Anamika Prasad
Shakti S. Gupta
R. K. Tyagi   *Editors*

Advances in Engineering Design

Select Proceedings of FLAME 2018

Springer

Lecture Notes in Mechanical Engineering

Anamika Prasad · Shakti S. Gupta ·
R. K. Tyagi

Editors

Advances in Engineering Design

Select Proceedings of FLAME 2018

Editors
Anamika Prasad
Department of Mechanical Engineering
South Dakota State University
Brookings, SD, USA

Shakti S. Gupta
Department of Mechanical Engineering
Indian Institute of Technology Kanpur
Kanpur, Uttar Pradesh, India

R. K. Tyagi
Department of Mechanical Engineering
Amity University
Noida, Uttar Pradesh, India

Preface

This book gets together the pool of cutting-edge research articles on different aspects of engineering design from the First International Conference on Future Learning Aspects for Mechanical Engineering (FLAME), which was organized by Amity University, Uttar Pradesh, Noida, India, from October 3 to 5, 2018.

The key task of this conference was to lay a platform that brings together academicians, scientists, and researchers across the globe to share their scientific ideas and vision in the areas of thermal, design, industrial, production, and interdisciplinary areas of mechanical engineering. FLAME 2018 played a key role to set up a bridge between academicians and industries.

The conference hosted almost 550 participants to interchange scientific ideas. During 3 days of the conference, researchers from academics and industries offered the most recent cutting-edge findings, went through several scientific brainstorm sessions, and exchanged ideas on practical socioeconomic topics. This conference also provided an opportunity to establish a network for joint collaboration between academicians and industries. Major emphasis was on the recent developments and innovations in various fields of mechanical engineering through plenary lectures.

The book covers mechanical design areas such as computational mechanics, finite element modeling, computer-aided designing, tribology, fracture mechanics, and vibration. The book brings together different aspects of engineering design and will be useful for researchers and professionals working in this field.

We would like to acknowledge all the participants who have contributed to this volume. We also deeply express our gratitude to the generous support provided by Amity University, Noida; Science and Engineering Research Board (SERB), an enterprise of Department of Science and Technology (DST), Government of India; Siemens; ISME; and Begell House. We also thank the publishers, and every staff of the department and institute who have directly or indirectly assisted to accomplish this goal. Finally, we would also like to express gratitude to the respected Founder President, Amity University, Dr. Ashok K. Chauhan, for providing all kinds of support and blessings.

In spite of sincere care, there might be typos and always a space for improvement. We would appreciate any suggestions from the reader for further improvements in this book.

Noida, India   Dr. R. K. Tyagi
Brookings, USA   Dr. Anamika Prasad
Kanpur, India   Shakti S. Gupta
January 2019

Contents

About the Editors

Dr. Anamika Prasad is an Assistant Professor in the Mechanical Engineering Department at South Dakota State University, Brookings, USA. She obtained her M.S. in Civil and Environmental Engineering, and Ph.D. in Material Science and Mechanics, both from Massachusetts Institute of Technology, Cambridge, USA. She was a postdoctoral scholar at Stanford University from 2009 to 2011, and also worked as an assistant professor at the Indian Institute of Technology, Delhi prior to her current position. She holds one patent to her credit.

Dr. Shakti S. Gupta is Associate Professor at the Indian Institute of Technology, Kanpur, India. He did his Master's from Indian Institute of Science, Bangalore and his Ph.D. from Virginia Tech, USA. His research interest includes linear and non-linear structural mechanics, mechanics of nanomaterials and their characterization, and engineering mechanics. He is a recipient of several awards such as DRDO's Silicon Medal for National Science Day oration, and the Daniel Fredrick Scholarship for excellent performance in the graduate program in the Department of Engineering Science and Mechanics, Virginia Tech.

Dr. R. K. Tyagi is Professor in the Department of Mechanical Engineering at Amity University, Noida, India. He holds a Ph.D. in the field of ion beam machining and spray technology. His areas of research include pollution control in internal combustion engines, ion beam machining, and design of agricultural equipment.

Static Analysis of Functionally Graded Plate Using Nonlinear Classical Plate Theory with von Karman Strains: A Complex Solution Analysis

Simran Jeet Singh and **Suraj Prakash Harsha**

Abstract The present study is based on the nonlinear bending analysis of Functionally Graded Material (FGM) plate with von Karman strain based nonlinear classical plate theory with in-plane displacement and moderate rotation subjected to thermal loading in the transverse direction. The equations of motion and boundary conditions are obtained using the Principle of Minimum Potential Energy (PMPE) method and material property is graded in thickness direction according to simple power-law distribution in terms of volume fractions of the constituents. The temperature is varying linearly through the thickness while temperature dependent material properties are nonlinear function of temperature. The effect of temperature-dependent material property is studied. It is observed that dependency of material property on the temperature cannot be neglected for analyzing the inhomogeneous FGM plate subjected to thermomechanical loading. The complex solution is obtained using analytical method, viz., Navier's Method which assures minimum error in the solution for simply supported plate. The results show that the response is transitional with respect to ceramic and metal and the complex solution predicts the real behavior of stresses and deflections in the FGM plate. The transverse deflection is in-between to that of metal and ceramic rich plates for FGM plates. The complex form of solution also gives information about the stress distribution in the thickness direction. The effect of temperature rise, side-to-thickness ratio and volume fraction exponent on nondimensional maximum central deflection and axial and transverse shear stresses of an FGM plate is studied.

Keywords Functionally graded materials (FGM) plate · von Karman strain · Nonlinear classical plate theory (NLCPT) · Navier's method

S. J. Singh (✉) · S. P. Harsha
Mechanical and Industrial Engineering Department, Indian Institute of Technology Roorkee, Roorkee 247667, Uttarakhand, India
e-mail: jeetsingh.simran@gmail.com

1   Introduction

Functionally Graded Materials are one of the smart materials introduced, nowadays, in which material properties of two materials are graded in one particular direction resulting in corresponding changes in the properties of the material. FGMs may be embodied as structural components and found to have great applications, where the operating conditions are harsh and subjected to extreme temperature such as heat exchanger tubes in power plant and heat shields of space crafts. Functionally Graded Materials was substantially advanced in the early 1980s in Japan [1].

The behavior of most of the FGM plate in literature is modeled using three-dimensional (3D) theory of linear elasticity or by two-dimensional (2D) plate theory of plane stress and plane strain. The 3D exact solution [2–5] provides benchmark results to access the validation and to predict the accuracy of various 2D plate theory. Zenkour [6] did a 3D bending analysis to derive the exact solutions for exponentially graded simply supported FGM plate subjected to a sinusoidal load using state-space method. The "*Classical Plate Theory*" (CPT) [7] being the simplest and most fundamental 2D plate model, does not take into account the transverse shear effect. Mohammadi et al. [8] presented an analytical method for the buckling analysis of Levy's FGM plate based on CPT. Bending analysis of FGM plate based on CPT [9, 10] has been done by several researchers. To avoid encountering shear correction factor, polynomial and non-polynomial based higher order theories were introduced. Levy et al. [11] obtained solutions for a wide range of values of the loading parameter and the Aspect ratio for the large deflections of rectangular plates using the asymptotic solution. Neves et al. addressed the analysis of functionally graded plates by collocation with radial basis functions, according to a sinusoidal shear deformation formulation [12], quasi-3D hyperbolic sine shear deformation theory [13], quasi-3D sinusoidal shear deformation formulation [14], quasi-3D higher order shear deformation theory and a meshless technique [15]. Tahar et al. [16] presented a theoretical formulation, of Navier solutions of rectangular plates based on a new higher order shear deformation model for the static response of functionally graded plates. Kamlesh et al. [17] attempted to extend inverse trigonometric shear deformation theory for the static and buckling analysis of FGM plate using an analytical solution.

Moreover, numerous studies have been done on the bending of functionally graded plates in the thermal environment. Reddy and Chin [18] studied the dynamic thermoelastic response of functionally graded cylinders and plates. In their formulation, Thermomechanical coupling was included and a finite element model of the formulation was developed. Shen [19] presented nonlinear bending analysis for a simply supported, functionally graded rectangular plate subjected to a transverse uniform or sinusoidal load and in thermal environments. Zenkour and Alghamdi [20] studied the bending response of sandwich plates subjected to thermomechanical loads. Material properties are assumed to be temperature independent.

It has been observed from the available literature that static and dynamic analysis of FGM plate based on different theories, viz., classical to shear deformation plate

theories have been studied and analyzed for stresses, deflection, and vibration using different numerical and analytical solutions but to the best knowledge of the author, none of the papers on the nonlinear bending analysis of plate subjected to thermomechanical analysis based on temperature dependent mechanical properties has been encountered. Thus, in the present study, the CPT together with von Karman's strain–displacement assumptions has been employed to derive the nonlinear governing partial differential equations with geometric nonlinearity and complex solution is analyzed.

2 Geometry

The thin plate is a planar structure having a transverse dimension much smaller as compared to the length and width dimensions. Let us consider a stiff plate whose transverse dimensions are small as compared to the other two dimensions and, therefore, the plate is considered to be two-dimensional lamina. Assume a mid-plane of the plate as a reference surface lie in the x-y plane and z-axis along the transverse direction, with z, coordinate positive upward, by forming a right-handed coordinate system. The reference surface is at the distance of $\pm h/2$ from both the top and bottom surfaces of the plate as shown in Fig. 1.

2.1 Sign Convention

The positive moment will make the upper fiber in compression and lower fiber in tension and the negative moment will make the upper fiber in tension and lower fiber in compression. Since curvature is proportional to moment, therefore, the positive moment will create positive curvature and the negative moment will create negative curvature. As concave upward is created by a positive moment, therefore, concave upward is considered to be positive and concave downward is considered to be negative.

Fig. 1 Coordinate system and reference surface
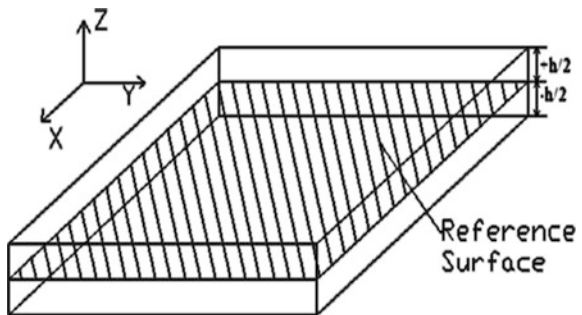
3 Governing Equations and Boundary Conditions

Kinematics of plate theory deals with the displacement of the mid-surface without considering the forces causing the displacements. The kinematic equation results in developing the relationship between strain and displacement. The plate under transverse loading, as shown in Fig. 2a, bends and slope of the mid-surfaces cause displacement in x- and y-direction as a linear function of transverse dimension (z). Let u, v, and, w are the real displacements of the body and $\bar{u}$, $\bar{v}$ and $\bar{w}$ are the displacements of the mid-surface, where, $\bar{u}$ and $\bar{v}$ are in-plane displacements and $\bar{w}$ is the out of plane displacement of the mid-surface as shown in Fig. 2b.

From kinematics of plate, displacement can be written as

$$u = \bar{u} - z\left(\frac{\partial \bar{w}}{\partial x}\right)$$
$$v = \bar{v} - z\left(\frac{\partial \bar{w}}{\partial y}\right) \tag{1}$$
$$w = \bar{w}$$

The nonlinear strain tensor is given by Lagrangian is given as

$$E_{ij} = \frac{1}{2}\left(\frac{\partial u_i}{\partial x_j} + \frac{\partial u_j}{\partial x_i} + \frac{\partial u_k}{\partial x_i}\frac{\partial u_k}{\partial x_j}\right) \tag{2}$$

On expanding and neglecting square of displacement gradient on the account of small deformation but assuming the rotation of transverse normal to be moderate $(10°–15°)$, therefore, the following terms are not neglected, $\left(\frac{\partial w}{\partial x}\right)^2$, $\left(\frac{\partial w}{\partial y}\right)^2$, $\left(\frac{\partial w}{\partial x}\right)\left(\frac{\partial w}{\partial y}\right)$.

This will induce geometric nonlinearity and thus strain becomes nonlinear and denoted by epsilon (ε) and substituting Eq. (1) in Eq. (2), we get
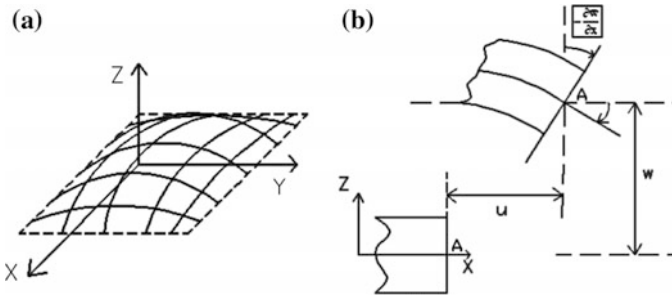
Fig. 2 a Plate under transverse loading in direction of Z **b** Kinematics of plate

$$\varepsilon_{xx} = \frac{\partial u}{\partial x} + \frac{1}{2}\left(\frac{\partial w}{\partial x}\right)^2 = \frac{\partial \bar{u}}{\partial x} - z\frac{\partial^2 \bar{w}}{\partial x^2} + \frac{1}{2}\left(\frac{\partial \bar{w}}{\partial x}\right)^2 \tag{3a}$$

$$\varepsilon_{yy} = \frac{\partial v}{\partial y} + \frac{1}{2}\left(\frac{\partial w}{\partial y}\right)^2 = \frac{\partial \bar{v}}{\partial y} - z\frac{\partial^2 \bar{w}}{\partial y^2} + \frac{1}{2}\left(\frac{\partial \bar{w}}{\partial y}\right)^2 \tag{3b}$$

$$\varepsilon_{xy} = \varepsilon_{yx} = \frac{1}{2}\left(\frac{\partial u}{\partial y} + \frac{\partial v}{\partial x} + \left(\frac{\partial w}{\partial x}\right)\left(\frac{\partial w}{\partial y}\right)\right)$$
$$= \frac{1}{2}\left(\frac{\partial \bar{v}}{\partial x} + \frac{\partial \bar{u}}{\partial y} - 2z\frac{\partial^2 \bar{w}}{\partial x \partial y} + \left(\frac{\partial \bar{w}}{\partial x}\right)\left(\frac{\partial \bar{w}}{\partial y}\right)\right) \tag{3c}$$

$\varepsilon_{zz} = \varepsilon_{xz} = \varepsilon_{yz} = 0$ ($\because$, there is no transverse linear and shear strain)
In matrices form, Eq. (3c) can be written as

$$[\varepsilon] = \begin{bmatrix} \varepsilon_{xx} \\ \varepsilon_{yy} \\ \varepsilon_{xy} \end{bmatrix} = \begin{bmatrix} \frac{\partial \bar{u}}{\partial x} + \frac{1}{2}\left(\frac{\partial \bar{w}}{\partial x}\right)^2 \\ \frac{\partial \bar{v}}{\partial y} + \frac{1}{2}\left(\frac{\partial \bar{w}}{\partial y}\right)^2 \\ \frac{1}{2}\left(\frac{\partial \bar{v}}{\partial x} + \frac{\partial \bar{u}}{\partial y} + \left(\frac{\partial \bar{w}}{\partial x}\right)\left(\frac{\partial \bar{w}}{\partial y}\right)\right) \end{bmatrix} + z\begin{bmatrix} -\frac{\partial^2 \bar{w}}{\partial x^2} \\ -\frac{\partial^2 \bar{w}}{\partial y^2} \\ -\frac{\partial^2 \bar{w}}{\partial x \partial y} \end{bmatrix} \tag{4}$$

Thus, $\varepsilon = \varepsilon^0 + z\varepsilon^1$
where

$$[\varepsilon^0] = \begin{bmatrix} \varepsilon_{xx}^0 \\ \varepsilon_{yy}^0 \\ \varepsilon_{xy}^0 \end{bmatrix} = \begin{bmatrix} \frac{\partial \bar{u}}{\partial x} + \frac{1}{2}\left(\frac{\partial \bar{w}}{\partial x}\right)^2 \\ \frac{\partial \bar{v}}{\partial y} + \frac{1}{2}\left(\frac{\partial \bar{w}}{\partial y}\right)^2 \\ \frac{1}{2}\left(\frac{\partial \bar{v}}{\partial x} + \frac{\partial \bar{u}}{\partial y} + \left(\frac{\partial \bar{w}}{\partial x}\right)\left(\frac{\partial \bar{w}}{\partial y}\right)\right) \end{bmatrix} \text{ and, } [\varepsilon^1] = \begin{bmatrix} \varepsilon_{xx}^1 \\ \varepsilon_{yy}^1 \\ \varepsilon_{xy}^1 \end{bmatrix} = \begin{bmatrix} -\frac{\partial^2 \bar{w}}{\partial x^2} \\ -\frac{\partial^2 \bar{w}}{\partial y^2} \\ -\frac{\partial^2 \bar{w}}{\partial x \partial y} \end{bmatrix}$$

The linear generalized Hooke's law for an orthotropic functionally graded material is given as

$$\sigma_i = \mathbf{C}_{ij}(\mathbf{z})\,\varepsilon_j; \quad i,j = 1 \text{ to } 6$$

where σ_i = stress vector; $\mathbf{C}_{ij}(\mathbf{z})$ = Stiffness matrix; and ε_j = Engineering Strain vector of the material. For Isotropic material, the Hooke's law reduces to

$$\begin{bmatrix} \sigma_{xx} \\ \sigma_{yy} \\ \tau_{xy} \end{bmatrix} = \begin{bmatrix} C_{11} & C_{12} & 0 \\ C_{12} & C_{22} & 0 \\ 0 & 0 & C_{66} \end{bmatrix} \begin{bmatrix} \varepsilon_{xx} - \alpha_{xx}T(x,y,z) \\ \varepsilon_{yy} - \alpha_{yy}T(x,y,z) \\ \gamma_{xy} \end{bmatrix} \tag{5}$$

where $C_{11} = C_{22} = \frac{E(z,T)}{1-v^2}$, $C_{12} = \frac{vE(z,T)}{1-v^2} = \frac{vE(z,T)}{1-v^2}$, $C_{66} = \frac{E(z,T)}{2(1+v)}$

$E(z, T)$ is the elastic modulus that is graded in the thickness direction and Poison's ratio v is constant, C_{ij}s are reduced stiffnesses and σ_{ij} is Piola–Kirchhoff stress tensor.

4   Equilibrium Equation

The equilibrium equation can be derived using the principle of virtual displacement given by the equation

$$\delta U + \delta V = 0 \tag{6}$$

where δU = virtual strain energy or variation of strain energy due to internal stresses

δU = virtual potential energy or variation of potential energy due to external forces

Now, virtual strain energy δU can be written as

$$\delta U = \iiint \sigma : \delta\varepsilon \, dv = \int_V \sigma_{ij}\delta\varepsilon_{ij} dz dx dy \tag{7}$$

where σ = Stress Tensor

ε = Green Lagrange Strain Tensor

$:$ = Operator called as double dot product

Therefore,

$$\delta U = \iiint \left[\sigma_{xx}\delta\varepsilon_{xx} + \sigma_{yy}\delta\varepsilon_{yy} + \sigma_{zz}\delta\varepsilon_{zz} + 2(\sigma_{xy}\delta\varepsilon_{xy} + \sigma_{yz}\delta\varepsilon_{yz} + \sigma_{zx}\delta\varepsilon_{zx})\right]dv$$

$$\tag{8}$$

In stiff plate problem, $\delta\varepsilon_{zz} = \delta\varepsilon_{yz} = \delta\varepsilon_{zx} = 0$
Thus, substituting above in Eq. (8), we get

$$\delta U = \iiint \left[\sigma_{xx}\delta\varepsilon_{xx} + \sigma_{yy}\delta\varepsilon_{yy} + 2\sigma_{xy}\delta\varepsilon_{xy}\right]dv$$

Taking variation of it, we get

$$\delta U = \left\{ \int\limits_A \left[\begin{array}{l} \int\limits_{-h/2}^{h/2} \sigma_{xx}\left(\frac{\partial \delta \bar{u}}{\partial X} + \left(\frac{\partial W}{\partial X}\right)\left(\frac{\partial \delta W}{\partial X}\right)\right) dz - \int\limits_{-h/2}^{h/2} \sigma_{xx} z \frac{\partial^2 \delta W}{\partial X^2} dz + \int\limits_{-h/2}^{-h/2} \sigma_{yy}\left(\frac{\partial \delta \bar{v}}{\partial y} + \left(\frac{\partial W}{\partial y}\right)\left(\frac{\partial \delta W}{\partial y}\right)\right) dz - \int\limits_{-h/2}^{-h/2} \sigma_{yy} z \frac{\partial^2 \delta W}{\partial y^2} dz \\ + \int\limits_{-h/2}^{h/2} \tau_{xy}\left(\frac{\partial \delta \bar{v}}{\partial X} + \frac{\partial \delta \bar{u}}{\partial y} + \frac{\partial \delta W}{\partial X}\frac{\partial W}{\partial y} + \frac{\partial \delta W}{\partial y}\frac{\partial W}{\partial X}\right) dz - \int\limits_{-h/2}^{h/2} 2\tau_{xy} z \frac{\partial^2 \delta W}{\partial X \partial y} dz \end{array} \right] dxdy \right\}$$

$$\delta U = \int\limits_A \left[\left(N_{xx}\delta\varepsilon_{xx}^0 + N_{yy}\delta\varepsilon_{yy}^0 + N_{xy}\delta\varepsilon_{xy}^0 \right) - \left(M_{xx}\delta\varepsilon_{xx}^1 + M_{yy}\delta\varepsilon_{yy}^1 + 2M_{xy}\delta\varepsilon_{xy}^1 \right) \right] dA$$

(9)

The virtual work done by the external force is given as

$$\delta V = -\iint q_z \delta \bar{w} dxdy \tag{10}$$

where, q_z = distributed transverse load applied on the top of the surface

$$\delta \bar{w} = \text{Applied virtual displacement}$$

Now, substituting Eqs. (9) and (10) into Eq. (6) and we get

$$\delta W = \int\limits_A \left[\left(N_{xx}\delta\varepsilon_{xx}^0 + N_{yy}\delta\varepsilon_{yy}^0 + N_{xy}\delta\varepsilon_{xy}^0 \right) - \left(M_{xx}\delta\varepsilon_{xx}^1 + M_{yy}\delta\varepsilon_{yy}^1 + 2M_{xy}\delta\varepsilon_{xy}^1 \right) - q_z\delta w \right] dA$$

(11)

Now solving above equation term by term and on rearranging, we get

$$\delta W = \int\limits_A \left\{ \left(-\frac{\partial N_{xx}}{\partial x} - \frac{\partial N_{xy}}{\partial y} \right)\delta\bar{u} + \left(-\frac{\partial N_{yy}}{\partial y} - \frac{\partial N_{xy}}{\partial x} \right)\delta\bar{v} + \left(\begin{array}{l} -\frac{\partial}{\partial x}\left(N_{xx}\frac{\partial \bar{W}}{\partial x} + N_{xy}\frac{\partial \bar{W}}{\partial y} \right) - \frac{\partial}{\partial y}\left(N_{yy}\frac{\partial \bar{W}}{\partial y} + N_{xy}\frac{\partial \bar{W}}{\partial x} \right) \\ -\left(\frac{\partial^2 M_{xx}}{\partial x^2} + \frac{\partial^2 M_{yy}}{\partial y^2} + 2\frac{\partial^2 M_{xy}}{\partial x \partial y} - q_z \right) \end{array} \right)\delta\bar{w} \right\} dA$$
$$+ \oint\limits_\Gamma \left\{ \begin{array}{l} \left(N_{xx}n_x + N_{xy}n_y \right)\delta\bar{u} + \left(N_{yy}n_y + N_{xy}n_x \right)\delta\bar{u} + \left[\begin{array}{l} \left(N_{xx}n_x + N_{xy}n_y \right)\frac{\partial \bar{W}}{\partial x} + \left(N_{yy}n_y + N_{xy}n_x \right)\frac{\partial \bar{W}}{\partial y} \\ + \left(\frac{\partial M_{xx}}{\partial x} + \frac{\partial M_{yx}}{\partial y} \right)n_x + \left(\frac{\partial M_{yy}}{\partial y} + \frac{\partial M_{xy}}{\partial x} \right)n_y \end{array} \right]\delta\bar{w} \\ \left(M_{xx}n_x + M_{yx}n_y \right)\frac{\partial \delta \bar{W}}{\partial x} - \left(M_{yy}n_y + M_{xy}n_x \right)\frac{\partial \delta \bar{W}}{\partial y} \end{array} \right\} ds$$

(12)

The Euler–Lagrange equation can be obtained by a fundamental lemma of variational calculus as

$$\delta\bar{u} : \quad \frac{\partial N_{xx}}{\partial x} + \frac{\partial N_{xy}}{\partial y} = 0 \tag{13a}$$

$$\delta\bar{v} : \quad \frac{\partial N_{yy}}{\partial y} + \frac{\partial N_{xy}}{\partial x} = 0 \tag{13b}$$

$$\delta\bar{w} : \left(\frac{\partial^2 M_{xx}}{\partial x^2} + \frac{\partial^2 M_{yy}}{\partial y^2} + 2\frac{\partial^2 M_{xy}}{\partial x\partial y} + q_z\right) + \frac{\partial}{\partial x}\left(N_{xx}\frac{\partial\bar{w}}{\partial x} + N_{xy}\frac{\partial\bar{w}}{\partial y}\right)$$
$$+ \frac{\partial}{\partial y}\left(N_{yy}\frac{\partial\bar{w}}{\partial y} + N_{xy}\frac{\partial\bar{w}}{\partial x}\right) = 0$$

$$(13c)$$

The boundary conditions are given by equating the term equal to zero of domain Γ, we get

$$
\begin{array}{lll}
\delta\bar{u} = 0 & \text{or} & N_{xx}n_x + N_{xy}n_y = 0 \\
\delta\bar{v} = 0 & \text{or} & N_{yy}n_y + N_{xy}n_x = 0 \\
\delta\bar{w} = 0 & \text{or} & \left[\begin{array}{l}\left(N_{xx}n_x + N_{xy}n_y\right)\frac{\partial\bar{w}}{\partial x} + \left(N_{yy}n_y + N_{xy}n_x\right)\frac{\partial\bar{w}}{\partial y} \\ + \left(\frac{\partial M_{xx}}{\partial x} + \frac{\partial M_{yx}}{\partial y}\right)n_x + \left(\frac{\partial M_{yy}}{\partial y} + \frac{\partial M_{xy}}{\partial x}\right)n_y\end{array}\right] = 0 \\
\delta\left(\frac{\partial\bar{w}}{\partial x}\right) = 0 & \text{or} & -\left(M_{xx}n_x + M_{yx}n_y\right) = 0 \\
\delta\left(\frac{\partial\bar{w}}{\partial y}\right) = 0 & \text{or} & -\left(M_{yy}n_y + M_{xy}n_x\right) = 0
\end{array}
$$

4.1 Relationship Between Stress Resultants and Middle Surface Displacements

Plate theory reduces the 3D continuum problem to 2D Lamina problem by applying certain assumptions on the plate is treated as a plane and therefore all the quantities depends on upon x and y alone. This is done by integrating the quantities in z-direction, i.e., through the plate thickness and thus the three-dimensional problem reduces to two-dimensional. Thus, therefore, the three stress components on the cross section are replaced by a set of resultant forces and moments and are known as stress resultants. Mathematically, stress resultant is defined as the integrals of stress over the thickness of the plate yielding following set of stress resultants:

$$\begin{Bmatrix} N_{xx} \\ N_{yy} \\ N_{xy} \end{Bmatrix} = \int_{-h/2}^{h/2} \begin{Bmatrix} \sigma_{xx} \\ \sigma_{yy} \\ \tau_{xy} \end{Bmatrix} dz \text{ and } \begin{Bmatrix} M_{xx} \\ M_{yy} \\ M_{xy} \end{Bmatrix} = \int_{-h/2}^{h/2} z \begin{Bmatrix} \sigma_{xx} \\ \sigma_{yy} \\ \tau_{xy} \end{Bmatrix} dz$$

Now, stress resultants and moment resultants gave in term of stiffness are

$$
\begin{Bmatrix} N_{xx} \\ N_{yy} \\ N_{xy} \end{Bmatrix} = \begin{bmatrix} A_{11} & A_{12} & 0 \\ A_{12} & A_{22} & 0 \\ 0 & 0 & A_{66} \end{bmatrix} \begin{Bmatrix} \varepsilon_{xx}^0 \\ \varepsilon_{yy}^0 \\ \gamma_{xy}^0 \end{Bmatrix}
$$
$$
+ \begin{bmatrix} B_{11} & B_{12} & 0 \\ B_{12} & B_{22} & 0 \\ 0 & 0 & B_{66} \end{bmatrix} \begin{Bmatrix} \varepsilon_{xx}^1 \\ \varepsilon_{yy}^1 \\ \gamma_{xy}^1 \end{Bmatrix} - \begin{Bmatrix} N_{xx}^T \\ N_{yy}^T \\ 0 \end{Bmatrix}
\tag{14}
$$

$$
\begin{Bmatrix} M_{xx} \\ M_{yy} \\ M_{xy} \end{Bmatrix} = \begin{bmatrix} B_{11} & B_{12} & 0 \\ B_{12} & B_{22} & 0 \\ 0 & 0 & B_{66} \end{bmatrix} \begin{Bmatrix} \varepsilon_{xx}^0 \\ \varepsilon_{yy}^0 \\ \gamma_{xy}^0 \end{Bmatrix}
$$
$$
+ \begin{bmatrix} D_{11} & D_{12} & 0 \\ D_{12} & D_{22} & 0 \\ 0 & 0 & D_{66} \end{bmatrix} \begin{Bmatrix} \varepsilon_{xx}^1 \\ \varepsilon_{yy}^1 \\ \gamma_{xy}^1 \end{Bmatrix} - \begin{Bmatrix} M_{xx}^T \\ M_{yy}^T \\ 0 \end{Bmatrix}
\tag{15}
$$

and in a compact form,

$$
\begin{Bmatrix} N \\ M \end{Bmatrix} = \begin{bmatrix} A & B \\ B & D \end{bmatrix} \begin{Bmatrix} \varepsilon^0 \\ \varepsilon^1 \end{Bmatrix} - \begin{Bmatrix} N^T \\ M^T \end{Bmatrix}
$$

where coefficients A_{ij}'s, B_{ij}'s, and D_{ij}'s are defined as extensional, extensional-bending, and bending stiffnesses, respectively. Mathematically,

$$
\{A_{ij}, B_{ij}, D_{ij}\} = \int_{-h/2}^{h/2} C_{ij}(z, T)\{1, z, z^2\} dz
$$

For Isotropic material,
$$
N_{xx}^T = N_{yy}^T = N^T = \int_{-h/2}^{h/2} \frac{E(z,T)}{1-v} \alpha(z, T) T(x, y, z) dz
$$

and,
$$
M_{xx}^T = M_{yy}^T = M^T = \int_{-h/2}^{h/2} \frac{zE(z,T)}{1-v} \alpha(z, T) T(x, y, z) dz
$$

The expressions for the curvatures and slopes defined in Eq. (4) are now substituted in Eqs. (14) and (15) and finally substituted in Eqs. (13a), (13b), and (13c) to obtain the equilibrium equations in terms of displacements.

Equilibrium equation in terms of displacement can be written as

$$A_{11}\left[\frac{\partial^2\bar{u}}{\partial x^2} + \left(\frac{\partial\bar{w}}{\partial x}\right)\left(\frac{\partial^2\bar{w}}{\partial x^2}\right)\right] + A_{12}\left[\frac{\partial^2\bar{v}}{\partial x\partial y} + \left(\frac{\partial\bar{w}}{\partial y}\right)\left(\frac{\partial^2\bar{w}}{\partial x\partial y}\right)\right]$$

$$+ A_{66}\left(\frac{\partial^2\bar{v}}{\partial x\partial y} + \frac{\partial^2\bar{u}}{\partial y^2} + \left(\frac{\partial^2\bar{w}}{\partial y^2}\right)\left(\frac{\partial\bar{w}}{\partial x}\right) + \left(\frac{\partial^2\bar{w}}{\partial x\partial y}\right)\left(\frac{\partial\bar{w}}{\partial y}\right)\right)$$

$$- B_{11}\left(\frac{\partial^3\bar{w}}{\partial x^3}\right) - (B_{12} + 2B_{66})\left(\frac{\partial^3\bar{w}}{\partial x\partial y^2}\right) = \frac{\partial N_{xx}^T}{\partial x}$$

$$(16)$$

$$A_{12}\left[\frac{\partial^2\bar{u}}{\partial x\partial y} + \left(\frac{\partial\bar{w}}{\partial x}\right)\left(\frac{\partial^2\bar{w}}{\partial x\partial y}\right)\right] + A_{22}\left[\frac{\partial^2\bar{v}}{\partial y^2} + \left(\frac{\partial\bar{w}}{\partial y}\right)\left(\frac{\partial^2\bar{w}}{\partial y^2}\right)\right]$$

$$+ A_{66}\left[\frac{\partial^2\bar{v}}{\partial x^2} + \frac{\partial^2\bar{u}}{\partial x\partial y} + \left(\frac{\partial^2\bar{w}}{\partial x^2}\right)\left(\frac{\partial\bar{w}}{\partial y}\right) + \left(\frac{\partial^2\bar{w}}{\partial x\partial y}\right)\left(\frac{\partial\bar{w}}{\partial x}\right)\right]$$

$$- B_{22}\left(\frac{\partial^3\bar{w}}{\partial y^3}\right) - (B_{12} + 2B_{66})\left(\frac{\partial^3\bar{w}}{\partial x^2\partial y}\right) = \frac{\partial N_{yy}^T}{\partial y}$$

$$(17)$$

$$B_{11}\left[\frac{\partial^3\bar{u}}{\partial x^3} + \left(\frac{\partial^2\bar{w}}{\partial x^2}\right)^2 + \left(\frac{\partial\bar{w}}{\partial x}\right)\left(\frac{\partial^3\bar{w}}{\partial x^3}\right)\right] + B_{22}\left[\frac{\partial^3\bar{v}}{\partial y^3} + \left(\frac{\partial^2\bar{w}}{\partial y^2}\right)^2 + \left(\frac{\partial\bar{w}}{\partial y}\right)\left(\frac{\partial^3\bar{w}}{\partial y^3}\right)\right]$$

$$+ B_{12}\left(\frac{\partial^2\bar{w}}{\partial x\partial y}\right)^2 + 2B_{66}\left(\frac{\partial^2\bar{w}}{\partial y^2}\right)\left(\frac{\partial^2\bar{w}}{\partial x^2}\right) - D_{11}\frac{\partial^4\bar{w}}{\partial x^4} - 2(D_{12} + 2D_{66})\left(\frac{\partial^4\bar{w}}{\partial x^2\partial y^2}\right) - D_{22}\frac{\partial^4\bar{w}}{\partial y^4}$$

$$+ (B_{12} + 2B_{66})\left[\frac{\partial^3\bar{u}}{\partial x\partial y^2} + \left(\frac{\partial^2\bar{w}}{\partial x\partial y}\right)^2 + \left(\frac{\partial\bar{w}}{\partial x}\right)\left(\frac{\partial^3\bar{w}}{\partial x\partial y^2}\right) + \frac{\partial^3\bar{v}}{\partial x^2\partial y} + \left(\frac{\partial\bar{w}}{\partial y}\right)\left(\frac{\partial^3\bar{w}}{\partial x^2\partial y}\right)\right]$$

$$+ \frac{\partial}{\partial x}\left(N_{xx}\frac{\partial\bar{w}}{\partial x} + N_{xy}\frac{\partial\bar{w}}{\partial y}\right) + \frac{\partial}{\partial y}\left(N_{yy}\frac{\partial\bar{w}}{\partial y} + N_{xy}\frac{\partial\bar{w}}{\partial x}\right) = -q_z + \frac{\partial M_{xx}^T}{\partial x^2} + \frac{\partial M_{yy}^T}{\partial y^2}$$

$$(18)$$

5 Analytical Solution

The Navier's-type solution is used to obtain the deflections and stresses for the functionally graded plate. The displacement fields that satisfy the boundary conditions and the governing equilibrium equations can be written as follows:

$$\bar{u} = \sum_{m=1}^{\infty}\sum_{n=1}^{\infty} U_{mn}\sin\left(\frac{m\pi x}{a}\right)\sin\left(\frac{n\pi y}{b}\right) \tag{19a}$$

$$\bar{v} = \sum_{m=1}^{\infty}\sum_{n=1}^{\infty} V_{mn}\sin\left(\frac{m\pi x}{a}\right)\sin\left(\frac{n\pi y}{b}\right) \tag{19b}$$

$$\overline{w} = \sum_{m=1}^{\infty} \sum_{n=1}^{\infty} W_{mn} \sin\left(\frac{m\pi x}{a}\right) \sin\left(\frac{n\pi y}{b}\right) \tag{19c}$$

The transverse load $q_z(x, y)$ using the double Fourier series is written as

$$q_z(x, y) = \sum_{m=1}^{\infty} \sum_{n=1}^{\infty} Q_{mn} \sin\left(\frac{m\pi x}{a}\right) \sin\left(\frac{n\pi y}{b}\right) \tag{20a}$$

$$T(x, y, z) = T_B(x, y) + \frac{z}{h} T_T(x, y) \tag{20b}$$

where

$$Q_{mn} = \frac{4}{ab} \int_0^a \int_0^b q_z(x, y) \sin\left(\frac{m\pi x}{a}\right) \sin\left(\frac{n\pi y}{b}\right) dx\, dy$$

$$\left\{ \begin{array}{c} T_B \\ T_T \end{array} \right\} = \left\{ \begin{array}{c} T'_B \\ T'_T \end{array} \right\} \sin\left(\frac{m\pi x}{a}\right) \sin\left(\frac{n\pi y}{b}\right)$$

Assuming the solution for uniform loading of q_0, that is, $q_z(x, y) = q_0$
Therefore,

$$Q_{mn} = \frac{16 q_0}{mn\pi^2}$$

Thus, transverse load $q_z(x, y)$ and $T(x, y, z)$ is defined as

$$q_z(x, y) = \frac{16 q_0}{\pi^2} \sum_{m=1}^{\infty} \sum_{n=1}^{\infty} \frac{1}{mn} \sin\left(\frac{m\pi x}{a}\right) \sin\left(\frac{n\pi y}{b}\right)$$

$$T(x, y, z) = \left(T'_B + \frac{z}{h} T'_T \right) \sin\left(\frac{m\pi x}{a}\right) \sin\left(\frac{n\pi y}{b}\right)$$

6 Numerical Results and Discussions

Functionally graded isotropic plate with different span-to-thickness ratio (a/h) is investigated to analyze the simply supported square plates ($a = b$) subjected to uniform transverse load (q_z) on the top surface ($z = h/2$), $q_0 = -1 \times 10^5\, \text{N/m}^2$. Six different span-to-thickness ratios are considered as 4, 10, 50, 70, 80, and 100 for analyzing the maximum central deflections.

The plate properties are graded from *Aluminum* (bottom) to *Alumina* (top) using rules of the mixture. Keeping temperature and Poisson ratio constant, Young's modulus is graded in the thickness direction using the following functional relationship:

$$E(z) = E_m + (E_c - E_m)\left(\frac{1}{2} + \frac{z}{h}\right)^f \qquad (21)$$

where $E_m = 70$ GPa and $E_c = 380$ GPa are Young's modulus for the metal (Aluminum) and ceramic (Alumina), respectively; f is the volume fraction exponent; h is the thickness of the plate. Poisson ratio (υ) considered for both metal and ceramic is 0.3.

6.1 Analysis of FGM Plate Without Thermal Loading

In deflection analysis, six different volume fraction exponent are considered 0.5, 2, 4, 6, 8, 10 along with two metal and, ceramic. On applying the Navier's solution, the solution so obtained is complex and plotted on a *complex plane* as shown in Fig. 3 and the *absolute solution* is shown in Fig. 4. It is observed that the solution of deflections in the case of pure metal and ceramic is approximately real with
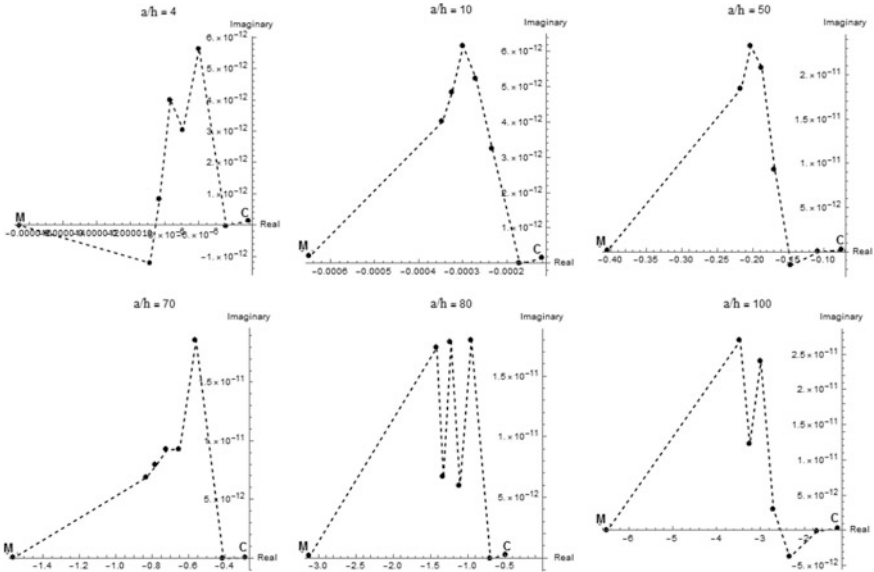
Fig. 3 Complex solution of deflection/thickness of the functionally graded plate for various volume fraction exponent (C,0.5,2,4,6,8,10,M) and a/h (4,10,50,70,80,100) (C and M stands for ceramic and metal, respectively)
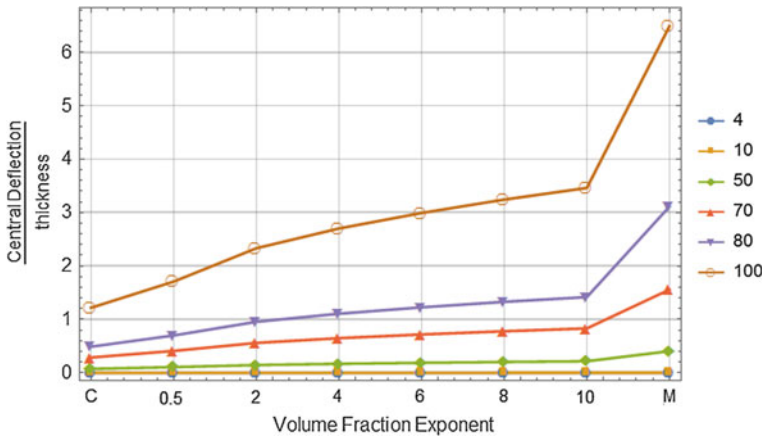
Fig. 4 Absolute solution of deflection/thickness of the functionally graded plate for various volume fraction exponent and the span-to-thickness ratio (C and M stands for ceramic and metal, respectively)

imaginary part approaches to zero, but for the functionally graded part solution is *complex*. Also, as thickness goes on decreasing, in the case of a thin plate (a/h = 80–100), the behavior reverses and deflection of the plate is due to the presence of metal and little effect of functionally graded material according to Nonlinear Classical Plate Theory.

The analysis has been done for the functionally graded and pure metal and, a ceramic plate for the absolute solution of deflection based on Fig. 4. It is observed that there is a sudden increase in the deflection of the plate for constant volume fraction exponent (excluding metal) and in the case of metal, there is a gradual increase in deflection for thick, moderately thick, and a flexible plate but the sudden increase in deflection takes place for thin plates.

6.2   Analysis of FGM Plate with Thermal Loading

Young's Modulus (according to ASME B31.1-1995) and coefficient of thermal expansion [21] for aluminum at various temperatures is interpolated, whereas for aluminum oxide it is taken from [22] and are given in Table 1.

Figure 5 depicts the effect of side-to-thickness ratios on the nondimensional deflection ($\hat{w}$) for the various material index (f). As expected, these results show that the nondimensional center deflection increases with a decrease in the side-to-thickness ratio for the flexible plate (a/h = 50–80) and membranes (a/h = 80–100) and it increases for thick (a/h < 10) and stiff plate (a/h = 10–50) due to thermal effect. The nondimensional deflection below the zero line indicates the thermal expansion of the plate in the thickness direction, because the

Table 1 Temperature dependent and independent material properties for ceramic and metal

Materials	Material property	Temperature independent (TID)[*]	Temperature dependent (TD)	
Aluminum	E (Pa)	70×10^9	$\left(\begin{array}{l} 72833.59262 + 92.02816T \\ -\ 0.86681T^2 + 0.00245T^3 \\ -\ 1.92332 \times 10^{-6}T^4 \\ -\ 3.04124 \times 10^{-9}T^5 \\ +\ 4.14613 \times 10^{-12}T^6 \end{array} \right)$	$\times 10^6$
	α (/K)	24×10^{-6}	$\left(\begin{array}{l} -\ 0.04382 + 0.0305T \\ +\ 7.78407 \times 10^{-4}T^2 \\ -\ 3.58141 \times 10^{-6}T^3 \\ +\ 6.49285 \times 10^{-9}T^4 \\ -\ 5.35578 \times 10^{-12}T^5 \\ +\ 1.67813 \times 10^{-15}T^6 \end{array} \right)$	$\times 10^{-6}$
Alumina	E (Pa)	380×10^9	$349.55 \left(\begin{array}{l} 1 - 3.853 \times 10^{-4}T \\ +\ 4.027 \times 10^{-7}T^2 \\ -\ 1.673 \times 10^{-10}T^3 \end{array} \right) \times 10^9$	
	α (/K)	8.1×10^{-6}	$6.8269 \left(1 + 1.838 \times 10^{-4}T \right) \times 10^{-6}$	

[*]Values for temperature-independent mechanical properties are taken at room temperature
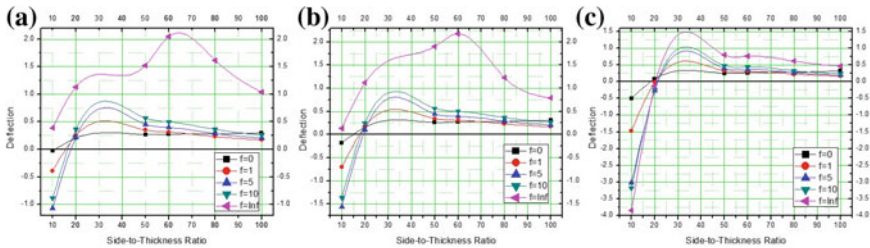
Fig. 5 Nondimensional deflection $(\hat{w})$ as a function of the side-to-thickness ratio (a/h) for various values of volume fraction exponent (f) of an FG square plate subjected to sinusoidal load at **a** $\Delta T = 200$ **b** $\Delta T = 300$ **c** $\Delta T = 500$

mechanical load is applied in negative direction and plate deflects in opposite direction. Thus, as expected, with the rise in temperature, the plate is more likely to lie below zero line, as shown in Fig. 5, where a plate with a/h = 20 is shifting toward zero line with the rise in temperature. Also, thermal loads cause more deflection for large values of volume fraction exponent (f). This shows clearly the effect of inhomogeneity inhibited in functionally graded materials. Also, with an increase in aspect ratio (a/h > 80, membranes) the results are almost the same for the different material index.
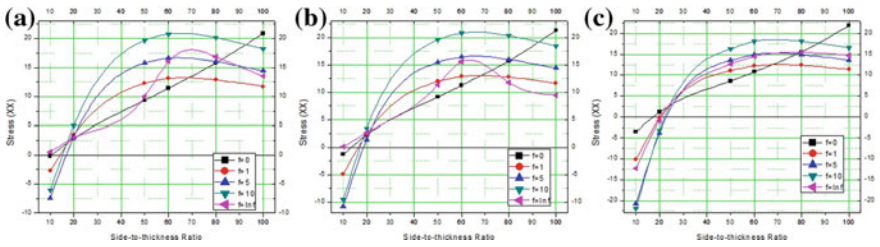
Fig. 6 Nondimensional in-plane longitudinal stress ($\hat{\sigma}_x$) as a function of the side-to-thickness ratio (a/h) for various values of volume fraction exponent (f) of an FG square plate subjected to a sinusoidal load at **a** $\Delta T = 200$ **b** $\Delta T = 300$ **c** $\Delta T = 500$

Figure 6 depicts the effect of side-to-thickness ratios on the nondimensional in-plane longitudinal stress ($\hat{\sigma}_x$) computed at the center and the top surface of the plate for the various material index (f). As expected, with the rise in temperature, nondimensional stress for the material index (f = 1, 5) reduces. Stress below the zero line indicates the nondimensional tensile stress. Thus, thick and stiff plates are subjected to tensile stresses due to thermal effect and as temperature increases the plates with a side-to-thickness ratio greater than 50, tensile stress will also induce in it.

Figure 7 depicts the effect of side-to-thickness ratios on the nondimensional in-plane transverse stress ($\hat{\tau}_{xy}$) computed at the corner and at ($z = -h/3$) for various material index (f). The figure shows that the results are almost same for the entire a/h ratios for the material index (f = 1, 10) up to $\Delta T = 300$, and for $\Delta T > 300$, the difference in results increases.

Nondimensional stresses and deflection for metal are suppressed with the rise in temperature for various aspect ratios. Also, as expected, due to thermal loads, the results for stresses and deflections are not intermediate [23] unlike, for only mechanical loading, in which the response is intermediate.

Figures 8 and 9 depict the through-the-thickness variation of nondimensional in-plane stresses. For smaller values of volume fraction exponent (f), there is a sharp gradient in both the stresses near the bottom surface of the plate and as material
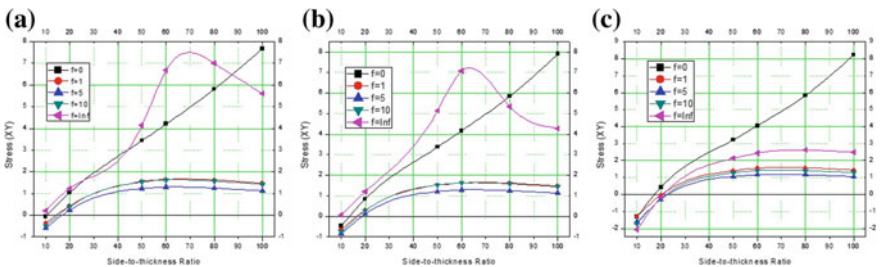
Fig. 7 Non-dimensional In-Plane transverse stress ($\hat{\tau}_{xy}$) as a function of the side-to-thickness ratio (a/h) for various values of volume fraction exponent (f) of an FG square plate subjected to a sinusoidal load at **a** $\Delta T = 200$ **b** $\Delta T = 300$ **c** $\Delta T = 500$
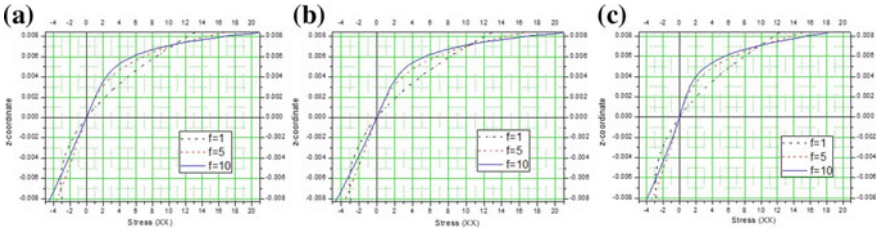
Fig. 8 Variation of nondimensional in-plane longitudinal stress ($\hat{\sigma}_x$) through-the-thickness of an FG square plate with a/h = 60 for different values of volume fraction exponent (f) at **a** $\Delta T = 200$ **b** $\Delta T = 300$ **c** $\Delta T = 500$
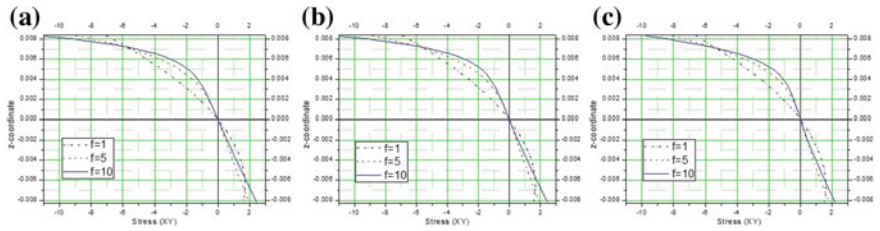
Fig. 9 Variation of nondimensional in-plane transverse stress ($\hat{\tau}_{xy}$) through-the-thickness of an FG square plate with a/h = 60 for different values of volume fraction exponent (f) at **a** $\Delta T = 200$ **b** $\Delta T = 300$ **c** $\Delta T = 500$

index increases, there is a steep gradient in stresses near the top surface. This is because of the sharp variation in the material properties near the top and bottom surfaces of the plate. With the increase in the exponent (f) the stresses increases at the top (maximum tensile (Fig. 8), maximum compressive (Fig. 9)) and a bottom surface (maximum compressive (Fig. 8), maximum tensile (Fig. 9)) of the plate and intermediate below the center of the plate. Also, with the rise in temperature figures shows almost the same results up to $\Delta T = 300$, and then the stress value reduces at $\Delta T > 300$ for a/h = 60.

Figure 10 depicts the through-the-thickness variation of nondimensional transverse shear stresses computed at $x = 0$, $y = b/2$. It can be seen that from the figure that the maximum value did not occur at the plate center as in the homogeneous case. This is due to the fact that, as the strain gradient increases, the inhomogeneity in the material property plays a vital role in stress distributions. The maximum value of stresses occurs at $z \cong 0.21\ h$ for $\Delta T = 200$, $z \cong 0.24\ h$ for $\Delta T = 300$, $z \cong 0.27\ h$ for $\Delta T = 500$. Thus, with the rise in temperature, the neutral plane on the edges of the plate shifted away from the center of the plate due to the combined effect of thermal loads and inhomogeneity.
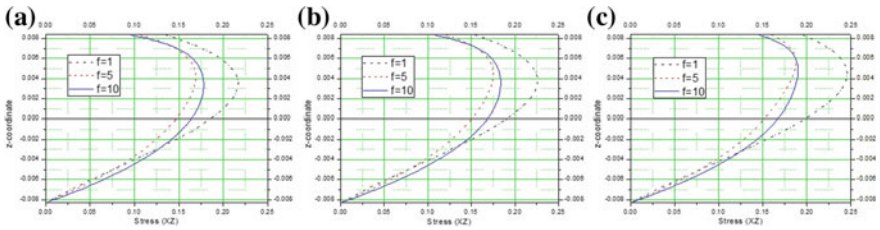
Fig. 10 Variation of nondimensional transverse shear stress $(\hat{\tau}_{xz})$ through-the-thickness of an FG square plate with a/h = 60 for different values of volume fraction exponent (f) at **a** $\Delta T = 200$ **b** $\Delta T = 300$ **c** $\Delta T = 500$
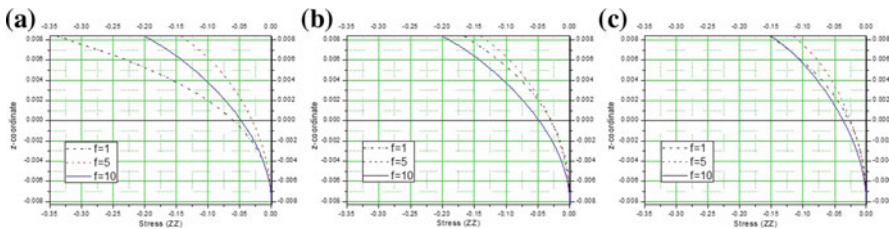
Fig. 11 Variation of nondimensional transverse normal stress $(\hat{\sigma}_z)$ through-the-thickness of an FG square plate with a/h = 60 for different values of volume fraction exponent (f) at **a** $\Delta T = 200$ **b** $\Delta T = 300$ **c** $\Delta T = 500$

Figure 11 depicts through-the-thickness variation of nondimensional transverse normal stresses computed at the center of the plate. The stresses are compressive throughout the plate with zero at the bottom surface and maximum compressive at the top surface of the plate. The stresses reduce with the increase in the exponent (f) up to 5 and then increases. Also, as expected, with the rise in temperature, the stress value reduces in the thickness direction.

Figure 12 shows the effect of the side-to-thickness ratio on the dimensionless center deflection $\hat{w}$ for three different volume fraction exponents (f = 1, 5, 10). The effect of thermal, mechanical, and thermomechanical load is taken into considerations. It is found that deflection is larger for the plates subjected to thermal load only whereas it is smaller for plates subjected to mechanical load only but with thermomechanical load, the deflection decreases with increase in the side-to-thickness ratio. Also, for mechanical and thermomechanical load, deflection increases with an increase in exponent whereas, for thermal load only, deflection increases up to exponent 5 and then decreases as depicted in most of the literature.

Fig. 12 Effect of mechanical, thermal, and thermomechanical load on the nondimensional center deflection of FG square plate for the different side-to-thickness ratio
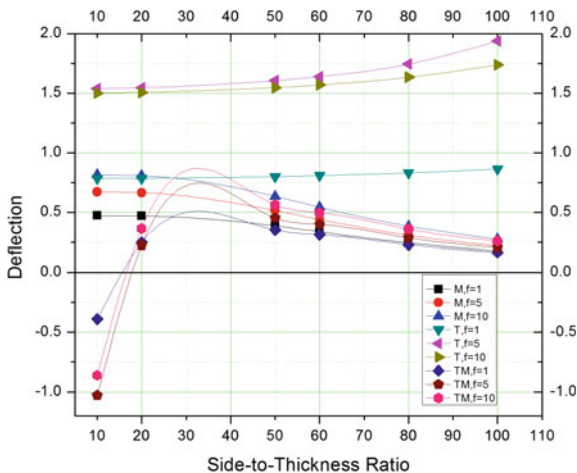
7 Conclusions

In this study, an analytical solution to functionally graded plate subjected to thermomechanical loading based on nonlinear classical plate theory is obtained. The solution obtained using Navier's method is complex, and hence complex analysis is done in the present study which only occurs because of nonlinearity in the strains. Nonlinear bending and stress under transverse uniform distributed load with diaphragm edge conditions are analyzed. It is found that the material property variation across the thickness according to simple power law is more effective for moderately thick (a/h = 5–10) and thick plates (a/h < 5), which are inferred by complex form of the solution. From the above study, the following conclusions are drawn:

- It was found that the dependency of material property cannot be neglected for the inhomogeneous functionally graded material at large values of temperature difference.
- For a certain side-to-thickness ratio, the dependency of material property on temperature becomes ineffective.
- The results show that the nondimensional center deflection increases with a decrease in the side-to-thickness ratio for the flexible plate (a/h = 50–80) and membranes (a/h = 80–100) and it increases for Thick (a/h < 10) and Stiff Plate (a/h = 10–50) due to thermal loading. Due to thermal loads, the results for stresses and deflections are not intermediate, unlike, for only mechanical loading, the response is intermediate.
- A sharp variation in the material properties near the top and bottom surfaces of the plate results in a sharp gradient near the bottom surface and steep gradient near the top surface with an increase in volume fraction exponent.

- With the rise in temperature, the neutral plane on the edges of the plate shifted away from the center of the plate due to the combined effect of thermal loads and inhomogeneity.
- The effect of thermal, mechanical and thermomechanical load is taken into considerations and it is found that deflection is larger for the plates subjected to thermal load only whereas it is smaller for plates subjected to mechanical load only but with thermomechanical load, the deflection decreases with increase in the side-to-thickness ratio.

References

1. Koizumi M, Niino M (1995) Overview of FGM research in Japan. MRS Bull 20(1):19–21
2. Levinson M (1985) The simply supported rectangular plate: an exact, three dimensional, linear elasticity solution. J Elast 15(3):283–291
3. Zhang H, Jiang JQ, Zhang ZC (2014) Three-dimensional elasticity solutions for bending of generally supported thick functionally graded plates. Appl Math Mech 35(11):1467–1478
4. Woodward B, Kashtalyan M (2011) Three-dimensional elasticity solution for bending of transversely isotropic functionally graded plates. Eur J Mech A Solids 30(5):705–718
5. Kashtalyan M (2004) Three-dimensional elasticity solution for bending of functionally graded rectangular plates. Eur J Mech A Solids 23(5):853–864
6. Zenkour AM (2007) Benchmark trigonometric and 3-D elasticity solutions for an exponentially graded thick rectangular plate. Arch Appl Mech 77(4):197–214
7. Love AE (1888) The small free vibrations and deformation of a thin elastic shell. Philos Trans R Soc Lond A 179: 491–546
8. Mohammadi M, Saidi AR, Jomehzadeh E (2010) Levy solution for buckling analysis of functionally graded rectangular plates. Appl Compos Mater 17(2):81–93
9. Chi SH, Chung YL (2006) Mechanical behavior of functionally graded material plates under transverse load—Part I: analysis. Int J Solids Struct 43(13):3657–3674
10. Chi SH, Chung YL (2006) Mechanical behavior of functionally graded material plates under transverse load—Part II: numerical results. Int J Solids Struct 43(13):3675–3691
11. Levy S (1942) Bending of rectangular plates with large deflections. National Bureau of Standards Gaithersburg, MD
12. Neves AM, Ferreira AJ, Carrera E, Roque CM, Cinefra M, Jorge RM, Soares CM (2011) Bending of FGM plates by a sinusoidal plate formulation and collocation with radial basis functions. Mech Res Commun 38(5):368–371
13. Neves AM, Ferreira AJ, Carrera E, Cinefra M, Roque CM, Jorge RM, Soares CM (2012) A quasi-3D hyperbolic shear deformation theory for the static and free vibration analysis of functionally graded plates. Compos Struct 94(5):1814–1825
14. Neves AM, Ferreira AJ, Carrera E, Roque CM, Cinefra M, Jorge RM, Soares CM (2012) A quasi-3D sinusoidal shear deformation theory for the static and free vibration analysis of functionally graded plates. Compos B Eng 43(2):711–725
15. Neves AM, Ferreira AJ, Carrera E, Cinefra M, Roque CM, Jorge RM, Soares CM (2013) Static, free vibration and buckling analysis of isotropic and sandwich functionally graded plates using a quasi-3D higher-order shear deformation theory and a meshless technique. Compos B Eng 44(1):657–674
16. Daouadji TH, Tounsi A (2013) Analytical solution for bending analysis of functionally graded plates. Sci Iran 20(3):516–523

17. Kulkarni K, Singh BN, Maiti DK (2015) Analytical solution for bending and buckling analysis of functionally graded plates using inverse trigonometric shear deformation theory. Compos Struct 15(134):147–157
18. Reddy JN, Chin CD (1998) Thermomechanical analysis of functionally graded cylinders and plates. J Therm Stress 21(6):593–626
19. Shen HS (2002) Nonlinear bending response of functionally graded plates subjected to transverse loads and in thermal environments. Int J Mech Sci 44(3):561–584
20. Zenkour AM, Alghamdi NA (2010) Bending analysis of functionally graded sandwich plates under the effect of mechanical and thermal loads. Mech Adv Mater Struct 17(6):419–432
21. Wilson AJ (1941) The thermal expansion of aluminium from 0 to 650 C. Proc Phys Soc 53 (3):235
22. Touloukian YS (1967) Thermophysical properties of high temperature solid materials: elements. Macmillan
23. Tanigawa Y (1993) Theoretical approach of optimum design for a plate of functionally gradient materials under thermal loading. In: Thermal shock and thermal fatigue behavior of advanced ceramics. Springer, Dordrecht, pp 171–180

Modelling, Fabrication and Characterization of Kevlar Reinforced Composite

Abhishek Rajpoot, **Vinay Pratap Singh**
and **Samar Bahadur Yadaw**

Abstract Kevlar fibre reinforced epoxy composites are extensively used for various applications. In this study, Kevlar fibres are used as reinforcement in the modified epoxy resin matrix. Epoxy resin is modified using polyetherimide (PEI). The content of polyetherimide in epoxy is derived up to 10 wt%. Mechanical properties improvement is observed around 7.5 wt% and 5 wt% of polyetherimide in blended epoxy as compare to pure epoxy. In the present work, Kevlar fibre in mat form is first introduced with epoxy resin. Then other samples were made by blending epoxy with different percentages of polyetherimide. Fabricated composites are subjected to various mechanical properties evaluation tests. Results exhibit an increase in strength values. Tensile, shear and impact strength is maximum for composite samples having 7.5 wt% PEI. Flexural strength is maximum for samples with 5 wt% PEI. DSC and TGA of samples are also done for material characterization of composites. During the TGA testing, the degradation of samples in the Nitrogen gas atmosphere at two different stages, 250–350 °C and 450–600 °C, are observed, where significant wt. loss has occurred. The DSC analysis of Epoxy resin and PEI-blended resin shows two different glass transitions at 90°C and 220°C, respectively.

Keywords Kevlar fiber · Composite · Polyetherimide

1 Introduction

For the past five decades, the utilization of fibre-reinforced components in engineering structures has been increasingly diversified from sports equipment and high-performance racing cars, to navy ships, helicopters and airplanes. There are

A. Rajpoot · V. P. Singh (✉)
Mechanical Engineering Department, H. B. T. U., Kanpur, UP, India
e-mail: vinayforus@gmail.com

S. B. Yadaw
Defence Materials and Stores Research and Development Establishment, Kanpur, UP, India

several kinds of fibres being used in laminated composites, but Kevlar has been used extensively due to its lightweight, tensile strength, toughness, and resistance to impact damage [1].

Composite materials have been developed to achieve enhanced properties such as strength, toughness, and improved performance at high temperature, etc. Strengthening mechanism of composite strongly depends on the type of reinforcement [2]. Yue and Padmanabhan studied interfacial strength of Kevlar fibre reinforced in epoxy matrix using fibre pull out test. It was observed that treatment of fibres with organic solvents prior to composite fabrication results in enhanced interfacial shear strength by about 60% compared to an untreated fibrous composite. Kevlar fibres are crystalline polyamide fibres consisting of carbon, hydrogen, oxygen and nitrogen elements. As compared to contemporary fibers, they have low density and high tensile strength to weight ratio. The Kevlar fibres are preferred over the carbon fibres as they do not fail by brittle cracking, but exhibit excellent toughness [3, 4].

Generally, structures and laminates made of fibrous composites consist of different layers of unidirectional laminae. Each lamina is made of the same constituents but, individual layers may differ by the relative volumes of reinforcements and constituent materials in them. Use of continuous or discontinuous fibers, woven or nonwoven reinforcement, and the orientation of fibres with respect to common reference axis influence the properties of fibrous composites [3, 4].

Previous research has assessed the influence of fiber positioning on the tensile strength by means of fracture testing. Parameters like fibre length, matrix pouring and compaction methods, specimen size influence the properties of composites [5].

In a fiber-reinforced composite, the orientation of fibers with respect to sliding surface is an important parameter required for the determination of wear rate and friction coefficient [6]. Epoxy resins with shorter curing cycles are in high demand for commercial applications as they provide economy in composite fabrication and higher toughness for better damage tolerance [7].

Many researchers have investigated the influence of temperature and light irradiation on the tensile fracture behaviour of fibres, exposure to thermal and light irradiating environment degrades the tensile strength of fibers [8]. Jang, W. Lee, Turmel and Partridge presented the work on polyetherimide modified high-performance epoxy resin. Polyetherimide-modified epoxy resin system resulted in an improved fracture toughness [9, 10].

In this paper, it is clearly observed that Kevlar fibre is introduced with epoxy and modified epoxy with different percentage of PEI (5%, 7.5% and 10% by wt.). Composites were prepared by the hand lay-up method. After fabrication, composite materials were cut by composite cutting machine as per ASTM standard. To identify the composite material strength, material undergoes mechanical characterization such as tensile, flexural, ILSS and impact properties for the composite material.

2 Materials and Methods

2.1 Fabrication of Composites

Four different types of composite samples are prepared as shown in Figs. 1, 2, 3 and 4. One type of samples are fabricated using Kevlar fibre with the only epoxy and other three are fabricated using Kevlar fibre with polyetherimide (PEI) modified epoxy in varying percentages of PEI as 5%, 7.5%, and 10%. Composites are prepared by hand layup technique involving alternate layers of Kevlar fibres in mat form and layer of Epoxy (LY556) resin. Samples are subjected to hydraulic press. A total thickness of 3 mm is maintained after layer by layer fabrication of composite. Samples were cut by composite cutting machine.

Fig. 1 Samples of Tensile Test by ASTMD 3039-76
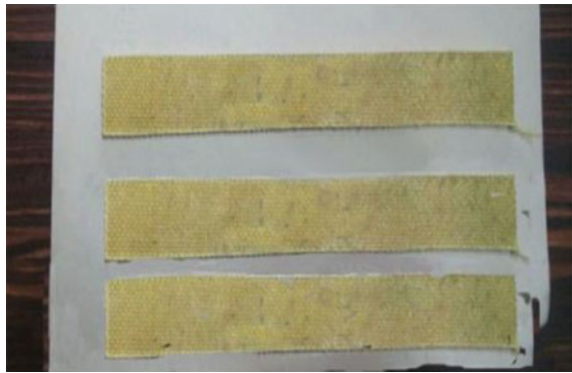
Fig. 2 Samples of Flexural Test by ASTMD 790-81
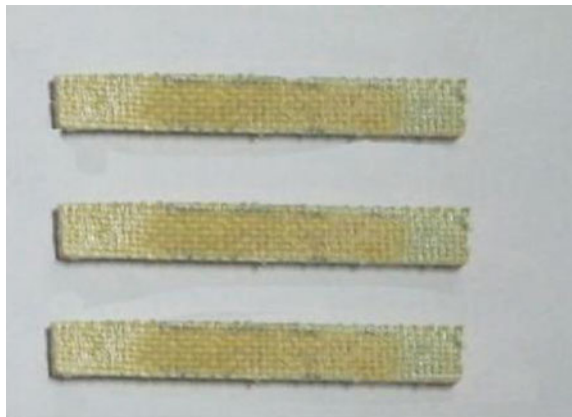
Fig. 3 Sample of ILSS test
ASTMD 2344-84
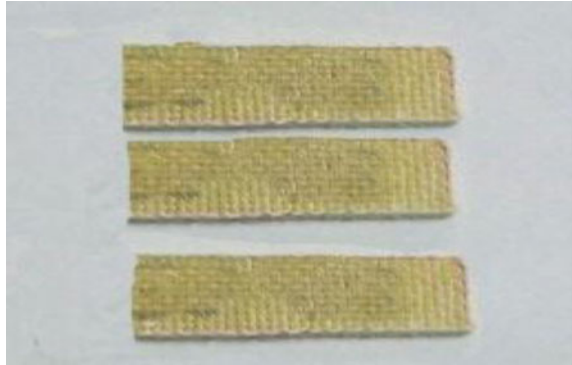
Fig. 4 Samples of impact
test by ASTMD 256
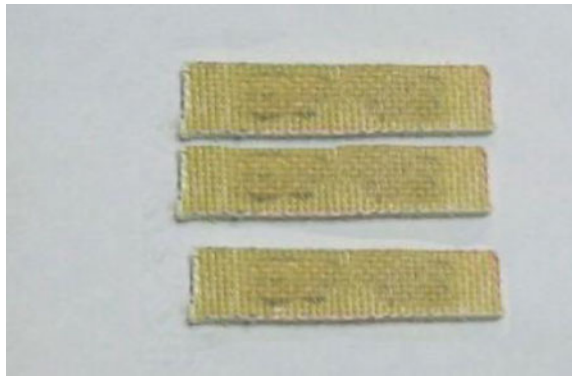
2.2 Mechanical Tests

Tensile strength of composite samples (Fig. 1) was evaluated in accordance with ASTM standard D 3039-76. The tensile test was performed at a recommended crosshead speed of 0.2 cm/min. Flexural strength of composite samples (Fig. 2) was determined by ASTM test method specified by D790-81. In this test, a composite beam specimen of rectangular cross section is loaded in a three-point bending mode. Interlaminar shear strength (ILSS) is defined as the strength preventing delamination, i.e. strength parallel to the plane of the lamination. ILSS is measured in a short beam shear test as per ASTM standard D 2344-84.

A flexural specimen (Fig. 3) with span (L)- depth (h) ratio of 5:1 is tested in three-point bending mode to produce a horizontal shear failure between the laminate piles.

The impact strength of the material is evaluated to find its toughness. In other words, impact strength indicates the capacity of the material to absorb and dissipate energies under shock or impact loading. ASTM standard D 256 is used to evaluate the impact resistance of fiber reinforced composite materials (Fig. 4).

Fig. 5 Samples of TGA and DSC
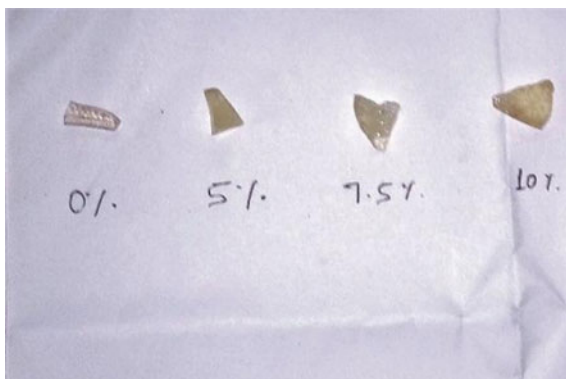
2.3 Thermal Gravimetric Analysis

Thermal gravimetric analysis (TGA) of the pure epoxy sample and other samples formed by blending PEI to epoxy have been performed. TGA provides information on the thermal stability of polymer samples (Fig. 5). TG analysis is carried out in the Nitrogen gas environment. Test chamber temperature was gradually increased at a heating rate of 10 °C/min from 30 °C to 600 °C. Such type of thermal analysis is carried out to understand the kinetics and thermodynamics of phase transformations in a variety of crystalline and non-crystalline materials. The major advantage of TGA is that it can be performed on non-crystalline, such as polymers and inorganic materials as well.

2.4 Differential Scanning Calorimetry

All the measurements of heat change values of the test samples as compared to standard reference were performed under nitrogen atmosphere. The masses of samples were 10–15 mg. Variation of differential heat for samples as a function of temperature can be plotted. Peaks in the plot indicate any phase transformation occurring in samples. Attributes like activation energy, amount of heat, transformation starting temperatures, etc., can be obtained from these plots.

3 Results and Discussion

In the unmodified epoxy, tensile strength comes out as 335.81 MPa, in modified epoxy with 5% PEI 344.23 MPa, with 7.5% PEI 427.39 MPa and with 10% PEI 313.81 MPa is found. Hence the tensile strength increases up to 7.5% then decreases

(Fig. 6). In the unmodified epoxy, flexural strength (Fig. 7) comes out as 166.48 MPa, in modified epoxy with 5% PEI 197.24 MPa, with 7.5% PEI 157.97 MPa and with 10% PEI 313.81 MPa is found. Hence, the flexural strength increases up to 5% then decreases. In the unmodified epoxy, shear strength comes out as 113.43 MPa, in modified epoxy with 5% PEI 100.69 MPa, with 7.5% PEI 136.39 MPa and with 10% PEI 117.21 MPa is found.

The results of the tensile test are different from flexural stress test because in tension only one type of stresses is predominantly observed in a specimen, however, under flexural load combination of tensile, bending and shear stresses are observed. The occurrence of a combination of stresses during bending affects the

Fig. 6 Maximum tensile strength of different samples
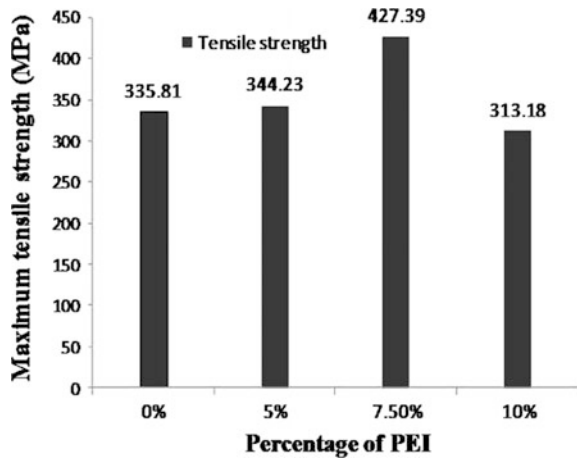
Fig. 7 Flexural strength of different samples
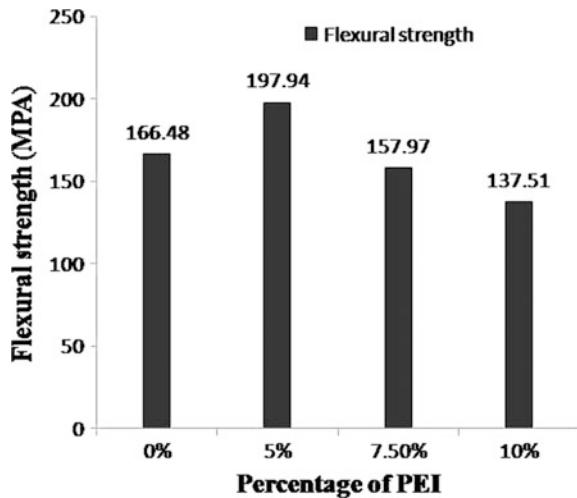
Fig. 8 Shear strength of different samples
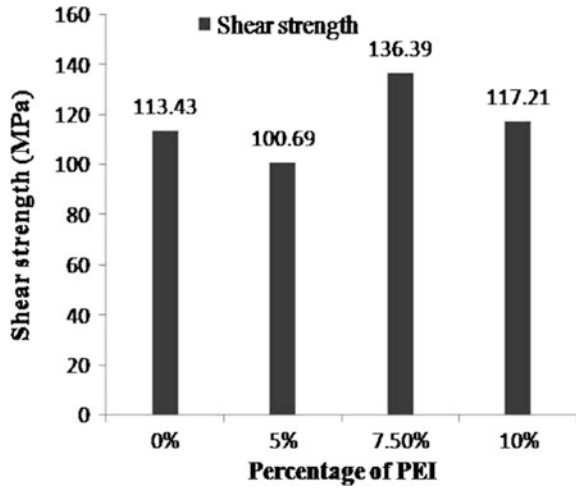
Fig. 9 Impact strength of different samples
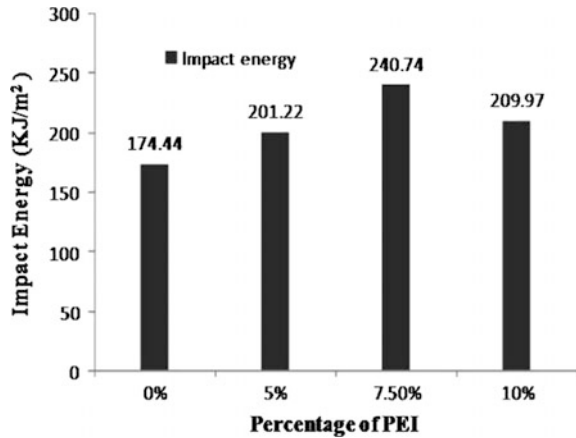
strength of the material component. Thus, in tension test strength of the composite is maximum at 7.50 wt% of PEI and in flexural test strength is maximum at 5 wt% of PEI [11].

Intelaminar shear strength (Fig. 8) first decreases at 5% then increases at 7.5% then again decreases. In the unmodified epoxy, impact energy (Fig. 9) comes out as 174.44 kJ/m^2, in modified epoxy with 5% PEI 201.22 kJ/m^2, with 7.5% PEI 240.74 kJ/m^2 and with 10% PEI 209.97 kJ/m^2 is found. Hence, impact energy increases up to 7.5% then decreases.

ILSS and impact strength of the composite is higher for 7.5% PEI blending of epoxy as compares to any other percentage. It was observed earlier that the toughening effect of PEI, when blended with epoxy resin, depends on the amount of curing. Lack of curing is the major cause of variation of results [14].

Thermal stability of polyetherimide-reinforced Epoxy blends was carried out in Fig. 10. The degradation blend in the N_2 atmosphere shows two different stages at 250–350 °C and 450–600 °C, where significant weight loss has occurred. In the first stage a loss in the mass of epoxy resin is observed due to the decomposition of the end group in the epoxy network. The loss in the second stage is primarily due to the degradation of main chains of epoxy. The Thermal degradation temperature of PEI percent resin is at 600 °C. The char yield in EP3 containing the highest percentage of PEI is less as most of the epoxy chains degrade at a lower temperature and gives a higher percentage of residue content. It also seems that the degradation profile does not change with respect to increase or decrease in wt% of PEI. It can be attributed to the absence of a compatiblizing agent between the epoxide and imide rings.

DSC utilized to measure the glass transition temperature (Tg) and enthalpy change in samples when subjected to heating Fig. 11. The wetting/attractive and repulsive/dewetting behaviour depends on the dispersion and homogeneity and compatibility of blends. The DSC thermogram shows two different glass transitions at 90 °C and 220 °C of Epoxy resins and PEI blend, respectively. DSC plots shows the curing temperature of epoxy resin is in the range of 120–180 °C. Glass transition temperature of PEI is about 220 °C. Decomposition of samples is observed around 350–400 °C. It further shows the degradation profile due to chain breaking and chain disintegration within the molecules.

The cross-linking of polymeric modifiers with another polymer is the most important and significant factor which affects the mechanical properties of unfilled and filled polymer blend system. The curing process or the crosslinking prevents slippage between chains when deformation causing stresses are applied to the sample. The increase in the crosslinking behaviour of blended resin attributes the change in the physical properties and adhesion characteristics of these resins lead to

Fig. 10 TGA analysis of pure epoxy (EP), 5% PEI (EP1), 7.5% PEI (EP2), 10% PEI (EP3)
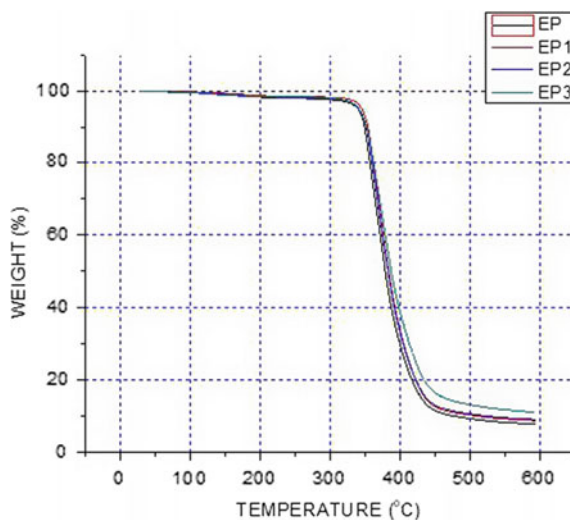
Fig. 11 DSC analysis of
pure epoxy (EP), 5% PEI
(EP1), 7.5% PEI (EP2), 10%
PEI (EP3)
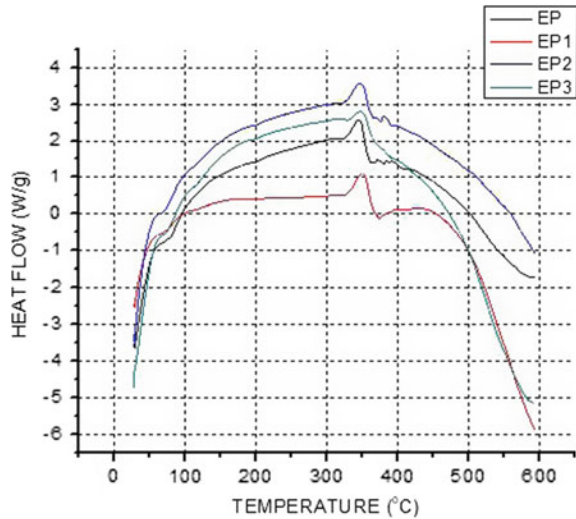
enhanced bonding of the fibre with the matrix. It further influences the mechanical
behaviour of the polymeric blend/composite by restricting the slippage of layer to
layer as well as the matrix to fabric debonding [12]. Epoxy polymers have inher-
ently low toughness and impact resistance. To improve the toughness and
mechanical properties, PEI is blended with the epoxy resin system. On blending the
PEI in epoxy toughness level is increases as the impact strength is improved.
From DSC curve it is observed that there are two distinct slope changes indicating
glass transition temperatures for epoxy and for PEI. These slope changes are not
very predominant also. Hence it can be inferred that the cross-linking between PEI
and epoxy is not sufficient [13]. However, for 7.5% blending of PEI the
cross-linking is better as compared to other samples.

4 Conclusions

In this work, an effort was made to develop Kevlar fibre with epoxy and
PEI-blended epoxy-based composites to be used for defence purpose. Experimental
investigations were performed to know the effect of fibre reinforcement in matrix
material to achieve the desired outcome. Tensile strength is found to be maximum
at 7.5% of PEI with epoxy as matrix material. Flexural strength is found to be
maximum at 5% of PEI with epoxy as matrix material. Shear strength is found to be
maximum at 7.5% of PEI with epoxy as matrix material. Impact strength is found to
be maximum at 7.5% of PEI with epoxy as matrix material. DSC investigations
show two different glass transitions at 90 °C and 220 °C of Epoxy resins and PEI
blend, respectively.

In the present work, PEI is blended with epoxy and it has been observed that there is a reduction in both tensile and flexural strength when the PEI percentage was increased to 10% as compared to its lower percentages. DSC results exhibit that there are two glass transition slope changes, so we can conclude that the excess quantity of hardener, improper mixing or improper manufacturing sequence followed influences the cross-linking between epoxy and PEI and thus the property of the fabricated composite. It is, therefore, necessary to mix optimum percentage of hardener while preparing the epoxy-PEI blend with the aim to modify epoxy by PEI. The blending of PEI with epoxy also increases the brittleness.

References

1. Yang S, Chalivendra VB, Kim YK (2017) Fracture and impact characterization of novel auxetic Kevlar/Epoxylaminated composites. J Compos Struct 168:120–129
2. Agrawal BD, Broutman LJ (1980) Analysis and performances of fibre composites, pp 2–3
3. Yue CY, Padmanabhan K (1999) Interficial studies on surface modified Kevlar fibre/epoxy matrix composite. J Compos, 205–217
4. Alhuthali A, Low IM, Dong C (2012) Characterisation of the water absorption, mechanical and thermal properties of recycled cellulose fibre reinforced vinyl-ester eco-nanocomposites. J Compos 2:2772–2781
5. Alberti MG, Enfedaque A, Gálvez JC, Agrawal V (2016) Fibre distribution and orientation of macro-synthetic polyolefin fibre reinforced concrete elements. J Const Build Mat, 505–517
6. Jun D, Yaohui L, Sirong Y, Handa D (2002) Effect of fibre-orientation on friction and wear properties of Al_2O_3 and carbon short fibres reinforced AlSi12CuMgNi hybrid composites. J Wear, 164–172
7. Chang IY (1985) Thermoplastic matrix continuous filament composites of Kevlar ® aramid or graphite fiber. Comp Sci Tech, 61–79
8. Cai G, Li D, Fang D, Yu W (2014) A new apparatus to measure the effect of temperature and light on the bending fatigue properties of Kevlar 49 and PBO fibers. J Poly Test, 143–148
9. Jang J, Lee W (1993) Polyetherimide high performance epoxy resin. J Poly, 513–525
10. Turmel DJP, Partridge IK (1996) Heterogeneous phase separation around fibres in epoxy/PEI blends and its effect on composite delamination resistance. J Comp Sci Tech, 1001–1007
11. Gorjipoor A, Simpson JF, Ganesan R, Hoa SV (2017) Computational and experimental strain analysis of flexural bending of thick glass/epoxy laminates. Comp Str, 133–134
12. Iijima K, Aoki D, Otsuka H, Takata T (2017) Synthesis of rotaxane cross-linked polymers with supramolecular cross-linkers based on g-CD and PTHF macromonomers: the effect of the macromonomer structure on the polymer properties. J Mat Chem, 1–5
13. Park JM, Kim D, Kong JW, Kim S-Ju, Jang JH, Kim M, Kim W, Lawrence K, DeVries (2007) Interfacial evaluation and self-sensing on residual stress and micro failure of toughened carbon fiber/epoxy-amine terminated (AT)-polyetherimide (PEI) composites. J Compos, 833–846
14. Hodgkin JH, Simon GP, Varley RJ (1998) Thermoplastic toughening of epoxy resins: a critical review. Ploy Adv Tech 9(1):3–10

Effects of Post-weld Heat Treatment on Microstructure and Mechanical Behavior of Friction Stir Welded Thick Section Al–Zn–Mg–Cu Alloy

T. Ramakrishna, S. Srinivasa Rao and G. Swami Naidu

Abstract Friction stir welding is considered to be a promising solution to successfully join high strength 7000 series aluminum alloys. However, questions related to a decrease in weld mechanical properties with an increase in plate thickness still remain unanswered. In this study, 16 mm thick AA7075–T651 aluminum alloy plates were successfully joined by friction stir welding. The welds were heat treated using a special solutionizing method called cyclic solution treatment (CST). The effects of CST on mechanical behavior and microstructures of the welds were studied using hardness, tensile, and impact tests and optical microscopy. The post-weld heat treatment significantly improves the hardness of the joint and homogenizes the hardness distribution across the welded joint. However, the tensile properties and impact toughness of the welds were not found to be beneficially affected. A significant grain growth in the weld nugget was observed after CST.

T. Ramakrishna (✉)
Department of Mechanical Engineering, Sir CRR College of Engineering,
Eluru 534007, Andhra Pradesh, India
e-mail: ramathadivaka@gmail.com

S. Srinivasa Rao
Department of Mechanical Engineering, MVGR College of Engineering,
Vizianagaram 535005, Andhra Pradesh, India

G. Swami Naidu
Department of Metallurgical Engineering, University College of Engineering,
JNTUK, Vizianagaram 535005, Andhra Pradesh, India

1   Introduction

Heat-treatable aluminum alloys such as alloy 7075 with favorable strength to weight ratios are widely used in aerospace industries [1]. However, the structural applications of these alloys inevitably include welding and it is considered difficult using conventional fusion welding processes. Friction stir welding (FSW), a solid-state process invented at The Welding Institute (TWI), is an alternate solution for joining aluminum alloys [2] since it offers many benefits over conventional joining methods. It is involved with lower heat during the process, no melting, low defects, and low distortion [3–5]. Though there is a quite a bit of research already reported on joining of AA7075 using friction stir welding in the literature [6–10], many questions on the poor mechanical behavior of the welded joint still remain unanswered [11, 12].

   In the recent past, there have been some efforts made to improve the mechanical properties of friction stir welded joints by changing tool geometry and welding parameters [13, 14]. Among the various techniques, post-weld heat treatment (PWHT) is found to be the most appropriate method for restoring degraded mechanical properties of the welds [15, 16]. Feng et al. [15] investigated the effect of solutionizing temperature on the tensile strength of the weld. Priya et al. [16] reported that direct aging of friction stir welded 2219 and 6061-T6 alloys at 165 °C for 18 h without solution treatment improves the hardness of weld nugget while it does not cause hardness recovery in the other zones of weld region.

   There are very few works reported on PWHT of friction stir welded AA7075 [17–21]. Barcelona et al. [17] reported that PWHT leads to a uniform distribution of precipitate particles in various zones of the weld. The PWHT was also found to cause a recovery in the strength of the joint and abnormal grain growth (AGG) in the weld region [18]. However, Mahoney et al. [19] realized that direct post-weld aging without solution treatment does not exhibit a useful effect on the yield strength of 7075-T651 weld. The solution treatment followed by aging was found to marginally improve the tensile properties of the welds [20]. Yeni et al. [21] also concluded that the post-weld aging increases the hardness across the weld. More recently, a new technique for heat treating high strength aluminum alloys has been devised based on cyclic solution treatment (CST) followed by artificial aging [22]. The beneficial effect of CST on mechanical properties of 7075 aluminum alloys has been earlier reported [23]. Furthermore, the effects of CST and artificial aging on mechanical properties of friction stir welded joints have been studied by Bayazid et al. [24].

   Most of the above studies have been carried out on the plates with a thickness ranging from 3 to 8 mm and in the majority of the cases positive effect of PWHT on friction stir welded Al alloy plates is very well established. However, the same has not been investigated on the welds with a plate thickness 10 mm and more. An unpublished work carried out very recently by the present authors on 10 mm thick friction stir welds revealed that the rightly selected post-weld heat treatments improve mechanical properties of the friction stir weld. In fact, as the thickness of

the plates to be welded increases, the reductions in mechanical properties increase. Hence, it is of prime interest to investigate that the loss in mechanical properties of friction stir welded thick section AA7075–T651 Al alloy can be recovered by PWHT. In this study, the possibility of restoring mechanical properties of 16 mm thick AA7075–T651 friction stir welds using cyclic solution treatment has been investigated.

2 Experimental Procedure

Friction stir welding trials were carried out on 16 mm thick plates of AA7075–T651 aluminum alloy. The chemical composition of the alloy is presented in Table 1. The plates were cut and machined to 110 mm width and 250 mm length coupons. The plates were longitudinally butt-welded using a friction stir welding machine. In one of the previous studies carried out on friction stir welding of 10 and 16 mm thick AA7075 plates, the 16 mm thick friction stir welded joints were developed using the process parameters given in Table 2 and they were found to be defect free [10]. Thus, the same was used in this work to produce the welds.

The post-weld heat treatments were carried out using a special solutionizing method called cyclic solution treatment (CST), a repeated heating between 400 and 480 °C for 1.5 h (0.25 h for each cycle) and water quenching (Fig. 1).

Microhardness surveys were conducted using a Vickers hardness testing machine under a load of 200 g applied for 15 s. The hardness measurements were made across the weld and at the mid-thickness of the weld cross-section with a spacing of 1 mm between adjacent indentations. Tensile specimens transverse to the welding direction were made according to ASTM B557 standard. Tensile tests were performed at room temperature using a computer-controlled universal testing machine. Weld microstructures were examined using stereo and optical microscopy. The samples were carefully prepared to the required sizes from the weld and then polished using emery papers of various grades. Final polishing was done using diamond compound (1 Âμm particle size) in a disk polishing machine. The polished samples were etched using standard Keller's reagent (5 ml HNO3, 2 ml HF, 3 ml HCL, and 190 ml distilled water) to understand the macro and microstructures of the weld.

Table 1 Chemical composition of 7075–T651 in wt%

Zn	Mg	Cu	Si	Fe	Cr	Ti	Mn	Al
6.0	2.5	1.4	0.03	0.08	0.20	0.05	0.01	Bal

Table 2 Friction stir welding process parameters

Nomenclature	Process parameter
Tool geometry	M2 tool steel Taper threaded pin (left-hand metric threads, 1.5 mm pitch) Pin diameter: 10 mm (shoulder end) and 8 mm (tip end) Pin length: 15.5 mm Shoulder diameter: 30 mm Flat shoulder
Tool rotational speed	500 rpm
Welding speed	25 mm/min
Tool tilt	1.5°
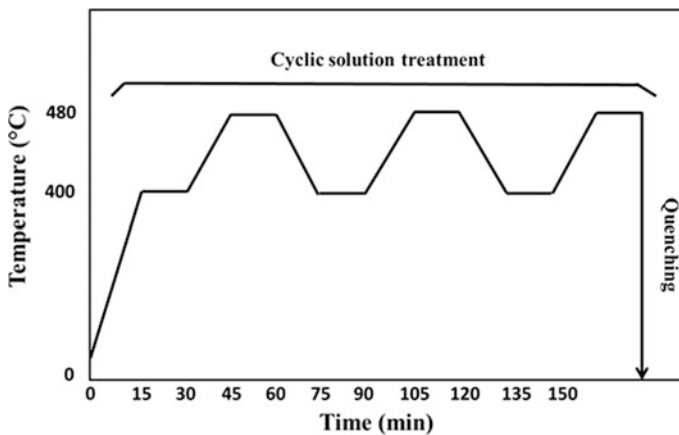
Fig. 1 Schematic illustration of cyclic solution treatment

3 Results and Discussion

3.1 Hardness Profiles

The hardness profiles of AA7075–T651 Al alloy friction stir welded joints in as-welded and cyclic solution treated (CS-treated) conditions are presented in Fig. 2. As it can be seen, the hardness of the weld region was found to be much lower across the weld zones such as weld nugget (WN), thermo-mechanically affected zone (TAMZ), and heat-affected zone (HAZ) than that of the base material. Also, the hardness measurements across the weld were found to be not homogenized exhibiting lower hardness values in the heat-affected zone and higher hardness values in the weld nugget. This happens to be a much disturbing issue in the

Fig. 2 Microhardness
profiles of the welds in
as-welded and CS-treated
conditions
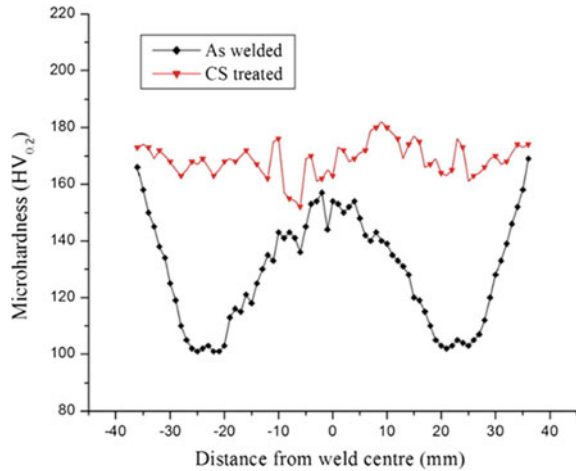
thick section friction stir welded high strength aluminum alloys such as AA7075–
T651, as the same was also reported in previous studies [10].

The cyclic solution treatment carried out on friction stir welds was found to
significantly improve the hardness across the weld. Interestingly, the CST was also
found to enhance the homogeneity in hardness values across various zones of
friction stir welded joint.

3.2 Tensile Properties

The results of tensile tests performed on the base material and friction stir welds,
both in as-welded and cyclic solution treated condition, are presented in Table 3.
Friction stir welding was found to cause reductions in the strength and elongation of
the base material. Tensile fractures occurred in the heat-affected zone of the welded
joint and this could be due to marginal grain growth and formation of precipitated
free zones taking place in the HAZ during friction stir welding, as the same was
also reported by the previous researchers [10].

The post-weld heat treatment conducted, intending to recover strength values, on
the welds did not show beneficial effects on tensile properties of the joint.
Particularly, the percent of elongation was adversely affected. This low elongation
displayed by the welds after cyclic solution treatment can be attributed to the
hardness increase in various zones of combined weld region, which do not plas-
tically deform during the testing, thus reducing the overall elongation of the
specimens. Similar statements were also made for thin section 7075 Al alloy plates
in T6 condition [18]. The CS treated welds were found to fracture in WN–TMAZ
interface (Fig. 3).

Table 3 Tensile properties of friction stir welds before and after post-weld heat treatment

Material	Yield strength (0.2% proof) (MPa)	Tensile strength (MPa)	% El	Joint efficiency in terms of YS	Fracture location	Impact toughness (J)
Base material	563	610	10	–	–	6.67
As-Welded	192	330	8	35	HAZ	5.5
CS treated	178	253	4	32	WN-TMAZ	5.33
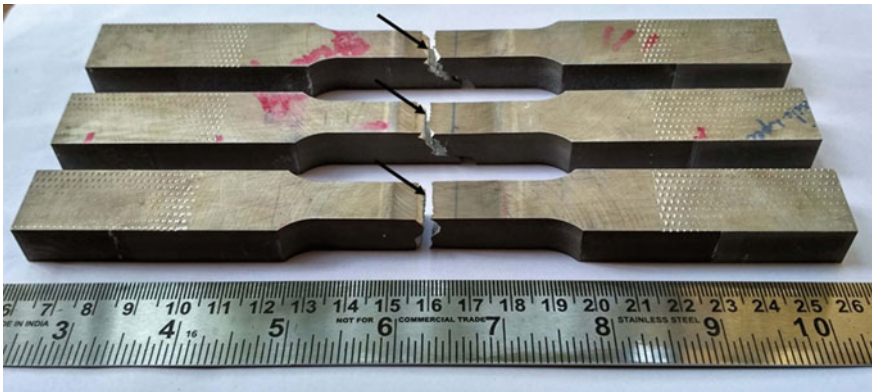
Fig. 3 Tensile-tested specimens showing fractures in WN-TMAZ interface (arrows show fracture location)

3.3 Impact Toughness

The results of the impact tests conducted on base material and the welds before and after post-weld heat treatment are presented in Table 3. The base material exhibited better impact toughness compared to the welds. The cyclic solution treatment caused a further decrease in the impact toughness of the welds. Failed impact test specimens are shown in Fig. 4.

3.4 Microstructure

The results of optical microscopy are presented in Figs. 5 and 6. The base material microstructure was characterized by pancake shaped large elongated grains, a type of hot-rolled structure (Fig. 5a). The typical TMAZ and HAZ zones of friction stir weld are shown in Fig. 5b and c. As can be observed, the transition zone between the base material and weld nugget was characterized by a highly deformed structure
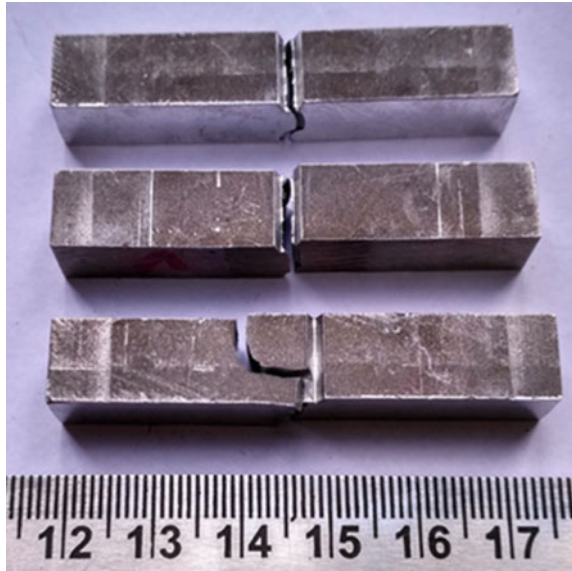
Fig. 4 Impact tested specimens of CS treated welds
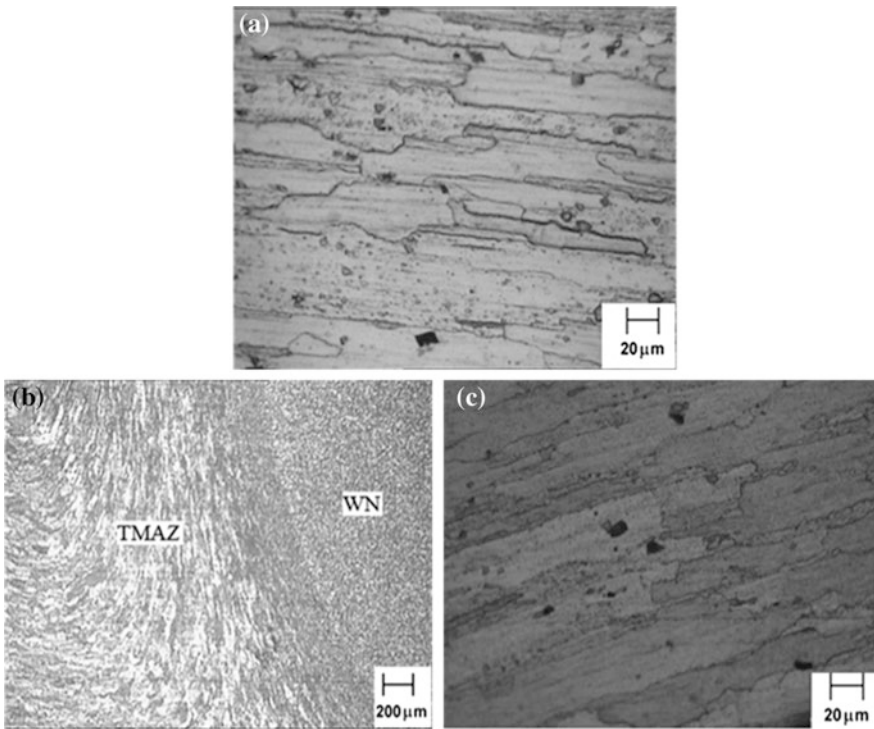
Fig. 5 Microstructures of base material and typical TMAZ and HAZ: **a** base material, **b** TMAZ, and **c** HAZ
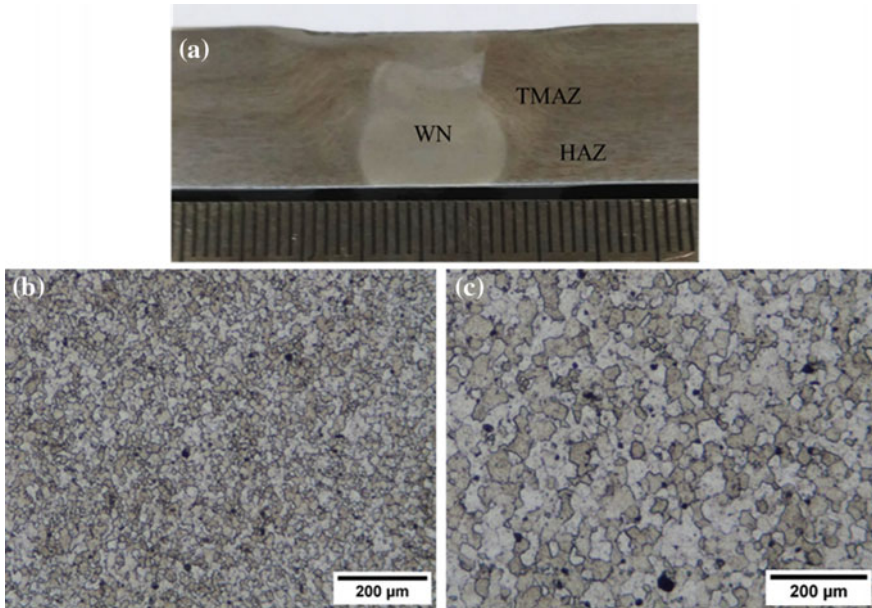
Fig. 6 Weld cross-section and weld nugget microstuctures: **a** typical macrostructure, **b** as-welded, and **c** CS-treated weld

(Fig. 5b) and the HAZ retained the same grain structure as the parent material excepting noticeable grain growth. The typical cross-sectional appearance of the friction stir weld is shown in Fig. 6a. The weld nugget microstructure of the friction stir welded joint exhibited very fine equiaxed grains (Fig. 6b) resulted from dynamic recrystallization phenomenon, that usually takes place during friction stir welding, due to severe plastic deformation and temperature rise of the welding area. The post-weld cyclic solution treatment was found to cause noticeable grain grown in the nugget zone of the weld region (Fig. 6c), usually known as (AGG) abnormal grain growth. This is likely to occur during the conventional solution treatment and the same has also been reported by several authors [21, 25].

4 Conclusions

- Friction stir welding can produce full penetration sound welds on 16 mm thick AA7075–T651 plates. However, it causes reductions in strength and hardness values.
- The post-weld cyclic solution treatment significantly improves the hardness of the joint and homogenized the hardness distribution across the welded joint.

- The cyclic solution treatment does not exhibit beneficial effects on tensile properties and impact toughness of the welded joint.

References

1. Abhay K, Sreekumar K (2008) Metallurgical studies on cracked Al–5.5 Zn–2.5 Mg–1.5 Cu aluminum alloy injector disc of turbine rotor. J Fail Anal Prev 8(4): 327–332
2. Thomas WM, Nicholas ED, Needham JC, Church MG, Temple-Smith P, Dawes CJ (1991) G. B. Patent Application No. 9125978.8
3. Sua JQ, Nelson TW, Sterling CJ (2005) Microstructure evolution during FSW/FSP of high strength aluminum alloys. Mater Sci Eng A 405:277–286
4. Fujii H, Cui L, Maeda M, Nogi K (2006) Effect of tool shape on mechanical properties and microstructure of friction stir welded aluminum alloys. Mater Sci Eng A 419:25–31
5. Chen HB, Yan K, Lin T, Chen SB, Jiang CY, Zhao Y (2006) The investigation of typical welding defects for 5456 aluminum alloy friction stir welds. Mater Sci Eng A 433:64–69
6. Mishra RS, Ma ZY (2005) Friction stir welding and processing. Mater Sci Eng R 50:1–78
7. Singh R, Sharma C, Dwivedi D, Mehta N, Kumar P (2011) The microstructure and mechanical properties of friction stir welded Al–Zn–Mg alloy in as welded and heat treated conditions. Mater Des 32(2):682–687
8. Nandan R, DebRoy T, Bhadeshia HKDH (2008) Recent advances in friction-stir welding–process, weldment structure and properties. Prog Mater Sci 53:980–1023
9. Srinivasa Rao T, Madhusudhan Reddy G, Srinivasa Rao G, Koteswara Rao SR (2014) Studies on salt fog corrosion behavior of friction stir welded AA7075–T651 aluminum alloy. Int J Mater Res 105:375–385
10. Srinivasa Rao T, Madhusudhan Reddy G, Koteswara Rao SR (2015) Microstructure and mechanical properties of friction stir welded AA7075–T651 aluminum alloy thick plates. Trans Nonferrous Metals Soc China 25:1170–1178
11. Elangovan K, Balasubramanian V (2008) Influences of post-weld heat treatment on tensile properties of friction stir-welded AA6061 aluminum alloy joints. Mater Charact 59(9):1168–1177
12. Krishnan KN (2002) The effect of post weld heat treatment on the properties of 6061 friction stir welded joints. J Mater Sci 37(3):473–480
13. Rajakumar S, Muralidharan C, Balasubramanian V (2011) Influence of friction stir welding process and tool parameters on strength properties of AA7075–T6 aluminium alloy joints. Mater Des 32(2):535–549
14. Rowe C, Thomas W (2005) Advances in tooling materials for friction stir welding. TWI and Cedar Metals Ltd, pp 1–11
15. Feng JC, Chen YC, Liu HJ (2006) Effects of post-weld heat treatment on microstructure and mechanical properties of friction stir welded joints of 2219-O aluminium alloy. Mater Sci Technol 22(1):86–90
16. Priya R, Subramanya Sarma V, Prasad Rao K (2009) Effect of post weld heat treatment on the microstructure and tensile properties of dissimilar friction stir welded AA2219 and AA6061 alloys. Trans Indian Inst Met 62(1):11–19
17. Barcellona A, Bua G, Fratini L, Palmeri D (2006) On microstructural phenomena occurring in friction stir welding of aluminium alloys. J Mater Process Technol 177(13):340–343
18. Pekolu G, Erim S, Cam G (2014) Effects of temper condition and post weld heat treatment on the microstructure and mechanical properties of friction stir butt-welded AA7075 Al alloy plates. Int J Adv Manuf Technol 70(1–4):201–213
19. Mahoney M, Rhodes C, Flinto J, Bingel W, Spurling R (1998) Properties of friction-stir welded 7075 T651 aluminum. Metall Mater Trans A 29(7):1955–1964

20. Sivaraj P, Kanagarajan D, Balasubramanian V (2014) Effect of post weld heat treatment on tensile properties and microstructure characteristics of friction stir welded armour grade AA7075–T651 aluminium alloy. Def Technol 10(1):1–8
21. Yeni S, Sayer O, Pakdil Erturul M (2008) Effect of post-weld aging on the mechanical and microstructural properties of friction stir welded aluminum alloy 7075. Arch Mater Sci Eng 34:105–109
22. Asgharzadeh H, Simchi A (2009) A new procedure for precipitation hardening of nanostructured Al–Mg–Si alloys and their nanocomposites. Iranian Patent, No. 57759
23. Radan L, Ghorbani H, Dehkordi O, Bayazid SM, Asgharzadeh H (2013) An investigation on the optimized precipitation hardening with Taguchi method and microstructure of 7075 aluminum alloy, 3th Ultrafine Grained and Nanostructured Materials (UFGNSM2013). Tehran, Iran
24. Bayazid SM, Farhangi H, Asgharzadeh H, Radan L, Mirhaji A (2016) Effect of cyclic solution treatment on microstructure and mechanical properties of friction stir welded 7075 Al alloy. Mater Sci Eng A 649(1):293–300
25. Threadgill PL, Leonard AJ, Shercli HR, Withers PJ (2009) Friction stir welding of Q5 aluminium alloys. Int Mater Rev 54:49–93

Temperature and Traverse Force Analysis During Underwater Friction Stir Welding

Mohd Atif Wahid, Nidhi Sharma, Pankul Goel, Zahid A. Khan and Arshad N. Siddiquee

Abstract Friction stir welding (FSW) is an auspicious clean welding method to join marine grade aluminum alloys (AAs). Underwater Friction Stir Welding (UFSW), can extend the marine application of the FSW due to its superior mechanical properties over its contemporary FSW. In FSW/UFSW the weld thermal cycles and tool forces exhibit a noteworthy effect on the weld properties. Force and temperature measurement during UFSW process play a pivotal role in understanding the process, prediction of tool life, microstructure and mechanical properties of the welded joints. As such an attempt has been made in this study to investigate the effect of welding speed (50–80 mm/min) on temperature distribution and traverse force during UFSW of AA 6082–T6. The results revealed that increase in welding speed caused high traverse force and low peak temperature. Furthermore, the increase in temperature was observed as the tool approaches the thermocouple near the weld center. After that, the temperature reduces due to a decrease in the thermal gradient. The maximum peak temperature of 137 °C was observed at the retreating side (RS) in heat affected zone (HAZ) at a low welding speed of 50 mm/min due to high heat input and slow cooling rate. Additionally, the maximum traverse force of 103 kgf was attained at a high welding speed of 80 mm/min due to high material flow stresses resulting from high strain rate and low temperature.

Keywords Friction stir welding (FSW) · Underwater friction stir welding (UFSW) · Temperature · Traverse force · Welding speed

M. A. Wahid (✉) · N. Sharma · P. Goel · Z. A. Khan · A. N. Siddiquee
Department of Mechanical Engineering, Jamia Millia Islamia, New Delhi, India
e-mail: wahidatif89@gmail.com

1 Introduction

A number of welding techniques have been developed in the past few years; still, welding of AAs seems to be challenging due to its high thermal conductivity and relatively low melting temperature [1, 2]. A recent joining technique, FSW has extended the application of AAs in different sectors, i.e., aerospace, automobile, and marine. FSW is a non-fusion joining technique developed by The Welding Institute (TWI) in 1991 [3]. This process does not cause melting of the material. Thus, undesirable fusion welding (FW) defects like solidification cracking, hydrogen embrittlement, etc. occurring due to the microstructural changes do not exist in FSW resulting in improved mechanical properties as compared to FW. In FSW, a specifically profiled tool with a shoulder and pin are inserted into the abutting faces of the base material (BM) and navigated along the joint line. The frictional heat generated amid the tool and the BM causes material softening leading to plastic deformation. Also, the material is transported from one side of the pin to the other side due to rotational and traverse movement of the tool. Intrinsically due to frictional heating and plastic deformation solid-state joining takes place [4–6] as shown in Fig. 1.

The FSW process is affected to a great extent by the heat generation and flow. Although the heat produced in FSW is less in comparison to FW, still it is sufficient enough to reduce the mechanical efficiency of the joints due to the dissolution and coarsening of the precipitates in heat treatable AAs. FSW regions most affected by this phenomenon are the HAZ and thermo–mechanically affected zone (TMAZ). So, the control of thermal cycles during FSW becomes necessary and this high heat generated can be overcome using different coolant, for instance, water, liquid nitrogen, etc. [7, 8]. In UFSW, water as a coolant is used to stabilize the temperature existing in the joints (see Fig. 2). Due to excellent absorption and transmission characteristic of water the heat is transferred readily from the HAZ and TMAZ

Fig. 1 Schematic representation of FSW
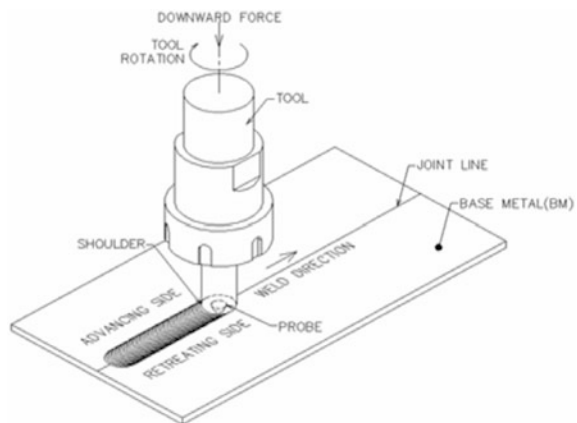
leading to lowering in the level of precipitate deterioration and improving the mechanical performance of the joints [8]. UFSW can be applicable in marine, shipbuilding, and several offshore construction and repair.

In recent years, UFSW has been adopted and investigated by some of the researchers due to its good joints efficiency as compared to FSW. Wahid et al. [9] recently FSWed AA–6082 using three cooling media (air, water, and water with crushed ice) and concluded that the controlled temperature distribution during water cooling ensured the maximum tensile strength of the joint. Fratini et al. [10] have also shown the potential use of water during UFSW of AA 7075 for improving joint strength and hardness due to low peak temperature. The effect of welding speed on temperature was investigated by Buchibabu et al. [11]. They stated a reduction in peak temperature as the welding speed was increased. The different forces encountered during FSW/UFSW are also influenced by the temperature generated and distribution [12, 13]. The traverse and axial forces were found to be significantly increased in water as compared to air during FSW of AA 7075 due to the lowering of peak temperature [12]. Leitão et al. [13] noted a substantial increase in tool torque with an increase in both plate thickness and welding speed. From the reported literature it is observed that both cooling media and the welding parameters offer substantial effect on the temperature generation and force measurement in FSW [9–14]. The available literature reveals very few studies on the UFSW process and also information about broad range of AAs are not available. Most of the studies target the role of thermal profiles on the properties of the joint and negligible information is reported on the measurement of forces.

During FSW/UFSW the temperature generated significantly affects the welded joint mechanical properties, and its measurement can provide the foundation for process improvement. The measurement of forces acting on the tool is also a prime requirement during FSW process as it may be used to design the optimum tool, predict tool life, understand the material flow, etc. Hence, considering the advantages of UFSW over FSW and importance of temperature and force measurement during FSW/UFSW, the present work aims at analyzing the influence of welding

speed on temperature and traverse force acting on the tool during UFSW of AA 6082–T6.

2 Experimental Procedure

The BM selected for the research work was AA6082–T6 of the dimension 180 × 50 × 3 mm and the butt joint configuration was considered for UFSW. AA6082–T6 is a marine grade AA having high corrosion resistance and good strength to weight ratio. The BM alloy composition and the other important properties are specified in Table 1 and Table 2 respectively. A tri-flute tool of 17 mm shoulder and 6 mm pin diameter was used to conduct welding on a robust vertical milling machine retrofitted to perform UFSW (see Fig. 3). The tests were performed at a fixed rotation speed of 1120 rpm, plunge depth of 0.25 mm, tilt angle of 2° and varying welding speed (50, 63 and 80 mm/min) after careful assessment of the trial runs.

Table 1 The alloy composition of the BM (wt%)

Mg	Mn	Cr	Si	Fe	Zn	Ti	Cu	Al
0.75	0.58	0.021	1.10	0.29	0.042	<0.005	0.051	Balance

Table 2 The important properties of the BM

UTS (MPa)	Microhardness (HV)	% Elongation	Melting point (°C)
305	105	13	550 approx

Fig. 3 FSW arrangement with temperature and load cell measuring unit
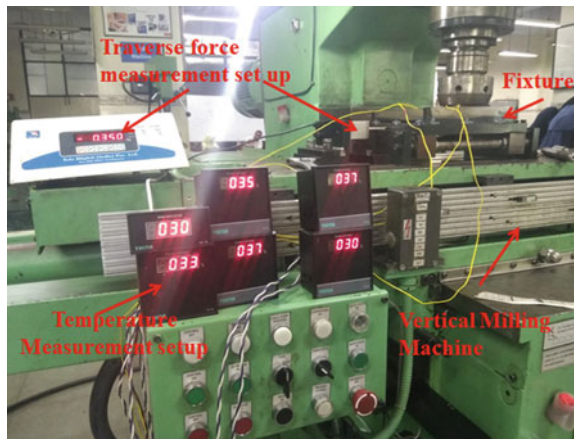
Fig. 4 The location of different thermocouples
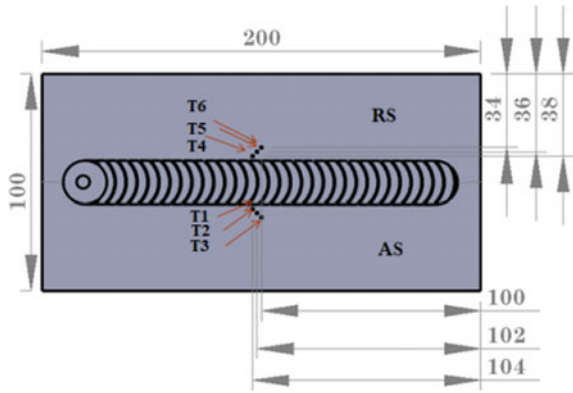
The temperature measurement was carried out using K type thermocouples (0 to 1200 °C, Mod: TDI-96) which were fixed on advancing side (AS) and RS during the welding. The thermocouple locations are demonstrated in Fig. 4. The traverse force experienced by the tool was measured as a function of distance during each experiment using a calibrated static load cell (10 kN, U9B) attached to the fixture (see Fig. 3).

3 Results and Discussion

Measurement of temperature and traverse force was successfully carried out, and the results were analyzed for investigating the influence of welding speed on the response variables. The results obtained are presented in Table 3 below.

3.1 Temperature Distribution

The degree of alteration in microstructure and mechanical properties during UFSW is reliant on the thermal history, which is influenced by welding parameters and

Table 3 Measured values of temperature and traverse force

Experiment no.	Welding speed (rpm)	Peak temperature (°C)	Peak temperature location	Maximum traverse force (kgf)
01	50	137	RS	72.33
02	63	123	AS	85.66
03	80	112	RS	103.00

cooling media involved during the welding [8, 10, 12, 14]. The temperature profiles generated at different parametric combinations are shown below in Fig. 5. During the initial tool plunging and dwelling the material below the surface of the tool gets properly stirred and the material undergoes extensive preheating and as the tool traverses the trailing portion of the tool is subjected to cooling. At the start the tool tries to push the cold material ahead of the stirred softens material resulting in initial peak values. As the preheating effect starts diminishing, further movement of the tool lowers the temperature and finally, temperature stabilizes. As such peak values are obtained initially and these values stabilize as the welding progresses.
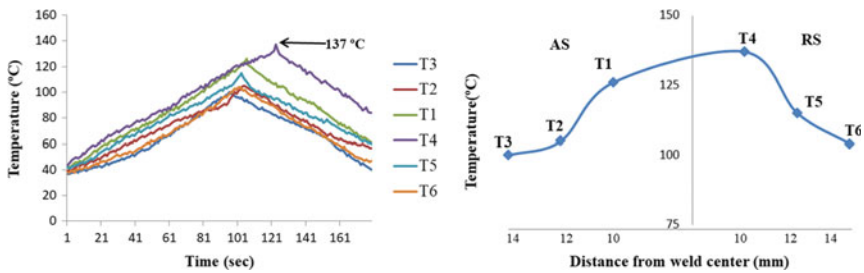
(a) The distribution of temperature along the direction of weld for Experiment 1

(b) Peak temperature along the transverse direction for Experiment 1
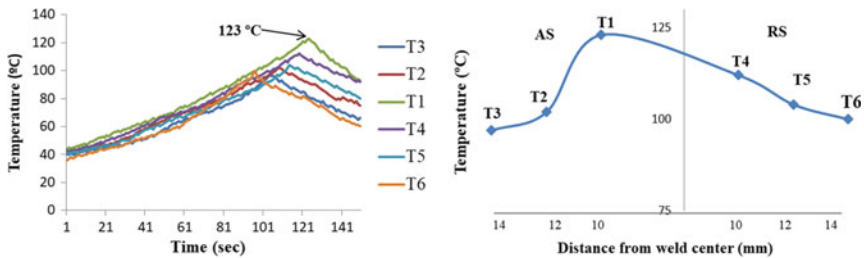
(c) The distribution of temperature along the direction of weld for Experiment 2

(d) Peak temperature along the transverse direction for Experiment 2
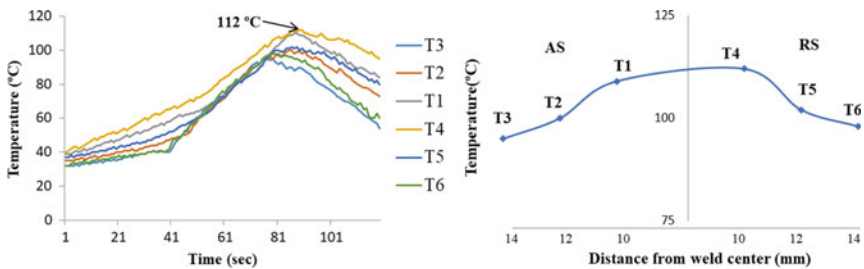
(e) The distribution of temperature along the direction of weld for Experiment 3

(f) Peak temperature along the transverse direction for Experiment 3

Fig. 5 The thermal cycle curves at a different welding speed

The increase in temperature is observed in all the welds when the tool approaches the thermocouples (T1–T6) [15]. A sudden decrease in temperature is observed as the tool moves away from the thermocouples (see Fig. 5a, c, e) because the cooling rate exceeds the rate of heat input rate just after the tool passes the thermocouples [15]. The rate of heat input decreases due to the increase in distance for heat conduction after the tool passes the thermocouples leading to a decrease in thermal gradient. The peak temperature was observed closest to the weld center in all the welds corresponding to the AS (T1) or RS (T4) during the UFSW (see Fig. 5b, d, f) [14, 15]. The peak temperature reduces due to heat dissipation as the distance from the weld center increases [14]. The peak temperature on AS was found to be higher than the RS in experiment no.2. This may be due to greater plastic deformation owing to the higher relative velocity of the tool at the AS in comparison to RS. In experiments, no.1 and 3 peaks temperature of RS were observed to be higher. In UFSW, the boiled water near the weld at AS is driven to move ahead opposing the cold water neighboring the weld and cools down rapidly and mandatorily while RS receives the warm water coming from AS, thus UFSWed joint show high temperature on RS. From the Fig. 5, it is also observed that with increasing welding speed the peak temperature decreases. The welding speed in UFSW governs the heat generation and material movement among which heat generation is significantly influenced by the welding speed. At higher welding speed less time is available for softening of the BM leading to a reduction in the heat input per unit length. Further, the cooling rate increases which causes lowering of the temperature. With the upsurge in welding speed, the strain rate also increases which lowers the temperature. As reported in the literature, a significantly low peak temperature and a thermal gradient is observed in UFSW as compared to FSW limiting coarsening of precipitates and causing enhancement in strength and hardness [8, 12, 14].

3.2 Traverse Force Generation

The synchronize traverse and rotational movement of the tool through the deforming material in UFSW process imposes a force and couple on the tool respectively. Material flow around the pin exerts traverse force during tool traverse in UFSW. The traverse force depends on the material flow stress which is linked to the temperature produced during the welding. Traverse force increases with a decrease in temperature due to increase in flow stress of the material [12].

The variation in traverse force for different welding speed is depicted in Fig. 6 and the corresponding peak values are given in Table 3. It is observed that the traverse force rises with the rise in welding speed [16]. The higher welding speed causes a rise in strain rate and a decrease in temperature. Both these situations augment the flow stress and lead to increase in traverse force [12, 17].

Initial peak and low values are observed as the tool traverse movement starts (see Fig. 6). At the starting, the tool tries to push the cold material ahead of the stirred

Fig. 6 Traverse Force plots
at the different welding speed
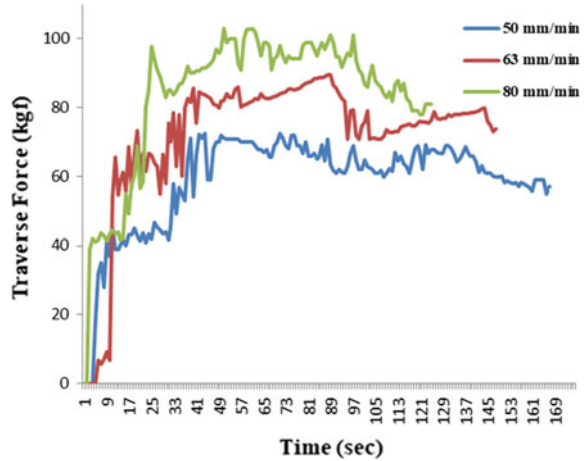
material resulting in initial peak values. The continuous deformation of the material
ahead induces additional heat which leads to a drop in flow stress of the material
causing a decrease in traverse force up to some limit. The force then stabilizes up to
some distance due to preheating effect of the tool dwell. As the preheating effect
starts diminishing, the further movement of the tool causes an increase in traverse
force due to the adequate stirring of the cold material [12].

4   Conclusion

UFSW of AA 6082–T6 was successfully performed on 3 mm thick plates at dif-
ferent welding speed. Following are some of the noticeable conclusions drawn from
the study:

- A higher welding speed resulted in lower heat generation leading to low peak
  temperature.
- The distribution of temperature during UFSW showed an identical trend as one
  moves away from the weld center at different welding speed.
- The increase in temperature was observed as the tool approaches the thermo-
  couple near to the weld center. After that, reduction in temperature is observed
  due to a decrease in thermal gradient.
- The variation in temperature and the thermal gradient is observed on AS and RS.
- An increase in traverse force was experienced with a rise in welding speed.
- A higher welding speed resulted in maximum traverse force caused by higher
  flow stresses due to high strain rate and lower temperature.
- The maximum peak temperature (137 °C) was observed at the RS in HAZ at a
  low welding speed of 50 mm/min and maximum traverse force of 103 kgf was
  attained at a high welding speed of 80 mm/min.

References

1. Cam G, İpekoğlu G (2017) Recent developments in joining of aluminum alloys. Int J Adv Manuf Technol 91(5–8):1851–1866
2. Lan S, Liu X, Ni J (2016) Microstructural evolution during friction stir welding of dissimilar aluminum alloy to advanced high-strength steel. Int J Adv Manuf Technol 82(9–12):2183–2193
3. Thomas WM, Nicholas ED, Needham JC, Murch MG, Temple-Smith P, Dawes CJ (1991) Friction stir butt welding. International Patent Application No PCT/GB92/02203 and Great Britain Patent Application No 9125978.8
4. Goel P, Siddiquee AN, Khan NZ (2018) Investigation on the effect of tool pin profiles on mechanical and microstructural properties of friction stir butt and scarf welded aluminium alloy 6063. Metals 8(1):74
5. Sharma N, Khan ZA, Siddiquee AN (2017) Friction stir welding of aluminum to copper—an overview. Trans Nonferrous Met Soc China 27:2113–2136
6. Wahid M, Siddiquee A, Khan Z, Asjad M (2016) Friction stir welds of Al alloy–Cu: an investigation on effect of plunge depth. Arch Mech Eng 63(4):619–634
7. Sharma C, Dwivedi D, Kumar P (2012) Influence of in-process cooling on tensile behaviour of friction stir welded joints of AA7039. Mater Sci Eng, A 556:479–487
8. Wahid MA, Khan ZA, Siddiquee AN (2018) Review on underwater friction stir welding: a variant of friction stir welding with great potential of improving joint properties. Trans Nonferrous Met Soc China 28(2):193–219
9. Wahid M, Siddiquee AN, Khan ZA, Sharma N (2018) Analysis of cooling media effects on microstructure and mechanical properties during FSW/UFSW of AA 6082–T6. Mater Res Express 5:046512. http://iopscience.iop.org/10.1088/2053-1591/aab8e3
10. Fratini L, Buffa G, Shivpuri R (2010) Mechanical and metallurgical effects of in process cooling during friction stir welding of AA7075–T6 butt joints. Acta Mater 58:2056–2067
11. Buchibabu V, Reddy GM (2017) Probing torque, traverse force and tool durability in friction stir welding of aluminum alloys. J Mater Process Technol 241:86–92
12. Papahn H, Bahemmat P, Haghpanahi M, Sommitsch C (2014) Study on governing parameters of thermal history during underwater friction stir welding. Int J Adv Manuf Technol 78:1101–1111
13. Leitão C, Louro R (2012) Using torque sensitivity analysis in accessing friction stir welding/processing conditions. J Mater Process Technol 212:2051–2057
14. Rui-dong F, Zeng-qiang S, Rui-cheng S, Ying L, Hui-jie L, Lei L (2011) Im-provement of weld temperature distribution and mechanical properties of 7050 aluminum alloy butt joints by submerged friction stir welding. Mater Des 32:4825–4831
15. Zhao Y, Wang Q, Chen H, Yan K (2014) Microstructure and mechanical properties of spray formed 7055 aluminum alloy by underwater friction stir welding. Mater Des 56:725–730
16. Kumar R, Singh K, Pandey S (2012) Process forces and heat input as function of process parameters in AA5083 friction stir welds. Trans Nonferrous Met Soc China 22:288–298
17. Colegrove PA, Shercliff HR (2006) CFD modelling of friction stir welding of thick plate 7449 aluminium alloy. Sci Technol Weld Join 11:429–441

Design and Analysis of a Novel Cloverleaf Combustor for Scramjet Engine

K. Naveen, Mukesh Kapoor, M. S. Prasad and S. Arunvinthan

Abstract In recent years, there has been an increased interest in the field of scramjet engine and its combustor design studies. Researchers started adopting several new technologies in fulfilling the design requirements of the combustor like mixing characteristics, shock elimination, low total pressure losses, high fuel penetration, and cooling. Among them, the shock eliminating capability and the total pressure losses are some of the key challenges. In this study, a novel idea of the cloverleaf-shaped combustor is proposed to eliminate both the shock and total pressure losses encountered in a scramjet combustor. A baseline circular combustor and the modified cloverleaf combustor have been numerically investigated at Mach 3 using density based K-ω SST (Shear Stress Transport) equations in CFD. The results show that the cloverleaf structure has the tendency to eliminate the shock formation in the combustor thereby helps reducing the total pressure losses incurred in the combustor. Moreover, the reason to use cloverleaf-structured combustor is twofold, one it reduces the shock formation and the other one it provides a 16.58% increase in the flow velocity at which the continuous stabilized combustion can be achieved. Additionally, attempts were made to identify the optimized number of cloverleaf structure by testing three cloverleaf structures to eight cloverleaf structures as briefly discussed.

Keywords Scramjet · Supersonic combustor · Cloverleaf · Pressure loss

K. Naveen (✉) · M. Kapoor · M. S. Prasad
AISST, Amity University, New Delhi, Delhi, India
e-mail: k14naveen14@gmail.com

S. Arunvinthan
SoME, SASTRA Deemed University, Thanjavur, India
e-mail: arunvinthan@sastra.ac.in

1 Introduction

Over the past few years, scramjet engines have become the major consideration in the field of the propulsion System. A scramjet engine is an enhancement of the ramjet engine, which in turn allows supersonic combustion over hypersonic speeds [1]. Unlike the other jet engines, ramjet and scramjet engines require high speeds to operate. The high-speed forward motion can be achieved with the help of missiles and rockets. Despite the hurdles faced, most of the developed countries are looking forward to design and develop their own Scramjet engines. Focusing on the performance of the scramjet engine, some of the factors taken into consideration are shock elimination, total pressure loss, and its corresponding increase in velocity. The scramjet engine consists of inlet section, isolator, combustor, and nozzle section.

One of the key challenges in designing the combustor is to provide effective fuel–air mixing characteristics. Several injector configurations like wall jets, struts and swept ramps have been developed and tested by various researchers during the past two decades. Still, there are many types of injector configurations which have been studied to produce enhanced fuel–air mixing characteristics. Figure 1a shows various types of fuel injectors [2]. The basic fuel injectors represents the wall jets, which are replaced by in-stream fuel injectors to provide adequate distribution of fuel to be mixed in the combustor. Hyper mixing injectors are used under high-speed combustors, which in turn also produce shocks in the combustor. Doster et al. [3] studied the fuel mixing characteristics on conventional circular combustor by means of various injection section pylon concepts. Even though the pylon concepts provide significant enhancement in the mixing characteristics, it is also accompanied by a large increase in total pressure loss, which lead to the drop in the overall engine efficiency.

(a)   **(b)**
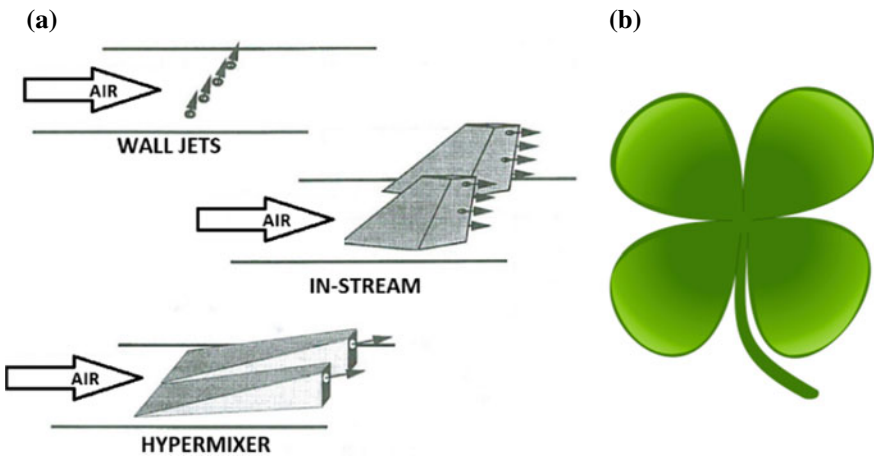
Fig. 1 a Various types of fuel injectors [2] **b** Typical cloverleaf shape

Recent studies by Rock et al. [4], presented the increase in fuel–air ratio with a large total pressure loss with four struts attached in a circular scramjet combustor. Hence, placing struts and pylons on the combustor causes large total pressure loss on fuel injection, which can overcome by proposing the shape transition.

Researchers came up with an idea of lobbed combustors to inject the fuel along the airflow. Such lobbed design gives an advantage of fuel injection as well as for improving the performance of the combustor on other parameters. Zheng et al. [5] analyzed comparison between different shape transitions like elliptical, rectangle and quasi-rectangle, of entry and exit of nozzle design which revealed to be more efficient than the conventional design. Among the various shapes of transition combustors developed, clover shape was also developed in the study. Samitha et al. [6] studied the performance of clover nozzle inspired from the cloverleaf shape as depicted in Fig. 1b. The results implied that the clover nozzle performs comparatively better than the conventional nozzle in terms of velocity distribution, momentum distribution, Mach number distribution, and stagnation pressure drop. Samitha et al. [7], also revealed that clover nozzle configuration can eliminate the use of pylon injectors for fuel injection, which in turn helps in eliminating the formation shocks. Similarly [8], they also have reported that the clover nozzle contributes effective fuel–air mixing characteristics without an excessive increase in pressure loss and the performance is enhanced over the conventional nozzle.

Ming-bo Sun et al. [9], studied a circular-to-clover shape transitioned combustor design. They numerically investigated that no shock pressure loss is formed in the clover combustor as the clover walls can initiate fuel injection in the supersonic combustor. Hence, the circular-to-clover shape transition enhances the combustor without a high supply of pressure along increasing Mach numbers.

The main objective of this work is to design and analyze a novel clover leaf combustor of a scramjet engine which increases velocity and reduces total pressure loss. Additionally, the cloverleaf combustor also reduces the formation of shock. The circular-to-clover transitioned combustor is tested at an initial condition of Mach 3. The novelty part of work is the design of transitioned shape of the cloverleaf combustor that is various configurations, from 3-cloverleaf to 8-cloverleaf, at the exit section of injection section was designed and tested at similar initial conditions. The tested cloverleaf shapes are compared in order to provide the optimum shape of cloverleaf combustor of a scramjet engine.

2   Computational Methodology

The general schematic representation of the circular combustor consisting of injection section, flame holding section, and expansion section is shown in Fig. 2. The baseline of the circular combustor injection section is presented in Fig. 3 and the 4-clover leaf combustor injection section is presented in Fig. 4.

As shown in Fig. 6, the cloverleaf combustor injection section is designed with an inlet section of 254 mm in diameter (D_1) and an outlet section of 350 mm in
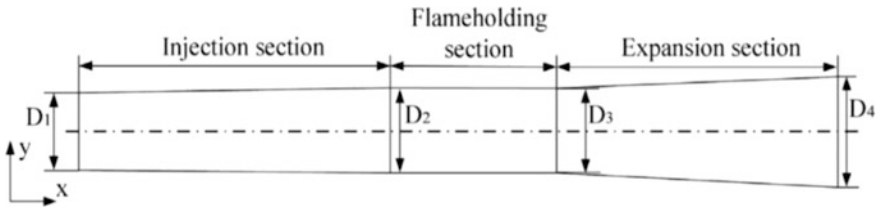
Fig. 2 A schematic diagram of the circular combustor [9]

Fig. 3 Baseline circular and clover combustor injection section
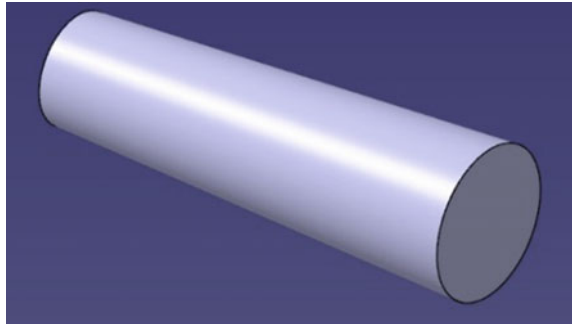
Fig. 4 Four cloverleaf combustor injection section
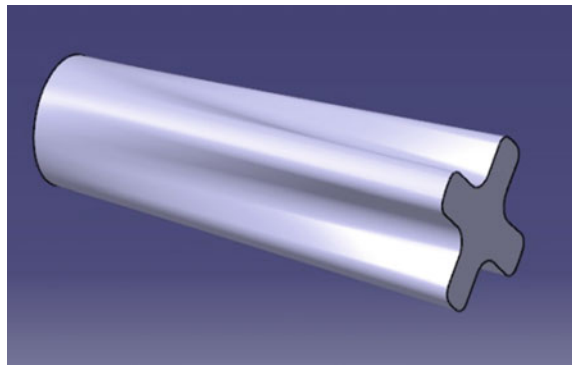
diameter (D_2) alongside a length of 1064 mm. The specification of clover shape is designed at the outlet section and it is inscribed within a circle (bigger dotted circle) of diameter D_2 350 mm. The internal circular space limit (smaller dotted circle) D_3, which is tangential to the clover troughs is 157.8 mm. Each clover troughs and clover crests are equally spaced over 360 degrees. Likewise, each clover trough and clover crest are designed at equal angles with respect to the number of cloverleaf structure to be designed in it. The angles for all the clover leaf shapes are shown in Table 1.

Fig. 5 Geometric sketch of 4-clover shape structure

Fig. 6 Front view of cloverleaf configuration
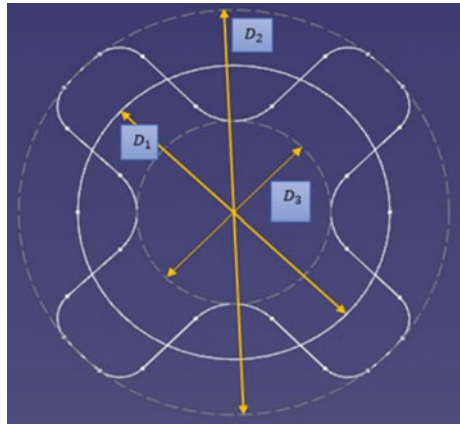
Table 1 Angle between clover crest and clover trough and the number of curvature points on various clover configurations

Model	Curvature points on each cloverleaf	Angle between clover crest and clover trough	Total curvature points on a clover shape design
3-clover	6	60°	18
4-clover	6	45°	24
5-clover	6	36°	30
6-clover	6	30°	36
7-clover	6	25.71°	42
8-clover	6	22.5°	48

Shape transition design from a circular inlet to a cloverleaf-shaped outlet has been made using the number of curvature points on the circular and clover sketches. As shown in Fig. 5, there are 6 curvature points on each of the cloverleaf. Hence, the shape transition is carried out on 24 curvature points from the circular inlet to 4-cloverleaf-shaped outlet. Similarly, the same methodology has been implied to design 3–8 clover-shaped combustors using the number of curvature points on the cloverleaf sketch. Table 1 illustrates the number of curvature points on 3–8 cloverleaf-shaped sketch designs. In Fig. 7, 3–8 cloverleaf shape structure has been shown with their respective curvature points as mentioned in Table 2.

From Fig. 7, it can be seen that the increase in the number of cloverleaves in the combustor reduces the cost of manufacturing. As the number of cloverleaves increases, the thickness between each clover leaf decreases. Hence, the 8-cloverleaf combustor requires a lesser quantity of material than the other clover shape combustors. The advantage of inscribing the clover shape inside a circle is that it can be easily implemented/installed over conventional circular existing scramjet engines. This gives us the benefit in the modification of an existing aircraft. The preliminary design of complete circular combustor and circular-to-clover transition combustor of a scramjet engine is shown in Figs. 8 and 9. From the geometric methodology, various configurations of cloverleaf combustors that are from 3 to 8 clover-shaped combustor injection sections were designed.

(a) 3-Clover leaf structure   (b) 4-Clover leaf structure   (c) 5-Clover leaf structure

(d) 6-Clover leaf structure   (e) 7-Clover leaf structure   (f) 8-Clover leaf structure
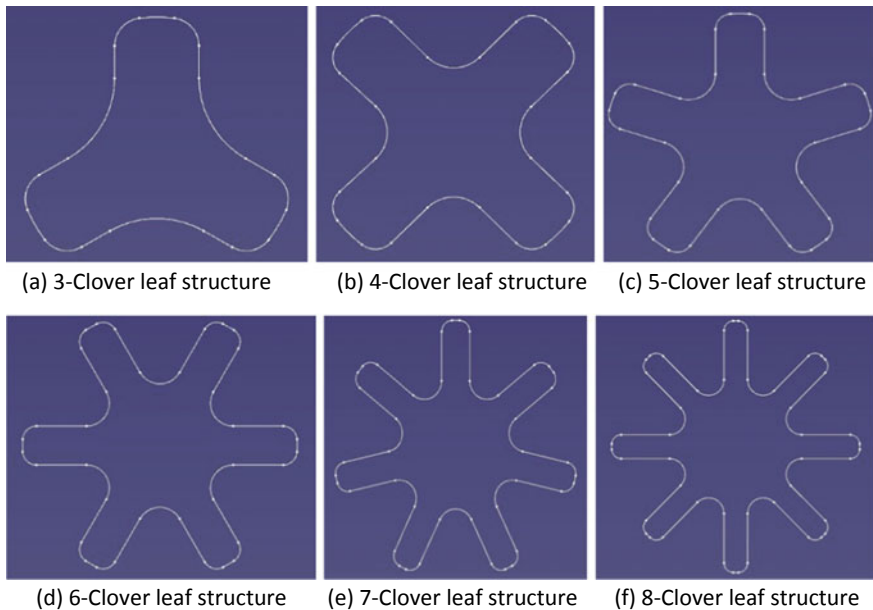
Fig. 7 Sketch of 3–8 cloverleaf combustors

Table 2 Initial conditions for the CFD simulations

Parameters	Initial conditions
Mach number	Ma = 3
Stagnation temperature	T_o = 1650 K
Stagnation pressure	P_o = 2000 kPa

Fig. 8 3D model of circular combustor scramjet engine
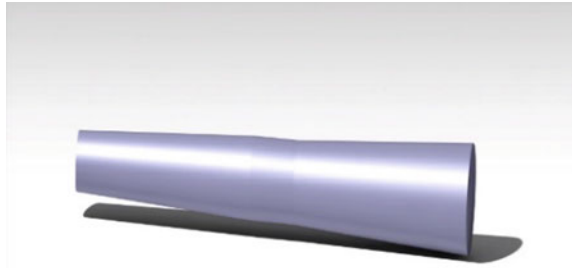
Fig. 9 3D model of circular —to—clover combustor scramjet engine

The respective cloverleaf combustor injection section models have been finely meshed. For the CFD simulations, k-ω SST model has been used. It is a 2-equation turbulence model which is used for simulating flow in the viscous sublayers.

In this work, it was assumed that the flow through the injection sections are compressible flows and the flow is also assumed to be viscous. The flow simulation for the clover combustor injection section has been performed using k-ω SST model because it is more suited for shape transition flows as the k-ω SST model is used on low Reynolds flow applications. Hence, for solution initialization, Reynolds Averaged Navier Stokes (RANS) equation using k-ω SST model for turbulent flow have been used on the cloverleaf combustor. For the RANS equation, the k-ω SST model has been used for viscous calculation. k-ω SST model is used to calculate the flow in near-wall conditions as the flow is calculated along the transitioned shape from circular to desired clover shape of the combustor. CFD simulations were performed on a steady state, double precision solver. For validation and verification, a comparison is performed between the novel clover combustor and the clover

combustor investigated by Ming-bo Sun et al. [9]. By verifying the increase in velocity on the cloverleaf combustors, the novel cloverleaf combustor obtained a deviation of 1.612% from the cloverleaf combustor of Ming-bo Sun et al. Table 3 represents the validation and verification of the novel clover leaf combustor. The initial conditions in Table 2 based on Ming-bo Sun et al. [9] have been utilized in this study.

To rely on the simulation results aiming at identifying the grid independence various mesh dimensions of 0.4, 0.55, 0.7, 0.9, and 1 million elements were tested and their corresponding results are depicted in Fig. 10. The mesh used for this entire simulation is chosen as 0.7 million elements as the Mach number results generated from these were found to be more accurate against the results produced by Ming-bo Sun et al. [9]. The CFD simulations were performed on the validated clover leaf combustor and the results were obtained on maximum velocity and total pressure loss. A similar analytic process has been performed on various configurations of cloverleaf combustor. The results were obtained for maximum velocity and total pressure loss. The test results were investigated and compared.

Table 3 Validation and verification of cloverleaf combustor

Attributes	Reference value (Ming-bo Sun et al. [9])	Numerical value
Mach No.	3.1	3.0559
Velocity	1063.61	1048.506
Deviation	1.612%	
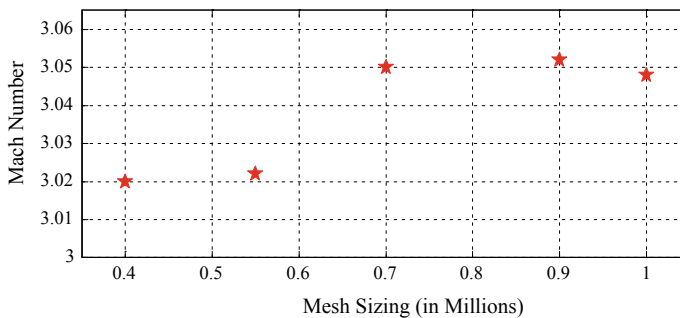
Fig. 10 Mesh independence study of Mach number and Mesh sizing (in millions)

3   Results and Discussions

3.1   *Maximum Velocity*

The results obtained from the above computational analysis, in the case of velocity, increases along the flow through the combustor. As shown in Table 4, the velocity at the outlet of the injection section is the maximum velocity of the combustor. Figure 12 represents the velocity contours from 3–8 clover leaf combustors. From Fig. 12, it is observed that the velocity increases from right to left side of each of the contour from 3–8 clover leaf combustors. Hence, there is an increase in maximum velocity from 3–8 clover combustors as mentioned in Table 4. Figure 11 represents the variation of maximum velocity (%) under various clover leaf configurations. It is because of the mass flow rate increases along the shape transition from circular to clover shape. Hence, the velocity increases greatly when it flows through asymmetric shapes. By increasing the cloverleaf from 3–8 clover in the combustor the asymmetric flow increases the maximum velocity along 3–8 clover leaf combustors. Therefore, an increase in velocity of the cloverleaf-structured scramjet engines is due to asymmetric flow along each cloverleaf structure.

From various shapes of clover combustors, the velocity contours for 3–8 cloverleaf combustors as shown in Fig. 12, the clover combustor with the 8-Cloverleaf structure has achieved an increase in velocity of 0.5 Mach that is 16.58% increase in velocity, as shown in Graph 1. It is also observed that the
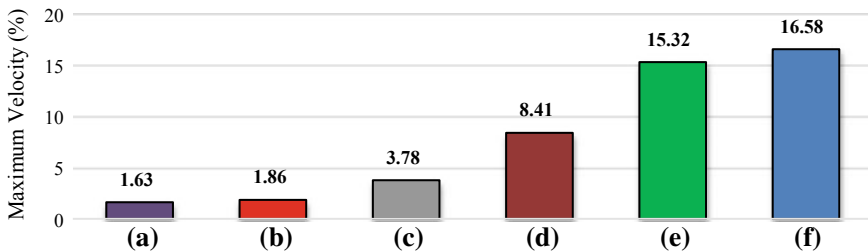
Fig. 11 Evaluation of Maximum velocity (%) under various clover configurations

Table 4 Overall Comparison of 3–8 clover combustor configurations

Models	Maximum total pressure (KPa)	Total pressure loss (KPa)	Maximum velocity (m/s)
3-Clover	733	1267	1046.15
4-Clover	667	1333	1048.506
5-Clover	753	1247	1068.21
6-Clover	790	1210	1115.89
7-Clover	801	1199	1187
8-Clover	838	1162	1200

(a) Velocity contour of 3-Clover leaf   (b) Velocity contour of 4-Clover leaf

(c) Velocity contour of 5-Clover leaf   (d) Velocity contour of 6-Clover leaf

(e) Velocity contour of 7-Clover leaf   (f) Velocity contour of 8-Clover leaf
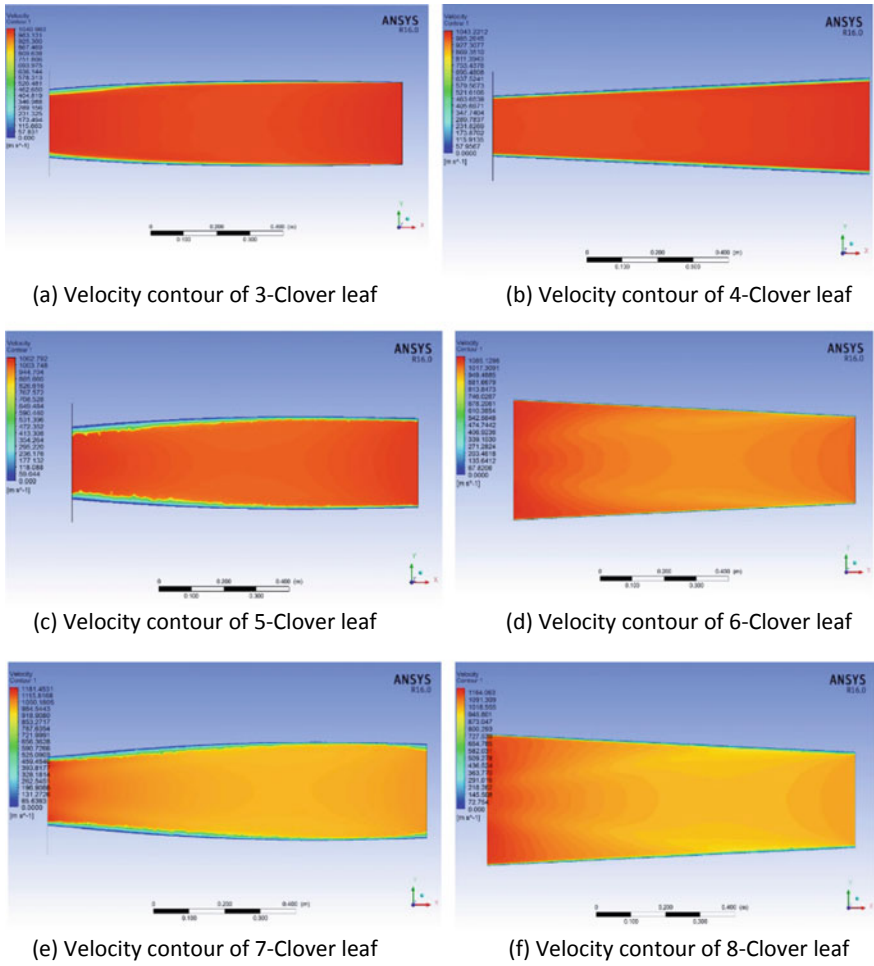
Fig. 12 Velocity contours of 3–8 cloverleaf combustors
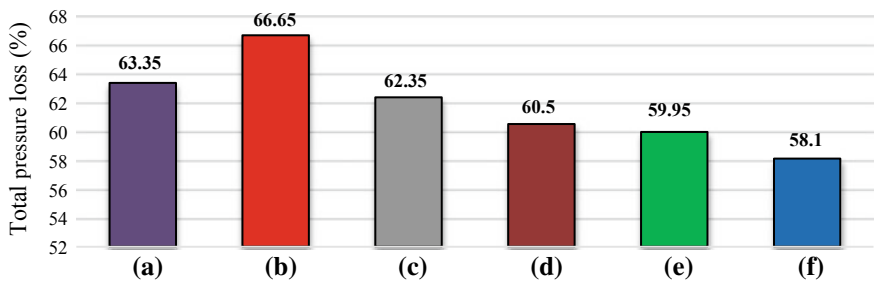
Fig. 13 Evaluation of Total Pressure Loss (%) under various clover configurations

velocity increases gradually from Mach 3 to 3.49 (3.5 approx.) with the increasing number of cloverleaf structures. From the above results, it is concluded that cloverleaf combustor injection section produces greater velocity along the supersonic flow of the scramjet engine.

3.2 Total Pressure Loss

The results obtained from the above computational analysis, in the case of total pressure, decreases along the flow through the combustor. As shown in Table 4, the total pressure at the outlet of the injection section is the maximum total pressure of the combustor. Figure 14 represents the total pressure contours from 3–8 clover leaf combustors. From Fig. 14, it is observed that the total pressure decreases from right to left side of each of the contour from 3–8 clover leaf combustors (total pressure drop from inlet to outlet of the combustor). Hence, there is an increase in maximum total pressure at the outlet of the 3–8 clover combustors as mentioned in Table 4. The total pressure loss is calculated as the difference between the pressure at initial condition and maximum total pressure obtained. Figure 13 represents the variation of total pressure loss (%) under various clover leaf configurations. It is observed that there is a gradual decrease in total pressure loss from 1333 kPa to 1162 kPa, as shown in Table 4, with an increase in the number of cloverleaf structures. Hence, 8-cloverleaf combustors produce a lesser total pressure loss of 58.1%, as shown in Fig. 13. The results imply that significantly the total pressure loss is less in 8-cloverleaf combustor as compared to the other clover leaf combustors. On such a combustor the reduction in shock formation also occurs since the shock downstream is less than the shock upstream. From the above results, it is concluded that cloverleaf combustor injection sections can reduce the loss in total pressure and additionally reduce shock formation along the supersonic flow of the scramjet engine.

3.3 Optimum Shape

From the results obtained, it is concluded that the clover shape combustor has achieved the objective that is, attaining greater velocity and reduced total pressure loss, as observed from Table 4. Cloverleaf combustor also demonstrates that it reduces shock since it produces a reduced total pressure loss than the conventional circular combustor. It is due to the asymmetric flow through the cloverleaf combustor which increases the velocity along the shape transition from circle to clover shape of the combustor. Due to increased velocity, the mass flow rate through the cloverleaf combustor is also increased. Hence at the edges of each cloverleaf shape

(a) Total pressure contour of 3-Clover leaf

(b) Total pressure contour of 4-Clover leaf

(c) Total pressure contour of 5-Clover leaf

(d) Total pressure contour of 6-Clover leaf

(e) Total pressure contour of 7-Clover leaf

(f) Total pressure contour of 8-Clover leaf
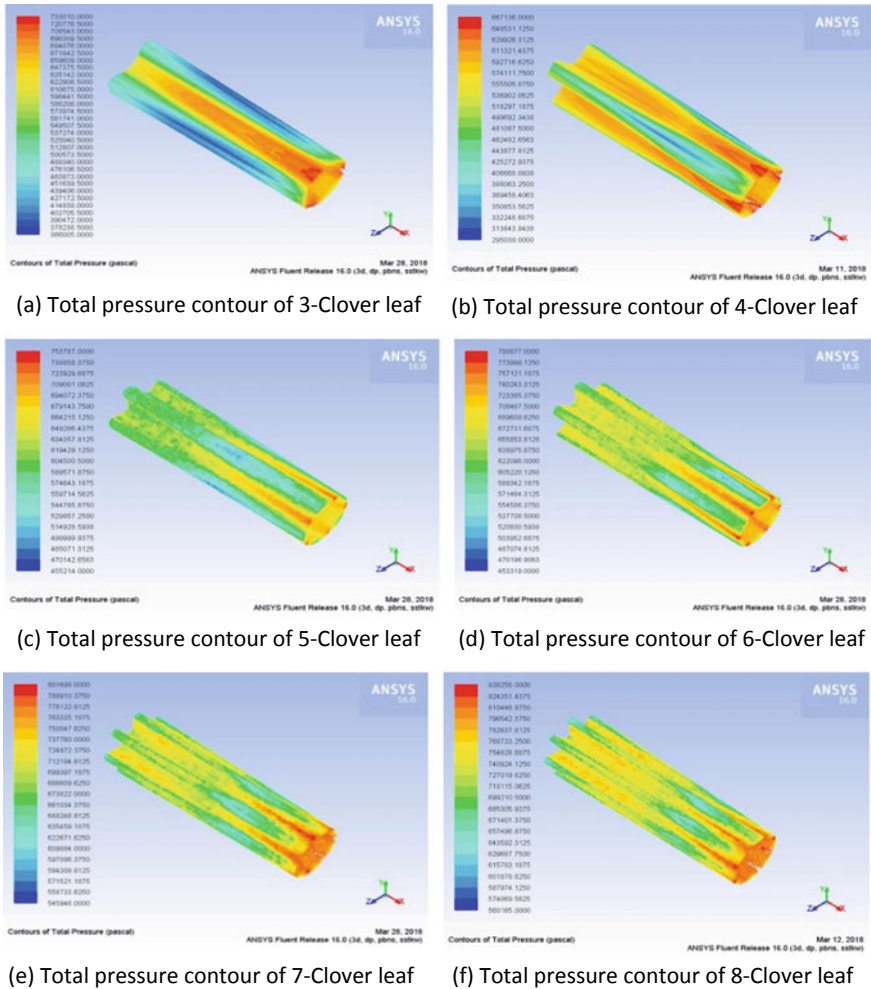
Fig. 14 Total pressure contours of 3–8 cloverleaf combustors

increases the velocity, thereby producing a greater increase in velocity than the conventional circular combustor. More the number of edges in the cloverleaf combustor more the increment in velocity.

Over the various configurations of cloverleaf combustor designed, 8-cloverleaf combustor has achieved: (i) maximum velocity (Fig. 12f), (ii) shock reduction and (iii) minimum total pressure loss (Fig. 14f) than the other clover leaf combustors. Hence, in this study, the 8-cloverleaf combustor has been identified as the optimum clover leaf combustor for a scramjet engine.

4 Conclusion

In this work, a novel clover leaf combustor for a scramjet engine has been designed. The circular-to-clover combustor has been analyzed for supersonic flow conditions at Mach 3. From the analysis, the cloverleaf combustor achieved greater velocity and reduced loss in total pressure. Additionally, the reduction in shock formation was investigated. Various shapes of clover combustors were designed, analyzed and compared under similar initial conditions. A circular combustor was tested for comparison. The results obtained from the comparison implied that 8-cloverleaf combustor is the most optimum clover leaf combustor, which produced 16.58% increase in velocity and 58.1% reduced total pressure loss. Additionally, it reduced the formation of shock in the cloverleaf combustor. Therefore, the results illustrate that the cloverleaf combustor will enhance the performance of the scramjet engine on velocity and total pressure loss. Therefore, the use of cloverleaf (8 cloverleaves) combustor provides a better efficiency on velocity and total pressure loss.

Further, the experimental and practical investigation is required on the novel clover leaf combustor to provide greater velocity and reduction in total pressure loss. The flame holding section of the combustor can further be designed and analyzed for producing enhanced Fuel–Air mixing characteristics. The expansion section of the combustor needs to be experimentally investigated with various clover leaf configurations in order to provide greater velocities after combustion and reduction in shock formation.

References

1. Segal C (2009) The scramjet engine: processes and characteristics. Cambridge University Press, The Edinburgh Building, Shaftesbury Road, Cambridge, UK
2. Kutschenreuter P (2000) Supersonic flow combustors in scramjet propulsion. In: Curran ET, Murthy SNB (eds). AIAA, New York
3. Doster JC, King PI, Gruber MR, Maple RC (2007) Pylon fuel injector design for a scramjet combustor. AIAA paper 2007–5404
4. Rock C, Schetz JA, Ungewitter R (2009) Experimental and numerical studies of a strut injector for round scramjet combustors. AIAA paper 2009–7313
5. Lv Zheng, Jinglei Xu, Mo Jianwei (2017) Design and analysis on three-dimensional scramjet nozzles with shape transition. Aerosp Sci Technol 71(2017):189–200
6. Samitha ZA, Kumar BS, Balachandran P (2008) Design and testing of clover nozzle. AIAA paper 2008–8094
7. Samitha ZA, Davis D, Balachandran P (2009) Computational study on supersonic mixing using clover nozzle. AIAA paper 2009-30
8. Samitha ZA, Swaraj Kumar B, Balachandran P (2007) Experimental study on supersonic mixing using clover nozzle. AIAA paper, 2007-8392007
9. Sun Ming-bo, Zhao Yu-xin, Zhao Guo-yan, Liu Yuan (2017) A conceptual design of shock-eliminating clover combustor for large scale scramjet engine. Acta Astronaut 130 (2017):34–42

Continuum Damage Mechanics Based Simulation of Ductile Fracture of Cylindrical Tubes

Dipankar Bora, Manoj Kumar and Sachin S. Gautam

Abstract The importance of impact problems has led to extensive research work over the years. In an impact phenomenon, the material is subjected to very short duration high force levels resulting in large plastic deformations and significant temperature rise. One of the most common phenomena of the impact problem is the occurrence of fracture. Fracture occurs when the velocity of impact is very high. In metal, it will lead to ductile fracture. Ductile fracture generally takes place due to void nucleation, then the growth of the nucleated voids and at last voids coalescence to form a micro-crack. A number of studies on ductile fracture and damage simulation in static condition have been carried out using this approach. But, there is a limited study on the prediction of fracture in impact problems. In impact problems, the effects of strain rate, stress triaxiality, and temperature on material behavior become significant. In the present work, damage growth, and effect of high strain rate are studied for ductile fracture during the high-velocity impact of cylindrical tubes using commercial finite element (FE) software ABAQUS/Explicit using continuum damage mechanics (CDM). It is shown that CDM-based modeling is able to capture the failure of the tubes.

Keywords Ductile fracture · High strain rate · Stress triaxiality

1 Introduction

Study of impact problems has important applications in various engineering fields such as automotive, aircraft, defence industry, etc. Impact problems always involve ductile fracture, which is very challenging to study. Some characteristic features of the impact problems are quick dissipation of energy, high plastic deformation, high

D. Bora · S. S. Gautam (✉)
Indian Institute of Technology Guwahati, Guwahati 781039, Assam, India
e-mail: ssg@iitg.ernet.in; ssg@iitg.ac.in

M. Kumar
National Institute of Technology Jalandhar, Jalandhar 144011, Punjab, India

strain rates, thermal softening and negative triaxiality. If the strain rate regime exceeds the limit of 10^3 s^{-1}, it is then considered as the high strain rate range. At high strain rate regime, thermal effects and strain sate effects become important and need to be considered. Mechanical response of a material varies under different loading rates including that of metals [1]. Clifton [1] has discussed a number of issues related to the dynamic response of materials and has suggested various potential research directions. Crack formation and sometimes complete fracture and fragmentation is also observed at high strain rates.

The structure of the remaining parts of the paper is as follows. Section 2 describes the plasticity model and the damage growth law. After that, the results and the necessary discussion are provided in Sect. 3. Finally, Sect. 4 concludes the paper.

2 Plasticity Model and Damage Growth Law

In the present work, AISI1045 steel [2] is used. Table 1 presents the material properties for this steel. In the present paper, the Johnson–Cook plasticity model [3] is utilized to model the plastic-hardening phenomenon. The current value of yield stress ($_Y^t\sigma$) depends on the equivalent plastic strain (ε_{eq}^P), the rate of equivalent plastic strain ($\dot{\varepsilon}_{eq}^P$) and the current value of temperature (T) as the following Johnson and Cook equation [3].

$$_Y^t\sigma = \left(_Y^0\sigma + K\left(\varepsilon_{eq}^P\right)^n\right)\left(1 - \left(\frac{T - T_{ref}}{T_m - T_{ref}}\right)^m\right)\left(1 + Cln\left(\frac{\dot{\varepsilon}_{eq}^P}{\dot{\varepsilon}_{ref}^P}\right)\right) \tag{1}$$

Here, $_Y^0\sigma$ denotes the initial yield stress, K is the hardening coefficient, and n is hardening exponent. T_{ref} is the reference temperature, T_m represents the melting point temperature and $\dot{\varepsilon}_{ref}^P$ denotes the reference strain rate. In the present work discontinuities in the form of micro-cracks or micro-voids are represented by the internal damage variable. If the voids are assumed to be distributed isotopically, then this internal damage variable can be assumed as a scalar quantity denoted by D. The damage variable is mathematically given by the area void fraction at a point in a plane as [4]

Table 1 Material properties of AISI1045 steel

E (GPa)	ν	(kg/m^3)	$_Y^0\sigma$ (MPa)	K (MPa)	n	m	C
210	0.30	7800	302	796	0.59	1.0	0.0134
$\dot{\varepsilon}_{ref}^P$	T_m (°C)	k	c (W/m °C)	α (J/kg °C)	T_{ref} (°C)	β (°C)	ς
1.0	1460	52	432.60	1.10×10^5	25	0.90	0.10

$$D = \lim_{dA \to 0} \frac{dA_v}{dA} \tag{2}$$

where dA and dA_v represent the infinitesimal area around that point and voids area covered in the plane contained by dA, respectively. Since the damage variable is introduced, it results in the concept of effective stress also. The effective stress is defined over the effective area $(dA - dA_v)$ that physically resists the applied forces. The effective Cauchy stress can be expressed as [4]

$$\sigma_{ij}' = \frac{\sigma_{ij}}{(1 - D)} \tag{3}$$

Damage growth law used in the present work is one proposed by Dhar et al. [5] for AISI-1090 spherodized steel. Damage growth law is given by

$$\dot{D} = c_d \dot{\varepsilon}_{eq}^P + (a_1 + a_2 D)(-Y)\dot{\varepsilon}_{eq}^P. \tag{4}$$

Here, c_d, a_1, and a_2 represent the material constants and Y denotes the conservative part of the thermodynamic force. The nonlinearity is introduced by utilizing the damage variable in explicit form. Dhar et al. [5] observed that the critical damage value can also be considered as material property for crack formation. Table 2 shows the value of the material constant used in the damage growth law.

3 Results and Discussion

This section presents the simulation of dynamic damage growth and various fracture patterns in thin-walled cylindrical tubes impacting against a rigid wall. A similar study has been carried out by Gautam and Dixit [2]. However, they did not show the whole fracture patterns. In this paper, a commercial FE software ABAQUS/Explicit is used to determine the stress, strain, and strain rate as well as temperature fields required for the evaluation of the damage. The damage growth law, along with the element deletion technique, is implemented in ABAQUS/ Explicit via user-defined VUMAT subroutine.

The friction coefficient (μ_f) is taken as 0.05. The range of impact velocity is 200–400 m/s. Figure 1 represents the initial geometry of the tube. The outer diameter (D_0) is 12.55 mm, length (L_0) is 62.75 mm and thickness of the tube (t_0) is 0.78 mm respectively.

Table 2 Various damage constants of AISI1045 steel

Material	c_d	a_1 (MPa^{-1})	a_2 (MPa^{-1})	D_{cr}
AISI1045	5.83×10^{-03}	4.04×10^{-04}	2.60	0.50

Fig. 1 Initial geometry of the
tube impact problem
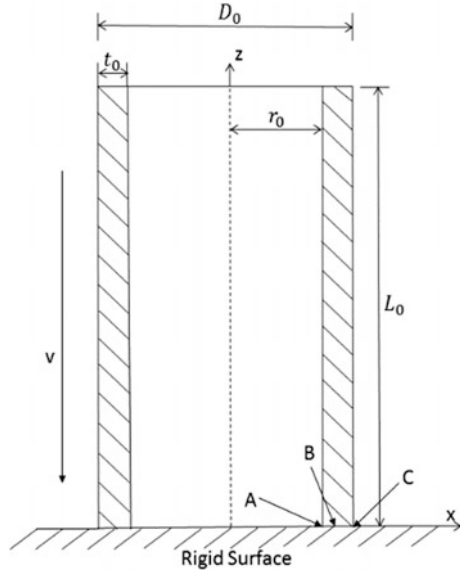
The simulated fracture patterns are not axisymmetric, therefore a solid 3-D finite
element (FE) model is created for the study. Eight-noded brick element (C3D8RT)
with a linear approximation for the displacement and temperature is employed
along with the reduced integration and hourglass control. The finite element mesh
consists of 56100 nodes and 50000 elements. The rigid wall is made as a discrete
rigid shell. The time step is chosen automatically within the solution algorithm by
ABAQUS considering the stability of the simulation. It is observed that the time
step is generally less than 0.01 μs.

3.1 Deformation of Tube Impacted at 250 m/s

In this section, the growth of equivalent plastic strain, equivalent stress and damage
is studied at the impacted end for impact velocity of $V = 250$ m/s. Deformed
configurations of the tube at different time steps is shown in Fig. 2. For a better
view, only zoomed view of the impact end is shown here.

From deformed configuration, it can be seen that deformation occurs only by
increasing the thickness of the tube at the impacting end. The material near the
impact face stops moving after the impact but the material in the upper part of the
tube is still moving with very high velocity in Z-direction, due to which bulging
occurs just above the impacted surface. Additionally, the initiation of local buckling
is also observed. As the deformation progresses, more and more buckling is
observed ($t = 20$ μs). Damage with time is plotted in Fig. 3a. From the figure, it can
be observed that damage increases more rapidly in the middle part of the impact

(a) t = 5.   (b) t = 10.   (c) t = 15.   (d) t = 20.
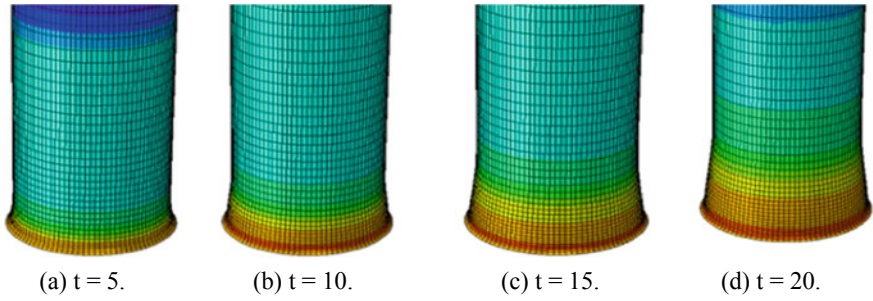
Fig. 2 The configurations of the tube at different times (in μ sec) for impact velocity V = 250 m/s. The colored contours show the von Mises stress distribution

surface. The equivalent plastic strain at three different points is shown in Fig. 3d. Damage at any part of the tube does not reach the critical value, therefore no fracture initiation takes place in the tube body.

(a) Damage with time   (b) Triaxiality with time

(c) Equivalent stress with time   (d) Equivalent plastic strain with time
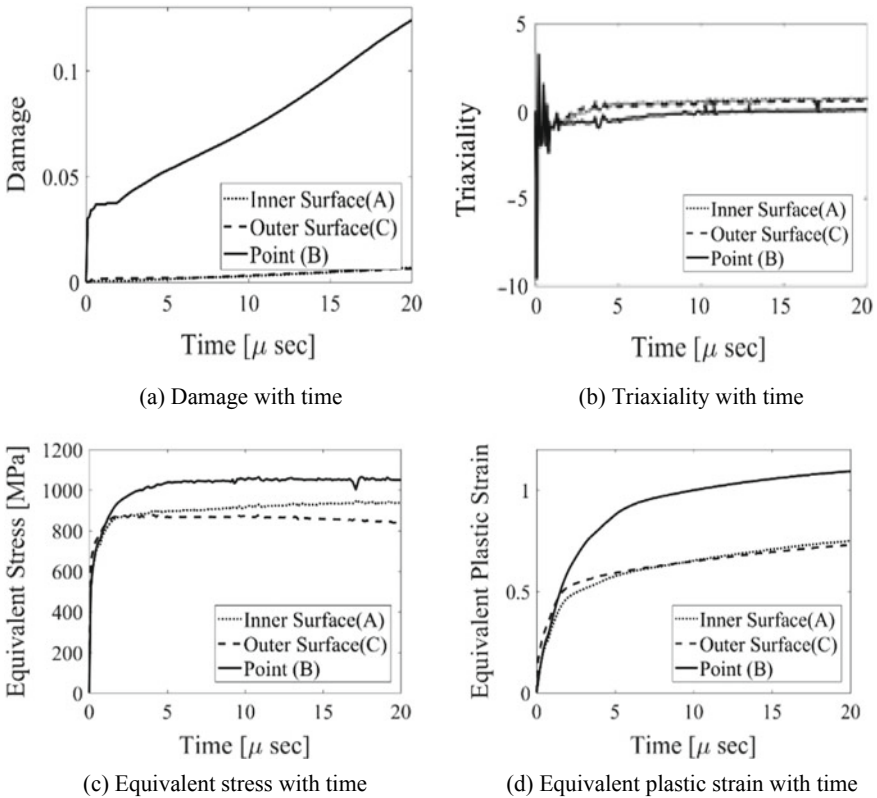
Fig. 3 Analysis of various characteristics of cylindrical tube impact at three different points on the impact surface at different time steps for V = 250 m/s

(a) t = 5.   (b) t = 10.   (c) t = 15.   (d) t = 20.
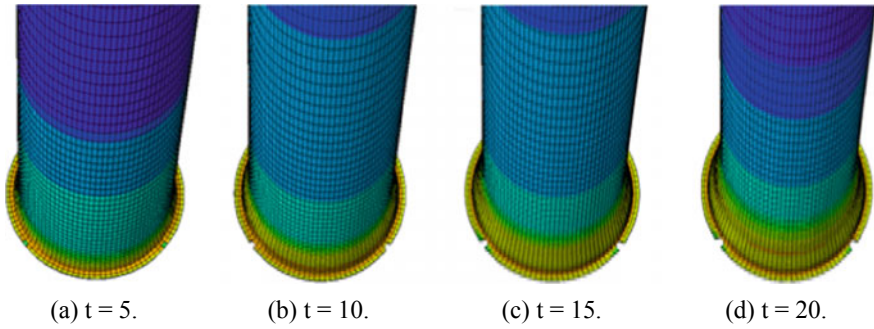
Fig. 4 The deformed configurations of the tube at different times (in μ sec) for impact velocity V = 350 m/s. The colored contours show the von Mises stress distribution

(a) Damage with time

(b) Triaxiality with time

(c) Equivalent stress with time

(d) Equivalent plastic strain with time
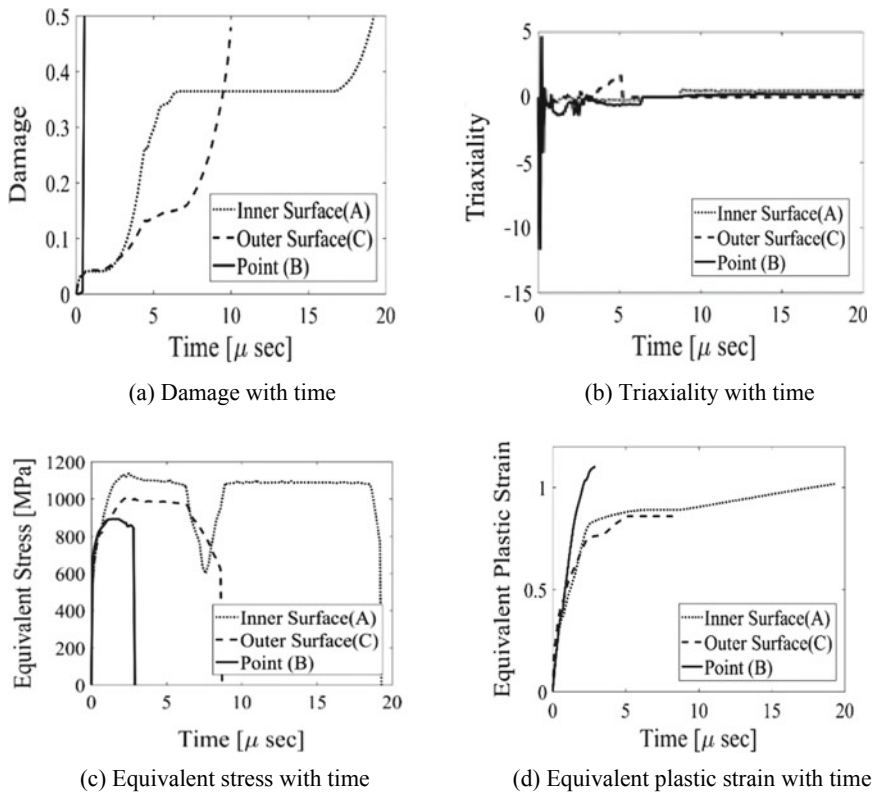
Fig. 5 Analysis of various characteristics of cylindrical tube impact at three different locations on the impact face with time for V = 350 m/s

3.2 Ductile Fracture of Tube Impacted at 350 m/s

The thickening of the tube wall just above the impact face takes place in the same manner as in the case of $V = 250$ m/s. The thickness of the tube wall increases, with the progress of deformation and grows along the length of the tube (see Fig. 4 b, d).

As the damage at the impact surface reaches the critical value, a crack initiates and grows as seen in Fig. 4b, d. Damage plot is shown in Fig. 5a. It is clear from the graph that at first damage occurs at point B followed by outer point A and inner point C. This is due to the movement of the material on either side in opposite directions. It is observed that both the plastic strain and the triaxiality plots (Fig. 5b, d) show that the failure occurs first at the middle point followed by the outer and then the inner point of the impacting surface. A similar observation has been reported by Gautam and Dixit [2].

4 Conclusion

Based on the present study it is observed that fracture has not occurred if the tube impacts the wall with $V = 250$ m/s velocity. Moreover, it is found that mushrooming and bulging takes place at the impacted end. On the other hand, fracture takes places in the middle part of the tube followed by outer part, and finally in the inner part of the tube on the impact surface for $V = 350$ m/s impact velocity. At this velocity, fracture starts at the midpoint of the tube spreads to the outer edge followed by the inner edge. The fracture pattern is quite similar to that of the experimental results on steel tubes presented by Wang and Lu [6].

References

1. Clifton RJ (2000) Response of materials under dynamic loading. Int J Solids Struct 37(1–2):105–113
2. Gautam SS, Dixit PM (2012) Numerical simulation of ductile fracture in cylindrical tube impacted against a rigid surface. Int J Damage Mech 21(3):341–371
3. Johnson GR, Cook WH (1985) Fracture characteristics of three metals subjected to various strains, strain rates and temperatures and pressures. Eng Fract Mech 21(1):31–48
4. Lemaitre J (1985) A continuous damage mechanics model for ductile fracture. Trans ASME: J Eng Mater Technol 107:83–89
5. Dhar S, Sethuraman R, Dixit PM (1996) A continuum damage mechanics model for void growth and micro crack initiation. Eng Fract Mech 53(6):917–928
6. Wang B, Lu G (2002) Mushrooming of circular tubes under dynamic axial loading. Thin Walled Struct 40(2):167–182

Modelling and Analysis of Magneto-Rheological Damper for Maximizing the Damping Force

Ashwani Kumar and **Rajat Joshi**

Abstract In this article, modelling of the magnetorheological (MR) damper and its finite element analysis (FEA) is presented. The axisymmetric FEM (finite element method) model of the MR damper was built using ANSYS Maxwell software. The MR damper was modelled using the geometrical parameters which were selected using the literature survey and then magnetic flux density was calculated and studied at the clearance space of the MR damper. The developed FEM model was used for determining the damping force of an MR damper with selected geometrical parameters. This article demonstrates that the developed FEM model for the MR damper can be used for predicting its damping force. The data gathered from this article will help the future researchers to know in depth the FEM modelling of MR damper and also provides a procedure to estimate the damping force.

Keywords Magnetorheological damper · Finite element analysis · Finite element method

1 Introduction

The behaviour of a magnetorheological damper is relatively the same when compared with the conventional fluid damper. However, MR damper behaviour changes in the presence of the magnetic field. The MR fluid is entirely different as compared with conventional fluid. MR fluid contains special elements such as polarized particles (carbonyl iron), stabilizers or a supplement, surfactants, etc. The

A. Kumar (✉) · R. Joshi
Mechanical Engineering Department, C.C.E.T. (Degree Wing), Sector -26, Chandigarh, India
e-mail: ashwanikumar@ccet.ac.in
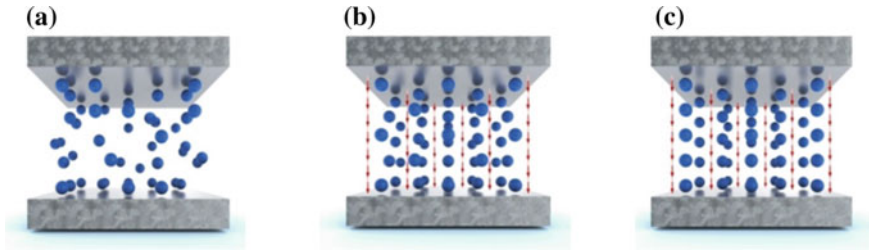
Fig. 1 Illustration of activation of the MR fluid

credit of developing the MR fluids was given to Jacob Rabinow when he was working at the US National Bureau of Standard [1]. The density of the MR fluid is very high in comparison with the density of the water and MR fluid appearance is like grease. When the flow of electric current is zero in the electromagnetic circuit of the MR damper, the MR damper behaves like a standard damper. However, as soon the electric current is increased from the zero value, the polarized particles in the MR fluid start to align in a particular fashion and formation of chain-like structure starts to begin, thereby increasing the viscosity of the MR fluid. All the polarized particles get aligned in a particular fashion at a distinct value of electric current. The MR fluid at that point has the maximum value of fluid viscosity [2, 3]. This full transformation of MR fluid from a fluid to a semi-solid is shown in Fig. 1.

The main elements of the MR damper are cylinder/housing, the piston which forms the electromagnet, piston rod and the MR fluid. The schematic diagram of the MR damper along with the MR device controller is shown in Fig. 2.
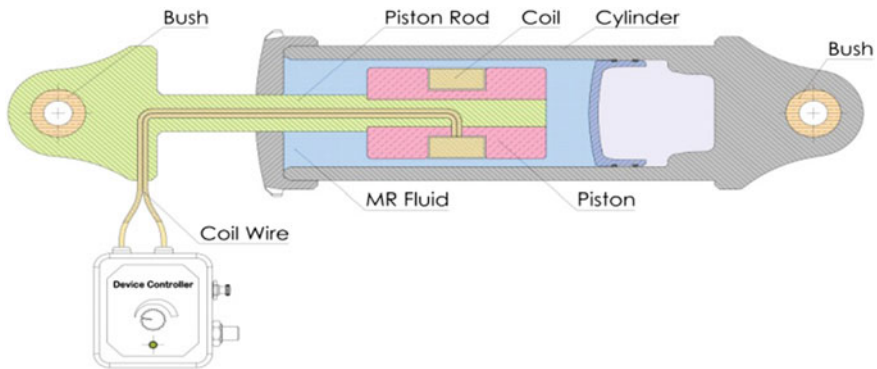
Fig. 2 Main elements of the MR Damper

The main objective of this article is to present an FEA model of MR damper which can be used to predict the damping force while considering the magnetic and MR effect resulting from the variation in the current provided to the electromagnetic coil. The finite element analysis (FEA) for the damper is essential for determining the maximum force which a magnetorheological damper can develop and for finding out its magnetic saturation [4, 5]. The advantage of having MR damper when compared with the conventional damper is that the desired and the preferred value of damping force can be obtained easily by just selecting the proper value of electric current for the MR damper. This feature of desired damping force makes the MR damper most interesting and exciting in the fields such as automotive, structural, seismic, etc. The only factor which limits or puts a brake on the value of increasing damping force is the saturation phenomenon which prevails after a particular value of the current.

2 Result and Discussion

The focus lies mainly on the range of damping force, while designing and modelling of the MR damper. The material selection plays a crucial role in the magnetic field induction and thereby on the total damping force, so the materials for the various components of the MR damper are to be selected judiciously. After the literature survey, the dimensions of MR prototype damper are selected and depicted in Fig. 3a, b.
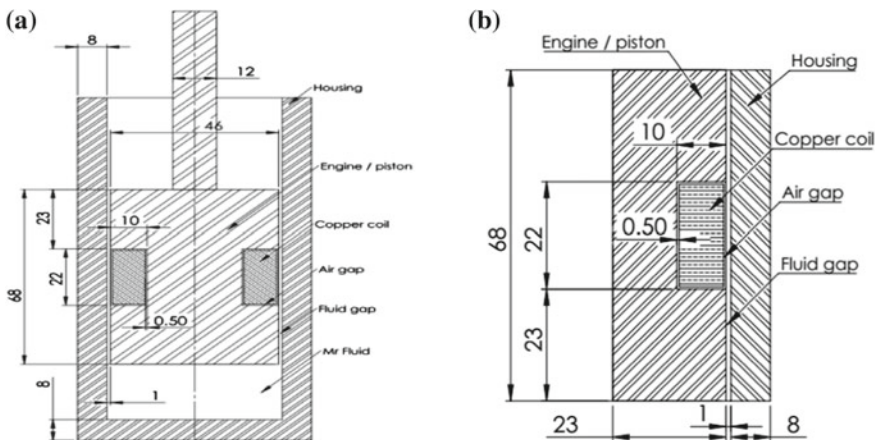
Fig. 3 **a** Various dimensions of MR fluid damper **b** Piston cross section with dimensions

Table 1 Design details of MR fluid damper

Sr. no.	Design details
1	Area of cross section of coil = 21 mm × 9 mm = 189 mm^2
2	Gauge of wire used = 24
3	Diameter of coil wire = 0.5054 mm
4	Total number of turns possible = 844 turns
5	Current through coil wire = 0.05A to 0.7 A in steps of 0.05A

During this study, the fluid gap or the clearance space or the distance between piston and cylinder was varied and during each such variation, the current through the coil was also varied. These details and variations performed on the MR damper are tabulated in Table 1. The aim of this analysis was to find the effect of changing the MR fluid gap on the overall damping force of the MR damper. During this analysis, the cross-sectional area of the coil of the MR fluid damper was kept constant.

In the analysis, a 2-D axis-symmetric model of the damper was created in ANSYS Maxwell software [6–10]. The magnetostatic analysis details for the MR fluid damper during the analysis were entered in the software and were shown in Table 2. Then, the software calculates the magnetic flux density in the various area of the MR fluid damper 2D model. Then the images of flux lines were taken out from the ANSYS software and the data values showing magnetic flux density in the desired region or the MR fluid gap region were also taken out so as to calculate the damping force produced by the damper.

Using the graphs between magnetic flux density (B) and shear stress (H) and Shear stress (H) and yield shear stress (τ_y) obtained from Lord Corp. Inc. USA [11] for MRF-132 DG, the data was gathered and processed using MATLAB software. Then, the value of shear stress was obtained using the code generated from MATLAB with respect to the magnetic flux density obtained at the various fluid gap at different levels of current ranging from 0.05 A to 0.7 A. The average value of the magnetic flux density and the shear stress over the fluid gap for various levels of current is shown qualitatively in Figs. 4 and 5. According to Bingham plastic model [12, 13], based on the plate modelling, the total damping force, F_D, is the sum of an induced yield stress component, F_τ, and viscous components, F_η, is given as

Table 2 Magneto static analysis details

1	Software used	Ansoft Maxwell		
2	Study type	Magnetostatics		
3	Model type	2D Axisymmetric about Z axis		
4	Material assigned			
	Part	Material	Material property	Value
	Piston, cylinder	Iron	Relative permeability	4000
	Coil area	Copper	Relative permeability	0.999991
	Air gap	Air	Relative permeability	1
	MR fluid gap	MRF-132DG	B-H Curve	Using Lord Corp. data
	Surrounding region	Air	Relative permeability	1
5	Excitation	Total current through the coil area was defined		
6	Analysis setup			
	Max no. of passes	18		
	Percent error	0.01%		
	Percent refine per Pass	40		
	Min. number of Passes	16		
	Min. converged Passes	1		
7	Optimization			
	Current variation	Current through coil wire = 0.05A to 0.7 A in steps of 0.05A		
	MR fluid gap Variation	The fluid gap varies from 0.5 mm to 1.5 mm in steps of 0.25 mm		
8	Result	Data table created for every parametric study and processed		
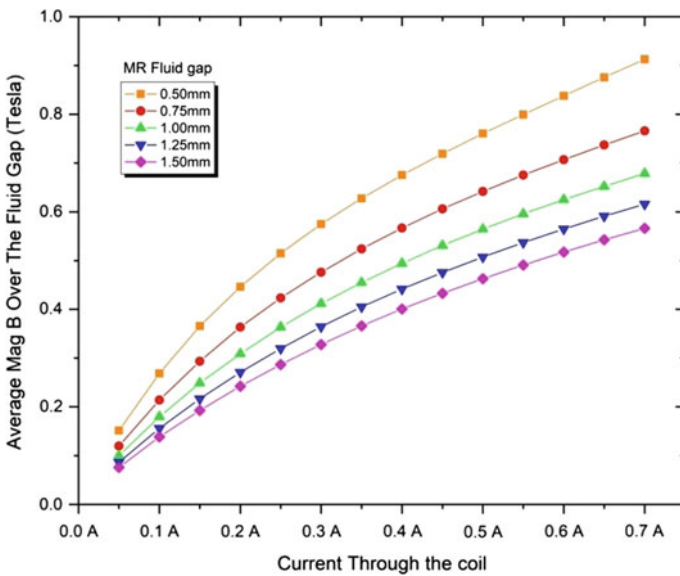
Fig. 4 Magnetic flux density at different levels of current
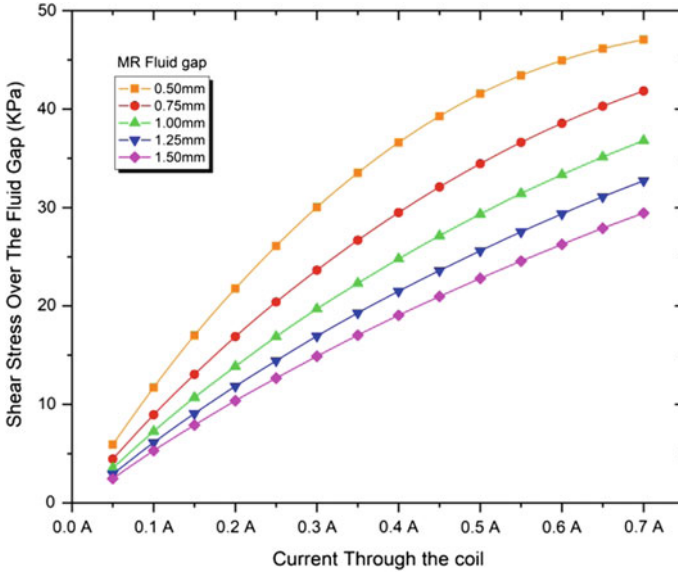
Fig. 5 Shear stress at different levels of current

$$F_D = F_\tau + F_\eta$$
$$= \left(2.07 + \frac{12Q\eta}{12Q\eta + 0.4wh^2\tau_y}\right)\frac{\tau_y LA_p}{h}\text{sgn}(v) + \left(1 + \frac{whv}{2Q}\right)\frac{12\eta QL_t A_p}{wh^3}$$

where

$$Q = A_p \times v \text{ and } A_p = \frac{\pi}{4}\left(D^2 - d_o^2\right)$$

The abbreviations used in the study are, Q is the volumetric flow rate, A_p is the effective cross-sectional area of piston, D is the diameter of the piston, d_o is the diameter of the piston rod, v is the piston velocity, τ_y is the yield shear strength of the MR fluid, η is the off-state (no magnetic field) viscosity of the MR fluid, L is the effective axial pole length, h is the gap between piston and cylinder, L_t is the total axial pole length, w is the mean circumference of the damper's annular flow path,
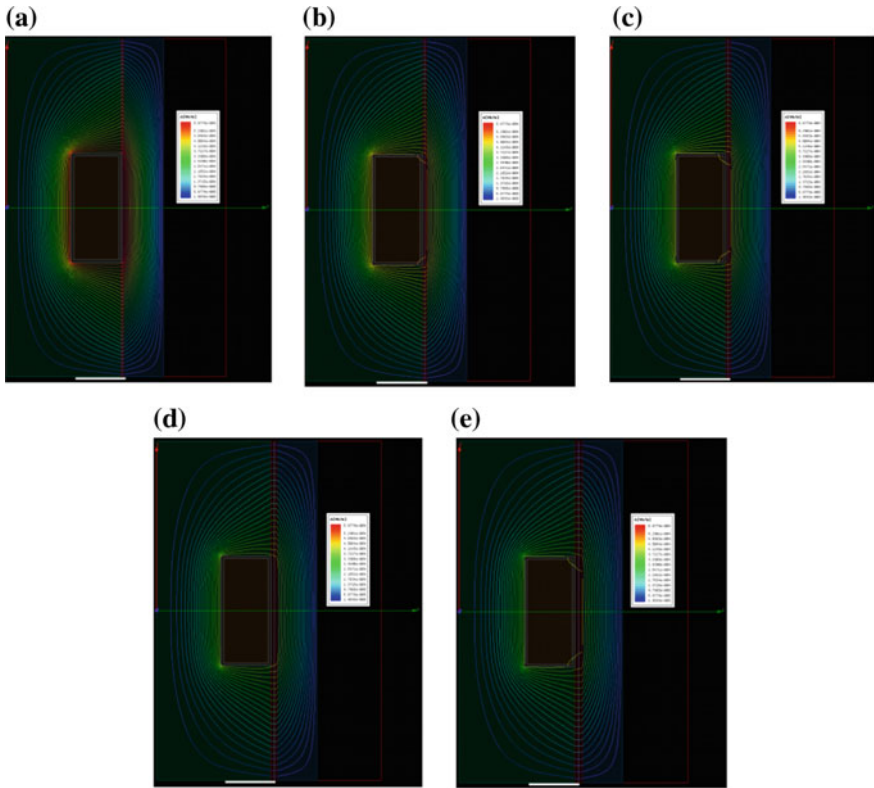
Fig. 6 **a** 2-D Flux Lines for fluid gap 0.50 mm **b** 2-D Flux Lines for fluid gap 0.75 mm **c** 2-D Flux Lines for fluid gap 1.00 mm **d** 2-D Flux Lines for fluid gap 1.25 mm **e** 2-D Flux Lines for fluid gap 1.50 mm

and *sgn(υ)* is used to consider the reciprocating motion of the piston. Total damping force of the FEM model is thus calculated using the data which is shown in Figs. 4 and 5. The 2- D flux lines for fluid gap ranging from 0.50 mm to 1.50 mm is shown in Fig. 6a–e. The magnitude of magnetic flux density for fluid gap ranging from 0.50 mm to 1.50 mm is shown in Fig. 7a–e. The damping force is calculated using the damping force equation and is tabulated in Table 3 and shown qualitatively in Fig. 8.
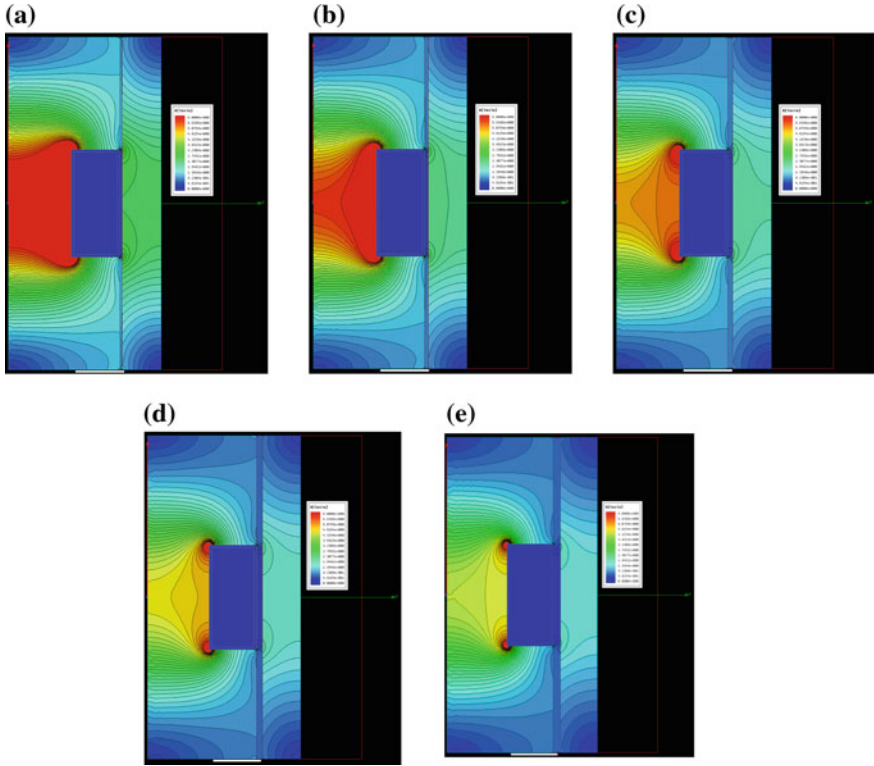
Fig. 7 a Magnetic flux density for fluid gap 0.50 mm **b** Magnetic flux density for fluid gap 0.75 mm **c** Magnetic flux density for fluid gap 1.00 mm **d** Magnetic flux density for fluid gap 1.25 mm **e** Magnetic flux density for fluid gap 1.50 mm

Table 3 Damping Force at different levels of current

Current in ampere (A)	Damping force (N) at various fluid gaps				
	0.50 mm	0.75 mm	1.00 mm	1.25 mm	1.50 mm
0.05	1006.84	474.36	272.29	173.81	118.42
0.1	1904.88	927.21	546.88	358.92	251.90
0.15	2722.98	1339.92	799.95	528.47	373.66
0.2	3460.09	1726.33	1033.09	687.73	489.22
0.25	4128.97	2080.71	1256.05	837.37	597.12
0.3	4735.83	2407.32	1463.58	981.50	700.96
0.35	5273.33	2713.11	1657.02	1117.12	801.22
0.4	5751.10	2995.45	1839.27	1244.51	896.35
0.45	6163.39	3256.89	2012.81	1365.84	986.44
0.5	6516.70	3494.24	2174.63	1481.44	1072.57
0.55	6803.37	3712.41	2328.57	1592.44	1155.06
0.6	7037.90	3907.05	2469.91	1696.96	1234.59
0.65	7223.89	4082.93	2602.16	1797.31	1311.26
0.7	7365.21	4237.93	2725.46	1891.37	1384.06
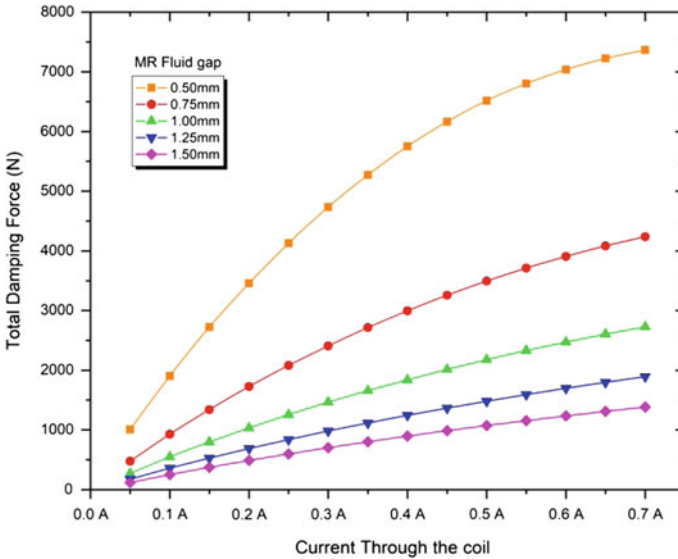
Fig. 8 Damping Force at different levels of current

3 Conclusion

In this paper, the FEM model of the magnetorheological damper and its FEA (finite element analysis) analysis was presented. The plots of 2-D flux lines and magnetic flux lines for the fluid gap which range from 0.5 mm to 1.5 mm were presented in the form of figures. It is a well-known fact that the fabrication cost of the magnetorheological damper is very high so the FEM modelling can be the best alternative to do the simulation and to find out the damping force range for the MR damper. In this study only one particular type of MR fluid, MRF-132DG Magnetorheological Fluid was used. However, there are other MR fluids available and the performance of MR damper can be checked using other available MR fluids.

References

1. Rabinow J (1948) The magnetic fluid clutch. Trans A IEEE 67:1308–1315
2. Spencer BF, Dyke SJ, Sain MK, Carlson JD (1996) Phenomenological model of a magnetorheological damper. ASCE J Eng Mech 123:1–22
3. Kumar A, Mangal S (2012) Properties and applications of controllable fluids: a review. Int J Mech Eng Res 2(1):57–66
4. Zhang HH, Liao CR, Chen WM, Huang SL (2006) A magnetic design method of MR fluid dampers and FEM analysis on magnetic saturation. J Intell Mater Syst Struct 17(8–9):813–818

5. Nguyen QH, Han YM, Choi SB, Wereley NM (2007) Geometry optimization of MR valves constrained in a specific volume using the finite element method. Smart Mater Struct 16 (6):2242

6. Sharma SK, Kumar A (2017) Ride performance of a high speed rail vehicle using controlled semi active suspension system. Smart Mater Struct 26(5):55026. https://doi.org/10.1088/1361-665X/aa68f7

7. Sharma SK, Kumar A (2018) Disturbance rejection and force-tracking controller of nonlinear lateral vibrations in passenger rail vehicle using magnetorheological fluid damper. J Intell Mater Syst Struct 29(2):279–297. https://doi.org/10.1177/1045389X17721051

8. Sharma SK, Kumar A (2018) Ride comfort of a higher speed rail vehicle using a magnetorheological suspension system. Proc Inst Mech Eng Part K: J Multi-body Dyn 232 (1):32–48. https://doi.org/10.1177/1464419317706873

9. Sharma SK, Kumar A (2016) Dynamics analysis of wheel rail contact using FEA. Procedia Eng 144:1119–1128. https://doi.org/10.1016/j.proeng.2016.05.076

10. Sharma SK, Sharma RC (2018) Simulation of quarter-car model with magnetorheological dampers for improving ride quality. Int J Veh Struct Syst 10(3) (2018)

11. LORD Homepage. http://www.lordmrstore.com/literature_231215/Data_Sheet_-_MRF-132DG_Magneto-Rheological_Fluid

12. Carlson JD, Catanzarite DM, Clair KAS (1996) Commercial magneto-rheological fluid devices. Int J Modern Phys B 10:2857–2865

13. Xu ZD, Jia DH, Zhang XC (2012) Performance tests and mathematical model considering magnetic saturation for magnetorheological damper. J Intell Mater Syst Struct 23(12):1331–1349

Multiscale Analysis of Bulk Metallic Glasses for Cardiovascular Applications

Vachhani Savan, Mehta Vatsal, Motru Suneel and M. H. Sachidananda

Abstract Bulk Metallic Glasses, an important class of amorphous metals with no long-range structural disorder, appear to have a futuristic potential for a wide range of applications. Some of the significant properties which bulk metallic glasses possess include optimistic Young's modulus, good fatigue endurance, higher strength, non-toxicity, improved wear resistance, and excellent corrosion resistance. Most vital property of Bulk Metallic Glasses is that it eliminates surface defects like cracks and crystalline defects like dislocations. These reasons have led to extensive research interest on bulk metallic glasses for biomedical applications such as implant materials. Research till date has a minimal contribution towards the development of Bulk Metallic Glasses as characteristic materials for biomedical applications. In this work, Cu-based bulk metallic glass with a compositional variation of Zr, Al and Ag alloying system is modelled using multiscale methods for cardiovascular stents. Analysis of the simulation results obtained using LAMMPS software, for various compositions of Bulk Metallic Glasses indicates an incremental change in Young's modulus, ultimate tensile strength, and fracture mechanism is by void formation. The variable strain rates have a considerable effect on the mechanical properties as well as failure mechanics. It is evident that the soft spots due to local structural variations tend to act as initiating points for fracture. The mechanical properties of Bulk Metallic Glasses obtained by Multiscale Modelling are in conformance with the requirements of cardiovascular stents, sufficing that the present compositions of Cu–Zr/Ag/Al can be considered as apt materials.

Keywords Bulk metallic glass · LAMMPS · Cardiovascular stent

V. Savan (✉) · M. Vatsal · M. Suneel · M. H. Sachidananda
Department of Mechanical Engineering, PES University, Bangalore, India
e-mail: savanvachhani10@gmail.com

1 Introduction

In 1960, an Au–Si system amorphous alloy was successfully fabricated by Klement et al. using fast cooling rates, but there were size limitations in their model [1]. In 1990, Inoue [2] suggested that the formation of an amorphous alloy is dependent upon its composition, cooling rates, and conditions namely large negative heat, three or more elements like palladium, zirconium, iron, titanium, and copper with 12% difference in atomic size. Inoue also discovered the glass-forming ability of amorphous alloys by measuring their thermal properties such as crystallization temperature (T_x), glass transition temperature (T_g) and a supercooled liquid region (ΔTx). The present-day diameters of BMG have been reported up to 2–30 mm [3, 4]. Since BMGs have superior properties such as high yielding strength which can range up to value of 6 GPa [5, 6], higher toughness, good ductility and excellent corrosion resistance, high viscosity in molten state, resistance to plastic deformation, lower thermal resistance, they have become a potential material with many applications like nuclear reactors, computer memories, coils, mobile phone cases and tennis racket. BMGs have recently attracted the attention of biomedical industry for applications like dental implants, cardiovascular stents (Co–Cr–Mo), while traditional alloys are still used in Bone-fixations (Ti-6Al-4 V), Artificial eardrum (SS316L), Screw-in bones ($Mg_{60}Zn_{35}Ca$) [7]. Stent, a metal or plastic tube in tubular or coil form is temporarily placed inside a duct, canal, blood vessel, open bile ducts, bronchi, or ureters, aids in healing or relieve an obstruction [8]. Cardiovascular stents are expandable metal mesh coils (see Fig. 1) used to improve blood flow immediately following a heart attack [9].

Stents can be manufactured using different materials like titanium–zirconium (Ti-Zr) alloys which are used in endosseous dental implants [10], biodegradable CaMgZn BMGs for skeletal applications [11], 316L stainless steel or Co–Cr alloy used for cardiovascular stents [12]. In the United States, the number of cardiac stents per 10,000 persons reported by AHRQ gradually increased from 1999 to 2006 which decreased thereafter [13].

H.M. Hsiao et al. reported that 18 mm stent is not at risk of bending or fatigue failure during respiratory motion by analysing micro-level FEA at various stresses and strains [14]. Review of stents fracture by Nair et al. [15] emphasized that fracture occurs at struts based on geometry and dimensions. The common stent

Fig. 1 Structural configuration of Cardiovascular stents
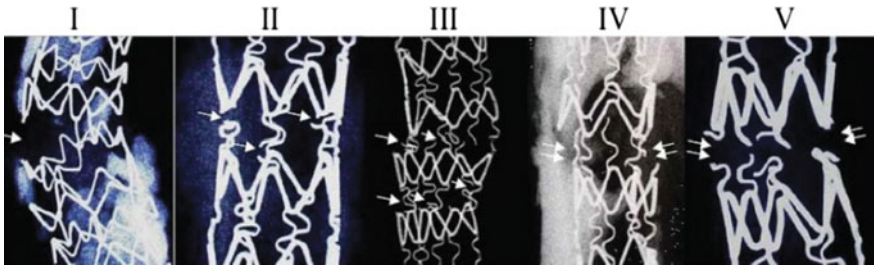
Fig. 2 Different types of fracture in a cardiovascular stent (Grade I–V) [16]

failure mechanism is due to compression, torsion, kinking and shear from repetitive cardiac contractions. According to Gaku Nakazawa et al. [16], there are different grades of fracture in a stent (See Fig. 2). In the above figure, we have grade I fracture of Taxus stent, grade II fracture of Cypher stent, grade III fracture of Cypher stent, grade IV fracture of Cypher stent and grade V fracture of Cypher stent and arrows are used to indicate the fracture in stents.

2 Research Insight

The failure of stents mainly depends on fatigue related to tension and compression. Metallic glasses undergo high cooling rates making it practically difficult to understand dynamic processes such as plastic deformation, recovery, recrystallization, and fracture, which can be studied in detail by the use of modelling and simulation [17]. Currently, the research work carried out on BMGs for biomedical applications is limited to components other than cardiovascular stents. In this research, multiscale analysis of BMGs for stents is done by LAMMPS, a parallel particle simulator at the atomic scale for the estimation of tensile properties. LAMMPS is a classical molecular dynamics code and runs on a single processor or in parallel using message-passing techniques [18].

3 Modelling Method: Molecular Dynamics Simulations

MD simulation facilitates the study on the dynamics of large macromolecules along with the optimization of resulting structures. Using the algorithm provided, MD gives a set of conformations of molecules. Atoms move under the action of instantaneous forces. There is a change in relative position and forces as the atoms moves. Initially, a set of atomic coordinates and potentials are created for the atoms in the system. Many-body potentials are used to include the effects of three or more particles interactions with each other. Embedded-Atom Method (EAM) has been

used to include the potential energies of three or more atom types. Input file consists of various parameters such as initialization, atom definition, force fields, settings, equilibration, and deformation. Under initialization, the cluster is considered to be metallic with periodic boundaries. An alloy cluster of $Zr_{40}Cu_{40}Al_{20}$ containing 32,000 atoms in a box of 66.20 Å and a system of $Zr_{40}Cu_{40}Ag_{20}$ containing 16,000 atoms in a box of 84.96 Å has been considered. The centrosymmetry parameter of each atom is calculated under the given parameters. The simulation is run using three basic files, an input file containing atomic models, a potential file containing interatomic bond energies between atoms and an executable file to run commands in the input file. Deformation of the structure is attained by applying tensile forces on the atomic cluster and can be studied by the use of an output data file, which contains the deformed atomic coordinates of the system. Thermodynamic parameters of the system like temperature, total energy, pressure and volume change as the simulation progresses, giving the desired result.

4 Result and Discussions

The molecular dynamics simulations performed using LAMMPS provide a deformed BMG under variable strain from 10^{12} to 10^{25} s^{-1}. A low strain rate revealed the effect of chosen potentials on deformation rate changing with a low deformation rate to high deformation rate with soft potentials. The quenching of BMG converts it to a rigid cluster where soft potentials do tend to require high strain rate accompanied by longer simulation times. The dependence of simulations on time steps varying from 0.002 to 0.1 made a significant improvement in reliable deformations acquired within the optimal simulation time frame. Energy minimization allowed the cluster to relax and restructure within periodic boundaries. The results obtained for multiple iterations under given parameters like quenching temperature, time step, strain rate and composition reflect upon the atom–atom interaction between different atom types (Cu–Zr–Al/Ag), interatomic separation, pair distribution function g(r), vacancy initiation followed by void formation leading to ultimate fracture. The tensile properties namely Young's modulus and ultimate tensile strength have been determined under varying strain rates for a given composition of the bulk metallic glass.

4.1 Mechanical Behavior of BMGs Stents

Under normal simulations, deformations of BMG stents take place under uniaxial tensile loading by stretching it from both ends at constant velocity and variable strain rate ranging from 10^{12} s^{-1} to 10^{25} s^{-1} as observed in Fig. 3. From the graph, it can be concluded that there is a sharp increase in the value of engineering stress
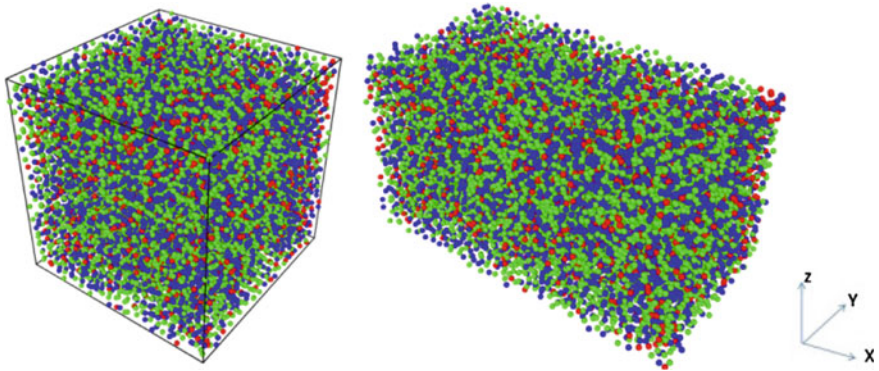
Fig. 3 Simulated modes of $Cu_{40}Zr_{40}Al_{20}$ BMG under uniaxial tensile loading at high strain rates of 10^{15} s^{-1}

when strain value is increased and thereafter fracture occurs suddenly without entering the plastic region due to the void formation as seen in Figs. 7 and 10. From the graph (Fig. 6), it can also be concluded that stress value decreases to a low value and it is analysed that $Zr_{40}Cu_{40}Al_{20}$ and $Zr_{40}Cu_{40}Ag_{20}$ BMGs are brittle in nature.

The pair distribution function of deformed clusters is calculated as shown in Fig. 4.

4.2 Young's Modulus Determination

For calculating Young's Modulus, a graph of Stress vs. Strain is plotted. The slope in the linear region gives the Young's Modulus for that composition. From the
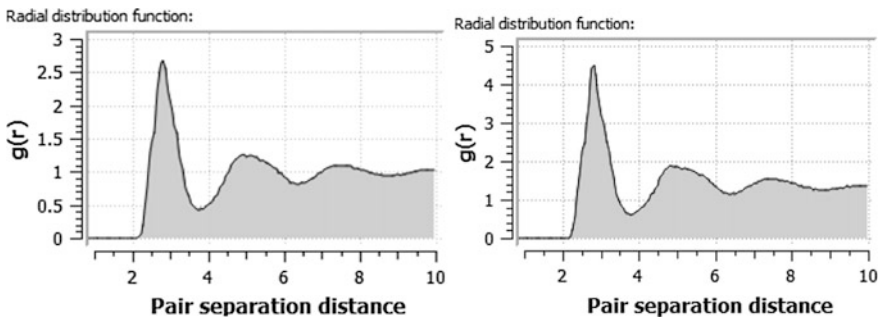
Fig. 4 Radial distribution function (RDF) showing the pair coefficient for $Cu_{40}Zr_{40}Al_{20}$ BMG. Cutoff radius is 10 Å. The figure on the left indicates RDF for non-deformed BMG and the figure on the right indicate the RDF for fractured BMG due to tensile deformation in the x-direction
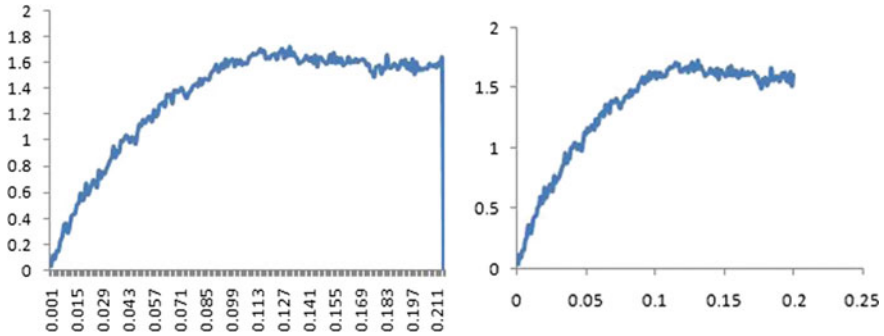
Fig. 5 Stress–Strain curves for $Cu_{40}Zr_{40}Al_{20}$ BMG for variable strains from a tensile test

Fig. 6 Stress–Strain curve for $Cu_{40}Zr_{40}Al_{20}$ BMG for the maximum strain. The slope of the stress–strain yields Young's modulus of 95.5 GPa for this composition of BMG, while the ultimate tensile strength is determined as 109 GPa
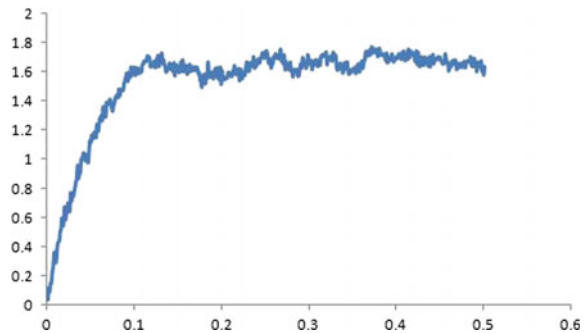
Stress vs. Strain graph of $Zr_{40}Cu_{40}Al_{20}$, Young's Modulus is found to be 95.5 GPa and from the Stress vs. Strain graph, (see Fig. 9) of $Zr_{40}Cu_{40}Ag_{20}$, Young's Modulus is found to be 108 GPa.

4.3 Effect on Properties by Changing the Composition

It is observed that properties like Young's Modulus and fracture are dependent on the composition of the bulk metallic glass. The iterations are performed by varying content of Al and Ag with the equal compositions of Cu (40%) and Zr (40%); the simulation of mechanical properties indicated an incremental change in Young's modulus. The elastic modulus increased from 72 GPa to 96 GPa for 8% to 20% Al composition, while it increased from 84 GPa to 108 GPa for the same percentage increase in Ag composition.
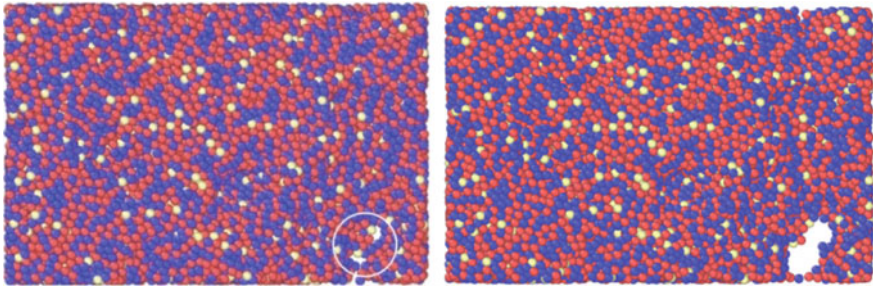
Fig. 7 Simulated modes of failure of $Cu_{40}Zr_{40}Al_{20}$ BMG by void formation during uniaxial tensile loading at high strain rates of 10^{25} s^{-1}
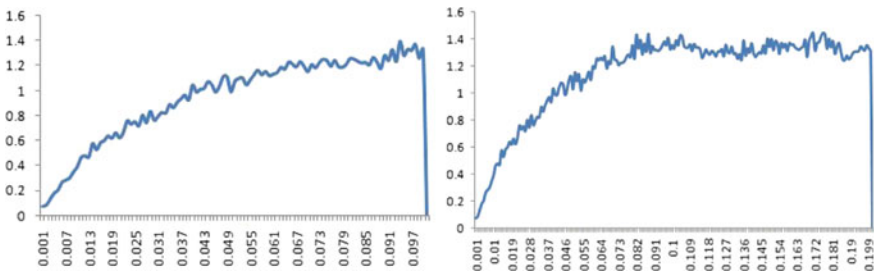
Fig. 8 Stress–Strain curves for $Cu_{40}Zr_{40}Ag_{20}$ BMG for variable strains

Fig. 9 Stress–Strain curve for $Cu_{40}Zr_{40}Ag_{20}$ BMG for the maximum strain. The slope of the stress–strain yields Young's modulus of 108 GPa for this composition of BMG, while the ultimate tensile strength is determined as 169 GPa
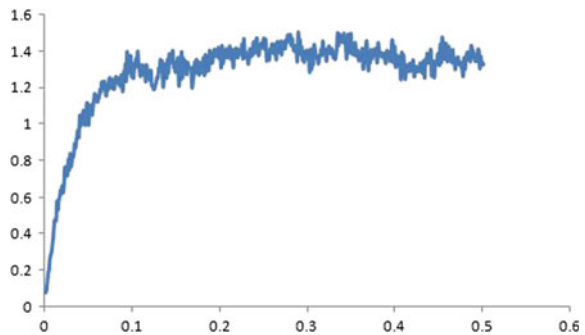
4.4 Effect of Varying Strain Rate on the Mechanical Properties

It can be observed from Fig. 5, that there is a significant change in the mechanical response of $Zr_{40}Cu_{40}Al_{20}$ for different strain rates and also from Fig. 8, for $Zr_{40}Cu_{40}Ag_{20}$ by varying strain rate, it is observed that the yield strength of the BMG is directly proportional to the strain rate, i.e. it increases with increasing strain
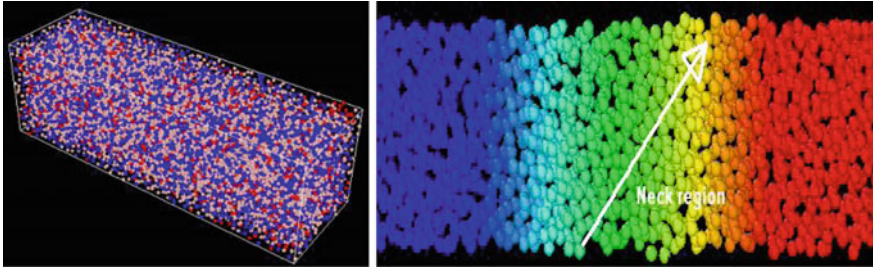
Fig. 10 Simulated modes of failure of $Cu_{40}Zr_{40}Ag_{20}$ BMG by void formation and subsequent neck formation during uniaxial tensile loading at high strain rates of 10^{25} s^{-1}

rate and vice versa. It is also observed that it takes longer for a BMG to fracture at a lower strain rate which indicates that the BMG is more brittle at higher strain rates and vice versa. The mechanical properties are determined from the respective stress–strain curve of Zr–Cu–Al/Ag compositions.

5 Conclusion

In this work, from the experimental results, it can be concluded that the fracture mechanism takes place without considerable plastic deformation when $Zr_{40}Cu_{40}Al_{20}$BMGs stent is subjected to uniaxial tensile deformation. From the tensile test result, it can be confirmed that $Zr_{40}Cu_{40}Al_{20}$ BMGs stents tend to act as brittle materials due to their characteristic failure by void formation. From the Stress vs. Strain graph of $Zr_{40}Cu_{40}Al_{20}$, Young's Modulus is found to be 95.5 GPa and from the Stress vs. Strain graph of $Zr_{40}Cu_{40}Ag_{20}$, Young's Modulus is found to be 108 GPa. From the results, we can analyse that yield stress of $Zr_{40}Cu_{40}Al_{20}$BMGs stent increases with increase in the strain rate, but fracture occurs in an early stage in case of higher strain rate and vice versa. However, it is stronger when compared to those with a lower strain rate. From observations, it can be noticed that there is a decrease in flow stress when there is in cross-section size of the sample deformed at a strain rate of 1×10^{15} s^{-1}. We can also notice that there is no significant change in the nature of stress–strain curves when the number of atoms is increased in the cluster. When strain rate increases, time to fracture reduces. Failure analysis indicates that the stress distribution was not uniform throughout the sample as the voids tend to occur near the soft spots created during the tensile deformation. Owing to their superior mechanical properties, bulk metallic glasses may become commonly used biomaterials for cardiovascular stent applications in the future.

References

1. Klement W, Willens RH, Duwez P (1960) Non-crystalline structure in solidified gold-silicon alloys. Nature 187:869–870
2. Inoue A (1995) High-strength bulk amorphous alloys with low critical cooling rates. Mater Trans, JIM 36:866–875
3. Wang JQ, Qin JY, Gu XN, Zheng YF, Bai HY (2011) Bulk metallic glasses based on ytterbium and calcium. J Non-Cryst Solids 3357:1232–1234
4. Jiang QK, Zhang GQ, Yang L, Wang XD, Saksl K, Franz H, Wunderlich R, Fecht H, Jiang JZ (2007) La-based bulk metallic glasses with critical diameter up to 30 mm. Acta Mater 55:4409–4418
5. Wang J, Li R, Hua N, Zhang T (2011) Co-based ternary bulk metallic glasses with ultra high strength and plasticity. J Mater Res 26:2072
6. Liu ZQ, Zhang ZF (2014) Strengthening and toughening metallic glasses: the elastic perspectives and opportunities. J Appl Phys 115:163505
7. Wikipedia. https://en.wikipedia.org/wiki/Amorphous_metal
8. Healthline Homepage. https://www.healthline.com/health/heart-disease/stent
9. Healthline. https://www.healthline.com/health/heart-disease/stent#procedure
10. Michelle Grandin H, Berner S, Dard M (2012) A Review of Titanium Zirconium (Ti Zr) alloys for use in Endosseous dental implants. MDPI Mater 5:1348–1360 (2012)
11. Wang YB, Xie XH (2011) Biodegradable CaMgZn bulk metallic glass for the potential skeletal application. Acta Biomater 7(8):3196–3208
12. AL-Mangour B, Mongrain R, Yue S (2013) Coronary stents fracture: an engineering approach (Review). Mater Sci Appl 4(10):606–621
13. HCUP Homepage. www.hcup-us.ahrq.gov/reports/statbriefs/sb128.jsp
14. Hsiao HM, Prabhu S, Nikanorov A (2007) Renealn, Renal artery stent bending fatigue analysis. Abbott Lab Vasc Solut J Medi Devices 1(2):113–118
15. Ravi N (2011) Nair, MD, and Kennet h Quadro's, MBBS, coronary stent fracture: a review of the literature. Cardiac Cath Lab Dir 1(1):32–38
16. Nakazawa G, Finn AV, Vorpahl M, Ladich E, Kutys R, Balazs I, Kolodgie FD, Virmani R (2009) Incidence and predictors of drug-eluting stent fracture in human coronary artery, a pathologic analysis. J Am College Cardiol 54(21):1924–1931
17. Dhal S, Raja Y (2012) Effect of size and strain rate of deformation behavior of $Cu_{50}Zr_{50}$ Metallic glasses: a molecular dynamics simulations study, B.Tech e-Thesis, NIT Rourkela
18. LAMMPS Homepage. http://lammps.sandia.gov/

Experimental Study on the Steady-State Performance of Closed-Circuit Hydrostatic Transmission Drives for the Rotary Head of Blast Hole Drill Machine Using Different Capacities Bent Axis Hydro-Motor

Alok Vardhan, K. Dasgupta and Mohit Bhola

Abstract Blast hole drill machines are used for drilling in rocks, which are of soft and medium-hard nature. In such machines, the drilling is accomplished via a hydrostatic transmission (HST) drive. This article presents the steady-state behaviours of two different HST drives for the rotary head of drill machine. In the first drive two high-speed low-torque (HSLT) hydro-motors, having an individual capacity of 10 cc/rev with the gear reducer having 15:1 gear ratio; whereas in the second drive identical numbers of hydro-motors, having an individual capacity of 16 cc/rev with the gear reducer having 10:1 gear ratio is employed. Bond graph technique has been used for modelling the drives. Based on the model, the analytical relations associating the torque loss, slip, and the overall efficiency linked with the drives are derived. By utilizing them, the performance corresponding to the HST drives is obtained in terms of the normal operating speed range linked with the drill machine utilized in mining applications. From the study it is observed that, for the constant load torque and the drill speed, the second drive (combination of two identical higher size hydro-motors along with a lower size gear reducer unit) shows better performance than the first drive (combination of two identical lower size hydro-motors along with a higher size gear reducer unit).

Keywords Blast hole drill machines · Hydrostatic transmission (HST) drive · Bond graph modelling · High-speed low-torque (HSLT) hydro-motor

Nomenclature

D_p	Volume displacement rate of the pump (m³/rad)
D_{pmax}	Maximum volume displacement rate of the pump (m³/rad)
D_m	Volume displacement rate of the hydro-motor (m³/rad)

A. Vardhan (✉) · K. Dasgupta · M. Bhola
Indian Institute of Technology (Indian School of Mines), Dhanbad,
Dhanbad 826004, Jharkhand, India
e-mail: alokvardhansinghh@gmail.com

G_r	Gear ratio of the gear reducer unit
J_{ld}	Load inertia of the driving shaft (kg m^2)
K_{cp}	Bulk stiffness of the fluid at pump plenum (N/m^5)
K_{cm}	Bulk stiffness of the fluid at hydro-motor plenum (N/m^5)
M_i	Angular momentum due to inertia load (kg m^2/s^2)
ω_p	Rotational frequency of the pump (rad/s)
Q_{mlkg}	Leakage flow of the hydro-motor (m^3/s)
Q_{plkg}	Leakage flow of the pump (m^3/s)
R_{ld}	Viscous load resistance (Nm-s)
R_{pl}	Leakage resistance coefficient of the pump (N-s/m^5)
α_{pd}	Displacement ratio of the pump
η_g	Efficiency of the gear reducer unit

1 Introduction

Hydrostatic transmission (HST) drive is the mainstay of the equipment used in the field of construction, mining, port handling sectors. The HST drive is utilized for transmitting power from one point to other in the absence of gears. The HST drive can provide the infinite combination of speed and torque, unlike gear-based system, which has a limited range depending upon the number of gear teeth. It plays a critical and important role in mobile drilling machine used in the mining operation. Considering the movement linked with the machine, rotations corresponding to the drill bit or drill penetration rate, almost all functions associated with the drill machine rely upon the functioning of its hydraulic systems.

Significant work has been carried out of late for enhancing the energy efficiency related to the HST drive. Ho et al. [1] have proposed a novel closed-loop energy saving HST system. The devised system consisted of an accumulator and flywheel in addition to pump and motor. Hui et al. [2] have contributed toward series HST system based hybrid vehicle in order to boost the fuel efficiency of the vehicle. Axin et al. [3] have analyzed the aspect of efficiency considering two systems, i.e., flow control and load sensitive intended toward multiple actuator drives. The results inferred the flow control system to be superior in energy saving and have the simpler structure and provide better stability. The efficiency features corresponding to the continuously variable transmissions, which comprise of pressure compensated pump and variable displacement motor is put forward through Vermillion [4].

Usually, in a blast hole drill machine, a primary controlled open-circuit otherwise closed-circuit low-speed high-torque (LSHT) hydrostatic transmission (HST) drive is used for rotating the drill bit. In order to accomplish that two alternative HST drive arrangements are furnished. Using two HSLT hydro-motors, having individual capacity of 10 cc/rev with the gear reducer having 15:1 gear ratio; alternatively identical numbers of hydro-motors, having individual capacity of

16 cc/rev with the gear reducer having 10:1 gear ratio are employed for driving the drill bit. A symbolic representation of the drives is depicted in Fig. 1 [5] and for controlling the speed linked with the hydro-motors, the inclination corresponding to the swash plate associated with the variable displacement pump is adjusted.

The motive of the present work is to examine the steady-state characteristics of two different primary controlled closed-circuit HST drives used in case of the rotary head of the blast hole drill machine through experimental investigations. In order to model the system, bond graph simulation technique [6] has been employed. The resistance linked with the model encompasses the losses associated with system components. Their dependence toward the system state variables is found out through experiments. By means of the type of losses, the performances of the drives are also estimated.

2 Hydrostatic Transmission Drive

Figure 1a represents the generalized figure of a closed-circuit HST drive intended during study, which basically represents two individual HST drives. The first drive comprises dual similar fixed displacement HSLT 10 cc/rev bent axis motors which successively drives the load via gear reduction unit having gear ratio 15:1, whereas the second drive consists of dual similar fixed displacement HSLT 16 cc/rev bent axis motors with gear reduction unit possessing gear ratio 10:1 driving the identical load. In case of both drives, a variable displacement axial piston pump which is being turned via a constant speed electric motor has been considered. Figure 1b indicates the loading system provided in the test setup for both the drives. The pump used in the loading system is same as that of the main pump of the hydraulic
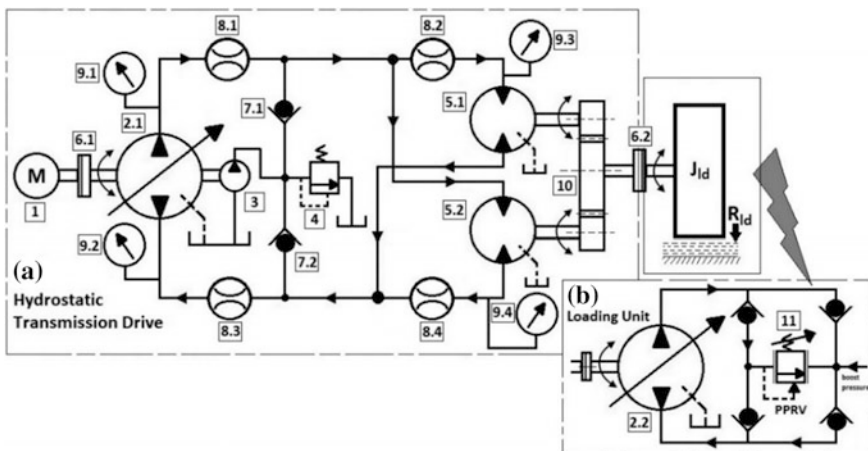
Fig. 1 Closed-circuit HST drive for the rotary head of blast hole drill machine

Table 1 List of the items

Sl. no.	Description	Item no.	Specifications
1	Electric motor	1	3-phase, 15 kW, 1460 rpm, 415 V
2	Axial piston pump	2.1, 2.2	28 cc/rev
3	Boost pump	3	Gear pump, 6.1 cc/rev
4	Pressure relief valve	4	DBDS10, 0 bar, 330 lpm
5	Bent axis hydro-motor	5.1, 5.2	10 cc/rev and 16 cc/rev
6	Speed and torque sensor	6.1, 6.2	0–2500 rpm and 0–1000 Nm
7	Check valve	7.1, 7.2	S10, 60 lpm, 315 bar
8	Flow metre	8.1, 8.2, 8.3, 8.4	Turbine flow sensor, 0–60 lpm
9	Pressure gauge	9.1, 9.2, 9.3, 9.4	S-10, 0–500 bar
10	Gear reducer unit	10	10:1 and 15:1
11	Proportional pressure relief valve	11	Pilot operated, Size 10, 0–200 bar

power unit. By adjusting the pump flow or cracking pressure corresponding to the proportional pressure relief valve (PPRV) utilized in the loading unit, the load torque experienced by the hydro-motors is varied.

The flow, speed, pressure and torque values are determined with the help of individual sensors and finally stored and recorded in the PC through DAQ. The performance of the drives was checked within the speed ranging from 20 rpm to 120 rpm and alongside the variation in torque ranging from 340 Nm to 540 Nm. While performing experiments, the temperature of oil was supposed to be kept constant at 50 ± 2 ºC by deploying cooler for keeping and maintaining the viscosity associated with the fluid approximately constant. The specification of the components employed in the test setup is given in Table 1.

3   Modelling of the HST Drive

Figure 2 depicts the bond graph representation corresponding to the model of the closed-circuit HST drive debated in Fig. 1. The subsequent system equations are deduced based on the model:

The torque due to inertia load:

$$\dot{M}_i = 2 P_m D_m G_r \eta_g - \omega_d R_{ld} \tag{1}$$

where the second quantity represents the torque developed by the hydro-motors and the third one represents torque as a result of viscous load.
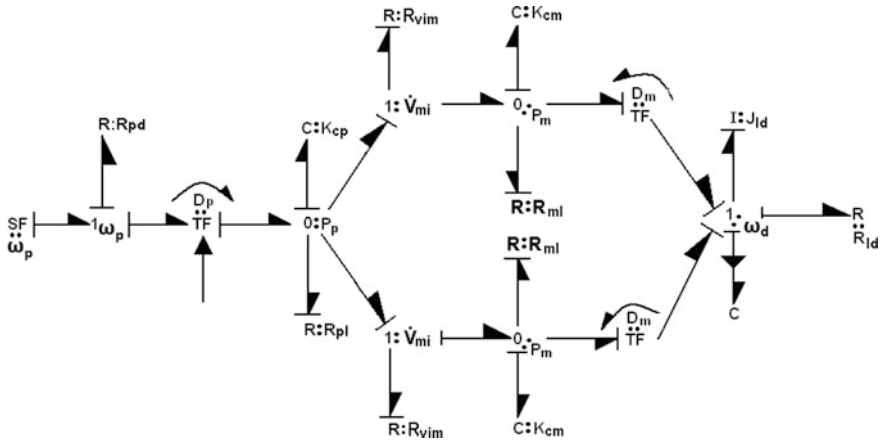
Fig. 2 Bond graph model pertaining to the considered system

The volumetric loss due to compression at the pump plenum:

$$Q_{cp} = \alpha_{pd}\omega_p D_{pmax} - \frac{P_p}{R_{pl}} - 2\left(\frac{P_p - P_m}{R_{vim}}\right) \tag{2}$$

Based on the prior equation, the second, third, and the fourth quantities correspond to the theoretical flow provided through pump, pump leakage flow, and the motors inlet flow, respectively.

The volumetric loss due to compression at the hydro-motor plenum:

$$Q_{cm} = \left(\frac{P_p - P_m}{R_{vim}}\right) - \frac{P_m}{R_{ml}} - \omega_m D_m \tag{3}$$

The third and the fourth quantities of Eq. (3) indicate the motor leakage flow and the outlet flow pertaining to the hydro-motor, respectively.

The plenum pressures associated with the pump alongside hydro-motor are given by

$$P_p = K_{cp} \int Q_{cp}dt \tag{4}$$

$$P_m = K_{cm} \int Q_{cm}dt \tag{5}$$

The rotational speed corresponding to the HST drive is

$$\omega_d = M_i/J_{ld} \tag{6}$$

And the rotational frequency of the hydro-motor is

$$\omega_m = \omega_d G_r \tag{7}$$

Neglecting the torque because of inertia load, from Eq. (1) during steady state, the load torque is stated as

$$2P_m D_m G_r \eta_g = \omega_d R_{ld} \tag{8}$$

$$\Rightarrow T_{ld} = 2P_m D_m G_r \eta_g \tag{9}$$

where load torque, $T_{ld} = \omega_d R_{ld}$.

Neglecting the volumetric loss due to compression of fluid in Eqs. (2) and (3), under steady-state condition the valve-port resistance (R_{vim}) linked with the hydro-motor is expressed as

$$R_{vim} = 2\left(\frac{P_p - \frac{T_{ld}}{2D_m G_r \eta_g}}{\alpha_{pd}\, \omega_p D_{pmax} - Q_{plkg}} \right) \tag{10}$$

$$\text{where, } \alpha_{pd} = D_p/D_{pmax} \text{ and } Q_{plkg} = P_p/R_{pl} \tag{11}$$

and the leakage resistance (R_{ml}) corresponding to the hydro-motor is stated as

$$R_{lm} = \frac{P_m}{Q_{mlkg}} = \left(\frac{T_{ld}}{2D_m G_r \eta_g Q_{mlkg}} \right) \tag{12}$$

During the condition of steady-state, the pump torque is provided through

$$T_{ip} = \omega_p R_{pd} + \alpha_{pd} D_{pmax} P_p \tag{13}$$

From Eq. (13), the drag resistance (R_{pd}) of the pump is

$$R_{pd} = \frac{T_{ip} - \alpha_{pd} D_{pmax} P_p}{\omega_p} \tag{14}$$

The slip, torque loss, and the overall efficiency of the HST drives are expressed by

$$S = \frac{\omega_{mi} - \omega_m}{\omega_{mi}} \tag{15}$$

where $\omega_{mi} = \frac{\alpha_{pd}\,\omega_p\,D_{pmax}}{2D_m}$

$$\Delta T_l = \frac{T_{ip} - T_{ld}}{T_{ip}} \qquad (16)$$

$$\eta = \frac{\omega_d\,T_{ld}}{\omega_p\,T_{ip}} \qquad (17)$$

4 Estimation of Resistances Pertaining to the Pump and the Hydro-Motors

The resistances R_{pl} and R_{ml} add up to the slip, on the other hand the resistances R_{pd} and R_{vim} add up to the torque loss associated with the drive. Using Eqs. (10), (11), (12), and (14) given in Sect. 3, the leakage resistances corresponding to the pump along with the hydro-motor, drag resistance of the pump and the valve-port resistance of the hydro-motor are estimated experimentally. The features linked with the resistances are plotted at various torque level by means of best-fit lines fitting the data points and they are shown in Figs. 3, 4 and 5, respectively.

With the decrement in the leakage resistances related to the pump alongside the hydro-motors (R_{pl} and R_{ml}), the flow losses associated with the drives increases and increase in the drag resistance (R_{pd}) pertaining to the pump and the valve-port resistance (R_{vim}) linked with the hydro-motor, results in the increment of the torque losses of the drives.
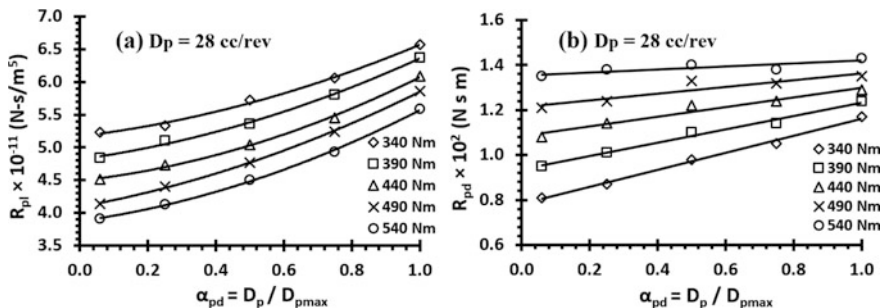
Fig. 3 Leakage resistance (R_{pl}) and the drag resistance (R_{pd}) features linked with the pump
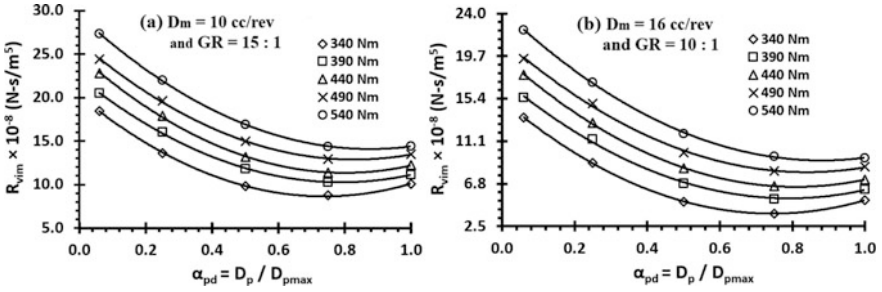
Fig. 4 Valve-port resistance (R_{vim}) features associated with the hydro-motors
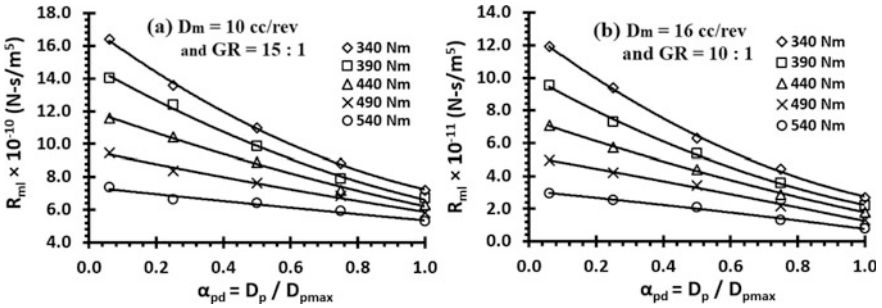
Fig. 5 Leakage resistance (R_{ml}) features corresponding to the hydro-motors

5 Results and Discussion

The speed of the drill bit utilized through drilling machine intended for its use in mining application changes from 20 to 120 rpm. By employing dual HSLT hydro-motors, capacity 10 cc/rev of each unit with reduction gear of 15:1 gear ratio; alternatively identical numbers of hydro-motors of 16 cc/rev with reduction gear of 10:1 gear ratio drives the drill bit. Both the gear unit has the same efficiency of 98%. Therefore, the performance of HST drives are examined where the lower capacity hydro-motors speed and torque changes under the boundary limit of 300 to 1800 rpm and 11 to 18 Nm; whereas, in case of higher capacity hydro-motors, these speed–torque range changes from 200 to 1200 rpm and 17 Nm to 27 Nm. Using the test data in Eqs. (15), (16) and (17), the performance parameters like slip, torque loss and the overall efficiency linked with the drives are found out.

Slip associated with the HST drives is basically a result of leakage resistances related to the pump (R_{pl}) along with the hydro-motors (R_{ml}). Utilizing Eq. (15) given in Sect. 3, the slip corresponding to the HST drives are obtained and it is shown in Fig. 6. The observations made from Fig. 6 are
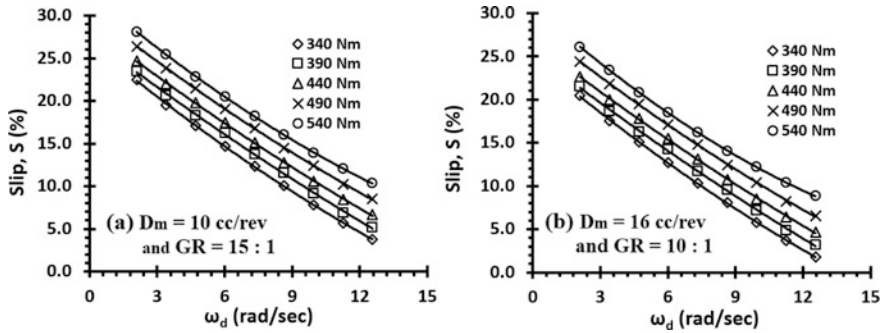
Fig. 6 Slip characteristics linked with the HST drives

- At a given speed, the increment corresponding to the torque level results in the enhancement in the slip.
- At a given torque level, the increment pertaining to the speed results in the decrement in the slip.

Torque loss associated with the HST drives is basically as a result of the drag resistance pertaining to the pump (R_{pd}) and the valve-port resistance linked with the hydro-motors (R_{vim}). Using Eq. (16) given in Sect. 3, the torque loss of the HST drives are obtained and it is shown in Fig. 7. The observations made from the Fig. 7 are

- At a given speed, percentage of torque loss depreciates as the torque level increases.
- At a given torque level, percentage of torque loss appreciates as the speed increases.

The slip and the torque loss decide the overall efficiency of the drives. Using Eq. (17) given in Sect. 3, the overall efficiency of the HST drives are obtained and it is shown in Fig. 8. The observations made from the Fig. 8 are
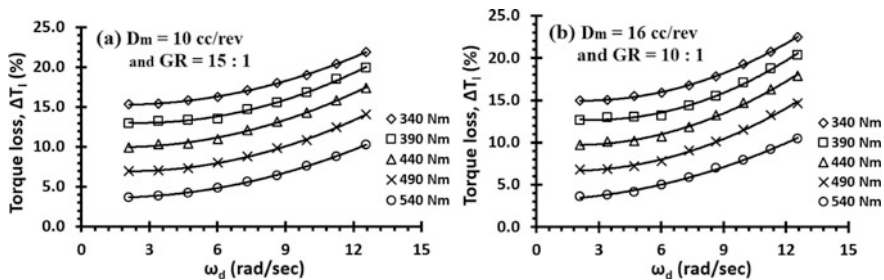
Fig. 7 Torque loss features linked with the HST drives
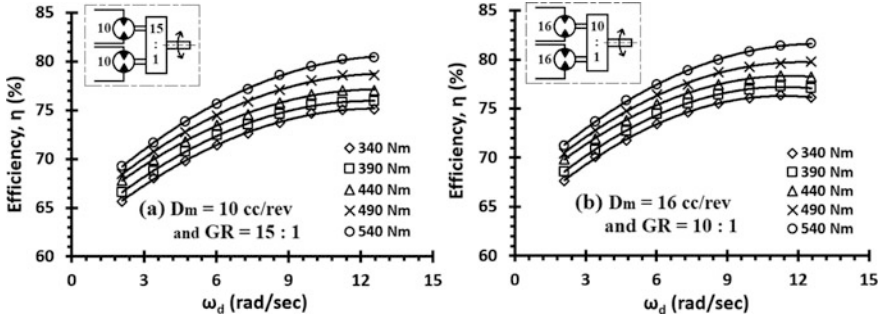
Fig. 8 Efficiency characteristics of the HST drives

- For a certain torque level, during the increment in the speed till 10.5 rad/sec (100 rpm), the overall efficiency linked with the drives enhances and furthermore, the efficiency almost remains constant.
- Under a given speed, the enhancement in the torque level results in the enhancement in the overall efficiency pertaining to the drives.
- For a particular speed and torque level, the HST drive having 16 cc hydro-motors and 10:1 gear reducer unit (Fig. 8b) has higher efficiency compared to the HST drive having 10 cc hydro-motors and 15:1 gear reducer unit (Fig. 8a).
- The maximum efficiency of the HST drive having 16 cc hydro-motors and 10:1 gear reducer unit (Fig. 8b) is 82% at 12.6 rad/sec (120 rpm) speed and 540 Nm torque level, whereas the maximum efficiency of the HST drive having 10 cc hydro-motors and 15:1 gear reducer unit (Fig. 8a) is 80% at 12.6 rad/sec (120 rpm) speed and 540 Nm torque level.

6   Conclusions

The present work describes the steady-state behaviors of two different closed-circuit HST drives for the rotary head of blast hole drill machine employed for mining applications. Bond graph technique has been employed for modelling the drives. Using them, the slip and torque loss along with the overall efficiency of the drives have been characterized. From the study, it is observed that at constant drill speed and the load torque, the HST drive having the higher size hydro-motors along with the smaller size gear reducer unit gives better performance compared to the HST drive having the smaller size hydro-motors along with the higher size gear reducer unit. The study also concluded that two-motor HST drive is apt for drilling softer rocks because softer rocks require higher drilling speed, however, this drive shows better performances at higher operating speed range.

References

1. Ho TH, Ahn KK (2010) Modeling and simulation of hydrostatic transmission system with energy regeneration using hydraulic accumulator. J Mech Sci Technol 24(5):1163–1175
2. Hui S, Ji-hai J, Xin W (2008) Factors influencing the system efficiency of hydrostatic transmission hybrid vehicles. In: Vehicle Power and Propulsion Conference 2008, pp 1–6. IEEE
3. Axin M, Eriksson B, Krus P (2014) Flow versus pressure control of pumps in mobile hydraulic systems. Proc Inst Mech Eng Part I: J Syst Control Eng 228(4):245–256
4. Vermillion SD (2011) Modeling a hydraulic hybrid drive train: efficiency considerations. PhD Thesis, University of Missouri, Columbia
5. Operation and maintenance manual of C-650 Drill, Revathi Equipment Limited Coimbatore, India
6. Borutzky W (2011) Bond graph modelling of engineering systems. Springer, New York

Design and Analysis of Solar Cabinet Dryer for Drying of Potatoes

Trinakshee Sarmah and S. K. Dhiman

Abstract A series of experiments were conducted on drying the potatoes via forced convection of heated air in an indirect-type solar cabinet dryer. Variation of the chamber temperature, the thickness of the potato slices and optimization of the water flow rate to the radiator was done. No pre-treatment of potatoes was carried out before commencing the experiments. The data, viz., the relative humidity inside the dryer, solar irradiation over the collector, temperature rise across the drying chamber and the weight lost by the specimen during the process of drying were collected. Analysis of data showed the increased drying rate with chamber temperature at a given air flow rate. For the slice thickness of 0.25 cm, the rectangular slices retained a faster drying rate compared to the square slices, while the circular slices showed the least drying rate. However, for the slice thickness of 0.5 cm, the rectangular slices still retained a faster drying rate, while square slices showed the least drying rate. The energy, exergy and cost analysis (simple payback period) of the setup was carried out.

Nomenclature

$\dot{m}_a$	Mass flow rate of air inside drying chamber (kg/s),
C_p	Specific heat of air (kJ/kg K)
T_{co}	Collector outlet temperature (K)
T_{ci}	Collector inlet temperature (K)
T_a	Ambient temperature (K)
Q	Heat energy used for drying process (kW)
η	System efficiency

T. Sarmah · S. K. Dhiman (✉)
Department of Mechanical Engineering, Birla Institute of Technology, Mesra, Ranchi, India
e-mail: sushil_k_dhiman@yahoo.co.in

T. Sarmah
e-mail: trinakshee1@gmail.com

η_{ex} System exergy efficiency
E_{xi} Collector inlet exergy
E_{xo} Collector outlet exergy

1   Introduction

Food processing is the transformation of any raw product such as vegetables, fruits, meat, fish, etc., through a process to make it consumable and increase its commercial value. The primary aim of the food processing industry is to extend the period for which a food product remains nutritious which is done by employing various methods that balance the organic or chemical changes in the raw food product and allows enough time for distribution, sale and storage. Drying, a method of food preservation, removes the moisture from the food and helps to extend the shelf life of food. The solar dryer is used extensively in the agricultural sector for drying of perishable food in a hygienic manner and at a lower operating and maintenance cost as compared to the conventional dryers. Several authors have carried out theoretical and experimental work in the solar drying of potatoes. Jabeen et al. [1] have constructed a forced convection solar cabinet dryer for studying the effect of temperature (60, 70 °C) and thickness (2.3, 3 mm) on the drying of potatoes. Patil et al. [2] have studied the drying of tomatoes in two solar cabinet dryers, which were ran simultaneously in natural (55 °C) and forced convection mode (46 °C). Chinenye et al. [3] have dried cocoa beans in a batch dryer at 55, 70 and 81 °C with air velocities of 1.3, 2.51 and 3.7 m/s for 4–6 h continuously in a day and reduced the moisture content from 79.6 to 6% (wet basis). Naderinezhad et al. [4] have designed a tunnel dryer and studied the effects of temperature (45–70 °C) and velocity (1.6–1.81 m/s) on the circle and square shapes of potatoes. Chouicha et al. [5] carried out experimental work to study an indirect type of solar dryer for drying of potato slices for velocities of (0.31, 0.4, 0.51 m/s) in the drying chamber.

   In the present work, the forced convection solar cabinet dryer has been designed. The objectives of the research are to study the drying of different thickness of potato slices by varying the temperature inside the drying chamber, to reduce the time required for drying of the potatoes as compared for open sun drying method and to bring the quality of the final product at par with the conventional electric dryers. Also, the cost of the dryer is low as the components of the model have been obtained from scrap yards and locally available materials have also been used.

2   Experimental Setup

As shown in Fig. 1, a box is constructed of 2 mm thick plywood board to house the radiator and the fan. It also serves as the duct for passing the hot air from the radiator to the drying chamber with the help of the fan. The SMPS (switched mode power

supply) is fitted at the top of the box and the required connections are made. The SMPS is used because supply is of 230 V and the setup has to be run on 12 V. The experimental setup is to be connected to a solar panel. A Maruti 800 radiator of the downward flow type has been used. There are 37 copper plates and the diameter of the tubes is of 10 mm. The capacity of the radiator is 3 L. The cooling fan used in the experimental setup has a speed of 1200–2400 rpm. It runs on 220/240 V single phase AC supply. A 0.5HP pump is used to pump the water from the evacuated type solar collector to the radiator. The pump runs on single-phase AC supply of 220/240 V, 2.5 A and 50 Hz. The speed of the pump is 2800 rpm. An evacuated tube solar collector is used as a supply of hot water to the radiator. The maximum temperature attained by the water inside the collector is about (80–90) °C. The dimensions of the drying chamber are 92 cm × 61 cm × 65 cm. The body of the drying chamber is made of glass fitted on a wooden frame. The thickness of the glass pane used is 3 mm. There are two trays inside the drying chamber. These trays are perforated wire- mesh in nature to obtain a uniform drying of the food products throughout. The dimensions of the tray are 81 cm × 54 cm × 3.5 cm. These trays are lightweight, free from corrosion and cheap. These factors are favourable for medium temperature drying. There are holes drilled at the top of the drying chamber to allow the warm air to escape from the chamber after absorbing the moisture from the food products.

3 Methodology

3.1 Sample Preparation

The potatoes were bought from the local market. They were washed, peeled and sliced. An industrial vegetable cutter was used to slice the potatoes. The sliced potatoes were then placed in a die to get the required shape. As shown in Fig. 2 three shapes were used for the experiment: rectangle, square and circle. Two thicknesses of potato slices were considered: 0.25 cm and 0.5 cm. All the samples of a particular shape were identical in dimensions. Five samples of a particular shape were considered for one set of experiments. No pretreatment of the potatoes was carried out.

3.2 Experimental Procedure

As shown in Fig. 4, the samples prepared were placed on the tray evenly. The temperature of the water inside the solar collector varied from (60–70) °C. To increase the temperature of the water entering the radiator an external electric heating rod was also used. So the final temperature of the water entering the radiator was in the range of (60–80) °C. The rotameter was used to measure the flow rate of water entering the radiator. The flow rate of water entering the radiator was approximately 2.5–3 litres per minute. The air inside the enclosed and insulated

Table 1 Complete list of sample shapes, dimensions, weight loss and change in moisture content of all the experiments conducted

Sample shape and dimensions (in cm)	Temperature (celsius)	Time required for complete drying of the samples (minutes)	Initial weight of the sample (grams)	Final weight of the sample after drying is completed (grams)	Initial moisture content (% w.b.)	Final moisture content after drying is completed (% w.b.)	Initial kg of water/ kg of dry matter	Final kg of water/ kg of dry matter
Square (3 × 3 × 0.25)	45	150	9.64	1.051	89.1	32.8	8.172	0.487
	55	135	9.76	1.059	59.1	30	8.216	0.3
	65	120	9.62	1.058	89	29.1	8.093	0.411
Square (3 × 3 × 0.5)	45	250	25.51	10.156	60.2	14.3	1.512	0.719
	55	235	25.53	10.153	60.6	19.4	1.514	0.237
	65	225	25.54	10.154	60.2	9.6	1.515	0.106
Rectangle (3.5 × 4.5 × 0.25)	45	175	11.55	2.208	79.8	20.1	4.231	0.317
	55	165	11.56	1.531	86.8	28.1	6.551	0.472
	65	150	11.54	1.582	99.58	20.3	6.295	0.351
Rectangle (3.5 × 4.5 × 0.5)	45	295	36.06	10.075	72.1	17.6	2.579	0.213
	55	280	36.05	10.074	72.1	7.9	2.579	0.086
	65	270	36.03	10.073	72	10.1	2.577	0.113
Circle (3 cm dia, 0.25 cm thick)	45	190	11.44	1.15	89.9	12.8	8.948	0.748
	55	170	11.43	1.12	89	10.1	9.205	0.596
	65	160	11.42	1.15	89.2	10.4	8.93	0.4
Circle (3 cm dia, 0.5 cm thick)	45	265	22.95	7.01	69.5	13.6	2.274	0.064
	55	240	22.93	7.03	69.3	10.6	2.262	0.118
	65	230	22.91	7.03	69.3	14.4	2.259	0.24

chamber was blown forcefully with the help of a fan. This air absorbed the heat from the water flowing inside the radiator. The hot air then entered the drying chamber through an inlet hole at the bottom. The hot air absorbed the moisture from the samples kept on top of the wire-mesh trays. The warm air was then expelled from the outlet holes neat the roof of the drying chamber. The warm water from the radiator was made to return back to the hot water tank through a pipe. Thus, the temperature of water in the hot water tank was kept constant and did not fall. The velocity of air inside the drying chamber was 2 m/s. The experiments were conducted for three temperatures of air inside the chamber 45, 55 and 65 °C. The ambient temperature was 34 °C. The direct solar radiation was 750 W/m^2. The experiments were conducted between 11 a.m. to 4 p.m. The samples were weighed after every 15 min. They were removed carefully from the trays as shown in Fig. 3 and enclosed in airtight bags so as to prevent any moisture from entering or escaping them. They were then carefully weighed in the electronic balance. The loss in weight of the samples was noted. The samples were dried until the three consecutive weights after drying were similar. This meant that the moisture was completely removed from the samples and they were dry. The dry bulb temperature and the wet bulb temperature were noted with the help of the psychrometer kept inside the drying chamber. These values gave the relative humidity inside the chamber from the psychometric chart. These values were also noted at regular intervals of time. The temperature inside the drying chamber and that at the outlet was measured by the digital thermometer (Table 1).

4   Results and Discussion

Three shapes of potato samples were taken (square, rectangle, and circle) and two thicknesses of samples were considered (0.25 and 0.5 cm). As observed from Figs. 5, 7 and 8, when the temperature inside the drying chamber was 45 °C and the 0.25 cm thick samples were being dried, the square samples took the least time to get dried completely as shown in Fig. 7 and the circular samples took the highest amount of time to dry as shown in Fig. 8. This trend was repeated when the temperature was 55 °C inside the drying chamber. However, for the temperature of 65 °C inside the drying chamber the time taken for the rectangular samples to dry was higher than the other shapes, which may be observed from Figs. 5, 7 and 8. Similarly, when the 0.5 cm thickness samples were being dried, the square-shaped samples dried the fastest as observed from Fig. 6 comparing with Figs. 9 and 10.

When the temperature inside the chamber was increased from 45 to 65 °C, the time required to dry the samples also decreased as the rate of removal of water from the samples was carried out at a faster pace. The flow rate of air inside the chamber was kept constant at 2 m/s throughout the entire time of the experiment.

Fig. 1 Experimental setup
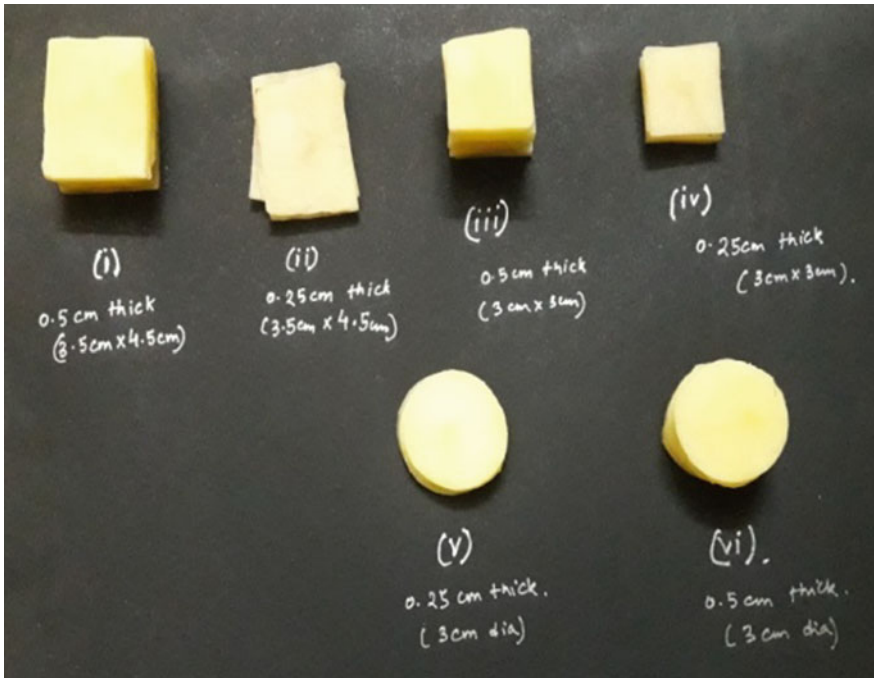
Fig. 2 Potato samples before drying

5 Energy, Exergy and Cost Analysis

5.1 Energy and Exergy Analysis

The equation for the amount of heat used for the drying process is given below [6]:-

$$Q = \dot{m}_a C_p (T_{co} - T_{ci}) \ldots \tag{1}$$

The equation for the system efficiency is given below [1]:

$$\eta = \frac{WL}{IA + P_f} \ldots \tag{2}$$

The equation for exergy at the inlet to the dryer is given below [6]:

$$E_{xi} = m_a C_p [(T_{ci} - T_a) - \left(T_a \ln\left(\frac{T_{ci}}{T_a}\right)\right) \ldots \tag{3}$$
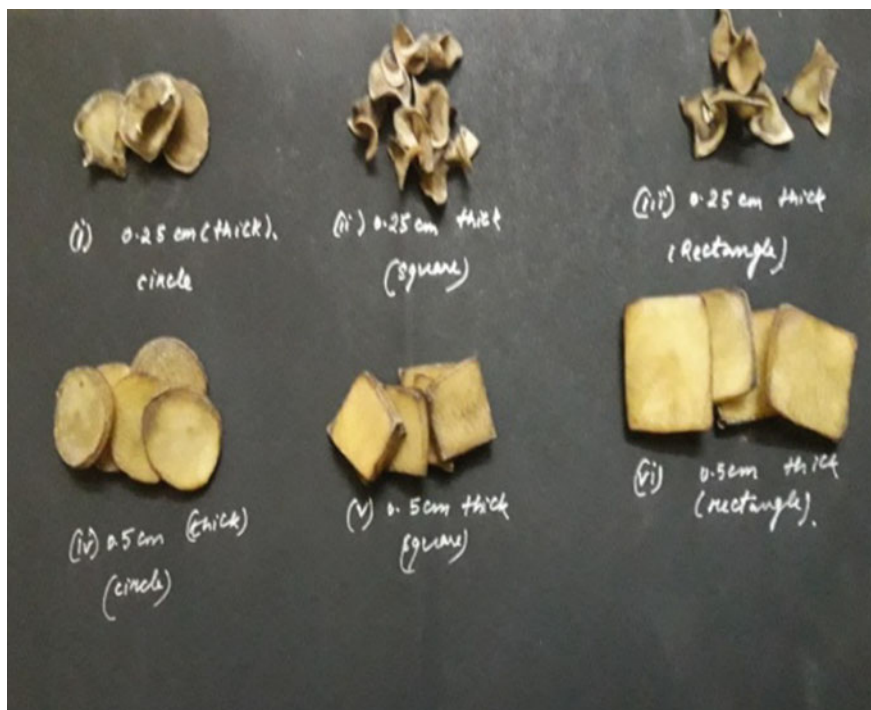
Fig. 3 Potato samples after drying
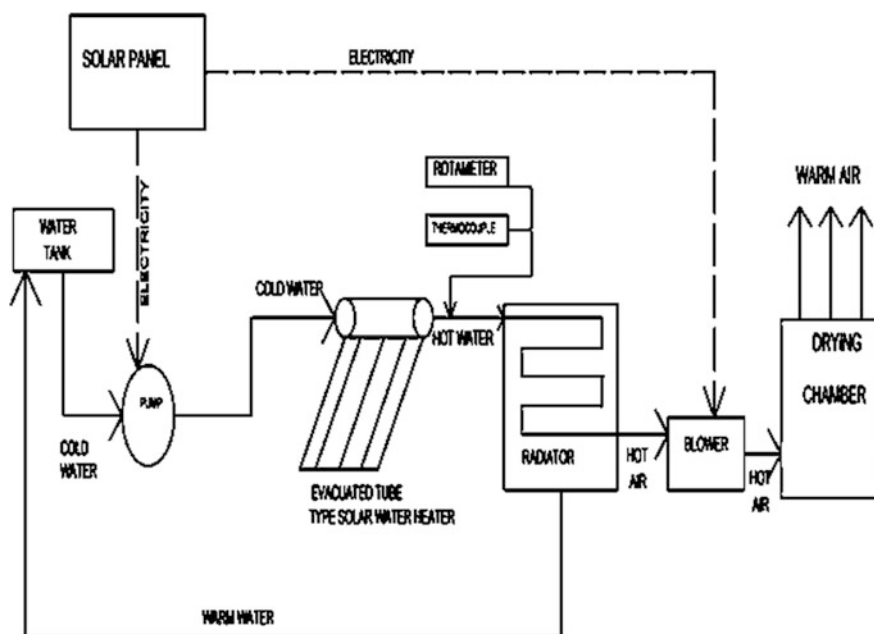
Fig. 4 Schematic diagram

Fig. 5 Variation of the
moisture content with time for
rectangular chips of 0.25 cm
thickness
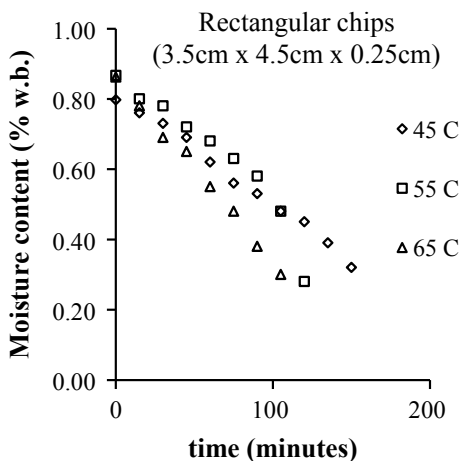
Fig. 6 Variation of the
moisture content with time for
rectangular chips of 0.5 cm
thickness
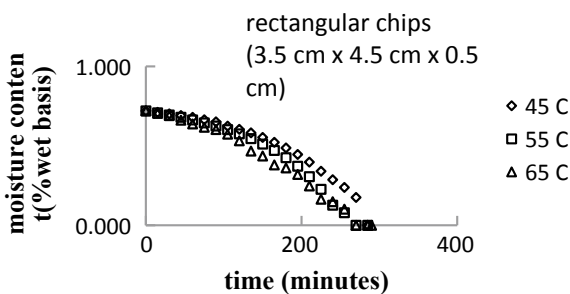
Fig. 7 Variation of the
moisture content with time for
square chips of 0.25 cm
thickness
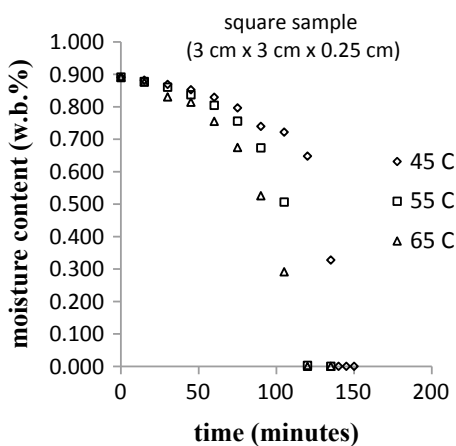
Fig. 8 Variation of the moisture content with time for circular chips of 0.25 cm thickness
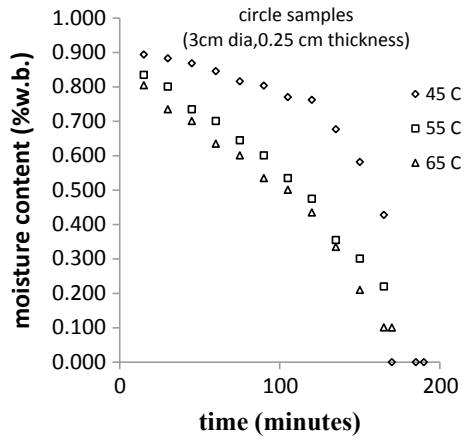
Fig. 9 Variation of the moisture content with time for square chips of 0.5 cm thickness
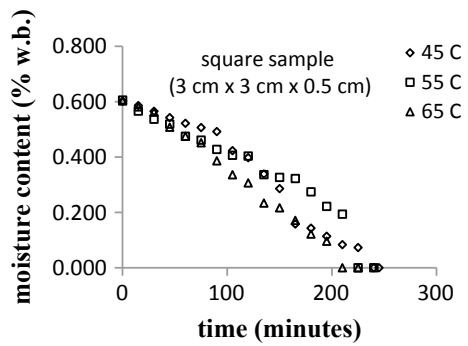
Fig. 10 Variation of the moisture content with time for circular chips of 0.5 cm thickness
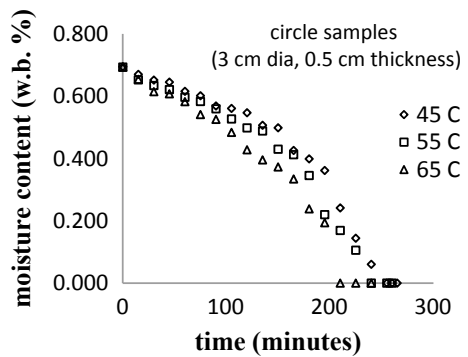
The equation for exergy at the outlet to the dryer is given below [6]:

$$E_{xo} = m_a C_p [(T_{co} - T_a) - \left(T_a \ln \left(\frac{T_{co}}{T_a} \right) \right) \dots \tag{4}$$

The equation for exergy efficiency is given below [6]:

$$\eta_{ex} = \frac{E_{xo}}{E_{xi}} \ldots \tag{5}$$

After the required calculations, it was found that the amount of heat energy used for the drying process is 5.2304 kW. The system efficiency for the forced convection solar dryer is 13.089%. The exergy efficiency of the solar dryer is 61.953%.

5.2 Cost Analysis

The total cost of the plywood box, heat exchanger fan, pipes etc. is Rs. 12100. The dryer capacity is 5 kg per batch and if it runs for 200 days a year, then the total cost of conventional energy used for one year is Rs. 4890.56. The expected lifetime of the dryer is 20 years. If the salvage value is taken as 10% of the total initial cost and the maintenance cost taken as 1% of the salvage value then the annual cash benefit comes out to be Rs. 4769.56. Hence, the simple payback period for the experimental setup is 1.328 years.

6 Conclusion

In the present work, the solar drying of potatoes in a forced convection solar dryer has been studied. The main results showed that when the temperature inside the chamber was 45, 55 and 65 °C, the moisture content of the potatoes reduced from 89.1% to 33% in an average time of 160 min for 0.25 cm thick slices and 260 min for 0.5 cm thick slices. For both thicknesses, the square samples took the least amount of time to dry. For 0.25 cm thick slices, the circular samples took the highest amount of time to dry and for 0.5 cm thick slices the rectangular samples took the maximum drying time. The average heat energy used for drying inside the chamber is 1.584 kW. The system energy efficiency was 13.089% and the exergy efficiency was 61.953%.

Certain improvements can be made to the existing setup. The wood used in the model may be replaced by Teflon which is a better insulator. Again an axial flow fan may be used instead of the exhaust fan. A biomass burner may be used to supplement the solar energy and increase the time of operation of the dryer.

References

1. Jabeen R, Aijaz T, Gul K.: Drying kinetics of potato using a self-designed cabinet dryer. Cogent Food Agric 1(1),1036485 (2015)
2. Patil R, Gawande, R.: Comparative analysis of cabinet solar dryer in natural and forced convection mode for tomatoes. Int. J Res Sci Innov (IJRSI) 3(7) (2016)
3. Ndukwu, MC (2009) Effect of drying temperature and drying air velocity on the drying rate and drying constant of cocoa bean. Agric Eng Int CIGR J
4. Naderinezhad S, Etesami N, Poormalek Najafabady A, Ghasemi Falavarjani M (2016) Mathematical modeling of drying of potato slices in a forced convective dryer based on important parameters. Food Sci Nutrition 4(1), 110–118
5. Chouicha S, Boubekri A, Mennouche D, Berrbeuh MH (2013) Solar drying of sliced potatoes. an experimental investigation. Energy Procedia 36: 1276–1285
6. Bennamoun Lyes (2012) An overview on application of exergy and energy for determination of solar drying efficiency. Int J Energy Eng 2(5):184–194

Graphene/MoS$_2$-Based Fix–Fix-Type RF-NEMS Switches—A Simulation Study

Aakif Anjum, Vishram B. Sawant and Suhas S. Mohite

Abstract In this work, modelling, simulation and analysis of a fix–fix-type RF-nanoelectromechanical switches (RF-NEMS) with very low actuation voltage and enhanced RF-Performance is presented. The switches are modelled using previously known theory from the literature. The various performance parameters are computed like modal frequencies, Casimir force, electrostatic force, capacitance, release time, actuation voltage and S-parameters are computed using ANSYS structural and HFSS software. The switch exhibits low actuation voltage <1 V for different thicknesses of graphene/MoS$_2$ as a beam material. Resonant frequency of graphene based beam for first, second and third mode are found to be 72.5 kHz, 86 kHz and 416 kHz, respectively, while for MoS$_2$-based beam 27 kHz, 34 kHz and 94 kHz, respectively. It is concluded that low actuation voltage NEMS switches can be realised using single-layer 2D material giving low insertion loss.

Keywords Graphene · MoS$_2$ · RF-NEMS · Actuation voltage · Insertion loss · Isolation

1 Introduction

Nanoelectromechanical system (NEMS) is an emerging field for future technology development. Radio frequency based NEMS switches in future will be widely used over MEMS switches to further reduce voltage, power consumption, and to enhance RF-performance [1]. The main reason is that RF-NEMS switches have low resistive losses, high isolation, low noise, and low actuation voltage. RF-NEMS

Aakif Anjum (✉) · S. S. Mohite
Mechanical Engineering Department, Government College of Engineering, Vidyanagar, Karad 415124, Maharashtra, India
e-mail: anjumaakif@gmail.com

V. B. Sawant
Mechanical Engineering Department, Rajiv Gandhi Institute of Technology, Versova, Andheri (W), Mumbai 400097, Maharashtra, India

switches work over a wide range of frequencies for various applications such as wireless communications, satellite system, cell phones, highly sensitive sensors, military applications, nano-tweezers, etc., [1–3].

There are various 2D materials, which are used in nanofabrication of devices to name a few are graphene, MoS_2, borophene, germanene, silicene, stanene, phosphorene [1–3]. These materials can be used as bridge materials in RF-NEMS switches [3–5]. RF-NEMS switches with two layers of graphene as a bridge material are presented by Milaninia et al. [3]. The dimensions used for beam are 20×3 μm (l × w) and g = 500 nm. The pull-in voltage is 4.5 V is obtained. The drawback of this switch is the limitation of contact resistance (200 kΩ). This is because of nonuniform surface of graphene due to chemical vapour deposition process. Fixed–fixed-type RF-NEMS switch consisting of graphene beam is modelled and simulated by Dragoman et al. [4]. CPW transmission line is formed using 20 nm gold, which is patterned on silicon. The voltage obtained by this switch is 2 V. Graphene-based RF-NEMS switches are modelled and analyzed for fixed–fixed beam by Pankaj et al. in 2014 [5]. The main disadvantage of all above switches is the actuation voltage are >1 V. Proper selection of 2D beam material so as to give minimum voltage is still challenging task and switch design has to be optimised at initial stage of design before fabrication. This motivates us to design RF-NEMS switch in order to get the minimum actuation voltage with low insertion loss and high isolation at various operating frequencies. In the following section schematic of RF-NEMS switch is presented.

2 Switch Description

The graphene-based RF-NEMS switch is shown in Fig. 1. The graphene membrane is attached between ground conductors. Ground conductors are attached to low loss substrate material. In this study, we have used silicon which is highly resistive. There is a central conductor which is in contact with thin dielectric layer, the dielectric layer is of Si_3N_4, and we have used Si_3N_4 due to its high K value. This dielectric layer is used to avoid the short-circuit between graphene membrane and bottom electrode. Mostly the dielectric layer is made very thin, in some switches it is reported from 1500 A to 2000 A [5–10]. Both the ground electrode and central electrode are made up of Au due to its high conductivity. DC voltage which is applied across graphene membrane and central electrode causes the generation of electrostatic force this electrostatic force causes the membrane to change its position from up-state to down-state. Detailed modelling is presented in the next section.
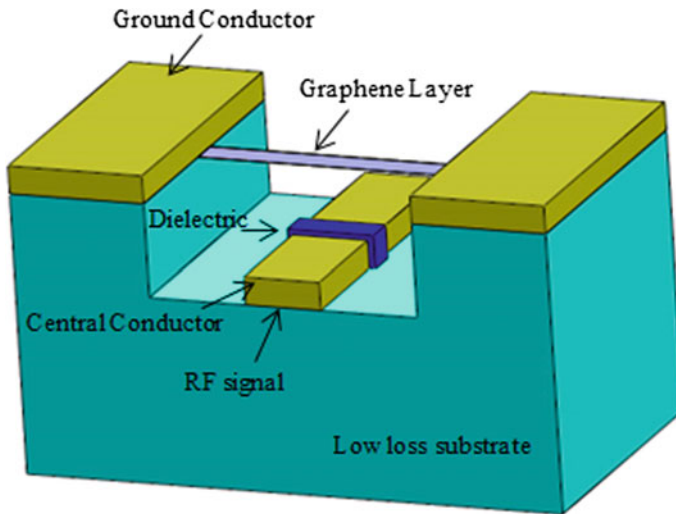
Fig. 1 Graphene-based RF-NEMS switch (not to scale)

3 Modelling

3.1 Mechanical Modelling

The mechanical modelling of RF-NEMS switch is involved by the three types of forces. The electrostatic force which acts due to the electrostatic charges induced between ground conductor and graphene beam. The second is elastic force, spring is modelled with the help of elastic force. This electrostatic force depends on size, shape, and material of beam. The third is intermolecular forces. These forces include Van der Waals and Casimir forces. The consideration of Van der Waals force is only when gap height (g) is less than 20 nm. Practically, fabrication of switch with gap height less than 20 nm faces difficulties. Packaging and population becomes difficult to control. Due to this reason, we have considered the Casimir force and designed the model with gap height greater than 20 nm. The consideration of Casimir force is only when gap height (g) is greater than 20 nm [6]. The governing equation of fixed–fixed-type switch is given as [6]

$$(EI)_{eff}\frac{d^4y}{dx^4} = F_{elec} + F_c + F_s \qquad (1)$$

Here, EI represents effective bonding rigidity of the beam. Deflection of beam is denoted by y. F_{elec}, F_c represents the electrostatic and Casimir force per unit length. While Fs represent elastic force.

According to fringe field of first order, F_{elec} per unit length of fixed–fixed beam is [6]

$$F_{elec} = \frac{1}{2} \frac{\varepsilon_0 V^2 w}{[g-y]^2} \left[1 + 0.65 \frac{g-y}{b} \right] \tag{2}$$

Where w represents width of beam, g is the distance between fixed–fixed beam and central conductor, ε_0 = Permittivity of free space and V is the applied voltage.

The force which is due to attraction between atoms is known as Casimir force. The Casimir force per unit length of the fixed–fixed beam is [6]

$$F_c = \frac{1}{240} \frac{\pi^2 hcw}{[g-y]^4} \tag{3}$$

Here, c is the speed of light that is 2.998×108 m s^{-1}, h is planks constant/2π. Material property does not affect the Casimir force.

Perpendicular load which acts due to small amount of deformation in a beam is elastic or transverse force. This force is computed as [6]

$$F_s = 2\tau^0 w \frac{d^2 y}{dx^2} \tag{4}$$

This force may soften the fixed–fixed type of switch. By combining Eqs. 2, 3, 4 the governing equation will be [6].

The actuation voltage for fixed–fixed-type RF-NEMS switch when Casimir force is neglected given as [7].

$$V_{pull-in} = \sqrt{\frac{8k}{27_{\varepsilon_0} W_\omega} g_0^3} \tag{5}$$

The actuation voltage for fixed–fixed-type RF-NEMS switch when Casimir force is considered given as [14].

$$V_{pull-in} = \sqrt{\left[k(g-g_0) - \frac{\pi^2 hcwL(g-g_0)}{240 g_0^4} \right] \frac{2g_0^2}{\varepsilon_0 wL}} \tag{6}$$

where g_0 = Pull-in gap, w = Fixed–fixed width, W = Length of CPW, k = Stiffness of spring.

The actuation voltage is dependent on stiffness and is given as [7].

$$k = 32 \, Ew(t/L)^3 + 17T/L \tag{7}$$

where

w, t, L is width, thickness and length of beam, E is Young's modulus of the beam.

Thus, from above equation, it is clear that release time is inversely proportional to frequency.

3.2 Electrical Modelling

RF-capacitive switch circuit diagram as shown in Fig. 2, modelled by a transmission line having a characteristic impedance, and concentrated series resistance of the bridge—inductor—capacitor model, in Fig. 2, graphene/MoS$_2$ bridge switches are mainly represented by the bridge inductance L, bridge resistor R and the variable C. Depending on the operating state of the variable bridge capacitance change switch. Impedance of the bridge, Z, is given by

$$Z = R + j\omega L + \frac{1}{j\omega C} \tag{8}$$

where $C = C_u$ or C_d depends on the operating state of the RF capacitive switch.

The up-state position, the reflection coefficient is

$$S_{11} = \frac{-j\omega C_u Z_0}{2 + j\omega C_u Z_0} \tag{9}$$

$$S_{21} = \frac{2R_s}{Z_0 + R_s} \tag{10}$$
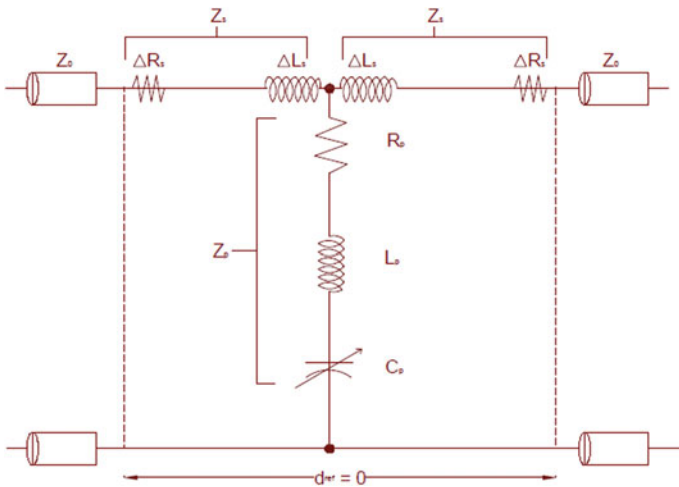
Fig. 2 Circuit diagram for switch

The S_{11} and S_{21} S parameter have been estimated in the up position of the bridge of NEMS, that represents the insertion loss and return loss. In position of downstate S_{21} represents the isolation of RF MEMS switch. Here, the return S_{11} losses have been estimated at both upward and downward positions. The total capacitance of RF MEMS switches in actuated state and un-actuated state to determine the insertion and isolation in the frequency range.

3.3 Material Properties of Graphene and MoS$_2$

Graphene, which is a typical flat monolayer of carbon atoms arranged in a honeycomb lattice and has great interest in electronic devices [1]. It was first mechanically exfoliated from graphite in 2004 [1].

Molybdenum disulphide is silvery black two-dimensional material can also be used for switching of RF-NEMS switches (Table 1).

4　Results and Discussion

4.1 Modal Analysis

The simulations were carried out to determine resonant frequency and deflection of fixed–fixed beam. Figure 3 shows the modal patterns of fixed–fixed-type graphene/MoS$_2$-based RF-NEMS switch. Resonant frequency of the switch is obtained with the help of modal analysis. Resonant frequency of graphene-based beam for first, second and third mode are 72.5 kHz, 86 kHz, and 416 kHz, respectively, while for MoS$_2$-based beam 27 kHz, 34 kHz, and 94 kHz respectively.

Table 1 Material properties of graphene and MoS$_2$

	Graphene	MoS$_2$	References
Doping	p-doped	p-doped	[5]
Single-layer thickness (SL) nm	0.34	0.3	[5, 11, 13]
Bilayer thickness (BL) nm	0.64	0.6	[5, 11, 13]
Multilayer thickness (ML) nm	2	1.7 to 1.8	[5]
Young's modulus TPa	0.8 to 1	0.3	[5, 10]
Density kg/m^3	2200	5060	[5, 10]
Poisson's ratio	0.4	0.125	[5, 10]
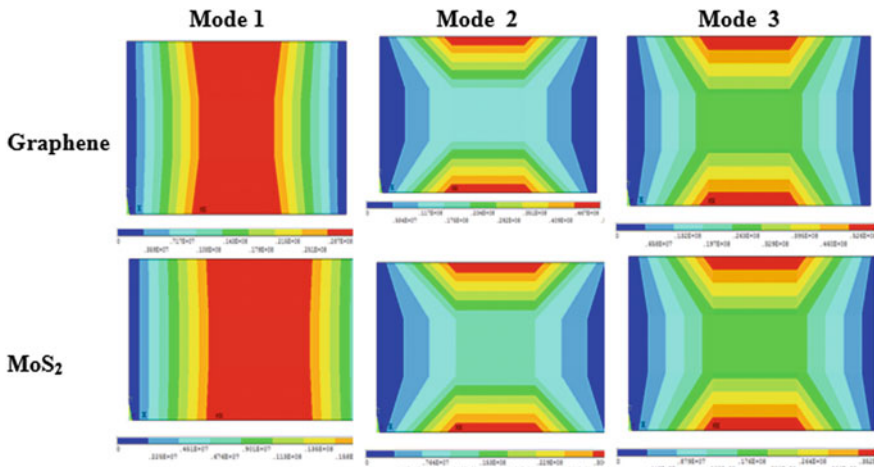
Fig. 3 Modal patterns of the beam structure for graphene/MoS$_2$

4.2 Pull-in Voltage with and Without Effect of Casimir Force

Analytical and simulation results are performed to study the mechanical and electrical parameters.

We considered the fixed–fixed beam with different thickness, that is 0.34 nm, 0.64 nm, and 2 nm for graphene beam, 0.301 nm, 0.602 nm and 2 nm for MoS$_2$ beam, we compute variation of the pull-in voltage with length shown in Figs. 4, 5, 6 and 7. From above figs, we notice that the effect of Casimir force on the pull-in voltage with the growth of thickness is more for the same length. This means, increase in thickness of the membrane causes the increase in the detachment length. The pull-in voltage with consideration of Casimir force is more than that of without consideration of Casimir force. At length of 10 μm, pull-in voltages are 1.16 and 1.15 with the effect of Casimir force while pull-in voltage of 0.44 is noted for graphene and MoS$_2$.
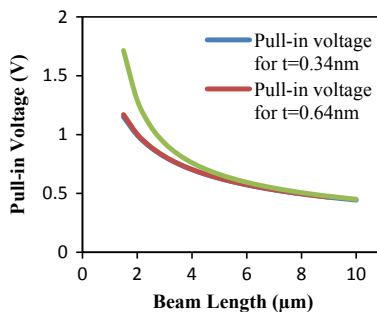
Fig. 4 Pull-in voltage without Casimir effect for graphene switch
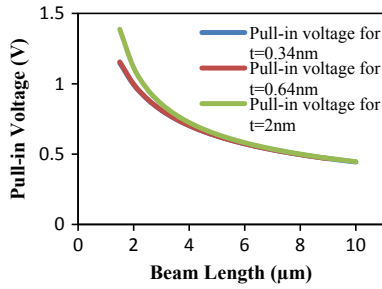
Fig. 5 Pull-in voltage without Casimir effect for MoS$_2$ switch
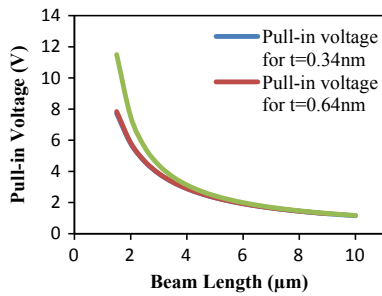
Fig. 6 Pull-in voltage with Casimir effect for graphene switch
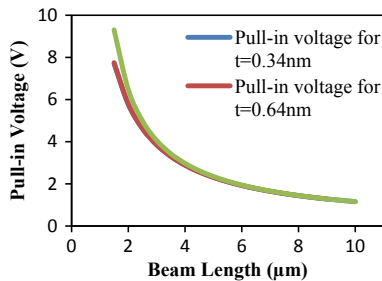
Fig. 7 Pull-in voltage with Casimir effect for MoS$_2$ switch

4.3 Insertion Loss, Isolation of RF-NEMS Switches

The S-parameters in the up- and down-state positions are shown in Figs. 8, 9, 10 and 11. The isolation and insertion loss values are obtained by simulations using ANSYS HFSS (High-Frequency Structural Simulator) for fixed–fixed-type RF-NEMS switches. The isolation and insertion loss values obtained are in the range of 10–12 dB and 0.054 dB for graphene and MoS$_2$ switches.
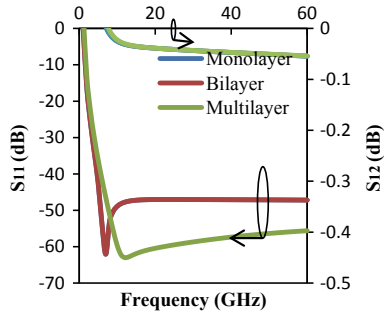
Fig. 8 S$_{11}$ and S$_{12}$ versus frequency in up-state position for graphene
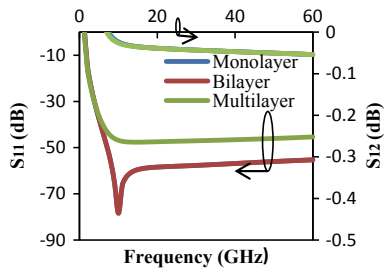
Fig. 9 S$_{11}$ and S$_{12}$ versus frequency in down-state position for graphene
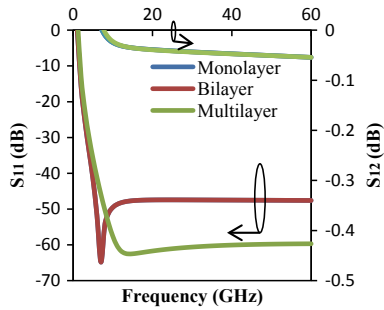
Fig. 10 S$_{11}$ and S$_{12}$ versus frequency in up-state position for MoS$_2$
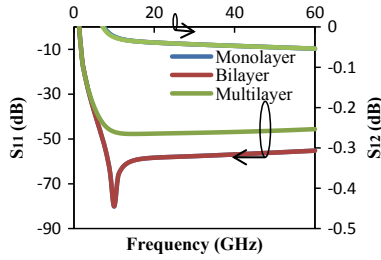
Fig. 11 S_{11} and S_{12} versus frequency in down-state position for MoS_2

Table 2 Comparisons of graphene and MoS_2 based RF-NEMS switch

References	Material	Pull-in voltage, $V_{pi}(V)$	Isolation	Insertion loss
Milaninia et al. [3]	Graphene	4.5 V	−30 dB at 60 GHz	–
Dragoman et al. [4]	Graphene	2 V	−40 dB at 60 GHz	–
Pankaj et al. [5]	SLG	0.3 V	>10 dB @ 1–60 GHz	0.01–0.3 dB
	MLG	1.4 V	>20 dB @ 1–60 GHz	0.01–0.2 dB
Simulated result for proposed graphene RF-NEMS switch	SLG, V_{pi} without Fc	0.44 V	$\approx$ −10 dB at 1 GHz	−0.054 dB at 60 GHz
	SLG, V_{pi} with Fc	1.150 V		
	BLG, V_{pi} without Fc	0.44 V	$\approx$ −5 dB at 1 GHz	−0.054 dB at 60 GHz
	BLG, V_{pi} with Fc	1.151 V		
	MLG, Vpull-in without Fc	0.45 V	$\approx$ −10 dB at 1 GHz	−0.054 dB at 60 GHz
	MLG, V_{pi} with Fc	1.166 V		
Simulated result for the proposed MoS_2 RF-NEMS switch	SLG, V_{pi} without Fc	0.44 V	$\approx$ −8.78 dB at 1 GHz	−0.054 dB at 60 GHz
	SLG, V_{pi} with Fc	1.150 V		
	BLG, V_{pi} without Fc	0.44 V	$\approx$ −9 dB at 1 GHz	−0.054 dB at 60 GHz
	BLG, V_{pi} with Fc	1.150 V		
	MLG, V_{pi} without Fc	0.44 V	$\approx$ −11 dB at 1 GHz	−0.054 dB at 60 GHz
	MLG, V_{pi} with Fc	1.156 V		

Table 3 Comparisons of graphene and MoS$_2$ based RF-NEMS switch @ 1 GHz

Design	Return loss (up) (dB) for graphene	Return loss (down) (dB) for graphene	Return loss (up) (dB) for MoS$_2$	Return loss (down) (dB) for MoS$_2$
For thickness 1	6.44	6.44	0.84	6.55
For thickness 2	0.81	6.0	0.84	6.57
For thickness 3	5.43	5.32	4.57	80

5 Comparison

We have further studied the MoS$_2$-based RF-NEMS switch and compared with the graphene-based RF-NEMS switch. These graphene/MoS$_2$-based switches are compared with the work done by various researchers previously. From Table 2, it is noted that graphene/MoS$_2$-based switches show low actuation voltage, low insertion loss and high isolation than that of work done by other researchers. The fixed–fixed-type RF-NEMS switches show good performance in terms of electrical and RF characteristics (Table 3).

6 Conclusions

Performance of fixed–fixed-type RF-NEMS switch based on graphene and MoS$_2$ is presented in terms of the performance parameters, viz., actuation voltage, insertion loss and isolation. It is further compared with the performance of RF-NEMS switches in the published literature. Resonant frequencies of graphene based beam for first, second and third mode are 72.5 kHz, 86 kHz and 416 kHz, respectively, while for MoS$_2$-based beam 27 kHz, 34 kHz and 94 kHz, respectively. The multilayer of graphene and MoS$_2$ switch offers superior isolation as compared to the monolayer and bilayer because of the lower surface resistance. The isolation 10 dB for multilayer graphene and 11 dB for multilayer MoS$_2$ are obtained. The switches exhibit low actuation voltage <1 V for different thickness of graphene/MoS$_2$ as a beam material without Casimir force and <1.5 V under the effect of Casimir force. The actuation voltage of MoS$_2$ switch is 0.86% less than that of graphene switch with the Casimir effect. However, MoS$_2$ switches have more return losses than graphene switch. In the down-state position, MoS$_2$ switch exhibits 1.75 times more return loss than that of graphene switch. It is concluded that graphene is the best material than MoS$_2$ for RF-NEMS switch when return loss is dominant while MoS$_2$ is more prominent in terms of actuation voltage and isolation.

Appendix

See Table 4.

Table 4 Parameters in the present paper

Symbol	Physical meaning	Symbol	Physical meaning
c	Speed of light (ms^{-1})	g_0	Pull-in gap (nm)
E	Young's modulus (TPa)	L	Length of beam (μm)
I	Moment of the inertia (m^4)	t	Thickness of beam (nm)
h	Planks constant/2π (J s)	w	Width of beam (μm)
K	Spring constant of beam (N m^{-2})	V	Applied voltage (V)
g	Gap height (nm)	ε_0	Vacuum permittivity (F/m)
V_{pi}	Pull-in voltage	F_c	Casimir force

References

1. Mafinejad Y, Kouzani A, Mafinezhad K, Mashad I (2013) Review of low actuation voltage RF MEMS electrostatic switches based on metallic and carbon alloys. J Microelectron Electron Compon Mater 43(2)
2. Jang WW, Lee JO, Yoon JB, Kim MS, Lee JM, Kim SM, Cho KH, Kim DW, Park D, Lee WS (2008) Fabrication and characterization of a nanoelectromechanical switch with 15-nm-thick suspension air gap. Appl Phys Lett 92: 103–110
3. Milaninia KM, Baldo MA, Reina A, Kong J (2009) All graphene electromechanical switch fabricated by chemical vapor deposition. Appl Phys Lett 95: 183105
4. Dragoman M, Dragoman D, Coccetti F, Plana R, Muller A (2009) Microwave switches based on graphene. J Appl Phys 105: 054309–054309-3
5. Sharma P, Perruisseau-Carrier J, Moldovan C, Ionescu AM (2014) Electromagnetic performance of RF NEMS graphene capacitive switches. IEEE Trans Nanotechnol 13
6. Ma JB, Jiang L, Asokanthan SF (2010) Influence of surface effects on the pull-in instability of NEMS electrostatic switches. Nanotechnology 21: 505708 9 pp. Iop Publishing. https://doi.org/10.1088/0957-4484/21/50/505708
7. Rebeiz GM (2003) RF MEMS: theory design and technology. Wiley, New Jersey
8. Sawant VB, More R, Mohite SS (2017) Numerical modeling and analytical verification for evaluating performance of RF microelectromechanical switches. J Adv Sci Technol 13(1) (Special Issue). ISSN 2230-9659
9. Sawant VB, Mohite SS, Cheulkar LN (2017) Effect of geometrical parameters on performance of RF MEMS switch at different temperature. In: Proceedings of international conference on nascent technologies in engineering (ICNTE)
10. Akinwande D, Petrone N, Hone J (2014) Two-dimensional flexible nanoelectronics. Nat Commun. https://doi.org/10.1038/ncomms66782
11. Yang FF, Huang YL, Xiao WB, Liu JT, Liu NH (2014) Control of absorption of monolayer MoS$_2$ thin-film transistor in one-dimensional defective photonic crystal. Physics Optics. https://doi.org/10.1209/0295-5075/112/37008

12. Bharadwaj BK, Nath D, Pratap R, Raghavan S (2016) Making consistent contacts to graphene: effect of architecture and growth induced defects. Nanotechnology 27(20). https://doi.org/10.1088/0957-4484/27/20/205705
13. Addou R, Colombo L, Wallace RM (2015) Surface defects on natural MoS$_2$. ACS Appl Mater Interfaces. https://doi.org/10.1021/acsami.5b01778
14. Lin W-H, Zhao, Y-P (2005) Casimir effect on the pull-in parameters of nanometer switches Microsystem Technologies. Springer, pp 80–85. https://doi.org/10.1007/s00542-004-0411-6

Optimization of Process Parameters for Erosion Wear in Slurry Pipeline

Kaushal Kumar, Ajay Kumar and Vinay Singh

Abstract In this paper, erosion wear behaviour of slurry flow has been investigated using a slurry erosion pot tester. Bottom ash is taken as the erodent material with varying concentrations. To assess test data, Taguchi's design of experimentation is used. The influence of test parameters on erosion wear could be estimated by computing signal-to-noise ratio and analysis of variance. L_9 (3^2) orthogonal array is used for the investigation. From analysis of test results, it is determined that speed has found as the most influencing parameter on erosion wear of base material. Based on experimental data, it is clearly revealed that erosion wear has strong dependence on rotational speed (N) as well as solid concentration (C_W) and testing time (T) also.

Keywords Slurry · Erosion · Bottom ash · Signal-to-noise ratio · ANOVA

1 Introduction

Basically, pipelines are used for transportation of slurry for short or long distances due to its little maintenance, throughout the year availability and being environmental friendly [1]. Brass is considered as appropriate pipe material having good mechanical properties and resistance to wear [2, 3]. As slurry contains some solid particles, which tend to impinge the base material, resulting various parts of the system, such as slurry pumps, pipelines and valves are prone to erosive wear. When two solid surfaces are in contact with each other, wear take place due to the mechanical deeds between them. Hard materials deform the softer material through mechanical action termed as erosion. This process can be a severe life-limiting

K. Kumar (✉) · A. Kumar
Department of Mechanical Engineering, K.R. Mangalam University,
Gurugram 122103, India
e-mail: ghanghaskaushal@gmail.com

V. Singh
Department of Mechanical Engineering, G.J.U.S. & T. Hisar, Hisar 125001, India

constraint in slurry pipeline by concerning unsettled flow of fluids, contains scratchy solid particles. Also, this damage can cause leakage and sudden failure of equipment without prior warning which can results in expensive repairs as well as loss of production time. Loss of material due to erosion is mainly subjected to different properties of particle such as shape, size, velocity, hardness, density, impact angle as well as slurry concentration, slurry viscosity, etc. [1, 4, 5] The erosion wear in wetted parts (pipes or pumps) affects overall life with their hydraulic efficiency [5]. A lot of factors are responsible for erosion wear and is more effective then corrosion, so its detailed analysis is done for the design of slurry transportation system [5–7]. However, the design and operation of such pipelines is still partially completed, thus extensive experimentation has been required to collect experimental data, and this is due to the fact that enormous parameters are involved in the design. The accurate prediction of wear rate with suitable DOE (Design of experimentation) is considered as the most influencing parameter that will also help in scheduling of maintenance work.

During last decade, various laboratory-scale test/setups have been developed to study erosion mechanism [8, 9]. Investigators documented that erosion wear depends on different operational conditions and parameters like velocity, solid concentration, erodent size, hardness of materials, etc. [10–12]. Researcher reported that erosion rate increases with concentration of solid in the slurry [13–17]. Although, a number of researchers significantly explored erosion wear behaviour of different slurry pipeline materials still there is no well-established study available for the material brass as a pipeline material.

The main objective of this paper is to provide a detailed data concerning with erosion wear behavior of material brass for multi-sized bottom ash slurry suspension.

2 Material and Method

2.1 Erodent Material Base Material

The erodent material is taken as bottom ash, collected from Rajiv Gandhi thermal power plant Hisar (Haryana). Bottom ash is collected from the bottom of combustion chamber. Energy-dispersive X-ray spectroscope (Model: JEOL, 6510LV) is used to measure Scanning electron microscopy (SEM) of bottom ash. The SEM image of bottom ash sample is shown in Fig. 1a. Particles of bottom ash are coarser, asymmetrical, darker grey in colour due to the existence of unburned carbon and having uneven surface texture. The particle size distribution (PSD) of bottom ash particle has been conducted with the help of sieve shaker having standardized sieves. About 62.50% particles of bottom are coarser than 150 µm, only 7.40% particles are finer than 53 µm as shown in Fig. 1b. The mixture of water and bottom ash has been used in the form of slurry.
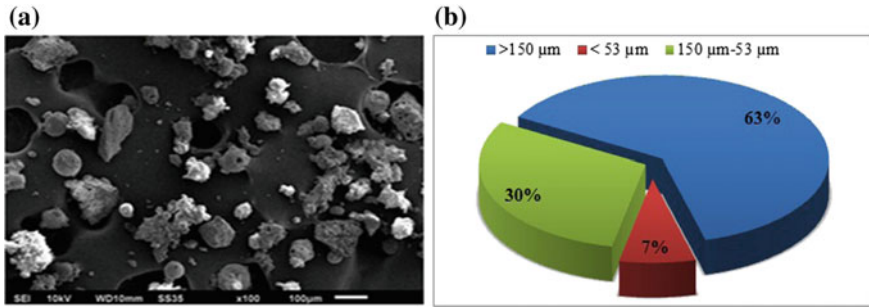
Fig. 1 **a** SEM **b** PSD of bottom ash sample

2.2 Base Material

The base material is cut into flat pieces of 75.10 mm × 25.10 mm × 5.02 mm with a central hole drilled (Ø = 5.20) to be held in rotating spindle of the tester. Erosion wear testing has been conducted on the brass substrates with geometry (shown in Fig. 2a). The chemical composition of brass substrates is shown in Fig. 2b, is measured by using Foundry Master spectrometer. The Vicker's hardness of base material is 228Hv, measured with the help of micro-Vickers hardness tester (Model MVH1, India). The micro hardness tests are conducted about three times and average value is taken as the hardness of base material. The surfaces of brass substrates are roughened prior the testing by grinding with 100-grade emery papers.

2.3 Experimental Method

In order to study the erosion wear, experimentation has been conducted at three different rotational speeds (N = 60, 800, 1000 rpm) at solid concentration (C_w) range of 30–50% (by weight) for time duration (T) of 90,120 and 150 min.
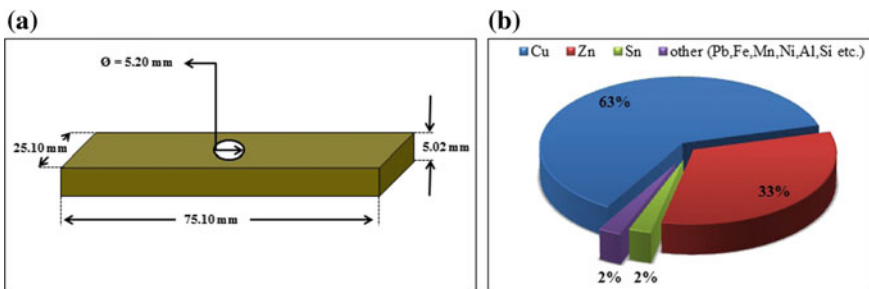
Fig. 2 **a** Geometry **b** Chemical composition of base material

The experiments are conducted on a bench scale apparatus, i.e. erosion wear pot tester (1.8 L, Ducom, India), as similar [18]. The tester contains a synchronized motor, spindle, specimen holder, jack and a pot. The specimen is fixed in holder attached to spindle. Screw jack is used to adjusting the position of pot. Tester's pot contains a cylindrical small cup inside over the larger cup in which slurry is poured. Erosion wear rate is determined in terms of mass loss (g/m^2). An electronic weighting machine of least count 1×10^4 g is used for the measurement of mass loss.

3 Result and Discussion

Design of Experiment (DOE) is one of the important and dominant statistical technique to study the effect of multiple variables simultaneously to yield an improved understanding of process performance. Taguchi technique is a powerful tool for the design of high quality systems [19, 20]. In the present work, Taguchi's design approach is used to study the effect of operating parameters on erosion wear of brass material with the help of MINITAB 16 software. In Taguchi's experimental design, the variables are expressed in two main categories, i.e. dependent variables and independent variables. There are three categories of quality characteristics, i.e. the-smaller-the-better, the-nominal-the-better, and the-bigger-the-better. In this study, the factors that are selected as independent variables are rotational speed, solid concentration and time duration. Erosion wear is considered as a response parameter or variable parameter. The experimental parameters (independent variables) have three levels. The level and factor are shown in Table 1.

Among the standard orthogonal arrays [21], the L_9 (3^2) orthogonal array is selected due to enabling the experimental design for the three factor with three levels.

3.1 Signal-to-Noise (S/N) Ratio

The S/N ratios for different parameters are determined by using L9 (32) orthogonal array as shown in Table 2. Difference between S/N ratios is also used to find the most influencing parameter. The S/N ratios are determined by applying smaller-is-better quality characteristic which is as follows:

Table 1 General presentation of factors with their levels

Parameters	Unit	Level 1	Level 2	Level 3
N	rpm	600	800	1000
C_w	% by weight	30	40	50
T	min.	90	120	150

Table 2 Experimental results based on L_9 (3^3) orthogonal array for the E_w and S/N ratios

Sr. No.	N	C_w	T	E_w	S/N ratios
1	600	30	90	6.23	−15.8898
2	600	40	120	7.88	−17.9305
3	600	50	150	9.00	−19.0849
4	800	30	120	8.60	−18.6900
5	800	40	150	9.43	−19.4902
6	800	50	90	9.01	−19.0945
7	1000	30	150	11.28	−21.0462
8	1000	40	90	10.98	−20.8120
9	1000	50	120	12.13	−21.6772

$$S/N = -10 \log(\text{M.S.D.}) \tag{1}$$

where M.S.D is the mean square derivation.

Table 2 shows the experimental results for S/N ratio using Eq. (1). Nevertheless the quality characteristic, S/N ratio with larger value resembles to better quality characteristics. Therefore, the level with minimum S/N ratio is considered as perfect level of the process parameters. In this experiment, the minimum S/N ratio is determined as −21.6772 and its trial number is 9. Thus, the optimum condition is observed as the 9th trial of the experiments. The effect of S/N ratios on erosion wear is shown in Fig. 3. Minimum value of erosion wear is found as 6.23 g/m^2 at N = 600 rpm with C_w = 30% for T = 90 min. While maximum value of erosion wear is found as 12.13 g/m^2 at N = 1000 rpm with C_w = 50% for T = 120 min.
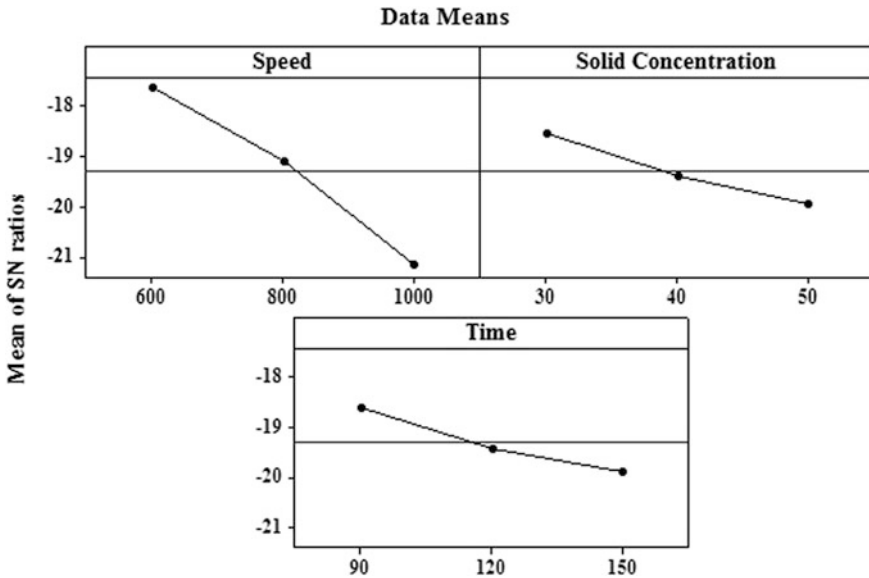
Fig. 3 The effect of S/N ratios on erosion wear

Table 3 Response table for S/N ratios

Level	N	C_w	T
1	−17.64	−18.54	−18.60
2	−19.09	−19.41	−19.43
3	−21.18	−19.95	−19.87
Delta	3.54	1.41	1.27
Rank	1	2	3

The minimum and maximum values of S/N ratio are observed as -21.6772 and −15.88 dB, respectively. It is observed that rotational speed have higher value of delta, which indicates that its rank is at most among other parameters. Similar trend was also observed by researcher [12]. With increase in relative motion between base material and erodent particles, the material removal rate increases. Table 3 represents the response table of S/N ratios for erosion wear. The value of delta provides the information about the most influencing parameters, i.e. highest influencing parameter have maximum value of delta. From Table 3, the value of delta is found as 3.54, 1.41 and 1.27 for N, Cw and T respectively.

3.2 Analysis of Variance (ANOVA)

Another approach to evaluate the results of erosion wear is ANOVA. The ANOVA is the statistical tool which is utmost applied to check the role of each factor in the form of percentage. A brief and detail analysis of ANOVA table provides the clarification about responsible factors, which need to be control for better outcomes. The results are shown in Table 4.

The DOF is equivalent of two, less than the factor's level. A sum of squares is a value that is used in calculating a variance and standard deviation for a set of scores. The F refers to variance and is equivalent to the value of the Mean square divided by the value of error. According to Table 4, the significant factors could be determined as to their individual contributions on results. So, the main factors which have significant effects on the quality criteria are determined as the N (83.15%). Also, it can be inferred that Cw (10.11%) and T (07.91%) are also important factor because of its small effect as compared to N.

Table 4 Results of ANOVA for E_w

Source	DF	Seq. SS	Adj. MS	F	P	C
N	2	21.86	10.93	210.02	0.00	83.15
C_w	2	2.71	1.36	26.07	0.03	10.11
T	2	2.12	1.06	20.40	0.04	7.91
Error	2	0.10	0.05			
Total	8	26.79				
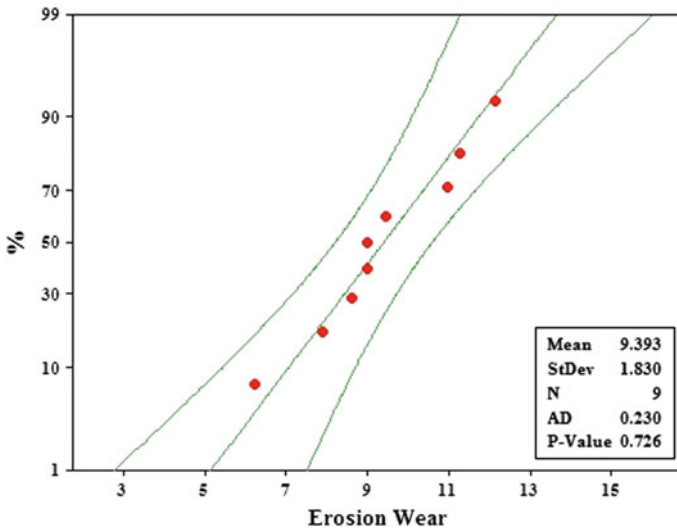
Fig. 4 Probability plot of erosion wear

Moreover, N is considered as the most dominating factor because it has maximum P-value and minimum F-value among all the parameters. It should be focused on the parameter values of main factors having highest effects on the quality criteria to estimate the optimum condition. The probability plot of erosion wear is evaluated by using Taguchi's DOE as shown in Fig. 4.

It has been detected that the normal distribution of residuals (errors) lies near about straight line accepting 5% level of confidence. It is also observed that the P-value is found as 0.72, which indicates the non-linearity in augmentation of erosion wear. Standard deviation was observed as 1.83. In order to found the interaction between different parameters, the interaction plots have been prepared as shown in Fig. 5. Maximum erosion wear is observed at maximum value of N, while it is not found in case of C_w and T.

3.3 Visual Analysis of Eroded Specimen

Surface morphology of eroded brass specimen was analysed with the help of Scanning electron microscopy (SEM). The eroded image of brass specimen (at N = 1000 rpm, C_w = 50% and T = 150 s.) is shown in Fig. 6. The dark phase of the topography represents the removal of softer elements of the composition. The presence of wear marks are detected on the worn surface due to pores, deep craters and lip formation. It is found that surface wear formed through deep-cratering is more responsible for loss of material. Researchers reported that cutting and fracture are the major modes of erosion wear mechanisms in the pipelines [19–21].
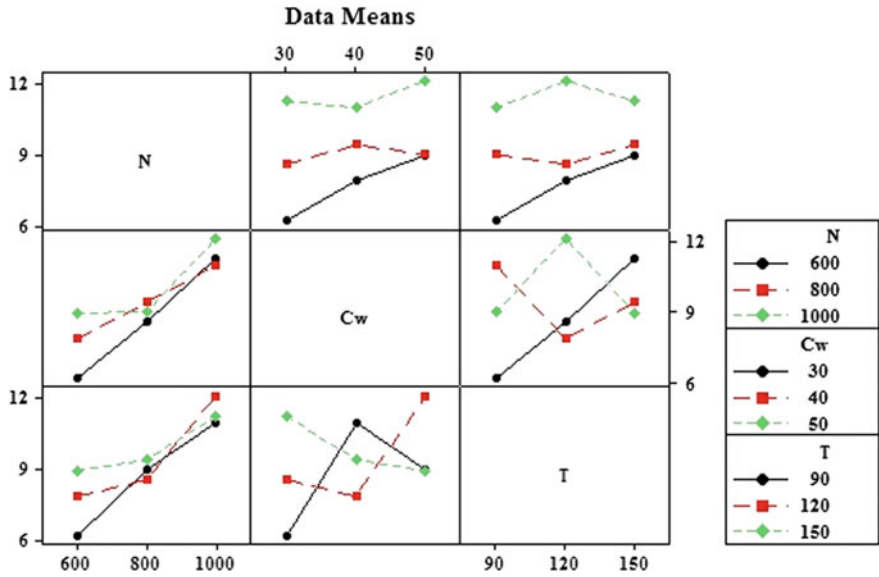
Fig. 5 Parametric interaction between different parameters
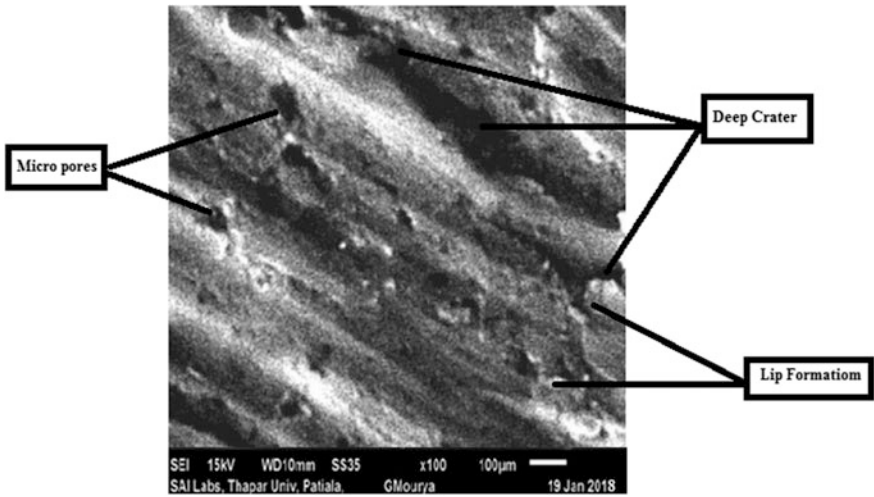
Fig. 6 Scanning electron microscopy (SEM) of eroded brass specimen

4 Conclusions

Experiments have been conducted to establish the effect of N, C_w and T on erosion wear of material brass. The existing study concludes that E_w rate increases with increase in rotational speed, solid concentration and time period. However, N is considered as the most pronouncing factor as compared to C_w and T. It is also observed that N has maximum values of delta and top rank among other parameters. Minimum F-value and maximum P-value also indicating towards the most dominating factor among all the parameters. Maximum erosion wear is observed at maximum value of N, while it is not found in case of C_w and T. Standard deviation was observed as 1.83.

References

1. Kumar S, Mohapatra SK, Gandhi BK (2013) Effect of addition of fly ash and drag reducing on the rheological properties of bottom ash. Int J Mech Mater Eng 8:1–8
2. Callcut V (2005) The brasses: properties & applications. CDA Publication, Hemel Hepstead
3. Namboodhiri TKG, Chaudhary RS, Prakash B, Agrawal MK (1982) The dezincification of brasses in concentrated ammonia. Corros Sci 22, 1037–1047
4. Desale GR, Gandhi BK, Jain SC (2009) Particle size effects on the slurry erosion of aluminium alloy (AA 6063). Wear 266:1066–1071
5. Pagalthivarthi KV, Gupta PK (2009) Prediction of erosion wear in multi-size particulate flow through a rotating channel. Fluid Dyn Mater Process 5:93–121
6. Elkholy A (1983) Prediction of abrasion wear for slurry pump materials. Wear 84:39–49
7. Shook CA, Haas DB, Husband WHW, Small M (1981) Relative wear rate determinations for slurry. J Pipelines 1:273–280
8. Roco MC, Addie GR, Dennis J, Nair P (1984) Modeling erosion wear in centrifugal slurry pumps. In: 9th international conference on hydraulic transport of solids in pipes, BHRA, Rome, Italy, vol 17–19, pp 291–309
9. Ghosh S, Sahoo P, Sutradhar G (2014) Wear characteristics optimization of Al-7.5% sic metal matrix composite using taguchi method. Adv Mater Manuf Charact 4, 93–99
10. Kumar D, Bhingole PP (2015) CFD based analysis of combined effect of cavitation and silt erosion on kaplan turbine. In: 4th International conference on materials processing and characterization. Materials Today Proceeding, vol 2, pp 2314–2322
11. Tarjan I, Debreczeni E (1972) In: 2nd International conference on hydraulic transport of solids in pipes, BHRA, Cranfield, UK, pp l–14
12. Gandhi BK, Singh SN, Seshadri V (1999) Study of the parametric dependence of erosion wear for the parallel flow of solid-liquid mixtures. Tribol Int 32:275–282
13. Desale RG, Gandhi BK, Jain SC (2005) Improvement in the Design of a pot tester to simulate erosion wear due to solid-liquid mixture. Wear 259:196–202
14. Gandhi BK, Singh SN, Seshadri V (2003) A study on the effect of surface orientation on erosion wear of flat specimens moving in a solid–liquid suspension. Wear 254:1233–1238
15. Cho TY, Yoon JH, Kim KS, Song KO, Joo YK, Fang W, Zhang SH, Youn SJ, Chun HG, Hwang SY (2008) A study on HVOF coatings of micron and nano WC-Co powders. Surf Coat Technol 202:5556–5559
16. Prasad BK, Jha AK, Modi OP, Yegneswaran AH (2004) Effect of sand concentration in the medium and traversal distance and speed on the slurry wear response of a zinc-based alloy alumina particle composite. Tribol Lett 17:301–309

17. Gupta R, Singh SN, Seshadri V (1995) Prediction of uneven wear in slurry pipeline on the basis of measurements in a pot tester. Wear 184:169–178
18. Kumar K, Kumar S, Singh G, Singh JP, Singh J (2017) Erosion wear investigation of HVOF sprayed WC-10Co4Cr coating on slurry pipeline materials. Coatings 7:1–11
19. Zhaohe T, Chuanxian D, Dongsheng Y (1992) A fracture model for wear mechanism in plasma sprayed ceramic materials. Wear 155:309–316
20. Martini C, Palombarini G, Poli G (2004) Sliding and abrasive wear behaviour of boride coatings. Wear 256:608–613
21. Modi OP, Mondal DP, Prasad BK, Singh M, Khaira HK (2003) Abrasive wear behaviour of a high carbon steel: effects of microstructure and experimental parameters and correlation with mechanical properties. Mater Sci Eng 343:235–242

Vibration Response of Human Subject Using FEM

Rajender Kumar, Sahil Savara, Sachin Kalsi and Ishbir Singh

Abstract Human body suffers when exposed to different vibration conditions that generated by traveling, working with machines etc. in sitting and standing posture both. In this study, modal analysis has been performed on 54 kg Indian human subject to find out the natural frequency and deformations for both sitting and standing posture under un-damped vibration conditions. An ellipsoidal approach has been used to model human subject as 3-D CAD model using physical dimensions and anthropometric data available in existing literature. Human subject is divided into different segments to convert complex human body into simple model using ellipsoidal shape of each segment. The results obtained in this study, will be helpful in designing components for human use like automobile seats, lifts, escalators, machine parts, etc. Also, in this study a comparison has been done in the results obtained in sitting and standing posture analysis. Further, it was found that with the increase in natural frequency, deformation increases in both the cases.

Keywords Modal analysis · Human body · Natural frequency · FEM · Standing posture · Sitting posture

1 Introduction

Human body experiences vibration whenever it comes in contact with vibrating surface and the possibilities are sitting on vibration seat (sitting posture), standing on a vibration floor (standing posture) or lying on a vibrating bed (recumbent posture). Vibration affects the comfort, performance, and efficiency of a person while travelling in vehicle, working on machines, daily life activities, etc. With increase in number of commentators during last few years in buses, cars, metro, aeroplanes, etc., human body in sitting and standing postures suffers from discomfort and injury due to different vibration conditions transferred from roads,

R. Kumar · S. Savara · S. Kalsi (✉) · I. Singh
Department of Mechanical Engineering, Chandigarh University, Chandigarh, Punjab, India
e-mail: phd.sachinkalsi@gmail.com

humps, seat interface, body parts of vehicle, etc. Taking this problem into consideration regarding a human body, study has been performed in this research work with sitting posture without backrest and standing posture without any support. In this work, natural frequencies and effect of vibration at different segments of human body in sitting posture and standing posture has been studied. The results obtained will be helpful in designing of seats and products for human use which will reduce the effect of vibration. Several researchers have considered different biodynamic models of human body using mass, density, stiffness, etc., similar to human body. In this research paper, finite element method (FEM) has been used to perform modal analysis when Indian male subject of 54 kg is exposed to free vibration conditions both in standing and sitting posture.

Several researchers have contributed their work in the field of WBV under different vibration conditions on different human subjects using different ranges of frequencies and accelerations using different postures. Singh et al. [1] generated a lumped parameter model (LPM) of 54 kg Indian male subject using 50th percentile anthropometric data. Liu et al. [2] developed a FEM of seated human subject supported by tri-axial apparent mass subjected to vertical vibration. Kitazaki and Griffin [3] used FEM to generate a 2-D human model. Nigam and Malik [4] developed a LPM model of U.S. male human subject 50th percentile anthropometric data. Blood et al. [5] conducted an experiment on 12 male subjects. Matsumoto and Griffin [6] evaluated the difference in biodynamic response in sitting and standing posture. Kitazaki and Griffin [7] used FEM to develop 2-D model of human. Ciloglu et al. [8] conducted an experiment to analyze whole body vibration (WBV). Griffin [9] used different methods to measure the WBV. Matsumoto and Griffin [10] analyzed the influence of standing human body on vibration. Shibata [11] find out the multiple scale factor for the discomfort of vertically standing persons. Rakheja et al. [12] studied the biodynamic response of standing human subjected to WBV. Singh et al. [13] performed modal analysis using ellipsoidal Indian subject of mass 54 kg in sitting posture.

From the literature review, it has been observed that lot of researchers have worked in the field of WBV under different dynamic conditions to increase the comfort level of human body and reduce the tendency of getting resonance with designed product for human use. Also, it is also observed that analytically, experimentally work has been performed on WBV than approach FEM. Taking this point into consideration, this study has been performed on Indian male human subject in standing and sitting posture under free un-damped conditions using FEM.

2 Methodology

In this study, 50th percentile Indian anthropometric data corresponding to 54 kg human subject in sitting posture without backrest and standing posture has been considered to perform modal analysis under un-damped free vibrations. The physical dimensions of human subject have been calculated using anthropometric

data of Indian male population [14] and formulae [1] to make a 3-D CAD model in SolidWorks 2016 software. FEM tool, i.e., ANSYS 16.0 software has been used to perform modal analysis using FEM under un-damped free vibration conditions.

Some assumptions have been considered during this study that is given below.

- Free un-damped vibratory model of human body has been considered.
- Subject is sitting without the support of any backrest.
- Subject in standing posture without any support is perpendicular to floor.
- Ellipsoidal shape has been considered to model different segments of a human body.

2.1 CAD Model of Human Subject

A physical model of human Indian male subject with mass of 54 kg, i.e., 50th anthropometric data of India population has been converted into CAD model using all segments of human body considered as in ellipsoidal shape [1]. A CAD model of human subject has been modeled in Solidworks 2016 software and is shown in Fig. 1. The dimensions to generate CAD model of human body using ellipsoidal shape has been taken from anthropometric data as given by Chakrabarti [14] and Singh et al. [1].

2.2 Modal Analysis of Human Subject

A 3-D CAD model of 54 kg Indian male subject has been generated using designing software i.e. Solidworks 2016 as shown in Fig. 1. FEM analysis has been
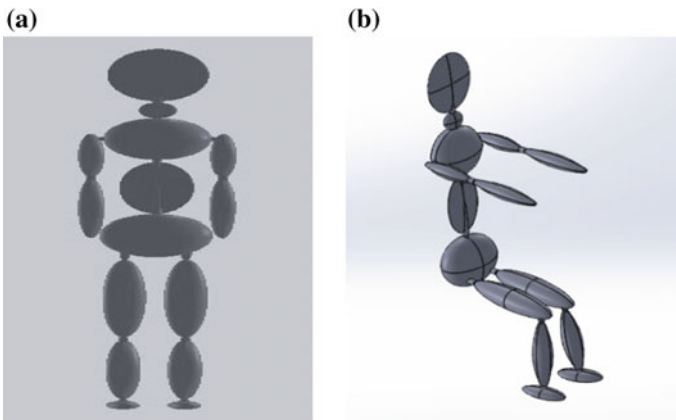
Fig. 1 CAD model of male subject in **a** standing and **b** sitting Posture
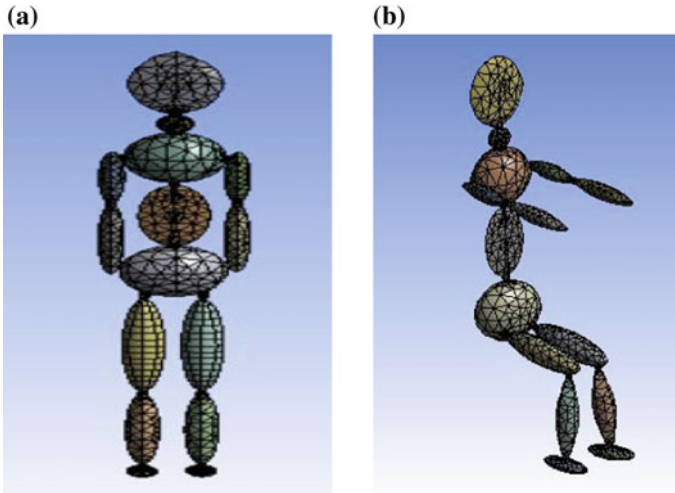
Fig. 2 Meshed model of human subject in **a** standing and **b** sitting Posture

performed using CAE (Computer Aided Engineering) ANSYS 16.0. To import 3-D model of human subject in ANSYS software to perform modal analysis, part file generated in Solidworks software was converted in Parasolid file. The physical properties of human subject have been considered as E (Modulus of elasticity) = 13 MN/m^2 [4] and human subject density = 1.062×10^3 kg/m^3 [1]. The material of human subject 3-D model has been assumed to be homogenous and isotropic in nature, i.e., the properties of the material are same in all the directions. The tetrahedral mesh elements have been considered for meshing of human segments in ANSYS software as tetrahedral mesh element is solid element and also, stiffer than other elements type which results in more accurate results. These elements result in smoother meshing for complex structures. The meshed model of human subject generated in ANSYS 16.0 is shown in Fig. 2.

2.3 Boundary Conditions

A human subject as shown in Fig. 3a has been assumed to be in standing posture with backbone in erect position, i.e., straight perpendicular to a floor. Both hands and arms have been considered to be straight and perpendicular to the floor without touching any part of human body. Also, feet have been considered to be straight parallel to floor and both legs to be straight with no bend. In this posture, only feet are assumed to be fixed to floor.
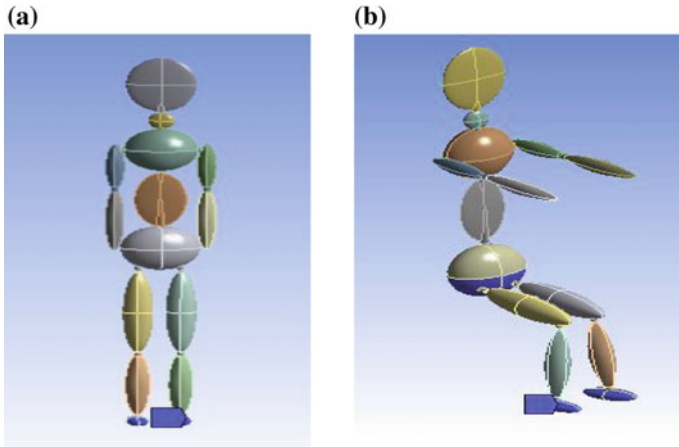
Fig. 3 Boundary condition of human subject in **a** standing and **b** sitting Posture

Similarly, for human subject in sitting posture as shown in Fig. 3b, hip joint is in touch with a seat and is assumed to be fixed support in ANSYS 16.0 software. In both the postures, it has been assumed that no external load or force is applied on human subject.

3 Results and Discussions

3.1 Modal Analysis of Human Subject in Sitting Posture

The results that have been obtained after performing modal analysis by using FEM on ANSYS 16.0 for Indian male human subject having mass 54 kg in sitting posture is shown in Table 1. It has been observed from Table 1 that with increase in natural frequencies, maximum deformation transmits from head (at initial modes) to lower arms (in final modes).

Table 1 Natural Frequency and maximum deformation in human segments for 54 kg human subject

Mode	Natural frequency (Hz)	Human segment (maximum deformation)
1	2.8	Head and lower arms
2	3.2	Head and lower arms
3	4.9	Lower arms
4	10.7	Lower arms
5	16.3	Lower arms
6	18.7	Lower arms
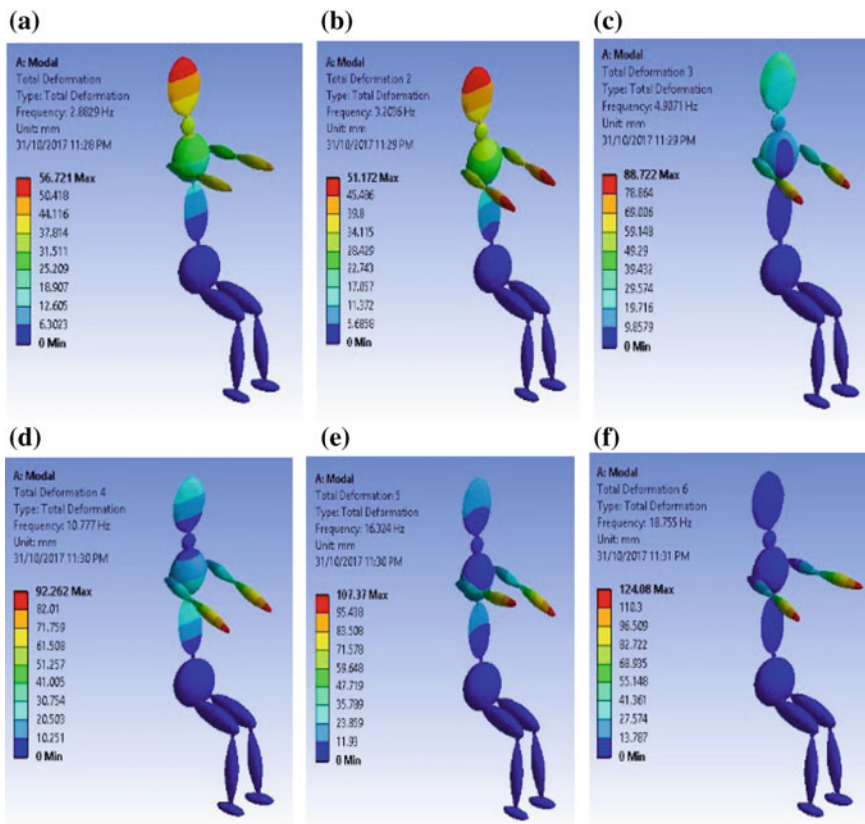
Fig. 4 **a** Mode shape at natural frequency 2.88 Hz; **b** Mode shape at natural frequency 3.20 Hz; **c** Mode shape at natural frequency 4.90 Hz; **d** Mode shape at natural frequency 10.77 Hz; **e** Mode shape at natural frequency 16.324 Hz; **f** Mode shape at natural frequency 18.75 Hz

At different value of natural frequencies, mode shapes as shown in Fig. 4 have been generated to observe the pattern of vibration transmission for 54 kg human body under free un-damped vibration conditions. The results obtained after performing modal analysis in sitting posture without backrest have been shown in Table 1.

- In first mode shape as shown in Fig. 4a, at natural frequency of 2.8 Hz the vibration effect has not been observed at upper body segments such as lower torso, upper legs, lower legs and feet, and maximum deformation is observed at head and lower arms. It might be due to a reason that lower torso and feet are in contact with seat and ground respectively. Also, human subject behaves like a first mode shape of a cantilever beam.
  In second mode at natural frequency of 3.2 Hz as shown in Fig. 4b, observed that to-and-fro motion of upper body segments is in lateral direction with

maximum deformation observed at head and lower arms about connecting point between central and lower torso. Also, no deformation has been observed at lower body segments. Also, no other motion of human subject in other directions has been noticed in this mode.

- As shown in Fig. 4c, at natural frequency of 4.9 Hz, i.e., at third mode shape of human subject, upper portion of body segments rotates along a vertical direction about a point that lies in central and lower torso. At lower arms, maximum effect of vibration has been observed. And effect of vibration has been transmitted from head segment to lower arms segments.
- In fourth mode, as shown in Fig. 4d at natural frequency of 10.7 Hz in upper body segments a fore-and-aft motion has been observed with slight bend at point which lies in between upper and central torso. And maximum deformation has occurred at lower arms and hands.
- At natural frequency of 16.3 Hz, as shown in Fig. 4e, i.e., at fifth mode, less deformation has been observed in body segments except at upper and lower arms. The maximum value of deformation is observed at lower arms and hands. In this mode, human body behaves like a rigid body.
- In the sixth mode, at natural frequency of 18.7 Hz as shown in Fig. 4f, except upper arms and lower arms no deformation has been observed at any other segment. At this mode, human body behaves like a rigid body.

3.2 Modal Analysis of Human Subject in Standing Posture

The results obtained after performing modal analysis, i.e., natural frequencies of 54 kg Indian male human subject in standing posture obtained under un-damped free vibration conditions is shown in Table 2.

The mode shapes obtained after modal analysis on the human subject at different natural frequencies are shown in Fig. 5a, b, c, d, e, f.

- It has been observed from Fig. 5a that at the natural frequency of 2.47 Hz, maximum effect of vibration is obtained at head with a deformation of 24.83 mm. At natural frequency of 5.16 Hz as shown in Fig. 5b, a maximum

Table 2 Natural Frequency and maximum deformation in standing posture

Mode	Natural frequency (Hz)	Human segment (with maximum deformation)
1	2.47	Head
2	5.16	Head
3	9.84	Head
4	12.21	Head
5	14.66	Lower arms and Hands
6	19.49	Lower arm and Hands
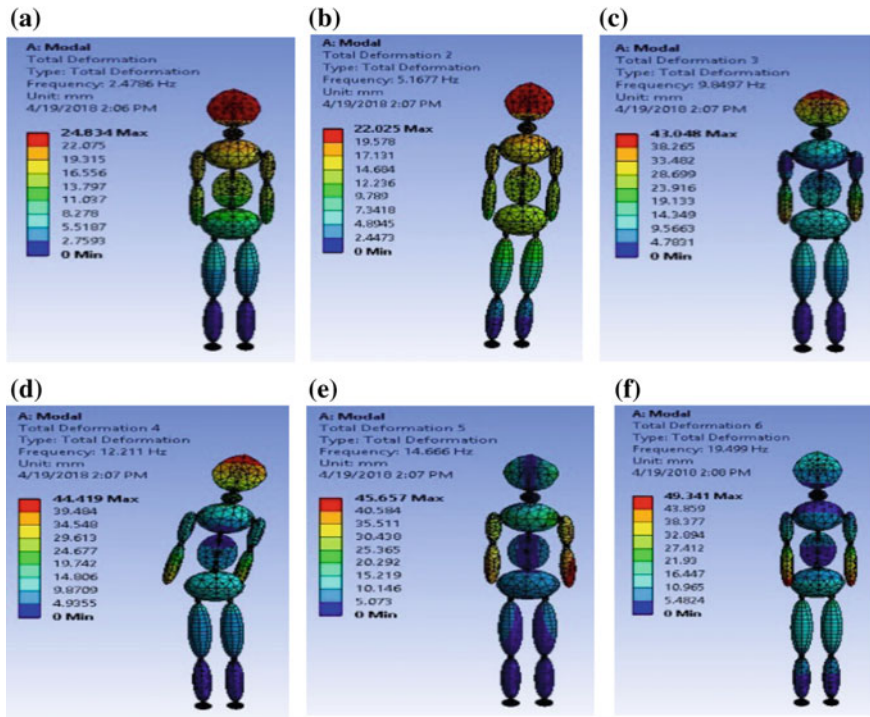
Fig. 5 **a** Mode shape at natural frequency 2.47 Hz; **b** Deformation at natural frequency 5.16 Hz; **c** Deformation at natural frequency 9.84 Hz; **d** Deformation at natural frequency 12.21 Hz; **e** Deformation at natural frequency 14.66 Hz; **f** Deformation at natural frequency 19.49 Hz

deformation, i.e., 22.02 mm is obtained at head and also, therefore the upper torso is slight bend towards the left side. At natural frequency of 9.84 Hz and 12.21 Hz as shown in Fig. 5c, central torso is at balanced position because feet is fixed and at this mode body acts like as a cantilever beam. At natural frequency of 12.21 Hz as shown in Fig. 5d, in fourth mode maximum deformation, i.e., 44.41 mm has been observed at head and upper portion of body moves toward right side.

- In fifth mode shape, upper torso of human subject has been rotated about hip joint towards the left side, as shown in Fig. 5e, at natural frequency of 14.66 Hz. At sixth mode as shown in Fig. 5f at natural frequency of 7.55 Hz; it has been observed that left lower arm and a motion of both arms in fore-and-aft direction is observed. With maximum deformation i.e. 49.34 mm at arms and hands.

- In standing and seated portion same trend of mode shape has been observed. The value of natural frequency can vary as obtained by for both cases. As in this study, 54 kg has been considered and also, FEM model has been used which is

an approximate method to find out results. The results in this study show that shoes might have more cushions to minimize the effect of vibration, and railing, supports should have a proper material for hands (so that resonance should not occur with the human subject).

4   Conclusions

In current study, modal analysis has been performed on 54 kg Indian human male subject using FEM approach. A human subject has been segmented into different segments in ellipsoidal shape and then, a 3-D CAD model generated in both postures, i.e., standing and sitting. In sitting posture, it has been found that with the increase in natural frequencies, a maximum effect of vibrations transmits from head at 2.8 Hz to lower arms at 18.75 Hz. In standing posture, a maximum effect of vibrations transmits from head (2.47 Hz) to lower arms (19.49 Hz) with an increase in natural frequency of human subject. In both the postures, human subject behaves as a cantilever. The results of this study can be used to design components for human use, i.e., automobile seats, railings, lifts, etc., to avoid resonance with a designed component. Further, the current study can be extended for different postures of human subject under damping conditions.

References

1. Singh I, Nigam SP, Saran VH (2014) Modal analysis of human body vibration model for Indian subjects under sitting posture. Ergonomic 58(7):1117–1132
2. Liu C, Qiu Y, Griffin MJ (2015) Finite element modelling of human-seat interactions: vertical in-line and fore-and-aft cross-axis apparent mass when sitting on a rigid seat without backrest and exposed to vertical vibration. Ergonomics 58(7):1207–1159
3. Kitazaki S, Griffin MJ (1997) A modal analysis of whole-body vertical vibration using a finite element model of human body. J Sound Vib 200(1):83–103
4. Nigam SP, Malik M (1987) A study on a vibratory model of a human body. J Biomech Eng 109(2):148–153
5. Blood RP, Ploger JD, Yost MG, Ching RP, Johnson PW (2010) Whole body vibration exposures in metropolitan bus drivers: a comparison of three seats. J Sound Vib 329(1):109–120
6. Matsumoto Y, Grffin MJ (1998) Dynamic response of standing human body exposed to vertical vibration: influence of posture and vibration magnitude. J Sound Vib 212(1):85–107
7. Kitazaki S, Griffin MJ (1997) A model analysis of whole body- vibration using a finite element model of the human body. J Sound 200(1):83–103
8. Ciloglu H, Alziadeh M, Mohany A, Kishawy H (2015) Assessment of the whole body vibration exposure and the dynamic seat comfort in passenger aircraft. Int J Ind Ergon 45:116–123
9. Griffin MJ (1998) A comparison of standardized methods for predicting the hazards of whole body vibration and repeated shock. J Sound Vib 215(4):883–914
10. Matsumoto Y, Grffin MJ (2002) Effect of phase on human response to vertical whole body vibration and shock- Analytical investigation. J Sound Vib 250(5):813–834

11. Shibata N (2015) Subjective response of standing persons subjected to fore-aft, lateral and vertical whole-body vibration. Int J Ind Ergon 49:116–123
12. Rakheja S, Dong RG, Patra S, Boileau PE, Marcotte P, Warren C (2010) Biodynamics of the human body under whole-body vibration: synthesis of the reported data. Int J Ind Ergon 40 (6):710–732
13. Singh I, Nigam SP, Saran VH (2016) Effect of backrest inclination on sitting subjects exposed to WBV. Procedia Technol 23:76–83
14. Chakrabarti D (1997) Indian anthropometric dimensions (For Ergonomics Design Practice). National Institute of Design, Ahmedabad

Experimental Investigations of Multiple Faults in Ball Bearing

S. P. Mogal and S. N. Palhe

Abstract Ball bearings are extensively used in many rotating machinery applications. Ball bearing failure is the main cause of breakdown of the rotating machineries. Local defects in ball bearing produced due to fatigue consist of cracks, pits and spalls on the rolling surfaces. Several researchers have studied the single fault in ball bearing, but in practice two or more faults (combined fault) are usually present. Fault diagnosis of a single row ball bearing has been extensively studied, however literature specific to double row ball bearings are sparse. This paper presents such cases, where single and multiple bearing faults of double row ball bearing are considered together. The objective is to experimentally investigate the single and multiple bearing faults of the inner race, outer race, cage and ball fault using envelope analysis. Envelope spectrum analysis is the best tool for bearing fault diagnosis like cracks and spalls in ball bearings. Bearing frequencies are excellently identified in the envelope spectrum.

Keywords Ball bearing · Multi-fault diagnosis · Envelope analysis

1 Introduction

In many rotating machinery applications rolling element bearings are widely used. Ball bearing failure is main cause of breakdown of the rotating machineries. To avoid failure of bearing various condition monitoring techniques like acoustic emission, current and temperature monitoring, wear debris detection and vibration

S. P. Mogal (✉) · S. N. Palhe
Department of Mechanical Engineering, NDMVPS's KBT College of Engineering,
Nashik, India
e-mail: spmogal10@gmail.com

analysis are used. Among these monitoring methods, vibration analysis is extensively used for identifying bearing faults. Vibration analysis is an important method for indicating bearing faults because it is an efficient and a non-disturbing method. For reducing downtime and improving the maintenance efficiency of ball bearing, vibration analysis is been commonly used. In this paper, envelope analysis technique for multi-fault diagnosis is proposed.

Cracks, pits, and spalls on the rolling surfaces are major local defects in ball bearing. Patel et al. [1] reported that local defects, such as spalls, pits and cracks on mating components of bearings are generated due to fatigue. Karacay and Akturk [2] reported that several researchers studied ball bearing defects by theoretically and experimentally and its effects on vibration level using scalar parameters such as peak-to-peak value, root mean square (RMS), crest factor and kurtosis. To predict fault locations an experimental investigation of a single row ball bearing faults by FFT spectrum analysis is presented. Rafsanjani et al. [3] proposed the analytical model for single row ball bearing with local defects on the inner race, outer race, and ball. They suggested that the analytical model can be used for design, predictive maintenance, and also condition monitoring of machines. Kiral and Karagülle [4] proposed in finite element method of dynamic loading models to investigate the effect of rotational speed on diagnostic of rolling element bearing for healthy and defected single row ball bearing. They examined that time and frequency domain techniques are sensitive to changes in rotational speeds. Choy et al. [5] checked out vibration results of faulty ball bearings using the time domain averaging, frequency component averaging, and the modified Poincare maps. They noticed that the average time signal technique does not provide clear information about faulty bearings, but the average frequency component and the modified Poincare map techniques provided much clear information about faulty bearing. Nikolaou et al. [6] proposed a wavelet packet transform signal processing technique for bearing faults. Samanta et al. [7] conferred artificial neural network (ANN) for rolling element bearings fault diagnosis. They used time domain signal of good and defective bearings as inputs to the ANN. Kankar et al. [8] used continuous wavelet transform (CWT) for bearing fault diagnosis. Artificial neural network (ANN) and support vector machine (SVM) are used for detection of bearing faults. Kankar et al. [9] suggested a response surface method for bearing defects such as spalls on outer race, inner race on ball are considered. Kilundu et al. [10] employed singular spectrum analysis to process vibration signals resulting from roller bearings and diagnosis of defective bearing. Wang et al. [11] presented adaptive spectral kurtosis (ASK) for multi-fault in rolling element bearing detection. A theoretical model of multiple bearing faults is developed. Feiyun Cong et al. [12] proposed a rolling bearing fault model which is based on dynamic load analysis of rotor bearing system. They investigated rotor bearing vibration model combined with both dynamic response and fault signal expression of rolling element bearing.

| Vibration signal | → | Band pass filter | → | Envelope | → | Envelope spectrum |

Fig. 1 Steps in envelope analysis

2 Envelope Analysis

Envelope analysis is the technique to extract the modulating signal from an amplitude-modulated signal. The result shows the time history of the modulating signal. This signal may be in time domain or it may be subjected to a subsequent frequency analysis. Envelope Analysis is the frequency spectrum of the modulating signal. It can be used for diagnosis of machinery fault where faults have an amplitude modulating effect on the characteristic frequencies of the machinery. The analyzer essentially tries to pick up some picks, otherwise be buried in the high frequency noise. Envelope analysis steps are as shown in Fig. 1.

3 Experimental Setup

The experimental test rig is as shown in Fig. 2. The test rig consists of a shaft with rotor disc and it was supported on two ball bearings. A DC motor coupled by a rigid coupling drives the shaft.
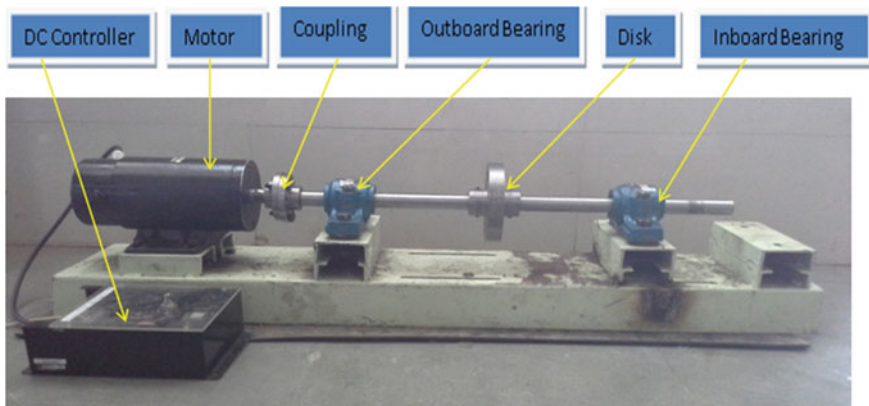
Fig. 2 Experimental setup

For the vibration measurement and analysis, four channels FFT analyser is used (Fig. 3). The three piezoelectric accelerometers are used to collect the vibration signals in three directions at a bearing-housing.

The ball bearing geometry is shown in Fig. 4. The self-aligning, double row deep groove ball bearing (SKF 1205 ETN) is used with the dimensions shown in Table 2. The fault in the Inner race, outer race and cage created using electro-discharge machining (EDM), the rectangular notch of 7.5 mm length, width 0.55 mm and depth 1.15 mm is created in outer race (Fig. 5). Similarly, rectangular

Fig. 3 FFT analyser
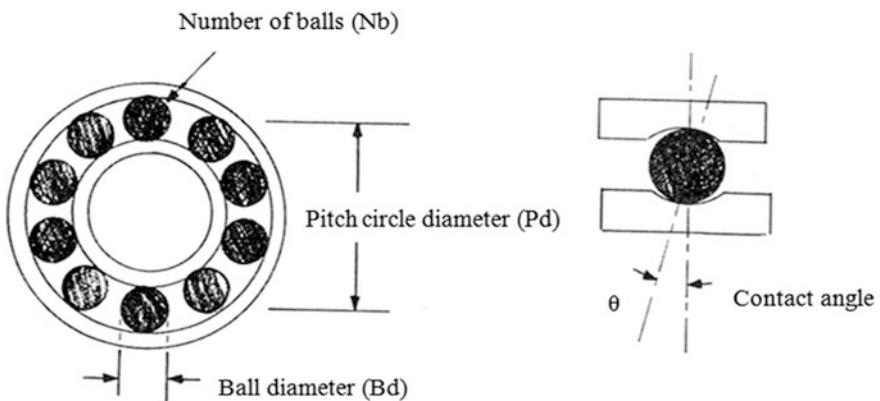
Fig. 4 Ball bearing geometry

Fig. 5 Outer race fault
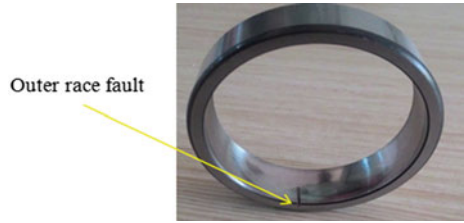
Fig. 6 Inner race fault
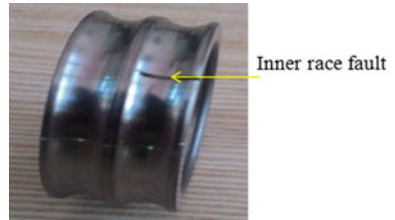
Fig. 7 Cage fault
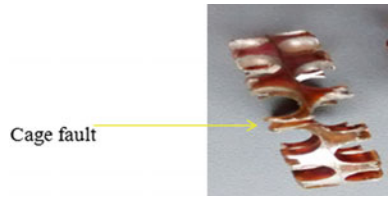
Fig. 8 Ball fault (Spall)

Table 1 Parameters for G-demod wideband measurement

DEMOD fmin (Hz)	500
DEMOD fmax (Hz)	25600
Samples	8192

Table 2 Specifications of rolling ball bearing

Bearing model	SKF 1205 ETN
Rolling element diameter, Bd	7.1 mm
Number of rolling elements, Nb	13
Pitch diameter, Pd	37.9 mm

notch of 7.5 mm length, width 0.5 mm and depth 1.15 mm, created in the inner race (Fig. 6), and rectangular notch of 6 mm length, width 0.7 mm and depth 1 mm, in cage (Fig. 7). The faulty ball (spall) from other bearing was used for analysis (Fig. 8). The signal is filtered in (DEMOD fmin, DEMOD fmax) range and demodulated. Parameters for G-demod wideband measurement is as shown in Table 1. The specification of rolling ball bearing as shown in Table 2.

3.1 Characteristic Fault Frequencies

The bearing characteristic frequency depends on the geometry of the bearing and on the type bearing defect. The characteristic fault frequencies of bearing are shown in Table 3. The characteristic fault frequencies obtained by the following equations [13]

Table 3 Characteristic fault frequencies of bearing (SKF 1205 ETN)

Types of fault	Characteristic fault frequency at the input frequency			
	1004 rev/min (16.73 Hz)	1021 rev/min (17.01 Hz)	1025 rev/min (17.08 Hz)	1048 rev/min (17.46 Hz)
Outer race	87.79	89.26	89.63	91.63
Inner race	129.67	131.84	132.38	135.33
Cage	6.75	6.86	6.89	7.04
Ball	41.80	42.51	42.68	43.63
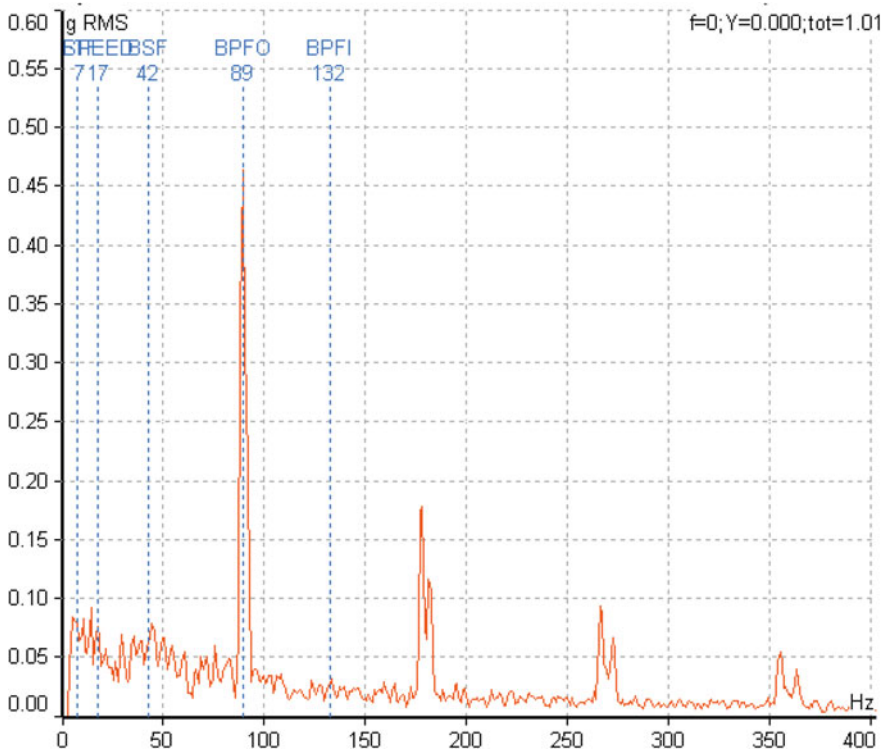
Fig. 9 Envelope spectrum of outer race fault at 1021 rev/min in vertical direction

$$\text{BPFI (Ball pass frequency } - \text{Inner)} = \frac{Nb}{2}\left(1 + \frac{Bd}{Pd}\cos\theta\right) \times F_s \qquad (1)$$

$$\text{BPFO (Ball pass frequency } - \text{Outer)} = \frac{Nb}{2}\left(1 - \frac{Bd}{Pd}\cos\theta\right) \times F_s(1) \qquad (2)$$

$$\text{FTF (Fundamental train frequency)(Cage)} = \frac{1}{2}\left(1 - \frac{Bd}{Pd}\cos\theta\right) \times F_s(1) \qquad (3)$$
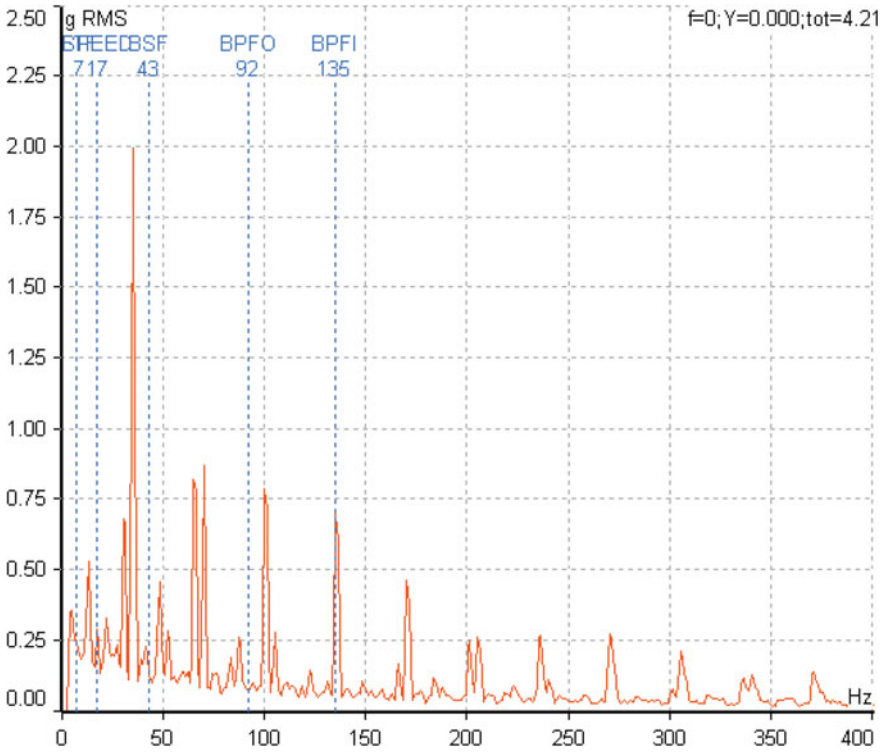
Fig. 10 Envelope spectrum of inner race fault at 1048 rev/min in vertical direction

$$\text{BSF (Ball spin frequency)} = \frac{Pd}{2Bd}\left(1 - \left(\frac{Bd}{Pd}\right)^2 (\cos\theta)^2\right) \times F_s \qquad (4)$$

where,

F_s =   = Shaft rotational frequency
Nb =   Number of balls
Bd =   Ball diameter (mm)
Pd =   Pitch diameter (mm)
θ =   contact angle in degree
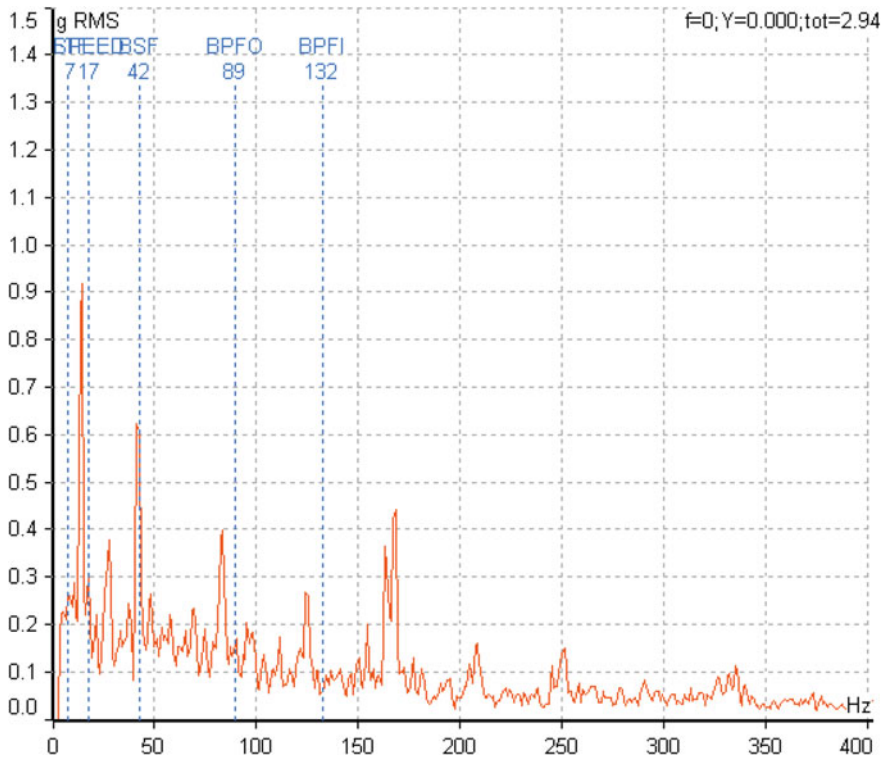
Fig. 11 Envelope spectrum of ball fault at 1021 rev/min in vertical direction

4 Result and discussion

Figure 9 shows envelope spectrum of outer race fault bearing. It is clear from it that Outer Race Fault Frequency (BPFO) at 89 Hz is generated and it is match to the theoretical value of 89.26 Hz (Table 3). The envelope spectrum of inner race fault is shown in Fig. 10. It is clear from it that the inner race fault frequency (BPFI) at 135 Hz is observed and it is matched to the theoretical value of 135.33 Hz (Table 3). Envelope spectrum of ball fault in vertical direction is shown in Fig. 11. Ball fault frequency (BSF) is observed at 42 Hz and it is matched to the theoretical
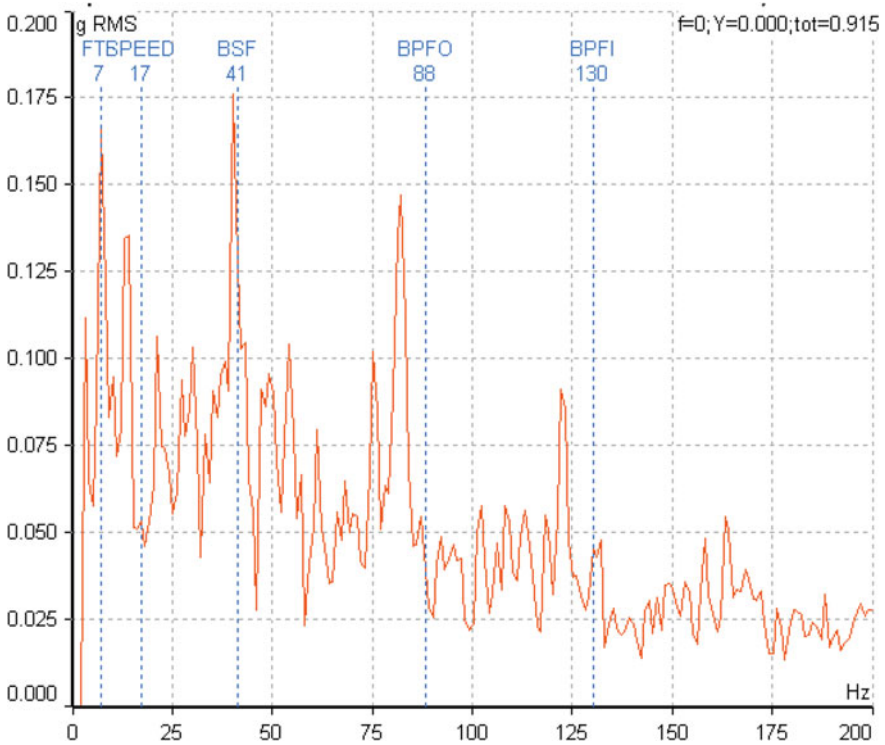
Fig. 12 Envelope spectrum of cage fault at 1004 rev/min in vertical direction

value of 42.51 Hz (Table 3). Figure 12 shows the envelope spectrum of cage fault in vertical direction. It can be seen from it that the cage fault frequency (FTF) at 7 Hz is present and it is matched to the theoretical value of 6.75 Hz (Table 3). Figure 13 shows cage, ball, outer and inner race fault frequency at 7 Hz, 42 Hz, 90 Hz and 132 Hz respectively, and it is matched to the theoretical value (Table 3).
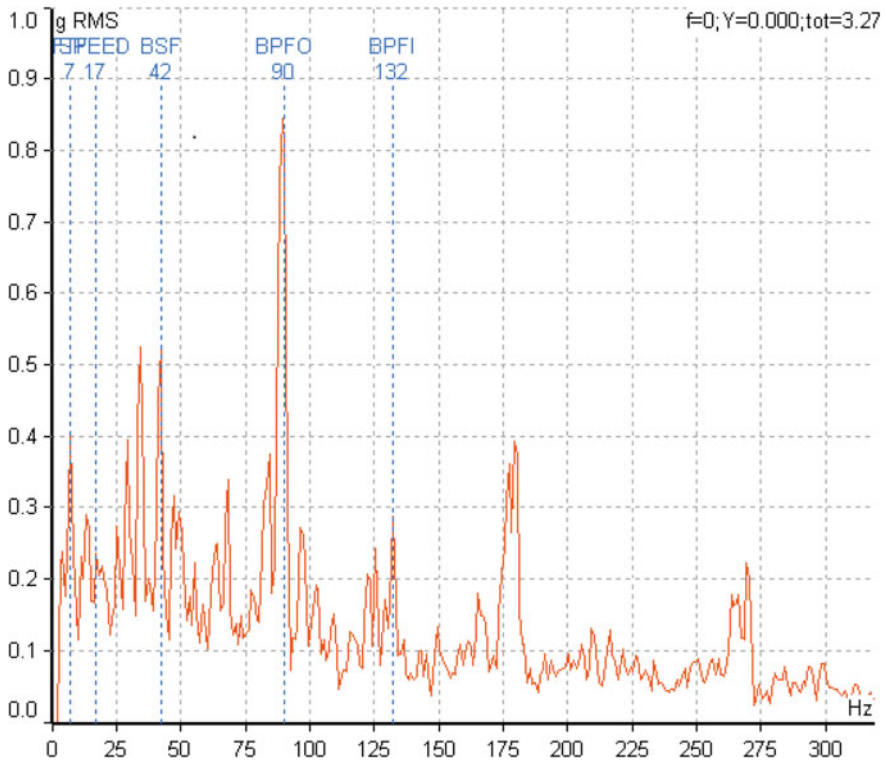
Fig. 13 Envelope spectrum of cage, inner race, outer race and ball fault at 1025 rev/min in vertical direction

5 Conclusion

- Experimental investigations of bearing single fault like inner race, outer race, ball and cage fault and also multiple faults is studied.
- Envelope spectrum analysis is best tool for bearing fault diagnostics like cracks and spalls in ball bearings.
- Bearing frequencies are excellently identified in the envelope spectrum.
- Envelop spectrum provide information about the type of defects.

References

1. Patel VN, Tandon N, Pandey RK (2014) Vibrations generated by rolling element bearings having multiple local defects on races. Procedia Technol 14:312–319
2. Karacay T, Akturk N (2009) Experimental diagnostics of ball bearings using statistical and spectral methods. Tribol Int 42:836–843
3. Rafsanjani A, Abbasion S, Farshidianfar A, Moeenfard H (2009) Nonlinear dynamic modeling of surface defects in rolling element bearing systems. J Sound Vib 319:1150–1174
4. Kiral Z, Karagülle H (2003) Simulation and analysis of vibration signals generated by rolling element bearing with defects. Tribol Int 36:667–678
5. Choy FK, Wu R, Konrad D, Labus E (2007) Damage identification of ball bearings for transmission systems in household appliances. Tribol Int 50:74–81
6. Nikolaou NG, Antoniadis IA (2002) Rolling element bearing fault diagnosis using wavelet packets. NDT and E Int 35:197–205
7. Samanta B, Al-alushi KR (2003) Artificial neural network based fault diagnostics of rolling element bearings using time-domain features. Mech Syst Signal Process 17:317–328
8. Kankar PK, Sharma SC, Harsha SP (2011) Fault diagnosis of ball bearings using machine learning methods. Expert Syst Appl 38:1876–1886
9. Kankar PK, Sharma SC, Harsha SP (2011) Fault diagnoses of ball bearings using continuous wavelet transform. Appl Soft Comput 11:2300–2312
10. Kilundu B, Chiementin X, Dehombreux P (2011) Singular spectrum analysis for bearing defect detection. J Vib Acoust 133, 051007-1-051007-7
11. Wang Y, Liang M (2012) Identification of multiple transient faults based on the adaptive spectral kurtosis method. J Sound Vib 331:470–486
12. Cong F, Chen J, Dong G, Pecht M (2013) Vibration model of rolling element bearings in a rotor-bearing system for fault diagnosis. J Sound Vib 332:2081–2097
13. Liu WY, Ha JG, Jiang JL (2013) A novel ball bearing fault diagnosis approach based on auto term window method. Measurement 46:4032–4037

Improvement in Tribological Behaviour of Brake Pad Material with CNT-Ni-P Composite Coating and Compare with Al_2O_3-Ni-P Composite Coating

Atul Kumar Harmukh, Santosh Kumar and Sushma Bharti

Abstract In mechanical machine components, the wear and friction are the major issues which are responsible for the fault and their failure. In this analysis, the tribological and mechanical properties of semi-metallic brake pad material were investigated. For improvement in the mechanical and triblogical properties of brake pad materials, Ni-P based multi-walled carbon nanotubes (MWCNT) and Ni-P-based nano Al_2O_3 composite coating was used. The electroless coating technique was used for the coating as it results in excellent tribological properties such as good wear and corrosion resistance, uniform coating thickness, good hardness, etc. Energy dispersive x-ray spectroscopy (EDX) test was used to find the composition of the brake pad sample. Tribological parameters like frictional force and wear rate were determined by pin-on-disc tribometer. The result shows that the tribological properties of brake pad were enhanced after the coating and wear rate and frictional forces were less as compared to without coated sample. Field emission scanning electron microscopy (FESEM) was used to validate the result of the test.

Keywords Tribological properties · Wear · Electroless coating ·
Carbon nanotubes

1 Introduction

In the brake pad system the wear is the main cause due to which the brake is worn out. For enhancing the life of brake pad we used the coating technology, electroless coating is one of them Selvamani and Premkumar [1] concluded that the Carbon

A. K. Harmukh (✉) · S. Kumar (✉) · S. Bharti
Department of Mechanical Engineering, Indian Institute of Technology (ISM) Dhanbad,
Dhanbad, India
e-mail: atulyitm707@gmail.com

S. Kumar
e-mail: santosh.kumar0190@gmail.com

nanotube is the one of the best coating material for the semi-metallic material. Carbon nanotube has good mechanical properties, good wear and corrosive properties. It is a good conductor of electricity, good thermal conductivity and chemically stable material. Ni-P coating is the one of the best coating material which gives the high wear and corrosion resistance, low coefficient of friction, high strength and high hardness [2]. Electromagnetic properties are increased by the coating of CNT through electroless coating and the permittivity properties are decreases and permeability properties are increases [3]. By the incorporation of SiC, ZrO_2, TiO_2, graphene, CNT, Carbon nanofibers (CNF's), diamond, and ZnO with Ni-P composite coating gives the high wear and corrosion resistance, high strength and hardness, low coefficient of friction [4]. Promphet and Rattanawaleedirojn [5] Investigated the use of the Ni-P-TiO_2 solution in steel exhibits a significant increase in corrosion resistance and electrical conductivity of the steel.

Afroukhteh and Dehghanian [6] concluded that the electroless coating of Ni-P with nano size TiC particle gives the good corrosion resistance. The improvement of corrosion resistance of the material depends upon the concentration of phosphorous in the coating. Popoola and Loto [7] concluded that wear and corrosion resistance of mild steel was increased by the coating of Sn in the Ni-P composting coating. Zhang, Cheng [8] concluded that the deposition of Ni-P coating in any substrate may increase the electrochemical property of the material. Karthikeyan and Jeeva [9] concluded that the incorporation of WS_2 with Ni-P composite coating improves the tribological properties of material. The wear and corrosion resistance, micro hardness were increased and coefficient of friction decreases. Panja and Sahoo [10] concluded that the electroless coating of Ni-P with alkaline medium gives the smooth coating surface with low porosity, and the coefficient of friction is decreased with higher percentages.

Duan and Li [11] concluded that the incorporation of Carbon nanotube with the Ni-P composite coating enhanced the damping quality of material. Atuanya and Obele [12] concluded that the incorporation of SiO_2 with Ni-Co composite coating improves the corrosion resistance and gives a better surface finish. Fayomi and Popoola [13] concluded that the incorporation of Zn with Al_2O_3-SiC composite coating increase the hardness of surface and give good crystal orientation. Incorporation of Ni-P coating reduces the wear as well as giving a good surface finish, low porosity and gives dense crystal structure [14]. RamPrabhu and Varma [15], it concluded that the by the use of composite material which made by layer by layer increased the corrosion and wear properties of the material.

Kumar and Mohanam [16] concluded that the incorporation of Ni coating on aluminium substrates increases the natural frequency of Aluminium and improves the dynamic behaviour of aluminium. Shibli and Suma [17] concluded that the incorporation of IrO_2 with Ni-P composite coating the stability of coating, gives good electrochemical properties and increase the hardness of the surface. Georjiza and Gouda [18] concluded that the Ni-B-SiC composite electroless coating improves the corrosion resistance and wear resistance and improves the hardness of the surface. Progress of wear finally determines the useful life and the quality of a product. Hence the nature of friction, wear and their control plays an important role

in different engineering operations. Though there are several research-based models and formulations in this regard [19–21].

The present study deals with the wear analysis of brake pad material. For improvement in the tribological behaviour of brake pad material, we were using the two different coatings of CNT-Ni-P and Al_2O_3-Ni-P on the surface of the brake pad and analyse the friction and wear.

2 Methodology

2.1 Pin and Disc Materials

The Pin-on-disc tribometer was used to test the friction and wear of brake pad material. The grey cast iron disc was used in this experiment has a specification of 100 mm diameter and 10 mm thickness. The average surface roughness of the disc is 0.18 μm. The "Energy dispersive X-Ray spectroscopy" (EDX) test was used to verify the composition of pin sample. The pin used in this experiment has a specification of 20 mm length and 6 mm diameter. Figure 1a shows the disc of grey cast iron, Fig. 1b, c, d shows the elemental composition of pin without coated and coated with CNT-Ni-P and Al_2O_3-Ni-P respectively.
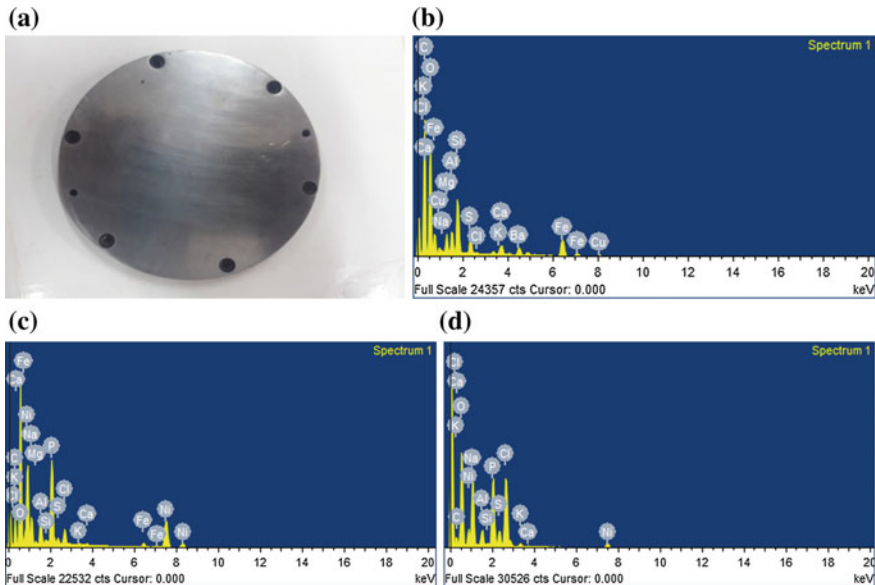
Fig. 1 Elemental analysis of brake pad pin by EDX **a** disc used in the experiment (grey cast iron) **b** elemental analysis of brake pad pin without coating **c** elemental analysis of brake pad pin with a coating of CNT-Ni-P **d** elemental analysis of brake pad pin with a coating of Al_2O_3-Ni-P

Table 1 (a). Elemental composition of brake pad pin (coated with CNT-Ni-P). (b). Elemental composition of brake pad pin (coated with Al_2O_3-Ni-P)

Sl. No.	Brake pad sample without coated			Brake pad sample with coated with Al_2O_3-Ni-P
	Material	wt%	Material	wt%
1.	C	55.89	C	24.52
2.	O	32.66	O	42.20
3.	Na	0.20	Na	10.79
4.	Mg	1.14	Mg	0.19
5.	Al	1.05	Al	8.95
6.	Si	2.76	Si	0.15
7.	S	1.01	P	7.75
8.	Cl	0.07	S	1.71
9.	K	0.19	K	0.42
10.	Ca	0.59	Ca	0.10
11.	Fe	3.38	Fe	0.75
12.	Cu	0.42	Ni	2.23
13.	Ba	0.64	Ba	0.24

Table 1 (a) shows the elemental analysis of brake pad pin of without coated sample and with coated sample of CNT-Ni-P.

Table 1 (b) shows the elemental analysis of brake pad pin without coated sample and with a coated sample of Al_2o_3-Ni-P.

2.2 Bath Concentration

For a change in tribological behaviour of brake pad material electroless coating technique was used. First, base solution was made by using all chemicals in the container. In this experiment, the base solution is common for both the CNT-Ni-P and Al_2o_3-Ni-P composite coating. All the chemicals are mixed in deionized water (250 ml). The magnetic stirrer and probe type ultrasonicator was used for mixing the solution and stable the coating solution, respectively. In this base solution sodium citrate, nickel sulphate, aluminium chloride and sodium hypophosphite

Table 2 Bath concentration of base solution (Ni-P)

Sl. No.	Chemicals	Weight (gm)
1.	Nickel sulphate	10
2.	Sodium hypophosphite	15
3.	Sodium citrate	7
4.	Aluminium chloride	12
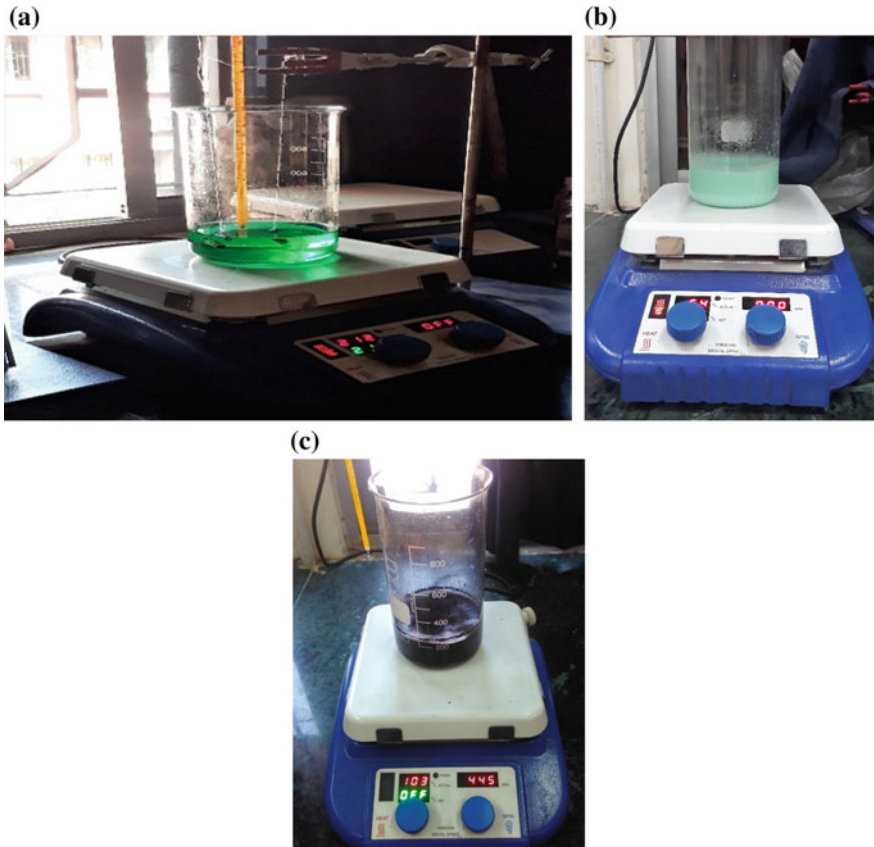
Fig. 2 a Coating performed with a base solution **b** Al_2O_3 mixed with a base solution **c** CNT mixed with a base solution

were used as buffering solution, complexing agent, and metal ion source respectively. Table 2 shows the bath concentration of base solution of Ni-P.

In this experiment, we were made the base solution of Ni-P in two different containers using all the chemicals mentioned in the above tables. Then we heated that up to 80 °C by using the magnetic stirrer for 30 min. After 30 min we put the carbon nanotube in one container and Al_2o_3 on another. And then dipped the pin in that container and then again heated up to 30 min. After 30 min remove the pin from the container and the pin was perfectly coated. Figure 2a, b, c shows the electroless coating arrangement.

3   Results and Discussion

Figure 3 shows the morphology of brake pad material surface which is taken by field emission scanning electron microscopy (FESEM) test.

In this study, we were coated the pin with two different composite materials which were CNT-Ni-P and Al_2O_3-Ni-P, respectively. We were investigated wear and friction test at 400 RPM and the load parameters are 3 kg and 4 kg respectively. Figures 4 and 5 shows the variation of wear and friction with respect to time for CNT-Ni-P and Al_2O_3-Ni-P coating, respectively.

1. Variation of wear and friction with time (coated with CNT-Ni-P)
   Load and speed parameters are as follows:

   - Speed—400 RPM
   - Load—3 kg & 4 kg
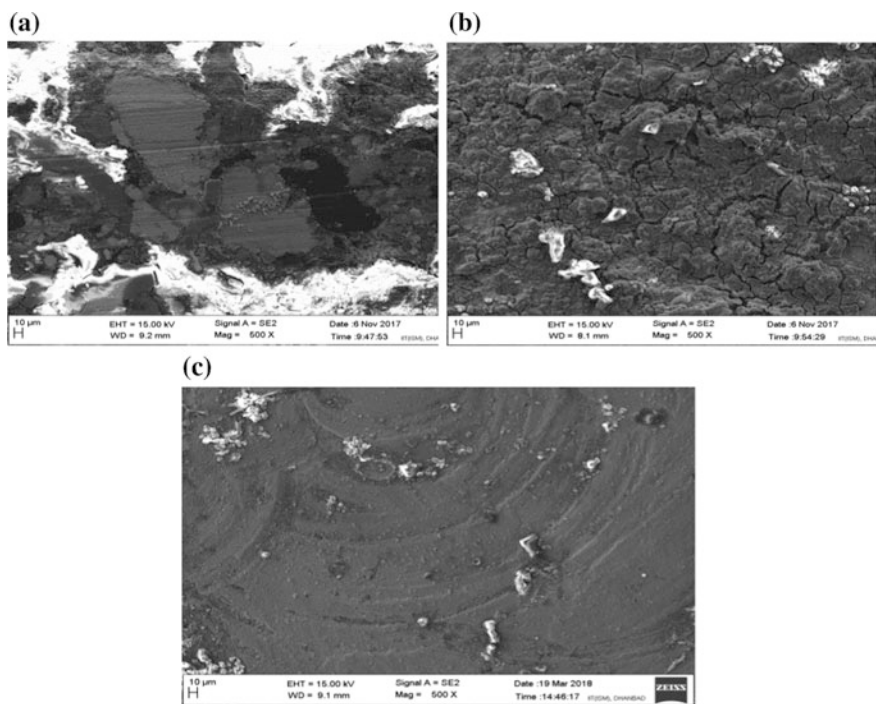
Fig. 3 FESEM images of brake pad pin **a** without coated **b** coated with CNT-Ni-P **c** coated with Al_2O_3-Ni-P

Fig. 4 **a** Variation of wear with time (CNT coating) **b** variation of coefficient of friction with time (CNT coating)
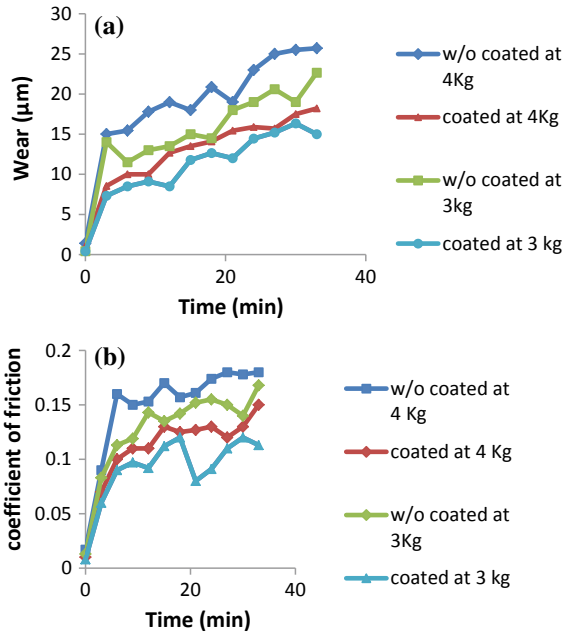
Fig. 5 **a** Variation of wear with time (Al_2O_3 coating) **b** Variation of coefficient of friction with time (Al_2O_3 coating)
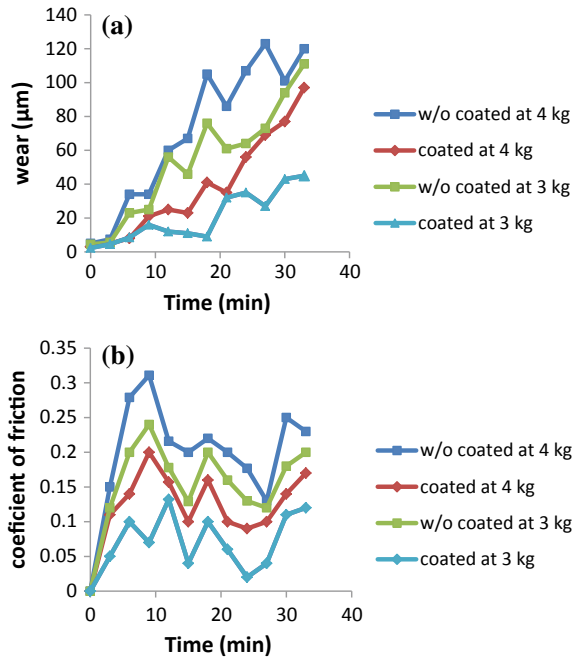
2. Variation of wear and friction with time (Al_2o_3-Ni-P coating)
   Speed and load parameters are as follows:

   - Speed—400 RPM
   - Load—3 kg and 4 kg

From this investigation, it has been observed that CNT coating is more efficient as compared to Al_2o_3 coating on the brake pad material. The wear and friction are less with CNT coating as compared to Al_2o_3 coating. This composite coating improves the surface morphology of brake pad. The wear resistance is improved as comparable to the uncoated material.

4   Conclusions

In this investigation, we concluded that the coating of carbon nanotube is more efficient and reliable on brake pad material as compare to Al_2o_3 coating, because CNT has good wear and corrosion resistance, give uniform coating thickness and provide good hardness and strength.

References

1. Selvamani ST, Premkumar S (2017) Influence of carbon nanotube on mechanical, metallurgical and tribological behavior of magnesium nanocomposites. J Magnes Alloy 5:326–335
2. Li ZH, Wang XQ (2006) Preparation and tribological properties of carbon nanotubes-Ni-P composite coating. Tribol Int 39:953–957
3. Yan Z, Hao, Z (2010) Studies of electromagnetic properties of MWCNTs after electroless plating with Co-Fe alloy. Chin J Aeronaut 23:377–380
4. Chen W, Gao W (2010) A novel electroless plating of Ni–P–TiO$_2$ nano composite coatings. Surf Coat Technol 204:2493–2498
5. Promphet N, Rattanawaleedirojn, P (2017) Electroless NiP–TiO$_2$ sol-RGO: a smart coating for enhanced corrosion resistance and conductivity of steel. Surf Coat Technol 325:604–610
6. Afroukhteh, S, Dehghanian, C (2012) Corrosion behavior of Ni–P/nano-TiC composite coating prepared in electroless baths containing different types of surfactant. Mater Int 22:480–487
7. Popoola API, Loto CA (2016) Corrosion and wear properties of Ni-Sn-P ternary deposits on mild steel via the electrolysis method. Alex Eng J 55:2901–2908
8. Zhang, S, Cheng L (2008) The effect of SiC particles added in electroless Ni-P plating solution on the properties of composite coating. Surf Coat Technol 202:2807–2812
9. Karthikeyan S, Jeeva PA (2013) Wear, hardness and corrosion resistance characteristics of Tungsten sulfide incorporated electroless Ni-P coatings. Procedia Eng 64:720–726
10. Panja B, Sahoo P (2014) Friction performance of electroless Ni-P coating in alkaline medium and optimization of coating parameters. Procedia Eng 97:47–55
11. Duan K, Li L (2017) Damping characteristic of Ni-coated carbon nanotube/copper composite. Mater Des 133:455–463

12. Atuanya CU, Obele CM (2008) Experimental study of microstructural and anti-corrosion behavior of Co-deposition Ni-Co-SiO$_2$ composite coating on mild steel. Def Technol 14:64–69
13. Fayomi OSI, Popoola API (2014) Study of Al$_2$0$_3$/SiC particle loading on the microstructural strengthening characteristic of Zn-Al$_2$O$_3$-SiC matrix composite coting. Egypt J Basic Appl Sci, 120–125
14. Wang LY, Tu JP (2003) Friction and wear behaviour of electroless Ni-based CNT composite coating. Wear 254:1289–1293
15. Ramprabhu T, Varma VK (2014) Tribological and mechanical behaviour of multilayer Cu/SiC-Gr hybrid composites for brake friction material application. Wear 317:201–212
16. Kumar AS, Mohanam K (2014) Influence of nickel coating on flexural and dynamic behavior of aluminium. Procedia Eng 97:1368–1378
17. Shibli SMA, Suma ND (2016) TiO$_2$-supported nano IrO$_2$ composite incorporated Ni-P coating for sensing Ethanol. Procedia Eng 24:754–760
18. Georjiza E, Gouda V (2017) Production and properties of composite electroless Ni-B-SiC coatings. Surf Coat Technol 325:46–51
19. Kumar S, Mukhopadhyay A (2016) Effect of microstructure on the wear behaviour of heat treated SS- 304 Stainless Steel. Int J Tribol Ind. www.tribology.fink.rs (Tribology in Industry Vol. 38, No. 4 (2016) 445–453)
20. Kumar S, Ghosh SK, Mukhopadhyay A (2018) Experimental Investigation on tribological behaviour of interacting surfaces with microstructral matrix. In: Proceedings of national conference on advanced materials, manufacturing and metrology (ncammm-2018), csir-cmeri, February, 2018. ISBN: 978-93-87480-56-8
21. Harmukh AK, Kumar S, Bharti S, Ghosh SK (2018) Effect of CNT-Ni-P composite coating on tribological behaviour for brake pad system. In: Proceedings of national conference on advanced materials, manufacturing and metrology (ncammm-2018), csir-cmeri, February, 2018. ISBN: 978-93-87480-56-8

Estimation of Load Carrying Capacity for Pin-Mounted Hydraulic Cylinders

Prakash Jatin, Nagargoje Aniket, P. K. Kankar, V. K. Gupta, P. K. Jain, Tamhankar Ravindra, Nyamgoudar Vinayak and Mulani Ismail

Abstract The standard hydraulic cylinder consists of two main parts, i.e., cylinder tube and piston rod. It operates by the reciprocation of either element and majorly used to transmit mechanical power using fluid linkage. The failure of such systems occurs usually because of piston rod failure. Being more specific, the buckling failure mode is more dominant over others. In this manuscript, the maximum allowable load is calculated for a standard hydraulic cylinder with pin-mounted at both ends analytically using analytically using ISO/TS 13725. Piston rod having less flexural rigidity (EI) is prone to buckling failure. The estimated load when applied on the piston rod end results into the stress condition of the cylinder tube. Von-Mises stress generated in the thick cylinder is discussed using Lame's theorem while axial and flexural stress for piston rod is deliberated. The results show that for lower slenderness ratio hydraulic cylinder may fail due to yielding of cylinder tube failure. The results obtained for slenderness ratio 19 of piston rod are compared with simulated results implemented in ANSYS.

Keywords Buckling · Flexural rigidity · Hydraulic cylinder · Lame's theorem · Slenderness ratio (SR)

Nomenclature

F_s	Factor of safety
P	Axial force applied
L_c	Length of the cylinder tube
L_p	Exposed length of the piston rod
L_{ph}	Width of the piston head
L_s	Distance between piston head center to piston rod bearing
e_p	Eccentricity of force at the piston rod

P. Jatin (✉) · N. Aniket · P. K. Kankar · V. K. Gupta · P. K. Jain
Machine Dynamics and Vibration Laboratory, Mechanical Engineering Discipline,
PDPM IIITDM Jabalpur, Jabalpur, India
e-mail: jatinprakash94@gmail.com

T. Ravindra · N. Vinayak · M. Ismail
Research and Development Establishment (Engineers) -R&dE (E) DRDO, Pune, India

e_c Eccentricity at cylinder bottom
R_{c_1} Reaction at the pin-end of the cylinder tube
R_j Reaction at the junction of cylinder tube and piston rod
R_{p_1} Reaction at the pin-end of the piston rod
M_j Moment at the junction of cylinder tube and piston rod
β Angle between deflection curves of cylinder tube and piston rod
ψ_{c_1} Angle at the pin-end of the cylinder tube
ψ_{p_1} Angle at the pin-end of the piston rod
φ_{c_1} Angle of deflection curve at the pin-end of the cylinder tube
φ_{c_2} Angle of the deflection curve at the end of cylinder tube
φ_{p_1} Angle of deflection curve at the pin-end of the piston rod
φ_{p_2} Angle of the deflection curve at the beginning of piston rod
D_{c_i} Inside diameter of the cylinder tube
D_{c_e} Outside diameter of the cylinder tube
d_p Outside diameter of the piston rod

1 Introduction

The hydraulic cylinder is an actuation device that is used to transfer mechanical power. To estimate critical buckling load in industries, fully extracted length of cylinder, i.e., Open Center Length (OCL) of the hydraulic cylinder is considered as a single column with uniform piston rod. In fact, a hydraulic cylinder cannot be considered as a single column with uniform piston rod diameter because of the relative moment between the piston rod and cylinder tube at piston-cylinder tube junction. Effect of flexural rigidity is also ignored in such assumption [1, 2]. Hoblit [3] considered the hydraulic cylinder as a structural element and calculated the critical load for instability. According to it, the piston rod is under compressive as well as flexural load whereas the cylinder tube is under flexural load and hoop stress due to the fluid inside it. In particular, Hoblit [3] and Flugge [4] incorporated the presence of fluid pressure inside the cylinder and thus treating it as a fluid column. Hoblit [3] concluded that the critical force considering fluid column is the same as that of in the solid column. Seshasai et al. [5] analyzed the stresses of hydraulic cylinders. Baragetti [6] had considered degradation in loading capacity of the cylinder due to the misalignment caused by wear in sealing. The ISO/TS 13725 (2001) standard [7] explained the method to calculate the cylinder buckling load. The ISO/TS 13725 (2001) standard [8] has been used in this work to estimate the critical load carrying capacity of the cylinder. The failure aspect of cylinder tube has not been considered in [8]. The pressure generated inside the tube results in hoop stress, radial stress, and longitudinal stress. Normalized Von-Mises stress of cylinder tube has been examined over the slenderness ratio (SR) of 11 to 65. The limit load carrying capacity of both end pin-mounted hydraulic cylinder is calculated and stress condition of both elements has been discussed.

2 Mathematical Formulation

2.1 Determinant Equation

In this section, the determinant equation to estimate the critical buckling load has been explained. The material properties and dimensions of the studied hydraulic cylinder are listed in Table 1 [7]. In Fig. 1, consider the reference axes at two extremes namely x_1-y_1 at the cylinder tube end and x_2-y_2 at the piston rod end.

Using Moment curvature relationship [9], the deflection equations for cylinder tube piston rod respectively are given by

$$E_c I_c \frac{d^2 y_1}{dx_1^2} = -kP y_1(x_1) \tag{1}$$

$$E_p I_p \frac{d^2 y_2}{dx_2^2} = -kP y_2(x_2) \tag{2}$$

The solutions to Eqs. (1) and (2) are given by Eqs. (3) and (4),

$$y_1 = A_{11} \cos(q_1 x_1) + A_{12} \sin(q_1 x_1) \tag{3}$$

$$y_2 = A_{21} \cos(q_2 x_2) + A_{22} \sin(q_2 x_2) \tag{4}$$

Table 1 Material properties and dimensions of cylinder tube and piston rod [7]

Cylinder outside diameter (D_{c_e})	32 mm
Cylinder inside diameter (D_{c_i})	25 mm
Piston rod diameter (D_p)	12 mm
Length of Cylinder tube (L_c)	115 mm
Length of the piston rod (L_p)	57 mm
Modulus of Elasticity (E)	220000 N/mm^2
Yield strength (σ_y)	360 N/mm^2
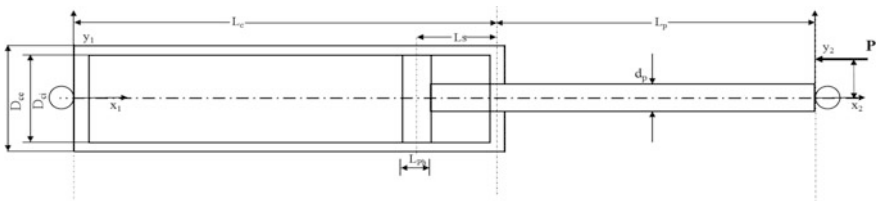
Fig. 1 Schematic view of hydraulic cylinder arrangement [7]

The boundary conditions of both end pin-mounted hydraulic cylinder are given by $y(0) = 0$, $y''(0) = 0$, $y(L) = 0$ and $y''(L) = 0$. Applying the boundary conditions in Eqs. (3) and (4), we get $A_{11} = A_{21} = 0$. At the junction point i.e. $y_1(L_c) = y_2(-L_p)$, using this condition yields

$$A_{12} \sin(q_1 L_c) + A_{22} \sin(q_2 L_p) = 0 \tag{5}$$

The moment at the cylinder-tube and piston junction is given as

$$M_j = kF y_2(-L_p) \tag{6}$$

The portion of piston rod inside the cylinder tube is considered to be simply supported between the piston head and cylinder head sealing. The angle between the slopes of cylinder tube deflection curve and piston rod deflection curve is given by $\beta = -M_j L_s / 3E_p I_p$ due to the moment acting at the junction.

Also, from Eqs. (3) and (4) the difference in the slope can be represented by

$$\frac{dy_1(L_c)}{dx_1} - \frac{dy_2(-L_p)}{dx_2} = \beta \tag{7}$$

$$A_{12} q_1 \cos(q_1 L_c) + A_{22} \left[-q_{22} \sin(q_2 L_p) + \frac{F_s P \sin(q_2 L_p) L_s}{3E_p I_p} \right] = 0 \tag{8}$$

Eqs. (5) and (8) can be rearranged in the matrix form as

$$\begin{pmatrix} \sin(q_1 L_c) & \sin(q_2 L_p) \\ q_1 \cos(q_1 L_c) & \left[-q_2 \sin(q_2 L_p) + \frac{kF \sin(q_2 L_p) L_s}{3E_p I_p} \right] \end{pmatrix} \begin{pmatrix} A_{12} \\ A_{22} \end{pmatrix} = 0 \tag{9}$$

The application of load on the system leads to the lateral deflection of the piston rod and cylinder tube. Theoretically, a system failure occurs when the deflection tends to infinity. For that, the determinant of Eq. (9) tends to zero. The determinant equation is given by [8]

$$\begin{aligned} F_s P L_s s_1 s_2 - 3E_p I_p q_1 c_1 s_2 - 3E_p I_p q_2 c_2 s_1 &= 0, \quad \text{where} \\ s_i = \sin(q_i L_i), c_i = \cos(q_i L_i), i, j &= c, p \end{aligned} \tag{10}$$

2.2 Maximum Safe Stress

The component having less value of rigidity (EI) is more prone to failure in buckling, thus piston rod can be treated as a critical element. Equation (10) determine critical load in buckling only, however, the piston rod may fail below
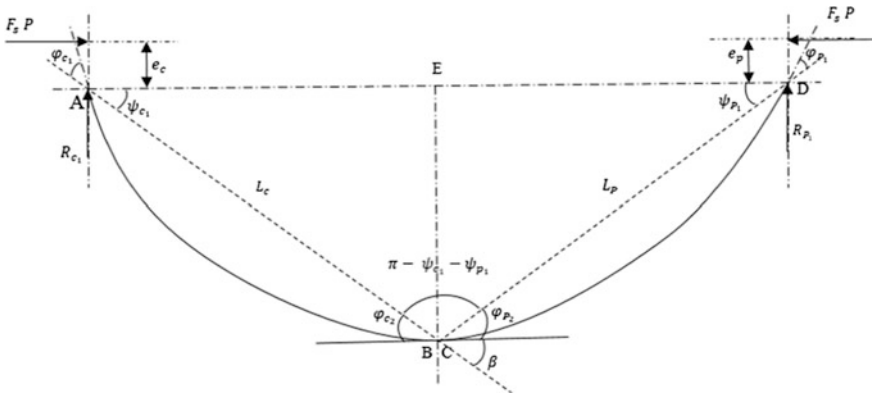
Fig. 2 Angle relationship between the piston rod and cylinder tube

critical load due to yielding if developed stresses are above yield point of the material.

In Fig. 2, the equilibrium condition of the piston rod and cylinder tube is shown in the coordinate axis *x-y*. According to free body diagram shown in Fig. 2, the equilibrium equation is written as

$$E_p I_p \frac{d^2 y}{dx^2} = -\frac{\rho_p \pi d_p^2 g}{8} x^2 + \left(R_j - kF\psi_{P_1}\right)x - M_j - F_s P y \tag{11}$$

Total solution of Eq. (11) is given by the summation of complementary and particular functions as

$$y = y_{C.F.} + y_{P.I} \tag{12}$$

The complementary function is given by

$$y_{C.F.} = C_1 \sin(q_2 x) + C_2 \cos(q_2 x) \tag{13}$$

and particular function is given as

$$y_{P.I.} = C_3 x^2 + C_4 x + C_5 \tag{14}$$

where C_1 and C_2 can be calculated by using boundary conditions: and

$$y(0) = y(L_2) = 0 \text{ and} \tag{15}$$

$$C_3 = -\frac{\rho_p \pi d_p^2 g}{8 F_s P}, \quad C_4 = \frac{\left(R_j - kF\psi_{P_1}\right)}{F_s P}, \quad C_5 = \frac{1}{F_s P}\left(-M_j + \frac{\rho_p \pi d_p^2 g E_p I_p}{4 F_s P}\right) \tag{16}$$

parameters can be calculated by employing angle relations, force, and moment equilibrium equations for cylinders and piston rod. This moment results in the bending stress in the system and total stress condition is given by the combination of axial and bending stresses.

$$\sigma_{\max} = \frac{4F_s P}{\pi d_p^2} + \frac{32 M_{\max}}{\pi d_p^3} \tag{17}$$

2.3 Equilibrium Equations and Angle Relations

Various angle relations between the piston rod and cylinder tube and the force and moment equilibrium equations have been listed below in Eqs. (18a–18i)

Angle relations:

The deflection at piston head-cylinder tube junction must be equal for the continuity of the system.

Equation (18a) states that lateral deflection of both articulations is equal at piston rod-cylinder tube junction.

$$L_c \psi_{c_1} - L_p \psi_{p_1} = 0 \tag{18a}$$

The geometrical relation between β, ψ_{c_1}, ψ_{p_1}, φ_{c_2} and φ_{p_2} can be shown by Eq. (18b) as shown in Fig. 2.

$$\beta - \psi_{c_1} - \psi_{p_1} + \varphi_{c_2} - \varphi_{p_2} = 0 \tag{18b}$$

The portion of piston rod inside the cylinder tube is assumed to be simply supported between the piston head and the cylinder tube sealing. It is subjected to moment M_j at one end as shown in Fig. 3. Thus, deflection is given by Eq. (18c).

$$\beta = -\frac{M_j L_s}{3 E_p I_p} \tag{18c}$$

Force and moment equilibrium equations for cylinder tube and piston rod:
Sum of forces acting on the cylinder tube in vertical direction must be zero as shown in Fig. 3.

Thus Eq. (18d) implies $\sum F_{cyl} = 0$

$$R_{c_1} + R_j + \rho_c L_c \frac{\pi}{4} \left(D_{c_e}^2 - D_{c_i}^2 \right) g = 0 \tag{18d}$$
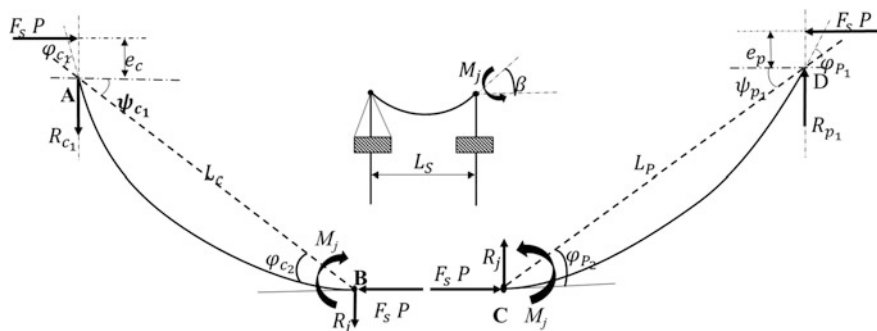
Fig. 3 Free body diagram of the cylinder tube and Piston rod

Similarly, the summation of the moment acting about point A on the cylinder tube be zero as shown in Fig. 3. Thus Eq. (18e) implies:

$$\sum M_A = 0$$
$$L_c R_j + M_j + F_s P L_c \psi_{c_1} + \rho_c L_c^2 \frac{\pi}{8} \left(D_{c_e}^2 - D_{c_i}^2 \right) g + F_s P e_c = 0 \tag{18e}$$

The slope of the cylinder tube deflection curve at the junction is given by $dy(0)/dx = \varphi_{C_1}$ as shown in Fig. 3.

$$(q_c L_c - s_1) R_j + q_1 (1 - c_1) M_j + F_s P (q_1 L_c - s_1) \psi_{c_1} + F_s P s_1 \varphi_{c_2}$$
$$- \frac{\rho_c \pi \left(D_{c_e}^2 - D_{c_i}^2 \right) g q_1}{4} \left[-\frac{L_c^2}{2} + \frac{1 - c_1}{q_1^2} \right]$$
$$= 0. \tag{18f}$$

In a similar way, equilibrium equations for piston rod are written as

Sum of forces acting on the piston rod in vertical direction must be zero as shown in Fig. 3.

Thus Eq. (18g) implies $\sum F_{rod} = 0$

$$R_{p_1} + R_j - \rho_p L_p \frac{\pi}{4} d_p^2 g = 0 \tag{18g}$$

Summation of the moment acting about point A on the cylinder tube be zero as shown in Fig. 3.

Thus Eq. (18h) implies $\sum M_d = 0$

$$-L_p R_j + M_j + F_s P L_p \psi_{p_1} + \rho_p L_p^2 \frac{\pi}{8} d_p^2 g + F_s P e_p = 0 \tag{18h}$$

The slope of piston rod deflection curve at the junction is given by $dy(0)/dx = \varphi_C$ as shown in Fig. 3, On further simplification written as

$$
\begin{aligned}
&\left(q_p L_p - s_2\right) R_j + q_2(1 - c_2) M_j + F_s P\left(q_1 L_p - s_2\right) \psi_{p_1} + F_s P s_2 \varphi_{p_2} \\
&\quad - \frac{\rho_p \pi\left(D_{c_e}^2 - D_{c_i}^2\right) g q_2}{4}\left[-\frac{L_p^2}{2} + \frac{1 - c_1}{q_2^2}\right] \\
&= 0.
\end{aligned} \tag{18i}
$$

Eqs. (18a–18i) can be rearranged in the matrix form the system of equations is obtained as below in accordance with [7].

This system of equations is solved to get the values of nine different unknown parameters. By a solving system of equations, maximum stress in the piston rod can be calculated with the help of Eq. (17). Thus, for the given actuator, maximum admissible force is calculated using an algorithmic method that generates a stress in the close vicinity to the limit stress of the material.

$$
\begin{pmatrix}
0 & 0 & 0 & 0 & 0 & L_c & -L_p & 0 & 0 \\
0 & 0 & 0 & 0 & 1 & -1 & -1 & 1 & -1 \\
0 & 0 & 0 & \frac{L_s}{3E_p I_p} & 1 & 0 & 0 & 0 & 0 \\
1 & 0 & 1 & 0 & 0 & 0 & 0 & 0 & 0 \\
0 & 0 & L_c & 1 & 0 & F_s P L_c & 0 & 0 & 0 \\
0 & 0 & q_1 L_c - s_1 & q_1(1 - c_1) & 0 & F_s P(q_1 L_c - s_1) & 0 & F_s P s_1 & 0 \\
0 & 1 & 1 & 0 & 0 & 0 & 0 & 0 & 0 \\
0 & 0 & -L_p & 1 & 0 & 0 & F_s P L_2 & 0 & 0 \\
0 & 0 & q_2 L_p - s_2 & -q_2(1 - c_2) & 0 & 0 & -F_s P(q_2 L_p - s_2) & 0 & F_s P s_2
\end{pmatrix}
\begin{pmatrix}
R_{c_1} \\
R_{p_1} \\
R_j \\
M_j \\
\beta \\
\psi_{c_1} \\
\psi_{p_1} \\
\varphi_{c_2} \\
\varphi_{p_2}
\end{pmatrix}
$$

$$
= \begin{pmatrix}
0 \\
0 \\
0 \\
-\rho_p L_p \frac{\pi}{4}\left(D_{c_e}^2 - D_{c_i}^2\right) g \\
-\rho_p L_p^2 \frac{\pi}{8}\left(D_{c_e}^2 - D_{c_i}^2\right) g - F_s P e_c \\
\frac{\rho_p \pi\left(D_{c_e}^2 - D_{c_i}^2\right) g q_1}{4}\left[-\frac{L_c^2}{2} + \frac{1 - c_1}{q_1^2}\right] \\
\rho_p L_p \frac{\pi}{4} d_p^2 g \\
-\rho_c L_c^2 \frac{\pi}{8} d_p^2 g - F_s P e_p \\
\frac{\rho_p \pi d_p^2 g q_1}{4}\left[\frac{L_p^2}{2} - \frac{1 - c_2}{q_2^2}\right]
\end{pmatrix}
\tag{19}
$$

2.4 Stress Developed in the Cylinder Tube

The Lame's Eq. (20) has been employed to evaluate the stresses in the cylinder. The critical buckling load by the method adapted according to ISO/TS 13725 is used to calculate the internal pressure developed due to oil inside the cylinder tube. The effect of bending stress has been considered in analyzing the stress condition of the cylinder tube. The bending stress obtained is arithmetically added to the longitudinal stress. The combined effect of radial stress, hoop stress, axial stress, and bending stress is used to calculate Von-Mises stress in the cylinder [7, 8]. Normalized Von-Mises stress ($\sigma_{Von-Mises}/\sigma_y$) is calculated to plot stress variation for different SR. The following equations have been used to calculate the stress considering external pressure to be zero [9]:

$$\text{Hoop stress}(\sigma_h) = \frac{p_i r_i^2}{r_o^2 - r_i^2}\left(1 + \frac{r_o^2}{r_i^2}\right) \quad \text{Longitudinal Stress}(\sigma_l) = \frac{p_i r_i^2}{r_o^2 - r_i^2}$$

$$\text{Bending Stress}(\sigma_b) = \frac{32 M_{max}}{\pi\left(d_{c_e}^4 - d_{c_i}^4 \big/ d_{c_e}\right)} \quad \text{Radial stress}(\sigma_r) = \frac{p_i r_i^2}{r_o^2 - r_i^2}\left(1 - \frac{r_o^2}{r_i^2}\right)$$

$$(20)$$

3 Results and Discussion

Figures 4 and 5 shows the theoretical results obtained for critical buckling load and Maximum allowable stress in piston rod respectively over the range of slenderness ratio (SR) 19 to 202.33. In this case, the length of piston rod varies from 0.057 m to 0.607 m with the step of 0.01. Figure 4 indicates that variation in the value of critical buckling load for the SR 19 to 45 is very less and after SR 45 its value decreases continuously.

Similarly, for corresponding values of stress in piston rod shown in Fig. 5 over SR 19 to 45 are constant approximately equal to yield point of the material and after SR 45 stresses in the piston rod are less than the yield point of the material. For SR 19 to 45, the stress due to the critical buckling load estimated by Eq. 10 exceeds the yield point of the material. To make it safe from failure, the algorithm is followed (as mentioned in Appendix) that gives the constant stress equal to yield stress of the material by limiting the buckling load up to SR 45.

Hydraulic cylinder of SR 19 with the mentioned dimensions in Table 1 has been modeled for the Finite Element Analysis as shown in Fig. 6. The load has been applied at the piston rod end and the Von-Mises stress of the hydraulic cylinder has been obtained. The Von-Mises stress obtained by the simulation differs by approximately 7% to that of theoretical results obtained. Further, it reports maximum stress in piston rod which again proves the piston rod to be a critical element.
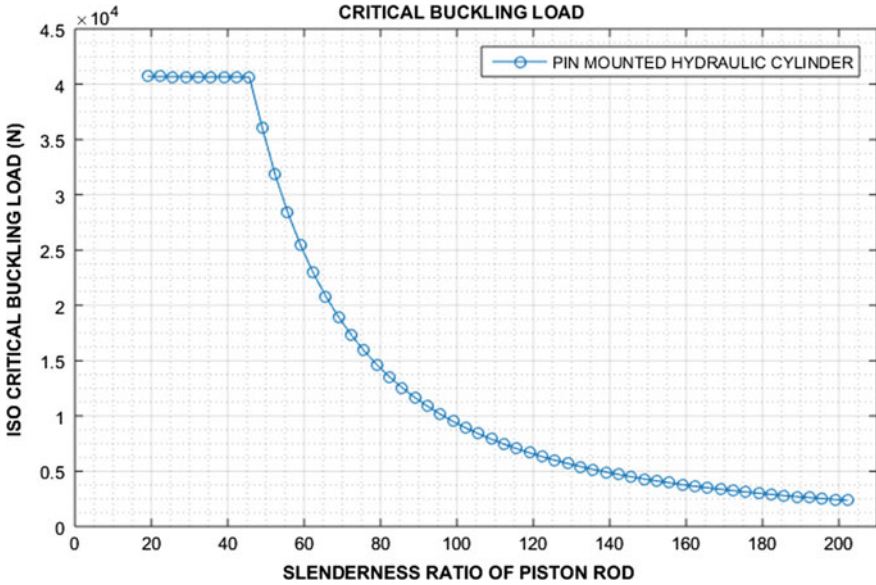
Fig. 4 Critical buckling load versus SR
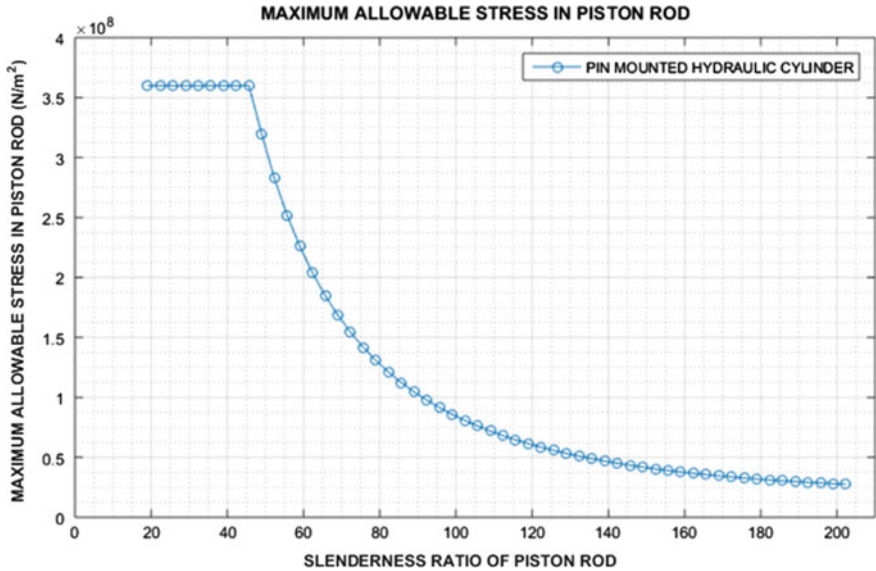
Fig. 5 Maximum allowable stress in piston rod

Figure 7 shows the Normalized Von-Mises Stress in a cylinder tube generated due to internal pressure developed inside the cylinder tube for the SR of the cylinder tube varying from 11 to 65. Normalized Von-Mises stress in the cylinder tube up to
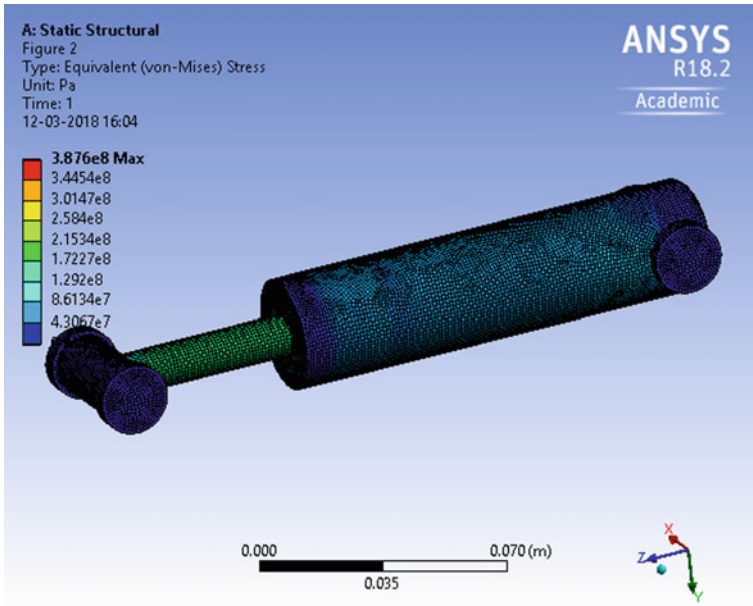
Fig. 6 Finite element simulation results
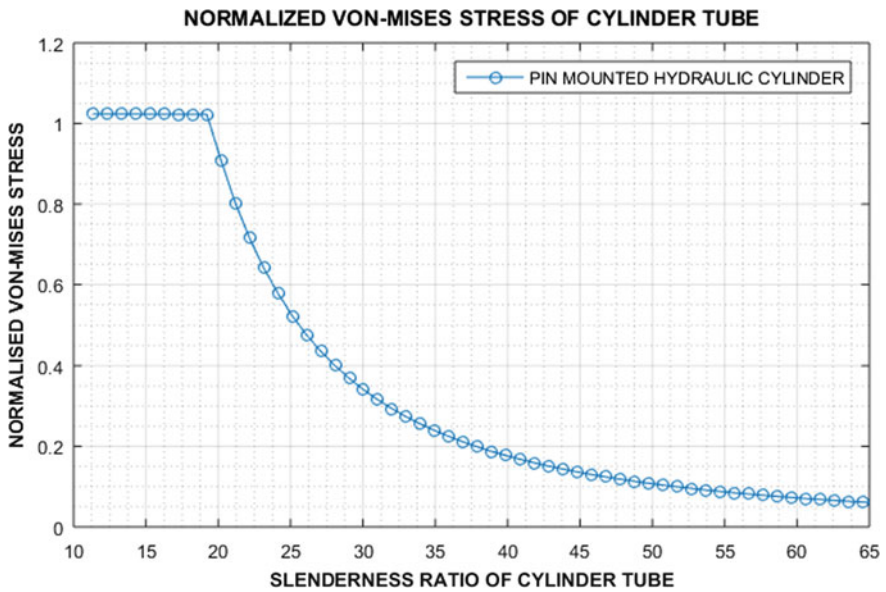
Fig. 7 Stress condition of cylinder tube

Table 2 Theoretical observation for different SR of the piston rod

Slenderness ratio of piston rod	Maximum allowable load (N)	Maximum stress in piston rod (MPa)	Slenderness ratio of Cylinder tube	Normalized Von-Mises Stress in cylinder tube
19	40694	360	11.32	1.0236
45.67	40660	360	19.20	1.0227
69	18956	168.56	26.10	0.4768
102.33	8918	80.74	35.95	0.2243
169	3368	34.52	55.65	0.0847
202.33	2368	27.59	65.50	0.0595

SR 19 is slightly more than unity i.e. up to the SR 19 of the cylinder tube, Von-Mises stress generated due to internal pressure is slightly greater than the yield stress of the cylinder tube material. After that as the stresses in the cylinder tube are below the yield point of the material. The yielding of the cylinder tube has been found for the lower SR up to 19. Table 2 summarizes the theoretical results obtained for the various slenderness ratio of the piston rod and cylinder tube. It is obvious that slender columns sustain lower compressive load in buckling. In the present analysis, it is confirmed that as slenderness ratio increases the critical buckling load decreases rapidly after SR 45.

4   Conclusions

In this study, theoretical estimation of critical buckling load of the pin-mounted hydraulic cylinder has been focused. The loading capacity degrades rapidly as slenderness ratio increases. The stresses induced are compressive in piston rod whereas tensile in a cylinder tube. Hence, cylinder tube fails only in yielding. The current research work will help in designing the hydraulic cylinder in various applications such as designing cylinders for heavy machinery and earth moving equipment etc. The outcomes of this work lead to the safe design of hydraulic cylinders used in Industries that determines more realistic failure load taking into consideration the material failure. According to the application, various factors like end friction, misalignment arising because of the wear rings can also be considered. The inclusion of such effects leads to the generation of the moment at the piston and cylinder tube junction.

References

1. Gamez-Montero PJ, Salazar E, Castilla R, Freire J, Khamashta M, Codina E (2009) Misalignment effects on the load capacity of a hydraulic cylinder. Int J Mech Sci 51(2): 105–113
2. Gamez-Montero PJ, Salazar E, Castilla R, Freire J, Khamashta M, Codina E (2009) Friction effects on the load capacity of a column and a hydraulic cylinder. Int J Mech Sci 51(2):145–151
3. Hoblit F (1950) Critical buckling for hydraulic actuating cylinders. Stress Engineer, Lockheed Aircraft Corporation. Product Engineering, 108–112
4. Flugge W (2013) Stresses in shells. Springer Science & Business Media
5. Seshasai KL, Dawkins WP, Iyengar S (1975) Stress analysis of hydraulic cylinders. In: Oklahoma State University, National Conference of fluid power
6. Baragetti S, Terranova A (1999) Limit load evaluation of hydraulic actuators. Int J Mater Product Technol 14(1):50–73
7. Hydraulic fluid power-cylinders: A method for determining the buckling load, Tech. Rep. ISO/TS 13725, ISO Standard (2001)
8. Timoshenko S (1970) Theory of elastic stability 2e. Tata McGraw-Hill Education
9. Timoshenko S (1953) History of strength of materials: with a brief account of the history of theory of elasticity and theory of structures. Courier Corporation

Kinematic Analysis of Bionic Vibratory Tillage Subsoiler

N. R. N. V. Gowripathi Rao, Himanshu Chaudhary and Ajay Kumar Sharma

Abstract The paper presents the kinematic analysis of bionic vibratory subsoiler used for agricultural tillage operation. Bionics is the study of the mechanical systems that function like living organisms or parts of the living organisms. Studies have reported that application of bionics in design procedure improves the working system efficiency. A crank-rocker mechanism is selected from the available literature for vibratory tillage operation in banana cultivation. The required trajectory of the crank-rocker mechanism for bionic vibratory subsoiler is examined through kinematic analysis. Velocity and acceleration required for the tillage tool operation are identified through kinematic analysis.

Keywords Vibratory tillage · Kinematics · Bionic tillage

1 Introduction

Agricultural tillage operations play an important role in crop growth. It results in the good tilth of the soil. Tillage is classified into two types primary and secondary tillage. The primary tillage aims to initially plough the land up to a depth of 20–25 cm. Secondary tillage is done once the primary operation is completed for better soil pulverization. The depth of secondary tillage operation is usually around 10–15 cm. There are different tillage implements available for these operations such as mould board plough, disc plough, cultivator, etc., as shown in Fig. 1. But among them, subsoiler is an important vertical tillage tool implement designed to minimize soil surface disturbance without soil inversion. It promotes aeration, increases water

N. R. N. V. Gowripathi Rao (✉) · H. Chaudhary
Department of Mechanical Engineering, Malaviya National Institute of Technology Jaipur, Jaipur, Rajasthan, India
e-mail: gowripathiraofmpe@gmail.com

A. K. Sharma
Department of Farm Machinery and Power Engineering, CTAE, MPUAT Udaipur, Udaipur, India
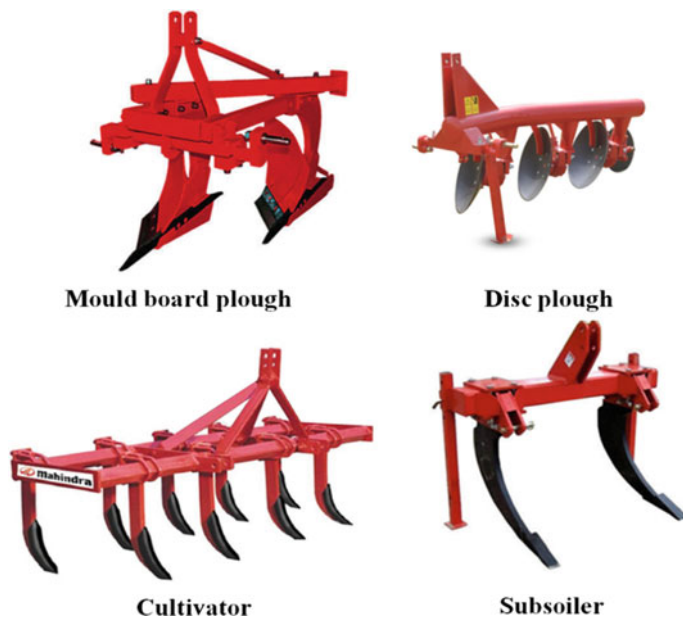
Fig. 1 Different types of primary and secondary tillage equipments

holding capacity, and improves root growth. Soil tillage devices nowadays are developing to meet the challenges of better utilization of the power and draft of the prime mower [1, 2].

Different applications are being used for the effective use of power in tillage operations. Among them, bionics is one of the area for solving engineering problems which uses the biological principles in design [3–5]. Some studies have reported that bionic design can improve the efficiency of tillage tool while operating in the soil. Thus the application of vibration in bionic design is one of the emerging area in agricultural mechanization [6].

Bionics is to mimic the living organisms and design a mechanical system for the required machines. A similar study is reported for design and development of vibratory subsoiler for banana cultivation. More work is reported on the application of bionics in subsoiler [5]. A study reported that subsoiling is an important tillage operation in conservation tillage and based on the application of biomimetics principle a cutting soil edge is designed and developed using the exponential function. Comparative experiments using two different types of subsoiler—one curve and another parabola-shaped were conducted. Results indicated that the cutting soil edge of shaft with exponential function curve structure has remarkable anti-drag property [7]. Another study reported the design and development of vibratory mechanism for banana cultivation using bionics principle. Experimental validation is performed for the designed bionic vibratory subsoiler. A significant reduction of draft force is reported [6]. Some studies on design of cutting blades using bionics is reported in the literature [8]. Performance study on effect of

biomimetics surface designs on furrow openers is also reported. Tool force and cutting power is increased with depth and speed, but cutting efficiency increased [4]. Thus the literature concludes that application of bionics can improve the design and effectiveness of the tillage tools.

The paper aims to carry out the kinematic analysis and to examine the required trajectory obtained through the vibratory mechanism in the literature [6], developed for the tillage operation in banana cultivation through MSC ADAMS. Velocity and acceleration required for tillage tool for operation are also identified through velocity and acceleration analysis in MATLAB.

2 Kinematic Diagram of the Vibratory Bionic Subsoiler

The literature suggests that vibratory subsoiler shown in Fig. 2 is used due to the reduction in draft force and increased power consumption. In the mechanism of literature [6], the vibrators are coupled with the frame through pin connection and connected with the gearbox and shank at the end. The principle of vibrating subsoiler in the literature [6], power is transmitted through the (PTO) power take-off shaft with the universal joint attached. PTO speed reduction takes place through the gearbox connected. The mechanism is provided motion through eccentric shaft attached to the crank. The vibratory mechanism is a crank-rocker and converts the rotating power of the crank into reciprocating motion of the rocker. Thus in this
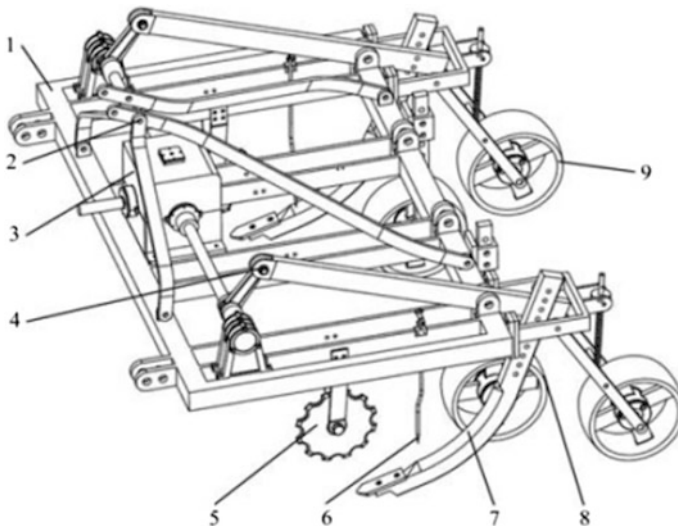
Fig. 2 1. Frame 2. Suspension bracket 3. Gear box 4. Vibrator 5. Coulter 6. Grass breaker 7. Shank 8. Gauge wheel 9. Press wheel (*Source* [6])
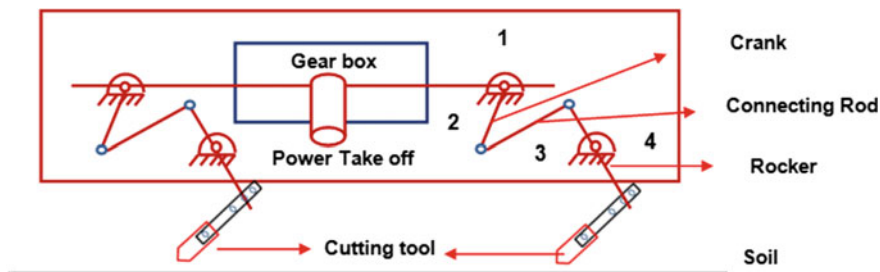
Fig. 3 Kinematic diagram of vibratory bionic subsoiler of literature [6]

way, the shank attached gains the vibrating action. Kinematic diagram of vibratory bionic subsoiler is shown in Fig. 3.

3 Materials and Methods

The analysis is done with the computer software MSC Adams, and it is one of the most widely used multi-function computing software. It helps in analysis of the proposed mechanical systems regarding dynamics, kinematic, and static analysis [9, 10]. Simulation of the mechanism can be carried out with the help of this simulation software. Therefore the following analysis method is chosen which can help to optimize and improve the system.

3.1 Model of the Vibratory Mechanism

The vibratory tillage mechanism [6] works on the principle of converting rotational motion of the power take-off shaft into the oscillatory motion. Figure 4 shows the kinematic diagram of the mechanism. Link 1 is the frame which is fixed one. Link O1A is crank which is given angular motion. Member AB is connected to the rocker O2B which is shown in Fig. 2.

3.2 Design of Elements Study

Compilation of the Model in MSC Adams

MSC Adams model of the crank-rocker mechanism consists of the several steps which are described further. The final assembled model will be ready to simulate the movement of the mechanism to be analyzed. The welcome window of the Adams which consist of the following option is shown in Fig. 5

Fig. 4 Kinematic diagram of vibratory mechanism [6]
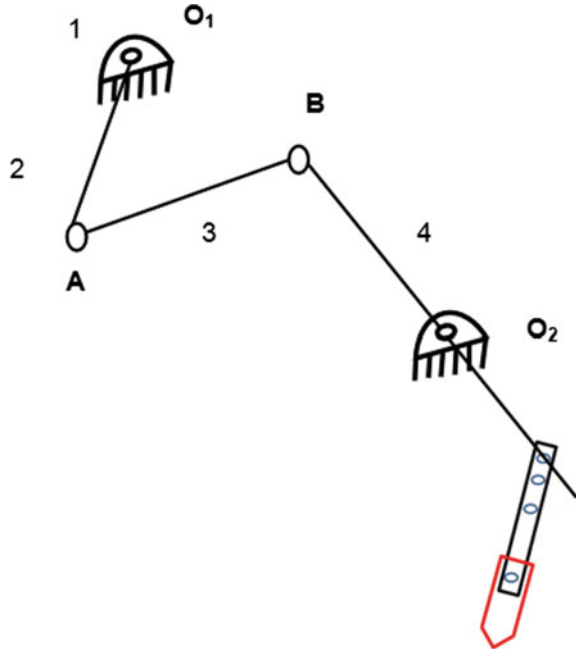
Fig. 5 Creating Model in MSC ADAMS
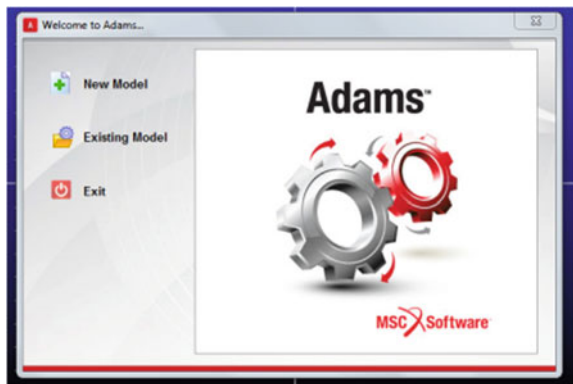
Creating Bodies in the MSC Adams

The mechanism is rendered in the plane by marking essential key points called as design points. The next step is to insert the members of the crank-rocker mechanism. Tool box to insert the solid body called rigid body link is available in the software. For the solid body (Link) a table of parameters is shown up to enter the width and thickness of the given member numerically. If we click left, then we place the member connecting the first and the second design point and so on. Inserting the individual members of the mechanism is shown in Fig. 6.
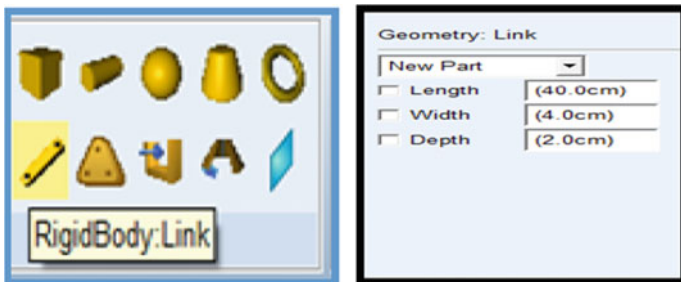
Fig. 6 Creating bodies

Fig. 7 Defining the joints between the member

Determining the Links

The members of the mechanism are defined for their respective joints for necessary moment. The relative position of the two bodies is defined by this joints. There are revolute joints between members of the mechanism. To create them a command
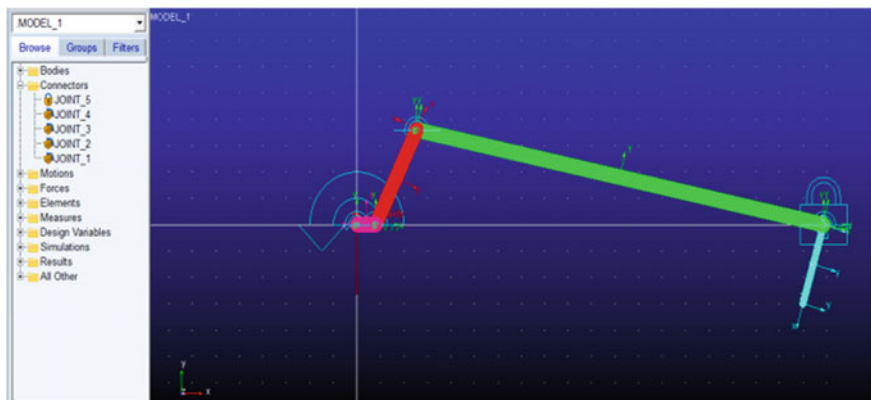
Fig. 8 Four-bar mechanism in MSC ADAMS
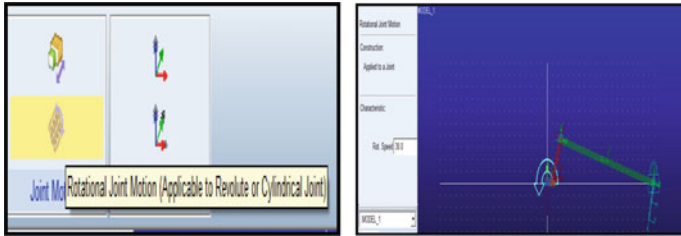
Fig. 9 Defining the motion of the crank in the four mechanism

window as shown in Fig. 7 called as connectors are used in MSC Adams. By selecting properly bodies and marker point a revolute joint can be placed between the links.

Figure 8 clearly shows the four-bar mechanism in MSC ADAMS interface. The mechanism is explained in Sect. 3.1.

Defining the Motion

The kinematic analysis of the mechanism can be performed by providing movement as shown in Fig. 9. This can be achieved by defining joint motion by ensuring the rotation of the driven member and consequent movement to the whole mechanism. Thus to do this, we select motions from the toolbox command in the main window. Then we select the rotational joint motion and set kinematic parameters rotation speed as 30 rad/sec. Thus left-click places the motion to the required design point that is the first revolute joint in this case as shown in Fig. 7.

Verification of the Model

After completing the model, it is ready for the simulation and kinematic analysis as shown in Fig. 10. This can be done with the help of simulation option in the toolbox. By clicking on the "start/pause animation" icon, we get the animation for the mechanism depending on the inputs provided in MSC Adams as shown in Fig. 7.
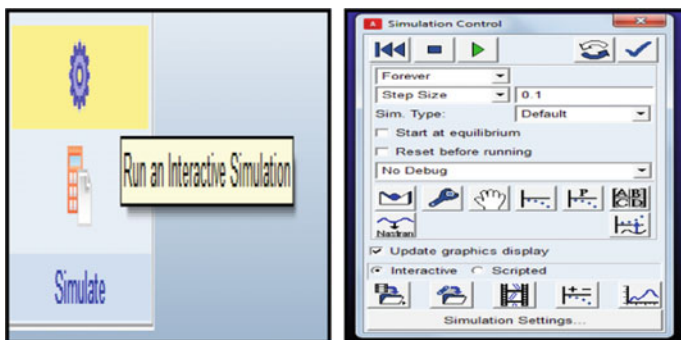
Fig. 10 Interactive simulation tool box
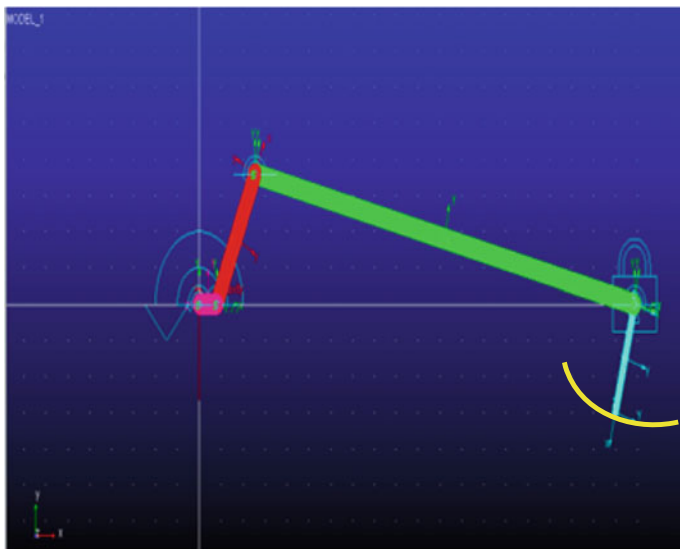
Fig. 11 MSC Adams model
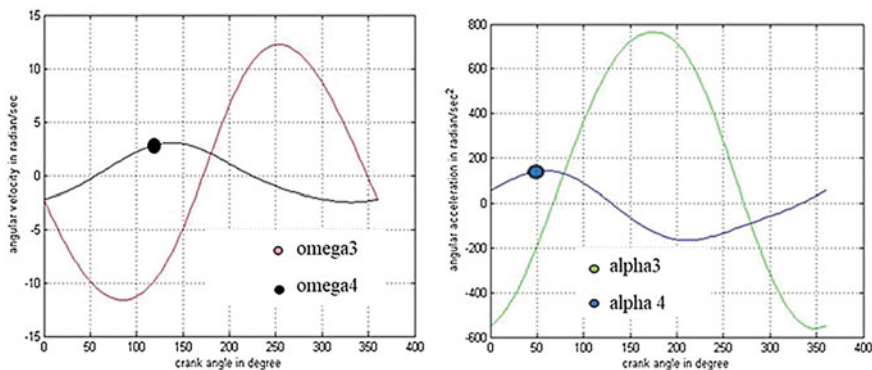
Fig. 12 Crank angle versus ang. velocity, Crank angle versus ang. acceleration

4 Results and Discussions

The required velocity and acceleration for the tillage tool are determined through MSC Adams software. The trajectory is observed to be a sinusoidal path; it follows two and fro motion. Figure 11 shows the tool path in Adams. The plot of omega (3, 4) versus crank angle is shown in Fig. 12, omega (3, 4) are the angular velocities of the coupler and rocker end. It is observed that maximum angular velocity for the tillage cutting tool at the rocker end (omega4) is observed to be 3 rad/sec and crank

angle is 1250. The cutting tool is attached at the rocker end. From the Fig. 12 acceleration is observed to be 170 rad/sec2 with crank angle 500.

5 Conclusion

The following study concluded that bionics and application of vibrations in soil tillage operation enables proper utilization of energy. The literature also suggests that draft requirement is comparatively less in vibratory tillage as compared to rigid tillage. Velocity and acceleration required by the link are identified. Thus there is a huge potential and scope for bionics in the design of vibratory tillage equipment in Indian agriculture which can improve the performance of the tillage operations and increase the wellness of the farmers.

References

1. Singh S (2016) Agricultural machinery industry in india agricultural mechanization in Asia Africa and Latin. America 47(2):26–35
2. Singh S, Singh RS, Singh SP (2014) Farm power availability on Indian farms Agricultural Engineering Today 38(4):44–52
3. Liu S, Weng S, Liao Y, Zhu D (2014) Structural bionic design for digging shovel of cassava harvester considering soil mechanics. Appl Bionics Biomech 11(1–2):1–11
4. Tong J, Moayad BZ, Ma YH, Sun JY, Chen DH, Jia H, Ren LQ (2009) Effects of biomimetic surface designs on furrow opener performance. J Bionic Eng 6(3):280–289
5. Zhijun Z, Honglei J, Jiyu S (2016) Review of application of biomimetics for designing soil-engaging tillage implements in Northeast China. Int J Agric Biol Eng 9(4):12
6. Xirui Z, Chao W, Zhishui C, Zhiwei Z (2016) Design and experiment of a bionic vibratory subsoiler for banana fields in southern China. Int J Agric Biol Eng 9(6):75
7. Zhang JB, Tong J, Ma YH (2014) Simulation of bionic anti-drag subsoiler with exponential curve feature using discrete element method. Appl Mech Mater 461:535–543(2014). Trans Tech Publications
8. Ji W, Jia H, Tong J (2012) Experiment on working performance of bionic blade for soil-rototilling and stubble-breaking. Trans Chin Soc Agric Eng 28(12):24–30
9. Hroncova D, Binda M, Sarga P, Kicak F (2012) Kinematical analysis of crank slider mechanism using MSC Adams/View. Procedia Eng 48:213–222
10. Vavro J, Kovacikova P, Bezdedova R (2017) Kinematic and dynamic analysis of planar mechanisms by means of the solid works software. Procedia Eng 177:476–481

Investigating Inlet Pipe Configuration of Muffler to Study the Performance Using CAE Modeling and Simulation

Eldhose James and Shubham Sharma

Abstract Mufflers are one of the integral components of the exhaust system of an automobile. Their main application is to attenuate the noise level caused by the exhaust gases coming from the combustion chamber. Designing and manufacturing of a muffler of our desire used to be a very long process of hit-and-trial method which would then be dragged by a number of tests. Due to environmental regulations, companies use reliable methods for modeling and testing of mufflers. Recent advancements in emission studies have made designing and testing a muffler numerically a convenient approach. This paper will deal with the experiments to study the performance of the muffler at the early stages of design. This study will deal with the outcome of different inlet pipe diameters and how that affects different parameters like transmission loss, acoustic pressure, and sound pressure.

Keywords Muffler · Acoustic pressure · Sound pressure · Transmission loss

1 Introduction

As the increase in demand for passenger cars in many countries is happening, the automobile industry is confronting many challenges from the pollution control board on noise pollution. Automobiles play one of the major parts in developing of any country, which makes transportation easier [1]. Though automobiles are a boon to the country because it provides a better way of transportation, it has a big negative effect on humans, because it causes environmental noise pollution. Automobile engines are the major reason for traffic noise pollution. This is why mufflers are vital to decrease the engine noise before it reaches the atmosphere. The muffler is an automotive component which is used to dampen the sound made in the exhaust of an engine or an internal combustion engine [2]. A drop-in pressure occurs inside the muffler. In an exhaust system, the muffler is placed after the

E. James (✉) · S. Sharma
Amity University Noida, Noida, UP, India
e-mail: e.eldhose03@gmail.com

catalytic converter and is the final automotive part in the exhaust system. The only job of an automobile muffler is to dampen the noise emission from the engine. A car without a muffler will have an admiration for the substantial difference in noise level a car with a muffler has. If automobiles run without a muffler, then an intolerable amount of exhaust noise will come from our cars and into the environment [3].

The pressure wave generated by pulses of interchanging high and low-pressure air is called sound. In an automobile engine, when the exhaust valve continuously opens, it allows high-pressure gas to enter the exhaust system, pressure waves are formed during this time. These pressure pulses are the reason for the sound coming from the engine. With the increase in the engine rpm the pressure fluctuations increase and because of this, the sound emitted is of a higher frequency. The variation in the ambient pressure is defined as back pressure and is caused because of the change in stagnation pressure through the various perforated elements and the immediate area discontinuities [4]. Back pressure and engine performance are directly related to each other. With the increase in back pressure, there is a significant reduction in thermodynamic efficiency and also the net power available [5].

Mufflers can be classified into two types

- Reactive muffler
- Absorptive muffler

A muffler which combines the properties of both reactive and absorptive type muffler is called as a hybrid muffler. This type of muffler is found commonly in most of the automobiles.

1.1 Reactive Muffler

The reactive muffler is also called as the reflective muffler, it uses the occurrence of destructive interference to dampen noise. Which means, that they are designed in such a way that the sound wave produced by an engine partially cancel itself out in the muffler. For total destructive interference to occur, a reflected wave of the pressure of equal amplitude which is out of phase by 180 degrees, needs to collide with the pressure wave that is being transmitted. Reflections happen when a change in area discontinuity or geometry occurs [6]. The outlet and inlet pipes are normally offset and have small holes that permit sound pulses to spread out in various directions inside a chamber which would result in destructive interference.

Reflective mufflers are extensively applied in the automobile exhaust system in which the exhaust gas flows and noise emission varies with time. They have the function of reducing noise at different frequencies because of the multiple chamber and difference in geometry that the exhaust gases are made to go through the muffler (Fig. 1).

Fig. 1 Reactive muffler
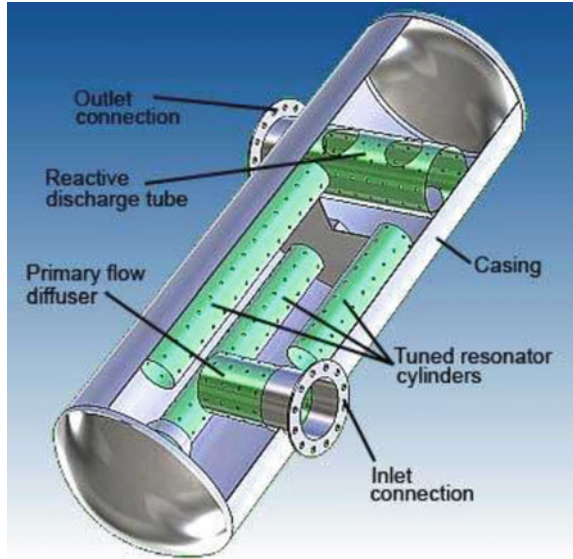
1.2 Absorptive Muffler

An absorptive muffler is also called as a dissipative muffler, it works on the principle of absorption to decrease the energy of sound. The energy of the sound waves is converted into heat in the absorptive material and thus diminished. A commonly used dissipative muffler is made up of a straight, circular and perforated pipe that is enclosed in larger steel covering. There is a coating of sound absorbing material between the casing and the perforated pipe that attracts some of the pressure pulses [7] (Fig. 2).

2 Material and Method

To find out the transmission loss, an equipment is used which works on the principle of Decomposition Theory [8] (Fig. 3).

The sound pressure is decomposed into two spectra's, the incident and reflected, SAA and SBB. Two sets of microphones are placed in the setup, one set which has two microphones is placed before the muffler and the third one after the muffler, this setup measures the transmission loss by comparing the difference in noise level between the two sets of microphones [9].

The equation used to measure the acoustic pressure p is a modified form of the Helmholtz equation
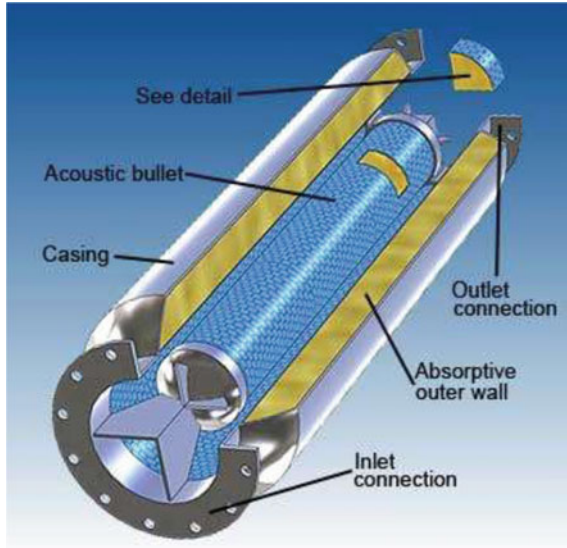
Fig. 2 Absorptive muffler
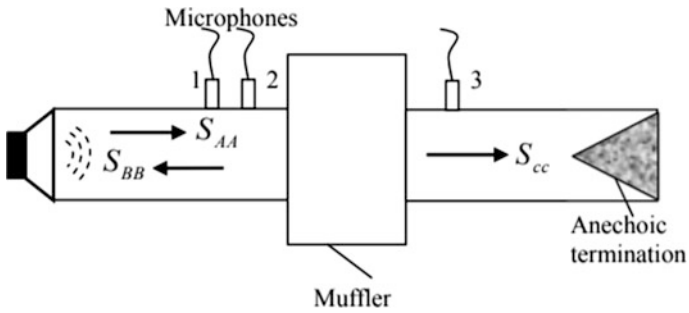
Fig. 3 Experimental setup of decomposition theory

$$\nabla \cdot \left(-\frac{\nabla p}{\rho} \right) - \frac{\omega^2 p}{c^2 p} = 0 \qquad (1)$$

where ω is angular frequency, c is sound of speed, and ρ is the density of material.

The equation used for transmission loss is

$$TL = 10 Log \left(\frac{P_{in}}{P_{out}} \right) \qquad (2)$$

TL is transmission loss, P_{in} and P_{out} denotes the sound power level at the inlet and outlet of the muffler.

3 Simulation

3.1 Parameters Used for the Model

See Table 1.

3.2 Meshing the Model

For this experiment we have taken two mufflers identical to each other in all ways except the inlet diameter, one model has a diameter of 35 mm and the other one has a diameter of 45 mm (Fig. 4).

These two designs are simulated on Comsol software and then compared to each other for different characteristics such as absolute pressure level, sound pressure level, acoustic pressure, and transmission loss at different frequencies. Depending on the result we will know the effect of inlet pipe diameter on the noise canceling property of the muffler.

Table 1 Parameters

Name	Value (mm)	Description
L	600	Muffler length
H	150	Muffler height
W	300	Muffler width
L_io	150	Inlet and outlet length
D	15	Liner thickness
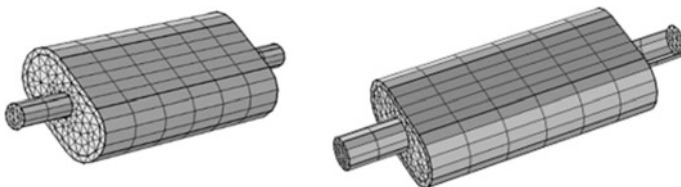
Fig. 4 Muffler with 35 mm (left) and 45 mm (right) inlet pipe

3.3   Transmission Loss Methodology for Comsol

See Fig. 5.

4   Result and Discussions

Figure 6 shows the absolute pressure for the two models, for a frequency of 1500 Hz it can be seen that for the 35 mm inlet pipe model, the value is 1.52 Pa and 1.37 Pa for the 45 mm model.
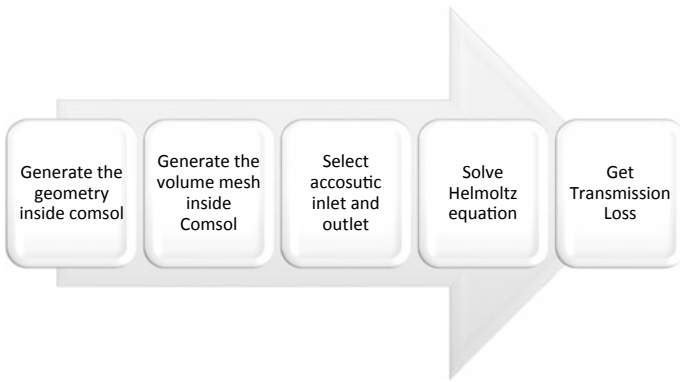
Fig. 5   Methodology for acquiring transmission loss in COMSOL
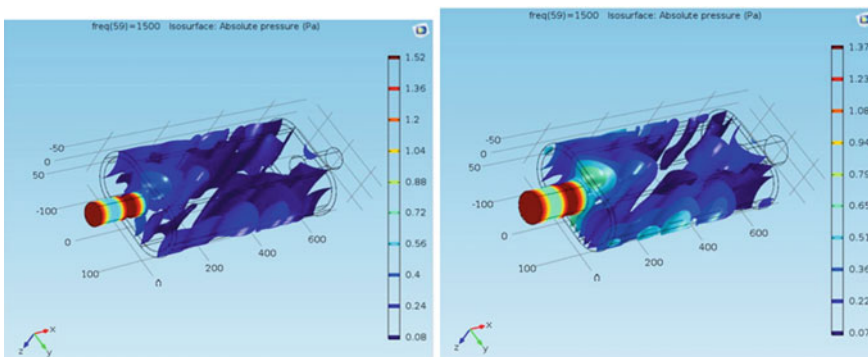
Fig. 6   Absolute Pressure Level for 35 mm (left) and 45 mm (right)
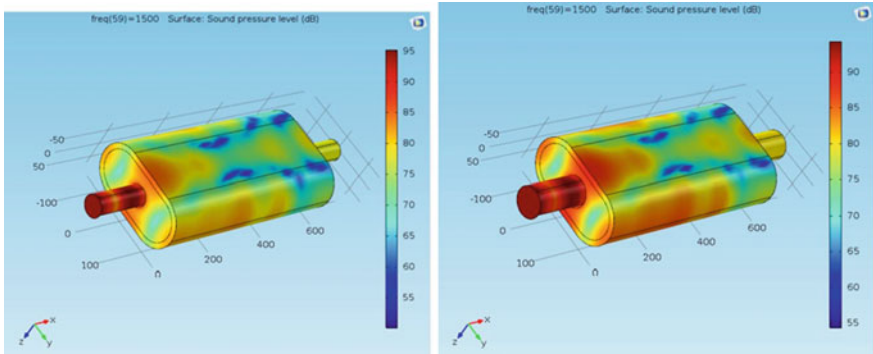
Fig. 7 Sound Pressure Level for 35 mm (left) and 45 mm (right)
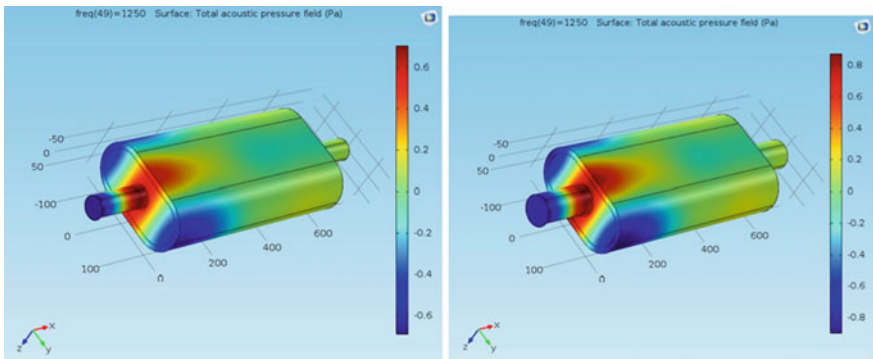
Fig. 8 Total Acoustic Pressure Field for 35 mm (left) and 45 mm (right)

Figure 7 shows the Sound Pressure for the two models at a frequency of 1500 Hz. It is 95 dB for the 35 mm model and 90 dB for the 45 mm model.

Figure 8 shows the Acoustic Pressure on the surface of the muffler at a frequency of 1250 Hz. It is 0.6 Pa for the 35 mm model and 0.8 Pa for the 45 mm model.

Figures 9 and 10 show graphs between transmission loss and frequency for the two models. From the figures, we can see that for the 35 mm model the maximum transmission loss is 23 dB and for that of the 45 mm model, it is 24 dB.
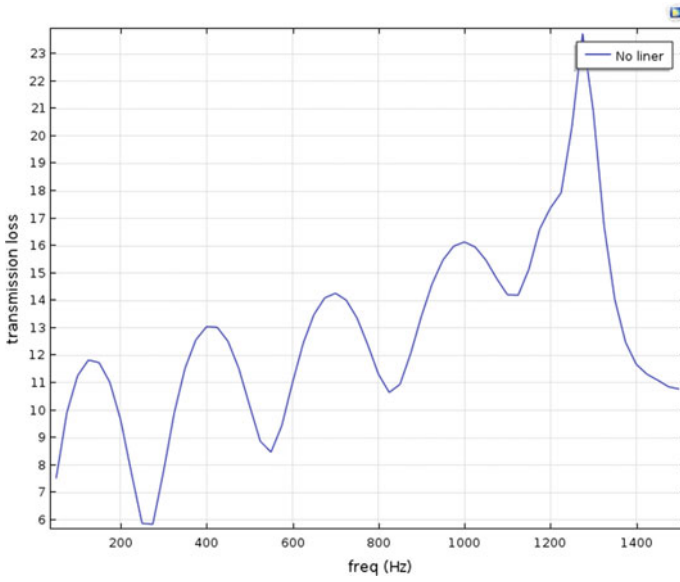
Fig. 9 Transmission Loss for 35 mm model
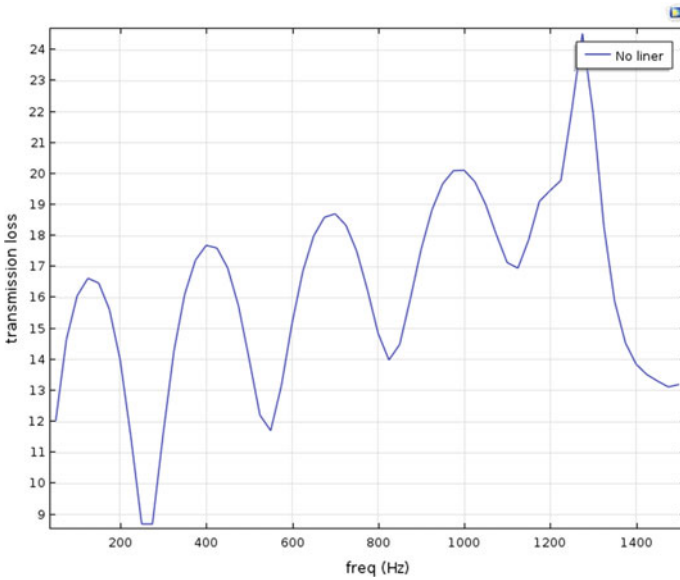
Fig. 10 Transmission Loss for 45 mm model
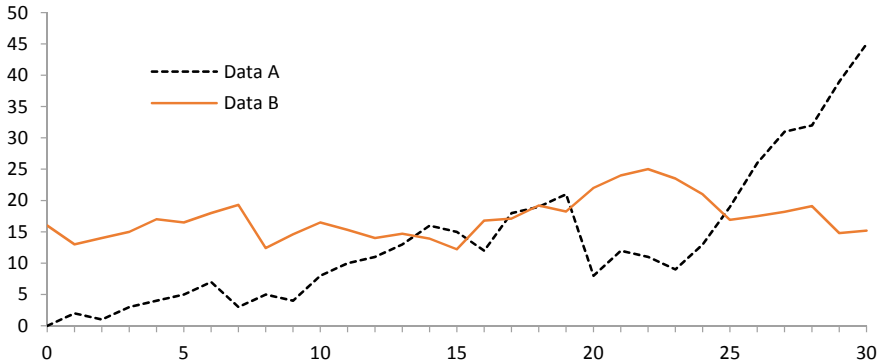
Fig. 11 A figure caption is always placed below the illustration. Short captions are centered, while long ones are justified. The macro button chooses the correct format automatically

5 Conclusion

We can clearly see that the transmission loss for the 45 mm model is greater than the 35 mm model. With this, we can come to the conclusion that as we increase the size of the inlet pipe, maximum transmission loss is also acquired. Thus, for better transmission loss the diameter of the inlet pipe of the muffler can be increased to make the muffler more efficient (Fig. 11).

For citations of references, we prefer the use of square brackets and consecutive numbers. Citations using labels or the author/year convention are also acceptable. The following bibliography provides a sample reference list with entries for journal articles [1], an LNCS chapter [2], a book [3], proceedings without editors [4], as well as a URL [5].

References

1. Yu X, Cheng L (2014) Duct noise attenuation using reactive silencer with various internal configurations. J Sound Vib 335:229–244
2. Yu X, Tong Y, Pan J, Cheng L (2015) Sub-chamber optimization for silencer design. J Sound Vib 351:57–67
3. Bilawchuk S, Fyfe KR (2003) Comparison and implementation of the various numerical methods used for calculating transmission loss in silencer systems. Appl Acoust 64:903–916
4. Barbieri R, Barbieri N (2006) Finite element acoustic simulation-based shape optimization of a muffler. Appl Acoust 67(4):346–357
5. Yao Y, Wei S, Zhao J, Chen S, Feng Z, Yue J (2013) Experiment and CFD Analysis of Reactive Muffler. J Appl Sci Eng Technol 6(17):3282–3288
6. Yu X, Cheng L (2014) Duct noise attenuation using reactive silencer with various internal configurations. J Sound Vib 335:229–244

7. Rahman M, Sharmin T, Hassan AFME, Nur MA (2005) Design and construction of a muffler for engine exhaust noise reduction. In: International conference on mechanical engineering, Dhaka
8. Tao Z, Seybert AF (2003) A review of current techniques for measuring muffler transmission loss, SAE-01-1653
9. Lee JW (2015) Optimal topology of reactive muffler achieving target transmission loss values: design and experiment. Appl Acoust
10. Author, F.: Article title. Journal 2(5), 99–110 (2016)
11. Author F, Author S (2016) Title of a proceedings paper. In: Editor F, Editor S (eds) CONFERENCE 2016, LNCS, vol 9999, pp. 1–13. Springer, Heidelberg
12. Author F, Author S, Author T (1999) Book title. 2nd edn. Publisher, Location (1999)
13. Author, F.: Contribution title. In: 9th International Proceedings on Proceedings, pp. 1–2. Publisher, Location (2010)
14. LNCS Homepage. http://www.springer.com/lncs. Accessed 21 Nov 2016

Performance Enhancement of an All-Terrain Vehicle by Optimizing Steering, Powertrain and Brakes

Anubhav Kumar Sinha, Ayush Sengupta, Himank Gandhi, Piyush Bansal, Krishna Mohan Agarwal, Sanjeev Kumar Sharma, Rakesh Chandmal Sharma and Sunil Kumar Sharma

Abstract All-Terrain Vehicle is an off-road vehicle which can withstand harsh terrains. The steering system, transmission system, and brakes are one of the integral parts of the buggy which is responsible for providing directional stability and power transmission, respectively. This paper focuses on the weight optimization and performance enhancement of the buggy by making alterations in the steering and transmission system of the vehicle. In the steering system, alternate material was used and in the transmission system, forward and reverse gearbox was replaced with continuously variable transmission and chain sprocket arrangement. A mathematical model was developed and compared with the result obtained from ADAMS/CAR. The decisions were made keeping in mind the safety, drivability, reliability, maneuverability, manufacturability, and performance aspects of the vehicle.

Keywords Steering · Chain sprocket · CVT · Brakes · Weight optimization · Adams

1 Introduction

An All-Terrain Vehicle (ATV) is defined by the American National Standards Institute (ANSI) as a vehicle that travels on low-pressure tires, with a seat that is straddled by the operator, along with handlebars for steering control which can

A. K. Sinha · A. Sengupta · H. Gandhi · P. Bansal · K. M. Agarwal · S. K. Sharma ·
S. K. Sharma (✉)
Department of Mechanical Engineering, Amity School of Engineering and Technology,
Amity University Uttar Pradesh, Noida, India
e-mail: sunilsharmaiitr@gmail.com

R. C. Sharma
Maharishi Markandeshwar (Deemed to be University), Mullana, Ambala 133207, India

withstand harsh terrains. This paper provides detailed insight regarding the steering, powertrain, and brakes of the ATV. The vehicle is designed in a way to keep the cost minimum, with no compromise on driver safety, ergonomics, and durability of the vehicle providing the thrill factor. The design is such that it can sustain in all weather conditions and must be mobile in rough terrain. A special emphasis has been put on weight reduction [1–20].

The design of the various components and assembly of the vehicle has been done using SolidWorks. It was made sure that the vehicle's weight is kept as light as possible, along with adequate strength and rigidity. The design is highly based on dynamic analysis of components and stress analysis to still ensure safety under the unwanted situation when there is an existence of impact forces. It is made sure, that the fabrication is easy, and affordable [21–29].

2 Steering

Steering works as a guiding mechanism which is used by the driver to follow a desired course. In this buggy, rack-and-pinion (manual steering system) assembly has been used [30, 31]. The vehicle has under steer, for which negative camber and damper stiffness have been provided. Though written data shows under steer, it has been rectified. Rack is connected with the tie rods directly of length 15.09 inch using appropriate connectors. The steering ratio is 7:1. The steering angles are: 25.56° (outside wheel) and 40° (inside wheel). The two angles are found with the help of MSC Adams. Table 1 shows the steering assembly specifications.

Most of the components are custom-made, with the exception of steering wheel, dampers, and rack-and-pinion assembly. Knuckle is to be directly connected to the wheels and made of aluminum because of lightweight, heat resistance, and in case of dynamic loading, fractures will not take place. Tie rods are to be manufactured of stainless steel as it provides high strength (Fig. 1).

Table 1 Steering assembly specifications		
Rack length	14 inch
Lock to lock	3 turns
Rack travel	4.25 inch
Steering angle	40(in), 25.56(out)
IBJ center distance	7 inch
OBJ center distance	22.09 inch
Turn lock to lock	0.778
Steering wheel diameter	13 inch
Turning radius	2.619 m
Ackerman percentage	50.40%
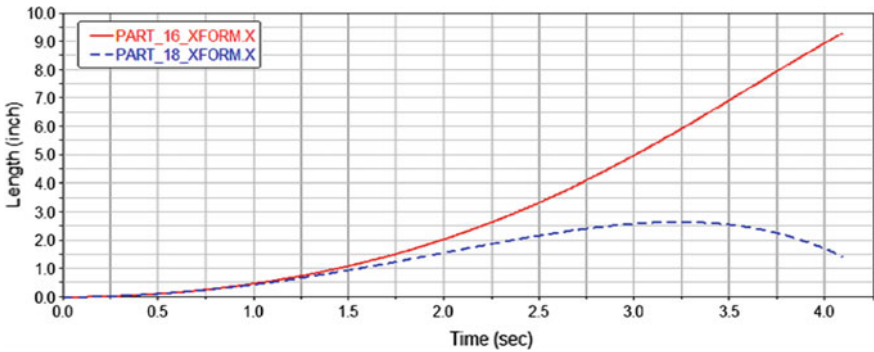
Fig. 1 Characteristic of wheel motion with rack movement per unit time

3 Powertrain

For the buggy, the following changes are shown in Table 2.

3.1 Engine

The engine considered is having Max power = 10 HP and Max Torque = 19.6 Nm@2600 rpm. By comparing the two, we have decided to go for CVT as our transmission because of the wide range of gear ratios and are easier to drive. As the terrain is tough the driver will have to change the gears very frequently to tackle the track, using a CVT removes that hassle and the driver is more focused on the track rather than just shifting to the correct gear.

3.2 Gear Reduction

To give the car the initial lift, an additional reduction is introduced which wil ladd to the acceleration. For that part, we are using a chain sprocket reduction as because it is easy to maintain, the ratios can be changed, during testing, if it is not suitable, more suitable according to the rear end of our buggy.

Table 2 The types of equipment change in ATV

Type	Manual	Automatic – CVT
Manufacturer	Mahindra, Mahindra Alfa gearbox	Cv Tech
Gear ratios	First 31.45:1; Second 18.70:1; Third 11.40:1; Fourth 7.35:1; Reverse 55.08:1	Low Ratio 3:1; High Ratio.43:1

Table 3 Tractive forces with respect RPM variations

RPM	CVT ratio	Total gear ratio	Torque output (engine) N-m	Torque on wheels N-m	Tractive force N
2000	3	42	18.4	772.8	2883.58
2200	2.68	37.52	18.5	694.12	2590
2400	2.36	33.04	18.8	621.152	2317.73
2600	2.04	28.56	19.2	548.352	2046.08
2800	1.72	24.08	18.8	452.704	1689.19
3000	1.4	19.6	18.5	362.6	1352.98
3200	1.08	15.12	18.4	278.208	1038.08
3400	0.76	10.64	18.1	192.584	718.597
3600	0.5	7	17.7	123.9	462.313

Also, since we are using CVT for the first time, a chain and sprocket are more feasible than a reduction through spur gears. First, we found the resistances with respect to ground that the buggy needs to overcome. The reduction required comes out to be 14:1. Moving on to the reduction design, since the ratio is high the reduction is completed in two steps where, it includes four sprockets and two roller chains. Sprocket N1 would be in axis with the output of the CVT and connected to sprocket N2 using a roller chain. Sprocket N3 would be in a compound with N2 and it would further be connected to N4, using a roller chain, onto the final drive. Referring to the sprocket manufacturers manual, the appropriate service factor was chosen for using a single strand sprocket with hub on both side sides considered that the car would travel at an avg. of 2600 rpm (for max torque). The variation in Tractive force is shown in Table 3. N1 = 23 teeth, N2 = 70 teeth, N3 = 17 teeth, N4 = 68 teeth, because of the design constraint the second reduction is carried out using smaller sprockets. The CVT is tuned to achieve a low ratio of 0.5:1 so that speed does not exceed above 60 kmph. Table 4 give the variation of speed and acceleration with respect to RPM.

Table 4 Tractive forces with respect RPM variations

RPM	Speed m/s	Speed kmph	Acceleration m/s^2
2000	1.33	4.81	9.84
2200	1.64	5.92	8.83
2400	2.03	7.33	7.91
2600	2.55	9.19	6.98
2800	3.26	11.74	5.76
3000	4.29	15.46	4.61
3200	5.93	21.38	3.54
3400	8.96	32.28	2.45
3600	14.43	51.95	1.57

3.3 Gear Torque Calculations

The gear torque calculations have been done to find the output torque provided by the engine at the wheels. The calculated amount of the torque is less than the rated torque of the engine which implies that the four sprocket arrangement will provide ample gear reductions to drive the vehicle. The rotational torque (T_r) can be calculated as

Rotational torque, $Tr = \mu W \cos \alpha r$
$\alpha = 30°$; Tire size = 22" = 0.279 m = 279.4 mm
$Tr = 0.3*293*9.81*\cos 30*(0.1359) = 104.17$ N-mm^2

Mass moment of inertia, $I = \frac{1}{2}r^2 W = \frac{1}{2}*293*9.81*(0.279)^2 = 11.18$ N-m^2
$V = r\omega \Leftrightarrow 16.66 = 0.2794 \omega$; ɯ = 59.62 rad/s; $\propto = \omega/t = 59.62/20 = 2.981$ rad/s^2
$I\alpha = 11.18*2.981 = 33.32$ N-mm.

Gear torque, $Tg = Tr + I*\alpha$; $Tg = 104.17 + 33.32 = 137.49$
Since, $\omega = 2\pi N$; $N = \omega/2 \pi = 9.49/s$ or 569.6 rpm;

Load power, $HP = 2\pi NT = 7.32$ HP
Therefore, $Tg > Tr$.

4 Brakes

The brakes were designed such that the vehicle stops in the least time and distance. Brakes are the most important of components, when it comes to the safety of the driver. Dual piston floating caliper would be used in our vehicle. This is primarily because it is effective with fewer prices, and even light-weighted [32–42]. Table 5 gives the braking specification [43–48].

Table 5 Braking specifications

Braking circuit	Specification
Brake master cylinder bore size	15.875 mm
Brake calliper cylinder (Bore size × No's)	25.4 mm; 2 cylinder per calliper;
	Area = 1012.9012 mm^2
Coefficient of friction	0.4
Weight transfer at 40 kmph to 0 kmph	452.219 N/m
Static rolling radius for tyre	0.285 m
Brake torque required per wheel	Front = 214.454 Nm;
	Rear = 169.426 Nm
Force required by caliper cylinder	6330.643 N
Stopping distance at 45 kmph	8.124 m
Pedal force	150 N
Pedal travel	3.038 inch

We have opted for Tandem Master Cylinder (TMC), the reason being that if a failure occurs in any of the linings, the remaining will still work and braking failure will be prevented. X-split arrangement would be used in our buggy. This is again because of the safety factor and if any of the brakes fail, the others would still work and bring the vehicle to halt. DOT 3 fluid is to be used in the brakes. It is a polyethylene glycol-based fluid and is commonly used in passenger vehicles. Its dry boiling point (205 °C) and wet boiling point (140 °C) is high and hence does not absorb moisture easily. It withstands high temperatures without getting boiled. SS 410 will be used as brake disc. The reason being that it has very favorable mechanical properties including high corrosion resistance and high strength.

5   Conclusion

After taking the design and calculation of the respective departments, the fabrication of an ATV was carried out and better results were achieved in all the departments, i.e., steering, transmission, and brakes department (Table 6).

A better arrangement for the steering mechanism has been installed, thus improving the steering ratio of the vehicle and the SS for the steering column and aluminum for the rack-and-pinion has reduced the weight as well as given better results for the same. Similarly, CVT has been preferred over manual transmission as it proves out to be over efficient over rough terrain. In the brakes department, comparatively smaller discs have been used thus contributing to the weight issues and size constraint of the buggy, also improving the stopping distance of the vehicle.

Table 6 Vehicle comparison

Specification	mBaja 2016	mBaja 2018
Width	61"	61"
Length	74"	82"
Height	48"	55"
Track width	F 49" R 54"	F 54" R 54"
Wheel base	68"	60"
Tyre size	F 23" R 23"	F 22" R 22"
Max speed	52 kmph	60 kmph
Max acceleration	3.8 m/s^2	9.84157 m/s^2
Gradeability	42.5%	60.32%
Transmission	Mahindra Alfa	CVTech CVT
Kerb weight	296 kg	155 kg
Stopping distance	9.5 m	6.5516 m
Steering	14:1 rack and pin	7:1 rack and pin

References

1. Kumar R, Garg MP, Sharma RC (2012) Vibration analysis of radial drilling machine structure using finite element method. Adv Mater Res 472:2717–2721
2. Palli S, Koona R, Sharma RC, Muddada V (2015) Dynamic Analysis of Indian railway integral coach factory bogie. Int J Veh Struct Syst 7(1):16–20. https://doi.org/10.4273/ijvss.7.1.03
3. Sharma RC (2011) Ride analysis of an Indian railway coach using Lagrangian dynamics. Int J Veh Struct Syst 3(4):219–224. https://doi.org/10.4273/ijvss.3.4.02
4. Sharma RC (2012) Recent advances in railway vehicle dynamics. Int J Veh Struct Syst 4 (2):52–63. https://doi.org/10.4273/ijvss.4.2.04
5. Sharma RC (2013) Sensitivity analysis of ride behaviour of Indian railway rajdhani coach using Lagrangian dynamics. Int J Veh Struct Syst 5(3–4):84–89
6. Sharma RC (2013) Stability and eigenvalue analysis of an Indian railway general sleeper coach using Lagrangian dynamics. Int J Veh Struct Syst 5(1):9–14
7. Sharma RC (2016) Evaluation of passenger ride comfort of Indian rail and road vehicles with ISO 2631-1 standards: part 1 - Mathematical modeling. Int J Veh Struct Syst 8(1):1–6
8. Sharma RC (2016) Evaluation of passenger ride comfort of Indian rail and road vehicles with ISO 2631-1 standards: part 2 – Simulation. Int J Veh Struct Syst 8(1):7–10
9. Sharma RC, Palli S (2016) Analysis of creep force and its sensitivity on stability and vertical-lateral ride for railway vehicle. Int J Veh Noise Vib 12(1):60–76
10. Sharma RC, Palli S, Koona R (2017) Stress and vibrational analysis of an Indian railway RCF bogie. Int J Veh Struct Syst 9(5):296–302
11. Sharma SK, Sharma RC, Kumar A, Palli S (2015) Challenges in rail vehicle-track modeling and simulation. Int J Veh Struct Syst 7(1):1–9
12. Sharma SK, Kumar A (2016) Dynamics analysis of wheel rail contact using FEA. Procedia Eng 144:1119–1128. https://doi.org/10.1016/j.proeng.2016.05.076
13. Sharma RC, Palli S, Sharma SK, Roy M (2017) Modernization of railway track with composite sleepers. Int J Veh Struct Syst 9(5):321–329
14. Sharma SK, Kumar A (2017) Impact of electric locomotive traction of the passenger vehicle ride quality in longitudinal train dynamics in the context of Indian railways. Mech Ind 18 (2):222. https://doi.org/10.1051/meca/2016047
15. Sharma SK, Kumar A (2017) Ride performance of a high speed rail vehicle using controlled semi active suspension system. Smart Mater Struct 26(5):55026. https://doi.org/10.1088/1361-665X/aa68f7
16. Sharma SK, Kumar A (2018) Ride comfort of a higher speed rail vehicle using a magnetorheological suspension system. Proc Inst Mech Eng Part K: J Multi-Body Dyn 232 (1):32–48. https://doi.org/10.1177/1464419317706873
17. Sharma SK, Kumar A (2018) Disturbance rejection and force-tracking controller of nonlinear lateral vibrations in passenger rail vehicle using magnetorheological fluid damper. J Intell Mater Syst Struct 29(2):279–297. https://doi.org/10.1177/1045389X17721051
18. Palli S, Koona R, Sharma SK, Sharma RC (2018) A review on dynamic analysis of rail vehicle coach. Int J Veh Struct Syst 10(3):204–211
19. Sharma RC, Sharma SK, Palli S (2018) Rail vehicle modeling and simulation using Lagrangian method. Int J Veh Struct Syst 10(3):188–194
20. Sharma SK, Sharma RC (2018) Simulation of Quarter-car model with magnetorheological dampers for ride quality improvement. Int J Veh Struct Syst 10(3):169–173
21. Sharma SK, Kumar A (2016) The impact of a rigid-flexible system on the ride quality of passenger bogies using a flexible carbody. In: Pombo J (ed) Proceedings of the third international conference on railway technology: research development and maintenance, Cagliari, Sardinia, Italy. Civil-Comp Press, Stirlingshire UK, 87. https://doi.org/10.4203/ccp.110.87

22. Sharma SK, Chaturvedi S (2016) Jerk analysis in rail vehicle dynamics. Perspect Sci 8:648–650. https://doi.org/10.1016/j.pisc.2016.06.047

23. Sharma SK, Kumar A (2014) A comparative study of Indian and worldwide railways. Int J Mech Eng Robot Res 1(1):114–120

24. Sharma SK (2013) Zero energy building envelope components: a review. Int J Eng Res Appl 3(2):662–675

25. Kumar P, Kumar A, Racic V, Erlicher S (2018) Modelling vertical human walking forces using self-sustained oscillator. Mech Syst Signal Process 99:345–363

26. Kumar P, Kumar A, Erlicher S (2018) A nonlinear oscillator model to generate lateral walking force on a rigid flat surface. Int J Struct Stab Dyn 18(2):1850020

27. Kumar P, Kumar A (2016) Modelling of lateral human walking force by self-sustained oscillator. Procedia Eng 144:945–952

28. Kumar P, Kumar A, Erlicher S (2017) A modified hybrid Van der Pol-Duffing-Rayleigh oscillator for modelling the lateral walking force on a rigid floor. Phys D 358:1–14

29. Kumar P, Kumar A, Racic V (2018) Modelling of longitudinal human walking force using self-sustained oscillator. Int J Struct Stab Dyn 18(6):1850080

30. Rao Dr CJ, Nageswara Rao Dr D, Srihari P (2013) Influence of cutting parameters on cutting force and surface finish in turning operation. J Procedia Engg, Elsevier Science Direct, pp 1405–1415

31. Swathi K, Srihari P (2015) Heat transfer enhancement in a tube using rectangular strip inserts. Int J Alied Eng Res, Research India Publications 10(20):41532–41544

32. Mohanty D, Jena R, Choudhury PK, Pattnaik R, Mohapatra S, Saini MR (2016) Milk derived antimicrobial bioactive peptides: a review. Int J Food Prop 19(4):837–846

33. Samantaray D, Mohapatra S, Mishra BB (2014) Microbial bioremediation of industrial effluents. In: Microbial biodegradation and bioremediation. Elsevier, pp 325–339

34. Mohapatra S, Rath SN, Pradhan SK, Samantaray DP, Rath CC (2016) Secondary structural models (16S rRNA) of polyhydroxyalkanoates producing bacillus species isolated from different rhizospheric soil: phylogenetics and chemical analysis. Int J Bioautomation 20(3):329–338

35. Mohapatra S, Samantaray DP, Samantaray SM, Mishra BB, Das S, Majumdar S, Pradhan SK, Rath SN, Rath CC, Akthar J, Achary KG (2016) Structural and thermal characterization of PHAs produced by Lysinibacillus sp. through submerged fermentation process. Int J Biol Macromol 93:1161–1167

36. Mohapatra S, Mishra R, Roy P, Yadav KL, Satapathi S (2017) Systematic investigation and in vitro biocompatibility studies on implantable magnetic nanocomposites for hyperthermia treatment of osteoarthritic knee joints. J Mater Sci 52(16):9262–9268

37. Bandekar D, Chouhan OP, Mohapatra S, Hazra M, Hazra S, Biswas S (2017) Putative protein VC0395_0300 from Vibrio cholerae is a diguanylate cyclase with a role in biofilm formation. Microbiol Res 202:61–70

38. Bandhu S, Khot MB, Sharma T, Sharma OP, Dasgupta D, Mohapatra S, Hazra S, Khatri OP, Ghosh D (2018) Single cell oil from Oleaginous yeast grown on sugarcane bagasse-derived xylose: an approach toward novel biolubricant for low friction and wear. ACS Sustain Chem Eng 6(1):275–283

39. Mohapatra S, Mohanta PR, Sarkar B, Daware A, Kumar C, Samantaray DP (2017) Production of Polyhydroxyalkanoates (PHAs) by bacillus strain isolated from waste water and its biochemical characterization. Proc Natl Acad Sci India Sect B Biol Sci 87(2):459–466

40. Sarkar MS, Segu H, Bhaskar JV, Jakher R, Mohapatra S, Shalini K, Shivaji S, Reddy PA (2018) Ecological preferences of large carnivores in remote, high-altitude protected areas: insights from Buxa tiger reserve, India. ORYX 52(1):66–77

41. Mohapatra S, Sarkar B, Samantaray DP, Daware A, Maity S, Pattnaik S, Bhattacharjee S (2017) Bioconversion of fish solid waste into PHB using bacillus subtilis based submerged fermentation process. Environ Technol, United Kingdom 38(24):3201–3208

42. Mohanty DP, Mohapatra S, Misra S, Sahu PS (2016) Milk derived bioactive peptides and their impact on human health – A review. Saudi J Biol Sci 23(5):577–583

43. Sharma SK, Sharma RC (2018) An investigation of a locomotive structural crashworthiness using finite element simulation. SAE Int J Commercial Veh 11(4):235–244. https://doi.org/10.4271/02-11-04-0019
44. Sharma RC, Sharma SK (2018) Sensitivity analysis of three-wheel vehicle's suspension parameters influencing ride behavior. Noise Vib Worldw 49(7–8):272–280. https://doi.org/10.1177/0957456518796846
45. Sharma SK (2018) Multibody analysis of longitudinal train dynamics on the passenger ride performance due to brake application. Proc Inst Mech Eng Part K: J Multi-Body Dyn 146441931878877. https://doi.org/10.1177/1464419318788775
46. Sharma SK, Kumar A (2018) Impact of longitudinal train dynamics on train operations: A simulation-based study. J Vib Eng Technol 6(3):197–203. https://doi.org/10.1007/s42417-018-0033-4
47. Sharma SK, Saini U, Kumar A (2019) Semi-active control to reduce lateral vibration of passenger rail vehicle by using disturbance rejection and continuous state damper controller. J Vib Eng Technol 7(2). https://doi.org/10.1007/s42417-019-00088-2
48. Sharma RC, Goyal KK (2017) Improved suspension design of Indian railway general sleeper ICF coach for optimum ride comfort. J Vib Eng Technol 5(6):547–556

Mechanical and Tribological Behaviour of Al-ZrO$_2$ Composites: A Review

Aasiya Parveen, Nathi Ram Chauhan and Mohd Suhaib

Abstract Aluminium metal matrix composites (AMCs) reinforced with hard ceramics are highly demanded composites which have the potential of fulfilling the current demands of advanced industrial applications due to its light weight and high strength properties. This paper attempts to review the various properties (microstructural, physical, mechanical and tribological) of the Al-ZrO$_2$ reinforced composites. The microstructural results obtained by the many researchers showed the uniform distribution of the reinforcement particles within the matrix and good bonding between them. The physical and mechanical behaviour of the composites enhances with the increment in the weight content of the ZrO$_2$ particles. It has been observed from the literature that the tribological properties also improved with the addition of the ZrO$_2$ particles within the Al matrix.

Keywords Aluminum metal matrix composites (AMCs) · Microstructural · Mechanical · Tribological

1 Introduction

Due to the advancement in the field of engineering, there is a huge requirement of metal matrix composites (MMCs) for the manufacturing of various structures that needs high strength to weight ratio [1, 2]. MMCs reinforced with the ceramic particles have the excellent properties by combining the properties of both matrix metal (low density and high ductility) and ceramics (high strength and high modulus) to achieve these applications [3, 4]. Al, Mg, Ti and its alloys are the commonly used matrices which are used as the base metals for the development of the MMC [5]. Other metallic alloys of Zn, Cu can also be used as the base metal

A. Parveen (✉) · N. R. Chauhan
Indira Gandhi Delhi Technical University for Women, Kashmere Gate, New Delhi, India
e-mail: aasiyaparveen346@gmail.com

M. Suhaib
Jamia Millia Islamia, New Delhi, India

matrices [6, 7]. Moreover, these AMCs have superior properties compared to other composites and thus are the most widely used MMCs in the various field such as automobiles, aircraft, etc. [8]. The properties like density, strength, stiffness and coefficient of thermal expansion are all appropriate for the use in the manufacturing of different structures [9]. AMC has improved tribological properties as compared to the conventional alloys [10]. Further, the type, compositions of the reinforcement and methods of fabrication are some of the major factors that do affects the properties of the MMCs [11–13]. Fibres and particulates type of the reinforcement are widely used in the development of the reinforcement [14]. MMC can be fabricated either by the solid-state method or liquid-state method [15]. Mostly, MMCs are fabricated by the powder metallurgy and stir casting method [16]. MMCs fabricated by the powder metallurgy method reported the more uniform distribution of the reinforcement with the matrix [17, 18]. During the stir casting process, it is difficult to achieve the uniform distribution of the reinforcement with the matrix and wettability in the liquid melt without the coatings of the reinforcement [19, 20]. The most commonly used ceramic reinforcements within the Al matrix are SiC, Al_2O_3, B_4C, ZrO_2, etc. [21, 22]. Zirconium dioxide (also called Zirconia) is a white crystalline ceramic material which has good mechanical properties. It has high strength and toughness which enhances the mechanical properties of the composites. Due to biocompatibility and strength properties, zirconia ceramics are used in the dentistry field to develop crowns and bridges. Apart from this, Zirconia also has industrial applications such as engine components, high-speed cutting tools, high resistant linings in furnaces [23, 24]. From the literature [25], it is reported that the Alumina reinforced with yttria-stabilized zirconia (YSZ) composites have popular applications in the dental field and as an electrolyte in the solid fuel oxide cells (SOFC) [26, 27]. Zirconia in the alumina matrix reduces the brittleness and improve the wear characteristics of the matrix [28].

This paper is aimed to review the effect of the reinforcement fraction, fabrication process on the various properties (microstructural, physical, mechanical and tribological) of the Al-ZrO_2 reinforced composites, as experienced by the previous researchers.

2 Literature Review

2.1 Microstructural Properties

Ramachandra et al. [29, 30] synthesized the nano- ZrO_2 powder by the combustion synthesis method and then fabricated the Al-ZrO_2 composites with the different wt % of the ZrO_2 (1, 2, 3 and 4%) through the powder metallurgy method. From the SEM images of the sintered compacts of the composites, as shown in Fig. 1, the presence of the clusters of the n-ZrO_2 within the matrix can be noticed. After sintering, the matrix and reinforcement particles bonded strongly which results to
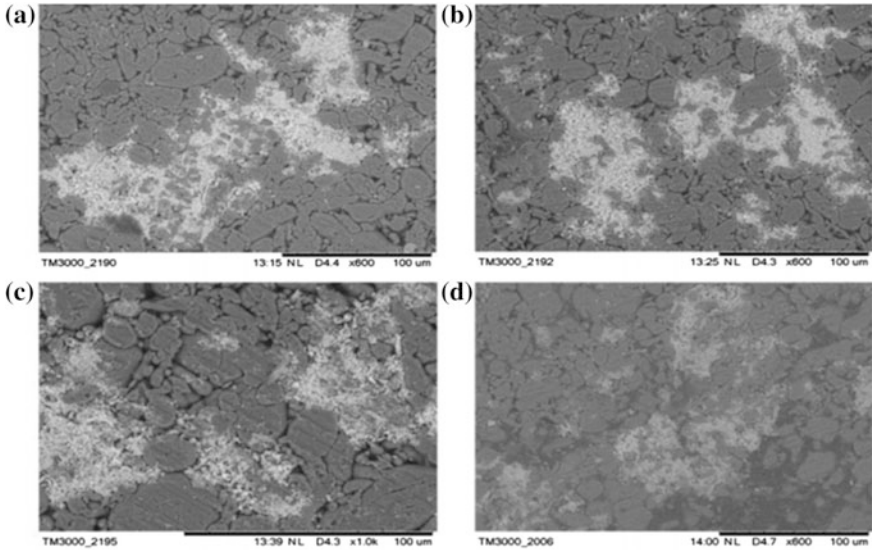
Fig. 1 SEM images of **a** 1% **b** 2% **c** 3% **d** 4% n-ZrO$_2$ reinforced with Al [29, 30]

Fig. 2 XRD pattern of Al-SiC/ZrO$_2$ [32]
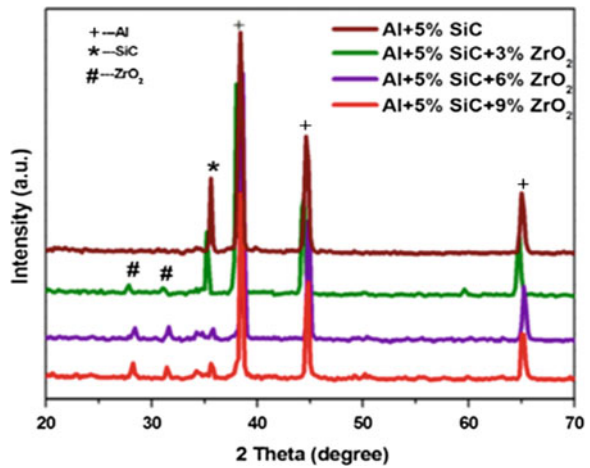
minimize the porosity. Radhika et al. [31] prepared the Aluminium LM25- 10 wt% ZrO$_2$ composites by the stir casting method and upon examination of the micro-structure Radhika et al., witnessed the homogeneous distribution of the reinforced particles with the matrix. Further, the improved interfacial bonding between the LM25 Al and ZrO$_2$ has been also established by the SEM images.

Arif et al. [32] fabricated the Al-5% SiC + (0, 3, 6 and 9%) ZrO$_2$ composites by the powder metallurgy method and studied its microstructural behaviour. Figure 2
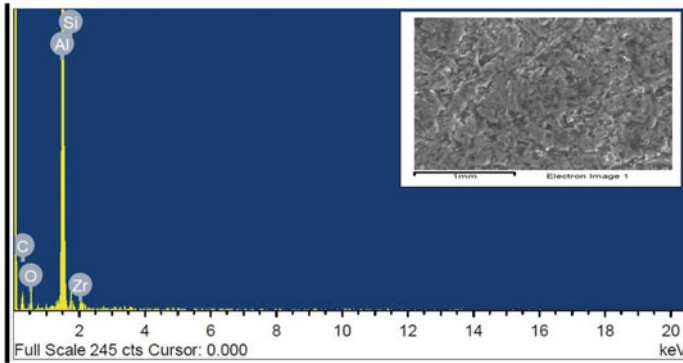
Fig. 3 EDS pattern of Al-SiC/ZrO$_2$ [32]

showed the XRD (X-ray diffractometer) pattern of the composites. According to the XRD pattern, the largest peak was observed of Aluminium. The presence of SiC and ZrO$_2$ with the matrix was also confirmed by the EDS (energy dispersive spectrum) analysis as shown in Fig. 3

Patoliya et al. [33] fabricated the Al6061-based composites with different wt% of ZrO$_2$ (0, 2.5, 5 and 7.5%) by the stir casting method and observed the uniform distribution and strong bonding between the reinforcement and matrix in the optical micrographs. Bhaumik et al. [34] prepared the Al6063-based composite by reinforcing the 5 wt% of ZrO$_2$ and 5 wt% of Al$_2$O$_3$ using the stir casting method. It is confirmed from the XRD image that Al, Al$_2$O$_3$ and ZrO$_2$ have the major peaks. The minor peaks were observed for Ti$_9$Al$_{23}$, Al$_3$Zr$_4$ and Al$_3$Zr. Madhushudhan et al. [35] reinforced the Al7068 alloy with the different weight percentages of ZrO$_2$ (0, 2, 4, 6 and 8) and produced the Al-based composites via the stir casting method. The optical micrographs revealed the uniform distribution of the reinforcement within the matrix and good interfacial bonding between them. The SEM images also observed the homogeneous distribution and good bonding between them. The presence of clustering is also observed which results to poor wettability of the reinforcement particles. Azevedo et al. [36] studied the effect of the different compaction pressure and sintering temperature on the microstructural properties of the Al-ZrO$_2$ composites prepared by the hot pressing method. The SEM images confirmed that the intermetallics (Al$_3$Zr) are formed at the high temperature (1273 K) and compaction pressure (300 MPa) with the high wt% (20%) of the ZrO$_2$ in the composite samples. Malhotra et al. [37] fabricated the Al6061-10 wt% fly ash composites with varying wt% of the ZrO$_2$ (5, 10 wt%) by the stir casting method and observed the uniform distribution of the reinforcement particles within the matrix. Ahmed et al. [38] produced the Al-ZrO$_2$ composites with different wt% (10, 15 and 20) by the stir casting method. The SEM images revealed the uniform

distribution of the reinforcement particles within the matrix. Pandiyarajan et al. [39] studied the microstructural properties of the Al6061- ZrO$_2$ (2, 4, 6, 8 and 10 wt%) composites produced by the stir casting method. From the microstructural studies, it was concluded that the reinforcement particles were uniformly distributed within the matrix and reduction in the clustering of the particles. Prasad et al. [40] fabricated the Al LM24 alloy composite by reinforcing the ZrO$_2$ with different volume % (1, 2 and 3%) through the vortex method and studied the microstructural properties of the developed composites. The SEM images confirmed that the reinforcement particles are distributed uniformly within the matrix alloy and the XRD graph confirmed the presence of the reinforcement within the matrix. Baghchesara et al. [41] investigated the effect of the three different casting temperatures on the Al356-ZrO$_2$ composites with different wt% (5, 10 and 15) and revealed the uniform distribution of the reinforcement particles within the matrix at the lowest value of casting temperature. The porosity level increases at the high temperature which affects the mechanical properties of the composites. Kumar et al. [42] studied the microstructural behaviour of the Al356.1/nano-ZrO$_2$ composites fabricated by the stir casting method with different wt% (2, 2.5, 3 and 3.5) of the nano-ZrO$_2$ particles. The XRD results confirmed the presence of the ZrO$_2$ particles within the matrix. The SEM revealed the uniform distribution of the ZrO$_2$ particles within the matrix and formation of clusters at the high wt% of the reinforcement.

2.2 Physical Properties

According to the study done by Arif et al. [32], it was revealed that the density, as well as the porosity of the Al-SiC/ZrO$_2$ composites, increased with the wt% of the reinforcements which may be due to the accumulation of the reinforcements having the high densities. Bhaumik et al. [34] calculated the actual and theoretical densities of the Al/(Al$_2$O$_3$ + ZrO$_2$) composites by the Archimedes principle and Rule of mixture method. The actual and theoretical density of the composites observed as 2.71 g/cm^3 and 2.89 g/cm^3 respectively. Azevedo et al. [36] evaluated that the sintering temperature has a significant effect on the density of the Al-ZrO$_2$ composites and observed that the density starts to decreases slightly with the rise in the temperature from 1073 K to 1273 K which may be due to the formation of the intermetallics results to deform the Al matrix and cause porosity.

Abdizadeh et al. [43] produced the A356-ZrO$_2$ (5, 10 and 15 wt%) composites by the stir casting method at three different casting temperatures (750, 850 and 950 °C) and studied the effect of the casting temperatures on the density of the composites for varying wt% of the reinforcement (Fig. 4). At 750 °C, the density increases with the wt% of the reinforcement. The density increases up to 10 wt% of the reinforcement at 850 °C and 5 wt% of the reinforcement at 950 °C after that it starts to decrease which may be due to the clustering and wettability of the reinforcement particles at high temperature.

Fig. 4 Variation of the
density of Al-ZrO$_2$
composites for different
casting temperatures [43]
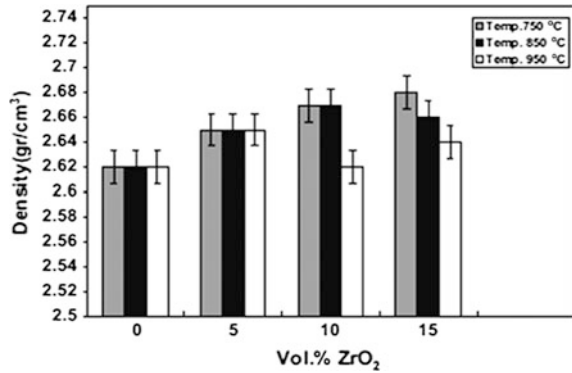
2.3 Mechanical Properties

Hardness. Ramachandra et al. [29] calculated the Brinell hardness of the Al/
n-ZrO$_2$ composites and observed that due to the enhanced weight percent of
n-ZrO$_2$, the hardness of the composites improved. Arif et al. [32] evaluated the
Rockwell hardness of the Al-SiC/ZrO$_2$ and revealed that the hardness of the Al
alloy was increased with the addition of 5 wt% of SiC which may be due to the high
hardness of the SiC. On further addition of the ZrO$_2$ reinforcement in the Al-SiC
alloy, the hardness will further increase with the wt% of the reinforcements. The
uniform distribution of the reinforcements within the matrix and the higher hardness
of the reinforcements results in the enhancement of the hardness of the composites.
Due to the addition of the hard reinforcement into the matrix, the hardness of the
composites also enhances [33]. The Rockwell hardness number of the Al6061 alloy
increases from 20 to 26 with 7.5% wt content of ZrO$_2$. Bhawmik et al. [34]
evaluated the Vickers hardness of the Al/5 wt% Al$_2$O$_3$/5 wt% ZrO$_2$ composites and
found the value of 91.1 HV.

Madhusudhan et al. [35] evaluated the Vickers hardness of the Al-ZrO$_2$ com-
posites and observed the direct variation in the hardness of the composites with the
different wt% of the reinforcements. The hardness of the Al7078 alloy increased
from 93.5 to 147.2 VHN with the 8 wt% of the ZrO$_2$ as shown in Fig. 5.

Fig. 5 Variation of the
Vickers hardness with the wt
% of the reinforcement [35]
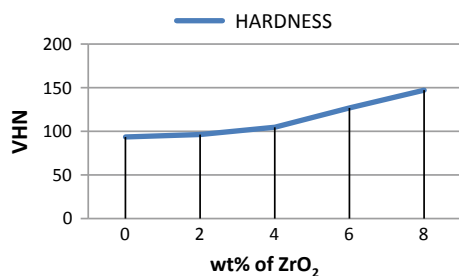
Azevedo et al. [36] observed that hardness of the Al-20 wt% ZrO$_2$ samples prepared through cold pressing decreases as the cold pressures increases from 150 MPa to 300 MPa whereas its increases in case of the samples prepared through hot pressing. Malhotra et al. [37] fabricated the Al6061-10 wt% fly ash composites with different wt% of the ZrO$_2$ (5, 10 wt%) by the stir casting method and calculated the Vickers hardness of the composites. The hardness of the Al6061, Al6061-(10% fly ash + 5% ZrO$_2$) and Al6061-(10% fly ash + 10% ZrO$_2$) was observed 78, 83 and 94 VHN. It was concluded that the hardness of the composites increased with the wt% of the reinforcement. According to Ahmed et al. [38], the hardness of the Al-ZrO$_2$ composites increases up to 15 wt% of the ZrO$_2$. The hardness of the composites starts to decrease on further increasing the wt% (20) of the ZrO$_2$. Pandiyarajan et al. [39] reported that the Rockwell hardness of the Al6061-ZrO$_2$ increases with the wt% of the reinforcement. This may be due to the addition of the hard ceramic reinforcement which has high resistance behaviour against the indentation. Prasad et al. [40] reported that the Brinell hardness of the Al LM24- ZrO$_2$ composites decreases with the addition of 2 vol.% of the reinforcement after that it starts increases with further increment in the vol.% of the reinforcement. Prasad et al. [40] reported that the Brinell hardness of the Al LM24-ZrO$_2$ composites decreases with the addition of 2 vol.% of the reinforcement after that it starts increases with further increment in the vol.% of the reinforcement. Abdizadeh et al. [43] studied the effect of the casting temperatures on the hardness of the A356-ZrO$_2$ composites for varying wt% of the reinforcement. At 750 °C, the hardness of the composites increases with the wt% of the reinforcement. The hardness of the A356 alloy increases with 5 wt% addition of the reinforcement and remained constant up to 10 wt% of the reinforcement at 850 °C. At high casting temperature 950 °C, the hardness increases only for 5 wt% of the reinforcement after that, it starts to decrease which may be due to the formation of defects at high temperature. Sreeniwas Rao et al. [44] investigated the Brinell hardness of the Al7075/n- ZrO$_2$ composites fabricated by the stir casting method with the different wt% of the ZrO$_2$ (0, 5 and 10%). The author investigated the average value of the three samples of each composition and found that the Al7075/n- ZrO$_2$ composites with 10 wt% of ZrO$_2$ have the maximum hardness. The hardness of the composites increases linearly with the wt% of the ZrO$_2$.

Tensile Strength (UTS). Patoliya et al. [33] prepared the ASTM E8 specimens for tensile testing for the Al6061 based composites with varying weight content of the ZrO$_2$. The tensile strength of the Al6061 alloy increased from 141 MPa to 156.5 MPa with the addition of the 7.5% wt content of the ZrO$_2$. The elongation rate decreased from 5% to 3.7% with the wt% of the reinforcement. According to Bhawmik et al. [34], the tensile strength of the Al/5 wt% Al$_2$O$_3$/5 wt% ZrO$_2$ composites was observed as 78.51 MPa which may be due to the brittle nature of the ceramic reinforcements. Madhusudhan et al. [35] evaluated the tensile strength

Fig. 6 Variation of tensile strength **a** and elongation rate **b** with the wt% of the reinforcement [35]
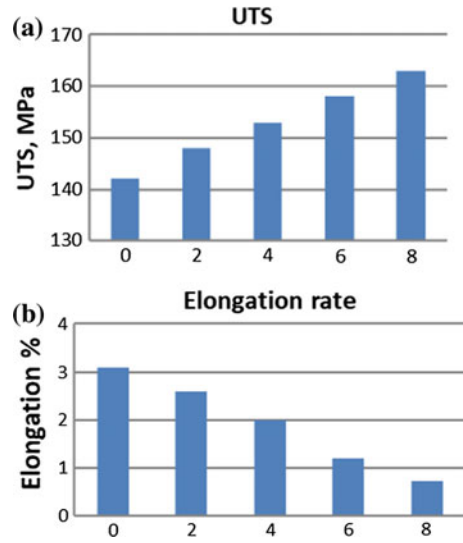
of the Al-ZrO_2 composites and observed the direct variation in the strength of the composites with the varying wt% of the reinforcements. The UTS of the Al7078 alloy increased from 142 to 163 MPa with the 8 wt% of the ZrO_2. The elongation rate decreases with the wt% of the reinforcement. It is observed to decrease from 3.1% to 0.73% for Al-8% ZrO_2 as shown in Fig. 6.

Malhotra et al. [37] evaluated the tensile strength of the Al6061, Al6061-(10% fly ash + 5% ZrO_2) and Al6061-(10% fly ash + 10% ZrO_2) as 233 MPa, 252 MPa and 275 MPa. It was concluded that the tensile strength of the composites increased with the wt% of the reinforcement. According to Ahmed et al. [38], the tensile strength of the Al-ZrO_2 composites increases up to 15 wt% of the ZrO_2. The strength of the composites starts to decrease on further increasing the wt% (20) of the ZrO_2. It was concluded from the study done by Pandiyarajan et al. [39], the tensile strength of the Al60621-ZrO_2 composites increases up to the addition of 6 wt% of the reinforcement and then starts to decrease on further increasing the wt% of the reinforcement. Prasad et al. [40] reported that the tensile strength of the Al LM24- ZrO_2 composites increases up to 60% of the tensile strength of the pure LM24 alloy. Abdzadeh et al. [43] observed that the tensile strength of the composites increases with the wt% of the reinforcement at 750 °C. Due to the occurrence of the porosity at high temperatures (850 and 950 °C), the tensile strength of the composites increases only up to 10 wt% of the reinforcement. Sreeniwas Rao et al. [44] in his study, observed that the Al7075/n- ZrO_2 composites with 5 wt% of ZrO_2 have the maximum value of the UTS of 135 MPa. The tensile strength of the composites increases with up to 5 wt% of the reinforcement after that it reduced.

2.4 Tribological Properties

Ramachandra et al. [29] evaluated the dry sliding wear of the Al-n ZrO$_2$ composites using the pin-on-disc apparatus and observed that the wear rate decreases with increasing the wt% of the reinforcement. The SEM micrographs confirmed the wear mechanisms, i.e. oxidation, micro-cutting and thermal softening during the dry sliding wear of the composites. Radhika et al. [31] evaluated the adhesive wear property of the Aluminium LM25 based composites under the varying load, sliding distance and sliding velocity conditions. On increasing the applied load from 15 N to 35 N, the wear rate also increases whereas it will decrease on increasing the sliding distance from 500 m to 2000 m and sliding velocity from 1.5 m/s to 3.5 m/s. It is confirmed by the ANOVA that the load (73.83%) has a significant effect on the wear characteristics. The SEM also confirmed that the higher wear rate occurs at the high load conditions. Arif et al. [32] investigated the wear loss of the Al-5% SiC for varying wt% of the ZrO$_2$ (3, 6 and 9%) using the pin-on-disc apparatus under the different conditions, i.e. applied load, sliding distance and sliding velocity. The wear loss of the aluminium hybrid composites increases with respect to the applied load, sliding distance as well as the sliding velocity. The aluminium hybrid composite with higher wt% of the ZrO$_2$ (9%) has the lower value of wear loss which showed the better wear characteristics. The same result was also confirmed by the SEM images of the worn surfaces which may be due to the uniform distribution of the reinforcement with the matrix which restricts the presence of grooves. Pandayirajan et al. [39] observed the variation of wear rate with the wt% of the reinforcements using the pin-on-disc apparatus. The wear rate (kg/m) of the composites decreases with the wt% of the reinforcement which may be due to the accumulation of the ceramic reinforcement. The SEM images of the worn surfaces confirmed the presence of the possible wear mechanism in the composites.

Kumar et al. [42] performed the pin-on-disc test on the Al356.1/nano-ZrO$_2$ composites with different wt% (2, 2.5, 3, and 3.5) of the nano-ZrO$_2$ particles under different load, speed and time conditions. The wear rate of the composites increases with respect to the load, speed as well as time. The Al356.1/3.5 wt% of the n-ZrO$_2$ showed the superior wear resisting properties under all different conditions. Zhu H et al. [45] investigated the tribological properties of the Al-C/ZrO$_2$ composites prepared by powder metallurgy method and studied the effect of the different molar ratios of C/ZrO$_2$ (0, 0.5 and 1) on the tribological properties under different temperature (373 K and 473 K) conditions as shown in Fig. 7. The wear loss of the composites increases with sliding velocity up to 0.6 m/s and then starts reduces under 373 K temperature whereas, at 473 K temperature, it reduces linearly with the sliding velocity. The wear properties enhanced with the molar ratios of the C/ZrO$_2$. The SEM images of the worn surfaces confirmed the adhesive, abrasive and oxidation wear. Omidvar et al. [46] studied the effect of the particle size of the ZrO$_2$ (4 μm and 40 nm) on the wear behaviour of the Al 1050-1 wt% ZrO$_2$ composites prepared by the accumulative roll bonding (ARB) process. The coefficient of friction of Al 1050 alloy reduced from 0.69 to 0.57 for the Al1050-1 wt% ZrO$_2$ composites

Fig. 7 Variation of the mass loss of Al-C/ZrO$_2$ composites with sliding velocity at the test temperature **a** 373 K and **b** 473 K [45]
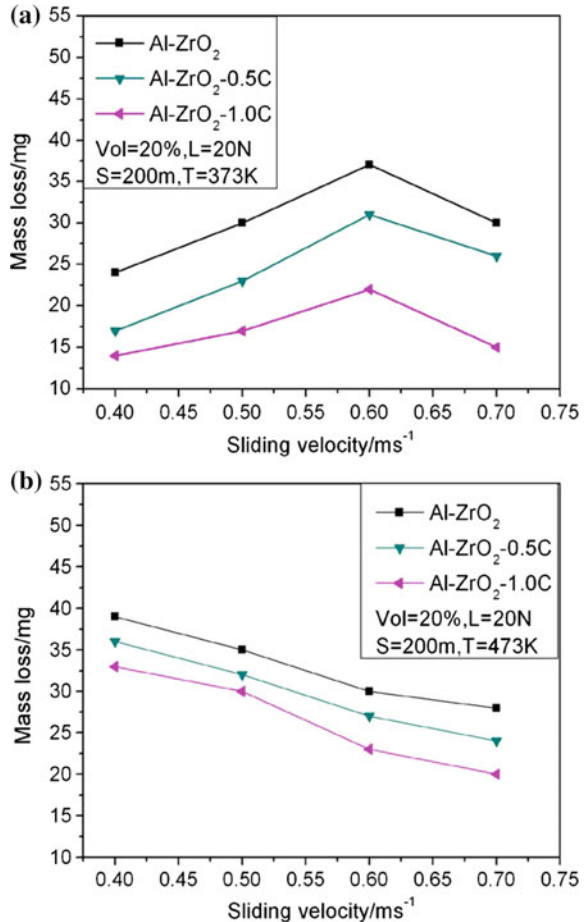
with a particle size of 4 μm. For the particles size of 40 nm, it again reduces to a value of 0.42 which may be due to the enhancement in the bonding of reinforcement and matrix with the particle size reduction which results to improve the wear resisting properties. The SEM images of worn surfaces confirmed the adhesive wear in both cases of particle sizes.

3 Conclusions

The review of the various properties of Al-ZrO$_2$ composites gives a few conclusions with respect to the influence of different parameters on the execution of the composites.

- First, the microstructural studies of the Al-ZrO$_2$ composites fabricated by the powder metallurgy method reported the more uniform distribution of the reinforcement with the matrix. During the stir casting process, it is difficult to achieve the uniform distribution of the reinforcement with the matrix and wettability in the liquid melt without the coatings of the reinforcement.
- The density of the composites increases with the weight fraction of the ZrO$_2$ which may be due to the high density of the reinforcement.
- The addition of the hard ceramic and uniform distribution of the reinforcement with the matrix also results to improve the mechanical and tribological properties. The hardness and tensile strength of the composites also increase with the weight fraction of the reinforcement.
- It has also been observed from the literature that the accumulation of the ZrO$_2$ particles into the matrix enhances the wear resistive properties and reduces the coefficient of friction.
- There is a need to explore the research regarding the fatigue and fracture behaviour of the Al/ZrO$_2$ as it is the important parameter for the application of marine and automobile fields.

References

1. Tjong SC (2013) Processing and deformation characteristics of metals reinforced with ceramic nanoparticles. Elsevier Ltd
2. Ibrahim IA, Mohamed FA, Lavernia EJ (1991) Particulate reinforced metal matrix composites - a review. J Mater Sci 26:1137–1156
3. Sinclair I, Gregson PJ (1997) Structural performance of discontinuous metal matrix composites. Mater Sci Technol 13:709–726. https://doi.org/10.1179/mst.1997.13.9.709
4. Hanumanth GS, Irons GA (1993) Particle incorporation by melt stirring for the production of metal-matrix composites. J Mater Sci 28:2459–2465. https://doi.org/10.1007/BF01151680
5. Bodunrin MO, Alaneme KK, Chown LH (2015) Aluminium matrix hybrid composites: a review of reinforcement philosophies; mechanical, corrosion and tribological characteristics. J Mater Res Technol 4:434–445. https://doi.org/10.1016/j.jmrt.2015.05.003
6. Casati R, Vedani M (2014) Metal matrix composites reinforced by nano-particles—A review. Metals (Basel) 4:65–83. https://doi.org/10.3390/met4010065
7. Kanayo Alaneme K, Apata Olubambi P (2013) Corrosion and wear behaviour of rice husk ash—Alumina reinforced Al–Mg–Si alloy matrix hybrid composites. J Mater Res Technol 2:188–194. https://doi.org/10.1016/j.jmrt.2013.02.005
8. Jiménez S, Rodríguez R, Lima R, Fuentes R, Rubio E, Herrera A, Castaño V (2000) Tribological improvement of aluminium infiltrated with zirconia nanoparticles. Mater Res Innov 2000:42–44
9. Surappa MK (2003) Aluminium matrix composites: challenges and opportunities. Sadhana 28:319–334. https://doi.org/10.1007/BF02717141
10. Rostami RB, Tajally M (2017) Wear properties of Al$_2$O$_3$/SiC. Emerg Mater Res doi:https://doi.org/10.1680/jemmr.16.00016
11. Ramnath BV, Elanchezhian C, Atreya TSA, Vignesh V (2014) Aluminum metal matrix composites - a review. Rev Adv Mater Sci 38:55–60. https://doi.org/10.1016/j.jmrt.2015.05.003

12. Sahu PS, Banchhor R (2017) Effect of different reinforcement on mechanical properties of aluminium metal matrix composites. Res J Eng Sci 6:39–45
13. Mortensen A, Llorca J (2010) Metal Matrix Composites. Annu Rev Mater Res 40:243–270. https://doi.org/10.1146/annurev-matsci-070909-104511
14. Jain P, Soni S, Baredar P (2014) Review on machining of aluminium metal matrix composites. Mater Sci Res India 11:114–120. https://doi.org/10.13005/msri/110204
15. Saravanani C, Subramanian K, Sivakumari DB, Sathyanandhani M, Narayanani RS (2015) Fabrication of aluminium metal composite - A review. J Chem Pharm Sci, 82–87
16. Kaczmar JW, Pietrzak K, Wlosinski W (2000) The production and application of metal matrix composite materials. J Mater Process Technol 106:58–67. doi:https://doi.org/10.1016/s0924-0136(00)00639-7
17. Idris J, Kabir MA (2001) Powder metallurgy development for the production of metal matrix composite. Process Fabr Adv Mater VIII:921–931. doi:https://doi.org/10.1142/9789812811431_0108
18. Patil OM, Khedkar NN, Sachit TS, Singh TP (2018) A review on effect of powder metallurgy process on mechanical and tribological properties of hybrid nano composites. Mater Today Proc 5:5802–5808. https://doi.org/10.1016/j.matpr.2017.12.177
19. Annigeri UK, Veeresh Kumar GB (2017) Method of stir casting of aluminum metal matrix composites: a review. Mater Today Proc 4:1140–1146. https://doi.org/10.1016/j.matpr.2017.01.130
20. Rajan TPD, Pillai RM, Pai BC (1998) Reinforcement coatings and interfaces in aluminium metal matrix composites. J Mater Sci 33:3491–3503. https://doi.org/10.1023/A:1004674822751
21. Yashpal S, Jawalkar CS, Verma AS, Suri NM (2017) Fabrication of aluminium metal matrix composites with particulate reinforcement: a review. Mater Today Proc 4:2927–2936. doi:https://doi.org/10.1016/j.matpr.2017.02.174
22. Vijaya Bhaskar K, Sundarrajan S, Subba Rao B, Ravindra K (2018) Effect of reinforcement and wear parameters on dry sliding wear of aluminum composites-A review. Mater Today Proc 5:5891–5900. https://doi.org/10.1016/j.matpr.2017.12.188
23. Anand A, Ul Haq MI, Raina A, Vohra K, Asgar A, Jha N, Ojha S, Kumar K, Singh Y (2016) Tribological and mechanical aspects of zirconia-reinforced aluminum metal matrix composites. Mater Focus 5:489–495. https://doi.org/10.1166/mat.2016.1346
24. Saheb N, Chia CY (2007) PM processing and characterisation of new ZrO_2–fly ash composites. Powder Metall 50:60–65. https://doi.org/10.1179/174329007X164916
25. Moraes M, Elias C (2004) Mechanical properties of alumina-zirconia composites for ceramic abutments. Mater Res 7:643–649. doi:https://doi.org/10.1590/s1516-14392004000400021
26. Wildan M, Edrees HJ, Hendry A (2002) Ceramic matrix composites of zirconia reinforced with metal particles. Mater Chem Phys 75:276–283. https://doi.org/10.1016/S0254-0584(02)00076-7
27. Choi SR (2005) 18 Alumina-reinforced zirconia composites. Handb Ceram Compos, 437–457. doi:https://doi.org/10.1007/0-387-23986-3_18
28. Mazzei AC, Rodrigues JA (2000) Alumina-mullite-zirconia composites obtained by reaction sintering. J Mater Sci 35:2807–2814
29. Ramachandra M, Abhishek A, Siddeshwar P, Bharathi V (2015) Hardness and wear resistance of ZrO_2 nano particle reinforced Al nanocomposites produced by powder metallurgy. Procedia Mater Sci 10:212–219. https://doi.org/10.1016/j.mspro.2015.06.043
30. Ramachandra M, Dilip Maruthi T, Rashmi R (2016) Evaluation of corrosion property of aluminium-zirconium dioxide ($AlZrO_2$) nanocomposites 2016:1321–1326
31. Radhika N, Venkata Priyanka ML (2017) Investigation of adhesive wear behaviour of zirconia reinforced aluminium metal matrix composite 12:1–12
32. Arif S, Alam T, Ansari AH, Siddiqui MA, Mohsin M (2017) Study of mechanical and tribological behaviour of $Al/SiC/ZrO_2$ hybrid composites fabricated through powder metallurgy technique. Mater Res Express

33. Patoliya DM, Sharma S (2015) Preparation and characterization of zirconium dioxide reinforced aluminium metal matrix composites, 3315–3321. doi:https://doi.org/10.15680/ijirset.2015.0405051
34. Maity K, Bhaumik M (1998) Fabrication and characterization of the Al6063/5 ZrO$_2$/5 Al$_2$O$_3$ composite. Braz Dent J 9:3–10. doi:https://doi.org/10.1088/1742-6596/755/1/011001
35. Madhusudhan M, Naveen GJ, Mahesha K (2017) Mechanical characterization of AA7068-ZrO$_2$ reinforced metal matrix composites. Mater Today Proc 4:3122–3130. https://doi.org/10.1016/j.matpr.2017.02.196
36. Azevedo G, Brand D (2000) Synthesis and characterization of aluminum – zirconium intermetallic composites 8:101–107
37. Malhotra S, Narayan R, Gupta R (2013) Synthesis and characterization of aluminium 6061 alloy-flyash & zirconia metal matrix composite. Int J Curr Eng Technol 3:1716–1719
38. Rao NSP, Murthy PLS, Suraj S (2015) Mechanical properties of aluminium alloy Al3562 matrix reinforced with zirconium particles, 1049–1052 (2015)
39. Pandiyarajan R, Maran P, Marimuthu S, Ganesh KC (2017) Synthesis and characterization of zirconium dioxide particulate reinforced aluminium alloy metal matrix composite 24:390–396
40. Prasad CV, Rao KM (2016) A study on effect of mechanical properties of Al-ZrO$_2$ composite by liquid routing element 4:189–192
41. Baghchesara MA, Abdizadeh H, Baharvandi HR (2010) Fractography of stir casted Al-ZrO$_2$ composites. Iran J Sci Technol Trans B Eng 33:453–462
42. Kumar R, RamachandraNaik AL, Ahamed S, Chaubey NK, Girish KB (2016) Microstructure and wear properties of zirconium nano metal matrix composites, 1–9
43. Abdizadeh H, Baghchesara MA (2013) Investigation on mechanical properties and fracture behavior of A356 aluminum alloy based ZrO$_2$ particle reinforced metal-matrix composites. Ceram Int 39:2045–2050. https://doi.org/10.1016/j.ceramint.2012.08.057
44. Chinna P, Rao S, Prasad T, Harish M (2017) Evaluation of mechanical properties of Al 7075 – ZrO$_2$ metal matrix composite by using stir casting technique. Int J Sci Res Eng Technol 6:377–381
45. Zhu H, Sun X, Huang J, Li J, Xie Z (2017) Dry sliding tribological behavior at elevated temperature of in situ aluminum matrix composites fabricated by Al-ZrO$_2$ -C system with different mole ratio of C/ ZrO$_2$. Powder Metall Min 6:1–5. doi:https://doi.org/10.4172/2168-9806.1000153
46. Omidvar H, Pabandi HK (2016) Effect of particle size ZrO$_2$ in the nano and micrometer scale on wear behavior of the arbed, 40–43

Design and Finite Element Simulation of a Trailing Arm Suspension System

Praveen Kumar, Suman Emmanuel and N. Rajesh Mathivanan

Abstract The suspension system of a vehicle is responsible for absorbing the vibrations during vehicle movement, thereby providing reliability and stability to the vehicle. The components of the suspension system enable damping the vibrations and avoid transmitting them to the frame. The major components of the suspension system along with their loading conditions are discussed in this paper. An attempt is made to analyze the structural behavior of the trailing arm of the suspension using FEM simulation by meshing and strength analysis using ANSYS analysis software. ANSYS static structural analysis module is used to verify the stress developed in the automobile suspension system. The distribution of the load on the trailing arm and the critical section are presented in this paper.

Keywords Suspension system · Trailing arm · FEM analysis

1 Introduction

Suspension system plays a vital role in an automobile by reducing the shock during the ride and keeps the car in control. The suspension system functions to isolate the chassis from rough terrain and provides vertical compliance; so that the wheel can follow the irregular terrain [1]. Georg [2] pointed out that one of the main functions of the suspension system is to maintain proper wheel alignment of the automobile. A good suspension system safeguards the other mounted systems from wear, damage and ultimately the vehicle itself, it contributes toward the vehicle's handling and braking, which provides the much-needed safety to the passengers [3]. Abhay et al. [4] emphasize that the suspension used in an automobile is a system which mediates between the vehicle and the road interface and its functions are associated with wide range of drivability such as handing ability, stability comfortability, etc. They also suggest that soaring performance on rough terrain is

P. Kumar (✉) · S. Emmanuel · N. R. Mathivanan
Department of Mechanical Engineering, PES University, Bangalore 560085, India
e-mail: praveenkumar13033@gmail.com

achievable using the multilink independent rear suspension configuration. The trailing arm is a component of a rear multilink-independent suspension system. It connects the knuckle and the frame, which influences the steering control and a stable rear wheel position. The suspension links and the wheels contribute toward the unsprung mass of the car and to experience a better ride quality, the unsprung mass of the car should be as low as possible [5]. Aluminum alloys are widely deployed in the transportation industry due to its relatively low density, on comparison with other metals [6]. The trailing arm is made of Aluminum 6082 and the knuckle is made of Aluminum 6063–T6 as the density of Aluminum is a third as that of steel and its low tensile properties on comparison to steel is compensated by its strength to weight ratio [7].

The trailing arm and the knuckle is welded using TIG welding process. Muyiwa and Paul pointed out that welding aluminum alloys can be problematic and welding defects like hot cracking, incomplete fusion, and porosity may arise [8]. Chandra and Vivekanand [9] indicated that the fracture in the specimen holder of a research reactor made using Aluminum alloy had occurred in a brittle mode without any gross plastic deformation at a location where the rod was welded. The reason for the weld failure was due to the low melting temperature eutectics, which are rich in Si and Fe and has led to weld cracking along the dendritic grains during solidification of the welds. Godefroid et al. [10] investigated the cause of failure of a control arm made of high strength and low alloy steel under the influence of fatigue loading. They discovered that the fatigue cracking of the component occurred during the application of standardized blocks of fatigue loading. In-depth analysis of the crack revealed the presence of stress concentration which initiated fatigue cracks on the weld bead. Variables like shielding gas flow rate, polarity of weld, welding speed, arc voltage, selection of filler rod, determine the quality of the weld [11, 12]. Vertical force F_Z is mainly responsible for the failure of rear suspension because when the vertical forces on left and right wheel are not equal during driving, a torque will be developed and exerted on the suspension component [13]. Emre et al. [14] conducted static and dynamic roll behavior and stability dynamics improvement based on increasing roll stiffness of the suspension system. They indicated that Virtual simulation can guide the designers to reach optimum suspension parameters for the vehicle.

Study on failures is common in automotive components like torsion beam, suspension arms, etc., have been done before [15]. Saayan Banerjee et al. [16] developed a mathematical model of full-tracked vehicle with trailing arm suspension system. The model is generic and computationally helpful in design of suspension system, while Hongbo [17] applied game theory for enhancing the vehicle suspension system. There is inadequate work done on design and characteristics of the trailing arm, so an attempt is made to the design and analyze the components of the trailing arm suspension system.

2 Structural Design

The primary objective of structural engineer is to design lighter components while ensuring reliability, durability and thereby reducing the cost of the components [18]. The suspension components of an All-Terrain Vehicle, designed with accordance to SAEINDIA mini-BAJA 2018 rulebook is investigated in this work. The suspension system consists of major components like the trailing arm, control arms, air shox, and wheel assembly components. The suspension components of a vehicle are designed to withstand three major forces; which gets generated at the tire contact patch and gets transmitted to the suspension components. The three major forces acting on the suspension components include a braking force, which acts in the negative X-axis, a cornering force, which acts in the negative Y-axis and a bump force acting in the positive Z-axis of the vehicle in accordance to the *ISO 8855* vehicle coordinate system. Braking force is obtained by determining the deceleration of the vehicle. A deceleration of 15.59 m/s^2 is obtained as per Newton's laws of motion under the assumption of the condition to bring a vehicle moving with a velocity of 45 km/hr to a standstill position within a distance of *5 meters*. A normal acceleration of 10.3986 m/s^2 is obtained under the assumption that the vehicle is traveling in a circular path of radius 15 m with a velocity of 45 km/hr to determine the cornering force. To determine the impact on the vehicle when it experiences a sudden fall or a drop, it is necessary to determine the bump force acting on the vehicle. The bump force is calculated in "*g*" units for sudden drops like the 5 feet drops, in mini-BAJA tracks. The maximum bump force experienced by the vehicle is determined to be 1156.3 N by using energy balance equation and Newton's laws of Motion. The rear suspension assembly is designed in such a way that it can move freely in the *Z-direction* when the air shox is not mounted to the system. Control arms and trailing arm constrains the motion of the suspension system along *X* and *Y directions* according to ISO coordinate system. Air shox suspensions are positioned in such a way that it takes the vertical load of the vehicle. The trailing arm maintains the stability of rear wheels. The length of the control arms and trailing arm are from the hard points of rear suspension geometry. The control arms are connected with chassis and knuckle with rod end bearing of size *M10*. Rod end bearing is chosen due to its ease of motion and its good strength. Rod end bearing of size *M12* is used to connect the one end trailing arm and chassis. Other end of the trailing arm is welded to the knuckle by aluminum TIG welding process as shown in Fig. 1. Welding is selected because it reduces complicated machining in the knuckle and trailing arm junction (Fig. 2).

The trailing arm experiences longitudinal forces caused due to acceleration and braking, vertical forces due to bump and road shocks. To meet the rough terrain conditions of the mini-BAJA event, the trailing arm is made of solid Aluminum 6082 rod due to its high tensile strength, good strength to weight ratio, good machinability and weldability. The knuckle is machined from a solid aluminum

Fig. 1 Trailing arm and knuckle assembly

Fig. 2 CAD model of the multilink independent rear suspension system. (1) Air Shox (2) Upper control arm (3) Lower control arm (4) Trailing arm (5) Wheel Hub (6) Knuckle

6063–T6 billet. Aluminum 6063–T6 is opted due to its good machinability and weldability properties. The control arms are made of AISI 4340 alloy steel of diameter 20 mm and wall thickness 3 mm.

3 FEM Simulation

Finite element analysis was adopted to simulate the structural analysis of suspension system to study the stresses on the trailing arm under worst-case scenario. The suspension system was modeled in SOLIDWORKS and exported to ANSYS workbench in step format. Step format is chosen over other CAD formats as it is

Table 1 Properties of materials used for simulation

	AISI 4340	Aluminum 6082	Aluminum 6063–T6
Density	7850 kg/m^3	2700 kg/m^3	2700 kg/m^3
Elastic modulus	20500 MPa	69000 MPa	69000 MPa
Poison's ratio	0.285	0.33	0.33
Tensile yield strength	470 MPa	260 MPa	215 MPa
Ultimate tensile strength	745 MPa	310 MPa	240 MPa

ISO 10303 standards and it keeps the all assembly hierarchy and maintains solid bodies. As the prime concern is to look at stress concentration in suspensions components the two piece rod ends were considered to be rigid as they have good strength and are easily replaceable. All the ground–body and body–body joints are specified in the workbench for rod ends and other components. The contact between the trailing arm and knuckle is defined as no separation in the weld region. Custom materials have been created in the ANSYS workbench to represent the AISI 4340 alloy steel and Aluminum 6082 by taking the properties from the SOLIDWORKS material database. The properties of the material used are listed in Table 1 (Figs. 3 and 4).

The suspension components are locally meshed in ANSYS mechanical workbench with a fine mesh of element size 1.5 mm. The total number of elements is 354255 and total number of nodes is 614287. The load values are obtained from the structural design calculations. Remote loads of 902.5 N, 600 N, 1156.3 N is applied on the inner wheel side bearing surface of the knuckle in *X, Y and Z directions,* respectively, from the tire contact point. The load is applied from a point to make the problem simpler. The knuckle is constrained to move in vertical direction from the upper damper end point and the model was subjected to analysis.
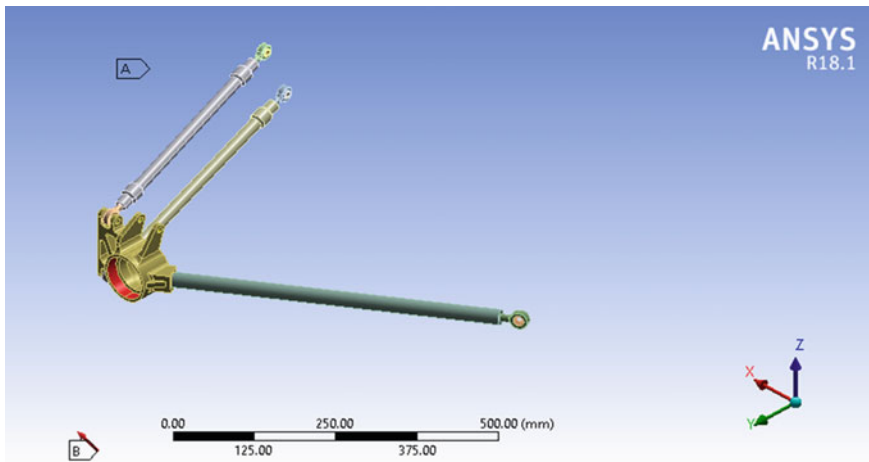
Fig. 3 Loads and constraints applied on the suspension component
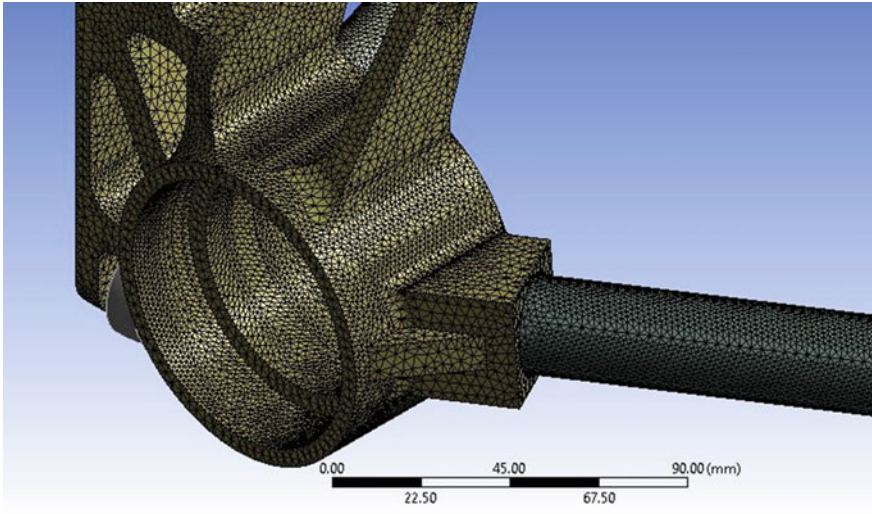
Fig. 4 Knuckle and trailing arm with fine mesh

4 FEM Results and Discussions

Figure 5 shows the stress distribution in the suspension components for the worst-case scenario the suspension components can experience, i.e., when the forces due to braking, bump and lateral are considered at the same time. From the above finite element analysis investigation it is clearly seen that the Von-Mises stresses induced in the suspension links are well within the yield region of the
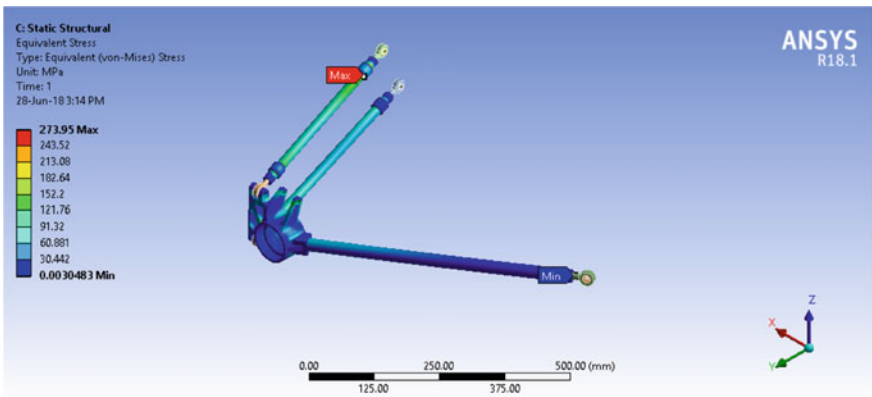
Fig. 5 Von-Misses stress distribution in the suspension components
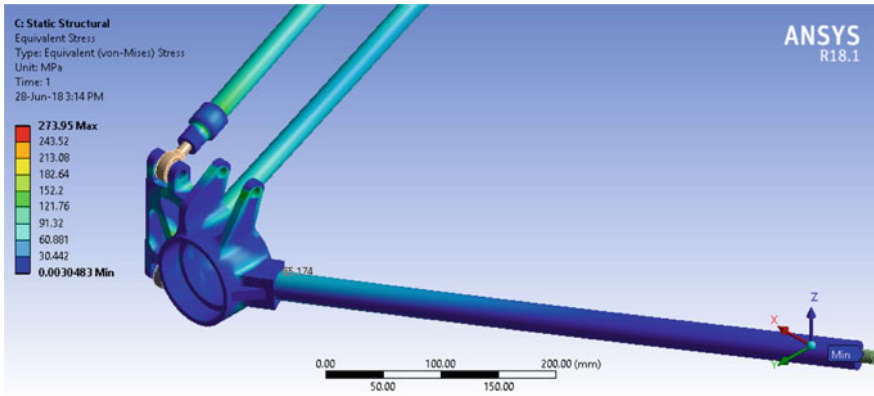
Fig. 6 Stress in the knuckle and trailing arm junction

materials, used for manufacturing the suspension components. Maximum stress $\sigma_{max} = 273.95$ MPa is induced in the upper control arm which is made of AISI 4340 alloy steel having an yield strength of 470 MPa.

A probe tool is used to find the stress in stress in knuckle and trailing arm junction as shown in Fig. 6. The probe tool indicates a stress value of 65.174 MPa. By calculations, it is found that a maximum load of 33024.15 N acts in the junction of knuckle and the trailing arm and the load are well within strength of aluminum weld. Hence, it is inferred that the design of the suspension system is safe and there is no need for redesign and it is also lighter in weight.

5 Conclusions

A detailed analysis of the suspension system is conducted using finite element analysis software. The component is modeled using a 3D modeling software and meshed and analyzed using simulating tool. The suspension system is designed considering the various loading condition and its material selection based on the weight criterion. The distribution of the load is even throughout the suspension system providing a lower stress concentration on critical junctions but within the limits. The upper control arm made of AISI 4340 alloy steel having yield strength of 470 MPa is induced with a maximum load of 273.95 MPa, which is a safe design.

References

1. Gillespie TD (1992) Fundamentals of vehicle dynamics. SAE International, USA
2. Rill G (2011) Road vehicle dynamics: fundamentals and modeling. CRC Press
3. Shijil P, Vargheese A, Devasia A, Joseph C, Jacob J (2016) Design and analysis of suspension system for an All-Terrain vehicle. Int J Sci Eng Res 7(3):164–190
4. Wable Abhay S, Londhe BC, Wable AD (2015) Multi-link structure for rear independent suspension of heavy vehicle. Int J Mech Eng Technol 6(5):01–09
5. Knowles Don (2007) Classroom manual for automotive suspension and steering systems, 4th edn. Cengage Delmar Learning, New York
6. Ambriz RR, Chicot D, Benseddiq N, Mesmacque G, de la Torre SD (2011) Local mechanical properties of the 6061–T6 Aluminium weld using micro-traction and instrumented indentation. Eur J Mech-A/Solids 30(3):307–315
7. Schmitt M, Paulmier D (2004) Tribological behaviour of diamond coatings sliding against Al alloys. Tribol Int 37(4):317–325
8. Olabode Muyiwa, Kah Paul, Martikainen Jukka (2013) Aluminium alloys welding processes: challenges, joint types and process selection. J Eng Manuf 227(8):1129–1137
9. Chandra K, Kain V (2013) Welding failure of as-fabricated component of aluminum alloy 5052. Eng Fail Anal 34:387–396
10. Godefroid LB, Faria GL, Cândido LC, Araujo SC (2014) Fatigue failure of a welded automotive component. Procedia Mater Sci 3:1902–1907
11. Adalarasan R, Santhanakumar M (2015) Parameter design in fusion welding of AA 6061 aluminium alloy using desirability grey relational analysis (DGRA) method. J Inst Eng (India): Series C 96(1), 57–63
12. Meseguer-Valdenebro Jose L, Martinez-Conesa Eusebio J, Serna Jose, Portoles Antonio (2016) Influence of the welding parameters on the heat affected zone for aluminum welding. Therm Sci 20(2):643–653
13. Zhao Li-Hui, Zheng Song-Lin, Feng Jin-Zhi (2014) Failure mode analysis of torsion beam rear suspension under service conditions. Eng Fail Anal 36:39–48
14. Sert Emre, Boyraz Pınar (2017) Optimization of suspension system and sensitivity analysis for improvement of stability in a midsize heavy vehicle. Eng Sci Technol Int J 20:997–1012
15. Nadota Y, Denier V (2004) Fatigue failure of suspension arm: experimental analysis and multiaxial criterion. Eng Fail Anal 11:485–499
16. Banerjee S, Balamurugan V, Krishnakumar R (2016) Ride comfort analysis of math ride dynamics model of full tracked vehicle with trailing arm suspension. Procedia Eng 144, 1110–1118
17. Wang Hongbo (2018) Enhancing vehicle suspension system control performance based on the improved extension control. Adv Mech Eng 10(7):1–13
18. Lee Yung-Li, Pan Jwo, Hathaway Richard, Bark Mark (2005) Fatigue testing and analysis: theory and practice, 1st edn. Elsevier Butterworth-Heinemann, Boston

Graphene: An Effective Lubricant for Tribological Applications

Pranav Dev Srivyas and M. S. Charoo

Abstract The objective of this review paper is to investigate the basic tribological behavior of graphene, the first existing 2D material and to enhance its performance as a self-lubricating material. The significant and prospective impact of this new class of material was first acknowledged in 2004 by Geim and Konstantin Novoselov who were awarded Noble prize for their discovery and development of graphene in 2010. In previous decades, reducing friction coefficient and wear-related failures in mechanical systems has gained serious attention due to friction's adverse impacts on effective life and durability of the mechanical systems. To reduce the friction and wear mechanism in the moving mechanical systems, the research proceeds in the development of novel materials, coatings, and lubricants (both liquid and solid) which have the potential of reducing friction and wear in materials. Despite intense research and development efforts on graphene for numerous existing as well as future applications, its tribological potential as a lubricant is still relatively uncharted. In this review, we provide relevant research of recent tribological studies on graphene especially, its use as a self-lubricating solid or as an additive for lubricating oils. A comprehensive review is provided with the aim to analyze such properties of graphene.

Keywords Graphene · Lubrication · Tribology · Wear · Friction

1 Introduction

In today's world, there is a need of energy resources to meet the growing energy demand, but these energy resources are depleting at a very fast rate which creates tremendous pressure on the engineers, scientist, and the designers. Comprehensive research is on the way to explore the entire possible alternative technologies to

P. D. Srivyas (✉) · M. S. Charoo
Mechanical Engineering Department, NIT Srinagar, Srinagar 190006,
Jammu & Kashmir, India
e-mail: devpranav.srivyas@gmail.com

conserve energy, economic demands, materials, and environment. Therefore, a better tribological property of the materials plays a vital role; is minimizing the energy depletion. Good tribological properties lead to reduce friction, increase the wear resistance of the material which is to be used in various moving mechanical systems and hence also reduce the emission to the environment [1]. Use of Liquid lubricants at the interface of the tribopair is one of the oldest but most effective methods of reducing friction and wear in the mechanical components and systems [2, 3]. According to a study, the worldwide production of the lubricant as well as a coolant during 2010 amounts to approx 170,046.9 metric tons [4]. But most of these lubricants are inherently toxic and of nonbiodegradable nature which affects the environment leads to demand the growth of eco-friendly self-lubricant materials. To enhance the properties of the lubricants and materials used in the composites, various other additives are added to it which enhances the antifriction and antiwear properties. Liquid lubricants reduce the wear and friction of the mechanical component and systems by providing the sliding contact interfaces from metal-to-metal contact by forming a low shear, high durability boundary film on the mating surfaces [5]. Nowadays solid lubricants have emerged as an integral part of materials science and engineering. Solid lubricants can be used in various forms to achieve the set of objectives. However, the use of solid lubricant as coating/filler has greatly expanded the use of solid lubricant materials. Different solid lubricants are used by their operating conditions. Example, MoS_2 is better to be used under a dry condition or in a vacuum; whereas graphite, boric acid shows better properties when used in the humid conditions. Therefore, solid lubricant properties mostly depend on the environment but they are highly durable and easy to deliver to the contact interface [6–9] (Table 1).

Graphene, a 2D carbon material has attained a considerable amount of popularity and scrutiny from the field of science and engineering [10]. Graphene is one such new solid lubricant which is having unusual physical, thermal, nontoxic, eco-friendly, mechanical, and tribological properties. Graphene an allotrope of carbon is a one-atom-thick planar sheet of sp2 bonded carbon atoms densely packed in a honeycomb crystal lattice. Graphene is strongest, chemically as well as thermally stable, gas-impermeable, and atomically thin. It is considered to be green lubricant as it contains C, O, and H instead of heavy metal elements. As in a modern world where the mechanical moving systems attracted a lot of the attention in various diverse applications; this newly emerged solid lubricant has the potential to reduce the friction, wear and increase the life of the system. Graphene nowadays is widely used both in the lubricants as a lubricant additive and as a filler reinforcement/graphene coating in the composites for lubrication means to decrease the friction and wear in tribological applications. It is proved to be equally well for the dry as well as a humid environment which is not in case of other commonly used solid lubricants. Of all the properties, tribological properties along with its applications are still the least explored. This review helps us to highlight these exceptional properties of graphene to reduce friction and wear in the micro- to nanoscale systems. As it is an ultrathin multilayer material, it can also be applied in micro-electromechanical-system (MEMS) and nano-electromechanical-systems

(NEMS) to reduce friction and wear from these systems. Graphene which is an anatomically smooth 2D material with low surface energy can replace the thin solid film is used to reduce adhesion and friction of various tribo surfaces.

In this review, various graphene synthesis techniques are reviewed along with a detailed discussion on the tribological properties of the graphene as a solid lubricant coating/filler in the composite and as a lubricant additive in the mineral/synthetic/biofluids. Also, the literature review is done on the operating conditions at which graphene shows excellent tribological properties. It is expected that this review will prove to be useful to the researchers working in the field of tribology.

2 Graphene Synthesis

Various synthesis routes are available for the synthesis of graphene. Properties of the graphene synthesized greatly depend on the type and quality of the synthesis root we adopt. Synthesis route adopted to generate the graphene has an effect on the grain size, shape, thickness, density, defect in structure, mechanical, and tribological properties of the graphene generated. The most basic and initially introduced method for the generation of the graphene is scotch tape method which is also called a mechanical exfoliation method. In this method of graphene synthesis, highly ordered pyrolytic graphite (HOPG) is used. Nowadays numerous synthesis process/methods are used for graphene generation. These include dry mechanical or chemical exfoliation; unrolling, and unzipping of carbon nanotubes by using physical, chemical or electrochemical methods; chemical vapor deposition (CVD)/epitaxial growth; arc discharge method; reduction of graphene oxide (GO), and many other organic/synthetic methods [11–20]. CVD is the best synthesis technique to get the best quality of graphene on the catalytic surfaces and it is done in the presence of hydrocarbon gases. Since there are various synthesis routes for the generation of graphene, some of them may be close to perfect but might be costly and some are not so perfect but cheap. It depends a lot that which grade of graphene is required and which synthesis route is adopted.

2.1 *Mechanical Exfoliation*

Mechanical exfoliation is the primary and the basic synthesis route used for the generation of graphene. It was first developed by Geim and Novoselov in the year 2004 for which they receive the noble prize in the year 2010. It includes isolating monolayer's of graphite. The basic mechanism is repetitive peeling of extremely oriented graphite. Highly ordered pyrolytic graphite (HOPG) is used in this process for the synthesis of graphene. This method is capable of generation of the atomically thin graphene sheet. This includes peeling off one or a few sheets of graphene

Table 1 Properties of graphene [54]

Thermal cond.	Thermal resistance	Specific surface area	Young's modulus	Fracture strength	Optical transmittance	Sheet resistance	Relaxation length	Phase coherence length	Mobility
$\sim 5000\ \mathrm{Wm^{-1}k^{-1}}$	$\sim 4 \times 10^{-8}\ \mathrm{km^2\ w^{-1}}$	$2300\ \mathrm{m^2 g^{-1}}$	~ 1 TPa	130 GPa	$\sim 97.7\%$	$1.3 \times 10^4 – 5.1 \times 10^4\ \Omega\ \mathrm{sq^{-1}}$	$15{,}000\ \mathrm{cm^2\ v^{-1}\ s^{-1}}$	3–5 μm	$10^8\ \mathrm{A\ cm^{-2}}$

using scotch tape and then depositing it on the substrates. The graphene produced by this synthesis route is of the highest quality with least defects but this process has some constraints, i.e., low productivity [21, 22].

2.2 Chemical Exfoliation

It is another possible synthesis route to obtain graphene which includes wet chemical processing. This processing route includes insertion of the graphite with the reactants which softens the Van-der Walls interactions and helps in the production of graphene sheets. In this synthesis route, the graphite is immersed in the acidic solution generally nitric or sulphuric acid. This method is generally done in two steps: Fist step includes thermal processing and Second includes ultra-sonication to disperse them. This result in the generation of the graphene chemical compounds sheets suspended in the colloidal suspension, which is further deposited on the substrate [23]. In order to achieve the pure quality graphene flakes, the chemical compounds must be removed from the colloidal suspension in the reduced atmosphere using alkaline solutions, by applying hydrogen plasma, by reducing hydrazine vapors or by heat treatments. This chemical exfoliation method has some disadvantages as the graphene flakes obtained are partially oxidized because the reduction processes are not so efficient. Another disadvantage is that the sp2 like graphene bonds are partially degraded to sp2–sp3 structure. The main advantage of this synthesis route is that it permits the correct management of the dimensions of graphene sheets. The dimension of the graphene sheet depends on the time period of sonication. Longer the sonication processes smaller the dimensions of graphene sheet [13]. Another advantage of this route is that high output of the graphene which makes it economically competitive. This route is best to be used for the production of composite materials, coating and for the biomedical applications.

2.3 Epitaxial Growth

It is another synthesis technique which involves the epitaxial growth on the crystalline carbide wafers substrate. In this process, a very thin layer of graphite is used under controlled atmosphere and proper conditions to produce graphene monolayer. A layer of monolayer graphene is produced on the SiC by heating the C–SiC at very high-temperature under the argon/vacuum atmosphere. The silicon which is close to the surface sublimates the carbon atoms but not at high-temperature the graphite reorganizes, and thus graphitization is achieved [24]. High surface roughness (Ra) of graphene is obtained from the Si–face. This synthesis route found is an application in semiconductor industry, semiconductor devices as it is easily deployable. But this synthesis route still required improvement for low-temperature

processes as compared to other synthesis processes. The main disadvantage of this method is that the graphene produces by this fabrication route have grain defect and grain boundaries due to which it cannot be perfectly homogenized. The quality as well as quantity produced by this synthesis route is not as much in comparison to the mechanical exfoliation and chemical exfoliation synthesis process, respectively.

2.4 Chemical Vapor Deposition

It is a well-known synthesis process in which the substrate is exposed to gaseous compounds. The graphene growth on the substrate surface is due to thermal decomposition of hydrocarbon gas molecules, i.e., methane/propane/acetylene catalyzed by a metal surface attribute to the segregation or precipitation of the carbon atoms from the metal. Mainly the transitions metals are used as a catalyst for the production of different allotropy of the carbon, so the main focus will be on them for the generation of graphene [25]. In the CVD process, the chemical constituents react in the vapor phase near/on a heated substrate to form a solid deposit. CVD process includes various chemical reactions such as thermal decomposition, reduction, hydrolysis, disproportion, oxidation, carburization, and nitridation. These processes can be used either individually or in combination. The main disadvantage of this processing route is that graphene is to be transferred from the metal to the actual appropriate substrate. It produces high-quality graphene and is mostly used for electronics applications, but the transfer of the graphene from the metal to the actual substrate sometimes leads to the improper alignment which increases the scope of error.

2.5 Hummer Method

This processing route is used for the synthesis of the graphene oxide. In this process, oxidation of graphite flakes are done to get the desired material. In this synthesis process, graphite flakes and sodium nitride are mixed in concentrated sulfuric acid in a volumetric flask kept at low temperature (0–5 °C) which is continuously stirred for 120 min. After that, the potassium permanganate is added to the suspension. The rate of addition of potassium permanganate is carefully controlled to keep the reaction temperature low (below 15 °C). The mixture is then stirred until it becomes pasty brownish. The paste is then kept stirring for two days after that its solution is diluted with the slow addition of water. The reaction temperature increases and the solution color changes to brown color. The solution is finally treated with hydrogen peroxide to terminate the reaction by the appearance of yellow color. Now, the process of purification takes place in which the mixture is washed by rinsing and centrifugation with hydrochloric acid and then with de-ionized water. The final step is the drying process under vacuum at room temperature, to produce graphene oxide as powder

Table 2 Synthesis methods and mechanisms [13, 21–28]

Synthesis method	Mechanism	Precursors used	Graphene produced/ number and size
Mechanical Exfoliation	Peeling off layers using scotch tape	Graphite	Pristine (SLG, FLG; 10 μm)
Chemical exfoliation	Decomposition of graphite based compounds, reduction, and subsequent exfoliation	Graphene oxide/ graphite flakes	Chemically Modified Graphene (SLG, FLG; > 100 μm)
Epitaxial growth	Thermal decomposition of hydrocarbons on top of SiC crystals	SiC	Pristine (SLG, FLG, > 50 μm)
Chemical vapor deposition	Carbon segregation or precipitation over transition metals	Transition metals, Polycrystalline Ni films, Copper Foils	Pristine (SLG, FLG, > 100 μm)
Liquid-phase exfoliation	Exposing graphite flakes or graphene oxide to solvents and applying sonication	Graphite/GO	Pristine (SLG, FLG, 20 μm)
Unzipped CNT	Longitudinal unzipping of CNT	MWCNT	Chemically Modified Graphene (SLG, FLG, 10 μm)
Solvothermal synthesis	Pyrolysis and filtering of solvothermal product	Solvothermal Products (Na + Ethanol)	Chemically Modified Graphene (SLG, FLG, 20 μm)

[26, 27]. Another improvement in the hummer method to get the high-quality graphene is the modified hummer method which involves both oxidation and exfoliation of graphite sheets due to thermal treatment of solution [28]. The summary of the synthesis methods and mechanisms are given in Table 2.

3 Tribological Behavior of Graphene

Graphene played a vital role in reducing friction and wear in various mechanical and tribological applications. So the detailed literature review of graphene as an antifriction, antiwear reinforcement in composites and as an additive in lubricants for low as well as high-temperature applications are discussed in the sections below.

3.1 Friction and Wear of Graphene

Many researchers worked a lot to reduce the friction and wear behavior at the micro as well as nanoscale by introducing graphene coatings as a solid lubricant in various tribological applications [29, 30]. Graphene produced by using chemical vapor

deposition synthesis route was estimated under the normal load up to 70 µN. While examining the frictional behavior of the CVD-graphene, it was found that the Coefficient of Friction (COF) is affected by various parameters as well as the materials of the initial substrate. It was observed that the coatings grown on the nickel exhibit better frictional behavior than that of the coating grown on the copper metal. It was also found that the COF considerably enhanced while the transfer of the graphene from the particular substrate like copper and nickel. The tribological properties of the coatings mostly depend on the adhesion between the substrate and the coatings. It was suggested from this research that few nanometer thick graphene samples proved to be good as solid lubricant at both micro as well as nanoscale [31]. Shin et al. in their investigation studied the COF of graphene produced by Epitaxial Growth and exfoliation method. The graphene with few layers under normal load up to 0.5 µN using an AFM tip radius of one meter was studied. It was observed that COF was not dependent on the number of layers. The COF for one to three-layer graphene was around 0.03. They also studied the defects in the structure of the defect. It was observed that the defects in the crystal structure of the graphene increase the COF by two to three times [32]. Won et al. studied the friction and wear mechanism of CVD produced graphene on the copper substrate under load of 20 µN with chrome steel ball as the counterbody (1 mm diameter). It was reported that the deposition parameters are crucial to get the graphene with minimum defect. It was also reported that the number of the layers varying from one to seven does not affect the COF a lot [33]. Yan et al. in their investigation studied the COF of graphene transferred on to the substrate under the load of up to 40 µN. It was reported that the applied load is a critical parameter which influenced the friction coefficient [34]. Berman et al. reported that the multilayer graphene flakes may be successfully used as a solid lubricant for chrome steel. It was observed that employing a low concentration of graphene flakes reduced the COF by six times [35, 36]. The brief summary of the friction behavior of graphene in micro- and nanoscale is given in Table 3.

3.2 Tribological Behavior of Graphene as Reinforcement in Composites

Several investigations have been done to study the tribological behavior of graphene as reinforcement in various composites materials. Tai et al. [37] studied the tribological behavior of Ultra-High Relative Molecular Mass Polythene (UHMWPE)/Graphene Oxide (GO) composite. The composite samples were fabricated using toluene-assisted mixing followed by hot-pressing technique. The tribological and mechanical properties of base composite and the GO/UHMWPE composites were examined. It was reported that GO nanosheets content up to 1 wt %, increases the wear resistance and hardness of the composites very significantly, while the friction coefficient will increase rapidly with the increase in the

Table 3 Tribological behavior of graphene on micro/nanoscale [29, 36]

Graphene in Microscale tribology					
Substrate	Deposition method	Ra (nm)	Counterbody	Contact pressure, load/operating conditions	COF
SiO_2	CVD	1	Fused silica lens	5–10 μm (Air, Room Temperature)	0.15
SiC	CVD	1	Diamond tip	0.05 μm (Air, Room Temperature)	0.07
Ni	CVD	–	Si_3N_4 ball	2 N (Air, 24 °C) (45% RH)	0.06
Cu	Solution	–	Steel ball	220 Mpa, 20 μN (Air, Room Temperature)	0.2
Steel C440	solution	15	Steel ball	1–5 N (Air, Room Temperature)	0.15
PET	Solution	5	SiO_2	20, 40 μN (Air, Room Temperature)	0.08
Ni	Exfol.	1	Fused silica lens	5–10 μm (Air, Room Temperature)	0.05
Si	Exfol.	1	Diamond tip	0.05 μm (Air, Room Temperature)	0.07
Si	Sputtering	–	Steel ball	100–400 μN (Air, Room Temperature)	0.12
Graphene in Nanoscale tribology					
Si	Exfol.	0.5	SiN	0.01–0.5 Nn (Air, Room Temperature)	0.025
SiO_2	Exfol.	0.5	Si	1 nN (Air, Room Temperature)	0.6–0.15
SiO_2	Exfol.	0.5	Si	1 nN (Air, Room Temperature)	–
Si	Exfol.	0.5	Si	1 nN (Air, Room Temperature)	–
SiO_2	Exfol.	0.5	DLC	5 nN (Air, Room Temperature)	0.4–1.0
Si	Exfol.	0.5	Si	3–30 nN (Air, Room Temperature)	0.02
Si	Solution	0.5	Si	1 nN (Air, Room Temperature)	0.10
SiO_2 (GNP Coated)	Solution	–	SiO_2 Ball (DLC coated)	1 nN (Dry Nitrogen)	0.004
SiO_2 (GNP Coated)	Solution	–	SiO_2 Ball	1 nN (Dry Nitrogen)	0.04
SiC	Thermal decomp	–	Si	40 nN (Air, Room Temperature)	0.2

reinforcement. Min et al. [38] investigated the Graphene Oxide (GO)/Polyimide (PI) Nanocomposite fabricated using situ polymerization. They studied the tribological behaviors of the composite under dry friction, seawater lubrication, and pure water lubrication conditions. The GO/PI composite exhibited better results beneath seawater-lubricated condition than other conditions because of the excellent lubricating effect of seawater. GO as reinforcement greatly improved the thermal stability of the composites. The tensile modulus and tensile stress of the nanocomposite improved significantly by adding graphene oxide (GO). The incorporation of GO under seawater lubrication can greatly improve the wear resistance of Polyimide. Best results were obtained with 0.5 wt% GO reinforced to PI composite. Zhu et al. [38] studied the dry sliding tribological behavior of Ni_3Al matrix composites (NMCs). It was reported that Ni_3Al matrix composites with 0.5 wt% graphene nanoplatelets (GNPs) sliding against different counter face balls with an applied load of 10 N and a sliding velocity of 0.234 ms^{-1}. When the composite

sliding against GCr15 steel, a consistent and thick friction layer is formed, leading to a lower COF, but when the composite sliding against Si_3N_4 and Al_2O_3, the formation and stability of the friction layers are restricted within the severe wear regime, and thus composite exhibit higher friction coefficients and wear rates. Yao et al. [40] studied the combined effect of lubrication of WS2 and multilayer graphene (MLG). The prepared sample of NiAl–5 wt% WS2 (NB)–1.5 wt% MLG exhibited excellent tribological properties. The MLG play the role of reinforcement particles and improved loading carrying ability. The addition of a combination of MLG and WS2 offered to possessed superior antifriction and the wear resistance. Gonzalez et al. [41] studied the dry sliding behavior of a graphene/alumina composite against alumina under dry conditions. The testing was done on the reciprocating tribometer with an applied load of 20 N, a sliding distance of up to 10 km and a sliding speed of 0.06 ms^{-1}. The composite showed a 10% lower friction coefficient and half the wear rate than the monolithic alumina. It has been also found that this behavior is related to the presence of graphene nanoplatelets (GNPs). GNPs form a self-lubricating layer that provides enough lubrication so as to decrease both friction coefficient and wear rate. These GNPs act as a self-lubricating layer on the contact surface between the composite and the Al_2O_3 ball that acts as counterpart material. Yazdani et al. [42] studied the tribological performance of the hot-pressed pure alumina and its composites containing numerous hybrid contents of GNPs and carbon nanotubes (CNTs) under different loading conditions. The composite reinforced with 0.5wt% graphene nanoplatelets reduced the COF up to 23% and enhance the wear rate by 70%. The hybrid reinforcement consisting of 0.3 wt% GNPs and 1 wt% CNTs shows even better performance, with an 86% reduction in the wear rate. GNPs played a vital role in the formation of a tribo-film on the worn surface by exfoliation. Llorente et al. [43] studied the friction and wear behavior of graphene/silicon carbide (SiC) composites under the dry sliding conditions and using silicon nitride balls as countersurface. GNPs composites showed an improvement in the wear resistance as compared to monolithic silicon carbide, with enhancements of 70 vol. % for the material containing up to 20 vol. % of GNPs. Under dry sliding conditions, the wear resistance of SiC ceramics considerably enhances with the addition of GNPs. 20 vol. % GNPs composite clearly showing the best wear resistant performance which is 70% more as compared to the monolithic SiC, whereas 5 vol. % reduced graphene oxides composites exhibit excellent fracture toughness. Kalin et al. [44] studied the effect of the morphology solid lubricant nanoparticles on Poly-Ether-Ether-Ketone (PEEK) composites on the mechanical and tribological characteristics. The results obtained under dry sliding tribological conditions show that the materials have an important effect on the friction coefficient and the wear, primarily by affecting their hardness. The carbon-based particles deteriorated the wear and tear behavior by 20 wt% (CNT) and the maximum amount of three times in the case of the GNP. Tabandeh et al. [45] studied the tribological behavior of Al matrix composites reinforced by GNPs, on a pin-on-disk tribometer. The results showed that the wear of Al-1 wt% GNP is enhanced with an increase in the normal loads. However, the friction coefficient of the Al-1 wt% GNP reduced with increasing normal loads. It has been

found that the GNPs reinforced nanocomposites showed excellent tribological properties. Belmonte et al. [46] studied the tribological properties of GNPs/Si_3N_4 composites in a reciprocating ball-on-plate tribometer under iso-octane lubrication. GNPs are excellent nanofillers which improve the tribological performance of ceramics. Under the high contact pressures, GNPs are able to decrease the friction and enhance the wear resistance up to 56% due to the exfoliation of the GNPs that creates a protective tribo-film. The exfoliation of the nanoplatelets (NPs) generates graphene flakes, which effectively limits wear volume by protective tribo-film. Xu et al. [47] studied the self-lubrication characteristics of multilayer graphene and high-temperature tribological properties of graphene titanium aluminum matrix composite from the temperature ranges from 100–700 °C using a rotating ball-on-disk tribometer at a load of 10 N and speed of 0.2 ms^{-1}. During the temperature range from 100 to 550 °C, MLG presents good lubricating properties. Above 600 °C, MLG lost their self-lubrication characteristics due to the formation of the oxide layer which improves the oxidation resistance of GTMC by restricting the grain boundaries and inhibiting the inflow of oxygen through grain boundaries. The brief summary of the test parameters of graphene as reinforcement composite in different materials are given in Table 4.

3.3 Tribological Behavior of Graphene as Lubricant Additives

Lin et al. [48] investigated the chemically modified the graphene platelets with oleic and stearic acids in a reflux reaction. They then investigated the tribological properties of modified graphene platelets based lubricant using a four-ball tester. The results show that the lubricants containing 0.75 wt% of the MGNP additive is efficient to reduce the wear of the materials and there is also an increase in the load carrying capacity of the lubricant. Senatore et al. [49] investigate the tribological behavior of graphene oxide nanosheets in mineral oil under boundary, mixed, and elastohydrodynamic lubrication regimes. The GO nanosheets were synthesized by using modified hummer method. Experimental studies were done on the pin-on-disc configuration tribometer. The studies concluded that the lubricant-containing GO additives are more efficient to reduce the friction behavior by forming a protective layer between two tribo surfaces which prevent direct metal-to-metal contact. Zhe et al. [50], in their study, compared the performance of lubricating oils with different additives. It was observed that most of the additives are toxic and produces poisonous gases when burnt in the environment; but the lubricant congaing GO as an additive is eco-friendly and green lubricant as GO consist of C, H, and O. It was also reported that the GO-based lubricating oil is efficient to reduce the wear and friction in the material even at high temperature. These GO-based lubricant also proved to be good for high sliding speed conditions. 0.5 wt% GO as an additive proved to be best in all the composition variations. Dou et al. [51] in their

Table 4 Tribological properties of graphene as reinforcement in composites [37–47]

Material	Reinforcement	Fabrication route	Test motion/counterbody/normal load (N)/temperature	Contact velocity/sliding distance	COF	Wear rate (mm³/Nm)/Weight loss (µg)
UHMWPE	0.1 wt% GO	Hot pressing	Reciprocating/ZrO$_2$ ball/5 N	9 cm/s	0.115	$1.35*10^{-5}$
UHMWPE	0.3 wt% GO				0.116	$1.53*10^{-5}$
UHMWPE	0.7 wt% GO				0.116	$1.1*10^{-5}$
UHMWPE	1.0 wt% GO				0.120	$1.1*10^{-5}$
UHMWPE	2.0 wt% GO				0.115	$1.05*10^{-5}$
UHMWPE	3.0 wt% GO				0.115	$1.03*10^{-5}$
Polyimide	0.1 wt% GO	Situ polymerization	Reciprocating/steel ball/3 N	0.156 m/s	0.41	$6*10^{-6}$
Polyimide	0.3 wt% GO				0.46	$13.5*10^{-6}$
Polyimide	0.5 wt% GO				0.54	$8*10^{-6}$
Polyimide	0.7 wt% GO				0.49	$7.9*10^{-6}$
Polyimide	1.0 wt% GO				0.55	$6.5*10^{-6}$
NiAl	1.5 wt% MLG	Spark plasma sintering	Rotary/Ni$_3$N$_4$ ball/2, 6, 12, 16 N	0.2 m/s	(0.6–0.8), (0.5–0.6), 0.5, 0.42	$2.82*10^{-5}$, $3.57*10^{-5}$, $4.02*10^{-5}$, $5.24*10^{-5}$
NiAl	1.5 wt%		Rotary/Al$_2$O$_3$ ball/10 N		0.35	$0.40*10^{-5}$
NiAl	MLG + 5 wt% WS$_2$		Rotary/Ni$_3$N$_4$ ball/10 N		0.21	$0.17*10^{-5}$
NiAl			Rotary/Al$_2$O$_3$ ball/10 N		0.25	$0.11*10^{-5}$
Al$_2$O$_3$	0.22 wt% GNP	Spark plasma sintering	Reciprocating/Al$_2$O$_3$/20 N	0.06 m/s/10 km	0.67	$3.5*10^{-9}$
Al$_2$O$_3$	0.5 wt% GNP		Reciprocating/Si$_3$N$_4$ Ball/5, 15, 25, 35 N	10 mm/s	0.40, 0.48, 0.58, 0.54	–, 2.3 µg, 6 µg, 5 µg
Al$_2$O$_3$	2 wt% GNP			10 mm/s	0.49, 0.55, 0.54, 0.53	–, 7 µg, 9 µg, 40 µg
Al$_2$O$_3$	5 wt% GNP			10 mm/s	0.45, 0.54, 0.51, 0.45	–, 62 µg, 80 µg, 160 µg

Table 4 (continued)

Material	Reinforcement	Fabrication route	Test motion/counterbody/normal load (N)/temperature	Contact velocity/sliding distance	COF	Wear rate (mm^3/Nm)/Weight loss (µg)
SiC	5 wt% GO	Spark plasma sintering	Reciprocating/Si_3N_4 Ball/5 N	0.1 m/s/360 m	0.71	$1.4*10^{-3}$
SiC	5 wt% GO				0.75	$1.3*10^{-3}$
SiC	20 wt% GO				0.96	$0.5*10^{-3}$
Al	0.1 wt% GNP	Spark plasma sintering	Reciprocating/440C steel disc/5 N, 10 N, 15 N	100 RPM/1.13 km	0.36, 0.34, 0.25	0.008 gms, 0.001gms, 0.016 grms
Al	1 wt% GNP		Reciprocating/440C steel disc/5, 10, 15 N	50 RPM/1.13 km	0.339, 0.36, 0.258	0.011gms, 0.0180 gms, 0.022 gms
Al	1 wt% GNP		Reciprocating/440C steel disc/5, 10, 15 N	100 RPM/1.13 km	0.33, 0.33, 0.239	0.0051 gms, 0.015 gms, 0.02 gms
Al	1 wt% GNP		Reciprocating/440C steel disc/5, 10, 15 N	150 RPM/1.13 km	0.33, 0.33, 0.239	0.0120 gms, 0.0155 gms, 0.027 gms
PEEK	2 wt% GNP	Spark plasma sintering	Reciprocating/100Cr6 PIN/1 MPa	0.05 m/s	0.62	$8.8*10^{-6}$
Si_3N_4	3 wt% GNP	Spark plasma sintering	Reciprocating/Si_3N_4 Ball/5, 100, 150, 200 N	0.1 m/s/360 m	0.225, 0.185, 0.169, 0.16	$1.0*10^{-3}$, $1.1*10^{-3}$, $1.3*10^{-3}$, $1.5*10^{-3}$
TiAl	3.5 wt% MLG	Spark plasma sintering	Rotary/Ni_3N_4 Ball/10 N/100 °C	0.2 m/s	0.360	$0.91*10^{-4}$
			Rotary/Ni_3N_4 Ball/10 N/200 °C		0.350	$0.95*10^{-4}$
			Rotary/Ni_3N_4 Ball/10 N/300 °C		0.375	$1.00*10^{-4}$
			Rotary/Ni_3N_4 Ball/10 N/400 °C		0.375	$1.01*10^{-4}$
			Rotary/Ni_3N_4 Ball/10 N/500 °C		0.370	$1.40*10^{-4}$
			Rotary/Ni_3N_4 Ball/10 N/600 °C		0.510	$2.30*10^{-4}$
			Rotary/Ni_3N_4 Ball/10 N/700 °C		0.525	$2.20*10^{-4}$

investigation used the crumpled graphene ball as an additive in the Poly Alpha Olefin (PAO) lubricating oil. It is proved to be high-performance additive. 0.01–0.1 wt% of the crumpled graphene ball proved to be best to reduce the friction and wear of materials. Azman et al. [52] studied the effect of GNP as an additive in the palm oil trimethylolpropane ester blended Poly Alpha Olefin. It was observed that there is a decrease in the COF and wear rate of the material by using the blended lubricating oil with 0.05 wt% GNP as an additive. Meng et al. [53] in their investigation studied the tribological behavior of engine oil with 0.06–0.10 wt% Sc–Ag/GN as an additive. The tests were conducted in the four-ball tester. It was reported that the oil with additive proved to behave better tribological properties than the base engine oil. As the nano–Ag and GN particles form a protective film between the two materials and prevent metal to metal contact, hence reduce the friction and wear of the tribopair. Rasheed et al. [54] investigated the tribological performance of graphene-based nanolubricant in a four-stroke IC engine test rig. The lubricating oil SN/CF API 20W50 was used and 0.01 wt% additive was added to the lubricating oil. It was observed that there is a reduction in the COF by 21%, increase in thermal conductivity at 80 °C by 23% and enhancement in the heat transfer rate by 70% is achieved. Wei al. [55] used liquid-phase exfoliated modified graphene by oleic acid as an additive in the lubricating oil. It was found that there was an increase in the wear and friction of the material by 14% and 17%, respectively. It was reported that modified graphene as an additive also increases the load carrying capacity of the lubricant. Kinoshita et al. [56] investigated the behavior of graphene oxide nanoparticles in a water-based coolant to reduce friction. It was reported that the COF is reduced to 0.05 and no surface wear was reported for over 60,000 cycles. Eswaraiah et al. [57] in their investigation reported that there is an increase in the frictional characteristics, wear resistance, and extreme pressure properties by 80, 33, and 40% by the use of 0.025 mg/ml of graphene as an additive in the engine oil. The brief summary of the test parameters of graphene as additive in different lubricants are given in Table 5 (Table 6).

Table 5 Tribological properties of graphene as an additive in lubricants [48–57]

Lubricant	Additive	Material	Counterbody	Test motion/ temperature/ normal load (N)	Frequency (Hz)/Speed (rpm)	Stoke (mm)	COF
HC Base oli	0.5 wt% GO	ALSI 52100 Steel	ALSI 52100 Steel ball	Recipro/50 °C/ 50 N Recipro/50 °C/ 100 N Recipro/50 °C/ 150 N	50 Hz	2	0.13, 0.11, 0.105
HC Base oli	0.5 wt% GO	ALSI 52100 Steel	ALSI 52100 Steel ball	Recipro/100 °C/ 50 N Recipro/100 °C/ 100 N Recipro/100 °C/ 150 N	50 Hz	2	0.17, 0.15, 0.14
HC Base oli	0.5 wt% GO	ALSI 52100 Steel	ALSI 52100 Steel ball	Recipro/150 °C/ 50 N Recipro/150 °C/ 100 N Recipro/150 °C/ 150 N	50 Hz	2	0.18, 0.15, 0.14

(continued)

Table 5 (continued)

Lubricant	Additive	Material	Counterbody	Test motion/temperature/normal load (N)	Frequency (Hz)/Speed (rpm)	Stoke (mm)	COF
HC Base oli	0.5 wt% GO	ALSI 52100 Steel	ALSI 52100 Steel ball	Recipro/50 °C/100 N	10 Hz, 20 Hz, 30 Hz, 40 Hz, 50 Hz	2	0.122, 0.12, 0.119, 0.18, 0.117
PAO40	0.05 wt% GO	ALSI 52100 Steel	ALSI 52100 Steel ball	Reciprocating/100 N Reciprocating/200 N Reciprocating/300 N Reciprocating/400 N Reciprocating/500 N	30 Hz	2	0.121, 0.119, 0.125, 0.126, 0.130
PAO40	0.5 wt% GO	ALSI 52100 Steel	ALSI 52100 Steel ball	Reciprocating/100 N Reciprocating/200 N Reciprocating/300 N Reciprocating/400 N Reciprocating/500 N	30 Hz	2	0.118, 0.118, 0.116, 0.118, 0.124
PAO40	0.1 wt% GO	ALSI 52100 Steel	ALSI 52100 Steel ball	Reciprocating/100 N Reciprocating/200 N Reciprocating/300 N Reciprocating/400 N Reciprocating/500 N	30 Hz	2	0.117, 0.114, 0.112, 0.113, 0.116
PAO40	1 wt% GO	ALSI 52100 Steel	ALSI 52100 Steel ball	Reciprocating/300 N	10 Hz, 20 Hz, 30 Hz, 40 Hz, 50 Hz	2	0.09, 0.16, 0.112, 0.113, 0.114
PAO4	0.01 wt% τ–GO	ALSI52100 Steel disc	M50 steel ball	Rotary/10 N	10 mm/s	–	0.132
PAO4	0.1 wt% τ–GO	ALSI52100 Steel disc	M50 steel ball	Rotary/10 N	10 mm/s	–	0.131
PAO 10	0.01 wt% GNP	ALSI 52100 Steel	ALSI 52100 Steel	Rotary/392 N	1200 rpm	–	0.08
PAO 10	0.03wt% GNP	ALSI 52100 Steel	ALSI 52100 Steel	Rotary/392 N	1200 rpm	–	0.081
PAO 10	0.05wt% GNP	ALSI 52100 Steel	ALSI 52100 Steel	Rotary/392 N	1200 rpm	–	0.073
PAO 10	0.1wt% GNP	ALSI 52100 Steel	ALSI 52100 Steel	Rotary/392 N	1200 rpm	–	0.087
PAO 10	0.2wt% GNP	ALSI 52100 Steel	ALSI 52100 Steel	Rotary/392 N	1200 rpm	–	0.081
PAO 10	0.5wt% GNP	ALSI 52100 Steel	ALSI 52100 Steel	Rotary/392 N	1200 rpm	–	0.080
PAO 10	1wt% GNP	ALSI 52100 Steel	ALSI 52100 Steel	Rotary/392 N	1200 rpm	–	0.086
PAO 10	3wt% GNP	ALSI 52100 Steel	ALSI 52100 Steel	Rotary/392 N	1200 rpm	–	0.089
SN 350	0.075wt% MGP	ALSI 52100 Steel	ALSI 52100 Steel ball	Rotary/75°C/147 N	1200 rpm	–	0.121
SN 150	0.1 wt% GO	X155CrVMo12–1 steel disc	X45Cr13 steel ball	Rotary/25 °C/60 N	1 m/s, 1.5 m/s, 2 m/s	–	0.134, 0.141, 0.152
SN 150	0.1 wt% GO	X155CrVMo12–1 steel disc	X45Cr13 steel ball	Rotary/50 °C/60 N	1 m/s, 1.5 m/s, 2 m/s	–	0.131, 0.141, 0.153

Table 5 (continued)

Lubricant	Additive	Material	Counterbody	Test motion/ temperature/ normal load (N)	Frequency (Hz)/Speed (rpm)	Stoke (mm)	COF
SN 150	0.1 wt% GO	X155CrVMo12–1 steel disc	X45Cr13 steel ball	Rotary/80 °C/ 60 N	1 m/s, 1.5 m/s, 2 m/s	–	0.141, 0.15, 0.16
SN/ CF20W50	Additive + G60	Steel Ball	Steel Ball	Rotary/40 N	1200 rpm	–	0.011
SN/ CF20W50	G60	Steel Ball	Steel Ball	Rotary/40 N	1200 rpm	–	0.014
SN/ CF20W50	G12	Steel Ball	Steel Ball	Rotary/40 N	1200 rpm	–	0.013
SN/ CF20W50	G8	Steel Ball	Steel Ball	Rotary/40 N	1200 rpm	–	0.014
SJ/ CF20W50	Additive + G60	Steel Ball	Steel Ball	Rotary/40 N	1200 rpm	–	0.017
SJ/ CF20W50	G60	Steel Ball	Steel Ball	Rotary/40 N	1200 rpm	–	0.018
SJ/ CF20W50	G12	Steel Ball	Steel Ball	Rotary/40 N	1200 rpm	–	0.017
SJ/ CF20W50	G8	Steel Ball	Steel Ball	Rotary/40 N	1200 rpm	–	0.017
10W40	0.1wt% GO	GCr15 steel ball	GCr15 steel ball	Rotary/343 N	1200 rpm	–	0.09
10W40	0.1wt% Ag/GN	GCr15 steel ball	GCr15 steel ball	Rotary/343 N	1200 rpm	–	0.09
10W40	0.1wt% Sc-Ag/ GN	GCr15 steel ball	GCr15 steel ball	Rotary/343 N	1200 rpm	–	0.078

Table 6 Overview of tribological properties of widely used solid lubricant [58, 59]

Solid lubricant coating	Deposition method	Coating thickness (μm)	COF	Friction/Wear mechanism
Graphite	Evaporation	0.2–5	Dry: 0.5–0.6 Humid: 0.1-0.2	Interlayer shear Water intercalation
DLC	Sputtering, Ion-Beam	1–3	Dry: 0.001–0.05 Humid: 0.2–0.3	High chemical inertness. The repulsive force due to hydrogen termination
Tetrahedral amorphous carbon	Ion-Beam, Cathode Arc, Pulsed Laser	0.01–1	Dry: 0.7 Humid: 0.1	Tribochemical induces a surface reaction Termination of a top carbon atom
Ultra Nano-Crystalline Diamond	MPCVD, HFCVD	0/5–1.5	Dry: 0.05–0.13 Humid: 0.007–0.1	Tribochemical induced reaction with H, O or OH
MoS_2&WS_2	Sputtering, Thermal Evaporation, CVD, ALD	0.2–2	Dry: 0.02–0.06 Humid: 0.15–0.25	Interlayer shear Transfer film formation
Graphene/Graphene Oxide (GO)	CVD, Mechanical and Chemical Exfoliation	0.001–0.002	Dry: 0.15–0.2 Humid: 0.15–0.2	Interlayer shear Prevention of tribo-corrosion

4   Conclusions

Graphene is proved as a unique and attractive material having promising mechanical, thermal, and tribological properties which found its application in the field of mechanical systems, electronic systems, and also in the field of biomedical. Several investigations make it clear that the graphene and its allotropes enhance the tribological properties of the composites as well as lubricants when used as reinforcement filler/coating or as additives, respectively. This review highlights the recent growth and development of graphene as a lubricant for micro as well as nanoscale applications in tribology. Despite its ultrathin nature it is proved to be effective for high temperature, high load dry sliding conditions. Graphene nanoparticles contributed directly to the latter film formation which plays an effective role in reducing the friction and wear of the tribopairs. Overall in this review graphene is proved to be a very effective material for reducing friction and wear. Growth in the synthesis process of graphene leads to explore some more applications in the field of tribology. The employment of graphene in tribological applications is expected to grow continuously shortly.

References

1. Wani MF, Anand A (2010) Life-cycle assessment modeling and life-cycle assessment evaluation of a triboelement. Proc Inst Mech Eng, Part J: J Eng Tribol 224(11):1209–1220. https://doi.org/10.1243/13506501JET747
2. Willing A (2001) Lubricants based on renewable resources–an environmentally compatible alternative to mineral oil products. Chemosphere 43(1):89–98. https://doi.org/10.1016/s0045-6535(00)00328-3
3. Farhanah AN, Syahrullail S (2016) Evaluation of lubrication performance of RBD palm stearin and its formulation under different applied loads. Jurnal Tribol 10:1–15
4. UN Data Industrial 23 Jan (2013) Commodity Statistics Database
5. Mercurio P, Burns KA, Negri A (2004) Testing the ecotoxicology of vegetable versus mineral based lubricating oils: 1. Degradation rates using tropical marine microbes. Environ Pollut 129(2):165–173. https://doi.org/10.1016/j.envpol.2003.11.001
6. Beerschwinger U, Mathieson D, Reuben RL, Yang SJ (1994) A study of wear on MEMS contact morphologies. J Micromech Microeng 4(3):95. https://doi.org/10.1088/0960-1317/4/3/001
7. Holmberg K, Andersson P, Erdemir A (2012) Global energy consumption due to friction in passenger cars. Tribol Int 47:221–234. https://doi.org/10.1016/j.triboint.2011.11.022
8. Kim HJ, Kim DE (2009) Nano-scale friction: a review. Int J Precis Eng Manuf 10(2):141–151. https://doi.org/10.1007/s12541-009-0039-7
9. Penkov O, Kim HJ, Kim HJ, Kim DE (2014) Tribology of graphene: a review. Int J Precis Eng Manuf 15(3):577–585. https://doi.org/10.1007/s12541-014-0373-2

10. Duplock EJ, Scheffler M, Lindan PJ (2004) Hallmark of perfect graphene. Phys Rev Lett 92 (22): 225502. https://doi.org/10.1103/physrevlett.92.225502

11. Novoselov KS, Geim AK, Morozov SV, Jiang D, Zhang Y, Dubonos SV, Firsov AA (2004) Electric field effect in atomically thin carbon films. Science 306(5696):666–669. https://doi.org/10.1126/science.1102896

12. Chen D, Tang L, Li J (2010) Graphene-based materials in electrochemistry. Chem Soc Rev 39 (8):3157–3180. https://doi.org/10.1039/B923596E

13. Soldano C, Mahmood A, Dujardin E (2010) Production, properties and potential of graphene. Carbon 48(8):2127–2150. https://doi.org/10.1016/j.carbon.2010.01.058

14. Lotya M, Hernandez Y, King PJ, Smith RJ, Nicolosi V, Karlsson LS, Duesberg GS (2010) Liquid phase production of graphene by exfoliation of graphite in surfactant/water solutions. J Am Chem Soc 131(10):3611–3620. https://doi.org/10.1021/ja807449u

15. Mohammadi S, Kolahdouz Z, Darbari S, Mohajerzadeh S, Masoumi N (2013) Graphene formation by unzipping carbon nanotubes using a sequential plasma-assisted processing. Carbon 52:451–463. https://doi.org/10.1016/j.carbon.2012.09.056

16. Kim KS, Zhao Y, Jang H, Lee SY, Kim JM, Kim KS, Hong BH (2009) Large-scale pattern growth of graphene films for stretchable transparent electrodes. Nature 457(7230):706. https://doi.org/10.1039/nature07719

17. Li X, Cai W, Colombo L, Ruoff RS (2009) Evolution of graphene growth on Ni and Cu by carbon isotope labeling. Nano Lett 9(12):4268–4272. https://doi.org/10.1021/nl902515k

18. Sutter PW, Flege JI, Sutter EA (2008) Epitaxial graphene on ruthenium. Nat Mater 7(5):406. https://doi.org/10.1038/nmat2166

19. Lee SW, Mattevi C, Chhowalla M, Sankaran RM (2012) Plasma-assisted reduction of graphene oxide at low temperature and atmospheric pressure for flexible conductor applications. J Phys Chem Lett 3(6):772–777. https://doi.org/10.1021/jz300080p

20. Rümmeli MH, Rocha CG, Ortmann F, Ibrahim I, Sevincli H, Börrnert F, Meyyappan M (2011) Graphene: piecing it together. Adv Mater 23(39):4471–4490. https://doi.org/10.1002/adma.201101855

21. Novoselov KS, Geim AK, Morozov SV, Jiang D, Zhang Y, Dubonos SV, Firsov AA (2004) Electric field effect in atomically thin carbon films. Science 306(5696):666–669. https://doi.org/10.1126/science.1102896

22. Zhang Y, Small JP, Pontius WV, Kim P (2005) Fabrication and electric-field-dependent transport measurements of mesoscopic graphite devices. Appl Phys Lett 86(7):073104. https://doi.org/10.1063/1.1862334

23. Parvez K, Wu ZS, Li R, Liu X, Graf R, Feng X, Müllen K (2014) Exfoliation of graphite into graphene in aqueous solutions of inorganic salts. J Am Chem Soc 136(16):6083–6091. https://doi.org/10.1021/ja5017156

24. Berger C, Song Z, Li T, Li X, Ogbazghi AY, Feng R, De Heer WA (2004) Ultrathin epitaxial graphite: 2D electron gas properties and a route toward graphene-based nanoelectronics. J Phys Chem B 108(52):19912–19916. https://doi.org/10.1021/jp040650f

25. Mattevi C, Kim H, Chhowalla M (2011) A review of chemical vapor deposition of graphene on copper. J Mater Chem 21(10):3324–3334. https://doi.org/10.1039/C0JM02126A

26. Hummers Jr WS, Offeman RE (1958) Preparation of graphitic oxide. J Am Chem Soc 80 (6):1339. https://doi.org/10.1021/ja01539a017

27. Paulchamy B, Arthi G, Lignesh BD (2015) A simple approach to stepwise synthesis of graphene oxide nanomaterial. J Nanomedicine Nanotechnol 6(1):1. https://doi.org/10.4172/2157-7439.1000253

28. Perera SD, Mariano RG, Vu K, Nour N, Seitz O, Chabal Y, Balkus KJ Jr (2012) Hydrothermal synthesis of graphene-TiO2 nanotube composites with enhanced photocatalytic activity. ACS Catal 2(6):949–956. https://doi.org/10.1021/cs200621c

29. Berman D, Erdemir A, Sumant AV (2014) Graphene: a new emerging lubricant. Mater Today 17(1):31–42. https://doi.org/10.1016/j.mattod.2013.12.003

30. Kim KS, Lee HJ, Lee C, Lee SK, Jang H, Ahn JH, Kim JH, Lee HJ (2011) Chemical vapor deposition-grown graphene: the thinnest solid lubricant. ACS Nano 5(6):5107–5114. https://doi.org/10.1021/nn2011865

31. Kim HJ, Yoo SS, Kim DE (2012) Nano-scale wear a review. Int J Precis Eng Manuf 13 (9):1709–1718. https://doi.org/10.1007/s12541-012-0224-y

32. Shin YJ, Stromberg R, Nay R, Huang H, Wee AT, Yang H, Bhatia CS (2011) Frictional characteristics of exfoliated and epitaxial graphene. Carbon 49(12):4070–4073. https://doi.org/10.1016/j.carbon.2011.05.046

33. Won MS, Penkov OV, Kim DE (2013) Durability and degradation mechanism of graphene coatings deposited on Cu substrates under dry contact sliding. Carbon 54:472–481. https://doi.org/10.1016/j.carbon.2012.12.007

34. Yan C, Kim KS, Lee SK, Bae SH, Hong BH, Kim JH, Ahn JH (2011) Mechanical and environmental stability of polymer thin-film-coated graphene. ACS Nano 6(3):2096–2103. https://doi.org/10.1021/nn203923n

35. Berman D, Erdemir A, Sumant AV (2013) Few-layer graphene to reduce wear and friction on sliding steel surfaces. Carbon 54:454–459. https://doi.org/10.1016/j.carbon.2012.11.061

36. Berman D, Erdemir A, Sumant AV (2013) Reduced wear and friction enabled by graphene layers on sliding steel surfaces in dry nitrogen. Carbon 59:167–175. https://doi.org/10.1016/j.carbon.2013.03.006

37. Tai Z, Chen Y, An Y, Yan X, Xue Q (2012) Tribological behavior of UHMWPE reinforced with graphene oxide nanosheets. Tribol Lett 46(1):55–63. https://doi.org/10.1007/s11249-012-9919-6

38. Min C, Nie P, Song HJ, Zhang Z, Zhao K (2014) Study of tribological properties of polyimide/graphene oxide nanocomposite films under seawater-lubricated condition. Tribol Int 80:131–140. https://doi.org/10.1016/j.triboint.2014.06.022

39. Zhu Q, Shi X, Zhai W, Yao J, Ibrahim AMM, Xu Z, Zhang Q (2014) Effect of counterface balls on the friction layer of Ni3Al matrix composites with 1.5 wt% graphene nanoplatelets. Tribol Lett 55(2):343–352. https://doi.org/10.1007/s11249-014-0362-8

40. Yao J, Shi X, Zhai W, Ibrahim AMM, Xu Z, Chen L, Wang Z (2014) The enhanced tribological properties of NiAlintermetallics: combined lubrication of multilayer graphene and WS2. Tribol Lett 56(3):573–582. https://doi.org/10.1007/s11249-014-0439-4

41. Gutierrez-Gonzalez CF, Smirnov A, Centeno A, Fernández A, Alonso B, Rocha VG, Bartolome JF (2015) Wear behavior of graphene/alumina composite. Ceram Int 41(6):7434–7438. https://doi.org/10.1016/j.ceramint.2015.02.061

42. Yazdani B, Xu F, Ahmad I, Hou X, Xia Y, Zhu Y (2015) Tribological performance of Graphene/Carbon nanotube hybrid reinforced Al2O3 composites. Sci Rep 5:11579. https://doi.org/10.1038/srep11579

43. Llorente J, Román-Manso B, Miranzo P, Belmonte M (2016) Tribological performance under dry sliding conditions of graphene/silicon carbide composites. J Eur Ceram Soc 36(3):429–435. https://doi.org/10.1016/j.jeurceramsoc.2015.09.040

44. Kalin M, Zalaznik M, Novak S (2015) Wear and friction behavior of poly-ether-ether-ketone (PEEK) filled with graphene, WS 2 and CNT nanoparticles. Wear 332:855–862. https://doi.org/10.1016/j.wear.2014.12.036

45. Tabandeh-Khorshid M, Omrani E, Menezes PL, Rohatgi PK (2016) Tribological performance of self-lubricating aluminum matrix nanocomposites: the role of graphene nanoplatelets. Eng Sci Technol Int J 19(1):463–469. https://doi.org/10.1016/j.jestch.2015.09.005

46. Belmonte M, Ramírez C, González-Julián J, Schneider J, Miranzo P, Osendi MI (2013) The beneficial effect of graphene nanofillers on the tribological performance of ceramics. Carbon 61:431–435. https://doi.org/10.1016/j.carbon.2013.04.102

47. Xu Z, Zhang Q, Jing P, Zhai W (2015) High-temperature tribological performance of TiAl matrix composites reinforced by multilayer graphene. Tribol Lett 58(1):3. https://doi.org/10.1007/s11249-015-0482-9

48. Lin J, Wang L, Chen G (2011) Modification of graphene platelets and their tribological properties as a lubricant additive. Tribol Lett 41(1):209–215. https://doi.org/10.1007/s11249-010-9702-5
49. Senatore A, D'Agostino V, Petrone V, Ciambelli P, Sarno M (2013) Graphene oxide nanosheets as an effective friction modifier for oil lubricant: materials, methods, and tribological results. ISRN Tribol. https://doi.org/10.5402/2013/425809
50. Chen Z, Liu X, Liu Y, Gunsel S, Luo J (2015) Ultrathin MoS 2 nanosheets with superior extreme pressure property as boundary lubricants. Sci Rep 5:12869. https://doi.org/10.1038/srep12869
51. Dou X, Koltonow AR, He X, Jang HD, Wang Q, Chung YW, Huang J (2016) Self-dispersed crumpled graphene balls in oil for friction and wear reduction. Proc Natl Acad Sci 113 (6):1528–1533. https://doi.org/10.1073/pnas.1520994113
52. Azman SSN, Zulkifli NWM, Masjuki H, Gulzar M, Zahid R (2016) Study of tribological properties of lubricating oil blend added with graphene nanoplatelets. J Mater Res 31 (13):1932–1938. https://doi.org/10.1557/jmr.2016.24
53. Meng Y, Su F, Chen Y (2016) Supercritical fluid synthesis and tribological applications of silver nanoparticle-decorated graphene in engine oil nanofluid. Sci Rep 6. https://doi.org/10.1038/srep31246
54. Rasheed AK, Khalid M, Javeed A, Rashmi W, Gupta TCSM, Chan A (2016) Heat transfer and tribological performance of graphene nano lubricant in an internal combustion engine. Tribol Int 103:504–515. https://doi.org/10.1016/j.triboint.2016.08.007
55. Zhang W, Zhou M, Zhu H, Tian Y, Wang K, Wei J, Wu D (2011) Tribological properties of oleic acid-modified graphene as lubricant oil additives. J Phys D Appl Phys 44(20):205303. https://doi.org/10.1088/0022-3727/44/20/205303
56. Kinoshita H, Nishina Y, Alias AA, Fujii M (2014) Tribological properties of monolayer graphene oxide sheets as water-based lubricant additives. Carbon 66:720–723. https://doi.org/10.1016/j.carbon.2013.08.045
57. Eswaraiah V, Sankaranarayanan V, Ramaprabhu S (2011) Graphene-based engine oil nanofluids for tribological applications. ACS Appl Mater Interfaces 3(11):4221–4227. https://doi.org/10.1021/am200851z
58. Donnet C, Erdemir A (2004) Solid lubricant coatings: recent developments and future trends. Tribol Lett 17(3):389–397. https://doi.org/10.1023/B:TRIL.0000044487.32514.1d
59. Scharf TW, Prasad SV (2013) Solid lubricants: a review. J Mater Sci 48(2):511–531. https://doi.org/10.1007/s10853-012-7038-2

Experimental, Computational, and Chemical Kinetic Analysis to Compare the Flame Structure of Methane-Air with Biogas–H$_2$–Air

Vinod Kumar Yadav, A. R. Khan, Shriyansh Srivastava and Vinay Yadav

Abstract This paper presents a numerical and experimental investigation of the laminar burning velocity and flame structure of methane, biogas, and hydrogen-enriched biogas. Experiments were performed on flat flame burners based on heat flux method, and numerical computations for the flame structure were conducted over the same burner using three-dimensional CFD simulations with DRM19 detailed chemistry. To get deeper insight of chemical reactions, sensitivity analysis of the studied mixtures was also conducted using ANSYS Chemkin-Pro® with GRI-Mech. 3.0 reaction mechanism. All experiments and numerical simulations were conducted at 1 atm and 298 K. The experimental results show that the laminar burning velocity of the methane-air mixture reduced by 47% when diluted with 50% carbon dioxide. On the other hand, 40% hydrogen addition in the biogas-air mixture (containing 30% methane + 30% carbon dioxide), enhanced the laminar burning velocity by 117% compared to pure biogas-air mixture at stoichiometry. The three-dimensional CFD computational results predicted a 580 K drop in temperature, 32% reduction in CH$_3$ concentration, and 30% reduction in CO concentration for methane, when diluted with 50% carbon dioxide. Chemical kinetic analysis of methane-air, biogas-air, and 40% hydrogen-enriched biogas-air mixture predicted H + O$_2$↔O + OH (R38) and H + CH$_3$(+M)↔CH$_4$(+M) (R52) to be most dominant reactions with positive and negative sensitivity coefficients, respectively. However, the dominance of these reactions were significantly higher in hydrogen-enriched biogas-air mixture compared to pure methane-air mixture due to the increased production of OH/H radicals in the reaction zone.

V. K. Yadav (✉)
G. L. Bajaj Institute of Technology and Management, Greater Noida 201306, India
e-mail: yadavvinod2004@gmail.com

V. K. Yadav · A. R. Khan
Department of Mechanical Engineering, Indian Institute of Technology Delhi,
New Delhi, India

S. Srivastava · V. Yadav
Department of Mechanical Engineering, G. L. Bajaj Institute of Technology
and Management, Greater Noida, India

259

1 Introduction

About 78% of the total GHG (Greenhouse gas) emissions rise from early 70's to 2010 was due to (CO_2) CO2 emissions emitted from combustion devices and industrial processes [1]. India strives to reduce the CO_2 level per unit economic activity. Biogas as an alternative fuel can play a major role in achieving this goal. Biogases, primarily containing methane (CH_4) and carbon dioxide (CO_2), are outcomes of anaerobic digestion of compost, wastes and organic derivatives from various natural resources. Biogas can be a good substitute for conventional fuel and may prove to be suitable for various domestic, industrial, and automotive applications. However, the low calorific value of biogas makes it inferior and degrades its combustion characteristics. Hence, it is not possible to replace the biogas with conventional fuel directly. The remedy to this problem is the enrichment of the biogas with hydrogen (H_2). To analyze the combustion characteristics of hydrogen-enriched biogas fuel, the Laminar burning velocity (LBV) is an essential parameter. LBV plays a key role in validating the chemical kinetics of any fuel. The studies [4–7] reported a reduction in LBV, reactivity and flame temperature due to the presence of CO_2 in biogas. CO_2 reduces the LBV by thermal, dilution and chemical effect [8]. The adverse effect of CO_2 presence in any fuel can be reduced by enriching it with high-grade fuels like hydrogen [9–14]. Many researchers have numerically studied the flame structures of methane and biogas using one-dimensional (1D) or two-dimensional (2D) numerical simulations [15–19]. However, actual flames can be modeled more realistically using three-dimensional (3D) simulations [20]. The objective of the present work is to experimentally determine the effect of CO_2 dilution and H_2 enrichment on the laminar burning velocity of CH_4-air and biogas-air mixtures, respectively. Additionally, 3D numerical simulations on the heat-flux burner are conducted to study the flame structure of aforementioned fuels. Furthermore, the chemical kinetic analysis is conducted to understand the role of important chemical reactions. The experimental and numerical analysis in this paper utilized 50% CO_2 diluted CH_4 representing one of the compositions of biogas and are also used by other groups [4–7, 21].

2 Methodology

Heat flux method (HFM) generating flat flames, proposed by De Goey et al. [2], modified by Bosschaart et al. [22] and used by many researchers [4, 7, 19, 23] was used in the present work for experimental measurements. The uncertainty associated with the heat flux method lies within ± 1 cm/s [3]. The detailed specifications of HFM can be referred from [2, 4, 19, 22, 23]. Here only a short description of the
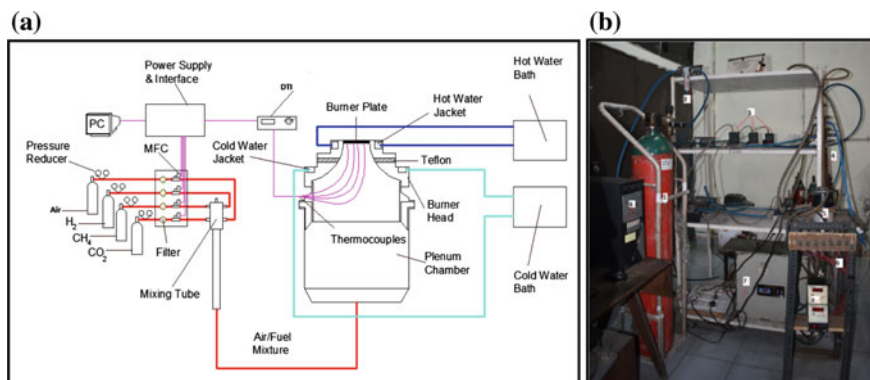
Fig. 1 **a** Schematic of the heat flux setup **b** Experimental setup based on heat flux method

setup is provided. The HFM has a burner drilled with 0.5 mm hole and 0.7 mm pitch (center to center distance). The plate, made of brass, has diameter and thickness of 30 mm and 2 mm respectively. Five K-type chromel-alumel thermocouples of 0.3 mm bead size are used to measure the plate temperature using a digital temperature indicator. A hot thermostatic bath containing warm water maintains the burner plate at 358 K. This ensures the minimization of the heat loss from the flame to the plate as desired by the HFM principle [22]. Figure 1a shows the setup schematic and Fig. 1b shows the experimental facility developed for LBV measurement of gaseous fuels.

2.1 Numerical Modeling

Chemical kinetic analysis, the burner stabilized flame module of ANSYS Chemkin-Pro® [24] is used to simulate 1D, unstretched and premixed flame. ANSYS Chemkin-Pro® solves equations of state, thermodynamic properties, and species production rates [24] under steady-state assumption. After grid convergence test, the following parameters were set for simulations: Grid points = 1000; Adaptive grid parameters: Grad 0.025, Curv 0.1; Soret effect; Multicomponent diffusion. GRI-Mech. 3.0 [25] with 53 species and 325 reversible reactions suitable for C1–C3 hydro-carbons was chosen to simulate 1D flames.

3D simulations of flat burner stabilized flames. The burner stabilized laminar premixed flames of the fuel-oxidizer mixture, used in present work, are simulated with DRM19 detailed (19 species and 84 reversible reactions) chemistry [31]. The flat burner plate used for experiments, made of brass with a hole diameter of 0.5 mm and pitch 0.7 mm was modeled with a domain having four side symmetry (Fig. 2). The cross-section of the rectangle extracted out of the plate (ABCD), forming the symmetry is shown at the bottom left of Fig. 2 with detailed
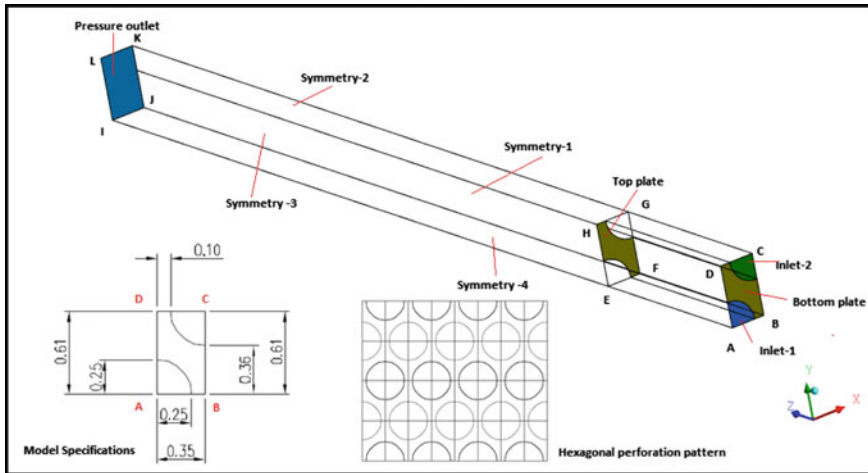
Fig. 2 Computational domain, specifications and boundary conditions for 3D simulations

specifications. ANSYS Fluent [26] solves 3D governing equations for mass, momentum, and energy conservations. Pressure-based numerical solver, with double precision, segregated solver using an implicit method for solving discretized set of algebraic equations was used. The laminar finite rate viscous model with a second-order upwind scheme for all governing equations was used. The 3D mesh was created using ANSYS® ICEM.

Boundary conditions, the premixed fuel-air mixture enters with uniform velocity through two inlets (Inlet-1 and Inlet-2) provided in the plate (Fig. 2). The species mass fractions and temperatures were set at these two inlets. The plate with thickness (CG) 2 mm was modeled. The length of the outer domain (GK) is kept 8 mm above the top burner plate (EFGH). The outlet of the domain (IJKL) was provided with pressure outlet boundary condition. The gauge pressure, air temperature and the oxygen mass fraction was specified at the pressure outlet. The four faces of the rectangle (BCKJ, CDKL, ADLI, and ABJI) represent the symmetry of the model which when extracted will lead to a hexagonal perforation pattern as shown at the bottom right of the Fig. 2. Cold flow simulations with the good convergence of governing equations up to 10-6 were ensured at the beginning. Then, the fuel-air mixture was ignited by patching a local region above the burner top to 2000 K. The solution was run with low under-relaxation factor (species 0.3, energy 0.1) for 10000–12000 iterations. After identifying the flame, the under-relaxation factors were set to 0.5 and 0.3 for species and energy, respectively. The grid independence test was conducted to obtain grid independent solutions. All 3D computations were performed at 1 atm and 298 K, similar to experiments. The corresponding measured LBVs were provided at velocity inlet boundary conditions.

3   Results and Discussions

The experiments were conducted at 298 $\pm$ 1 K temperature, and 1-atm using HFM. The maximum calculated uncertainty for the present setup with 95% confidence interval was $\pm$ 1 cm/s. Figure 3a shows the measured LBV of CH_4-air mixture as a function of equivalence ratio (ϕ). The present results agree well with the results available in the literatures [23, 28–30]. Further, the numerical predictions of ANSYS Chemkin-Pro[®] [24] using GRI-Mech. 3.0 [25] is also in good agreement at most of the equivalence ratios. Figure 3b presents the experimental results of CH_4-air, CH_4 diluted with 50% CO_2 (representing biogas)-air and, 20 and 40% H_2-enriched biogas-air (with $CH_4/CO_2 = 1$). For biogas-air mixtures, a consistent decrease in the LBV at all equivalence ratios can be observed. At stoichiometry, the LBV of biogas-air mixture decreased by about 47% compared to CH_4-air. This is due to the dilution, chemical and thermal effect of CO_2 [8, 27]. When the same biogas (with $CH_4/CO_2 = 1$), was enriched with 20 and 40% H_2, an increase in LBV at all equivalence ratios was observed. This was due to the increased H_2 concentration that had resulted in an increase in LBV. Furthermore, the effect of H_2 enrichment is more prominent for the rich fuel-air mixture compared to leaner and stoichiometric mixtures. In addition, the increased H_2 concentration in the biogas blends had shifted the peak LBV from $\phi = 1.0$ to 1.1. About 117% rise in the LBV of the biogas-H_2 fuel containing 40% H_2, compared to the base biogas-air mixture, was observed.

To understand the chemistry behind an appreciable rise in LBV due to H_2 enrichment, the sensitivity analysis of CH_4-air, biogas (50% CH_4 + 50% CO_2)-air, and 40% H_2-enriched biogas-air was conducted using ANSYS Chemkin-Pro with GRI-Mech. 3.0 and results were plotted in Fig. 4a (at $\phi = 1.0$). The normalized sensitivity coefficients of seven common reactions which are among the top most sensitive reactions for selected fuel blends were considered for analysis. For the biogas-air mixture, the most dominant chain branching reaction producing O and OH radicals is R38: $H + O_2 \leftrightarrow O + OH$. However, R52: $H + CH_3$ (+M) $\leftrightarrow CH_4$
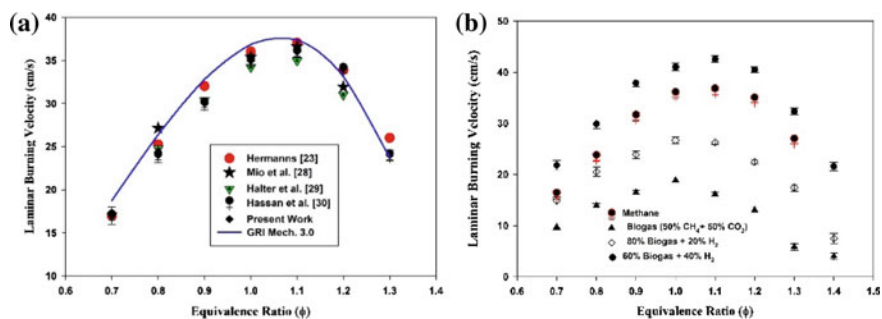
Fig. 3 Measured LBV as a function of equivalence ratio at 1 atm and 298 K for **a** CH_4-air mixture compared to literature and numerically predicted results **b** CH_4-air, Biogas-air and H_2-enriched biogas-air

(+M), that consumes H radical was most sensitive in the negative direction. On the other hand, with 40% H_2-enrichment, the normalized sensitivity coefficients of reactions R38 and R52 further decreased, due to enhanced creation of H radical, thereby minimizing the effect of CO_2 dilution.

For a better and in-depth understanding of the flame structure of the used fuel blends, 3D computations were conducted using ANSYS Fluent [26] with DRM19 detailed chemistry [31]. All simulations were conducted at 1 atm and 298 K.

Sensitivity analysis predicted that H plays an important role in LBV, hence, H radical profile of all fuels was compared. The 3D computational results with DRM19 chemistry, along a vertical line, at the center of one of the inlets, is plotted in Fig. 4b. It can be observed that the mole fraction of H radical is highest for biogas containing 40% H_2 and is minimum for biogas (50%CH_4 + 50%CO_2). Due to increased production of H for H_2-enriched fuels, the sensitivity of R38 and R52 have shown a decreasing trend (Fig. 4a). Figure 5a–c compares the flame structure and temperature profiles of CH_4-air, biogas (50%CH_4 + 50%$CO2_2$-air and (30% CH_4–30%CO_2–40%H_2)-air mixtures. It can be depicted from Fig. 5a–c that the point where CH_4 diminishes, the CO peaks. CH_4 concentration reaches zero at 0.2, 0.6, and 0.3 mm for CH_4-air, 50%CO_2 diluted CH_4 (biogas)-air and 40% H_2-enriched (30%CH_4–30%CO_2), respectively, after the mixture leaves the top surface of the burner. An axial distance of 0.002 m corresponds to burner top surface in Fig. 5a–d. The delay in CH_4 consumption for 50% CO_2 diluted CH_4 (biogas)-air mixture (Fig. 5b) signifies the thickening of the reaction zone, compared to pure CH_4-air mixture (Fig. 5a). However, the delay and thickening effects are reduced due to the presence of H_2 (Fig. 5c). For CH_4-air flame, the pre-flame reactions start immediately after passing through the burner rim and become rapid with an increase in temperature. Hence, the consumption of the CH_4 is faster in CH_4-air flame as compared to a biogas-air flame. Further, with 50% CO_2 diluted CH_4, the flame temperature drops by about 580 K compared to pure CH_4-air mixture.
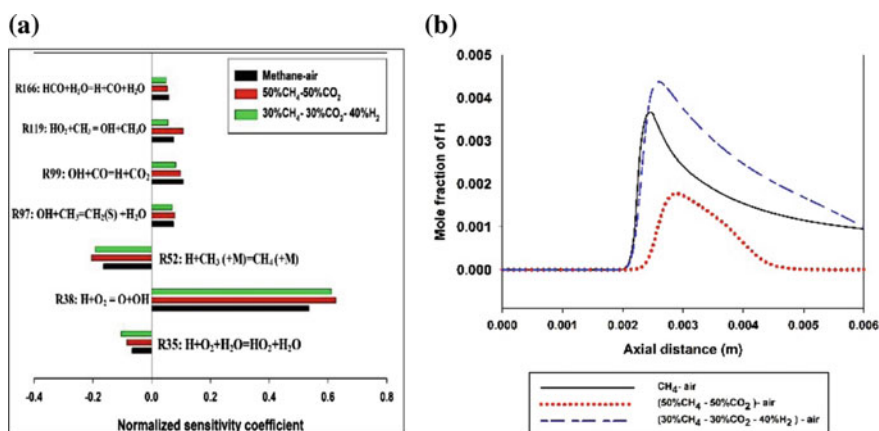
Fig. 4 a Normalized sensitivity coefficients (1D results) b Mole fraction of H (3D results)
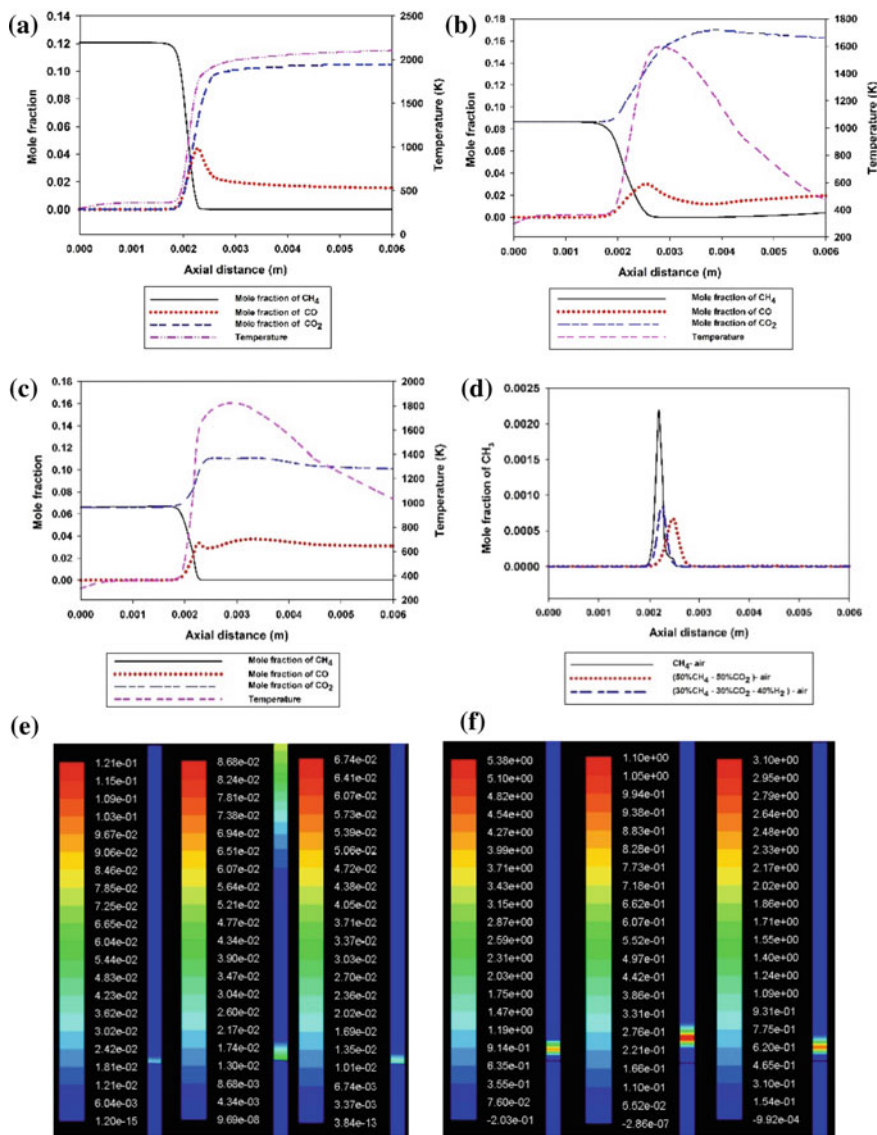
Fig. 5 Fluent 3D numerical predictions **a** CH$_4$-air mole fraction **b** Biogas-air mole fraction **c** 40% H$_2$-enriched biogas-air mole fraction **d** CH$_3$ mole fraction comparison (three fuels) **e** CH$_4$ mol fraction contour comparison (three fuels: left-CH$_4$-air, mid-Biogas-air, right–40% H$_2$ enriched biogas-air) **f** Kinetic reaction rate of R22 comparison (three fuels: left-CH$_4$-air, mid-Biogas-air, right–40% H$_2$ enriched biogas-air). All computations are conducted with DRM19 at 1 atm and 298 K

This drop in temperature affects the reactivity of the mixture and had resulted in thickening of the reaction zone. The peak mole fraction of CH_3, the first intermediate formed when CH_4 is attacked by H and OH, decreased by about 32% when CH_4 was diluted with 50% CO_2 (Fig. 5d). This may be attributed to the delayed formation of H radical (Fig. 4b), which has its peak at 0.4 mm above the burner top for CH_4-air mixture and 0.9 mm above the burner top for 50% CO_2 diluted CH_4-air mixture. Further, 50% CO_2 concentration in CH_4, decreased the CO production for biogas-air mixtures compared to pure CH_4-air mixture by about 30%. The CH_4 mol fraction contour, and kinetic reaction rate contours are plotted in Fig. 5e and Fig. 5f respectively. Figure 5e demonstrates the delay in consumption of CH_4 for the biogas-air flame (mid contour) compared to CH_4-air Flame (left contour). This indicates that the flame had appeared closer to the burner top surface for CH_4-air mixtures. However, with 40% H_2 enrichment, the concentrations return back towards CH_4-air type flames. From Fig. 5f, a clear lifting of biogas-air flame (mid contour) can be observed over the burner rim compared to CH_4-air flame (left contour). The reaction rate contour of the H_2 enriched fuel, analogous to CH_4 mol fraction contour, lies between stoichiometric CH_4 and biogas flames. 1D sensitivity analysis with ANSYS Chemkin-Pro with GRI 3.0 and DRM19 reaction mechanisms predicted $H + O_2 \leftrightarrow O + OH$ (R38 for GRI or R22 for DRM19) as the top chain branching reaction for all the studied mixtures. The kinetic reaction rate (of R38 or R22) determined through three-dimensional CFD analysis revealed that the reactivity of pure CH_4-air mixture decreased by about five times when diluted with 50% CO_2 (Fig. 5f). The results indicated that the presence of CO_2 in biogas fuel decreases LBV, flame temperature, mixture reactivity and increases the thickness of the reaction zone. However, these adverse effects may be minimized by H_2 enrichment.

4 Conclusions

Based on the experimental and computational investigation of combustion characteristics and flame structure of methane-air, biogas (containing 50% CO_2)-air, and biogas enriched with 40% H_2-air, over a flat flame burner, the following conclusions were drawn.

The presence of CO_2 in biogas fuel results in decreased flame temperature. As a consequence, the flame reactions become slow resulting in decreased laminar burning velocity and increased reaction zone thickness.

The LBV of CH_4, when diluted with 50% CO_2, decreased by about 47%. However, when the biogas mixture (containing 50% CO_2) is enriched with 40% H_2, about 117% rise in LBV of biogas is observed. Further, with the addition of H_2 in biogas, the peak LBV shifted from $\phi = 1.0$ to 1.1.

The reactions R38: $H + O_2 \leftrightarrow O + OH$ and R52: $H + CH_3 (+M) \leftrightarrow CH4 (+M)$ are most dominant reactions with positive and negative normalized sensitivity coefficients, respectively. With 50% CO_2 dilution in CH_4, the magnitude of these

reactions increased in their respective directions. However, with 40% H_2 addition in biogas, the normalized sensitivity coefficients of these fuels exhibited a decreasing trend due to enhanced production of H.

The results of the present work are useful in understanding the flame structure of CH_4-air and biogas-air mixtures. Also, the inferences of the present work can be used by the I.C. engine researchers to prepare an H_2-enriched biogas fuel that may be a good substitute for natural gas with lesser emissions.

References

1. Pachauri RK (2014) Climate Change 2014 Synthesis Report: Intergovernmental Panel on Climate Change. http://www.ipcc.ch/report/ar5/syr/. Accessed 05 Mar 2018
2. De Goey LPH, Maaren AV, Quax RM (1993) Stabilization of adiabatic premixed laminar flames on flat flame burner. Combust Sci Technol 92:201–207. https://doi.org/10.1080/00102209308907668
3. Alekseev VA, Jenny DN, Moah C, Elna JK, Nilsson Evgeniy NV, De Goey LPH, Konnov AA (2016) Experimental uncertainties of the heat flux method for measuring burning velocities. Combust Sci Technol 188.6:853–894. https://doi.org/10.1080/00102202.2015.1125348
4. Kishore VR, Ravi MR, Ray A (2011) Adiabatic burning velocity and cellular flame characteristics of H_2–CO–CO_2–air mixtures. Combust Flame 158:2149–2164. https://doi.org/10.1016/j.combustflame.2011.03.018
5. Nonaka HOB, Pereira FM (2016) Experimental and numerical study of CO_2 content effects on the laminar burning velocity of biogas. Fuel 182:382–390. https://doi.org/10.1016/j.fuel.2016.05.098
6. Liu C, Yan B, Chen G, Bai XS (2010) Structures and burning velocity of biomass derived gas flames. Int J Hydrog Energy 35:542–555. https://doi.org/10.1016/j.ijhydene.2009.11.020
7. Hinton N, Stone R (2014) Laminar burning velocity measurements of methane and carbon dioxide mixtures (biogas) over wide ranging temperatures and pressures. Fuel 116:743–750. https://doi.org/10.1016/j.fuel.2013.08.069
8. Hu E, Jiang X, Huang Z, Lida N (2012) Numerical study on the effects of diluents on the laminar burning velocity of methane-Air Mixtures. Energy Fuels 26(7):4242–4252. https://doi.org/10.1021/ef300535s
9. Zhen HS, Leung CW, Cheung CS, Huang ZH (2016) Combustion characteristic and heating performance of stoichiometric biogas–hydrogen–air flame. Int J Heat Mass Transfer 92:807–814. https://doi.org/10.1016/j.ijheatmasstransfer.2015.09.040
10. Chen Z, Tang C, Fu J, Jiang X, Li Q, Wei L, Huang Z (2012) Experimental and numerical investigation on diluted DME flames. Thermal and chemical kinetic effects on laminar flame speed. Fuel 102:567–573. https://doi.org/10.1016/j.fuel.2012.06.003
11. Leung T, Wierzba I (2008) The effect of hydrogen addition on biogas non-premixed jet flame stability in a co-flowing air stream. Int J Hydrog Energy 33:3856–3862. https://doi.org/10.1016/j.ijhydene.2008.04.030
12. Pizzuti L, Martins CA, Lacava PT (2016) Laminar burning velocity and flammability limits in biogas: a literature review. Renew Sust Energy Rev 62:856–865. https://doi.org/10.1016/j.rser.2016.05.011
13. Chandra R, Vijay VK, Subbarao PMV, Khura TK (2011) Performance evaluation of a constant speed I C engine on CNG, methane enriched biogas and biogas. Appl Energy 88:3969–3977. https://doi.org/10.1016/j.apenergy.2011.04.032

14. Subramanian KA, Mathad VC, Vijay VK, Subbarao PMV (2013) Comparative evaluation of emission and fuel economy of an automotive spark ignition vehicle fuelled with methane enriched biogas and CNG using chassis dynamometer. Appl Energy 105:17–29. https://doi.org/10.1016/j.apenergy.2012.12.011

15. Maaren V, Thung DS, de Goey LPH (1994) Measurement of flame temperature and adiabatic burning velocity of ethane/air mixtures. Combust Sci Technol 96:327–344. https://doi.org/10.1080/00102209408935360

16. De Goey LPH, Bosch WMML, Somers LMT, Mallens RMM (1995) Modeling of the small scale structure of flat burner-stabilized flames. Combust Sci Technol 104:387–400. https://doi.org/10.1080/00102209508907729

17. Maaren V (1994) One step chemical reaction parameters for premixed laminar flames. Ph. D thesis, Eindhoven University of Technology. https://doi.org/10.6100/ir417400

18. Konnov AA, Riemeijer R, Kornilov VN, de Goey LPH (2013) 2D effects in laminar premixed flames stabilized on a flat flame burner. Exp Therm Fluid Sci 47:213–223. https://doi.org/10.1016/j.expthermflusci.2013.02.002

19. Goswami M, Derks S, Coumans K, Slikker WJ, de Andrade OMH, Bastiaans RJM, Konnov AA, de Goey LPH (2013) The effect of elevated pressures on the laminar burning velocity of methane + air mixtures. Combust Flame 160:1627–1635. https://doi.org/10.1016/j.combustflame.2013.03.032

20. Jithin EV, Kishore VR, Varghese RJ (2014) Three-dimensional simulations of steady perforated-plate stabilized propane-air premixed flames. Energy Fuels 28:5415–5425. https://doi.org/10.1021/ef401903y

21. Park O, Veloo PS, Liu N, Egolfopolous FN (2010) Combustion characteristics of alternative gaseous fuels. Proc Comb Inst 33:887–894. https://doi.org/10.1016/j.proci.2010.06.116

22. Bosschaart KJ, de Goey LPH (2003) Detailed analysis of heat flux method for measuring burning velocities. Combust Flame 132:170–180. https://doi.org/10.1016/S0010-2180(02)00433-9

23. Hermanns RTE (2007) Laminar burning velocities of methane-hydrogen-air mixtures. Ph. D thesis, Eindhoven University of Technology. https://doi.org/10.6100/ir630126

24. ANSYS Chemkin-Pro® Release 17.0 (Chemkin-Pro 15151) ANSYS, Inc. (2016-01-11)

25. Smith GP, Golden DM, Frenklach M, Moriarty NW, Eiteneer B, Goldenberg M, Bowman CT, Hanson RK, Song S, Gardiner WC, Lissianski VV, Qin Z

26. http//www.me.berkeley.edu/gri_mech/data/nasa_plnm.html. Accessed 05 Aug 2017

27. ANSYS Fluent Release 17.2. ANSYS, Inc. USA. (ANSYS R17.2 Academic)

28. Lee K, Kim H, Park P, Yang S, Ko Y (2013) CO_2 radiation heat loss effects on NOx emissions and combustion instabilities in lean premixed flames. Fuel 106:682–689. https://doi.org/10.1016/j.fuel.2012.12.048

29. Miao H, Liu Y (2014) Measuring the laminar burning velocity and Markstein length of premixed methane/nitrogen/air mixtures with the consideration of nonlinear stretch effects. Fuel 121:208–215. https://doi.org/10.1016/j.fuel.2013.12.039

30. Halter F, Tahtouh T, Rousselle CM (2010) Nonlinear effects of stretch on the flame front propagation. Combust Flame 157:1825–1832. https://doi.org/10.1016/j.combustflame.2010.05.013

31. Kazakov, A., Frenklach, M.: DRM19/ DRM22 reaction mechanisms. http://www.me.berkeley.edu/drm/. Accessed 22 Mar 2018

A Comparative Study for Transmission Efficiency of ABS, POM, and HDPE Spur Gears

Akant Kumar Singh[ID]**, Siddhartha**[ID]**, Sanjay Yadav**[ID]
and Prashant Kumar Singh[ID]

Abstract Application of polymer gears is increasing due to some of their inherent properties. Nowadays, polymer gears are replacing metal gears in various applications. They have less weight, lower inertia, and run much quieter in comparison to metal gears. In this work, the transmission efficiency of polymer gears running at different speed (600, 800, 1000, and 1200 rpm) and torque (0.8, 1.2, 1.6, and 2 Nm) are studied. Three different thermoplastic materials viz. Acrylonitrile Butadiene Styrene (ABS), Polyoxymethylene (POM), and High-Density Polyethylene (HDPE) are used to fabricate polymer gears using injection molding machine. Gears are operated for 1.2×10^5 cycles to investigate the transmission efficiency. The experiments are carried out using a power absorption type polymer gear test rig. It is concluded from this work that transmission efficiency of these polymer gears is significantly affected by torque. Speed has less significant effect on transmission efficiency of polymer gears.

Keywords Polymer gears · Polymer gear test rig · Transmission efficiency

1 Introduction

Plastics gears are found today in both commercial and precisiontype applications to transfer the motion and power. Transmission efficiency is an important parameter for power and motion transmission applications. The overall mechanical system efficiency in some power transmission applications is improved by using the plastic gears [1]. Plastic gears are used in various applications nowadays. However, the transmission efficiency of polymer gears has not been investigated much so far.

A. K. Singh (✉) · Siddhartha · P. K. Singh
Department of Mechanical Engineering, NIT Hamirpur, Hamirpur 177005, HP, India
e-mail: akant.nith@gmail.com

S. Yadav
Department of Mechanical Engineering, I.T.S Engineering College,
Greater Noida 201308, India

Walton et al. [2, 3] observed that speed and loads are the key factors that significantly affect the transmission efficiency of polymer gears. They investigated the effect of different materials and geometries on the transmission efficiency of polymer gear pairs.

Many researchers are working on polymer gears since the last decade [4]. Senthilvelan and Gnanamoorthy [5] investigated the efficiency of polymer gears and found that carbon fiber filled composite gear performed better than neat gears due to its enhanced gear tooth stiffness and thermal characteristics. Transmission efficiency of polymer gears is also improved with the addition of nanoclay particles [6]. Transmission efficiency of polymer gears is improved about 2% by using compressed air cooling at the mating surface of master and test gears [7]. Rayudu and Nagarajan [8] studied the effect of gear wear and tooth deformation on the transmission efficiency of plastic gear. Luscher et al. [9] studied the transmission error and geometry of polyketone gears in which transmission efficiency and effect of packing pressure on gear run out is studied. Mertens and Senthilvelan [10] investigated the surface durability of injection-molded carbon nanotube–polypropylene spur gears and found that inclusion of carbon nanotube improved the efficiency of plastic gears. Experimental and numerical evaluation of transmission characteristics of polymer spur gears are done by Kodeeswaran et al. [11]

Wear and thermal resistance of polymer gear tooth is increased with the reinforcement of fibers in polymer gear material [12–14]. However, fiber-reinforced composite gears also has better transmission efficiency [2, 5]. Damping capability of polymer gears is reduced with the reinforcement of glass fibers and noise emission is also increased [15]. Singh and Siddhartha [16] fabricated the functionally graded materials (FGMs) gears through a novel fabrication technique. The transmission efficiency of FGM gears are found better than the conventional polymer gears. Transmission efficiency has been investigated for different material based polymer gears. However, authors found that transmission efficiency has not been investigated for gears fabricated with ABS, POM, and HDPE materials. Therefore, the focus of this investigation is to develop ABS, POM, and HDPE based polymer gears and compare their transmission efficiency.

2 Materials and Method

2.1 Gear Fabrication

Polymer gears are fabricated using injection molding process. ABS, HDPE, and POM polymer materials are used to fabricate the polymer gears. ABS, HDPE, and POM materials are heated at 80 °C, 60 °C, and 90 °C, respectively, in a dryer for 4 h to remove the moisture. Gears are fabricated at the injection pressure of 50 MPa for ABS, 60 MPa for HDPE and 70 MPa for POM. Injection-molded gears are shown in Fig. 1.
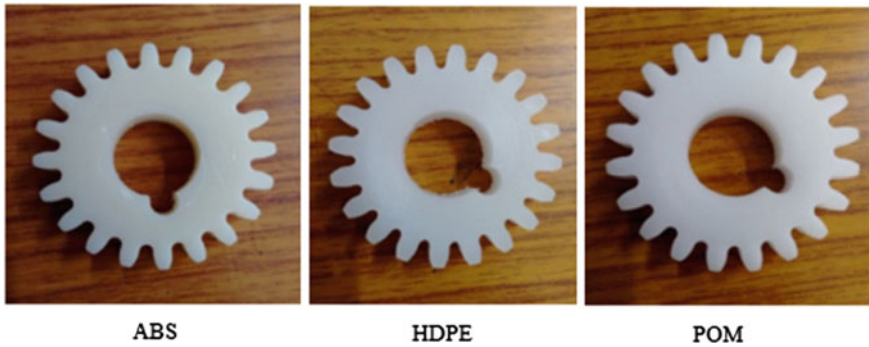
Fig. 1 Injection-molded polymer gears

2.2 Polymer Gear Test Rig

A gear test rig (CM-9108) has been used for the testing of the polymer gears. This test rig is fabricated by the DUCOM Instruments, India. Figure 2 shows a complete arrangement of gear test rig. Each polymer gear meshes with a metal gear having same design specifications. Polymer gear is placed on a shaft attached to a DC motor while the metal gear shaft is driven by an AC motor. The AC motor is able to run at any speed up to 1500 rpm. Test gears (Polymer gears) are loaded by applying the load on DC motor with the help of a rheostat. The torque acting on both the gears (polymer and metal) is measured by torque sensors with an accuracy of $\pm$ 0.2%. The temperature fluctuations during each test were continuously monitored by a non-contact type infrared sensor (make: OMEGA; model: OS 100EV2–Series) fixed

Fig. 2 Polymer gear test rig

vertically on an acrylic chamber above the mating surface of gears. The infrared sensor can measure the temperature from ambient to 130 °C with least count of 1 °C. Accuracy of the infrared sensor is $1 \pm 1\%$ measured value in °C. Testing of polymer gears is performed at the speeds of 600, 800, 1000 and 1200 rpm and torque values of 0.8, 1.2, 1.6, and 2 Nm. Test gears are operated for 1.2×10^5 cycles.

2.3 Dynamic Mechanical Analysis and Transmission Efficiency

Dynamic mechanical analysis (DMA) of ABS, POM, and HDPE is carried out as per ASTM D5023 with the help of a dynamic mechanical analyzer. DMA is performed within the temperature range of 20–140 °C and a constant frequency (1 Hz). Transmission efficiency of fabricated gears is investigated. Following relation is used to evaluate the transmission efficiency by neglecting the power loss at couplings and bearings.

$$\text{Transmission efficiency} = \frac{\text{Driven gear torque}}{\text{Driver gear torque}} \tag{1}$$

3 Results and Discussions

3.1 Dynamic Mechanical Analysis of Gear Materials

DMA is performed so as to have insight about storage modulus (E′), and damping factor (tan δ). DMA provides insight about the thermal response of gear materials under the application of cyclic mechanical stresses. Stiffness and impact properties of the gear materials can be predicted by damping behavior of the materials. There are three regions in DMA, i.e., glassy region, glass transition region, and rubbery region. The temperature at which the rubbery region initiates is known as glass transition temperature (Tg). Figures 3 and 4 shows the effect of temperature on the storage modulus and damping factor of ABS, POM, and HDPE materials.

Fig. 3 Storage modulus of gear materials
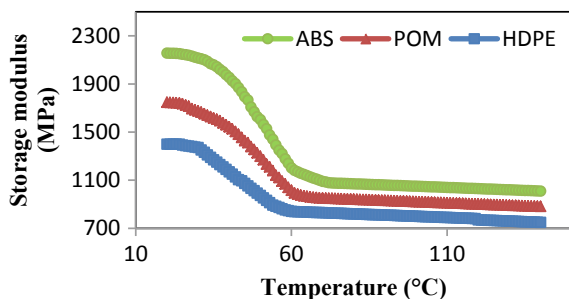
Fig. 4 Damping factor of gear materials
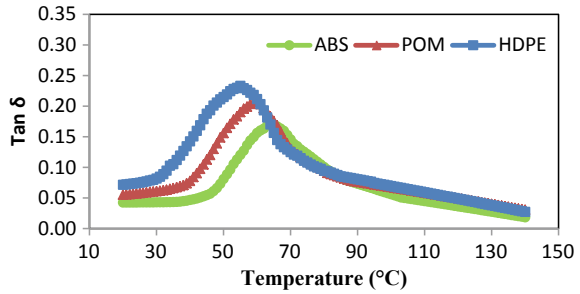
It is observed from Fig. 3 that the value of storage modulus of ABS, POM, and HDPE materials is found to be spacious below glass transition temperature (Tg). It shows a greater contribution of materials characteristics toward the stiffness at low temperature. The integral constituent of polymeric material becomes loose and lose their close packing arrangement as the temperature increases, and thus results in decreased value of storage modulus in the glass transition region (32–72 °C). The order of storage modulus of gear materials in the glass transition region is: ABS > POM > HDPE. There is no noteworthy change observed in storage modulus for rubbery region. The damping factor (tan δ) represents the ration of loss to the storage in a visco-elastic system or precisely the quantum of internal friction and is a dimensionless number [17]. The highest value of tan δ corresponds to glass transition temperature (GTT). Damping factor of all fabricated composites are shown in Fig. 4. The GTT of ABS, POM and HDPE materials are 5 wt% reinforced and 10 wt% reinforced nanofiller filled composites are 68 °C, 60 °C, and 55 °C, respectively. ABS and HDPE materials have highest and lowest damping factor (tan δ), respectively.

3.2 Variation in the Transmission Efficiency of Polymer Gears Due to Speed and Torque

Gear material plays a significant role in transmission efficiency (TE) of the polymer gears. TE is also affected by speed and the torque acting on the polymer gears. Figure 5a and b represents the variation in the surface temperature and TE of polymer gears due to the acting torque at the speeds of 600 and 1200 rpm. Figure 5 shows that the surface temperature of gear tooth increases and TE decreases with increase in the torque. Flexibility of polymer gear tooth is very sensitive to the gear tooth temperature. Gear tooth surface temperature increases with increase in torque causes teeth deflection. After completion of 1.2 million cycles, some amount of torque (Driven torque) is lost on the test gear due to deflected gear tooth. Therefore, TE of test gears decreases with increase in the torque [3].
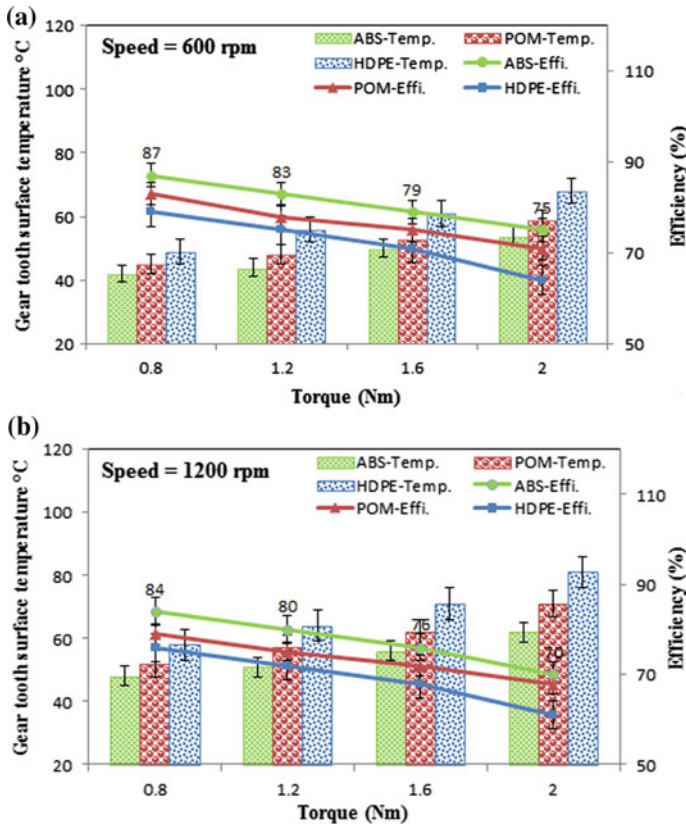
Fig. 5 **a** TE of the test gears at speed of 600 rpm after 1.2×10^5 cycle **b** TE of the test gears at 1200 rpm after 1.2×10^5 cycle

Transmission efficiency of ABS gear is higher in comparison to POM and HDPE gears. It happens due to low surface temperature of gear tooth, low damping factor and high storage modulus. TE of ABS, POM, and HDPE materials based gears is higher at 600 rpm as compared to 1200 rpm as observed from Fig. 5a and b. High gear tooth surface temperature at 1200 rpm causes less TE for ABS, POM, and HDPE gears. Among the three types of gears, ABS has highest and HDPE has lowest TE for both constant speeds (600 and 1200 rpm) and at each torque. TE of manufactured gears decreases by 20% for HDPE gear, 16% for POM gear and 14% for ABS gear when the torque increases from 0.8 to 2 Nm. Therefore, ABS gear has minimum declination for TE.

At the constant speed of 1200 rpm, ABS gears have 3 and 13% higher TE as compared to POM and neat HDPE gears, respectively, at 2 Nm torque. However, at 600 rpm, ABS gears have higher TE of 5 and 15% as compared to POM and neat HDPE gears, respectively, at the torque value of 2 Nm.
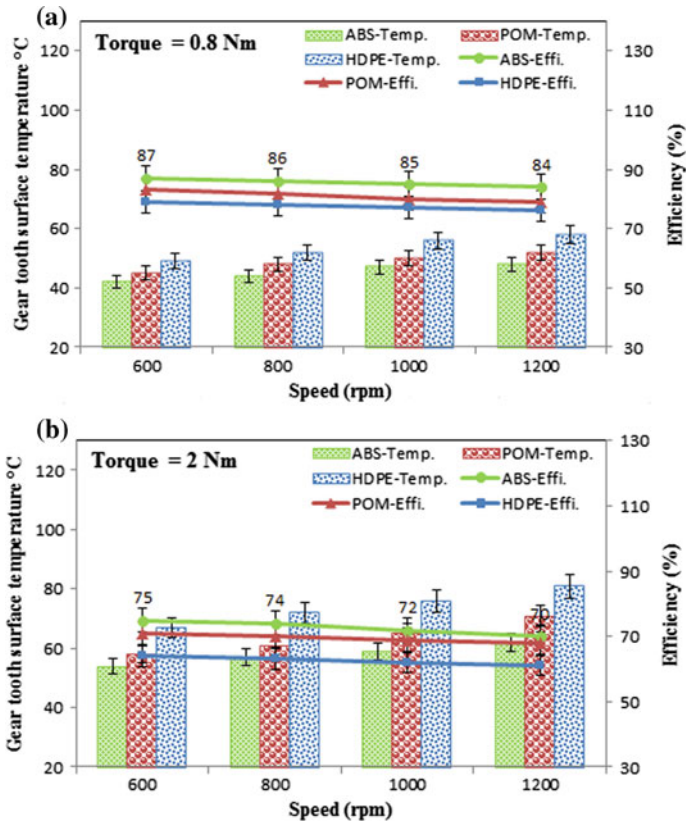
Fig. 6 **a** TE of the test gears at 0.8 Nm after completing 2×10^5 cycle **b** TE of the test gears at 2.6 Nm after completing 2×10^5 cycle

TE of ABS, POM, and HDPE gears is not much affected by variation in speed, as observed in Fig. 6. It shows that TE of ABS, POM, and HDPE gears reduces with increase in speed.

Walton et al. [2, 3] also found the similar results for several other plastic gear materials. TE of ABS, POM and HDPE gears is higher at the torque of 0.8 Nm in comparison to 2 Nm at each constant speed as evident from Fig. 6. TE of ABS, POM and HDPE gears is lower at 2 Nm in comparison to that at 0.8 Nm. It happens due to the fact that the tooth surface temperature of the gears is higher at 2 Nm. TE of ABS, POM, and HDPE gears reduces slightly from 4 to 6% when the speed increases from 600 to 1200 rpm.

At the constant torque of 0.8 Nm, ABS gears have 6 and 10% higher TE in comparison to POM and neat HDPE gears, respectively, at 1200 rpm. However, at 2 Nm torque, ABS gears have 3 and 13% higher TE as compared to POM and HDPE gears, respectively at the speed of 1200 rpm. Therefore, it is clear that performance of ABS gear is superior to POM and HDPE gears.

4   Conclusions

The following conclusions are drawn from this study:

- ABS, POM, and HDPE materials based polymer gears are successfully fabricated by injection molding process.
- Transmission efficiency of fabricated gears is significantly affected by torque rather than speed.
- ABS gear has higher transmission efficiency as compared to POM and HDPE gears. At 600 rpm, ABS gears have higher TE of 5 and 15% as compared to POM and neat HDPE gears, respectively, at the torque value of 2 Nm.
- HDPE gear has minimum transmission efficiency among all three fabricated gears, i.e., 60%.

References

1. Adams CE (1986) Plastic gearing: selection and application, 2nd edn. Marcel Dekker, New York
2. Walton D, Cropper AB, Weale DJ, Meuleman PK (2002) The efficiency and friction of plastic cylindrical gears. Part 1: influence of materials. J Eng Tribol 216:75–92
3. Walton D, Cropper AB, Weale DJ, Meuleman PK (2002) The efficiency and friction of plastic cylindrical gears. Part 2: influence of tooth geometry. J Eng Tribol 216:93–103
4. Singh AK, Siddhartha, Singh PK (2017) Polymer spur gears behaviors under different loading conditions: a review. J Eng Tribol. https://doi.org/10.1177/1350650117711595
5. Senthilvelan S, Gnanamoorthy R (2009) Efficiency of injection-moulded polymer composite spur gears. J Eng Tribol 223:925–928
6. Kirupasankar S, Gurunathan C, Gnanamoorthy R (2012) Transmission efficiency of polyamide nanocomposite spur gears. Maters Des 39:338–343
7. Mertens AJ, Senthilvelan S (2015) Durability enhancement of polymer gear using compressed air cooling. J Mat Des Appl 230:515–525
8. Nagarajan T, Rayudu GVN (1987) Investigation of the transmission characteristics of plastic involute fine mechanism gears. In: Proceedings of the 7th World Congress on the Theory of Machines and Mechanisms Sevilla. Spain, pp 1335–1338
9. Luscher A, Houser D, Snow C (2000) An investigation of the geometry and transmission error of injection molded gears. J Injection Molding Technol 4:177–190
10. Mertens, A.J. Senthilvelan, S.: Surface durability of injection-moulded carbon nanotube–polypropylene spur gears. J Mat Des Appl (2016). https://doi.org/10.1177/1464420716654308
11. Kodeeswaran M, Suresh R, Senthilvelan S (2016) Transmission characteristics of injection moulded polymer spur gears: experimental and numerical evaluation. Int J Power Trains 5:246–263
12. Gurunathan C, Kirupasankar S, Gnanamoorthy R (2011) Wear characteristics of polyamide nanocomposite spur gears. J Eng Tribol 225:299–306
13. Kurokawa M, Uchiyama Y, Iwai T, Nagai S (2003) Performance of plastic gear made of carbon fiber reinforced polyamide. Wear 254:468–473
14. Singh PK, Siddhartha, Singh AK (2017) An investigation on the effects of the various techniques over the performance and durability of polymer gears. Mater Today 4:1606–1614

15. Senthilvelan S, Gnanamoorthy R (2006) Damping characteristics of unreinforced, glass and carbon fiber reinforced nylon 6/6 spur gears. Polym Test 25:56–62
16. Singh AK, Siddhartha (2017) A novel technique for in-situ manufacturing of functionally graded materials based polymer composite spur gears. Poly Compos https://doi.org/10.1002/pc.24682
17. Joseph PV, Mathew G, Joseph K, Groeninckx G, Thomas S (2003) Dynamic mechanical properties of short sisal fibre reinforced polypropylene composites. Compos A 34:275–290

Energy Saving Analysis Using Pilot Operated Counter Balance Valve

R. Sreeharsha, Mohit Bhola, N. Kumar and Alok Vardhan

Abstract Counter balance valves are used in hydraulic systems to withhold the vertical loads by preventing the free flow of the hydraulic fluid for the safety purpose. But due to this safety feature of the valve, it creates back pressure on the actuator, when the actuation of the cylinder is required in upward direction, to lift the load. This increases the pressure losses across the actuator in the hydraulic system and in turn heat the oil unnecessarily. This, in turn, causes the system to be energy inefficient. But, in today's competitive world development of energy efficient systems (EES) is an important aspect. In this article, comparison of energy efficient hydraulic system is done using Pilot Operated Counter Balance Valve (POCBV) and Conventional Counter Balance Valve (CCBV) through MATLAB®/Simulink environment. It has been found that POCBV is more energy efficient than CCBV for a particular set of operating conditions. Effects of physical parameters like pilot ratio, spring rate on stability and efficiency used in designing of POCBV are also studied and compared using MATLAB®/Simulink environment. This model is beneficial for hydraulic machine manufacturers engaged in designing of lifting devices in selecting a suitable valve for particular load application and for the designers to design the main components of the valve.

Nomenclature

F_S	Spring setting
k	Spring stiffness
x	Valve opening
P_{pilot}	Pilot pressure at opening port of "P"
P_{back}	Back Pressure at port "b"
P_{load}	Load Pressure at port "L"

R. Sreeharsha (✉) · M. Bhola · N. Kumar · A. Vardhan
Indian Institute of Technology (Indian School of Mines) Dhanbad,
Dhanbad 826004, Jharkhand, India
e-mail: sriharsha153@gmail.com

A_{pilot} Valve effective area at port "P"
A_{load} Rod area of the actuator at port "L"
A_{back} Valve effective area at port "b"
Ψ Pilot ratio
a_{back} Back pressure ratio
C_p Spring stiffness (Pa/m)
P_{set} Valve setting pressure

1   Introduction

In the present scenario, technology of Heavy Earth Moving Machineries (HEMM) are developing in a very rapid manner. Hydraulic systems employed in HEMM's accomplishes not only the desired task, but it should be in energy efficient manner and within a specified time. With today's design of hydraulic components, flexibility of hydraulic technology has been significantly increased. Energy efficient systems can be developed in two ways: one by improving the efficiency of each component in the system and other by incorporating energy saving devices like accumulators in case of hydraulic systems. As this article is being focused on analysis of energy efficient hydraulic system to balance heavy loads. This is a task which includes identifying the components where losses are occurring and implementing a better alternative to save the losses. As this article focuses on one such component in hydraulic systems of, i.e., Counter balance valve.

Conventional Counter Balance Valve (CCBV) is basically a pressure relief valve but used in special application in combination with check valve to develop a back pressure in a hydraulic system. This valve creates a back pressure to prevent load running away when the actuator is retracting. The main limitation of this valve is that it reduces the available force from the actuator that is lost in overcoming the back pressure set up by the counter balance valve. So this loss is identified and an alternative component is suggested that can reduce it without altering its basic function, i.e., Pilot Operated Counter balance valve (POCBV).

Both valves, i.e., CCBV and POCBV are multifunctional and serves the purposes like leak tight load holding, Shock absorption, and cavitation protection at load lowering, and no pressure drop before lift, cope with hose failure and more.

During hoisting load is raised or lowered as per the requirement. When the load is being lowered there is chance of overrun due to gravity, so to counteract this a back pressure need to be generated to ensure the safety and smooth running of system. In case of HEMM, especially the hoisting machineries like cranes and excavators which runs on hydraulic system, a load holding valve is a most crucial

component. To make the load lifting/lowering mechanism energy efficient and more stabilized system, study of steady state and dynamic characteristics of valves is necessary. Maiti et al. [1] studied the static and dynamic characteristics of two-stage pressure relief valve (PRV) with proportional solenoid control pilot stage has been modeled. Liu et al. [2] researched on dynamic characteristics of CCBV in time domain and frequency domain using AMESim simulation software and validated experimentally. Zhao et al. [3] studied on influencing parameters of CCBV on stability of the system. The analysis result indicates that the pressure pulsation of the lifting system is closely related to dynamic characteristic of the counter balance valve, and stability of the system can be improved by means of the flow area of counter balance valve with linear small gradient. Handroos et al. [4] in his article, provided the detailed study on steady state and dynamic characteristics of CCBV. Overshoot with CCBV in dynamic responses are high. This is due to high sealing friction provided to bear the load. To improve the dynamic response of load-holding devices, Kjelland and Hansen [5] conducted numerical and experiential study on pressure feedback system indirectly to eliminate oscillations and to improve stability of the hydraulic system using over center valve. Xu and Liu [6] build a model of POCBV based on the AMESim software and performance analysis has been done through simulation. The simulation results show that POCBV has good dynamic response and stability and its controlled spool opening is independent of the load. Yao et al. [7] studied about the stability analysis of POCBV for flow rates around 2000 lpm. The analysis results indicate that such systems are unstable for normal range of parameters. To stabilize such systems incorporation of accumulators in the main pressure line is suggested. Another novel approach for stabilizing hydraulic circuit containing POCBV was experimented by Sorensen et al. [8]. This concept utilizes a low-pass filtered value of the load pressure from the secondary circuit for the pilot connection of POCBV valve. Rydberg [9] has analyzed on various possible types of load holding hydraulic systems in mobile and industrial applications in regard of energy saving potential. Ritelli and Vacca [10] addressed the problems and approach in aspect of energy saving analysis of CCBV.

The present article is based on comparing the energy saving analysis of the hydraulic system containing CCBV and POCBV valves. Effects of physical parameters like pilot ratio, spring rate on the stability, i.e., overshoot and settling time and energy efficiency used in designing of POCBV has been analyzed using MATLAB®/Simulink environment. The study of individual parameters will help the hydraulic lifting machine manufacturers in selecting a suitable valve for particular load application (variable/constant) and for the designers to design the main components of the valve.

2   Material and Method

The conventional and pilot operated counter balance hydraulic circuits are shown in
Fig. 1. In circuit 1(a) load is raised or lowered with the help of pressure relief valve
used in combination with the check valve. Here PRV holds the load of the system
and raising of the load attained with the help of check valve. For lowering of the
load, back pressure should reach the cracking pressure of the PRV. Whereas, in
case 1(b) of pilot operated counter balance valve (POCBV) main flow to the
actuator is passed through check valve and for lowering of the load along with the
resultant back pressure of load pilot line (low pressure) from the main supply is
provided for opening of the backflow which facilitates lowering of the load. The
other major components of the hydraulic circuits are actuator with load, 4/3 tandem
centered type DCV, a high-pressure line source and low-pressure line source.

2.1   Mathematical Equations Involved in Working of POCB
Valve

The pilot operated counter balance valves are used in hydraulic systems working
with overriding or for hanging loads. Generally employed in excavators or cranes
for heavy load lifting/holding purpose. This POCBV has better dynamic response
when compared to conventional counter balance valve (CCBV). The working of
POCBV is shown in Fig. 2. To study of different factors on which functioning of
the POCBV depends can be analyzed with the help of mathematical equations.
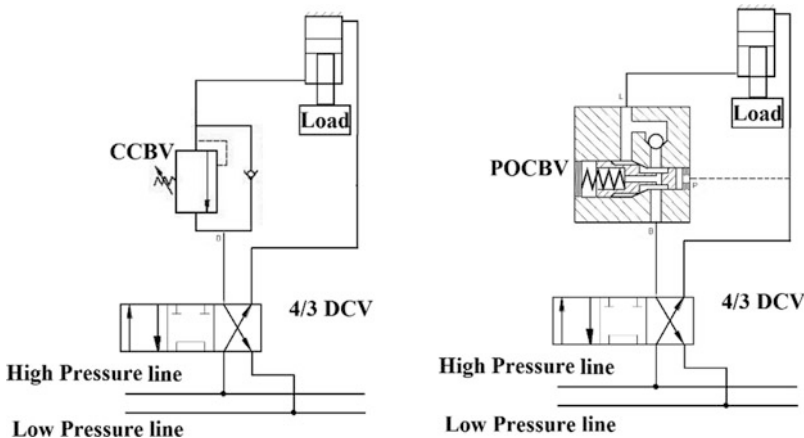
Fig. 1 Conventional hydraulic circuits of CCBV and POCBV. **a** Conventional counter balance
circuit. **b** Pilot operated counter balance check valve

Fig. 2 Working of POCB valve
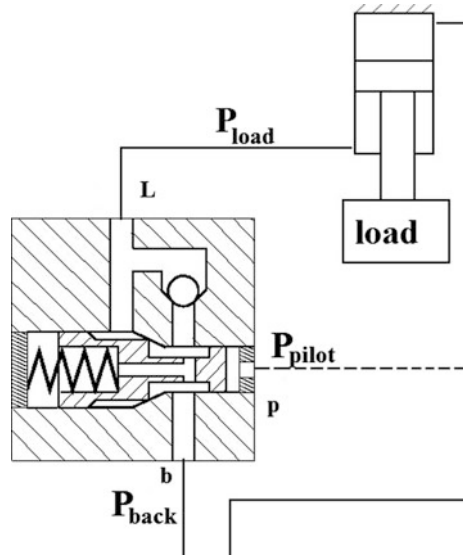
Lowering operation of the load is possible when there is possibility of flow through a passage is created between the rod side and the tank port. When DCV is operated in such a position so that to lowering operation of the load has to occur, considering the static condition if pressure at port P and pressure at port L is higher than the spring force then only lowering of the load takes place.

$$F_s + k.x = P_{pilot}.A_{pilot} + P_{load}.A_{load} - P_{back}.A_{back} \tag{1}$$

Dividing with load side area of the rod

$$P_{set} = \frac{F_S}{A_{load}}; \ C_p = \frac{k}{A_{load}}; \ \Psi = \frac{A_{pilot}}{A_{load}}; \ a_{back} = \frac{A_{back}}{A_{load}} \tag{2}$$

The equation for valve displacement is determined as

$$x = \left(\frac{P_{pilot}.a_{pilot} + P_{load} - P_{back}.a_{back} - P_{set}}{C_p} \right) \tag{3}$$

The above equations are considered with the assumption that inertia, friction, and hydraulic forces acting on the valve member are neglected.
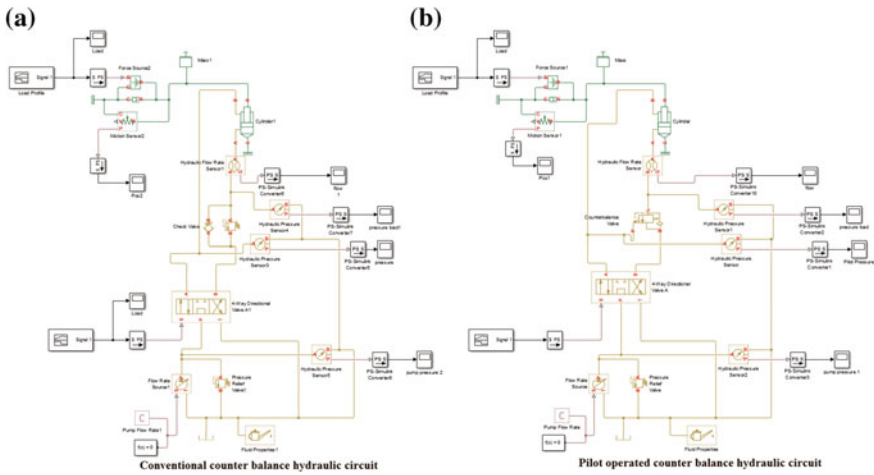
Fig. 3 Modeling of CCBV and POCBV hydraulic circuits. **a** Conventional counter balance hydraulic circuit. **b** Pilot operated counter balance hydraulic circuit

Table 1 The major system parameters considered for the simulation analysis

S. No.	System parameters	Magnitude	Unit
1.	Main pump flow rate	1e-3	m³/s
2.	Main PRV cracking pressure	100	bar
3.	Set pressure of counter balance valve	32.5	bar
4.	Rod side area of the piston	0.004	m²
5.	Piston side area of the piston	0.008	m²

2.2 System Modeling

The above mentioned conventional hydraulic circuits using CCBV and POCBV as shown in Fig. 1 is modeled in the MATLAB®/Simulink environment and shown in Fig. 3. The major system parameters considered for the simulation analysis are given in Table 1. The study of POCBV valve parameters like pilot ratio, spring stiffness with load pressure has been analyzed. A comparative study in energy saving aspect between these two circuits has also been performed. The external load imposed on the system is a type of variable load given in step with an increment of 5 kN, starting from 5 to 15 kN.
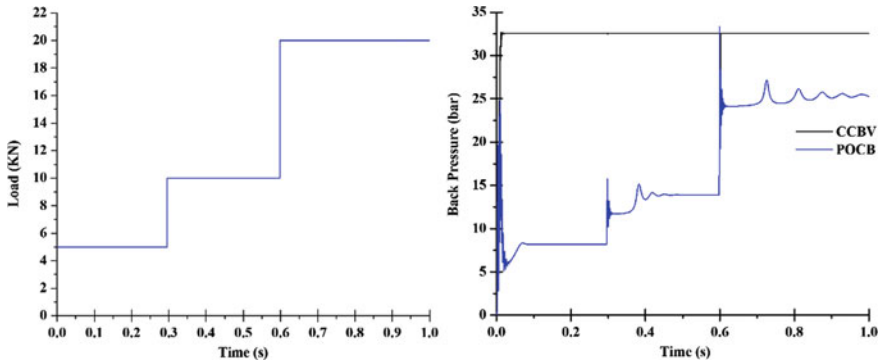
Fig. 4 Comparing the back pressure attained in case CCBV and POCBV. **a** Load profile used for the analysis. **b** Comparison of CCBV and POCBV at varying load profile

3 Results and Discussions

Figure 4a describes the load profile for the machine during counter balance valve in operation. For 0–0.3 s the load is kept at 5 kN, for 0.3–0.6 s there is step change in load to 10 kN than to 20 kN for 0.6–1 s.

Referring to Fig. 4b, the comparison of the CCBV and POCBV has been carried out for a given load profile as shown in Fig. 4a. The pre-compression setting of the spring is set about 1.3 times the maximum load carried by the machine. It is found that in the POCBV the back pressure adjusts itself according to the load profile of the machine. But in the CCBV, in which the pressure relief valve acts as the counter balance valve, the back pressure is almost constant which the pre-compression setting of the spring of the CCBV. This feature of the POCBV helps to make the hydraulic circuit of the machine more efficient during low load operating conditions by avoiding unnecessary back pressure due to high pre-compression setting of the spring in CCBV.

Referring to Fig. 5a, it is observed that the for the energy efficient point of view, the pilot ratio of the POCBV should be kept high, as the back pressure for the high pilot ratio is less as compared to low pilot ratio valve which contributes to the higher energy losses during upward stroke of the cylinder. It is also observed that the valve with high pilot ratio is less stable as compared to the valve with lower pilot ratio. So, the machines which has minimum variation of load during operation (stable load application like hydraulic press/lift), the valve with higher pilot ratio is suitable for energy efficiency and for the applications like excavators boom cylinder which has higher variation of load during its operation compromise has to be made between greater stability and energy efficiency. Referring to Fig. 5b, the effect of spring stiffness on the stability and backpressure has been found. It is observed that valve with higher spring stiffness has higher overshoot in pressure as compared to
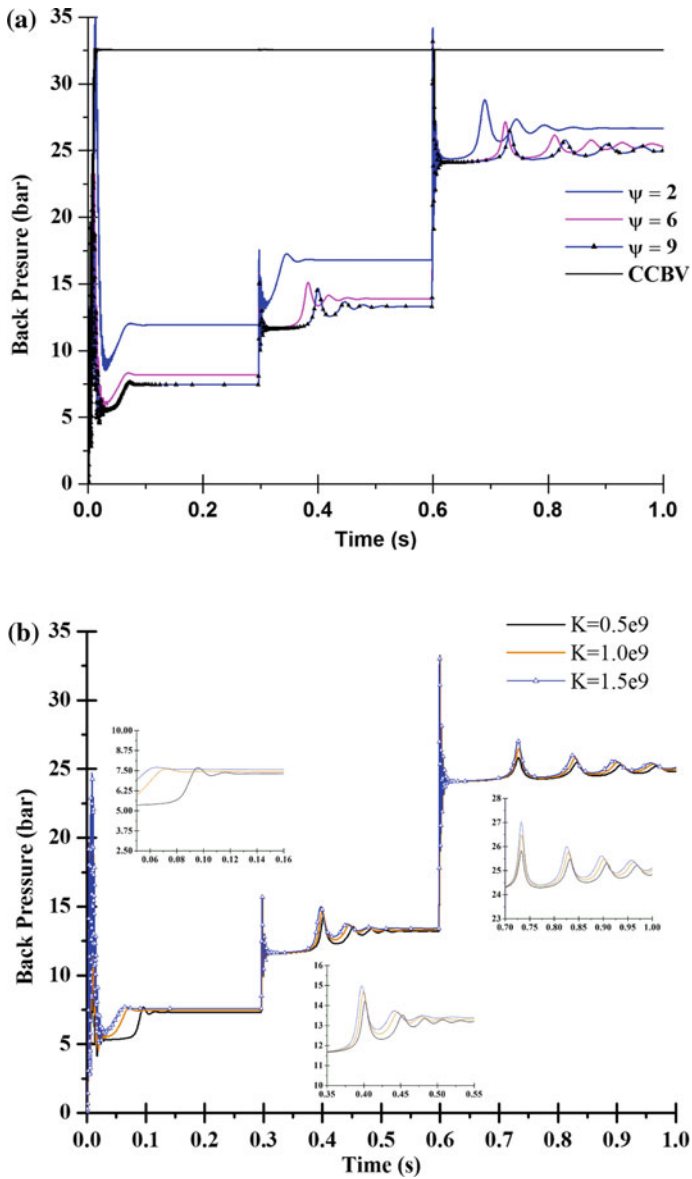
Fig. 5 Studying the effect of pilot ratio and spring stiffness of POCBV

the valve with lower spring stiffness. The settling time of the response is slightly fast for the higher stiffness spring as compared with lower stiffness spring.

4 Conclusion

In this article, comparison of energy efficient hydraulic system is done using Pilot Operated Counter Balance Valve (POCBV) and Conventional Counter Balance Valve (CCBV) through MATLAB®/Simulink environment. Based on the simulation results it has been found that POCBV is more energy efficient than CCBV. The variation of pilot ratio increases the energy saving of the POCBV system when compared to CCBV but with the increase in the pilot ratio also causes the increase in instability of the system. Increase in spring stiffness decreases the energy efficient operation of the system. An overall, using POCBV one can perform energy efficient operation when compared to CCBV based above results.

References

1. Maiti R, Saha R, Watton J (2002) The static and dynamic characteristics of a pressure relief valve with a proportional solenoid-controlled pilot stage. Proc Inst Mech Eng Part I J Syst Control Eng 216(2):143–156
2. Liu X, Liu X, Wang L, Chen J (2010) The dynamic analysis and experimental research of counter balance valve used in truck crane. In: International conference on electrical and control engineering 2010 (ICECE). IEEE, pp 2332–2335
3. Zhao L, Xinhui L, Wang T (2010) Influence of counterbalance valve parameters on stability of the crane lifting system. In: International conference on mechatronics and automation 2010 (ICMA). IEEE, pp 1010–1014
4. Handroos H, Halme J, Vilenius M (1993) Steady state and dynamic properties of counterbalance valves. In: 3rd Scandinavian international conference on fluid power
5. Kjellander MB, Hansen MR (2013) Numerical and experiential study of motion control using pressure feedback. In: 13th Scandinavian international conference on fluid power 2013, vol 092. Linköping University Electronic Press, Sweden, pp 337–345
6. Xu J, Liu XN (2012) Simulation analysis of the counterbalance valve used in cranes based on AMESim software. Appl Mech Mater 233:55–61
7. Yao Y, et al (2014) Stability analysis of a pilot operated counterbalance valve for a big flow rate. In: Symposium on fluid power and motion control 2014 (ASME/BATH). American Society of Mechanical Engineers
8. Sørensen JK, Hansen MR, Ebbesen MK (2016) Novel concept for stabilizing a hydraulic circuit containing counterbalance valve and pressure compensated flow supply. Int J Fluid Power 17(3):153–162
9. Rydberg KE (2015) Energy efficient hydraulics: system solutions for loss minimization. In: The national conference on fluid power 2015, Sweden
10. Ritelli GF, Vacca A (2013) Energetic and dynamic impact of counterbalance valves in fluid power machines. Energy Convers Manag 76:701–711

Enhancing Learning of Kinematics and Fatigue Failure Theories Using CAD Modeler

Prathivadi Ravikumar, Blair McDonald, Il-Seop Shin, Khaled Zbeeb and N. Puneeth

Abstract Mechanical Engineering is the branch of engineering that specializes in the design, production, and uses of machines. The physics of mechanics is widely used in mechanical engineering. Educators make continuous improvements in providing quality education to ensure that mechanical engineering students understand important concepts and develop skills to apply them in practice upon graduation. Engineering software tools are enabling educators to develop innovative new techniques that enhance the learning of many mechanical engineering topics. This paper discusses the use of *SolidWorks* CAD modeler to develop learning tools that support the understanding of concepts of mechanical engineering topics such as kinematic synthesis, kinematic analysis, and fatigue failure theories. Specifically, three-position synthesis with specified moving pivots of a four-bar mechanism, symmetrical linkage with synthesis of one of its cognates, and 3D fatigue diagram that extends the traditional 2D fatigue diagrams are described. Effective use of sketch, drawing, and solid model tools with solid modeler are discussed. The productivity of CAD tools in significantly enhancing learning is recognized through the discussion.

Keywords Kinematics · Synthesis · Analysis · Fatigue · Failure · SolidWorks · CAD · Mechanical · Engineering

P. Ravikumar (✉) · B. McDonald · I.-S. Shin · K. Zbeeb (✉)
Western Illinois University, Moline, IL 61265, USA
e-mail: p_b_ravikumar@yahoo.com
e-mail:

N. Puneeth
Vivekananda College of Engineering and Technology, Puttur 574203, Karnataka, India
e-mail: puneethn0015@gmail.com

289

1   Introduction

Mechanical Engineering is the branch of engineering that specializes in the design, production, and uses of machines. The physics of mechanics is widely used in mechanical engineering [1]. Educators make continuous improvements in providing quality education to ensure that mechanical engineering students understand important concepts and develop skills to apply them in practice upon graduation. Engineering software tools are enabling educators to develop innovative new techniques that enhance the learning of many mechanical engineering topics. This paper discusses the use of *SolidWorks* CAD modeler to develop learning tools that support the understanding of concepts of mechanical engineering topics such as kinematic synthesis, kinematic analysis, and fatigue failure theories. Effective use of sketch, drawing, and solid model tools with solid modeler are discussed.

  As per various studies carried out [2] on increase in productivity due to computer-aided design (CAD), it has been found that at lower ends the increase in productivity is in the ratio 3:1 and in many cases it is 10:1 (even 100:1 gains have been reported in some cases). This increase in productivity is measured against the traditional designing process in which most of the calculations are done manually and drafting is done by using the drawing board. Although these productivity gains are in the industry, one can extrapolate comparable benefits in education in using CAD, more in terms of enhanced learning due to better understanding of the concepts than in terms of sheer productivity. Interestingly, there is a productivity gain in using CAD modelers, albeit much smaller in scale, by accomplishing more of taught/learnt material for the same or better quality of education. Many mechanical engineering topics are best understood by a combination of content language, engineering principles, mathematics, and graphical representations. It then makes sense to use CAD modelers to address the graphical aspects that are present in such topics. Kinematics and fatigue failure theories are important mechanical engineering topics that involve significant graphical content. This background is the genesis for the topic and content of this paper.

2   Material and Method

2.1   *Kinematic Synthesis*

Mechanics is the branch of scientific study which deals with motions, time, and forces. Mechanics is made up of two parts, statics and dynamics. *Statics* deals with stationary systems and *dynamics* deals with which move or change with time. Within dynamics, *kinematics* deals with only the motion aspects such as position or velocity, and *kinetics* deals with motion and the cause of that motion such as forces or moments. Kinematics (dynamics in general) can be applied to objects modeled as particles, rigid bodies, combination of rigid bodies called linkages/mechanisms, or

flexible systems. Such studies can be extended to more complex models such as flexible bodies. Kinematics can be further sub-divided into *kinematic synthesis* and *kinematic analysis*. Just as any engineering design practice involves a combination of synthesis and analysis, so does kinematic synthesis and analysis. Most engineering courses deal primarily with analysis techniques for various situations. However, one cannot analyze anything until it has been synthesized into existence [3]. Many machine design problems require the creation of a device with particular motion characteristics. Examples vary greatly from tracing out a particular path in space to inserting a part into an assembly in a certain path. It is thus evident that knowledge and skills in kinematic synthesis must be developed, especially for mechanical engineering students. Graphical methods are a powerful means to accomplish kinematic synthesis of mechanisms. Examples of graphical synthesis problems and use of CAD modelers to graphically solve or supplement the solution by other means is discussed next.

2.2 Graphical Three-Position Synthesis with Specified Moving Pivots

As a practical application, three positions of a line as shown in Fig. 1 may need to be matched by a line on a link of a moving four-bar mechanism with the additional requirement that the line on the link be the end points of the pivots on the link. A graphical procedure can be undertaken as the means for this three-position synthesis with specified moving pivots situation. The procedure is known from the literature [3].

The graphical procedure requires that the following steps be followed to accomplish the synthesis:

- Draw link CD in the three given positions C_1D_1, C_2D_2, and C_3D_3.
- Draw construction lines from C_1 to C_2 and C_2 to C_3.
- Bisect line C_1C_2 and line C_2C_3 and extend them until they meet at some point O_2.
- Repeat steps 3 and 4 for lines D_1D_2 and D_2D_3 to get point O_4.
- Connect O_2 with C_1 and call it link 2 (crank). Connect O_2 with D_1 and call it link 4 (rocker).
- Link C_1D_1 is link 3 (coupler). Link O_2O_4 is Link 1 (ground).
- Check the Grashof condition. Any Grashof condition is potentially acceptable.

The above graphical procedure can be implemented by using tools like a paper, pencil, compass, and protractor as needed as a manual method or by using a CAD program such as *SolidWorks* [4] as a computer method. It is best to have students use the manual method first to solve for every different type of graphical synthesis problem to grasp the concepts well. It is equally important to teach them to start using computer methods such as *SolidWorks* to reflect real-world practice. Figure 2
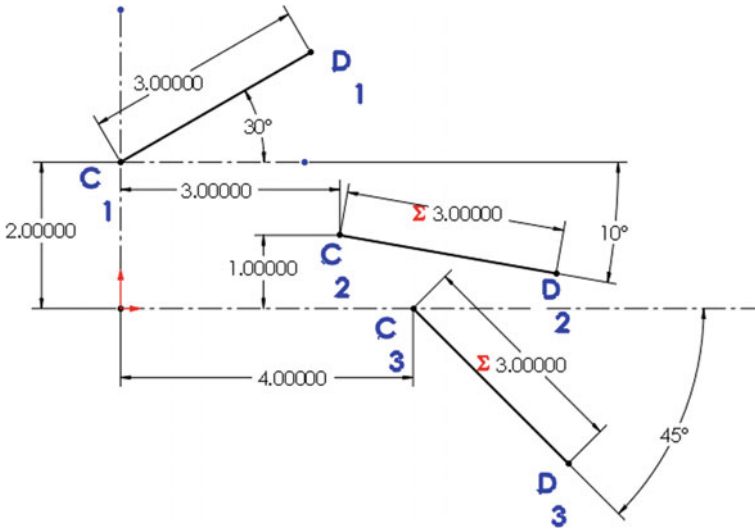
Fig. 1 Three positions C_1D_1, C_2D_2, and C_3D_3 to be matched by moving pivots of a link of a four-bar mechanism

shows the implementation of the graphical procedure in the "sketch" mode within a SolidWorks part file and the synthesized four-bar mechanism that solves the problem. The synthesized mechanism parameters are: 2.400 units long Ground link positioned as shown; 5 units long Crank pivoted at the lower end located as shown; 4.746 units long rocker pivoted at its lower end located as shown; 3 units long Coupler that connects the Crank and the Rocker. The 3 units long Coupler will match the three positions given in Fig. 1 as the Crank is rotated. It is also easy to rotate the crank to see how the mechanism moves and verify that the three positions are matched by the Coupler. This ability to do this design verification using CAD modelers such as *SolidWorks* has alternatives that are not easy or productive such as checking by manual constructions or by building models with wood or plastic or metal. Note that Figs. 1 and 2 can be made as two separate sketches within the same *SolidWorks* file so that it is easy to copy necessary information from the sketch of Fig. 1 to the sketch of Fig. 2 before making the additional constructions as shown in Fig. 2. Such as approach minimizes human errors such as using incorrect dimensions and maximizes efficiency of completing the task because everything is in one file and is less error-prone as pointed out.

After synthesis and design verification as described, the Solid Modeling capabilities of *SolidWorks* can be utilized to make the solid models of the links as parts using sketches first and then make an assembly of the parts as a mechanism. Assembly, as a mechanism, implies that we take advantage of options such as different types of mates (for example, setting concentric mates between the surfaces of the pin holes of links that connect as a pin joint). It is then possible to use more features of *SolidWorks* to study the mechanism assembly further such as attaching a
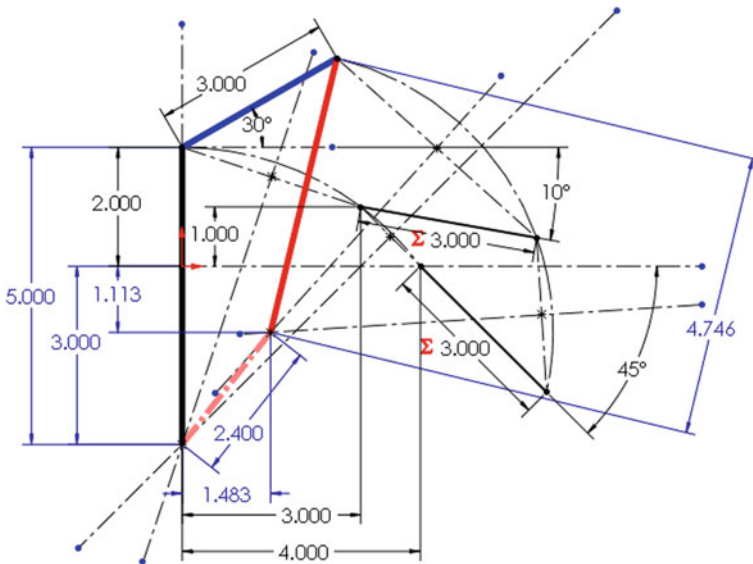
Fig. 2 Graphical three-position synthesis with moving pivots using *SolidWorks*

motor to the crank to examine its motion, velocity, or acceleration. Such studies are possible in the advanced "Motion Analysis" segment of "Motion Study" portion of *SolidWorks*. It should be pointed out that "simpler" studies can also be done in *SolidWorks* using the "Animation" segment of "Motion Study". Figure 3 shows the solid model assembly as a planar front view (the mechanism is after all a planar mechanism in the kinematic sense) on the left and as an actual 3D model in the trimetric view on the right. It is obviously not possible to demonstrate the motion study aspects such as motion animation in a passive document such as this but can always be demonstrated at any presentation opportunity. It should be noted that the synthesized mechanism shown in Fig. 3 is a Grashof four-bar because it meets the requirement that the sum of the shortest and longest links' lengths (Ground 2.4 units plus crank 5 units = 7.4 units) is less than the sum of the other two links' lengths (Coupler 3 units plus Rocker 4.746 units = 7.746 units). In fact, because the shortest link is grounded, the mechanism is a double-crank in that both the Crank and Rocker are capable of complete rotation and hence a motor can be attached to either the Crank or the Rocker. It should also be noted that the coupler can go past the three given positions and if it is required to limit the motion of the coupler to the extreme positions 1 and 3 in Fig. 1, a suitable two-link DYAD can always be added to the mechanism.
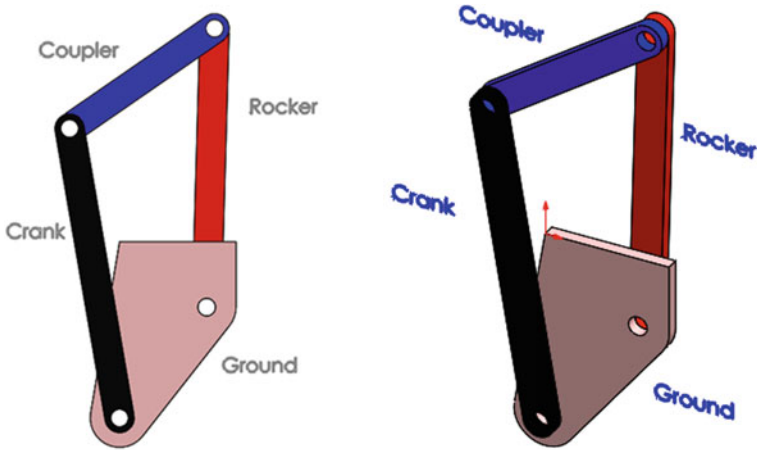
Fig. 3 Frontal view (left) and trimetric view (right) of the synthesized mechanism for the three-position synthesis with specified moving pivots

2.3 Symmetrical Linkage and Synthesis of One of Its Cognates

When the lengths of the coupler and rocker are equal pin-to-pin in a four-bar linkage, every coupler point on a circle centered on the coupler-rocker joint with radius equal to the coupler length will generate symmetrical coupler curves. *Symmetrical coupler curves* have an axis of symmetry. Linkages that generate such symmetrical coupler curves are called Symmetrical Linkages. An example is shown in Fig. 4 as a schematic sketch on the left and as a solid model frontal view on the right.
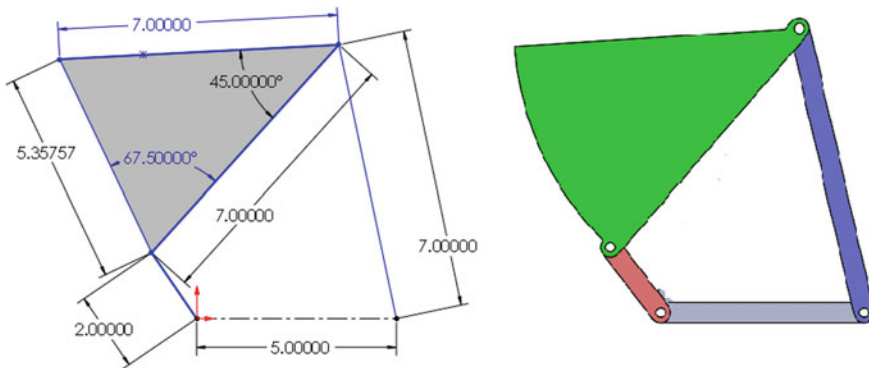
Fig. 4 A symmetrical linkage as a schematic (left) and as frontal view solid model (right) created using *SolidWorks*
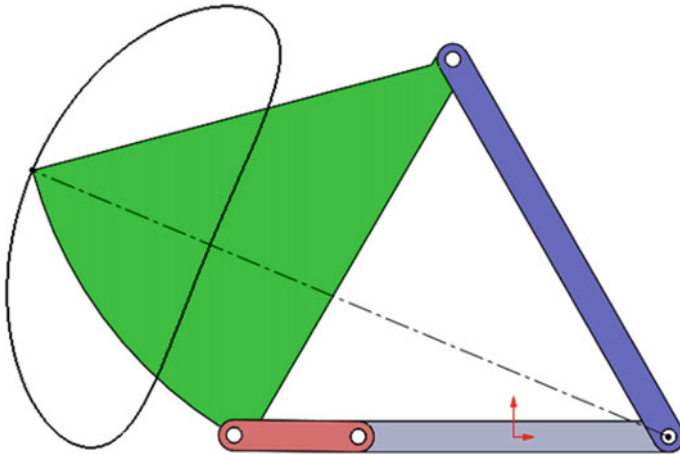
Fig. 5 A symmetrical linkage

The coupler curve generated by the point at the end of the arc on the coupler as shown on the right in Fig. 4 (the point is the same as the free corner of the triangle-shaped link on the left of Fig. 4) is shown in Fig. 5. The symmetry of the coupler curve is identified as the line joining the ground-rocker joint point to the coupler curve trace point when the crank is collinear with the ground as shown. Although the Symmetrical Linkage is interesting and practical in and of itself, the focus here is on the more involved concept of synthesizing the cognate of this linkage. The word *cognate* was used by Hartenburg and Denavit [5] to describe a *linkage of different geometry that generates the same coupler curve (as another linkage).*

To synthesize a cognate, a very robust procedure is to create the Cayley Diagram and then the Roberts Diagram [3]. The Cayley Diagram is shown in Fig. 6 and was generated using *SolidWorks*. Links 1 (ground), 2 (crank), 3(coupler), and 4 (rocker) form the original linkage (Cognate #1) which is the same as the linkage shown in Fig. 4. Cayley Diagram construction starts with keeping link 3 fixed and rotating links 2 and 4 about their respective pivots on link 3 until they are both collinear with the line joining the coupler-crank joint and the coupler-rocker joint. Then a line that will eventually contain link 10, a side of link 9, and link 8 is drawn parallel to one side of link 3 as shown. Another line that will eventually contain link 5, a side of link 6, and link 7 is drawn parallel to a side of link 3 as shown. This is followed by extending two sides of link 3 until they meet the two lines that were just generated as shown. This results in a large triangle consisting of four parallelograms and three triangles forming the Cayley Diagram. The top apex of the large triangle will relocate when a similar triangle to the large triangle is constructed with the line joining the original ground pivots as the base of that triangle. This similar triangle construction is shown as a dotted line in Fig. 6 wherein link 1 is one side, and the other two sides meet at the third ground pivot (which is seen over link
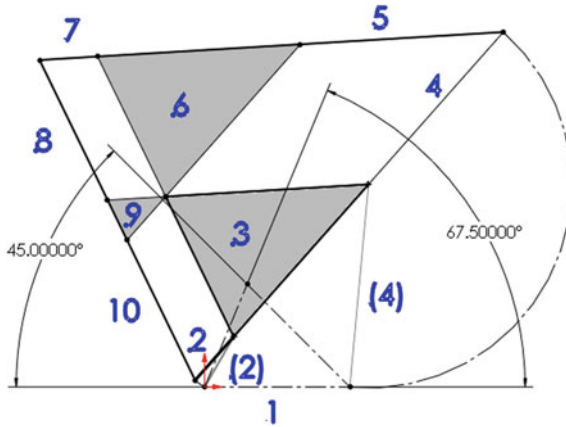
Fig. 6 Cayley diagram showing all three eventual cognates
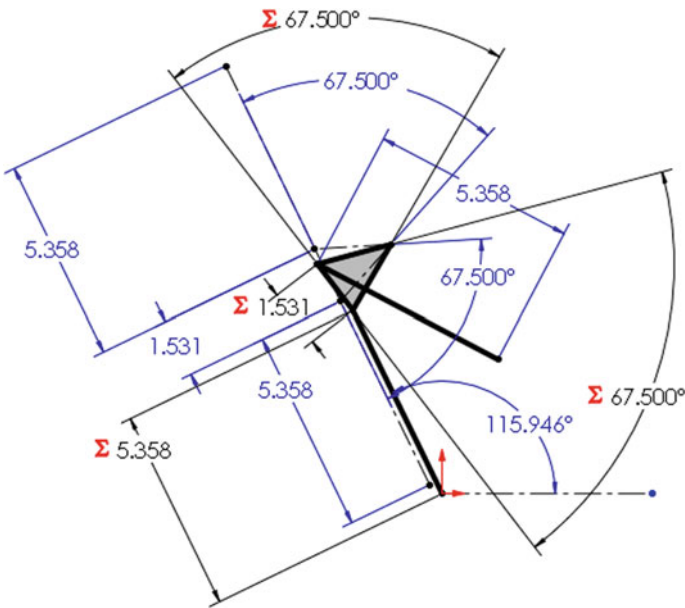
Fig. 7 Robert's diagram for cognate #2

3 in this example). Roberts Diagram then follows as seen in Fig. 7. To construct this, while not allowing the common point between the three triangles (each one which is a ternary link of each of the three cognates) to move, links for the cognates are moved to their appropriate locations to synthesize the cognates. That is, link 8 is connected to the new ground pivot, and link 10 is connected to the original ground pivot on the left. Link 9 will rotate to its correct orientation. Thus, the original
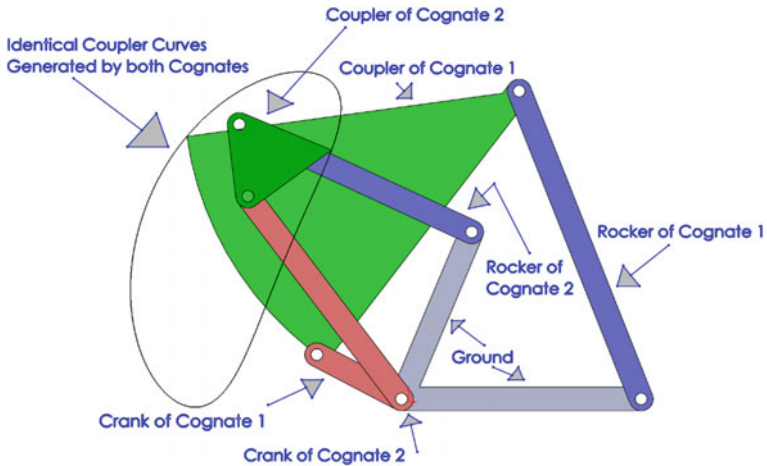
Fig. 8 Frontal plane view of *SolidWorks* assembly of solid models of two cognates and the identical coupler curves traced by them

ground pivot at the bottom left and the new ground pivot are part of the ground for a cognate (say Cognate #2) and other links of Cognate #2 are 8, 9, and 10. Similarly, the original ground pivot at the bottom right and the new ground pivot are part of the ground for Cognate #3 and the other links for Cognate #3 are 4, 5, and 6. To illustrate that true cognates have been synthesized, Solid Models of Cognate #1 and Cognate #2 were assembled as mechanisms and superimposed using *SolidWorks* as shown in Fig. 8. Coupler curves were traced using the motion analysis tools in *SolidWorks* to compare the coupler curves which must be identical to qualify as cognates. Motion animations in *SolidWorks* confirm that they are cognates. Only discrete point or points on the coupler curve can be shown on paper being reached by each cognate's coupler curve point. Figure 8 shows that the coupler curve is touched by each cognate's coupler curve point in some general or arbitrary positions.

2.4 Content and Methodology of Using CAD for Fatigue Failure

2.4.1 Fatigue Diagrams in 2D

The 2D Fatigue Diagram representing various failure criteria such as the Soderberg Line, the Modified Goodman Line, the Gerber Line, the ASME Line, and the Yield (Langer) Line are well-known in the literature [6] and is shown in Fig. 9.

The fatigue diagram of Fig. 9 shows the limiting value combination of Mid-Range Stress (x-axis) and Alternating Stress (y-axis) for each of the failure
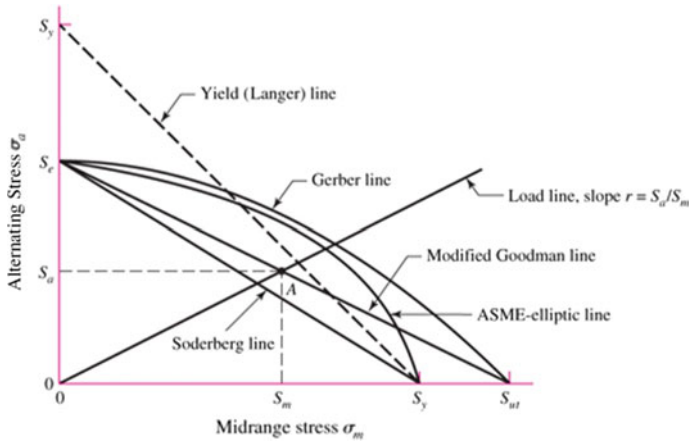
Fig. 9 2D fatigue diagram

criterion for infinite life. For example, any point represented by a particular value of Mid-Range Stress and Alternating Stress that is inside the bounds formed by the Soderberg Line, the x-axis, and the y-axis is considered to be safe for infinite life by the Soderberg criterion. (Looking at the figure, it can also be seen that the Soderberg Line is the most conservative). Failure theories, vitally important in the design of mechanical components and systems, must be clearly understood by the graduating student to be able to apply them skillfully in industry practice. The 2-D Fatigue Diagram is the culmination of significant theoretical as well as experimental developments and equations in failure analysis wherein many aspects such as the S-N Diagram, infinite life, fully reversed stress, and fluctuating stress are involved.

2.4.2 Fatigue Diagrams in 3D

When the discussion is further extended to finite life under fluctuating stresses, it is often done so with theory and equations and only. Just as a 2D Fatigue Diagram is a very useful supplement to learning the underlying aspects for infinite life, it will be greatly helpful if finite life fatigue failure aspects can be represented diagrammatically to relate finite life to Mid-Range Stress and Alternating Stress values for various failure criterion. This results in a 3D Fatigue Diagram as shown in Fig. 10 (created in *SolidWorks*) which has been created using the theoretical basis and equations for finite life for each of the failure criterion. The x-axis represents the Mid-Range Stress and the y-axis represents the Alternating Stress. The information in the third direction has been presented along the negative z-axis so as to show the 2D Fatigue Diagram clearly as a special case of the 3D Fatigue Diagram on the nearest x–y plane in the front. The failure criteria are now surfaces in the 3D diagram instead of 2D curves in the 2D diagram. Any point in the y–z plane
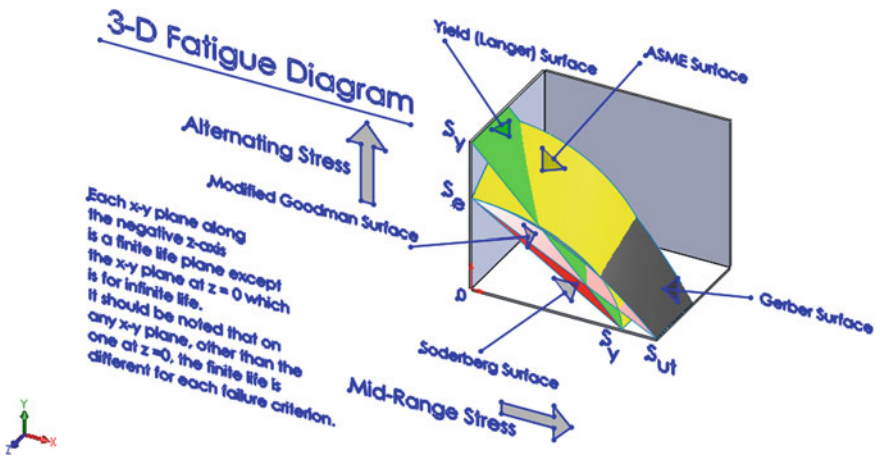
Fig. 10 3-D fatigue diagram

represents a particular value of completely reversed stress for a particular value of finite life for a specific failure criterion. Such a point is achieved by replacing the endurance limit (for infinite life) in any specific failure criterion's well-known equation with the completely reversed stress and calculating it for a given combination of mid-range stress and alternating stress. Once that value of completely reversed stress is found, the S-N diagram's equation in the high-cycle range between 1000 cycles to 1,000,000 cycles can be used to find the finite life. Although the numbers are best found by using equations to calculate them as just described, the 3D Fatigue Diagram is very useful for student's understanding of the concepts.

The above approach is discussed below through the modified Goodman theory as an illustration, best applicable for ductile steels:

Completely reversed stress = Alternating Stress/(1 − Mid-Range Stress/Tensile Strength)

Finite Life = (Completely reversed stress/a)$^{(1/b)}$, where

a = (Fraction of strength at 1000 cycles to tensile strength × tensile strength)^2/ Endurance limit

b = −(1/3) log (Fraction of strength at 1000 cycles to tensile strength × tensile strength/Endurance Limit).

3 Results and Discussion

The use of CAD modeler such as SolidWorks as described in this paper was adopted in ENGR 321 Mechanical Design I and ENGR 322 Mechanical Design II courses that are taken by students majoring in mechanical engineering and general

engineering. Student evaluations showed that the strategy and methods of using CAD modeler were very effective. Other evidence of the effectiveness was observed through the application of the CAD modeler by students on projects in kinematics in the ENGR 322 course. The productivity and outcome capabilities for kinematics that CAD modelers provide serve as incentives for students to learn and apply the concepts much more effectively.

Cited references include excellent content in the areas of kinematics and fatigue theories. Supplementing the teaching of the concepts in them using 3D CAD modelers as described in this paper to emphasize synthesis of mechanisms and extend 2D fatigue diagrams to 3D fatigue diagrams has been a novel, productive, and practical approach.

4 Conclusions

This paper discussed the use of *SolidWorks* CAD modeler to develop learning tools that support the understanding of concepts of mechanical engineering topics such as kinematic synthesis, kinematic analysis, and fatigue failure theories. Effective use of sketch, drawing, and solid model tools with solid modeler were discussed. The productivity of CAD tools in significantly enhancing learning was recognized through the discussion.

Compared to using earlier 2D CAD modelers or using only the 2D aspects of 3D CAD modelers, the approach of using the 3D capabilities of 3D CAD modelers provides benefits such as better visualization of geometry, checking for interference/collision, and simulating advanced kinematic and kinetic aspects. As for fatigue failure theories, 3D CAD modeler has been demonstrated here to show concepts in new ways.

References

1. Dictionary.com. http://www.dictionary.com/browse/mechanical-engineering. Accessed 9 May 2018
2. Bright Hub Engineering. https://www.brighthubengineering.com/cad-autocad-reviews-tips/19769-benefits-of-using-computer-aided-design-cad-software-increase-in-productivity/. Accessed 5 April 2018
3. Norton (2012) Design of machinery, 5th edn. McGraw-Hill, New York, NY
4. Dassault Systems SOLIDWORKS Corp Homepage: https://www.solidworks.com/. Accessed 5 April 2018
5. Hartenberg R, Denavit S (1964) Kinematic synthesis of linkages. McGraw-Hill, New York, NY
6. Budynas R, Nisbett JK (2015) Shigley's mechanical engineering design, 10th edn. McGraw-Hill, New York, NY

Performance Analysis of Special Design Single Basin Passive Solar Distillation Systems: A Comprehensive Review

D. B. Singh, Ashok Kumar Singh, Kumar Navneet, V. K. Dwivedi, J. K. Yadav and Gajendra Singh

Abstract Solar desalting systems are used for maintaining the shortage of fresh water in distant areas where sunlight is available in great quantity. These solar stills are working on the principle of evaporation and condensation for generating potable water. These systems are about maintenance-free requiring minimum manpower and can be made-up by materials voluntarily available in local market. A variety of designs of single basin passive solar stills are used to enhance the efficiency and rate of fresh distillate output. It helps in fulfilling the existing gap between the demands against the fresh water supply. Guarantee of freshwater availability for the world is an immense challenge. In the present work, various types of specially designed single basin passive solar distillation systems have been reviewed and concluded on behalf of economic, self-sustainable, and production rate with some new challenges.

Keywords Single basin solar distillation systems · Efficiency · Productivity

1 Introduction

Water is very important for life on Earth. Out of the total estimated water on the earth, 97% salty water and 3% potable water is available for use. Day by day, the demand for potable water increases which cannot be fulfilled by conventional sources of water especially in remote areas. There are various systems available for desalting the brackish and saline water form solar energy like active distillation system, passive distillation system, single basin, double basin, multi basin, wick

D. B. Singh · A. K. Singh (✉) · K. Navneet · V. K. Dwivedi · J. K. Yadav
Mechanical Engineering Department, Galgotias College of Engineering and Technology, Greater Noida 201306, UP, India
e-mail: agashok26@gmail.com

G. Singh
Department of Mechanical Engineering, Indian Institute of Technology (ISM) Dhanbad, Dhanbad 826004, Jharkhand, India

type, diffuser type, cascade type, fin type, heat exchanger type, flat plate collector type, evacuated tubular collector type, thermal storage material type, additional condenser type etc. and all these systems are based on the simple working principle of evaporation of water and condensation of vapor by utilizing solar radiation energy. Out of those, there are some special designs of single basin passive solar stills which have very important role among all other solar stills in comparison with performance and productivity which is highlighted in the present work with appropriate discussions and conclusions.

Solar stills are very easy to fabricate by using easily available materials in the local market. Malik et al. [1] showed the past conditions of solar distillation also revealed the work of passive solar distillation systems in their book. Solar still was first ever utilized by Arab alchemists in 1551 and further a Swedish engineer Charles Wilson had developed the first conventional solar still in 1872 [2]. Al-Hayek and Badran [3] studied the various designs of solar still and its effects also. Lost minerals during distillation process were recovered by providing marble bed while trickling the distillate. The past background of solar distillation was presented by Nebbia and Menozzi [4]. After that Garg and Mann [5] showed the different aspects of design, working conditions, climatic parameters based on daily, monthly and annual routine of passive solar stills.

2 Solar Still

Solar still is a brackish water desalting device which utilizes solar radiation comes on the inclined glass cover of still. Solar radiation is absorbed by water surface and still basin liner after that evaporation happens from the top cover of still basin. Then after by releasing its latent heat to the glass cover, vapor gets condensed and condensed water trickles to the glass cover and collected in container through a particular passage under gravity [6]. A review of different solar distillation systems has been presented by different reviewers [7–9].

2.1 Passive Single Basin Solar Still

Passive solar distiller receives direct solar heat from sun which is directly used to vaporize the brackish water. It is configured as single slope, double slope or other special design type solar distillation systems without connecting any external or internal, direct or indirect power source and if external power source like photovoltaic modules, etc., are used than those systems are called active solar stills as reviewed by Singh et al. [10]. Generally fiber-reinforced plastic and transparent glass cover (readily available in the local market) is used to prepare solar distillation system. Still basin liner is painted dark black for better solar absorption [11, 12]. Such type of passive solar stills as shown in Fig. 1 produces 2.1 l/m^2 per day

Fig. 1 Schematic view of Passive single slope solar still
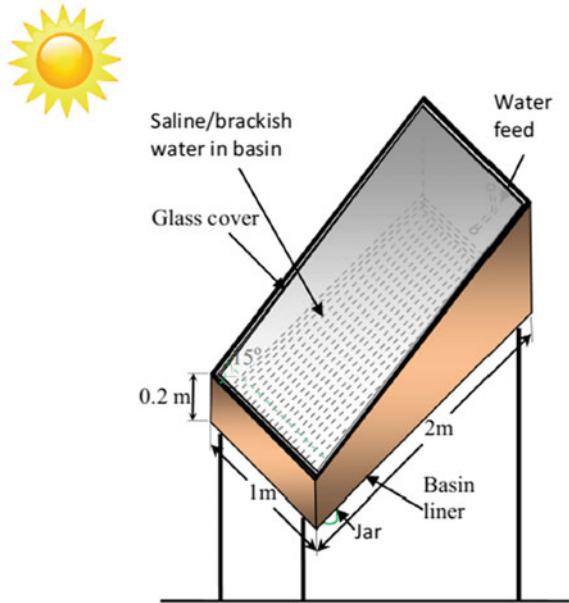
maximum distillate and 34% efficiency for 2 cm basin water depth based on the experimental results revealed by Phadatare and Verma [13].

2.2 Special Design Single Basin Passive Solar Still

Special designs of solar still came into picture for further improvement of conventional solar distillation systems which needs many improvements because of much heat losses, less productivity, and high cost of distillate and these are most often not recovered. Such type of stills performed with maximum efficiency up to 40% and yield up to 6 l/m^2, revealed by Kunze [14]. So stills which are modified with new designs with enhanced productivity are called special designed single basin passive solar still.

Abdallah et al. [15] studied three types of modified designs for the performance of single basin passive solar still as shown in Fig. 2 and found incremental improvement in the performance like first system with internal mirror showed 30% improvement, second system with stepped basin showed 180% improvement and third system with solar radiation tracking system showed 380% improvement.

Velmurugan et al. [16] studied and experimented on fin type, sponge type, and wick type solar still as shown in Fig. 3 to find the productivity deviation. The productivity was found 29.6% for solar still with fins, 15.3% for solar still with sponge and 45.5% for solar still with wick.
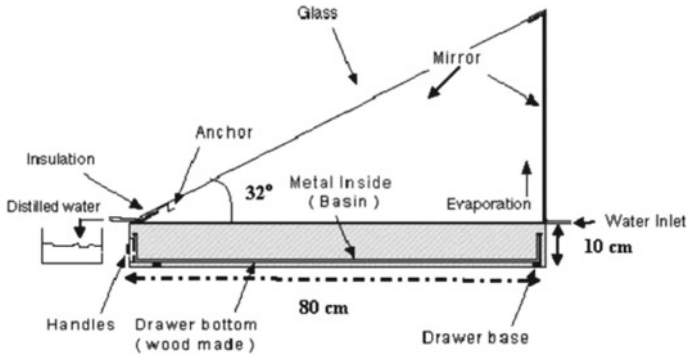
Fig. 2 Line diagram for single basin solar still with internal mirrors [15]
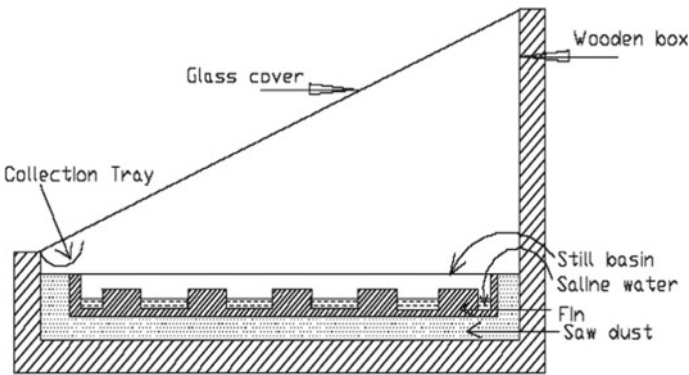
Fig. 3 Schematic diagram for fin-type solar still [16]

Shanmugan et al. [17] experimented on solar still with boosting mirror installed just above the top glass cover of still as shown in Fig. 4. This boosting mirror improves the reflection of solar radiation toward basin water, in this way performance improvement appeared as 35% (without boosting mirror) and 45% (with boosting mirror).

Tiwari and Suneja [18] presented the experimental analysis of solar still with inverted absorber as shown in Fig. 5 which improves the solar radiation transmission to basin water at its lower side directly. This improves the heat gain to basin and ultimately performance gets improved.

Kabeel [19] presented a pyramid type solar still along with wick as shown in Fig. 6 and showed the improved performance of about 45% and 4.0 l/m^2 per day productivity because wick increases the effective evaporative surface area.

Dhiman Naresh [20] presented a spherical solar still as shown in Fig. 7 and found better efficiency than conventional solar still. Basel [21] revealed the new concept of hemispherical solar still transportable type and found 33% average
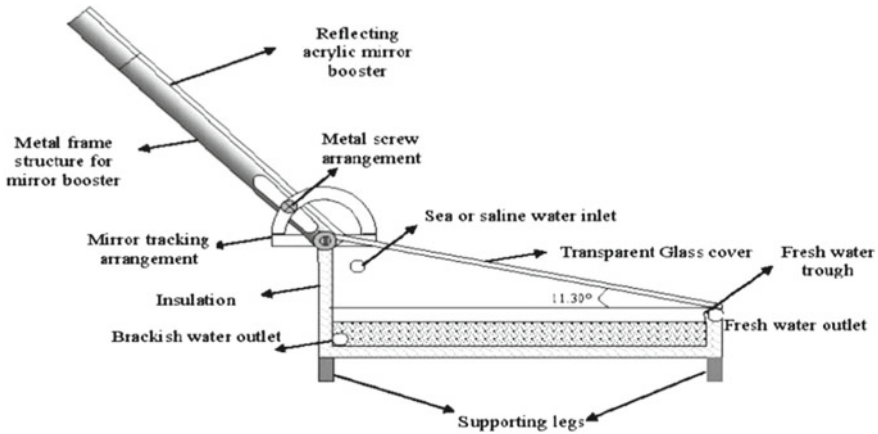
Fig. 4 Schematic diagram of solar distillation system with boosting mirror [17]
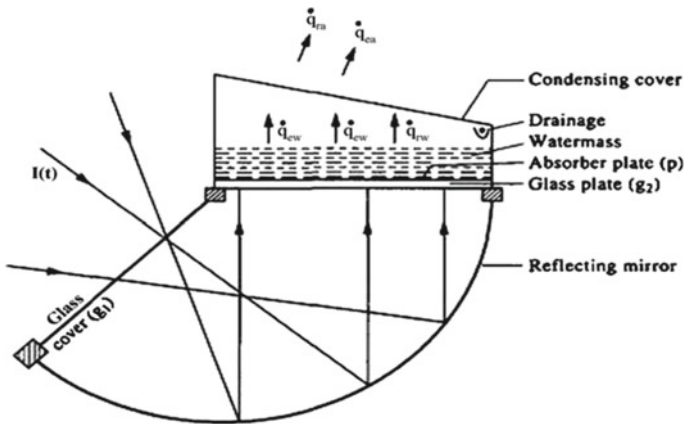
Fig. 5 Schematic diagram of solar still with inverted absorber [18]

efficiency. Arunkumar et al. [22] presented a solar still with hemispherical top covering as shown in Fig. 8. They have experimented with and without the flow of water over the top cover and the result found as 34 and 42% efficiency without and with water flow over the top cover of still basin.

Ahsam et al. [23] presented the new design of tubular solar still which have more exposure for solar radiation hence more evaporation as 77% produces more distillate. Tiwari and Kumar [24] experimented on tubular solar still during off light time at night and found better performance than conventional solar still. Kumar and Anand [25] presented tubular solar still of tray type with multi-wick. In this system, due to overall higher heat gain more evaporation and ultimately more distillate output. Arunkumar et al. [26] studied a tubular solar still with rectangular tray type
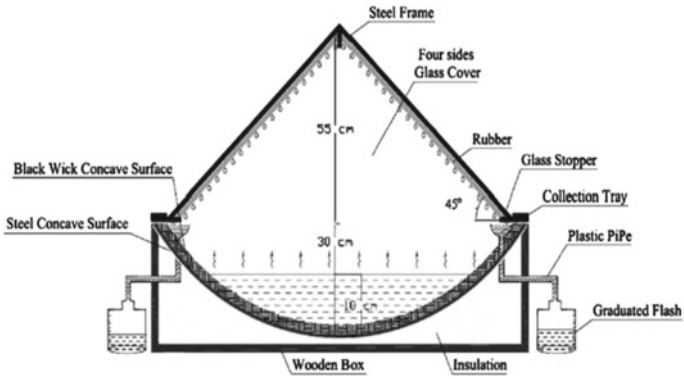
Fig. 6 Schematic diagram of pyramid solar still [19]
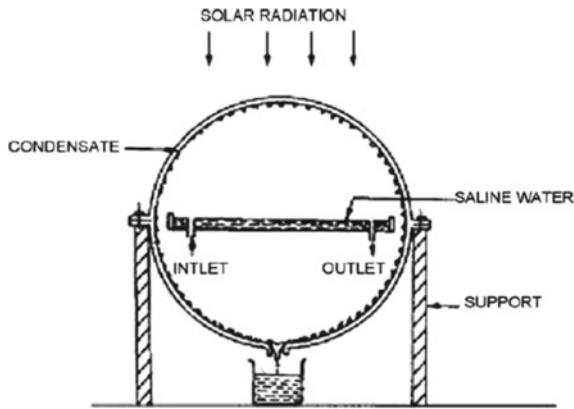
Fig. 7 Schematic diagram of spherical solar still [20]
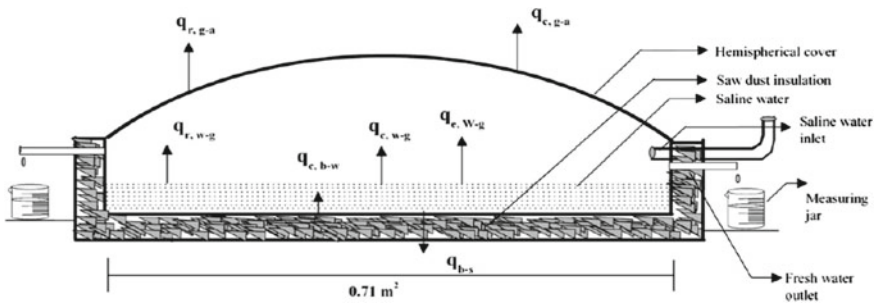
Fig. 8 Schematic diagram of hemispherical solar still [22]
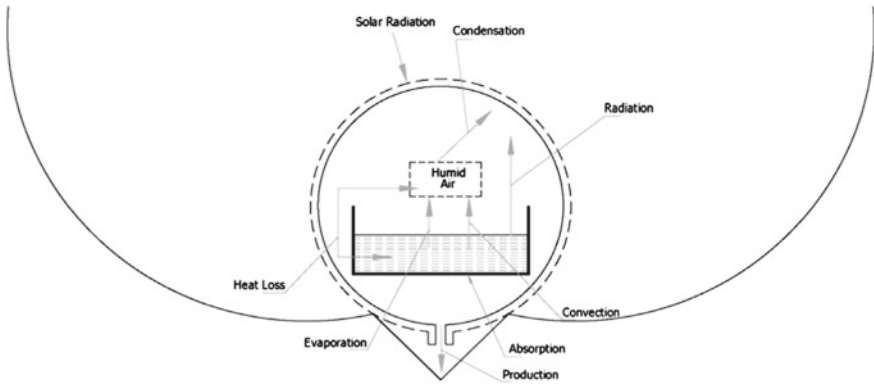
Fig. 9 Schematic diagram of tubular solar still with reflectors [26]

Fig. 10 Line diagram of V-type solar distillation system with boosting mirror [27]
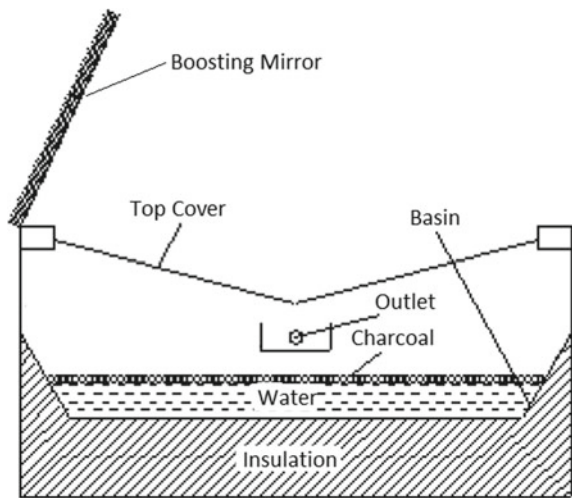
water basin and with water and air flow through basin top cover as shown in Fig. 9. The result was found as 2.05 l/day distillate output for without cooling condition, 3.05 l/day productivity for air-cooled condition and 5 l/day productivity for water-cooled conditions.

Selva Kumar et al. [27] investigated the performance of V-type solar distillation system associated with charcoal absorber as shown in Fig. 10 and found 24.47% and 11.92% overall efficiency without and with the boosting mirror, respectively. The next experiment was done with charcoal along with and without boosting mirror and found 14.10% and 30.05% distillate output, respectively.

3   Result and Discussions

In the above study, various types of specially designed single basin solar stills have been carried out and found overall productivity and efficiency as 2.1 l/m^2 per day and 34%, respectively, for conventional single basin solar still with plastic cover which is further improved by specially designed solar stills. Still with internal mirrors, with stepped basin along with solar tracking device showed better results like first system with internal mirror showed 30% improvement, second system with stepped basin showed 180% improvement and third system with solar radiation tracking system showed 380% improvement in comparison with passive solar distillation systems. The third combination of still gives the best performance because this combination has the maximum possibility to receive excessive solar radiation energy. Solar still with wick type found better result (45.5% higher productivity than conventional solar still) than fin or sponge type (29.6% and 15.3% productivity, respectively) because of greater effective evaporative and condensation surface area is provided by fins in still basin. V-type solar still with boosting mirror produces 30.05% yield but tubular still reflectors performs better and produces 5 l/day distillate output due to better solar gain for smaller basin water depth.

4   Conclusion

In the present study, on the basis of performance analysis for specially designed single basin passive solar stills have been reviewed and the conclusions have been represented as follows:

- A brief review have been done for specially designed single basin solar stills with plastic cover, with internal mirror, stepped basin, and solar tracking device, with fin, sponge, and wick, with boosting mirrors, with inverted absorber, pyramid-type solar still, spherical and hemispherical solar still, tubular solar still, and V-type solar still.
- Tubular solar still with compound parabolic concentrator produces maximum distillate output.
- It is observed that productivity, efficiency, and overall performance of a solar still depend on solar collector surface area, effective evaporative area, basin water depth, and design of solar still, which influences heat transfer coefficients and ultimately affects the performance of solar still.
- Solar still with special design are having maximum possibility to trap and utilize the thermal energy of solar radiation (direct, indirect or diffused solar radiation) along with larger evaporative surface area and better effective condensation area, hence produce better distillate.
- The present study emphasizes the further improvement of solar still with new designs that shows better performance and efficiency with great economy. In this way, it is difficult to find out most economic and efficient solar still among

the all studied stills as conventional single basin solar still itself is not much economic due to lower production of distillate. So, there is much scope available for preparing more economic, self-sustainable and efficient solar distillation system onwards.

References

1. Malik MAS, Tiwari GN, Kumar A, Sodha MS (1982) Solar distillation. Pergamon Press, Oxford, UK
2. Frick G, Hirschmann J (1973) Theory and experience with solar still in Chile. Sol Energy 14(4):405–412
3. Al-Hayek I, Badran OO (2004) The effect of using different designs of solar stills on water distillation 169:121–127
4. Nebbia G, Menozzi GN (1966) Historical aspects of dissalzione. Acqua Ind. 41(42):3–20
5. Garg HP, Mann HS (1976) Effect of climatic, operational and design parameters on the year round performance of single sloped and double sloped solar still under Indian arid zone conditions. Solar Energy 18:159–163
6. Tiwari GN, Mishra RK (2012) Advanced renewable energy sources. RSC Publishing, Cambridge, UK
7. Tiwari GN (2009) Dimri Vimal and Chel Arvind: parametric study of an active and passive solar distillation system: energy and exergy analysis. Desalination 242:1–18
8. Tiwari GN, Lovedeep S (2017) Review on the energy and economic efficiencies of passive and active solar distillation systems. Desalination. http://dx.doi.org/10.1016/j.desal.2016.08.023
9. Singh AK, Singh DB, Mallick A, Kumar N (2018) Energy matrices and efficiency analyses of solar distiller units: a review. Sol Energy 173:53–75
10. Singh AK, Chattopadhayaya S, Singh DB, Kumar N (2017) Performance study for active solar stills based on energy metrics: a short review. J Refrig Air Cond Heat Vent 4(3):21–26
11. Dev R, Tiwari GN (2009) Characteristic equation of passive solar still. Desalination 245:246–265
12. Dev R, Singh HN, Tiwari GN (2011) Characteristic equation of double passive solar still. Desalination 267:261–266
13. Phadatare MK, Verma SK (2007) Influence of water depth on internal heat and mass transfer in a plastic solar still. Desalination 217(1–3):267–275
14. Kunze HA (2001) A new approach to solar desalination for small and medium size use in remote areas. Desalination 139:35–41
15. Abdallah S, Badran O, Abu-Khader MM (2008) Performance evolution of a modified design of a single slope solar still. Desalination 219:222–230
16. Velmurugan V, Gopalakrishan M, Raghu R, Srithar K (2008) Single basin solar still with fins for enhancing productivity. Energy Convers Manag 49:2602–2608
17. Shanmugan S, Rajamohan P, Mutharasu D (2008) Performance study on an acrylic mirror boosted solar distillation unit utilizing seawater. Desalination 230:281–287
18. Tiwari GN, Suneja S (1998) Performance evaluation of an inverted absorber solar still. Energy Convers Manag 39(3–4):173–180
19. Kabeel AA (2009) Performance of solar still with a concave wick evaporation surface. Energy 34:1504–1509
20. Dhiman Naresh K (1988) Transient analysis of a spherical solar still. Desalination 69(1):47–55

21. Basel Ismail I (2009) Design and performance of a transportable hemispherical solar sill. Renew Energy 34:145–150
22. Arunkumar T, Jayaprakash R, Denkenberger D, Ashan A, Okundamiya MS, Sanjay K, Tanaka H, Aybar HS (2012) An experimental study on hemispherical solar still. Desalination 286:342–348
23. Ashan A, Imteaz M, Rahman A, Yusuf B, Fukuhara T (2012) Design, fabrication and performance analysis of an improved solar still. Desalination 292:105–112
24. Tiwari GN, Kumar A (1988) Nocturnal water production by tubular solar stills using waste heat to preheat brine. Desalination 69(3):309–318
25. Kumar A, Anand JD (1992) Modeling and performance of a tubular multiwick solar still. Energy 17(11):1067–1071
26. Arunkumar T, Jayaprakash R, Ahsan A, Denkenberger D, Okundamiya MS (2013) Effect of water and air flow on concentric tubular solar water desalting system. Appl Energy 103: 109–115
27. Selva Kumar B, Sanjay K, Jayaprakash R (2008) Performance analysis of a V type solar still using a charcoal absorber and a boosting mirror. Desalination 229:217–230

The Advancement of United Acceleration–Brake Pedal: A Review

Rahul Garjola(ORCID)**, Rohit Yadav**(ORCID)**, Ravi Yadav**(ORCID)
and Dinesh Chawla(ORCID)

Abstract In the modern time, vehicles are equipped with the dedicated accelerator and brake control pedals. Right foot is mostly engaged in operating the pedals having contrasting and dissimilar behaviour. To operate a pedal, a driver needs to leave the other. The switching time between the pedals in various situations has been determined by the ability and response time of the driver. Another critical parameter for safety is the time required for the vehicle to stop completely. Switching foot between the pedals takes time, and consequently, the vehicle will travel more distance before stopping. The delay between the shifts from one pedal to the other reduces the effective stop time of the vehicle and leads to serious accident sometimes. In recent years, automobile designers have developed several coupled accelerator–brake pedal systems to reduce the response time in braking and to eliminate the possibility of pressing the incorrect pedal during panic situations. This study aims to summarize and discuss the recent development of combined acceleration–brake pedal and its usefulness for future vehicles.

Keywords Ergonomics · Combined acceleration–brake pedal · Automobile

1 Introduction

There are three foot pedals employed for the smooth and safe functioning of a vehicle. These three pedals are named as the clutch, brake and acceleration pedals placed customarily at left, middle and right, respectively. Therefore, right foot is mostly engaged in operating the accelerator and the brake simultaneously. This arrangement also ensures the release of throttle while braking. There is a predefined distance between an accelerator and brake pedals always evidently increase brake reaction time. In case of a panic situation during driving, foot might incorrectly

R. Garjola (✉) · R. Yadav · R. Yadav · D. Chawla
Department of Mechanical Engineering, Manav Rachna International Institute of Research and Studies, Faridabad 121003, Haryana, India
e-mail: rahulgarjola@gmail.com

place on the brake or it may wrongly hit the throttle instead of the brake [1, 2]. Inaccurate foot placement on brake leads to the poor braking performance of the vehicle. As per Schmidt's [1] study, unintended acceleration is even worse in case of the cars running on automatic transmission due to the absence of clutch pedal. On the other hand, the driver is able to discover the mistake quickly in case of manual transmission because the vehicle will gain race when clutch released. Automakers implemented levelling difference between the acceleration and brake pedals to minimize the danger of mishandling. These two pedals are typically placed at different heights; the brake pedal is usually mounted higher than the accelerator one. On the contrary, this arrangement further escalates foot switching time between pedals. An easy solution for such type of problem is to use combined accelerator–brake pedal in place of traditional pedals [3]. In recent times, several models of united accelerator–brake pedals were proposed, but most of them were more or less impractical. Some interesting designs were also proposed and implemented at laboratory scale but not commercialized yet. A lot of work is still needed to make this design safe and ergonomically suitable for the use of general public. This study aims to comprehensibly summarize the research contributions of various peoples in the field of the combined acceleration–brake pedal system.

2   Standard Pedal Drive System

A vehicle is able to dodge the collision with moving or stationary obstruction by proper braking. Sometimes drivers misjudge the actual situation on the road and apply the brakes too late to stop the car at a required distance. Unfortunately, collision is unavoidable in such type of situation. As per the Johansson and Rumar [4], if the brakes were applied 0.4–0.8 s earlier, the collision could be prevented. A delay in braking is due to the driver's reaction time and foot movement time from the accelerator to brake. Automaker might not change the driver's response time but time spend during foot movement could be reduced using some innovative designs. As suggested in some literature, the time lag could be reduced by the optimization of a vertical and horizontal position of the two pedals. Additionally, the clearance between the pedals should also be optimized for preventing the accidental hit of the wrong pedal in emergency situations. Again, the foot travel time is a critical issue in such type of arrangement and minor improvement in the braking is expected. Davies and Watts [5] suggested that if the vertical height difference between the two pedals is 152 mm the foot movement time varies in between 0–16 s at different situations. Snyder [6] found that the optimum foot movement time could be achieved when the brake and accelerator are situated at similar height with 62.5 mm horizontal separation. From the studies, it was found that the placement of the pedals at optimum distances did not provide required braking efficiency.

Therefore, people worked on innovative pedal designs which can minimize or eliminated foot travel time. Konz et al. [7], Poock et al. [8] and some others have proposed designs of combined accelerator–brake pedal operated by the heel-toe movement for a significant reduction in braking durations.

3 Combined Pedal Drive System

In combined pedal, the acceleration is achieved by the forefoot movement in the forward direction. Whereas, brakes are applied if whole foot is hitting the pedal in the forward direction. Therefore, instant acceleration or brake can be engaged by the movement of the foot in one direction. Additionally, when brake applied, the accelerator will switch to idle condition instantly. The horizontal movement of the right foot is completely eliminated if combined accelerator–brake pedal is utilized instead of conventional pedal arrangements in the vehicle for safe driving. It was reported that incorporation of Winkelman's pedal model reduced the brake reaction time up to 0.2 s [7–9]. As the single pedal is employed and foot is always placed on it, there is no possibility of misapplication or accidental hit of accelerator instead of the brake [1]. The manoeuvre of foot in the combined pedal is mostly up and down whereas, in case of conventional pedal it is up, down, right and left. Therefore, driving fatigue is reduced efficiently for extended driving sessions. All these advantages are encouraging researchers to propose or devise innovative configurations of combine accelerator–brake pedal.

Glass and Suggs [10] studied the foot movement time between stimulus and incidence of braking. They divided their study into two sections. In the first part of the study, relative vertical heights of conventional pedal systems were considered, and its effect on effective braking was discussed. They proposed if the accelerator pedal was located 25–50 mm higher than brake pedal, the foot travel time is reduced by 12.5% as shown in Fig. 1. The second part of the study explained the effectiveness of a new design in which acceleration and braking can be done by a single pedal. They found 74% reduced braking time with this new design. The comparison of braking efficiency of conventional and combined accelerator–brake pedal is shown in Fig. 1. It can be clearly understood from the figure that the effective braking could be achieved using combined accelerator–brake pedal. There is no height difference exist in the combined pedal system (CPS) that is why zero foot movement time is shown in Fig. 1.

Poock et al. [8] studied the braking efficiency of a single pedal drive and conventional pedal drive system as per the ergonomic point of view. They designed their study in two parts. The first part is to derive optimal parameter settings for seating posture. The second part is to compare the reaction time of braking in one pedal drive and conventional pedal drive system.

Fig. 1 Effect of foot pedal heights on reaction time in conventional and combined accelerator–brake pedal (Reconstructed from [10])
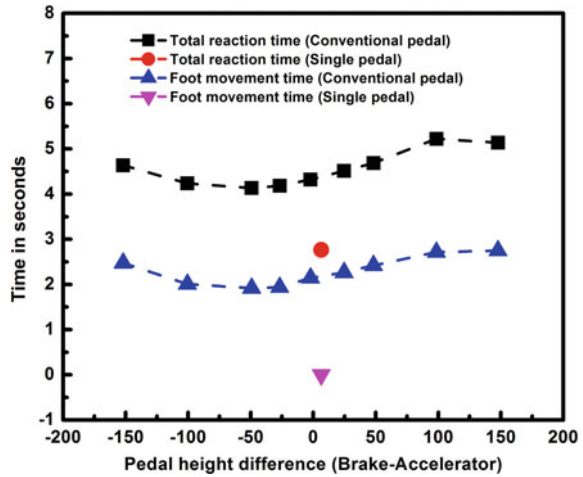
Table 1 The optimal parameters of driving posture [4]

S.no.	Parameters	Setting limits
1.	Seat distance from pedal	As per the driver's comfort level
2.	Seat height	Around 8–11 in. above heal end of pedal
3.	Seat tilt angle	0–5° tilt toward back
4.	Ankle angle	85–95° at zero acceleration
5.	Floor angle	Around 60° in most vehicles
6.	Knee angle	Around 150°
7.	Angle of twist	5–10° to the right vertical

The average reaction time of conventional and one pedal system was 0.468 and 0.256 s, respectively, for the optimal seating arrangements as listed in Table 1. It is around 45% better than the conventional brake system. It means if a car is running at 96 kmph, the margin of safety provided by the single pedal drive system is around 5.8 m.

Nilsson [3] studied the human behaviour towards accepting the combined accelerator–brake pedal system. He divided his study into five different sections. Eighteen participants have participated in his study. Out of 18, nine were male, and nine female of age group ranges from 18–79. They were asked to perform specific tasks over the 9 months of time in all the five sessions and instructed to document the necessary feedback in their diaries. The five sections of the test were included the basic functioning of the CPS, asked to do first manoeuvre test, provided training for a period of time, asked to drive alone in several terrains, asked to perform second manoeuvre test, and finally, they have to share the experience with the investigator. He also recorded the reaction time for prepared braking. The feedback

Fig. 2 Number of reported errors per 1000 km for driving stretches of 200 km (Reconstructed from [3])
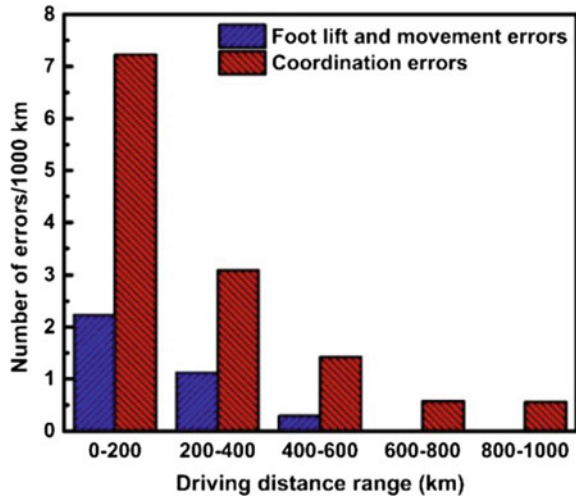
diaries were collected, and the recorded data were analyzed. On the basis of data analysis, some important conclusions were drawn by him.

The main conclusions drawn by the Nilsson [3] from his study are summarized below:

- Transition from the conventional pedal systems to the combined brake–accelerator system is comparatively stress-free and unproblematic and adopted easily by all the categories of drivers irrespective of age and gender.
- The initial mistakes committed by the drivers owing to unfamiliarity of the system are quickly abated. In most cases, the problems were rectified on or before completing 500 km of driving as shown in Fig. 2.
- Women and older men drivers struggled most to get acquainted fully with the new system. Besides, they managed well in normal traffic conditions after experience.
- Sometimes erroneous driving behaviours were also reported by the drivers. In some cases this erroneous driving behaviours of drivers continued even after they gained significant experience.
- The outcomes of misapplications were not fetal because of high level of awareness and braking response time provided by the new pedal design. Therefore, combined brake–accelerator pedal provided better safety with fewer inconsequential accidents with respect to standard braking system.

The problems of transition between pedal systems are surprisingly low. The drivers are adopting the new system really quickly. Additionally, the higher braking efficiency provided by the design prevented the accidents successfully. Therefore, the survey provided by Nilsson supports the replacement of standard brake system by more advanced combined brake system.

3.1 Different Designs of Combined Pedal Drive System

Various designs of combined accelerator–brake pedals have been proposed and patented. Some innovative designs are explained in this section.

Winkelman Design. Winkelman Design. It is mainly based on the heel–toe pivoted movement of plungers as shown in Fig. 3a. It is a simple design in which rare ends of a flat board is attached with cylindrical plunger rods. It consists of some locking arrangement for one plunger when the other one is moving and vice versa. The vehicle will get accelerated when the driver presses the plunger using toe. In that case, the plunger below the heel is non-operative. On the other hand, the vehicle will stop when the driver presses the plunger using the heel. Likewise, the plunger below the toe is non-operative. Therefore, simultaneous acceleration and brake could be achieved using a single pedal [11].

Naruse Design. In his design, clockwise movement of right foot accelerates the vehicle whereas, pushing down the same pedal applies the brake (shown in Fig. 3b). This idea was fascinating, but it created the problem as per the ergonomic standpoint especially for extended driving sessions [12, 13]. Matsunaga et al. [14] examined the effectiveness of Naruse pedal system during emergency or panic braking situation. They observed that the car housed Naruse pedal system is stopped 1.6 m earlier than the car with the conventional pedal system at a speed of 40 km/h.

Gustafsson Design. The combined pedal devised by Gustafsson consist of two distinct gestures of the foot for acceleration and brake (shown in Fig. 3c). In his design, a single pedal was used, and acceleration was achieved when the pivoted motion of foot took place with respect to heal, i.e. when forefoot was pressing the pedal in the forward direction while heal was at rest. On the other hand, the brake was applied when the whole foot was moving toward forwarding direction [15, 16].
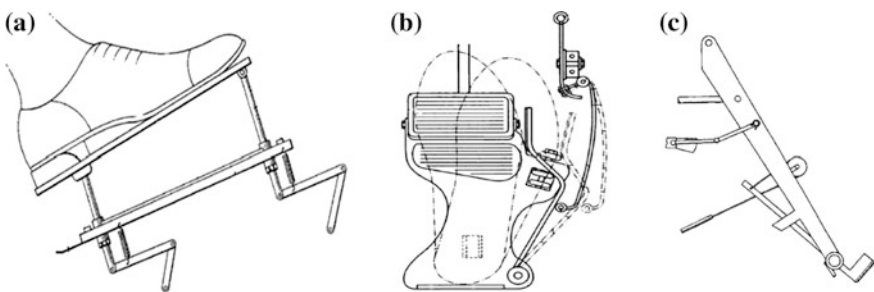
Fig. 3 Combined accelerator–brake pedal design **a** Winkelman's pedal (Reconstructed form [11]) **b** Naruse's pedal (Reconstructed from [12]) **c** Gustafsson's pedal (Reconstructed from [15])

3.2 Modelling Based Approach for Combined Pedal Drive System

To analyze the performance of combined pedal system (CPS), CAD modelling and FEM analysis were also performed in some studies. Arora [17] prepared a pivoted design of a CPS in CATIA V5. A prototype of this 3D model was manufactured using mild steel (AISI 1018) and tested accordingly. They claimed that the proposed design significantly reduced the interference between two contrasting actions, i.e. acceleration and braking. Pawar et al. [18] studied the robustness of the CPS using ANSYS 14. The comfort level as per ergonomic consideration was also investigated. The pressure on different components of the pedal was also studied. The materials were selected by considering cost, strength and availability. However, the fasteners used for the design optimization were selected on the basis of loading condition results.

3.3 Combined Pedal Drive System for Electric/Hybrid Electric Vehicle

In electric and hybrid electric vehicle, mostly advanced regenerative braking technology is employed for charging the batteries using braking power. Schmitz et al. [19] investigated the standalone design of combined accelerator–brake pedal equipped with an electronic brake which is shown in Fig. 4. The simulator used by them consists CPS with an additional hydraulic brake pedal. They observed that drivers preferred the CPS more often for stopping the vehicle over the hydraulic brake. The driving efficiency was also improved with combined accelerator–brake pedal. Constant observation of power gauge is a prerequisite for monitoring acceleration, deceleration or sailing of the vehicle when CPS is utilized. On the

Fig. 4 A new design of combined accelerator–brake pedal for electric or hybrid electric vehicles (Reconstructed from [19])

S.no.	Automobile company	Model	References
1.	Nissan	Leaf	[20]
2.	Toyota	Cresta	[14]
3.	Tesla	Model S	[21]
4.	Volkswagen	eGolf	[22]
5.	Chevrolet	Bolt EV	[23]
6.	BMW	i3 eV	[24]
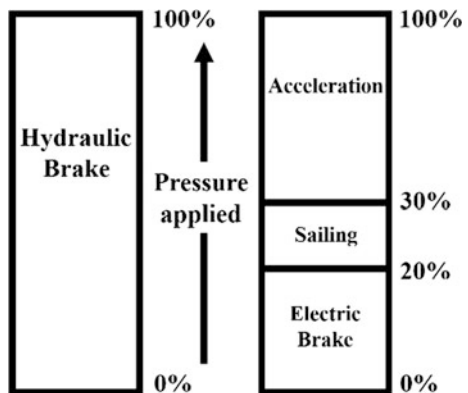
Table 2 Utilization of one pedal drive system in various car models

contrary, the braking process is more predictable and easy when strong electronic brakes are incorporated in the CPS. Again, the comfort level of the driver increased because of no foot movement involved while braking. The use of hydraulic brake pedal along with CPS guaranteed the additional safety since the driver can use the hydraulic brake in the state of confusion [19].

The development of electric vehicles (EV) or hybrid electric vehicles (HEV) has got pace in recent years. The way of driving has been completely changed due to the incorporation of the regenerative brake system in electric vehicles. The regenerative braking system stimulates the charging cycle of batteries while braking. To fully extract the potential of regenerative braking, the EVs or HEVs are fitted with one pedal drive system. The model and make of the cars running on one pedal drive configuration is summarized in Table 2. These cars housed advanced design and configuration of a combined accelerator–brake pedal for full regenerative energy absorption during deceleration.

3.4 Risks Associated with Combined Pedal Drive System

The main risks associated with the CPS are listed here [3, 10].

- Switching cars of the different pedal system may create a state of confusion in drivers mind. He/She can move his foot away from the combined pedal when brakes are required because of already instilled habits.
- The reduced brake reaction time may provoke the drivers to compensate with smaller safety-margins. He/She might drive fast or maintain shorter distance to the leading vehicles.
- The new or radical design includes economic considerations for automakers. Changing already instilled habits and learning new procedures are some other more significant challenges. Also, the availability of data related to performance and public acceptability is not up to the mark.

4 Conclusions

In this article, a review on the significance of combined accelerator–brake pedal is presented. In the discussion, several aspects of one pedal drive and its importance is enclosed. It was reported in the literature that the problems with the separate pedal system such as accidental hit of accelerator pedal instead of brake, poor braking and high foot switching time between pedals could be eliminated using combined pedal system (CPS). Additionally, the foot switching time is eliminated and breaking efficiency is improved around 45% when conventional pedals were replaced by CPS. The effect of driver's seating posture on average reaction time is improved significantly for CPS resulted in higher margin of safety. The CPS is recently incorporated in several electric or hybrid electric vehicles for encouraging one pedal drive and it was branded as an additional safety feature in the cars.

References

1. Schmidt RA (1989) Unintended acceleration: a review of human factors contributions. Hum Factors 31:345–364
2. Wu Y, Boyle LN, McGehee DV (2018) Evaluating variability in foot to pedal movements using functional principal components analysis. Accid Anal Prev
3. Nilsson R (2002) Evaluation of a combined brake–accelerator pedal. Accid Anal Prev 34:175–183
4. Johansson G, Rumar Kare (1971) Drivers' brake reaction times. Hum Factors 13:23–27
5. Davies BT, Watts JM Jr (1970) Further investigations of movement time between brake and accelerator pedals in automobiles. Hum Factors 12:559–561
6. Snyder HL (1976) Braking movement time and accelerator-brake separation. Hum Factors 18:201–204
7. Konz S, Wadhera N, Sathaye S, Chawla S (1971) Human factors considerations for a combined brake-accelerator pedal. Ergonomics 14:279–292
8. Poock GK, West AE, Tobbn TJ, Sullivan JPT (1973) A combined accelerator-brake pedal. Ergonomics 16:845–848
9. Higginbotham III HW, Frost JA (1972) A road test comparison of reaction times using an operational combined brake-accelerator pedal and the conventional brake pedal
10. Glass SW, Suggs CW (1977) Optimization of vehicle accelerator-brake pedal foot travel time. Appl Ergon 8:215–218
11. Winkelman CN (1959) Automotive vehicle foot pedals. https://patents.google.com/patent/US2878908A/en
12. Naruse M (2004) Automobile accelerator and brake pedal device. https://patents.google.com/patent/US20040139818/en
13. Farrier J (2010) One pedal for both the brake and the accelerator. http://www.neatorama.com/2010/08/04/one-pedal-for-both-the-brake-and-the-accelerator/

14. Matsunaga K, Naruse M, Muto F, Kitamura F (1996) New brake pedal and accelerator bar system to prevent the mistake of pressing down the accelerator instead of the brake in emergency situations. In: International conference on traffic and transport psychology. Valencia, Spain

15. Gustafsson S (2003) Single-pedal system in motor vehicles and a method for forming such a single-pedal system. https://patents.google.com/patent/EP0877977B1/en

16. Combined accelerator brake pedal (2002) http://www.btb.termiumplus.gc.ca/tpv2alpha/alpha-eng.html?lang=eng&i=1&index=alt&srchtxt=COMBINED%20ACCELERATOR%20BRAKE%20PEDAL

17. Arora S (2016) A combined pedal for brake and accelerator. Int J Res Aeronaut Mech Eng 4:131–138

18. Pawar S, Buchade S, Patil O, Maneri A (2017) Design and development of combination of brake and accelerate pedal. Imp J Interdiscip Res 3:144–146

19. Schmitz M, Maag C, Jagiellowicz M, Hanig M (2013) Impact of a combined accelerator–brake pedal solution on efficient driving. IET Intel Transport Syst 7:203–209

20. Gibbs S (2017) New nissan leaf has one-pedal driving mode for both accelerating and braking. http://www.theguardian.com/technology/2017/sep/06/new-nissan-leaf-has-one-pedal-driving-mode-for-both-accelerating-and-braking

21. Voelcker J (2017) What IS "one-pedal driving" in an electric car?. https://www.greencarreports.com/news/1109539_what-is-one-pedal-driving-in-an-electric-car

22. Volkswagen e-golf electric vehicle test|review (2016). http://www.caranddriver.com/reviews/2016-volkswagen-e-golf-electric-vehicle-test-review

23. Bolt EV goes the distance…with one pedal (2016) https://media.gm.com/content/media/us/en/chevrolet/home.detail.html/content/Pages/news/us/en/2016/sep/0906-bolt-ev.html

24. BMW i3—one pedal driving video (2015) https://insideevs.com/bmw-i3-one-pedal-driving-video/

Additive Manufacturing and 3D Printing: A Perspective

Kunal Govil, Vinay Kumar, Divya P. Pandey, R. Praneeth and Ajay Sharma

Abstract Additive manufacturing is another word for Rapid Prototyping (RP). Rapid Prototyping in its earlier form was done using Stereolithography (a term coined by Chuck Hull in 1984). According to a variety of literature, additive manufacturing (AM) is incontestable to bring about a revolution in the way products are designed, manufactured, and supplied to end users. AM technology has gained significant academic as well as industry interest due to its ability to create complex structures with customizable features and materials. The goal of this review paper is to organize this body of knowledge surrounding AM, and present current barriers, findings, and future prospects for manufacturers and researchers. The evolution due to AM in areas such as material, design, and production also has been discussed.

Keywords Rapid Prototyping · 3D printing · Additive manufacturing · CAD

1 Introduction

Additive manufacturing (AM), also referred to as 3D printing has gained popularity in media and captured the imagination of the public as well as researchers in many fields. With recent interests, this technology is continuously being changed, reimagined and customized to a wide domain of applications ranging from automotive, aerospace, engineering, medicine, biological systems, and food. A historical analysis of AM reveals its roots lie in photo sculpture (in the 1860s) and topography (in the 1890s) [1].

An earlier form of additive manufacturing included photopolymer curing (Stereolithography), filament deposition (FDM) and sheet lamination (laminated object manufacturing, LOM). With literature and experiments performed in the

K. Govil (✉) · V. Kumar · D. P. Pandey · R. Praneeth · A. Sharma
Department of Mechanical and Automation Engineering, Amity University Noida, Noida, Uttar Pradesh, India
e-mail: kunalgovil345@gmail.com

past, additive manufacturing now includes processes like powder metallurgy, laser sintering, electron beam sintering/welding, binder jetting, etc. The significant amount of interest and investment in development AM technologies does not come as a surprise, as its capability for layerwise additive fabrication method is an innovative concept that is different from conventional material removal process and its ability to build complex shapes and patterns using a wide variety of materials. The recent boom in electronics and automation resulted in a reduction in the cost of programmable controllers, lasers, ink jet printing, and computer-aided design (CAD) software has enabled variation in conventional design limitations, allowing individuals to innovate, utilize and tinker with new design concepts. The current technology is being used by companies to create prototypes and concept parts for visualization and testing and small parts that require less amount of mechanical or structural integrity. Companies that use 3D printing technology currently range from General Electric (world leader in mechanical and electrical appliances), Boeing, Koenigsegg, and Ford Motors (automobile manufacturers) and Hasbro (world leader in toy manufacturing).

The goal of this review paper is to organize the body of knowledge we have culminated and present our understanding and observations on this large spectrum of AM technology. We believe that this technology is at a critical stage as advancements in material science and engineering are putting the stepping stones towards the future of manufacturing. For example, advancement in related technologies (such as new material, or topology optimization) can significantly affect or sometimes give rise to advancements in AM technology. This paper starts by describing fundamental of AM processes in Sect. 1. We also put forward an overview of all types of AM technologies with illustrations. In Sect. 2, we present a literature review of older and most recent scientific papers on Additive Manufacturing. Next, in Sect. 3, we provide an overview of the attributes and barriers of AM technology and help give perspective on how to improve upon them. Section 4 summarizes developments in the industries like Manufacturing, Construction, and Education. We conclude our paper by outlining important future trends in Sect. 5.

1.1 Additive Manufacturing

Working principle of a 3D printer is very simple and in relevant with the current CNC operated manufacturing systems. Like all other systems, 3 coordinate axes are used to move different motors (x and y usually being the extruder and z being the bed). Conventional material removal processes require metal to undergo a primary form of manufacturing (casting and forging), whereas in AM the material is directly placed in regions that require structure (based on CAD design).

AM processes fabricate parts by creating successive cross-sectional layers of an object. The model is sliced into thousands of layers (depending on the resolution) by slicing software (for example Cura). Each layer is created via the selective

deposition of material (and/or energy to fuse the material) to form a printed surface as shown in Fig. 1.

1.2 Fused Deposition Modeling

As depicted in Fig. 1. Fused Deposition Modeling (FDM) is one of the most basic forms of 3D printing. Filaments of thermoplastics like PLA (polylactic acid) or ABS (acrylonitrile butadiene styrene) are used in FDM. A hot extruder head with a very fine nozzle is used to lay down layer after layer till the part is complete. Most DIY home printers work on FDM technology and while most extrusion systems process thermoplastic materials, efforts have been made in processing ceramic and metal pastes. The FDM printing process can be seen in Fig. 1a.

1.3 Powder Bed Fusion

Powder bed technology generally requires a high powered energy beam (Laser or electron Beam) to selectively melt a bed of metallic powder, for example, Stainless steel, titanium, etc. After each scanning process, a fine layer of powder is spread with the help of a roller. Processes like Direct Metal Laser Sintering (DMLS), Selective Laser Melting (SLM) and Electron Beam welding are a part of powder bead type 3D printing, seen in Fig. 1b. This AM process has to be done in a vacuum-like environment to avoid metal oxidization at higher temperatures and requires high temp heating in post-processing.
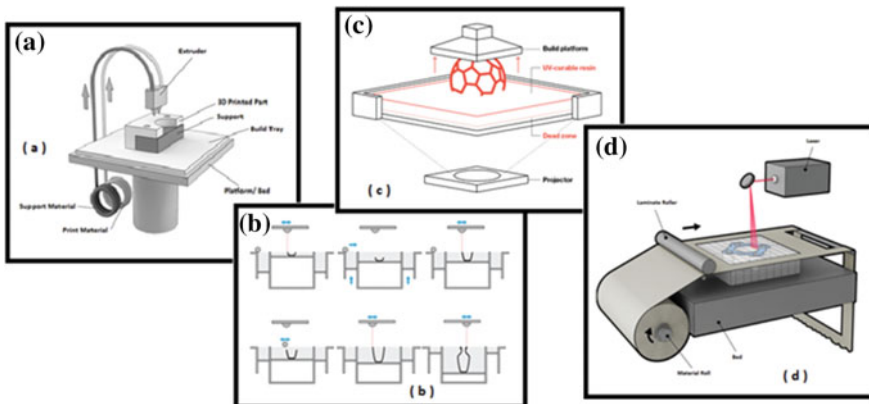
Fig. 1 a FDM [2], b DMLS [3], c STL [4], d LOM [5]

1.4   Photopolymerization

Photopolymerization is a new name given to Stereolithography (STL) and Digital Light Projector (DLP). In photopolymerization, a UV light source is used to cure photosensitive resins into solid objects. Some problems with STL are over curing and cost of necessary supplies. Many improvements have been made to make use of other resin materials like elastomers, nylons, etc. A revolutionary photopolymerization printer, the Carbon M1 had been introduced into the market in 2015. Its technological works on DLP and has brought advancement allowing a part that usually took 3 h to make to be made in less than 15 min Fig. 1c.

1.5   Material Jetting

Material Jetting 3D printing is very similar to normal inkjet printing. In material jetting, material such as wax or photopolymer is printed on a substrate and then cured via heating or UV curing. This repeated deposition of material and curing process results in a 3D solid object. Due to limitations in viscosity of the material, most materials cannot be used as the material is sprayed on the substrate and thus colloidal solutions cannot be used.

1.6   Binder Jetting

This process of additive manufacturing is very similar to powder metallurgy and powder bed fusion technique. In this process, a binder is deposited on a powdered bed. The binder adheres to the powder on the layer and the process continues. After fabrication, the part is put in a furnace for post-processing to cure the binder and melt the powder to form a structurally stronger part. This process is successful in processing ceramics, metals, foundry sand (silica sand), concrete and polymer materials.

1.7   Laminated Object Manufacturing

LOM is one of the earliest forms of additive manufacturing with its origination in 1987. In this, multiple layers of material are cut with a calibrated CO2 laser and placed on top of one another to form a three-dimensional object. LOM provided standardization, larger production size and a better surface finish than STL, and thus was used to prototype metal parts Fig. 1d.

1.8 AM in Current Industries

Nowadays AM technology is widely used in manufacturing, civil engineering, and in education sector.

1.8.1 Manufacturing

Manufacturing is a field that is profiting with the addition of 3D printing machines in their arsenal. General Electric (manufacturing giant) which had taken responsibility to produce a new engine for the Black Hawke helicopter with the help of 3D printed parts under the armies improved turbine engine program (ITEP), is under testing. The parts are working as predicted and with lesser overall weight. Another Manufacturing giant, Electrolux is developing spare parts for their electronics and machines with 3D printers. This reduces their dependencies on suppliers, hence increase part availability and reduces overall costs [6, 7].

1.8.2 Civil/Construction

With the ability to produce complex structures and without difficulty has sparked interest of designers and architects all around the world. Amt-Spetsavia (a company in Europe) has managed to build an entire home using a concrete 3D printer. Unlike other printers, they produce blocks that interconnect to form a solid structure. Sculptures, unlike the times when Michelangelo used to sit with a stone block and hammers, are now easy to make. The artist just has to make a 3D model of the sculpture sitting on a computer to produce the most exquisite pieces of art [6, 8].

1.8.3 Education

With the younger generation growing up in a modern time with the ultimate form of technology makes the older generations feel how their parents did when they used their first television. Most countries imply keeping vocational training on 3D printers, a part of their curriculum. Using 3D printers in education will improve the basic understandings of subjects like engineering fundamentals with focus on materials and their properties, and manufacturing process, pragmatic approach to skills development, problem-solving and critical thinking, design principles tools, etc.

2   Literature Review

Gao and Zhang [1] give an overview of 3D printing technology and its applications in industries like Automobiles, Medicine, Engineering, Education, etc. In the paper, they describe different materials along with their construction characteristics like max particle size, minimum size, layer thickness, tolerances, and applications.

Cheng et al. [9] they give requirement and reason for topology optimization. This term, according to them, has its origin in casting. Due to complexities in design, certain design changes have to be made in order to obtain a specific output. Increase in complexity may lead to reduction in both material and production costs. With experimentation, they gave forward constraints, faced during fabrication.

Scaffold structures for overhanging structures, Curling and Warping in metal printers (at high temperatures), Building accuracy, Surface finish, Size constraint, and Inability for multi-material printing.

Brackett and Ashcroft [10] State the concept of Additive Manufacturing and the processes through which a part is fabricated. They explain each and every step starting from the modeling in CAD software to slicing into layers. Their paper emphasizes more toward the post-processing aspect of 3D printing in which they give an overview of processes like sanding, heat treatment, and finishing.

Doubrovski et al. [11] worked on electromechanical systems that has lead the science of rapid prototyping to the next level. Their success in building a 3D-printed stepper motor has built up a storm in the department of aerospace engineering. This process improves volumetric efficiency, with reduced production costs and leads the path to on-demand production of specialized parts. Their tests show that because of limitations in production quality, the motor cannot match with the market produced motors, but may in the future.

Aguilera and Ramos [12] is on multi-material 3D printing technology, especially integration of electronic circuits. In their industrial study, they observed that cost of a material is dependent on "Time to market" aspect of production. To counter multi-stage manufacturing and assembly, they introduce printed electronics. With success in building a flashlight (leaving out the bulb and battery), they suggest this type of manufacturing as the technology of the future.

Goh and Agarwala [13] gave forward a practical paper based on the basic mechanical models like linkages, slider crank mechanism, and gears, etc. Inspired by the old mechanisms present in museums all across the world, they recreated the mechanism with 3D printing to find problems such as clearance between surfaces, warping, and friction in joints due to the resolution of current printers.

Ang [14] revolve around the designing process of an additive manufactured part. Talking about Cellular Models, they put forward how minimum material can be used to produce more structurally stable parts taking under consideration properties like design factor, stress concentration, and size effect. Cellular structure (truss) design or topology optimization focuses on creating porous materials to minimize weight and to maximize strength, stiffness, thermal conductivity. Their

conclusion statement accentuates on improvements in the interconnected domains like material science and structural engineering.

Hwa and Rajoo [15] did a study on power consumption, when any kind of manufacturing process is to be considered, energy input and consumption becomes a priority. Their study presents an overview of electricity consumption in different AM technologies. According to their study, AM is more transparent and can be easily monitored. Their conclusion states the consumption characteristics of a system are dependent on Build Volume, the requirement of heat (according to material requirements), Pre and Post heating, Layer Thickness, quantities produced per cycle.

Reference [16] Paper on Cost of AM focusses on the current aspects of AM technology and the monetary costs associated with part production. The aspects focused on in the paper are Impact on Health, Energy consumption, and environment.

Supply chain improvement, Incomplete utilization of AM technologies, harmful nature of natural binding materials, build time and energy consumption are aspects due to which this process of manufacturing is still not used for mass production. According to their finding, only positive of AM is reduction in operating costs, elimination of fixed costs of dies, tooling and promotes innovation in design.

Junk and Kuen [2] give insight on challenges and the future of AM technology, characterize the challenges of AM technology like the ones mentioned below

Lack of comprehensive design principles.

Cost and quality of marketed machines.

Variables like extrusion, curing, and geometrical positioning.

Dependencies on other domains like material modeling, tool design, computing, and process design.

Some barriers that need to be overcome for the success of this technology in the future are Personal and Mass production, Scalability and Layer Resolution, Material heterogeneity and Structural Reliability and Standardization.

3 Fundamentals of AM Technology

3.1 Attributes of AM

Design flexibility—a distinguishing feature of Additive manufacturing that differs from conventional manufacturing processes. In relation to subtractive manufacturing, traditional processes imply constraints like inability to produce complex geometry, diverse tooling, and design. Secondary manufacturing techniques (contouring, stamping, thread cutting) impose additional constraints. Unlike Subtractive manufacturing, AM gives the advantage of multi-material objects as well as topologically complex structures.

On-demand manufacturing—most current manufacturing industries focus on automation of their industry as well as increasing the flexibility of the preexisting setup. AM technology or 3D printing is one of the most flexible systems that are present in the market today. It can make anything and everything, and may not even require assembly. On-demand makes the part customizable according to customer demand and this intern increase profit and reduces requirement of tertiary machines or systems.

Design complexity and cost—current 3D printing technology has allowed freedom to designers to make more complex structures. Complexity does not increase additional expenses, whereas to make complex structure with casting, there is a direct relationship between complexity and die/mold costs.

Dimensional characteristics—properties like accuracy, resolution, and bias are some of the basic properties that allow standardization of manufactured parts. Older rapid prototyping technologies like LOM and STL lacked resolution and hence produced mere prototypes. With the improvement in AM technology, parts being produced are both according to ASME standards and functional. One property that current AM technologies are unable to achieve is tentative tolerance of assembly parts.

Assembly—unlike most manufacturing processes, 3D printed parts may or may not require assembly. Printing technologies like metal sintering produce very high-resolution and therefore the parts which need to be assembled can be printed together. Taking an example of meshed gears, both the gears can be simultaneously made. This reduces "time to market" as mentioned above which intern reduces both production fixed costs (conveyer lines) and final cost of product.

Efficiency in production—other plastic forming and molding technology include injection molding, which is faster than 3D printing but uses excess material. In production scenarios, AM can lower inventory and storage as well as reduce cost related to supply chain management. A term "buy-to-fly" ratio is the ratio of raw material bought and the material that ends up in the part is very low in AM techniques, which makes it feasible in terms of economics of manufacturing.

3.2 Barriers of AM

Build time—build time is a very important aspect of any manufacturing setup, i.e. more time means more cost. In 3D printing, the time to finish is dependent on many variables such as layer thickness, printing speed of printer and in general the total height of the part. Part orientation, resolution, quantity of parts printed per cycle, distance from origin can also impart to total build time.

Resolution and surface finish—high-resolution of a printer allows printing of very fine and subtle intricacies present in the design. Extrusion type AM technologies usually have larger deposition (in terms of size) with a minimum layer thickness of 0.25 mm whereas other systems like Metal Sintering and Vat photopolymerization have more concentrative binding features which allow layers as

fine as 0.1 mm. Surface finish is interlinked with resolution, the finer the layer thickness the better is the surface finish of the produced part. When compared FDM type printers produce distinctive layers which give rise to a rougher texture against LMS which gives very smooth surfaces (much smoother after post-processing). Other factors like vibrations, belt tautness and calibrations also affect resolution and surface finish.

Support structures—extrusion based printed parts require support structure for overhangs (most printers require support in angles upwards of 30°), and water solvable infill material to produce gaps between assembled parts. This support and infills are removed during post-processing and end up in waste. Material jetting printers do not require supports as excess powder present around the piece provide support. Metals printer do require supports to inhibit curling and warping, which are caused due to high temperatures and residual stresses.

Post-processing—current AM processes require post-processing to produce more stable and hard parts. STL requires ultraviolet hardening, FDM requires annealing, Metal Sintering requires heat treating, etc. In most cases, the post-processing requires more energy than the actual printing process. This imparts both time and cost to the final product. Curing time is also a part of post-processing. Different materials take their own distinct time to harden/solidify, this indirectly affects total build efficiency.

Material selection—with improvements in printing processes, materials that are printer ready are restricting the flexibility of the entire system. Binder Jetting being the most flexible in incorporating newer materials (due to its emphasis on post-processing) and FDM being the least flexible with only a few materials that are currently present in the market (in most cases PLA and ABS). Each material or composite provide different material characteristics, in order to make requirement-specific products, field of material science has to develop and improve.

Software—with DIY and the Maker movement has influenced the production of smaller/personal printers. As most printer work on a software interface to make CAD models and their STL counterparts, the software is required to be more user-friendly. To make these interfaces less complicated, some aspects of design have to be neglected. This neglect results in lesser quality of produced parts. Other printers like the CubeX from 3D systems work on proprietary software which constricts the flexibility of the printer.

Mass manufacturing—the printers that exist in the market today, personal or industrial, require time to print individual parts let alone when printing in bulk. Mass production is a form of manufacturing that produces large quantities of similar parts (same or from the same family of parts) at very high rates, in order to meet customer demand. The reason for this drawback is the less responsiveness and accuracy of current servo motors.

Scalability—printers have to trade one property over another to make scalability possible. Printing with thinner layer thickness produce very smooth surfaces, but intern ends up increasing the total build time. To make larger models, the machines have to print faster and thus have to sacrifice resolution and surface finish. Most printers today can easily make smaller prototypes within standards but their success is not scalable for large dimensional objects.

Structural reliability—most parts produced by AM method of manufacturing lack structural strength and material properties due to discrepancies in the fusion of the multiple layers and infill ratios. Some properties like density and malleability also change due to building parameters and high temperatures which the material is subjected to during printing. This problem can be solved by creating Heterogeneous parts, but most printers can only work with one material at any given moment.

3.3 *Improvements Required*

With our research, we have observed that most of the barriers mentioned above are due to dependency of Additive manufacturing on other fields of manufacturing like Material Management, Structural Engineering, Topology Management, Material Sourcing, Supply chain management and most importantly Electronics and Software Design. Some of the improvements that are required are mentioned below –

Material limitations can be reduced by development in the field if Material Sciences. Newer substitutes for standard materials can lead to better structural properties.

Development in Electrical and Electronic components like Fast acting servos, Position correction accelerometers for servo feedback, Artificial Intelligence for better algorithm controllers.

Topology optimization for determining the maximum strength that can be achieved using minimum raw material.

Network connectivity to the internet for improvement in machine capability by training Artificial Intelligence to learn and reduce time as well as improve productivity.

Setting Standards of design for 3D printed parts. Most current manufacturing standards are for metallic parts. Standards have to be introduced to increase reliability of the produced parts. These standards require material and design testing to introduce a universal guideline (Fig. 2).

Olson 3 link model (1997) is a diagram that correlates or shows linear relationship between performance, properties, structure and process of a manufactured part.

Fig. 2 Olson's three-link model [17, 18]
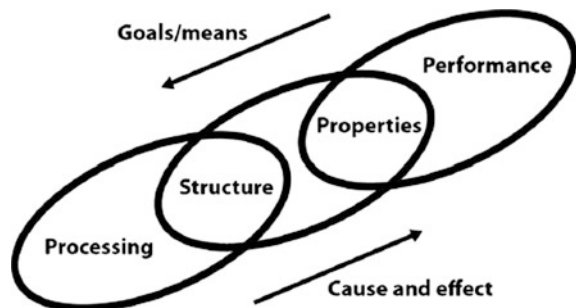
Table 1 Types of AM technologies, their positives and drawbacks [2–6, 9–15, 17, 19–28]

S.no.	Process	Findings
1.	Fused deposition	• Cost of raw material is least, compared to other processes • Ease of manufacture and post-processing • Machines are much compact, thus ideal for small spaces • Parts can be recycled to produce filaments • Adhesion is easy with the use of acetone • Annealing process of PLA makes the part as strong as other materials like Bakelite • Material deposition is slower when compared to other technologies • Layers are distinct and visible • Reliability of layer binding is low • Structural integrity is influenced by infill ratios • Correct temperature has to be maintained for proper material and layer properties • Composites are difficult to produce • Limitations on size of produced part • Restrictions on materials. Only heat meltable or light curable materials can be used • Poor surface finish
2.	Metal sintering	• Fully dense parts can be produced • Quality and Resolution is very high • High accuracy and detail • No requirement of support structures • Dependent on the field of Powder Metallurgy • Raw material can be recycled • Parts produced have to be heat treated within a matter of days to avoid reduction in intra-particle adhesion • Post-processing requires high heat and thus consumes more power • Higher physical properties than some traditional manufacturing processes like casting (with practical results) • Poor surface finish before post-processing • Very sensitive to oxygen, have to be done in enclosed space/chamber • Properties of metal may change due to high temperatures • Special alloys can be produced using this process
3.	Steriolithography	• Least power consuming AM technology • Very High build speeds • Moderate-resolution of produced parts • Problems faced in STL technology– – Over curing – Irregular deposition – Bumps and drops – Irregular hardening • Low structural strength • High cost of raw material, due to their photo-curable properties • Materials like rubber, nylons, and resins can be used to made dampers, shock absorbers, and flexible meshes • Require time in post-processing to cure the material throughout

Table 1 (continued)

S.no.	Process	Findings
4.	Binder jetting	• Very high-resolution parts can be produced • Full-color objects can be manufactured • Requires infiltration during post-processing • A wide variety of materials can be used in this type of AM technology • Most of the fusion of material and layers happen in post-processing • Current binders produce harmful fumes during post-processing •. Parts produced have high porosity • Ideal for smaller parts like Jewelry, ornaments etc
5.	Laminated object manufacturing	• Able to produce large models • Raw materials in inexpensive. Usually PVC sheets or pape • Medium to high-resolution of built parts • Moderate Strength • Does not require post-processing • Extra material cut left around the cut section acts as support • Requires decubing (the process of removing excess material) which is labor intensive • Produces fumes which contain carbon dioxide and carbon monoxide • Requires an open system to avoid environment contamination • May lead to fires (as paper is highly combustible at high laser temperatures) • Cannot make very complex geometrical structures due to inability of making hollow parts • Prototypes or parts produced are not functional, they normally form a cast • Low machining cost and high surface finish

4 Result and Discussion

The Table 1 is the compilation of all the observations made by the authors. Study of the various forms of additive manufacturing processes, their positives as well as the drawbacks are also mentioned.

5 Conclusion

Additive Manufacturing or 3D printing had become the new field of manufacturing starting from the late 1980s. Many manufacturing, aerospace, and industrial sectors are investing heavily in AM processes. The current AM process requires

advancement, for problems mentioned above, which will make the process faster and more efficient in the near future. Advancements such as in the field of electronics, material sciences, and standardization of the production process, as per our research will pave the way to AM being the future of production.

References

1. Gao W, Zhang Y (2015) The status, challenges, and future of additive manufacturing in engineering. Elsevier
2. Junk S, Kuen C (2016) Review of open source and freeware cad systems for use with 3D-printing. Elsevier
3. Campbell I, Bourell D (2012) Additive manufacturing: rapid prototyping comes of age. Emerald Insight
4. Compton BG, Lewis JA (2014) 3D-printing of lightweight cellular composites
5. Baumers M, Tuck C (2011) Energy inputs to additive manufacturing: does capacity utilization matter? ResearchGate
6. Upadhyay M, Sivarupan T (2017) 3D printing for rapid sand casting
7. Haria R, BJ (2017) 3D printing industry. https://3dprintingindustry.com
8. Imaterialise. https://i.materialise.com/blog/going-strong-how-3d-printing-in-ceramics-really-works/
9. Cheng Y, Pu H, Dongping D (2013) Modeling and fabrication of heterogeneous three-dimensional objects with AM
10. Brackett D, Ashcroft I (2011) Topology optimization for additive manufacturing
11. EL. Doubrovski, Verlinden JC, Geraedts JMP (2011) Design methods for on-demand additive manufacturing (Retrieved from Research Gate.)
12. Aguilera E, Ramos J (2013) 3D printing of electro mechanical systems
13. Goh GL, Agarwala S (2017) Additively manufactured multi-material free-form structure with printed electronics. Springer
14. Ang KC (2006) Investigation of the mechanical properties and porosity relationship in FDM structures. Emerald Insight
15. Hwa LC, Rajoo S (2017) Recent advances in 3D printing of porous ceramics
16. Manufacturing Guide. https://www.manufacturingguide.com/en/laminated-object-manufacturing-lom
17. Mahindru DV, Priyanka Mahendru SR, Ganj T (2015) Review of rapid prototyping-technology for the future
18. Carbon. Carbon 3 (https://www.carbon3d.com/)
19. Ramya SL (2016) 3D printing technologies in various application
20. Pîrjan A, Petroşanu D-M (2011) The impact of 3D printing technology on the society and economy
21. Roberson D, Shemelya CM (2015) Expanding the applicability of FDM-type technologies through material development. Emerald Insight
22. Lipson H, Moon FC (2005) 3D-printing the history of mechanisms
23. Jaideep Shuklaa, AM (2012) Review of development in 3D printing and its impact on industrial
24. Lee J-Y, An J (2017) Fundamentals and applications of 3D printing for novel materials. Elsevier

25. Yang L, Harryson O (2016) Design for additively manufactured lightweight structure. Solid Freeform Fabrication
26. Baumers M, Dickens P (2015) The cost of additive manufacturing: machine productivity, economies of scale & technology push. Elsevier
27. Samer Mukhaimar, SM (2014, March 16). 3D Printing (Retrieved from Research Gate.)
28. Yang L (2017) Microstructure, mechanical properties & design considerations for AM. Springer

Design Issues in Multi-finger Robotic Hands: An Overview

Eram Neha, Mohd Suhaib and Sudipto Mukherjee

Abstract Multi-finger Robotic hands (MFRH) are desired similar to human hands in order to perform stable grasping and fine manipulation of different objects. Their industrial applications including material handling fulfills the requirement of unique end-effector tool empowering specific reach, payloads, and flexibility. The design and control of dexterous and prosthetic robotic hands is of important concern these days. The performance of these hands depends on their mechanical design, prosthetics etc. The mechanical range of movement must be properly controlled and monitored to get the best performance of the robotic hand. In order to obtain the desired outcome from these robotic hands, various design parameters are discussed. The control issues of the multi-finger hand-arm system in order to interact with the human environment are also discussed. The objective of this paper is to evaluate multi-finger robotic hands capable of grasping a large variety of products. An overview of the relations between the designing features for the robotic hand, its anthropomorphism and dexterity is reported. Also, the best known robotic hands developed so far are reviewed emphasizing on their ergonomics and mechanical features. Based on these parameters, a newly designed four fingered tendon actuated robotic hand is discussed along with its mechanical structure.

Keywords Multi-finger gripper · Grasping · Manipulation · Dexterity · Exoskeletal

E. Neha (✉) · M. Suhaib
Department of Mechanical Engineering, Jamia Millia Islamia, New Delhi, India
e-mail: eramneha@gmail.com

M. Suhaib
e-mail: msuhaib@jmi.ac.in

S. Mukherjee
Department of Mechanical Engineering, Indian Institute of Technology Delhi,
New Delhi, Delhi, India
e-mail: sudipto@iitd.ac.in

1 Introduction

The robot grippers or end effectors are aimed to provide an interaction of the robotic arm with the near environment in order to replace manpower and perform a task similar to human beings. The robotic grippers which resemble the human hand are known as anthropomorphic robotic hands. The human hand is capable of adapting a task, as it is a sensory and communicating organ. Multi-finger robotic hand is an end effector located at the free end of the robotic arm such that the robot can hold parts, tools, and materials for performing a variety of task [1]. A multi-finger robotic gripper is a dexterous hand aimed for grasping and manipulation of various items. It is examined that a lot of investigators attempted to design a MFRH resembling the human hand. Since beginning robots have been used for industrial purposes executing monotonous tasks like the pick and place operations [2]. Newly developed and commercialized robotic hands are now days utilized as service robots, humanoids and rehabilitation prosthetics [3]. The MFRH are designed to perform various tasks which are difficult to perform by human hands. A prosthetic hand is vital to give rehabilitation for persons with disability in hand. It offers cosmetic as well as functional support [4]. The compact design of these multi-finger robotic grippers made it possible to acclimatize the hand to the wounded wrist. The new prosthesis is able to firmly grasp objects having a variety of sizes and shapes. The anthropomorphic human scale robot hands are also used for space-based works [5].

Numerous technical and scientific concerns are associated with the development and advancement of anthropomorphic robotic hands possessing dexterity and flexibility of high level [6]. Furthermore, the kinematic structure of the robotic hand, newly designed sensors and their unification in the hand, newly designed actuators with specific abilities of torques/velocities and given dimensions plays a crucial role in the growth and development of the advanced technology of dexterous robot hands [7]. In this paper, the design parameters along with the control issues of multi-finger robotic hands are discussed. A standard review of dexterous robot hands is conducted. Then, the new Four Fingered robotic hand is developed, based on the study which is presented with more details.

2 Design Characteristics of Robotic Hands

2.1 Actuation

For modular robotic hands, it is ideal that the actuators are placed within the hand or should occupy least possible space. The solution comes in the form of tendons, driven by DC motors and mini motors coupled with gear reductions. A very compact design can be achieved using tendons but it is coupled with the problem of friction, compliance, etc. [8]. The Hill's muscle model presented a muscle actuator

design made up of conventional DC motors with cable tendon transmission [9]. Commonly used actuation consists of DC motors driving tendons or using gear reductions. Improvement in same was conceptualized and presented various shape memory alloy actuators on the basis of the functioning of biological muscles for driving a five-fingered hand [10, 11]. SMA wire actuators can be applied to control hand prosthesis wherein two actuators are used to control a single degree of freedom [12]. A miniature pneumatic McKibben artificial muscle is also developed and applied to actuate a robotic hand [13]. Ionic polymer-metal composite (IPMC) based muscle were also developed which are actuated by EMG signals [14].

2.2 Sensing

Sensors are used in robotic hands in order to identify the type of object which comes in its contact. It is difficult to replicate sensing mechanism of human hand due to its great redundancy; however, some sensors need to be placed on the surface of the prostheses, for providing appropriate feedback. Research on the subject is directed towards creating new sensors and to incorporate and integrate the different sensing capabilities in the hand tasks. Embedded sensors [15] are one of the options for hand prostheses. Another kind of sensor is a slip sensor which can be applied to hand prostheses to obtain grasping information [16]. Transmitting sensory feedback to the prosthetic hand user is another major research area [17].

2.3 Grasping and Manipulation

Grasping is defined as restricting any object from moving relative to the hand on the application of disturbing forces. Fingertips are used for finer manipulation and distal phalanges are used to grasp the object in human hand. Such grasp is called precision grasp and manipulation is dexterous and nonprehensile. Inner phalanges are used to hold larger objects by enveloping. Such grasp is called power grasp or enveloping grasp and manipulation are prehensile. The robustness of grasp is defined by form closure and force closure grasps. The ability of grasp to completely or partially constrain the motions of the manipulated object and apply arbitrary contact forces on the object without violating friction constraints at the contact is determined based on it. Researchers investigated that 4 fingers are necessary for grasping any 3-D object and 3 fingers for 2-D objects [18]. These results hold good provided that friction coefficient is non-zero.

Manipulation is defined as the ability of robotic hands to vary the position and orientation of any grasped object securely. It is desirable that the designed hand excel in a particular job or replicates human hand in performance. This is achieved by incorporating various sensors to detect forces, vibrations or pressure distributions. A number of technologies which support the general-purpose manipulation

are present these days [19]. These robotic hands are incorporated as end effectors of robotic arms for grasping and manipulation tasks. This combination enables the robot to add compliance and fine motion due to small inertia at the hand, along with an increase of the overall range of motion with the arm [20].

2.4 Dexterity

The dexterity of any hand is its capability of manipulating an object in order to change its configuration from initial to a final one. A number of techniques developed by researchers for object manipulation are finger gaiting and regrasping [21]. In this process, a firm grasp is attained by performing a number of grasping operations. As a result, a large amount of time is wasted in order to get a perfectly secure grip. Regrasping of irregular and 3D shaped objects are more concerning because they possess very limited secure grasp positions. All these processes involve a number of tasks to be controlled including kinematics and dynamics, slipping of object, contact points monitoring etc. This requires the hand to enhance its degree of flexibility by making the hand to slide some contacts with the grasped objects as in case of human hands [22]. The modeling of friction and synthesis of contact points is a challenging problem for the researchers. It is always desirable to choose the simplest engineering process in terms of mechanical structure, sensors, number of actuators etc. in order to obtain any dexterous robotic hand. The minimum no. of actuators in any robotic hand for dexterous manipulation is nine, but for a complex hand structure, the number of actuators can go up to 32 [23].

3   Overview of Robotic Hands

A number of factors are responsible for the design and proper utilization of robotic hands in order to achieve a dexterous and anthropomorphic robotic hand. This is resolved by calculating the kinematics, the exact size of links, contact surface smoothness etc.

In 1979, the Okada Hand was built consisting of two fingers and an opposable thumb having eleven controlled DOF possessing exoskeleton structural design. The hand is equipped with motor, joint position sensors and motor effort sensors [24]. In 1983, Stanford/JPL Hand was developed consisting of nine actuated joint and three fingers having an integrated design. This hand is designed for tip prehension and the contact surface is not very smooth. The size of this gripper is equal to human hand having exoskeletal design and tendons offer remote transmission. Sensors are equipped with the hand to check the motion position and tension in the tendon wires [25]. The Utah/MIT hand was developed at Utah University in 1988, and it comprises of 4 fingers having a total of 16 joints which are controlled by an integrated exoskeletal design. The size of the hand is equal to a hand of human and

the whole hand including the palm is designed to grasp different objects offering good smoothness on the surface of objects. It comprises of remote actuation system, pneumatic actuators, different motors and sensors to monitor joint position, tension in tendons etc. [26]. In 1988, the Barrett Hand was developed comprising of three fingers, out of which two the fingers rotate synchronously in a symmetric manner about the base joint in a spreading action [27]. A single DC brushless servo motor is employed to drives the two joints of each finger. In 1999, NASA Johnson Space Center developed the Robonaut hand for space-based operations having an endoskeleton design. This hand consists of five fingers having 22 joints and 14 of them having controlled DOF. The hand aims to approximate an astronaut's hand in terms of environment, strength, and kinematics [28]. Research on DLR hand started in 1997 when the two multisensory dexterous robot hands: DLR Hand I and II were developed. It consists of 4 fingers having a total of 17 joints with 13 number of actuation. This hand is an extremely integrated mechatronic device which is more powerful and accurate. The hand and main microprocessor are connected by eight cables. A fingertip force of around 30 N is exerted with the accumulation of BLDC motors, harmonic drives, belt transmission and differential bevel gear transmission. The thumb of this hand contains one extra degree of freedom due to which it can exert a good amount of grasping power along with fine manipulation. The DLR Hand II is considered one of the fine robotic hand developed so far. Since 2001, research is being conducted to build a smaller hand that can be easily fabricated and mimics the human hand [29]. The Ultralight hand was developed in 2000 comprising of five fingers and 18 joints having 13 actuated joints making it an integrated exoskeletal designed hand. The size is much bigger than a hand of human having a frictionless, smooth contact surface. The hand consists of motor sensors, tactile and joint position sensors. The Gifu Hand was developed in 2001, with the aim to perform dexterous object manipulation similar to human hands [30]. It is a five-fingered hand having twenty joints with sixteen degrees of freedom. Each finger of this hand has four joints but three degrees of freedom whereas its thumb comprises of four joints with four degrees of freedom. In 2013, a robotic hand having 4 fingers along with an opposing thumb was developed known as the anthropomorphic hand [31]. Each finger has 3 joints similar to human hand. These finger joints are controlled by the tendon routing mechanism.

4 Results and Discussion

The robotic hands developed in past are unable to replicate the motor capabilities of the human hand as the kinematic characteristics similar to human hand are difficult to achieve. Dexterity, anthropomorphism, grasping, manipulability and control were the main focus of research. They aimed at achieving one or two specific properties based on the area of application of the particular robot hand. The efforts made to increase dexterity and manipulating capability of the hand requires more

number of fingers and joints resulting in more complex control system of the hand which lead to decrease in load carrying capacity.

The multi-finger hands having jointed fingers like human hand possess the properties of dexterity. Multi fingered hand research so far has focused on grasping control and manipulability of the grasped object. Most of the research on grasping and synthesis carried out during last two decades resulted in complex and bulky mechanisms which are partially applicable to the real world applications and unstructured environments. Along with dexterity and manipulating capability, there is an apparent gain in the need of low friction, small volume and light weight grippers with an efficient and simple actuation and transmission system for improving manipulator performance. The anthropomorphic design of the hands is not paid much attention which is also an important factor for rehabilitation applications of hand. The palm of most of multi finger hand designs is developed as a non-flexible part, however, the palm of human hand is flexible and plays very important role in grasping very small objects. Most of the work done on grasping planning strategy for different type grasps considering the number of contact points only. Not much work is found in the area of force exerted by the fingers at the contact points on the object for grasping and the stress distribution over the fingers due to these forces. The kinematics of full-actuated tendon mechanisms have been analyzed and classified but kinematics of under-actuated tendon mechanisms has not been analyzed clearly.

Therefore, based on the above literature the Four-fingered tendon actuated robotic hand is developed as shown in Fig. 1.

The purpose of this hand is to perform various grasping and manipulation tasks [32]. Each finger and thumb has one actuator for their movement. The working principle of this hand is to transfer the movement of actuators from one link to another simultaneously due to which the gripper can make partially wrap-around grasp. This hand is designed with aim of simplicity of mechanisms and lightness of weight. For this purpose, tendon transmission is used with a simple arrangement of one tendon per finger. The structure of the hand is kept in close proximity with the human hand to expand its area of application. The hand is designed with three fingers identical in all aspects and with the separate design of thumb. The placement of thumb opposite to fingers makes the precision gripping easy and possible.
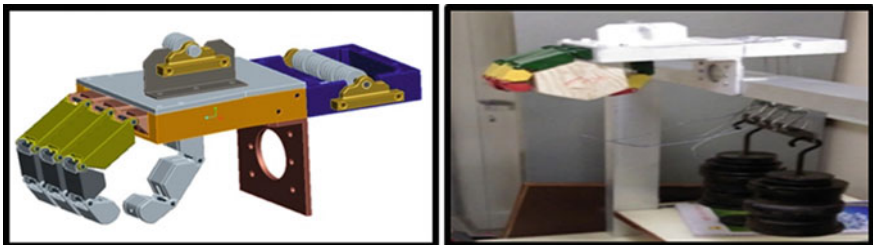
Fig. 1 Four-fingered robotic hand [32]

With this design sensor and actuators can be easily incorporated for testing purposes. The tendon selection is done on the basis of high tensile strength and subsequently, its load carrying capacity is calculated with safety margins. The pin joints of fingers are incorporated with torsion springs for retraction. Since twisting moment about each joint is not same, therefore a different number of springs are used at different joints, one at proximal, two at middle and four at distal joint. A string passes through each finger, one end of the string is attached to the fingertip and other end is left free for connection with actuator. The mechanism of the gripper allows the phalanges to contract when the force (tension) is applied on the free end of the rope. The finger is released to its home position by torsion springs provided at each joint. In absence of specific task and usage of the gripper for general purpose while human hand taken as model, and various dimensions are approximately taken double the size of human hand.

5 Conclusions

It has been observed from the past research that human hand is the main point of inspiration and design follow up to develop a multi-fingered robotic hand. The multi-fingered hands are used as the end effector in a robotic system, where each individual finger is considered as an open loop kinematic chain or independent robot manipulator. After reviewing the various multi-finger robotic hands, it can be concluded that a large number of efforts are being made in the field of robotics to develop these multi-finger robotic hands with the aim to mimic a human hand. It is desirable that the hands provide motions and perform the task with maximum accuracy and precision. To fulfill these demands these hands employ various methodologies of control with a different number of fingers and degrees of freedom. Based on this study the four-fingered multipurpose robotic hand is developed consisting of three fingers and one thumb. It has total eleven joints. The working principle of this gripper is similar to human hand with ability to handle various shaped work pieces. Various researchers are still working in this area to overcome the problems related to the size of the hand, accuracy and resolving the weight issues by choosing appropriate materials etc., as there is a lot more to achieve in robotic hand to fully replicate a human hand. The flexibility of the human hand is still a big challenge for the researchers in this regard.

References

1. Bekey GA et al (1990) Control architecture for the Belgrade/USC hand, dextrous robot hands. Springer, New York, pp 136–149
2. Kumar V, Bicchi A (2000) Robotic grasping and contact: a review. In: Symposium proceedings of IEEE, vol 348, p 353

3. Pylatiuk C, Bretthauer G (2001) A new ultralight anthropomorphic hand. In: Proceedings of 2001 ICRA IEEE international conference on robotics and automation, vol 3(1), pp 2437–2441

4. Butterfass J, Grebenstein M, Liu H, Hirzinger G (2001) DLR-Hand II: next generation of a dextrous robot hand. In: Proceedings of the IEEE international conference on robotics and automation, pp 109–114

5. Folgheraiter M, Gini G (2001) Human-like hierarchical reflex control for an artificial hand. In: Proceedings of IEEE humanoids, Tokyo, Japan

6. Caffaz A, Cannata G (1998) The design and development of the dist-hand dextrous gripper. In: Proceedings of the IEEE international conference on robotics and automation

7. Takaki T, Omata T (2009) High-performance anthropomorphic robot hand with grasp force magnification mechanism. In: Proceedings of IEEE international conference on robotics and automation, pp 1697–1703

8. Bundhoo V, Park EJ (2005) Design of an artificial muscle actuated finger towards biomimetic prosthetic hands. In: Proceedings of the 12th international conference on advanced robotics, ICAR 05, 18–20 July 2005

9. Gialias N, Matsuoka Y (2004) Muscle actuator design for the ACT hand. In: Proceedings of the 2004 IEEE international conference on robotics and automation, May 2004

10. Cho KJ, Asada H (2005) Multi-axis SMA actuator array for driving anthropomorphic robot hand. In: Proceedings of the 2005 IEEE international conference on robotics and automation, Barcelona, Spain, 18–22 April 2005

11. Cho K-J, Rosmarin J, Asada H (2006) Design of vast DOF artificial muscle actuators with a cellular array structure and its application to a five-fingered robotic hand. In: Proceedings of the 2006 IEEE international conference on robotics and automation, Orlando, FL, USA, 15–19 May 2006

12. Loh CS, Yokoi H, Arai T (2005) New shape memory alloy actuator: design and application in the prosthetic hand. In: 27th annual international conference of the engineering in medicine and biology society, IEEE-EMBS

13. Lee YK, Shimoyama I (2002) A multi-channel microvalve for micro pneumatic artificial muscle. In: The 15th IEEE international conference on micro electro mechanical systems, 20–24 Jan 2002

14. Lee MJ, Jung SH, Lee S, Mun MS, Moon I (2006) Control of IPMC-based artificial muscle for myoelectric hand prosthesis. In: Proceedings of the 1st IEEE/RAS international conference on biomedical robotics and biomechatronics, BioRob 06, Pisa, Italy, 20–22 Feb 2006

15. Dollar AM, Wagner CR, Howe RD (2006) Embedded sensors for biomimetic robotics via shape deposition manufacturing. In: Proceedings of the 1st IEEE/RAS International Conference on Biomedical Robotics and Biomechatronics, BioRob 06, Pisa, Italy, 20–22 Feb 2006

16. Dubey VN, Crowder RM (2005) Photoelasticity based dynamic tactile sensor. In: Proceedings of ASME IDETC/CIE 2005 international design engineering technical conferences and computers and information in engineering conference, Long Beach, CA, USA, 24–28 Sept 2005

17. Kim G, Asakura Y, Okuno R, Akazawa K (2005) Tactile substitution system for transmitting a few words to a prosthetic hand user. In: 27th Annual international conference of the engineering in medicine and biology society, IEEE-EMBS 2005, 01–04 Sept 2005

18. Salisbury KS, Roth B (1983) Kinematics and force analysis of articulated mechanical hands. J Mech Trans Actuat Des 105:35–41

19. Grupen RA, Henderson TC et al (1989) Survey of general-purpose manipulation. Int J Robot Res 8(1):38–62

20. Nagai K, Yoshikawa T (1995) Grasping and manipulation by arm/multi-fingered-hand mechanisms. In: IEEE international conference on robotics and automation, vol 1(3), Nagoya, Japan, pp 1040–1047

21. Hong J, Lafferriere G, Mishra B, Tan X (1990) Fine manipulation with multi finger hands. In: Proceedings of IEEE international conference robotics and automation, pp 1568–1573
22. Goyal S (1989) Planar sliding of a rigid body with dry friction: limit surfaces and dynamics of motion. Ph.D. dissertation, Cornell University, Ithaca, NY
23. Farooqi MA, Tanaka T, Nagata K, Ikezawa Y, Omata T (1999) Sensor-based control for the execution of regrasping primitives on a multi-fingered robot. In Proceedings of IEEE international conference robotics and automation
24. Soto Martell JW, Gini G (2007) Robotic hands: design review and proposal of new design process. Int J Mech Aerosp Ind Mech Manuf Eng 1(2)
25. Salisbury K (1984) The Stanford/JPL hand: mechanical specifications, Salisbury Robotics. Inc., Palo Alto, CA
26. Jacobsen SC, Iversen EK, Knutti DF, Johnson RT, Biggers KB (1986) Design of the Utah/M. I.T. dextrous hand. In: Proceedings of IEEE international conference on robotics and automation, pp 1520–1532
27. Townsend WT (2000) The Barrett Hand grasper-programmably flexible part handling and assembly. Ind Robot Int J 10(3):181–188
28. Lovchik C, Distler M (1999) The Robonaut hand: a dexterous robot hand for space. In: Proceedings of the 1999 IEEE international conference on robotics and automation, vol 2(1), pp 907–912
29. Gao XH et al (2003) The HIT/DLR dexterous hand: work in progress. In: Proceedings of the 2003 IEEE international conference on robotics & automation, pp 3164–3168
30. Mouri T, Kawasaki H, Yoshikawa K, Takai J, Ito S (2002) Anthropomorphic Robot hand: Gifu hand III. ICCAS
31. Townsend WT (2000) MCB—industrial robot feature article—Barrett hand grasper. Ind Robot Int J 27(3):181–188
32. Neha E, Suhaib M, Mukherjee S.: Motion planning for a four-fingered robotic hand. In: Advances in Robotics, ACM digital library. ACM (2017)

Structural Analysis of Pechora Missile System's Launcher Beam

**Daamini Visaalaakshi, Gouresh Sood, Vishakha Baghel
and Anupam Tiwari**

Abstract Pechora missile system is an old and vintage system used for launching surface-to-air missiles. The launcher beams of the Pechora missile system undergo fatigue over time due to structural load, wear and tear, and ageing. This results in crack propagation which ultimately leads to the failure of the launcher beam structure. In this research work, the structural integrity of the launcher beam is investigated by performing analysis of launcher beam using Finite Element Method (FEM). The paper concludes by suggesting methods to optimize the design of the launcher beam to overcome structural failure.

Keywords FEM · Structural · Analysis · Missile · Beam · Fatigue · Optimization

1 Introduction

Pechora missile launcher beam is a missile launcher for SAM (Surface-to-Air)-3 Missile. The weight of launcher is approximately 13 tonnes. The launcher can be operated manually as well as functionally through launcher cabin. It has a guide rail and roller support to hoist the missile. Four missiles are kept on this launcher and two missiles can be launched together within 0.5 s. Based on the field performance, the kill probability of the missile is 98%. It can achieve velocity up to 900 m/s. Targets can be engaged even in extreme and severe conditions of environment using the Pechora.

D. Visaalaakshi (✉) · G. Sood (✉)
UTC Aerospace Systems, Bengalore, India
e-mail: daamini.visaalaakshi@utas.utc.com

G. Sood
e-mail: gouresh.sood@utas.utc.com

V. Baghel
Amity Institute of Space Science and Technology, Amity University Noida, Noida, UP, India

A. Tiwari
Indian Air Force, New Delhi, India

For the operation of Pechora missile launcher, there are two gears: one is azimuth and the other is elevation gear. The launchers provide pre-launch preparation of missiles in azimuth and elevation angles. Rotation (azimuth movement) is 360° and elevation angle is 3° 25'—65° 55'. There is also an azimuth receiver, elevation receiver and a transmitter in the launcher. Four cables are connected to launcher for power, control, communication and signal. A separate Bogey is used for the transportation of the launcher. It can pull the launcher and carry it for longer distances [1]. The major problem in the old and vintage Pechora missile launcher beam was the occurrence of cracks and crack propagation around welded areas. This paper focuses on addressing this issue. Alternate methods have been studied and suggested to reduce the cracks and minimize the occurrence of new cracks beside the welded cracks.

1.1 SAM-3

SAM-3 Missile is a surface-to-air guided missile system used by the Indian air force. BRD-7 specializes in working on missiles, their servicing, relay change, seal change and repairs the defects. The missile consists of six sections, namely, radio fuse, control surface, warhead, all airborne equipment (electrical), sustainer motor and booster motor. Radio fuse contains all the radio and transmission equipment [1]. Control surface contains rudder and elevator and is controlled by servo motors. Warhead contains heavy explosives containing 4800 fragments which explode when the target is within 300 m range of the missile. The airborne equipment contains RCG, autopilot, two relays and turbine which produces electricity with the help of compressed gas. The blast radius is 300 m of the missile. The range of the missile is 25 km. The velocity that it approximately achieves is 1100 m/s.

1.2 MGR—Missile Guidance RADAR

MGR is a complex radar used for searching and tracking with a range of 85 km approximately. It has three antennas and all are semi-parabolic type. It has a 100 kV generator to supply power. For noise reduction, there is a superheterodyne receiver. RF waves are converted into intermediate frequencies.

2 Methodology

The methodology adopted for structural analysis of Pechora missile launcher beam can be explained with help of a process flow [2] diagram as shown in Fig. 1.
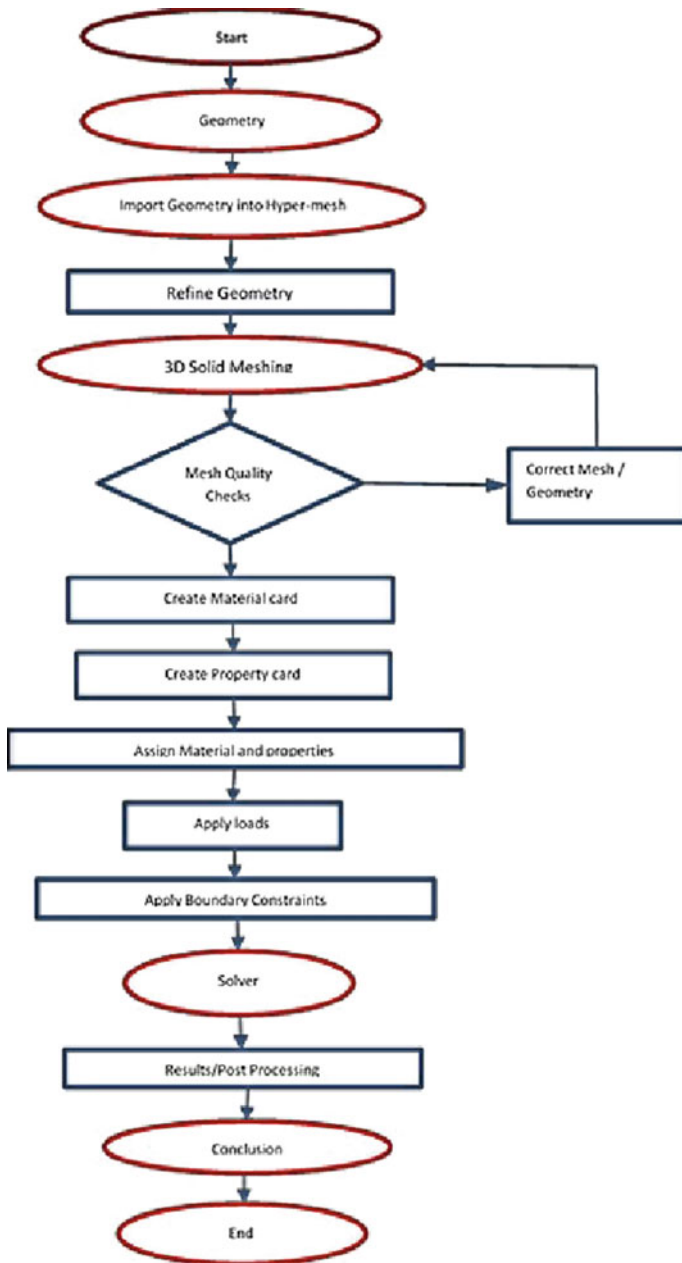
Fig. 1 Process flow diagram of structural analysis

2.1 Geometry Creation

The Pechora missile launcher beam was modelled using UniGraphics NX 8.5. A simple sketch was created and the sketch was extruded. Rectangular slits were modelled on the surface of the beam using 'subtract' command. These rectangular slits or guide rails are the areas of importance for the analysis. They are the structural members where the maximum load is applied as the Pechora missile is hoisted here. There are smaller rectangular protrusions which are modelled on the top surface of the box beam (Fig. 2).

On the front portion of the model, a trapezoidal-shaped structure was modelled by sketch creation and then extrusion. To this surface, a wing-like section was created and mirrored on both sides. The two mirrored wings like structures are connected using a rectangular rib to give support at the free end as it behaves like a cantilever beam. The entire box beam is hollow inside and was modelled accordingly. Two rectangular boxes were modelled inside the hollow beam. These boxes are used to store the electrical equipment of the launcher (Fig. 3).

2.2 Mesh Creation

After creating the geometry, the CAD model is imported as igs format into Altair hypermesh tool. Once the geometry is imported, 'Mixed' option is selected to show the topology from visualization toolbar. The edge edit option in the geometry is then used to suppress the free edges or incorrect edges using the toggle option for the purpose of cleaning the model topology [3]. Cleaning is an exhaustive but an important process before the creation of mesh.
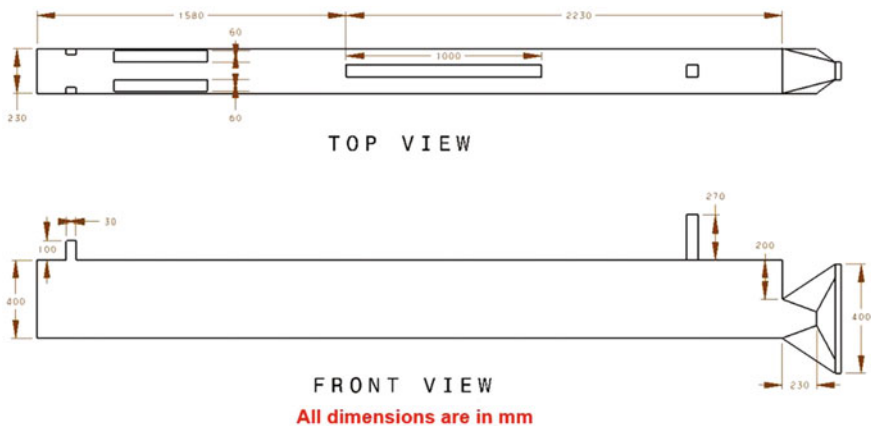
Fig. 2 Schematic of a Pechora missile launcher beam
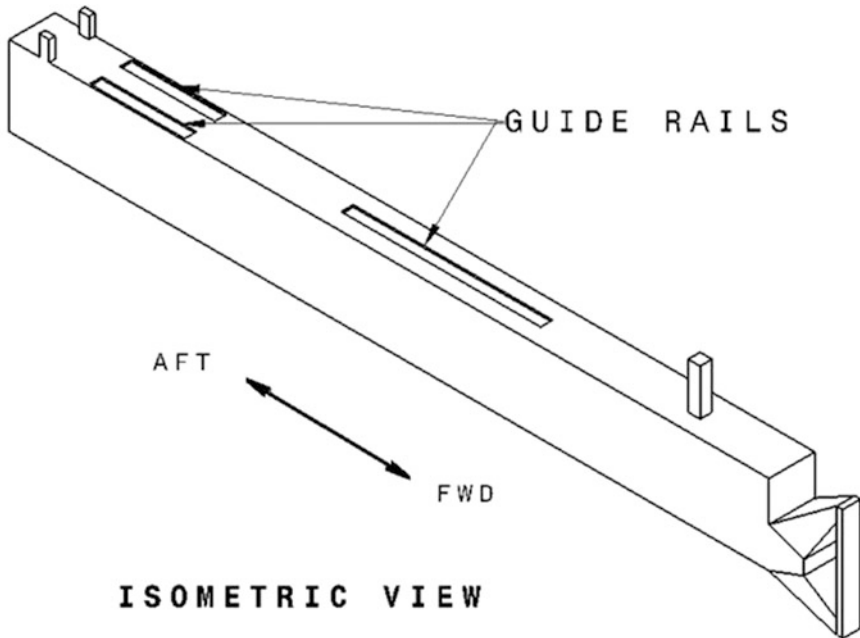
Fig. 3 Isometric view of a Pechora missile launcher beam CAD model

Disconnected nodes are joined, additional lines are removed or stitched to one, irregular edges are smoothened and many such modelling errors which will affect the smoothness of a mesh are removed through cleaning. Split-surf node from Quick edit is also used to create edges/surface lines.

3D meshing was done to create an appropriate mesh for the Pechora missile launcher beam [4]. After the selection of the 3D option, 'tetramesh' was selected to create mesh made of tetrahedral elements. Selecting 'Volume tetra', the 'use proximity' and 'use curvature' boxes are checked to improve the mesh refinement and quality. It helps to lower the element size as per the shape of elements [4]. Now the important properties which determine the mesh are selected. First 'the minimum element size' which is given as 0.001, the 'feature angle' is 45° and lastly the 'element size' is given as 0.03. The enclosed volume of the Pechora missile launcher beam is selected and the mesh is then generated. The element size is selected by convergence. Convergence is widely used to obtain the most accurate single solution. The multiple numbers of solutions are iterated till it converges to a single point. Hence, at least two solutions are required to determine convergence. The word convergence is used because the output from the finite element programme is converging on a single correct solution. The solution from the finite element programme is checked with a solution of increased accuracy. If the more accurate solution is different from the original solution, then the solution is not converged. If the solution does not change much (less than a few percent difference), then the solution is considered converged [4, 5].

Once the mesh is created, the quality of the mesh can be checked and refined by modifying various parameters which define the mesh structure, mesh quality can be checked by changing from 3D to tool option and then select 'check elems' or simply by using F10 shortcut key [5].

The different mesh quality checks are done using this option [6]. In the 3D option here in the check elems tab, it is made sure that 'Warpage' is less than 5. Aspect ratio is a dimensionless parameter which is obtained by dividing the maximum length by the minimum length of the element. Irrespective the number of faces in an element the aspect ratio is calculated in the same manner. For a refined mesh the aspect ratio should be less than 5, the maximum aspect ratio of the mesh was 3.68. Skewness of elements is calculated in the units of angle. The maximum skew angle is 62.90.

Tet collapse should be greater than 0.1. The minimum Tet collapse of the model is 0.24. The Jacobian ratio is a measure of the deviation of a given element from −1.0 to 1.0, where 1.0 represents a perfectly shaped element. Jacobian has to be always positive for the mesh to have quality elements. The ideal shape for an element depends on the element type. The check is performed by mapping an ideal element in parametric coordinates onto the actual element defined in global coordinates. For example, the coordinates of the corners of an ideal quad element in parametric coordinates are (−1, −1), (1, −1), (1, 1), and (−1, 1). The minimum Jacobian is 0.96.

If any of these properties have failed, then the mesh needs further refinement [5]. Until all the properties of the mesh are within the range repeat the procedure of meshing. This is done through trial and error.

The component collector is created after achieving a refined mesh by performing quality checks. Here various components within the model can be assigned individually. The beam component is named as 'aluminium beam' and a colour is assigned for the particular component. Even properties can be assigned to each component if required.

The material properties can be assigned through the material collector. Respective materials are assigned based on the design of the model. The materials used in the Pechora missile launcher beam are aluminium and steel. Aluminium material is selected for the beam and a colour is assigned for the particular component. MAT1 can be selected for metals. Once the required material is selected, properties like density, modulus of elasticity and Poisson's ratio which are inbuilt in the software are displayed. Any changes to be made to the values of the physical/ mechanical properties can be done if required. The material is then updated.

Next properties are assigned using the property collector. The type is here the type is selected as 3D and the property is selected as PLSOLID. The material is then given to the property.

To apply the loads, the main option is changed from '3D' to 'tools'. Using the force option nodes where the force is applied in the structure is selected. The system of axis is changed to local system. The magnitude of the force can be varied accordingly here.
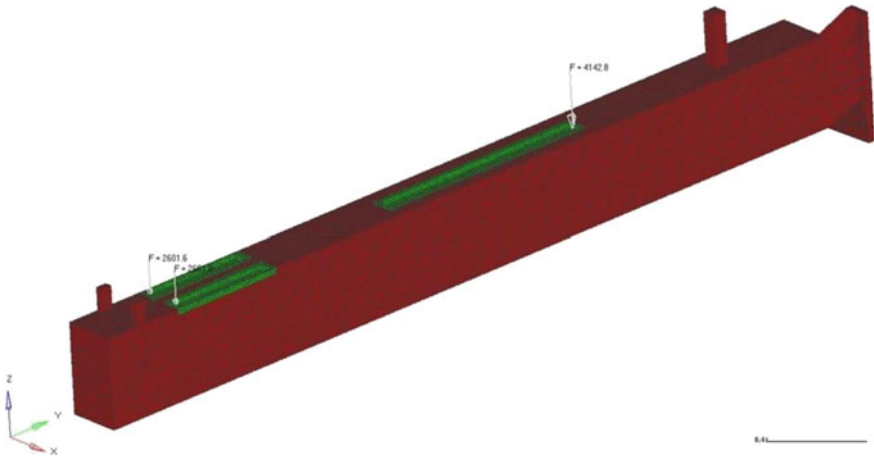
Fig. 4 Pechora missile launcher beam mesh

The model is constrained using the constraint option. For any point in space, there can be six possible degrees of freedom of motion: three translational motion, namely, motion about x-axis, y-axis and z-axis, and three rotational motion about x-axis, y-axis and z-axis. The Pechora missile is mounted on the beam till the missile is launched. It remains stationary and does not undergo any motion on application of load. Hence, the beam model is constrained in all the degrees of freedom (Fig. 4).

The next step after completion of modelling and meshing is to validate the model through FEM validation check. This is to check how accurately the model represents the governing equations. For example, to validate the deflection of a spring system on application of force, the model is checked if it obeys the underlying equation F = kx. This vital step enables to calibrate the model and achieve accurate results. For the Pechora missile launcher beam under the equilibrium check, free-free modal check (SOL 103) or a rigid body static analysis check (SOL 101) was done. This helps to verify load paths, stress distribution and displacement of the FEA model [6].

3 Results and Discussion

The solver is used to run the mesh model and provide results. These results are then post-processed to get the following plots.

The structure will appear on the system with deformed shape and we will get the deflection value (Figs. 5 and 6).

The observations were in line with the problem statement. The stresses are high in the region where cracks are developed. Even when those cracks are welded the
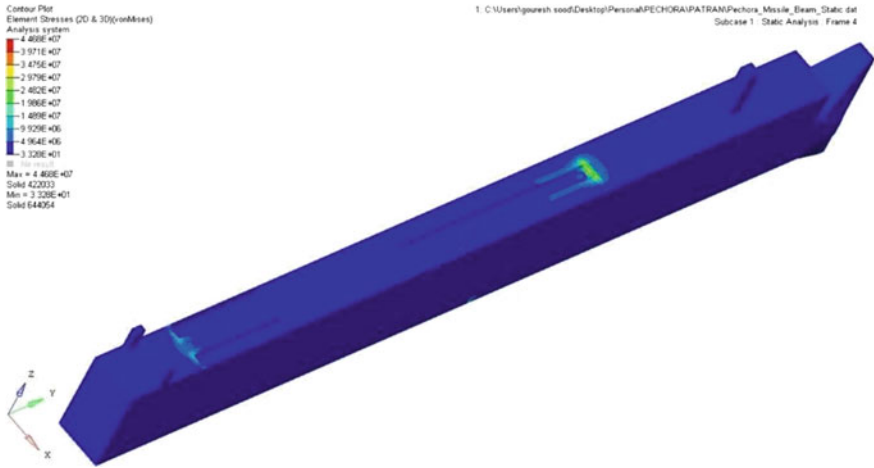
Fig. 5 Displacement plot
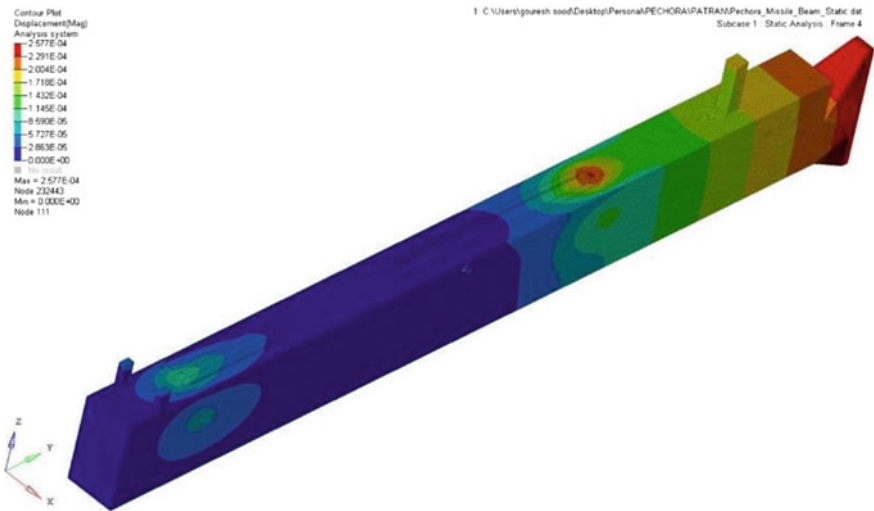
Fig. 6 Stress plot

stress will still be similar so different ways of optimizing the Pechora missile launcher beam are given.

Different types of stiffeners are placed at the high-stress location so as to provide support to the load carrying member.

The load path shifts to the stiffener so the member can avoid developing cracks.

3.1 Placing Stiffener I.E. Structural Members in Weakened Areas

There are various shapes and size of stiffeners which are used to provide structural strength. Z, T and I are the basic shapes of stiffeners which are connected to the main structure by rivets. When stiffeners are placed along the length of the structure, its load-carrying capacity increases and it reduces bending. Considering this approach of using stiffeners, we will calculate the load-carrying capacity of the given structure when stiffeners of various shape made up of same material and same dimensions are introduced with the body

- Buckling stress for a stiffener is given by

$$Cu = K * E*[t/b]2 \qquad (1)$$

where

Cu = buckling stresses (N/m^2)
K = end fixity constant
E = Young's modulus of elasticity (GPa)
T = thickness (cm)
B = length (cm)

- Load carried by stiffeners is given by

$$P = \sigma c * [(6 * W + 2 * W1) * t + A] \qquad (2)$$

where

P = load carried (N)
σc = bucking stresses (N/m^2)
W = width when both sides are simply supported (m)
W1 = width when one side simply supported and one side fixed (m)
A = area of stiffener (m^2)
T = thickness (m)
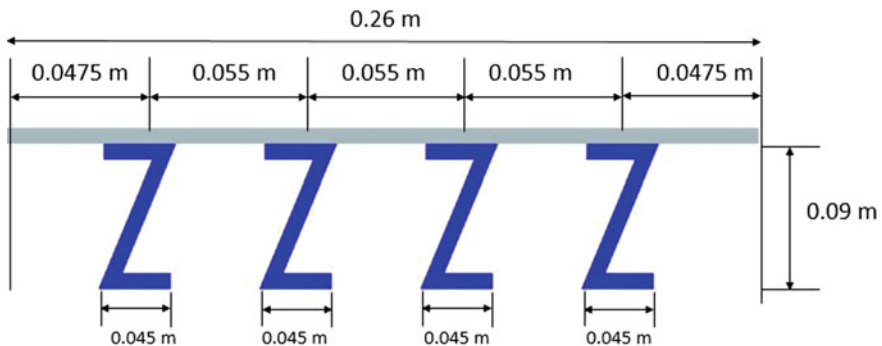
Fig. 7 Placement of Z-, T- and I-shaped stiffeners on surface (with dimensions)

Fig. 8 Z-shaped stiffener
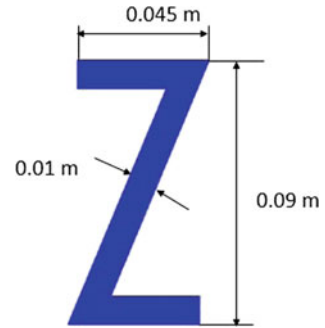
Here W and W1 are given as

$$W = 0.85 * t * (E/\sigma c) * 0.5 \tag{3}$$

$$W1 = 0.60 * t * (E/\sigma c) * 0.5 \tag{4}$$

Now, by making an arrangement of stiffeners in manner as shown in Fig. 7 we will calculate load-carrying capacity of each stiffener.

The dimensions and material of stiffeners are assumed to be same for Z, T, I sections so same buckling stresses will develop on the structure, which are as follows.

4   Conclusion

The Z section/Z-shaped stiffener has a maximum strength among all the three stiffeners. The load-carrying capacity of the structure increases at its maximum level with the help of Z-shaped stiffener. So as to increase the structural strength of the weakened region of the launcher beam, it is suggested to place Z-shaped stiffeners in the manner as shown in Fig. 8. An optimized design modification was suggested to improve the structure and load-bearing characteristics of the launcher beam.

References

1. S-125 Neva/Pechora (Surface-to-air missile system). https://en.m.wikipedia.org/wiki/s-125_Neva/Pechora
2. Qing L. Xian-Jun H (2008) Structure topology optimization design of vehicle parts based on HyperMesh/OptiStruct [J]. Equip Manuf Technol 10: 42–44
3. Reddy JN (1993) An introduction to the finite element method. McGraw-Hill Inc. Google Scholar

4. Gokhale NS (2008) Practical finite element analysis. Finite to Infinite
5. Loseille A et al (2007) Achievement of global second order mesh convergence for discontinuous flows with adapted unstructured meshes. In: 18th AIAA computational fluid dynamics conference
6. http://altairuniversity.com/wp-content/uploads/2014/02/elemquality.pdf

Design of Microfluidic Paper-Based Device for the Detection of Nitrogen Dioxide in Atmosphere

Surya Tiwary, Yameen Hassan and Rajeev Kumar Singh

Abstract Pollutant gases from industries and certain processes like welding, exhaust of internal combustion engines, use of explosives, use of nitric acid, etc., are the sources of sulfur dioxide (SO_2) and nitrogen oxides (NO_2 and N_2O_5) which become the part of atmosphere. The heterogeneous reactions of atmospheric aerosol convert these gases to sulphuric, nitrous, and nitric acids which precipitate as acid rain and thus severely affect human health. In this paper, the design of colorimetric paper-based microfluidic device is presented to detect and quantify nitrogen dioxide (NO_2). In order to reduce the cost of device and ease of fabrication, wax printing for fabricating paper-based analytical device (μPAD) is proposed.

Keywords Microfluidics · μPADs · Nitrogen dioxide

1 Introduction

Microfluidics involves the manipulation of very small volume of fluids in devices having micron-sized channels and features. Microfluidic devices are used as micro total analysis system (μTAS), point-of-care diagnostic systems, etc. Traditional substrates like silicon, glass, and polymers are used in the past to fabricate these devices due to low cost and simple fabrication techniques. During the last decade, chemically patterned paper is widely used to fabricate microfluidic devices as it offers unique advantages like power-free fluid transport due to capillary action, easy disposability, lightweight, long shelf life, and high surface area-to-volume ratio availability for chemical reaction. Since paper is porous hydrophilic material, it can

S. Tiwary · Y. Hassan · R. K. Singh (✉)
Department of Mechanical Engineering, Amity University Noida, Noida, UP, India
e-mail: rksingh4@amity.edu

store reagents in active form within fiber network [1]. The paper-based device can be easily disposed of without any harm to the environment apart being the low cost of material (i.e., paper in this case).

2 Materials and Methods

Variety of techniques like wax patterning, inkjet printing, flexographic printing, photolithography, paper cutting and shaping, indelible ink stamping, screen printed polydimethylsiloxane (PDMS), lacquer spraying, and vapor phase polymer deposition are developed by various researchers to pattern the paper. In order to define the flow, the flow barriers are made. This can be accomplished by making hydrophobic and hydrophilic regions in the paper. The hydrophobic region prevents the flow and is used as boundary of flow while the flow takes place through the hydrophilic region. Photoresist was used earlier to define flow boundaries in μPADs but its use is limited due to the high cost of fabrication and potential for background reactivity. Due to this limitation, other low-cost techniques were developed making use of wax and other materials in place of photoresist. Wax is a low cost, relatively inert material that can be used for patterning paper by the application of available fabrication techniques. After patterning, the paper is heated so that wax melts and forms three-dimensional barriers. A variety of methods like metallic stamp, wax dipping, screen printing, manual wax application, etc., are available for wax application on paper but all these suffer low throughput and resolution. An alternative to this is the use of a commercially available office printer. This printer uses wax based ink offering high throughput and resolution. In this case, user is not required to generate new mask of each different design and can print the design in less than a minute on paper. After printing, the paper is heated so that wax melts through the paper and forms open, hemi, or fully enclosed channels [2]. The fabrication flowchart and associated equipment are shown in Fig. 1.

Wax printing technique is capable to print 100–200 μPADs in the paper of size 8.5 inch × 11.5 inch in less than 5 min including heat cycle. The device cost mainly depends on the quality of paper used and is generally less than $0.001. The resolution obtained by wax printing is not as high as obtained by the photolithography technique because while heating wax spreads in both vertical and lateral directions. Since paper is anisotropic and more fibers are laid in horizontal direction than in vertical direction, the wax spreads more in horizontal direction than vertical direction while heating cycle and this deteriorates the resolution of channel produced. Along thickness of paper, the channel width in top portion of paper (where printing is done by printer) is more than bottom portion due to this reason. So μPADs are designed for intended flow taking into consideration of this spreading of wax in vertical and lateral directions [3].
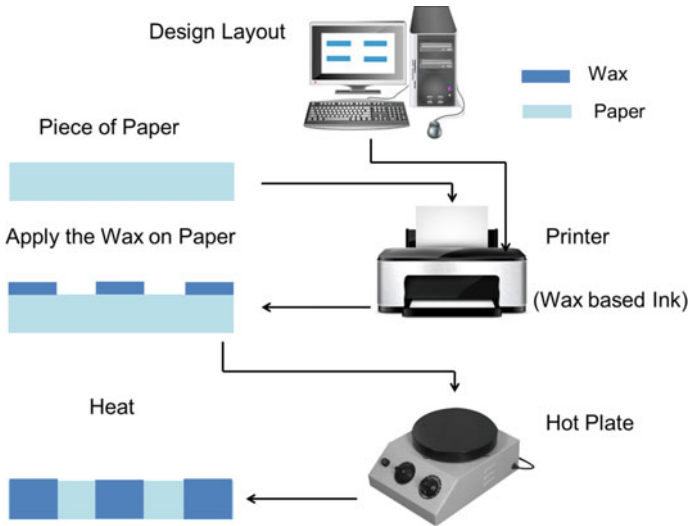
Fig. 1 Schematic of fabrication flowchart of wax printing on paper using commercially available office printer

3 Model for Spreading of Molten Wax

The wax in molten state represents the capillary flow in porous materials if it spreads in the paper. Washburn's equation best describes the lateral flow of wax in the paper which is as follows:

$$L = \sqrt{\frac{\gamma D t}{4\eta}} \tag{1}$$

where L is lateral flow of liquid of viscosity η and surface tension γ, respectively, in porous material having average pore diameter D in time t.

If wax and paper temperature is maintained constant, it will furnish reproducible results. The width of hydrophobic barrier after heating step can be represented by

$$X = L + 2N \tag{2}$$

where L is the width of original printed line using office printer, and L represents lateral spreading of wax on one side of the printed line. If two parallel lines are printed on paper having initial distance W, then on heating the hydrophobic barrier
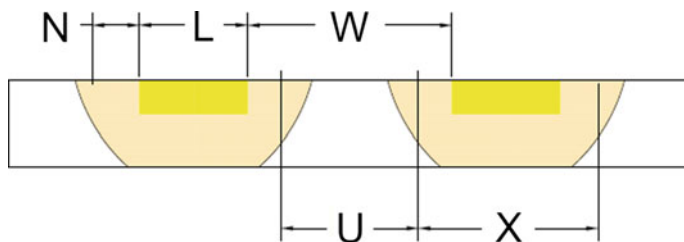
Fig. 2 Wax spreading after heating cycle

distance will be increased, and consequently, the hydrophilic distance will be reduced as is clear from Fig. 2. The average width of hydrophilic channel after heating will be [4]

$$U = W - 2N \tag{3}$$

4   Result and Discussion

The µPADs are designed for Whatman no. 1 chromatography paper (thickness 180 µm) because it is homogeneous, biocompatible, hydrophilic, and easily available. The design involves wax printing method. In wax printing, the patterns are printed on paper, and then, it is heated to penetrate wax to entire thickness and after cooling step the µPAD are ready for use. These are having a long shelf life. In wax printing, the line width cannot be kept less than 300 µm as sufficient wax will not be available to cover the entire thickness. In this design, line width and channel width are taken as 350 µm and 5 mm, respectively. The final dimension of the channel after wax melting will be 4450 ± 50 µm. At that end of the channel, a circular test zone with inner diameter 8 mm is provided. The aim to keep channel dimension and test zone dimension large is to make reagent loading and subsequently color change measurement with ease and without any optical aid. The reagents for the assay which are in liquid form will be supplied at the base of channel, which will flow to the test zone due to capillary action. The NO_2 gas present in the atmosphere will react with reagent and thus color change will take place in the channel and test zone. This µPAD is designed for colorimetric detection so the color intensity will be measured at the test zone. There are 10 test zones in the µPAD to overcome any bias and error. The average value of all test zones will be the final value. One µPAD dimension is 250 mm × 30 mm. The paper sheet dimension that can be directly fed to the printer is 215 mm × 280 mm. So in one printer sheet, 7 µPADs can be printed [3]. The µPAD with dimension is shown in Fig. 3a and b.
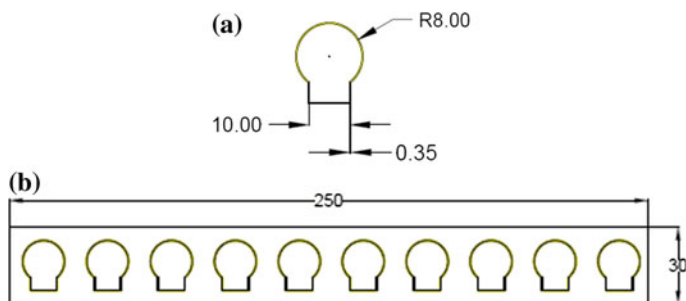
Fig. 3 a Single μPAD; **b** an array of μPAD. All dimensions are in mm

Reagent most suitable for this device may be prepared by dissolving sulfanilic acid in water containing glacial acetic acid and adding N-(1-naphthyl)-ethylene-diamine dihydrochloride to it [5].

5 Conclusion

A design of paper-based μPAD for the detection of NO_2 using wax printing is presented in this paper. The fluid flow takes place due to capillary action in the paper (substrate) so no external pump is required. The μPAD is disposable as it is printed on paper and no threat to environment is created. The fabrication time is within a few minutes, and it is a low-cost device because of the low cost of paper and materials used. In the further work, this μPAD will be fabricated in paper using wax printing method and real-time detection of NO_2 will be done.

References

1. Meredith NA, Quinn C, Cate DM, Reilly TH III, Volckens J, Henry CS (2016) Paper-based analytical devices for environmental analysis. Analyst 141: 1874–1887
2. Cate DM, Adkins JA, Mettakoonpitak J, Henry CS (2015) Recent developments in paper-based microfluidic devices. Anal Chem 87:19–41
3. Carrilho E, Martinez AW, Whitesides GM (2009) Understanding wax printing: a simple micropatterning process for paper-based microfluidics. Anal Chem 81:7091–7095
4. Washburn EW (1921) The dynamics of capillary flow. Phys Rev 17: 273–283
5. Saltzman BE (1954) Colorimetric microdetermination of nitrogen dioxide in the atmosphere. Anal Chem 26(12):1949–1955

Free In-Plane Vibration of a Cracked Curved Beam with Fixed Ends

Soumajit Talukdar and Sankar Kumar Roy

Abstract Curved beam is extensively used in different engineering fields, presence of crack weakens the curved beam and introduces local variation in stiffness. This leads to varying dynamic responses of the beam. Therefore, analysis of dynamic behavior of a cracked curved beam is an important issue in order to identify the crack. Hence, in this paper, the curved beam has been modelled by Timoshenko beam model and in plane free vibration of the cracked curved beam with both end fixed conditions has been numerically studied.

Keywords Curved beam · Crack · Free vibration

1 Introduction

Curved beam has many engineering applications in bridges, railways, roads, buildings etc. The curved beam can readily be used where the curved structure is required. However, straight beams are mostly used in engineering applications as it is simple from user point of view and analysis point of view. Due to geometrical reason, the analysis of curved beam becomes more complex as compared to straight beam as it considers rotational and radial displacements and coupled tangential displacement due to its curvature effect. The literature review reflects that studies on curved beam are less as compared to straight beam. Wolf [1] used Euler-Bernoulli beam segments for free vibration analysis of curved arches. Petyt and Fleischer [2] developed three different finite element model for radial vibration of a curved beam for different boundary conditions. Austin and Veletsos [3] determined natural frequencies of a curved arches without considering rotary inertia and shear deformation effect. Davis et al. [4] investigated that shear deformation and rotary inertia

S. Talukdar · S. K. Roy (✉)
Mechanical Engineering Department, National Institute Technology Patna,
Patna 800005, Bihar, India
e-mail: sankar.roy@nitp.ac.in

can be neglected for thin curved beam with constant curvature. Auciello and Rosa [5] reviewed free vibration of circular arches. In which, they did not consider the shear deformation and rotary inertia. So far researchers [1, 3, 5] simplified the curved beam as uniform circular arc, where curvature effect was hardly considered. However, analysis of thick curved beam needs to consider effects of shear deformation and rotary inertia and coupling of radial and tangential displacement. Hence, Timoshenko beam theory will be much more appropriate as it considers those effects. Eisenberger and Efraim [6] used Timoshenko beam theory for the analysis of curved beam. Friedman and Kosmatka [7] applied Ritz method to estimate stiffness matrix with the help of two noded curved beam using trigonometric function. The interpolation function meets the homogeneous form of the governing differential equations. Thus it makes free from shear and membrane locking. Also they investigated that this element meets to a shear deformable straight beam with reducing thickness. Kang et al. [8], Irie et al. [9] used differential quadrate technique and transfer matrix method, respectively to solve the equation of motion for a curved beam. Litewka et al. [10, 11] investigated the static and dynamic responses of a curved beam with the help of similar trigonometric interpolation functions developed by Friedman and Kosmatka [7]. The stiffness matrix is determined for static analysis using trigonometric functions and result matches with the analytical solution. Further, they used the consistent mass matrix for free vibration analysis and studied explored the effects of shear and axial forces together with rotary and tangential inertia on natural frequencies. Yang et al. [12] modelled tangential displacement in terms of polynomial function of order five. Recently, Yang et al. [13] have reviewed in plane vibration of a curved beam. In which, the review detailed the analysis of curved beam with and without taking axial deformation, rotary inertia, shear deformation.

Based on above literature review, very less amount of work has been done on dynamic analysis of curved beam. During working condition, the crack may generate in the curved beam. The generation of crack reduces the local stiffness of the beam. Reduction of stiffness will affect the dynamic behaviour of the beam. Hence, in this paper, in plane free vibration of a cracked curved beam has been analyzed.

1.1 Equations of Motion

Modelling of curved beam has been done based on the paper [7]. The Fig. 1 shows the geometry of curved beam with constant cross section. The radius of curvature of the beam is R and angle subtended by the beam is ϕ. Here, among the three different axes x, y, and z, x is directed along centroidal axis and y, z is showing the two principle direction of the beam cross section. Hence, u, v, θ are tangential, radial and rotational displacements, respectively. w is the displacement in the z direction which is at out of plane direction.
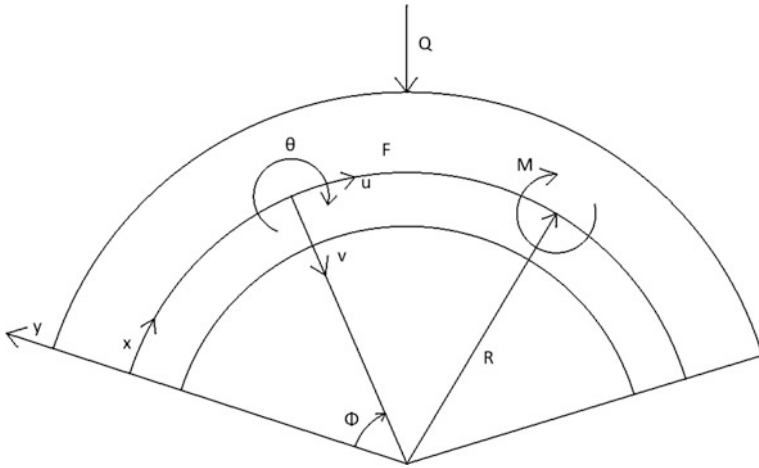
Fig. 1 Geometry of curved beam

F and *Q* are the externally applied loads in axial and transverse directions and *M* is the externally applied moment.

Hence, Modelling has been done based on following assumptions:

- The material of the beam is homogeneous and isotropic.
- Out of plane displacement and rotations are assumed to zero.
- The modelling has been done without considering damping.
- Effects of rotary inertia and shear deformation are significant.

The deflection of the curved Timoshenko beam can be written as

$$u(x, y, z, t) = u(x, t) - y\theta(x, t) \tag{1}$$

$$v(x, y, z, t) = v(x, t) \tag{2}$$

$$w(x, y, z, t) = 0 \tag{3}$$

The strains for the curved beam in curvilinear coordinate system can be written as

$$\varepsilon_{xx} = \frac{\partial u}{\partial x} - \frac{v}{R} - y\frac{\partial \theta}{\partial x} \tag{4}$$

$$\gamma_{xx} = \frac{\partial v}{\partial x} - \theta + \frac{u}{R} \tag{5}$$

Hence, the system is conservative as damping is not considered for the modelling. Therefore, according to Hamilton principle

$$\int_{t_1}^{t_2} [\delta(T-U)+\delta W_e]dt = 0 \tag{6}$$

where, T, U, W_e are kinetic energy, potential energy, and work done by the external forces, respectively. Here, T, U, W_e can be written as

$$T = \frac{1}{2}\int_0^L \left[\rho A\left(\frac{\partial u}{\partial t}\right)^2 + \rho A\left(\frac{\partial v}{\partial t}\right)^2 + \rho I\left(\frac{\partial \theta}{\partial t}\right)^2\right]dx \tag{7}$$

$$U = \frac{1}{2}\int_0^L \left[EA\left(\frac{\partial u}{\partial x}-\frac{v}{R}\right)^2 + EI\left(\frac{\partial \theta}{\partial x}\right)^2 + kGA\left(\frac{\partial v}{\partial x}-\theta+\frac{u}{R}\right)^2\right]dx \tag{8}$$

$$W_e = \int_0^L [uF+vQ+\theta M]dx \tag{9}$$

where F, Q, M is axial force, transverse force, moment along the length of the beam. Hence, the equation of motion can be written as

$$\rho A\frac{\partial^2 u}{\partial t^2} + \left(EA\frac{\partial^2}{\partial x^2}-\frac{kGA}{R^2}\right)u - \frac{EA+kGA}{R}\frac{\partial v}{\partial x} + \frac{kGA}{R}\theta - F = 0 \tag{10}$$

$$\rho A\frac{\partial^2 v}{\partial t^2} - \frac{EA+kGA}{R}u - \left(kGA\frac{\partial^2}{\partial x^2}-\frac{EA}{R^2}\right)v + kGA\theta - Q = 0 \tag{11}$$

$$\rho I\frac{\partial^2 \theta}{\partial t^2} - \frac{kGA}{R}u - kGA\frac{\partial v}{\partial x} - \left(EI\frac{\partial^2}{\partial x^2}-kGA\right)\theta - M = 0 \tag{12}$$

1.2 Finite Element Formulation

The finite element formulation has been done by considering 2-Node, 6 DOF curved beam element. Trigonometric shape function is used for the analysis [7]. The shape functions are

$$v = a_1+a_2x+(a_3+a_4x)\cos\frac{x}{R}+(a_5+a_6x)\sin\frac{x}{R} \tag{13}$$

$$\theta = b_1+b_2x+(b_3+b_4x)\cos\frac{x}{R}+(b_5+b_6x)\sin\frac{x}{R} \tag{14}$$

$$u = c_1+c_2x+(c_3+c_4x)\cos\frac{x}{R}+(c_5+c_6x)\sin\frac{x}{R} \tag{15}$$

Finally, the kinetic energy and potential energy can be written as

$$T = \frac{1}{2}\{\dot{d}\}^T \int_0^L [T]^T[N]^T[P][N][T]\{\dot{d}\}dx \tag{16}$$

$$T = \frac{1}{2}\{\dot{d}\}^T[ma]\{\dot{d}\} \tag{17}$$

$$U = \frac{1}{2}\{d\}^T \int_0^L [T]^T[B]^T[D][B][T]\{d\}dx \tag{18}$$

$$U = \frac{1}{2}\{d\}^T[ka]\{d\} \tag{19}$$

where,

$$[ma] = \int_0^L [T]^T[N]^T[P][N][T]dx \tag{20}$$

$$[ka] = \int_0^L [T]^T[B]^T[P][B][T]dx \tag{21}$$

1.3 Crack Modelling

Presence of crack changes the local compliance of the beam [14–16]. The local compliance matrix for the crack can be written as

$$C_{ij} = \frac{\partial U_i}{\partial P_j} = \frac{\partial^2}{\partial P_i \partial P_j} \int_0^a J da \tag{22}$$

where, U_i is the strain energy due to displacement in the direction of P_i and J is the strain energy release rate. Which can be expressed as

$$J = \frac{1}{E}\left[\left(\sum_{k=1}^{6} K_{Ik}\right)^2 + \left(\sum_{k=1}^{6} K_{IIk}\right)^2 + \left(\sum_{k=1}^{6} K_{IIIk}\right)^2\right] \tag{23}$$

Here K_I, K_{II}, K_{III} are stress intensity factor for Mode I, II, III, respectively and 1–6 shows 3 forces and three moments in three directions (x, y, and z directions). Hence, in case of in-plane problem, three forces have been considered for the analysis. The forces are axial force (P_1), shear force (P_2) and bending moment (P_6). Hence, stress intensity factor [15, 16] can be written as

$$K_{I1} = \frac{0.278P_1}{2\sqrt{h}} \sqrt{\frac{[1+2(a/h)]^3}{(a/h)(1-a/h)^3}} \tag{24}$$

$$K_{I6} = \frac{6P_5}{bh^{3/2}} \frac{0.482}{\sqrt{(1-a/h)^3}} \tag{25}$$

$$K_{II2} = \frac{P_3\sqrt{\pi a}}{bh} \frac{0.725}{\sqrt{(a/h)(1-a/h)}} \tag{26}$$

Hence, a is depth of crack, b and h are breadth and height of the beam, respectively. The compliance matrix can be derived with the help of Eq. (9). Due to presence of crack, it requires force equilibrium and additional crack across the crack [14]

$$-\{P\}^+ = \{P\}^- \tag{27}$$

$$\{w\}^+ - \{w\}^- = [C]\{P\}^+ \tag{28}$$

Combining above two equations, it can be written as

$$\begin{Bmatrix} \{P\}^- \\ \{P\}^+ \end{Bmatrix} = \begin{bmatrix} [C]^{-1} & -[C]^{-1} \\ -[C]^{-1} & [C]^{-1} \end{bmatrix} \begin{Bmatrix} \{w\}^- \\ \{w\}^+ \end{Bmatrix} \tag{29}$$

$$\{P\} = [K]\{w\} \tag{30}$$

2 Results and Discussions

The analysis has been performed on a curved beam whose physical parameters are given below [17]

Modulus of Elasticity (E) = 200 GPa = 2×10^{11} Pa
Modulus of Rigidity (G) = 76.9 GPa = 7.69×10^{10} Pa
Shear Correction Factor (k) = 0.85
Cross Sectional Area (A) = 0.005 m^2
Area Moment of Inertia (I) = 4.16×10^{-6} m^4
Radius of Curvature (R) = 0.5 m
Density (ρ) = 7850 kg/m^3
Angle subtended by beam (ϕ) = 90 deg

Based the above values, the mass and stiffness matrix have been evaluated for each element by using the Eqs. (20) and (21). Further, global mass matrix has been

formed and global stiffness matrix has been formed by incorporating local stiffness for the crack by using the Eq. (30). The equation of motion for the beam will be

$$[ma]_{global}\{\ddot{d}\}_{global} + [ka]_{global}\{d\}_{global} = \{0\} \tag{31}$$

Now, the solution of $\{d\}$ assumed as

$$\{d\}_{global} = \{X\}e^{j\omega t} \tag{32}$$

where, $\{X\}$ and ω are mode shape and natural frequency, respectively. The Eq. (32) has been solved to find out natural frequencies. Obtained natural frequencies of a cracked and without cracked curved beam with different edge crack depth ratio (a/h) have been shown in Table 1. The crack depth ratio has been considered for analysis are 0.2, 0.4 for first 10 modes. The results show that the natural frequency of the cracked beam decreases as crack depth increases

Further, the equations of motion (31) are decoupled by multiplying modal vector and each equation has been solved for free vibration analysis. Next, v, u, θ are formed by using appendix (1.5)–(1.7). The mode shape results for the radial displacement 'v' for first ten modes of a cracked beam under clamped—clamped end conditions are shown in Fig. 2.

The mode shape results for the tangential displacement 'u' for first ten modes of a cracked beam under clamped-clamped end conditions are shown in Fig. 3. The mode shape results for the rotational displacement 'θ' for first ten modes of a cracked beam under clamped-clamped end conditions are shown in Fig. 4. The crack introduces discontinuity and it is modelled as a spring. Therefore, higher displacement in different modes have been observed at the vicinity of the crack.

Table 1 Natural frequencies of a curved beam with edge crack of varying crack depth ratios under clamped-clamped end condition

Mode	Natural frequency without crack (Hz)	Natural frequency with crack depth ratio 0.2 (Hz)	Natural frequency with crack depth ratio 0.4 (Hz)
1	770.90	693.27	638.23
2	1690.84	1552.98	1393.15
3	2721.50	2697.13	2609.42
4	3451.10	3266.94	2898.41
5	3959.06	3711.43	3669.19
6	4988.19	3963.25	3684.97
7	6564.81	6069.61	5968.50
8	8446.74	6340.42	6027.41
9	9781.79	9412.24	9314.93
10	9854.49	9444.93	9333.16
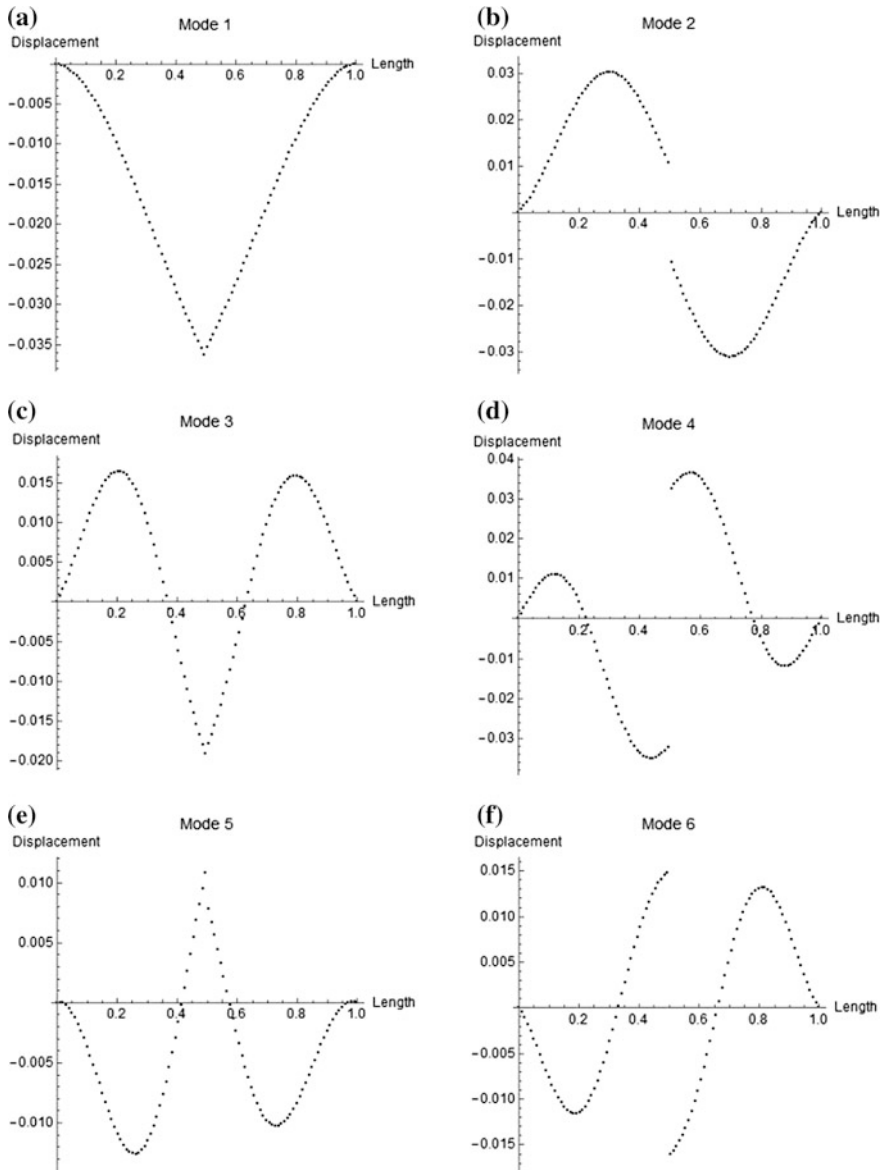
Fig. 2 Mode shapes for radial displacement 'v' for a cracked beam under clamped—clamped end conditions for first ten modes
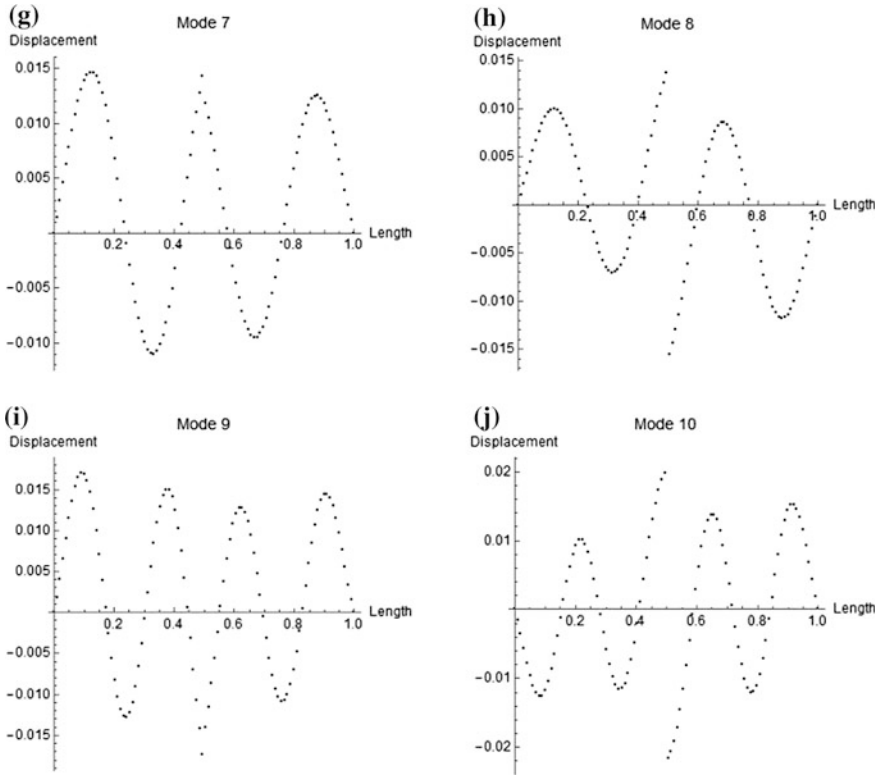
Fig. 2 (continued)
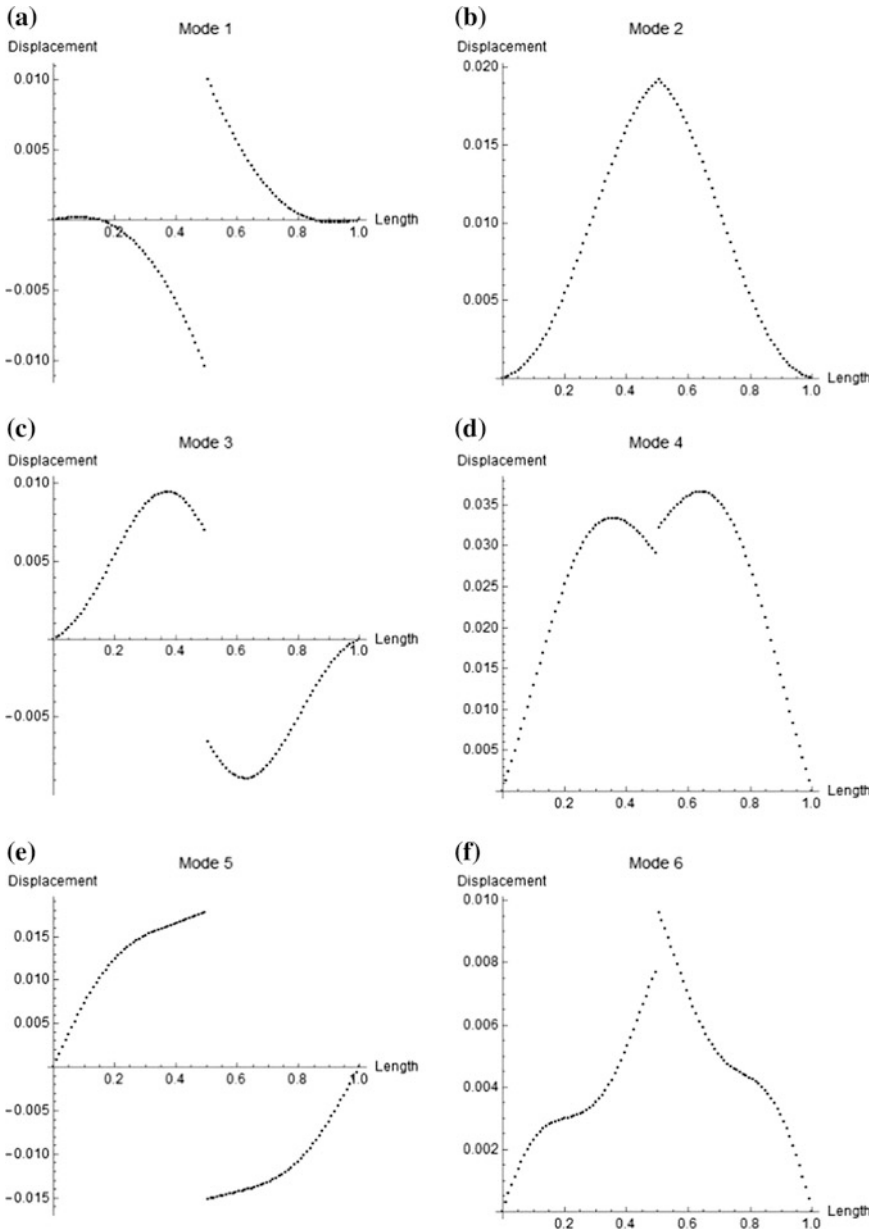
Fig. 3 Mode shapes for axial displacement 'u' for a cracked beam under clamped-clamped end conditions for first ten modes

(g) Mode 7

(h) Mode 8

(i) Mode 9

(j) Mode 10
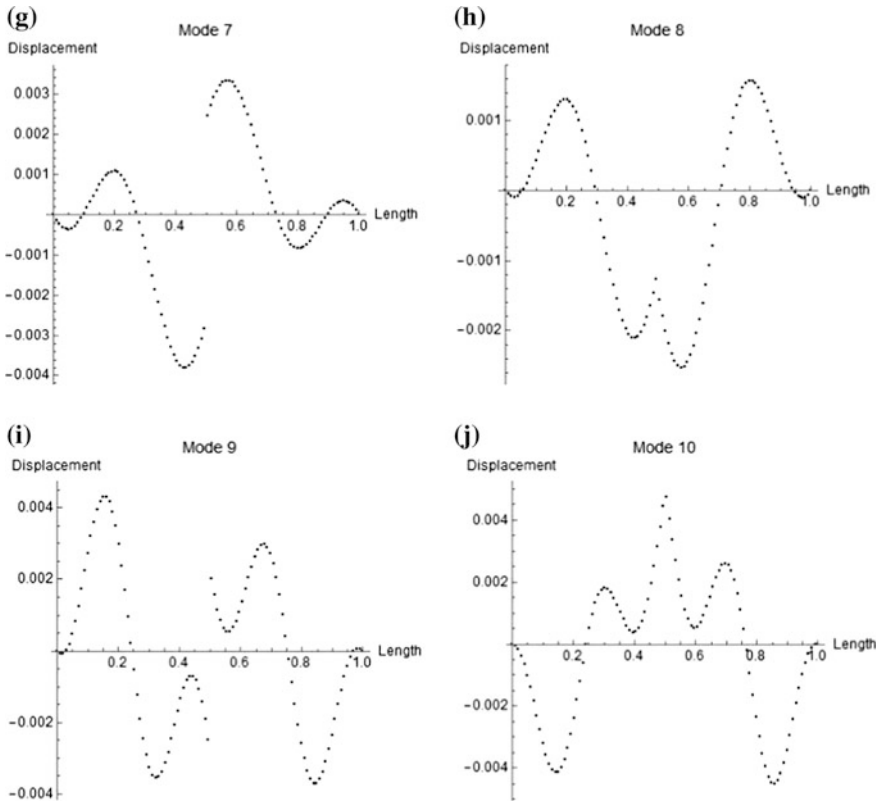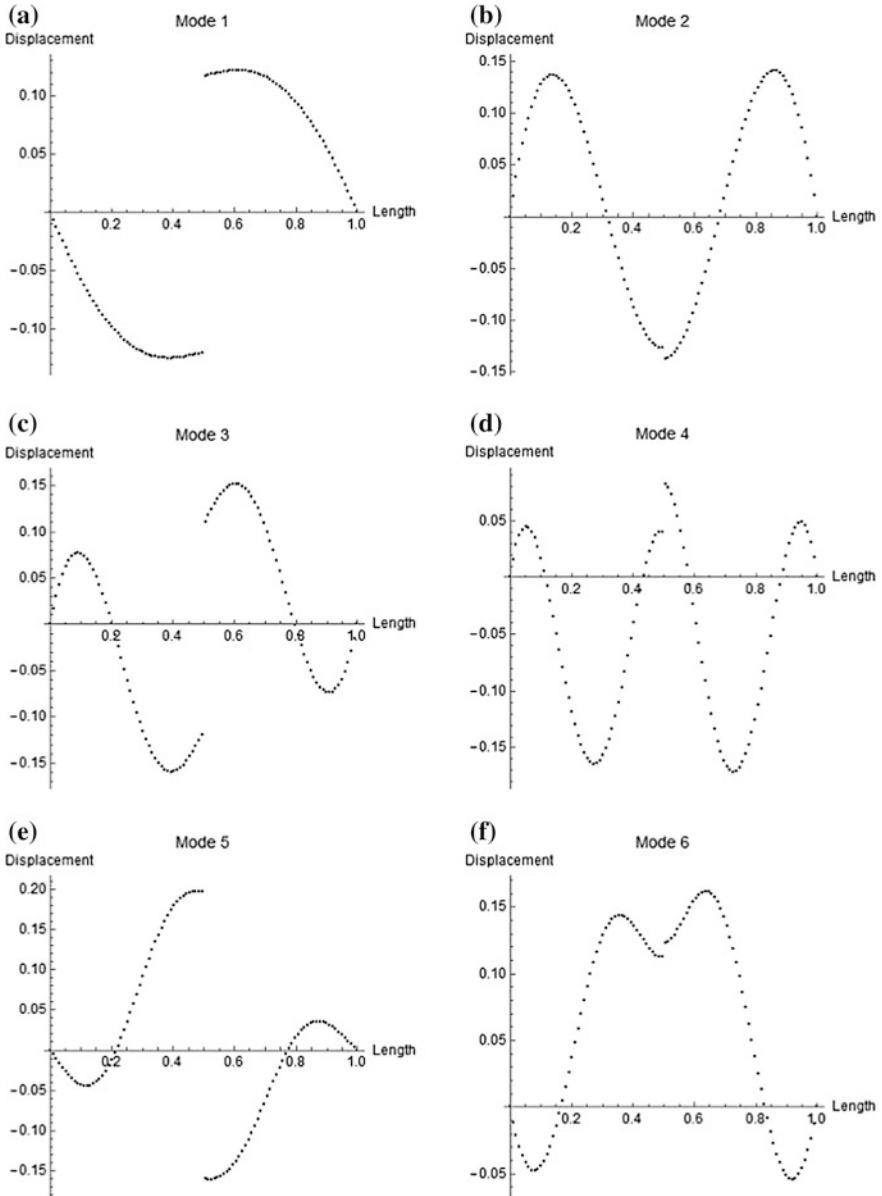
Fig. 3 (continued)

Fig. 4 Mode shapes for rotational displacement 'θ' for a cracked beam under clamped—clamped end conditions for first ten modes
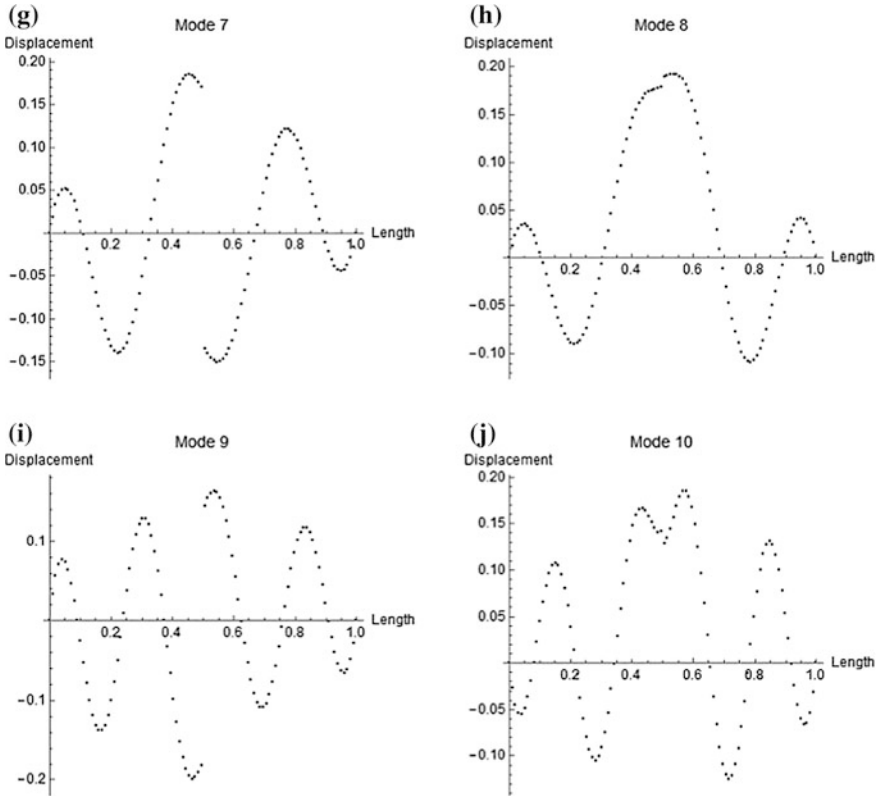
Fig. 4 (continued)

3 Conclusions

An edge crack was introduced in the curved beam and the natural frequencies were evaluated under varying crack depths. It is seen that the natural frequency decreases with increasing crack depth. It is also seen from the mode shape results for a cracked beam that there is a discontinuity at the crack location for the displacements and rotations. Both of these results are expected. The decrease in natural frequency suggest a decrease in stiffness of the beam with increase in crack depth and there will be a sudden change in deflection at the location of the crack.

References

1. Wolf JA (1971) Natural frequencies of circular arches. J Struct Division ASCE 97:2337–2350
2. Petyt M, Fleischer CC (1971) Free vibration of a curved beam. J Sound Vib 18(1):17–30
3. Austin W, Veletsos A (1972) Free in-plane vibrations of circular arches. J Eng Mech ASCE 98:311–329

4. Davis R, Henshell RD, Warburton GB (1972) Constant curvature beam finite elements for in-plane vibration. J Sound Vib 25(4):561–576
5. Auciello NM, Rosa MAD (1994) Free vibrations of circular arches: a review. J Sound Vib 176(4), 433–458
6. Eisenberger M, Efraim E (2001) In-plane vibrations of shear deformable curved beams. Int J Numer Methods Eng 52:1221–1234
7. Friedman Z, Kosmatka JB (1998) An accurate two-node finite element for shear deformable curved beams. Int J Numer Methods Eng 41:473–498
8. Kang K, Bert C, Striz H (1995) Vibration analysis of shear deformation circular arches by the differential quadrature method. J Sound Vib 181(2):353–360
9. Lee SY, Yan QZ (2015) Exact static analysis of in-plane curved Timoshenko beams with strong nonlinear boundary conditions. Math Probl Eng 4:1–12
10. Litewka P, Rakowski J (1998) The exact thick arch finite element. Comput Struct 68:369–379
11. Litewka P, Rakowski J (2001) Free vibrations of shear-flexible and compressible arches by FEM. Int J Numerical Methods Eng 52:273–286
12. Yang F, Sedaghati R, Esmailzadeh E (2008) Free in-plane vibration of general curved beams using finite element method. J Sound Vib 318(4–5):850–867
13. Yang F, Sedaghati R, Esmailzadeh E.: Free in-plane vibration of curved beam structures: a tutorial and the state of the art. J Vib Control, 1–8 (2017)
14. Gounaris G, Dimarogonas A (1988) A finite element of a cracked prismatic beam for structural analysis. Comput Struct 28(3):309–313
15. Nobil L (2000) Mixed mode crack initiation and direction in beams with edge crack. Theor Appl Fract Mech 33:107–116
16. Nobil L (2001) Mixed mode crack growth in curved beams with radial edge crack. Theor Appl Fracture Mech 36:61–72
17. Talukdar S (2017) Dynamic analysis of a curved timoshenko beam using finite element method. NIT Patna, India, July 2017, Thesis for the degree of master of technology in mechanical engineering

Planar Vehicle Dynamics Using Bicycle Model

Akshay Mistri

Abstract There is a limit to which a vehicle will remain directionally stable during a steering maneuver. Vehicle configuration factors like position of center of gravity and vehicle state factors like velocity and steer angles have a huge influence on the stability of a vehicle in motion. A lot of investments are made during a vehicle design process to make it stable and safe for occupants, which include study of dynamics of the vehicle configuration. This study of dynamics can be achieved by studying the equations of motion for that vehicle configuration and by performing actual road tests which could be expensive sometimes. Thus, the bicycle model discussed further is a quick and inexpensive way to analyze a vehicle configuration for its stability. Along with stability, the model can provide useful information like velocity vectors, yaw rates for a given input wheel torques, and steer angles. The model is developed by deriving equations of motion for a simple two-wheel vehicle setup. The paper discusses in detail the process of deriving equations for a bicycle model and the way in which various factors affect the vehicle turn responses.

Keywords CG—Center of gravity · δ—Steering angle · α—Sideslip angle · ω—Angular velocity · C_α—Cornering stiffness · G_{acc}—Lateral acceleration gain

1 Introduction

Primary forces which influence the dynamics of a motor vehicle are developed at tire–road interface patches which are nearly the size of a human hand. By motor vehicle, it is meant that further discussion will be applicable to automobiles like cars, buses, and trucks. The tire patches are the only contact between the vehicle and the road which if analyzed properly could give an insight to vehicle handling characteristics.

A. Mistri (✉)
Wayne State University, Detroit, MI 48201, USA
e-mail: akshay14september@gmail.com

To analyze the dynamics of vehicle while making a turn, bicycle model was developed which was relatively easy to understand. It can provide useful information for a given vehicle configuration like velocity of the center of gravity (CG) of vehicle in longitudinal and lateral directions and the vehicle's yaw rate for a given steering angle. It could also be used to judge the steering response of a given vehicle configuration and how the turn radius of a vehicle changes with vehicle speed when the steering angle is kept constant. The bicycle model also includes the sideslip phenomenon occurring in high-speed maneuvers. Sideslip is developed in tires due to the friction force acting on tire to counteract the centrifugal forces acting on the vehicle during a turn. Thus, a bicycle model is an analytical method of understanding various vehicle handling characteristics in a relatively simple way and could be used in initial vehicle design phase.

One ground-based stationary frame (X−Y) and a body-fixed reference frame (x−y) with x-axis as the longitudinal axis of the model are chosen. Origin of the body-fixed reference frame is taken as the CG of the vehicle configuration.

The velocity of the bicycle model is described in the body-fixed reference frame and then its time derivative is taken to get the equation of motion. Forces acting on tire are first described in body-fixed reference frame and using their relationships with slip angles and torque equations of motion are resolved into required control variables.

These equations of motion were simulated in the software Simulink (The MathWorks, Inc., Massachusetts, USA) and were validated by supplying time-varying inputs and getting the desired pre-validated outcomes for those given inputs, discussed further in the paper in detail.

2 Method

2.1 Model Setup

Consider the two reference frames and the bicycle model as shown in Fig. 1.

Fig. 1 Bicycle model setup
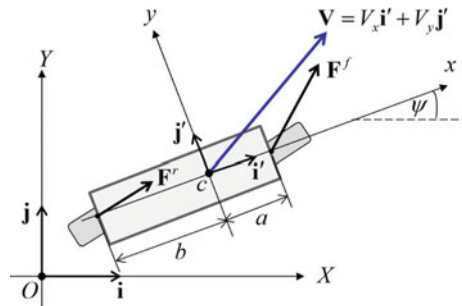
X−Y shows the ground reference frame while x−y represents the body-fixed reference frame. Velocity vector V is shown in blue, and force vectors acting on front and rear tire from ground are shown in body-fixed reference frame. Distances "a" and "b" are from CG of the model to the centers of the front and rear tire, respectively. "Ψ" is the angle between the x-axes of the two reference frames.

2.2 Equations Used

Velocity vector

$$\vec{V} = V_x \mathbf{i'} + V_y \mathbf{j'} \tag{1}$$

Using the differential operator on vector V,

$$\frac{d}{dt} = \left(\frac{\tilde{\mathbf{d}}}{\mathbf{dt}}\right) + [(\boldsymbol{\omega}) \times \ ]$$

We get

$$\frac{d\vec{V}}{dt} = \left(\frac{dV_x}{dt} - \omega_z . V_y\right) \mathbf{i'} + \left(\frac{dV_y}{dt} + \omega_z . V_x\right) \mathbf{j'} \tag{2}$$

where ω_z is the angular velocity of model about z-axis.

Also, this gives us the acceleration vector

$$\frac{d\vec{V}}{dt} = \vec{a} = a_x \mathbf{i'} + a_y \mathbf{j'} \tag{3}$$

Now, for getting equation of motion, we can use

$$F_{net} = m \cdot \vec{a}$$

Using Eqs. (2) and (3),

$$m\left(\dot{V}_x - \omega_z . V_y\right) = \mathbf{F^f i'} + \mathbf{F^r i'} \tag{4}$$

$$m\left(\dot{V}_y + \omega_z . V_x\right) = \mathbf{F^f j'} + \mathbf{F^r j'} \tag{5}$$

Considering I_{zz} as the inertia of the model about z-axis, we can write the moment equation as

$$I_{zz} \dot{\omega}_z = a\mathbf{F^f j'} - b\mathbf{F^r j'} \tag{6}$$

Now, we can disintegrate the forces acting on tires into the body-fixed reference frame

$$\mathbf{F^f} = \left(F_{xf}\cos\delta_f - F_{yf}\sin\delta_f\right)\mathbf{i'} + \left(F_{xf}\sin\delta_f - F_{yf}\sin\delta_f\right)\mathbf{j'} \tag{7}$$

$$\mathbf{F^r} = \left(F_{xr}\cos\delta_r - F_{yr}\sin\delta_r\right)\mathbf{i'} + \left(F_{xr}\sin\delta_r - F_{yr}\sin\delta_r\right)\mathbf{j'} \tag{8}$$

where δ_f and δ_r are the front and the rear wheel steering angles ($\delta_r = 0$ if the rear wheel cannot be steered) (Fig. 2).

Slipping of tires occur since there is a difference in direction of tire travel and the direction of vehicle travel. The angle between these two directions is the slip angle for that tire, shown in Fig. 3 as α_f.

Slipping can also be understood as the wheel want to travel in direction of the vector $\mathbf{V^f}$ but is dragged in direction of the vector $\mathbf{V}$ by the vehicle CG.

For getting an expression of the slip angle, velocity of the wheel in its own axis system (x-wheel and y-wheel, see Fig. 2) must transformed to body-fixed reference frame using normal vector from CG to wheel center r^f as shown below:

Velocity vector of wheel, V^f = (Velocity vector of CG, V) + (Angular rotation about CG)

$$\begin{aligned} V^f &= V + \left(\Omega \times r^f\right) \\ &= V_x\mathbf{i'} + V_y\mathbf{j'} + \begin{bmatrix} \mathbf{i'} & \mathbf{j'} & \mathbf{k'} \\ 0 & 0 & \dot{\Psi} \\ a & 0 & 0 \end{bmatrix} \\ &= V_x\mathbf{i'} + (V_y + \dot{\Psi}a)\mathbf{j'} \end{aligned} \tag{9}$$

Fig. 2 Forces on front wheel
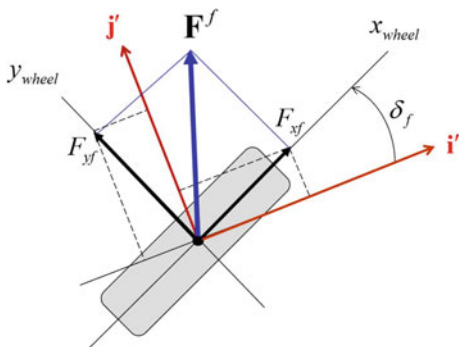
Fig. 3 Bicycle model
showing slip angle
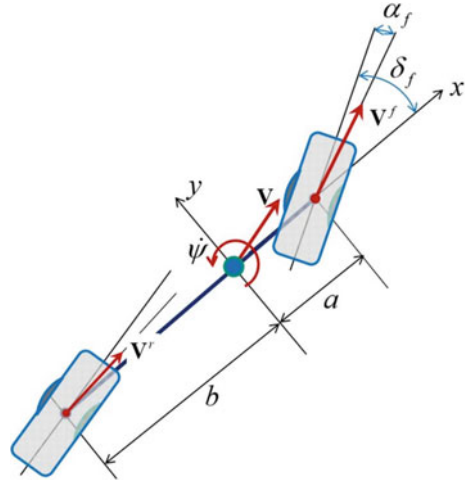
Now, the ratio of the x and y components of vector V^f obtained above can be expressed as

$$\tan(\delta_f - \alpha_f) = V_y^f / V_x^f = \frac{V_y + \dot{\Psi} \, a}{V_x} \tag{10}$$

Using small angle approximations (for simplicity),

$$\alpha_f = \delta_f - \frac{V_y + \dot{\Psi} a}{V_x} \tag{11}$$

Similarly, for rear tire,

$$\alpha_r = \delta_r - \frac{V_y - \dot{\Psi} b}{V_x} \tag{12}$$

Now, the relationship between the slip angles α_f, α_f and the lateral tire forces F_{yf}, F_{yr} can be established by linearizing the forces,

$$F_y = \frac{\partial F_y}{\partial \alpha} . \alpha = C_\alpha . \alpha \tag{13}$$

where C_α called as cornering stiffness coefficient.

Using ,

$$F_{yf} = C_{\alpha f}.\alpha_f = C_{\alpha f}\left(\delta_f - \frac{V_y + \dot{\Psi}a}{V_x}\right) \tag{14}$$

$$F_{yr} = C_{\alpha r}.\alpha_r = C_{\alpha r}\left(\delta_r - \frac{V_y - \dot{\Psi}b}{V_x}\right) \tag{15}$$

For the longitudinal forces, F_{xf}, F_{xr} relationship between input torque to wheels and their effective radii can be established as

$$F_{xf} = \frac{Q_f}{R_{fe}} \tag{16}$$

$$F_{xr} = \frac{Q_r}{R_{re}} \tag{17}$$

Finally, the equations are disintegrated into require control variables. To sum up the bicycle model equations:

Inputs:

1. Front wheel torque, Q_f [N-m].
2. Rear wheel torque, Q_r [N-m].
3. Front wheel steer angle, δ_f [rad].
4. Rear wheel steer angle, δ_r [rad] (taken 0 in our case).

Outputs:

1. Velocity in x-coordinate axis, V_x [m/s].
2. Velocity in y-coordinate axis, V_y [m/s].
3. Yaw rate in x-y plane, $\dot{\Psi}$ [rad/s].
4. Yaw angle, Ψ [rad].

Equations Modeled in Simulink:

1.
$$F_{xf} = Q_f/R_{fe}$$

2.
$$F_{xr} = Q_r/R_{re}$$

3.
$$F_{yf} = C_{\alpha f}\left(\delta_f - \frac{V_y + \dot{\Psi}a}{V_x}\right)$$

4.
$$F_{yr} = C_{\alpha r}\left(\delta_r - \frac{V_y - \dot{\Psi}b}{V_x}\right)$$

5.
$$m\left(\dot{V}_x - \dot{\Psi}V_y\right) = F_{xf}\cos\delta_f - F_{yf}\sin\delta_f + F_{xr}$$

6.
$$m\left(\dot{V}_y + \dot{\Psi}V_x\right) = F_{xf}\sin\delta_f - F_{yf}\cos\delta_f + F_{yr}$$

7.
$$I_{ZZ}\dot{\Psi} = a\left(F_{xf}\sin\delta_f - F_{yf}\cos\delta_f\right) - b.F_{yr}$$

3   Nonlinear Tire Models

Several nonlinear tire models exist and are developed by various automotive bodies.

1. The linear relationship discussed in Eq. (13), Sect. 2.2, is valid for small slip angles (<5°). For higher slip angles, the relation becomes nonlinear and is given as

$$F_{yf} = A.\sin\left[B.\tan^{-1}\left(C_{\alpha f}.\alpha_f/AB\right)\right] \tag{18}$$

$$F_{yr} = A.\sin\left[B.\tan^{-1}\left(C_{\alpha r}.\alpha_r/AB\right)\right] \tag{19}$$

where
A and B are shape factors

- A = $\mu.F_{zf}$ or $\mu.F_{zr}$, respectively, for F_{yf} and F_{yr}.
- $F_{zf} = bmg/L$ $F_{zr} = amg/L$

Fig. 4 Lateral force variation with slip angle [1]
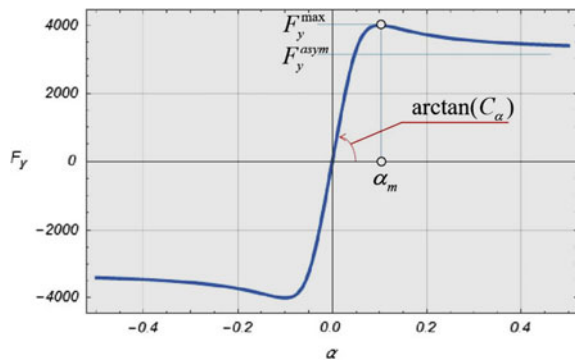
Fig. 5 GM nonlinear tire
model
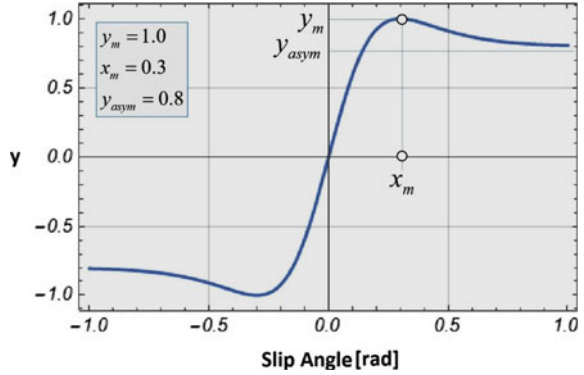
- B = 2; L is the wheelbase for the given configuration, = a + b. The variation of lateral force vs. slip angle can be seen in Fig. 4.

2. Model developed by General Motors (GM), Michigan, USA [2] (Fig. 5).

   Equation for the model:

$$y(x) = y_m \sin\left[b. \tanh(cx)\right]$$

$$b = \pi - \arcsin\left(\frac{y_{asym}}{y_m}\right)$$

$$c = \frac{\operatorname{arctanh}\left\lfloor\frac{\pi}{2b}\right\rfloor}{x_m}$$

4   Directional Stability

For analyzing the directional stability of the model, lateral dynamics of the body should be observed. Hence, the longitudinal forces are taken as negligible and rear wheel steer angle is taken as zero. Therefore, Eqs. (5) and (6) will reduce to

$$m\left(\dot{V}_y + \omega_z.V_x\right) = \boldsymbol{F}_{yf} + \boldsymbol{F}_{yr} \tag{20}$$

$$I_{zz}\,\dot{\omega}_z = a\boldsymbol{F}_{yf} - b\boldsymbol{F}_{yr} \tag{21}$$

Using Eqs. (14), (15) in (20), (21),

$$m\left(\dot{V}_y + \omega_z . V_x\right) = C_{\alpha f}\left(\delta_f - \frac{V_y + \dot{\Psi}a}{V_x}\right) + C_{\alpha r}\left(\delta_r - \frac{V_y - \dot{\Psi}b}{V_x}\right) \qquad (22)$$

$$I_{zz}\,\dot{\omega}_z = aC_{\alpha f}\left(\delta_f - \frac{V_y + \dot{\Psi}a}{V_x}\right) + bC_{\alpha r}\left(\frac{V_y - \dot{\Psi}b}{V_x}\right) \qquad (23)$$

Taking

$$a_1 = \frac{C_{\alpha f} + C_{\alpha r}}{V_x}; \qquad a_2 = mV_x + \frac{aC_{\alpha f} - bC_{\alpha r}}{V_x}$$

$$a_3 = \frac{aC_{\alpha f} - bC_{\alpha r}}{V_x}; \qquad a_4 = \frac{a^2 C_{\alpha f} + b^2 C_{\alpha r}}{V_x}$$

Equations (22) and (23) reduce to

$$m\,\dot{V}_y + a_1 V_y + a_2 \dot{\Psi} = C_{\alpha f}\delta_f \qquad (24)$$

$$I_{zz}\,\dot{\omega}_z + a_3 V_y + a_4 \dot{\Psi} = aC_{\alpha f}\delta_f \qquad (25)$$

Reducing the above equations to eigenvector—eigenvalue problem, we get

$$m\,\dot{V}_y + a_1 V_y + a_2 \dot{\Psi} = 0$$

$$I_{zz}\,\dot{\omega}_z + a_3 V_y + a_4 \dot{\Psi} = 0$$

Solving the above differential equations using,

$$V_y = A_1 e^{\lambda t} \quad \text{and} \quad \dot{\Psi} = A_2 e^{\lambda t}$$

we get

$$\begin{vmatrix} m\lambda + a_1 & a_2 \\ a_3 & I_{zz}\lambda + a_4 \end{vmatrix} = 0$$

For stability,

$$a_1 a_4 + a_2 a_3 > 0$$

which reduces to

$$L + \frac{V_x^2}{g} K_{US} > 0 \qquad \text{(stability condition)}$$

where K_{US} is called as the understeer coefficient,

$$K_{US} = \frac{W_f}{C_{\alpha f}} - \frac{W_r}{C_{\alpha r}} \qquad (26)$$

where the front and rear axle weights are used as

$$W_f = \frac{b}{L} mg \quad W_r = \frac{a}{L} mg$$

The understeer coefficient is useful factor to understand the dynamic response of a given vehicle configuration. It provides the steering response of a vehicle when it is accelerated as follows:

$$\partial_f = \frac{L}{R} + K_{US} \frac{a_y}{g} \qquad (27)$$

where a_y lateral acceleration of vehicle and is R turn radii (Fig. 6).

4.1 Effect of Understeer Coefficient K_{US}

When $K_{US} > 0$, the configuration is said to be **understeer**:

- Steering angle required for a given turn radius increases with the square of vehicle speed.

Fig. 6 Steering geometry for bicycle model
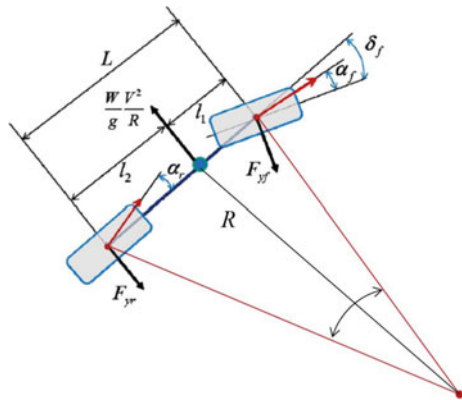
- Due to lateral acceleration of the CG, front tires will have greater slip than the rear ones.

$$\partial_f = \frac{L}{R} + K_{US}\frac{a_y}{g} > \frac{L}{R}$$

- For understeer situation, characteristic speed $V_{char} = \sqrt{\frac{gL}{K_{US}}}$ is the speed at which the steer angle required to make a turn of a given radii doubles.

When $K_{US} = 0$, the configuration is said to be **neutral steer**:

- Steer angle required for a given turn radii is independent of the vehicle speed.
- The lateral acceleration of CG induces an equal amount of slip on front and rear tires.

$$\partial_f = \frac{L}{R}$$

When $K_{US} < 0$, the configuration is said to be **oversteer**:

- To maintain a constant turn radius during acceleration, the steering angle should be reduced.
- More slip occurs at the rear tire than the front due to the lateral acceleration of the CG.
- For oversteer situation, a critical speed is present, $V_{critical} = \sqrt{\frac{gL}{-K_{US}}}$ at which the vehicle would become directionally unstable (Fig. 7).

Fig. 7 Effect of understeer coefficient on directional stability
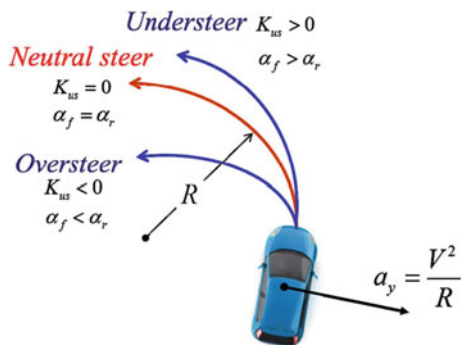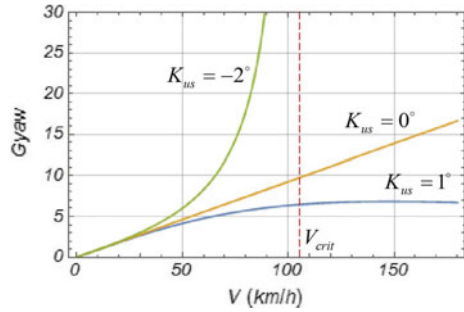
4.2 Yaw Rate Response Versus Understeer Coefficient $\mathbf{K_{US}}$

Figure 8 shows the variation of yaw rate response with velocity of vehicle for different understeer coefficients.

$$G_{yaw} = \frac{V}{L + \mathrm{K_{US}}\frac{V^2}{g}} \tag{28}$$

4.3 Lateral Acceleration Response Versus Understeer Coefficient $\mathbf{K_{US}}$

A typical figure below shows the variation of lateral acceleration of vehicle for different vehicle speeds, for different values of understeer coefficient (Fig. 9).

$$G_{acc} = \frac{V^2}{gL + \mathrm{K_{US}}V^2} \tag{29}$$

Fig. 9 Lateral acceleration
versus vehicle velocity for
different K_{US}
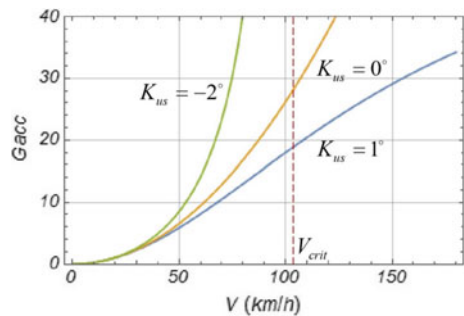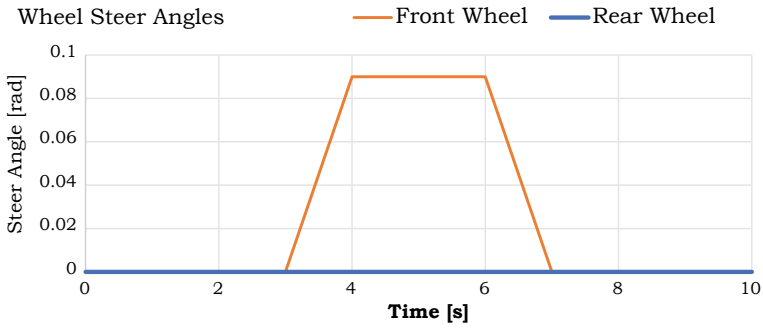
Fig. 10 Wheel steer angles

5 Results

The bicycle model was validated using various input and output sets which were taken from the official website of MathWorks [3]. The model showed accurate outputs for given inputs which are discussed below (Fig. 10).

5.1 Inputs Used

See Fig. 11.
Model Configuration Factors Used:

Sprung mass, m [Kg]	3090
I_{ZZ} [Kg.m^2]	5980
a [m]	1.65
b [m]	1.37
$C_{\alpha f}$ [N/rad]	76666
$C_{\alpha r}$ [N/rad]	186300
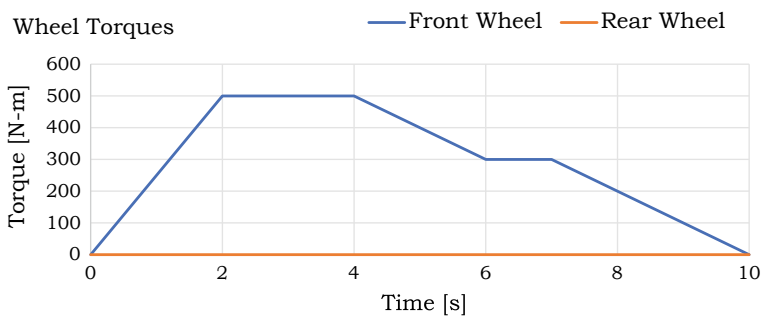
Fig. 11 Wheel input torques

5.2 Outputs Obtained: Dynamic States

See (Figs. 12, 13).

5.3 Lateral Force Versus Sideslip (Linear and Nonlinear Relationship)

The first thing to observe is the variation of lateral tire forces with sideslip angles for linear and nonlinear case. It is quite evident that in the first two linear models, the variation is linear, and for the nonlinear, it is linear at the vicinity of zero but as sideslip angle increases, the variation is nonlinear (Fig. 14).
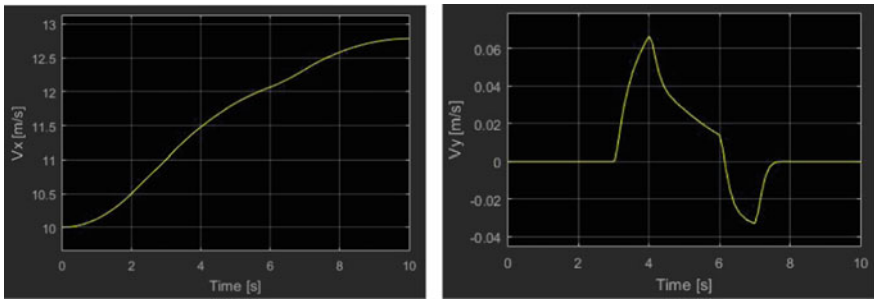
Fig. 12 Output velocities
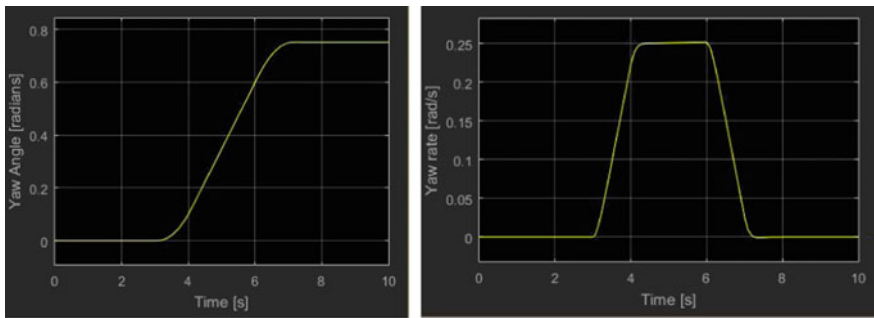
Fig. 13 Output yaw angle and yaw rate
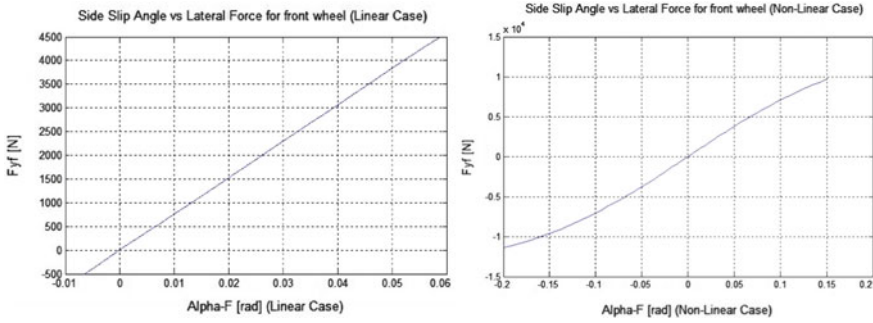
Fig. 14 Linear versus nonlinear case: lateral force versus sideslip

5.4 Lateral Acceleration Gain

For analyzing the lateral acceleration gain of the model for a situation involving a sudden lane change is considered. A sudden change of front steer angle (0.1 rad) is provided as the input keeping longitudinal force on front wheel constant. Lateral acceleration gain is found from both sides the equation: LHS to show dynamic behavior of sudden steer angle change while RHS to show the theoretical aspect.

$$G_{acc} = \frac{a_y/g}{\delta_f} = \left(\frac{V_x^2}{g.L + V_x^2.K_{US}} \right)$$

Inputs taken:
Input 1: δ_f See (Fig. 15).
Input 2: F_{xf} See (Fig. 16).
Input 3: $F_{xr} = 0$ **Input 4**: $\delta_r = 0$
Output: See (Figs. 17, 18).
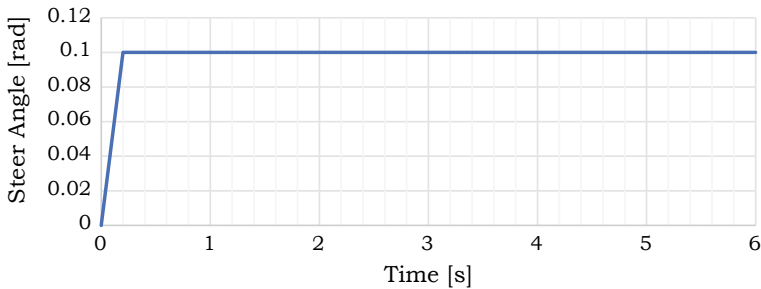
Fig. 15 Front steering angle as a time (sec) input

Longitudnal Tire Force
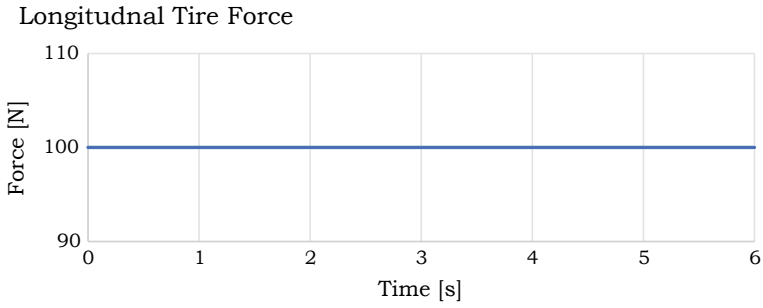
Fig. 16 Longitudinal front tire force as time (sec) input
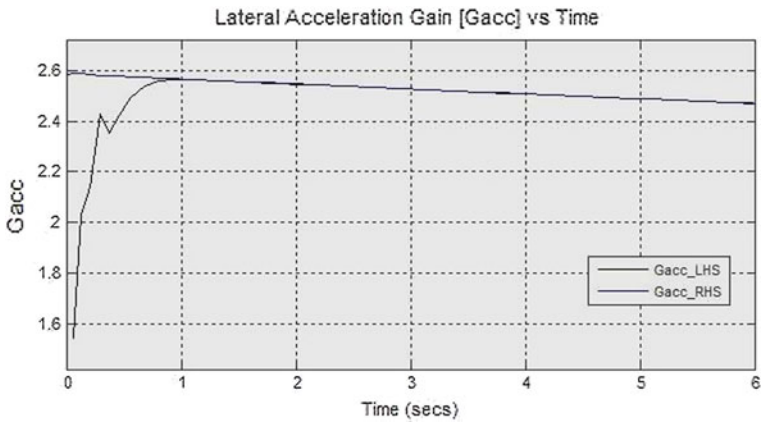
Fig. 17 Lateral acceleration gain
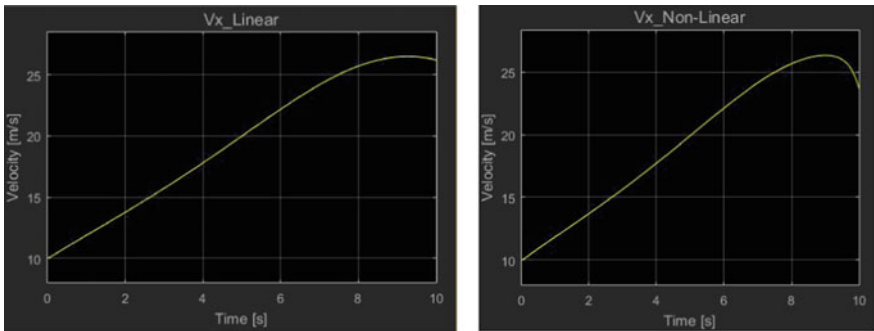
Fig. 18 Longitudinal velocity: linear versus nonlinear tire model—1

5.5 Dynamic States of Linear Versus Nonlinear Tire Models

Velocity of CG in x-coordinate axis: Linear and nonlinear.

These velocities clearly show the differences due to nonlinear sideslips. Variation in nonlinear case is more realistic in the end as shown (Fig. 19).

Note: These outputs were obtained keeping:

- Front steer angle $\delta_f = -0.2$ to 0.2 for both linear and nonlinear model.
- Front wheel torque $Q_f = 2200$ Nm for both models (Figs. 20, 21).
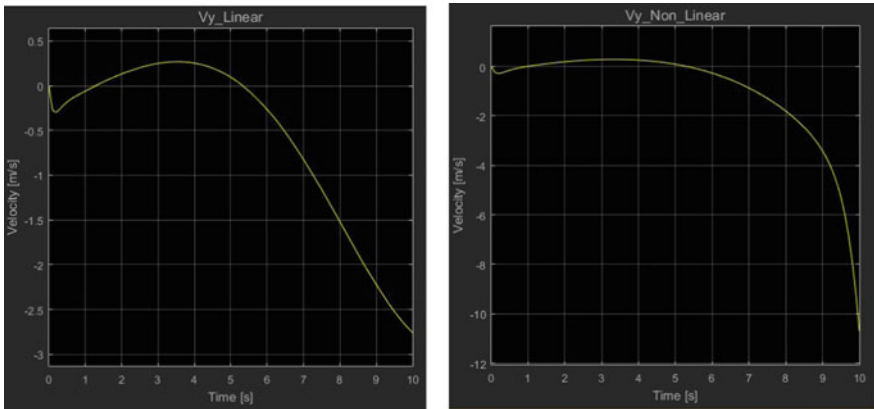
Fig. 19 Lateral velocity: linear versus nonlinear tire model—1
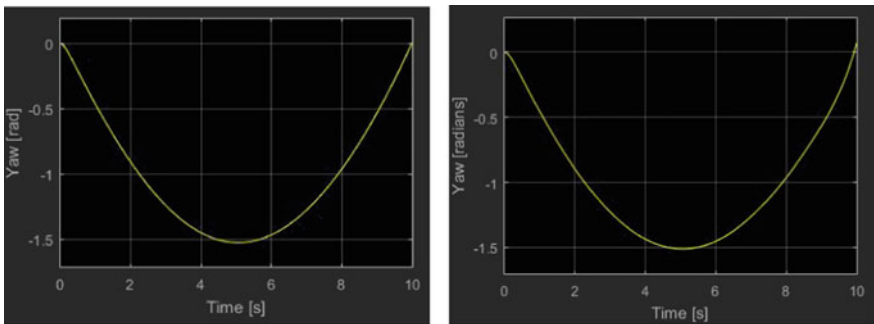
Fig. 20 Yaw angle: linear versus nonlinear tire model—1
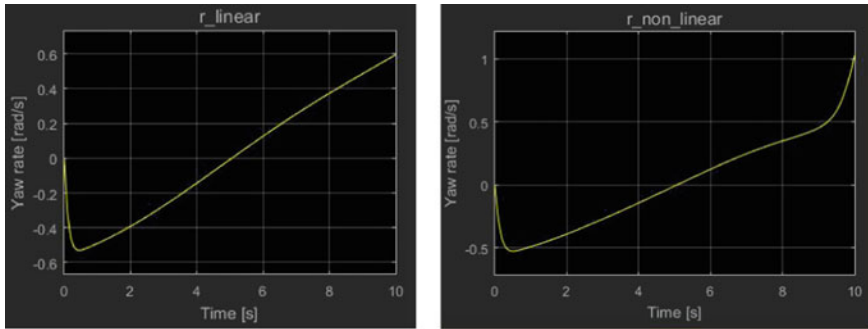
Fig. 21 Yaw rate: linear versus nonlinear tire model—1

6   Conclusion

The bicycle model obtained from equations of motion can provide dynamics states, i.e., velocities for given input wheel steer angles and wheel torques. In the model, nonlinear tire models developed experimentally can be added for a more realistic behavior. Effect of adding nonlinear tire models to the basic bicycle model can be seen by observing changes in wheel velocities. Finally, the condition for directional stability for a given vehicle configuration is derived by focusing on lateral dynamics of the body. Eigenvector and eigenvalue equation lead to the concept of understeer coefficient which is based on weight distributions on front and rear axles of the vehicle and has a huge influence on the stability of a vehicle. The model could be used for analyzing different vehicle configurations for their:

- dynamic states for various steering and speeds as inputs;
- lateral forces being generated for different sideslip angles;
- directional stability;
- understeer coefficient.

References

1. Pacejka HB, Besselink IJM (1997) In: Processing of the 2nd international colloquium on tyre models for vehicle dynamic analysis, pp 234–249
2. Pylypchuk V, Chen SK, Moshchuk N, Litkouhi B (2011) Slip-based holistic corner control. In: Proceedings of the ASME 2011 international mechanical engineering congress & exposition 2011, Denver, Colorado, US
3. Modelling a Vehicle Dynamics System, MathWorks—Examples. https://www.mathworks.com/help/ident/examples/modeling-a-vehicle-dynamics-system.html#responsive_offcanvas. Accessed 28 Jan 2018

Evaluation of Tensile Properties of Hot Rolled Carbon Steel Using Finite Element Analysis

Joginder Singh, M. R. Tyagi, Abdul Ahad, Abhinav Chawla, Dinesh Kashyap and Vinay Prabhakar

Abstract The steel undergoes rolling above the recrystallization temperature is termed as hot rolled steel. In this process, steel billet is transformed into a thin sheet with some specific properties. These thin sheets are easy to form or work with for several applications. Finite element analysis (FEA) technique is a powerful numerical method for solving several engineering problems. This technique not only reduced the experimental testing cost of materials but also provided the reliable test results for the same. In this article, the commercial HR1 steel was analyzed for tensile properties using FEA technique. The specimen dimensions were adopted from ASTM E8M standard. The 3D design of the specimen was created in CATIA and analyzed in ANSYS. When the applied load is 14 kN, the maximum stress obtained from the virtual analysis is matching well with the numerically obtained values. The maximum stress and strain in the gauge length were 279 MPa and 0.0014, respectively. Also, the calculated value of the maximum elongation was 7% for a 14 kN load.

Keywords Hot rolled steel · FEA · CATIA · ANSYS · Stress · Strain

1 Introduction

In the automobile industry, the steel has been a favorable material for the manufacturing of motorized vehicle parts from the early development stage. It has an ability to achieve required stiffness and strength by alloying, hardening, and work hardening processes. However, it has drawbacks like poor corrosion resistance and high weight. An adequate profile of a material could be achieved when it has been subjected to various metalworking processes. A thin and flat sheet of a metal is formed using a suitable rolling process as per the application need. If the rolling was carried out at a temperature ranges 0.50–0.75 T_m (melting temperature), it is

J. Singh (✉) · M. R. Tyagi · A. Ahad · A. Chawla · D. Kashyap · V. Prabhakar
Department of Mechanical Engineering, Manav Rachna University, Faridabad, India
e-mail: joginder@mru.edu.in

termed as hot rolling. This process has several advantages like low power consumption, the low pressure required for deformation, better deformation achieved, able to deform near brittle material, etc. An instilled malleability of hot rolled steel is providing freedom to manufacture a variety of different shapes. Therefore, it is an ideal material for the fabrication of structural components in various industries [1, 2]. In the past, several models using different algorithms were proposed to check the possible behavior of the materials during different loading conditions. Liu et al. [3] established a model using the artificial neural network (ANN) to precisely predict the mechanical properties of hot rolled C-Mn steels. They observed a close agreement between predicted and experimentally observed results. Ozerdem and Kolukisa [4] used ANN-based model for predicting the mechanical properties of hot rolled carbon steel bars (AISI 10xx series). They noticed that the model had predicted the mechanical characteristics within an acceptable accuracy under prescribed conditions. Apart from ANN, another dominant method to predict the possible mechanical behavior of hot rolled steel is finite element analysis (FEA) technique [5, 6]. FEA technique is frequently employed for examining the behavior of materials in several operational parameters. It is further helpful to test the materials and predict their behavior under different loading conditions even without destroying it. It is not only minimizing the product design time but also enhancing the quality and performance. The increased computing speed of modern computers boosted the utilization of FEA in several domains. As time passed by, the FEA software equipped with more advanced and sophisticated features. Currently, powerful FEA packages are available for modeling and simulation purpose. These packages are not only improved the modeling practices but also helped in sound interpretation of the obtained results [7, 8]. The present investigation aims to study the tensile behavior of the HR1 hot rolled steel using the FEA package. A 3D model of the flat tensile specimen was developed in CATIA and imported into ANSYS for tensile property analysis. A comparison of theoretical and numerical analysis was also carried out for a better understanding of the approach.

2 Experimental Procedure

The HR1 grade of the hot rolled carbon steel was selected for the investigation. The chemical composition of the same is given in Table 1.

The design of flat plate tensile specimen was chosen from the standards provided in ASTM E8M [10]. A 3D drawing of flat plate tensile specimen was prepared in

Table 1 Chemical composition of HR1 grade hot rolled carbon steel [9]

Designation	Type	C	Mn	P	S	Micro alloy	Fe
HR1	Commercial	0.15	0.60	0.05	0.035	–	Remaining
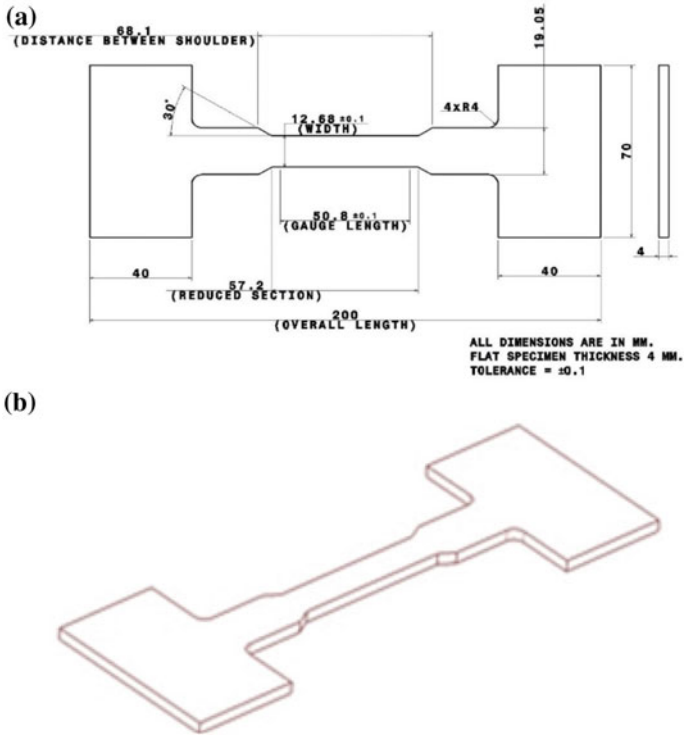
Fig. 1 Flat plate tensile specimen drawing: **a** 2D drawing and **b** isometric view

CATIA V5R20 software. A 3D and 2D design is interlinked, and any change made in 3D design is directly reflected in the 2D model or vice versa. A 2D drawing along with all the necessary dimensions of the tensile specimen and its isometric view is shown in Fig. 1a and b. The required dimensions are taken from ASTM E8M standard.

Finite element analysis (FEA) was carried out using ANSYS R18.2 software. It is a mathematical illustration of a physical object. The analysis is usually conducted in two sections. In the first section, a model of the object is developed and analyzed by collectively using material properties and necessary boundary conditions. It is a preprocessed mathematical model related to the associated problem. In the second section, the post-processing is carried out in terms of study and solution of the predefined mathematical problem. The complete process of FEA is illustrated in Fig. 2.

A 3D model of the flat plate tensile specimen developed in CATIA was saved with a.stp file extension. This popular file format is mainly utilized for communicating 3D graphical representation among several designing and analysis software. The virtual analysis of the component was carried out using ANSYS. The 3D model of the specimen is imported in ANSYS and discretized into a finite number of

Fig. 2 Block diagram of
FEA steps
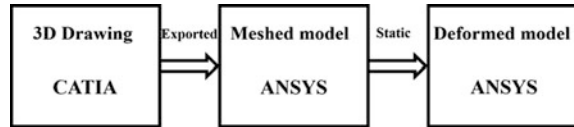
Fig. 3 Meshing of flat plate
tensile specimen of HR1
grade hot rolled carbon steel
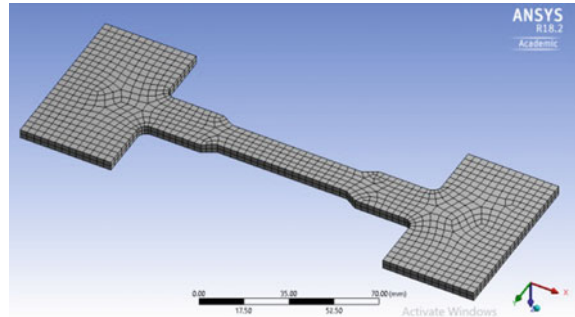
elements. This process is commonly known as meshing. The purpose of meshing is to distribute the load equally on the entire body. A proper meshing leads to higher accuracy in the results. A fine meshing of the specimen was chosen using 1648 elements and 9981 nodes (Fig. 3).

After meshing, the required constraints are imposed on the specimen in the form of boundary conditions. There are six degrees of freedom used for a component in ANSYS. In the present investigation, the movement of one end of the specimen is restricted by fixed support as shown in Fig. 4a. Besides, an axial force of tensile nature is applied to the other end of the specimen as per Fig. 4b.

After setting out the boundary and load conditions, the linear- and nonlinear-type virtual analysis was carried out using isotropic hardening model as per the requirement. In this model, von Mises yield criteria are utilized along with isotropic work hardening assumption. In a bilinear isotropic hardening (BISO), the elastic and plastic regions in complete stress–strain curve are facilitated by just two lines (as shown in Fig. 5). On the other hand, several straight lines are used for the analysis of stress–strain curve in the multilinear isotropic hardening (MISO) analysis. The BISO is more or less as an approximation of the more realistic MISO analysis. The material properties listed in Table 2 are entered as inputs for bilinear isotropic and multilinear isotropic hardening analysis, respectively. Both BISO and MISO analysis is carried out for examining the materials behavior under loading conditions beyond yield point or in plastic region.
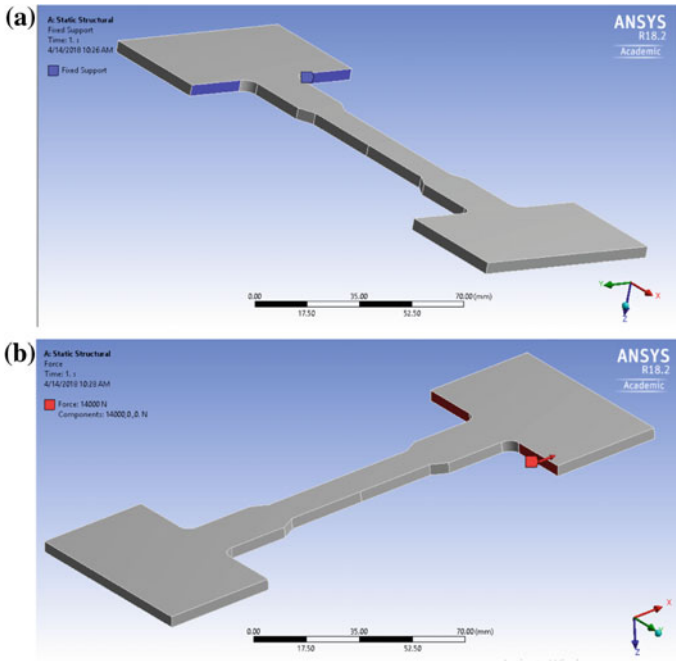
Fig. 4 **a** Boundary condition and **b** loading condition of tensile specimens
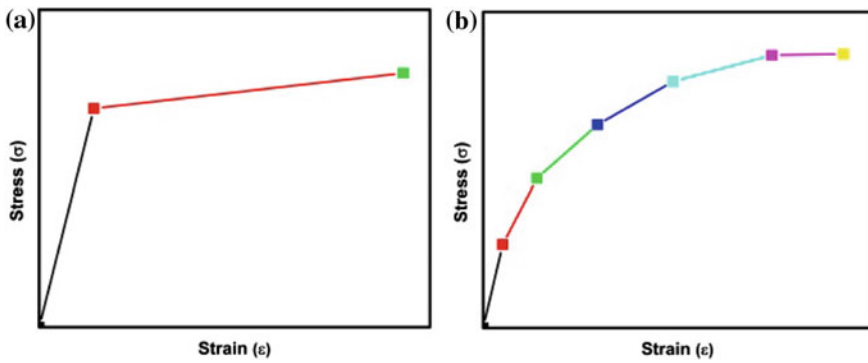
Fig. 5 Schematic diagram of uniaxial tensile loading behavior of **a** BISO and **b** MISO model

Table 2 Required material properties for the analysis

Material properties	Standard values
Ultimate tensile strength	440 MPa
Young's modulus	2×10^5 MPa
Poisson's ratio	0.3
Yield strength	250 MPa
Tangent modulus	1450 MPa

3 Results and Discussion

3.1 Theoretical Calculations of Tensile Strength

The standard material properties are listed in Table 2. The theoretical calculation of yield strength was done via Hook's law:

$$\sigma = E\varepsilon \tag{1}$$

where σ is applied stress, ε is the resulting strain, and E denotes Young's modulus.

The cross-sectional area of the flat plate tensile specimen employed in the present investigation is 50.8 mm^2. The tensile stress is calculated using the following equation for a particular applied load:

$$Tensile\ stress = \frac{Applied\ load}{Cross-sectional\ area} \tag{2}$$

For a load of 14 kN, the tensile stress is 275.5 MPa. Similarly, tensile stress can be calculated for other loads such as 15 kN, 16 kN, etc. The strain aroused in the specimen due to 275.5 MPa stress is calculated using Hooks law, and its value is 0.0014.

3.2 Stress–Strain Curve Analysis Using FEA

The BISO program in ANSYS was utilized for modeling the stress–strain behavior of the HR1 steel for different loading condition. The results of the analysis are summarized in Table 3. It was observed that if the load is below 20 kN, the observed value of the UTS is lower than the experimentally observed value, i.e., 440 MPa. Therefore, it can be concluded that the material is exhibiting better tensile strength when the applied load is below 21 kN.

Table 3 Stress–strain curve analysis using virtual analysis

S. no.	Load (kN)	Stress (MPa)	Strain (mm/mm)
1	14	279.3	0.0013965
2	15	300.4	0.0015023
3	16	320.1	0.0016009
4	17	345.6	0.0017469
5	18	380.6	0.0019221
6	19	413.5	0.0020867
7	20	443.6	0.0022374
8	21	472.1	0.0023807
9	22	500.4	0.0025223
10	23	528.2	0.0026623

3.3 von Mises Stress Analysis

Virtual analysis of the materials behavior was carried out in elastic and plastic regions under different loading conditions. The von Mises stress profile of flat plate specimen of HR1 material is shown in Fig. 6. The study of von Mises stress reemphasized the suitability of the metal for defined loading parameters. As per the figure, it can be observed that the maximum stress is distributed at the gauge length of the specimen. The load is evenly distributed along the gauge length and extended till the fillet region. Apart from the gauge length, these fillet radius regions are the prone areas for the failure of the specimen when load distribution is not uniform. But it could be reduced in the virtual analysis if the meshing of those corners were intense than the remaining body. The load distribution in the grip section is relatively lower than that of the gauge section. The maximum and minimum loads are 279 MPa and 119 MPa in the gauge length and grip section, respectively. The load variation range in the gauge section of the specimen is 259–279 MPa. The reported experimental yield strength value of HR1 steel in literature is 250 MPa. The results obtained from the virtual analysis indicates that the yielding is just started for 14 kN load. The material is entered into a strain hardening region for the applied load as maximum stress is very close to yielding strength.

3.4 von Mises Strain Analysis

The strain profile of the HR1 steel is shown in Fig. 7. The maximum strain was observed at the gauge region as expected. There is an almost uniform distribution of strain was observed along the gauge length except the points near to the reduced section. The maximum and minimum strain was 0.0014 and 0.00013 at gauge length and fillet section, respectively.
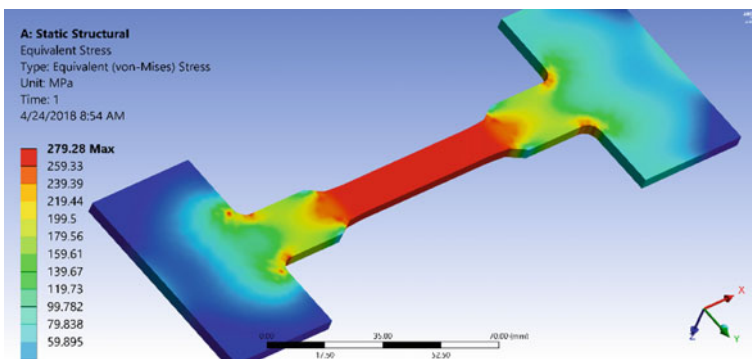
Fig. 6 von Mises stress or equivalent stress profile in HR1 specimen
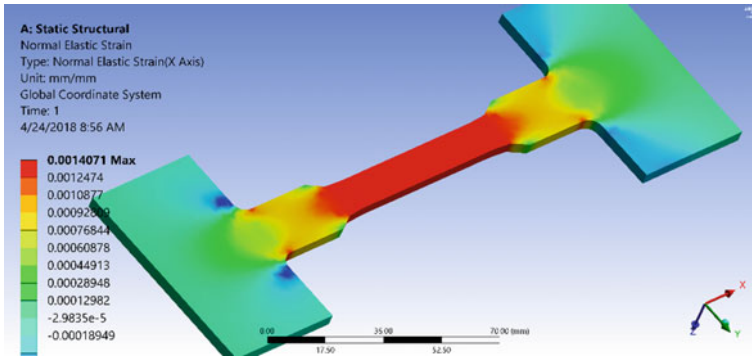
Fig. 7 von Mises strain or equivalent strain profile in HR1 specimen

4   Conclusion

In this article, the finite element analysis method is utilized to study the stress–strain behavior of the commercially available hot rolled steel (HR1). The maximum stress was observed in the gauge region of the specimen when the applied load is 14 kN. Therefore, the maximum load distribution is around gauge length if fillet region is not considered or considered after fine meshing in that region. This is the required situation in the tensile test. The color contour of gauge region exhibits the maximum and uniform distribution of load in that section. The load variation in the gauge section lies in between 259 and 279 MPa. The maximum strain in the gauge section ranges in between 0.0013 and 0.0014. The specimen was elongated around 7% when 14 kN load was applied. The stress, strain, and elongation values indicated that the material just started yielding when the applied load was 14 kN. Therefore, the virtual analysis conducted in the present study is very consistent with the calculated numerical values for low loading conditions.

References

1. Panigrahi BK (2001) Processing of low carbon steel plate and hot strip—an overview. Bull Mater Sci 24:361–371
2. DeGarmo EP, Black JT, Kohser RA, Klamecki BE (1997) Materials and process in manufacturing. Prentice Hall
3. Liu ZY, Wang W-D, Gao W (1996) Prediction of the mechanical properties of hot-rolled C-Mn steels using artificial neural networks. J Mater Process Technol 57:332–336

4. Ozerdem MS, Kolukisa S (2008) Artificial Neural Network approach to predict mechanical properties of hot rolled, nonresulfurized, AISI 10xx series carbon steel bars. J Mater Process Technol 199:437–439
5. Sharma SK, Kumar A (2018) Ride comfort of a higher speed rail vehicle using a magnetorheological suspension system. Proc Inst Mech Eng Part K J Multi-Body Dyn 232 (1):32–48. https://doi.org/10.1177/1464419317706873
6. Sharma SK, Kumar A (2016) Dynamics analysis of wheel rail contact using FEA. Procedia Eng 144:1119–1128. https://doi.org/10.1016/j.proeng.2016.05.076
7. Chung KF, Ip KH (2000) Finite element modeling of bolted connections between cold-formed steel strips and hot rolled steel plates under static shear loading. Eng Struct 22:1271–1284
8. Stolarski T, Nakasone Y, Yoshimoto S (2018) Engineering analysis with ANSYS software. Butterworth-Heinemann
9. Hot rolled carbon steel sheet and strip (2008). http://www.bis.org.in/sf/mtd/MTD4(4730).pdf
10. Standard Test Methods for Tension Testing of Metallic Materials (ASTM E8/E8M). https://www.astm.org/Standards/E8.htm

Serviceability Analysis of a Footbridge Subjected to Pedestrian Walking

Prakash Kumar , **Anoop Kumar Godara and Anil Kumar**

Abstract The paper presents a methodology to study the vibration response of beam-type footbridges subjected to loads due to walking of pedestrians in groups. A simply supported concrete beam is modeled in Ansys, and modal analysis is performed. Some of the natural frequencies of the bridge fall in the range of human walking frequencies. The pedestrian load is considered only in the vertical direction and represented as a Fourier series of five dominant harmonics. Identical individual pedestrians walk on the bridge centerline with the same walking frequency such that at any time there is a group of one, three, five, and ten pedestrians on the bridge. Moreover, another case considers three parallel groups of pedestrians walking in a row. The acceleration response of the bridge shows that the bridge vibration is unstable at the resonance condition for the first mode. The bridge fails to satisfy the pedestrian comfort limit defined in the design codes. It requires some vibration mitigation measures or structural modification to reduce the vibration.

Keywords Pedestrian walking · Serviceability · Vertical vibration ·
Pedestrian group

1 Introduction

Due to advancement in materials and construction technology, architects and engineers can build modern civil engineering structures ever longer, taller, and lighter. Some of these structures such as pedestrian bridges, grandstands, gymnasia, and staircases are commonly subjected to dynamic loads due to normal human

P. Kumar (✉)
Department of Production Engineering, Birla Institute of Technology, Mesra,
Mesra 835215, India
e-mail: pkiitr87@gmail.com

A. K. Godara · A. Kumar
Department of Mechanical and Industrial Engineering, IIT Roorkee,
Roorkee 247667, India

activities such as walking, running, and jumping [1, 2]. On the one hand, these structures may very well satisfy the design strength criteria based on the ultimate limit state. On the other hand, these light and slender structures have one or more natural frequencies often below 5 Hz that are within the range of common human actions, thus creating serious vibration serviceability problems [1–4]. Some notable example of vibration serviceability problems is the London Millennium bridge [5], the Paris Solferino bridge [6], and the Toda Park bridge [7] which triggered research on human–structure interaction (HSI) [1, 8–10] and pedestrian loading in various activities [3, 11].

Predicting the dynamic performance of these structures under pedestrian-induced load has thus become a critical aspect of structural design [1, 12, 13]. To this end, multiple practical design methodologies have been developed such as French guide Sétra [14] and the European guide HiVoSS [15] that enable designers to check the vibration serviceability of the footbridge based on the prediction of the maximum acceleration levels for a different pedestrian number and crowd density.

The paper addresses the issue of evaluation of the dynamic response of a beam-type pedestrian bridge subjected to group pedestrian loading. The group activity is more severe for triggering of vibration than individual pedestrian load or crowd load. Few practical examples are: (i) military personnel moving at the same walking speed on a bridge and (ii) vandal loading generated by a group.

2 Serviceability Analysis of Footbridge

2.1 Modal Analysis of a Footbridge

To study the vibration serviceability of a footbridge, a simply supported beam structure (see Fig. 1) is taken, which is equivalent to a concrete footbridge. Geometric and material specifications of the beam are given in Table 1. The modal analysis of the beam using Ansys 18.0 [16] shows that some natural frequencies lie in the human walking range. Thus, the structure is prone to the serviceability problem. Table 2 summarizes the first 10 natural frequencies (in Hz) and the mode shape for the beam.

Fig. 1 A schematic representation of simply supported beam-type bridge
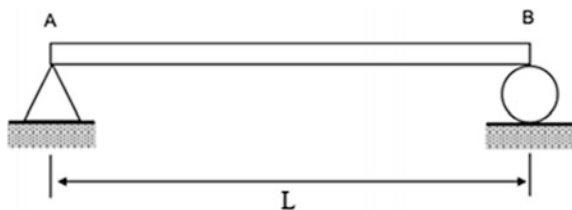
Table 1 Specifications of a beam-type bridge

Length (m)	Width (m)	Height (m)	Young modulus (GPa)	Poisson's ratio	Density (kg/m^3)
18	3	0.3327	27.3	0.18	2500

Table 2 First 10 natural frequencies of the beam

Vibration mode	First	Second	Third	Fourth	Fifth	Sixth	Seventh	Eighth	Ninth	Tenth
Vibration frequency	1.54	6.15	12.96	13.81	24.47	25.92	27.13	38.06	38.89	45.90
Mode shape direction	Vertical	Vertical	Lateral	Vertical	Vertical	Twisting	Lateral	Vertical	Twisting	Twisting

Damping plays a vital role in the dynamic analysis of structures and foundations. To make it easier and simple we treat the damping value as an equivalent Rayleigh damping as follows:

$$[C] = \alpha[M] + \beta[K] \tag{1}$$

Here [C], [M], and [K] are damping, mass, and stiffness matrix of the physical system, and α and β are constants. The orthogonal transformation of the damping matrix reduces the matrix [C] to the form

$$2\xi_i\omega_i = \alpha + \beta\omega_i^2 \tag{2}$$

In which ξ_i and ω_i are damping ratio and natural frequency for the ith mode. For systems with large degrees of freedom, it is difficult to guess meaningful values of Rayleigh damping coefficients α and β at the start of analysis.

Since the first few modes have a prominent effect on dynamic behavior, we consider the first 15 modes. The average damping ratio for the concrete structure is 1.3% and light concrete footbridges excited by intentional loading can undergo large vibrations and lead to higher damping ratios of around 5% [17–26]. Therefore, we take the first modal damping ratio as 1.5% and fifteenth modal damping ratio as 5%. By modal analysis of beam, we get ω_1 = 9.688 rad/sec and ω_{15} = 482.87 rad/sec. Now putting values of ξ_1 = 0.015, ξ_{15} = 0.05, and ω_1 and ω_{15} in Eq. (2), we get α = 0.2713 and β = 20.59 × 10^{-5}.

2.2 Serviceability Criteria for a Footbridge

Due to the movement of pedestrians, the bridge starts vibrating in lateral or vertical direction, depending on its natural frequency. A response of the bridge shows that

Table 3 Comfort classes and related acceleration limits [14, 15]

Comfort level	Maximum	Average	Minimum	Discomfort
Vertical (m/s^2)	<0.5	0.5–1	1–2.5	>2.5
Lateral (m/s^2)	<0.1	0.1–0.3	0.3–0.8	>0.8

whether it is suitable for pedestrian walking or not and what is the critical number of pedestrians for safe walking. Comfort criteria due to bridge vibration are given in Table 3.

2.3 Modeling the Pedestrian-Induced Load

The present study focuses only on the serviceability problem arising due to the vertical walking force of the pedestrian. For sake of simplicity, human walking force is considered as periodic force and it can be expressed in form of Fourier series [27–32]

$$F(t) \approx W + W \sum_{k=1}^{5} C_k \cos\left(2\pi k f_w t - \Delta\phi_{1,k}\right) \tag{3}$$

Table 4 Frequency, DLF, and phase difference of the Fourier force [27]

Speed (km/h)	f_w (Hz)	C_1	C_2	C_3	C_4	C_5	$\Delta\emptyset_{1,2}$ (rad)	$\Delta\emptyset_{1,3}$ (rad)	$\Delta\emptyset_{1,4}$ (rad)	$\Delta\emptyset_{1,5}$ (rad)
3.0	1.54	0.098	0.010	0.047	0.029	0.016	4.95	5.59	0.67	0.72
6.0	2.06	0.366	0.099	0.023	0.037	0.026	3.05	4.84	5.71	5.44
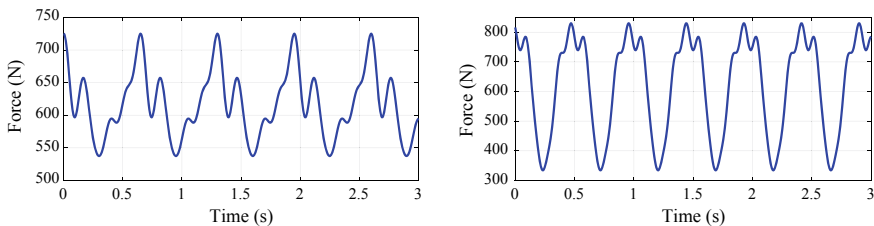
Fig. 2 Fourier representation of vertical force generated by pedestrian at walking frequencies of 1.54–2.06 Hz

Here, W is the mean value of the vertical force which is equal to the body weight; C_k and f_w are the dynamic load factor (DLF) and walking frequency. Here, $\Delta\phi_{1,k}$ is the phase difference of kth harmonic with respect to the first harmonic.

The Fourier components of a pedestrian (body mass = 63.1 kg) at two walking speeds are provided in Table 4 [27] for serviceability analysis in this study. Using the data of Table 4, a typical force plot for a vertical walking force for walking frequencies of 1.54–2.06 Hz is shown in Fig. 2.

2.4 Analysis of a Beam-Type Bridge

The finite element model of the beam bridge is developed in ANSYS 18.0 using beam188 element and modal analysis is performed to get natural frequencies and mode shapes. To study the serviceability problem, two different types of pedestrian groups, i.e., pedestrians walk in one row and three parallel rows, are analyzed for four different conditions. In the first condition, a pedestrian walks on the structure such that when he leaves from one end then a new pedestrian enters from another end. In the second condition, a new pedestrian keeps on entering after covering L/3 distance such that at any instant, there are three pedestrians present on the bridge. Accordingly, in third and fourth condition, 5 and 10 pedestrians walk on the structure such that the gap between pedestrian is kept the same throughout the simulation. For analysis purpose, two different walking speeds are used: the first one is 3 km/h, i.e., slow walking, and walking frequency is 1.54 Hz matching to the first mode of the structure. The second walking speed is 6.0 km/h that is fast walking and walking frequency is 2.06 Hz. The third harmonic of the fast walking that is 6.18 Hz is close to the second mode of the structure. For dynamic analysis, a force represented by Eq. (3) is applied at a node for one time period, and for the next time period, a load is applied to another node which is
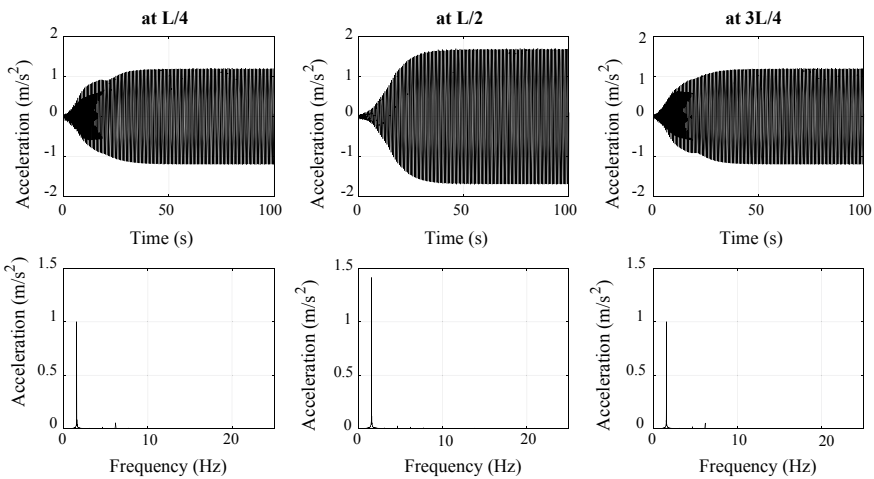
Fig. 3 Vibration response of the beam and frequency spectra at a pedestrian walking frequency of 1.54 Hz for three different locations
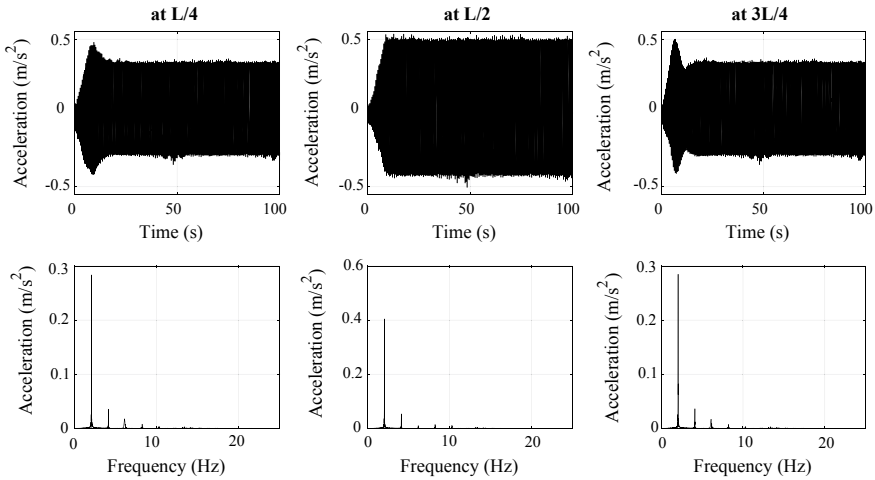
Fig. 4 Vibration response of the beam and frequency spectra at pedestrian walking frequency of 2.06 Hz, i.e., one-third of the second mode at three different locations

at a distance equal to the step length from the previous node. The acceleration and displacement time history of the beam is recorded for 100 s at three points L/4, L/2, and 3L/4 for all simulations with sampling rate 250 Hz.

3 Results and Discussion

Figure 3 shows vibration response and frequency spectra of the bridge when three groups of ten pedestrians are walking on it at 3 km/h and the walking frequency is 1.54 Hz. In the first mode, the maximum deflection occurs at the mid-span. Therefore, the maximum acceleration is obtained at L/2 distance from the end. FFT of the acceleration signal for L/4 and 3L/4 shows spectra at 6.18 Hz but this is unavailable for L/2 as at this location, node formation occurs for the second mode.

As the third harmonic (at walking speed of 6.0 km/h) is matched with the second mode of the bridge, it also tends to excite the bridge excessively. Figure 4 also shows vibration response and frequency spectra of the structure when ten groups of three pedestrians are walking on it at 6 km/h at a walking frequency of 2.06 Hz, and the third harmonic is equal to the second natural frequency of the structure. Vibration response in Fig. 4 is lower than that in Fig. 3 as in earlier case resonance occurred in the first mode whereas in this case, the resonance occurred in the second mode. The maximum vibration occurred at L/4 and 3L/4 in the second mode so FFT of the response shows the presence of 6.153 Hz frequency at L/4 and 3L/4 whereas at L/2 node formation takes place so 6.153 Hz frequency is not available at L/2 span.

Table 5 RMS vibration response (m/s^2) of beam-type bridge at three points

No. of pedestrian	Walking frequency of 1.54 Hz			Walking frequency of 2.06 Hz		
	L/2	L/2	3L/4	L/2	L/2	3L/4
1	0.035	0.040	0.035	0.020	0.013	0.020
3	0.078	0.109	0.078	0.024	0.032	0.024
5	0.128	0.180	0.128	0.037	0.051	0.037
10	0.254	0.357	0.254	0.072	0.101	0.072
1*3	0.105	0.120	0.105	0.059	0.039	0.058
3*3	0.234	0.328	0.234	0.072	0.096	0.072
5*3	0.384	0.540	0.384	0.110	0.154	0.111
10*3	0.763	1.072	0.763	0.215	0.303	0.216

Table 6 Maximum vibration response (m/s^2) of beam-type bridge at three points

No. of pedestrian	Walking frequency of 1.54 Hz			Walking frequency of 2.06 Hz		
	L/2	L/2	3L/4	L/2	L/2	3L/4
1	0.102	0.086	0.105	0.061	0.038	0.066
3	0.144	0.198	0.155	0.068	0.076	0.077
5	0.218	0.298	0.217	0.090	0.109	0.087
10	0.402	0.566	0.402	0.160	0.178	0.167
1*3	0.306	0.259	0.315	0.184	0.115	0.198
3*3	0.431	0.593	0.465	0.205	0.227	0.230
5*3	0.654	0.895	0.650	0.270	0.326	0.261
10*3	1.205	1.698	1.205	0.479	0.535	0.501

Vibration responses of all the simulated results are compiled in Tables 5 and 6. Table 5 shows the root mean square (RMS) of the acceleration response for all the eight cases and at all the three locations. RMS vibration response of the bridge shows that the response is maximum at mid-span and increases with an increase in the number of pedestrians. Similar trends are observed for the maximum vibration response listed in Table 6.

4 Conclusions

The modal analysis of the beam bridge reveals that the bridge is susceptible to vibration serviceability as its natural frequencies lie in the range of human walking loads. To analyze the serviceability problem, two walking speeds (3–6 km/h) are selected. The fundamental frequency of walking for 3 km/h is 1.54 Hz which matches with the first vertical frequency of the structure. Therefore, large vibration amplitudes of 0.357 and 1.072 m/s^2 were observed at the midpoint of the structure when 10 pedestrians walk in a single row and in three parallel rows, respectively.

For the second speed (6 km/h), the third harmonic of the walking force matched with the second modal frequency of the structure and caused excessive vibration of 0.535 m/s^2, i.e., beyond the comfort limit for a group of 10 pedestrians walking in three parallel rows. In both cases, with the increase in the number of pedestrians in a group, the vibration magnitude increases but a rate of increase is lesser in the second case. The bridge requires some vibration mitigation measures or structural modification to reduce the vibration.

References

1. Živanović S, Pavic A, Reynolds P (2005) Vibration serviceability of footbridges under human-induced excitation: a literature review. J Sound Vib 279:1–74
2. Jones CA, Reynolds P, Pavic A (2011) Vibration serviceability of stadia structures subjected to dynamic crowd loads: a literature review. J Sound Vib 330:1531–1566
3. Racic V, Pavic A, Brownjohn JMW (2009) Experimental identification and analytical modelling of human walking forces: literature review. J Sound Vib 326:1–49
4. Nimmen KV, Lombaert G, Roeck GD, Broeck PV (2014) Vibration serviceability of footbridges: evaluation of the current codes of practice. Eng Struct 59:448–461
5. Dallard P, Fitzpatrick T, Flint A, Low A, Smith RR, Willford M et al (2001) London millennium bridge: pedestrian-induced lateral vibration. J Bridg Eng 6:412–417
6. Danbon F, Grillaud G (2005) Dynamic behaviour of a steel footbridge, characterization and modelling of the dynamic loading induced by a moving crowd on the solferino footbridge in Paris. In: FOOTBRIDGE 2005
7. Fujino Y, Pacheco BM, Nakamura S, Warnitchai P (1993) Synchronization of human walking observed during lateral vibration of a congested pedestrian bridge. Earthq Eng Struct Dynam 22:741–758
8. Shahabpoor E, Pavic A, Racic V (2016) Identification of mass-spring-damper model of walking humans. Structures 5:233–246
9. Shahabpoor E, Pavic A, Racic V (2016) Interaction between walking humans and structures in vertical direction: a literature review. Shock Vib 22
10. Bocian M, Brownjohn JMW, Racic V, Hester D, Quattrone A, Monnickendam R (2016) A framework for experimental determination of localised vertical pedestrian forces on full-scale structures using wireless attitude and heading reference systems. J Sound Vib 376:217–243
11. Bocian M, Macdonald JHG, Burn JF (2013) Biomechanically inspired modeling of pedestrian-induced vertical self-excited forces. J Bridg Eng 18:1336–1346
12. Brownjohn J, Fok P, Roche M, Moyo P (2004) Long span steel pedestrian bridge at Singapore Changi Airport – Part 1: prediction of vibration serviceability problems. Struct Eng 82:21–27
13. Brownjohn J, Fok P, Roche M, Omenzetter P (2004) Long span steel pedestrian bridge at Singapore Changi Airport – Part 2: crowd loading tests and vibration mitigation measures. Struct Eng 82:28–34
14. SETRA (2006) Technical guide footbridges assesment of vibrational behavior of footbridges under pedestrian loading. SETRA, Paris, France
15. Heinemeyer C, Butz C, Keil A, Schlaich M, Goldack A, Lukić M, Chabrolin B, Lemaire A, Martin P, Cunha A, Caetano E (2008) Design of lightweight footbridges for human induced vibrations - Background document in support to the implementation, harmonization and further development of the eurocodes
16. ANSYS. Swanson Analysis Systems Inc., Houston, Pennsylvania, USA, version 18.0

17. Mårtensson A, Nilsson M (2014) Dynamic analysis of pedestrian load models for footbridges, a review of current load models and guidelines. Master thesis, Chalmers University of Technology
18. Sharma SK, Sharma RC, Kumar A, Palli S (2015) Challenges in rail vehicle-track modeling and simulation. Int J Veh Struct Syst 7(1):1–9
19. Sharma SK, Kumar A (2016) Dynamics analysis of wheel rail contact using FEA. Procedia Eng 144:1119–1128
20. Sharma SK, Kumar A (2017) Impact of electric locomotive traction of the passenger vehicle ride quality in longitudinal train dynamics in the context of Indian railways. Mech Ind 18 (2):222
21. Sharma SK, Kumar A (2017) Ride performance of a high speed rail vehicle using controlled semi active suspension system. Smart Mater Struct 26(5):55026
22. Sharma SK, Kumar A (2018) Ride comfort of a higher speed rail vehicle using a magnetorheological suspension system. Proc Inst Mech Eng Part K: J Multi-Body Dyn 232 (1):32–48
23. Sharma SK, Kumar A (2018) Disturbance rejection and force-tracking controller of nonlinear lateral vibrations in passenger rail vehicle using magnetorheological fluid damper. J Intell Mater Syst Struct 29(2):279–297
24. Sharma SK, Sharma RC, Palli S (2018) Rail vehicle modeling and simulation using lagrangian method. Int J Veh Struct Syst 10(3)
25. Sharma SK, Sharma RC (2018) Simulation of quarter-car model with magnetorheological dampers for improving ride quality. Int J Veh Struct Syst 10(3)
26. Sharma SK, Kumar A (2014) A comparative study of Indian and worldwide railways. Int J Mech Eng Robot Res 1(1):114–120
27. Kumar P, Kumar A, Racic V, Erlicher S (2018) Modelling vertical human walking forces using self-sustained oscillator. Mech Syst Signal Process 99:345–363
28. Kumar P, Kumar A, Erlicher S (2018) A nonlinear oscillator model to generate lateral walking force on a rigid flat surface. Int J Struct Stab Dyn 18(2):1850020
29. Kumar P, Kumar A (2016) Modelling of lateral human walking force by self-sustained oscillator. Procedia Eng 144:945–952
30. Kumar P, Kumar A, Erlicher S (2017) A modified hybrid Van der Pol-Duffing-Rayleigh oscillator for modelling the lateral walking force on a rigid floor. Phys D 358:1–14
31. Kumar P, Kumar A, Racic V (2018) Modelling of longitudinal human walking force using self-sustained oscillator. Int J Struct Stab Dyn 18(6):1850080
32. Kumar P, Kumar A (2014) Human induced vibration in structures. Int J Mech Eng Robot Res 1:44–54

Development of AHP Framework of Sustainable Product Design and Manufacturing of Electric Vehicle

Zareef Askary, Abhishek Singh, Sumit Gupta, R. K. Shukla and Piyush Jaiswal

Abstract In the present scenario, the success of an industry depends on its sustainable manufacturing performance where competitiveness is followed by superior performance. To remain competitive in the market, the manufacturing companies need to evaluate their performance through the manufacturing sustainability. This paper presents an AHP-based model for the enablers of sustainable manufacturing evaluation in Indian manufacturing companies. A hierarchy structure is established based on the proposed key enablers of sustainable. The company's score is calculated to assess sustainability in manufacturing against the enablers and the companies rank is determined based on their scores.

Keywords AHP · Rank and weight · Sustainable manufacturing

1 Introduction

In these days, the reliance on fossil fuels and conventional sources of energy is not sustainable for future generations. It is because of this necessity that adoption of sustainability in each aspect of our life is required.

Sustainability is about meeting the needs of the present without compromising the ability of future generations to meet their needs [1]. The categorization of sustainability is divided into three classes economic, social and environmental. With the population of over 1 billion people, there is enormous pressure on transportation sector to meet the needs of the people, and as a result, the cheapest

Z. Askary · A. Singh · S. Gupta (✉)
Amity School of Engineering and Technology, Amity University Noida,
Noida 201313, UP, India
e-mail: sumitgupta2007@gmail.com

R. K. Shukla
ABES Engineering College, Ghaziabad 201009, UP, India

P. Jaiswal
NIT Jamshedpur, Jamshedpur 831014, Jharkhand, India

and most economical path is to use fossil fuels. According to the previous years' data, it is expected that by 2030, about 40% of the population will live in urban areas. As a result, the demand for transportation is bound to increase. This puts pressure on the use of fossil fuels which has already shown signs of exhaustion. In urban areas, emission from conventional powered vehicles has become a detriment to human health, whereas in rural areas, distribution of fuels remains a challenge.

Although fossil fuels are the cheapest fuel for transport there are unwanted consequences like emission of harmful gases and noise pollution. Diseases like asthma, reduced lung function, pulmonary cancer are caused due to inhalation of these harmful gases like CO, SOx and NOx. The combustion of fossil fuels also leads to the release of greenhouse gases like water vapour and CO_2, which is harmful for the environment and causes global warming.

Ever since the industrial revolution has started, most of the world's industrialized nations have been hinged onto cheap fossil fuel energy. As developing countries are rising in industrial sector, the global demand and price of fossil fuels will also increase, as well as CO_2 and greenhouse emissions. The continuous increase in the prices of non-renewable resources is also a result of the increased demand.

As the demand of fossil fuels increases, in the coming years, there will be a shortage of these resources. As a result, this leads to the importing of fossil fuels from other countries which may add to the overhead and ultimately increase the price of the fuel. This makes it difficult for an average man who will not be able to afford transportation charges like they can do so now. As the above points have highlighted the ill effects of non-sustainable technologies, it is paramount to change our technologies to be sustainable and environment friendly. The aim of this research is to find out the prominent enabler of sustainable product design and manufacturing of electric vehicles.

2 Literature Review

After reviewing several papers, it is clear that the gaps of the research in this field are in the area of key enablers. This is a new field so the research done here is lacking the necessary amount of literature. Although some papers have highlighted the enablers but it does not provide a clear view of the enablers.

Firms not only satisfy customer needs but also fulfil the expectation of other stakeholders. It is necessary for the firms to understand these expectations and define appropriate sustainability goals, strategies and objectives at both cooperate and industrial level [2].

The researchers proposed that the electric vehicles have lowered the terrestrial acidification potential and global warming potential and can also overcome many other environmental impacts as compared to internal combustion engine vehicles. They also suggested that the effectiveness of electric vehicles can be improved if their power source is a renewable source of energy [3].

The diesel consumption is a serious problem in Brazil. According to the paper the diesel fuel consumption per day is reaching up to 40 billion litres per year. The paper proposes that utilization of biodiesel instead of diesel would lower the emissions of greenhouse gases and also gives advantages on environmental and social aspects [4].

The researchers have highlighted the use of biofuels and sustainable energy development in Brazil by assessing three decades of Alcohol Program. The paper shows how policies regarding to production of biomass can cause direct benefit in energy improvement, economic savings and reduction in emission of CO_2 and reduce pollution of air. They also suggested that there are certain government policies to reduce the emissions of CO_2 and to enhance the use of bio fuels [5].

It has been found that as the raw materials are depleting day by day a day may come when these resources get exhausted. Therefore, investments are to be done in R&D, in order to overcome different challenges. One of the biggest challenges in EV is power source, i.e. battery. Designing green and sustainable battery units are necessary, so replacing conventional energy resources have become critical [6].

As the manufacturing industry is becoming highly competitive, this necessitates the implementation of cost-effective and energy efficient methods of manufacturing. The paper aims to highlight the barriers for the execution of efficient energy in the manufacturing industry of Sweden. They have also concluded that not much is known about acceptance of new technologies in the non-energy intensive manufacturing industry and further research is needed. The major driving force in the adoption of energy efficiency is the increasing energy prices from conventional sources of energy. They have also concluded that the people with real drive to adopt energy-efficient solutions are a key driver [7].

Researchers have proposed environmentally sustainable product innovation through a framework and found the factors that drive product innovation. They have concluded that the main factors are market; law and regulation knowledge; inter-functional collaboration; innovation-oriented learning; and R&D investments [8].

The author proposed in his paper that the demand for the vehicle has increased specially for personal transport. So, with increase in the number of vehicles in market, the demand for fuel also increases and hence, the global warming potential gases will also increase. He also proposed that using battery-powered vehicle or electric vehicle can overcome the energy crisis and global warming issues [9].

The author described the state of the automobile industry and urban road transportation management in China. It highlights the fact that the state government has invested heavily in the automotive industry. Foreign investment has also driven their automotive industry [10].

3 Problem Novelty

Even though there have been lots of researches done on the manufacturing process to be sustainable, still, there are very small number of studies have verily applied sustainability as a part of manufacturing process.

Sustainability has been integrated into manufacturing management areas such as product development supply chain management, lean manufacturing, and supplier evaluation and selection [11].

Based on several literature reviews, the purpose of our research is (i) to find the enablers that drive the manufacturing company to adopt sustainability in electric vehicle and (ii) to analyse these enablers and find out which factor has the highest priority.

The objective of this research is to highlight the key enablers that drive the manufactures and the customers to adopt sustainable practices in electric vehicles.

4 Methodology

This study begins with the identification of enablers of sustainable product design and manufacturing for electric vehicles from literature. This study utilizes the expert opinion collected for selected enablers. In the survey, the set of questions have been framed and put forwarded after brainstorming session with experts.

An analysis of enablers of sustainable product design and manufacturing breakdown into Environmental, Economical and Social categories and modelled through AHP. Table 1 shows different categories and Table 2 shows different number of enablers.

4.1 Analytical Hierarchy Process (AHP)

AHP is a structured approach for classifying and analysing complex decisions, based on established from mathematics and psychology. It is a decision-making technique which breaks complex problem into a hierarchy, in which each level consists of specific elements.

Table 1 Different categories

Symbol	Description
C1	Economical
C2	Social
C3	Environmental

Table 2 List of enablers

Sl no.	Categories	Symbols	Enablers
1	Economical	E1	Government policies [8]
		E2	Increase of non-renewable fuel prices [7]
		E3	R&D investment [8]
		E4	Inter-functional collaboration [8]
2	Social	E5	Stakeholder integration [2]
		E6	Customer responsibility [12]
		E7	Role of institution [8]
		E8	Environmental impact on community [12]
3	Environmental	E9	Emissions Standard
		E10	Lower greenhouse gas [12]
		E11	Reduction in carbon content [13]
		E12	3Rs (reduction, recycling and remanufacturing) [13]

Research shows that different matrixes are made for different categories and then value is given in the cells accordingly by deciding which factor will dominate over other. And then, normalized weight is found out followed by global weight using formula. The final objective of the decision will have the biggest value in the hierarchy [12].

It has been found that some of the areas where AHP is used are the selection of best alternatives from various other alternatives, optimization, strategic planning, resolving conflict, forecasting, business process re-engineering, resource allocations, health care, public policy, etc. This methodology is used by various private and public sector organizations, as well as individual practitioners. It can be easily understood and is able to produce results that agree with expectations [13].

Some advantages of AHP are, it gives information how higher priority factors affects lower priority one and instead of suggesting an exact decision, AHP helps the decision makers to find out the best factors that meets their goal and their understanding of the problem [14].

Since there are twelve enablers and this is a new field so we have chosen AHP in our analysis. The analysis has been done from an Indian perspective as so the research done in this field has not been adequate as compared to the research done in developing countries so it is in our best interest to find the key enablers which drive the automobile manufacturing companies to adopt sustainable practices and enablers in which less weightage can be given.

5   Problem Analysis

On the basis of global weight, the ranking of the enablers has been done. It can be concluded that E9 (Emissions Standard), E12 (3Rs (reduction, recycling and remanufacturing)), E11 (Reduction in carbon content) and E1 (Government policies) have the highest weightage (Table 3).

6   Result

It can be concluded that the government plays an important role in propelling people and companies towards the adoption of sustainable practices. They can give certain guidelines and policies that give benefits to the customer and the manufacturers in the electric vehicle sector. They can make laws, which restrict the use of conventional resources and can minimize the utilization time of them. They can also enact policies which drives the automobile manufacturers to adopt sustainable practices in their production.

As the government has the power to shift the conventional power transport sector towards sustainability practices in their production, this also results in the reduction of carbon content in the atmosphere. Presently, the government has enforced the use of emission standard called Bharat Stage which is based on the Euro standard to control the emission of air pollutants from conventional engines and equipment. As the carbon content reduces in the air, the overall health of our population also improves.

Another enabler is the use of 3Rs, which means reduce, recycle and remanufacture in the production process. Reduce means to use the raw materials in a

Table 3   Ranking of enablers

Categories	Enablers	Weight	Rating	Global Weight	%	Ranking
Economic	E1	1.8678	1	1.4090	12	4
	E2	0.6103	3	0.4604	4	9
	E3	1.0663	2	0.8043	7	5
	E4	0.4556	4	0.3437	3	10
Social	E5	1.1835	2	0.5640	5	8
	E6	0.3227	4	0.1538	1	12
	E7	0.7280	3	0.3469	3	10
	E8	1.7658	1	0.8415	7	5
Environmental	E9	1.4644	1	2.5907	22	1
	E10	0.4817	4	0.8521	7	5
	E11	0.8906	3	1.5756	13	3
	E12	1.1633	2	2.0580	17	2

judicious manner, recycle means to the conversion of waste material into usable form. It also means to salvage parts from one machine and using it in another. Remanufacture means to build a product to specifications of the original product by cannibalizing an old product, or reused, repaired and new parts (Johnson and McCarthy 2014). Solely owning an electric vehicle will not contribute to sustainability, its manufacturing must also be eco-friendly. The fabrication of the body parts of the vehicle, for example dashboard, seat and seat cover and other aesthetics of vehicle must also be made of such materials that contain less carbon content.

One of the barriers of an EV is power-to-weight ratio. Since there will be weight (self-weight of vehicle and weight of passenger and luggage) of the vehicle and other forces acting on it (drag forces, frictional forces between wheels and road, etc.), this means a high powered battery would be required which is light to reduce the self-weight of the vehicle. This is only possible if there are more investments made in research and development (R&D). R&D will help in finding out better product and better technology that would enhance the performance of the battery and vehicle.

There are other advantages of using electric vehicle for example, conventional vehicles have combustion chamber, lubrication unit, fuel unit and other rotating parts (like camshafts, governors, etc.) whereas electric vehicles will have only battery unit, motor assembly and transmission. This will lead in profit for manufacturing industries as it will avoid manufacturing and assembly of these units. Also, the inventory and shop floor area to store these things will minimize to transmission only.

7 Conclusion

Electric vehicles are a new technology and as with any new technology adoption is slow. So, in order for adoption to take place in a faster rate, there should be other enablers. The enablers make it easier for adoption of new technologies rather than being adopted for the merits of the technology alone. We have concluded that E9 (Emissions Standard), E12 (3Rs (reduction, recycling and remanufacturing)), E11 (Reduction in carbon content) and E1 (Government policies) have the highest weightage. These enablers will eventually lead to the adoption of electric vehicles in a large scale.

References

1. Brundtland GH (1987) Report of the World Commission on environment and development: our common future. United Nations (1987)
2. Wolf J (2011) Sustainable supply chain management integration: a qualitative analysis of the german manufacturing industry. J Bus Ethics 102(2):221–235

3. Hawkins T, Singh B, Majeau-Bettez G, Strømman A (2012) Comparative environmental life cycle assessment of conventional and electric vehicles. J Ind Ecol 17(1):53–64

4. Westkämper E, Alting L, Arndt G (2001) Life cycle management and assessment: approaches and visions towards sustainable manufacturing. Proc Inst Mech Eng Part B: J Eng Manuf 215 (5):599–626

5. La Rovere E, Pereira A, Simões A (2011) Biofuels and sustainable energy development in Brazil. World Dev 39(6):1026–1036

6. Armand M, Tarascon JM (2008) Building better batteries. Nature 451(7179):652–657

7. Rohdin P, Thollander P (2006) Barriers to and driving forces for energy efficiency in the non-energy intensive manufacturing industry in Sweden. Energy 31(12):1836–1844

8. De Medeiros J, Ribeiro J, Cortimiglia M (2014) Success factors for environmentally sustainable product innovation: a systematic literature review. J Clean Prod 65:76–86

9. Chan CC (2007) The state of the art of electric, hybrid, and fuel cell vehicles. Proc IEEE 95 (4):704–718

10. Gan L (2003) Globalization of the automobile industry in China: dynamics and barriers in greening of the road transportation. Energy Policy 31(6):537–551

11. Amrina E, Yusof SM (2011) Key performance indicators for sustainable manufacturing evaluation in automotive companies. In: IEEE International conference on industrial engineering and engineering management, Singapore, 2011, pp 1093–1097. IEEE (2011)

12. Hassini E, Surti C, Searcy C (2012) A literature review and a case study of sustainable supply chains with a focus on metrics. Int J Prod Econ 140(1):69–82

13. Gunasekaran A, Spalanzani A (2012) Sustainability of manufacturing and services: investigations for research and applications. Int J Prod Econ 140(1):35–47

14. Partovi FY, Burton J, Banerjee A (1990) Application of analytical hierarchy process in operations management. Int J Oper Prod Manag 10(3):5–19

Design and Analysis of Steering Knuckle Joint

Mohd Shuaib[ID]**, Abid Haleem**[ID]**, Lalit Kumar**[ID]**, Rohan**[ID]
and Divyam Sharma[ID]

Abstract The steering knuckle joint acts as a connection between wheels and suspension system with the help of which the wheels of the vehicle are turned. Here spindle-type steering knuckle of an ATV was taken as a specimen. It was analyzed and redesigned according to specific external conditions with the help of CAE. The point cloud data of the component in .STL file format was prepared with 3D scanning, and then this cloud data was used to get the CAD file with NX software. The CAD data file is common input file which can be read easily by any design and analysis software, so conversion was necessary for further processing the collected data. The collected data was analyzed with ANSYS software for stress optimization. The analysis was done while considering two main factors, which were weight and failure. Then the CAD model was tested for different loading conditions. After analysis, the steering joint was redesigned according to the results obtained. The results show that redesigned knuckle has more curved edges, which reduces the stress concentration, and also it was optimized further to improve its performance.

Keywords Steering knuckle joint · SolidWorks · NX · ANSYS · 3D printing · Scanning · CAE · Meshing

M. Shuaib · Rohan
Department of Mechanical Engineering, Delhi Technological University,
New Delhi, India
e-mail: shuaib89141@gmail.com

A. Haleem · L. Kumar (✉)
Department of Mechanical Engineering, Jamia Millia Islamia,
New Delhi 110025, India
e-mail: rathee.lalit.2007@gmail.com

D. Sharma
Department of Mechanical Engineering, SRM University, NCR Campus,
Modinagar, India

1   Introduction

A spindle-type steering knuckle of ATV of **Dirt Rangers** (BAJA Team, SRM University, Ghaziabad Campus, UP) was analyzed for mostly weight reduction. Several minor changes of dimensions, compactness, cost cutting, etc., were also done. The original knuckle taken as sample was made of cast iron (carbon content greater than 2%) [1]. This knuckle was then scanned at **JMI University laboratory** and STL file was generated. Using **NX** software, STL file was converted to CAD file which was further processed for analysis. The analysis was done on ANSYS. On studying stresses and deformations, optimization was done. On basis of optimization values, steering knuckle was redesigned. Further, it is 3D printed in gypsum (again in JMI University laboratory) for representation purpose only.

2   Steering Knuckle Joint

It is also called *upright*, *hub*, *wheel carrier*, or *spindle*. Steering Knuckle is a stub axle which acts as a connection between wheels and suspension system. It helps in turning front wheels. It comes in different shapes and sizes but can be mainly classified into two categories, out of which a spindle-type steering knuckle is used (other type is hub) [2, 3]. Table 1 and Fig. 1 show the data and the image of the knuckle joint that was used.

3   3D Scanning, CAD Modeling, and Analysis

3.1   3D Scanning

3D scanning is a process of converting a specimen or environment into a three-dimensional digital model. It takes data for making geometry, using 3D scanner. The scanner is similar to a camera; the main difference is that it can also take distance parameter into consideration, which generates a 3D view instead of a 2D image. It creates a bundle of points (point cloud) on the surface of the specimen. These points are extrapolated to generated contours (reconstruction) which can be

Table 1 Steering knuckle joint data

Parameter	Value
Scrub radius (in mm)	118.618
King pin angle/inclination (in degree)	8
Camber	+1.5
Caster	−1.5
Ackerman %	72
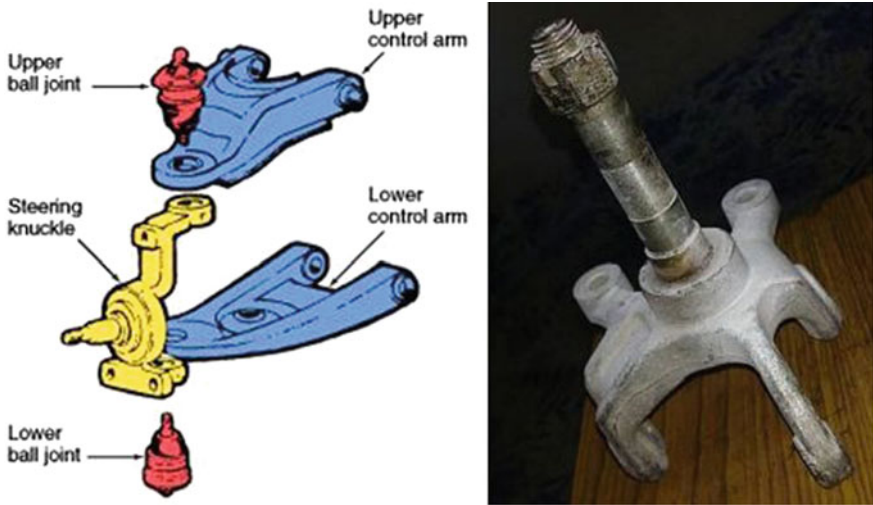
Fig. 1 Steering knuckle in front suspension [11]

further processed into well-defined surfaces. For constructing a complete model, hundreds of scans were done in different directions to obtain a dataset of all sides of the specimen. These scans were then mapped according to a common reference system (alignment) and merged to generate the whole model [4].

3.2 3D Scanning of Knuckle

Scanning of the steering knuckle was done at JMI University laboratory. 3D scanner (Steinbichler Comet L3D) was used for scanning [5, 6], and then .STL format file was obtained from scanning. The procedure of scanning is shown in Fig. 2.
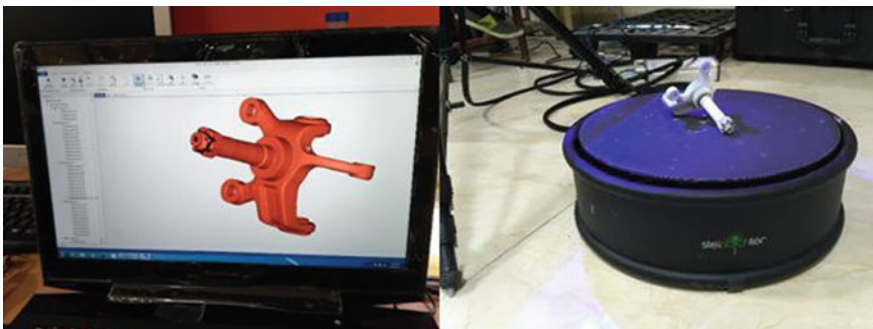
Fig. 2 Generation of 3D scanned model using Comet software

3.3 CAD Model of Knuckle

CAD model of steering knuckle was prepared using the .STL file using SolidWorks software [7, 8]. Images of Knuckle's CAD design are shown in Fig. 3.

3.4 Analysis of Knuckle

The final generated CAD model was then analyzed using ANSYS (software of Ansys, Inc. for realistic simulation). The software has many uses from designing products to creating simulations that test its durability, temperature distribution, fluid movements, and electromagnetic properties. Here analysis and meshing were done in ANSYS. The obtained values of different stresses can be found in Table 2 and Fig. 4. For the boundary conditions for each kind of loads, the weight of ATV vehicle was taken as 260 kg (inclusive of driver), kerb weight was 180 kg, load division in front: rear axle is 2:3, load division among tires is 1:1, jump ht. is considered as 6 feet (1.828 m) and the load and respective stress values are obtained as in Table 2.

Fig. 3 First and second views of CAD model (cast iron material)

Table 2 Value of stresses in ANSYS

Sr. No	Analysis type	Load type	von Mises Stress value (MPa)
1	Static structural	Braking (420 N)	47.991
2	Static structural	Bump (600 N)	83.062
3	Static structural	Lateral (800 N)	257.36

4 Topology Optimization

Topology optimization refers to finding the best solution of any problem with a given set of constrains and objective function [12–18]. It is a systematic method to optimize layout and material within limited design space. Here, the developed model involves three parameters, namely, design variables (materials density), design objective (weight reduction), and design constraints (volume). The topology of any structure is its spatial arrangement of members of the structure and internal boundaries. Optimizing topology means changing connectivity between structural members of discrete structures or between domains of continuum structures. It can be implemented using finite element methods for the analysis and techniques of optimization using the method of moving asymptotes, optimality criteria method, genetic algorithms, topological derivatives, and level sets [19–22]. The topology optimization results can be seen in Fig. 5, and it shows that on an average, 3% of mass was reduced using topology optimization. The assumptions were taken as study is in static condition, and the material is flawless and homogeneous; no cracks, blowholes, and other deformities present in it. The factor of safety is 2, and the ultimate tensile strength is 260 MPa (gray cast iron). Also for the optimization purpose, the meshing was used with the following specifications, i.e., element type: quadratic, mesh Size: 2.25e-002 m, no. of elements: 1,45,059, no. of nodes: 2,28,728, finer meshing at edges, holes to obtain stresses more accurately. Also, the thickness of the high stress point on calliper mount was increased and several other dimensions were changed in get result.
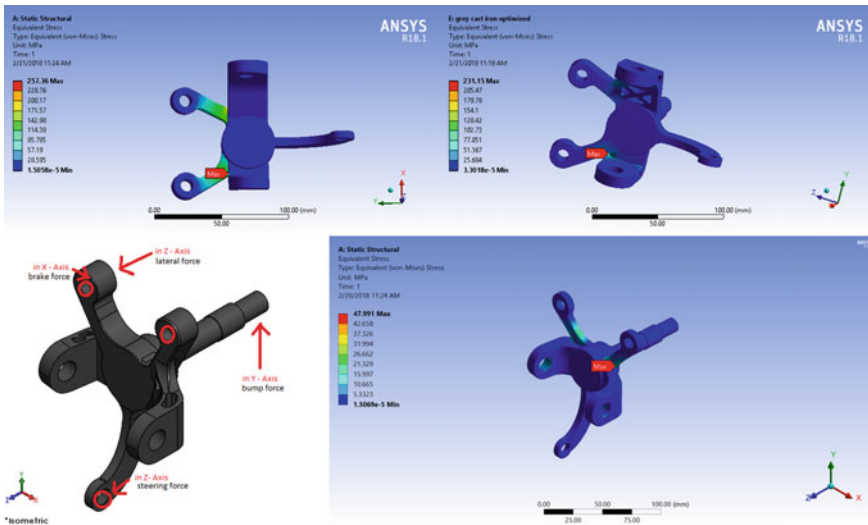
Fig. 4 Analysis in ANSYS
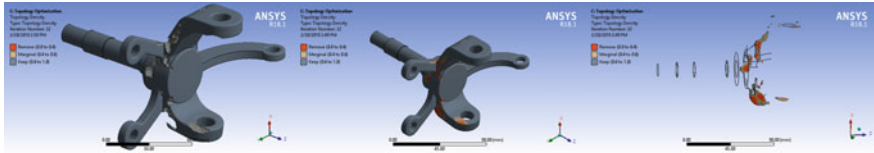
Fig. 5 Topology optimization

4.1 *Optimized Cad Model*

By putting the constraint of stress (UTS) in **ANSYS** of less than 250 MPa, important points on knuckle were found and shape was optimized. Fillets were added to make stress concentration uniform. Unlike sharp edges and more curved edges (Fig. 6) to delocalize the stresses, hence lesser chances of sudden failure in improved design. The weight of Knuckle is almost similar after optimization. This is due to the reason that in one portion thickness was increased while the material was removed from some other portion. From the comparison in Table 3, we can conclude that there is a considerable reduction in failure due to lateral loading condition (-26 MPa) in the expense of a slight increase in stress during bump ($+2$ MPa).

5 3D Printing

It is also called as Additive Manufacturing because the specimen is created using an additive process. The 3D specimen is produced by laying down thinly sliced successive horizontal layers of binder material over top of other. Either from the 3D model or from additive manufacturing file (AMF), the specimen of any kind of
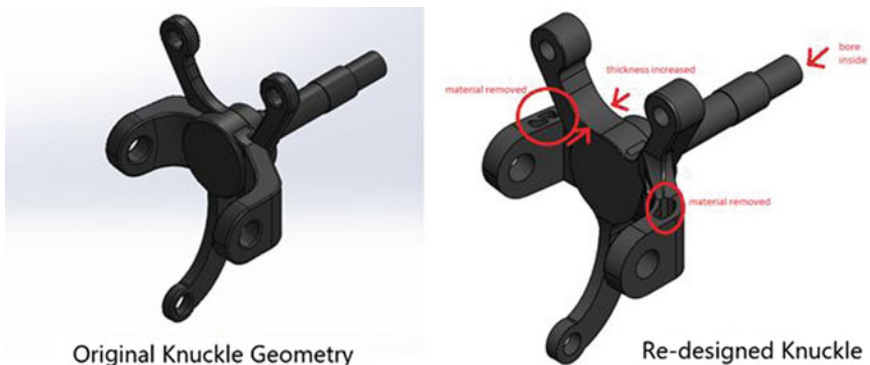
Fig. 6 Shape optimization

Table 3 Comparison of first and optimized model

Analysis type	Load type	Stress von misses	Values of von Mises Stress after optimization
Static structural	Braking (420 N)	47.991 MPa	31.724 MPa
Static structural	Bump (600 N)	83.062 MPa	85.79 MPa
Static structural	Lateral (800 N)	257.36 MPa	231.15 MPa
Weight	–	653.28 grams	639.30 grams
Material	–	Gray cast iron	Gray cast iron

geometry can be created. Before feeding it into the 3D printer, slicing has to be performed. Slicing is basically splitting 3D model into thousands of horizontal layers. Then printer understands every sliced image (almost 2D) and prints it layer by layer [9, 10].

ASTM (American Society for Testing and Materials) F42—Additive Manufacturing developed a set of standards which classify the AM processes into different types according to standard terminology for AM, but here 3D printing was used.

5.1 3D Printing of New Design of Knuckle

After optimization, steering knuckle was redesigned in Dassault's SolidWorks. Several parameters were changed to enhance knuckle according to the needs. It can be seen from the above image that redesigned knuckle had more curved edges which reduces stress concentration. Several dimensional changes have also been incorporated. Thickness was changed at several points. This modified design was printed to verify the changes using the three-dimensional printing machine.

6 Conclusion

Three important factors for optimization of any design are cost, weight, and failure. Design should be such that it helps in reducing the above three. Steering knuckle comes under unsprung mass. Its weight reduction helps greatly in the reduction of overall weight of the suspension system. This results in lesser fuel consumption. Using the above analysis, the design was optimized according to these three factors. However, some companies even optimize the joint further for abovementioned reasons. This analysis helped in achieving the required suspension characteristics. Further in future with the help of metal 3D printer, the actual model of the steering knuckle can be printed and used in the real ATV with more improvements. The future improvements can be in material selection as different materials have

different mechanical and chemical properties, and the effect of material is seen in knuckle's strength and its weight. The low weight of materials can help in optimizing fuel level consumption.

References

1. Gillespie TD (1992) Fundamentals of vehicle dynamics. Society of Automotive Engineers (SAE), Inc., ISBN-13: 978-1560911999, 15 Feb 1992
2. Miller R, Miller MR (2004) Machine shop tools & operations. Audel, ISBN-13: 978-0764555275, 5th edn, February 27, 2004
3. http://www.qpluslabs.com/node/2195. Accessed 15 May 2017
4. Raj RP, Palpandi K (2015) Static analysis and topology optimization of steering knuckle by using finite element method. Int J Innov Res Sci Eng Technol 4(13):220–227
5. Haleem A, Kumar V, Kumar L (2017) Computational analysis of poly lactic acid (PLA) feed wire in fused deposition modelling machine. Int J Recent Sci Res (IJRSR) 8(6):17971–17976 ISSN: 0976-3031 (O). https://doi.org/10.24327/ijrsr
6. http://grabcad.com/library?query=steering%20knuckle. Accessed 15 May 2017
7. Kumar L, Tanveer Q, Kumar V, Javaid M, Haleem A (2016) Developing low cost 3 D printer. Int J Appl Sci Eng Res (IJASER) 5(6):433–447 ISSN: 2277-9442. https://doi.org/10.6088/ijaser.05042. http://www.computeraideddesignguide.com/steering-knuckle/. Accessed 16 May 2017
8. Kumar L, Haleem A, Tanveer Q, Javaid M, Shuaib M, Kumar V (2017) Rapid manufacturing: classification and recent development. Int J Adv Eng Res Sci (IJAERS) 4(3):029–040 ISSN: 2349-6495(P), 2456-1908(O). https://doi.org/10.22161/ijaers.4.3.5. http://3dprinting.com/what-is-3d-printing. Accessed 17 May 2017
9. Bhimrao BK, Belkar SB, Kulkarni SS (2016) Topology optimization of steering knuckle arm using finite element method. Int J Sci Res Manag Stud (IJSRMS) 2(8):346–351
10. Kumar V, Kumar L, Haleem A (2016) Rapid prototyping technology ranking using an ANP approach and its sensitivity analysis. Int J Eng Sci Res Technol (IJESRT) 5(9):93–103 ISSN: 2277–9655. https://doi.org/10.5281/zenodo.61471
11. Fox S (2010) Lecture on cockpit control forces or how robust do driver controls really need to be? Soc Autom Eng (SAE), July 2010
12. Kumar L, Shuaib M, Tanveer Q, Kumar V, Javaid M, Haleem A (2018) 3 D scanner integration with product development. Int J Eng Technol (UAE) 7(2.13):220–225 ISSN: 2227-524X. https://doi.org/10.14419/ijet.v7i2.13.11690, 15 April 2018
13. Kamble AV, Patil SS, Harugade ML, Pol PS, Design and development of steering knuckle with spindle and its optimization- a review. Int J Eng
14. Research & Technology (IJERT), 5(3):96–104, March 2016
15. Bhusari A, Chavan A, Karmarkar S (2016) FEA & optimisation of steering knuckle of ATV in Proceedings of 54th IRF international conference, Pune, India, ISBN: 978-93-86083-10-4 (8th May, 2016)
16. Beer F, Johnston R, Dewolf J (2002) Mechanics of materials. 1st Edn, McGraw-Hill Companies, Inc., ISBN: 0-07-365935-5

17. Shigly J, Mischke C, Budynas R (2003) Mechanical engineering design. 7th edn, McGraw Hill Companies, Inc., ISBN-10: 0072520361, ISBN-13: 978-0072520361, 1 July 2003
18. Kumar V, Haleem A, Kumar L (2016) Design and development of thermal rapid prototyping machine and its application. Int J Emerg Technol Eng Res (IJETER) 4(2):101–106 ISSN 2454-6410
19. Haleem A, Kumar V, Kumar L (2017) Mathematical modelling & pressure drop analysis of fused deposition modelling feed wire. Int J Eng Technol 9(4):2885–2894 ISSN: 0975-4024 (O). https://doi.org/10.21817/ijet/2017/v9i4/170904066
20. http://optotechnik.zeiss.com/en/products/3d-scanning/comet-l3d. Accessed 17 may 2017
21. Gore SR, Gund KK, Patane PM, Mohite NV, Chimote CV (2017) Topology optimization of automotive steering knuckle using finite element analysis. Int J Curr Eng Technol 7:230–234
22. Javaid M, Haleem A, Kumar A (2015) Product design and development using Polyjet rapid prototyping technology. Int J Control Theor Inf 5(3):12–19 ISSN 2224-5774 (Paper) ISSN 2225-0492

Assembly of Mechanical Parts in Virtual Environment

Anuj Kumar Sehgal, Vineet Kumar, Nitesh Kumar and Aman Gupta

Abstract A virtual reality headset device is developed to get the virtual environment of a real world with the help of VR convertor software. The virtual headset is used to assemble the 3D design of automobile engine part in virtual environment using Autodesk Fusion 360, VR headset, VR convertor (Trinus VR software), Arduino IDE software, ATMEGA 320P, hand gesture reader device, gyro sensors, magnetometer sensor, and 5.7-inch screen display. The programming language used in the present study is Arduino IDE software is C++. The computer read the gesture of gyro sensor with the help of selected codes. The assembly simulation of the costly products can be carried out before actual practice and the financial loss pertaining to accidents and monitory damages can be minimized.

Keywords CAD · VR convertor · Virtual environment

1 Introduction

Virtual reality is a new technical device like other electronics device, for example, mobile, computer, camera, etc. The birth of VR headset technology in the market was considered in 2016. But the Oculus Rift Company made the first prototype in 2010, and then after that, Sony, HTC, PlayStation, and Samsung company released their own VR headset in the market. Virtual reality headset is very capable to give the users a new experience of a 3D virtual environment by immerging it into that world with giving the vision, hearing, touch, and smell types of senses. This type of feel can be done by wearing VR goggles or by standing in VR room/cave. From VR room and VR goggles, a person can get two types of virtual effect, Computer-Generated-based and Reality-based VR effect, Computer-Generated VR is generally used for gaming, watching movies (best for Sci-Fi movies because it

A. K. Sehgal (✉) · V. Kumar · N. Kumar · A. Gupta
Department of Mechanical Engineering, SET, Sharda University,
Greater Noida 201306, UP, India
e-mail: anujsehgal2000@gmail.com

give the best VFX), and for reality based is used for treating people from phobia, for scientific visualization, military training, virtual tourism, etc. Brough et al. [1] discussed about the virtual training studio in virtual environment where the user first learns a video and after that, they perform it. All these things were done by VR headset, wireless wand, optical tracker, gyroscope, and the combination of C++, Python, open CGI programming language, and WorldViz wizard for the transformation of VRML model.

Zhong et al. [2] mentioned about constrained-based methodology to work in virtual reality environment precisely by mentioning the rule for designing and assembling of parts. Arne et al. [3] mentioned about a new system CAD design through VR called MEMPHIS system. This system is an improved version of product data management (PDM) system, MEMPHIS system allow to synchronized the CAD geometry to VR without storing the VR data on one computer. It can also convert CAD data to VR data. Weidlich et al. [4] discussed about the virtual training studio in virtual environment where the user first learns a video and after that, they perform it. All these things were done by VR headset, wireless wand, optical tracker, gyroscope, and the combination of C++, Python, open CGI programming language, and WorldViz wizard for the transformation of VRML model. Hilfert et al. [5] approaches a new designing method with the help of virtual reality. By linking the VR system, CAD and navigation system together and also by using some algorithm like CAD, java, C++, and Boolean subtraction method, the design becomes possible through VR. Wang et al. [6] described his work of about making virtual reality headset for engineering and construction purpose in low budget. The system is worked with the help of VR headset (oculus rift) UE4 for programming, BIM server, leap motion, and some other sensors also. Gao et al. [7] presents a novel force rendering approach, which focuses on mechanical part assembly based on three basic mechanical fit types, namely clearance fit, interference fit, and transition fit. The algorithm to calculate the assembly force is formulated by analyzing the tolerance variation along the assembly length between two mating parts. Mengoni et al. [8] focused on simulating and analyzing the influence of the human factors involved in the assembly process, on the basis of performance done in previous paper. Assembly operations are simulated in a virtual environment, and the human factors including the visibility of an assembling part, posture, reachability, and fatigue of an operator are quantified. The new calculation methods of the estimated final position and the assembly force are presented to perform a more realistic assembly operation. Seth et al. [9] explores the potentialities of virtual reality (VR) to improve the learning process of mechanical product design. It is focused on the definition of a proper experimental VR-based set up whose performance matches mechanical design learning purpose, such as assimilability and tolerances prescription.

2 Set up Requirements

The VR headset with virtual screen of 720 × 1440 pixels resolution and a USB cable for connecting the headset with a computer for the data transmission. Autodesk software for generating the mechanical part, while, Arduino UNO and MPU 6050 gyro sensor with Arduino software are used for interfacing with the VR headset device. The following steps were used for implementing VR headset.

- Connect the headset to CAD by Trinus VR software.
- For continuous communication between VR world and PC system, USB cable/ HDMI cable is used.
- Arduino software is used to control the VR world through the human hand, which converts the hand gesture into a coded command acceptable to PC system.

3 Result and Discussion

3.1 Trinus VR Software

Trinus VR software is used to provide the virtual effect by connecting the PC to smartphone through Wi-Fi and USB cable. It uses the phone display and sensor of the smartphone to convert it into a portal to software. Figure 1 shows the Trinus VR Server software. The specification of software is as follows.
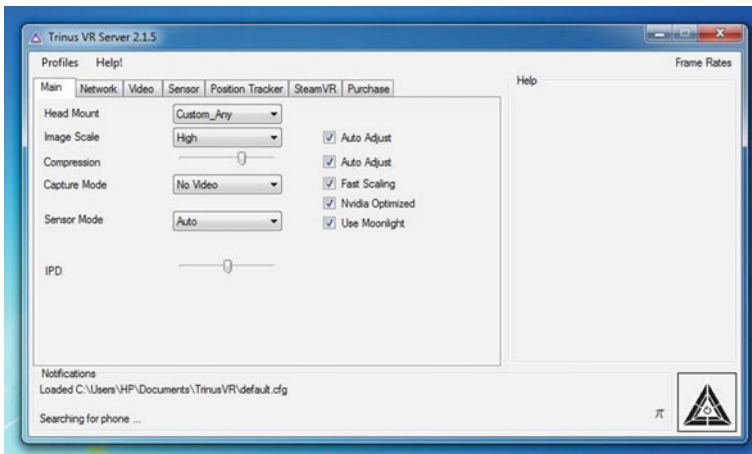
Fig. 1 Trinus VR Server 2.1.5 software

- Maximum frame rate of 90.
- Reading of streaming scale 720 × 720.

3.2 CAD (Computer-Aided Design)

Autodesk Fusion 360 software is used for designing and assembly of V4 engine parts as a case study, which is shown in Fig. 2.

3.3 Arduino

Arduino is an open-source physical computing platform based on a simple input and output (I/O) system capable of implementing the processing language (C++ language is used in this study). Arduino is composed of two major parts, viz., the Arduino board (hardware) and the Arduino IDE (software) which is used to develop standalone interactive objects. The technical specifications of the microcontroller board based on ATMEGA 328P Arduino are given in Table 1. Figure 3 shows the Arduino UNO used in the present study.

3.4 Mpu 6050

It is a 6-Axis MEMS motion tracking device (3 gyro + 3 accelerometer) with an onboard digital motion processor (DMP), which can process 6-axis motion fusion
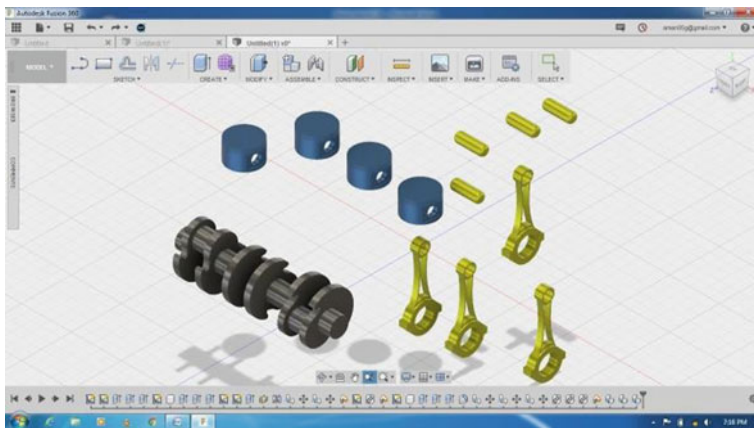
Fig. 2 V4 engine assembly parts (case study)

Table 1 Microcontroller board based on ATMEGA 328P specifications

Microcontroller AT mega 328P specifications	
Length	68.6 mm
Width	53.4 mm
Weight	25 g
Operating voltage	5 V
Input voltage	Recommended -(7–12 V), limit -(6–20 v)
Digital I/O pins	14 (of which 6 provide PWM)
PWM Digital I/O pins	6
Analog input pins	6
DC current per I/O pins	20 mA
DC current for 3.3v pins	50 mA
Flash memory	32 KB of which 0.5 KB used by boot loader
SRAM	2 KB
EEPROM	1 KB
Clock speed	16 MHz
LED_BUILTIN	13

Fig. 3 Arduino UNO (microcontroller board)

algorithm. Motion AppTM platform supported to Linux, Android, and Windows. The size of this device is 25.5 mm × 15.2 mm × 2.48 mm. The specifications of MPU 6050 motion tracking device are given in Table 2

Table 2 MPU 6050 motion tracking device specifications

Gyro full-scale range (°/sec)	±250	±500	±1000	±2000
Gyro sensitivity (LBS/°/sec)	131	65.5	32.8	16.4
Gyro rate noise (dps/ Hz)	0.005	0.005	0.005	0.005
Accel full-scale range (g)	±2	±4	±8	±16
Accel sensitivity (LSB/g)	16384	8192	4096	2048
Logic supply voltage (v)	1.8 V ± 5%			
Operating voltage supply (V +/−5%)	2.375–3.46 v			

3.5   CAD to VR Implementation

The file format used in this CAD software are Archive Files (*.f3d), IGES Files (*. igs*.iges), SAT Files (*.sat), SMT Files (*.smt), and STEP Files (*.stp *.step). For the implementation of VR effect, head mount, image scale, capture mode, sensor mode, and IPD are the main settings in Trinus VR software and were set in accordance with the headset product. In this device, a normal homemade headset is used; size of the screen is 5 inch and shows 2049 × 1096 streaming input notification on Trinus VR after connecting to the CAD at 90 maximum frame rates. Figure 4 shows the result of VR CAD screen.

3.6   Hand Gesture Recognition Method

Hand gesture recognition method is used with the help of hand glove-type gyro sensor, which is attached with an aim to control the system by waving the hand in air.
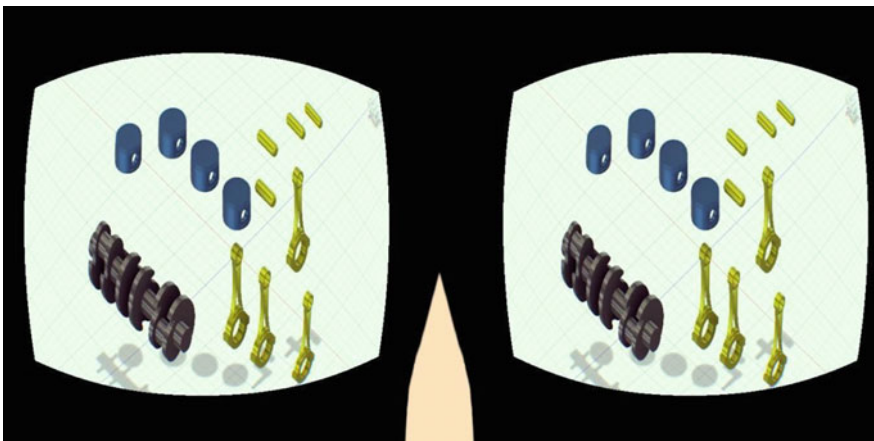
Fig. 4 Results of VR CAD screen

The hardware used in this method are MPU 6050, Arduino UNO, Arduino software, male–female wire, switches ON/OFF button, 10 kΩ resistor, and breadboard. The step of connecting the wire from Arduino UNO to MPU 6050 are VCC—5 V, GND-GND, SCL-AREF, SDA-GND, respectively. After connecting the wire in sequence connect the Arduino to PC through USB cable for uploading the code in Arduino UNO, virtual reality headset device is developed to get the virtual environment of a real world with the help of VR convertor software. The virtual headset is used to assemble the 3D design of automobile engine part in the virtual environment using Autodesk Fusion 360, VR headset, VR convertor (Trinus VR software), Arduino IDE software, ATmega320P, hand gesture reader device, gyro sensors, magnetometer sensor and 5.7-inch screen display. The programming language used in the present study is Arduino IDE software is C++. The computer read the gesture of gyro sensor with the help of selected codes. The assembly simulation of the costly products can be carried out before actual practice and the financial loss pertaining to accidents and monitory damages can be minimized

4 Conclusions

Virtual reality headset device is developed using Autodesk Fusion 360, VR headset, VR convertor (Trinus VR software), Arduino IDE software, ATMEGA 320P, hand gesture reader device, gyro sensors, magnetometer sensor, and 5.7-inch screen display. In present work, the assembly of V4 engine parts is conducted by connecting VR headset to the Trinus VR software, CAD file, and hand gesture recognition device. Figure 4 shows the actual VR image of CAD file which is converted with the help of Trinus VR software. The maximum frame rate of this image is 90 and streaming input of 2049 × 1096 pixels with the help of hand gesture recognition device using MPU 6050 (gyro) sensor is implemented on the user hand with Arduino UNO and Arduino IDE software. The developed VR headset is implemented in order to confirm its application with a case study involving assembling and disassembling of V4 engine parts in the virtual environment offline prior to performing the actual prescribed practice. Therefore, the study concludes that this device can be very useful in the future for product design, research, and development in industries before assembling and disassembling of product.

References

1. Brough JE, Schwartz M, Gupta SK, Anand DK, Kavetsky R, Pettersen R (2007) Towards the development of a virtual environment- based training system for mechanical assemble operations. Springer-Verlag London Limited (2007) 111:189–206. https://doi.org/10.1007/s10055-007-0076-4
2. Zhong Y, Shrinzadeh B, Ma W (2005) Solid modelling in a virtual reality environment, Springer. 21:17–40. https://doi.org/10.1007/s00371-0004-0268-9

3. Arne S, Seokryul K, Daniel W, Ziying T, Sangsu C (2006) CAD- VR geometry and meta data synchronization for design review application. J Zhejiang Univ Sci A 7(9):1482–1491. www.zju.edu.cn/jzus
4. Weidlich D, Cser L, Polzin T, Cristiano D, Zickner H (2009) Virtual reality approaches for immersive design. Int J Interact Des Manuf (2009) 3:103–108. https://doi.org/10.1007/s12008-009-0063-y
5. Hilfert T, Konig M (2016) Low-cost virtual reality environment for engineering and construction. A Springer Open J 4:2. https://doi.org/10.1186/s40327-015-0031-5
6. Wang QH, Huang ZD, Ni JL, Xiong W, Li JR (2016) A novel force rendering approach for virtual assembly of mechanical parts. Int J Adv Manuf Technol (2016) 86:977–988. https://doi.org/10.1007/s00170-015-8255-z
7. Gao Wei, Shao Xiao-Dong, Liu Huan-Ling (2016) Enhancing fidelity of virtual assembly by considering human factors. Int J Adv Manuf Technol 83:873–886. https://doi.org/10.1007/s00170-015-7628-7
8. Mengoni M, Germani M, Peruzzini M (2011) Benchmarking of virtual reality performance in mechanics education. Int J Interact Des Manuf 5:103–117. https://doi.org/10.1007/s12008-011-0119-7
9. Seth A, Vance JM, Oliver JH (2011) Virtual reality for assembly methods prototyping: a review. Virt Real 15:5–20. https://doi.org/10.1007/s10055-009-0153-y

Comparative Model Analysis of Brake Rotors

Mohit Bhardwaj, Shivam Mittal, Vikas Kumar, Rohit Sharma and Jaspreet Heera

Abstract Brakes in any vehicle are of an utmost important device. Since, brakes by converting the kinetic energy of wheel to be precise that of the brake rotors to heat energy and bring the vehicle to a complete stop. Computation of the stresses and analysis of vibration characteristics of brake rotors considerably help to avoid failure and possess the ancillary benefits of having optimal weight and cost. The present paper deals with designing two different designs of brake rotors, conventional and a periphery brake rotor using Solid Works software and its structural analysis using ANSYS software. Modal analysis is done to enhance the natural frequency of the brake rotors, so as to compare which design of the rotor, in particular, shows the lesser deformation and much more susceptible frequencies. Finite element analysis (FEA) is generally used to show the dynamic response of a structure, and has the advantage that complex geometries can be modeled to high accuracies. But accuracy of the FEA can be sketchy and the unwavering quality of the FE model must be approved by looking at the anticipated outcomes of natural frequencies and mode shapes of the FE model with the experimental results. The results show that natural frequencies of original model and natural frequencies of simplified model are in great concurrence with each other.

1 Introduction

In automobile engineering, the brakes are the topic of utmost importance and thus, an appreciated level of attention is given to the problems arising in the speed reduction of a vehicle with the help of brakes, since all automobiles use either drum brakes or the disc brakes in order to shed their speed and momentum. Though, the braking action for the drum brakes is achieved by the mechanical, pneumatic, or

M. Bhardwaj (✉) · S. Mittal · V. Kumar · R. Sharma · J. Heera
Amity University Noida, Noida 201313, Uttar Pradesh, India
e-mail: mohit6296@gmail.com

S. Mittal
e-mail: mittalshiv17@gmail.com

fluid actuation. While in the disc brakes, we can only use the brake fluid for actuating the brake piston's calipers.

Therefore, all designers need to acquire the most ideal performance with agreeable condition (diminish the noise and vibration as much as could be expected) for the brakes with less amount of brake fade and resistance over the brake rotor. So thus, using two different designs for the brake disc or rotors, and then analysis their deformation and reaching a conclusion which design stays till last.

1.1 Periphery Disc

The disc brake rotors, wherein the disc is bolted through its outer perimeter and the calipers are mounted from the inner perimeter of the disc. This is done so that a larger size disc can be accommodated and a lesser torque has to be worked upon.

1.2 Conventional Disc

The disc brake rotor is generally used on the vehicle in which the screws are bolted around the center hub of the disc brake. The calipers are mounted over the perimeter of the disc and thus braking actions is achieved.

2 Methodology

2.1 Modeling of Brake Rotors

The brake rotor models have been entirely modeled by the Solid Works software. The sketch command of the Solid Works is used to create 2D sketch, by the means of various other geometrical commands. Then, the 3D model of clutch is extruded from the recently created 2D sketch. Additional features can be incorporated using revolve, copy, or mirror commands.

2.2 Modal Analysis

The modal analysis or modular investigation is viewed as a basic advance in the planned procedure to gauge the vibration attributes of the planned structure. Thus, the objective of a modular investigation is deciding the normal frequencies and

mode shapes. The modular examination can likewise be taken as a reason for other more nitty-gritty dynamic investigations, for example, a transient dynamic investigation, a symphonious investigation, or even a range examination in view of the modular superposition system. The principle presumption in the modular examination is that the framework is direct and disregarded nonlinearity in the framework.

2.3 Material Selection

Using structural steel as the material for both the designs, the research has been conducted.

2.4 Comparing the Results

A comparison for the various natural frequencies observed for the different models of the brake rotors. And check if the design and parameters fails or turn out to be giving the positive results.

3 CAD Modeling of Brake Rotors

The brake rotor models have been entirely modeled by the Solid Works software. The sketch command of the Solid Works to create 2D sketch is used. Then, the 3D model of disc brake rotors is extruded from the recently created 2D sketch. Additional features can be incorporated using revolve, copy, or mirror commands (Figs. 1, 2 and Tables 1 and 2).

4 Meshing

For free vibration analysis, finite element-based software ANSYS is used. The discretized FEA models of the conventional disc and periphery disc are shown in Figs. 3 and 4, respectively. The mesh model consists of 23803 nodes and 12991 elements for the peripheral brake rotor and the conventional disc also consists of 23803 nodes and 12991 elements. The minimum edge length is 0.000635 mm, while the element size is 5 mm. the meshing is coarse and the finesse is geometry dependent.

Fig. 1 Model of
conventional disc brake rotor
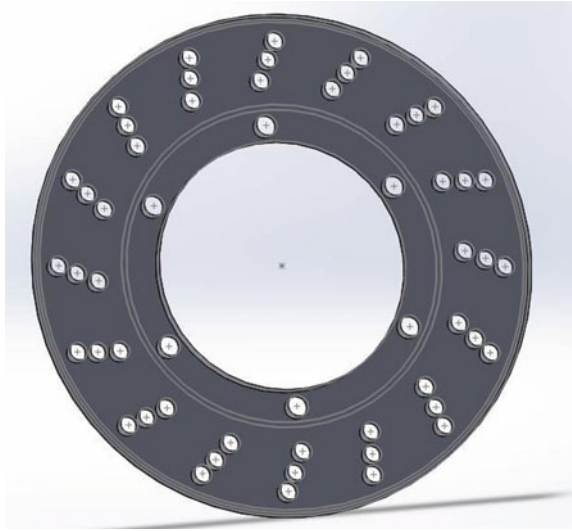
Fig. 2 Model of a periphery
disc brake rotor
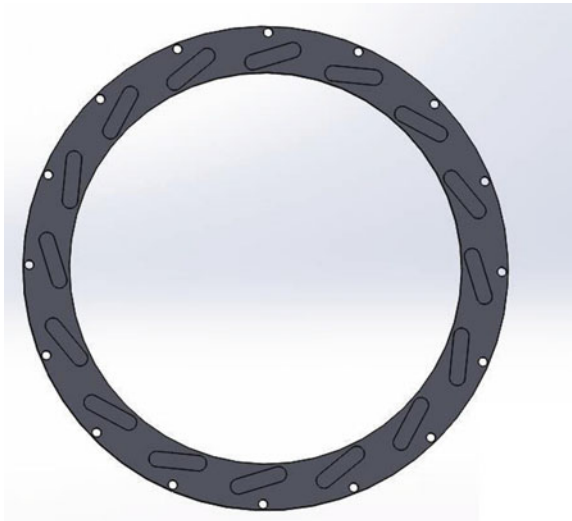
Table 1 Properties of
conventional disc brake rotor

Properties	Values
Radius of disc	0.2667 m
Thickness of disc	7.62e-003 m
Volume of disc	5.5622e-004 m^3

Table 2 Properties of periphery disc brake rotor

Properties	Values
Radius of disc	0.2667 m
Thickness of disc	7.62e-003 m
Volume of disc	5.5622e-004 m^3

Fig. 3 Mesh model of conventional disc
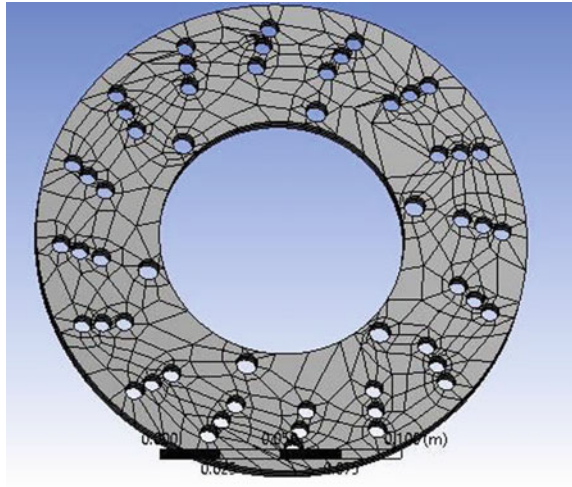
Fig. 4 Mesh model of periphery disc
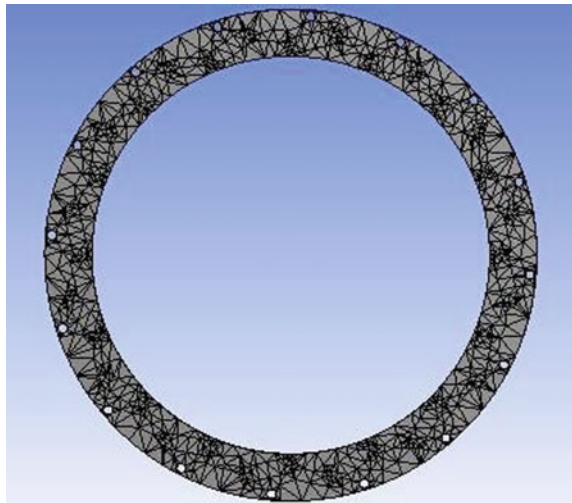
For free vibration analysis, finite element-based software ANSYS is used. The discretized FEA models of conventional disc and periphery disc are shown in Figs. 3 and 4, respectively. The mesh model consists of 23803 nodes and 12991

elements for the peripheral brake rotor and the conventional disc also consists of 23803 nodes and 12991 elements. The minimum edge length is 0.000635 mm, while the element size is 5 mm. The meshing is coarse and the finesse is geometry dependent.

5   Result and Discussion

The FEA-based free vibration analysis evaluates both the discs for the first six natural frequencies and mode shapes. Zero displacement constraint-based boundary conditions were applied for the simulation. Table 3 shows the natural frequencies for both discs.

The finite element analysis of both the designs of the brake rotors was done using structural steel as the material of the construction, and the results obtained are not much different when the brake rotors were designed for a wheel size of radius 12 inches. The frequencies vary from 2443.9 Hz to 2684.3 Hz for a conventional disc brake rotor while from 2454.8 Hz to 2715.7 Hz for the peripheral disc brake rotor.

The result of the frequencies are effective and very much distinguishable in a way that from first to sixth mode, the frequencies observed for the conventional discs are lower than that of the peripheral disc rotor for the deformation observed.

The total maximum total deformation observed is 1.5419 m for both conventional and peripheral brake rotor. The total deformation and directional deformation for the x-axis are exactly the same but the frequencies for the six modes observed are higher for the peripheral rotor. The conventional disc which is bolted around its inner perimeter makes for a bowl shape for maximum deformation and the peripheral disc deforms in a way that waves are observed over its surface. This surely does show that peripheral disc can take up larger frequencies and ever after maximum deformation, it would not change the geometry of any other parts of the automobile (Figs. 5, 6, 7, and 8).

Table 3 Natural frequency

Mode	Conventional disc	Periphery disc
1	2443.9	2454.8
2	2462.6	2482.7
3	2471.8	2493.7
4	2560.4	2577.7
5	2571	2586.5
6	2684.3	2715.7

Fig. 5 Deformation of conventional disc brake rotor
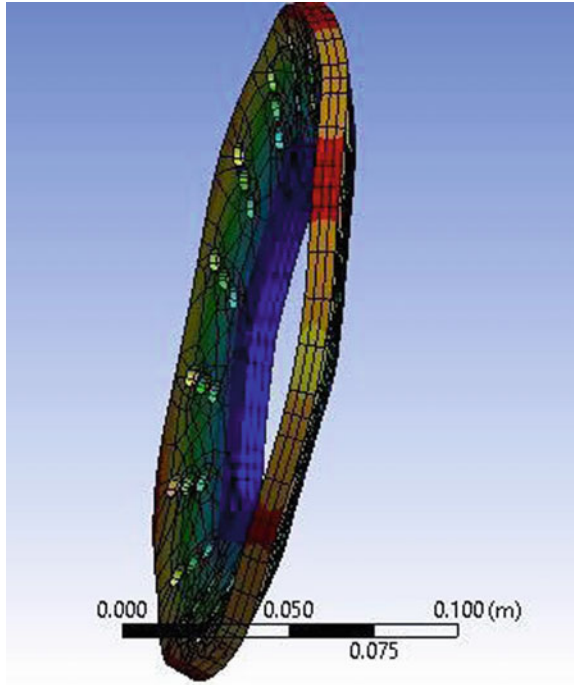
Fig. 6 Deformation of periphery disc brake rotor
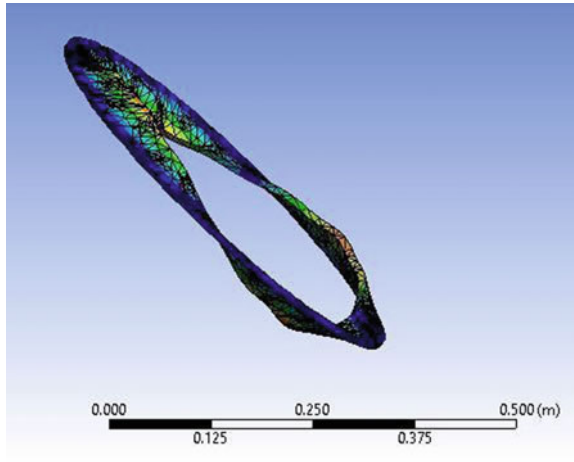
Fig. 7 Natural frequencies for conventional disc
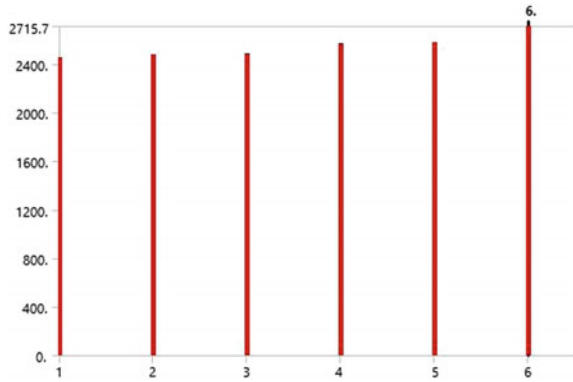
Fig. 8 Natural frequencies for periphery disc
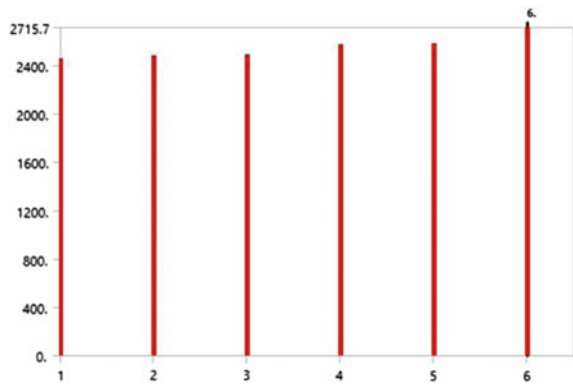
6 Conclusion

This study has showcased how the natural frequencies for the conventional brake rotor disc and the peripheral brake rotor disc are made up of structural steel. The natural frequencies observed for the conventional disc brake setup are lower than the one observed on the peripheral disc. This translates that the peripheral discs can be worked over at higher frequencies for lesser damages and deformations.

The maximum deformation observed for the conventional disc as well as peripheral disc is exactly the same, since both the discs are designed for R14-inch scooter tyres with a disc designed with a radius of 11 inches. The volume of the material is also the same for both the disc rotors, thus, the maximum deflection is also identical. But, there is a huge difference in the directional deformation of the discs. The conventional disc has positive deformation in the z-axis or in other words, the disc is deformed/bent on to just one side, while the peripheral disc has observed deformation in both the directions of the z-axis generating a wave pattern.

The directional deformation observed in the x-axis is positive in both cases means that disc is going to hamper the calipers in the case of conventional rotor,

while the bolts by which the disc is mounted will be affected in case of a peripheral rotor, which will lead the deformation to the rim.

Weight, natural frequency, and mode shapes of the two designs of the rotors for the particular size of wheel rim have been evaluated based upon the simulation results. This study will provide a reference in the design of brake rotors of both the patterns for commercial vehicle and also for the theoretical aspect of NVH levels.

References

1. Kumar V, Kumar P, Manjunatha, Pawar MD, Shivaramakrishna, Finite element analysis of two wheeler disc brake rotor. Imp J Interdiscip Res
2. Quadri SA, Dolas DR (2015) Comparative modal analysis of conventional spur gear with modified involute spur gear. Int Res J Eng Technol (IRJET) 02(04)
3. Harak SS, Sharma SC, Harsha SP, Modal analysis of prestressed draft pad of freight wagons using finite element method. J Mod Transp
4. Das S (2014) Design and weight optimisation of aluminium alloy wheel. Int J Sci Res Publ 4(6)
5. Venkatramanan R, Kumaragurubaran SB, Vishnu KC, Sivakumar S, Saravanan B, Design and analysis of disc brake rotor. Int J Appl Eng Res
6. Mittal S, Peripheral disc brake system and its comparison with conventional disc brake system for use in motorcycle front wheel. Int J Aerosp Mech Eng 3

Research on Braking Performance Using Scaling Methodology on Disc Pad in Disc Brake System

Pankaj Kumar, Pritish Shubham and Akshaykumar Vijayendernath

Abstract Automobile is a big invention in itself, which comprises of engine, clutch, transmission, suspension brakes and other major components. Out of these components, brakes are the only vital components over which not much research has been done. Many advancements have been made in braking technologies over the time. Among which, disc brake system is the safest and advanced braking mechanism. The performance of a disc brake system depends upon parameters like heat generated, speed of the vehicle, rotor and disc pad material and other environmental conditions. Later on, these parameters result in stopping distance, braking power, deceleration time and thermal gradient, which depend upon disc pad and rotor contact region. If this contact region undergoes any change, parameters like temperature distribution, contact pressure distribution, total deformation and equivalent stress, it will ultimately get changed. This research paper emphasis on the using scaling methodology in disc pad to analyze and simulate the outcomes of changing measurements of disc pad in disc brake system. This paper aims to determine disc temperature and to examine stress concentration, structural deformation and contact pressure of brake disc and pads during single braking stop event. The thermal-structural analysis is then used with coupling to determine the deformation on both the assemblies. Temperature and equivalent stress analysis are carried out in fluent. The designs have been made in SolidWorks and analyzed in ANSYS workbench.

Keywords Smaller pad · Bigger pad · Rotor · Analysis

P. Kumar (✉) · P. Shubham · A. Vijayendernath
Amity School of Engineering and Technology, Amity University Noida, Noida,
Uttar Pradesh, India
e-mail: pankajsoni3956@gmail.com

1 Introduction

Disc brake system is the most popular and reliable type of braking system in an automobile. Every vehicle comes with disc brake. In disc brake system, several components come into play when brakes are applied by the driver during the braking process, the main components which play a vital role in braking performance which will govern the overall efficiency of the brakes are brake pads and rotor. The brake rotor is being squeezed from both the sides by the brake pads, which results into stopping of the vehicle.

This report aims on changing brake pad size on the same-sized rotor. The same rotor will be assembled with a smaller pad and then with a bigger pad, and then calculate the parameters which will decide its performance and efficiency. Structural and thermal analysis will be performed on 3D models in ANSYS workbench and temperature or pressure in CFD fluent of these two assemblies [1].

Here, are the literature reviews related to this paper: Viraj and Kunal (2014) [1] designed a disc and simulated it for structural and thermal analysis for three different materials in ANSYS. The thermal properties of these materials were analysed and concluded that stainless steel offers better braking performance. Prof. Mitpatel, Mansi Raval, Jenish Patel (2016) [2] analysed the thermo-mechanical behaviour of the brake disc during the braking phase. This analysis was done to determine deformation established in the disc. Swapnil and Bhaskar (2014) [3] did the thermal and modal analysis on a two-wheelers disc brake system to calculate the deflection, heat flux and temperature of the disc brake model. Belhocine, Rahim Abu Bakar and MostefaBouchetara (2016) [4] did an analysis on a disc brake to determine disc temperature and stress concentration and structural deformation using ANSYS. The thermo-structural later on used with coupling to determine the deformation.

2 Methodology

A normal disc brake system is selected and recorded all its dimensions, material and properties and calculated its frictional surface area. All the calculations for braking force, braking distance and heat flux are done using formulae and recorded the results. Now, same calculations are done on the disc pad but after increasing its length, dimension and area is recorded and used them in the calculations. Both the smaller and bigger pads were assembled with a same-sized rotor separately. Now, a 3D model of both of the assemblies before and after increasing the disc pad length is created. 3D design is simulated in ANSYS workbench for further analysis. Temperature and pressure analysis was done in CFD fluent. Difference in the output parameters were observed and stated in the report. The results will be discussed and concluded.

3 Design and Calculations

3.1 Input Data

(See Fig. 1 and Table 1).

(A) Rotor

Material – Carbon ceramic Mixture
Internal Dia – 111.97 mm
External Dia – 240 mm
No. of holes for studs – 4
Dia of each hole – 10 mm
Dia of central hole – 60 mm
Total Thickness of the Rotor – 15 mm
Mass – 0.5 kg [3]
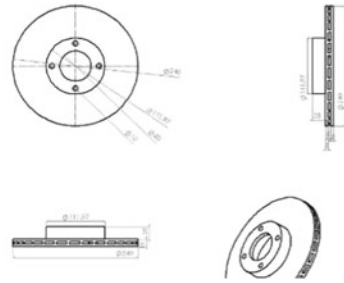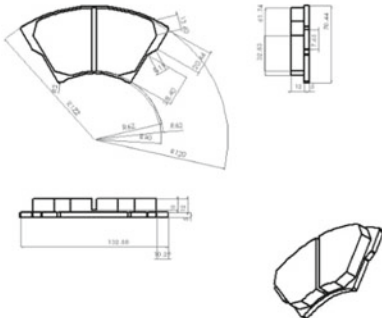
(B) Smaller Pad   **(C) Bigger Pad**
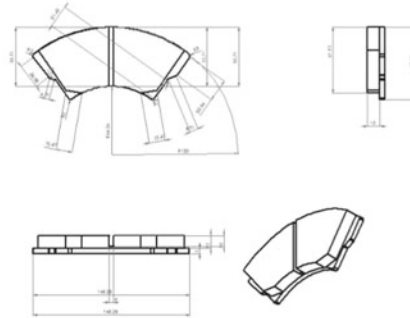
Fig. 1 **A** Rotor, **B** Smaller pad, **C** Bigger pad

Table 1 Input data of smaller and bigger pad

Properties	Smaller pad (mm)	Bigger pad (mm)
Material	Asbestos	Asbestos
Dimensions	51 × 58	71 × 58
Thickness	17	17
Outer radius	120	120
Inner radius	62	62

4 Calculations for Smaller and Bigger Pad

4.1 For Smaller Pad

- Kinetic Energy of Vehicle = $(M \times V^2)/2$ = 269910.515 Joule
  where

  M = mass of the vehicle (kg)
  V = Linear velocity of vehicle (m/s) = 100 kmph = 27.77 m/s

- Tangential force between pad and rotor (inner face), FTRI = $\mu1.$FRI = 1415.4N.
  Where,

  FTRI = Normal force between pad brake And Rotor (Inner)
  $\mu1$ = Coefficient of friction **= 0.5**
  FRI = $P_{max}/2 \times A$ (pad brake area) [Area = 5661.6 mm^2]

- Brake Torque (TB) = FT. R = (FTRI + FTRO) × R = 339.69 N.m
  where

$$R = \text{radius of rotor}$$

- Brake Distance (x) = $(mv^2)/2$ FT = 95.34 m
- Time taken to stop the vehicle, t = V/a = 5.66 Seconds
  where

  V = Linear velocity of vehicle (m/s)
  a = F/M = $(\mu \times M \times g)/M$, (m/s^2)

- Heat generated, Q = M.Cp. ΔT = 6000 J
  where

  M = mass of the disc, (kg)
  Cp = Specific heat capacity = 800 J/kg°C ΔT = Developed temperature difference

- Heat Flux = Heat Generated/Second/area = 42.576 kw/m^2
- Thermal Gradient = Heat Flux/Thermal Conductivity = 1064.4 k/m
  Thermal conductivity is assumed to be 40 W/m-k (Watts per metre-kelvin).

4.2 For Bigger Pad

- Kinetic Energy of Vehicle = $(M \times V^2)/2$ = 269910.515 J
- Tangential force between pad and rotor (Inner face), FTRI = $\mu1.$ FRI = 1415.4 N. [Area = 6624.6 mm^2]

- Brake Torque (TB) = FT. R = (FTRI + FTRO) × R = 339.69 N.m
- Brake Distance (x) = (mv^2)/2 FT = 95.34 m
- Time taken to stop the vehicle, t = V/ = 5.66 s
- Heat generated, Q = M.Cp. ΔT = 6000 J
- Heat Flux = Heat Generated/Second/area = 42.576 kw/m^2
- Thermal Gradient = Heat Flux/Thermal Conductivity = 1064.4 k/m
  Refer 5.1 to get to know what these symbols stand for.

5   Result and Discussion

Both smaller and bigger disc brake pad have been designed in SolidWorks and simulated in ANSYS workbench for structural analysis, and temperature distribution and stress analysis was done in CFD fluent [4].

5.1   Deformation

When brakes are applied, rotor and pad undergoes total deformation due to the pressure applied by the brake pads against the rotor. Smaller and bigger disc pad assemblies were simulated to test the effects of deformation at four specific time intervals. The images plotted below shows the deformation on smaller pad (a, c, e, g) and bigger pad (b, d, f, h) for Figs. 2 and 3.

(a) Smaller Pad   **(b)** Bigger Pad   **(c)** Smaller Pad   **(d)** Bigger Pad

(e) Smaller Pad   **(f)** Bigger Pad   **(g)** Smaller Pad   **(h)** Bigger Pad

Fig. 2 Smaller pad (**a**, **c**, **e**, **g**) and bigger pad (**b**, **d**, **f**, **h**)

At 1.1 seconds **At 2.2 seconds**

(a) Smaller Pad   **(b)** Bigger Pad   **(c)** Smaller Pad   **(d)** Bigger Pad

At 3.6 seconds   **At 5 seconds**
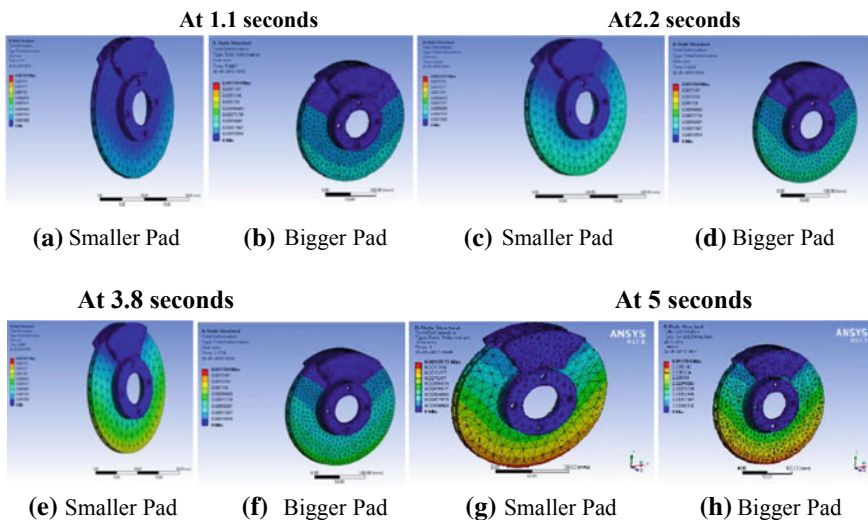
(e) Smaller Pad   **(f)** Bigger Pad   **(g)** Smaller Pad   **(h)** Bigger Pad
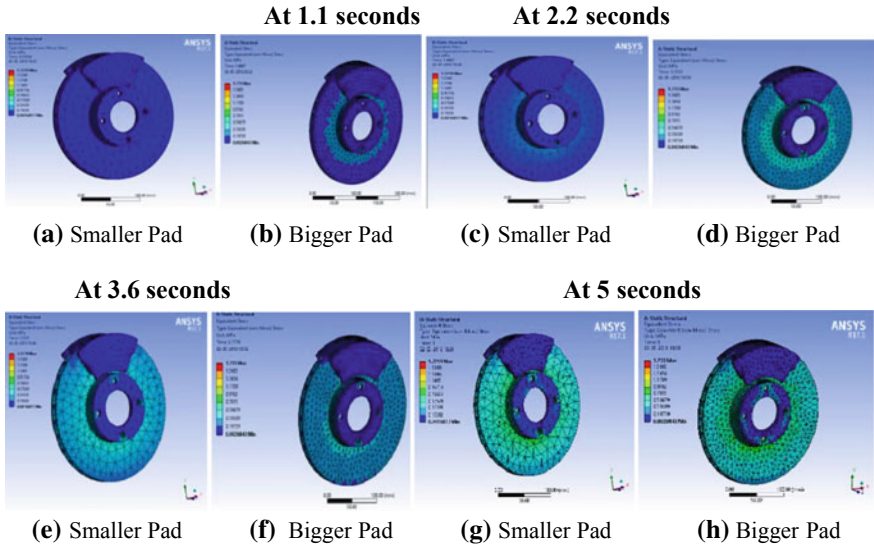
Fig. 3 Smaller pad (**a**, **c**, **e**, **g**) and bigger pad (**b**, **d**, **f**, **h**)

5.2 Equivalent Stress

Like total deformation, equivalent stress is also measured at four intervals of time and results are shown below.

Smaller pad (a, c, e, g) and bigger pad (b, d, f, h) under (Fig. 4).

Static Temperature   **Total Temperature**

(a) Smaller Pad   **(b)** Bigger Pad   **(c)** Smaller Pad   **(d)** Bigger Pad

Static Pressure   **Total Pressure**

(e) Smaller Pad   **(f)** Bigger Pad   **(g)** Smaller Pad   **(h)** Bigger Pad
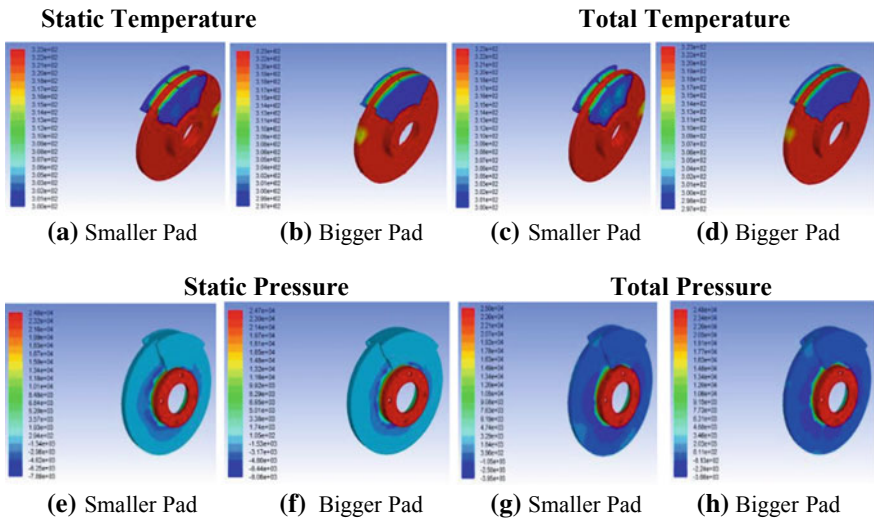
Fig. 4 Smaller pad (**a**, **c**, **e**, **g**) and bigger pad (**b**, **d**, **f**, **h**)

5.3 Temperature

A temperature difference has been recorded from the starting of the analysis to the end of it.

5.4 Pressure

6 Presentation of Results and Their Analysis

Considering all the results of analysis and simulation of both the assemblies in ANSYS workbench and CFD fluent, a table has been plotted which clearly differentiates the parameters between smaller pad assembly and bigger pad assembly (Tables 2 and 3).

Table 2 Numerical calculation data

S. no.	Parameters	Smaller pad	Bigger pad
1.	Kinetic Energy (joule)	269910.515	269910.515
2.	Tangential Force (N)	1415.4	1656.15
3.	Brake Torque (N-m)	339.69	397.47
4.	Braking Distance (m)	95.34	81.48
5.	Stopping Time (s)	5.66	5.66
6.	Heat Flux (kw/m^2)	42.576	41.192
7.	Thermal Gradient (k/m)	1064.4	1029.8

Table 3 Presentation of results and their analysis

S. no	Parameters	Minimum value		Maximum value	
		Small pad	Bigger pad	Small pad	Bigger pad
1	*Deformation* (mm)				
	1.1 s	0	0	0.00018968	0.00056801
	2.2 s	0	0	0.00056903	0.00075734
	3.8 s	0	0	0.00075871	0.00094688
	5 s	0	0	0.00170710	0.00170400
2	*Equivalent Stress* (MPa)				
	1.1 s	0.0016817	0.0026843	0.19282	0.39209
	2.2 s	0.0016817	0.0026843	0.38395	0.78150
	3.8 s	0.0016817	0.0026843	0.76622	0.97620
	5 s	0.0016817	0.0026843	1.7219	1.75500
3	*Pressure* (Pa)				
	Static	−7889.3	−8077.2	24844.5	24652.2
	Total	−3947.8	−3660.5	25007.8	24814
4	*Temperature* (K)				
	Static	300	297.3	323	323
	Total	300	297	323	323

7   Conclusion

If we consider only numerical values, after increasing the brake pad size, the **brake assembly with the bigger pad is more efficient** in terms of tangential force, braking torque, braking distance.

But if we consider the simulation results, after using this numerical data as an input in analysis and simulation**, brake assembly with the smaller pad is more durable** and less prone to any kind of failure or wear and tear. Smaller pad will possess less braking torque, which will result into more stopping distance but it will increase the life of braking system. Bigger pad will provide more braking torque resulting into less stopping distance but it will degrade the life of brake system. It will quickly need a replacement with a new one.

For example, if a person modifies his bike with just hit-and-trial method for just looks and performance, definitely, the bike will perform well. But if that person runs analysis on those modifications, he will get to know its negative results over the time. Only the analysis can examine the positive or negative outcomes of any type of modifications. The same applies here in the case of disc pad size alteration. If the driver uses larger pad without any analysis or deep research, he will experience good performance. But if he analyses this alteration, he will get to know about its less durability. If a driver prefers hard braking and does not pay attention to the brake system life and durability, then he should opt for bigger brake pad. If a driver likes to drive smoothly and takes care of his vehicle and its components, then he should opt for smaller brake pad.

References

1. Parab V, Naik K, Dhale P (2014) Structural and thermal analysis of brake disc. Int J Eng Dev Res www.ijedr.org
2. Patel P, Raval M, Patel J (2016) Design of disc Brake's rotor. Int J Eng Dev Res
3. Pophale A (2015) Ansys analysis of braking rotor of two wheeler. Int J Adv Eng Res Stud
4. Belhocine A, Rahim Abu Bakar A, Bouchetara M (2015) Thermal and structural analysis of disc brake assembly during single stop braking even. Aust J Mech Eng

Design of EGR Cooler for Improving the Effectiveness to Constraint NOx Emission

Akshay Kumar Vijayendernath, Rahul Ajitkumar and Ram Tyagi

Abstract In diesel motors, it is exceptionally needed to decrease the measure of NOx in the exhaust gas. NOx arrangement is a temperature subordinate marvel, and it happens mostly when the temperature in the ignition chamber surpasses 2000 K. In this way, so as that to diminish NOx outflows in the fumes, it is important to keep the top ignition temperatures under control. One effective path for guaranteeing this is by exhaust gas re-flow (EGR). This procedure is for the most part finished by utilizing a heat exchanger in which fumes gas flows inside the tube and coolant flows inside the shell. The exhaust framework decreases the ignition temperature, due to this arrangement of NOx is lessened. ANSYS Fluent is utilized to solve and recreate the stream fields and temperature appropriation of liquids inside the EGR cooler. Four models of EGR coolers were made using SolidWorks. Model-I is a single shell with square helical tubes inside. Model II is a single shell with circular helical tubes. Model-III and Model-IV have square and circular helical tubes with fins, respectively. The inlet conditions were kept constant for all the models and analysis was done to find out the outlet conditions. Of the four models, square helical tubes with fins (Model III) was found to give the best optimum results because of the greater surface area and better heat dissipation.

Keywords NOx reduction · Exhaust gas recirculation (EGR) · ANSYS fluent · EGR cooler

1 Introduction

An imperative method for the advancement of IC engine is done by the lessening of emissions to control pollution [1]. As an individual portability on our planet is expanding and the need for transportation division is improving and developing,

A. K. Vijayendernath (✉) · R. Ajitkumar · R. Tyagi
Amity School of Engineering and Technology, Amity University, Noida,
Uttar Pradesh, India
e-mail: akshayk1504@gmail.com

it imperative is to constrain the effect of activity on both, i.e., earth and the prosperity of the people. The primary ignition items that are being contained in motor fumes gases are water vapor (H_2O), carbon dioxide (CO_2), nitrogen oxides (NO_X), particulate issue (PM), and hydrocarbons (HC) and lastly, carbon monoxide (CO) in it [2–5]. These, with the exception of the water vapor, are being considered ecologically harmful. And, this is additionally reflected in the way that administrations everywhere throughout world sanction is limited for these gases of emissive property. In this way, motor designers take shot for lessening these discharges. An approach to diminish the evolution of NO_X inside diesel engine motors is by employing the EGR, recycled exhaust emissions [6]. Some portion of these fumes gas was followed up by another path directed into the ignition chamber, into which it serves to lessen these arrangements of NOX with diminishing the response temperature. Thus, the measure of EGR that could be utilized is restricted because of various factors. One of those is the requirement to convey sufficient outside air for ignition to occur, other is the abatement of motor productivity which can be caused due to high measures of EGR. Besides, on the turbocharged motors, in the stack concentrates on the turbocharger effectiveness, by this the weight of insertion is high than that of exhaust weight [7]. This proves it is difficult to obtain any EGR, as there is no weight contrast for driving it. To beat these issues, distinctive EGR enrooting could be utilized. One crucial part in frosty or cool EGR is the exchange of heat plan and assembling, which will be utilized to chill the gas. EGR coolers are generally used as in shell tube sort for this situation when the gas moves through tubes and coolant (motor coat water) streams in the shell [8].

In the content of this paper, we are proposing multiple designs and models of EGR coolers. By expanding the surface area, heat dissipated can be reduced and so the designs were used as models in various design categories. Models were designed with fins and without fins in the form of helical tubes inside the heat exchanger. The use of helical tubes was to increase the overall area, as well as to give a proper flow inside the tubes [8]. Simulation and analysis were done in ANSYS Fluent to understand the heat flow throughout the heat exchanger [9]. We have performed a reenactment examination to decide how the inner state of EGR cooler tubes influences its productivity. The stream conduct of liquids moving inside this heat exchanger is reproduced. This similar investigation can be helpful while choosing the most practical plan of EGR coolers [9].

2 Methodology

See Table 1.

2.1 Design Specification of EGR Cooler

Shell

Diameter = 80 mm

Table 1 Here, EGR cooler was designed based on helical tubes with fins and without fins for a particular diesel engine [8]

Description	Specifications
Displacement	1248 cc
Induction type	Turbocharger
Bore*Stoke	69.6 mm*82 mm
Maximum power output	75/4000
Compression ratio	17.6
EGR process	Cooled system
Maximum torque	190/2000

Thickness of wall = 10 mm

Box Helix

Length × Breadth = 5 × 5 mm
Total length of tubes = 200 mm
Number of tubes = 10

Circular helix

Outer diameter of circle = 5 mm
Inner diameter of circle = 4.5 mm
Total length of tubes = 20 mm
Number of tubes-10

2.2 Boundary Condition

See Table 2.

2.3 According to NTU Method

Overall heat transfer coefficient for gases = 70 W/m^{2}K
Area of tubes

$$A_s = \pi \times L \times d_0 \times N_t = 0.067 m^2 \tag{1}$$

$$NTU = UA/C_{min} = 1.031 \tag{2}$$

Table 2 Initialization condition for conducting computational analysis

Properties	Cold water	Exhaust gases
Mass flow rate (Kg/Sec)	0.01	0.005
Inlet temperature (K)	323	739

The following values for calculation are used in Ansys for simulation of the EGR [8].

Effectiveness of counter flow EGR cooler

$$\epsilon = \frac{1 - \exp(-NTU(1 - R))}{1 - R\exp(-NTU(1 - R))} = 61.1\% \tag{3}$$

Heat transfer coefficient

$$h_t = N_u k_t d_i$$
$$h_t = 240.48 \, W/m^2 - k \tag{4}$$

Shell-side Reynolds number

$$Re = G_s \, d_e / \mu$$
$$R_e = 48619.36 \tag{5}$$

$$Nu_s = 1.04 \, R_e \cdot 4 \, P \, r^3$$
$$= 117.3 \tag{6}$$

Shell-side heat transfer coefficient (hs) (Figs. 1 and 2).

$$h_s = (Nu_s \times k_f)/d_e$$
$$h_s = 105.47 \, W/m2 - K \tag{7}$$

2.4 Mesh Information

See Fig. 3, Tables 3, 4 and 5.

Fig. 1 Assembly of the EGR cooler with all tubes arranged in a circular manner with side closing covers
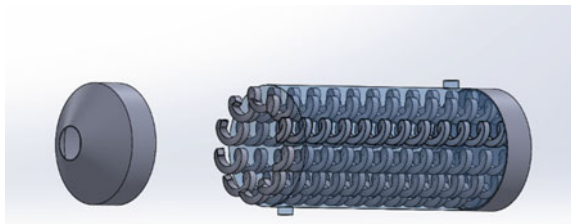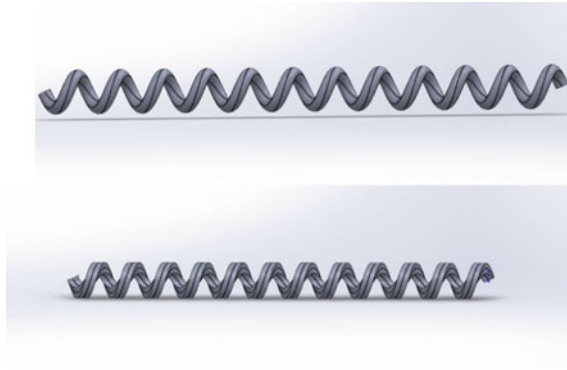
Fig. 2 Solid view of the circular and square finned helix tubes
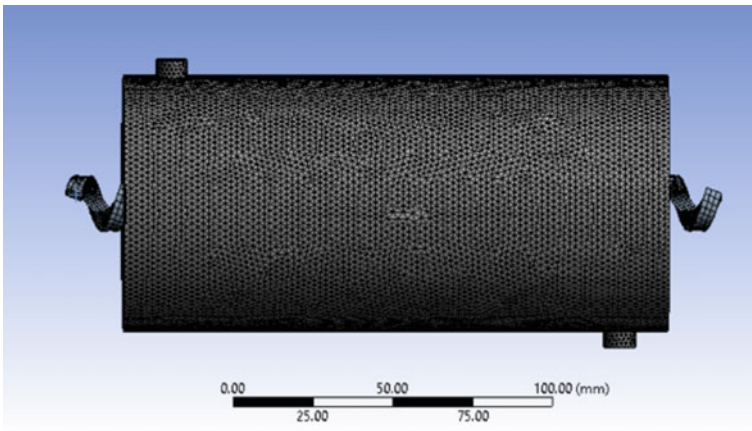
Fig. 3 Mesh contours of the Fluid model assembly of Square helix tube

Table 3 Mesh report information for the components

Domain	Nodes	Elements	Tetrahedra	Hexahedra
Fluid domain int1 int2 src	4800	2691	0	2691
pipe int1 int2 trg	7368	3672	0	3672
shell int1 int2 src	18019	91063	91063	0
All domains	30187	97426	91063	6363

Table 4 Statistics of the mesh for the components

Domain	Min. face angle (degree)	Max. face angle (degree)	Max. edge length ratio	Max. element volume ratio	Range of connections	
Fluid domain int1 int2 src	66.0304	117.691	3.02837	3.85699	1	8
pipe int1 int2 trg	40.5225	137.829	10.5467	3.53514	2	4
shell int1 int2 src	21.8483	118.445	2.65422	10.0164	3	38
All Domains	21.8483	137.829	10.5467	10.0164	1	38

Table 5 Boundary physics for component

Domain	Boundaries and conditions	
Fluid domain int1 int2 src	**Boundary—exhaust_gas_inlet**	
	Type	VELOCITY INLET
	Boundary—exhaust_gas_out	
	Type	PRESSURE OUTLET
	Boundary—wall fluid_domain int1 int2 src	
	Type	WALL
Pipe int1 int2 trg	**Boundary—wall pipe int1 int2 trg**	
	Type	WALL
Shell int1 int2 src	**Boundary—water_inlet**	
	Type	VELOCITY INLET
	Boundary—water_out	
	Type	PRESSURE OUTLET
	Boundary—wall shell int1 int2 src	
	Type	WALL

3 Result and Discussion

By observing the table, we got the CFD results for different models, and now we can claim that the outlet temperature of square helix with fins is comparatively low than the other models. So, we can manufacture this model for better cooling of EGR for reducing the NOx formation (Figs. 4, 5, 6, 7, 8 and Table 6).

From the above temperature contours diagrams, we can observe the change in temperature or the heat transfer in the shell and the square helical tube without fins. The difference in the temperature along the tube is shown with the changing color along the tube. The maximum temperature can be observed at the inlet of the tube where the exhaust gas enters into the tube and outlet temperature is calculated at the end of the tube using a probe in the CFD analysis software. This gives an overview of how the flow and heat transfer takes place in the EGR cooler.
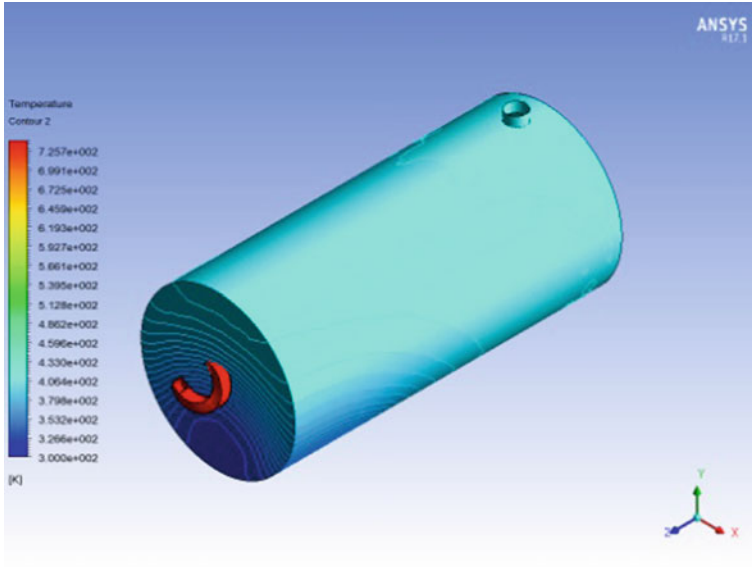
Fig. 4 Temperature contour of EGR cooler
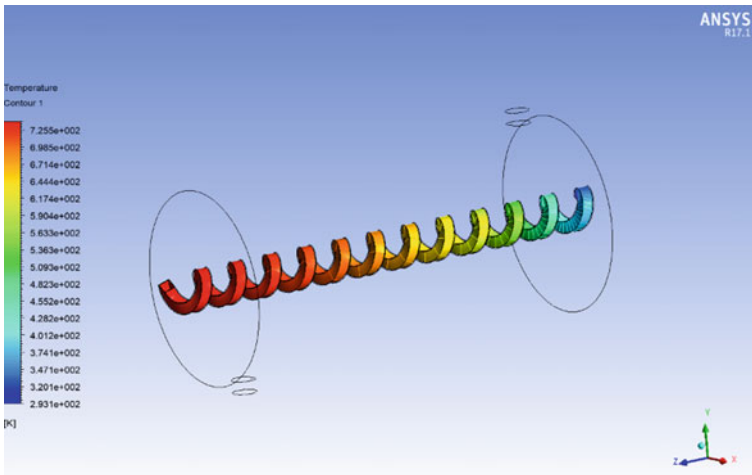
Fig. 5 Temperature contour for square helical tube without fins
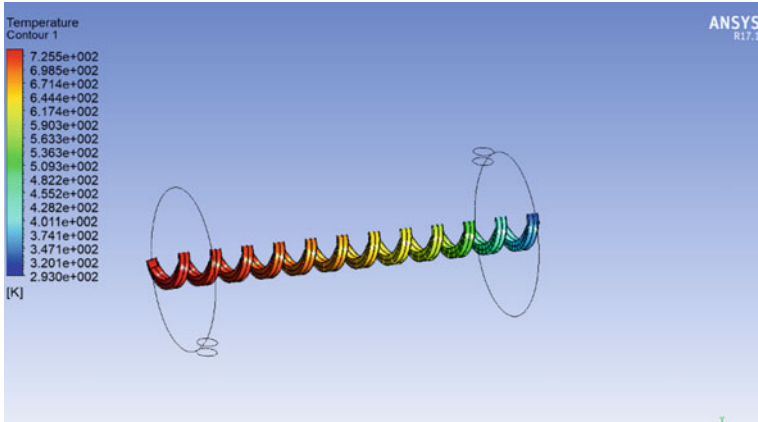
Fig. 6 Temperature contour of square helical tube having fins
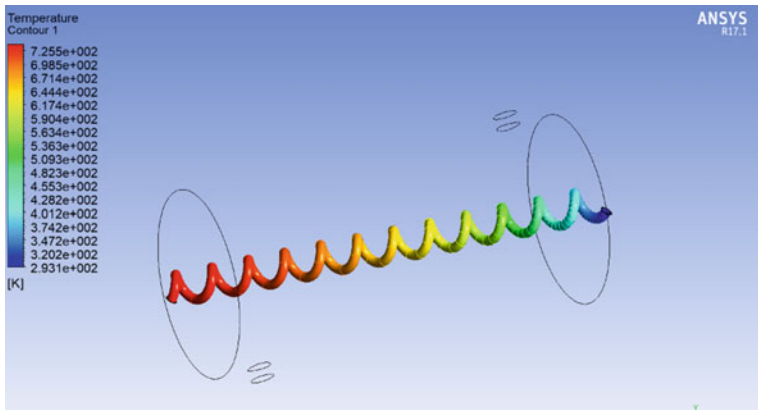
Fig. 7 Temperature contour for circular helical tube without fins
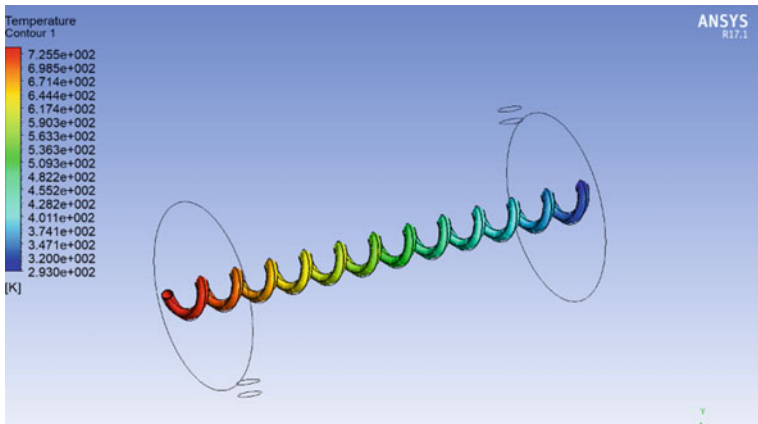
Fig. 8 Temperature contour of circular helical tube having fins

Table 6 CFD results for different models

Parameter	Square helix without fins	Square helix with fins	Circular helix without fins	Circular helix with fins	Rectangular tube with fins [9]
Mean temperature of exhaust gas (K)					
Inlet	739.0	739.0	739.0	739.0	739.0
Outlet	343.89	315.29	365.42	351.45	582.76

4 Conclusion

We have undergone some comparative study based on heat transfer and temperature drop within the plane square and circular helical tubes having fins and without fins. Usually, the temperature of exhaust gases using the EGR cooler is maintained around 350 K–400 K [9], which would provide an advantage for complete combustion of fuel and in reducing emissions by means of exhaust gas recirculation. Here, further reduction in the temperature has been shown, which would provide further reduction in the emissions due to the reduced temperature obtained from EGR cooler.

It is observed that the finned tubes dissipate more heat compared to the plain ones so this improves the effectiveness of the EGR cooler if the conventional plain tubes are replaced by the helical finned tubes, and in this case, the most efficient is the square helical finned tubes, which dissipate 36.2% more heat compared to the conventional rectangular finned tubes [9] and circular helical tubes with fins contributes 28.8% compared to the rectangular finned tubes. Therefore, the effectiveness of EGR cooler has improved in both cases. So, an experimental approach can be carried out by fabricating the model based on the proposed design in near future, and the results can be compared with that of the analysis results of CFD.

References

1. Reifarth S (2010), EGR-systems for diesel engines, licentiate thesis KTH CICERO, Department of Machine Design Royal Institute of Technology, SE-100 44 Stockholm
2. Kumar Vivek, Gaurav Varshney Kumar, Sakyasingh Tripathy, Agrawal Avinash Kumar (2013) Design of an experimental EGR system for a two cylinder diesel engine, department of mechanical engineering. I. I.T, Kanpur
3. Ghassembaglou N, Rahmatfam A, Ranjbar F (2014) World Acad Sci Eng Technol Int J Mech Mechatron Eng 8(11); Optimum design of heat exchanger in diesel engine cold EGR for pollutants reduction
4. Vashahi Foad, Kim Jintaek, Kim Daesuk (2014) A Numerical study on thermal and strain characteristics of EGR cooler 7:241–252
5. Byrne RC (1999) Standards of the tubular exchanger manufacturers association. (TEMA) 8th Edn, TEMA Inc., pp. 2–9 and 28–35
6. Rathore MM (2006) Engineering heat and mass transfer, 2nd Ed, pp. 300–305

7. ANSYS 15.0 Help Library
8. Coulson & Richardson, Chemical engineering design, 4th Edn, pp. 671–672
9. Shah IH, Singh B (2015) Assistant Professor, 2 PG scholar, Department of Mechanical Engineering. (2015) A comparative analysis to enhance the effectiveness of EGR coolers used in diesel engines

Erosion Analysis of Aramid Fiber–Epoxy Composite

Chinmaya Sharma and Shiv Ranjan Kumar

Abstract All the industries are mostly affected by the financial loss due to the Tribological problem. Especially, when slurry particles pass through pipes and pumps, erosion occurs in tidal turbine blades. The surface erosion is increased on interaction with seawater. In this work, epoxy composite reinforced with Kevlar fiber was prepared using VARTM technique and tested for erosive wear characterization using slurry jet erosion tester. The parameters for erosive wear test were taken as fiber content, impact velocity, slurry concentration, and impingement angle. The fiber content was varied as 52, 55, and 58 wt%. The result was analyzed by the Taguchi Design of Experiments. The finding of result indicated that the wear rate of epoxy composite reinforced with different fiber contents was minimum at the impact velocity of 30 m/s, slurry concentration 160 gm/min, impingement angle of 60°, and fiber content of 55 wt%.

Keywords Slurry erosive wear · Kevlar fiber · Taguchi Orthogonal Array

1 Introduction

Slurry erosion is one of the serious concerns during the continuous impact of slurry jet on the target application. Various experiments have been conducting by the researchers to reduce friction and wear during the working of machine parts. Slurry erosive wear rate mostly depends upon impingement angle, impact velocity, slurry concentration, etc. Gandhi et al. [1] tested erosion wear of seven different materials under the parameters of concentration as 10% wt, velocity as 3 m/s, and particle size as 550 mm. It was concluded that the erosive wear rate was dependent on the ratio of hardness of slurry-to-hardness of target material. However, it was independent of individual hardness slurry particle and target material. Patnaik et al. [2] fabricated glass–polyester hybrid composites filled with different particulate fillers

C. Sharma (✉) · S. R. Kumar
Mechanical Engineering Department, JECRC University, Jaipur, India
e-mail: chinmaya567@gmail.com

such as fly ash, aluminum oxide, and silicon carbide. In their study on erosion wear characteristics, it was revealed that the wear rate was decreased with the addition of hard particulate filler. Aluminum oxide-reinforced composite indicated less wear rate as compared to SiC and fly ash-reinforced composites. Mishra et al. [3] reported that the impact angle was the most significant factor influencing the erosion wear of composite material. It was also revealed that the erosive wear rate was increased with the increase in particle size of slurry. Tian et al. [4] tested the erosive wear for three formulations of iron alloys containing 25, 30, and 40% of chromium. The sand particle size was also varied as 10, 148, and 660 microns. They concluded that the increase in sand particle increased the erosive wear rate. Hu, et al. [5] suggested that Ni–Al$_2$O$_3$ coating can be used to improve the surface with better hardness and less erosive wear rate. Miyazaki [6] studied solid particle erosion behavior of polymer matrix composites. The experimental results were also verified by the theoretical model and FEA technique. Thakur et al. [7] conducted wear tests to study the effect of slurry erosion parameters such as impact angle, slurry concentration, impact velocity, and particle size on erosion wear. They concluded that the maximum weight loss was observed at 30° angle of impact. Chaudhari et al. [8] studied and compared slurry erosion behavior of thermomechanical processed 13Cr4Ni stainless steel. It was seen that there was less wear in the thermomechanically processed specimens as compared to stainless steel. Razzaque et al. [9] evaluated the erosive wear rate of carbon steel specimens in sand water slurry system by varying the erodent particle size. Slurry concentration was also varied. The surfaces of the eroded specimens are examined using Scanning Electron Microscopy (SEM). They concluded that an increase in slurry concentration increased the erosive wear rate irrespective of erodent particle size. However, for the same concentration, larger particles led to more erosive wear rate. Extensive research on solid particle erosion behavior of polymer composite with different particulate filler materials has been conducted by Patnaik et al. [10–14]. They analyzed the influence of various control factors like impact velocity, impingement angle, erodent size, standoff distance, etc., on erosion behavior. Their study of wear mechanism was based on the microstructure of eroded surface. Nilkar et al. [15] reported that maximum wear was observed at 30° impingement angle for ductile material and at normal to the surface for brittle materials. Khan et al. [16] tested for slurry erosive wear characterization of Al–Si alloy composite reinforced with 10 and 15 wt% of SiC particle. It was revealed that the addition of SiC decreased the wear rate of alloy and an increase in sand volume content increased the wear rate.

Hence, the aim of this work was to fabricate Aramid Fiber–Epoxy Composite, study the effect of different fiber content on the wear erosive wear behavior, and finally optimize a combination of various parameters that influence the erosive performance of Aramid Fiber–Epoxy Composite.

2 Experimental Procedure

2.1 Materials and Sample Preparation

Kevlar (fiber), Epoxy Araldite LY 1564(resin), and Hardener 22962 were procured from the local market, Jaipur, India. Both the epoxies and hardener were mixed in the ratio of 10:1 by weight. The composite was prepared by Vacuum-Assisted Resin Transfer Molding (VARTM). VARTM is a variation of Resin Transfer Molding (RTM), which involves the use of a vacuum to facilitate resin flow uniformly into a fiber layup. Hence, there is very less chance of void formation as compared to the Hand Layup method. After the impregnation occurred, the composite part was allowed to cure at room temperature.

2.2 Slurry Jet Erosion Test

The experiments were conducted on Slurry Jet Erosion Tester with ASTM standards of G131. The machine used was made by DUCOM Instruments, Asia and the model number is TR-411. The sand used was of 355 micron and 60 kg was hand sieved, which required a lot of hard work. Care was taken that any unwanted particle should not reach the hopper or else it could clog the nozzle.

2.3 Design of Experiment (DOE)

The experiments were performed as per Taguchi orthogonal Design of Experiment to study the effect of parameters on the wear rate of composite materials. Equation (1) was used to find out the S/N ratio.

$$\frac{S}{N} = 10 \, log \left[\frac{1}{n} \sum\nolimits_{i=1}^{n} y_i^2 \right] \tag{1}$$

where y_i is the value of experimental result of the ith test and n is the number of tests. The characteristics of S/N ratio can be divided into three parts, i.e., smaller the better, larger the better, and nominal the better. However, in the case of erosion wear, smaller-the-better characteristic has been selected. Table 1 indicates the factors and levels selected for experimental analysis using the Taguchi method. The orthogonal array chosen in this study is L9 (3^4), which has nine rows corresponding to the number of variables selected.

Table 1 List of factors and levels in Taguchi Orthogonal Array

Factor	Type	Level	Value	Unit
Impact velocity	Fixed	3	20, 25, 30	m/sec
Impingement angle	Fixed	3	30, 60, 90	degree
Fiber content	Fixed	3	52,55,58	wt. %

3   Result and Discussion

Experiments were performed as per Taguchi Orthogonal Array to study the effect of parameters on the erosive wear rate of composites. As per Taguchi Orthogonal Array, nine different combinations of parameters were taken and experiments were performed as per those parameters. Taguchi Array L9 (3^4) having four factors, three levels, and nine runs was used. The erosion rate and concern S/N ratios were presented in Table 2. The analysis was performed using the software MINITAB 18 to analyze the wear rate of epoxy composite reinforced with different weight percentages of fiber content. The overall mean for the S/N ratio of the slurry erosion rate is found to be −15.17 db. The graph shows graphically the effect of the four control factors on slurry erosion rate. Minimum and maximum slurry erosion wear by the individual experimental parameter is shown in above Fig. 1. Figure 1 depicted the analysis related to S/N (signal-to-noise) ratio. It was revealed that the factor combination of A1, B1, C1, and D2 would result in a minimum erosion rate for the prepared sample. Therefore, it can be concluded that the wear rate of epoxy composite reinforced with different fiber contents was minimum at the impact velocity of 30 m/sec, slurry concentration 160 gm/min, impingement angle of 60°, and fiber content of 55 wt%.

Table 2 SN ratio for different experiments

Velocity (m/s)	Slurry Conc. (gm/min)	Angle (Deg)	Layer (wt. %)	Erosion (mg)	SNRA1
30	160	60	52	4	−12.0412
30	190	75	55	4	−12.0412
30	230	90	58	7	−16.9020
35	160	75	58	7	−16.9020
35	190	90	52	6	−15.5630
35	230	60	55	4	−12.0412
40	160	90	55	6	−15.5630
40	190	60	58	10	−20
40	230	75	52	6	−15.5630
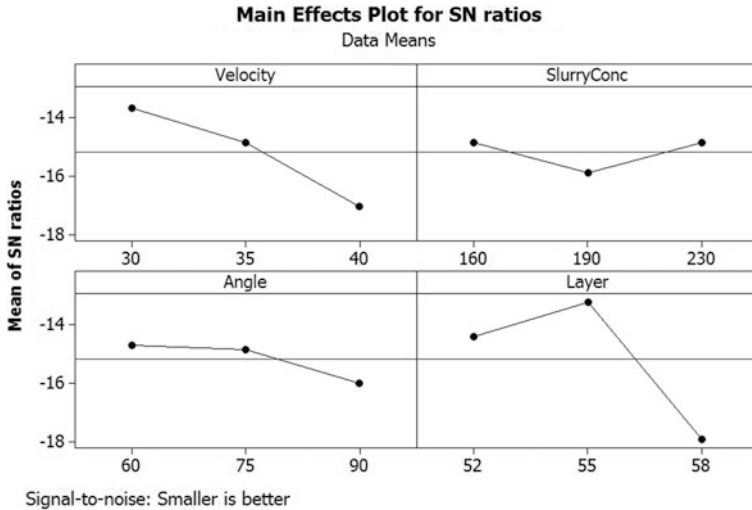
Fig. 1 Effect of control factors on erosive wear rate

4 Conclusions

Epoxy composite reinforced with different weight percentages of fiber content were successfully fabricated using Vacuum-Assisted Resin Transfer Molding (VARTM). Erosive wear tests have been performed to study the effect of various parameters such as impingement angle, impact velocity, fiber content, and slurry concentration on the wear behavior of the material. The experiments were conducted as per Taguchi Orthogonal Array L9 (3^4). Erosion wear increased with the increase in impact velocity. Finally, it can be concluded that the wear rate of epoxy composite reinforced with different fiber content was minimum at the impact velocity of 30 m/sec, slurry concentration 160 gm/min, impingement angle of 60°, and fiber content of 55 wt%.

References

1. Gandhi BK, Desale GR, Jain SC (2008) Slurry erosion of ductile materials under normal impact condition. Wear 264:322–330
2. Patnaik A, Satapathy A, Mahapatra SS, Dash RR (2008) A Taguchi approach for investigation of erosion of glass fiber–polyester composites. J Reinf Plast Compos 27 (8):871–888
3. Mishra SC, Praharaj S, Satpathy A (2009) Evaluation of erosion wear of a ceramic coating with Taguchi approach. Manuf Eng 4:241–246
4. Tian HH, Addie GR, Visintainer RJ (2009) Erosion–corrosion performance of high—Cr cast iron alloys in flowing liquid–solid slurries. Wear 267(11):2039–2047

5. Hu HX, Jiang SL, Tao YS, Xiong TY, Zheng YG (2011) Cavitation erosion and jet impingement erosion mechanism of cold sprayed Ni–Al$_2$O$_3$ coating. Nucl Eng Des 241:4929–4937
6. Miyazaki N (2015) Solid particle impact erosion of polymer matrix composites—a critical review. J Compos Mater 50(23):3175–3217
7. Thakur PA, Khairnar HS, Deore ER, More SR (2015) Development of slurry jet erosion tester to simulate the erosion wear due to solid-liquid mixture. IJNR Eng Sci 2(1):14–20
8. Kishor B, Chaudhari GP, Nath SK (2016) Slurry erosion of thermo-mechanically processed 13Cr4Ni stainless steel. Tribo Int 93:50–55
9. Razzaque MM, Alam MK, Khan MI (2016) Effect of erodent particles on the erosion of metal specimens. In: AIP conference proceedings, vol 1754. https://doi.org/10.1063/1.4958459
10. Patnaik A, Satapathy A, Mahapatra SS, Dash RR (2008) A Taguchi approach for investigation of erosion of glass fiber-polyester composite. J Reinf Plast Comp 27:871–881
11. Patnaik A, Satapathy A, Mahapatra SS, Dash RR (2008) Parametric optimization of erosion wear of polyester-GF-alumina hybrid composite using Taguchi method. J Reinf Plast Comp 27:1039–1098
12. Patnaik A, Satapathy A, Mahapatra SS, Dash RR (2008) Implementation Taguchi design for erosion of fiber reinforced polyester composite system with SiC filler. J Reinf Plast Comp 27:1093–1111
13. Patnaik A, Satapathy A, Mahapatra SS, Dash RR (2008) A modeling approach for prediction of erosion behavior of glass fiber-polyester composite. J Polym Res 15:147–160
14. Patnaik A, Tejyan S (2012) A Taguchi approach for investigation of solid particle erosion response of needle-punched nonwoven reinforced polymer composites: Part II. J Ind Text. https://doi.org/10.1177/1528083712460264, 2012
15. Nilkar KM (2017) Experimental study and analysis of slurry erosion wear of SS304L material. IOSR J Mech Civ Eng 17(1):29–34
16. Khan MM, Dixit G (2017) Effects of test parameters and sic reinforcement on the slurry erosive wear response of Al-Si alloy. Mater Today Proc 4(2):3141–3149

A Fatigue Crack Growth Life Prediction Model for Discontinuous Reinforced Metal–Matrix Composite: Influence of Microstructure

Abhishek Tevatia

Abstract Under the fully strain-controlled conditions, a closed-form multistage fatigue crack growth (MSFCG) life prediction model has been developed for discontinuous reinforced MMCs (DRMMCs) considering the effect of microstructural features. The model considers crack nucleation, small crack, and long crack life. The crack initiation is evaluated on the bases of slip steps deepening into a fatigue crack under the cyclic strain. Next, the small crack growth life is investigated within the microstructural threshold. Finally, for long fatigue crack propagation, previously developed model by Tevatia and Srivastava is modified and incorporated in the current model. Under the total strain-controlled conditions, reinforcement in the matrix results in an increase in both (i) the level of cyclic plastic deformation and (ii) cyclic plastic zone size near the vicinity of crack tip. The effect of initiation and small crack growth life is significant for low cycle fatigue applications.

Keywords Microstructural · Multistage fatigue · Small crack growth life · Fatigue crack initiation · DRMMCs

1 Introduction

Today, the demand of metal–matrix composites (MMCs) is increasing in the development of engineering components/structure due to its high stiffness, strength, and fatigue life [1–4]. The damage due to cyclic/variable loading is one of the crucial limiting factors for estimating the life of discontinuous reinforced metal–matrix composites (DRMMCs) [5, 6]. The damage evolves successively from fatigue crack nucleation/initiation resulting in small crack followed by long crack leading to sudden failure of the component. It has been established that analytical modeling of fatigue crack growth evolution performed well in advance, and is

A. Tevatia (✉)
Division of Manufacturing Process and Automation Engineering,
Netaji Subhas University of Technology, Sec-3, Dwarka, New Delhi 110078, India
e-mail: abhishek_tevatia@yahoo.co.in

useful in the evaluation of the performance of composite materials so that maintenance/replacement can be scheduled before any catastrophic failure [5].

Though a number of fatigue models were developed for DRMMCs [7–16] over the last two decades, these models excluded the effect of microstructural features of composites on the fatigue damage evolution. The presented model includes this important feature. Here, the fatigue damage has four stages: (i) nucleation, (ii) microstructural short crack growth, (iii) physically short crack growth, and (iv) long crack growth. The sum of these different stages is cumulative total fatigue life, which here is termed as multistage fatigue crack growth (MSFCG) life [7]

$$N_T = N_i + N_{msc} + N_{psc} + N_{lc} \tag{1}$$

where N_T is the total fatigue life, N_i is the life of crack initiation, N_{msc} is the life of microstructural small crack growth and N_{psc} is the life of physically small crack growth life (the MSC and PSC stages are often combined), and N_{lc} is fatigue life of long crack.

In the present work, the total fatigue life prediction model is developed for DRMMC considering the effect of microstructural features such as crack nucleation/initiation period with small crack life and long crack propagation life under the fully strain-controlled condition. The crack initiation model is developed on the bases of slip steps deepening into a fatigue crack under cyclic strain. The small crack growth life is evaluated in DRMMC within the microstructural threshold based on the elastic stresses distribution. Finally, the long crack propagation life is evaluated using modified Tevatia et al. [12] life prediction model. The analytical results are compared with the experimental data [10–14].

2   Analytical Fatigue Model

As mentioned above, the whole fatigue degradation process in DRMMCs can be divided into four different stages. The model derivation assumes that the nucleation is controlled by the crack tip displacement and surface displacement. The small cracks nucleate from the surface defects and are evolved into the rest of the stages in microstructural elements within the fatigue damage zone.

2.1   Fatigue Initiation Life

Harvey et al. [17] proposed initiation model for the high strength low alloy steel with plastic strain, slip height displacement, and slip band spacing. The model uses the plastic strain fraction contributing to surface upset based on the assumptions that the surface displacements are similar to the crack [18] and nucleation is

controlled by the displacement of the crack tip. When cumulative displacement reaches the microstructural threshold value, initiation life can be expressed as [17]

$$N_i = \frac{\Delta K_{th}^2}{4\sigma_{ys}Ef\Delta\varepsilon_{pl}h} \tag{2}$$

where N_i initiation crack life, ΔK_{th} stress intensity threshold, E modulus of elasticity, σ_{ys} yield strength, f the plastic strain fraction range which created the surface displacement, $\Delta\varepsilon_{pl}$ plastic strain amplitude, and h width of slip band in DRMMCs. Without losing the generality, the expression for fatigue nucleation life for DRMMCs is written as

$$N_i = \frac{\Delta K_{th}^2}{4\sigma_{cy}E_cf\Delta\varepsilon_{pl}S_r} \tag{3}$$

where σ_{cy} DRMMC yield strength, E_c DRMMC Young's modulus, and S_r is the average spacing between the discontinuous reinforcements.

The value of stress intensity threshold for crack based on the average spacing between the discontinuous reinforcements is expressed as [19]

$$\Delta K_{th} = (1-R)\sigma_{my}(2S_r)^{\frac{1}{2}} \tag{4}$$

where R load ratio and σ_{my} matrix cyclic yield strength.

The cyclic yield stress of DRMMCs, considering the microstructural effect is calculated by the expression [20]

$$\sigma_{cy} = \left[1 + \frac{8V_f^2s^2\left(E_f - E_m\right)}{3\left(E_f + 4V_fs^2E_m\right)}\right]\sigma_{my} \tag{5}$$

where V_f reinforcement volume fraction, s is the aspect ratio of reinforcements (length to diameter), E_f, and E_m are Young's moduli of reinforcement and matrix materials, respectively. Thus, the threshold intensity can be rewritten as

$$\Delta K_{th} = (1-R)\sigma_{cy}\left[1 + \frac{8V_f^2s^2\left(E_f - E_m\right)}{3\left(E_f + 4V_fs^2E_m\right)}\right]^{-1}(2S_r)^{\frac{1}{2}} \tag{6}$$

Thus, the fatigue crack nucleation (Eq. 2) life can be calculated using the expression

$$N_i = \frac{1}{4E_cf}(1-R)^2\sigma_{cy}\left[1 + \frac{8V_f^2s^2\left(E_f - E_m\right)}{3\left(E_f + 4V_fs^2E_m\right)}\right]^{-2}\left(\frac{\Delta\varepsilon_{pl}}{2}\right)^{-1} \tag{7}$$

2.2 Microstructural Small Crack Life

For small crack life, Chan et al. [21] model are extended. The Chan's model proposed a relationship (for metals) for propagation of the small crack growth near the threshold of long crack growth. Without losing the integrity of Chan's, the expression for DRMMCs is

$$\frac{da}{dN} = \left(\frac{E_c s'}{4\sigma_{cy}\varepsilon'_f d_o}\right)^{\frac{1}{b}}(2s')^{1-\frac{1}{b}}\left[\frac{\Delta K_{eff}}{E_c}\right]^{2b} \tag{8}$$

where d_o is the dislocation barrier spacing, ε'_f is the fatigue ductility coefficient, s' is the strain spacing, b is the fatigue ductility exponent, and ΔK_{eff} is the effective stress intensity factor.

Chapetti [22] expressed the range of effective stress intensity for small crack growth as

$$\Delta K_{eff} = \Delta K - \Delta K_{th,a} \tag{9}$$

where ΔK is the applied range of stress intensity and $\Delta K_{th,a}$ the threshold range of stress intensity, often depends on the length of small crack growth from nucleation/initiation, is expressed as [23]

$$\Delta K_{th,a} = \Delta K_{th}\left(\frac{a}{a+a_D}\right)^{\frac{1}{2}} \tag{10}$$

where ΔK_{th} is the threshold range for crack based on the average spacing between the discontinuous reinforcements; a is the crack length; size of the critical defect $a_D = a_o/\beta^2$; a_o is the critical defect. In the present work, the value of geometrical factor (β) for is 0.65; and a_o is the same as a_i [21–23].

From Eqs. (6) and (10), the law of threshold from nucleation is rearranged to

$$\Delta K_{th,a} = (1-R)\sigma_{cy}\left[1+\frac{8V_f^2 s^2\left(E_f-E_m\right)}{3\left(E_f+4V_f s^2 E_m\right)}\right]^{-1}\left(2S_r.\frac{a}{a+a_D}\right)^{\frac{1}{2}} \tag{11}$$

The applied stress intensity range $\Delta K = \Delta\sigma Y\sqrt{\pi a}$; where $\Delta\sigma$ is the cyclic stress amplitude and Y is the crack geometry correction factor [24]. The effective stress intensity range in DRMMC for small crack growth is

$$\Delta K_{eff} = \Delta\sigma Y(\pi a)^{\frac{1}{2}}-(1-R)\sigma_{cy}\left[1+\frac{8V_f^2 s^2\left(E_f-E_m\right)}{3\left(E_f+4V_f s^2 E_m\right)}\right]^{-1}\left(2S_r.\frac{a}{a+a_D}\right)^{\frac{1}{2}} \tag{12}$$

Finally, the microstructure fatigue small crack growth rate can be expressed as

$$
\frac{da}{dN} =
\left(\frac{E_c s'}{4\sigma_{cy}\varepsilon'_f d_o}\right)^{\frac{1}{b}}(2s')^{1-\frac{1}{b}}\left\{\frac{1}{E_c}\left(\Delta\sigma Y(\pi a)^{\frac{1}{2}}-\right.\right.
$$
$$
\left.\left.(1-R)\sigma_{cy}\left[1+\frac{8V_f^2 s^2\left(E_f-E_m\right)}{3\left(E_f+4V_f s^2 E_m\right)}\right]\left(2S_r\cdot\frac{a}{a+a_D}\right)^{\frac{1}{2}}\right)\right\}^{2b}
\tag{13}
$$

The microstructural small crack growth life is calculated by integrating Equation (13) between the initial (i.e., initiation) crack size a_i and small crack size a_{sc}.

2.3 Fatigue Long Crack Propagation Life

The fatigue crack growth model with microstructural features is influenced by the load ratio [25, 26]. The existing model [25] is improved by including the effect of load ratio in the estimation of fatigue life of DRMMCs. The relationship between the range of the stress intensity factor with the load ratio is given as [7, 8, 25, 26]

$$
\Delta K_{eff} = U_R \Delta K
\tag{14}
$$

where $U_R = 1/(1-R)$ for $R < 0$; $U_R = 1$ for $R \geq 0$; and $U_R = 0$.

The modified fatigue long crack propagation life [12], including the effect of load ratio, based on the accumulated cyclic plastic zone (CPZ) Eq. (14) is expressed as

$$
2N_{lc} = \frac{64C_\varepsilon^2}{\lambda_l U_R Y^2 \pi^2}\left[1+\frac{8V_f^2 s^2\left(E_f-E_m\right)}{3\left(E_f+4V_f s^2 E_m\right)}\right]^{-2}\left(\frac{n'}{n'+1}\right)\left(\frac{\sigma_{cy}}{K'}\right)^3 ln\left(\frac{a_f}{a_{sc}}\right)\left(\frac{\Delta\varepsilon_{pl}}{2}\right)^{-(3n'+1)}
\tag{15}
$$

where λ_l is the correction factor under the large-scale yielding, C_ε constraint, K' is the cyclic strength coefficient, n' is the cyclic strain hardening exponent, and a_f is the final crack length.

2.4 MSFCG Life Prediction Model

The fatigue degradation process is the cumulative effect of the four stages, namely (i) crack initiation/nucleation, (ii) microstructural/physical small crack, and (iii) long crack size. In composite materials, the nucleation life is almost negligible compared to the metals [5]. Thus, the total fatigue life of DRMMCs is (Eq. 1)

$$N_T = N_i + N_{msc/psc} + N_{lc} \tag{16}$$

where N_i, $N_{msc/psc}$ and N_{lc} can be estimated using Eqs. (7), (13), and (15), respectively.

3   Result and Discussion

The values for modeling parameters for various aluminum-based DRMMCs are compiled in Table 1. The fraction of plastic strain range (f) is estimated from plastic strain amplitude experimental value (Eq. 7). The dislocation barrier spacing can be evaluated (Eq. 8) from Hall–Petch relation [23], $d_o = D_o \left(\frac{1-V_f}{V_f}\right)^{\frac{1}{3}}$. The average spacing (S_r) between the discontinuous reinforcements is assumed to be equal to the dislocation barrier spacing (Table 1). The other parameters used in the modeling are constraint, $C_\varepsilon = 0.2$ for aluminum DRMMCs [27] and crack geometry-based correction factor, $Y = 1.12$ assuming semi-elliptical crack [28]. The CPZ correction factors λ_l are estimated by substituting the experimental values of plastic strain amplitude into $\lambda_l = \frac{\pi}{18}\left(\frac{1}{2} + \frac{2}{3}\sqrt{\frac{2}{3}\frac{\Delta\sigma_{eff}}{2\sigma_{cy}}}\right)$ [29]. The initial, small crack, and final critical crack lengths are taken as 5 µm [14], 300 µm [19], and 2 mm [14].

Table 1   Modelling parameters of the different aluminum-based DRMMCs

Composite	AA6061-Al$_2$O$_3$-T6 tested at 25 °C [9]	Al99.85-Al$_2$O$_3$-T6 tested at 25 °C [10]	AA6061-Al$_2$O$_{3(P)}$-T6 tested at 25 °C [11]	AA2014-Al$_2$O$_{3(P)}$ tested at 100 °C [14]
E_c (GPa)	89	84	93.3	89
E_m (GPa)	71	71	71	72
E_f (GPa)	300	300	312	312
s	66.67	66.67	1.7	1.7
n'	0.22	0.22	0.16	0.14
K' (MPa)	1579	560	1066	580
σ_{cy} (MPa)	402	143	387	467
σ_{my} (MPa)	280	35	340	414
V_f	0.2	0.2	0.15	0.15
λ_l	0.3838	0.278	0.3497	0.1885
D_o µm	3	3	8	7.3
d_o µm	4.76	4.76	14.26	13.02
ε_f'	0.0921	0.1115	0.1782	1.1795
b	−0.6024	−0.6024	−0.6757	−0.7042
a_o µm	1.88	1.88	5	4.56
a_D µm	4.44	4.44	11.83	10.79

Fig. 1 Total fatigue crack growth life for **a** Al99.98-Al$_2$O$_3$-T6, **b** AA6061-Al$_2$O$_3$-T6, **c** AA6061-Al$_2$O$_{3(P)}$-T6, **d** AA2014-Al$_2$O$_3$ DRMMCs

Figure 1a–d displays the fatigue crack growth lives for different DRMMCs fitted using Eq. (16). The nucleation life is more prominent within the first 100 cycles at high plastic strain amplitudes. As a result, the effect of nucleation and microstructural small crack life is more significant for low cycle fatigue compared to the crack propagation life. Low cycle fatigue (below 10^5 cycles) shows good agreement between the predicted and experimental values. However, the experimental and predicted results for very high plastic strain amplitudes (Fig. 1) are comparably varied.

4 Conclusion

A new model to predict the cumulative fatigue life cycle of a composite is simplified with its analytical solution. The current model is unique as it combines all physical processes involved during the fatigue life. This MSFCG life prediction model is implemented for different DRMMCs displaying good agreement with the respective experimental data sets. This model has superiority over the MSL model as it includes very early stages of nucleation and microstructural components of the material.

References

1. Clyne TW Withers P (1992) An introduction to metal matrix composites. Cambridge University Press, Cambridge
2. Gupta P, Kumar D, Parkash O, Jha AK (2013) Structural and mechanical behavior of 5% Al_2O_3 reinforced Fe metal matrix composites (MMC) produced by powder metallurgy (P/M) route. Bull Mater Sci 36:859–868
3. Gupta P, Kumar D, Parkash O, Jha AK (2014) Effect of sintering on wear characteristics of Fe-Al_2O_3 metal matrix composites. In: Proceedings of the Institution of mechanical engineers, Part J: J Eng Tribol 228:362–368
4. Khosla P, Singh HK, Katoch V, Dubey A, Singh N, Kumar D, Gupta P (2017) Synthesis, mechanical and corrosion behaviour of iron-silicon carbide metal matrix nanocomposites. J Compos Mater. https://doi.org/10.1177/0021998317702439
5. Llorca J (2002) Fatigue of particle and whisker reinforced metal-matrix composites. Prog Mater Sci 47:283–353
6. Hartmann O, Kemnitzer M, Biermann H (2002) Influence of reinforcement morphology and matrix strength of metal-matrix composites on the cyclic deformation and fatigue behaviour. Inter J Fatigue 24:215–221
7. McDowell DL, Gall K, Horstemeyer MF, Fan J (2003) Microstructural based fatigue modeling of cast A356-T6 alloy. Eng Fract Mech 70:49–80
8. Bruzzi MS, McHugh PE (2004) Micromechanical investegation of the fatigue crack growth behaviour of Al-SiC MMCs. Inter J Fatigue 26:795–804
9. Ding H-Z, Biermann H, Hartmann O (2002) A low cycle fatigue model of small-fiber reinforced 6061 aluminum alloy metal matrix composites. Comp Sci Tech 62:2189–2199
10. Ding H-Z, Biermann H, Hartmann O (2003) Low cycle fatigue crack growth and life prediction of small-fiber reinforced aluminum matrix composites. Inter J Fatigue 25:209–220
11. Ding H-Z, Hartmann O, Biermann H, Mughrabi H (2002) Modelling low-cycle fatigue life of particulate-reinforced metal-matrix composites. Mater Sci Eng A 333:295–305
12. Tevatia A, Srivastava SK (2015) Modified shear lag theory based fatigue crack growth life prediction model for small-fiber reinforced metal matrix composites. Inter J Fatigue 70: 123–129
13. Tevatia A, Srivastava SK (2016) Influence of residual thermal stresses on the fatigue crack growth life of discontinuous reinforcement in metal matrix composites. Fatigue Fract Eng Mater Struct 40:81–88
14. Levin M, Karlsson B (1993) Crack initiation and growth during low-cycle fatigue of discontinuously reinforced metal–matrix composites. Int J Fatigue 15(5):377–387
15. Tevatia A, Srivastava SK (2018) The energy-based multistage fatigue crack growth life prediction model for DRMMCs. Fatigue Fract Eng Mater Struct, 1–11. https://doi.org/10.1111/ffe.12853
16. Zhang Q (2005) A model for the low cycle fatigue life prediction of discontinuously reinforced MMCs. Inter J Fatigue 27:417–427
17. Harvey SE, Marsh PG, Gerberich WW (1994) Atomic force microscopy and modeling of fatigue crack initiation in metals. Acta metal mater 42:3493–3502
18. Ma B-T, Laird C (1989) Overview of fatigue behavior in copper single crystals—I. Surface morphology and stage I crack initiation sites for tests at constant strain amplitude. Acta Metal 37:325–36
19. Li CS, Ellyin F (1995) On crack phases of particulate-reinforced metal matrix composites. Fatigue Fract Eng Mater Struct 18:1299–1309
20. Jiang Z, Lian J, Yang D, Dong S (1998) A new modification to shear lag model as applied to stiffness and yield strength of small fiber reinforced metal matrix composites. J Mater Sci Tech 14:517–522
21. Chan KS (1993) Scaling laws for fatigue crack growth of large cracks in steels. Metall Trans A 24:2474–2485

22. Chapetti MD (2003) Fatigue propagation threshold of small cracks under constant amplitude loading. Int J Fatigue 25:1319–1326
23. Santus C, Taylor D (2009) Physically small crack propagation in metals during high cycle fatigue. Inter J Fatigue 31:1356–1365
24. Rice JR (1967) Mechanics of crack tip deformation and extension by fatigue. In: Fatigue crack propagation. ASTM STP 415, ASTM, PA, pp 247–309
25. Kanazawa T, Machida S (1975) On the effect of cyclic stress ratio on the fatigue crack propagation. Eng Fract Mech 7:445–455
26. Robertson IM (1994) Correlation of fatigue crack growth rate at different stress ratios for quenched and tempered steels and other alloys. Fatigue Fract Eng Mater Struct 17:327–338
27. Davidson DL, McClung RC (1997) Local constraint near fatigue cracks in alloys and particulate composites. Inter J Fract 84:81–98
28. Mowbray DF (1967) Derivation of a low-cycle fatigue relationship employing the ΔJ-integral approach to crack growth. In: Cracks and fracture. ASTM STP 601, PA, ASTM, pp 33–46
29. Lu TJ, Chow CL (1990) A modified Dugdale model for crack tip plasticity and its related problems. Eng Fract Mech 37:551–568

Augmented Reality-Based Simulation of Spring–Mass System

Rohit Singla, Saurabh Kumar Yadav and Jaspreet Hira

Abstract In recent decades, various user interaction technologies have made their presence to visualize the complex behavior patterns of a dynamical system. Out of these, technology Augmented Reality (AR) emerged as a viable choice for studying the interaction between reality and simulation. Augmented reality-based simulation involves computer-based superimposition of an image on another image. In the present work, MATLAB and Unity3D-based simulation techniques have been used for a spring–mass system. Computer-based image processing has been performed in MATLAB. A tracking algorithm and simulation code is developed using MATLAB to get enhanced interaction between the real and the virtual systems. The results of this study shall prove to be quite useful in the rapid prototyping and vibration engineering fields.

Keywords Spring mass · Augmented reality · Mechanical vibration · Unity3D

1 Introduction

Numerical analysis of mechanical engineering problems is widely conducted by many engineers to predict the behavior of real-world physical systems. Numerical investigation is a widely accepted tool, which helps to analyze the behavior of real systems. It is carried out in a pure virtual environment.

In the last few decades, augmented reality technology and its applications in the analysis of mechanical engineering problems have been widely developed to increase the perception of users about its interaction with the numerical simulation. In augmented reality, superimposition of one image (generated by analysis) over

R. Singla (✉) · J. Hira
Department of Mechanical Engineering, Amity University Noida, Noida, India
e-mail: rohitsinglaonline@gmail.com; rsingla1@amity.edu

S. K. Yadav
Department of Mechanical Engineering, IITRAM, Ahmedabad, India
e-mail: saurabhme.iitr@gmail.com

another real-world image is done. Superimposing the numerical results onto the corresponding real objects results in wider exploration of the subject and deeper examination of the results.

Augmented reality is a relatively new field, wherein most of the research has occurred in the past two decades. In this technology, real-world picture is captured by a moving camera and it is enriched by computer-generated analysis and computer-generated objects [1]. Augmented reality visualization system has been applied in various fields such as medical intervention and patient information systems [2], presentation of museum, historic and cultural heritage [3], and to support teaching, learning, robotics, and academics [4]. In recent years, great progress has been achieved in improving the quality and computation efficiency in the area of augmented simulation [5].

Conventional analysis is usually carried out in offices or virtual environments like computer-aided design software that do not promote the user intelligence and interaction with the real system, thereby limiting the application of analysis [6, 7]. With the sole purpose of enhancing the analysis with augmented reality, the paper presents a method which integrates the analysis done with augmented reality with the real system. The paper proposes a novel method that integrates numerical simulation with real-world problems.

The main contributions of this paper are:

1. An integrated framework for performing dynamic analysis interactively by using augmented reality has been developed.
2. An interface application has been developed by using MATLAB and Unity3D.
3. A real-time interaction method to apply dynamic boundary condition has been developed. The complete application uses the mobile sensor.
4. Interactive methods have been developed for resonance model and damped system.

2 Procedure and Methodology

A different/novel AR implementation that focuses on the use of commodity smartphones/tablets as AR platforms employ an approach which implements a video see-through AR, where the real environment is composed of a live video feed from the smartphone/mobile device camera and virtual objects are superimposed on this live video feed [8]. The complete process to do augmented simulation has been implemented by using the following steps.

1. Parameters are initialized in MATLAB.
2. Complete equation of motion is solved by using state space model and OBJ file compatible for augmented simulation is generated in MATLAB.
3. MATLAB is coupled with augmented reality application program developed in Unity3D.
4. Object is tracked by using gyroscopic sensor, camera and magnetic compass.
5. Simulation is ended by using exit Command in Augmented reality application (Fig. 1).
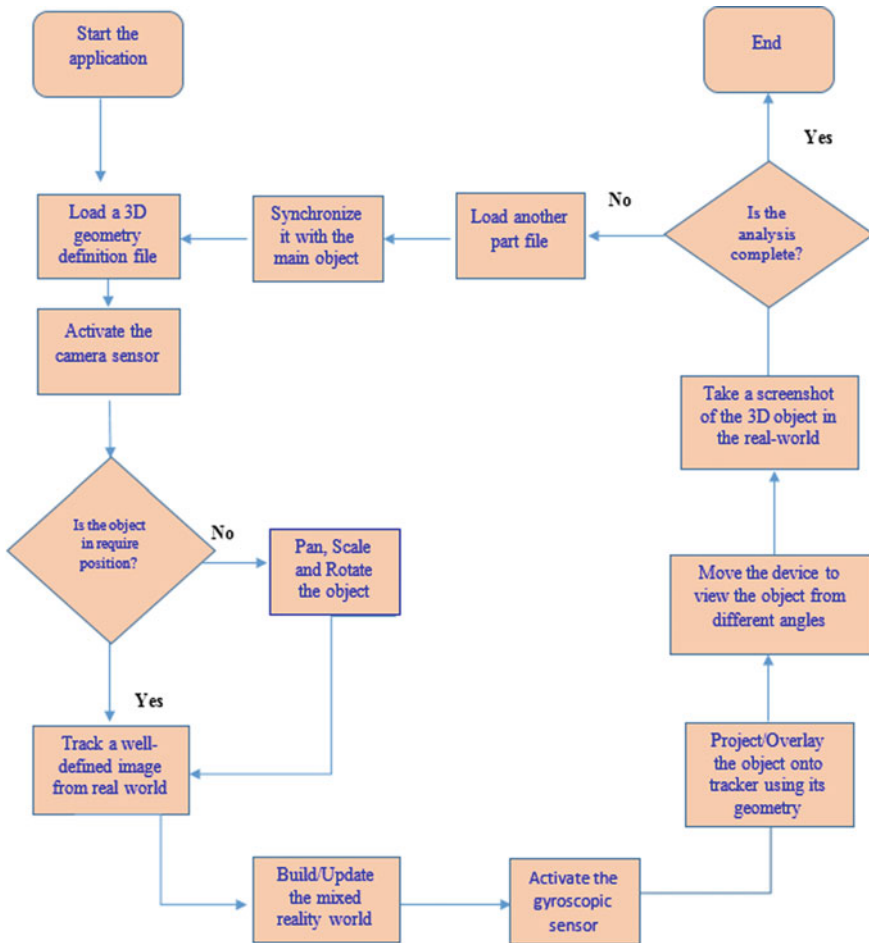
Fig. 1 Application solution procedure

3 Results and Discussion

Augmented reality-based simulation of developed methodology has been performed for a chosen benchmark problem. Therefore, spring–mass problem has been simulated in augmented reality and augmented reality simulation is performed. The following equation of motion is used for spring–mass simulation (Fig. 2).

$$mx + kx = \ddot{F}_0 \cos \omega t \tag{1}$$

Fig. 2 Augmented reality
application to represents the
dynamic model
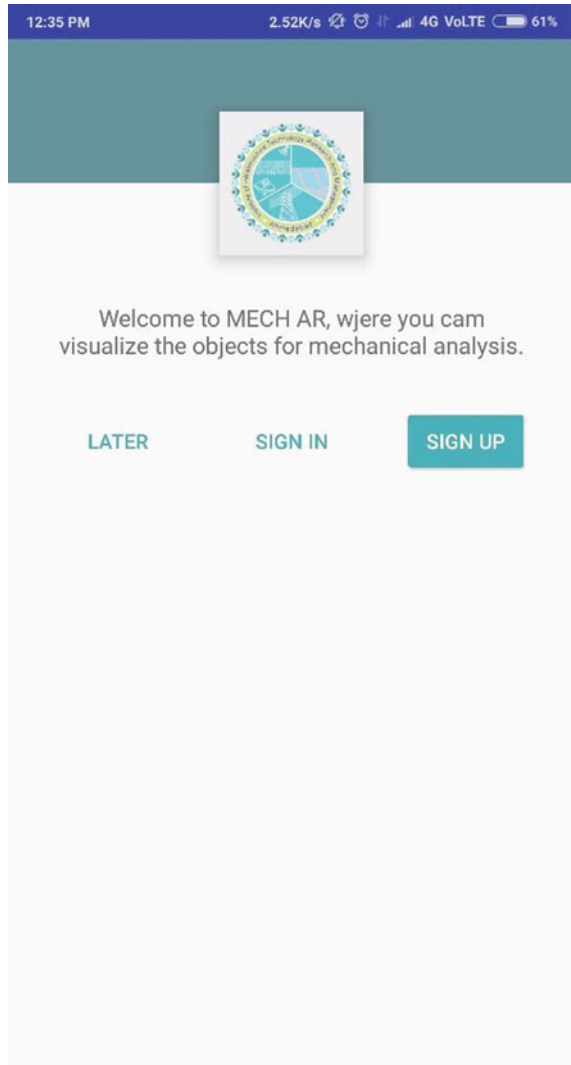
OBJ file for augmented reality has been generated by using MATLAB.
Therefore, a specialized program for augmented object generation and tracking is
generated. Figure 3 shows the dynamic response of spring–mass system with time.

In Fig. 4, the augmented object has been shown for a vibrating object with
spring. The complete simulation has been performed in software MATLAB 2016
on Windows 7 and Unity3D on Android 7.0. The hardware used in the system is
Xenon processor-based Dell Precision Desktop and REDMI Note 5.
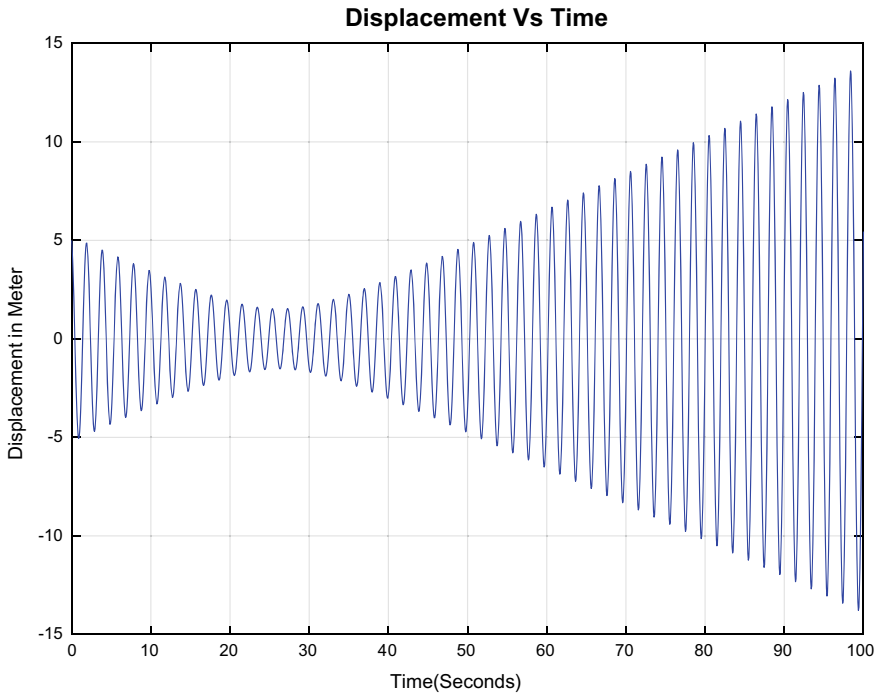
Fig. 3 Augmented simulation results

We can also apply the results of present methodology to the problem [9, 10], which deals with the analysis of 2-link robot system to get augmented reality-based simulation.

4 Conclusion

In this paper, an augmented reality-based dynamic simulation has been proposed which integrates and presents a scientific visualization method. A novel Android application interface has been developed to enhance the visualization and interaction of dynamic nature. The complete process has been automated and it required computation process. The system has automated tracking method. With simplified and automated augmented interfaces, the user can modify the model and can apply the boundary condition in the system. The system is coupled with MATLAB and mobile AR platforms to investigate the outdoor and the on-site dynamic analysis. On the basis of the approach developed, the following conclusions have been drawn.

Fig. 4 Vibrating object augmented reality simulation
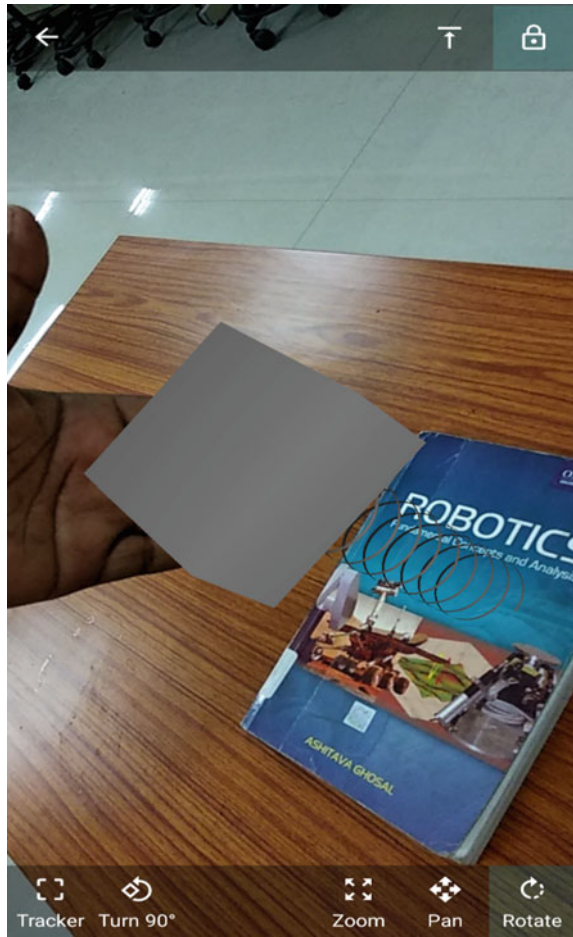
1. A successful implementation of a benchmark problem of vibration analysis is done by using augmented reality. The implementation of this problem will open doors for others to develop augmented reality applications.
2. The developed method will be quite useful for the dynamic analysis of mechanical engineering simulation.
3. Further, the work can be applied for rotor dynamic analysis, XFEM stress analysis and vibration of plates.

References

1. Azuma RT (1997) A survey of augmented reality. Presence Teleoperators Virtual Environ 6 (4):355–385
2. Navab N et al (2012) First deployments of augmented reality in operating rooms. Computer 45(7):48–55
3. Miyashita T et al (2008) An augmented reality museum guide. In: Proceedings of the 7th IEEE/ACM international symposium on mixed and augmented reality. IEEE Computer Society
4. Billinghurst M, Duenser A (2012) Augmented reality in the classroom. Computer 45(7):56–63
5. Dong F-H (2018) Virtual reality research on vibration characteristics of long-span bridges with considering vehicle and wind loads based on neural networks and finite element method. Neural Comput Appl 29(5):1303–1309
6. Huang J, Ong S-K, Nee AY (2017) Visualization and interaction of finite element analysis in augmented reality. Comput Aided Des 84:1–14
7. Liverani A, Kuester F, Hamann B (1999) Towards interactive finite element analysis of shell structures in virtual reality. In: IEEE international conference on information visualization (Cat. No. PR00210)
8. Li W, Nee A, Ong S (2017) A state-of-the-art review of augmented reality in engineering analysis and simulation, vol 1
9. Singla R, Agarwal V, Parthasarathy H (2015) Statistical analysis of tracking and parametric estimation errors in a 2-link robot based on Lyapunov function. Non-linear Dyn 82:217–238
10. Singla R, Parthasarathy H, Agarwal V, Rana R (2016) Feedback optimization problem for master-slave teleoperation tracking in the presence of random noise in dynamics and feedback. Non-linear Dyn 86:559–586

Comprehensive Review on Hybrid Vehicle Powertrain

Shivam Mahajan, **Jai Prakash Sharma**, **K. Aditya**,
Himanshu Gupta and **Kunal Singh**

Abstract In the automobile sector, the use of a hybrid powertrain is considered as one of the essential steps for reducing environmental temperature and pollution. The demand for non-polluted renewable fuel, especially for light-duty vehicles continues to increase with economic growth and development of the nation. With regard, the upgrading technology of current hybrid electric vehicles can be considered as progression in this field of developing zero emission. The main purpose of the present work is to compare the functionality of series, parallel, and combined hybrid powertrains. This article also explained the favorable and unfavorable areas of all configurations that are usually faced by the owner. The functionality of hybrid powertrain used in the Maruti Suzuki Ciaz is also explained in the article. Hybrid vehicles are far more fuel efficient and emit fewer greenhouse gases as compared to the conventional gasoline light-duty vehicles. The hybridization of vehicles could assist in solving the greenhouse gas emission and global warming. This paper provides a glimpse of the upgraded technology and production capacity of all the hybrid configurations in vehicles. The use of upgraded hybrid technologies in the vehicle is not only economical but also environment-friendly. The emission of carbon monoxide (CO), nitrogenous product (NOx), and hydrocarbon (HC) are effectively checked with the vehicle that uses hybrid technology.

Keywords Hybrid vehicles · Engine simulation · Regenerative braking ·
Energy saving · Zero emission · Conventional vehicle

S. Mahajan (✉) · J. P. Sharma · K. Aditya · H. Gupta · K. Singh
Department of Mechanical Engineering, Manav Rachna University,
Faridabad, Haryana, India
e-mail: mahajanshivam18@gmail.com

1   Introduction

A conventional fuel vehicle is a vehicle that runs on one power output that mean's power generates by internal combustion engine (ICE). Due to the presence of many factors, such as environmental pollution, high oil prices day by day, and low-quality oil, the dependence on conventional vehicle is not possible for any country, so the countries have to shift toward the hybrid vehicle and new technology power system that help us to fight against the major problem of global emission, and now it becomes a high priority for many governments and vehicle manufacturing vompany around the world. The major causes of emission are saturated or unsaturated unburnt hydrocarbon (HC), carbon oxides (COx), nitrogen oxides (NOx), sulfur oxide (SOx), and solid particulars [1].

The vehicle which uses two or more different types of power sources to run the vehicles is known as a hybrid vehicle like electric and fuel, solar and fuel, and electric and solar. The most common type of hybrid vehicle is a hybrid electric vehicle (HEVs), which combines the power of ICE that means gasoline power and electric power of more than one motor with battery. A hybrid vehicle uses multiple propelling forces that provide motive power to move vehicles [2]. The main motive of the electric vehicle powertrain is to attain better fuel conservation than a conventional vehicle for achieving better efficacy [3].

2   Hybrid Vehicle Power Train Configurations

A hybrid electric vehicle can be designed with the many types of technological framework, namely parallel hybrid, series hybrid, or combined hybrid (power split).

2.1   Series Hybrid

In the series hybrid, the heat engine inculcates a power which is directly used by electric generator instead of direct contact with the wheels. And, the output power of the engine is stored in a battery that conveys through the motor to the rear wheel and front wheel depend on drive assembly that is shown in Fig. 1. When we necessitate ample amounts of power like when a vehicle drive on a hilly area and high pitch area where high torque is required, then the motor take electricity from the generator as well as battery both because of high power requirement.

The combustion engine of the series hybrid is smaller in size because it has to meet with a certain power requirement; because of large battery storage and powerful than parallel hybrids in order to provide the extra power needs and effective in extensive city driving [4]. The examples are: Honda Insight, Honda Accord, and Renault Kangoo, etc.
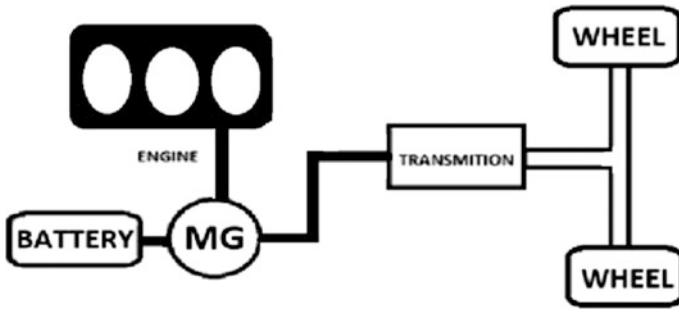
Fig. 1 Block diagram of series hybrid

2.2 Parallel Hybrid

In a parallel hybrid system, power comes from both engine and an electric motor which is parallelly connected with power transmission. In this hybrid vehicle, the electric motor and ICE are settled such that it produce and gave power to the vehicle either discretely or as one that is shown in Fig. 2. On recent researches, most of ICE, the gear box and electric motor are coupled by automatically controlled clutches or multi-plate clutches [5].

In parallel hybrid vehicle, there is another source to charge the battery with the help of regenerating braking system and excess power output of engine that is not required for that speed. There is a permanent shaft between the wheels and the motor. One major disadvantage is battery cannot be charged when the vehicle is at steady state. The examples are: Lohner-Porsche Mixte Hybrid, Ferdinand Porsche, and Honda Civic etc.

Fig. 2 Block diagram of parallel hybrid
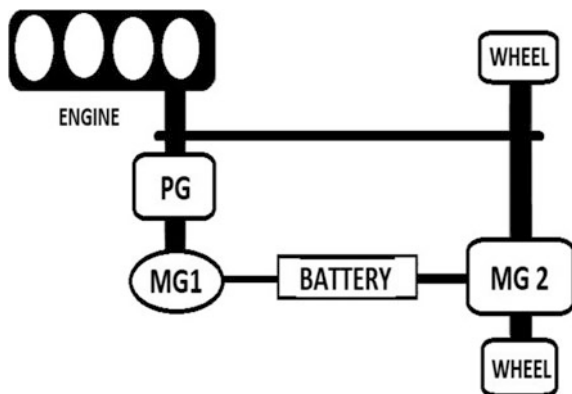
2.3   *Combined Hybrid (Power Split Hybrid)*

Combined hybrid systems have characteristics of both parallel and series hybrids. There is a duos connection between the engine and the driven axle: electrical as well as mechanical both that is shown in Fig. 3. The interconnecting power of electrical and mechanical makes the hybrid vehicle very complicated [6]. The power transmit to the wheels can be either electrical or mechanical or both. Parallel hybrids also show this phenomenon of combined hybrid powertrain [7].

As conclude, power split hybrid are more effective because series hybrids are more efficient at lower speeds and parallel tend to be more efficient at high speeds; however, the cost of combined hybrid is higher than parallel hybrid because combined powertrain merge the benefits and complexity of series and parallel powertrain. Examples: Lexus RX, BMW X6, Lexus GS450, etc. (Table 1).

3   On the Basis of Electric Vehicle Speed Configuration

3.1   *Single-Speed Vehicle Configuration*

The main difference between the electric motor car and the conventional car is their powertrain. The conventional car has a multi-speed gearbox that allows better gearing for different speeds ratio, and mostly electric vehicle comes with single-speed configuration, including the Nissan Leaf, BMW i3, and generally all Tesla models. Tesla Model S comes with single-speed gearbox having a ratio of 9.7 [8]. Electric vehicle generates 100% of their torque as soon as they activate the motor. Generally, the combinations of ability to meet an inclusive range of driving handle condition using the electric motor and the desire for high efficacy. The desired performance of the electric vehicle depends on motor design because drivetrain have one and final gear ratio.

Fig. 3 Block diagram of combined hybrid
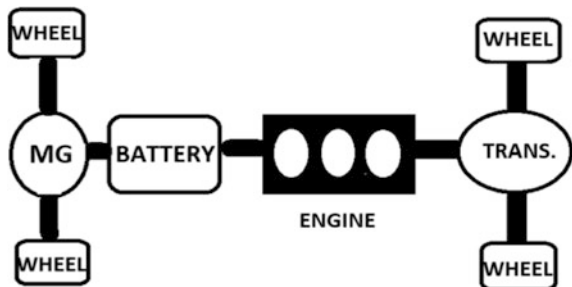
Table 1 It shows the advantage and disadvantage of all hybrid vehicle powertrain

Vehicle configuration	Advantages	Disadvantages
Series hybrid	No direct linking between engines to wheel ICE can be usually stop at zero emission areas Fewer floors require	Due to energy conversion there is energy loss too This hybrid is mostly suitable for city driving Weight, cost and size of the powertrain can be unreasonable
Parallel hybrid	ICE directly connected to wheels; then less power loss Most of the parallel hybrid vehicle doesn't require generator It gives better efficiency during long distance driving	Floor requirement is large There is not constant RPM range in ICEs, thus there is loss in efficiency Too much complicated system
Combined hybrid	ICE can be turned off when battery is full charge or at zero emission zones ICE speed can be chosen by adjusting generator speed Decoupling of the power supplied by the engine that allows for a smaller, lighter, and more efficient ICE design	Power vicious cycle may lead to low efficacy Relatively complex in structure Due to complicated assembled part, this hybrid is more expensive than parallel hybrid

3.2 Two, Three, and Four Speeds Vehicle Configuration

A two-speed or even multi-speed electric vehicles, having a high-speed ratio, and high economic requirements of driving of the vehicle from the torque power to the motor speed with the technology of multiple speed gear ratios likely improve the overall performance of the hybrid electric vehicle. It is completely feasible to design a vehicle having multiple gear ratios but it is completely unnecessary what is being demanded from the motor output. The designing of multi-speed gear ratio into the electric hybrid vehicle is possible but it creates complexity, having extra weight that decreases the overall efficiency of the hybrid vehicle.

The multiple speeds transmissions having two parallel gears that are coupled with a single common clutch with the electric motor. Generally, multiple gears system require a synchronize device for changing gears but in two-speed gear transmission system, it does not require any synchronizer for shifting because shifting is performed between the clutch. But in a three-speed transmission system, a synchronizer pair is used for first and third gears to select alternate gear ratios, while in the four-speed gear ratio structure, it has two synchronizers pairs. The decrease in efficiency is viewed in different components [9], in the driveline, and there are several losses which are present:

- Differential having 5% (approx.) loss
- Single gear friction having 1% (approx.) loss
- Single gear viscous having 1% (approx.) loss

- Due to wet clutches 2–3% loss
- In dynchronizer mechanism device having 1–2% loss.
- Other losses are also occurring (about 4–5% higher) when dry clutches were used instead of wet clutches, and gear to gear losses are also increased by 2–3% [9].

4   Technologies Used in Hybrid Cars

The hybrid vehicles have significant technology that helps us to provide better efficacy and save fuel during that time:

Braking Regeneration: The electric motor applied resistance (obstruct) to slow down the wheels of vehicle. In return, the inertia of wheels rotates the motor in opposite direction that is recaptured by generator and convert waste energy of coasting or braking into electricity, which is further stored [10].

Electric Motor Drive: The electric motor supply extreme power to driveline of heat engine while accelerating in pitching or inclined areas. In most of the areas, the motor is only responsible for providing power in low-speed driving requirement where heat engines are not more efficient. In several vehicles, the power for low-velocity conditions are transmitted by the motor itself and it is eco-friendlier as compared to the conventional vehicle.

Automatic ignition on/off: Self-executing technology shuts off the heat engine when the vehicle is at idling state and restarts the engine when accelerating. According to the research, the highest air pollution is recorded in the vicinity of traffic lights areas. Therefore, a new hybrid technology could help in reducing the pollution in those areas along with less energy consumption in heavy traffic driving [10].

5   Analysis

Hybrid vehicles are more fuel efficient; like two to three times than conventional vehicle. That means the hybrid vehicle can exhale only one-third to one-half of the greenhouse gases as compared to conventional gasoline cars (petrol or diesel cars). As we see normal vehicles are one of the tremendous contributors to a global warming, for this reason, hybrid vehicle plays an important role or a significant contribution to fight against global warming problem.

In addition, hybrids also have a function to automatically shutoff the heat engine when the vehicle is in the rest state that is why these vehicles are efficient at traffic lights [11]. All this new technology comes with very high price than a conventional vehicle because manufacturing of hybrid vehicle is complex to assemble and the parts are also expensive than normal vehicles because of these technologies like a regenerative braking system, batteries, and using of more than one motors. Sometimes, the owner of the hybrid vehicle can spend more time in the repairer

shop with a high repairer bill. Hybrid vehicle is not only responsible for generating low pollution is also responsible for less noise pollution because nowadays, noise pollution is being a big issue of World Health Organization but indirectly, this technology is unsafe to those who rely with their ears that means visually impaired who determine the road with the noise of vehicle whether it is safe to cross the road or walk through a parking area [12]. Mostly, hybrid vehicle has two types of batteries: (1) nickel metal hydride or (2) lithium-ion battery; both are regarded as more environmentally friendly than lead-based batteries that incredibly bad for the environment [13].

There is no need of any change when drive hybrid vehicle because these vehicles also take gasoline from fuel stations to operate exactly the same as conventional gasoline vehicles but the technology used in hybrid vehicle is apart from conventional vehicle. That is proving with these points of hybrid vehicle over conventional vehicle:

- Energy loss during braking is minimizing in hybrid vehicle.
- There is no requirement of high peak load of engine so it reduces the engine weight as compare to normal vehicle.
- Hybrid vehicle is more fuel efficient than conventional vehicle. It also runs with zero emission in highly polluted areas.
- Hybrid vehicle using alternative fuels so it does not depend on fossil fuels only [14].

6 Hybrid Powertrain Used in Maruti Suzuki Ciaz

Maruti's new Ciaz known as Smart Hybrid Vehicle System (SHVS) uses an upgraded version of starter motor through which power is transmitted with the help of belt drive that connect with the engine. This technical arrangement makes them completely quiet at the starting of vehicle. The Maruti Ciaz performs three general purposes: Hybrid electric motor that connect with engine, starter motor, and use generator to charge the battery when the car apply brake or when it reduces their speed.

- The Maruti hybrid Ciaz also has an arrangement of start/stop and save fuel when the car is at traffic light areas. The engine will restart instantly when the clutch is released and works very silently because starter motor starts the engine with a belt drive rather than the noisy gear.
- The Maruti Suzuki Ciaz Hybrid's braking system, coupled with Integrated Starter Generator that helps the engine in start–stop technology that automatically stops the engine at a traffic area and start when releasing the clutch.
- With all these features the Maruti Ciaz Hybrid has a mileage of over 28.09 km in 1 liter of diesel.
- Ciaz have a power of 88.5 bhp @ 4000 RPM with 200 Nm @ 1750 RPM torque.

Although it has basic start-stop system that only comes into play when the car comes to a halt, there is already a more advanced system that works even when the car is in motion. This system cuts off the engine but continues to run all the car's equipment's like power steering, brake regenerative boosters, climate control sensors, and electronic systems with the help of an electric generator [15].

7 Conclusion

After reading this paper, the developing need for the hybrid vehicle for a sustainable transportation system is efficiently demonstrated. This paper shows all beneficial and critical areas for all hybrid configurations, and the problem faced by the owner in different situations with the impressive new technology of hybrid electric vehicle. Hybrid vehicles not only offer a great encroachment of air emissions, it also helps us to save the unnecessary use of fuel with their new technology to minimize losses that occur during ideal and moving state. It is concluded that Hybrid Electric Vehicles (HEVs) is able to merge the power generated by electric motors and heat engines. In this configuration, both the sources can be employed either in combination or individually as per the requirements.

References

1. Ganesan V (2012) Internal combustion engines. McGraw Hill Education (India) Pvt Ltd
2. Neubauer JS, Wood E, Pesaran A (2015) A second life for electric vehicle batteries: answering questions on battery degradation and value. SAE Int J Mater Manuf 8:544–553
3. Pesaran A, Santhanagopalan S, Kim GH (2013) Addressing the impact of temperature extremes on large format li-ion batteries for vehicle applications (presentation). National Renewable Energy Lab. (NREL), Golden, CO (United States)
4. Subramoniam C, Mugilan M, Krishna BV, Harne V (2015) Hybrid powertrain smoothness improvement. In: 2015 IEEE international transportation electrification conference (ITEC). IEEE, pp 1–7
5. Shirk M, Gray T, Wishart J (2014) 2011 Hyundai sonata 3539-hybrid electric vehicle battery test results. Idaho National Laboratory (INL)
6. Kim N, Cha S, Peng H (2011) Optimal control of hybrid electric vehicles based on Pontryagin's minimum principle. IEEE Trans Control Syst Technol 19:1279–1287
7. Balmoor P, Boorgu H, Cummiskey R, Einhorn J, Gunay G, Kodandapani P, Min JKJ, Nelson A, Song D, Timothy S (2009) Better place feasibility study: first draft
8. Trade (2017) New, A.A.I.B. with a P. for I.E. with, book, exciting technologies H. is also a published children's book author whose most recent, Vehicles, Z.G. the, Engineering, I.A. at I.Y.K. to H. an I. in: Why do electric cars only have one gear? http://shortsleeveandtieclub.com/why-do-electric-cars-only-have-one-gear/

9. Zhou X, Walker P, Zhang N, Zhu B, Ruan J (2014) Numerical and experimental investigation of drag torque in a two-speed dual clutch transmission. Mech Mach Theory 79:46–63

10. How hybrids work. https://fueleconomy.gov/feg/hybridtech.shtml

11. Taymaz I, Benli M (2014) Emissions and fuel economy for a hybrid vehicle. Fuel 115:812–817

12. Information on http://www.noiseoff.org/evs.php

13. Smith K, Warleywine M, Wood E, Neubauer J, Pesaran A (2012) Comparison of plug-in hybrid electric vehicle battery life across geographies and drive-cycles. National Renewable Energy Laboratory (NREL), Golden, CO

14. http://ode.engin.umich.edu/publications/PapalambrosReports/ComparativeStudyofSeriesandParallelHybridVehicles.pdf

15. Maruti Suzuki Ciaz Diesel Hybrid technology and features explained-ZigWheels. https://www.zigwheels.com/news-features/news/maruti-suzuki-ciaz-diesel-hybridtechnology-and-features-explained/22929/

Kinematic Synthesis of a Crossed Four-Bar Steering Linkage for Automobiles

Santiranjan Pramanik and Sukrut Shrikant Thipse

Abstract A crossed four-bar mechanism has been synthesized in a recent work using Hooke and Jeeves optimization method. The maximum rotation of the outer wheel is 49°. The track-to-wheelbase ratio is four-tenth. In the present work, kinematic synthesis has been carried out using precision point technique for a benchmark vehicle with track-to-wheelbase ratio of 0.326. There are two design parameters only. The mechanism has two equal links which are the input and output links. The nondimensional length of these links is one design parameter. The other design parameter is the angle of inclination of these links with the longitudinal axis of the vehicle. Two nonlinear equations have been obtained in this synthesis. These are solved using Newton–Raphson method. Five precision points have been obtained with maximum steering error of 0.01°. The mechanism needs two equal spur or helical gears to be added to it so that it can produce a coordinated motion of the front wheels. It has been found that the present method is more efficient than the Hooke and Jeeves method since less number of iterations are required by this method.

Keywords Kinematic synthesis · Crossed Four-bar mechanism · Algebraic method · Newton–Raphson method · Steering mechanism · Steering error

S. Pramanik (✉)
Symbiosis International (Deemed University), Lavale, Mulshi, Pune 411042, India
e-mail: santiranjan_pramanik@rediffmail.com

S. Pramanik
College of Military Engineering, Pune 411031, India

S. S. Thipse
The Automotive Research Association of India, Pune 411004, India

503

1 Introduction

Steering mechanisms are very important for four-wheel vehicle for cornering motions as accurately as possible. The design of steering mechanism should be such that there is pure rolling motion of the wheels of the vehicles. There are several types of steering mechanisms. The simplest mechanism is the four-bar mechanism popularly known as Ackermann steering. This mechanism has four links out of which two links are equal in length and other two links are unequal. The Ackermann steering has progressive deviation in the steering error curve at the end of rotation of inner wheel. Fahey and Huston [1] modified an Ackermann steering to an eight-bar mechanism to increase the number of precision points in the error curve in an extended range of motion. They considered the rotation of inner wheel up to 61°. The maximum steering error is 0.03° only. But the whole mechanism is placed ahead of the front axle. Also, there are two small links in the mechanism and this disproportionate link is the cause of reduction of accuracy in the long run. That is why their mechanism is not implemented in practice. A lot of research has been carried out to improve the steering accuracy of the four-wheel vehicles.

Pramanik and Thipse [2] considered a crossed four-bar mechanism (CFBM) for investigating its performance in regard to steering accuracy and transmission angle. In comparison to Ackermann steering, CFBM has more number of precision points in the error curve. They used Hooke and Jeeves method (HJM) to optimize the mechanism. In the present work, algebraic method is used to synthesize the mechanism. The procedure leads to a set of two nonlinear equations which are solved by Newton–Raphson method (NRM). It has been found that both synthesis methods are accurate but the NRM is more efficient as less number of iterations are required by this method to achieve the final solution.

2 Crossed Four-Bar Mechanism

The crossed four-bar mechanism has been shown by linkage AGFB in the mean position while the vehicle moves along a straight path. In this mechanism links AG and BF are equal in length. These two links make equal angles with the vehicle longitudinal axis. This means that the angles KAG and FBH are equal. These angles are equal to β, one design parameter k_2. The distance AB is taken as d. The steering arm AG is equal to r and r/d is k_1, another design parameter. Two spur gears are used for producing coordinated motion of the two front wheels.

When the outer wheel rotates by angle GAD or α, then the inner wheel rotates by angle FBE, i.e., θ. So using Ackermann formula, we write the following ideal equation.

Fig. 1 A crossed four-bar
steering mechanism
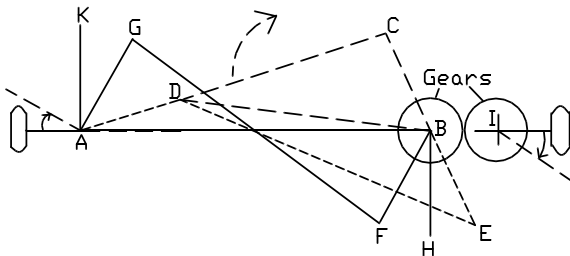
$$\cot \alpha - \cot \theta = t/w \qquad (1)$$

In the above equation, t is the wheel track AI and w is wheelbase.
By referring to Fig. 1, the coordinates of the points D and E are as under:

$$D = \{r \sin(\beta + \alpha), -r \cos(\beta + \alpha)\} \quad \text{and } E = \{d + r \sin(\theta - \beta), r \cos(\theta - \beta)\}$$

Now, $DE^2 = GF^2$ gives the following relation.

$$\{d + r \sin(\theta - \beta) - r \sin(\beta + \alpha)\}^2 + \{r \cos(\theta - \beta) + r \cos(\beta + \alpha)\}^2$$
$$= (d - 2r \sin \beta)^2 + (2r \cos \beta)^2$$

Writing $r/d = k_1$ and $\beta = k_2$, we get

$$\{1 + k_1 \sin(\theta - k_2) - k_1 \sin(k_2 + \alpha)\}^2 + k_1^2 \{\cos(\theta - k_2) + \cos(k_2 + \alpha)\}^2$$
$$= \{1 - 2k_1 \sin(k_2)\}^2 + 4k_1^2 \cos^2(k_2)$$

or,

$$k_1^2 \{\sin(\theta - k_2) - \sin(k_2 + \alpha)\}^2 + 2k_1 \{\sin(\theta - k_2) - \sin(k_2 + \alpha)\} + k_1^2 \{\cos(\theta -$$
$$k_2) + \cos(k_2 + \alpha)\}^2 = -4k_1 \sin(k_2) + 4k_1^2 \qquad (2)$$

or,

$$k_1^2 \{2 + 2 \sin(k_2 - \theta) \sin(k_2 + \alpha) + 2 \cos(k_2 - \theta)\cos(k_2 + \alpha)\} - 2k_1 \{\sin(k_2 -$$
$$\theta) + \sin(k_2 + \alpha)\} = -4k_1 \sin(k_2) + 4k_1^2$$

or,　　$$-2k_1^2 + 2k_1^2 \cos(\alpha + \theta) = 2k_1 \{\sin(k_2 - \theta) + \sin(k_2 + \alpha)\} - 4k_1 \sin(k_2)$$

or,　　$$k_1 \{\cos(\alpha + \theta) - 1\} - \sin(k_2 - \theta) - \sin(k_2 + \alpha) + 2 \sin(k_2) = 0$$

3　Numerical Analysis and Result

The Newton–Raphson method has been used to solve the nonlinear equations
involving two design parameters. The Eq. (2) can be rewritten as

$$y = 0 \tag{3}$$

When (α, θ) combination is replaced by (α_i, θ_i) in the Eq. (3), then y is replaced by y_i where $i = 1, 2$. This gives two equations with two unknowns. The function y_i can be written as

$$y_i = y_i(k_1, k_2) \tag{4}$$

The initial estimates for the roots of the system of equations have been taken as under:

$$r = 0; \quad K_{10} = r/d = 0$$
$$\beta = 0; \quad K_{20} = \beta = 0$$

Let K_{10} and K_{20} be the initial estimates of the design parameters. Let ΔK_1 and ΔK_2 be the respective corrections so that the Eq. (4) are satisfied, i.e.,

$$f_1(K_{10} + \Delta K_1, K_{20} + \Delta K_2) = y_1$$
$$f_2(K_{10} + \Delta K_1, K_{20} + \Delta K_2) = y_2 \tag{5}$$

Expanding the Eq. (5) by Taylor's theorem about the initial solution and neglecting the higher order terms, we obtain the following matrix equation.

$$\begin{bmatrix} y1 - f1(K10, K20) \\ y2 - f2(K10, K20) \end{bmatrix} = \begin{bmatrix} \partial f1/\partial K1 & \partial f1/\partial K2 \\ \partial f2/\partial K1 & \partial f2/\partial K2 \end{bmatrix} \begin{bmatrix} \Delta K1 \\ \Delta K2 \end{bmatrix}$$

This can be written as

$$P = [J]Q$$
$$\text{or} \quad Q = [J]^{-1}P$$

where [J] is called Jacobian Matrix, Q the correction vector, and P the error.

The correction thus obtained is used to update the initial estimate, i.e.,

$$K_{10'} = K_{10} + \Delta K_1 \text{ and}$$
$$K_{20'} = K_{20} + \Delta K_2$$

The wheel track-to-wheel base ratio has been taken as 0.326 from a benchmark vehicle. The precision points are taken as 27° and 40° rotations of the inner wheel.

The solution to the nonlinear equations is found as under:

$k_1 = 0.3833$; $k_2 = 0.4970$ rad= 28.48°.

The dimensions of various links are d = 10 unit; r = 3.833 unit; β = 28.48°.

The maximum value of the steering error is 0.007° over a range of rotation of 40° of the inner wheel.

4 Conclusion

The steering error curves have been shown in Fig. 2 to compare the accuracies of the two methods. It has been found that both methods are accurate but in the Hooke and Jeeves method, the designer has no control on the location of the precision points. In Newton–Raphson method the selected precision point is achieved. The steering range has been increased in Fig. 3 up to 60° and errors have been
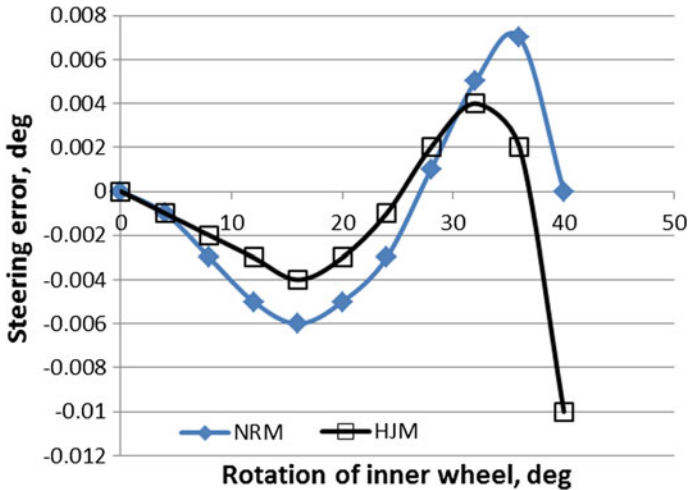
Fig. 2 Steering error curve
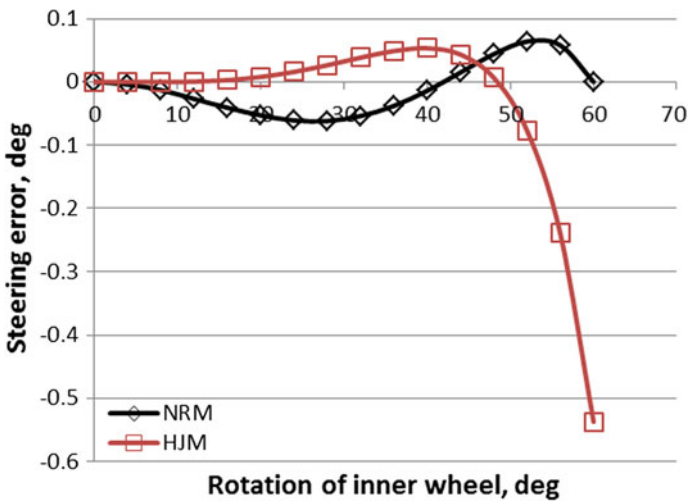
Fig. 3 Steering error curve
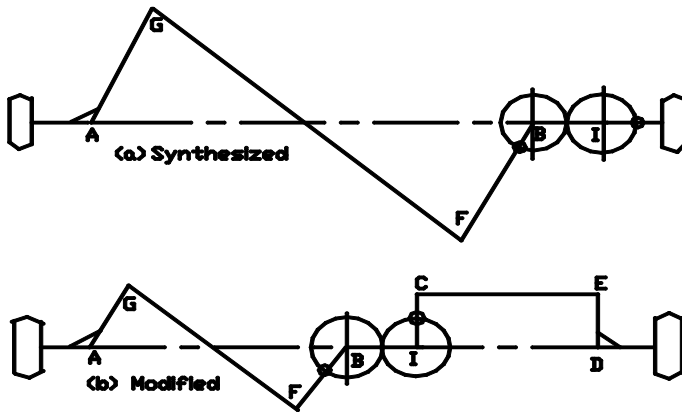
Fig. 4 Modification of steering mechanism

compared. It has been observed that in case of large rotation of the inner wheel, the divergent end behavior of the curve is more prominent for the Hooke and Jeeves method. In case of Newton–Raphson method, the initial solution of zero values of the design parameters can progress toward the final solution. This is not true for the other method. Hence, the algebraic method is better than the Hooke and Jeeves method. The length of steering arm is high and therefore, the mechanism has been reduced to half size and a parallelogram mechanism has been added in Fig. 4. In this way, the steering linkage has been reduced to acceptable size.

References

1. Fahey SO'F, Huston DR (1997) A novel automotive steering linkage. ASME J Mech Des 119:481–484
2. Pramanik S, Thipse SS (2017) Kinematic synthesis of a crossed four-bar mechanism for automotive steering. Int J Veh Struct Syst 9(3):169–171

Designing a Biomimetic Flapping-Wing Air Vehicle Capable of Controlled and Sustained Flight

Burela Ramesh Gupta, Kartikaye Uniyal and Anunay Kausteya

Abstract Flying vehicle that is propelled by flapping wings also known as flapping-wing air vehicles (FWAV)/Ornithopters has been a subject of exploration due of its possible use towards unmanned air vehicles (UAV), micro air vehicles (MAVs). Birds and insects fly with unprecedented agility in flight. These FWAVs seek to mimic the motions of such naturally found species. They can find their use in military surveillance or for forestry and wildlife survey. Ornithopters are vehicles that generate the necessary thrust and lift by flapping motion. This exploration work contains a detailed description of the mechanical and the electrical systems used in the FWAV. This paper also focuses on the production process involved in the making of FWAV. This paper also gives an insight about the initial control experiments that were performed. Instead of focusing on problems of small MAV which revolves around miniaturization of the mechanism and electrical energy storage. Our work concerns itself more with the topic of robot locomotion. Thus, it will give details about how one can achieve better stability and control on the flight of an Ornithopter. The developed FWAV has a wingspan of 1.17 m, designed for a kerb weight of 1000 grams. The prototype has been designed specifically for the use of exploration. The designing make extra efforts to enhance payload size, control stabilization, wing efficiency and crash survivability.

Keywords Ornithopter · FWAV · Flapping wing

B. Ramesh Gupta (✉) · K. Uniyal (✉) · A. Kausteya
Shiv Nadar University, Greater Noida 201314, UP, India
e-mail: rg468@snu.edu.in

K. Uniyal
e-mail: uniyalkatikaye@gmail.com

1 Introduction

In cutting-edge years, the improvement and exploration done on the flapping wing are getting the upward push. That is because of the development of the technology of micro additives consisting of an electric motor. The army specifically may be very interested in its improvement. Though, the exploration is in particularly new, there is some achievement within the try to simulate the bird's flight. Due to the present day enhancements in other unmanned aerial cars (UAVS), the progress of flapping wing MAV has been slowing behind, because of the complication of the layout and the unstable aerodynamic effects of the flapping wing. Flapping wing MAV have been regularly being picked up and exploration similarly. The flapping wing MAV has a couple of advantages in comparison to the alternative sorts of MAV (quadcopters, single rotor drones, double rotor drones, helicopter drones and so forth). Flapping wing MAV is capable to float and might achieve this instead of making a lot of noise. But the most notable advantage is that it mimics either an insect or a bird. Be it at the war zone or for exploration of wildlife in which mixing among the encompassing and no longer being found is key to the success of mission. Flapping wing MAV can be classified into: Entomopters (like insect— flapping) and Ornithopters (bird like flapping). While the entomopters is capable of flying; the ornithopter is able to best flying ahead and float as well.

On these studies, a new kind is developed to carry the payload. First, three birds resembling FWAV, which has more than one wings, as a biomimetic, is fabricated; layout is built totally on the features of formerly superior FWAVs. The goal is to manufacture the prototype which is lightweight and cost-effective, so as to make the product commercially viable (Table 1).

Table 1 Overview of investigated FWAV

Parameter	Model	
	Park Hawk design by Sean Kinkade [1]	Phoneix (MIT) [1]
Wing size	1.3 m	1.8 m
Fuselage length	28 cm	32 cm
Weight	395 g	1197 g
Stroke angle	10–30°	25–40°
Max frequency	12 Hz	15 Hz

2 Process of Production and Design

The general format and production manner is offered in Fig. 1. Layout specs for a successful flight are described in desk 1. As an example, numerous situations along with the fuselage length, flight time and wing length are decided.

The following steps will be able to pick out additives inside the layout of an FWAV. The detailed mechanism of flapping by using SolidWorks software program, fuselage and wings are designed. The design of this step is also determined by the association of several components of electronic nature together with a pace controller, a transmitter and a battery
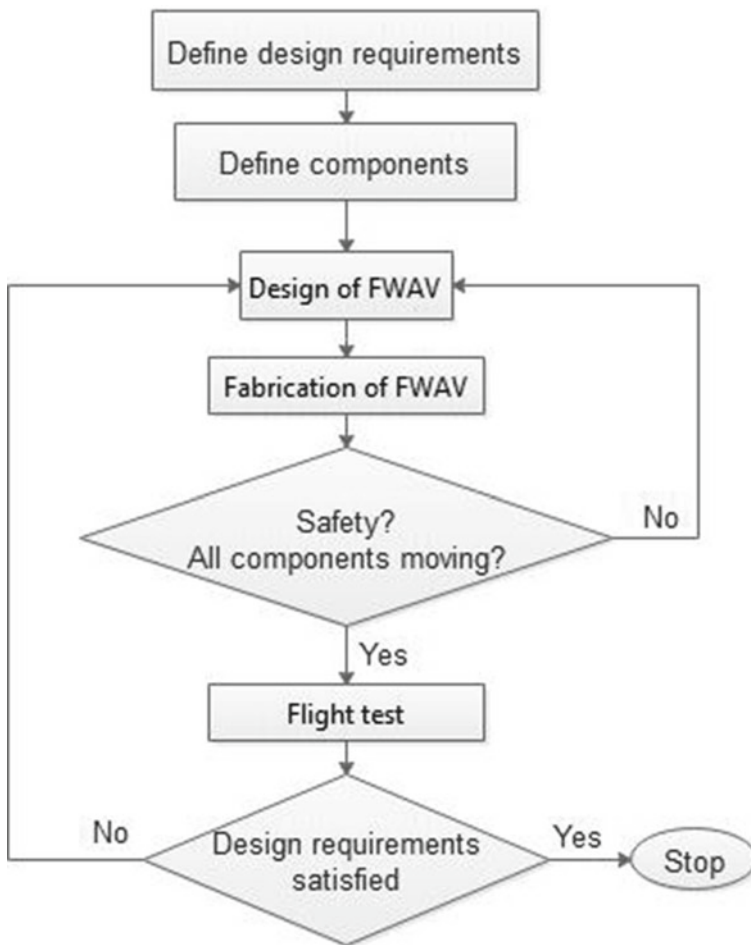
Fig. 1 The design and production process of the FWAV [2]

Afterwards, the layout step of each part is fabricated using several production techniques with excessive precision of the FWAV. Several elements of subsystems are to be assembled, after being made separately. The tolerance and accuracy of the elements are checked throughout the metric system. In further steps, the FWAV that has been assembled is the specific layout of the FWAV. When manufactured, the flapping wing movement should comply with the initial layout and design for the flapping wing mechanism.

Else, the required procedure will go back to the previous step as explained by the flow diagram in Fig. 1. This process is repeated until the working of all the subsystems is achieved. At the last step, the layout needs to be described at step one and is checked via the test of flight. The flight time and most of the frequencies are specifically checked in this step. If the design requirements are not reached, the design will be further changed according to the needs and the process will be repeated once more. If the design requirements are satisfied, the format and production techniques are further decided.

2.1 CAD Design

In the design criteria, using the dimensions (Table 2), using SolidWorks a CAD design was modelled. This could integrate a horizontal stabilizer tail design and a transverse shaft mechanism. Both roll control and pitch can be provided, here the design of horizontal stabilizer tail was chosen. The preliminary design (CAD model) is shown in Fig. 2.

Table 2 The bird mimicking FWAV design requirements definition

ITEMS	Design Req.
Wing type	A pair of wings
Wing size	1–1.5 m
Fuselage length	30 m
Weight	1000 grams (at max)
Stroke angle	40–50°
Maximum frequency	5
Flight time	>10 Min

Fig. 2 CAD model
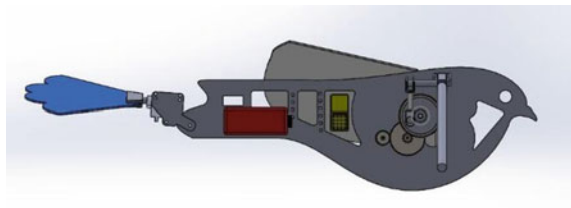
Table 3 Weights of individual components

Components	Weight	Unit
BLDC motor	72	g
Receiver of Radio	10	g
Servos	32	g
Battery Li Po	152	g
Controller electronic speed	30	g
Fuselage	167	g
Transverse shaft	95	g
Gears	44	g
Tail holder	34	g
Wings	156	g
Tail	60	g

Initially, the components to be used were decided. After procurement of material, each component was weight as shown in Table 3. To compare the possible lift that can be generated, the components of total weight could be used.

2.1.1 CAD—Dimensions for Design

To determine accurately the payload for flight and dimensions, a lift equation was used. Some of the suppositions that have to be made prior to using this following equation:

(1) Due to assumptions made there are certain forces that contribute to the generation of lift while flapping will be neglected.
(2) The location of the wing and time do not affect the coefficient of lift.
(3) Blade element theory has been ignored by induced inflow. The rectangular wing-shaped equation for a lift could be expanded to, from the suppositions made

$$L = \frac{1}{3} \varphi^2 \pi^2 C_l \, \rho \, C_o \, l^3 \tag{1}$$

Table 4 Design parameters

Parameter	Values	Unit
Amplitude of flapping	40	Degree
frequency of flapping	4.603	Hz
Coefficient of lift	0.27	–
Density of air	1.225	Kg/m^3
Length of chord	0.27	M
Span of wing	o.54	M
Lift	9.514	N

where the angle of flapping is φ, the frequency of flapping is f, chord length is C_o and the length of wingspan is l. For a wing that is shaped rectangular this is the equation, however, the equation, as mentioned above, gives us only a preliminary estimate of the lift achieved, for the given specifications mentioned in Table 4.

2.2 Production Material

Balsa wood, carbon fibre and acrylic were the three materials being considered due to their high strength to weight ratios. The first material of choice was to use carbon fibre. Carbon fibre is relatively expensive and can only be laser cut, therefore, once the sheet is cut, it is difficult to do alteration with the fuselage as laser cutting can burn some of the components attached to the body. Balsa wood is a suitable material because it is extremely light and it is easy to machine it. However, the desired strength cannot be achieved with the use of balsa wood. Acrylic sheet and carbon fibre were the solitary choices remaining. Like carbon fibre, acrylic is not as strong and light but was used for the initial design. For precision cutting, Laser cutting machine was put to work. Later, medium-density fibreboard (MDF) was used to make the fuselage as it has better strength then acrylic sheet and is much lighter in weight.

2.3 Wings Design and Production

Crafted from spokes utilized in cycle; the wings have a triangular guide shape. A strut connects from the rear of the Ornithopter s body to a point near the stop of the number one spar and the primary spar runs along the main fringe of the wing. There are numerous small spokes that are joined together by welding, which contribute to the desired shape of the wing. The wing is connected with a small joint at the trailing edge. The wings have a triangular guide shape. There are support structures in form of additional wire structure to divide the load on the wing and in order to support the wing spar. The wing has three subparts a wing spar rod, wire support structure and thin slices of SELIG 1020 airfoil in between. The usage of
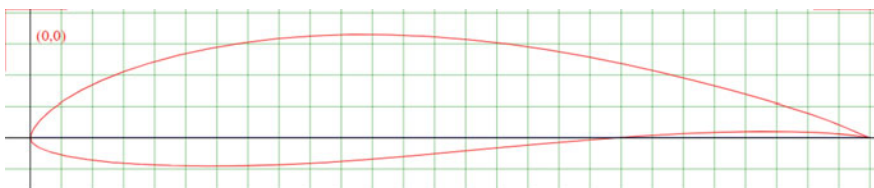
Fig. 3 Airfoil SEIG 1020

Fig. 4 Wing with wire mesh and slices of styrofoam sheets cut in the desired airfoil shape

these thin slices offers the popular airfoil form to the wings, at the same time, there may be minimal weight addition (Fig. 3).

'Because the lift coefficient of the rigid span wise is higher that that of the flexible span wise in unsteady state flight' [3], we used plastic(Nylon) rods to make the span structure of a mechanical Ornithopter which is sufficiently rigid. With wire mesh along the trailing edge, from a woven nylon membrane the wings are made, and near the tail to a point on the centreline, diagonally transverse masts from the leading edge, to the body by hinges at the centreline of the body the leading edge masts connect. 'The arrangement of the spars in the wings create a taught membrane most of the wing surface, with a small amount of flexing toward the wing tips. This flexing provides the forward thrust when the wings are flapping' [4] (Fig. 4).

2.4 Tail

With its intended use, the tail design varies. Only for stability, but in most cases, they are used for control. Around the angle 15° or less, the tail is tilted upwards mostly for the nose to pitch up. The more common designs that are put forth for control are the swinging and the tilting tail due to their simplicity. To a point when

Fig. 5 Swinging tail
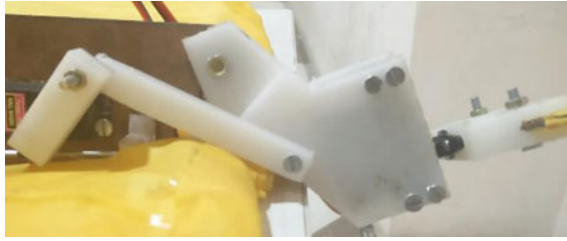
Fig. 6 Tilting tail

it swings, a rolling moment of the swinging tail works to either side. The tilting tail works like a rudder, when it rotates to the right it causes the MAV to tilt to the right side for pitch and rolling motion, a horizontal stabilizer can act as an aileron providing additional control. This design requires two servos to be used and a crank link to connect both the motors to give a complete movement (Figs. 5 and 6).

2.5 Electronics

'In remote controlled planes an elevator and a rudder are sued for the control of the direction. Likewise an elevator and a rudder are attached for the FWAV in the tail wing. A lightweight receiver and a speed controller are also required for the radio control' [2]. A speed controller and lightweight receiver are also needed for the radio control. For the purpose of tail movement, two MG996R servo motors have been used at the tail link, 'this servo is very fast and commonly used in helicopters as well as other kind of applications that needs a very fast output speed' [5]. Which gives the yaw movement via a crank link mechanism. This tail link also houses the second motor, which is directly connected to the tail and is responsible for the rolling movement. Hence, a combined component, which comprises of two-servo motors, a speed controller and a receiver, is selected as demonstrated in Fig. 7.
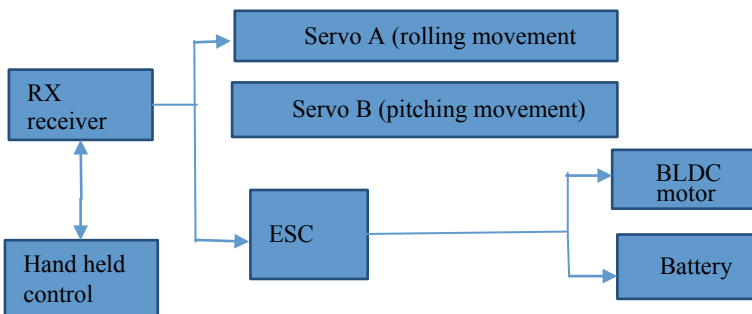
Fig. 7 Block diagram of the electronic circuit

To supply the whole system, a battery must be selected as such that it has higher resilience, light weight, portable and economic. In order to have a better understanding of how the model reacts in gliding conditions, a battery which can give a longer run time was selected. To serve this purpose, a battery of 11.1 V 2200 mAh was selected. The calculated battery runtime in the current electronic setup is 10 min 24 s.

2.6 Gear and Motor Selection

The drive mechanism converting the electric power from the battery to the flapping motion of the wings is the most critical part of the Ornithopter. To manufacture and design gearbox is complex, because it must endure major forces which reverse directions numerous times, while at the same time it should be very durable and light. Because small gears in the gear assembly must be made of metal which makes it necessary to trim as much weight as possible, the following can be achieved by performing dynamic analysis on the gear assembly. The system of drive views a breakdown of four different parts:

1. The electric motor.
2. Stage of gear reduction.
3. The high torque rotation is converted by a linkage into a reciprocating movement.
4. A connection for the wing spars.

A highly integrated design is required to maximize the power to weight ratio but through that, the analysis of parts comes down evenly. 'For the gearbox, multiple stages add to its complication, but it allowed us to attain better reduction ratios without using extremely large gears' [1]. 'The transverse shaft design is usually used for a bigger MAV designwhere weight could be overcome by large wings' [5]. For the gearbox, multiple stages add to its complication, but allow to attain better reduction ratios without using extremely large gears. We have achieved the desired gear reduction ratio of 21:1 with a three-stage gear mechanism detail of which is given in Table 5 (Fig. 8):

In the marketplace, the gears available were either too big or too small. Hence, they had to be fabricated as per custom design. The design of gears depends upon

Table 5 Details of the gears

Details	No of teeth	Module	Dia. of gear (mm)	Material
Motor gear	26	0.7	18.2	Brass
Small gear (2 gear assembly)	11	0.9	12.6	Brass
Big gear (2 gear assembly)	77	0.7	55.30	Nylon
Gear of motor	66	0.9	61.20	Nylon

Fig. 8 Gear assembly

Table 6 Specification of motor

Specification/motor	Motor 1	SG90
Stall torque (6.0 V)	13 kg/cm	2.4 kg/cm
Voltage (V)	4.8–6.0 V	4.8–6.0 V
Weight (g)	32	11

RMP on which the motor rolls because it is required to bring down the speed at which the motor is running as the flapping speed requires to be at a much slower pace than the speed at which the motor is revolving.

The rating of motor impacts the gear ratio, which in turn impacts the frequency of flapping, and here, the frequency of this is

$$Flapping\,frequency = \frac{Motor\,load\,speed}{Gear\,ratio\,\times\,60} \tag{2}$$

Brushless outrunner motor is the motor that is used here. Outrunner motors ratings are having low KV which means the torque is more but speed is less. For this project more than speed, as the motors have to turn the gears to flap, higher torque is needed. In order for the motor to be attached to the frame of flapping mechanism, with ease, instead of a separate mount so that the COG could be centrally aligned, two motors were selected based on the parameters, and we chose the one based on the maximum output in terms of torque generated, which tapers down to two motors as displayed in Table 6.

Motor 1 was chosen because we needed a motor that could generate high torque at low RPM so that gear reduction could be reduced (Fig. 9).

Fig. 9 FWAV made

3 Results

The phenomenon of a hovering flight based on an MAV was the goal of this paper, which majorly focused on the improvement of the wing design and the controllability of the several iterations in the connections of the wing spar rod. These targets were fully achieved. The mechanism selected for turning the gyration of the DC motors for flapping movement of wings is precise and take it towards its running, which can be referred to as error free.

The use of the transverse shaft enables two cranks to be connected to the same output gear. This approach is lighter, since it saves one gear but usually presents greater friction in the joints, both at the crank and at the wing, as well as being slightly more difficult to build. For smooth power transmission, several iterations was done to make the meshing of the gears accurate. There was some free movements in the initial set up of the gearbox when the shaft and the driven gear was fixed with adhesives, Later, the driven gear was designed with a hub so that the

Fig. 10 Transverse shaft assembly
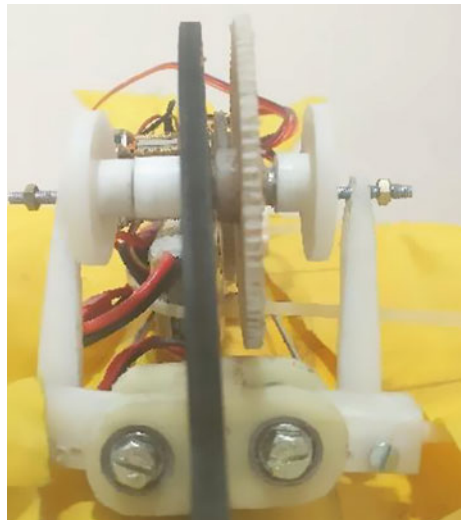
link between the shaft and gear can be fixed firmly and there is no play involved (Fig. 10).

Eight iterations were made in the FWAV so that flapping motion could be with the desired shape of wings. The flapping was not enough to generate lift for a sustained flight. For finding the optimal wing and mechanical configuration instead of confining our design to be as close to investigated FWAV and their parameters, we can extend our search space to generate more lift. There were no enhancements so far on the motors. With different parameters such as velocity constant, many suppliers have DC motors of the same size, but advancements should be made regarding the controlling ability by the way of regulating the motors and decreasing play in the structure. Furthermore, for further improvements, the gained knowledge can be used.

The use of two servo motors adds more weight at the trailing edge of the Ornithopter, thus, the use of smaller servo motors is suggested. The flight tests conducted with the Ornithopter confirmed that it has very less weight capacity to accommodate complicated sensor packages and onboard computers.

Two options thereby come into focus:

1. Either increase the payload capacity of the Ornithopter or to use miniaturized sensor pack so that the overall payload decreases. A preliminary analysis of the payload and carrying size displayed would be possible to make an Ornithopter sufficiently big. Besides the advantage of using sensors and a computer, we have already been adapted with a greater vehicle which would have slower dynamics and would be easier to examine and manage when the project is advanced.
2. To accommodate the weight, an increased payload to allow the extension of the system with the adding of more sensors in the future and if the computer was also downsized, will result in improved performance.

4   Conclusion

With sensors like an inertial measurement unit, at the lab, instrumentation could be done either onboard or offboard with the capture system of Vicon motion. The Vicon environment presented delivers brilliant data and is simple to set up, but it is short to grab data of free flight for the 1.17 m wingspan vehicle with its grabbing area of approximately $3 \times 3 \times 2$ m.

In the physical structure of the bird such as using another kind of material instead of fibreglass to construct the body, we could change a lot of different characteristics, although relatively light, the fibreglass still corresponds to almost one-third of the global weight of the robot. Using balsa wood or another kind of light material like carbon fibre, the body could be constructed.

References

1. Jackowski ZJ (2009) Design and construction of an autonomous ornithopter. Doctoral dissertation, Massachusetts Institute of Technology
2. Jung HK, Choi JS, Wang C, Park GJ (2015) Analysis and fabrication of unconventional flapping wing air vehicles. Int J Micro Air Veh 7(1):71–88
3. Park JH, Yoon KJ (2008) Designing a biomimetic ornithopter capable of sustained and controlled flight. J Bionic Eng 5(1):39–47
4. Hunt R, Hornby GS, Lohn JD (2005) Toward evolved flight. In: Proceedings of the 7th annual conference on genetic and evolutionary computation. ACM, pp 957–964
5. Bin Jumat MR, Srigrarom S (2014) Design and development of UGS flapping wing MAVs. In: International micro air vehicle conference and competition

Electrical Discharge Diamond Grinding (EDDG): A Review

**Rajat Sharma, Ayush Gupta, Umesh Kumar Vates
and Gyanendra Kumar Singh**

Abstract Due to the lower productivity of electrical discharge machining (EDM) process, it is not widely used for machining purpose. So, a new hybrid machining process (HMP) has been discovered, namely electrical discharge diamond grinding (EDDG). This EDDG is the combination of electric discharge machining (EDM) and grinding wheel with metal-bonded diamond grit. EDDG gives better performance than EDM due to the spark generation the rotating diamond wheel. This paper aims to summarize the work done by various researchers on EDDG process along with developments in the same area. Various output responses such as Wheel Wear Rate (WWR), Surface Roughness (Ra), Average Surface Roughness (ASR) and Material Removal Rate (MRR) have been analysed by different researchers considering various factors like pulse current, wheel speed, pulse on time, duty factor, Abrasive Particle Size (APS), infeed, pulse off time and abrasive particle concentration (APC) as input parameters, to compare the performance of the process considering different configurations of EDDG. The study reveals that EDDG can be efficiently used for grinding, super alloys, MMCs, cremates and various combinations of carbide steel. Further, it was concluded that online dressing, thermal softening of the workpiece and de-clogging of the wheel are remarkable features of EDDG. This process has a great future scope as it provides us the surface finish in order of few nanometers.

Keywords Electrical discharge diamond grinding (EDDG) ·
Electric discharge machining (EDM) · Hybrid machining processes (HMPs)

R. Sharma (✉) · A. Gupta · U. K. Vates
Amity School of Engineering and Technology, Amity University Noida,
Noida, UP, India
e-mail: rajat44017@gmail.com

G. K. Singh
Technical and Vocational Education and Training, Addis Ababa, Ethiopia

1 Introduction

Grinding generally is the last and important step in manufacturing processes, therefore, the improvements in this process are necessary. The improvements in this process are basically measured in terms of WWR, Ra, MRR. The visible surfaces of the final workpiece need to be faultless and with minimum marks on it [1]. The major problem arising during the grinding of the workpiece is found to be the presence of microcracks. Therefore, the hybrid grinding process is developed to overcome this problem and for grinding electrically conductive hard to be machined materials, which combines EDM and metal-bonded diamond grinding known as EDDG [2].

Spark is generated during the process, as shown in Fig. 1, which thermally softens the workpiece, hence decreasing the normal forces which further reduce the grinding power [3]. This results in lowering the WWR and Ra and increasing the MRR. Therefore, online dressing, thermal softening of the workpiece and de-clogging of the wheel are noticeable features of EDDG [4].

The diamond wheel with metal bonding is connected or attached to the EDM apparatus in one or another way. The workpiece is completely soaked in dielectric liquid. An electric motor drives the wheel usually through a belt-pulley arrangement. Variable speed drive provided helps in changing the speed of the motor. The whole apparatus is resting on a solid base, as shown in the Fig. 2. Servo system helps in preventing physical contact between wheel and the work. The MRR and quality of the surface are improved by the abrasive action in the given process [5].

2 Classification of Electro Discharge Diamond Grinding

EDDG can be broadly classified in the following three different configurations:

1. Surface configuration of Electrical Discharge Diamond Grinding (EDDSG).
2. Cut-off configuration of Electrical Discharge Diamond Grinding (EDDCG).
3. Face configuration of Electrical Discharge Diamond Grinding (EDDFG).

Figure 3 shows the various configurations of EDDG.

Fig. 1 Schematic representation of wheel-work interface in EDDG [2]
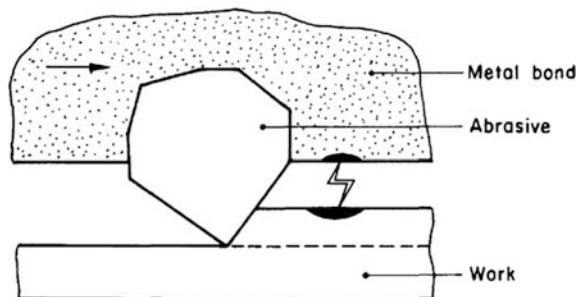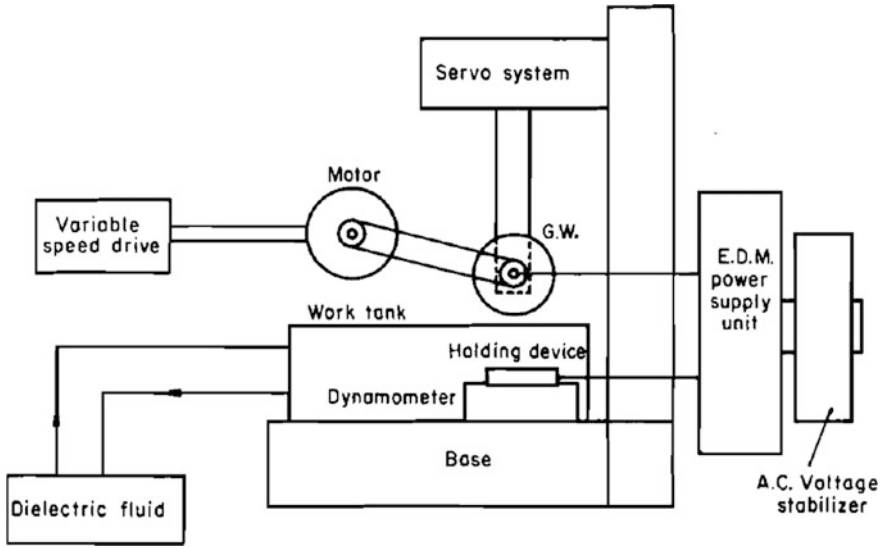
Fig. 2 Schematic diagram of EDDG process [27]
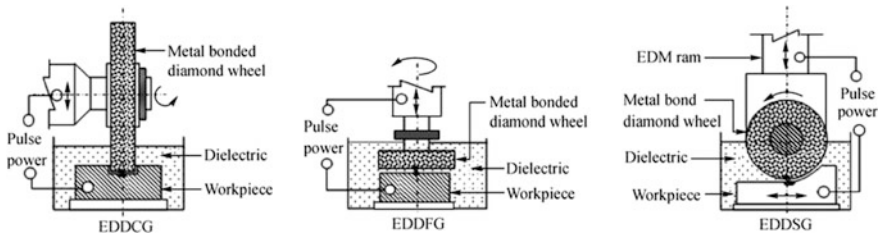
Fig. 3 Configurations of Electrical Discharge Diamond Grinding (EDDG) [23]

2.1 Surface Configuration of Electrical Discharge Diamond Grinding (EDDSG)

The periphery of grinding wheel helps to grind the surface of the workpiece in EDDSG. Wheel, which is mounted on the ram, acts as an electrode having its axis parallel to the workpiece. The grinding wheel is allowed to rotate about its horizontal axis under the action of servo system. The reciprocating action of work helps in achieving relative motion between job and grinding wheel which further results in grinding of the required work. Thickness of the job in this process under normal conditions is more than that of the wheel.

The Finite Element Method (FEM) was implemented by Yadava et al. [6] to find out the temperature distribution in the job due to EDDSG. They stated that generation of high temperature during the process leads to the generation of

microcracks, thermal stresses and burn marks. The effects of heat flux, heat distribution, table speed and depth of cut on the temperature of the topmost surface of the workpiece during grinding of a High-Speed Steel are studied. From their experiments, they concluded that temperature at the topmost surface increases with an increment in depth of cut and table speed (V_t). The temperature rise at the topmost layer of the workpiece seems to be reduced when a bigger wheel was used [6].

Yadav and Yadava [4] predicted wear and Ra in EDDG process using different techniques, namely design of experiments technique and neural network technique. The material used for experimentation purpose was HSS. Input parameters chosen were pulse current (I), duty ratio, wheel speed (N) and grain size. From their study, they concluded that for minimum WWR, ranges of I, duty ratio, N and grain size should be low. For better surface finished workpiece, range of I, duty ratio and grain size should be low, whereas N should be high [7].

Sunder and Yadava [8] examined EDDSG by keeping Al–SiC metal matrix composite under observation. They declared the grinding of MMCs to be difficult due to the presence of hard ceramic in them. They studied how MRR and Ra are affected by I, pulse on time (T_{on}), N, duty factor (d_f). A conclusion was made from their observations that lower I, d_f, T_{on} and high N must be selected to achieve better Ra. On the other hand, for higher (MRR), I, N, T_{on} should be high and d_f must have lower range [8].

Balaji and Yadava [9] proposed that the higher values of temperature and huge thermal stress generated during EDDG acts as an obstruction to good surface integrity of the workpiece. 3D thermal finite element (FE) simulation of EDDSG has been studied. The experiments were performed on HSS workpiece. The effect of various dielectric fluids, d_f and partition of energy during the process on the temperature distribution and MRR are reported. Near the top surface, it was found that there is high-temperature gradient. This results in the generation of thermal stresses during the process. MRR was observed to be increased with increase in Energy partition, d_f and Discharge voltage (V_d). It is found to be inversely proportional to feed [9].

Taguchi methodology was made into use by Choudhary et al. [10] to determine the optimum conditions for grinding AISI D2 Die Steel employing Electrical Discharge grinding under surface configuration. From their experiments, they determined that increase in MRR is observed with increasing abrasive particle size (APS), I, N and T_{on} and decreases with increase in Abrasive Particle Concentration (APC) and T_{off}. It was also observed that larger size abrasives show more participation as compared to the smaller particles. I, APS and rotational speed of the electrode were declared as most consequential parameters affecting the EDSG process [10].

Sunder and Yadava [8] discussed the optimization of MRR and Ra in EDDSG process in terms of N, depth of cut, V_t, T_{on}, I and d_f. Experiments were carried out on Al–Al2O3 metal matrix composite (MMC). The categorization of the effect of different input factors in percentage contribution of decreasing order was as shown in Table 1 [11]. Almost similar analysis was done in Agarwal and Yadava [12]

Table 1 Percentage contribution of various parameters during EDDSG [11, 12]

References no.	Wheel speed (N)	Current (I)	Depth of cut	Pulse on time (T_{on})	Table speed (V_t)	Duty factor (d_f)
[11]	44.15	25.12	13.00	11.69	3.50	2.40
[12]	46.36	22.66	10.76	9.80	6.45	3.97

keeping Al–SiC composite under observation. The percentage contribution of different factors is shown in Table 1 [12].

2.2 Cut-Off Configuration of Electrical Discharge Diamond Grinding (EDDCG)

As in EDDSG, outer edges of the metal-bonded diamond grinding wheel are used in EDDCG to cut the workpiece in pieces. The grinding wheel is placed on the ram having machining table parallel to wheel's axis. Servo control system controls the upward and downward motion of the rotating wheel. The physical contact between wheel and job is avoided. Electric sparks occurring between diamond wheel and workpiece surface results in simultaneous heating and softening of the work surface. The wheel used in EDDCG is usually thinner than that of EDDSG.

Yadav and Yadava [13] reported Artificial Neural Network (ANN) for modelling and Grey Relational Analysis (GRA) analysis for multi-objective optimization of EDDCG by performing experiments on cemented carbide. In their work, the main objective was to find the optimize parameters to improve the MRR and decrease the Ra. The optimum input parameters found were I = 5A, T_{on} = 50 μs, d_f = 0.70 and N = 1300 RPM. The percentage improvements with respect to initial experimental arrangements were 87.23% in MRR and 18% in Ra [14].

Yadav and Yadava [13] examined EDDCG of Ti–Al–Mo–V for MRR and Ra. The effects of N, I and T_{on} were studied by them. The influence of abrasion and electro erosion on the surface of the workpiece has also been observed by making Scanning Electron Microscope (SEM) technology in use and concluded that on increasing the current (3A–9A) grooves generated by abrasives on the surface reduces in number [13]. Almost similar work was done by Yadav and Yadava [13] by performing experiments on cemented Carbide. The effect of N, I, T_{on} and duty factor on MRR and Ra was studied and SEM of the surface was done by taking current 3A and 5A. Surface of the workpiece machined at 5 A was seen to have better finish [15].

Unune and Mali [16] determined the optimal machining parameters EDDCG. Job under consideration was Inconel 718 workpiece. Taguchi orthogonal array with grey relational analysis was utilized to determine multiple performance characteristics. The wheel speed was reported to be the most significant factor in EDDCG.

The optimal values of process parameters suggested were N 1200 rpm, I 10 amp, T_{on} 100 μs and d_f of 0.69 for improvement of grey relation grade by 4.321% [17].

2.3 Face Configuration of Electrical Discharge Diamond Grinding (EDDFG)

In EDDFG, face of the grinding wheel is used to perform the operation. The feed is provided in the direction perpendicular to the workpiece and rotation is allowed along the vertical spindle. The upward and downward motion to the wheel is provided using servo mechanism, which also prevents physical contact between job and the electrode wheel. Softening of the workpiece occurs as a result of electric sparks. The diameter of workpiece is generally kept smaller than that of the diameter of grinding wheel with diamond grit.

Singh et al. [18] combined conventional grinding and EDM to overcome problems like presence of re-solidified layer, large tool wear rate and thermal cracks while performing electro discharge face grinding of WC–CO composite. They put Taguchi method and grey relational analysis in use to determine optimum machining parameters. They analysed the effect of input parameters like N, I, T_{on} and d_f on the output parameters like MRR, WWR and ASR. They concluded that the MRR increased with increase in I, while N decreased with increase in Ton. WWR and ASR increased with N and I. N was observed to be the most significant factor affecting EMDFG. Overall, MRR witnessed improvement by 86.49%, WWR witnessed reduction by 21.70% but ASR reported deterioration by 14.86% [2].

Singh et al. [19] proposed an experimental study and optimization of parameters of EDDFG. They conducted experiments on ELEKTRA PULS EDM machine. They reported the used of Taguchi method along with GRA and entropy measurement for multi-performance characteristics. It was observed that increasing N, I and T_{on} increased the MRR and also the same decreased with increasing d_f. T_{on} along with d_f were identified as the most influencing factors affecting EDDFG [16].

Shrivastava and Dubey [20] used Taguchi methodology and response surface methodology for optimization of EDDFG process. They adopted a hybrid machining process comprising diamond grinding and electro discharge grinding. Experiments along with the use of specially designed orthogonal array were performed on high-speed steel workpiece with spark erosion oil as dielectric liquid. They machined each workpiece for 60 min. They analysed quality characteristics like MRR, ASR and WWR [18]. Similar work was done by Singh et al. and Shrivastava and Dubey [19, 20] in which EDDFG of cemented carbide–cobalt composite was done. Tungsten carbide and cobalt was chosen as the workpiece due to its high hardness and perfect resistance to shock and wear. Optimum valued obtained from their TM approach and hybrid approach is shown in Table 2. [19].

Yadav et al. [21] proposed experimental model for optimization of EDDFG. Process performance of copper–iron–graphite metal matrix composite has been

Table 2 Optimum valued obtained from TM approach and hybrid approach [18, 19]

References no.	Approach type	MRR (mm^3 m^{-1})	WWR (g min^{-1})	ASR (μm)
[20]	TM	1.8254	0.005223	3.312
	Hybrid	1.9457	0.001266	2.91
[21]	TM	0.3945	0.008104	3.11
	Hybrid	0.7982	0.006122	2.78

studied by optimizing MRR and SR. Input parameters taken were peak I, T_{on}, T_{off} and grit size. They identified that I and grit size of diamond were significant factors for MRR while I and T_{on} were significant factors for SR. The improvements of 95% and 29% were reported in optimization results of MRR and SR respectively [20].

Yadav et al. [22] investigated multi-objective optimization of process parameters in electro discharge diamond face grinding based on ANN-NSGA-II hybrid technique. High-speed steel cylindrical workpiece of diameter 25 mm was kept under consideration. In their research, they proposed that combination of high N, moderate pulse I, high T_{on} and moderate d_f are suitable for higher MRR, whereas combination of moderate N, low I, high T_{on} and high d_f of process parameter are suitable for better surface finish [23].

Unune and Mali [17] used response surface methodology and genetic algorithm for the optimization of electro discharge diamond face grinding of tungsten carbide–cobalt composite. Input parameters considered for their research were N, I, T_{on} and d_f, whereas output parameters took under consideration were MRR and Ra. The conclusion drawn from their work was that a suitable combination of input parameters and optimal parameters settings provides higher MRR and Ra [21].

Yadav et al. [24] applied non-dominated sorting genetic algorithm for multi-objective optimization of electric discharge diamond face grinding process on cylindrical high speed workpiece of 25 mm diameter. In their study, they considered pulse I, T_{on} and d_f as input parameters and studied their effect on MRR and surface finish. They proposed that optimal solution provides many combination of lower surface roughness with varying MRR, which facilitates selecting a better combination of process parameters as per product or design requirement [22].

2.4 Some Newly Developed Configurations of EDDG

Slotted-Electrical Discharge Diamond Grinding (S-EDDG)

A new configuration of EDDG process in cut-off configuration with slotted wheel is reported by Yadav and Yadava [25]. The experiments were performed on Al/SiCp/B4Cp hybrid MMC. They described that the need to find this new configuration was that in EDDG process, the loss of diamond particles was very frequent moreover entrapment of leftover chips into the gaps of wheel was a disadvantage. Therefore a slotted abrasive grinding wheel was used to remove these drawbacks. I,

T_{on}, T_{off}, N and abrasive grit number were taken as input parameters while MRR and Ra were taken as output parameters. They reported that the S-EDDCG gives about five times higher MRR than electric discharge cut-off machining (EDCM) and two times higher MRR than electric discharge cut-off grinding (EDCG), respectively. It also gives about three times better surface finish than EDCM and 1.5 times improves surface finish than EDCG processes [24].

Yadav and Yadava [26] describes modelling and optimization of EDDG process in face configuration with slotted wheel by machining Aluminium–silicon carbide–graphite composite and by applying techniques like ANN and non-dominated sorting genetic algorithm-II (NSGA-II). Input parameters taken were I, T_{on}, T_{off}, grit number and N whereas MRR and Ra were considered as output parameters. Their results showed a good support with experimental data with absolute percentage error of 4.28% and 5.09% for MRR and Ra respectively [25].

Electrical discharge diamond face surface grinding (EDDFSG)

This was a new configuration was investigated by Yadav and Yadava [27]. As per experimental setup, two aluminium plates are placed perpendicular to each other in vertical and horizontal direction. EDM RAM is attached to horizontal plate and axis of grinding wheel is perpendicular to work table. This table is allowed to move in x and y-direction with help of two bipolar stepper motors. The experiments were performed on hybrid MMC, Al/SiCp/B4Cp. I, T_{on}, T_{off}, abrasive grit size, N and V_t were considered as input process parameters and their effect was determined on MRR and Ra. SEM was used to study the surface characteristics which helped them to make a conclusion that diamond wheel having higher grit number yields better results than lower grit numbers [26].

3   Conclusions

As grinding is generally the last stage of all the manufacturing processes, it has attracted the attention of various researchers. EDDG has been found very productive for grinding electrically conductive hard materials, super alloys, MMCs, cremates and various combinations of carbide steel. Experiments have revealed that various factors like pulse current, wheel speed, pulse on time, duty factor, abrasive particle size (APS), infeed, pulse off time and Abrasive Particle Concentration (APC) have impact on MRR, Ra and WWR. Current, duty factor and their interaction highly influence WWR. Higher MRR can be obtained by using high values of peak current, rotational speed, abrasive particle size (APS), pulse on time, infeed, table speed and low ranges of APC, duty factor and pulse off time. For better surface roughness, pulse on time, duty factor, pulse current, infeed and table speed must be low. High generation of temperature and thermal stresses during EDDG process results in bad surface conditions. Increase in depth of cut and wheel speed is seen to result in increment of surface temperature which can be reduced by using grinding wheel of bigger size. Life of the metal-bonded diamond grinding wheel is

also believed to increase 10 times more than the traditional process. It has also been seen that a new configuration of EDDG are attracting the interest of researchers, namely electrical discharge diamond face surface grinding (EDDFSG) and slotted electrical discharge diamond cut-off grinding (S-EDDCG) on which much work is not yet done.

4   Future Scope

After the study of various research papers, it can be said that much work is not done yet on EDDG. This process is the unique development in EDM and grinding process for machining materials with good surface parameters. So, the advancements in Electric Discharge Grinding (EDG) process can be made by adding different abrasives to the grinding wheels. Developing some new configurations of EDDG process can also lead to enhance the quality of the surface generated. This study may be useful to researchers who make efforts to machine difficult to be machined materials.

References

1. Wegener K, Bleicher F, Krajnik P, Hoffmeister HW, Brecher C (2017) Recent developments in grinding machines. CIRP Ann Manuf Technol 66(2):779–802. https://doi.org/10.1016/j.cirp.2017.05.006
2. Singh GK, Yadava V, Kumar R (2010) Diamond face grinding of WC-Co composite with spark assistance: experimental study and parameter optimization. Int J Precis Eng Manuf 11 (4):509–518. https://doi.org/10.1007/s12541-010-0059-3
3. Koshy P, Jain VK, Lal GK (1996) Mechanism of material removal in electrical discharge diamond grinding. Int J Mach Tools Manuf 36(10):1173–1185 (1996). https://doi.org/10.1016/0890-6955(95)00103-4
4. Yadav RS, Yadava V (2017) Experimental investigations on electrical discharge diamond peripheral surface grinding (EDDPSG) of hybrid metal matrix composite. J Manuf Process 27:241–251. https://doi.org/10.1016/j.jmapro.2017.04.004
5. Kumar S, Choudhury SK (2007) Prediction of wear and surface roughness in electro-discharge diamond grinding. J Mater Process Technol 191:206–209. https://doi.org/10.1016/j.jmatprotec.2007.03.032
6. Yadava V, Jain VK, Dixit PM (2005) Temperature distribution in the workpiece due to electro-discharge diamond surface grinding using FEM. Int J Manuf Technol Manag 7(2–4):246–267. https://doi.org/10.1504/IJMTM.2005.006832
7. Kumar S, Choudhury SK (2007) Prediction of wear and surface roughness in electro-discharge diamond grinding. J Mater Process Technol 191:206–209. https://doi.org/10.1016/j.jmatprotec.2007.03.032
8. Sunder S, Yadava V (2012) Development, experimental investigation and neural network modelling of surface-electrical discharge diamond grinding of Al-SiC metal matrix composite. Int J Abras Technol 5(3):223–244. https://doi.org/10.1504/IJAT.2012.051033

9. Balaji PS, Yadava V (2013) Three dimensional thermal finite element simulation of electro-discharge diamond surface grinding. Simul Model Pract Theor 35:97–117. https://doi.org/10.1016/j.simpat.2013.03.007

10. Choudhary R, Kumar H, Singh S (2013) Machining performance and surface integrity of AISI D2 die steel machined using electrical discharge surface grinding process. J Mater Eng Perform 22(12):3665–3673. https://doi.org/10.1007/s11665-013-0679-8

11. Sunder S, Yadava V (2014) Modelling and optimisation of material removal rate and surface roughness in surface-electrical discharge diamond grinding process. Int J Ind Syst Eng 17(2):133–151. https://doi.org/10.1504/IJISE.2014.061990

12. Agrawal SS, Yadava V (2015) Development and Experimental Study of Surface-Electrical Discharge Diamond Grinding of Al–10 wt%SiC Composite. J Inst Eng (India) 97(1):1–9. https://doi.org/10.1007/s40032-015-0183-z

13. Yadav SKS, Yadava V (2013) Experimental investigation of electrical discharge diamond cut-off grinding of Ti Alloy. Mater Manuf Process 28:557–561. https://doi.org/10.1080/10426914.2012.718469

14. Yadav SKS, Yadava V (2011) Neural network modelling and multi objective optimisation of electrical discharge diamond cut-off grinding (EDDCG). Int J Abras Technol 4(4):346–362. https://doi.org/10.1504/IJAT.2011.044509

15. Yadav SKS, Yadava V (2013) Experimental investigations to study electrical discharge diamond cutoff grinding (EDDCG) machinability of cemented carbide. Mater Manuf Process 28(10):1077–1081. https://doi.org/10.1080/10426914.2013.792414

16. Singh GK, Yadava V, Kumar R (2011) Experimental study and parameter optimization of electro-discharge diamond face grinding. Int J Abras Technol 4(1):14–40. https://doi.org/10.1504/IJAT.2011.039001

17. Unune DR, Mali HS (2016) A study of multi objective parametric optimization of electric discharge diamond cut-off grinding of Inconel 718. Int J Abras Technol 7(3):187–199. https://doi.org/10.1504/IJAT.2016.078281

18. Singh GK, Yadava V, Kumar R (2012) Robust parameter design and multi-objective optimization of electro-discharge diamond face grinding of HSS. Int J Mach Machinabil Mater 11(1):1–19. https://doi.org/10.1504/IJMMM.2012.044919

19. Singh GK, Yadava V, Kumar R (2012) Modelling and optimisation of electro-discharge diamond face grinding of cemented carbide–cobalt composite. Int J Ind Syst Eng 12(2):141–164. https://doi.org/10.1504/IJISE.2012.048858

20. Shrivastava PK, Dubey AK (2013) Experimental modeling and optimization of electric discharge diamond face grinding of metal matrix composite. Int J Adv Manuf Technol 69:2471–2480. https://doi.org/10.1007/s00170-013-5190-8

21. Yadav RN, Yadava V, Singh GK (2014) Application of response surface methodology and genetic algorithm for optimisation of electro-discharge diamond face grinding of tungsten carbide-cobalt composite. Int J Ind Syst Eng 18(1):76–94. https://doi.org/10.1504/IJISE.2014.064342

22. Yadav RN, Yadava V, Singh GK (2014) Application of non-dominated sorting genetic algorithm for multi-objective optimization of electrical discharge diamond face grinding process. J Mech Sci Technol 28(6):2299–2306. https://doi.org/10.1007/s12206-014-0520-9

23. Yadav RN, Yadava V, Singh GK (2013) Multi-objective optimization of process parameters in Electro-discharge diamond face grinding based on ANN-NSGA-II hybrid technique. Front Mech Eng 8(3):319–332. https://doi.org/10.1007/s11465-013-0269-3

24. Yadav RN, Yadava V (2014) Slotted-electrical discharge diamond cut-off grinding of Al/SiC/B4C hybrid metal matrix composite. J Mech Sci Technol 28(1):309–316. https://doi.org/10.1007/s12206-013-0968-z

25. Yadav RN, Yadava V (2015) Application of soft computing techniques for modeling and optimization of slotted-electrical discharge diamond face grinding process. Trans Indian Inst Met 68(5):981–990. https://doi.org/10.1007/s12666-015-0536-6
26. Yadav RS, Yadava V (2017) Performance study of Electrical discharge diamond face surface grinding (EDDFSG) on hybrid metal matrix composite. J Mech Sci Technol 31(1):317–325. https://doi.org/10.1080/10426914.2016.1221089
27. Choudhury SK, Jain VK, Gupta M (1999) Electrical discharge diamond grinding of high speed steel. Mach Sci Technol 3(1):91–105. https://doi.org/10.1080/10940349908945685

Stress Analysis of Infinite Plate with Elliptical Hole

Sandeep Soni and Udaykumar Saindane

Abstract The stress field around different geometries like circular, rectangular, triangular, and elliptical having different orientations and loaded with different loading conditions can be find out using methods discovered by several researchers. One similar attempt has been made to determine the stresses around elliptical hole with infinite plate loaded in X-direction and Y-direction subsequently. The elastostatic problem of the homogeneous isotropic infinite plate with the loading at infinity (in X and Y-direction) for the elliptical hole is considered in this paper. Boundary value problem is solved with complex stress functions using complex variable approach. For this work, the Schwarz's alternating technique given by Sokolnikoff and Ukadgaonkar is used, and the derived analytical solution can be used for generation of code in C++ to find out the stress components at a given particular point.

Keywords Stress analysis · Infinite plate · Elliptical hole

1 Introduction

The presence of elliptical hole in plates and machined components are subjected to loading introduces stress concentration in the vicinity of holes. Sudden changes in cross section lead to stress concentration at a localized point. It is impossible to estimate the rise of stresses in neighborhood of hole using elementary theory of strength of materials. The stress concentration depends on geometry of components, size of hole, and loading condition. A classic example of plate loaded with tension which contains centrally located hole is considered here. The solutions in the form of simple analytical equations from the method of complex variable approach can

S. Soni · U. Saindane (✉)
S. V. National Institute of Technology, Surat 395007, Gujarat, India
e-mail: udaysaindane@gmail.com

give us the check against the effect of change in the parameter in design process. The method of using complex variables for the solution of elastostatic problems was first introduced by Kolosoff in his doctoral dissertation work. It was further extended by Muskhelishvili to solve the two and three-dimensional problems of theory of elasticity.

2 Material and Method

Two cases are considered with loading at x-direction and y-direction separately. These problems can be solved by various methods. The elastoplastic problem for homogeneous isotropic plate with loading at infinity for elliptical hole is solved using a novel method called Schwarz's alternating method given by Sokolnikoff and Ukadgaonkar with successive approximations. Initially, a plate without any hole is considered. The boundary condition on the hole boundary is found out. To nullify this, the negative of this boundary condition is applied on the hole. The solution of this problem is superimposed on the first solution which gives the required closed-form solution [1, 2].

By the method, we can superimpose the two problems to get the final solution [3].

2.1 First Case

In this, the load is applied along x-direction. It is discretized into first problem and second problem (Fig. 1).

Boundary Condition

$$\sigma_x^\infty = P;$$
$$\sigma_y^\infty = 0;$$
$$\tau_{xy}^\infty = 0;$$

First Problem   Second Problem
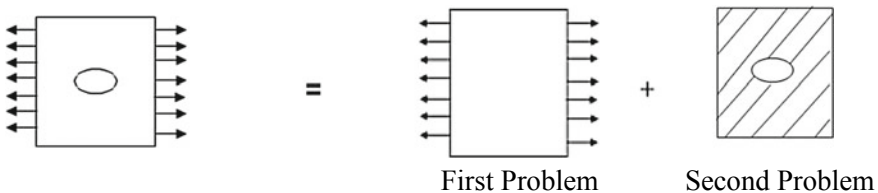
Fig. 1 Infinite plate (neglecting edge effect) first case

Solution

The boundary condition for the first problem can be found out as given by the formula

$$f(t) = \phi(z) + z\overline{\phi'(z)} + \overline{\psi(z)}$$

For the second problem, boundary condition can be imposed as $= f(t)_2 - f(t)_1$

A. *First problem*

$$\sigma_X + \sigma_Y = 2\left\{\phi'(z) + \overline{\phi'(z)}\right\}$$
$$= 4\,\mathrm{Re}\left\{\phi'(z)\right\}$$

Putting the given boundary condition and integrating, we get the

$$\phi_0(z) = Pz/4;$$

Now

$$\sigma_Y - \sigma_X + 2i\tau_{XY} = 2\left\{\bar{z}\phi''(z) + \psi'(z)\right\}$$

We get

$$\psi_0(z) = -Pz/2;$$

Now, we use the conformal mapping for mapping the region outside of elliptical hole to region outside the unit circle (Fig. 2).

$$f(z) = R(w + m/w)$$
$$f'(z) = R(1 - m/w^2)$$
$$M = (a - b)/(a + b)$$
$$f'(z) = R(1 - mw^2)$$
$$R = a + b/2;$$

Fig. 2 Conformal mapping from Z Plane to W Plane

Z Plane

W Plane

$$f_0(t) = \phi(t) + \frac{f(t)}{f'(t)}\overline{\phi'(t)} + \overline{\psi(t)}$$

$$= PR(t+m/t)/4 + R(t+m/t)/(R(1-mt^2) * PR(1-mt^2)/4 + PR(1/t+mt)/2$$

$$= \frac{PR}{2}[t^2 + m + 1 + mt^2]/t$$

(t is boundary point lie on hole)……. (t.t = R2)

B. *Second Problem* (Fig. 3)

$$\phi_1(w) = -\frac{1}{2\pi i}\int \overset{f(t)_2 = -f(t)_1}{\overbrace{\frac{f(t)d\sigma}{\sigma - w}}}$$

$$= \frac{PR}{2}\frac{1}{2\pi i}\oint [\frac{m}{t(t-w)} + \frac{1}{t(t-w)} + \frac{mt}{t-w} + \frac{t}{t-w}]$$

$$= -\frac{PR}{2}[\frac{m+1}{w}]$$

Solving Cauchy's integral

$$\phi_1(w) = -\frac{PR}{2}[\frac{m+1}{w}]$$

$$\psi_1(w) = -\frac{1}{2\pi i}\int \frac{\overline{f}(t)dt}{t-z} - \frac{w(1+mw^2)}{w^2-m}\phi'(w)$$

$$\psi_1(w) = -\frac{1}{2\pi i}\int [-\frac{PR(1+t^2+mt^2+m)}{t(t-w)}] - \frac{w(1+mw^2)}{w^2-m}\frac{PR(m+1)}{2w^2}$$

$$= -\frac{PR(m+1)}{2}[\frac{1}{w} + \frac{1+mw^2}{w(w^2-m)}]$$

Fig. 3 Second problem of first case after conformal mapping
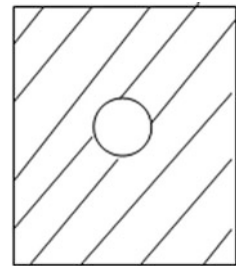
Finally, we get

$$\phi(z) = \phi_0(z) + \phi_1(z)$$
$$= \frac{PR}{4}(w + \frac{m}{w}) - \frac{PR}{2}(\frac{m+1}{w})$$
$$= \frac{PR}{4}[w - \frac{m}{w} - \frac{2}{w}]$$
$$\psi(z) = \psi_0(z) + \psi_1(z)$$
$$= \frac{PR}{2}(w + \frac{m}{w}) - \frac{PR}{2}\frac{(m+1)}{w}[1 + \frac{1+mw^2}{w^2 - m}]$$
$$= \frac{PR}{2}[w - \frac{1}{w} - \frac{(m+1)(1+mw^2)}{w(w^2 - m)}]$$

Finding stresses

$$\sigma_X + \sigma_Y = 4\,\mathrm{Re}\left\{\phi'(z)\right\}$$
$$= 4\,\mathrm{Re}\{\frac{\phi'(w)}{f'(w)}\}$$
$$= \frac{P}{4}[\frac{w^2 + m + 2}{w^2 - m}]$$

Separating real and imaginary part and converting in polar form, we get

$$\sigma_r + \sigma_\theta = \frac{r^4 - m^2 + 2(r^2 \cos 2\theta - m)}{r^4 - 2r^2 m \cos 2\theta + m^2}$$
$$\sigma_\theta - \sigma_r + 2i\tau_{r\theta} = 2\left\{\bar{z}\phi''(z) + \psi'(z)\right\}e^{2i\theta}$$

Separating real and imaginary part

$$\tau_{r\theta} = \frac{P}{2}\left\{\frac{N2*D1 + N1*D2}{D1^2 + D2^2}\right\}$$
$$\sigma_\theta - \sigma_r = P\left\{\frac{N1*D1 + N2*D2}{D1^2 + D2^2}\right\}$$

where

$$N1 = AA + AB \cos 2\theta + AC \sin 2\theta + AD \cos 4\theta + AE \sin 4\theta$$
$$N2 = BB + BC \sin 2\theta + BD \cos 2\theta + AD \sin 4\theta - AE \cos 4\theta$$
$$D1 = (J + K) \cos 2\theta + L \cos 4\theta + M$$
$$D2 = (J - K) \sin 2\theta + L \sin 4\theta$$
$$AA = B + (A + G)$$
$$AB = D + C + F + H$$
$$AC = 0 \, AE = 0 \, BB = 0 \, BD = 0$$
$$AD = E$$
$$BC = D + C + F - H$$
$$A = 2r^4 - m^2 r^2 - 3r^2$$
$$B = mr^2 - 2mr^4 + m^3 r^2$$
$$C = 2mr^2 - mr^4$$
$$D = r^2 - 2mr^2 + m^2 r^4$$
$$E = -r^6$$
$$F = 2mr^4$$
$$G = -m^2 r^2$$
$$H = m$$
$$J = r^6 + 2m^2 r^2$$
$$K = m^2 r^2$$
$$L = -mr^4$$
$$M = -2mr^4 - m^3$$

So finally,

$$\sigma_x = (\sigma_r * \cos^2 \theta) + (\sigma_\theta * \sin^2 \theta) - (2\tau_{r\theta} \sin \theta \cos \theta)$$
$$\sigma_y = (\sigma_r * \sin^2 \theta) + (\sigma_\theta * \cos^2 \theta) + (2\tau_{r\theta} \sin \theta \cos \theta)$$
$$\tau_{xy} = (\sigma_r - \sigma_\theta) * \cos \theta * \sin \theta + 2\tau_{r\theta}(\cos^2 \theta - \sin^2 \theta)$$

2.2 Second Case

In this, the load is applied along y-direction. It is discretized into first problem and second problem (Fig. 4).

First Problem   Second Problem
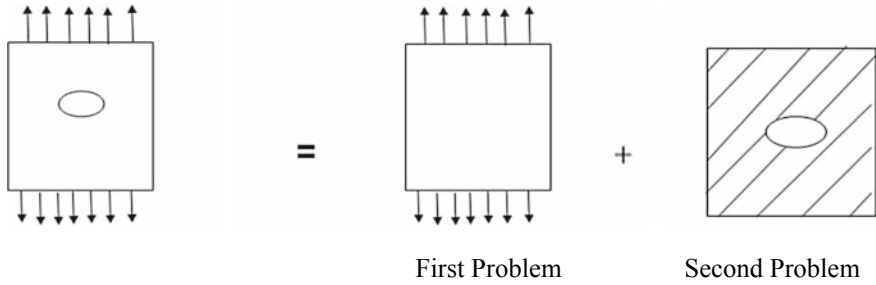
Fig. 4 Infinite plate (neglecting edge effect) second case

Boundary Condition

$$\sigma_x^\infty = 0;$$
$$\sigma_y^\infty = P;$$
$$\tau_{xy}^\infty = 0;$$

Solution

By the method, we can superposition the two problems to get the final solution.

The boundary condition for the first problem can be found out as given by the formula

$$f(t) = \phi(z) + \overline{z\phi'(z)} + \overline{\psi(z)}$$

For the second problem, boundary condition can be imposed as $= f(t)_2 - f(t)_1$

C. *First problem*

$$\sigma_X + \sigma_Y = 2\left\{ \varphi'(z) + \overline{\varphi'(z)} \right\}$$
$$= 4\,\mathrm{Re}\left\{ \varphi'(z) \right\}$$

Putting the given boundary condition and integrating, we get the

$$\phi_0(z) = Pz/4;$$

Now

$$\sigma_Y - \sigma_X + 2i\tau_{XY} = 2\left\{ \bar{z}\varphi''(z) + \psi'(z) \right\}$$

We get

$$\psi_0(z) = Pz/2;$$

Now, we use the conformal mapping for mapping the region outside of elliptical hole to region outside the unit circle (Fig. 5).

$$f(z) = R(w + m/w),$$
$$f(z) = R(1 - m/w^2),$$
$$f'(z) = R(1 - mw^2)$$
$$R = a + b/2;$$
$$M = (a - b)/(a + b)$$

$$f_0(t) = \phi(t) + \frac{f(t)}{\overline{f'(t)}}\overline{\phi'(t)} + \overline{\psi(t)}$$

$$= PR(t + m/t)/4 + R(t + m/t)/(R(1 - mt^2) * PR(1 - mt^2)/4 + PR(1/t + mt)/2$$

$$= \frac{PR}{2}[t^2 + m + 1 + mt^2]/t$$

$$= Pt/4 + tP/4 + Pt/2$$

$$= Pt/2 + PR2/(2Z)(t.t = R2)$$

(t is boundary point lie on hole)

D. *Second Problem* (Fig. 6)

$$f(t)_2 = -f(t)_1$$

$$\phi_1(\zeta) = -\frac{1}{2\pi i}\int\frac{f(t)d\sigma}{\sigma - \zeta}$$

$$= -\frac{1}{2\pi i}\int\frac{Ptdt}{t - z} + -\frac{1}{2\pi i}\int\frac{PR^2dt}{t - z}$$

Fig. 5 Conformal mapping from Z Plane to W Plane

Z Plane   W Plane
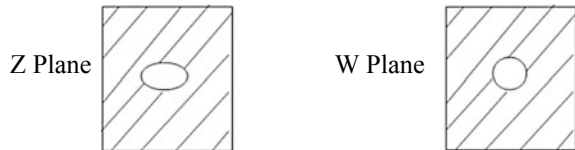
Fig. 6 Second problem of
second case after conformal
mapping
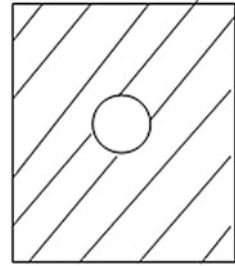
Solving Cauchy's integral

$$\phi_1(\zeta) = -PR2/(2z)$$
$$\psi_1(\zeta) = -\frac{1}{2\pi i}\int\frac{\overline{f(t)}dt}{t-z} - \overline{z}\,\phi'(z)$$

Finally, we get

$$\phi(z) = \phi_0(z) + \phi_1(z)$$
$$= \frac{Pz}{4} - \frac{PR^2}{2z}$$
$$\psi(z) = \psi_0(z) + \psi_1(z)$$
$$= \frac{Pz}{2} - \frac{PR^2}{2}(\frac{1}{z} + \frac{R^2}{z^3})$$

Finding stresses

$$\sigma_X + \sigma_Y = 4\,\mathrm{Re}\left\{\phi'(z)\right\}$$
$$= \left[\frac{P}{4} + \frac{PR^2}{2z}\right]$$

Separating real and imaginary part and converting in polar form, we get

$$\sigma_r + \sigma_\theta = P\left\{1 + \frac{2R^2}{r^2}\cos 2\theta\right\}$$
$$\sigma_\theta - \sigma_r + 2i\tau_{r\theta} = 2\left\{\overline{z}\,\phi''(z) + \psi'(z)\right\}e^{2i\theta}$$

$$(1)$$

Separating real and imaginary part

$$\sigma_\theta - \sigma_r = \left\{ \frac{PR^2}{r^2} + P(1 + \frac{3R^4}{r^4} - \frac{2R^2}{r^2}) \right\} \cos 2\theta \tag{2}$$

$$\tau_{r\theta} = \frac{P}{2} \left\{ 1 + \frac{2R^2}{r^2} - \frac{3R^4}{r^4} \right\} \sin 2\theta \tag{3}$$

Solving Eqs. 1 and 2, we get

$$\sigma_\theta = \frac{P}{2} \left\{ (1 + \frac{R^2}{r^2}) + (1 + \frac{3R^4}{r^4}) \cos 2\theta \right\}$$
$$\sigma_r = \frac{P}{2} \left\{ (1 - \frac{R^2}{r^2}) + (\frac{4R^2}{r^2} - 1 - \frac{3R^4}{r^4}) \cos 2\theta \right\}$$
$$\tau_{r\theta} = \frac{P}{2} \left\{ 1 + \frac{2R^2}{r^2} - \frac{3R^4}{r^4} \right\} \sin 2\theta$$

3 Result and Discussion

$$\sigma_\theta = \frac{P}{2} \left\{ (1 + \frac{R^2}{r^2}) + (1 + \frac{3R^4}{r^4}) \cos 2\theta \right\}$$
$$\sigma_r = \frac{P}{2} \left\{ (1 - \frac{R^2}{r^2}) + (\frac{4R^2}{r^2} - 1 - \frac{3R^4}{r^4}) \cos 2\theta \right\}$$
$$\tau_{r\theta} = \frac{P}{2} \left\{ 1 + \frac{2R^2}{r^2} - \frac{3R^4}{r^4} \right\} \sin 2\theta$$

The above equations are useful to find out stress field of two-dimensional iso-tropic homogeneous infinite plate with elliptical hole. An attempt is made to give general solution to plate problem. Knowing the values of hole radius (R), load (P) applied at the edge of plate and angle of inclination (θ), one can find out all three stress components that is σx, σy, and $\tau r\theta$ at a distance of (r) from plate origin. Here lower left corner of the plate is taken as origin. Thus, assigning numerical values to the above-listed plate parameters, the values of all three stress components can be find out and represented in tabular form. Further, the stress functions given above can be reduced to solve various types of hole boundary problems such as circular, rectangular, square hole, and crack. Also, it can generate the text result file of all the nodes (in the region which is four times the hole radius) [6, 8].

The solution is based on classical theory of elasticity given by Muskhelishvili, N. I. Various boundary value problems are solved in his book. An attempt is made to formulate one of the boundary value problems and solution is provided using advanced mathematics in terms of mathematical equations which consist of com-plex Stress functions and Cauchy's integral formulae. This solution is very useful in stress calculation for any type of similar cases in lap/riveted joints in aircraft structures. Thus, this closed-form solution saves the computer time compared to finite element solutions.

4 Conclusion

The solution is obtained using stress functions by Schwarz's alternating method, which gives stress distribution of infinite plate with elliptical hole by varying input parameters. By adopting the computer code, we can find out the stress at any given particular point in the neighborhood of circular hole. The result file so as generated can be used for visual display of result so obtain such as meshing and then contour plot for the stress components [4, 5, 7, 9].

References

1. Muskhelishvili NI (1963) Some basic problems of the mathematical theory of elasticity. P. Noordoff Ltd
2. Ukadgaonkar VG, Awasare PJ, A novel method of stress analysis of an infinite plate with elliptical hole with uniform tensile stress. IE (I) Journal-ME 73:309–311
3. Comer J, Bannantine J (1997) Fundamentals of metal fatigue analysis. 1st edn. Prentice Hall
4. Love AEH (1944) Mathematical theory of elasticity, 4th edn. Dover Publications, New York
5. Ameen Mohammed (2011) Computational elasticity theory of elasticity and finite and boundary element methods. Alpha Science International Ltd., Harrow, UK
6. Sokolnikoff IS (1956) Mathematical theory of elasticity. McGraw Hill Book Co., New York
7. Chavan KS, Bakare AK, Dharap MA, Saindane UV (2010) Stress analysis of infinite plate with inclined elliptical hole cutout. Int J Adv Eng Appl, 267–269
8. Saindane UV (2011) Crack analysis of rivet hole and its repair using composite patch. M.Tech Thesis. University of Pune
9. Bakare AK (2001) Fatigue crack growth at riveted fuselage lap joint of aircraft. M.Tech. Dissertation, Jan 2001, Dept. of Mechanical Engg, Indian Institute of Technology, Bombay

Formation of Hole Flanges Through Incremental Forming: A Review

Yogesh Dewang, Nitin Tenguria, Vipin Sharma
and Maneesh Kumar Dubey

Abstract Hole flanges are formed around a hole with precut hole on sheet metal, which is used for fixation and guiding cables. The present study presents a critical and concise review on the formation of hole flanges through incremental forming. Aluminum alloys, steel alloys, and polymers are used in the majority of investigations of hole flanging through SPIF. The number of stages with different tool trajectories utilized by researchers are found to be efficient as compared to single-stage hole flanging through SPIF. A variety of shapes of tool with hemispherical tooltip, high-speed tool, and new featured tool are utilized by the researchers for hole flange forming through incremental forming. Circle grid analysis is found to be a handy tool for prediction of formability in terms of forming limiting diagrams (FLD). It is found that through developed experimental set ups, cost of tooling sets and cycle time have reduced considerably. Higher formability is attained in hole flanging through SPIF as compared to conventional press working due to absence of necking. It is found that in majority of investigations, shell and solid elements are used for meshing of sheets in FEM simulation of hole flanging through incremental forming.

Keywords Incremental forming · Hole flanging · Sheet metal forming · Hole flange · Circle grid analysis · Forming limit

1 Introduction

A sheet metal forming process, in which hole is formed with the help of dedicated sets of tooling such as punch and die is known as conventional hole flanging process. Hole flanging is widely applied in the aeronautics and automotive industries.

Y. Dewang (✉) · V. Sharma · M. K. Dubey
Lakshmi Narain College of Technology, Bhopal, India
e-mail: dewang.yogesh3@gmail.com

N. Tenguria
Sagar Institute of Research & Technology, Bhopal, India

Conventional hole flanging is found to be economical, only when it is applied in mass production [1]. On the other hand, hole flanges can also be formed by using other forming technique known as incremental forming, in which there is no requirement of dedicated tooling sets. Saving in tooling costs makes incremental forming an economical technique as compared to conventional press working for the formation of hole flanges [1, 2]. Researchers in the past had contributed in the area of formation of hole flanges through incremental forming. Petek and Kuzman [2] introduced a novel strategy named as backward incremental hole flanging technique, which can be performed in multiple steps. Centeno et al. [3] found that formability in hole flanging through single-stage incremental forming has increased as compared to conventional hole flanging due to restricted necking before fracture. Montanari et al. [4] integrated the concept of circle grid analysis and laws of plasticity to investigate the development of stresses and strains as well as to investigate deformation history in hole flanging through single-point incremental forming. Silva et al. [5] employed polymer sheets as workpiece material for the formation of hole flanges through multistage single point incremental forming and found that polyethylene tereph-thalate (PET) is more suitable as compared to polycarbonate (PC). Silva et al. [6] found that fracture forming limit lines are situated above forming limiting curve in principal strain space, which yielded higher limiting ratio in hole flanging through incremental forming as compared to conventional press working. Bambach et al. [7] applied an adaptive blank holder for actuating hole flanging operations which yielded fast and accurate formation of hole flanges. Cristino et al. [8] presented an effective methodology for the determination of critical values of damage and fracture toughness at crack initiation by conducting experiments of hole flanging. Montanari et al. [9] reported a peculiar outcome as higher limiting forming ratio in hole flanging of AISI304L sheets through conventional press working in comparison to incre-mental sheet forming. Yonan et al. [10] presented a methodology for direct evalu-ation of in-plane stresses and accumulated damage at different positions over the conical and pyramidal PVC parts through experimentation. Cristino et al. [11] found cracks around circumferential direction in hole flanging through incremental forming at the flange walls whereas meridional cracks in hole flanges formed through press working. Borrego et al. [12] encountered failure at the vertical wall instead of flange edge due to postponed necking followed by the ductile fracture in hole flanging of AA 7075-O through SPIF. Cristino et al. [13] investigated defor-mation behavior of square hole flanges through multistage SPIF and found that failure occurred due to thinning until fracture with no sign of previously localized necking. Hussain et al. [14] recommended 80 mm as a threshold size of hole in hole flanging through incremental sheet metal forming for achieving maximum forma-bility. Cao et al. [15] developed a new flanging tool with a new and improved version of incremental sheet forming process for ensuring uniform thickness across hole flange due to the combined deformation mode of bending-dominated zone. Dewang et al. [16] reviewed various aspects of hole flanging process and found that incremental sheet forming technique to be more suitable and economical as

compared to conventional press working. The objective of the present paper is to review the various aspects of hole flanging process by application of single point incremental forming techniques for formation of hole flanges.

2 Various Aspects of Hole Flanging Through Incremental Forming

2.1 Single-Point Incremental Forming of Hole Flanges

Single-point incremental forming is a novel technique for the formation of axisymmetric sheet metal parts. In SPIF, a sheet metal blank with precut hole, blank holder, and rigs with backing plate and rotating tool, which follows the path defined by CNC machine are required. Figure 1 shows the experimental set up of incremental forming of hole flanging, in which a flat sheet with a precut hole is rigidly fixed onto a forming fixture which is mounted onto the table of a three-axis CNC machine [1]. SPIF hole flange tool is suspended through a spindle and forms the flange in number of increments as instructed via CNC codes. The tool contacts at single point on to the sheet and moves in the horizontal plane and deformation of
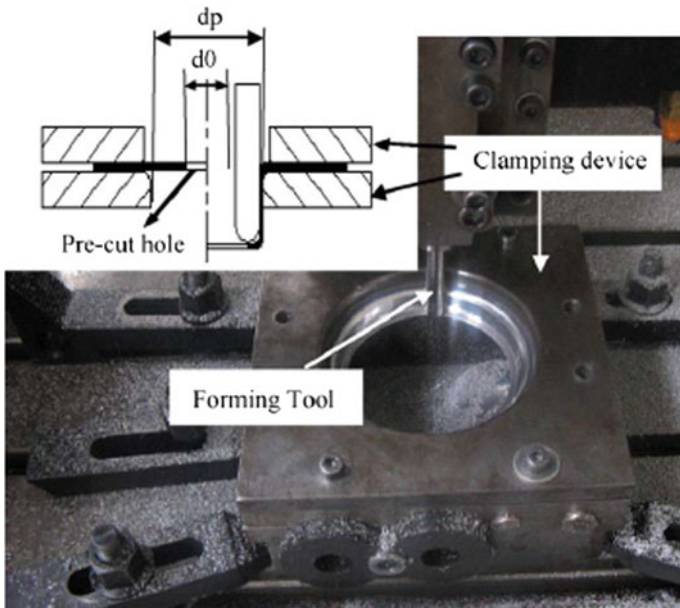
Fig. 1 Experiemental setup of single incremental forming on tabletop of CNC machine for formation of flanges [1]

flange occurs progressively in vertical direction. SPIF hole flanging offers various advantages over conventional press working such as flexibility in manufacturing, low-cost tooling sets, higher formability, capability of withstanding very short life cycles, and reducing lead times in development and production [1].

2.2 Parameters in Hole Flanging Process Through Incremental Forming

Hole flanging through incremental forming depends on different process and operating parameters. There are number of geometrical, operational, and materials parameters, which govern this process which researchers considered in past investigations of hole flanging through incremental forming. Various input parameters in incremental forming are as follows:

(i) Tool diameter, (ii) vertical step size of spiral, (iii) horizontal step size, (iv) feed rate, (v) initial drawing angle, (vi) precut hole diameter of sheet metal blank, (vii) thickness of sheet metal blank, (viii) forming strategies (diameter and wall angles), (ix) number of stages, (x) materials of sheet, (xii) rotational speed of tool, (xiii) lubricants, and (xiv) anisotropy of sheet.

The representation of output results and feasibility of the hole flanging can be expressed in terms of output parameters, which are as follows:

Output parameters are:(i) Neck height, (ii) thinning, (iii) limiting forming ratio, (iv) fracture toughness, (v) maximum hole expansion ratio, (vi) necking (vii), formability limit, (viii) ductile damage, (ix) stresses, and (x) strains.

2.3 Materials Used for Hole Flange Formation Through Incremental Forming

Materials are the essence and prime requirement for the formation of hole flanges. Proper selection of materials for the formation of hole flanges is a crucial task, which will certainly reduce risk of failure in hole flanges. Sheet metals, as well as various grades of polymer sheet materials, are utilized by various researchers in the past, in order to study formability of materials in hole flanges through incremental forming. Table 1 shows a description of materials used in forming hole flanges through single-point incremental forming technique. In majority of investigations of hole flanging through SPIF, the researchers had opted for different grades of aluminum alloys and steel alloys as workpiece material.

Table 1 Materials used in past for formation of hole flanges through incremental forming

S. no	Author	Year	Material	Thickness of material (mm)
1.	Cui and Gao [1]	2010	1060 aluminum sheet	1
2.	Petek and Kuzman [2]	2012	DC05 steel sheet	1.2
3.	Centeno et al. [3]	2012	AA1050-H111	1
4.	Montanari et al. [4]	2013	AA1050-H111	1
5.	Silva et al. [5]	2013	Commercial polymer sheets (a) polyethylene terephthalate (PET) (b) polycarbonate (PC)	3
6.	Silva et al. [6]	2013	(a) AA1050-H111 (b) Titanium (grade 2 unalloyed titanium, standard oxygen)	(a) 1 (b) 0.7
7.	Bambach et al. [7]	2014	Mild steel (DC04)	1
8.	Cristino et al. [8]	2014	AA1050-H111	1
9.	Montanari et al. [9]	2014	AISI304L stainless steel blanks	0.5
10.	Yonan et al. [10]	2014	(a) Polyvinylchloride (PVC)	3
11.	Cristino et al. [11]	2015	(a) AISI304L stainless steel blanks (b) Polyethylene terephthalate (PET)	(a) 0.5 (b) 3
12.	Borrego et al. [12]	2015	AA 7075 O sheets	1.6
13.	Cristino et al. [13]	2015	AA1050-H111	1
14.	Hussain et al. [14]	2016	Rolled AA1060 aluminum sheet	1
15.	Cao et al. [15]	2016	AA5052	1

2.4 Tool Geometry

Geometry of tools utilized in hole flanging through SPIF is a vital issue for confirming formability of hole flanges. A tool with spherical tool head is utilized in backward hole flanging process [2] as shown in Fig. 2a. Besides this, a forming tool with hemispherical tip for hole flanging through SPIF is also utilized in majority of cases as shown in Fig. 2b [3–6, 8, 9, 11, 12]. This tool is generally made up from cold working of 120WV4-DIN tool steel, which is hardened and tempered to 60 HRc and has diameter of 8 mm. Figure 2c shows a tool used in high-speed incremental forming [7]. In another analysis, a forming tool with ball circular tip of diameter of 12 mm is applied in hole flanging through SPIF as shown in Fig. 2d [14]. A new flanging tool with hyperbolic and cylindrical sections below tool arm is

also developed in order to achieve the condition of uniform thickness in hole
flanges and to overcome thinning during forming through conventional ball-nose
tool [15] as shown in Fig. 2e.

2.5 Tool Path and Strategies

In multistage SPIF of hole flanging, Cui and Gao [1] employed three different tool
paths with increment in diameter of hole, angle of bending, and combination of
diameter and angle. Petek and Kuzman [2] defined tool path in backward hole
flanging process, with change in x and change in z which represents an increase in
the horizontal x-direction and the spiral step in the vertical z-direction, respectively.
Centeno et al. [3] and Silva et al. [5] adopted a helical tool path with a step size per
revolution, which is equal to 0.2 mm in multistage incremental forming of hole
flanges. Silva et al. [5] and Cristino et al. [8] utilized tool strategy with increment in
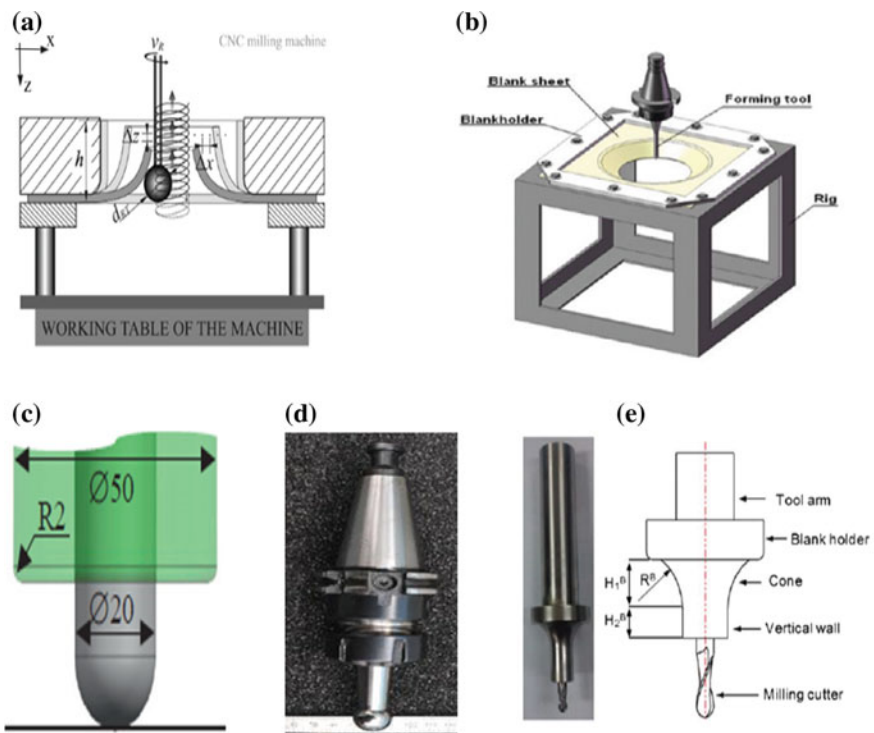
Fig. 2 Tools used in hole flanging through single-point incremental forming **a** Tool with spherical
tooltip used in BIHF process set up [2] **b** Tool used with hemispherical tooltip used in hole
flanging through SPIF [3–6, 8, 9, 11, 12] **c** Tool used in high-speed incremental forming for hole
flanging [7] **d** Tool with ball-nose tool tip [14] **e** Tool with milling cutter [15]

wall bending angles with increment of 50 from 65 to 90°. Silva et al. [6] and Cristino et al. [11] employed six stages in multistage SPIF of hole flanging in a step of 50 in the range from 650 to 900. Cristino et al. [11] adopted similar tool paths for the formation of square-shaped hole flanges through SPIF. Silva et al. [6] adopted nine stages for Titanium (grade2) for formation of hole flanges through SPIF. A similar six-stage strategy with increment of 50 in drawing angles are adopted by Montanari et al. [9] for AISI304L stainless steel sheets and Yonan et al. [10] applied similar strategy for PVC sheets for hole flange forming through multistage SPIF. Bambach et al. [7] employed tool path strategies with increment of 5 mm in hole diameter and increment in wall angle by 100. Tool paths with different trajectories [12] are shown as given in Fig. 3a.

In the initial step, the tool is moved in the vertical downward direction (z-direction) in such a manner that it will follow conical frustum with variation in slope for proper positioning of sheet over supporting plates. In second part of tool path, the tool is now moved to follow a cylindrical helical path for formation of hole flanges. This entire movement of tool path is actuated and controlled through CNC control resolution with a step down of 0.2 mm/turn in both stages. Hussain et al. [14] adopted a four-stages strateg in the range of 45°–90° with an increment of 15°. Cao et al. [15] used a ball-nose tool as shown in Fig. 3b, which follows a path from periphery of the sheet toward of center of sheet with precut hole which moves down a three-dimensional profile layer in Z-direction. They also presented a new featured tool as shown in Fig. 3c with milling cutter in which the tool moves from inward to outward in horizontal path in X-Y plane. The contact between tool and sheet occurs along a vertical band area region which enables the sheet to deform gradually for formation of flange without outward movement of new featured tool.
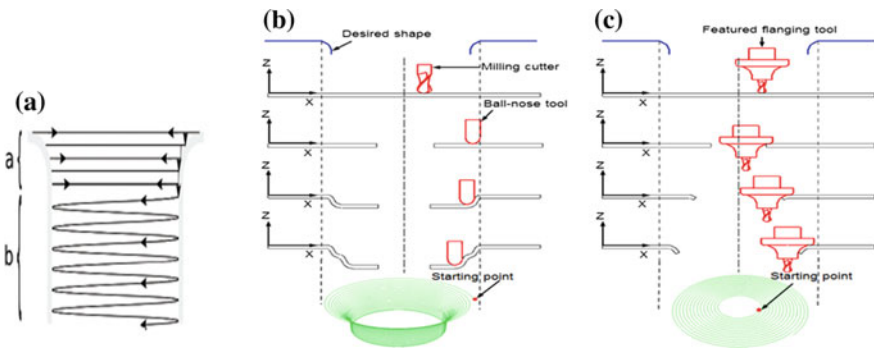
Fig. 3 Different hole flanging tool path strategies **a** Tool path with portion "a" representing Z-level trajectory for conical frustum and "b" representing cylindrical helical path [12] **b** Tool path with ball-nose tip **c** tool path with milling cutter tool

3   Research Gap

The following are the recommendations for the work, which can be included in the future for better understanding of the process of hole flanging through single-point incremental forming:

(i) Solid three-dimensional elements and solid shell combined elements can be used more for discretization of sheet metal blank for prediction of location of ductile damage and fracture in hole flanges through FEM simulation, which is not extensively carried out by previous researchers and can be taken as future work.
(ii) Tools as well as tips of the tools can be made by using composite materials and fibrous materials to study the analysis of formability of hole flanges through SPIF.

4   Results and Discussion

4.1   Finite Element Analysis of Hole Flanging Through Incremental Forming

Bambach et al. [7] utilized the concept of an adaptive blank holder by using FEM simulation in order to reduce the bulges around the primary deformation zone. Figure 4 shows the contour plots of hole flanges formed with and without adaptive blank holder. Hussain et al. [14] developed a finite element model for hole flanging through incremental forming. Figure 5 shows the finite element model of hole flanging in which sheet metal blank is shown along with rigid ball-nose spherical tip tool. They discretized the sheet metal blank with shell elements for reducing computational time while tools are considered as rigid entity. Cao et al. [15] developed FEM model in LS-DYNA FEM software package as shown in Fig. 6, with ball-nose tool and a new featured tool for hole flanging through incremental sheet forming. They discretized the sheet metal blank with three-dimensional fully integrated 8-noded S/R solid elements and considered tools as rigid elements. They found through FEM simulation that strain at point A and B gradually increases because new featured tool is in contact with forming area which will keep deformation of sheet all the time as tool moves inward to outward. Figure 7 shows the contour plot of effective plastic strain in which conventional tool has smaller contact area with forming zone as compared to new featured tool. Besides this, less through-thickness shear deformation is observed by using new featured tool [15].

Fig. 4 Contour plot of hole flanges with and without adaptive blank holder in hole flanging [7]
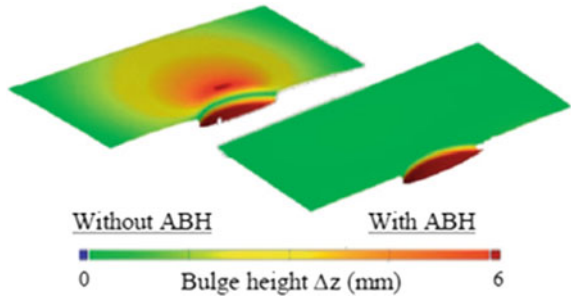
Fig. 5 FEM model of hole flanging [14]
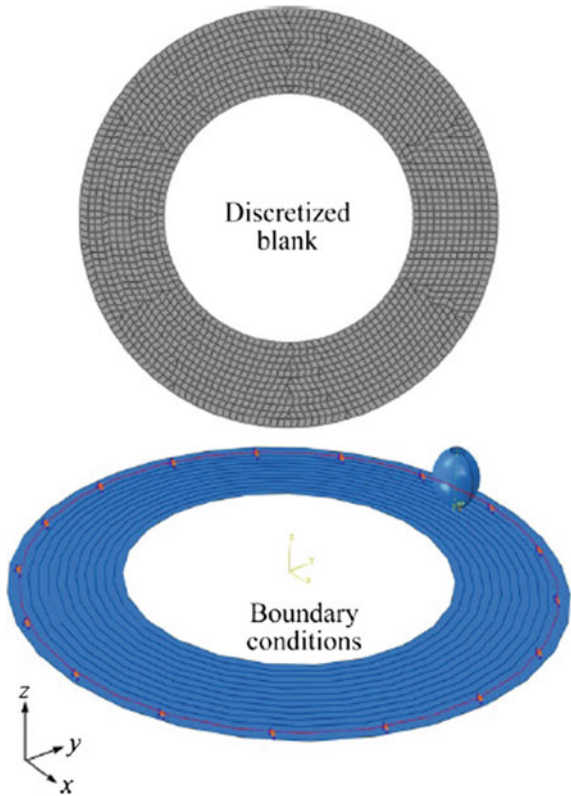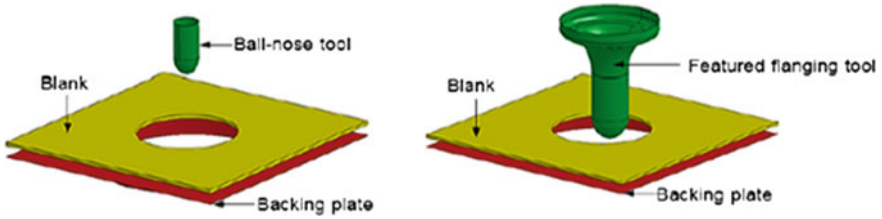
Fig. 6 FEM model of conventional ISF process and new featured tool ISF process [15]
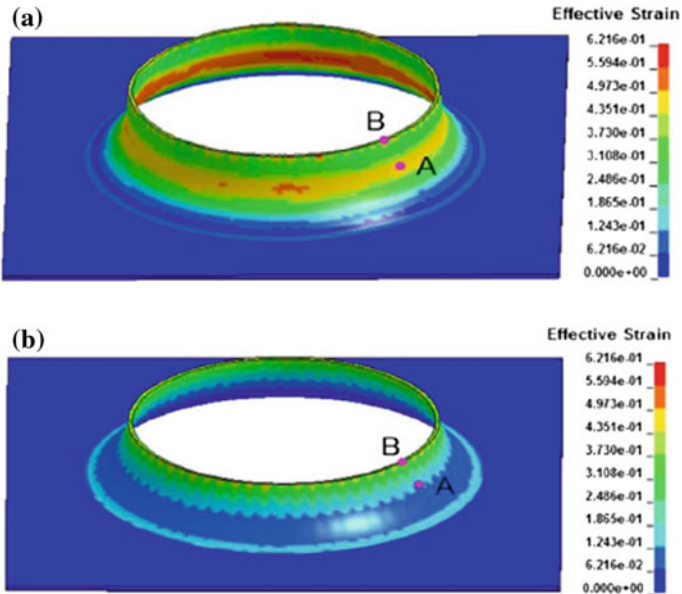
Fig. 7 Contour plot of effective stain developed in hole flanges by incremental forming **a** Conventional ball-nose tip tool **b** New featured tool with milling cutter [15]

4.2 Experimental Analysis of Hole Flanging Through Incremental Forming

4.2.1 Experimental Set Up and Procedure

Experimental set up mounted on tabletop of CNC machine is shown in Fig. 1, which comprises of forming tool and clamping device [1]. Another experimental set up for backward hole flanging is shown in Fig. 2a, in which tool moves in helical path in upward direction. Figure 2b shows the experimental set up in cubical form, which is made up of metallic bars, in which a sheet metal blank is clamped rigidly with the help of screws between blank holder and backing plate and forming tool

with spherical tooltip is placed centrally to form hole flange [3–6, 8, 9, 11, 12]. Experimental set up [7] with rotating tool to perform high-speed incremental operations is shown in Fig. 2c. High-speed tool is situated in radial direction which utilizes a slide mechanism for displacement in axial direction as shown in Fig. 9a, b [7]. Another experimental setup is made up of rigs, blank holder, backing plates, forming tool, and dynamometer is shown in Fig. 9c [12]. Experimental set up for conventional ISF process and new featured tool ISF process are shown in Fig. 9d, e, respectively (Fig. 8).
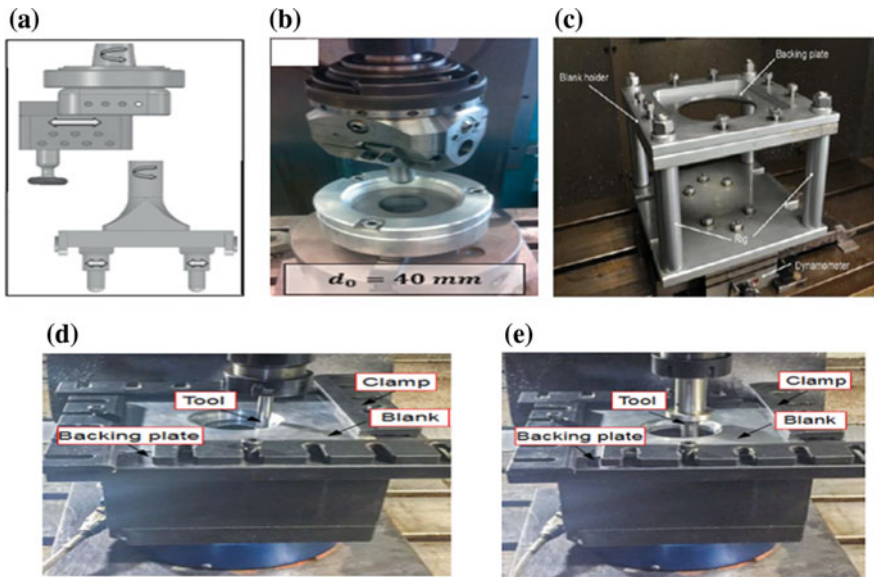
Fig. 8 **a–e** Experimental set up used in hole flanging through single point incremental forming **a**, **b** [7], **c** [12], **d**, **e** [15]
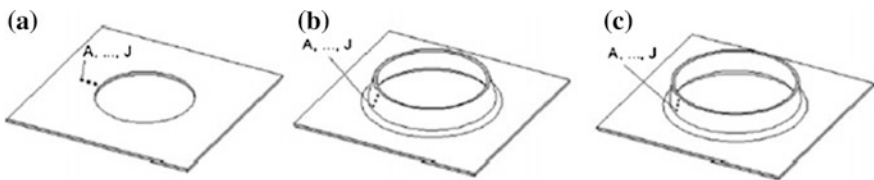
Fig. 9 Representation of marking of grid points for locating strain paths of interest **a** before deformation **b** intermediate stage **c** final deformed stage [4, 8]

4.2.2 Role of Circle Grid Analysis

Circle grid analysis is utilized for strain analysis (loci of strains) in hole flanging through SPIF. This methodology helps in determining the failure points in principal strain space for prediction of formability in terms of forming limit diagrams (FLD). In this method, generally a grid of circles of diameter in a range of 2–2.5 mm initial diameter of circle are screen printed or electrochemical etched on the sheet surface before deformation. For strain analysis, path of interest is defined initially, which will become strain path after deformation. Figure 9 shows the marking of grid points (A–J) before deformation on to the sheet metal blank with precut hole, intermediate stage of deformation and final stage of deformation [4, 8].

Computer-aided measuring system (CAMS) system is adopted by researchers which comprises of a 3Com USB camera and the GPA 3.0 software as shown in Fig. 11 [8, 11]. This camera takes a picture before forming and after forming. After deformation, the circles got converted into ellipses of major and minor axis, and these axes are measured by using computer-aided measuring system (CAMS) as shown in Fig. 10. Principal logarithmic strains can be computed by using the following relationships:

$$\varepsilon_1 = \ln\left[\frac{a}{d}\right] \tag{1}$$

$$\varepsilon_2 = \ln\left[\frac{b}{d}\right] \tag{2}$$

where d = diameter of circle; a = major axis of ellipse; b = minor axis of ellipse

$$\varepsilon_1 = \ln\left(\frac{a}{d}\right) \qquad \varepsilon_2 = \ln\left(\frac{b}{d}\right)$$
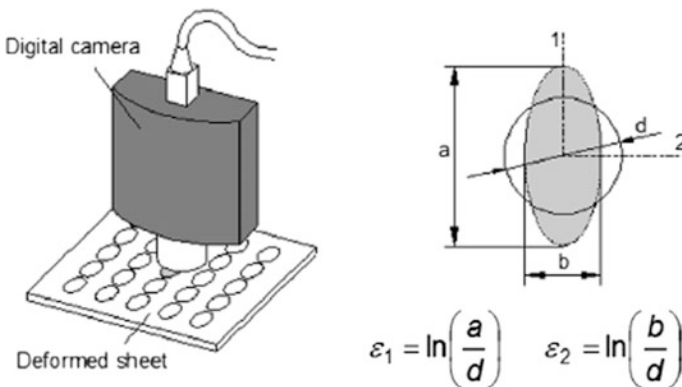
Fig. 10 Schematic representation of the procedure utilized for measuring the major and minor in-plane strains that resulted from plastic deformation of the circle during sheet formability tests [8, 11]

4.2.3 Formability Analysis

Forming limit diagrams (FLDs) and fracture forming limit line (FFL) are the two powerful tools for failure points and range strains envelope for formability prediction in hole flanging by SPIF. FLD is generated on the basis of outputs (major strains and minor strains) given by circle grid analysis after deformation. It also shows clearly limiting strains onset of localized necking and fracture strains. FLDs can be plotted after preparing sheet samples as per different types of test namely tensile test as per ASTM standard, circular bulge test, elliptical bulge test, Nakazima test and hemispherical dome test, etc. After performing these tests, limiting strains for different stress states which ranges from uniaxial to plane strain and biaxial loading conditions can be obtained [8]. In FLD major strain is plotted against minor strain and the zone below forming limiting curve (FLC) is designated as safe zone and above the zone, where fracture will occur as shown in Fig. 11. Fracture forming limit (FFL) is the line which can be obtained by measuring thickness before and after fracture as shown in Figs. 11 and 12 [8]. A–J points are marked on the precut hole sheet samples are deformed progressively by SPIF as shown in Fig. 12 [4, 8]. A solid black curve is the strain envelope and other black
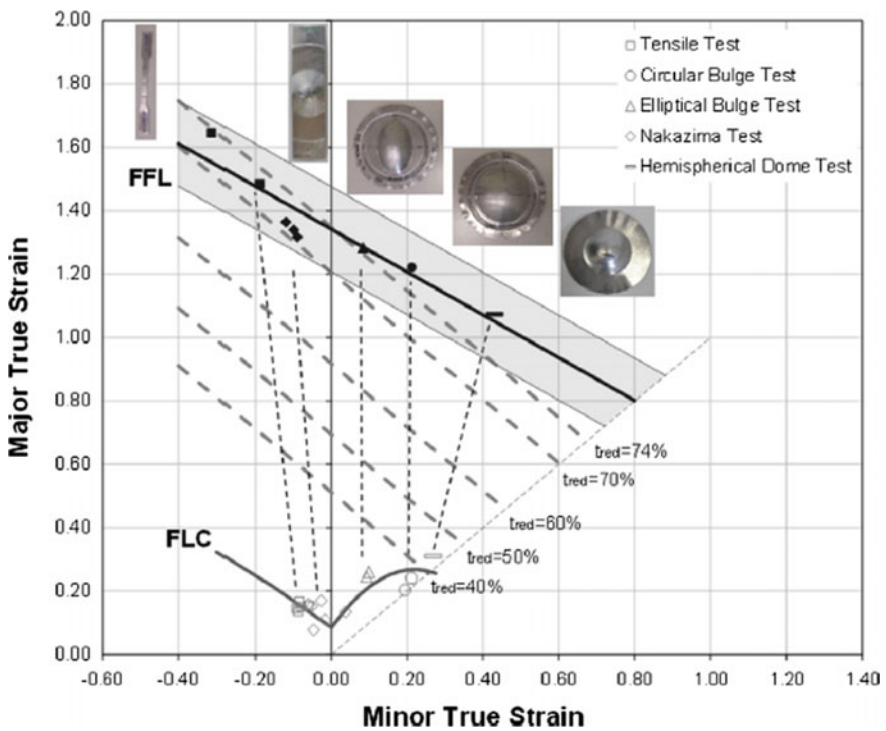
Fig. 11 Forming limit diagrams with forming limiting curve (FLC) and fracture forming limit (FFL) [8]
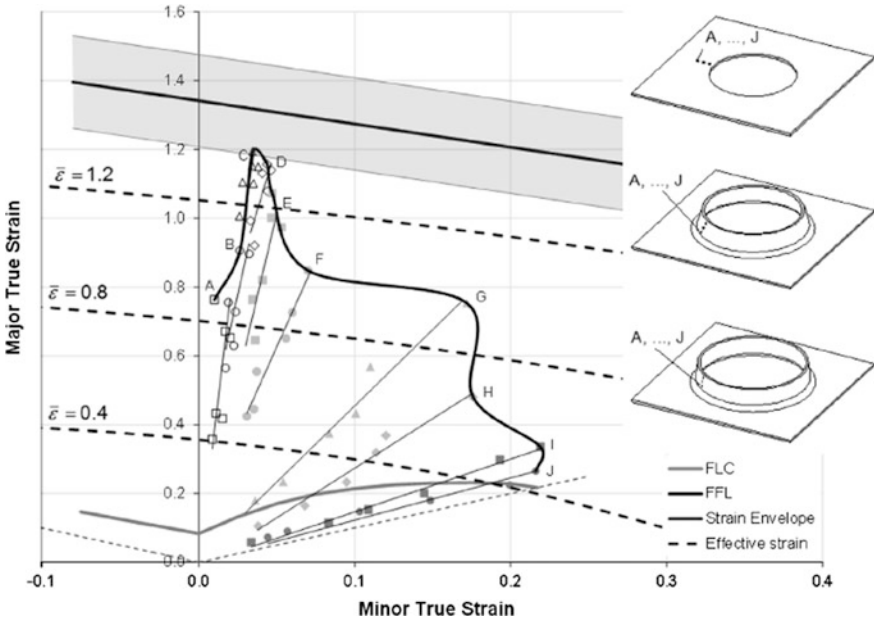
Fig. 12 Representation of the strain paths in the principal strain space, the black curve is the strain envelope [8]

solid line represents fracture forming limit lines. The region from C–E is nearest to the FFL and largest strain proved to be critical region which is located near flange wall but not at the flange wall which is found in hole flanging through conventional press working. Suppression of localized necking with low growth rate of strains above forming limiting curve in hole flanging by SPIF increases formability as compared to conventional press working.

5 Conclusions

In the present work, various attributes and capabilities of hole flanging process through incremental forming are studied. It can be concluded that formation of hole flanges through SPIF found to be more efficient and economically feasible as compared to conventional press working. Metallic alloys of aluminum and steel are found to be used in majority case of hole flanging as compared to polymeric materials. Tools with hemispherical ball-nose, high-speed tools, and new featured tools are utilized in most of the investigations of hole flanging through SPIF. Multistage forming strategies found to be more beneficial as compared to single stage direct forming. Circle grid analysis found to be very handy and efficient methodology for clear and better understanding of deformation mechanics of hole

flanging through SPIF. The design of experimental set ups of hole flanging through SPIF certainly eliminated die requirement of tool sets, which has reduced cycle time and cost of manufacturing. It is found that that the auppression of necking is the prime reason for higher formability limits of hole flanging through incremental forming as compared to conventional press working. Fewer attempts are reported in the area of FEM analysis of hole flanging via incremental forming in which mainly shell elements and solid elements are utilized for discretization of blank.

References

1. Cui Z, Gao L (2010) Studies on hole-flanging process using multistage incremental forming. CIRP J Manuf Sci Technol 2(2):124–128
2. Petek A, Kuzman K (2012) Backward hole-flanging technology using an incremental approach. Stroj Vestn- J Mech E 58(2):73–80
3. Centeno G, Silva B, Vallellano C, Martins P (2012) Manufacturing of sheet metal flanged parts using multi-stage SPIF. In: 14th International conference on metal forming, pp 271–274. Wiley-VCH Verlag GmbH & Co. KGaA, Weinheim
4. Montanari L, Cristino VA, Silva MB, Martins PAF (2013) A new approach for deformation history of material elements in hole-flanging produced by single point incremental forming. Int J Adv Manuf Technol 69(5–8):1175–1183
5. Silva MB, Martinho TM, Martins PAF (2013) Incremental forming of hole-flanges in polymer sheets. Mater Manuf Process 28(3):330–335
6. Silva MB, Teixeira P, Reis A, Martins PA (2013) On the formability of hole-flanging by incremental sheet forming. Proc Inst Mech Eng LJ Mater Des Appl 227(2):91–99
7. Bambach M, Voswinckel H, Hirt G (2014) A new process design for performing hole-flanging operations by incremental sheet foming. Procedia Eng 81:2305–2310
8. Cristino VA, Montanari L, Silva MB, Atkins AG, Martins PAF (2014) Fracture in hole-flanging produced by single point incremental forming. Int J Mech Sci 83:146–154
9. Montanari L, Cristino VA, Silva MB, Martins PAF (2014) On the relative performance of hole-flanging by incremental sheet forming and conventional press-working. Proc Inst Mech Eng L J Mater Des Appl 228(4):312–322
10. Yonan SA, Silva MB, Martins PAF, Tekkaya AE (2014) Plastic flow and failure in single point incremental forming of PVC sheets. Express Polym Lett 8(5):301–311
11. Cristino VAM, Silva MB, Wong PK, Tam LM, Martins PAF (2015) Hole-flanging of metals and polymers produced by single point incremental forming. Int J Mater Product Technol 50 (1):37–48
12. Borrego M, Palma DM, Donaire AJM, Centeno G, Vallellano C (2015) On the study of the single-stage hole-flanging process by SPIF. Procedia Eng 132:290–297
13. Cristino VAM, Montanari L, Silva MB, Martins PAF (2015) Towards square hole-flanging produced by single point incremental forming. Proc Inst Mech Eng L J Mater Des Appl 229 (5):380–388
14. Hussain G, Valaei H, Ghamdi KAA, Khan B (2016) Finite element and experimental analysis of cylindrical hole flanging in incremental forming. Trans Nonferrous Met Soc China 26 (9):2419–2425
15. Cao TT, Lu B, Ou H, Long H, Chen J (2016) Investigation on a new hole-flanging approach by incremental sheet forming through a featured tool. Int J Mach Tools Manuf 110:1–17
16. Dewang Y, Purohit R, Tenguria N (2017) A study on sheet metal hole-flanging process. Mater. Today: Proc 4(4) PD:5421–5428

Prediction of Ride Comfort of Two-Wheeler Riders Exposed to Whole-Body Vibration

Mohd Parvez and Abid Ali Khan

Abstract Two-wheelers, being an important mode of transportation, exposes the rider to a higher level of whole-body vibration (WBV) compared to cars. However, the assessment and design modification to reduce WBV in two-wheelers have not been explored in conjunction to the ride comfort. The present study develops a simulation model which can predict the effects of WBV on comfort level of two-wheeler riders as per ISO 2631-1. A 9-dof lumped mass parameter vibration model consisting of 4-dof seated human biodynamic model coupled with 5-dof two-wheeler model has been developed and represented mathematically in state space form. Further, the model has been simulated in LabVIEW and the ride comfort on a two-wheeler in different simulated driving conditions, comprising of road profiles, vehicle speed and duration of exposure were assessed. Road profiles, vehicle speeds and the duration of exposure were found to have a statistically significant effect on ride comfort.

Keywords Whole-body vibration · Two-wheeler · Ride comfort

1 Introduction

Two-wheeler is one of the most important modes of transportation for millions of peoples around the world because of its cost-effectiveness and usefulness in traffic congested areas. In developing country like India, its sale is increasing at a rate of 1 million per year and in recent years, 17.6 million two-wheelers has been sold, making it the most popular vehicle among the other categories [13]. Two-wheelers are used mostly for short distances and short durations of time, but for the professional drivers like postmen, deliverymen and courier boys, this is a vehicle of work and used for 8–10 hrs per day. Apart from the professionals, all two-wheeler

M. Parvez (✉) · A. A. Khan
Ergonomics Research Division, Department of Mechanical Engineering,
Aligarh Muslim University, Aligarh, India
e-mail: parvez0527@gmail.com

riders are exposed to different kind of environmental stressors like noise, temperature, vibration, etc. Among these environmental stressors, the exposure to vibration has found to create the whole-body vibration (WBV) effects, which have always been a matter of concern for automobile industries. It was found that the two-wheeler riders are likely to a have higher level of whole-body vibration exposure as compared to car drivers [5, 11].

WBV is an unavoidable environmental stressor found in all types of vehicle and has become a major cause of discomfort [9]. Apart from causing discomfort, WBV leads to musculoskeletal disorder such as low back pain depending on the intensity of the WBV parameters which are amplitude, frequency, duration of exposure and method of exposure [4, 10].

In attempts to solve the problem associated with WBV, the mathematical modelling cum simulation approach has found to be interesting among researchers in recent days. The popularity of this technique is because of its cost-effectiveness, less time consumption, and no human subject's intervention. For this purpose, many seated human biodynamic models had been developed form single degree of freedom to multi-degree of freedom. Among thesebio-dynamics models,the 4 degree of freedom (dof) human biodynamic model has been found to be the most suited to analyse and assess the ride comfort [2] with respect to the vehicle model.

In the present study, a simulation model was developed that can predict the effects of WBV on comfort level of two-wheeler riders. A 9-dof lumped mass parameter model has been used in state space form. The respective coding of the simulation model was done in LabVIEW12.0. The model provided a simulation interface that can be used to vary the model parameters and driving conditions to predict the effect of WBV on ride comfort.

2 Development of a Simulation Model

2.1 Vibration Model

A 9-dof lumped mass parameter vibration model (Fig. 1) has been developed which consists of 5-dof two-wheeler model (front wheel, rear wheel, vehicle body and vehicle seat) and 4-dof seated human rider biodynamic model (lower torso, viscera, upper torso and head and neck). The 4-dof biodynamic seated human model has been adopted from [15].

The assumptions made while modelling were as: (1) the model is linear time-invariant (LTI), (2) source of vibration to the human rider is vehicle seat, (3) source of vibration to the vehicle is road profile undulation, (4) rider is in erect sitting position without backrest and (5) the vertical axis vibration is the major cause of WBV.
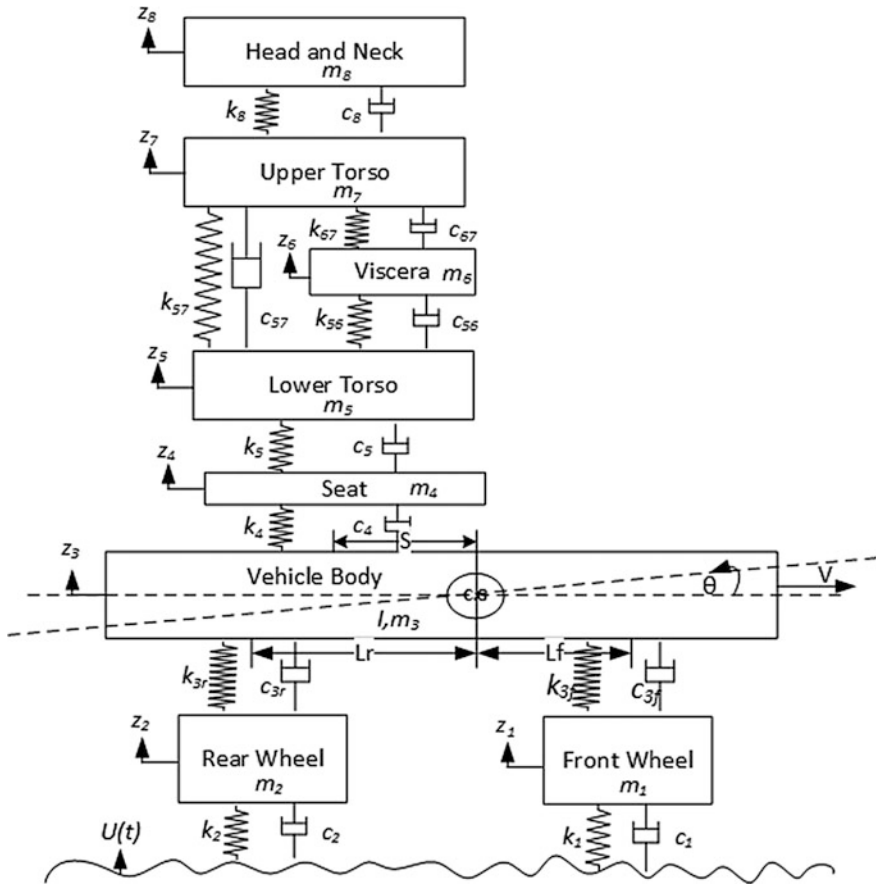
Fig. 1 Vibration model of two-wheeler coupled with rider

2.2 State Space Modelling

The presented 9-dof model (Sect. 2) was represented into state space form by using the following equations of motion. These equations were obtained by applying the D'Alembert's principle.

$$m_1\ddot{z}_1 - c_{3f}\left(\dot{z}_3 - \dot{z}_1 + L_f\dot{\theta}\right) - k_{3f}\left(z_3 - z_1 + L_f\theta\right) = k_1u(t) + c_1\dot{u}(t) \tag{1}$$

$$m_2\ddot{z}_2 - c_{3r}\left(\dot{z}_3 - \dot{z}_2 - L_r\dot{\theta}\right) - k_{3r}\left(z_3 - z_2 - L_f\theta\right) = k_2u(t) + c_2\dot{u}(t) \tag{2}$$

$$m_3\ddot{z}_3 + c_{3f}\left(\dot{z}_3 - \dot{z}_1 + L_f\dot{\theta}\right) + c_{3r}\left(\dot{z}_3 - \dot{z}_2 - L_r\dot{\theta}\right) - c_4\left(\dot{z}_4 - \dot{z}_3 + s\dot{\theta}\right)$$
$$+ k_{3f}\left(z_3 - z_1 + L_f\theta\right) + k_{3r}(z_3 - z_2 - L_r\theta) - k_4(z_4 - z_3 + s\theta) = 0 \tag{3}$$

$$I\ddot{\theta} + c_{3f}\left(\dot{z}_3 - \dot{z}_1 + L_f\dot{\theta}\right)L_f - c_{3r}\left(\dot{z}_3 - \dot{z}_2 - L_r\dot{\theta}\right)L_r + c_4\left(\dot{z}_4 - \dot{z}_3 + s\dot{\theta}\right)s$$
$$+ k_{3f}\left(z_3 - z_1 + L_f\theta\right)L_f - k_{3r}(z_3 - z_2 - L_r\theta)L_r + k_4(z_4 - z_3 + s\theta)s = 0 \tag{4}$$

$$m_4\ddot{z}_4 + c_4\left(\dot{z}_4 - \dot{z}_3 + s\dot{\theta}\right) - c_5(\dot{z}_5 - \dot{z}_4) + k_4(z_4 - z_3 + s\theta) - k_5(z_5 - z_4) = 0 \tag{5}$$

$$m_5\ddot{z}_5 + c_5(\dot{z}_5 - \dot{z}_4) - c_{56}(\dot{z}_6 - \dot{z}_5) - c_{57}(\dot{z}_7 - \dot{z}_5) + k_5(z_5 - z_4) - k_{56}(z_6 - z_5)$$
$$- k_{57}(z_7 - z_5)$$
$$= 0 \tag{6}$$

$$m_6\ddot{z}_6 + c_{56}(\dot{z}_6 - \dot{z}_5) - c_{67}(\dot{z}_7 - \dot{z}_6) + k_{56}(z_6 - z_5) - k_{67}(z_7 - z_6) = 0 \tag{7}$$

$$m_7\ddot{z}_7 + c_{57}(\dot{z}_7 - \dot{z}_5) + c_{67}(\dot{z}_7 - \dot{z}_6) - c_8(\dot{z}_8 - \dot{z}_7) + k_{57}(z_7 - z_5) + k_{67}(z_7 - z_6)$$
$$- k_8(z_8 - z_7)$$
$$= 0 \tag{8}$$

$$m_8\ddot{z}_8 + c_8(\dot{z}_8 - \dot{z}_7) + k_8(z_8 - z_7) = 0 \tag{9}$$

The state space equations were written in the following matrix form:

$$\{\dot{x}\} = [A]\{x\} + [B]\{u\} \tag{10}$$

$$\{y\} = [C]\{x\} + [D]\{u\} \tag{11}$$

where $[A]$ is the system matrix, $[B]$ is the input matrix, $[C]$ is the output matrix and $[D]$ is the transmission matrix. For a vibrating system, the two state variables viz. displacement and velocity are selected for each degree of freedom. The matrix A and B were obtained from nine equations of motion, the matrix C were selected for the desired nine displacement outputs while the D matrix is zero matrix for most of the dynamical LTI physical systems [12].

2.3   Model Parameters

The model parameters needed for the development of simulation model were adopted from the literature [2, 3] and is given in the Table 1.

Table 1 Inertial, oscillatory and geometrical parameters

Inertial parameters		Damping of rear suspension (c_{3r})	1165 N-s/m
Mass of front wheel with axle (m_1)	11.9 kg		
Mass of rear wheel with axle (m_2)	14.7 kg	Stiffness of seat (k_4)	15000 N/m
Mass of vehicle body (m_3)	85 kg	Damping of seat (c_4)	150 N-s/m
Moment of inertia of vehicle body about C.G (I)	22.013 kg-m^2	Stiffness of lower torso (k_5)	49340 N/m
Mass of the vehicle seat (m_4)	3.4 kg	Damping of lower torso (c_5)	2475 N-s/m
Mass of the lower torso (m_5)	36 kg	Stiffness between upper torso and lower torso (k_{57})	192000 N/m
Mass of the viscera (m_6)	5.5 kg	Damping between upper torso and lower torso (c_{57})	909 N-s/m
Mass of the upper torso (m_7)	15 kg	Stiffness between viscera and lower torso (k_{56})	20000 N/m
Mass of the head and neck (m_8)	4.170 kg	Damping between viscera and lower torso (c_{56})	330 N-s/m
Oscillatory parameters		Stiffness between viscera and upper torso (k_{67})	10000 N/m
Stiffness of front tire (k_1)	130000 N/m	Damping between viscera and upper torso (c_{67})	200 N-s/m
Damping of front tire (c_1)	200 N-s/m	Stiffness between upper torso and head and neck (k_8)	134400 N/m
Stiffness of rear tire (k_2)	141000 N/m	Damping between upper torso and head and neck (c_8)	250 N-s/m
Damping of rear tire (c_2)	300 N-s/m	Geometric parameters	
Stiffness of front suspension (k_{3f})	25000 N/m	Location of front suspension joint from C.G (L_f)	0.595 m
Damping of front suspension (c_{3f})	2134 N-s/m	Location of rear suspension joint from C.G (L_r)	0.70 m
Stiffness of rear suspension (k_{3r})	58570 N/m	Location of seat from C.G (s)	0.30 m

2.4 Modelling of Road Profiles

The road profiles act as a major source of vibration for any ground vehicles. ISO 8608 (2016) [8] has provided a guideline for the mathematical modelling of different classes of road profile for the purpose to study the dynamics of a ground vehicles. In the present study, Gaussian random and stationary road profiles of different classes were generated using the sinusoidal approximation method which

has also been used in previous studies [14]. The following equation gives the time domain excitation of road profiles.

$$u(t) = \sum_i^N A_i \cos(\omega_i t + \alpha_i) \tag{12}$$

3 Simulation Interface

The simulation model was developed in LabVIEW using control design and simulation module. The front panel of the simulation model is shown in Fig. 2. It provide a user interface for controlling the simulation parameters. The results were displayed in the front panel that further was exported for statistical analysis.

4 Comfort Level Assessment

In order to predict the comfort level of rider during WBV exposure, a full factorial analysis was performed by varying three important driving parameters, i.e. road profile (good and average), vehicle speed (20 km/h, 40 km/h and 60 km/h) and duration of exposure (300 s, 600 s and 900 s). The comfort level assessment was done in accordance with ISO 2631-1 (1997) based on the weighted RMS acceleration (Table 2) of vehicle seat.

In addition to weighted RMS acceleration, the model also evaluates the Vibration Dose Values (VDV), which is most widely used quantitative method to
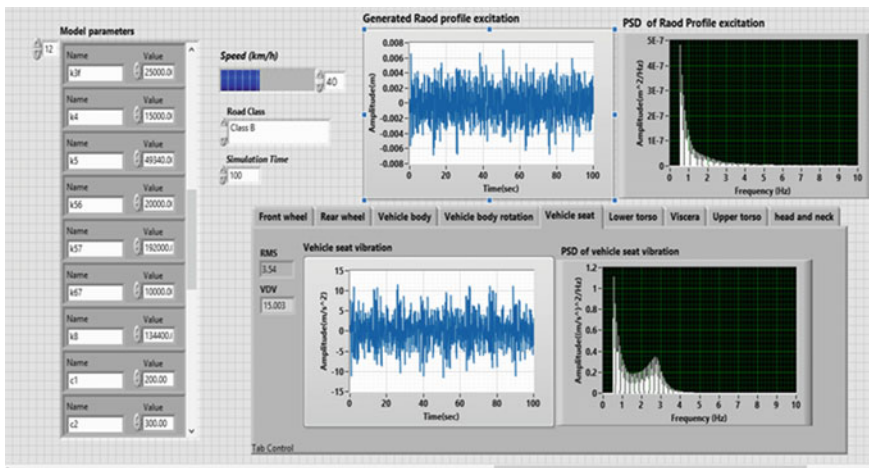
Fig. 2 Simulation interface

Table 2 Comfort level criteria as per ISO 2631-1 (1997) [7]

Acceleration (m/s^2)	Category
Less than 0.315	Not uncomfortable
0.315–0.63	A little comfortable
0.5–1	Fairly uncomfortable
0.8–1.6	Uncomfortable
1.25–2.5	Very uncomfortable
Greater than 2.5	Extremely uncomfortable

assess the WBV exposure from the safety point of view. Two limiting values, i.e. Exposure Action Value (EAV: 0.5 m/s^2 RMS acceleration or 9.1 m/s$^{1.75}$ VDV) and Exposure Limit Value (ELV: (1.15 m/s^2 RMS acceleration or 21 m/s$^{1.75}$ VDV) were provided by 2002/44/EC (2002) [1]. If the WBV exposure exceeds above the EAV, the corrective action must be taken to reduce the exposure level. On the other hand, the WBV exposure must not be exceeded above ELV.

5 Results and Discussion

Analysis of variance (ANOVA) in SPSS was performed on a total of 18 simulation runs. It was observed that there were significant main effects ($p < 0.05$) of vehicle speed and road profile on comfort level of the rider. It predicts that the road profiles should be smooth and the speed of the vehicle should be low in order to have a comfortable ride. Also, the interaction effect of road profile and vehicle speed was found significant ($p < 0.05$). It indicates that comfortable ride can also be achieved on rough road profiles if vehicle speed is kept low and there may exist an optimum combination of road profile and vehicle speed for comfortable ride. However, the effect of duration exposure on RMS acceleration was not significant ($p > 0.05$) while it showed a significant contribution on VDV ($p < 0.05$). This indicated that the RMS acceleration is a time-independent parameter while VDV is a time-dependent parameter. The same characteristicsof the duration ofexposure was also found in the previousexperimentalinvestigation [6]. Similar effects were also observed in the interaction of road profile and vehicle speed on duration of exposure.

It is clearly evident from Fig. 3 that the RMS acceleration is independent on the duration of exposure while the VDV is dependent on the duration of exposure and increases with the increase in the duration of exposure. It is also clear that the road profile increases the WBV exposure as the driving condition is moved from the Good road profile to the Average road profile. However, the increasing pattern of WBV exposure with the vehicle speed was found to be increasing on both types of road profiles. Numerical values show that the RMS accelerations were predicting
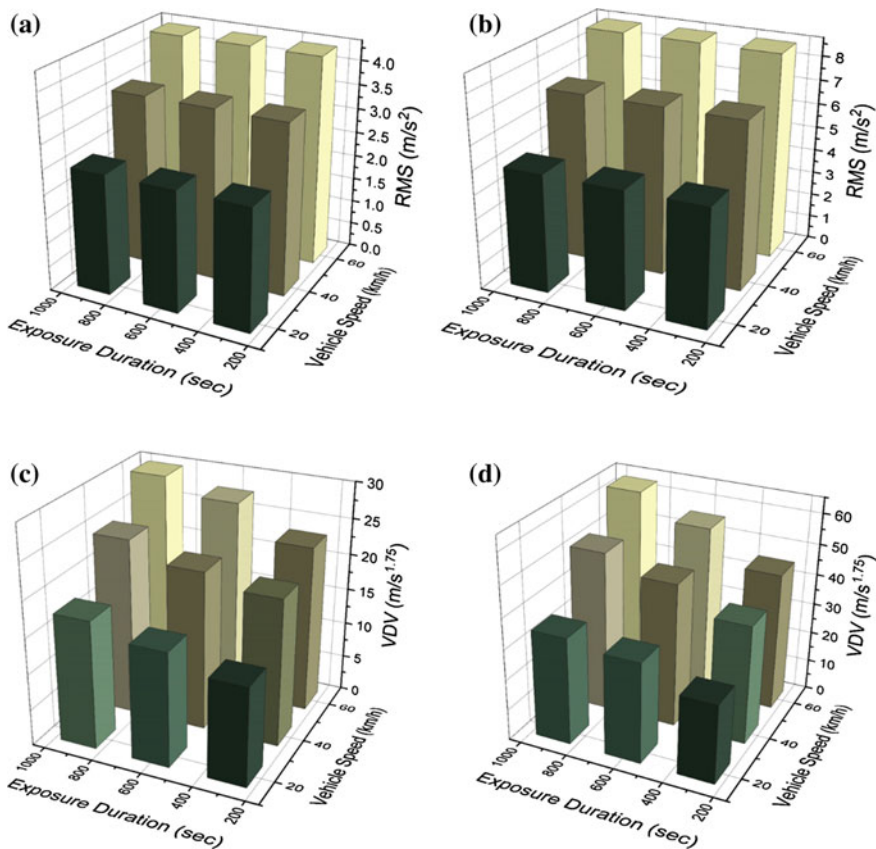
Fig. 3 WBV exposure varying with the vehicle speed and the duration of exposure: RMS acceleration for **a** Good road profile, **b** Average road profile and VDV values for **a** Good road profile, **b** Average road profile

the exposure to be extremely uncomfortable and VDV values were within the limits on Good road profiles, low speed and short duration of exposure while it moved beyond the permissible limits in the other driving conditions.

6 Conclusions

Whole-body vibration is one of the major issues causing the discomfort and health risk to the two-wheeler riders. Mathematical modelling and simulation have proven to be less time-consuming and cost-effective way to analyse the WBV exposure and finding the vehicle design improvement for comfortable ride. The present study developed a simulation model to predict the ride comfort of any two-wheeler in

different simulated driving conditions. The model predicted the ride comfort of a rider on a two-wheeler in different driving condition and found that the road profile has a greater significant effect on ride comfort followed by the vehicle speed and the duration of exposure. This whole study may be considered as an important way to further investigate the effects of WBV on two-wheeler riders as well as other vehicle drivers.

Further work is needed to validate the model, after which, it can be used to design a control strategy to reduce the WBV in various driving conditions by optimizing the vehicle design parameters.

References

1. /44/EC: European Parliament and the Council of the European Union Directive 2002/44/EC (EU Directive) on the minimum health and safety requirements regarding the exposure of workers to the risks arsing from physical agents (vibration). Off J Eur Communities. L, 177:13–19 (2002)
2. Bai X et al (2017) On 4-degree-of-freedom biodynamic models of seated occupants: lumped-parameter modeling. J Sound Vib 402:122–141
3. Benjamin NW et al (2015) Investigation of motorcycle design improvements with respect to whole body vibration exposure to the rider. J Multidiscip Eng Sci Technol 2(3):321–327
4. Bovenzi M (2010) A longitudinal study of low back pain and daily vibration exposure in professional drivers. Ind Health 48(5):584–595
5. Chen H-C et al (2009) Whole-body vibration exposure experienced by motorcycle riders – An evaluation according to ISO 2631-1 and ISO 2631-5 standards. Int J Ind Ergon 39:708–718
6. Duarte MLM et al (2018) Correlation between weighted acceleration, vibration dose value and exposure time on whole body vibration comfort levels evaluation. Saf Sci 103, November 2017, 218–224
7. ISO 2631-1: Mechanical vibration and shock—Evaluation of human exposure to whole-body vibration—Part 1: General requirements (1997)
8. ISO 8608: Mechanical vibration – Road surface profiles – Reporting of measured data (2016)
9. Mansfield N et al (2015) Driver discomfort in vehicle seats - Effect of changing road conditions and seat foam composition. Appl Ergon 50:153–159
10. Moraes GF, de S et al (2016) Whole-body vibration and musculoskeletal diseases in professional truck drivers. Fisioter. em Mov 29(1):159–172
11. Moreno R et al (2011) Predictors of whole body vibration exposure in motorcycle riders Estimadores de la vibración de cuerpo entero para motociclistas. Fac Eng Univ Antioquia 61:91–103
12. Rowell D (2002) State-Space representation of LTI systems
13. Statistica: • Two-wheeler sales in India 2017| Statistic, https://www.statista.com/statistics/318023/two-wheeler-sales-in-india/
14. Tyan F et al (2009) Generation of random road profiles. J Adv Eng 4(2):151–156
15. Wan Y, Schimmels J (1995) A simple model that captures the essential dynamics of a seated human exposed to whole body vibration. Adv Bioeng

Design and Analysis of Reciprocating Screw for Injection Moulding Machine

Vipul Parmar and Mitesh Panchal

Abstract In this paper, the design and analysis of the reciprocating screw of injection moulding machine has been presented. The flow of melted material is controlled by the reciprocating screw inside the barrel, where the raw material of the product is melted. The proper flow of melted material is required to obtain better quality of the product. Thus, the reciprocating screw can be considered as a critical component of injection moulding machine and its size varies model to model. The work presented is based on parametric modelling of reciprocating screw. The parametric modelling is carried out by merging Creo parametric and Excel spreadsheet using Excel analysis, as well as by using pro/programming of Creo Parametric modelling package. Using developed parametric model of reciprocating screw, three parameters (radius of screw, feed flight depth and metering flight depth) are required to generate the three-dimensional (3D) model for further analysis. The ease of present approach is very useful for the development of the different types of reciprocating screw in terms of variation in the said dimensions. The 3D model generated using parametric modelling has been analysed for different materials (EN-41B, EN24, EN9 and EN8). The static structural and steady-state thermal analysis has been considered to analyse stresses, total deformation, total heat flux and directional heat flux. The obtained result depicts that EN-41B has higher yield strength and EN24 has low total heat flux value. Thus, EN-41B can be considered where higher strength is required and for higher wear resistance EN24 is preferred for reciprocating screw.

Keywords Injection moulding machine · Reciprocating screw · Parametric modelling · Static structural analysis · Transient thermal analysis

V. Parmar (✉) · M. Panchal (✉)
Mechanical Engineering Department, Institute of Technology, Nirma University, Ahmedabad 382481, Gujart, India
e-mail: vvparmar82@yahoo.in

M. Panchal
e-mail: mitesh.panchal@nirmauni.ac.in

1   Introduction

In injection moulding processes, plastics are the most adaptable of all known materials and have built up themselves in good position. The aggregate utilization of plastic is more than 750,000 MT and is evaluated to cross 2500,000 MT, i.e. more than four times before this present decade's over. Injection moulding process is one of the well-known techniques to convert crude material into an article of utilization. This procedure is most regularly utilized for thermoplastic materials which might be progressively softened, reshaped and cooled. The injection moulding process is a practically useful process of manufacturing in the cutting-edge world from the automobile components to the food bundling. The injection moulding process enables us to produce simple as well as complex components/engineering products.

The most commonly used thermoplastic materials are polystyrene, acrylonitrile butadiene styrene (ABS), polyamide, polypropylene, polyethylene, and polyvinyl chloride (PVC). Most popular methods for converting plastics into useful products are blow moulding, compression moulding, injection moulding and extrusion. The injection moulding machine has two basic components; injection unit and clamping unit. The injection unit includes the melting process of the product material and it includes the mechanism, which inject the melted material into the mould to get the final product. Both these important processes of injection moulding process are carried out in the injection unit. The reciprocating screw is the important component inside the injection unit as it is useful to perform both the task of melting of product material as well as injecting melted material into the mould. The reciprocating screw is divided into three zones namely; feed zone, transition zone and metering zone. Thus, reciprocating screw is an important part/component of the injection moulding machine.

Several literatures can be found for addressing the design and analysis of the reciprocating screw of injection moulding machines [1–3]. Many industries are available, which are manufacturing the injection moulding machines, for which design of reciprocating screw is an important component. So to ease and quick designing process, the parametric modelling process of the reciprocating screw needs to be developed. To overcome this requirement of industries, the present work covers the parametric modelling of the reciprocating screw. Also, the static structural analysis and transient thermal analysis have been presented in this paper.

The present analysis has been carried out to analyse the factor of safety of the reciprocating screw for different possible materials (EN8, EN9, EN4 and EN-41B). The obtained results depict that the EN-41B material is having higher factor of safety of 5. 68359. And, the performed transient thermal analysis also suggest the suitable material as EN-41B. The presented analysis is very useful for design of reciprocating screw.

2 Modelling of Reciprocating Screw for Injection Moulding Machine

2.1 Modelling of Reciprocating Screw

Modelling of reciprocating screw of diameter 79.8 mm is carried out using Creo Parametric (a modelling software) as shown in Fig. 1.

2.2 Parametric Modelling of Reciprocating Screw

The term 'Parametric' describes here the dimension's ability of a 3D model to change the shape of model geometry as soon as the dimension value is varied. Feature-based is a term used to describe the various components of a model. For example, a part can consists of various types of features such as holes, grooves, fillets, and chamfers. A 'feature' is the basic unit of a parametric solid model.

In a parametric model, each entity like line or arc in a wireframe, or a filleting operation has parameters connected with it. These parameters control the different geometric properties of the entity, like length, width and height of a model. They also control the locations of these entities within the model. Parametric modelling uses the computer to design objects or systems that model part attributes with real-world behaviour. Parametric models use feature-based, solid and surface modelling design tools to manage the system attributes.

One of the main features of parametric modelling is that attributes that are interlinked automatically change their features. In other words, parametric modelling allows the designer to define entire classes of shapes, not just specific instances. Before the advent of parametric modelling, editing the shape was not an easy task for designers. For example, to modify a 3D solid, the designer had to change the length, the breadth and the height. However, with parametric modelling, the designer need only alter one parameter; the other two parameters get adjusted automatically.

Parametric modelling becomes one of the requirements for the design of reciprocating screw, as this involves exacting requirements and manufacturing criteria. The industries (specially injection moulding machine manufacturer) often go for parametric modelling when making families of parts that involve slight variations on a core design, because the designer will need to create design between dimensions, parts and assemblies. This supports designs that will need to be

Fig. 1 Model of reciprocating screw of 79.8 mm

Table 1 Excel spreadsheet of reciprocating screw of diameter 69.8 mm

Parameter	(mm)
Main Dia.	70
L/D Ratio	22.9226261
Compression Ratio	2.30555556
Diameter	69.8
Total Length (L)	1600
Feed Length (Lf)	800
Compression Length (Lc)	480
Metering Length (Lm)	320
Pitch (P)	70
Flight Width	7
Metering Flight Depth (Dm)	3.6
Feed Flight Depth (Df)	8.3
Under Cut Diameter	69.5
Under Cut Length	262.5
Under Cut Thickness	0.125
Shank Diameter 1	69.4
Shank Diameter 2	69
Shank Diameter 3	60
Spline Diameter	69.31
Shank Length 1	83
Shank Length 2	199
Shank Length 3	100
Spline Length	80
Leading Radius	7
Trailing Radius	3.5
Profile Length	63
Extension in Helical Profile	35

modified or iterated on a regular premise. It also creates models with single features that can be modified or changed—such as holes and chamfers—those are captured in a model tree.

Parameters of reciprocating screw of diameter 69.8 mm is linked with the excel spreadsheet which is shown in below Table 1.

Table 1 linked with the Creo model of reciprocating screw of diameter 69.8 mm for the parametric modelling of diameter 79.8 mm. Model of reciprocating screw of diameter 69.8 mm was modified by changing few parameters highlighted in Table 2 and reciprocating screw of 79.8 mm was obtained.

Parametric modelling is carried out by merging Creo parametric and MS Excel using Excel analysis function. Excel analysis is used to carry out parametric modelling in that you change a few specific parameters and get a new modified model. An Excel spreadsheet file is made consisting of different relative dimension

Table 2 Excel spreadsheet of reciprocating screw of diameter 79.8 mm

Parameter	(mm)
Main Dia.	80
L/D Ratio	20.05012531
Compression Ratio	2.289473684
Diameter	79.8
Total Length (L)	1600
Feed Length (Lf)	800
Compression Length (Lc)	480
Metering Length (Lm)	320
Pitch (P)	80
Flight Width	8
Metering Flight Depth (Dm)	3.8
Feed Flight Depth (Df)	8.7
Under Cut Diameter	79.55
Under Cut Length	300.1074499
Under Cut Thickness	0.125
Shank Diameter 1	79.4
Shank Diameter 2	79
Shank Diameter 3	70
Spline Diameter	79.31
Shank Length 1	83
Shank Length 2	199
Shank Length 3	100
Spline Length	80
Leading Radius	7
Trailing Radius	3.5
Profile Length	72
Extension in Helical Profile	40

parameters of reciprocation screw and it is then linked with the Creo parametric model using excel analysis function. Once the spreadsheet file is linked with Creo parametric, any change in parameters given in a spreadsheet will lead to change in parametric model as well.

3 Design of Reciprocating Screw

Figure 2 shows the different zones of reciprocating screw of injection moulding machine and the empirical relations of different dimensions in terms of core diameter of the screw. For the design of reciprocating screw, different dimensions can be determined by the following relations [4].
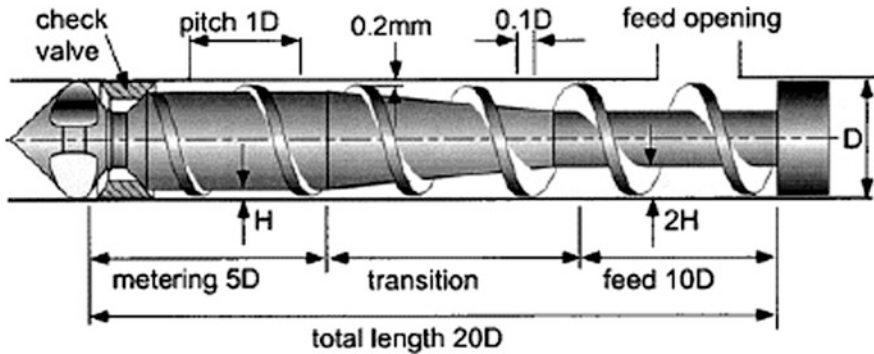
Fig. 2 Terminology of reciprocating screw [4]

where

D = Core Diameter of Reciprocating Screw = 70 mm
Total Length of Flighted Section of Screw = 20D = 1400 mm
Length of Feed Section = 10D = 700 mm
Length of Transition Section = 5D = 350 mm
Length of Metering Section = 5D = 350 mm
Pitch of Screw = 1D = 70 mm
Width of Flight of Screw = 0.1D = 7 mm
Flight Depth in Feed Section = 0.16D to 0.18D = 11.2 to 12.6 mm
Flight Depth in Metering Section = 0.06D to 0.07D = 4.2 to 4.9 mm.

4 Result and Discussion

4.1 Static Structural Analysis

Static structural analysis has been carried out in ANSYS workbench. The different material properties applied to carry out this analysis are density, thermal expansion, Young's modulus, Poisson's ratio, yield tensile strength, ultimate tensile strength, specific heat, thermal conductivity. The geometry of reciprocating screw was modelled in Creo parametric, and then it is imported into the ANSYS workbench. The meshing of model was done. Three boundary conditions are applied as follows [1, 5, 6]. The properties of all considered materials are summarized in Table 3 [5–8].

- One end of the reciprocating screw was kept fixed, which is near to the metering zone.
- Other end was kept free and applied moment from the machine manual, which is near to the drive zone.
- The injection pressure was applied to the model of reciprocating screw.

Table 3 Physical properties for different materials of reciprocating screw

Materials	Young's modulus (PA)	Poisons ratio	Density (kg/m^3)	Thermal expansion	Yield tensile strength (PA)	Ultimate tensile strength (PA)	Specific heat (J/g-K)	Thermal conductivity (W/m-K)
SAE52100 (EN-41B)	210×10^9	0.3	7810	11.9×10^{-6}	9.1×10^8	672×10^6	0.475	46.6
SSAE4340 (EN 24)	205×10^9	0.292	7850	12.3×10^{-6}	4.7×10^8	689×10^6	0.475	44.5
SAE1040 (EN 9)	203×10^9	0.292	7810	10.7×10^{-6}	3.5×10^8	632×10^6	0.473	42.7
SAE4040 (EN 8)	200×10^9	0.292	7845	11.3×10^{-6}	3.5×10^8	585×10^6	0.486	51.9

4.2 Transient Thermal Analysis

Transient thermal analysis has been carried out in ANSYS workbench. The different material properties applied to carry out this analysis are density, thermal expansion, Young's modulus, Poisson's ratio, yield tensile strength, ultimate tensile strength, specific heat, thermal conductivity. The geometry of reciprocating screw was modelled in Creo Parametric, and then it is imported into the ANSYS workbench. The meshing of model was done. One boundary condition is applied as follows [2]. The temperatures of different considered mould materials at different zones of reciprocating screw are summarized in Table 4. These values of the required temperature of mould materials at different zones have been utilized to perform transient thermal analysis.

4.3 Static Structural Analysis

The static structural analysis of reciprocating screw has been done by the ANSYS Workbench. The same model is analysed for different materials such as EN 8, EN 9, EN 24 and EN-41B. The results obtained from the analysis are summarized in Table 5.

Table 4 Temperatures for mould materials applied at various zones of screw

Materials	Mould temperatures (°C)			
	T1 (Metering Zone)	T2 (Compression Zone)	T3 (Feed Zone)	T4 (Drive Zone)
Nylon-66	240	275	280	60
Low-Density Polyethylene	150	170	190	60
Polypropylene	200	230	240	60
Flexible Pvc	140	160	170	60
Polystyrene	170	220	230	60

Table 5 Results of static structural analysis of different materials

Property	EN 8	EN 9	EN 24	EN-41B
Total Deformation, m	Max: 0.00175	Max: 0.00177	Max: 0.00173	Max: 0.00169
	Min: 0	Min: 0	Min: 0	Min: 0
Equivalent Stress, Pa	Max: 1.602e8	Max: 1.602e8	Max: 1.602e8	Max: 1.601e8
	Min: 2.103e5	Min: 2.103e5	Min: 2.103e5	Min: 2.114e5
Shear Stress, Pa	Max: 7.794e7	Max: 7.794e7	Max: 7.794e7	Max: 7.790e7
	Min: −7.818e7	Min: −7.818e7	Min: −7.818e7	Min: −7.815e7
Factor of Safety	2.18463	2.20585	2.93364	5.68359
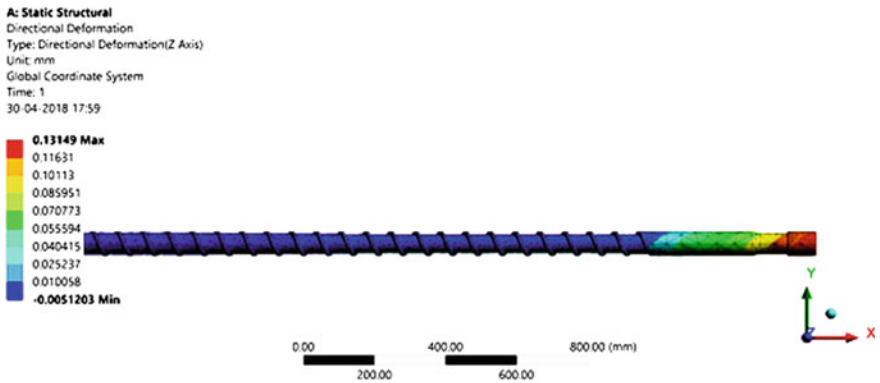
Fig. 3 Directional deformation of reciprocating screw of EN-41B material

The finite element method (FEM) based simulations have been performed for static structural analysis using ANSYS workbench. Figure 3 shows, simulated result for directional deformation. And, Figs. 4 and 5 show the simulated results for
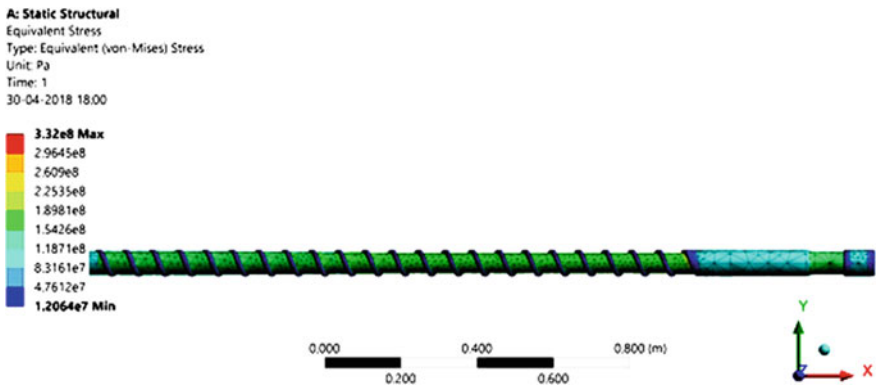
Fig. 4 von Mises stress of reciprocating screw of EN-41B material

A: Static Structural
Shear Stress
Type: Shear Stress(XY Plane)
Unit: Pa
Global Coordinate System
Time: 1
30-04-2018 18:00

7.2021e7 Max
5.2392e7
3.2762e7
1.3132e7
-6.4972e6
-2.6127e7
-4.5756e7
-6.5386e7
-8.5015e7
-1.0465e8 Min

0.000   0.400   0.800 (m)
     0.200   0.600
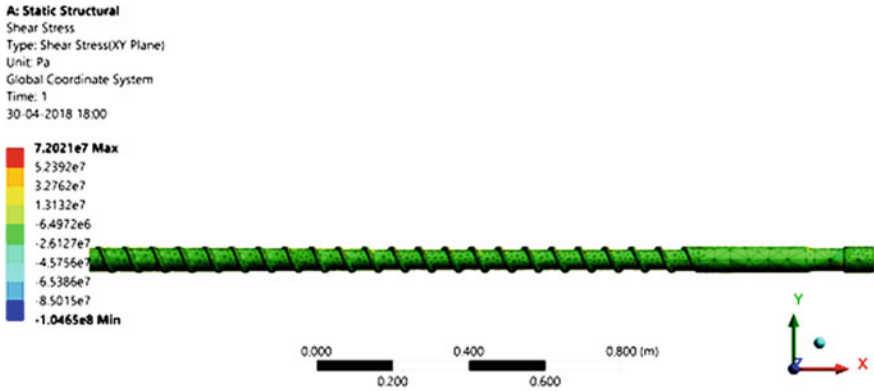
Fig. 5 Shear stress of reciprocating screw of EN-41B material

von Mises stresses as well as shear stress analysis, respectively, for the applied boundary conditions to the reciprocating screw of EN-41B material.

The FEM-based simulated results are summarized in Table 5 for different considered materials of reciprocating screw. The obtained results depict that for the same dimensions of reciprocating screw, the EN-41B material provides higher factor of safety as 5.68359. While for other considered materials factor of safety varies in the range of 2.1–3.0. The performed analysis suggests that EN-41B is the most suitable material for the reciprocating screw.

4.4 Transient Thermal Analysis

Figure 6 shows the meshed of 3D model of reciprocating screw for transient thermal analysis.

The transient thermal analysis also has been done for reciprocating screw by the ANSYS workbench. The same model is analysed for different materials such as EN8, EN9, EN24 and EN-41B. The results of transient thermal analysis of reciprocating screw of different materials for different mould materials are shown in Tables 6, 7, 8 and 9.

The obtained results depict that the EN-41B material is most suitable as it is having lower heat flux value, ultimately which reduces wear of thread of reciprocating screw.

Fig. 6 Meshed model of reciprocating screw for transient thermal analysis

Table 6 Results of transient thermal analysis using EN8 material

Property	Nylon	LDPE	Polypropylene	Flexible PVC	Polystyrene
Temp., °C	Max: 337.58	Max: 224.99	Max: 291.3	Max: 198.79	Max: 274.5
	Min: 16.599	Min: 18.593	Min: 17.651	Min: 19.6	Min: 17.117
Total heat flux, W/m^2	Max: 1.022e7	Max: 6.433e6	Max: 8.859e6	Max: 5.954e6	Max: 8.003e6
	Min: 2.304e-12	Min: 2.648e-12	Min: 0	Min: 1.300e-12	Min: 7.617e-28
Directional heat flux, W/m^2	Max: 7.968e6	Max: 4.150e6	Max: 7.375e6	Max: 6.282e6	Max: 5.831e6
	Min: −5.348e6	Min: −5.3226	Min: −7.398e6	Min: −3.785e6	Min: −4.135e6

Table 7 Results of transient thermal analysis using EN9 material

Property	Nylon	LDPE	Polypropylene	Flexible PVC	Polystyrene
Temp., °C	Max: 337.59	Max: 224.03	Max: 287.12	Max: 198.79	Max: 274.5
	Min: 17.158	Min: 18.996	Min: 18.617	Min: 18.548	Min: 17.254
Total heat flux, W/m^2	Max: 1.224e7	Max: 7.471e6	Max: 1.0219e7	Max: 6.378e6	Max: 9.635e6
	Min: 2.801e-12	Min: 3.218e-12	Min: 1.295e-12	Min: 1.448e-12	Min: 5.110e-27
Directional heat flux, W/m^2	Max: 1.072e7	Max: 4.905e6	Max: 8.855e6	Max: 5.277e6	Max: 7.107e6
	Min: −6.495e6	Min: −3.452e6	Min: −5.315e6	Min: −3.247e6	Min: −5.023e6

Table 8 Results of transient thermal analysis using EN24 material

Property	Nylon	LDPE	Polypropylene	Flexible PVC	Polystyrene
Temp., °C	Max:337.59	Max: 224.03	Max: 289.98	Max: 200.32	Max: 274.5
	Min:17.533	Min: 18.58	Min: 17.887	Min: 19.39	Min: 18.334
Total heat flux, W/m^2	Max:1.0737	Max: 6.474e6	Max: 9.279e6	Max: 5.673e6	Max: 8.309e6
	Min:5.379e-12	Min: 2.759e-12	Min: 0	Min: 1.241e-12	Min: 1.664e-27
Directional heat flux, W/m^2	Max:7.887e6	Max: 5.526e6	Max: 7.549e6	Max: 4.557e6	Max: 6.079e6
	Min: −5.576e6	Min: −3.291e6	Min: −7.678e6	Min: −4.655e6	Min: −4.309e6

Table 9 Results of transient thermal analysis using EN-41B material

Property	Nylon	LDPE	Polypropylene	Flexible PVC	Polystyrene
Temp., °C	Max: 317.3	Max: 224.02	Max: 289.26	Max: 199.4	Max: 274.5
	Min: −33.504	Min: 20.743	Min: 19.668	Min: 19.038	Min: 17.731
Total heat flux, W/m^2	Max: 5.565e6	Max: 6.945e6	Max: 9.751e6	Max: 5.954e6	Max: 8.739e6
	Min:7.213e-13	Min: 3.265e-12	Min: 0	Min:1.300e-12	Min: 2.322e-27
Directional heat flux, W/m^2	Max: 4.491e6	Max: 4.905e6	Max: 6.690e6	Max: 4.081e6	Max: 6.366e6
	Min: −3.261e6	Min: −3.452e6	Min: −7.975e6	Min: −4.891e6	Min: −4.511e6

5 Conclusion

Parametric modelling of reciprocating screw of injection moulding machine has been created of diameter 79.8 mm. The excel analysis function of Creo (modelling software) has been used to generate parametric modelling of reciprocating screw of injection moulding machine. The required sizes of the reciprocating screw can be easily incorporated in terms of core diameter and model can be generated based on the Excel analysis. The result obtained for the static structural analysis depict that EN41B material has the higher factor of safety compared to other materials like EN8, EN9 and EN24. The obtained results based on transient thermal analysis depict that among all the considered steel grade materials, the SAE 52100 (EN-41B) has been found as the most suitable material for reciprocating screw, as it exhibits the minimum heat flux generation while processing. The EN-41B material which is having higher value of factor of safety for the considered dimensions of reciprocating screw and the minimum value of heat flux generation is the most suitable material for the reciprocating screw of injection moulding machine.

References

1. Ganesh K (2015) Design and analysis of new coupling system in injection moulding machine to improve screw life. Int J Innov Eng Res Technol 2(3):1–6
2. Vikas RR, Jadhao PK (2013) Finite element analysis of reciprocating screw for injection moulding machine. Int J Innov Res Sci Eng Technol 2(7):3137–3143
3. Nagrale NB, Baxi RN (2011) Finite element analysis of reciprocating screw for injection moulding machine. Int J Eng Technol 3(3):191–199
4. https://www.plasticsportalasia.net/wa/plasticsAP∼zh_CN/function/conversions:/publish/comon/upload/technical_brochures/TI_Screwdesigns.pdf

5. Bull SJ, Zhou Q (2001) A simulation test for wear in injection moulding machines. Wear 249:372–378. (PII: S0043-1648 (01) 00543-9)
6. Ke Y, Furong G, Frank A (2008) Barrel temperature control during operation transition in injection molding, The Hong Kong university of science and technology. Control Eng Pract 16:1259–1264
7. Fantoni G, Tosello D, Gabelloni HN (2012) Modelling of injection molding machines for micro manufacture applications through functional analysis. Procedia CIRP 2:107–112
8. Venugopal PK, Shailesh P, Baig Z (2015) Finite element analysis and validation of reciprocating screw and coupling of injection molding machine. IOSR J Mech Civil Eng (IOSR-JMCE) 88–94

A Neural Network Classification of sEMG Signals for Estimation of Force While Gripping

Salman Mohd Khan, Abid Ali Khan and Omar Farooq

Abstract In recent years, surface electromyography (sEMG) has been an important aspect in the control of prosthetic and orthotic devices. However, such devices are still subject to discussion because of the inability to perform actions of daily living. One such issue is the retrieval of clear neural information from noise-free EMG signals. In this paper, the objective is to identify optimal time domain sEMG features for a task of low-level gripping force by performing classification with neural networking technique. The classifier was designed using an artificial neural network for different gripping force level. The gripping gestures were performed at two levels: first, simple gripping, when no force was applied and second, simple gripping with a force of 10 N. The multichannel sEMG signals were recorded from six forearm muscles namely ECD, ECR, ECU, FCU, FCD, and FCR. This paper helps to identify the merits of ANN and importance of different forearm muscles for feature selection. The results are obtained from the neural networking indicated root mean square (RMS) and waveform length (WL) as superior time domain features. Further; extensor muscles were found to be more responsive as compared to flexor muscles.

Keywords EMG feature extraction · Neural networking · ANN

1 Introduction

Surface electromyograms (sEMG) are extensively used in prosthetic devices as well as in assistive devices. These devices are controlled by electromyogram (EMG) signals, which take information from the muscles in the form of electrical activity. These signals are retrieved when the muscles undergo contraction. The

S. M. Khan (✉) · A. A. Khan
Ergonomics Research Division, Department of Mechanical Engineering, AMU, Aligarh, India
e-mail: salmanmkhan225@gmail.com

O. Farooq
Department of Electronics Engineering, AMU, Aligarh, India

upper limb myoelectric prosthetic devices are based on surface EMGs, which help to restore the functionalities lost after amputation. Several studies have been carried out for the upper limb prosthetic devices to discuss the role of EMG signals for grasping of objects [1], the posture of hand [2], and applied force for gripping purposes [3].

The authenticity of the relationship between sEMG and grip force depends on muscles selection, features derived from muscle signals, and method to derive to relations. The earliest known research was done by Duque and Masset for different postures and forces varying with respect to maximum voluntary contraction (MVC). The EMG signals were measured on the flexor muscles of a forearm [4]. In 2010; Matheiesen [5] recorded the EMG signals from only flexor digitorum profundus muscle for prediction of power grip. Baranski [6] also analyzed the role of flexor muscles. However, very few researchers [3, 7] have incorporated extensor muscles in their study.

The features most often used in the development of EMG-grip force relation are integrated EMG (iEMG), Variance (VAR), Mean Absolute Value (MAV), Waveform Length (WL), Wilson Amplitude (WAMP), Power Spectrum ,and autoregressive model. [8] In general; the optimality was obtained for iEMG, waveform length, VAR and autoregressive models [9, 10].

The performance of features to predict force can be modeled by using techniques/algorithms named as linear discriminant analysis, support vector machines, [11] artificial neural networking (ANN), etc. Often, the researchers investigated linear relationship between EMG and grip force, but this resulted in poorer performance and predictability than techniques mentioned earlier [2, 5, 11]. The most frequently used and much predictable algorithm has been artificial neural networking [5, 11, 12]. More importantly; there isn't any work to our knowledge where more than three muscles of the forearm are used as input in a single model to predict low-level force.

In this study; an artificial neural network based classifier has been proposed to identify best features to predict a gripping task at different low-level force. Further, sensitivity analysis was performed to reveal the importance of the muscles for classification of the task. The focus of this study was on the low-level grip forces in the robotic prosthetic hand, which are essentially required for light and fragile objects. The models relating sEMG and force were developed with the help of artificial neural networking or multilayer perceptron. This would further help to identify the features and forearm muscles which respond most to low-level forces.

2 Methodology

The experiment was performed on eight able-bodied human subjects (age range: 23–27 years; mean: 25.625 years). All the subjects were right handed. The subjects were asked to provide their written consent prior to the experiment.

2.1 Experimental Procedure

The subjects were seated on an adjustable chair with their right arm placed on the armrest shown in Fig. 1. The arm on the armrest with all fingers in the direction of the arm was considered as the home position. The subjects performed a gripping action (i.e., bringing four fingers and a thumb simultaneously around the Jamar handgrip dynamometer).

The objective of the experiment was to retrieve the data for no force and low grip forces which can be subsequently used to design a system for the classification of these cases of grip forces. The whole gripping process was completed in 12–15 s. It involved the following steps: starting from the home position to forming a grip; maintaining a grip for 4–5 s (prescribed time was 5 s); bringing back fingers to home position. Each subject was asked to perform each case for multiple trials. In each case; the subjects were asked to rest for 2 min in between each trial. After one case; the rest period was 5 min.

Before the recording; all subjects were allowed to get used to the experimental setup and practice to maintain a grip with a required force.

A Jamar handgrip dynamometer (Biometrics) with an adjustable grip was used to measure the grip force. The grip size was changed accordingly for the convenience of the subject as well as ensuring that the grip is formed by the proximal phalanges and metacarpals of fingers and thumb.

The EMGs were recorded using bipolar wire electrodes from six muscles: Flexor Digitorum Superficialis (FDS), Flexor Carpi Radialis (FCR), Flexor Carpi Ulnaris
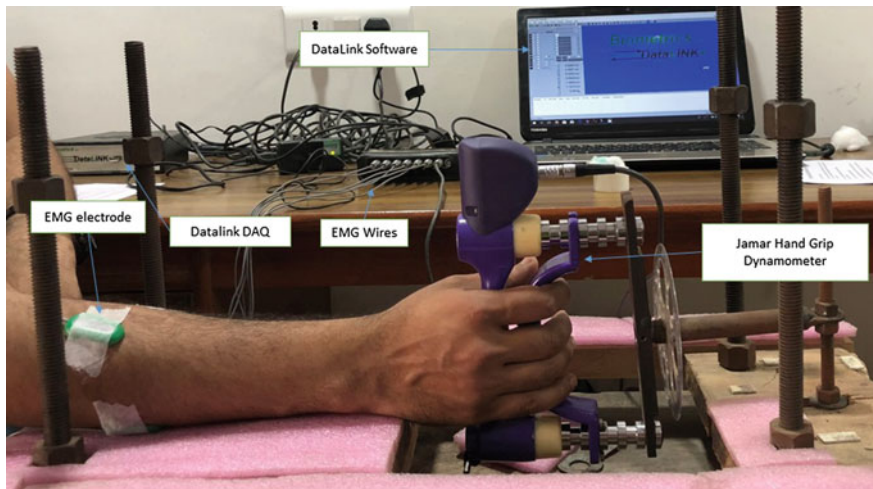
Fig. 1 Data acquisition setup for the recording of EMG signals

(FCU), Extensor Carpi Ulnaris (ECU), Extensor Carpi Radialis (ECR), and Extensor Digitorum Superficialis (EDS). The standard protocol for surface electromyography for noninvasive assessment of muscles (SENIAM) was followed for the placement of electrodes. The reference electrode was placed behind the earlobe. The EMG signals were recorded using a Datalink system with a sampling rate of 1000 Hz. The force signals were sampled at a rate of 50 Hz.

2.2 Feature Extraction

The features were extracted over the entire interval of gripping; Altogether, six features were extracted from six EMG channels placed on six different muscles mentioned earlier. These features are most commonly used to estimate muscle behavior for gripping actions. They are as follows:

Mean Absolute Value: It is calculated as an average of absolute values of the EMG signal amplitude in a segment [8].

Integrated EMG: Integrated EMG is defined as a summation of absolute values of the EMG signal amplitude [8].

Root Mean Square: RMS is the quadratic mean of the EMG signal [8].

Waveform Length: This feature provides information about the frequency, duration, and waveform amplitude of the EMG signal [8, 11].

Variance: Variance is the average of square values of the deviation of the EMG values.

Power Spectrum: Power spectrum, also called total power is an aggregate of the EMG spectrum.

The individual ability of the feature to estimate grip force of a hand can be established by using a neural networking method named as a multilayer perceptron. A multilayer perceptron is one of the earliest neural networking techniques based on feedforward artificial neural networking.

The models were designed for each feature involving six muscles; thus forming a network of six muscles as input. The network designed; consist of a single hidden layer; with 10 neurons. The activation functions for the hidden layer and the output layer were sigmoid functions. The batch training was performed based on the gradient descent algorithm. The output module consisted of two neurons; one with no force and other with force of 10 N. 70% of the data was used for training of the network while the rest was used to test the model. The number of epochs was set as 1000. The resulting data was analyzed on the basis of the sum of squares of error (Fig. 2).

Fig. 2 Neural network for RMS feature
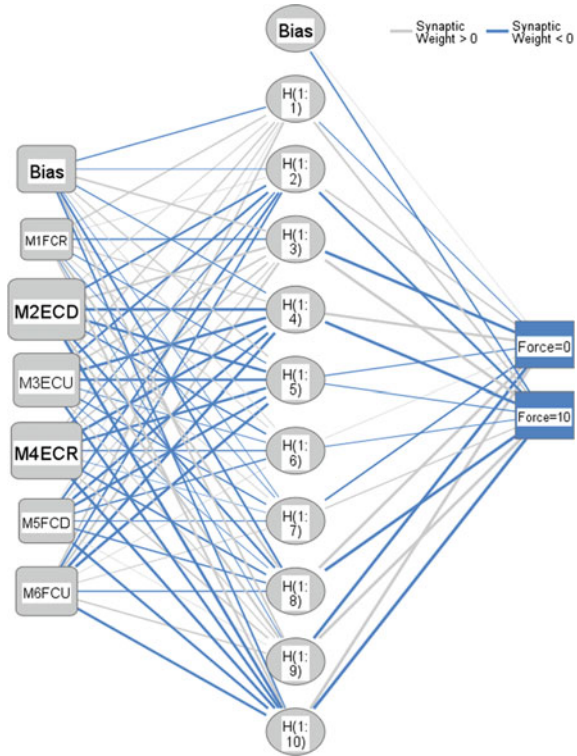
3 Results and Discussion

The superiority of features extracted for classification of grip force was estimated by sum of squares of error and the percent of correct prediction. The range of the sum of squares of error for all features was 1.62-0.34. The highest percent correct predictions were 94.9% and 93.8% for RMS and waveform length (WL) features, respectively. The overall analysis depicted that the performance was worst for power spectrum feature. The second worst performance was of integrated EMG (iEMG) feature. The sum of squares of error and percent correct prediction for iEMG feature were 1.15 and 83.3%, respectively. Figure 3 shows sum of squares of error and percent correct prediction for each feature.

Figure 4 shows the behavior of different muscles for different features. The data is in terms of normalized importance. These graphs helped to identify the significance of different muscles in features, showing superior classification.

Extensor Carpi Digitorum (ECD) and Extensor Carpi Ulnaris (ECU) are the most significant muscles for generating a relation between EMG feature and grip force outcome. Based on the electromyography signal; ECD muscle showed highest influence in the classification models of RMS, MAV, iEMG and Variance features. However, in rest of the cases, not all muscles were heavily involved in generating a

(a)

(b)
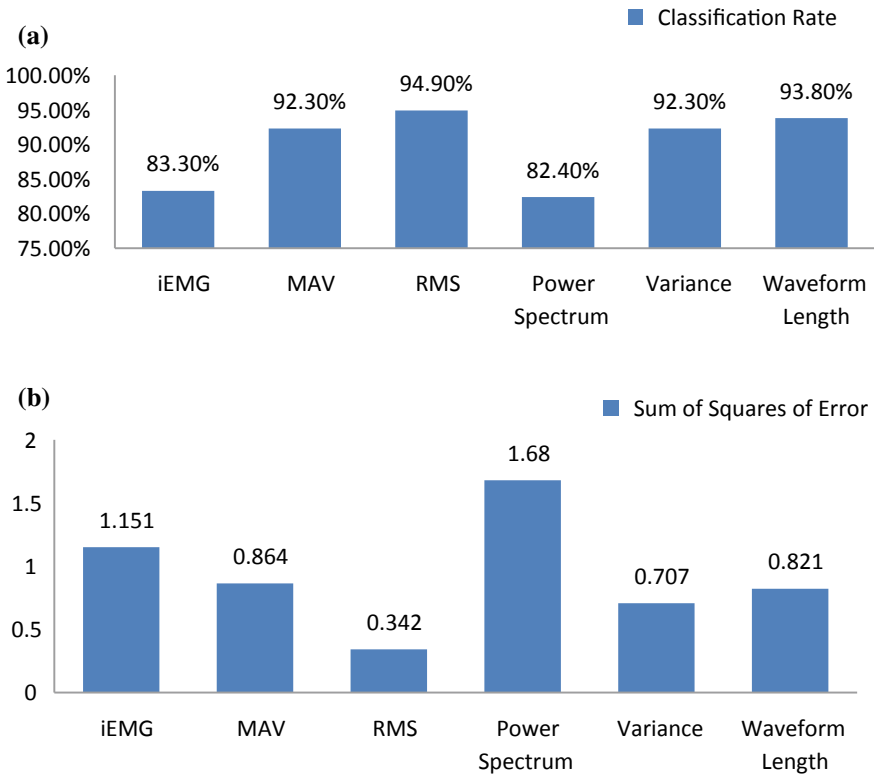
Fig. 3 **a** Classification rate of six time domain features; **b** Sum of squares of error for all features extracted

model relationship between input features of all muscles and respective grip force. For instance; to define a model relation of MAV and force/no force output, three muscles were relatively important.

Although the classification of all features was quick and precise, the most optimal classification of data was from RMS and waveform length.

3.1 Force Prediction Using ANN

Using ANN helped better nonlinear force sEMG feature of muscles relationship resulting in improved correct prediction and lower sum of squares error for the tested data. This is in concurrence with the results of the Kamavuoko et al. [13], where ANN performed better than first-order polynomial. Apart from it, ANN classification error for RMS was 5.1% compared to the classification error of 10%
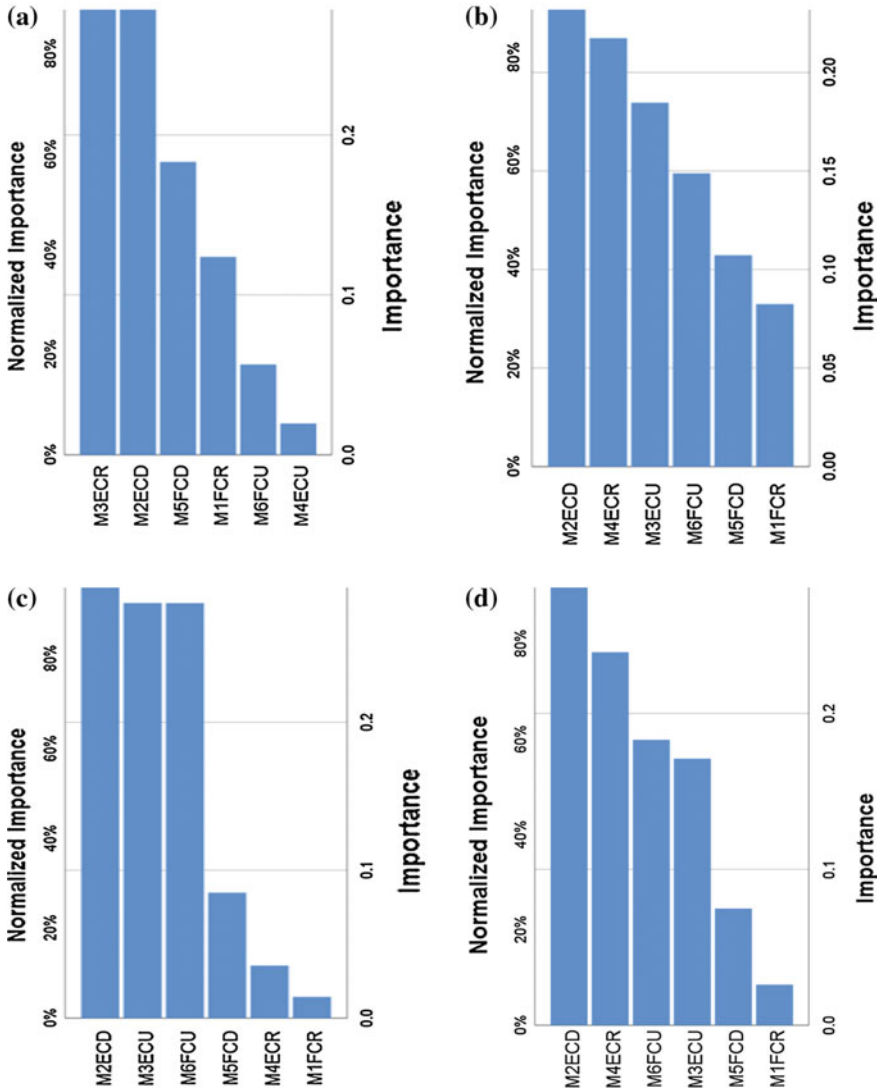
Fig. 4 **a** Muscle importance graph of muscles for MAV feature, **b** Importance graph of muscles for RMS feature, **c** Importance graph of muscles for variance feature, **d** Importance graph of muscles for WL feature

by linear discriminant analysis (LDA) for low-level forces [12]. The emphasis has been laid on small change in force. Such forces are specifically important to hold objects which are small, fragile, and easily deformable. The performance of a model also depends on the features selected for the application in myoelectric prosthetic devices. Off the six features analyzed, RMS, waveform length (WL) mean absolute

value (MAV), and variance features were found to be better predictor of the grip force from the ANN classifiers designed. ANN didn't perform well on power spectrum and iEMG. The features mean absolute value (MAV) and variance also performed well but not as good as the root mean square (RMS) and waveform length (WL).

3.2 Muscles Behavior

The muscles which were predominantly affecting no force/force output were extensor muscles and flexor carpi digitorum (FCD) (Fig. 4). However, this partially contradicts the work by Hoozemans et al. [3] where extensor digitorum and flexor carpi radialis resulted in the lowest validity of the EMG model. These contradictions may be because of the fact that high-level handgrip force up to 300 N was taken in their study. Another study by Baranski et al. [6] found the contribution of FCU and FCR muscles was significantly low among all forearm flexor muscles. This conforms to our results. The muscles contributing most, in most of the models designed were extensor carpi digitorum and extensor carpi ulnaris. Thus, for this task especially while grasping at no force or low force, extensor muscles were found to be a better predictor than flexor muscles. The focus has been more on flexor muscles. In this study, flexor as well as extensor muscles have been incorporated.

As a future scope, different combinations of upper limb muscles can be tested to increase the prediction rate. It is evident from the study that intensity of the gripping task (gripping force) needs to be addressed differently for classification purposes.

4 Conclusion

The aim of this study was to investigate the features contributing highest in the classification of no force/low force condition using neural networking. It has been found that root mean square (RMS) and waveform length (WL) responds best for the designed classifier. Also, correct predictions rate in percentage for MAV and variance was estimated as well. This study helped us to identify the muscles which are most responsive to these forces. The extensor muscles play a significant role during gripping along with flexor muscles. The least responsive muscle was FCR. Thus, it can be concluded that neural networking can be used as an essential tool/ technique to further discriminate in different levels of low-level grip forces.

References

1. Batzianoulis I, El-Khoury S, Pirondini E, Coscia M, Micera S, Billard A (2017) EMG-based decoding of grasp gestures in reaching-to-grasping motions. Rob Auton Syst 91:59–70
2. Yamanoi Y, Morishita S, Kato R, Yokoi H (2017) Development of myoelectric hand that determines hand posture and estimates grip force simultaneously. Biomed Signal Process Control 38:312–321
3. Hoozemans MJ, Van Dieën JH (2005) Prediction of handgrip forces using surface EMG of forearm muscles. J Electromyogr Kinesiol 15(4):358–366
4. Duque J, Masset D, Malchaire J (1995) Evaluation of handgrip force from EMG measurements. Appl Ergon 26(1):61–66
5. Jakob ENK, Mathiesen R, Bøg MF, Erkocevic E, Niemeier MJ, Smidstrup A (2010) Prediction of grasping force based on features of surface and intramuscular EMG. In: 7th semester conference paper, pp. 1–9. Denmark)
6. Barański R, Kozupa A (2014) Hand grip-EMG muscle response. Acta Phys Pol, A 125(4):7–11
7. Keir PJ, Mogk JPM (2005) The development and validation of equations to predict grip force in the workplace: contributions of muscle activity and posture. Ergonomics 48(10):1243–1259
8. Phinyomark A, Phukpattaranont P, Limsakul C (2012) Feature reduction and selection for EMG signal classification. Expert Syst Appl 39(8):7420–7431
9. Al-Timemy AH, Bugmann G, Escudero J (2013) A preliminary investigation of the effect of force variation for the control of hand prosthesis. In: Annual international conference of the IEEE engineering in medicine and biology society, pp. 0–3. IEEE, Japan
10. Al-Timemy AH, Bugmann G, Escudero J, Outram N (2013) Classification of finger movements for the dexterous hand prosthesis control with surface electromyography. IEEE J Biomed Heal Inform 17(3):608–618
11. Sidek SN, Mohideen AJM (2012) Measurement system to study the relationship between forearm EMG signals and wrist position at varied hand grip force. In: International conference on biomedical engineering ICoBE 2012, February, pp. 169–174
12. Al-Timemy AH, Khushaba RN, Bugmann G, Escudero J (2016) Improving the performance against force variation of EMG controlled multifunctional upper-limb prostheses for transradial amputees. IEEE Trans Neural Syst Rehabl Eng 24(6):650–661
13. Kamavuako EN (2013) Influence of the feature space on the estimation of hand grasping force from intramuscular EMG. Biomed Signal Process Control 8(1):1–5

Estimation of Plastic Zone at Crack Tip Under Fatigue Loading of AA6061-T6 Aluminum Alloy by Finite Element Analysis Using ANSYS

Yatika Gori and Rajesh P. Verma

Abstract The plastic zone shape and size are analytically estimated at crack tip under fatigue loading (at stress ratio $(R) = 0.1$ and 0.5) of AA6061-T6 aluminum alloy by finite element analysis using ANSYS. The stress intensity factor (SIF) is a measure of the mechanical force required for crack growth and is closely related to the plastic zone formed in the vicinity of the crack tip. The stress intensity factor range (ΔK) was determined by finite element analysis using ANSYS and was compared with the experimental data obtained as per ASTM standard to decide the applicability of the analytical method in the present work. The comparison exhibited that the error to determine SIF using ANSYS is less than 20%, which lie under acceptable range. The finite element analysis was applied to determine the plastic zone shape and size at crack tip using ANSYS. A butterfly type of cyclic plastic zone was observed in the plane strain condition. At lower ΔK, smaller plastic zone was measured for $R = 0.5$ in comparison to $R = 0.1$. After $\Delta K = 12.00$ MPa√mm, comparatively larger area of plastic zone was observed for $R = 0.5$. At constant $\Delta K = 12.88$ MPa√mm, the value of maximum SIF (K_{max}) was obtained as 14.29 MPa√mm and 16.11 MPa√mm at stress ration $(R) = 0.1$ and 0.5, respectively. It was also observed that at same $K_{max} = 16.55$ MPa√mm, the value of ΔK is 14.86 and 18.13 for R = 0.1 and 0.5, respectively. The increased value of ΔK results in larger plastic zone for $R = 0.5$ at later stage of crack growth.

Keywords Crack growth · Plastic zone · Stress intensity factor · AA6061-T6

Y. Gori (✉) · R. P. Verma
Department of Mechanical Engineering, Graphic Era (Deemed to be University),
Dehradun, Uttarakhand, India
e-mail: yatigori@gmail.com

1 Introduction

The design of any mechanical component needs the proper examination of failure mechanism of the component. Fracture is the common mode of failure in engineering applications. Fracture mechanics deals with a crack and the crack becomes very dangerous under fatigue loading. Fatigue fracture covers approximately 90% failure in engineering applications [1]. The growth of crack under fatigue loading is a primary concern of any designer. In real conditions, the stresses at the crack tip are very large that they cause an elastic deformation in the front of the crack tip. The elastic deformation forms a plastic zone near crack tip [2]. It is very useful to know the plastic zone at crack tip to designers so that it may be analyzed to understand the crack growth behavior.

Many researchers have proposed methods to determine the plastic zone size and shape at crack tip. Benrahou et al. [3] have studied the formation of plastic zone under mode I, II, and combination of the two. von Mises and Tresca criteria were applied to estimate the plastic zone and the estimated plastic zone area was compared to those measured by FEA (ABAQUS). Paul [4] stated that the nature of cyclic plastic deformation and damage on a fatigue crack tip is expressible to understand the failure mechanism under cyclic loading. The plastic zone size was studied and effect of stress intensity factor was investigated. Park et al. [5], Wu et al. [6], Mohanty et al. [7] also proposed various methods to estimate plastic zone at crack tip under fatigue loading.

The fatigue crack growth phenomenon is different for different materials. There are a number of experimental and analytical techniques available to determine the plastic zone size in literature [3–7]. But there is limited information available on plastic zone formation in AA6061-T6 aluminum alloys. AA6061-T6 aluminum alloy is the most used aluminum alloys in structural applications. In the present work, fatigue plastic zone at crack tip of compact tension specimen of AA6061-T6 aluminum alloys was estimated by finite element analysis. The plastic zone size at stress ratios, R = 0.1 and 0.5, were compared to understand the crack growth at different stress ratios.

2 Methodology

Finite element analysis (FEA) of compact tension (CT) specimen was carried out to estimate the plastic zone size using ANSYS. The result obtained from ANSYS model was verified with experimental data to ensure the suitability of ANSYS model. The methodology followed in the present work is presented in (Fig. 1).

The experimental data were obtained for CT specimens of AA6061-T6 aluminum alloys. Commercial plates of AA 6061-T6 [8] were used. Chemical composition of the alloy AA6061-T6 is given in Table 1. The dimension and geometry of CT specimen were as per ASTM E647-08 (Fig. 2). The CT specimens were cut

AA 6061-T6

CT Specimen

Experimental Analysis

Analytical Analysis

FEM Analysis

- ASTM
- Crack length (*a*) vs No. of Cycles (*N*)
- Crack length (*a*) vs SIF (∆*K*)
- At R = 0.1, 0.5

FEM Analysis

- ANSYS
- Crack length (*a*) vs No. of Cycles (*N*)
- Crack length (*a*) vs SIF (∆*K*)
- At R = 0.1, 0.5

Comparison experimental data to Analytical data
(To check the applicability of ANSYS to the present application)

Crack tip plastic zone estimation using FEM

Fig. 1 Methodology followed in present work

Table 1 Chemical composition of AA6061-T6

Material	Si	Cu	Fe	Zn	Mg	Ni	Mn	Cr	Ti	Sn	Pb	Al
6061-T6	0.79	0.19	0.02	0.07	0.98	0.03	0.17	0.04	0.03	0.02	0.024	Rem

Fig. 2 a A CT specimen
b Geometry specification of
CT specimen as per ASTM
standard
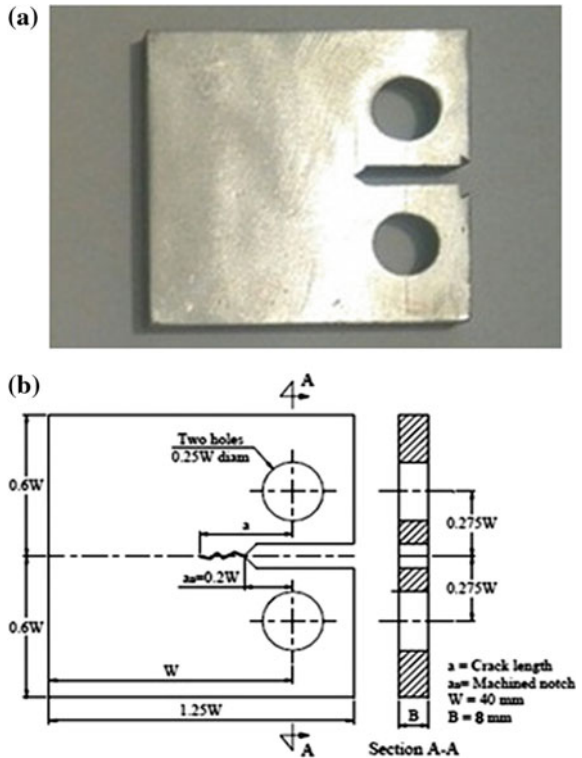
by power hacksaw from the plates of AA6061-T6. The fatigue crack growth tests
were performed at two stress ratios, R = 0.1 and 0.5. The crack progress was
observed and corresponding number of cycles (N) and stress intensity factor (ΔK)
were observed.

3 Finite Element Analyses

Finite element analysis was applied to estimate the fatigue crack growth rate and
formation of plastic zone with the help of ANSYS Workbench 15 for CT specimen
of AA6061-T6 aluminum alloys. The CT specimen was modeled in SolidWorks
and fatigue failure analysis was carried out in ANSYS environment. The following
steps were followed for the finite element analysis of CT specimen:

(a) Modeling of CT specimen in SolidWorks,
(b) Importing model to ANSYS,
(c) Meshing,
(d) Applying boundary conditions and loading conditions in fatigue module of ANSYS,
(e) Applying fracture tool in ANSYS, and
(f) Obtaining data (a versus N and a versus ΔK).

Fig. 3 **a** 2D CAD model in SolidWorks **b** Solid CAD model in ANSYS
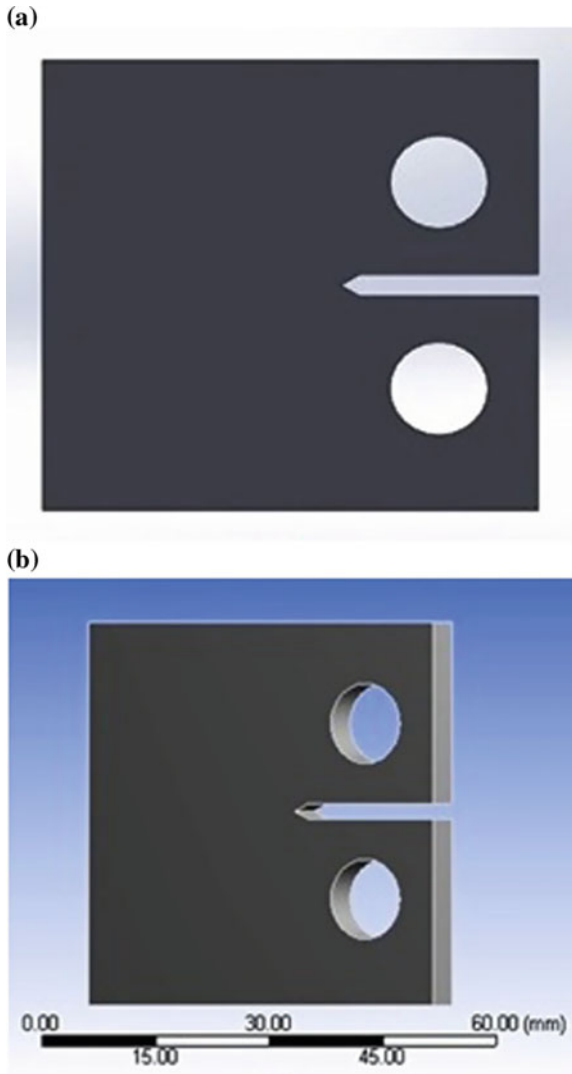
Fig. 4 **a** Meshing of CT specimen geometry **b** Meshing near crack tip
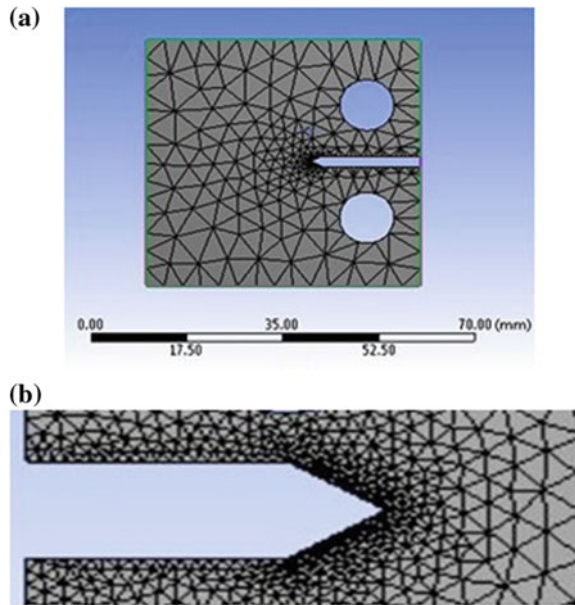
In the present work, the 2D model of CT specimen was used (Fig. 3a). The dimensions of CT specimen were taken according to ASTM standards as shown in Fig. 1. The 2D model of CT specimen was imported in ANSYS and was converted into 3D CAD model (Fig. 3b) of 6 mm thickness.

Meshing is the process of dividing or discretizing the geometry into finite elements. In the present analysis, the model of CT specimen was discretized into 4054 elements with 7483 nodes. Three-noded triangular elements were used in meshing, as it is sufficient to analyze the fatigue crack growth. The meshing of CT specimen is shown in Fig. 4a, in which the crack tip region was discretized with refined meshes to capture the large strain gradients. The refined meshes near the crack tip (Fig. 4b) were used as the crack tip region which is the critical region. The sizes of element in the fine mesh zone increase linearly along the crack line in the present investigation.

After meshing, boundary conditions were applied to the model. The CT specimen contains two holes of 10 mm diameter on upper and lower edges of the specimen to hold the grip. Fixed support is applied to the lower grip (Fig. 5a) and a tension load of 2.2 kN (Fig. 5b) is applied to the upper grip of the specimen. In fatigue tool, stress ratios, R = 0.1 and 0.5, were taken with frequency, f = 10 Hz. The crack growth rate of CT specimen along with the values of stress intensity factor (SIF) at the crack tip was estimated using fracture tool.

Fig. 5 **a** Fixed support at the lower edge of CT specimen **b** Tension load on the upper edge of the CT specimen

(a)

(b)
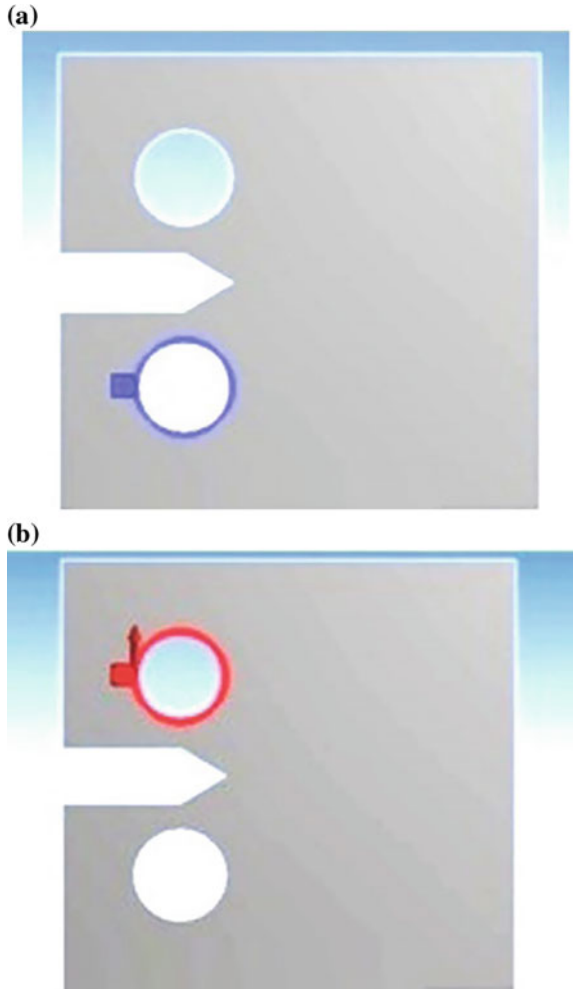
4 Result and Discussion

4.1 Comparison of FEA with Experimental Data

The data obtained from the FEA analysis was compared with the experimental data. The experimental fatigue crack growth tests were performed on a servo-hydraulic universal testing machine (Make: BIS Solutions (P) Ltd. India) having a load capacity of 25 kN with graphic interface. The comparison of FEA and experimental data is shown in Figs. 6 and 7.

A slight fast crack growth is observed experimentally as compared to FEA analysis. The reason may be that the mechanical analysis is the only analysis
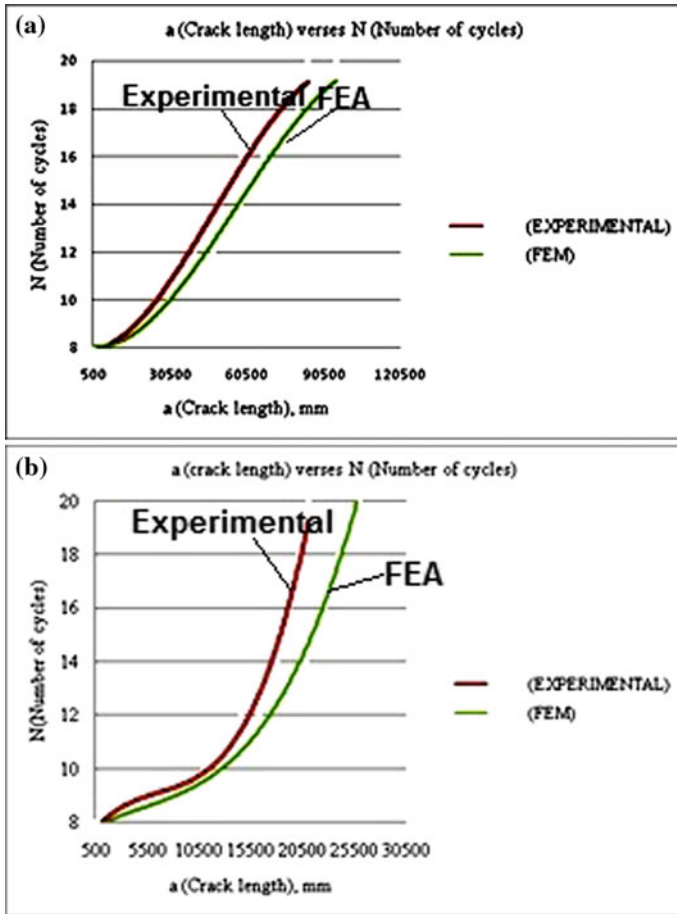
Fig. 6 **a** Crack length, *a* versus number of cycles, *N* **a** at *R* = 0.1 **b** at *R* = 0.5

considered in the FEA analysis, the microhardness is not considered. The error in obtaining the data from FEA was found less than 20% at any point, which is acceptable. Therefore, the same finite element model was used to estimate the plastic zone at crack tip.

4.2 Estimation of Plastic Zone at Crack Tip

It is very useful to know the plastic zone at crack tip so that it may be analyzed to understand the crack growth behavior and designed to avoid fracture failure in machine components. The plastic zone shape and size at crack tip of the specimen
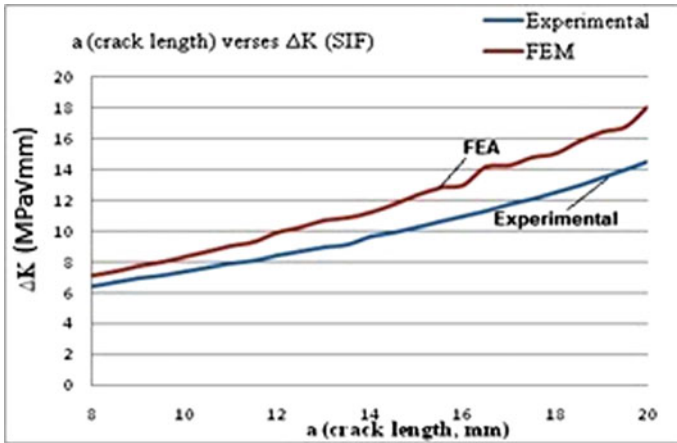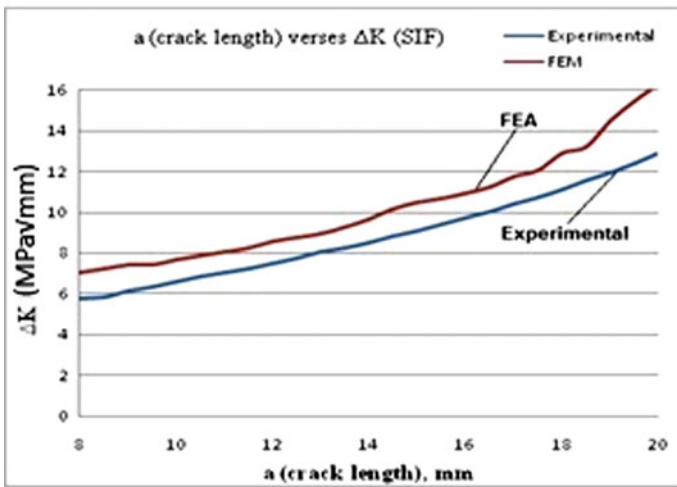
Fig. 7 Crack length, a (mm) versus SIF, ΔK (MPa√mm) at **a** R = 0.1 **b** R = 0.5

were determined using FEA in ANSYS environment. In the present study, the modeling is purely mechanical, i.e., the force was the only loading condition and the microstructure was not considered. Plain strain condition is assumed for the formation of plastic zone as the thickness of CT specimen is small. Figure 8 shows the formation of plastic zone at the crack tip for stress ratio, R = 0.1. A butterfly type of cyclic plastic zone was observed in the plane strain finite element analysis (for both R = 0.1 and 0.5). Figure 9 shows the size of plastic zones obtained at R = 0.1 and 0.5.
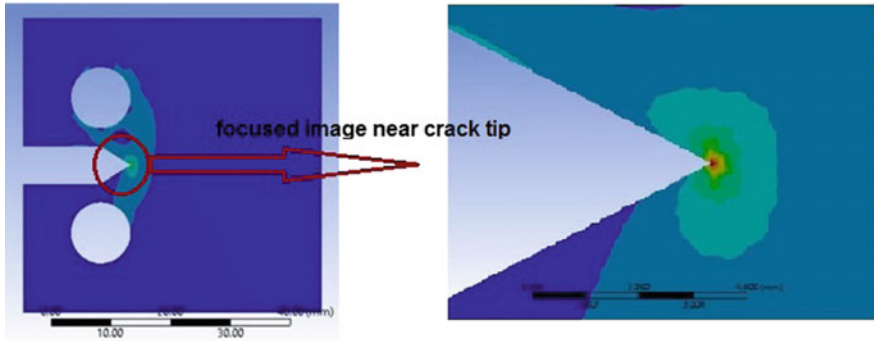
Fig. 8 Fatigue plastic zone at crack tip (at $R = 0.1$)
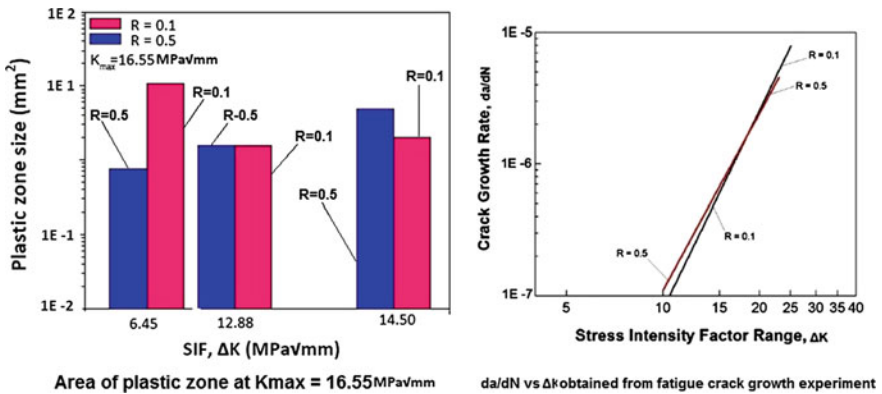
Fig. 9 Area of plastic zone at $K_{max} = 16.55$ MPa√mm and da/dN vs ΔK obtained from fatigue crack growth experiment

The maximum and minimum values of von Mises stress at crack tip of the CT specimen were found 2.0541 MPa and 2.21×10^{-5} MPa, respectively. It was observed that as the size of the plastic zone increases with the decrease in von Mises stresses. Therefore, it might be concluded that the large plastic zone size helps in reducing the value of stresses at the crack tip [9], which, in turn, increases the life of the component.

It is clear from the figure that the plastic zone area for R = 0.5 at lower ΔK ($\Delta K = 6.45$ MPa√mm) is smaller than that for R = 0.1. At $\Delta K = 12.00$ MPa√mm, the plastic zone areas for R = 0.1 and 0.5 are approximately equal. At higher $\Delta K = 14.50$ MPa√mm, the plastic zone area for R = 0.5 is greater than that for R = 0.1. Larger plastic zone leads to great difficulty in crack growth. It means that the crack growth for R = 0.1 at lower ΔK is lower than that for R = 0.5. It increases with an increase in ΔK with respect to R = 0.5. This trend was also verified from experimental data as shown in Fig. 9.

At lower ΔK, lower plastic zone area was obtained for R = 0.5. After $\Delta K = 12.00$ MPa√mm, larger plastic zone area was observed than that for R = 0.1. The crack growth depends on the values of Kmax. Kmax is the main driving force of crack propagation [1]. At constant $\Delta K = 12.88$ MPa√mm, the value of Kmax is 14.29 MPa√mm for R-ratio 0.1, whereas the value of Kmax for R-ratio 0.5 is 16.11 MPa√mm. There is a slight increase in the value of Kmax for R-ratio 0.5 as compared to R-ratio 0.1, which means that there is an increase in the size of plastic zone. The plastic zone area at lower ΔK for R = 0.1 and 0.5 is dependent on Kmax.

5   Conclusion

The following conclusions are made from the present work:

- There was less than 20% error (with comparison to experimental data) to estimate crack growth (Δa) and stress intensity factor (SIF, ΔK) by FEA using ANSYS. Therefore, FEA may be applied satisfactorily to study the fatigue crack growth phenomena for AA6061-T6 aluminum alloys.
- It was observed that as the size of the plastic zone increases with the decrease in von Mises stresses. Therefore, it might be concluded that the large plastic zone size helps in reducing the value of stresses at the crack tip, which, in turn, increases the life of the component.
- Before $\Delta K = 12.00$ MPa√mm, comparatively smaller plastic zone was observed at R = 0.5. In initial stage of crack growth, the AA6061-T6 aluminum alloy shows significant higher crack growth resistance at stress ratio, R = 0.1 as compared to R = 0.5.
- In later stage (after $\Delta K = 12.00$ MPa√mm), comparatively larger plastic zone was observed at R = 0.5. That is, faster crack growth was observed in AA6061-T6 aluminum alloys for R = 0.1.
- Butterfly shape of plastic zone was formed during the plain strain FEA analysis.

References

1. Verma RP, Pandey KN (2018) Study of fatigue crack growth rate of AA6061 at different stress ratios. In: Seetharamu S, Bhanu K, Raghunath SR, Khare W (eds) FatigueDurability 2017. LNME, Springer, Singapore, pp 67–74. https://doi.org/10.1007/978-981-10-6002-1_6
2. Stanzl-Tschegg SE, Mayer H (2001) Fatigue and fatigue crack growth of aluminium alloys at very high numbers of cycles. Int J Fatigue 23:231–237
3. Benrahou KH, Benguediab M, Belhouari M, Nait-Abdelaziz M, Imad A (2007) Estimation of the plastic zone by finite element method under mixed mode (I and II) loading. Comput Mater Sci 38(4):595–601
4. Paul SK (2016) Numerical models of plastic zones and associated deformations for a stationary crack in a C(T) specimen loaded at different R-ratios. Theoret Appl Fract Mech 84:183–191

5. Park HB, Kim KM, Lee BW (1996) Plastic zone size in fatigue cracking. Int J Press Vessel Pip 68(3):279–285
6. Wu T, Wagner D, Kirk D (2016) Analysis of the plastic zone of a circle crack under very high cycle fatigue. Int J Fatigue 93:415–421
7. Mohanty JR, Verma BB, Ray PK (2009) Prediction of fatigue crack growth and residual life using an exponential model: part I (constant amplitude loading). Int J Fatigue 31(3):418–424
8. Verma RP, Pandey KN (2017) Fracture behavior of GMA welded joints of dissimilar and similar aluminum alloys of 6061-T6/5083-O. J Failure Anal Prev 17(2):248–254
9. Chen J, Huang Y, Dong L, Li Y (2015) A study on evaluation method of crack tip reverse plastic zone size for the center cracked steel plate model under tension–compression cyclic loading. Eng Fract Mech 133:138–151

Detection of Crack and Unbalancing in a Rotor System Using Artificial Neural Network

Ram Babu Gupta and Sachin Kumar Singh

Abstract Crack and unbalance are two important effects experienced by a rotor system during its motion. These are a common source of high vibration and undesirable functioning in rotating machinery. The methods of detection of rotor faults have improved from time being such as single fault identification at any given instance, but generally more than one fault is existent in a rotor system simultaneously which has not been discussed so far. In this work, a method is being devised to critically identify unbalance and crack in rotor system using artificial neural networks (ANN) by statistical features. Moreover, a confusion matrix is also obtained by statistical features. Then, by the help confusion matrix, the class of crack and unbalance was decided. Validation and testing of the neural network have been done with simulation data.

Keywords ANN · Confusion matrix · Crack · Unbalance

1 Introduction

Rotating machinery is of prime importance for industrial applications. Unbalance and crack are a common source of high vibration and malfunction in rotating machinery. In rotating system, main cause of vibration is fault. In a continuous process industry, an undesirable failure of rotating system may result in huge economical losses in terms of maintenance cost as well as huge production losses. Vibration analysis seems to be an effective tool in diagnosis of problems related to rotating machinery. There are many vibration-based diagnosis techniques available for rotating machinery [1]. Lei et al. [2] proposed a new way to carry out fault

R. B. Gupta (✉) · S. K. Singh
Department of Mechanical Engineering, IIT (ISM) Dhanbad, Dhanbad 826004, India
e-mail: rb108786@gmail.com

problems diagnosis in rotating machinery using statistical analysis, and adaptive neuro-fuzzy interface system (ANFIS). In literature, different techniques are used for modelling and identification of unbalance and crack response of the system. Genta and Bona [3] obtained unbalance response of the system using a modal approach. Considering one loose pedestal in a rotating machine, unbalance response has been studied using experimental, analytical and numerical approaches [4]. There are many methods used for obtaining the periodical response in rotor systems, such as the series expansion method [5] and the harmonic balance method [6, 7]. Curti et al. [8] used dynamic stiffness method for the rotor-bearing system and obtained unbalance response. Sekhar [9] proposed a method based on the online identification of unbalance and crack in a rotor and simulated identification process when simultaneous occurrence of unbalance and crack exists on the rotor. Recently, Kankar et al. [10] have successfully examined fault diagnosis of problems pertinent to ball bearings using ANN.

In this paper, the work is mainly focused on crack and unbalance in rotor system using Artificial Neural Network. A Simulink model of rotor has been generated with the help of linearised stiffness and damping coefficient, simple model which enables investigation of unbalance in rotor system. This model helps to provide some insight into rotor system when unbalance and crack are present in rotor system. The rotor model has been given a specific spin speed and numerically simulated rotor displacements are generated. For crack and unbalance, various vibration data are taken as time-domain signals for various eccentricity values ranging from 0 to 0.000007 m and taken 20 data set for each statistical feature at additive stiffness of 16100 Nm^{-1} and 18000 Nm^{-1}. ANN uses trained and tested statistical features extracted from time-domain signal.

2   Analytical Model by Simulink

The system of equations for motion

$$\mathbf{M}\ddot{u} + \mathbf{C}\dot{u} + \mathbf{K}u = \mathbf{F}_{st} + \mathbf{F}_{unb}, \tag{1}$$

where [M], [C] and [K] are defined as the mass, damping and stiffness matrices, respectively, for the given system, $\{F_{st}\}$ is given as the force vector to take into account the static deflection in the specified system, $\{F_{unb}\}$ is defined as the force vector to accommodate the disc unbalance and$\{u\}$ is the displacement vector of the disc, m is the disc mass and c is the viscous damping.

$$[M] = \begin{bmatrix} m & 0 \\ 0 & m \end{bmatrix}, [C] = \begin{bmatrix} c & 0 \\ 0 & c \end{bmatrix}, [K] = \begin{bmatrix} k_0 & 0 \\ 0 & k_0 \end{bmatrix}, [u] = \begin{bmatrix} u_x \\ u_y \end{bmatrix}.$$

Final equation of motion

$$\begin{bmatrix} m & 0 \\ 0 & m \end{bmatrix}\begin{bmatrix} \ddot{u}_x \\ \ddot{u}_y \end{bmatrix} + \begin{bmatrix} c & 0 \\ 0 & c \end{bmatrix}\begin{bmatrix} \dot{u}_x \\ \dot{u}_y \end{bmatrix} + \begin{bmatrix} k_0 & 0 \\ 0 & k_0 \end{bmatrix}\begin{bmatrix} u_x \\ u_y \end{bmatrix}$$
$$= \frac{1}{2}s(t)\Delta k\begin{bmatrix} (1+\cos 2\omega t) & \sin 2\omega t \\ \sin 2\omega t & (1+\cos 2\omega t) \end{bmatrix}\begin{bmatrix} \omega_y \\ 0 \end{bmatrix} + me\omega^2 \begin{Bmatrix} \cos(\omega t + \beta) \\ \sin(\omega t + \beta) \end{Bmatrix}. \tag{2}$$

Rotor system data for the numerical simulation:

Disc mass, m = 2 kg, Intact shaft stiffness, $k_0 = 3.2135 \times 10^{-5}\mathrm{Nm}^{-1}$;
Additive (negative) crack stiffness, $\Delta k = 1.601 \times 10^4\mathrm{Nm}^{-1}$;,
Viscous damping in rotor system, $c = 16.03\,\mathrm{N} - \mathrm{s\,m}^{-1}$;
Phase of unbalance, $\beta = 10(\pi/180)$ rad;
Shaft deflection due to disc weight, $\omega_y = 6.105 \times 10^{-5}$ m and
Disc eccentricity, e = 0.000007 m.

2.1 Simulink Model

See Fig. 1.

2.2 Unbalance Identification

Various unbalance conditions are taken such as unbalance at e = 0 m, e = 0.00000233 m, e = 0.00000467 m and e = 0.000007 m. In each case, 20 sets of data are taken. The preprocessing is performed on the time-domain signal to extract the required statistical features like mean (μ), root mean square (RMS) and variance (σ^2), standard deviation and skewness using MATLAB. Training and testing of the neural network are done with the extracted data from Simulink diagram and confusion matrix is obtained in two different cases. First one is with statistical features in X-direction, second one is with statistical features in Y-direction. Unbalance severity of the rotor system is classified according to the various explained methods and also using ANNs.

Fig. 1 Simulink model for **a** x-direction and **b** y-direction

2.3 Unbalance and Crack

In the present work, the results of a theoretical study on a simple linear rotor dynamic model are being analysed, capable of simulating the effects of crack and unbalance across a rotor system. The mathematical model for dynamics of a cracked rotor is presented. A Laval rotor, which is a simply supported elastic shaft with a centrally located disc, is considered. It is based on lumped modelling with the assumption that the shaft is massless. Take rotor speed of 600 rpm and taken eccentricity values range between 0 and 0.000007 m. In each case, 20 sets of data are taken such as statistical features like mean (μ), root mean square (RMS) and variance (σ^2) standard deviation, and skewness using MATLAB software. Extract the statistical features by performing the preprocessing on the whole signal. Neural network is trained and tested with the Simulink data. Moreover, a confusion matrix is also obtained by statistical features. Unbalance and crack of the rotor system are classified based on the abovementioned two methods and using ANNs.

2.4 Feature Extraction

A complete list of features that are evaluated from the vibration signals using statistics are given below:

(a) Mean value: Mean value is the average value of a signal,

$$\text{mean} = \frac{\sum_{i=1}^{n} X_i}{n};$$

(b) RMS value: The RMS value is given by

$$\text{rms} = \sqrt{\sum_{i=1}^{n} X_i^2 \frac{1}{n}};$$

(c) Standard deviation: It is a measure of energy content in the vibration signal and is termed as standard deviation, which is given by

$$\text{Standard deviation} = \sqrt{\frac{\sum_{i=1}^{n} (X_i - \bar{X})^2}{n-1}};$$

(d) Variance: Variance is the square of the standard deviation, which is given by

$$\text{Variance} = std^2;$$

(e) Skewness: Measure of symmetry is skewness, or the lack of symmetry, which is given by

$$\text{Skewness} = \frac{n}{(n-1)(n-2)} \sum_{i=1}^{n} \left(\frac{Xi - \bar{X}}{\sigma} \right)^3.$$

2.5 Application of Neural Network

ANNs working mechanism is based on biological neurons and it is used for pattern recognition in many situations where data are incomplete or fuzzy. ANN's advantages are automatic detection and diagnostics of rotating machines. However, they require a large number of training examples. The basic building block for an artificial neural network is the neuron. ANN is working with input and output numerical values. Each neuron consists of many inputs and outputs. Each connection, which is present between artificial neurons, is capable of transmitting a signal from one to another. The artificial neuron which is receiver of the signal can successfully process it and then signal artificial neurons attached to it. Two-layered feedforward neural network consists of two layers as given below:

 (i) First layer which is hidden and processes the data and
(ii) Second layer is the output layer that gives the result by the analysis, i.e. unbalance severity class.

The configuration of the feedforward neural network is explained in Fig. 2. Input layer consists of five neurons, no of hidden neurons are 10 and output layer consists of four neurons. Initially, the random weights are taken varying from 0 to 1.

Fig. 2 Artificial neural network

3 Results and Discussion

ANN training and classification of faults are being analysed and explained using MATLAB software. This study is mainly focused on crack and unbalance, and are classified using ANN as shown in the confusion matrices shown in Figs. 3 and 4.

3.1 Unbalance Severity Identification

As explained in Sect. 2.2, the Simulink model is conducted with different unbalance conditions at additive stiffness (Δk) value 16010 Nm^{-1} to 18000 Nm^{-1}. Each case is considered as a separate class like unbalance at e = 0 m, e = 0.00000233 m, e = 0.00000467 m and at e = 0.000007 m. From the Simulink data, various statistical features are extracted in both X-direction and Y-direction. The rotor runs at 600 rpm. Data is fed to the neural network and confusion matrices in all four cases.
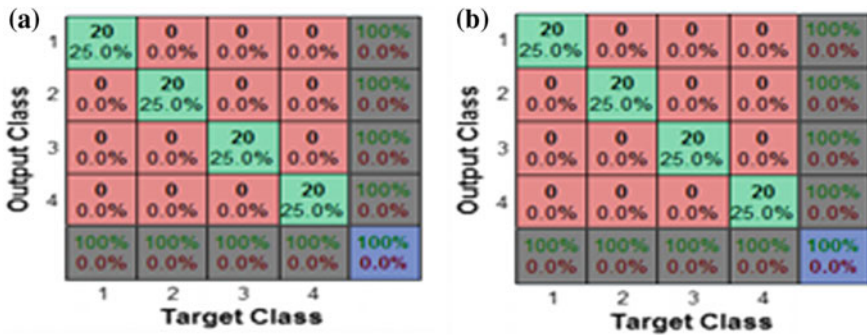

Fig. 3 Confusion matrix for unbalance **a** Statistical features in X-direction and **b** Statistical features in Y-direction
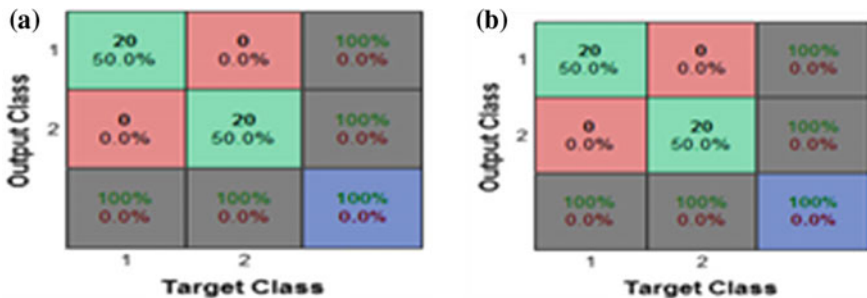
Fig. 4 Confusion matrix for crack and unbalance **a** Statistical features in X-direction and **b** Statistical features in Y-direction

Table 1 Statistical features at eccentricity (e) = 0

S.N.	Mean (m)	RMS (m)	Variance (m^2)	Std. deviation (m)	Skewness
1	−2.46E-09	9.79E-07	9.79E-07	9.59E-13	0.041051
2	−2.75E-09	1.09E-06	1.09E-06	1.20E-12	0.041051
3	−1.82E-10	9.96E-07	9.96E-07	9.91E-13	0.033355
4	−2.03E-10	1.11E-06	1.11E-06	1.24E-12	0.033355
5	−1.36E-09	9.81E-07	9.81E-07	9.62E-13	0.036061
6	−1.53E-09	1.10E-06	1.10E-06	1.20E-12	0.03606
7	8.15E-09	9.82E-07	9.82E-07	9.65E-13	0.041668
8	9.12E-09	1.10E-06	1.10E-06	1.21E-12	0.041668
9	−1.26E-09	9.81E-07	9.81E-07	9.63E-13	0.035445
10	−1.41E-09	1.10E-06	1.10E-06	1.20E-12	0.035445
11	7.21E-09	9.82E-07	9.82E-07	9.63E-13	0.037293
12	8.06E-09	1.10E-06	1.10E-06	1.20E-12	0.037292
13	−1.48E-09	9.82E-07	9.82E-07	9.64E-13	0.036118
14	−1.65E-09	1.10E-06	1.10E-06	1.20E-12	0.036118
15	1.29E-09	9.78E-07	9.78E-07	9.56E-13	0.034385
16	1.44E-09	1.09E-06	1.09E-06	1.20E-12	0.034385
17	−1.03E-09	9.82E-07	9.82E-07	9.64E-13	0.034902
18	−1.15E-09	1.10E-06	1.10E-06	1.20E-12	0.034902
19	−1.20E-09	9.77E-07	9.77E-07	9.55E-13	0.035641
20	−1.35E-09	1.09E-06	1.09E-06	1.19E-12	0.03564

Some typical ANN training data are presented in Table 1 at e = 0. Table 1 gives the statistical features at e = 0 m unbalance and at Δk = 16010 Nm^{-1} statistical features of 10 data sets and at Δk = 18000 Nm^{-1}, another 10 data sets are taken in X-direction. Similar results have been generated for other unbalances and in both X- and Y-directions, these are, however, not shown in here. In this case, similar data for vertical direction have also been developed. The result obtained on a test set is often shown as a 2-D confusion matrix with a row and column for each class. Each matrix element depicts the counts of test examples for which the actual class is designated as the row and for predicted class as the column. The confusion matrix shown in Fig. 3a corresponds to the statistical features in X-direction while Fig. 3b corresponds to that of in the Y-direction. From Fig. 4b, it can be inferred that ANN has correctly predicted 20, 20, 20 and 20 cases for four classes, i.e. at e = 0, e = 0.00000233 m, e = 0.00000467 m and at e = 0.000007 m, respectively, with statistical features in Y-direction. It can be noticed from Figs. 3a to 4b that statistical features are giving 100% accuracy by analytical model. In confusion matrix, the percentages are calculated in the last rows and columns as count of samples which are classified in correct sense to the total number of samples classified. Hence, the horizontal ANN results and vertical results are giving 100% accuracy due to analytical model of Simulink. Hence, ANN's results are the same in X- and Y-directions. The time-domain vibration signals response at rotor running speed of 600 rpm with various unbalance situations which are depicted from Figs. 5a to 8b.

(a)

(b)
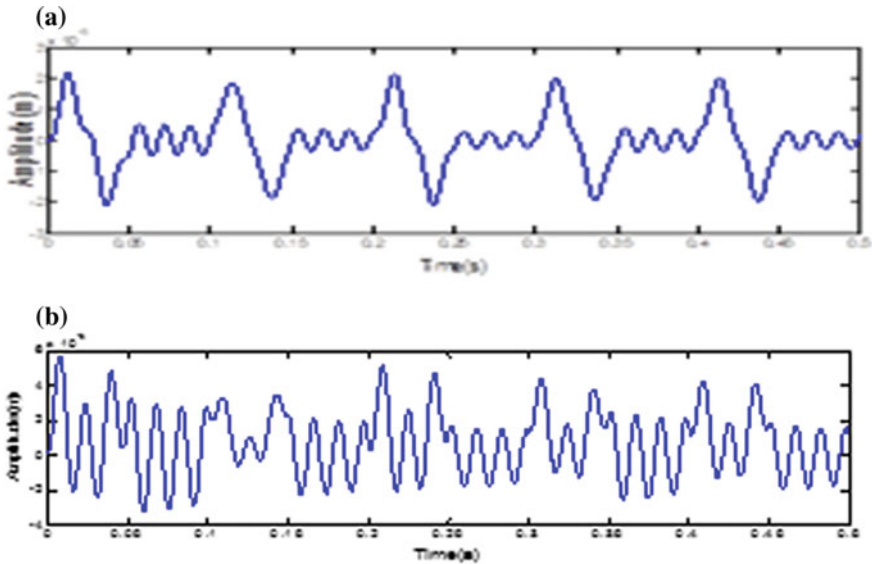
Fig. 5 Eccentricity (e) = 0 m **a** X-direction and **b** Y-direction

3.2 Unbalance and Crack Identification

Data are extracted from Simulink diagram and obtained statistical features. Each case is considered as a separate class like (i) crack at $\Delta k = 0$ Nm^{-1} v and e value at 0.0000035 m and 0.000007 m change w.r.t. time (ii) unbalance at e = 0 and $\Delta k = 16010$ Nm^{-1} and $\Delta k = 18000$ Nm^{-1} change w.r.t. time. From the Simulink data, various statistical features are extracted. Neural network is modelled as a classification problem. Data is fed into the neural network and obtained confusion matrices as shown in Fig. 4a and b in X-direction and Y-direction, respectively. It shows that 100% of the data is classified accurately in X-direction and 100% of the data is classified accurately in the Y-direction. It shows how classification is done between target class (actual class) and output class. Once the neural network is stabilised that can be used to take the new values and it tells which class it belongs to. From this, we can make decision by knowing the fault to which it belongs to, whether unbalance or crack depending on the class to which it belongs to. Different data sets used for training and testing, 70% of the data are used for training and 30% of the data are used for testing. In each data set, 20 data points are used. The network is modelled as a two-class problem and trained and tested accordingly. Here, unbalance and crack faults are separately simulated. It is a two-class problem, it just tells whether the fault is unbalance or crack. Because of mathematical simulation, vertical data classification and horizontal data classification are the same. Here, we will

not get the severity of the problem, we get only type of problem, i.e. unbalance or crack. Based on the input (statistical features) given to the ANN and the ANN toolbox of MATLAB program will form the confusion matrix (Figs. 6, 7, 8).
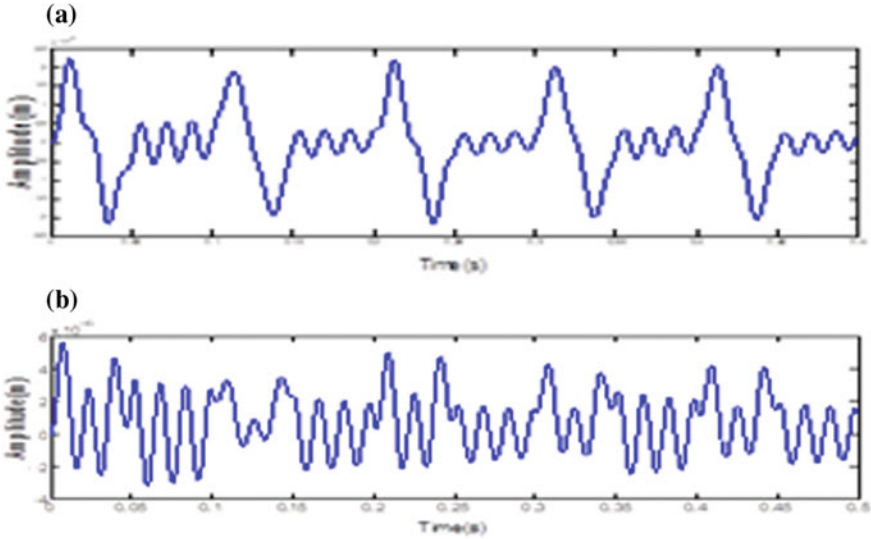
Fig. 6 Eccentricity (e) = 0.00000233 m **a** X-direction and **b** Y-direction
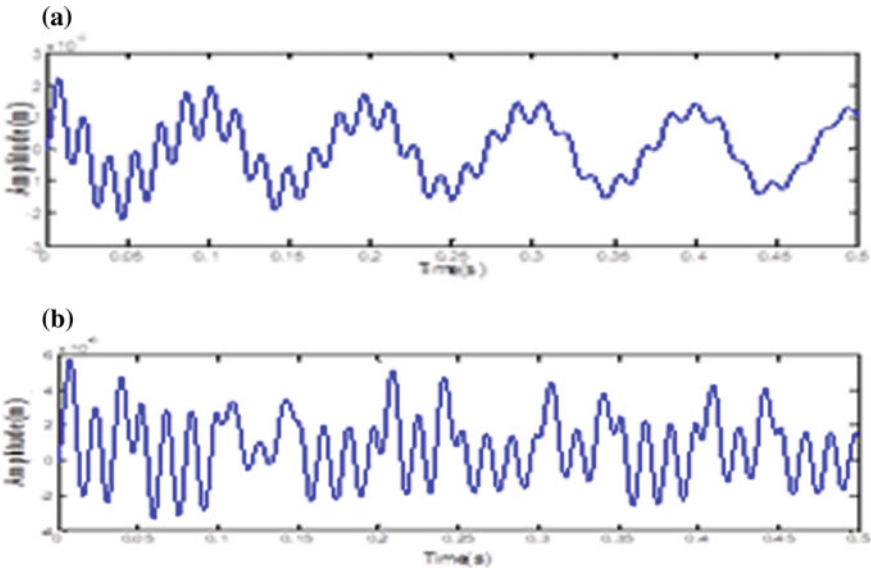
Fig. 7 Eccentricity (e) = 0. 00000467 m **a** X-direction and **b** Y-direction
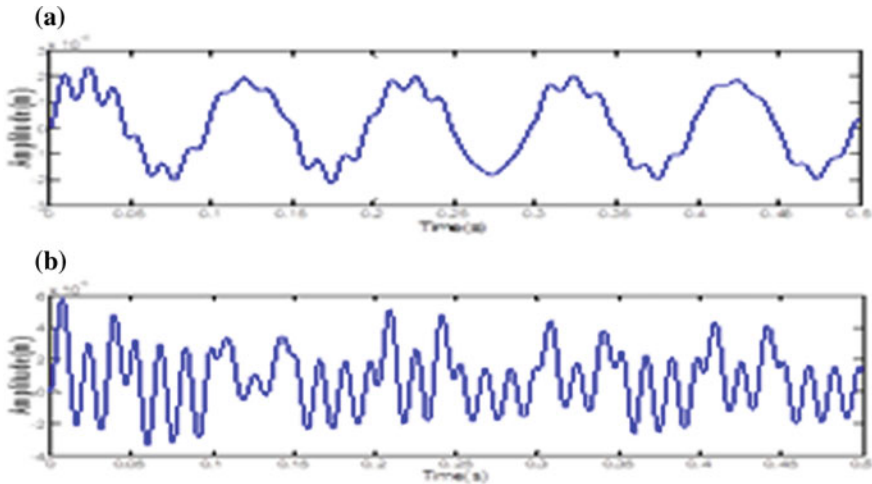
Fig. 8 Eccentricity (e) = 0. 000007 m **a** X-direction and **b** Y-direction

4 Conclusions

The work presented in this paper an analytical procedure, which is conducted by simulating different unbalances and cracks that occur in the system comprising rotor-bearing system. The statistical features were given as input to the ANN. Then, for the cases of crack and unbalance, confusion matrix was obtained. In both cases, ANN is trained and tested by both X-direction and Y-direction readings.

By modelling the neural network as a classification problem, the data was classified. It was observed that Y-direction readings are classification results and X-direction vibration readings are giving the same result as that obtained by Simulink model. These results are quite useful for making a maintenance decision based on unbalance severity, whether the machine is allowed to run or not. The present neural network is classified with 100% accuracy by statistical features in X-direction for unbalance identification and with 100% accuracy by statistical features in Y-direction for cracks. The present model can be improved by adding measurement noise in this model. Addition of measurement noise will mimic the actual system more closely. The working of the algorithm can be tested after adding measurement noise in the model.

References

1. Braun S (1986) Mechanical signature analysis: theory and application. Academic Press, London
2. Lei Y, He Z, Zi Y (2008) A new approach to intelligent fault diagnosis of rotating machinery. Expert Syst Appl 35(1):1593–1600

3. Genta G, Bona FD (1989) Unbalance response of rotors: a modal approach with some extensions to damped natural systems. J Sound Vib 140(1):129–153
4. Goldman P, Muszynska A (1991) Analytical and experimental simulation of loose pedestal dynamic effects on a rotating machine vibrational response. In: Rotating machinery and vehicle dynamics. ASME DE, vol 35, pp 11–17
5. Chu F, Zhang Z (1998) Bifurcation and chaos in a rub-impact Jeffcott rotor system. J Sound Vib 210(1):1–18
6. Kim YB, Noah ST (1991) Stability and bifurcation analysis of oscillators with piecewise-linear characteristic: a general approach. Trans ASME J Appl Mech 58(1):545–553
7. Chu F, Holmes R (1998) Efficient computation on nonlinear responses of a rotating assembly incorporating the squeeze-film damper. Comput Methods Appl Mech Eng 164(1):363–373
8. Curti G, Raffa FA, Vatta F (1992) Unbalance response of rotor systems by dynamic stiffness method. Mech Res Commun 19(4):351–359
9. Sekhar AS (2005). Identification of unbalance and crack acting simultaneously in a rotor system: modal expansion versus reduced basis dynamic expansion. J Vib Control 11(9):1125–1145
10. Kankar PK, Satish CS, Harsha SP (2011) Fault diagnosis of ball bearings using machine learning methods. Expert Syst Appl 38(1):1876–1886

Characterization of ABS Material in Hybrid Composites: A Review

Nitin Kumar Gupta, Pankaj Pandey, Samarth Mehta, Shilpi Swati, Shubham Kumar Mishra and Kevin Jose Tom

Abstract The importance of polycarbonate/acrylonitrile butadiene styrene (PC/ABS) alloy is increasing day by day in today's world. In this work, we have analyzed and compiled the ABS substrate both qualitatively and quantitatively in various fields like doping, surface modification, polymerization, conductivity, and electroplate decomposition. Also, an in-depth overview of the mechanical behavior, thermal properties, metallization, and modulus of materials has been investigated here. ABS plates with nickel and copper serve good in industrial applications. Apart from this, their widespread applications in automobiles, communication instruments, electrical and electronics equipment, injection molding, and fused deposition modeling were studied to analyze the mechanical behavior of virgin ABS because of its user-friendly behavior and simplicity for machinery actions. The degeneration of ABS substrate caused due to less amount of nitrogen obtained from the paralysis of DABS has been discussed thoroughly. Quasi-static mechanical properties of FDM–ABS materials were also taken into account. In order to improve flame retardancy, it was advised to promote char formation using tin- and zinc-based Lewis acid salts as charging additives on ABS during combustion. Also, flame-retardant properties in ABS were observed by the reaction of hexachlorophosphazene with phenol and catechol. ABS rubber resin and fumed hydrophobic silica nanoparticles were dispersed together to get the best wear abrasion resistant polymer, Taguchi method was introduced to calculate signal-to-noise (S/N) ratio. Later, the study on laser transmission welding of polymer joints by two ABS sheets has also been taken into consideration. The emphasis on production of innovative models using ABS waste has been laid. The discussion on the tribological behavior of composites has also been studied. Boiling effects of ABS fraction on glassy transition temperature and strain rate on deformation behavior of PC, ABS alloy are theoretically concluded in this work.

N. K. Gupta (✉) · P. Pandey (✉) · S. Mehta · S. Swati · S. K. Mishra · K. J. Tom
Department of Mechanical Engineering, DIT University, Dehradun, Uttarakhand, India
e-mail: Nitin.gupta@dituniversity.edu.in

P. Pandey
e-mail: pandeypankaj1920@gmail.com

1 Introduction

Thermal resistance, lightweight, easy formability, and reflectivity are some of the
properties of a plastic material due to which plastics are useful in many ways. These
properties of plastic are helpful in fabrication of materials like ABS/PS. The study
of ABS material can be helpful in reducing economics, energy, and environmental
issue of a country. Acrylonitrile, Butadiene, and styrene are three monomers of
ABS polymers. A nonconductive material can be made conductive by several
methods. Applying a conductive layer on the nonconductive material is one of the
very useful methods and is called metallization which is done for the determination
of property of any alloy. After adding additives, it is important to know the effect of
additives on the alloy [1, 2]. An alternative of additive has been developed recently
which can be useful in having similar properties as before with less price. In this
approach, the polarity range of the system can be enlarged by the use of ionic liquid
(ILS) as adjuvant in ABS [3]. Combination of properties of individual components
is useful in giving an optimum price–service ratio because of its low cost and high
performance [4]. Introducing pores to the material system helps in further weight
reduction and energy absorption through large compressive deformation, and this is
(fabricating porous structures) easier and cost-effective compared to metals and
ceramics [5].

An environmental-friendly surface etching and activation technique for ABS
material is a replacement for conventional chromic acid bath. By using this, peel
strength increases and adhesion strength reaches its maximum value [6]. If ther-
moplastic polymers (ABS/PC) were treated with atmospheric plasma, the slower the
plasma treatment tends to the greater wetability of the treated polymers, somehow
which gives idea about surface modification [7]. During the recycling of ABS from
waste electrical and electronic equipment (WEEE) voids, defects can occur (caused
by the evolution of volatile substances) and it was found that flexural strength and
ductility, in particular, decreased with increased level of voids [8]. Nickel elec-
troplating of ABS plastic has been achieved without any palladium pretreatment
which is environmental friendly [9]. ABS material has wide range of applications
and use of polymeric composites has grown at a rapid rate since 1960s. Hence, in
this review paper, we are theoretically summing up all the physical and chemical
properties of ABS/PC and its effect on environment.

2   Literature Review

1. **ABS material and organic polymeric varistor**: Varistors are the electronic devices which cause a variation in the resistance with the applied voltage. The relationship between resistance and applied voltage in varistor is inversely proportional. The resistance of the varistors is high at lower voltage and decreases as the voltage is raised. The varistors have an inverse relation between applied voltage and resistance, and hence it shows a nonlinear/nonohmic behavior of current and voltage characteristics. Varistors are used in controlling and compensating devices, and hence it was built at large scale as controlling devices. Due to availability and cheap in price, varistors are made from the ceramic materials. These varistors are made from ceramic materials, and hence known as ceramic varistors. Basically, these ceramic varistors are made up of n-type semiconductors. These n-type grains are then surrounded by insulating electrical barriers at the grain boundary [10]. To protect these systems against transient overvoltages, low-voltage varistors are developed [9]. Varistors till now were being built by using ceramic materials which were showing a nonlinear electric behavior on polymerization. The limitation of using ceramic-based varistors is its preparation and uses. The preparation of ceramic varistors is done at high temperature and with toxic chemicals, and hence these things are making it less desirable. Also, non-flexibility in the mechanical behavior and high density is also a cause of its undesirability [11].

    To overcome with abovementioned problems, a new varistor is investigated [11]. Organic varistors are made by the combination of the low-cost dielectric polymer and condensing polymers, polyaniline, acrylonitrile–butadiene–styrene copolymer. Preparation of PANI emeraldine-salt form (PANI-ES) is done by oxidative polymerization synthesis in which 6.0 ml of aniline in presence of 1.0 mol/L of HCl is combined with 3.756 g of $(NH_4)_2S_2O_8$. This synthesis is done by stirring the mixture for 2 h. Aqueous solution of 0.1 mol/L of NH_4OH when stirred with PANI-ES for 24 h, it gives PANI emeraldine-base form (PANI-EB). PANI-ES with ABS composite dissolves in adequate amount of ABS in chloroform [11]. The dispersion of PANI particles takes place in polymer matrix of dielectric. ABS was chosen because of its mechanical and thermal properties [12] as well as because recycling is possible. One more advantage of using ABS is that the composition of acrylonitrile, butadiene, and styrene in ABS can be varied which will cause new physical and chemical properties.

    The following figure, Fig. 1a, shows SEM micrographs of PANI-DBSA/ABS and Fig. 1b shows SEM micrographs of OPV composites. In both the composites, the percentage of PANI is 20%. In Fig. 1a, the homogeneous phase of PANI-DBSA/ABS can be seen. While in Fig. 1b, i.e., in the varistor sample, the grains of PANI are closely packed and it can be distinguished by normal methods. This can be concluded that the PANI gets dispersed in the ABS matrix.
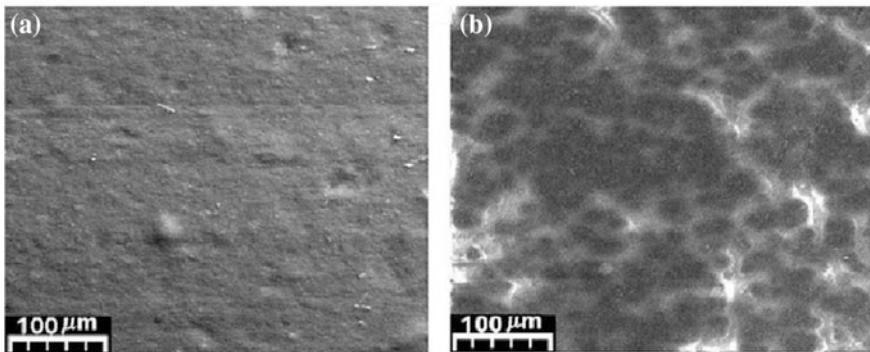
Fig. 1 a SEM micrographs of PANI–DBSA/ABS **b** PANI/ABS composites varistor

E–J curve of PANI-DBSA/ABS Blend and PANI/ABS varistor is shown in Fig. 2. Comparative study of both is done on the curve which is shown. PANI-DBSA/ABS blend shows a linear ohmic behavior while PANI/ABS varistor shows nonlinear ohmic characteristics [12]. In the recent time, it was the first attempt for the preparation of organic polymeric varistors in which a nonlinear coefficient of $\alpha = 5.0$ and breakdown voltage of 10 V/mm is taken. Its characterization was also done with flexible, inexpensive, and stable properties [12].

2. **ABS material modification by treating with an atmospheric pressure plasma**: In this, the effect of treating ABS with atmospheric pressure plasma has been discussed. It is observed that about 80% of the tensile strength is recovered

Fig. 2 Current density electric field (J–E) curve for 20% wt of PANI–DBSE/ABS blend and PANI/ABS varistor composites
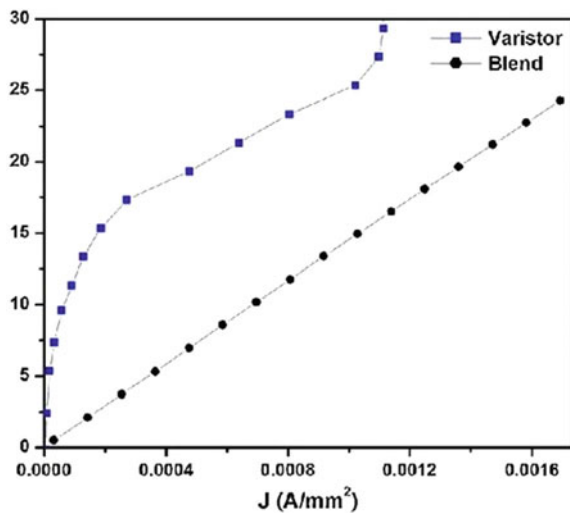
by using this process [13]. Atmospheric pressure plasma treatment is an alternative surface preparation method for plastics and organic matrix composites prior to structural adhesive bonding [14]. Atmospheric pressure plasma is the best technique for replacement of traditional method of preparation. By acquiring the plasma treatment, the oxygen content increases [14]. The use of plasma results in only minor changes to composite surface structure. The use of this method in the joining of composite surface has been the subject of several publications [14].

Wet chemical cleaning and mechanical abrasion are two techniques of replacement of traditional method for surface preparation. The traditional preparation method also causes the environmental issue when used to prepare the ABS material [14]. By treatment of ABS with atmospheric pressure plasma, there is an increase in O peak and decrease in C peak, respectively, and also the strength of adhesive bonding increases considerably [14]. Also, the strength of repaired sample is increased by 12% up to 92% of virgin specimen. Atmospheric pressure plasma activation not only improves static bond strengths, but also significantly increases the durability of joint [14].

3. **ABS material copper metallization**: In this work, we studied an environmental-friendly surface metallization on ABS copolymer as a replacement of conventional chromic acid etching bath [8]. By using copper metallization, its peel strength and adhesion strength improves, and at the temperature of 50 °C adhesion strength reaches its maximum value. It is also theoretically studied that there is no difference between "Cu and Pd" catalyst on crystalline of electroless-plated copper film. Copper (Cu) has an excellent electrical conductivity and is relatively inexpensive. In the following work, it has been widely studied for POP and variety of plastics which are being Cu plated that includes acrylonitrile–butadiene–styrene (ABS), polypropene, and Teflon. Conductive Cu layers were developed on ABS from bath of H_2SO_4, CH_3COOH, and H_3PO_4 to increase the electrical performance [15].

Further, at low temperature, CuS nanoparticles were prepared under hydrothermal reaction between $Cu(NO_3)_2.4H_2O$ and thioglycolic acid. CuS nanostructure added to acrylonitrile–butadiene–styrene copolymer and influence of copper sulfide on the thermal stability and flame retardancy of ABS matrix were studied. As a result, it was concluded that CuS nanostructure can enhance the thermal stability of the ABS Matrix [16].

In Fig. 3, XRD pattern of pure ABS polymer and ABS–CuS nanocomposites have been shown. XRD pattern of any composite shows the phase identification of it. Figure 3a shows the phase pattern of pure ABS polymer. Figure 3b shows the phase pattern of ABS–CuS nanocomposites. From the figure, it can be concluded that the peaks of CuS in XRD pattern of nanocomposite confirm the existence of copper sulfide in the polymeric matrix [16].

Most common durable plastic is acrylonitrile butadiene styrene (ABS). Copper and nickel have large industrial uses and are used in different processes. These are used in making of toys, automotive, electronic housing, computer body
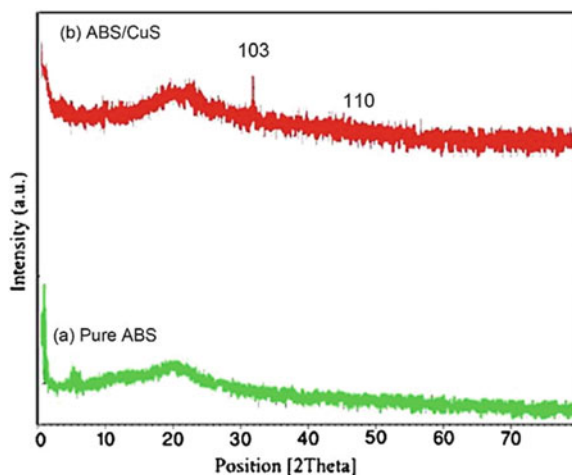
parts, pipes, switches, etc. [4]. Due to large-scale uses of nickel, it is selected as the coating material in direct metal electroplating on ABS. Because of its eco-friendly behavior, less in cost and quick in process, it is largely in demand for planting industries [4]. In this paper, we have studied and analyzed the electrodeposition of nickel (Ni) on the ABS material with the help of electroplating process. The main reason for adopting this process of electroplating is its eco-friendly properties and less cost of operation.

The electroplating of nickel on the surface of ABS takes place in three steps. In first step, polypyrrole is chemically deposited on the layer of ABS surface. Second, the electroplating of copper on ABS surface is done. At the end, nickel is deposited on the top layer of ABS. This process of electroplating has some advantages over the conventional methods of electroplating. This method may be completed in three steps but it is quicker than conventional method. This is because several steps like palladium autocatalysis and chromium etching are reduced here. Homogeneity, thickness, and adherent of coating can be analyzed by SEM, X-ray mapping, and EDS [17]. In this work, an effect of alkaline nickel sulfate and aqueous acid nickel chloride on the ABS is analyzed when ABS is dipped in it. As a conclusion, it was found that the acid nickel chloride bath had a greater stability and wide operating range. Also, acid nickel chloride bath gave better coating thickness than alkaline nickel sulfate bath. Later on, effects of sodium hypophosphite and sodium citrate concentrations on the electroless nickel plating thickness were discussed.

4. **ABS material surface etching**: Surface etching of ABS using electroless deposition method is responsible for achieving good conditions for metal–plastic bonding and we studied that chromic acid etched samples show better electrical performance. Etching generally provides anchoring sites for activator material, increase in the surface area, and some residual remaining also got eliminated in the etching [18]. In this section, an environmental-friendly etching

system containing MnO_2–H_3PO_4–H_2SO_4 was developed to investigate surface etching for ABS–polycarbonate (PC/ABS) as the replacement for conventional chromic acid etching solutions. When the ABS substrates were treated in optimal swelling and etching conditions, preferable surface hydrophilic conditions were studied by SEM observation and surface contact angle measurement to obtain desirable surface finish conditions and thus adhesion strength was improved. The result showed that the TMAH–NMP–H_2O swelling treatment and the MnO_2–H_3PO_4–H_2SO_4 etching treatment were very effective and environmental friendly for ABS surface treatments [19]. Further, a device made up of ABS and fabricated by FDM was treated to render their surfaces impervious to water and grafting of PEGMA, which was presented and evaluated for increasing the hydrophilicity and biocompatibility of the ABS surface. In order to overcome this problem, sealing an FDM–ABS surface with an acetone treatment was implemented to the device and the grafting of PEGMA into ABS is a viable method to increase surface hydrophilicity and biocompatibility [20]. Copper particles were deposited on the ABS surface which served as a replacement for $SnCl_2$/$PdCl_2$ colloid, and thus Cu proved to be a feasible replacement for Pd catalyst [21].

In Fig. 4, FT-IR spectra of treatment of PC/ABS substrates with swelling and etching has been shown. The variation in the wave number range with percentage of treatment is shown in the graph. When there was no treatment of PC/ABS substrate with swelling, there is a long dotted line present in the graph. This shows that the wave number range is decreasing initially when the percentage of transmittance is decreasing till a point and then the wave number range is decreasing even increasing the percentage of transmittance. After swelling treatment of PC/ABS, a small dotted line is shown in the graph. In this, comparatively high-transmittance percentage is giving approximately the same

Fig. 4 FTIR spectra of PC/ABS substrates with swelling and etching treatments, wave number range: 1650–1800 cm
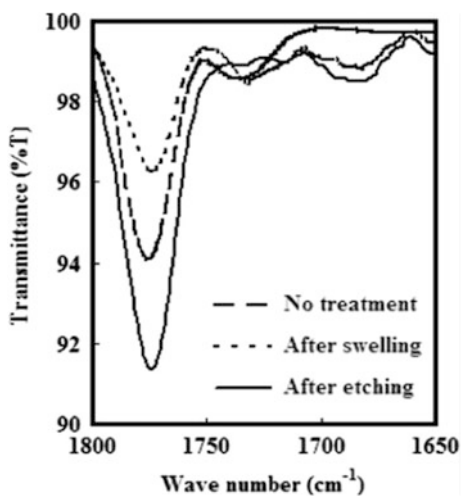
wave number range. After the etching process, a continuous line is shown. In this, comparatively high variation of percentage of transmittance is showing very less variation in the wave number range.

From the above information, this can be concluded that the surface absorption capacity of PC/ABS has increased when the process of etching is done on it. Low value of transmittance percentage is showing that less amount of light beam is detected on the other side of the sample [19].

5. **ABS material metallization**: Whenever any nonmetallic plastic components or part is imparted by a metallic property, then this process is called metallization. The process of metallization is done by decomposing the thin metallic film over the surface of plastic material. In this literature, the metallization of part material, i.e., acrylonitrile–butadiene–styrene copolymer is done. To do this, fused decomposing modeling machining is required. The metals which are used for the metallization are silver (Ag), Gold (Au), copper (Cu), and nickel (Ni) [18]. Having good electrical conductivity and comparatively less expensive, copper is widely used. Different techniques are available for the metallization process. These techniques are spray metal techniques, vacuum decomposition techniques, sputtering, dipping the part in metal paint, paint by brush, and electroless plating [22]. Fused decomposition method is a method to fabricate the part of specific dimensions. By use of this method, the prototyping is done rapidly, as the layer-by-layer decomposition principle is used to fabricate. In this method, the CAD design model is directly converted into fabrication.

Before the process of electroless decomposition, it is essential to prepare the surface on which decomposition is achieved. This surface preparation method is also known as conditioning of surface. The conditioning of the surface of the metal or plastic surface increases the adhesiveness between the plastic and
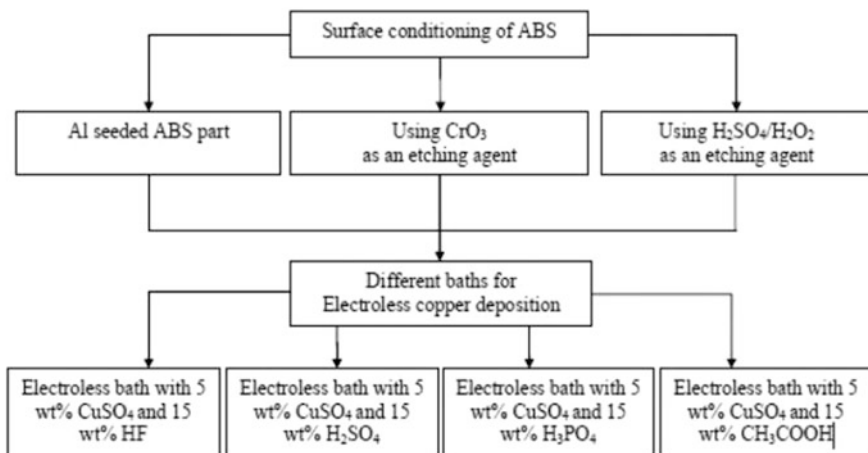
Fig. 5 Surface conditioning of ABS through different routes

decomposed materials [23]. The optimum time for the conditioning of the surface depends upon the properties of the plastic which is dependent upon the composition and fabrication used in the production of the plastics [24]. For the preparation of the ABS surface for electroless surface decomposition, two different routes are identified. These routes are shown in Fig. 5.

In Fig. 5, it is shown that the surface preparation of ABS materials can be done through different methods. These methods are represented in the form of routes in the image. Also, bath of different materials with its wt% with ABS is indicated at the lower of the image.

For the surface conditioning through Route 1, chromium acid is used as an etching agent in different processes of the surface. These processes are cleaning, etching, neutralization, activation, acceleration, and electroless decomposition. At the end of the process, the sample is washed with the water and dipped in the acidic solution. In second route, all the processes remain same other than etching process. In the second route, the composition and the constituents also remain the same. For the etching process, chromium acid is replaced by sulphuric acid (H_2SO_4) and hydrogen peroxide (H_2O_2). After all steps in the first route, the ABS part is immersed in the 192 ml solution of H_2O_2, 160 ml of sulphuric acid (H_2SO_4), and 448 ml of deionized water. All these are maintained at room temperature.

Figure 6 is showing the SEM image of copper-deposited ABS for different–different time periods. The analysis of sample of Route 1 is done on SEM and EDM. These crystals are observed when electroless copper decomposition is done in acidic solution of HF for 24 h and 48 h at room temperature [25].

SEM and EDS images of sample dipped in HF bath at room temperature is shown in Figs. 6 and 7. In Fig. 6, the deposition of copper is not clearly visible. However, some crystals can be seen from EDS mapping.

In Fig. 7, the copper distribution on the Al-seeded ABS surface is shown. This pattern is obtained by EDS mapping to examine the distribution of copper.
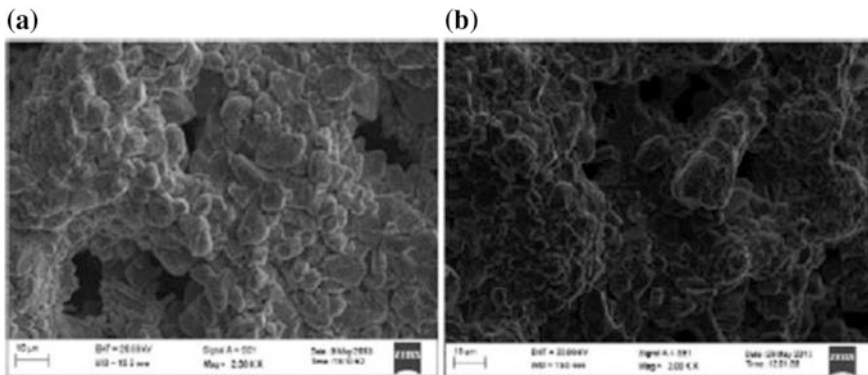
Fig. 6 SEM image of copper-deposited ABS part surface in HF bath **a** For 24 h **b** for 48 h
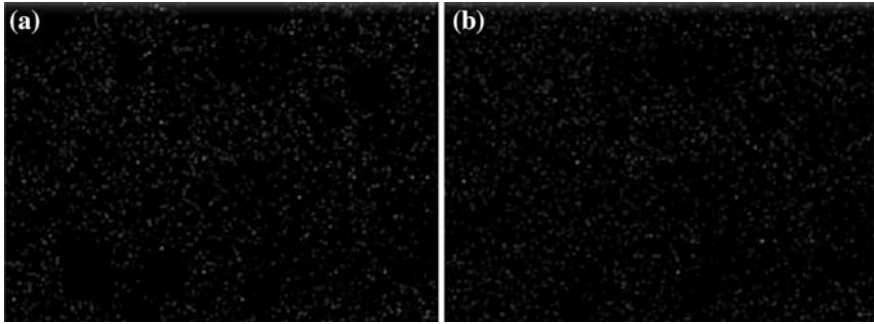
Fig. 7 EDS map of copper-deposited ABS part surface in HF bath **a** 24 h **b** 48 h
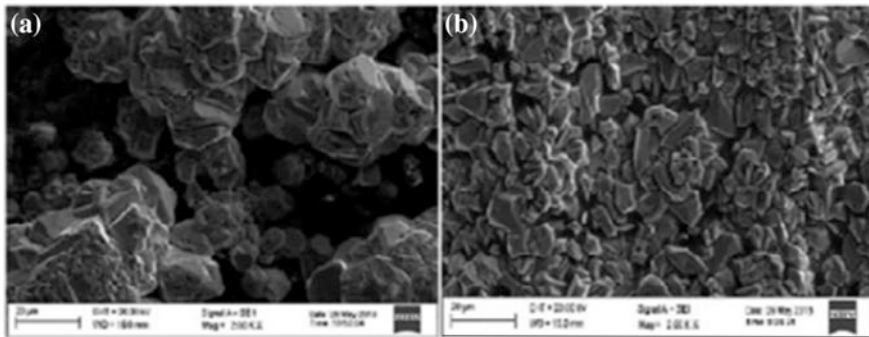
Fig. 8 SEM image of copper-deposited ABS part surface in CH_3COOH bath **a** 24 h **b** 48 h

Figure 8a shows the copper distribution after 24 h and Fig. 8b shows the copper distribution after 48 h [25].

Now, from this, we can conclude that whenever the observation likes electrical performance, SEM image and EDS analysis are examined, and then the following results appear:

- Copper can be obtained on the surface of ABS by all three routes.
- The conductivity of specimen prepared by different route differs in some scale.
- Also, the conductivity has been affected by different types of acidic baths.
- In Route 1, resistance value was noted in all the points but not in Route 2.
- When we prepare the ABS surface by way 1, it removes the stages that we did in Route 2.
- Route 2 is not cheap because of the seeding of the plastic surface with the catalyst, e.g., palladium (Pd) and/or tin (Sn).
- Hence, way 1 is the best because it involves less stages [26].

3 Result and Conclusion

In this literature, we have reviewed the effect of different decomposition methods on the conductivity of ABS material, effect of different methods on use of ABS as varistors, E–J curves of ABS plastic, etc. From considering all the above literature and the theory, we came to the following conclusion:

1. In the varistor preparation, the dispersion of PANI in the ABS matrix is more than the dispersion of PANI in ABS–DBSA. This shows that for the preparation of varistor, PANI should be dispersed in the ABS material.
2. The ABS surface modification by atmospheric plasma is discussed. This affects the surface of ABS materials. The tensile strength of the ABS material is recovered by 80%. This conclude that plastic materials when treated with atmospheric plasma increases the tensile strength.
3. The copper metallization of ABS plastic material is done by the bath of acidic solution of nickel chloride and alkaline nickel sulfate solution. Effects of both the methods have been compared and the conclusion is brought that the acid nickel chloride bath had a greater stability and wide operating range. Also, acid nickel chloride bath gave better coating thickness than alkaline nickel sulfate bath.
4. The surface modification of the ABS material is done to ensure the proper bonding between the metallization metal and ABS surface. The etching of the ABS surface gives better surface absorbing capacity. Low value of the transmittance percentage gives high absorbing capacity.
5. In the last section of the paper, we have reviewed the different processes involved in ABS material metallization. The results are obtained and we concluded that before the ABS material metallization, it is essential to modify the surface of the ABS material. The surface modification is obtained best when it is etched by chromium acid. Also, the conductivity of the ABS material is increased when different acidic baths are used.

References

1. Zhang J (2016) Research on thermostability of flame-retardant PC/ABS-Blends with PyGC. Procedia Eng 135:83–89
2. Merijs RM, Zicans J, Ivanova T, Berzina R, Saldabola R, Maksimovs R (2015) The effect of introduction of montmorillonite clay (MMT) on the elastic properties of polycarbonate (PC) composition with acrylonitrile-butadiene styrene (ABS). Contents lists available at Science Direct

3. De Souza RL, Campos VC, Ventura SP, Soares CM, Coutinho JA, Lima ÁS (2014) Effect of ionic liquids as adjuvants on PEG-based ABS formation and the extraction two probe dyes. S0378-3812(14)00223-4

4. Salinas SA, Kusch P, Knupp G, Steinhaus J, Sülthaus D

5. Al Jahwari F, Huang Y, Naguib HE, Lo J (2016) Relation of impact strength to the microstructure of functionally graded porous structures of acrylonitrile butadiene styrene (ABS) foamed by thermally activated microsphes 98:270–281

6. Xu W, Zhuang M, Cheng Z (2016) Environmentally friendly copper metallization of ABS by Cu-Catalysed electroless process 45(7):1709–1713

7. Abenojar J, Torregrosa-Coque R, Martinez MA, Martin-Martinez JM (2009) Surface modifications of polycarbonate (PC) and acrylonitrile butadiene styrene (ABS) copolymer by treatment with atmospheric plasma 203:2173–2180

8. Anold JC, Alsoton S, Holder A (2009) Void formation due to gas evolution during the recycling of Acrylonitrile-Butadiene-Styrene copolymer (ABS) from waste electrical and electronic equipment (WEEE)

9. Bazzaoui M, Martins JI, Bazzaoui EA, Albourine A (2012) Environmentally friendly process for nickel electroplating of ABS 258:7968–7975

10. Cristovan FH, Pereira EC (2011) Polymeric varistor based on PANI/ABS composite 161:2041–2044

11. Cristovan FH, Pereira EC (2011) Polymeric varistor based on PANI/ABS composite

12. Pud A, Ogurtsov N, Korzhenko A, Shapoval G (2003) Prog Polym Sci 28:1701

13. Kumar S, Abhishek G, Ullattil A, Elangundran TVA, Bhowmik S, Devadathan S, Kim CG, Baluch A (2016) Effect of atmospheric pressure plasma treatment for repair of polymer matrix composite for aerospace applications

14. Williums TS, Yu H, Woo R, Grigoriev M, Cheng D, Hick RF

15. Li Y, Shimizu H (2009) Improvement in toughness of poly (L-lactide) (PLLA) through reactive blending with acrylonitrile–butadiene–styrene copolymer (ABS): morphology and properties 45:738–746

16. Ghanbari D, Salavati-Niasari M, Esmaeili-Zare M, Jamshidi P, Akhtarianfar F (2014) Hydrothermal synthesis of CuS nanostructures and their application on preparation of ABS-based nanocomposite

17. Electroless nickel plating on ABS plastics from nickel chloride and nickel sulfate baths. J Chem Soc Pak 27(3):246–249 (2005)

18. Equbal A, Sood AK (2015) Investigations on metallization in FDM build ABS part using electroless deposition method 19:22–31

19. Ma Q, Zhao W, Li X, Li L, Wang Z (2013) Study of an environment - friendly surface pretreatment of ABS-polycarbonate surface for adhesion improvement 44:243–249

20. Magallón-Cacho L, Pérez-Bueno JJ, Meas-Vong Y, Stremsdoerfer G, Espinoza-Beltrán FJ (2011) Surface modification of acrylonitrile-butadiene-styrene (ABS) with heterogeneous photocatalysis (TiO$_2$) for the substitution of the etching stage in the electroless process 206:1410–1415

21. Singh R, Singh R, Dureja JS, Farina I, Fabbrocino F (2017) Investigations for dimensional accuracy of Al alloy/Al-MMC developed by combining stir casting and ABS replica based investment casting, S1359-8368(16)32171-0

22. Charbonnier M, Romand M (2003) Polymer pretreatments for enhanced adhesion of metals deposited by the electroless process. Int J Adhes Adhes 23:277–285

23. Luan B, Yeung M, Wells W, Liu X (2000) Chemical surface preparation for metallization of stereolithography polymers. J Appl Surf Sci 15:26–38

24. Gui-xiang W, Ning L, Hui-li H, Yuan-chun Y (2006) Process of direct copper plating on ABS plastics. J Appl Surf Sci 253:480–484

25. De Bruyn K, Van Stappen M, De Deurwaerder H, Rouxhet L, Celis JP (2003) Study of pretreatment methods for vacuum metallization of plastics. Surf Coat Technol

26. Li D, Goodwin K, Yang C (2008) Electroless copper deposition on aluminium seeded ABS plastics. J Mater Sci 43

Experimental Investigation of Mechanical Strength and Temperature of Friction Stir Welded Joint

Jitender Kundu, Siddhartha Kosti, Mandeep Kumar, Nav Rattan, Gyander Ghangas and Satish Kumar Sharma

Abstract Friction stir welding (FSW) is one of the primary technologies in the manufacturing industry for joining. In the present article, an experimental investigation has been carried out to reveal the temperature range for the maximum mechanical strength of friction stir welded (FSWed) joint. In a total, 30 experiments have been designed by response surface methodology (RSM) for four input process parameters. These experiments have been carried out and welding temperature data are recorded through thermocouples. The mechanical testing results indicated that tool rotational speed is the most dominating parameter which influences the joint strength. Other parameters like traverse speed, tool tilt angle, and dwell time also have a significant impact on ultimate tensile strength. Both response, i.e., ultimate tensile strength and frictional temperature also have a correlation which can predict the joint quality. An optimization of the process parameters has been done for ultimate tensile strength keeping frictional temperature in the range. The optimized parameter settings have been validated by confirmation experiments.

Keywords Friction stir welding · Tool rotational speed · Aluminum alloy temperature · Ultimate tensile strength

J. Kundu (✉)
Jorhat Engineering College, Jorhat 786007, Assam, India
e-mail: rsjk005@gmail.com

S. Kosti
Rajkiya Engineering College Banda, Banda 210201, Uttar Pradesh, India

M. Kumar
National Institute of Technology Kurukshetra, Kurukshetra 136119, India

N. Rattan
Women Institute of Technology, Dehradun 248007, India

G. Ghangas
Panipat Institute of Engineering and Technology, Panipat 132102, India

S. K. Sharma
Thapar Institute of Engineering and Technology, Patiala 147004, India

1 Introduction

With the rapid change of product variety in manufacturing industry, experts need to use innovative manufacturing techniques which must be cost-wise as well as quality-wise effective. FSW is one of the important joining processes among these new and innovative techniques. FSW is invented at The Welding Institute, UK in 1991 [1, 2]. FSW process is one of the joining material techniques which produce sound- and defect-free welding. FSW process is widely used in advanced manufacturing industries like aviation, space, marine, etc. [3, 4]. FSW is a solid-state welding in which a cylindrical rotation tool moves on weld line of two metal plates. The high temperature is produced due to the friction between tool shoulder and material plates. This high temperature transforms welded edge material into plasticized form which is further stirred by the rotation of tool pin. Tool pin is firmly attached with bottom of the shoulder. At the optimized value of the process parameters, this FSWed joint produces the same or 90% strength of base material. This process has number of advantages, e.g., no melting of materials, and therefore welding defects like entrapment of gases, blow holes can be avoided [5, 6]. Heat-affected zone is narrow as compared to conventional welding processes. Nonconducting materials like plastics also can be welded easily. The effect of different parameters has been investigated by researchers [7–9].

A number of researchers have been doing optimization of process parameters to get the efficient and quality weld. Taguchi approach with the GRA has been used which also gives considerable good results [10–12]. RSM has been used comparatively less but this technique is widely accepted. With the increase of its applications, FSW optimization is needed for the industrial use.

2 Materials and Methods

For the current research, aluminum alloy 5083-T321 has been used. The working material is widely used in aviation industry and marine industry due to its higher strength-to-weight ratio and resistance to corrosion. For the experimental planning, a statistical technique named "Design of Experiment" has been used. Four process parameters such as tool rotational speed, traverse speed, tool tilt angle, and dwell time have been selected. Dwell time is the time interval when tool shoulder is kept at initial point of actual welding before giving traverse speed. Dwell time provides initial heat so that better weld occurs at the starting point. The response parameters for the experimental study are ultimate tensile strength and frictional temperature.

Table 1 Chemical composition of working material AA5083-T321

Element	Mg	Mn	Fe	Si	Zn	Cr	Cu	V	Ti	Al
Weight %	4.9	0.5	0.33	0.13	0.11	0.0	0.05	0.01	0.01	93.78

Table 2 Working process parameters with minimum and maximum values

Process parameter	Notation	Units	Level values	
			Minimum	Maximum
Traverse speed	A	mm·min^{-1}	16	40
Tool rotational speed	B	rpm	500	1400
Tool tilt angle	C	degree	1	3
Dwell time	D	second	8	20

Table 3 Experimental settings and recorded response data

Std no	Run	A	B	C	D	Ultimate tensile strength			Frictional temperature		
						Test 1	Test 2	Avg.	Test 1	Test 2	Avg.
29	1	28	950	2	14	317	319	318	287.4	283.2	285.3
2	2	40	500	1	8	193	197	195	201.4	203.6	202.5
20	3	28	1400	2	14	253	253	253	298.6	300.6	299.6
27	4	28	950	2	14	305	303	304	272.8	267.4	270.1
19	5	28	500	2	14	239	245	242	244.6	244	244.3
6	6	40	500	3	8	236	246	241	243	244	243.5
23	7	28	950	2	8	309	311	310	255	259.2	257.1
13	8	16	500	3	20	236	234	235	275.6	277.6	276.6
7	9	16	400	3	8	250	264	257	337.6	340	338.8
28	10	28	950	2	14	314	316	315	274.5	268.1	271.3
16	11	40	1400	3	20	254	252	253	252.6	259	255.8
10	12	40	500	1	20	207	213	210	211.1	213.1	212.1
8	13	40	1400	3	8	255	255	255	322.8	319.6	321.2
22	14	28	950	3	14	312	318	315	276	276	276
24	15	28	950	2	20	315	313	314	240.6	238.4	239.5
25	16	28	950	2	14	315	319	317	266.7	272.9	269.8
11	17	16	1400	1	20	154	166	160	287.7	291.9	289.8
3	18	16	1400	1	8	175	171	173	298.5	299.7	299.1
26	19	28	950	2	14	317	317	317	256.6	251.4	254
15	20	16	1400	3	20	212	216	214	318.1	313.7	315.9
4	21	40	1400	1	8	170	172	171	268.3	271.3	269.8
30	22	28	950	2	14	318	310	314	245.4	253.8	249.6
12	23	40	1400	1	20	171	169	170	225.4	233.6	229.5
18	24	40	950	2	14	278	276	277	272.4	279.2	275.8
17	25	16	950	2	14	290	272	281	289.9	290.5	290.2
21	26	28	950	1	14	278	280	279	242.6	246.4	244.5
9	27	16	500	1	20	209	205	207	242	244.2	243.1
14	28	40	500	3	20	233	237	235	236.2	237.4	236.8
5	29	16	500	3	8	230	232	231	265.3	264.1	264.7
1	30	16	500	1	8	206	204	205	226	223.6	224.8
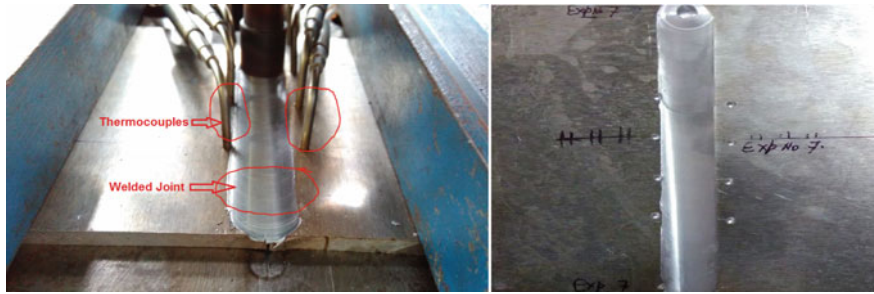
Fig. 1 Picture of FSW in action and welded joint for experiment number 7

The working material constituents have been reported in Table 1. Two plates of aluminum alloy 5083 of 150 mm*75 mm*4.5 mm have been used for experimentation. The pilot study and literature survey has been used for estimation of minimum values and maximum values of different process parameters.

For the FSW process, a tool steel H13 has been used. Tool fabrication is also an important factor for FSW of aluminum alloy. Tool pin profile affects the frequency of the stirring pulses under the tool shoulder, which, in turn, affects mechanical properties of joint. Therefore, a concave shoulder with diameter 18 mm, pin diameter 6 mm, and pin length 4.4 mm has been fabricated. Table 2 reported these minimum and maximum values of process parameters. These intervals confirm the good weld strength for aluminum alloys.

Totally 30 experiments with single iteration have been performed to reduce the effect of noise factors. Central composite design of RSM has been used for the number of experiments and find out the effect of process parameters on responses. The central composite design consists of 30 experimental points in random order: 16 factorial points, 8 axial points, and 6 central points, as given in Table 3. The experimental data from the central composite design were utilized to fit second-order polynomial equation. Vertical milling machine has been used with a cast iron fixture for the FSW. Figure 1 shows welding process and the welded joint produced. L-type thermocouples and infrared temperature measuring device have been used for estimation of the temperature on the welded joint.

3   Result and Discussion

Tensile strength testing samples have been prepared as per ASTM-8 M standard. The main objective of this experimental study is to maximize the tensile strength. The frictional temperature has a particular effect on the welding joint strength. At very small frictional heat, there is low temperature and low mixing of plasticized material. As frictional heat is increased, the tensile strength also increases and at a particular critical point higher frictional heat starts producing adverse effect on weld

joint. Higher frictional heat means higher temperature and aluminum is a good conductor of heat. Repeated thermal cycles make detrimental effect on the properties of aluminum alloy. High temperature produces wide heat-affected zone and welded joints break from the HAZ region. Therefore, optimum heat is necessary for the FSWed joint. The desirability approach has been used for the optimization of both responses.

3.1 Analysis of Variance for Ultimate Tensile Strength

Analysis of Variance (ANOVA) has been utilized to find out significant factors for the tensile strength and temperature. A quadratic model has been solved through statistical software Design Expert v7 (trial version). Backward ANOVA for the ultimate tensile strength and frictional temperature have been given in Tables 4 and 5. All the significant process parameters and their interactions have been selected at 95% confidence level.

From Table 4, significant process parameters and their interactions are B, C, BC, A^2, and B^2. Interaction terms also have significant effects on the ultimate tensile strength. R-square has a considerably desired value of 0.97 which is near to the predicted R-square. Tool rotational speed plays a most significant role in the frictional heat generation as well as intermixing of the plasticized material. At higher

Table 4 ANOVA for ultimate tensile strength

Source	Sum of squares	df	Mean square	F value	p-value Prob > F	
Model	74941.68	9	8326.85	97.49	<0.0001	significant
A-Traverse speed	107.56	1	107.56	1.26	0.2751	
B-Tool rotational speed	501.39	1	501.39	5.87	0.0250	
C-Tool tilt angle	12064.22	1	12064.22	141.25	<0.0001	
D-Dwell time	88.89	1	88.89	1.04	0.3198	
BC	2025.00	1	2025.00	23.71	<0.0001	
BD	342.25	1	342.25	4.01	0.0591	
A^2	2296.56	1	2296.56	26.89	<0.0001	
B^2	10200.01	1	10200.01	119.42	<0.0001	
C^2	309.59	1	309.59	3.62	0.0714	
Residual	1708.19	20	85.41			
Lack of fit	1573.36	15	104.89	3.89	0.0705	not significant
Pure error	134.83	5	26.97			
Cor total	76649.87	29				

Table 5 ANOVA for frictional temperature

Source	Sum of squares	df	Mean square	F value	p-value Prob > F	
Model	27451.02	9	3050.11	38.78	<0.0001	significant
A-Traverse speed	4867.56	1	4867.56	61.89	<0.0001	
B-Tool rotational speed	12329.73	1	12329.73	156.76	<0.0001	
C-Tool tilt angle	5481.04	1	5481.04	69.69	<0.0001	
D-Dwell time	832.32	1	832.32	10.58	0.0040	
AD	635.04	1	635.04	8.07	0.0101	
BD	1827.56	1	1827.56	23.24	0.0001	
CD	235.62	1	235.62	3.00	0.0989	
A^2	894.09	1	894.09	11.37	0.0030	
D^2	1190.19	1	1190.19	15.13	0.0009	
Residual	1573.09	20	78.65			
Lack of fit	731.10	15	48.74	0.29	0.9718	not significant
Pure error	841.99	5	168.40			
Cor total	29024.11	29				

tool rotation speed, intermixing is more uniform in advancing side as well as retreating side which creates a uniform crystallized nugget zone, i.e., high ultimate tensile strength. Dwell time and traverse speed have lower effect on the performance of the FSWed joint. A quadratic model has been given in Eq. (1) for the ultimate tensile strength.

$$\text{Ultimate Tensile Strength} = -168.66 + 11.265 * A + 0.53 * B + 43.91 * C + 1.25694 * D + 0.025 * B * C - 1.71E - 003 * B * D - 0.2 * A^2 - 2.966E - 004 * B^2 - 10.44 * C^2.$$

$$(1)$$

3.2 Analysis of Variance for Frictional Temperature

From the ANOVA table, it has been estimated that all input process parameters are significant with five interactions. R-square for the frictional temperature is 0.94 which is in a good agreement with the predicted R-square. Therefore, generation of heat is the combined result of all the involved process parameters. To keep the value of frictional heat in a target is necessary so that flow of material under the tool shoulder is good. A quadric model for the friction heat has been given in Eq. (2).

Frictional Temperature $= +112.27 - 6.41 * A + 0.11 * B + 26.40 * C + 20.81 * D - 0.09 * A * D - 3.96E - 003 * B * D - 0.64 * C * D + 0.11 * A^2 - 0.52 * D^2$.

$$(2)$$

For the ultimate tensile strength, a contour plot has been drawn (Fig. 2) which depicts that the increase in tool rotational speed also increases ultimate tensile strength with shallow pace.

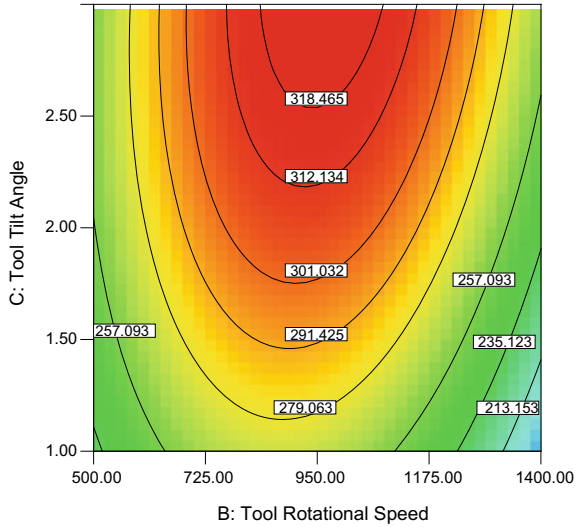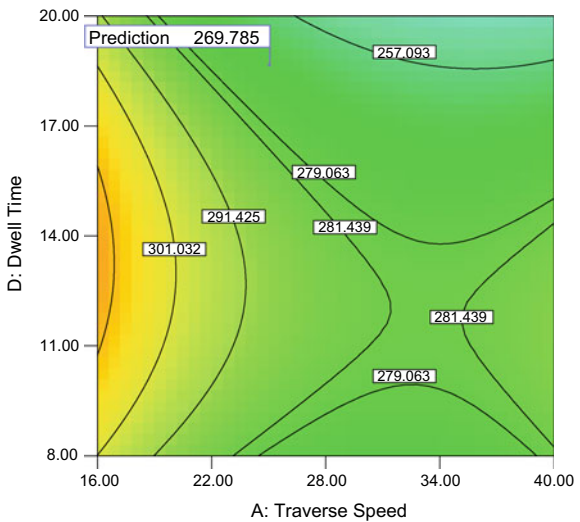**Fig. 2** Contour plot for ultimate tensile strength

Fig. 3 Contour plot for frictional temperature

In other significant process parameters, an increase in tool tilt angle sharply increases ultimate tensile strength which is due to the high pressure of tool shoulder on the plasticized material. The contour plot for the frictional temperature is also shown in Fig. 3. From contour, it has been identified that lower the value of the traverse speed the higher will be the friction temperature because number of rotations per unit area will be maximum and number of thermal cycles will be more at a given region. But, it will also increase the heat-affected zone which decreases the strength around the joint.

3.3 Optimal Setting for Process Parameters

Desirability approach has been used for the optimal setting of the input process parameters. In this approach, our desirability is considered 1.000 and respective to this input process parameters have been given some values. In current experimental study, maximum ultimate tensile strength is our desirability. The response frictional temperature must be in a given range otherwise it will decrease joint strength. Multi-response optimization has been utilized for best results.

A ramp function graph has been plotted which showed all the predicted values of input process parameters and corresponding response values (Fig. 4).

The predicted maximum value for the ultimate tensile strength is 325.22 MPa at a frictional temperature of 291.95 °C. The corresponding values for input process parameters have been given in Fig. 4.

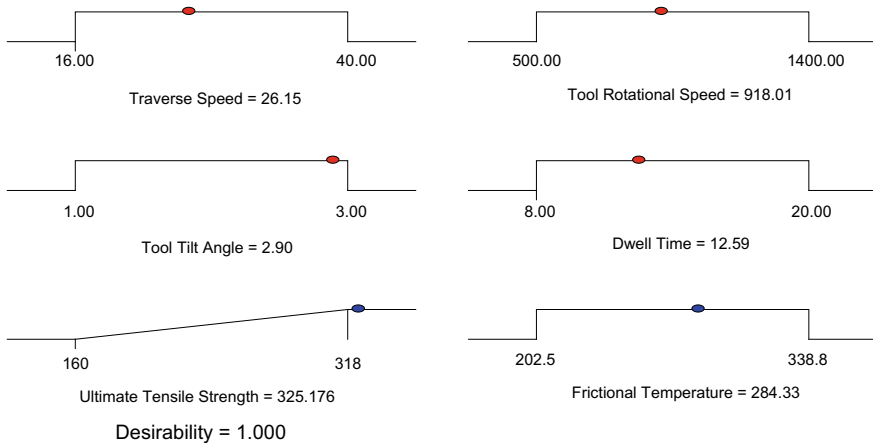|	
16.00 40.00	500.00 1400.00
Traverse Speed = 26.15	Tool Rotational Speed = 918.01
1.00 3.00	8.00 20.00
Tool Tilt Angle = 2.90	Dwell Time = 12.59
160 318	202.5 338.8
Ultimate Tensile Strength = 325.176	Frictional Temperature = 284.33
Desirability = 1.000	

Fig. 4 Ramp function graph of input process parameters and responses

For the validation of the results, two confirmation experiments have been performed and the value of ultimate tensile strength has been found out. The average value for the confirmation experiments comes out to be 318.37 MPa which is 95% confidence interval of the predicted optimal range.

4 Conclusions

From the above experimental study, following conclusions are drawn:

- The tool rotational speed and tool tilt angle are most significant factors for sound FSWed joint.
- The optimized setting for input process parameters suggested by desirability approach are traverse speed $= 25.10$ mm min^{-1}, tool rotational speed $= 1044.23$ rpm, tool tilt angle $= 2.96º$, and dwell time $= 9.74$ s.

References

1. Thomas WM, Norris I, Nicholas ED, et al (1991) Friction stir welding process developments and variant techniques. Google Patents, 1–21
2. Ma ZY (2008) Friction stir processing technology: a review. Metall Mater Trans A 39 (3):642–658
3. AWS D17 Committee on welding in the aircraft and aerospace industries (2010) Specification for friction stir welding of aluminum alloys for aerospace applications. An American National Standard 53
4. Thomas WM, Nicholas ED (1997) Friction stir welding for the transportation industries. Mater Des 18:269–273
5. Kundu J, Singh H (2016) Friction stir welding of AA5083 aluminium alloy: multi-response optimization using taguchi-based grey relational analysis. Adv Mech Eng 8:1–10
6. Mishra RS, Ma ZY (2005) Friction stir welding and processing. Mater Sci Eng R Rep 50(1–2):1–78
7. Padmanaban R, Balusamy V, Nouranga KN (2015) Effect of process parameters on the tensile strength of friction stir welded dissimilar aluminum joints. J Eng Sci Technol 10:790–801
8. Kundu J, Singh H (2016) Friction stir welding of dissimilar Al alloys: effect of process parameters on mechanical properties. Eng Solid Mech 4:125–132
9. Ghangas G, Singhal S (2018) Effect of tool pin profile and dimensions on mechanical properties and microstructure of friction stir welded armor alloy. Mater Res Express 5(6)
10. Pawar SP, Shete MT (2013) Optimization of friction stir welding process parameter using taguchi method and response surface methodology: a review. Int J Res Eng Technol 2 (12):551–554
11. Kundu J, Singh H (2018) Modelling and analysis of process parameters in friction stir welding of AA5083-H321 using response surface methodology. Adv Mater Process Technol 4(2):1–17
12. Sharma SK, Maheshwari S (2016) Multi-objective optimization of HAZ characteristics for submerged arc welding of micro-alloyed high strength pipeline steel using GRA-PCA approach. J Manuf Sci Prod 16(4):263–271

Effect of Front Slant Angle on Aerodynamics of a Car

Vishal Dhiman, Tanuj Joshi and Gurminder Singh

Abstract In this study, flow over the surface of a simplified car body is investigated using computational fluid dynamics. 3D modeling is carried out in Creo and simulation is carried out in ANSYS Fluent. Car is assumed to be moving at 40 m/s ($\sim$150 kmph). Flow behavior such as velocity profile, static pressure, and coefficient of drag and lift is determined. Three different cases of slant angles of the front windshield are taken, i.e., $20°$, $25°$, and $30°$ and their effect on aerodynamics of the car is determined. Comparison is then performed for static pressure, velocity profile, drag, and lift coefficient. Simulation results showed that the slant angle of $25°$ is most suitable of all, as the coefficient of drag and lift is minimum in this case.

Keywords CAD modeling · CFD · Drag · Lift · Static pressure · Velocity vector

1 Introduction

Automotive aerodynamics has become a subject of significant importance nowadays. Its main objectives are reducing drag, preventing undesired lift forces, and other causes of aerodynamic instability, producing downforce to improve traction, improve cornering abilities at high speeds and minimizing noise emission. Designing a vehicle by considering airflow over its surface makes it to accelerate faster. As a result, it can achieve better fuel economy. Coefficient of drag (C_d) is a commonly used term for a vehicle's aerodynamic smoothness. Multiplying drag coefficient by frontal area of the vehicle gives an index of total drag, i.e., *drag area*.

V. Dhiman
Chandigarh University, Mohali 140413, Punjab, India
e-mail: vishal.dhiman029@gmail.com

T. Joshi (✉) · G. Singh
Indian Institute of Technology, Hauz Khas, New Delhi 110016, India
e-mail: tanujptd@gmail.com

G. Singh
e-mail: gurmindersingh2012@gmail.com

641

By controlling frontal design of the vehicle, we can significantly reduce drag coefficient and frontal area, and thus the drag resistance experienced by the vehicle.

Janusz Piechna explained that any airflow at front region of a vehicle strongly influences overall flow pattern around the vehicle. Even relatively small changes in the values of pressure, distributed over the big car body region, change aerodynamic forces significantly [1]. Jovan Doric modeled and designed the car body using CCM+ on the basis of elements of aerodynamics and vehicle dynamics and impact of external influences on it. Based on analytical and CFD simulation, he concluded that varying the geometry of the model contributes significantly to the change in the values of lift and drag forces and coefficients [2]. Yong-Jun Jang investigated the ability of nonlinear eddy viscosity to determine the flow around the "Ahmed body" with the steady RANS formulation. He predicted separation from and reattachment of streamlines onto the slanted rear roof portion at slant angle of 25° and consequently production of lift and circulation [3]. Emmanuel Guilmineau compared numerical results with experimental data and concluded that at slant angle of 25°, the simulation result predicts significant separation, and experiment reveals that halfway down the center of the face, reattachment is taking place [4]. Saurabh Banga investigated the effect of variation of rear slant angle of the "Ahmed body" on drag and lift coefficients. He also determined the optimum rear slant angle giving minimum drag coefficient (C_d) and minimum positive coefficient of lift (C_l) to reduce inefficiencies and losses [5–9].

The present study is aimed to determine important aerodynamic characteristics of a car such as coefficient of drag, coefficient of lift, static pressure, and velocity vectors over the surface. CFD is performed for three different slant angles of front windshield of an arbitrary car model, i.e., 20°, 25°, and 30° and results are compared.

2 Theory

For a fluid flow, basic governing equations can be obtained by applying the fundamental laws of mechanics. Computational fluid dynamics involves some fundamental fluid flow equations based on conservation of mass, conservation of momentum, and conservation of energy.

For a compressible fluid, continuity equation or the equation of conservation of mass can be expressed as follows:

$$\frac{\partial \rho}{\partial t} + \nabla \cdot (\rho \vec{v}) = 0.$$

It is followed by the equations of conservation of momentum, also called Navier–Stokes equations. The Navier–Stokes (N–S) equations are the basic governing equations for a heat conducting, viscous fluid and are obtained by applying Newton's II law of motion to a fluid element.

For a compressible Newtonian fluid, N–S equations can be written as follows:

$$\rho\left(\frac{\partial u}{\partial t} + u.\nabla u\right) = -\nabla p + \nabla.\left(\mu\left(\nabla u + (\nabla u)^T\right) - \frac{2}{3}\mu\left(\nabla.u\right)I\right) + F.$$

Here, $\vec{u}$ and $\vec{v}$ are the fluid velocity and p, ρ, *and* μ are pressure, density, and fluid dynamic viscosity. The above N–S equation consists of pressure, inertial, viscous, and external forces that are experienced by the flowing fluid. These above equations, together with the equation of conservation of energy form a set of coupled, nonlinear partial differential equations which are then solved to get pressure and velocity values.

For the applications, where Reynolds number is very large, turbulent flow problems are often transient in nature. And, a fine mesh that is capable of resolving size of even the smallest eddies in the flow is required. Solving such simulations for complex engineering problems, using above N–S equations, require such massive computational power that is often beyond the capabilities of most of the computers and supercomputers. That is why, a Reynolds-averaged formulation of the basic Navier–Stokes equations is used, also termed as RANS. It averages pressure and velocity fields in time. These RANS equations are then solved in a stationary way on a coarser mesh, thus drastically reducing computing power and time.

Reynolds-averaged formulation of Navier–Stokes equations is as follows:

$$\rho(U.\nabla U) + \nabla.\left(\mu_T\left(\nabla U + (\nabla U)^T\right) - \frac{2}{3}\mu_T(\nabla.U)I\right)$$
$$= -\nabla P + \nabla.\left(\mu\left(\nabla U + (\nabla U)^T\right) - \frac{2}{3}\mu(\nabla.U)I\right) + F.$$

Here, **P** and **U**—time-averaged pressure and velocity.

$\boldsymbol{\mu_T}$—turbulent viscosity, i.e., effects of time-dependent small-scale fluctuations of velocity.

The turbulent viscosity ($\boldsymbol{\mu_T}$) can be calculated using turbulence models. **K-εpsilon** turbulence model is the most common and is often used in industrial applications because of its robustness and computationally inexpensiveness. Above equations are the core of fluid flow modeling. These equations need to be solved, for a set of specific boundary conditions (inlet, outlet, and wall), in order to determine fluid pressure and its velocity for a given control volume. From these two parameters, all other required variables can be evaluated.

Drag coefficient can be calculated as $C_D = \frac{F_D}{0.5 \times \rho \times u^2 \times A}$.

Lift coefficient can be calculated as $C_L = \frac{F_L}{0.5 \times \rho \times u^2 \times A}$.

For complex engineering problems, above equations of fluid flow are nearly impossible to solve analytically. But, it is possible to determine computer-based approximate solution (numerically) of fluid flow equations for most of the engineering problems [10].

3   CFD Simulation

Analysis and comparison study are done through modeling and simulation using Pro-E and ANSYS Fluent as shown in Figs. 1 and 2. A control volume (enclosure) is generated around the car body. In order to obtain accurate and reliable results for the simulation, meshing of the CAD model must be properly carried out. There are various element sizes and types available in ANSYS. Solution time grows with the cube of the number of nodes. Hence, lesser is the element size, more accurate will be the results, but due to greater number of elements/nodes computational time is increased significantly. So, selection of element size and type should be done so as to get optimum results in lesser computational time [11].
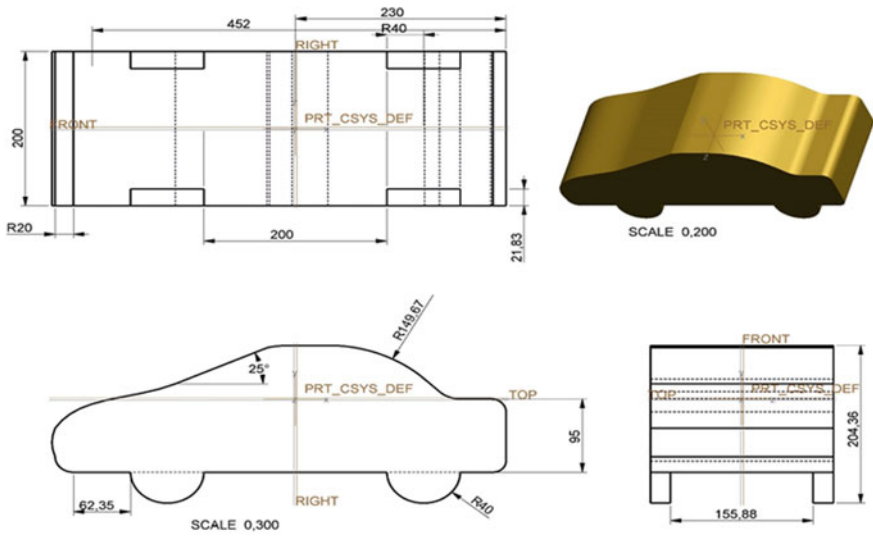
Fig. 1 Dimensions of car model
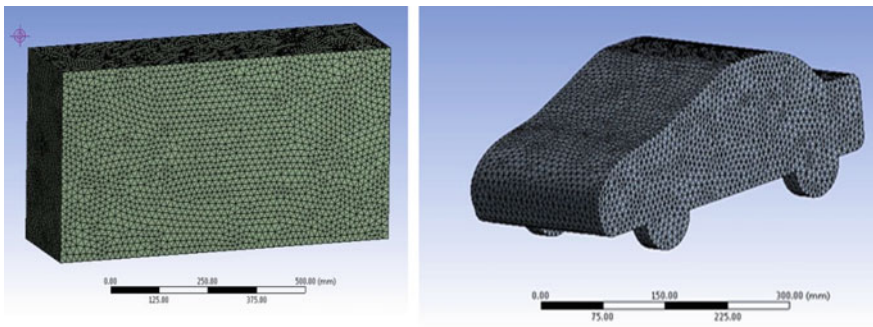
Fig. 2 Meshing of CAD model

In our study, triangular surface mesh is adopted for car body and 3D tetrahedral elements are opted for 3D enclosure as it covers curvatures and irregularities (holes/slots) more efficiently. Element size of 20 mm is selected. Simulation is then performed for car model with three different slant angles of front windshield, i.e., 20°, 25°, and 30° and results are then analyzed.

3.1 Boundary Conditions

In order to get more accurate solutions (i.e., near to experimental) using Fluent, boundary condition inputs need to be more realistic. Following are the values of input parameters fed in Fluent:

Dynamic viscosity (air) = 1.7894×10^{-6} kg-m/s,
Density (air) = 1.246 kg/m^3,
Flow velocity at Inlet = 40 m/s,
Pressure outlet = 0 Pa (gage pressure),
Wall = Stationary No Slip,
Reference area = 0.2446547 m^2, and
Reference density = 1.246 kg/m^3.

Lift and drag coefficients are monitored along with residuals [12].

3.2 Results: Slant Angle 20°

(See Figs. 3, 4, 5, 6).

Fig. 3 CAD model of car with 20° front slant angle
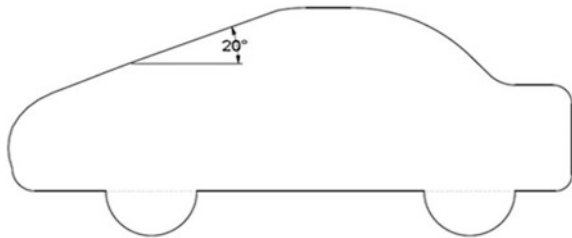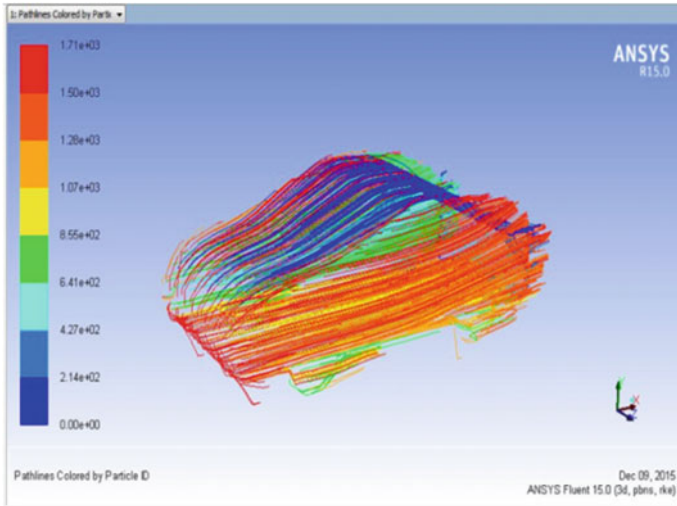
Fig. 4 Contours of particle path lines
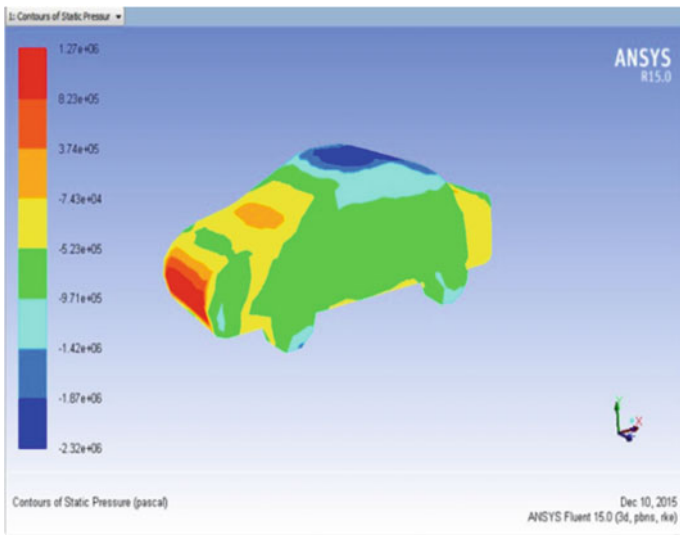
Fig. 5 Contours of static pressure
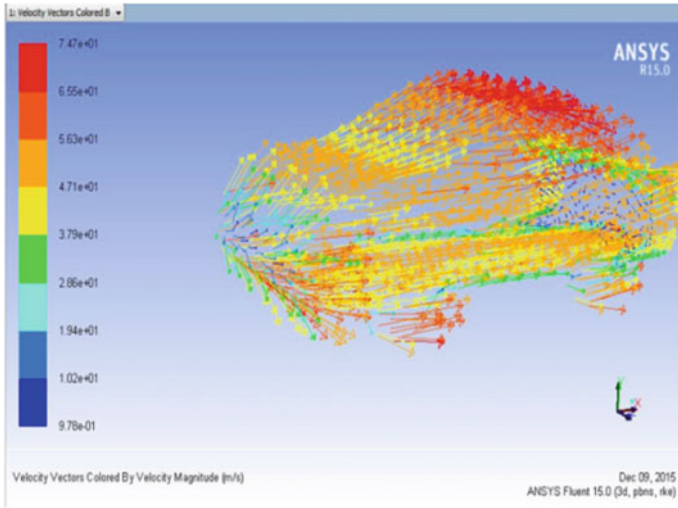
Fig. 6 Contours of velocity vectors

3.3 Results: Slant Angle 25°

(See Figs. 7, 8, 9, 10).
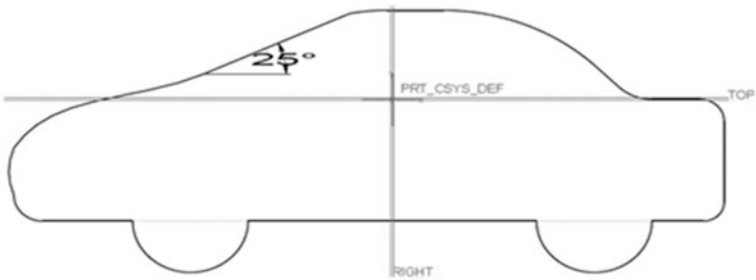
Fig. 7 CAD model of car with 25° front slant angle
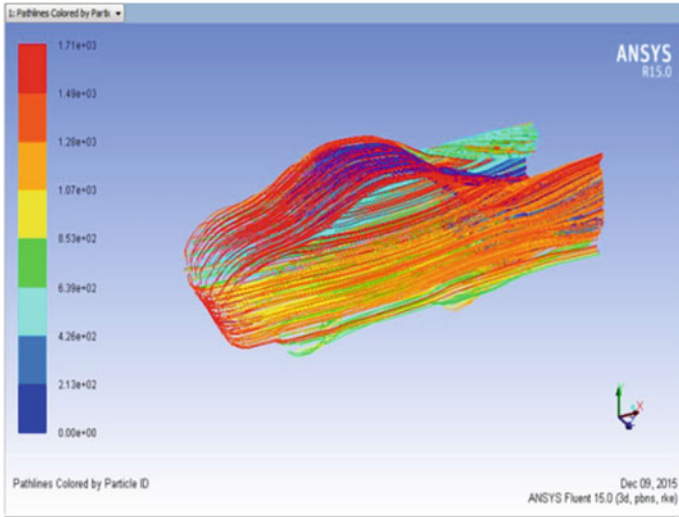
Fig. 8 Contours of particle path lines
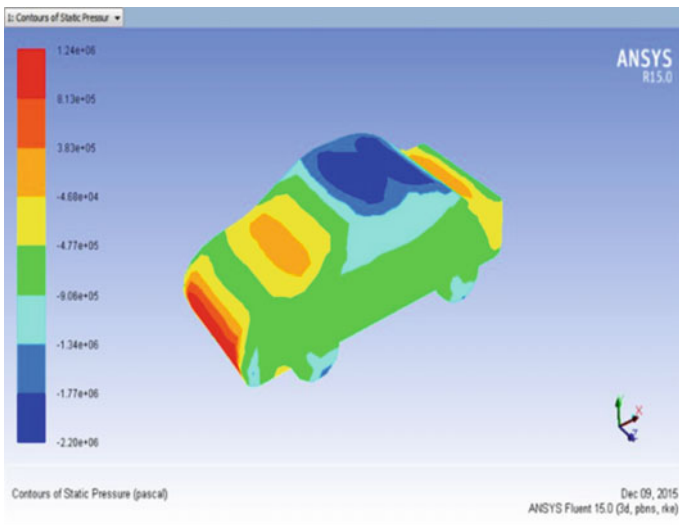
Fig. 9 Contours of static pressure
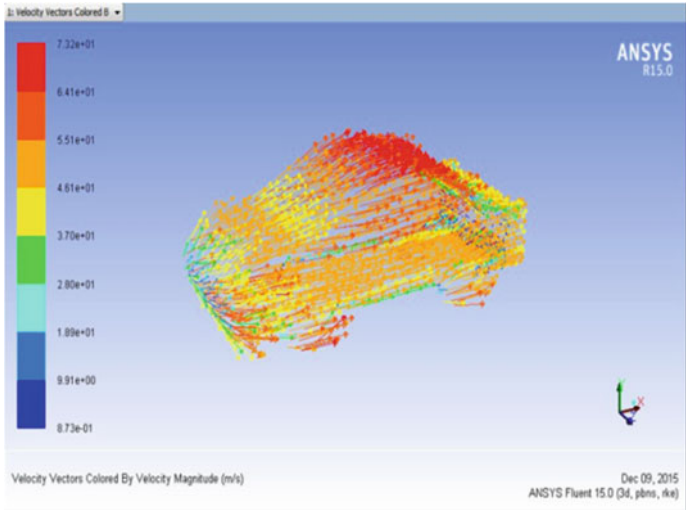
Fig. 10 Contours of velocity vectors

3.4 Results: Slant Angle 30°

(See Figs. 11, 12, 13, 14 and Table 1).
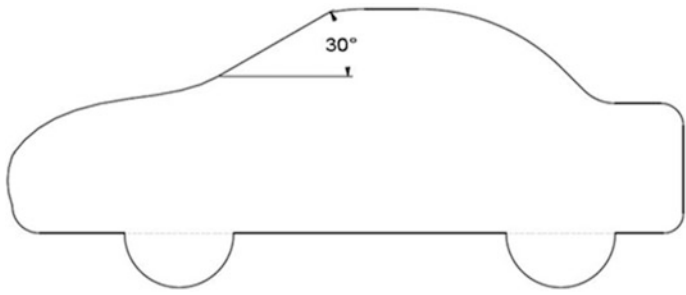
Fig. 11 CAD model of car with 30° front slant angle
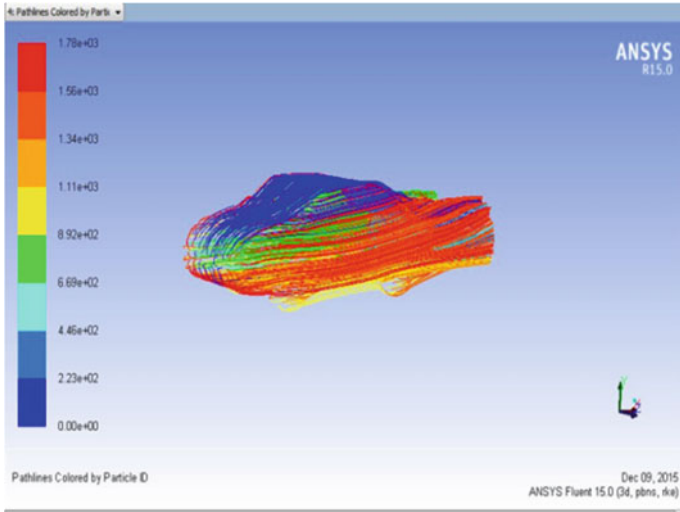
Fig. 12 Contours of particle path lines
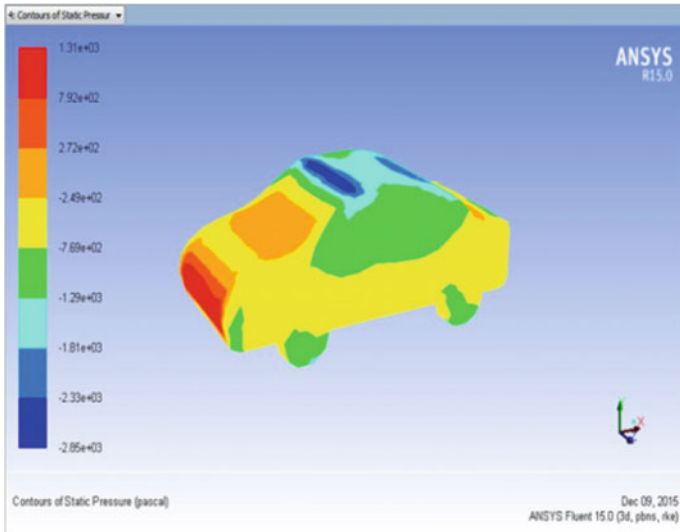
Fig. 13 Contours of static pressure
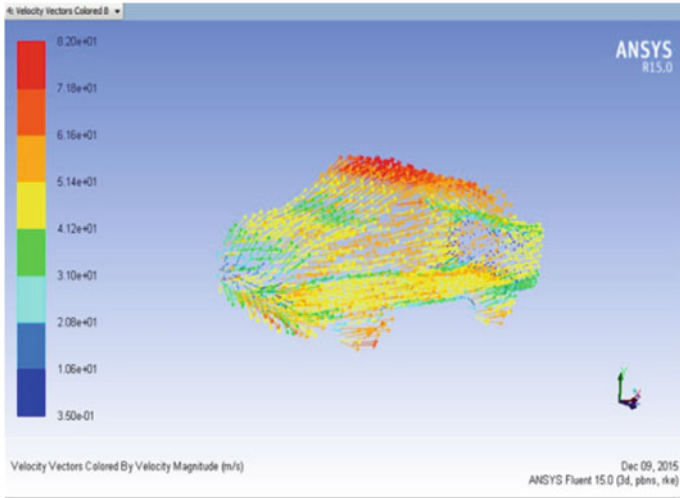
Fig. 14 Contours of velocity vectors

Table 1 Drag and lift coefficients for three different front slant angles

	20° slant	25° slant	30° slant
Coefficient of drag (C_d)	0.1032	0.1011	0.1052
Coefficient of lift (C_l)	0.1025	0.0873	0.0982

Table 2 Aerodynamic characteristics for three different front slant angles

|	20° slant	25° slant	30° slant
Particle path line (max.)	1.71×10^3	1.71×10^3	1.78×10^3
Static pressure (max.)	1.27×10^6	1.24×10^6	1.31×10^3
Velocity vectors (max.)	7.47×10^1	7.32×10^1	8.20×10^1

From the above table, it is clearly observed that

- Minimum drag coefficient (C_d) of 0.1011 is obtained for configuration of car body with 25° front slant angle.
- Minimum positive lift coefficient (C_l) of 0.0873 is obtained for configuration of car body with 25° front slant angle.

From Table 2, it is clearly observed that

- Variation of front shape of the car does not affect particle path line maximum value.
- Particle path line maximum magnitude is approximately the same for all three cases but path line shapes are different, which can be examined from path line contours.
- Due to more slant in the third case, i.e., 30° static pressure value is lower than the other two cases, which shows advantage of using more slant angle.
- One of the main disadvantage of increasing slant angle is that it increases area of static pressure on the front and consequently leads to more drag force value.
- Velocity vectors at the top surface increase with increase in slant angle.

4   Conclusion

In the above study, CFD results for three different slant angles of front windshield are presented. Comparison is done by tabulating different coefficients obtained and optimum rear slant angle is determined, giving minimum drag and lift coefficient. Considering results obtained from simulations, it is inferred that the front design of a vehicle significantly affects airflow pattern around whole vehicle body. Minimum drag coefficient (C_d) and minimum positive lift coefficient (C_l) are obtained for the car body with front slant angle of 25°.

References

1. Piechna J, Rudniak L, Piechna A (2009) CFD analysis of the central engine generic sports car aerodynamics. In: 4th European automotive simulation conference, Munich
2. Doric J, Galambos S (2015) Design and analysis of car body using CFD software. In: 12th international conference on accomplishments in electrical and mechanical engineering and information technology. ResearchGate, Banja Luka, pp 693–696
3. Jang Y (2008) An investigation of higher-order closures in the computation of the flow around a generic car. J Mech Sci Technol, 1019–1029. Springer, Korea
4. Guilmineau E (2007) Computational study of flow around a simplified car body. J Wind Eng Ind Aerodyn 96:1207–1217
5. Banga S, Zunaid M, Ansari N, Sharma S, Dungriyal R (2015) CFD simulation of flow around external vehicle: ahmed body. IOSR J Mech Civ Eng 12:87–94
6. Sharma SK, Kumar A (2017) Ride performance of a high speed rail vehicle using controlled semi active suspension system. Smart Mater Struct 26(5):55026. https://doi.org/10.1088/1361-665X/aa68f7
7. Sharma SK, Kumar A (2018) Disturbance rejection and force-tracking controller of nonlinear lateral vibrations in passenger rail vehicle using magnetorheological fluid damper. J Intell Mater Syst Struct 29(2):279–297. https://doi.org/10.1177/1045389X17721051
8. Sharma SK, Kumar A (2018) Ride comfort of a higher speed rail vehicle using a magnetorheological suspension system. Proc Inst Mech Eng Part K: J Multi-Body Dyn 232(1):32–48. https://doi.org/10.1177/1464419317706873

9. Sharma SK, Kumar A (2016) Dynamics analysis of wheel rail contact using FEA. Procedia Eng 144:1119–1128. https://doi.org/10.1016/j.proeng.2016.05.076
10. COMSOL Multiphysics Pvt. Ltd., Multiphysics CYCLOPEDIA. https://www.comsol.co.in/multiphysics/navier-stokes-equations/
11. Altair University. Practical aspects of finite element simulation—a study guide, pp 65–67 (2015) https://www.training.altairuniversity.com/
12. edX (2017) Drag monitor implementation. A hands-on introduction to engineering simulations. https://www.edx.org/course/a-hands-on-introduction-to-engineering-simulations/

An Isogeometric-Based Study of Mortar Contact Algorithm for Frictionless Sliding

Vishal Agrawal and Sachin S. Gautam

Abstract Apart from the material, geometrical, and boundary non-linearities, the enforcement of the contact constraint in an accurate manner is considered to be a major issue for the numerical simulation of the contact problems. So far, due to the default features of NURBS-based isogeometric analysis (IGA), e.g. ability to represent the exact form of a geometry even with a very coarse mesh, it has been widely utilized for the study of contact problems. For the application of IGA to the contact problem, the mortar contact algorithm has been preferably employed in comparison to the other contact algorithms. As of now, significant efforts have been made and is still continuing to effectively simulate the different class of contact problems varying from small to large deformation through the application of the IGA-based approach. In this contribution, the mortar-based isogeometric contact algorithm is utilized for the numerical simulation of a large deformation frictionless contact problem. For the purpose of validation and to ensure the convergence of presented simulation, second and fourth order of the NURBS basis functions are used for modelling of the considered problem.

Keywords Computational contact mechanics · Isogeometric analysis · NURBS · Mortar method

1 Introduction

Since the introduction of the NURBS-based IGA technique [1], it has drawn the attention of many researchers and has been successfully applied to a wide range of problems such as plate and shells, fluids, fluid–structure interaction, structural vibration, optimization, fatigue and crack and biomedical engineering. The reader

V. Agrawal (✉) · S. S. Gautam (✉)
Indian Institute of Technology Guwahati, Guwahati 781039, India
e-mail: v.agrawal@iitg.ernet.in

S. S. Gautam
e-mail: ssg@iitg.ac.in

referred to the monograph by Cottrell et al. [2] and Agrawal and Gautam [3] for the detailed description of this technique and its implementation procedure within the existing FEA code structure. The application of NURBS-based IGA technique for the treatment of contact problem was first reported by Temizer et al. [4] and Lu [5] in 2011. They applied the NURBS-based IGA technique to the frictionless contact problems. Lu [5] introduced the NURBS-based Isogeometric formulation for the analysis of the two- and three-dimensional frictionless contact problems. In his work, a surface-to-surface-based contact treatment approach, in which contact constraints are enforced directly at the quadrature points of the contact surface and is denoted by Gauss-point-to-surface (GPTS) contact algorithm, has been adopted. Temizer et al. [4] have analysed the thermo-mechanical, frictionless two- and three-dimensional contact problems using the NURBS-based isogeometric formulation. From the analysis of various finite deformation contact problems, it has been found that the results obtained with the GPTS contact algorithm are qualitatively satisfactory. However, based on the quantitative examination of the classical Hertz contact problem, it has been found that the GPTS approach yields over-constraint contact formulation which leads to non-physical oscillations of the contact tractions. Moreover, it has been shown that the magnitude of the oscillations further increases on increasing the value of penalty parameter. In order to relax the over-constraining, a mortar contact algorithm, in which contact constraints are enforced in a weak sense at the control points, has been presented. With this, stable and superior quality results are obtained even for large value of penalty parameter in comparison to GPTS contact algorithm.

Later, the mortar contact algorithm by Temizer et al. [4] has been extended by Lorenzis et al. [6] for the simulation of large deformation frictional two-dimensional contact problems. In their work, Lorenzis et al. [6] have found that the non-physical oscillation, which has been obtained with GPTS contact formulation [4], becomes significant for the frictional Hertz contact problem. While the proposed mortar contact algorithm within the context of NURBS-based IGA delivers the considerably improved results in comparison to GPTS or its counterpart mortar-based standard finite element formulation. The distribution of the contact pressure improves monotonically on increasing the mesh resolution, which is not a case with the standard FE-based mortar contact formulation. Based on these noted features of mortar-based isogeometric formulation of contact problems, this technique has been extensively applied for the isogeometric-based simulation of wide range of the contact problems, e.g. for the three-dimensional large deformation frictionless contact problem [7], three-dimensional finite deformation frictional problem [8], for the analysis of two-dimensional frictionless linearly elastic contact problems [9]. A review paper that thoroughly covers the available isogeometric-based treatment procedures for various contact problems has been presented by Lorenzis et al. [10]. Based on the literature survey, it has been found that a significant amount of research efforts have been made and is still continuing for the numerical simulations of various contact problems using the mortar-based IGA formulation. In this contribution, a two-dimensional, quasi-static, frictionless, two bodies deformable ironing problem is numerically simulated using the mortar-based isogeometric formulation.

To the best of author's knowledge, no such analysis is available in the literature. A penalty-based approach is employed for the enforcement of contact constraint. For the purpose of numerical simulation, an in-house code incorporating the NURBS toolbox presented in [11] is developed.

The remainder of the paper is organized as follows. In Sect. 2, the mortar-based isogeometric formulation of the contact problem using the penalty method is briefly described. After that in Sect. 3, the numerical simulation of the considered problem along with the results and necessary discussion are provided. Finally, in Sect. 4, the conclusion and the scope of the future work are presented.

2 Formulation

In this section, a mortar-based isogeometric formulation, presented by Lorenzis et al. [6], for two-dimensional frictionless contact between two elastic bodies undergoing large deformation is briefly described. In order to distinguish the two bodies one is denoted as the slave, $\mathcal{B}^s$, and the other as the master, $\mathcal{B}^m$. The relation between the initial configuration of bodies $\mathbf{X}^k$, where the superscript $k = \{s, m\}$ denotes the slave and master bodies, the displacement field $\mathbf{u}^k$ and the current configuration of a $\mathbf{x}^k$ point of a body is given by $\mathbf{x}^k = \mathbf{X}^k + \mathbf{u}^k$. When both bodies are in contact, the contribution of the contact tractions to the virtual work is expressed as [12]

$$\delta W_c = \int_{\Gamma_{0c}^s} t_{\mathrm{N}} \delta g_{\mathrm{N}} \, \mathrm{d}\Gamma \tag{1}$$

and the linearization of the virtual work is given by [12]

$$\Delta \delta W_c = \int_{\Gamma_{0c}^s} \left(\Delta t_{\mathrm{N}} \delta g_{\mathrm{N}} + t_{\mathrm{N}} \Delta \delta g_{\mathrm{N}} \right) \mathrm{d}\Gamma \tag{2}$$

where $g_{\mathrm{N}} = (\mathbf{x}^s - \bar{\mathbf{x}}^m) \cdot \mathbf{n}$ denotes the normal gap between a given point $\mathbf{x}^s$ on the contact surface of the slave body Γ_{0c}^s and a projection point $\bar{\mathbf{x}}^m$ on the contact surface of the master body Γ_c^m. The penalty regularized normal traction is given by $t_{\mathrm{N}} = \epsilon_{\mathrm{N}} \langle g_{\mathrm{N}} \rangle$. The reader referred to the monographs by Laursen [13] and Wriggers [12] for more details.

In case of the NURBS-based discretization of the contacting bodies, the parameterization for the contact surface is directly inherited from the parametrization of the bulk of the domain. Based on the isoparametric concept,

displacement field $\mathbf{u}$, its variation $\delta\mathbf{u}$ and the coordinates of the discretized form of the contact surface within its current configuration $\mathbf{x}^e$ are given by [2, 14]

$$\mathbf{u}^e = \sum_{l=1}^{n_{cpe}} R_l\mathbf{u}_l, \quad \delta\mathbf{u}^e = \sum_{l=1}^{n_{cpe}} R_l\delta\mathbf{u}_l, \text{ and } \mathbf{x}^e = \sum_{l=1}^{n_{cpe}} R_l\mathbf{x}_l \tag{3}$$

where $n_{cpe} = 1+p$ denotes the number of control points having support within the element 'e'. The above-described parametrization will be used for the contact surface of slave and master bodies by adding the appropriate superscript s or m, respectively, in the following discussion.

For the case of mortar-based contact formulation, the contact constraints are enforced in a weak sense at the control points and the weak form, shown in Eq. (1), translates to the following form [6]:

$$\delta W_c = \sum_A^{n_{cp}^s} (p_{N_A}\delta g_{N_A})A_A \tag{4}$$

where n_{cp}^s denotes the total number of control points across the slave contact surface and the normal gap evaluated at the control point is given by $g_{N_A} = \frac{1}{A_A}\int_{\Gamma_{0c}^s} R_A g_N \, d\Gamma$. The normal contact pressure is defined as $p_{N_{int}} = \epsilon_N \sum_A^{n_{cp}^s} g_{N_A} R_A$ and $A_A = \int_{\Gamma_{0c}^s} R_A \, d\Gamma$ represents the area of competence for a control point. Based on the discretization shown in Eq. (3), the virtual work done by contact traction, Eq. (4), can be cast into the following matrix form [6, 12]:

$$\delta W_c = \delta\mathbf{u}^T \int_{\Gamma_{0c}^s} p_{N_{int}}\mathbf{N} \, d\Gamma = \delta\mathbf{u}^T\mathbf{R}_c \tag{5}$$

where $\mathbf{N}$ is the NURBS basis functions matrix and $\mathbf{R}_c$ is the expression for the contact force vector. Using the Gauss–Legendre quadrature rule

$$\mathbf{R}_c = \sum_g^{n_{gp}^s} p_{N_{intg}}\mathbf{N}_g J_g w_g \tag{6}$$

where n_{gp}^s denotes the total number of Gauss points used for the integration of above equation, J_g is the determinant of Jacobian matrix and w_g is the weight

associated to Gauss point g. In order to obtain the consistent tangent stiffness matrix a full linearization of the virtual work expression is carried out. It yields [6, 12]

$$\Delta\delta W_c = \int_{\Gamma^s_{0c}} \left(\Delta p_{N_{int}}\delta g_N + p_{N_{int}}\Delta\delta g_N \right) \mathbf{d}\Gamma \tag{7}$$

$$\Delta\delta W_c = \sum_A^{n^s_{cp}} \left(\frac{\epsilon_N}{A_A} \int_{\Gamma^s_{0c}} R_A\delta g_N \, \mathrm{d}\Gamma \int_{\Gamma^s_{0c}} R_A\Delta g_N \, \mathrm{d}\Gamma \right) + \int_{\Gamma^s_{0c}} \epsilon_N \left(\sum_A^{n^s_{cp}} R_A g_{N_A} \right) \Delta\delta g_N \, \mathrm{d}\Gamma \tag{8}$$

From the above equation, the expression for the consistent contact tangent stiffness matrix is obtained as [6]

$$\mathbf{K}_c = \sum_A^{n^s_{cp}} \left[\frac{\epsilon_N}{A_A} \int_{\Gamma^s_{0c}} R_A\mathbf{N} \, \mathrm{d}\Gamma \int_{\Gamma^s_{0c}} R_A\mathbf{N}^T \, \mathrm{d}\Gamma \right] + \\ \int_{\Gamma^s_{0c}} \left[\epsilon_N p_{N_{int}} \left(-g_N m_{11}\bar{\mathbf{N}}_1\bar{\mathbf{N}}_1^T - \mathbf{D}_1\mathbf{N}_1^T - \mathbf{N}_1\mathbf{D}_1^T + k_{11}\mathbf{D}_1\mathbf{D}_1^T \right) \right] \mathrm{d}\Gamma \tag{9}$$

Using the Gauss–Legendre rule, the contact tangent stiffness matrix is numerically computed as

$$\mathbf{K}_c = \sum_A^{n^s_{cp}} \left[\frac{\epsilon_N}{\sum\limits_g^{n^s_{gp}} R_{A_g} J_g w_g} \sum_g^{n^s_{gp}} R_{A_g}\mathbf{N} J_g w_g \sum_g^{n^s_{gp}} R_{A_g}\mathbf{N}_g^T J_g w_g \right] + \\ \sum_g^{n^s_{gp}} \left[\epsilon_N p_{N_{int_g}} \left(-g_{N_g} m_{11_g}\bar{\mathbf{N}}_{1_g}\bar{\mathbf{N}}_{1_g}^T - \mathbf{D}_{1_g}\mathbf{N}_{1_g}^T - \mathbf{N}_{1_g}\mathbf{D}_{1_g}^T + k_{11_g}\mathbf{D}_{1_g}\mathbf{D}_{1_g}^T \right) \right] J_g w_g \tag{10}$$

3 Result and Discussion

For the simulation of a large deformation contact problem using the NURBS-based IGA technique, a frictionless version of the problem presented in [6] is considered. The set-up of the problem in the undeformed configuration is shown in Fig. 1. This problem is analysed in two steps. In the first, a cylindrical die is pushed against the elastic block. After that, in the second step, it is moved along the tangential direction. For this, the vertical and horizontal displacements, $U_y = -0.075$ mm and $U_x = 2.0$ mm in 10 and 140 time steps, respectively, are applied at the top boundary line of the die during the two analysis steps. For the modelling of cylindrical die, a hyper-elastic material with $E = 1000$ GPa and $v = 0.3$ under the plane strain conditions are used. The block is also modelled with same material and conditions except with $E = 1$ GPa and $v = 0.3$. It is considered that the control

points at the bottom surface of the block is fixed along the x and y directions. For the overall numerical simulation of this problem, 48×8 and 48×24 mesh resolution for the cylindrical die and the block, is used, respectively. For the enforcement of contact constraints, the penalty parameter is $\epsilon_N = 100$. The deformed configuration of the bodies after the application of vertical and after that, horizontal displacement for second-order NURBS discretization is shown in Fig. 2a and b, respectively. At the end of each displacement step, the resultant normal and tangential contact reaction forces are accounted and the resultant plot for the overall simulation of this problem is shown in Fig. 3. Theoretically, due to the absence of friction, the normal contact reaction force remains constant during the second stage of analysis. Moreover, no tangential force act on the bodies and its contribution remains zero throughout the analysis. These theoretical results of the contact
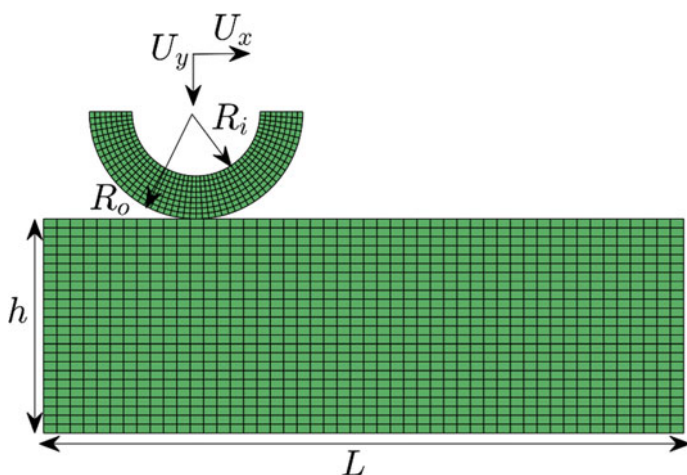
Fig. 1 The set-up of the undeformed geometrical configuration of the frictionless ironing problem for displacement step $t = 0$
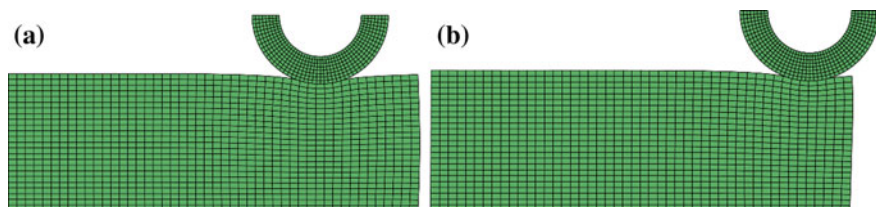
Fig. 2 The deformed configuration of the problem after **a** first analysis step at displacement step $t = 10$ and **b** second analysis step at displacement step $t = 150$
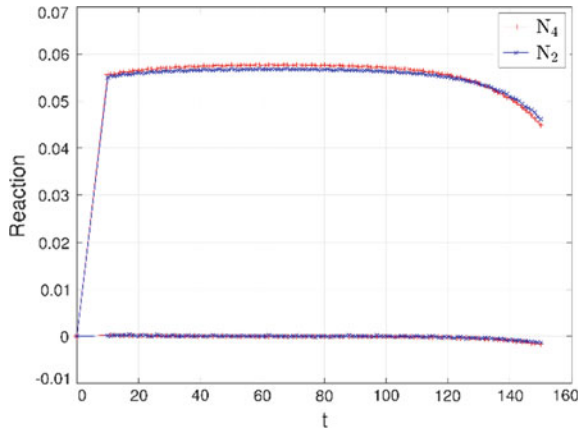
Fig. 3 The resultant normal and tangential contact reaction forces for the overall simulation process
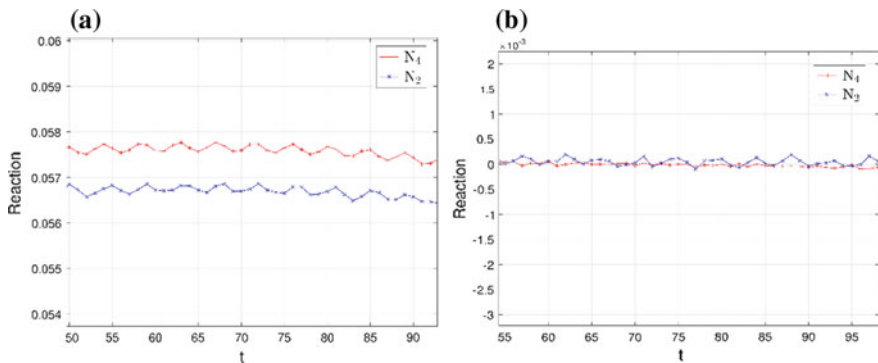
Fig. 4 Zoomed view of the variation of **a** normal contact reaction force and **b** tangential contact reaction force shown in Fig. 3

tractions are used as a reference. In order to ensure the validity and convergence of the numerical simulation, the fourth-order NURBS basis functions have also been used to describe the bulk of the die and block bodies. The resultant curve for the normal and tangential contact reaction forces is also included in Fig. 3. In Fig. 4, the zoomed view of the variation of the normal and tangential reaction forces for the second and the fourth order of NURBS discretization are also shown. From Figs. 3 and 4, it can be observed that on increasing the order of NURBS basis functions, the evaluated result converges towards the theoretical solution.

4   Conclusion

Based on the numerical simulation of large deformation frictionless ironing problem, it is found that the presented NURBS-based IGA formulation using the mortar contact algorithm matches well with the theoretical solution for this problem. Moreover, the amplitude of oscillations is reduced on discretizing the bulk of bodies with fourth-order NURBS functions. This ensures the validation as well as the convergence of the implementation. However, for the considered mesh resolution and discretization, artificial oscillations are present which are needed to be eliminated. For this purpose, the future objective is to utilize the enhanced formulation to improve the accuracy and efficiency of the numerical result in comparison to present formulation.

References

1. Hughes TJR, Cottrell JA, Bazilevs Y (2005) Isogeometric analysis: CAD, finite elements, NURBS, exact geometry and mesh refinement. Comput Methods Appl Mech Eng 194(39–41):4135–4195
2. Cottrell JA, Hughes TJR, Bazilevs Y (2009) Isogeometric analysis: toward integration of CAD and FEA. Wiley
3. Agrawal V, Gautam SS (2018) IGA: A simplified introduction and implementation details for finite element users. J Inst Eng (India) Ser C. https://doi.org/10.1007/s40032-018-0462-6
4. Temizer I, Wriggers P, Hughes TJR (2011) Contact treatment in Isogeometric analysis with NURBS. Comput Methods Appl Mech Eng 200(9–12):1100–1112
5. Lu J (2011) Isogeometric contact analysis: geometric basis and formulation for frictionless contact. Comput Methods Appl Mech Eng 200(5–8):726–741
6. De Lorenzis L, Temizer I, Wriggers P, Zavarise G (2011) A large deformation frictional contact formulation using NURBS–based isogeometric analysis. Int J Numer Meth Eng 87 (13):1278–1300
7. De Lorenzis L, Wriggers P, Zavarise G (2012) A mortar formulation for 3D large deformation contact using NURBS–based isogeometric analysis and the augmented Lagrangian method. Comput Mech 48(1):1–20
8. Temizer I, Wriggers P, Hughes TJR (2012) Three–dimensional mortar– based frictional contact treatment in Isogeometric analysis with NURBS. Comput Methods Appl Mech Eng 209–212:115–128
9. Kim JY, Youn SK (2012) Isogeometric contact analysis using mortar method. Int J Numer Meth Eng 89(12):1559–1581
10. De Lorenzis L, Wriggers P, Hughes TJR (2014) Isogeometric contact: a review. 37(1):85–123
11. De Falco C, Reali A, Vãzquez R (2011) GeoPDEs: a research tool for isogeometric analysis of PDEs. Adv Eng Softw 42(12):1020–1034
12. Wriggers P (2006) Computational contact mechanics, 2nd edn. Springer, New York
13. Laursen TA (2003) Computational contact and impact mechanics: fundamentals of modeling interfacial phenomena in nonlinear finite element analysis. Springer
14. Piegl L, Tiller W (2012) The NURBS book (Monographs in Visual Communication). Springer

Optimization Design for Aerodynamic Elements of Indian Locomotive of Passenger Train

Bhargav Goswami, Anmol Rathi, Sharf Sayeed, Pulakesh Das,
Rakesh Chandmal Sharma and Sunil Kumar Sharma

Abstract The objective of this paper is to optimize the WAP-5 Indian locomotive with the help of a multi-objective optimization technique so as to steady the plural aerodynamic factors. An evolutionary algorithm along with shape parameterization method, which makes use of B-spline curves and Coons patches and also a computational simulation, which makes use of a message-passing interface that are involved in this multi-objective design optimization method. For determining the efficiency of this technique, we design a train head which has optimized aerodynamic drag and aerodynamic forces in relation to affecting other trains. Reasonable Pareto results were obtained with the help of a 10th generation evolutionary algorithm.

Keywords Aerodynamic · Locomotive nose shape · Optimization · CFD

1 Introduction

While optimizing the head shape of the locomotive, various aspects have to be considered, and some of them are manufacturing price, aerodynamic properties, mechanical structures, and ease with which the maintenance will be done. Of all these, the most important factor for a WAP-5 is its aerodynamic properties, for which factors such as aerodynamic drag, car vibrations induced due to flow, crosswind response, and aerodynamic forces affecting the other trains and trackside structures must be taken into consideration [1–9]. The aerodynamic drag is calculated using wind tunnel and CFD analysis [10–13]. For minimizing the drag force, a guiding principle is being used. As mentioned above, so many researches

B. Goswami · A. Rathi · S. Sayeed · P. Das · S. K. Sharma (✉)
Department of Mechanical Engineering, Amity School of Engineering and Technology,
Amity University Uttar Pradesh, Noida, Uttar Pradesh, India
e-mail: sunilsharmaiitr@gmail.com

R. C. Sharma
Maharishi Markandeshwar (Deemed to be University), Mullana, Ambala 133207, India

have been done just to improve aerodynamic properties of a WAP-5 Indian loco-motive [14–19]. Regardless of how, it is very difficult to meet the necessities of multiple aerodynamic properties at the same time. Multi-objective optimization has been widely used in aerospace and aeronautical engineering to design an aircraft [20–30]. However, this method is not much used in the field of railways. Despite the fact that the idea of multi-objective optimization for a magnetic elevated vehicle, but they only studied an optimum two-dimension nose shape. So, in this study, a multi-objective optimization method is developed for the three-dimensional shape of a train with the aim of supporting the train design process.

2 Methodology

2.1 Outline of the Method

The following figure describes the process of multi-objective optimization. At first, the random generation of initial train shapes. Then, the calculation of aerodynamic
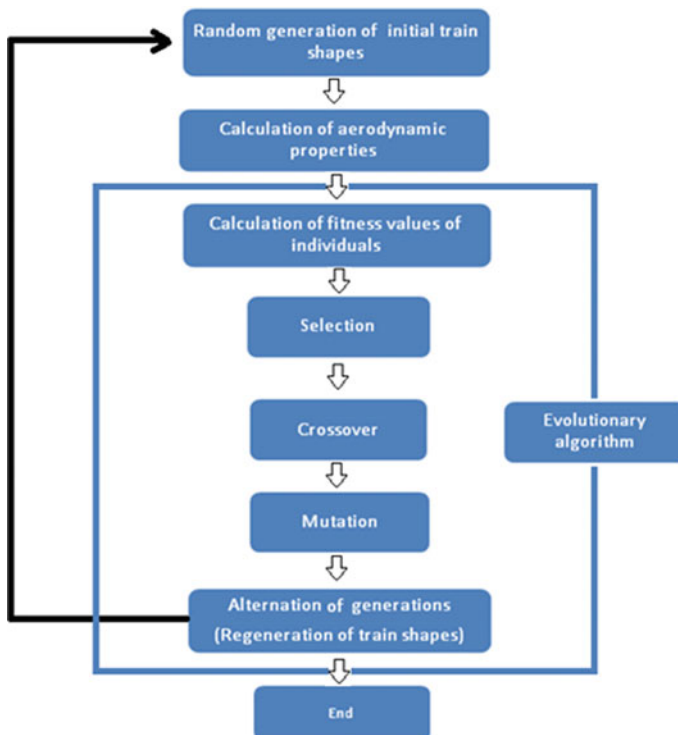
Fig. 1 Flowchart of the proposed method

properties is carried out. Before recurring to the flow simulation phase, new feasible design constraints are recognized with the help of using an evolutionary algorithm. The cycle will keep on repeating until and unless the objective is achieved (Fig. 1).

2.2 Train Shape Definition

The important technique of optimization is the shape parameterization, and some parameters are required for higher degree of flexibility in representing shapes. In this, B-spline curves first define the cross section shapes, which are mostly used for airfoil designs. Next, the bilinear Coons patches are used for determining the surface between the cross section shapes. In this, the B-spline curve of third order with multiple points to define the cross section shape. The "d" as a distance of a concern points, V_1 and V_2 set to be constant, to reduce the computational cost and the curvature of corners should be the same. Equation A is defined as cross-sectional area in Eq. 1. [20]:

$$\frac{A(x)}{\pi b^2} = (1 - \alpha_2)\left[(1 - \alpha_1)\frac{x}{a} + \alpha_1\sqrt{\frac{x}{a}}\right] + \alpha_2\left(\frac{x}{a}\right)^2. \tag{1}$$

where x = front end distance; a = train nose length, πb^2 = maximum part of the nose area, which is said to be 11 m^2. α_1 1 = 4.18 and α_2 = 0.75 are design variable, where a/b = 5 (Figs. 2 and 3).

2.3 Multi-objective Evolution Algorithm

At constant condition, the objective function lies between maximizing or minimizing value. It is said to be multi-objective optimization problem. It is a Pareto-optimal solution rather than a unique solution [20], and it denotes the

Fig. 2 Representation of train nose shape
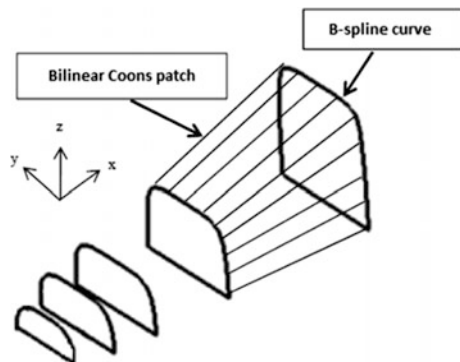
Fig. 3 Definition of cross
section by third-order
B-spline curve
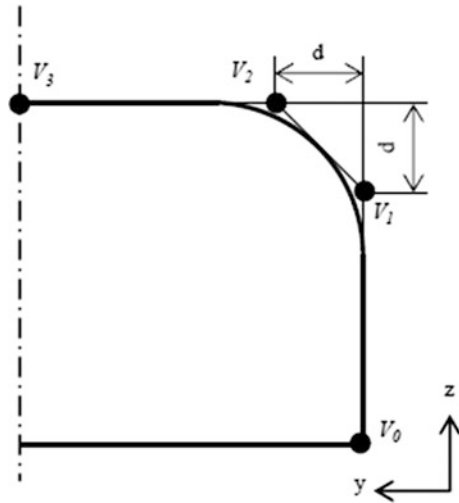
Fig. 4 Pareto solution
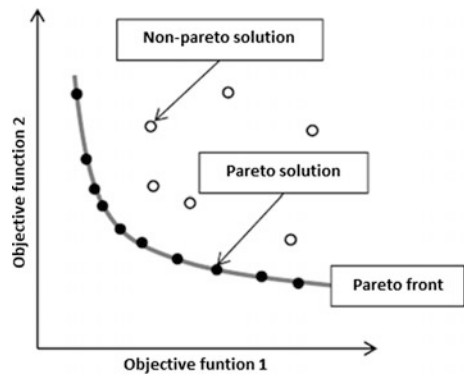
competing objectives of a trade-off information. The optimization procedure is
divided into two groups: stochastic ones and deterministic methods. When the
deterministic method struck with local optima having a number of peaks in a
maximum value of the function is said to be stochastic method. In the deterministic
method, the objective function has a single peak. Mostly, in the problems of
aerodynamic, it has stochastic methods [20]. Stochastic Universal Sampling
(SUS) is applied to stop diversity loss of population (Fig. 5). In this study, the
numbers of indicators are two (Fig. 4).

The value of fitness after modification is as follows (2):

$$f_i' = f_i / \sum_{j=1}^{N} s(d_i, j) \tag{2}$$
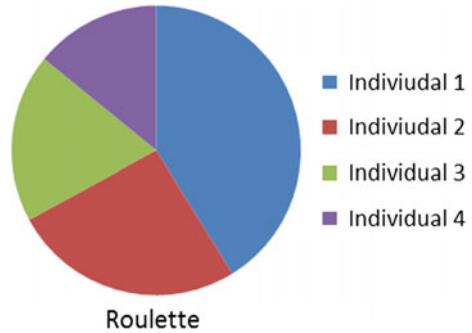
where N = populations size, s = function of the population density (3).

$$s(d_i,j) = \begin{cases} 1 \\ 0 \end{cases} - \left(\frac{d_i,j}{\sigma_{share}} \right)^x \cdot \begin{array}{l} d_i,j < \sigma_{share} \\ d_i,j \geq \sigma_{share} \end{array} \tag{3}$$

where d_i, j = Euclidean distance between i and j of the function. x = 0.25; σ_{share} = is the value which controls the increase and decrease of the optimal value relative with the population density. Solving the following value (4)

$$N\sigma_{share}^{q-1} - \frac{\prod_{i=1}^{q-1}(M_i - m_i + \sigma_{share}) - \prod_{i=1}^{q}(M_i - m_i)}{\sigma_{share}} = 0. \tag{4}$$

where M_i and m_i is the maximum and minimum number of objective function. q = number of objective function. As the two equation becomes (5),

$$(N - 1)\sigma_{share}^2 - (M_1 + M_2 - m_1 - m_2)\sigma_{share} - 2(M_1 - m_2)(M_2 - m_2) = 0 \tag{5}$$

Crossover: Crossover means the exchange of genes between some individuals who are selected. In our case, here the design parameters are the genes. BLX-α technique have an area which is wide for exploring, and generally is used to combine the design parameters or genes of the two parents [31–41].

$$x_{child1} = \gamma \cdot x_{parent1} + (1 - \gamma) \cdot x_{parent2}.$$

$$x_{child} = (1 - \gamma) \cdot x_{parent1} + \gamma \cdot x_{parent2}.$$

where x_{child1} = design parameter of children; x_{child2} = design parameter of children, $x_{parent1}$ = design parameter of parents; $x_{parent2}$ = design parameter of parents

$$\gamma = (1 + 2\alpha)u - \alpha$$

where u = uniform random variable $(0 < u < 1)$. As per α, the parameters of design for the child is set to be exterior and in middle of the parameters of design of the parents in a stochastic manner $\alpha = 0.5$.

2.4 Objective Functions and Numerical Solution

Two aerodynamic properties are used in this study as objective functions: aerodynamic drag on the nose of the locomotive and pressure variation around the locomotive, which influences aerodynamic forces affecting other locomotives and trackside structures [42–47]. First, a surface grid generation method is used, which is based on the unstructured grid to create a surface grid on the surface. The length of the grid is 2.5 times the length of the locomotive. The whole grid has a total of 17,7500 nodes with 95,0000 elements approximately. Figure 6 shows an example of the grid system. The pressure drag acting from the upper edge to the tip of the nose section is used to evaluate the aerodynamic drag on the nose. The maximum and minimum pressures along a line on the side of an oncoming train (absent in computation) is used to estimate the pressure variation around the locomotive (Fig. 7).

Fig. 6 An example of grid system
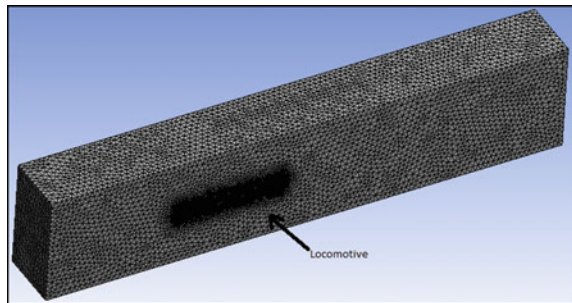
Fig. 7 Sampling location of pressure variation
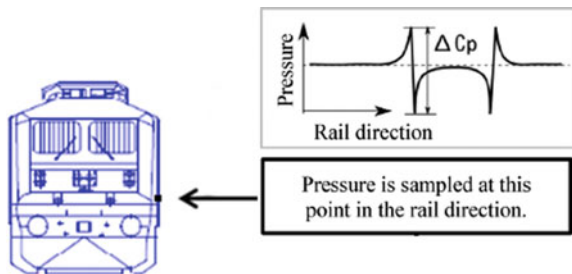
3   Result and Discussion

The feasibility of this method is shown by optimizing the WAP-5 locomotive shape using the two objective functions described above. The evolutionary calculation was done, until the 10th generation with 520 individuals. The computation was done on ANSYS fluent and the approximate computational time required for each generation was 3 h. The objective value distribution for each generation is shown in Fig. 8. Pareto-optimal solutions and examples of their train shape are shown in Fig. 9.

A total of 110 Pareto-optimal solutions were found. The locomotive with minimum pressure variation along the body has a shape, which gradually expands in sideways and upwards directions with a shorter nose length. A comparison between the simulated aerodynamic properties of the real WAP-5 locomotive and the Pareto-optimal solutions are shown in Fig. 10.
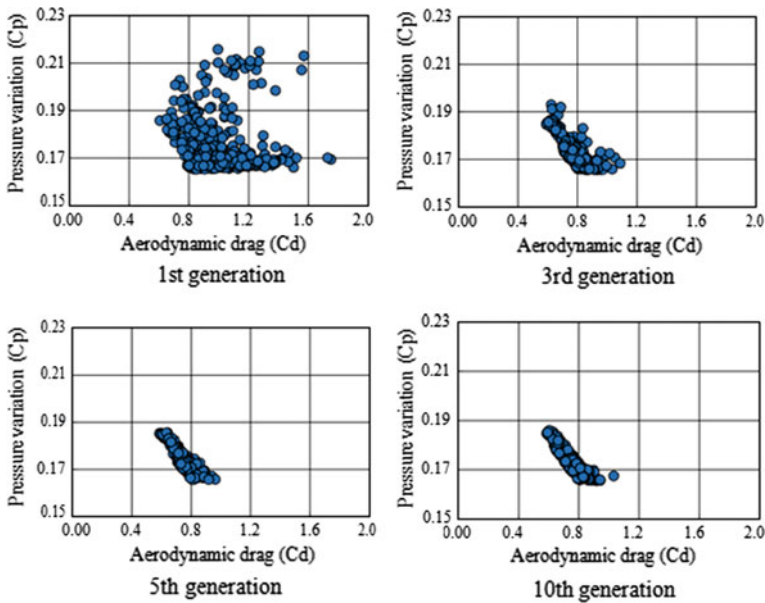
Fig. 8   Objective value distribution at each generation
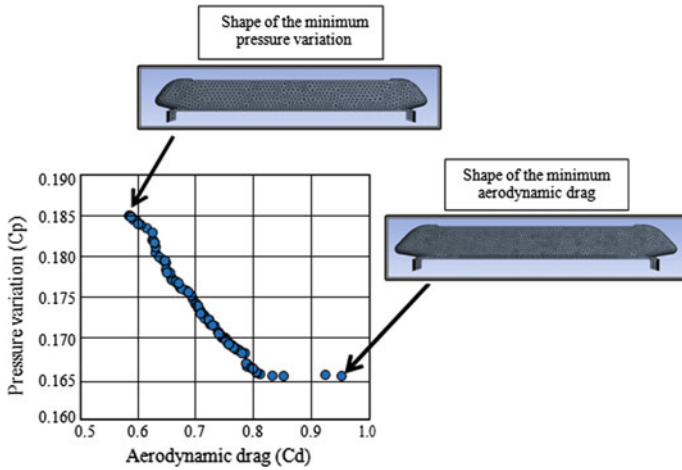
Fig. 9 Pareto solutions and examples of nose shapes
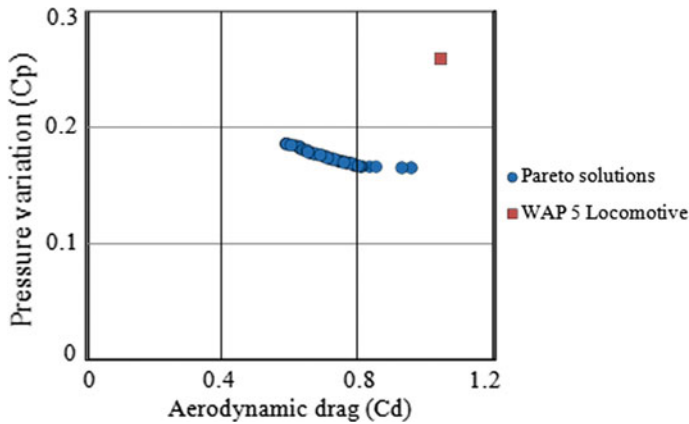
Fig. 10 Comparison of aerodynamic properties between present results and original WAP-5 locomotive

4   Conclusion

Optimization of the nose shape of WAP-5 locomotive to meet requirements for aerodynamic properties using a numerical flow simulation and an evolutionary algorithm was done. Its feasibility was demonstrated with the help of two objective functions, pressure variation along the body and aerodynamic drag. Optimization was done for a relatively simple locomotive shape using the two objective functions

in this study. More objective functions can be employed for more practical shapes and in the future study, this method can be applied for the design process of actual locomotives also.

References

1. Kumar R, Garg MP, Sharma RC (2012) Vibration analysis of radial drilling machine structure using finite element method. Adv Mater Res 472:2717–2721
2. Palli S, Koona R, Sharma RC, Muddada V (2015) Dynamic analysis of indian railway integral coach factory bogie. Int J Veh Struct Syst 7(1):16–20. https://doi.org/10.4273/ijvss.7.1.03
3. Sharma RC (2011) Ride analysis of an Indian railway coach using Lagrangian dynamics. Int J Veh Struct Syst 3(4):219–224. https://doi.org/10.4273/ijvss.3.4.02
4. Sharma RC (2012) Recent advances in railway vehicle dynamics. Int J Veh Struct Syst 4 (2):52–63. https://doi.org/10.4273/ijvss.4.2.04
5. Sharma RC (2013) Sensitivity analysis of ride behaviour of Indian railway Rajdhani coach using Lagrangian dynamics. Int J Veh Struct Syst 5(3–4):84–89
6. Sharma RC (2013) Stability and eigenvalue analysis of an Indian railway general sleeper coach using Lagrangian dynamics. Int J Veh Struct Syst 5(1):9–14
7. Sharma RC (2016) Evaluation of passenger ride comfort of Indian rail and road vehicles with ISO 2631-1 standards: Part 1—mathematical modeling. Int J Veh Struct Syst 8(1):1–6
8. Sharma RC (2016) Evaluation of passenger ride comfort of Indian rail and road vehicles with ISO 2631-1 standards: Part 2—simulation. Int J Veh Struct Syst 8(1):7–10
9. Sharma RC, Palli S (2016) Analysis of creep force and its sensitivity on stability and vertical-lateral ride for railway vehicle. Int J Veh Noise Vib 12(1):60–76
10. Sharma RC, Palli S, Koona R (2017) Stress and vibrational analysis of an Indian railway RCF bogie. Int J Veh Struct Syst 9(5):296–302
11. Sharma SK, Sharma RC, Kumar A, Palli S (2015) Challenges in rail vehicle-track modeling and simulation. Int J Veh Struct Syst 7(1):1–9
12. Sharma SK, Kumar A (2016) Dynamics analysis of wheel rail contact using FEA. Procedia Eng 144:1119–1128. https://doi.org/10.1016/j.proeng.2016.05.076
13. Sharma RC, Palli S, Sharma SK, Roy M (2017) Modernization of railway track with composite sleepers. Int J Veh Struct Syst 9(5):321–329
14. Sharma SK, Kumar A (2017) Impact of electric locomotive traction of the passenger vehicle ride quality in longitudinal train dynamics in the context of Indian railways. Mech Ind 18 (2):222. https://doi.org/10.1051/meca/2016047
15. Sharma SK, Kumar A (2017) Ride performance of a high speed rail vehicle using controlled semi active suspension system. Smart Mater Struct 26(5):55026. https://doi.org/10.1088/1361-665X/aa68f7
16. Sharma SK, Kumar A (2018) Ride comfort of a higher speed rail vehicle using a magnetorheological suspension system. Proc Inst Mech Eng Part K J Multi-Body Dyn 232 (1):32–48. https://doi.org/10.1177/1464419317706873
17. Sharma SK, Kumar A (2018) Disturbance rejection and force-tracking controller of nonlinear lateral vibrations in passenger rail vehicle using magnetorheological fluid damper. J Intell Mater Syst Struct 29(2):279–297. https://doi.org/10.1177/1045389X17721051
18. Palli S, Koona R, Sharma SK, Sharma RC (2018) A review on dynamic analysis of rail vehicle coach. Int J Veh Struct Syst 10(3):204–211
19. Sharma RC, Sharma SK, Palli S (2018) Rail vehicle modeling and simulation using Lagrangian method. Int J Veh Struct Syst 10(3):188–194
20. Sharma SK, Sharma RC (2018) Simulation of quarter-car model with magnetorheological dampers for ride quality improvement. Int J Veh Struct Syst 10(3):169–173

21. Sharma SK, Kumar A (2016) The impact of a rigid-flexible system on the ride quality of passenger bogies using a flexible carbody. In: Pombo J (ed) Proceedings of the third international conference on railway technology: research development and maintenance stirlingshire UK 5–8 April 2016, Cagliari, Sardinia, Italy. Civil-Comp Press, Stirlingshire UK, p 87. https://doi.org/10.4203/ccp.110.87

22. Sharma SK, Chaturvedi S (2016) Jerk analysis in rail vehicle dynamics. Perspect Sci 8:648–650. https://doi.org/10.1016/j.pisc.2016.06.047

23. Sharma SK, Kumar A (2014) A comparative study of Indian and worldwide railways. Int J Mech Eng Robot Res 1(1):114–120

24. Sharma SK (2013) Zero energy building envelope components: a review. Int J Eng Res Appl 3(2):662–675

25. Kumar P, Kumar A, Racic V, Erlicher S (2018) Modelling vertical human walking forces using self-sustained oscillator. Mech Syst Signal Process 99:345–363

26. Kumar P, Kumar A, Erlicher S (2018) A nonlinear oscillator model to generate lateral walking force on a rigid flat surface. Int J Struct Stab Dyn 18(2):1850020

27. Kumar P, Kumar A (2016) Modelling of lateral human walking force by self-sustained oscillator. Procedia Eng 144:945–952

28. Kumar P, Kumar A, Erlicher S (2017) A modified hybrid Van der Pol-Duffing-Rayleigh oscillator for modelling the lateral walking force on a rigid floor. Phys D Nonlinear Phenom 358:1–14

29. Kumar P, Kumar A, Racic V (2018) Modelling of longitudinal human walking force using self-sustained oscillator. Int J Struct Stab Dyn 18(6):1850080

30. Mohanty D, Jena R, Choudhury PK, Pattnaik R, Mohapatra S, Saini MR (2016) Milk derived antimicrobial bioactive peptides: a review. Int J Food Prop 19(4):837–846

31. Samantaray D, Mohapatra S, Mishra BB (2014) Microbial bioremediation of industrial effluents. In: Microbial biodegradation and bioremediation. Elsevier, pp 325–339

32. Mohapatra S, Rath SN, Pradhan SK, Samantaray DP, Rath CC (2016) Secondary structural models (16S rRNA) of polyhydroxyalkanoates producing bacillus species isolated from different rhizospheric soil: phylogenetics and chemical analysis. Int J Bioautomation 20(3):329–338

33. Mohapatra S, Samantaray DP, Samantaray SM, Mishra BB, Das S, Majumdar S, Pradhan SK, Rath SN, Rath CC, Akthar J, Achary KG (2016) Structural and thermal characterization of PHAs produced by Lysinibacillus sp. through submerged fermentation process. Int J Biol Macromol 93:1161–1167

34. Mohapatra S, Mishra R, Roy P, Yadav KL, Satapathi S (2017) Systematic investigation and in vitro biocompatibility studies on implantable magnetic nanocomposites for hyperthermia treatment of osteoarthritic knee joints. J Mater Sci 52(16):9262–9268

35. Bandekar D, Chouhan OP, Mohapatra S, Hazra M, Hazra S, Biswas S (2017) Putative protein VC0395_0300 from Vibrio cholerae is a diguanylate cyclase with a role in biofilm formation. Microbiol Res 202:61–70

36. Bandhu S, Khot MB, Sharma T, Sharma OP, Dasgupta D, Mohapatra S, Hazra S, Khatri OP, Ghosh D (2018) Single cell oil from oleaginous yeast grown on sugarcane bagasse-derived xylose: an approach toward novel biolubricant for low friction and wear. ACS Sustain Chem Eng 6(1):275–283

37. Mohapatra S, Mohanta PR, Sarkar B, Daware A, Kumar C, Samantaray DP (2017) Production of Polyhydroxyalkanoates (PHAs) by bacillus strain isolated from waste water and its biochemical characterization. Proc Natl Acad Sci India Sect B Biol Sci 87(2):459–466

38. Sarkar MS, Segu H, Bhaskar JV, Jakher R, Mohapatra S, Shalini K, Shivaji S, Reddy PA (2018) Ecological preferences of large carnivores in remote, high-altitude protected areas: insights from buxa tiger reserve, India. ORYX 52(1):66–77

39. Mohapatra S, Sarkar B, Samantaray DP, Daware A, Maity S, Pattnaik S, Bhattacharjee S (2017) Bioconversion of fish solid waste into PHB using Bacillus subtilis based submerged fermentation process. Environ Technol (United Kingdom) 38(16):3201–3208

40. Mohanty DP, Mohapatra S, Misra S, Sahu PS (2016) Milk derived bioactive peptides and their impact on human health—a review. Saudi J Biol Sci 23(5):577–583
41. Sharma SK, Kumar A (2018) Multibody analysis of longitudinal train dynamics on the passenger ride performance due to brake application. Proc Inst Mech Eng Part K J Multi-Body Dyn. https://doi.org/10.1177/1464419318788775
42. Sharma SK, Sharma RC (2018) An Investigation of a locomotive structural crashworthiness using finite element simulation. SAE Int J Commer Veh 11(4):235–44. https://doi.org/10.4271/02-11-04-0019
43. Sharma RC, Sharma SK (2018) Sensitivity analysis of three-wheel vehicle's suspension parameters influencing ride behavior. Noise Vib Worldw 49(7–8):272–280. https://doi.org/10.1177/0957456518796846
44. Sharma SK, Kumar A (2018) Impact of longitudinal train dynamics on train operations: A simulation-based study. J Vib Eng Technol 6(3):197–203. https://doi.org/10.1007/s42417-018-0033-4
45. Sharma SK, Saini U, Kumar A (2019) Semi-active control to reduce lateral vibration of passenger rail vehicle by using disturbance rejection and continuous state damper controller. J Vib Eng Technol 7(2). https://doi.org/10.1007/s42417-019-00088-2
46. Sharma RC, Goyal KK (2017) Improved suspension design of Indian railway general sleeper ICF coach for optimum ride comfort. J Vib Eng Technol 5(6):547–556
47. Sharma RC (2017) Ride, eigenvalue and stability analysis of three-wheel vehicle using Lagrangian dynamics. Int J Veh Noise Vib 1:13–25

A Comparative Study of Five Explicit Time Integration Algorithms for Non-linear Dynamic Systems

Amandeep Sahu, Rishiraj K. Thakur, Vishal Agarwal and Sachin S. Gautam

Abstract For the numerical simulation of the dynamic structural problems special attention is needed to be paid while choosing the time integration algorithm. The task becomes even more challenging if any non-linearity (especially the boundary non-linearities) is involved in the system. In the literature, a number of time integration algorithms are available. However, the choice of an appropriate time integration algorithm is an essential criterion to ensure the efficiency and the robustness of the numerical simulations. The difficulty in this choice resides in being able to combine the robustness, accuracy and the stability of the algorithm. Time integration algorithms are usually classified into two categories: (1) explicit and (2) implicit. For stability reasons, explicit algorithms use smaller time-step in comparison to implicit algorithms. Explicit algorithms are used for the multi-degree-of-freedom system having various non-linearities, e.g. geometrical, material and boundary, for which carrying out the iterations operation becomes prohibitively expensive, and convergence issues are frequent. In this contribution, the stability, robustness and the accuracy of popularly employed explicit time integration algorithms are investigated and compared through a number of single and multi-degree-of-freedom non-linear systems.

Keywords Non-linear · Dynamic system · Time integration algorithms · Multi-degree-of-freedom

1 Introduction

Numerical simulation of dynamic problems, represented by equation of motion, requires numerical integration in time, which in turn requires time integration algorithm.

A. Sahu · R. K. Thakur · V. Agarwal · S. S. Gautam (✉)
Indian Institute of Technology Guwahati, Guwahati 781039, Assam, India
e-mail: ssg@iitg.ernet.in

The direct time integration algorithms for the linear and the non-linear equations of motion are categorized into two different families: collocation-based algorithms and momentum-based algorithms [1]. In the momentum-based algorithms, the equation of motion is developed over the time interval. The idea is to integrate the equation of motion over the respective time interval. In collocation-based algorithms, the equation of motion is satisfied at discrete points in time.

Collocation-based algorithms are further divided into implicit algorithms (IA's) and explicit algorithms (EA's) [1]. In EA's, the solution at current time depends upon the solution of previous time point, while in IA's the solution at current time depends on some quantities at current time point too requires the use of iterative solution procedure like Newton–Raphson methods. Also EA's are conditionally stable while IA's are unconditionally stable—at least for linear problems.

Currently, active research is carried out in the area of EA's. A number of EA's have been proposed for example Noh and Bathe [2], Pajand and Rad [3], Zhai [4], Groβeholz et al. [5]. However, a comparative study of these has not been carried out.

The objective of the present work is to study the performance of some recently proposed explicit time integration algorithms for non-linear dynamic systems. The rest of the paper is structured as follows: Sect. 2 gives the background on some explicit time integration algorithms. Section 3 presents the results of some numerical problems which show the performance of the EA's. Section 4 concludes the paper.

2 Explicit Time Integration Algorithm

A general non-linear and non-dissipative system at time $t + \Delta t$ is governed by the following equation [1]

$$M\ddot{U}_{t+\Delta t} + F_{int_{t+\Delta t}} + F_{c_{t+\Delta t}} = F_{ext_{t+\Delta t}} \tag{1}$$

where U is the displacement vector, and M is the mass stiffness matrix. The internal, contact and the external force vectors at $t + \Delta t$ are represented by $F_{int_{t+\Delta t}}$, $F_{c_{t+\Delta t}}$ and $F_{ext_{t+\Delta t}}$, respectively. The superimposed dote denote the derivative of the quantity with respect to time. To obtain the solution of the above-described system at time $t + \Delta t$, direct time integration algorithms are employed. Based on the application, direct time integration algorithms are broadly classified into two categories: (1) explicit, and (2) implicit time integration algorithms. Explicit time integration algorithms (EA's) utilize the state or values of quantities evaluated at the previous time-step, i.e. t, to obtain the solution at the current time-step. Moreover, EA's have computational advantages over IA's and are found to be more appreciable for the wave propagation problems [5]. In this contribution, five most popular

explicit time integration algorithms are considered for their comparative study. The description of each algorithm is presented in the following.

2.1 Standard Central Difference Algorithm [1]

With the standard central difference (CD) algorithm, the equation for displacement, and velocity quantities at the time t $+ \Delta$t are given by the following equations [1]

$$U_{t+\Delta t} = U_t + \Delta t \dot{U}_t + 0.5\Delta t^2 \ddot{U}_t \tag{2}$$

$$\dot{U}_{t+\Delta t} = \dot{U}_t + 0.5\Delta t (\ddot{U}_t + \ddot{U}_{t+\Delta t}) \tag{3}$$

where U is the displacement vector, and Δt is the time-step. Equations (2) and (3) are the iterative equation, which are used to calculate U and $\dot{U}$ quantities at successive time-steps. After that $\ddot{U}$ is evaluated from Eq. (1). As being the explicit algorithm, it is conditionally stable. Therefore, it should satisfy the condition Δ t $\omega \leq 2$. Here, ω denotes the highest natural frequency of the system.

2.2 Stabilized Central Difference Algorithm [5]

With the stabilized CD algorithm, proposed by Großeholz et al. [5], the original equation given by Eq. (1), is first modified to the below form

$$(M + a\Delta t^2 DF|_u) \ddot{U} + F_{int_{t+\Delta t}} + F_{c_{t+\Delta t}} = F_{ext_{t+\Delta t}} \tag{4}$$

The above equation then discretized according to the standard CD algorithm. In Eq. (4), the term $DF|_u$ denotes the Jacobian matrix of $(F_{int_{t+\Delta t}} + F_{c_{t+\Delta t}})$ evaluated at U, $a = 0.25 \tanh(\alpha\Delta t\omega)$ is a positive scalar function, and ω is taken as the highest natural frequency of the differential equation. The value of α is taken as 0.25, which is determined from the stability analysis of the stabilized CD algorithm [5].

2.3 Noh and Bathe Explicit Algorithm [2]

Noh and Bathe [2] proposed a two-step EA, which yields the second order of accuracy, for the problems with and without considering the damping. In this algorithm, each time-step Δt is further subdivided into two sub-steps. The size of each sub-step is given by pΔt and (1 − p)Δt, respectively, where p $\in$ (0,1). The values of the displacement, velocity and the acceleration at time t and (t − 1) are

known. For the first sub-step, the velocity and displacement quantities are calculated using the following expression [2]

$$U_{t+p\Delta t} = U_t + a_0 \dot{U}_t + a_1 \ddot{U}_t \tag{5}$$

$$\dot{U}_{t+p\Delta t} = \dot{U}_t + a_2 (\ddot{U}_t + \ddot{U}_{t+p\Delta t}) \tag{6}$$

After that, for the second sub-step, these values are evaluated as

$$U_{t+\Delta t} = U_{t+p\Delta t} + a_3 \dot{U}_{t+p\Delta t} + a_4 \ddot{U}_{t+p\Delta t} \tag{7}$$

$$\dot{U}_{t+\Delta t} = \dot{U}_{t+p\Delta t} + a_5 \ddot{U}_t + a_6 \ddot{U}_{t+p\Delta t} + a_7 \ddot{U}_{t+\Delta t} \tag{8}$$

where the constants used in above equations are defined as follows:

$$a_0 = p\Delta t, \quad a_1 = 0.5(p\Delta t)^2, \quad a_2 = 0.5a_0, \quad a_3 = (1-p)\Delta t$$

$$a_4 = 0.5((1-p)\Delta t)^2, \quad a_5 = q_0 a_3, \quad a_6 = (0.5 + q_1)a_3, \quad a_7 = q_2 a_3$$

$$q_1 = \frac{1-2p}{2p(1-p)}, \quad q_2 = 0.5 - pq_1, \quad q_0 = -q_1 - q_2 + 0.5$$

For higher accuracy, the value of p suggested by [2] is 0.54. In order to be conditionally stable, the above algorithm satisfies the following criteria: $\frac{\Delta t}{T} \leq 0.2$. This algorithm can easily be extended for a non-linear system.

2.4 Zhai Explicit Algorithm [4]

The following relationships give the algorithm proposed by Zhai [4] to solve the equilibrium Eq. (1):

$$U_{t+\Delta t} = U_t + \Delta t \dot{U}_t + (0.5 + \phi)\Delta t^2 \ddot{U}_t - \phi \Delta t^2 \ddot{U}_{t-\Delta t} \tag{9}$$

$$\dot{U}_{t+\Delta t} = \dot{U}_t + (1+\varphi)\Delta t \ddot{U}_t - \varphi \Delta t \ddot{U}_{t-\Delta t} \tag{10}$$

The algorithm is controlled by two parameters: ϕ and φ. From stability analysis, $\phi = \varphi = 0.5$ is considered. For this algorithm, the stability criteria are same as that for standard CD algorithm, i.e. $\Delta t \omega \leq 2$.

2.5 *Pajand and Rad Explicit Algorithm [3]*

Pajand and Rad [3] proposed a new family of EA's for calculating displacement, velocity and acceleration as follows:

$$U_{t+\Delta t/2} = U_t + \frac{\Delta t}{2}\dot{U}_t, \ \dot{U}_{t+\Delta t/2} = \dot{U}_t + \frac{\Delta t}{2}\ddot{U}_t \tag{11}$$

$$M\ddot{U}_{t+\Delta t/2} + F_{int_{t+\Delta t}} + F_{c_{t+\Delta t}} = \frac{1}{2}\left(F_{ext_t} + F_{ext_{t+\Delta t}}\right) \tag{12}$$

$$\dot{U}_{t+\Delta t} = \dot{U}_t + \Delta t\ddot{U}_{t+\Delta t/2} \tag{13}$$

$$\hat{U}_n = U_t + \frac{\Delta t}{2}\dot{U}_t + \frac{\Delta t^2}{4\alpha}\ddot{U}_{n+\Delta t/2} + \frac{(\alpha-2)\Delta t^2}{8\alpha}\ddot{U}_t \tag{14}$$

$$U_t = \frac{4}{3}\hat{U}_t - \frac{1}{3}U_t + \frac{\Delta t}{3}\dot{U}_{t+\Delta t} \tag{15}$$

Within this algorithm, the least relative period error occurs in the range of $0.8 \leq \alpha \leq 1$. Pajand and Rad [3] have shown that the algorithmic damping ratio is negligible when $\Delta t \omega \leq 0.6$.

3 Numerical Examples

To compare the performance and to investigate the difference in the performance of above mentioned explicit time integration algorithms following non-linear problems are considered: (1) a single-degree-of-freedom problem, (2) a two-degrees-of-freedom spring pendulum problem and (3) one-dimensional adhesive contact problem. The obtained result and the necessary discussion for each problem are included in the respective following section.

3.1 *Single-Degree-of-Freedom Non-linear Problem*

Consider the following equation of a non-linear conservative system

$$\ddot{U} + U^3 - 2U^2 - 411U + 6 = 0 \tag{16}$$

with initial conditions as $U(0) = \dot{U}(0) = 0$ [5]. For further details, the reader is referred to Groβeholz et al. [5]. The critical time-step for the standard CD

Table 1 Maximum error produced in total energy at different time-steps

Time-step	Noh [2]	CDM [1]	STB [5]	Zhai [4]	Rad [3]
1×10^{-6}	2.31×10^{-6}	6.118×10^{-3}	6.141×10^{-5}	3.311×10^{-5}	3.147×10^{-5}
1×10^{-5}	2.316×10^{-4}	6.112×10^{-4}	6.112×10^{-4}	3.3×10^{-3}	1.6×10^{-3}
1×10^{-4}	2.38×10^{-2}	6.11×10^{-2}	6.11×10^{-2}	3.314×10^{-3}	1.8×10^{-1}

algorithm, stabilized CD algorithm [5] and Zhai explicit algorithm [4] is $\Delta t = 0.0453$ s. Also, critical time-step for Noh and Bathe [2] and Pajand and Rad [3] is $\Delta t = 0.0285$ and 0.0136 s, respectively. Therefore, solution is calculated for following time-steps: 1×10^{-3}, 1×10^{-4}, 1×10^{-5} and 1×10^{-6} s. Total time for simulation is taken as 10 s. As the problem is non-dissipative and self-excited, the total energy of the system is conserved. From the initial condition, total energy at every time-step should remain constant. Due to paucity of the space, the plots for the variation of the displacement and energy quantities over time are not shown. In Table 1, the maximum error in the total energy for all the explicit time integration algorithms is shown.

Based on the evaluated result, it can be summarized that the algorithm proposed by Noh and Bathe [2] produces the least maximum error and algorithm proposed by Zhai [4] produces the maximum error in the total energy for all the time-steps except 1×10^{-4} s.

3.2 Non-linear Two-Degree-of-Freedom Problem

The schematic arrangement of the considered problem is shown in Fig. 1a [3]. The details of the problem can be found in Pajand and Rad [3]. The solution is calculated for following time-steps: 1×10^{-3} s, 1×10^{-4} s, 1×10^{-5} s and 1×10^{-6} s, respectively. The equation of motion for a spring pendulum can be written as follows:

$$m\ddot{r} - m(L_0 + r)\dot{\theta}^2 - mg\cos(\theta) + kr = 0$$

$$m\ddot{\theta} + \frac{m\left(2\dot{r}\dot{\theta} + g\sin(\theta)\right)}{L_0 + r} = 0$$

By solving the above equation, it can be observed that almost all the algorithms produce the same variation of displacement. While looking into Fig. 1b, the algorithm proposed by Pajand and Rad [3] shows least radial displacement error, and is also relatively stable with respect to the other algorithms over the time, followed by Noh and Bathe algorithm [2] and the standard CD algorithm. It can be noted that increase in the radial displacement error over the time produced by the algorithm proposed by [4] is more as compared to others. With respect to
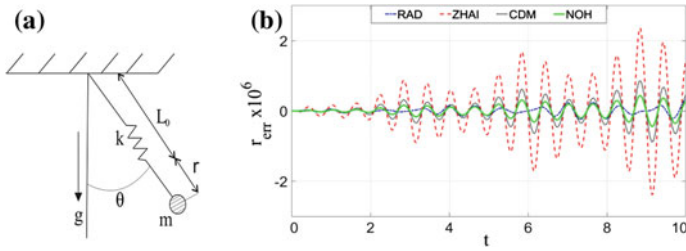
Fig. 1 **a** The spring pendulum problem [3]. Variation of displacement error in radial displacement (rerr) at time-step $\Delta t = 1 \times 10^{-4}$ s with respect to time taking standard CD algorithm at time-step $\Delta t = 1 \times 10^{-6}$ s as reference

computational time, the algorithm proposed by [3] is found to be more economical because of its simpler mathematical formulation.

3.3 One-Dimensional Adhesive Contact Problem

A two point mass system, in which a fixed mass and a free mass are interacting under the application of adhesive forces, is taken from Gautam and Sauer [6]. In this problem two cases are considered: (1) free mass is connected with spring, and (2) both masses freely interact with each other. The set-up of the system is shown in the Fig. 2. The reader is referred to Ref. [6] for further details. For solving the problem four different time-steps, i.e. 1×10^{-3} s, 1×10^{-4} s, 1×10^{-5} s and 1×10^{-6} s are considered. The definition of the error in energy E_{err} can be found in Ref. [6].

From the Fig. 3a and b, it can be observed that the relative error produced by the Noh and Bathe [2] is less when compared with other algorithms followed by the
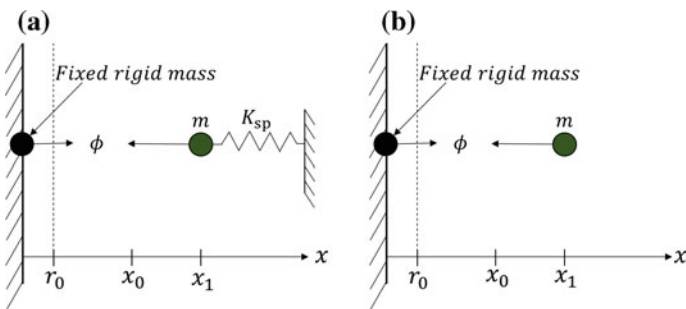
Fig. 2 Two point mass (fixed and free) interacting with each other through van der Waals adhesive force **a** under the application of spring, and **b** without spring

Fig. 3 Variation of the logarithmic of relative error in total energy over time for time-step $\Delta t = 1 \times 10^{-5}$ s: **a** with spring **b** without spring

stabilized CD algorithm [5] and the standard CD algorithm [1]. It is worth mentioning that the maximum relative error produced by the [2] is in the order of 1×10^{-9}, while algorithm proposed by [4] produces in the order of 1×10^{-6}.

4 Conclusions

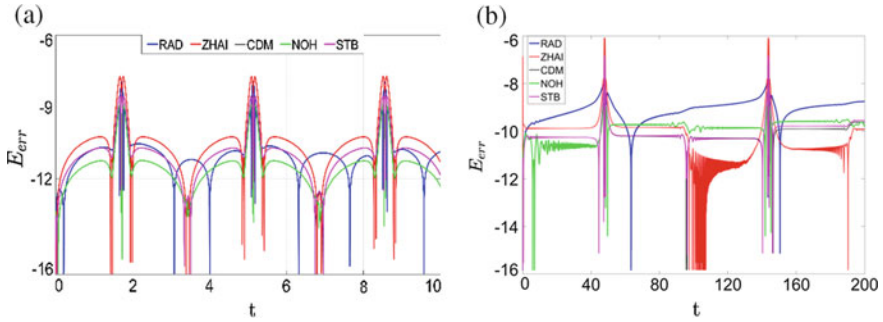From the numerical examples analyzed in this paper, it can be stated that the performance of the EA's depends on the various parameters. Some of these are stiffness of the equation, the time-step and the highest natural frequency of the considered system. These parameters play a key role in determining the performance of the algorithm. For non-linear problems, additional efforts are needed to determine the natural frequency of the system, especially in case of stabilized CD algorithm. The algorithm proposed by Pajand and Rad [3] takes relatively less computational time for the considered numerical examples because of its simpler mathematical formulation. However, their algorithm proposed performs best in case of the spring pendulum problem but is not good enough in case of other two numerical examples. While, the algorithm proposed by Noh and Bathe gives the best result in one degree non-linear and adhesive contact problem, and also performs well in case of spring pendulum problem. The standard CD algorithm also performs well in the above-discussed numerical examples after algorithm proposed by Noh and Bathe. But in spring pendulum problem, standard CD algorithm transforms into implicit algorithm due to the complicated mathematical formulation and needs Newton–Raphson method to obtain the solution, hence utilizes more computational efforts. Performance of standard CD and stabilized CD algorithm is of the same order for all the three problems discussed above. However, the standard CD is conditionally stable, so, it can be only used for lower time-step but stabilized CD algorithm can be used for higher time-step considering some tolerance value in result. The algorithm proposed by Zhai has the highest order of error for discussed

problems followed by the algorithm proposed in [5] for one degree non-linear and adhesive contact problem. Standard CD algorithm, Stabilized CD algorithm and algorithm proposed by Noh and Bathe, all perform well in the above-discussed problems. Considering the accuracy and the computational cost, the algorithm proposed by Noh and Bathe is found to be performing better than the standard CD and the stabilized CD algorithm.

References

1. Bathe KJ (1996) Finite element procedures. Prentice-Hall, Englewood Cliffs
2. Noh G, Bathe KJ (2013) An explicit time integration scheme for analysis of wave propagation. Comput Struct 129:178–193
3. Pajand MR, Rad MK (2017) A family of second-order fully explicit time integration schemes. Comput Appl Math. https://doi.org/10.1007/s40314-017-0520-3
4. Zhai WM (1996) Two simple fast integration methods for large-scale dynamics problem in engineering. Int J Numer Meth Eng 39(24):4199–4214
5. Groβeholz G, Soares D Jr, Estorff O (2015) A stabilized central difference scheme for dynamical analysis. Int J Numer Meth Eng 102(11):1750–1760
6. Gautam SS, Sauer RA (2012) An energy-momentum conserving temporal discretization schemes for adhesive contact problem. Int J Numer Meth Eng 93(10):1057–1081
7. Rio G, Soive A, Grolleau V (2005) Comparative study of numerical explicit time integration algorithms. Adv Eng Softw 36(4):252–265

Static and Dynamic Characteristics of Two-Lobe Hydrostatic Journal Bearing

Sandeep Soni and **Dnyaneshwar V. Kushare**

Abstract The behavior of multi-recess hydrostatic journal bearings is now very well known because of stability and many numerical and experimental studies that have been carried out in this area. Noncircular or multi-lobe journal bearings are also used in high-speed machinery, gas turbines, and test equipments due to their excellent shaft stability characteristics and capability to suppress the whirl. Capillary and orifice are most commonly used restrictors for hydrostatic bearings because of simple manufacturing. The two-lobe bearings are among the commonly used noncircular journal bearings. The aim of this study deals with the theoretical investigation of a two-lobe six-recess hydrostatic journal bearing systems to present static and dynamic performance characteristics with different restrictors such as capillary, orifice, etc. and comparison of characteristics of capillary and orifice restrictor. Recent years have witnessed quite a substantial amount of research work in the area of fluid film lubrication. The analysis and design of two-lobe six-recess hydrostatic journal bearing is quite a complex process. There are various parameters such as bearing configuration, lobe position, type of restrictor, number of recesses, shape of recesses, lubricant supply pressure, external load, bearing operating and geometric parameters, etc., which influences this class of bearing quite significantly. The analysis of a two-lobe multi-recess hydrostatic bearing would become more realistic by incorporating physical effect of method of compensation device. Further, a designer may improve the performance of bearing by varying the number of recess.

Keywords Hydrostatic · Multi-lobe · Restrictors

S. Soni (✉)
Department of Mechanical Engineering, SVNIT, Surat, Gujarat, India
e-mail: sandytit2004@gmail.com

D. V. Kushare
Department of Mechanical Engineering,
NDMVPS's College of Engineering, Nashik, India

1   Introduction

The multi-lobe hydrostatic journal bearing consists of two, three, and four lobes. The multi-lobe bearing is designed to overcome the disadvantages of circular hydrostatic bearing. The bore is made of two arcs of larger radius; the bearing has larger clearances on the two horizontal sides and smaller clearance in the upper and bottom sides. Noncircular journal bearings are also used in high-speed machinery, gas turbines, and test equipments due to their excellent shaft stability characteristics and capability to suppress the whirl. In general, the two-lobe multi-recess hydrostatic journal bearing for high-speed applications offers meritorious properties such as a multi-lobe bearing geometry which improves shaft stability. Two-lobe bearing is more stable than the circular bearings. Two-lobe (elliptical) bearing is easier to manufacture [1].

Figure 1 shows the basic operating principle of two-lobe six-recess hydrostatic journal bearing. The lubricant at constant supply pressure is pumped into the bearing clearance space. The lubricant first passes to the restrictor and then to a pocket or recess. The recess is usually quite deep so that it offers a little resistance to the flow of lubricant. The lubricant in a multi-recess journal bearing system is introduced to various recesses through separate entry ports.
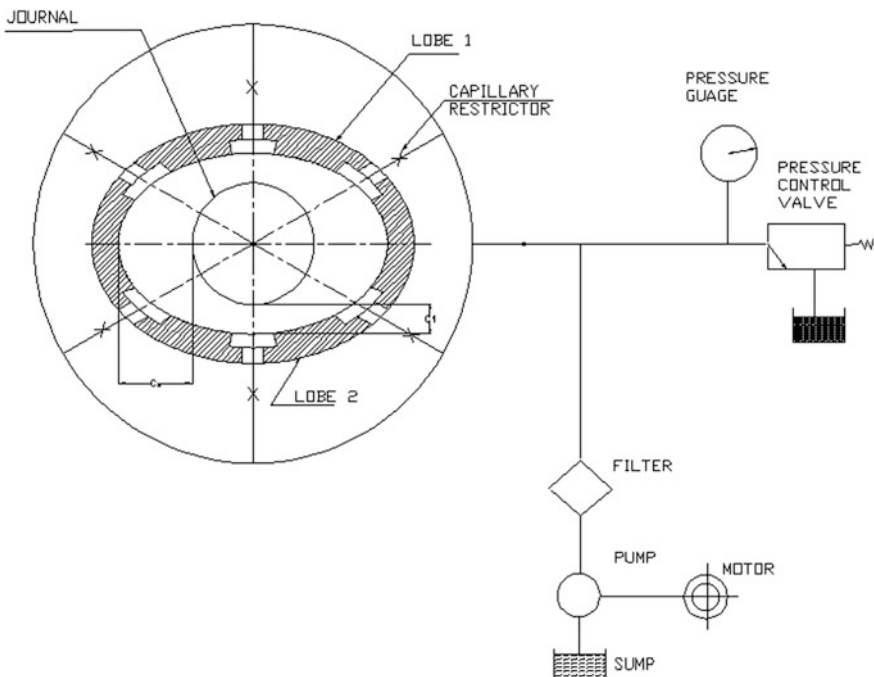
Fig. 1   A two-lobe six-recess hydrostatic journal bearing [2]

Recent years have witnessed quite a substantial research work in the field of fluid film lubrication. Design and analysis of two-lobe multi-recess hydrostatic journal bearing is quite a complex process. There are various parameters such as bearing configuration, lobe position, type of restrictor, number of recesses/pockets, shape of recesses, lubricant supply pressure, external load, bearing operating and geometric parameters, etc., which influences this class of bearing quite significantly. The analysis of a two-lobe multi-recess hydrostatic bearing would become more realistic by incorporating physical effect of method of compensation device. Further, a designer may improve the performance of bearing by varying the number of recess.

The aim of this study deals with the theoretical investigation of a two-lobe six-recess hydrostatic journal bearing systems to present static and dynamic performance characteristics with capillary restrictor and orifice restrictor and comparison with circular journal bearing [3].

2 Analysis of Journal Bearing

2.1 Fluid Flow Reynolds Equation in Nondimensional Form

The Reynolds equation in nondimensional is written as [4, 5]

$$\frac{\partial}{\partial \alpha}\left(\frac{\bar{h}^3}{6}\frac{\partial \bar{p}}{\partial \alpha}\right) + \frac{\partial}{\partial \beta}\left(\frac{\bar{h}^3}{6}\frac{\partial \bar{p}}{\partial \beta}\right) = \Omega\frac{\partial \bar{h}}{\partial \alpha} + 2\frac{\partial \bar{h}}{\partial \tau}. \tag{1}$$

The nondimensional parameter in the above equation is as follows:

$$\bar{p} = \frac{p}{p_s};\ \alpha = \frac{x}{R_J};\ \bar{h} = \frac{h}{c};\ \beta = \frac{y}{R_J};\ \bar{z} = \frac{z}{h};$$

$$U = \omega_j R_j;\ \bar{\mu} = \frac{\mu}{\mu_r};\ \Omega = \omega_J\left(\frac{\mu_r R_J^2}{c^2 p_s}\right);\ \tau = t\left(\frac{c^2 p_s}{\mu_r R_J^2}\right).$$

2.2 Nondimensional Fluid Film Thickness

The following equation gives the film thickness:

$$\bar{h} = \bar{h}_0 + \Delta\bar{h}. \tag{2}$$

The above expression for a multi-lobe multi-recess bearing is modified and written as [6, 7]

$$\bar{h} = \frac{1}{\delta} - \left(\bar{X}_j + \bar{x} - \bar{X}_L^i \right) \cos \alpha - \left(\bar{Z}_j + \bar{z} - \bar{Z}_L^i \right) \sin \alpha. \tag{3}$$

2.3 Equation for Capillary and Orifice Restrictor

The various flow control devices used in hydrostatic multi-lobe multi-recess journal bearings are capillary restrictor, orifice restrictor, and constant flow valves. In this work, for two-lobe six-recess journal bearings, capillary and orifice restrictors are used as a compensating element. The equation for capillary and orifice restrictor is as follows [8, 9]:

$$\bar{Q}_R = \bar{C}_{s2}(1 - \bar{p}_c) \quad \text{(Capillary)} \tag{4}$$

$$\bar{Q}_R = \bar{C}_{s2}(1 - \bar{p}_c)^{\frac{1}{2}} \quad \text{(Orifice)}. \tag{5}$$

2.4 Boundary Conditions

1. Nodes situated on the external boundary of the bearing have zero pressure.
2. Nodes on pocket/recess have equal pressure.
3. The nodal flows are zero at internal nodes except those situated on pockets.
4. Flow of lubricant through the restrictor is equal to the bearing input flow.

3 Result and Discussion

3.1 Maximum Fluid Film Pressure $(\bar{P}_{\max})$ [2, 10, 11]

The restrictor design parameter $(\bar{C}_{s2})$ and variation in fluid film pressure $(\bar{P}_{\max})$ are presented as shown in Fig. 2. At given fixed load $(\bar{W}_0)$ as offset factor (δ) increases, the maximum fluid film pressure $(\bar{P}_{\max})$ also increases. Due to alteration in the bearing geometry on the account of lobing is responsible for the increase in the values of $(\bar{P}_{\max})$ at a offset factor $(\delta) = 1.50$ for a capillary restrictor two-lobe journal bearing and given fixed load $\bar{W}_0 = 0.6$. The value of $(\bar{P}_{\max})$ increases by 40.76% as compared to circular six-recess journal bearing for the values of $(\bar{C}_{s2}) = 0.4$ and the value of $(\bar{P}_{\max})$ increases by 42.61% for orifice restrictor bearing.

Fig. 2 Maximum peak
pressure
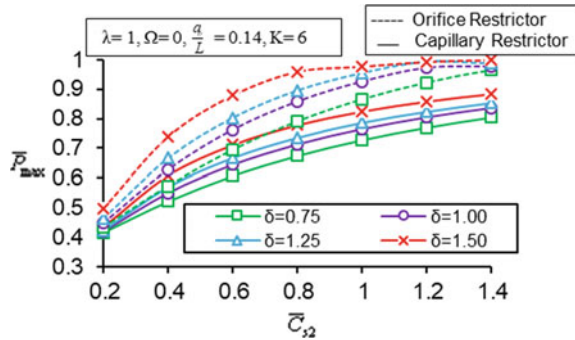
3.2 Bearing Flow $(\bar{Q})$ [2, 10, 11]

Figure 3 shows the restrictor design parameter $(\bar{C}_{s2})$ and the variation of bearing flow $(\bar{Q})$. As restrictor parameter $(\bar{C}_{s2})$ increases, the $(\bar{Q})$ also increases. When restrictor design parameter $(\bar{C}_{s2}) = 0.2$, the bearing flow $(\bar{Q})$ is minimum and when restrictor design parameter $(\bar{C}_{s2}) = 1.4$, the bearing flow $(\bar{Q})$ is maximum. When there is an increase in the offset factor (δ), the bearing flow $(\bar{Q})$ decreases for a given value of $(\bar{C}_{s2})$. For two-lobe six-recess bearing when offset factor $(\delta) = 1.50$, the bearing flow $(\bar{Q})$ is less than circular bearing.

3.3 Fluid Film Stiffness Coefficient $(\bar{S}_{ii}; i = 1, 2)$ [2, 10, 11]

The restrictor parameter $(\bar{C}_{s2})$ and the variation of direct fluid film stiffness coefficient $(\bar{S}_{ii}; i = 1, 2)$ have been presented for a two-lobe bearing shown in Fig. 4. As the restrictor design parameter $(\bar{C}_{s2})$ and offset factor (δ) increase, the fluid film

Fig. 3 Fluid flow
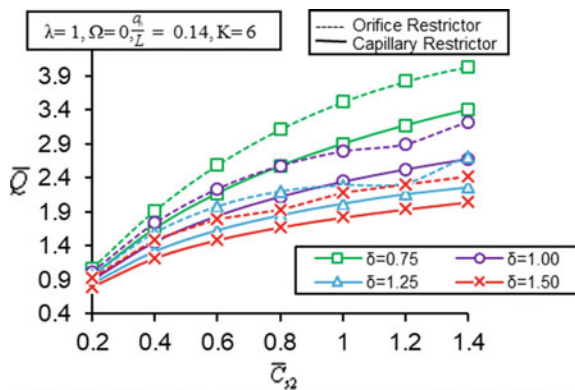
Fig. 4 Direct stiffness
coefficient
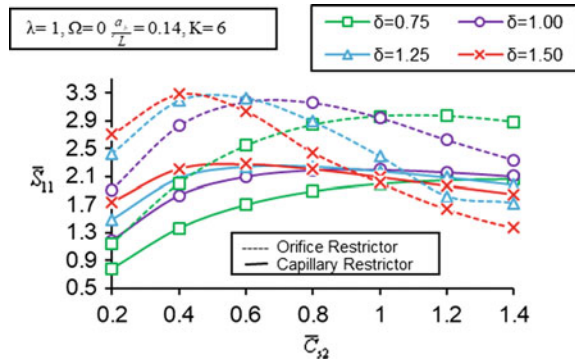
stiffness coefficient ($\bar{S}_{11}$) increases. Figure 4 reveals that fluid film stiffness coefficient ($\bar{S}_{11}$) increases with an increase in offset factor after certain value of ($\bar{C}_{s2}$), and the change in the fluid film stiffness coefficient is marginal for capillary-compensated bearing as compared to the orifice-compensated bearing.

3.4 Fluid Film Damping Coefficient ($\bar{C}_{ii}$; $i = 1, 2$) [2, 10, 11, 12]

The restrictor design parameter ($\bar{C}_{s2}$) and the direct fluid film damping coefficient ($\bar{C}_{11}$) for the lobe bearing are shown in Fig. 5. The fluid film damping coefficient ($\bar{C}_{11}$) decreases with increase in restrictor parameter ($\bar{C}_{s2}$). When offset factor is above one, the fluid film damping coefficient is maximum and when offset factor is equal to 0.75, the fluid film damping coefficient is smallest. The increase in offset factor (δ) improves the damping of the system. At a constant ($\bar{C}_{s2}$), when the offset factor (δ) increases, the value of damping coefficient ($\bar{C}_{11}$) also increases (Fig. 5).

Fig. 5 Direct damping
coefficient
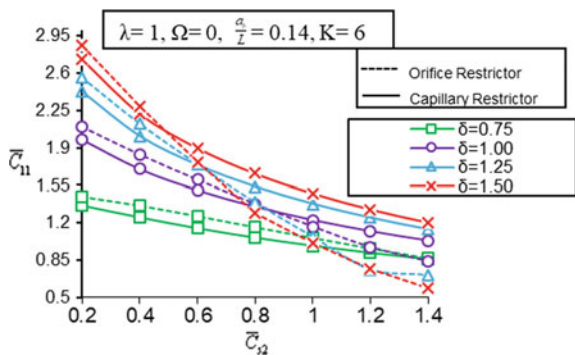
Figure 6 shows the percentage variation for maximum peak pressure, Fig. 7 shows percentage variation for fluid flow, Fig. 8 shows percentage variation for direct stiffness coefficient and Fig. 9 shows percentage variation for direct damping coefficient.
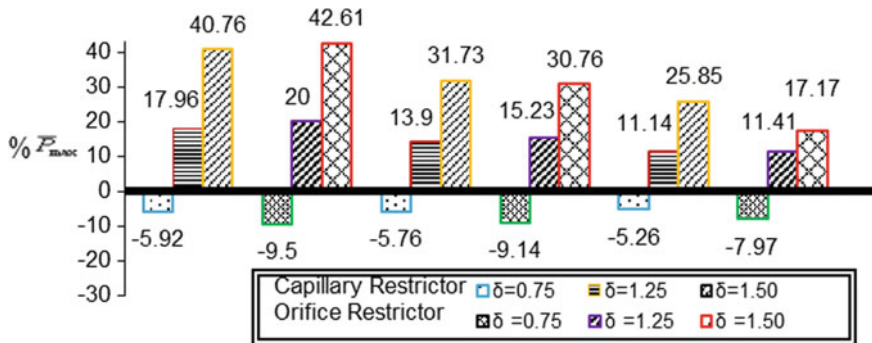
Fig. 6 Percentage variation for maximum peak pressure [13]
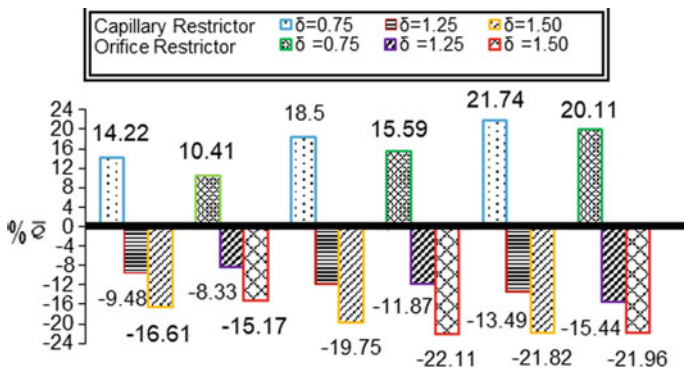
Fig. 7 Percentage variation for fluid flow [13]
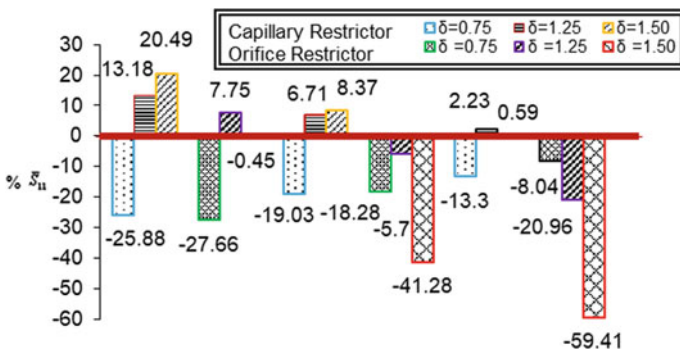
Fig. 8 Percentage variation for direct stiffness coefficient [13]
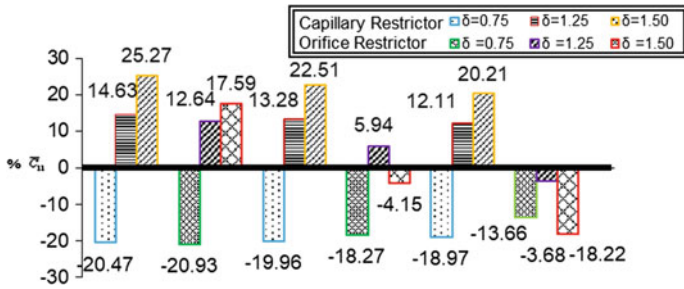
Fig. 9 Percentage variation for direct damping coefficient [13]

4   Conclusion

- In the present work for hydrostatic lobe bearings, the fluid film pressure $(\bar{P}_{max})$ is greater than a circular six-recess hydrostatic bearing. When offset factor (δ) increases from lower value to higher value, maximum fluid film pressure $(\bar{P}_{max})$ increases. Thus, from maximum fluid film pressure $(\bar{P}_{max})$ point of view, a two-lobe six-recess hydrostatic journal bearing with offset factor (δ) above one will be desirable as compared to circular six-recess journal bearing.
- Suitable offset factor (δ) will be chosen to get an improved performance from a two-lobe hydrostatic bearing as compared to a circular six-recess bearing for the range external load $(\bar{W}_0)$ and restrictor used.

References

1. Malik M (2008) A comparative study of some two-lobed journal bearing configurations. ASLE Trans 26(1):118–124. https://doi.org/10.1080/05698198308981485
2. Phalle VM, Sharma SC, Jain SC (2011) Influence of wear on the performance of a 2–lobe multirecess hybrid journal bearing system compensated with membrane restrictor. Tribol Int 44:380–395. https://doi.org/10.1016/j.triboint.2010.11.011
3. Ho YS, Chen NNS (1984) Pressure distribution in a six–pocket hydrostatic journal bearing. Wear 98(8):89–100. https://doi.org/10.1016/0043-1648(84)90219-9
4. Sinhasan R, Sharma SC, Jain SC (1989) Performance characteristics of an externally pressurized capillary compensated flexible journal bearings. Tribol Int 22(4):283–293. https://doi.org/10.1016/0301-679X(89)90087-X
5. Sharma SC, Jain SC, Sinhasan R, Shalia R (1995) Comparative study of the performance of six pocket and four pocket hydrostatic/hybrid flexible journal bearings. Tribol Int 28(8):531–539. https://doi.org/10.1016/0301-679X(96)85541-1
6. Ghosh MK, Satish MR (2003) Rotordynamic characteristics of multilobe hybrid bearings with short sills-part I. Tribol Int 36:625–632. https://doi.org/10.1016/S0301-679X(03)00006-9
7. Ghosh MK, Satish MR (2003) Rotordynamic characteristics of multilobe hybrid bearings with short sills-part II. Tribol Int 36:633–636. https://doi.org/10.1016/S0301-679X(03)00007-0

8. Jain SC, Sinhasan R, Sharma SC (1992) Analytical study of flexible hybrid journal bearing system using different flow control device. Tribol Int 25(6):387–395. https://doi.org/10.1016/0301-679X(92)90076-Y
9. Chen CH, Kang Y, Chang YP, Lee HH, Shen PC (2005) Influences of recess depth on the stability of the Jeffcott rotor supported by hybrid bearings with orifice restrictor. Ind Lubr Tribol 57(1):41–51. https://doi.org/10.1108/00368790510575978
10. Kushare PB, Sharma SC (2013) A study of two lobe non recessed worn journal bearing operating with non-Newtonian lubricant. Proc Inst Mech Eng Part J J Eng Tribol 227 (12):1418–1437. https://doi.org/10.1177/1350650113496083
11. Basavaraja JS, Sharma SC, Jain SC (2008) Performance of an orifice compensated two-lobe hole-entry hybrid journal bearing. Adv Tribol 2008 (871952):10. https://doi.org/10.1155/2008/871952
12. Ajeet S, Gupta BK (1984) Stability analysis of orthogonally displaced bearings. Wear 97 (1):83–92. https://doi.org/10.1016/0043-1648(84)90083-8
13. Phalle VM, Sharma SC, Jain SC (2012) Performance analysis of a 2-lobe worn multirecess hybrid journal bearing system using different flow control devices. Tribol Int 52:101–116. http://doi.org/10.1016/j.triboint.2012.03.009

Numerical Methods to Estimate Fracture Parameters in Ceramics

Subbaiah Arunkumar, Ravi Kiran Bollineni and Parameswaran Vignesh

Abstract Ceramic materials are widely used in most of the industries due to their outstanding mechanical properties like high strength, high modulus of elasticity, corrosion resistance, low coefficient of thermal expansion, etc. It is therefore vital to understand the deformation and fracture of ceramics to take preventive measures to circumvent catastrophic failure. The deformation process and fracture of ceramics can be understood through fracture mechanics of brittle materials. In the first part of this work, an overview of the fracture mechanics and the various approaches employed to predict the failures of isotropic and homogeneous materials is briefly presented. Following this, a brief overview of the numerical methods used to estimate fracture parameters to analyze the failure of ceramic materials is discussed. Estimation of stress intensity factor of a typical ceramic material used in industry through numerical simulation and the associated result is presented in this work.

Keywords Fracture · Ceramics · J-integral · Stress–energy criterion · Numerical method · Stress intensity factor · Alumina

1 Introduction

Ceramic materials are compounds between metallic and nonmetallic elements which are held together in covalent and/or ionic bonds. These are classified as carbides, fluorides, nitrides, oxides, and sulfides based on their composition. Based on their application, ceramics are further classified as abrasives, cement, clay products, glasses, refractories, and advanced ceramics. In general, the strength and stiffness of ceramic materials are comparable to metals and are extremely brittle. Ceramics are resistant to heat and electricity and can withstand high temperature and harsh ambience [1]. The compressive strength of ceramics is higher than their

S. Arunkumar (✉) · R. K. Bollineni · P. Vignesh
Department of Mechanical Engineering, Amrita Vishwa Vidyapeetham,
Amritapuri, Kollam, India
e-mail: arunkumars@am.amrita.edu

tensile strength and it is resistant to wear and corrosion. Due to these excellent properties, these have become attractive materials for high-temperature applications like in gas turbines [2]. They are also used in the field of dentistry [3]. One of the limitations of ceramics is that they have very low fracture toughness (due to their brittle nature) which promotes the crack to propagate at much higher speeds. This results in catastrophic failure of the structure without any prior warning. The brittle nature is attributed by the defects (present in the bulk volume or on the surface) formed either during the processing or secondary manufacturing processes. These defects act as the sites of stress concentration and, in turn, promote the propagation of the crack leading to failure of the component [4–6]. The various defects that could be the origin of failure in ceramics are classified as (i) processing defects like pores, foreign particles, etc. (ii) machining defects (iii) environmental- and service-induced defects. As the size of the specimen increases, the probability of having more number of defects increases. In addition, specimen shape also determines the nature of the flaw. From the shape of the specimen, accessible direction of machining and the uniformity of the machining can be determined. The processing defects show a preferential direction with the type of processing, and hence with the specimen shape. The number of defects in the component can be reduced significantly, but this increases the cost of processing [7]. These defects can be detected by failure analysis procedures through nondestructive examination in combination with fracture mechanics. Nondestructive testing identifies the location and size of the flaw in the component, while with fracture mechanics, the critical size of the flaw and time necessary for the growth of the flaw to its critical size can be assessed. In other words, the remaining life of the component can be determined through fracture mechanics. In addition, the severity of crack can also be quantified using fracture mechanics. The aim of this work is to elaborate the techniques, particularly, of numerical methods in estimating the fracture parameters which is otherwise difficult to find experimentally.

2   The Mechanics of Fracture

The branch of fracture mechanics came into existence to analyze the flaws present in the components which cause failure. Thus, the basic assumption in fracture mechanics is that all materials contain cracks from which the failure nucleates. At the microscopic level, fracture mechanics investigates with the nucleation and growth of cracks. Fracture of materials, in general, can be classified into brittle and ductile fractures. In the case of ductile fracture, the components undergo substantial plastic deformation prior to failure. This serves as a warning from which preventive measures can be taken to circumvent the catastrophic failure. However, in brittle fracture (for example, ceramics), the components undergo little or no plastic deformation. Hence, the cracks propagate at much faster rate in brittle materials and there are remote chances for avoiding catastrophic failure. In addition, the brittle materials have least resistance in the presence of defects in comparison to the

ductile materials and lack an exact strength parameter like yield strength. In these situations, fracture mechanics approach becomes more promising as it helps in characterizing the load-bearing capacity of the brittle materials using fracture parameters. Fracture mechanics can be classified into linear elastic fracture mechanics (LEFM) and elastic–plastic fracture mechanics (EPFM).

2.1 LEFM

A cracked body when loaded, the tip of the crack will be subjected to plastic strain leading to nonlinear mechanical behavior except in a perfectly brittle material. In situations, where the magnitude of the plastic deformation and nonlinearity is very small relative to the size of the crack, the linear theory is sufficient for the determination of stress–strain field at the crack tip. Thus, LEFM deals with quantifying the severity of crack situation subjected to linear elastic stress field [8]. Basically, there are three approaches in LEFM: (i) energy balance approach, (ii) stress intensity approach, and (iii) damage tolerance approach. The energy balance approach originally proposed by Griffith (1893–1963) uses energy release rate as a parameter to predict the fracture of a material. If the energy release rate is equal to or greater than the surface energy of the material, then the crack propagation takes place which leads to the failure of the material. In fact, the energy release rate serves "driving force" for the growth of the crack. Griffith claimed that the energy necessary for the formation of two new surfaces of a crack comes entirely from the surface energy. One of the major limitations of this approach is that it gives no information about the state of stress at tip of the crack and the estimation of the energy is difficult in situations where there is considerable plastic deformation. However, the former information can be obtained through the stress intensity approach. In 1957, George R Irwin (1907–1998) developed the stress intensity approach. In this approach, the fracture of a material is predicted by a parameter known as "stress intensity factor" (SIF). The SIF characterizes the state of stress field near the tip of the crack. This approach states that, the component fractures when the SIF reaches a critical value and is applicable only for materials with linear elastic behavior. The damage-tolerant approach is a major tool in the remaining life assessment of the in-service component. The phrase "damage tolerant" means the ability to resist fracture from a preexistent flaw for a specified period. Using this approach, it is thus possible to prevent the catastrophic failure of the components in service that could lead to loss of property and life. The damage or flaw in a component could occur due to manufacturing or design errors and also during service by unexpected sources. The size of the flaw present in the component is found through nondestructive techniques. Then, by applying this approach, the time taken for the flaw to reach to critical size (which is obtained through the stress intensity approach) can be estimated [9–11].

2.2 EPFM

As mentioned above, the LEFM is applicable when the plastic strain is restricted to a very small area around the tip of the crack (which is called as small-scale yielding). In addition, it estimates infinite stresses at the tip of the crack. The material, however, undergoes yielding at the tip of the crack in reality. Thus, when the material behavior is nonlinear and small-scale yielding cannot be assumed, it is not possible to apply LEFM, and hence an alternative approach is needed. The stress situation near the tip of the crack with significant plastic deformation can be characterized using EPFM. The two parameters used in EPFM to describe the crack tip conditions are the crack tip opening displacement (CTOD) and the J-integral. The CTOD was first proposed by Wells [12] in 1961. During his experiments on structural steels, Wells observed that application of LEFM for these materials was not possible. He also noticed that the crack faces of specimens made from these materials had moved apart with severe blunting prior to failure. The amount of crack blunting increased with the increase in the materials' toughness. This led to the proposal of CTOD as a fracture criterion by Wells. Another EPFM parameter was proposed by Rice in 1968 [13] called as J-integral which characterizes the stress field near the tip of the crack. J-integral is also a measure of material fracture toughness. It is applicable for both linear and nonlinear elastic materials. When an elastic–plastic material is loaded monotonically, the response after yielding is assumed to be equivalent of nonlinear elastic material provided no unloading occurs. It is under this assumption, J-integral is used to estimate the stress field ahead of the tip of the crack [14, 15]. Fracture occurs when either CTOD or J-integral approaches a critical value. CTOD is widely used in Britain while J-integral in United States. There are certain misunderstandings held about these EPFM parameters. Since J-integral is defined using a complex mathematical expression, it has been granted a high rank while CTOD is relatively simple parameter that quantifies the fracture toughness of a material. It is not appropriate to say definitely that one criterion is superior to the other as both J-integral and CTOD are related to each other. The numerical estimation of the J-integral is relatively easy than CTOD as numerical estimation of CTOD requires special elements to model the crack blunting. On the contrary, experimental determination of CTOD is easier than J-integral and many researchers prefer CTOD as it can be understood naturally [16].

3 Numerical Methods

The main objective of fracture mechanics is to obtain stress–strain distribution in the cracked body submitted to external loads. In simple cases, it is easy to arrive at closed-form solutions using analytical methods. As the geometry, loading and boundary conditions become intricate, it becomes too difficult for the analytical

methods to handle. In such circumstances, numerical techniques can be used to solve such complex problems. However, these techniques give approximate solutions. But, with the use of high-performance computers, the accuracy of the solution can be improved. There are several numerical methods available as of today to predict the onset of fracture. But, those which are reliable and frequently used are discussed below very briefly.

3.1 Stress–Energy Criterion

One of the new methods to enhance the fracture toughness of the ceramic material is to fabricate several layered ceramics with the internal layers subjected to residual compressive stresses which inhibit the propagation of cracks. Hence, it is imperative to understand the crack propagation in layered ceramics. The crack propagation investigation in brittle materials is often carried out in one of the standard specimen shapes like single edge notch bend. In order to perform this experiment, a sharp notch or a crack needs to be introduced in the specimen which is very difficult in brittle materials. Since the application of LEFM which uses Griffith's or Irwin's law to predict the fracture is not sufficient in this case as it cannot envisage the nucleation of a new crack particularly starting from a notch. Thus, an alternate method which predicts both nucleation and growth of the surface cracks in layered ceramics is needed. In this context, the stress–energy criterion was developed in the last decade. The stress–energy criterion specifies two conditions which are to be satisfied concurrently for the onset of a crack. The first condition is based on energy and the second is based on the stress. If the amount of energy available is sufficient to create a crack and the applied tensile stress is greater than the ultimate strength of the material, the crack propagates steadily. Thus, the crack nucleation is due to the energy aspect and propagation is due to stress aspect. Both criteria must be satisfied together for the stable crack growth [17].

3.2 Strain Energy Density Criterion

The Griffith or Irwin's theory of fracture mechanics is used to predict the onset of crack growth in brittle materials. In energy approach (Griffith's theory), the entire cracked body is assumed as a system and crack propagation is predicted based on the condition that if the elastic strain energy released is more than the energy required to form two new surfaces. On the other hand, Irwin used a stress parameter to predict the beginning of the growth of a crack. If the stress situation near the tip of the crack reaches a critical intensity, the crack growth occurs. These theories are limited to materials submitted to mode I loading where the crack propagates along the initial crack plane. Suppose if the material is subjected to combined loading, LEFM cannot give the whole picture of the crack mixed mode crack propagation.

Sih (1974) proposed a new theory based on strain energy density (SED) to address this problem. The theory states that crack nucleates along a particular direction having minimum strain energy density and it grows when the strain energy density reaches the critical value [18, 19]. Later several theories based on SED were proposed by various researchers like maximum tangential SED [20], minimum distortional SED [21], maximum dilatational SED [22], and averaged SED [23]. The averaged strain energy density criterion postulates that the component fractures when the averaged deformation energy within the control volume (the volume of material around the tip of the crack) approaches a critical value.

3.3 Discrete Element Method

Linear elastic fracture mechanics has seasoned enough to address the problem of fracture of brittle materials through the theory and experiments. Nevertheless, certain vital aspects like the crack meandering and branching have not been able to give complete explanation. Crack meandering is most often found in heterogeneous materials. The computational techniques can be promising in this situation to understand the stress situation around the heterogeneity. This could possibly lead to some understanding about the crack meandering [24, 25]. The polycrystalline ceramics contains pores and distinct particles bonded together arbitrarily. Techniques based on continuum models like finite element method, meshless methods, etc. can be employed to model the behavior of ceramics but struggle to simulate the finite deformations and relative movement of the discrete particles. However, the discrete element method (DEM) can model the behavior of granular particles and particle–fluid interaction. DEM was developed by Cundall [26] for analyzing the rock and soil mechanics (which requires modeling of granular materials). DEM is used in many fields like agriculture, mining, concrete technology, machining, and geotechnical applications [27]. This method considers a body or material as an assembly of different particles or blocks. Thus, it models the finite displacements and rotations of particles and identifies the new contacts on its own during the modeling process [28].

3.4 Finite Element Method

Finite element method (FEM) is a numerical method employed to arrive at approximate solutions to fracture mechanics problems. With the advent of computers, this method has become a famous tool as it can handle multidisciplinary problems and can deliver the solution at much faster rate. In this approach, the domain under investigation is divided into several small elements. The governing equation for each of the element is formulated in terms of the independent variables (also called as field variables) and is solved to obtain its values at the

interconnecting points. The values of the independent variables within the element are obtained through approximating functions or shape functions. The coefficients in the shape functions are obtained using the boundary conditions. The governing differential equation can be solved using variational principles like Rayleigh–Ritz and weighted residual methods. The accuracy of the solution can be improved by dividing the domain with more elements. In the context of fracture mechanics, FEM is used to obtain both LEFM and EPFM fracture parameters. The subroutines to estimate these parameters are readily available in most commercial finite element packages. In this work, the basic procedure to estimate the SIF is illustrated in the next section [9].

4   Numerical Simulation

Standard compact tension (CT) specimen is used to estimate the fracture toughness (K_{IC}) or the mode I SIF as per ASTM E399 standard [29]. The schematic of the CT specimen geometry and its dimensions is shown in Fig. 1. A 2D plane strain model is used for the estimation of the fracture toughness. A commonly used ceramic material like alumina (Al_2O_3, 99.5% pure) is used. Alumina has superior properties like high mechanical strength, wear resistant, temperature resistant, resistance to abrasion and corrosion, etc. Since the material behavior is under linear elastic regime, a linear elastic constitutive model is used in the analysis. The mechanical properties of alumina (99.5% pure) used in this analysis are given in Table 1. The

Fig. 1 Compact tension specimen geometry as per ASTM standard
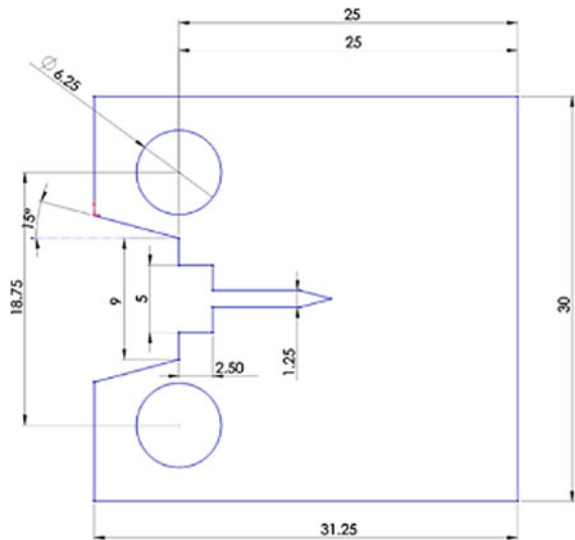
Table 1 Mechanical properties of Alumina

Material	Young's modulus E (*GPa*)	Poisson's ratio (*v*)	Density (ρ) *gm/cm³*
Al₂O₃	372	0.22	3.98

analysis is carried out in standard ABAQUS analysis package. The width of the specimen is 25 mm. The crack-length-to-width ratio was 0.5 as specified in the ASTM E399 standard.

After creating the geometry and uploading the material properties, the crack contour and the crack front using interaction option are specified. The contour integral method is selected in this analysis. In this method, the user will be prompted to specify the contour region around the tip of the crack and the crack extension direction. The next step is to mesh the model. The domain was discretized with CPS4R—A four-node bilinear plane stress quadrilateral, and reduced integration with hourglass control is used (Fig. 2). For benchmarking the problem, grid-independent analysis is carried out. The number of elements in the model was increased till a constant stress intensity factor (SIF) is reached. The variation of SIF with respect to the number of elements is shown in Fig. 3 modeling with different numbers of elements and SIF graph is plotted.

As can be seen from Fig. 3 that SIF steeply rise when the total number of element in the model is between 200 and 450. Then, the SIF decreases slightly and then maintains a constant value nearly after 600 elements. This indicates that the results are grid independent. In this analysis, nearly 900 elements are used. Figure 4

Fig. 2 Meshed geometry of CT specimen
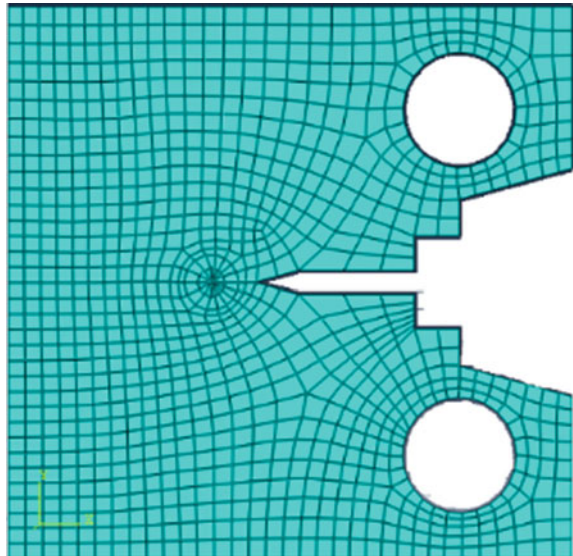
Fig. 3 Variation of SIF vs number of elements
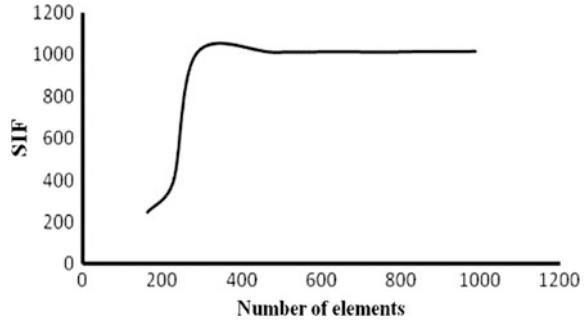
Fig. 4 Effect of a/w ratio on the SIF
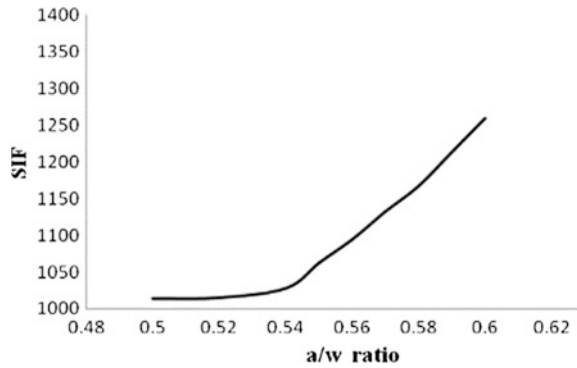
shows the influence of a/w ratio, where a is the crack length and w is the width of the specimen, on the SIF of the specimen. As the a/w ratio increases, the SIF increases. This is obvious as the crack length increases the stresses around the crack increases dramatically.

5   Conclusions

In this paper, a brief introduction to ceramics and their properties are listed. Due to the superior properties of ceramics, these are the most sought materials in various applications like gas turbines and components subjected to harsh environments. Therefore, it is vital to know about the techniques that give information about the remaining life of the components made of ceramics. In this context, the fracture mechanics is a viable tool as it can characterize the stress situation around the flaw using various fracture parameters. In addition, there are several numerical techniques which can help in determining these fracture parameters like stress–energy criterion, strain energy density criterion, SIF, J-integral, CTOD, etc. All of these

techniques have proven to be reliable and are used in in-service components. By using finite element method, these parameters can be easily estimated with the help of computers. This was exemplified in this work.

References

1. Callister Jr, Rethwisch DG (2005) Materials science and engineering—an introduction, 8th edn. Wiley, New York
2. Kwon SG, Lee YS, Kim JH, Lee JH, Hwang KT, Yoon SJ (2010) Fracture evaluation in a ceramic spherical dome port under shock impact. Expt Mech 50:589–597
3. Silva LH, Lima E, Favero SS, Lohbauer U, Cesar PF (2017) Dental ceramics: a review of new materials and processing methods. Braz Oral Res 31:133–146
4. Leguillon D, Martin E, Sevecek O, Bermejo R (2015) Application of the coupled stress-energy criterion to predict the fracture behavior of layered ceramics designed with internal compressive stresses. Eur J Mech A/Solids 54:94–104
5. Leguillon D (2002) Strength or toughness? a criterion for crack onset at a notch. Eur J Mech A/Solids 21:61–72
6. Evans AG (1974) The role of inclusions in the fracture of ceramic materials, J Mater Sci 9:1145–1152
7. Rice RW, Mecholsky JJ, Freiman SW, Morey SM (1978) Failure causing defects in ceramics: What NDE should find. In: Proceedings of the ARPA/AFML Review of Progress in Quantitative NDE, September 1976–June 1977, p 44
8. Gdoutos EE (2005) Fracture Mechanics—an introduction, 2nd edn. Springer, Dordrecht
9. Anderson TL (2005) Fracture mechanics—fundamentals and applications, 3rd edn. Taylor and Francis, Florida
10. Hertzberg RW (1976) Deformation and fracture mechanics of engineering materials. Wiley, New York
11. Grandt JrF (2011) Damage tolerant design and nondestructive inspection—keys to aircraft airworthiness. Procedia Eng 17:236–246. Elsevier
12. Wells AA (1961) Unstable crack propagation in metals: cleavage and fast fracture. In: Proceedings of the Crack Propagation Symposium, 1, Paper 84. Cranfield, UK
13. Rice JR (1968) A path independent integral and the approximate analysis of strain concentration by notches and cracks. J of App Mech 35:379–386
14. Hutchinson JW (1968) Singular behavior at the end of a tensile crack tip in a hardening material. J Mech Phy Sol 16:13–31
15. Rice JR, Rosengren GF (1968) Plane strain deformation near a crack tip in a power-law hardening material. J Mech Phy Sol 16:1–12
16. Anderson TL (1988) A Comparison of J-Integral and CTOD as Fracture Toughness Parameters. In: Read DT, Reed RP (eds) Fracture Mechanics: 18th Symposium, ASTM STP 945. Philadelphia, pp 741–753
17. Leguillon D, Martin E, Sevecek O, Bermejo R (2015) Application of the coupled stress-energy criterion to predict the fracture behaviour of layered ceramics designed with internal compressive stresses. Eur J Mech-A/Solids 54:94–104
18. Sih GC (1974) Strain-energy-density factor applied to mixed mode crack problems. Int J Fract 10(3):305–321
19. Ayatollahi MR, Rashidi Moghaddam M, Berto F (2015) A generalized strain energy density criterion for mixed mode fracture analysis in brittle and quasi-brittle materials. Theor Appl Fract Mech 79:70–76
20. Koo JM, Choy YS (1991) A new mixed mode fracture criterion: maximum tangential strain energy density criterion. Eng Fract Mech 39:443–449

21. Nabil Yehia AB (1991) Distortional strain energy density criterion: the Y-criterion. Eng Fract Mech 39:477–485
22. Theocaris PS, Andrianopoulos NP (1982) The mises elastic–plastic boundary at the core region in fracture criterion. Eng Fract Mech 16:425–432
23. Lazzarin P, Zambardi R (2001) A finite-volume-energy based approach to predict the static and fatigue behavior of components with sharp V-shaped notches. Int J Fract 112(3):275–298
24. Hedjazi L, Guessasma S, Della Valle G, Benseddiq N (2011) Finite element modelling of crack propagation in carbohydrate extruded starch with open void structure. Carbohyd Polym 83:1696–1706
25. Jiang SQ, Li X, Tan YQ (2017) Discrete element simulation of SiC ceramic with preexisting random flaws under uniaxial compression. Ceram Int 43:13717–13728
26. Jiang S, Li T (2015) Tan Y A DEM methodology for simulating the grinding process of SiC ceramics. Procedia Eng 102:1803–1810
27. Review Coetzee C J (2017) Calibration of the discrete element method. Powder Technol 310:104–142
28. Lisjak A, Grasselli G (2014) A review of discrete modeling techniques for fracturing processes in discontinuous rock masses. J Rock Mech Geotech Eng 6:301–314
29. ASTM E399–09 Standard Method for Linear-Elastic Plane Strain Fracture Toughness K_{IC} of Metallic Materials

Low Rolling Resistance Tires for E-Rickshaws for Increasing Range and Capacity

Prateek Bhatt and Umesh Kumar Vates

Abstract In the next 30–40 years, there will be an immediate need for an alternative method of transportation. Pollution is another major issue. Hence, electrically charged transport system is logically the best alternative for the future. I have focused on the electric rickshaws running in my city and it is the best and cheapest mode of transportation for city hops. In one charge, these e-rickshaws can run up to 80 km. But, what if the range of the e-rickshaw could be increased by reducing the energy losses and increase its range. One way this can be achieved is by reducing frictional resistance of tires used in e-rickshaws. It is found that 15% of the fuel is used in overcoming rolling resistance of the tires. This paper has presented different methods for reducing the rolling resistance on the tires of e-rickshaws. Silica is the most preferable material that can replace the traditionally used carbon black fillers. Various other methods are presented in this paper. Finally, the results are analyzed using Ansys software taking load factor and inflation pressure into consideration.

Keywords Silica · Carbon black fillers · Rolling resistance · Ansys · Inflation pressure

1 Introduction

The world is now facing a fuel crisis and fossil fuels are depleting at an alarming rate. Of all the CO_2 emissions in the United States, 33% comes from the transportation sector. Hence, electrically charged transport system is logically the best alternative for the future. I have focused on the electric rickshaws that are running in my city and are the best and cheapest mode of transportation for city hops. The e-Rrickshaws generally can carry up to five passengers. In one charge, these e-rickshaws can run up to 80 km but takes around 7–8 h to get a full charge again. But what if the range of the e-rickshaw could be increased by reducing the energy

P. Bhatt (✉) · U. K. Vates
Department of Mechanical Engineering, Amity University Noida, Noida, Uttar Pradesh, India
e-mail: prateek.bhatt777@gmail.com

losses and increase its range. In one way this can be achieved is by reducing the frictional resistance of the tires used in e-rickshaws. It is found that 15% of the fuel is used in overcoming the rolling resistance of the tires. This paper has presented different methods for reducing the rolling resistance on the tires of the e-rickshaws.

Silica is the most preferable material that can replace the traditionally used carbon black fillers [1]. Carbon black uses petroleum products for being used in a tire, and hence using silica will help protect the environment. In this paper, I have depicted the use of natural rubber instead of styrene–butadiene rubber [2, 3]. Natural rubber when used with a filler agent like TESPT (coupling agent) helps in cross-linking that increases the filler–filler interaction. Rolling resistance with silica-filled natural rubber decreases as temperature increases. Using vulcanized NR, silica interactions are highly improved. Now, industries are also using epoxidized natural rubber for obtaining more efficient results [4]. Research on using dynamically vulcanized rubber (DVA), that is, using resins with rubber for increasing its strength and ability to perform at high temperature and pressure [5]. Yokohama has been doing research on using orange peel juice in tires to make use of environmental friendly materials and reduce rolling resistance. Finally, analysis has been done comparing effect of load on rolling resistance of a vehicle, and effect of inflation pressure and speed on rolling resistance of a tire. The final results are observed using graphs [6, 7].

2 Tire Properties of an E-Rickshaw

The tire used in e-rickshaw is a 10-inch wheel containing air inside it. It is generally made of synthetic rubber, natural rubber, wires and fabric, and carbon black mixed with other alloys. The tires manufactured today consist of cord that contains the ply and an elastomer which encases them. The cord provides the tensile strength necessary to contain the high inflation pressures. It can be made of natural fibers like silk cotton or synthetic fibers like nylon and Kevlar.

The elastomer encases the cords to protect them from wearing and to hold the cord in place. An elastomer is a composite of rubber materials like styrene–butadiene rubber along with other chemical compounds like silica and carbon black for giving it strength. The tire used e-rickshaw is made slimmer (lesser width) to reduce the rolling resistance while running on the road. But, at the same time, it has to be made strong enough to have up to 1 ton loading capacity without any failure.

The industrial tire grade of e-rickshaw is 314(90/90-12),

Tire diameter = 526 mm (under normal inflation),

Minimum tire inflation = 514 mm (under low inflation)/Maximum tire inflation = 538 mm (under high inflation),

Section width = 80 mm,

Minimum section width = 77 mm/Maximum section width = 86 mm,

Tire strength (Ply Rating) = 6 pr,

Loading index = 165 kg,

Maximum allowable speed = 65 km/hr,
Inflexion pressure = 40 psi, and
Inflexion pressure is the maximum allowable air pressure inside the tire.

3   The Rolling Resistance of a Tire Can Be Expressed As

$$F_r = cW,$$

where F_r is the rolling resistance in Newton, c is the coefficient of rolling resistance,

$W = ma_g$, where W = weight of the body or the normal force (N),
m = mass of body (in kg), and
a_g = acceleration due to gravity (9.81 m/s^2).

The rolling coefficient for air-filled tires on a dry road is calculated as

$$c = 0.005 + (1/p)\left(0.01 + 0.0095\left(v/100^2\right)\right),$$

where

p = tire pressure (bar),
v = velocity (km/hr).

4   How to Reduce the Rolling Resistance on These Tires Using Silica Fillers

A conventional tire contained about 28% natural rubber, 28% synthetic rubber along with 28% carbon black filler which is produced by burning fossil fuels. To make the system eco-friendly, now silica fillers that contain surface-treated sand micro-particles are used to replace the carbon black fillers. This compound helps in reducing the frictional heat created by the rubber during operation. Hence, this way a tire containing about 97% of natural ingredients reduces the environmental impact steadily. But now with more efforts into research, polymeric fillers are replacing the silica in many countries. These fillers are more efficient and use only 10–12 phr of its constituents instead of 30–60 phr of silica filler used to reinforce rubber. This helps in reduction of overall weight of the tire, thus making them more efficient to use. Another advantage of polymeric fillers is that they do not need the use of polycyclic oils, mineral/vegetable oils for aiding in dispersion of filler for reducing the viscosity of the compound.

Silica fillers used today applies solution-polymerized elastomer butadiene rubber and solution styrene–butadiene rubber (S-SBR). However, using natural rubber with silica fillers remains a challenge. Silica is a polar and hydrophilic reinforcing

filler. There are a number of non-rubber constituents in natural rubber. Hence, using epoxidized natural rubber (ENR) and deproteinized natural rubber (DPNR) are being developed for better interactions between natural rubber and silica. Good dispersion properties of silica into rubber mixture are very important. Coupling agents are pre-reacted with the rubber compound during the mixing stage of rubber and silica. TESPT and bis(triethoxysilylpropyl)disulphide (TESPD) are the most effective coupling agents used till now. TESPT is actually a tetrasulphide that is a mixture of silane groups. When mixing silica with rubber compounds, these coupling agents react with silica resulting in the hydrophobation of the surface of silica. This process stops the formation of silica–silica bonds, thus making silica compatible to mix with a nonpolar rubber. The hydrolyzable group of silane affects the reactivity of the coupling agent. Among all the groups, ethoxy group C_2H_5O- is the most preferred silanization agent because its toxicity can be controlled and it reacts fast enough to make the reactions on time.

During tests, it is observed that at temperatures above 150 °C, viscosity of the rubber compound increased due to premature curing of rubber. The premature curing takes place due to sulfur in TESPT (coupling agent). At higher temperatures, rubber becomes softer, breaking down of chains of natural rubber and silica structures. The natural rubber reacts with TESPT at temperatures starting at 120 °C and reaction rate increases at higher temperatures. But, at temperatures above 150 °C, the reaction rate decreases. Hence, viscosity of silica-TESPT depends on premature cross-linking reaction of sulfur along with the salinization reaction. Filler–filler interaction also takes place (known as Payne effect). But, at the optimum temperature range of 135–150 °C, the filler–rubber interaction is maximum instead of filler–filler interaction. It is due to hydrophobation, a light cross-linked networked due to smaller amount of cross-linking during mixing. The rolling resistance of tires with silica filled NR decreases as the tires temperatures are increased to most optimum in the range of 135–150 °C along with 10 min of mixing interval of silica–silane rubber after mastication, thus improving the fuel efficiency and decreasing the environmental effect of tire manufacturing process.

5   Result and Discussion

Steady-state thermal analysis is performed using proper boundary conditions. Hence, temperature distribution in a rolling tire is obtained. While performing the simulation isotropic, homogeneous, and hyper-elastic properties of rubber are taken. In this simulation, the variation of rolling resistance with respect to different loading conditions is taken. After simulation, it is found that rolling resistance increases as load on the vehicle is increased. Inflation pressure is applied on the internal surface of the tire. The coefficient of friction between tire and road is set at 0.7, to avoid any slip condition between the two surfaces during simulation. The von Mises stress is maximum on the contact region between tire and the road. The principle strain is maximum on sidewalls of the tire. The stresses and strains caused
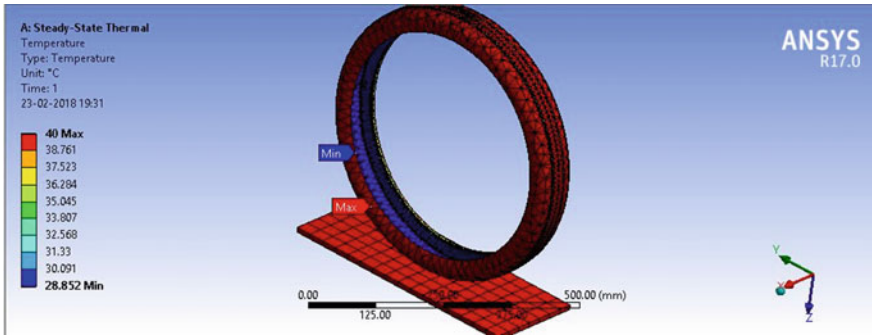
Fig. 1 Temperature variation in the tire using Steady state thermal analysis

by external loading help in evaluating the total strain energy stored in the tire. High strain energy is obtained near the contact region. As the load on the tire increases, the energy dissipation also increases, thus increasing the rolling resistance (Figs. 1, 2, 3, 4, 5, 6, 7, 8, 9, and 10).

Temperature variation in the tire using Steady state thermal analysis. The minimum temperature is around 29 °C at the inner surface and maximum goes up to 40 °C on the outer tread surface. Although with increasing speed tread temperature increases and causes wear to the tires.

The stress analysis (von Mises) is performed. Maximum stress is observed at the sidewalls of the tire.

The strain energy is maximum at the contact patch between tire and road. More the strain energy density, more are hysteresis losses, which lead to more rolling resistance.

Three loading conditions are taken. Initially, only the kerb mass of vehicle is taken, i.e., 350 kg. Then, load of five passengers is taken as 300 kg that makes the total mass up to 650 kg. Finally, luggage load of 40 kg is taken that makes the total
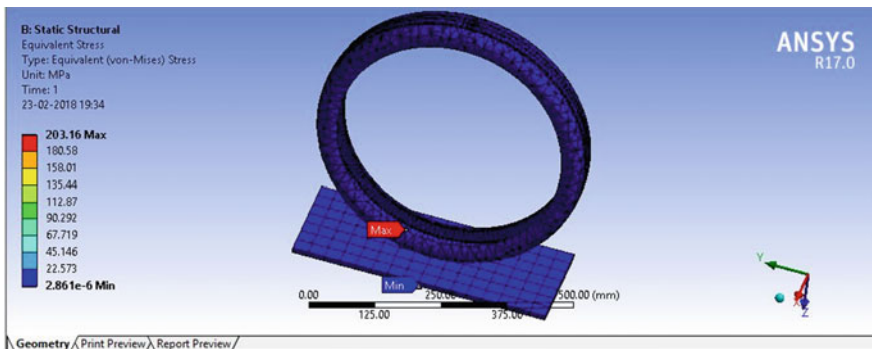
Fig. 2 Stress is observed at the side walls of the tire
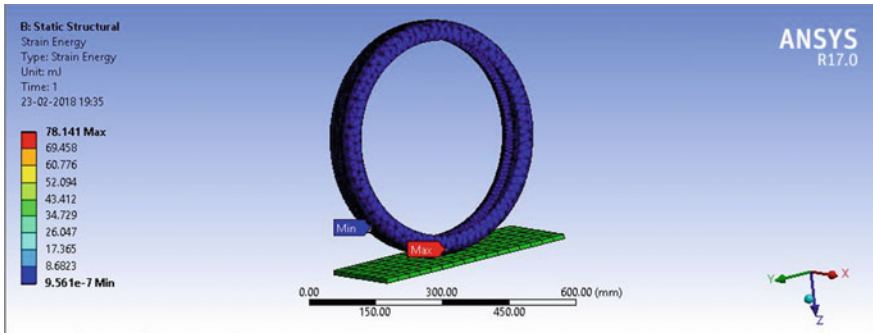
Fig. 3 Strain at the contact patch between tire and road
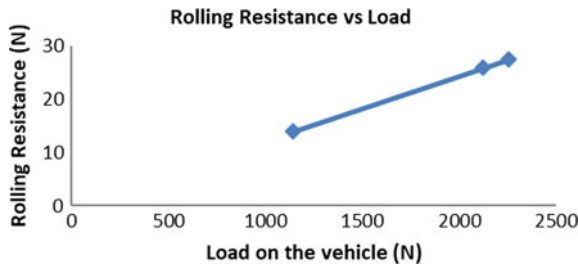
Fig. 4 As the load on the vehicle increases, rolling resistance also increases
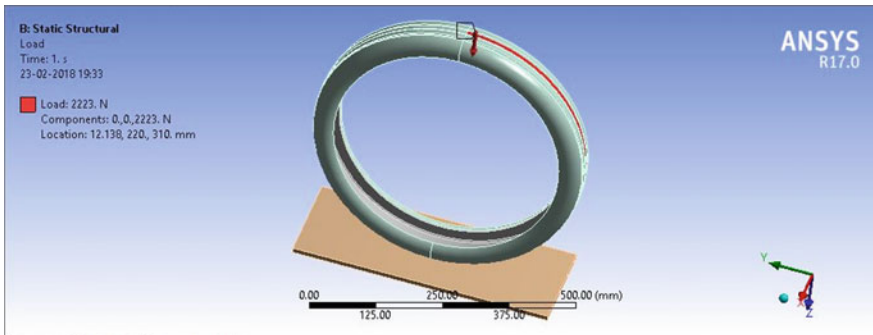
Fig. 5 Maximum loading capacity on each tire

mass equal to 690 kg. Weight of the vehicle will be = 690∗9.81 = 6768.9 N. Hence, load on each wheel = 6768.9/3 = 2256.3 N. This load is used to calculate the rolling resistance on each wheel, $F_r = cW$, where F_r is the rolling resistance in Newton, c is the coefficient of rolling resistance, $W = ma_g$. In this way, different rolling resistances are calculated for different loading conditions.
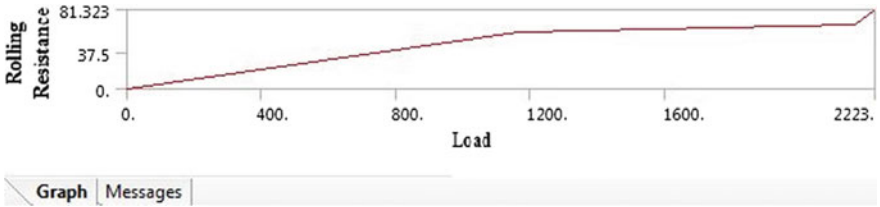
Fig. 6 Rolling resistance versus load obtained after analysis of the result in Ansys
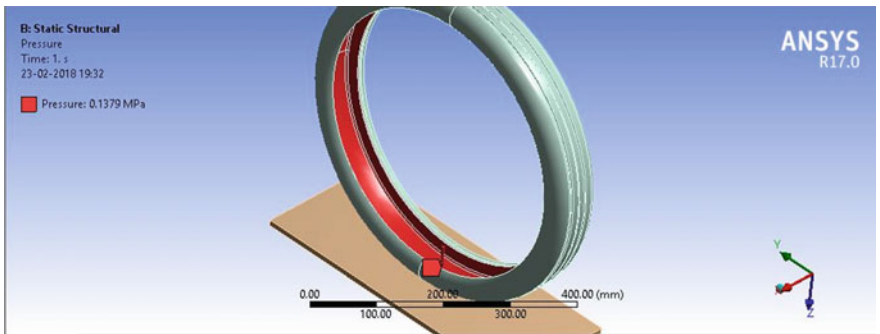
Fig. 7 Inflation of pressure on tires
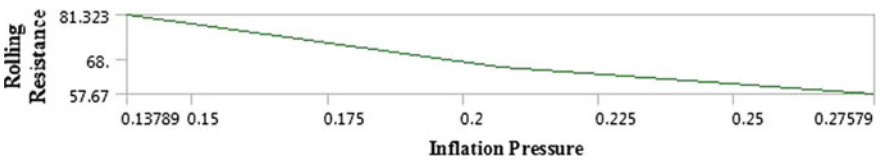
Fig. 8 Graph obtained by performing static analysis in Ansys

Case 1 Keeping inflation pressure and speed constant, variation of rolling resistance with load on the vehicle is shown in Table 1.

It is observed that with the increase in the load on the vehicle, the contact patch of tire and road also increases. Due to this, more energy dissipation takes place. The strain energy density also increases that increases the rolling resistance on the tire. With the maximum amount of stress at the contact region of tire and road, by evaluating stress and strains caused by external loading, the strain energy and rolling resistance can be calculated.

Fig. 9 Rolling resistance vs
inflation in pressure of tires
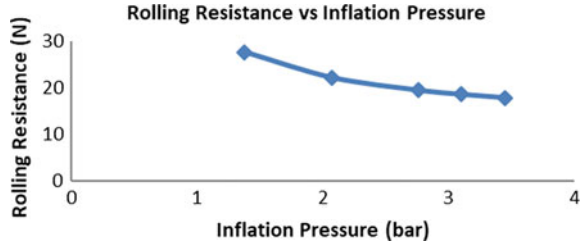
Fig. 10 Rolling resistance vs
vehicles speed in pressure of
tires
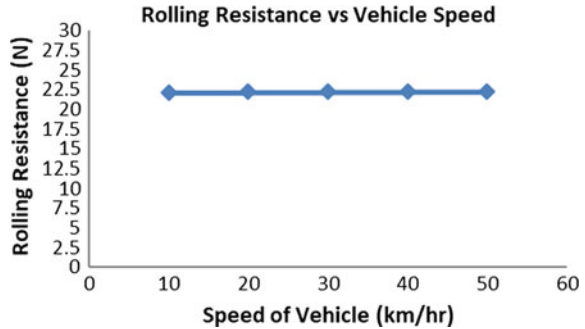
Table 1 Keeping inflation pressure and speed constant, variation of rolling resistance with load
on the vehicle

S.No.	Rolling resistance (N)	Inflation pressure (bar)	Load (N)	Speed (km/hr)
1	13.962	1.378	1144.5	20
2	25.931	1.378	2125.5	20
3	27.526	1.378	2256.3	20

The load of the vehicle + Passenger weight + Luggage is assumed to be dis-
tributed equally among three tires of the e-rickshaw, with the maximum loading
capacity on each tire to be 2256.3 N

Case 2 Taking a constant load of 2256.3 N (maximum loading condition) and a
constant speed of 25 km/hr, the inflation pressure is varied. It is calculated from the
result that as the inflation pressure increases, rolling resistance decreases as shown
in Table 2.

Table 2 Taking a constant load of 2256.3 N (maximum loading condition) and a constant speed
of 25 km/hr, the inflation pressure is varied

S.No.	Rolling resistance (N)	Inflation pressure (bar)	Load (N)	Speed (km/hr)
1	27.66	1.378	2256.3	25
2	22.21	2.0684	2256.3	25
3	19.48	2.7579	2256.3	25
4	18.57	3.102	2256.3	25
5	17.84	3.4473	2256.3	25

Table 3 Observing the variation of rolling resistance with the vehicle speed, the load and inflation pressure are kept constant

S.No.	Rolling resistance (N)	Inflation pressure (bar)	Load (N)	Speed (km/hr)
1	22.20	2.0684	2256.3	10
2	22.21	2.0684	2256.3	20
3	22.21	2.0684	2256.3	30
4	22.23	2.0684	2256.3	40
5	22.24	2.0684	2256.3	50

Pressure on the inner liner (inflation pressure) plays a vital role in reducing rolling resistance. More the inflation pressure, less the amount of energy dissipated, and hence less is the rolling resistance.

As the inflation pressure is increased, rolling resistance decreases. With 50% increase in inflation pressure, rolling resistance decreases by 19.7% (keeping Load and speed constant).

Case 3 For observing the variation of rolling resistance with the vehicle speed, the load and inflation pressures are kept constant. Finally, rolling resistance at different speeds is calculated as shown in Table 3.

6 Conclusion

From the above results, it is observed that rolling resistance remains almost constant with the increasing vehicle speed. Although between 30–40 km/hr, it increases slightly. But, at speeds above 80 km/hr, rolling resistance becomes a factor of concern as heat dissipation starts to increase. This also increases tire wear and reduces efficiency of the vehicle.

References

1. Sarkawi SS, Kaewsakul W, Sahakaro K, Dierkes WK, Noordermeer JWM (2015) A review on reinforcement of natural rubber by silica fillers for use in low-rolling resistance tires. J Rubb Res 18(4):203–233
2. Cho JR, Shin SW, Yoo WS (2005) Tyre performance optimization for enhancing tire wear performance by ANN. Comput Struct 83:920–933
3. Duez B (2016) Towards a substantially lower fuel consumption freight transport by the development of an innovative low rolling resistance truck tyre concept. Transp Res Procedia 14:1051–1060. Goodyear Innovation Center, Rue Gordon Smith, L-7750 Colmar-Berg, Luxembourg
4. Sarkawi SS, Kaewsakul W, Sahakaro K, Dierkes WK, Noordermeer JW (2015) A review on reinforcement of natural rubber by silica fillers for use in low-rolling resistance tyres. J Rubb Res 18(4):203–233

5. Hara Y, Kirino Y (2012) Environmental compound technology for tyres. Int Polym Sci Technol 6:187–192. Nippon Gomu Kyokaishi
6. Shida Z, Koishi M, Kogure T, Kabe K (1999) A rolling resistance simulation of tires using static finite element analysis. Tire Sci Technol 27(2):84–105
7. Ebbott TG, Hohman RL, Jeusette JP, Kerchman V (1999) Tire temperature and rolling resistance prediction with finite element analysis. Tire Sci Technol 27:2–21
8. Hall DEAND, Moreland JC (2000) Fundamentals of rolling resistance. Rubb Chem Technol 74:525–539
9. Korunović N, Madić M, Trajanović M, Radovanović M (2015) A procedure for multi-objective optimization of tire design parameters. Int J Ind Eng Comput 6:199–210
10. Lin Y-J, Hwang S-J (2004) Temperature prediction of rolling tires by computer simulation. Math Comput Simul 67:235–249
11. Kraus G (1978) Reinforcement of elastomers by particulate fillers. In: Eirich F (ed) Science and Technology of Rubber. Academic Press, New York
12. Tang T, Johnson D, Ledbury E, Goddette T (2012) Simulation of thermal signature of tires and tracks. In: 2012 NDIA ground vehicle systems engineering and technology, August 14–16, Michigan
13. Golbakhshi H, Namjoo M (2015) An efficient numerical scheme for evaluating the rolling resistance of a pneumatic tire. Dep Mech Eng Bio Syst 78671–61167. University of Jiroft, Jiroft, Iran

A Comparison of Recent Experimental Techniques to Measure Acoustic Properties of a Muffler

Utkarsh Chhibber, Ranjeet Kumar, Sunali and R. N. Hota

Abstract The transmission loss (TL) is an important acoustic property to evaluate the performance of a muffler, which needs to be thoroughly discussed and analyzed. In this work, the two most commonly used techniques for obtaining TL, i.e., two-load method and two-source method are discussed and compared experimentally. The experiments have been done using various in-house fabricated mufflers with different geometrical dimensions. The muffler being used for experiments is extended tube resonator. An impedance tube has been used for determination of TL experimentally. Experimental results obtained for TL using the two methods are compared qualitatively and it has been observed that in some cases, two-load method gives clear frequency information as compared to the two sources in high-frequency ranges. However, good agreements between the two methods were obtained in most cases.

Keywords Two-load method · Two-source method · Transmission loss

1 Introduction

The most common technique today to characterize a muffler experimentally is by the use of an impedance tube. In the recent past, various methods have been developed to measure the bulk acoustic properties of a muffler using an impedance tube starting from two-cavity method [1], four-pole parameter method [2], and two-wave decomposition method [3].

Initially, Yaniv et al. [1] gave the two-cavity method which determines the characteristic impedance and propagation constant by investigation of standing wave patterns inside the tube driven at one end by sound source and at another end by a sample backed by a rigid wall and a sample backed by an air space, a quarter wave long, itself terminated in a rigid wall. However, there are some sources of

U. Chhibber (✉) · R. Kumar · Sunali · R. N. Hota
Department of Mechanical Engineering, IIT (ISM) Dhanbad, Dhanbad 826004, India
e-mail: chhibber.utkarsh@yahoo.in

inaccuracies in it, like the variation associated with the mounting of the sample in the impedance tube, which could lead to unequal compression of the acoustic sample. Utsuno and Seybert [4] later gave an improved two-cavity method in 1989.

Another method developed was standing wave ratio technique (SWR) [5] in which a traveling microphone is used to find the location and magnitude of consecutive maxima and minima of a standing wave pattern in an impedance tube. After obtaining their ratio, the reflection coefficient is calculated and absorption coefficient is obtained. The main drawback of this method is the traversing microphone. Use of traversing microphone increases errors while taking the measurements.

However, all of the abovementioned methods gave absorption coefficient, but transmission loss (TL) being one of the essential parameters used in design and development of Mufflers is not obtained by any of the aforementioned. In 1990, Munjal and Doige [2] gave a two-source method in which an acoustic-based element was modeled using a four-pole parameter method. In this method, the wave is assumed to follow plane wave propagation at the inlet and the outlet sections of the element inside an impedance tube. Four pole is basically a method to relate velocity and pressure at inlet to outlet of the element. By applying the four-pole parameter method, the inevitable properties like transmission loss of a muffler as well as any acoustical element like liners can be calculated.

Later, in 2004, ASTM began developing a standard for obtaining normal incidence absorption coefficient. In this method, an impedance tube is used inside which the test sample is mounted. A sound source such as a speaker is attached to one end of the tube. To get transmission loss, four microphones are mounted on each side of the sample at two locations. Further, the wave is segregated into forward and backward traveling waves by measurement of complex sound pressure level simultaneously at four locations, and then examination of their relative amplitude and phase, which is why it is called wave decomposition method [3].

In this paper, the two most preferred techniques; two-load method (ASTM E 26 11) and two-source method are presented in detail. Also, in comparative analysis, the results of the two methods and the advantages of the two-load method in determination of TL are presented. The following paper is organized as in Sect. 2, the two-source method is presented; in Sect. 3, two-load method is discussed; and in Sect. 4, experimental results and discussion are given.

2 Two-Source Method

Two-source method envisages that an acoustical specimen can be successfully modeled using the four-pole parameters. It is based on transfer matrix approach. A transfer matrix relates the input parameter to the output parameter of the selected

Fig. 1 The four poles
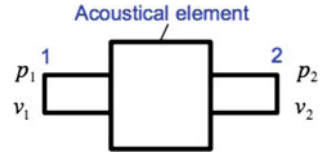
element. A schematic of four poles is shown in Fig. 1. The transfer matrix can be written as

$$\begin{bmatrix} p_1 \\ v_1 \end{bmatrix} = \begin{bmatrix} A & B \\ C & D \end{bmatrix} \begin{bmatrix} p_2 \\ v_2 \end{bmatrix},$$

(1)

where

p_1: pressure amplitude of sound wave at inlet section,
p_2: pressure amplitude of sound wave at outlet section,
v_1: velocity amplitudes at inlet section,
v_2: velocity amplitude at outlet section, and
A, B, C, and D are the four-pole parameters.

The sound source placement in two sources is shown in Fig. 2. Two configurations are shown in "a" and "b". First configuration "a" will be analyzed. We can easily obtain four-pole equations using transfer matrix method for the elements between microphones 1–2 and 3–4. Likewise, for element 2–3, the four-pole equation can also be expressed. Here, the example element is taken as a muffler, and it could also be a screech liner in its place. The four-pole equation of element is given as

$$\begin{bmatrix} p_{2a} \\ v_{2a} \end{bmatrix} = \begin{bmatrix} A & B \\ C & D \end{bmatrix} \begin{bmatrix} p_{3a} \\ v_{3a} \end{bmatrix},$$

(2)

Fig. 2 Schematic of two-source method

where "a" in the subscript is used for Configuration "a" as shown in Fig. 2. Then, comparing the four-pole expressions for different elements, i.e., 1–2, 3–4, and 2–3, the equation

$$
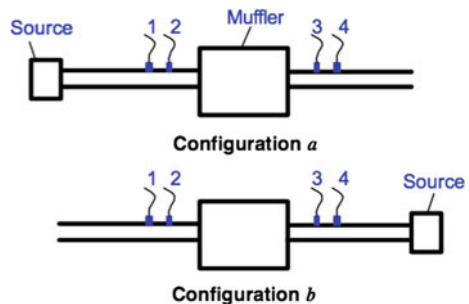\begin{bmatrix} p_{2a} \\ \frac{1}{B_{12}}(p_{1a} - A_{12}p_{2a}) \end{bmatrix} = \begin{bmatrix} A_{23} & B_{23} \\ C_{23} & D_{23} \end{bmatrix} \begin{bmatrix} p_{3a} \\ \frac{D_{34}}{B_{34}}p_{3a} + (C_{34} - \frac{D_{34}A_{34}}{B_{34}})p_{4a} \end{bmatrix}
\tag{3}
$$

is obtained, where A_{ij}, B_{ij}, C_{ij}, and D_{ij} are the respective notations for the four poles defined for test specimen i–j, p_{ia} and v_{ia} are the respective sound pressure and particle velocity at point "i" for Configuration a.

Here, in Eq. (3), we can see that there are two equations and four unknowns. We can get two additional equations by displacing the sound source from one end to the other end and all four poles of element 2–3 can be obtained. For Configuration "b", it can be then written as

$$
\begin{bmatrix} p_{3b} \\ v_{3b} \end{bmatrix} = \begin{bmatrix} A_{23} & B_{23} \\ C_{23} & D_{23} \end{bmatrix} \begin{bmatrix} p_{2b} \\ v_{2b} \end{bmatrix} = \frac{1}{\Delta} \begin{bmatrix} D_{23} & B_{23} \\ C_{23} & A_{23} \end{bmatrix} \begin{bmatrix} p_{2b} \\ v_{2b} \end{bmatrix},
\tag{4}
$$

where Δ is the value of the determinant of the matrix, where $\Delta = A_{23}D_{23} - B_{23}C_{23}$ and minus sign "−" is for change in the direction of velocity.

By applying the same methodology as used earlier, another equation can be written comprising of four poles as

$$
\begin{bmatrix} p_{3b} \\ \frac{-1}{B_{34}}(\Delta_{34}p_{4b} - D_{34}p_{4a}) \end{bmatrix} = \frac{1}{\Delta} \begin{bmatrix} D_{23} & B_{23} \\ C_{23} & A_{23} \end{bmatrix} \begin{bmatrix} p_{2b} \\ (\frac{C_{12}}{\Delta_{12}} - \frac{A_{12}D_{12}}{\Delta_{12}B_{12}})p_{1b} - (\frac{p_{2b}A_{12}}{B_{12}}) \end{bmatrix},
\tag{5}
$$

where $\Delta_{12} = A_{12}D_{12} - B_{12}C_{12}$, $\Delta_{34} = A_{34}D_{34} - B_{34}C_{34}$. p_{ib} are the respective sound pressures and v_{ib} is the respective particle velocity for point i of Configuration "b". Then, from Eqs. (3) and (5), the four poles for Configuration "b" can now be simplified as

$$
A_{23} = \frac{\Delta_{34}(H_{32a}H_{34b} - H_{32b}H_{34a}) + D_{34}(H_{32b} - H_{32a})}{\Delta_{34}(H_{34b} - H_{34a})}
\tag{6}
$$

$$
B_{23} = \frac{B_{34}(H_{32a} - H_{32b})}{\Delta_{34}(H_{34b} - H_{34a})}
\tag{7}
$$

$$
C_{23} = \frac{(H_{31a} - A_{12}H_{32a})(\Delta_{34}H_{34b} - D_{34}) - (H_{31b} - A_{12}H_{32b})(\Delta_{34}H_{34} - D_{34})}{B_{12}\Delta_{34}(H_{34b} - H_{34a})}
\tag{8}
$$

$$
D_{23} = \frac{B_{34}(H_{31a} - H_{31b}) + A_{34}(H_{32b} - H_{32b})}{B_{12}\Delta_{34}(H_{34b} - H_{34a})},
\tag{9}
$$

where $H_{ij} = p_j/p_i$, which is evaluated by the assumption of neglecting flow, then four poles for respective elements 1–2 and 3–4 can be given by [6]

$$\begin{bmatrix} A_{12} & B_{12} \\ C_{12} & D_{12} \end{bmatrix} = \begin{bmatrix} \cos kl_{12} & j\rho \, \sin kl_{12} \\ j \, \sin kl_{12}/\rho c & \cos kl_{12} \end{bmatrix}, \Delta_{12} = 1 \tag{10}$$

$$\begin{bmatrix} A_{34} & B_{34} \\ C_{34} & D_{34} \end{bmatrix} = \begin{bmatrix} \cos kl_{34} & j\rho \, \sin kl_{34} \\ j \, \sin kl_{34}/\rho c & \cos kl_{34} \end{bmatrix}, \Delta_{34} = 1, \tag{11}$$

respectively. In Eqs. (10) and (11), l_{12} and l_{34} are the spaces between the microphones designated for respective elements 1–2 and 3–4. The TL is then represented in terms of two parameters, i.e., the four poles and tube area, as [7]

$$TL = 20 \log_{10} \left\{ A_{23} + \frac{B_{23}}{\rho c} + \rho c C_{23} + D_{23} \right\}, dB. \tag{12}$$

3 Two-Load Method

As the name signifies, the two-load method requires two different terminations (loads) for obtaining the absorption coefficient.

In this method also, like all other methods, an impedance tube is used, but here we use four microphones, two on either side of the test sample. Here also, we use a loudspeaker on one end of the impedance tube. The test specimen is mounted inside the tube. All the four microphones with the support of holders are flush mounted inside the tube. A broadband signal generator is used for generation of plane waves inside the tube which results in the formation of a pattern as shown by standing waves, which is further segregated into forward and backward traveling waves A, B, C, and D as shown in Fig. 3.

This wave decomposition is done by the measurement of complex sound pressure amplitude at four specified locations simultaneously, and then analyzing their relative amplitude and phase. From there, the pressure and particle velocity are obtained, which are further used to obtain transfer matrix elements. And, these transfer matrix elements can yield us, the absorption coefficient, acoustic impedance, and other important properties as shown in Fig. 3 [3].

In this method, collection of microphone data for two loads (in the form of complex acoustic transfer functions between the reference and the remaining microphones) is the first step.

For each load case, on each side of the specimen, the acoustic wave field inside the tube is decomposed into forward and backward traveling waves, indicated in Fig. 3 using equations (Using microphone 1 as reference microphone).
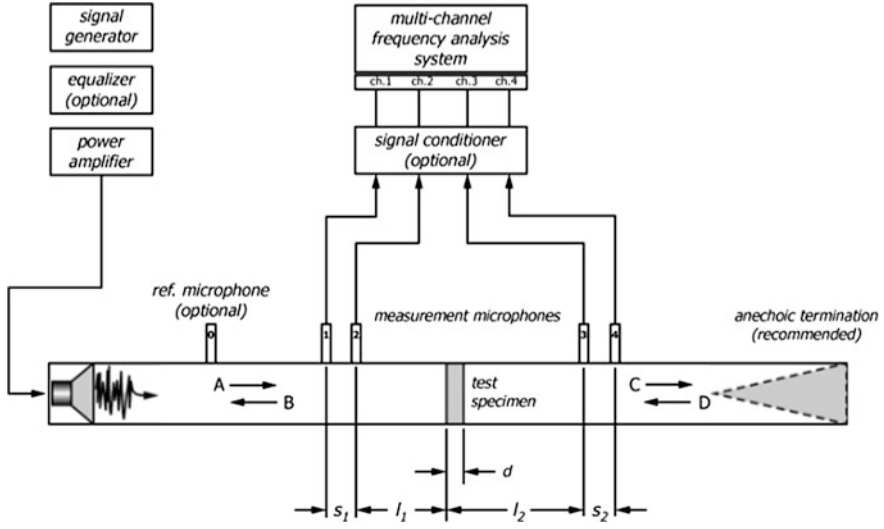
Fig. 3 Set up for two-load method

$$A = i\frac{\left[H_{11}e^{-ikl_1} - H_{21}e^{-ik(l_1 + s_1)}\right]}{2\sin(ks_1)} \tag{13}$$

$$B = i\frac{\left[H_{21}e^{ik(l_1 + s_1)} - H_{11}e^{ikL_1}\right]}{2\sin(ks_1)} \tag{14}$$

$$C = i\frac{H_{31}e^{ik(l_2 + s_2)} - H_{41}e^{ikl_2}}{2\sin(ks_2)} \tag{15}$$

$$D = i\frac{\left[H_{41}e^{-ikL_2} - H_{31}e^{-ik(l_2 + s_2)}\right]}{2\sin(ks_2)}. \tag{16}$$

Calculating the pressure and velocity at each side of the specimen, we will get

$$p_0 = A + B \tag{17}$$

$$u_0 = \frac{(A - B)}{c\rho} \tag{18}$$

$$p_d = Ce^{-ikd} + De^{ikd} \tag{19}$$

$$u_d = \frac{(Ce^{-ikd} - De^{ikd})}{c\rho}. \tag{20}$$

From the pressure and particle velocity values in each load case, calculate the transfer matrix for the specimen as given below:

$$\begin{bmatrix} p_0 \\ u_0 \end{bmatrix}_{loada} = \begin{bmatrix} T_{11} & T_{12} \\ T_{21} & T_{22} \end{bmatrix} \begin{bmatrix} p_d \\ u_d \end{bmatrix}_{loada}. \tag{21}$$

Determination of transfer matrix elements:

Relation to find transfer matrix as per ASTM 2611-09 [5] using pressure and velocity is

$$\begin{bmatrix} p_0 \\ u_0 \end{bmatrix}_{loadb} = \begin{bmatrix} T_{11} & T_{12} \\ T_{21} & T_{22} \end{bmatrix} \begin{bmatrix} p_d \\ u_d \end{bmatrix}_{loadb}. \tag{22}$$

From Eq. (22), we have four unknowns and four equations. By solving this, we will get

$$T_{11} = \frac{p_o^a.u_d^b - p_o^b.u_d^a}{p_d^a.u_d^b - p_d^b.u_d^a} \tag{23}$$

$$T_{12} = \frac{p_o^b.p_d^a - p_o^a.p_d^b}{p_d^a.u_d^b - p_d^b.u_d^a} \tag{24}$$

$$T_{21} = \frac{u_o^a.u_d^b - u_o^b.u_d^a}{p_d^a.u_d^b - p_d^b.u_d^a} \tag{25}$$

$$T_{22} = \frac{p_d^a.u_0^b - p_d^b.u_0^a}{p_d^a.u_d^b - p_d^b.u_d^a}. \tag{26}$$

After calculating transfer matrix, using elements of transfer matrix (T_{11}, T_{12}, T_{21}, T_{22}), we can calculate all the acoustic properties of an acoustic material.

Transmission Coefficient:

$$t = \frac{2e^{ikd}}{T_{11} + \frac{T_{12}}{\rho c} + T_{12}\rho c + T_{22}}. \tag{27}$$

Normal Incidence Transmission Loss:

$$TL_n = 20 \log_{10}(1/t). \tag{28}$$

4   Experimental Results and Discussion

Figure 4 shows a schematic line diagram for the test element taken in this study which is an extended outlet type muffler. The extended part L_1 is varied by several lengths to perform different experiments. Different mufflers have been fabricated to test by both techniques, i.e., two-load and two-source methods.

An impedance tube of 43.54 mm dia was used having a cutoff range of 5 kHz and B&K sensors and signal generators were used to take the measurements using a random white noise.

The test elements geometric dimensions are given as follows:
Inner diameter = 43.54 mm, Outer diameter = 70.40 mm,
Length of chamber = 50.38 mm,
Outlet lengths taken are L_1 = 10.90 mm, 11.58 mm, and 19.68 mm.
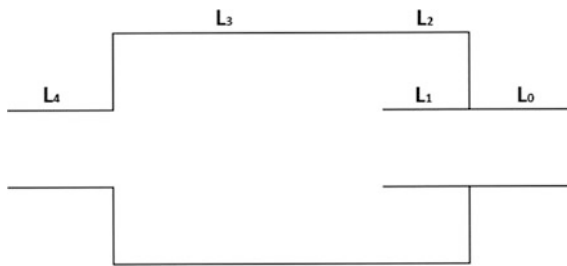
Fig. 4 Block diagram of test muffler
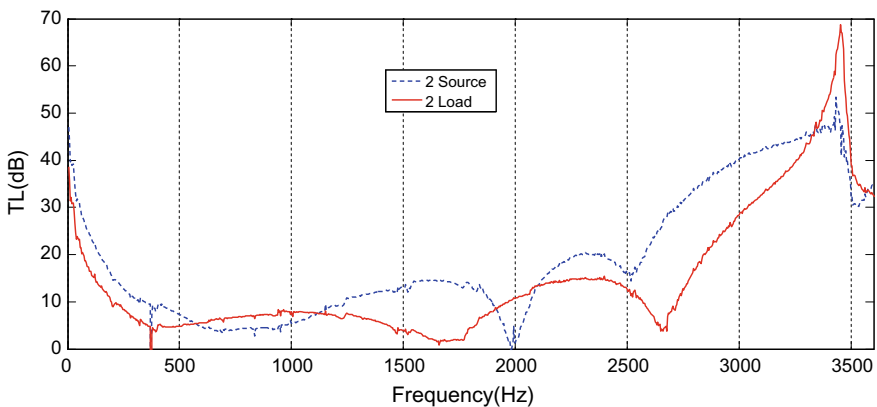
Fig. 5 Comparison of experimental results for two-source and two-load methods for L1 = 10.90 mm
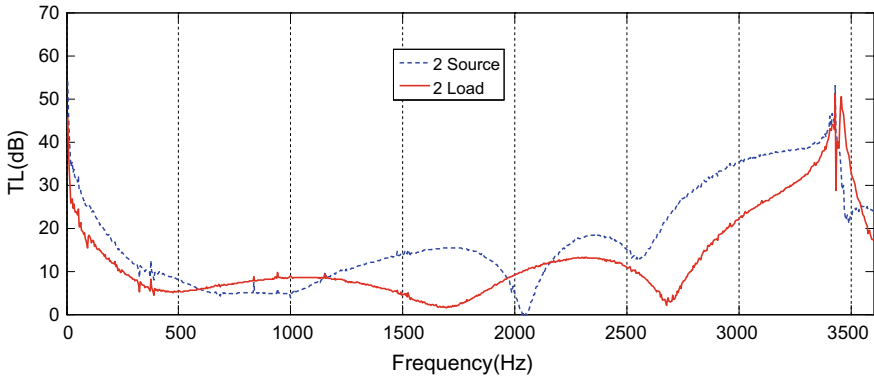
Fig. 6 Comparison of experimental results for two-source and two-load methods for L1 = 11.58 mm
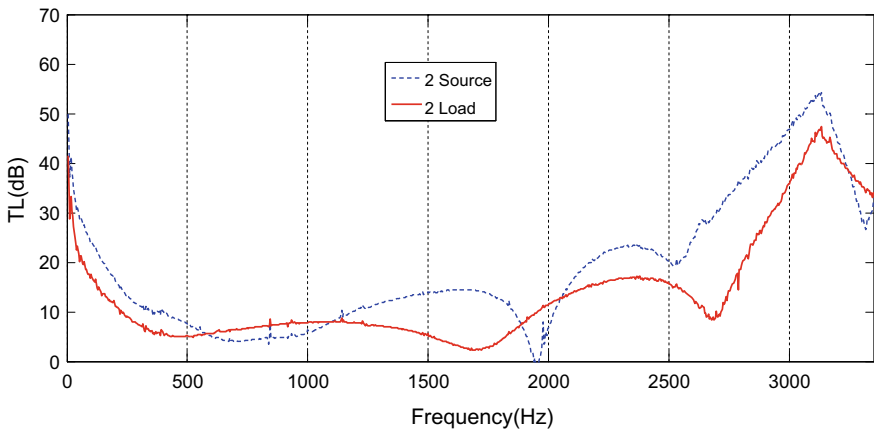
Fig. 7 Comparison of experimental results for two-source and two-load methods for L1 = 19.68 mm

The outlet lengths were taken randomly to conduct the experiments without any mean flow. Figures 5, 6, and 7 show the comparison of results obtained by two-load and two-source methods.

Above results clearly show that the fluctuations in two-load method are less as compared to the two-source method. The reason for this can be the error during taking measurements because of moving the sound source from one place to another. Another reason for this can be due to insufficient impedance difference between the two two-source configurations (two sides). As we know that for almost geometrically symmetric materials where there is no impedance difference from two sides, the two-source method cannot be applied.

5 Conclusions

The TL of muffler samples was determined separately by two-load method and then using two-source method. The results obtained using both methods are compared and the comparison shows a good agreement of respective results. During this process, following points were observed:

1. Two-source method is very useful but its main drawback is that the sound source has to be moved from one end to the other end of the tube, which is a bit time consuming and may be prone to error while taking measurements.
2. Two-load method offers numerous advantages in comparison with the two-source method. It is a considerable saving of time and labor, as the source does not have to be displaced from one end of the impedance tube to other unlike that of two-source method.
3. It is also observed that in some cases, the peak frequency information of two-source method is not very good as compared to two load. The reason for this may be the extended length of the muffler, which does not provide the suitable impedance difference from one side as to other.
4. For the case of two-load method, the main limitation can be the impedance difference of the two loads, i.e., the two loads should be different to each other or the solution can be indeterminate due to similarity of impedance of both loads.

Nevertheless, the obtained results from both methods show good agreements, but the authors suggest the use of two-load method for better accuracy. The results presented in the present work may be helpful for researchers in selecting the best technique for measurement and evaluation of the acoustic performance of mufflers.

References

1. Yaniv SL (1973) Impedance tube measurement of propagation constant and characteristic impedance of porous acoustic material. J Acoust Soc Am, 3049–3056
2. Munjal ML, Doige AG (1990) Theory of a two source-location method for direct experimental evaluation of the four-pole parameters of an aero acoustic element. J Sound Vib 141(2):323–333
3. Standard test method for measurement of normal incidence sound transmission of acoustical materials based on the transfer matrix method, ASTM standard E 2611-09 (2011)
4. Utsuno H, Tanaka T, Fujikawa T, Seybert AF (1989) Transfer function method for measuring characteristic impedance and propagation constant of porous materials. J Acoust Soc Am 86 (2):637–643
5. Standard test method for impedance and absorption of acoustical material by impedance tube method, ASTM standard C 384–04 (2011)
6. Tao Z, Seybert AF (2003) A review of current Techniques for measuring muffler transmission loss. University of Kentucky, SAE Inc., 01-1653
7. Munjal ML (1987) Acoustics of ducts and mufflers. Wiley–Interscience, New York

Dimensional Errors During Scanning of Product Using 3D Scanner

Mohd Javaid , **Abid Haleem** **and Lalit Kumar**

Abstract Non-contact scanners are available commercially as there is a need to understand their application in the current processes and products. This work tries to, explore the dimensional errors in the scanning process and also the best process parameters for using a 3D scanner. COLIN software was used with the scanner to convert the data of physical product into cloud data (3D CAD) file. Used UNIGRAPHICS software used to check the actual dimension of the digital file. Two tensile test specimens were taken to verify the scanning accuracy of the products by using the scanner. Results identified that there was scanning error in tensile test specimen 1 and specimen 2 during the first time. The scanning error occurred due to seven main reasons, i.e. selection of wrong reference point, out of field of view, alignment in measurement not appropriately done, calibration of the scanner, temperature out of range, software problem and post-processing. The scan depth and projected angle also affect the dimensional accuracy. After studying these parameters and finding the causes of error, we tried to improve these factors to improve scanning accuracy. Then again scanning of the same tensile test specimen 1 and specimen 2 was done and data obtained, as compared with first scan data. From this comparison, we identified lesser dimensional errors comparatively during the second scan which was taken after improving the factors. So factors identified to improve the dimensional errors.

Keywords 3D scanner · Dimensional accuracy · Comparison · Errors · Methodologies · Specimen

M. Javaid (✉) · A. Haleem · L. Kumar
Department of Mechanical Engineering, Jamia Millia Islamia, New Delhi 110025, India
e-mail: mohdjavaid0786@gmail.com

1   Introduction

The 3D scanner is a digital device, which is used to convert real object data into a digital form. The data acquired with the help of 3D Scanner is in the form of the point cloud. A 3D scanner is used to create a 3D model in the digital form of the physical object. The data which is obtained by the 3D scanner can be put for different purposes through software for modification in design, build of the product and in reverse engineering [1, 2]. Structured light is a technique which captures an image in 3D form with the help of a 3D Scanner. Series of light patterns cast by the projector on an object, while the camera captures an image of the object. The expensive and specialised hardware is required for operating these 3D scanning technologies [3]. 3D scanners have various medical applications that help to create a medical implant by using additive manufacturing technologies [4]. 3D scanner obtains 3D point cloud of the scene when scanned from different positions around the object. For the quality of point cloud, scanning geometry plays an important role. Range quality and point cloud density variant concerning scanning geometry [5]. Conventional coordinate measurement machines (CMMs) have three simple blocks, i.e. handling system of 3D motion, touch probe and collector and reduce measurement uncertainty. The touch probe has a limitation in its application [6]. Contactless 3D scanners give more reliable measurements as compared to the contact system. These provide high precision and fast measurement. It has various advance applications in reverse engineering, environmental construction, plastic surgery, cultural heritage and constructions of 3D optical sensors [7–9]. 3D Scanner is a convenient and straightforward 3D laser measurement technology usually for complex shape and small volume data acquisition of the object. Mainly this technology uses the camera self-calibration method for construction of 3D model algorithm which creates the measurement environment of the measuring technique in hardware and machinery [10, 11].

1.1   The Occurrence of Dimensional Errors During Scanning

Wrong Reference Points. The first significant factor which affects the dimensional accuracy of the product is the selection of wrong reference point. During scanning of tensile test specimens after two rotation of rotary table, Colin software required reference point. If the selection of the reference point is not made correctly, it creates problems in dimensional accuracy of the product.

Out of Field of View. When an object which is to be scanned is out of a field of view of projector and camera, it creates problem in dimensions of scanning object's digital file. So it is clear that proper selection of camera and projector is essential for

the field of view and scanning with accuracy. This error affects the length of the product.

Aligning of the Measurement. Any product which is scanned by the 3D from both sides (front and back). During alignment of both sides, if proper alignment has not done it also creates problem. These errors affect the thickness of the product as in the tensile test specimen 1 in which the thickness is reduced 2.9 mm to 2.4 mm.

Calibration of the Scanner. Like other measuring devices, 3D scanner also required proper calibration to produce accurate results. By calibration, process scanner provides more precise data. It used a standard calibration plate as the specification.

Temperature Difference. Proper temperature range of this scanner is 18–30 °C. If there is difference between the temperatures, the scanner does not produce an accurate result.

Software Problem. When software creates a problem during the scanning the dimensional accuracy is also affected, and acquired shape in such case is not accurate.

2 Steinbichler Comet L3D Scanner

The Steinbichler Comet 3D Scanner is non-contact type optical scanner which is installed in Jamia Millia Islamia, New Delhi, used for scanning of product. It is a portable scanner (due to its small size and weight) in which scanning head is placed upon the tripod head. The product can be scanned in the various positions with or without the assistance of a rotary table as shown in Fig. 1.

The product is first scanned only from the top view in different rotations, and then it is scanned from the back and side positions depending upon required types,

Fig. 1 Steinbichler 3D scanner

shape and rotation of the product. During different rotation, it required the reference points. It is essential to give exact reference points manually, then align all the 3D scan arrangements to complete the digital form of the product. After completion of scanning, data is exported in STEP, IGES, STL and other formats. Sometimes 3D scanner also works as a mobile scanner for scanning of a large size product without a rotary table. During this case, we have removed the rotary table, and we rotate the scanner in the differential rotation and completing scanning process.

3 The Algorithm Used in the 3D Scanner for Mesh Generation

The 3D Scanner used here is a blue light scanner, in which the projector sends the light fringes of different thickness, and the camera used to detect the reflected light. There are two methods, and the first method is finite element method in which small elements are created from discretising of measured field. For two dimensions commonly triangles or quadrilaterals are created which measures angles, area or height, edge lengths of the elements. In each display image, for each camera, the machine determines whether the projector directly illuminates the given pixel or not. If it illuminates in any given frame, the code bit is correspondingly set high, otherwise, it is set low. The algorithm used in this scanner consists of camera and projector, which project light to an object. This method is computationally precise and efficient [12]. 3D scanning is based on the triangulation principle. For scanning of the object, it projects different fringe pattern which are captured by camera. Each measurement generates millions of data points. The visible part is recorded by the camera in a single scan to convert the object from physical to digitised form.

4 Comparison of Dimensional Accuracy of Product

3D scanner acquires geometry data from the physical object, and this data is used to create a physical object and used for various applications such as inspection, reverse engineering, quality management, restoration, rapid prototyping and cultural heritage documentation. We took two tensile test specimen as scanned by a Steinbichler 3D scanner, then different errors are calculated in the scanning. The software used by the Stenbichler 3D scanner is COLIN 3D for scanning. The functions of COLIN create an entirely clean and watertight 360-degree virtual model. The three-dimensional operated the Scanner and the rotary table through the host computer. In this process, first the data registration is performed automatically, then edit the captured scanned data (decimate, fill holes, smooth), then the scans are merged into a single watertight mesh, and finally, can be exported to a variety of three-dimensional data formats. In this case, data is exported in STL format.
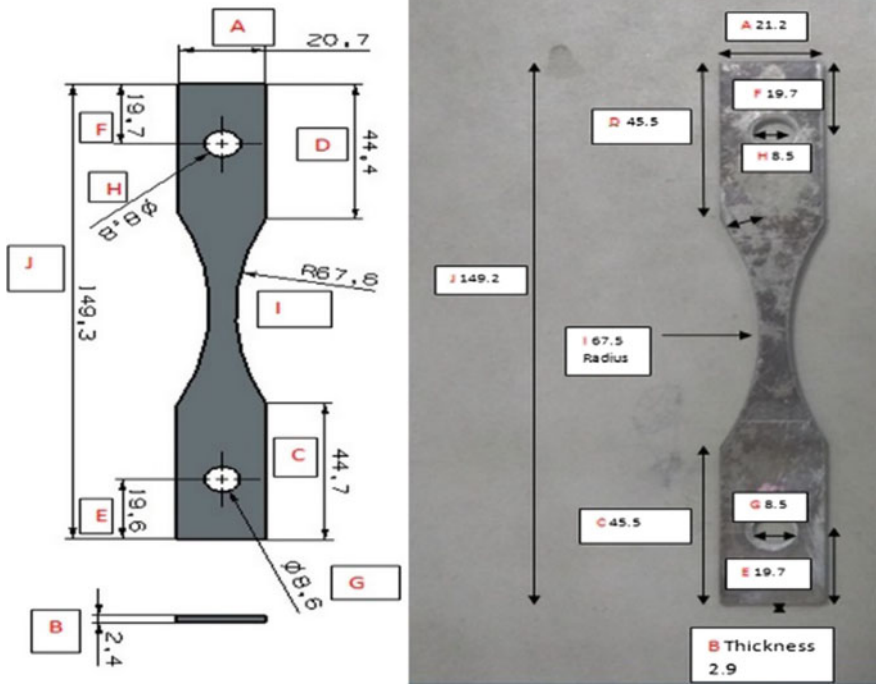
Fig. 2 Scanned and actual dimensions of tensile test specimen 1

COLIN 3D has manual and automatic data registration, smoothing, point decimation, data merging, polygon checking (degeneration, intersections), holes filling, and texture blending and merging options. Consider the tensile test specimen 1 shown in Fig. 2. In case of a hole in specimen there is an increase in the dimensions, and also the total length of the specimen increases marginally. Scanner shows an error in thickness (B) which is 0.5 mm. The percentage error of 1st specimen as shown in Table 1, during scanning is −0.00772 (decrease in dimension of product). Now consider the 2nd specimen as shown in Fig. 3. The scanning errors are calculated for specimen 2 as shown in Table 2. It shows that there is a reduction in length of scanning and some dimensional errors are reduced (i.e. A and B are of same dimensions but have a large error after scanning.

5 Post-Processing

When scanning is completed, post-processing is an important step which is done manually. In such type errors are occurs, in the form of errors in the holes, in the product. For reducing the dimensional errors during scanning, the focus is given on

Table 1 Comparison of results of tensile test specimen 1

Part no	Actual dimension (1)	Dimension after scanning (2)	Absolute error in scanning = 2–1
A	21.2	20.2	−1
B	2.9	2.4	−0.5
C	45.5	44.7	−0.8
D	45.5	44.4	−0.9
E	19.7	19.6	−0.1
F	19.7	19.7	0
G	8.5	8.6	0.1
H	8.5	8.8	0.3
I	67.5	67.5	0
J	149.2	149.3	0.1
Percentage error			−0.00772
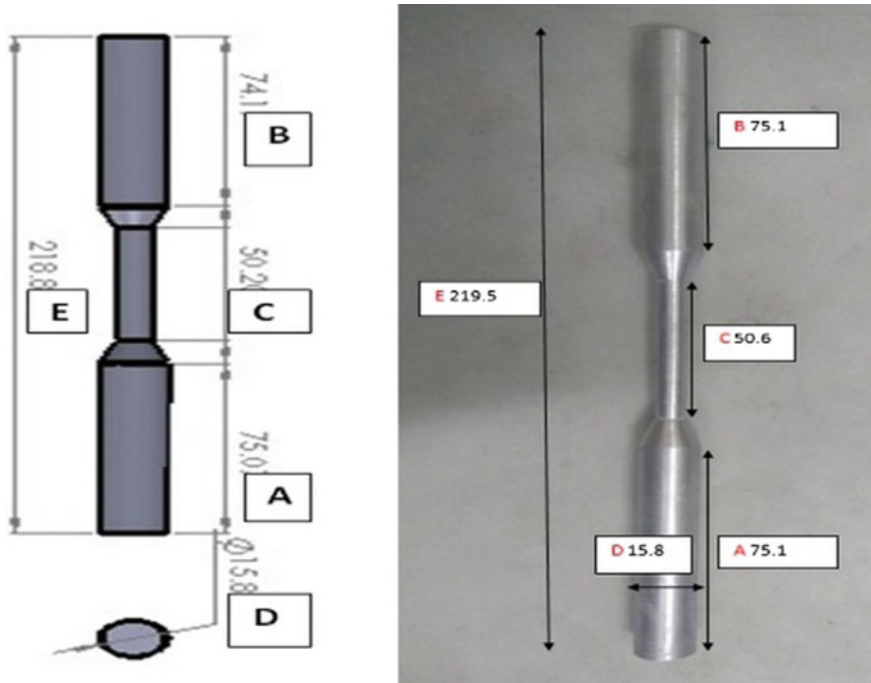
Fig. 3 Scanned and actual dimensions of tensile test specimen 2

the proper selection of reference point, proper alignment, calibration process, post-processing and also examine the software problem, proper temperature and field of view. Then again scanning of specimen 1 and 2 is done as shown in Figs. 4 and 5.

Table 2 Comparison of results of tensile test specimen 2

Part no	Actual dimension (1)	Dimension after scanning (2)	Absolute error in scanning = 2−1
A	75.1	75.0	−0.1
B	75.1	74.1	−1
C	50.6	50.2	−0.4
D	15.8	15.8	0
E	219.5	218.7	−0.8
Percentage error			−0.00592

Moreover, from the calculation, as shown in Table 3, it has been analysed that there is a reduction in the scanning errors. The percentage error is reduced from −0.00772 to −0.0054. From the Table 4, scanning error is calculated again after scanning of specimen 2. It shows that there is a great reduction in scanning errors. The percentage error is reduced from −0.00592 to 0.0009. Observed that by proper utilisation of scanner and proper management of the factors which cause scanning errors good results can be acquired and errors can be minimised during scanning.
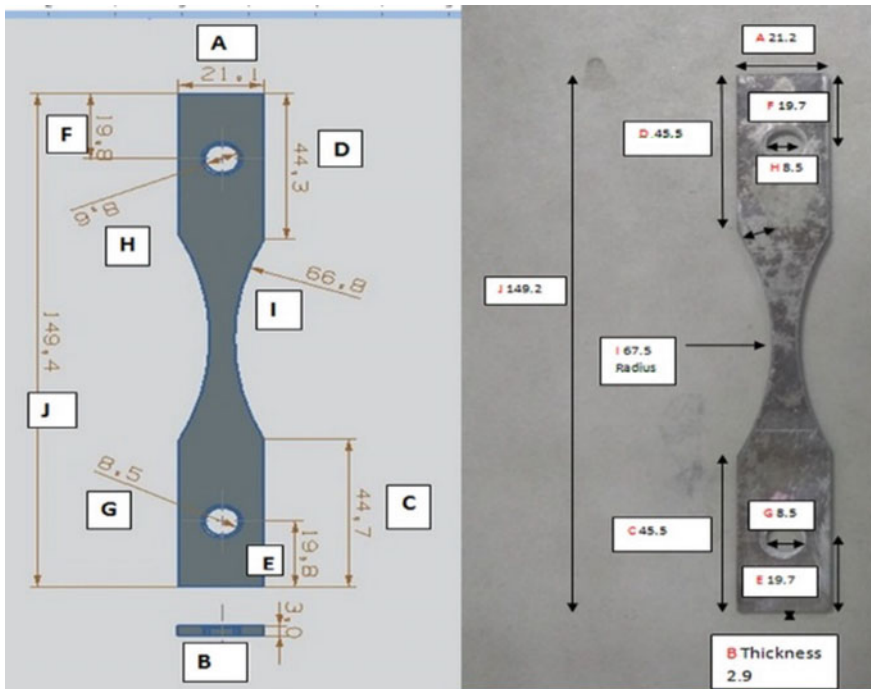
Fig. 4 Scanned and actual dimensions of tensile test specimen 1
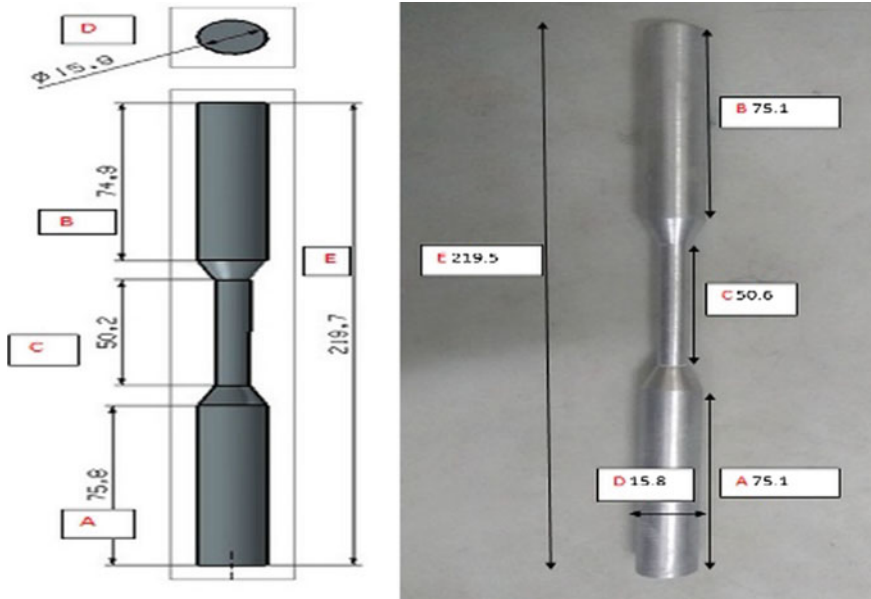
Fig. 5 Scanned and actual dimensions of tensile test specimen 2

Table 3 Comparison of results of tensile test Specimen 1

Part no	Actual dimension (1)	Dimension after scanning (2)	Absolute error in scanning = 2−1
A	21.2	21.2	0
B	2.9	3.0	0.1
C	45.5	44.7	−0.8
D	45.5	44.3	−1.2
E	19.7	19.8	0.1
F	19.7	19.8	0.1
G	8.5	8.5	0
H	8.5	8.6	0.1
I	67.5	66.8	0.7
J	149.2	149.4	0.2
Percentage error			−0.0054

6 Result and Its Discussion

The errors in the scanning can be due to the neglected selection of wrong reference point, the product is out of a field of view, improper aligning of measurement, software problems and manual post-processing. All of these errors affect the

Table 4 Comparison of results of tensile test specimen 2

Part no	Actual dimension (1)	Dimension after scanning (2)	Absolute error in scanning = 2−1
A	75.1	75.8	0.7
B	75.1	74.9	−0.2
C	50.6	50.2	−0.4
D	15.8	15.9	0.1
E	219.5	219.7	0.2
Percentage error			0.0009

successful scanning. Projected angle, scanning depth and proper lightning also create errors. These affect the overall performance of the scanner. A 3D scanner is capable of capturing a 360-degree snapshot of the object. Main errors occur in the thickness of product which is due to improper aligning of the digital scanned file. It cannot take exact geometry measurement. The proper scanning process is important to avoid these types of errors during scanning, and we achieve high accuracy in the digital CAD file. 3D scanners are more suitable for measure the geometry of complex shape product which is not measured by manual measurement. This paper contributes to the selection of input parameters of scanning to achieve reasonable accuracy. The seven parameters discussed are the main cause to affect the dimensional accuracy of the scanned product.

7 Conclusion

3D Scanners capture XYZ coordinates of millions of points all over an object to recreate it digitally. 3D Scanner, scan products by using Colin software to convert the physical form of product into 3D digital form. If the reference point is taken precisely and carefully, the scanning quality can be improved. During scanning, the product must be in 'field of view' for achieving accurate scanning. Calibration is maintained by maintaining the temperature during the scanning and by proper handling of the software issues. The final step of post-processing is vital for removing errors and for global optimisation. As compared to touch probe a 3D scanner, is efficient because it easily measures the geometry of complex shape products. To achieve accuracy in scanning, we need to remove the errors that affect the scanning of product.

References

1. Tóth T, Živčák J (2014) A comparison of the outputs of 3D scanners. In: 24th DAAAM International symposium on intelligent manufacturing and automation procedia engineering, vol 69, pp 393–401
2. Javaid M, Haleem A, Shuaib M, Kumar L (2017) Product design and development using combination of steinbichler comet 3D scanner and projet 3D printer. In: National conference on innovative trends in mechanical engineering held at department of mechanical engineering, Shri Mata Vaishno Devi University Katra, Jammu
3. Pogacar V (2007) The integrated renaissance of design. In: Proceedings of the 1st DAAAM international specialized conference on additive technologies in science direct, pp 9–12
4. Javaid M, Haleem A (2017) Additive manufacturing applications in medical cases: a literature review. Alex J Med. https://doi.org/10.1016/j.ajme.2017.09.003
5. Kumar L, Tanveer Q, Kumar V, Javaid M, Haleem A (2016) Developing low cost 3 D printer. Int J Appl Sci Engineering Res 5(6):433–447
6. Zhang G, Veale R, Charlton T, Borchardt B, Hocken R (1985) Error compensation of coordinate measuring machines. CIRP Ann 34(1):445–448
7. Sansoni G, Trebeschi M, Docchio F (2009) State-of-the-art and applications of 3D imaging sensors in industry, cultural heritage, medicine, and criminal investigation. Sensors 9(1):568–601
8. Lina J, Hu D, Chen H (2015) Desktop 3D laser scanning technology research. In: AASRI international conference on industrial electronics and applications, pp 321–323
9. Haleem A, Khan A, Javaid M (2016) Design and development of smart landline using 3D printing technique. Int J Adv Res Innov 4(2):438–447
10. Kumar L, Shuaib M, Tanveer Q, Kumar V, Javaid M, Haleem A (2018) 3D scanner integration with product development. Int J Eng Technol 7(2):220–225
11. Javaid M, Kumar L, Kumar V, Haleem A (2015) Product design and development using polyjet rapid prototyping technology. Control Theory Inform 5(3):12–19
12. Lamovsky D, Lasaruk A (2011) Calibration and reconstruction algorithms for a handheld 3D laser scanner. In: International Conference on advanced concepts for intelligent vision systems, vol 6915. Lecture Notes in Computer Science, pp 635–646

Friction and Wear Characteristics of Heat-Treated Medium Carbon Alloy Steel

Abhijit Mukhopadhyay

Abstract The microstructure of a material can produce excellent mechanical properties as well as they have strong influence on mechanical properties like strength, toughness, rigidity, ductility, hardness, corrosion resistance, wear resistance and so on. The microstructure of alloy steel again depends on the types of alloying constituent present in the particular steel, their concentrations and the heat treatment procedure of the alloy steel. Heat treatment is basically the heating process of the material at desired temperature, allowing the material to dwell at that temperature for a specified time and finally cooling at room temperature. Various categories of microstructures may be developed depending on the cooling process. In the present research work, medium carbon alloy steel has been heat treated to give annealed, normalized and quenched samples. Heating has been done in an electric muffle furnace followed by cooling inside the furnace, in open air and in cutting grade oil (grade 44) to give annealed, normalized, and quenched samples respectively. Hardness of all the samples have been measured in Rockwell C scale and compared accordingly. Microstructures of all the samples have also been observed using an optical trinocular microscope and discussed. Finally tribo characteristics, that is, the study of friction and wear of the heat treated samples have been conducted in dry condition and under fixed parametric combinations of normal load on job, speed of the wheel (rpm) and cycle time. "Winducom 2006" software supported multi-tribotester "TR-25" (Ducom) has been used for this experimental study. All the test results have been tabulated, compared and concluded accordingly.

Keywords Heat treatment · Microstructure · Tribotesting

A. Mukhopadhyay (✉)
Mechanical Engineering Department, Jadavpur University, Kolkata 700032, India
e-mail: m_obiji@yahoo.com

1   Introduction

Tribological studies, that is, the study of friction, wear, and associated lubrication, if any, plays very important role in different engineering and other applications particularly where interacting surfaces under relative motions are prominent. Control of friction and wear in case of sliding or rolling contact pairs is necessary to maintain desired functional reliability of the components. This will not only increase the product quality but the life cycle will also be enhanced. Needless to be mentioned that to achieve such control friction and wear-related knowledge base is very much essential. Friction and wear are system dependent properties [1–4, 18–20].

Several research based models and data have been available for different tool-work pair combinations and in different work situations. However, it is hardly feasible to foretell the tribological behavior of a particular work situation based on those available data. This necessitates the experimental investigation of friction and wear study in each and every work situation.

Medium carbon steel with a carbon content of 0.425 along with nickel, chromium and molybdenum as alloying elements had been procured from the market and is used for the present experimental studies. Chemical compositions of the procured/as received steel have been obtained through spectrographic analysis. The values of the ingredients have been furnished in Table 1. Comparing the test results, the procured steel may closely be approximated as AISI 4340 steel. AISI 4340 steel has wide applications in military and commercial vehicles, structural steel, heavy duty axle, connecting rod, shaft, etc. All these application areas are highly stressed and the steel used in such application requires high strength and rigidity, resistance to wear and deformation and so on [5].

Heat treatment is the process of heating and subsequent cooling of metals to achieve some desired properties [7]. It makes the material suitable for different engineering applications. Heat treatment affects the microstructure by internal stress removal and grain refinement. Radhika et al. [6] conducted heat treatment on Aluminum Metal Matrix Composites (AMMCs) to get maximum concentration of the solutes in the solvent and thus generating a single phase. Without heat treatment solute and solvent remains in separate phases. Heat treatment enhances several desired properties of AMMCs. However, medium carbon steel exhibits improved toughness due to heat treatment whereas hardness is not increased considerably [7]. Surface properties of metals are enhanced due to the development of different microstructures which again depend on the temperature of heating and subsequent cooling.

Some important heat treatments like annealing, normalizing and quenching have been conducted on medium carbon alloy steel in the present experimental work. Annealing is meant for the improvement of toughness, ductility and reduction of hardness. Normalizing on the other hand improves the strength with some ductility and quenching takes care of improved hardness in case of steel with higher percentage of carbon [8].

Finally friction and wear tests have been conducted on the heat treated steel samples. Multi tribotester "TR-25" (Ducom) supported with "Winducom-2006" software has been utilized for this purpose [9]. Load on job (N), rotational speed of the wheel (rpm) and cycle time (sec) have been considered as the working parameters in tribological testing. All the samples have been slid against the standard roller of the tribotester at fixed parametric combinations and in dry condition.

2 Experimental

2.1 Test Material

Medium carbon alloy steel has been selected as the test material in the present study. The material has been procured directly from the market. Samples of size 20 mm × 20 mm × 8 mm have been machined from the larger work piece as per the dimension requirement of the sample holder of the tribotester. The chemical composition of "as received" material has been tested by spectrographic analysis and the result has been furnished in Table 1.

2.2 Heat Treatment

Microprocessor controlled electric muffle furnace [N.R. Scientific] with a maximum temperature limit of 1100 °C has been used to heat the material at desired temperature and allowed to dwell for specified time. Several ways of softening processes have been discussed by different researchers in their research studies [1, 7, 10–12]. Based on the feasibility of studies in the laboratory, some basic heat treatment processes have been selected. These operations have been discussed in the following sub-sections. In all the cases the rate of increment of heat has been selected as 10 °C per minute.

Annealing. Samples have been heated from room temperature to 930 °C and allowed to dwell for 2 h at that temperature inside the furnace. At the end of the operation the furnace has been switched off and the samples have been allowed to cool inside the furnace, that is, furnace cooling.

Normalizing. Samples have been heated to attain a temperature of 930 °C and allowed to dwell inside the furnace at that temperature for 2 h. Then the samples have been taken out of the furnace and allowed to cool in open air to attain room temperature.

Table 1 Chemical composition of medium carbon alloy steel used in the study

Elements	C	Si	Mn	P	S	Ni	Cr	Mo	F
Percentage	0.425	0.238	0.55	0.031	0.032	1.41	1.09	0.228	Rest

Quenching. After heating the samples at 930 °C inside the furnace and allowing a soaking time of 2 h, the samples are dipped into cutting grade oil (grade 44) and allowed to attain room temperature. This sudden cooling in oil is the quenching process.

2.3 Friction and Wear Test

A "Ducom" make multi tribotester "TR-25" has been used to conduct friction and wear test. The frictional force, coefficient of friction and wear data have automatically been recorded through "Winducom-2006" data acquisition software. Block-on-roller configuration of the tester has been utilized for the tribo tests. Wear has been measured in terms of displacements in microns with the help of a linear voltage resistance transducer [13] as designed in the said tribotester. Samples have been cleaned with acetone prior to the test to remove any trace of grease, oil, dirt or dust. Based on different research studies [1, 14–20 and references there in] rotational speed of the wheel (rpm), load on job (N) and duration of test run (sec) have been identified as the most important parameters for the wear test in multi tribotester. Fixed values of the said parameters have been considered in the present study and the values have been fixed at 375 rpm, 50 N, and 900 s, respectively. All the samples have been slid against a hardened steel roller of diameter 50 mm and hardness of 82 HRC. Weights of all the specimens have been measured before and after the wear test using an electronic analytical and precision balance (Sartorius BSA 223S, Germany; maximum range is 220 gm with a readability of 0.001 gm). The specimens have been cleaned thoroughly with acetone to remove any traces of oil, dust, grease, etc., before taking the weights. Difference of the two values indicates the weight loss of the specimen due to wear [17].

3   Results and Discussions

Hardness values of the heat treated samples have been furnished in Table 2.

The hardness of the normal sample has been measured at 50 HRC. The improvement of hardness has been observed in case of oil quenched sample. Sudden cooling from elevated temperature gives rise to the development of

Table 2 Hardness (HRC) of different heat treated steel

Heat treatment	1st reading	2nd reading	3rd reading	Average
Annealing	52.0	51.5	47.0	50.0
Normalizing	67.0	69.0	69.5	68.5
Quenching	73.0	72.5	73.9	73.0

Table 3 Weight loss (gm) of the samples due to wear

Specimen type	Initial weight (w_1)	Final weight (w_2)	$\Delta w = (w_1 - w_2)$
Original	24.426	24.415	0.011
Annealed	21.290	21.281	0.009
Normalized	21.595	21.589	0.006
Quenched	22.290	22.287	0.003

martensite due to the presence of higher percentage of carbon in the medium carbon steel sample as used in the present study. In normalized samples cooling is comparatively faster than that of annealed samples and hence the hardness is little bit higher in case of normalized sample. Annealing is not meant for improving hardness. It is, in general, a softening operation and the hardness remains almost the same as that of the original sample. It is not out of place to mention that medium carbon alloy steels may be toughened by heat treatment process; however hardness cannot be improved to a greater extent [7].

Table 3 indicates the weight loss data due to wear during friction studies in tribotester. The microstructures of the original as well as heat treated samples have been depicted in Fig. 1a–d.

The annealed sample shows an iron carbide layer to curl up in spherical form (cf Fig. 1b). Alternate layers of ferrite and iron carbide (Fe_3C), that is, cementite is formed in this process as the cooling is very slow. This alternate layer of ferrite and cementite is known as pearlite. In Fig. 1b these layers are prominent along with grain boundaries in places. In Fig. 1c normalized sample shows more refined and uniform grain structure and as it is a modified annealing process it shows spheroidized iron carbide. Normalizing produces harder surface than annealing and this has been supported by the respective hardness values as shown in Table 2. Oil quenched sample of steel used in the study shows an interlaced needle like structure, known as martensite. This structure gives a harder surface. However, martensite is also very unstable structure. The hardness of oil quenched samples is more than normalized samples. This may also be attributed due to the presence of ferrite, martensite and particularly chromium carbide as the alloy steel specimen used in the study contains larger fraction of chromium. To conclude regarding the actual composition and percentages of these structures in the heat treated samples, micro hardness test supported by feritscopic study is needed [1].

Friction and wear characteristics of all the heat treated as well as normal samples have been conducted. The wear values have been furnished in Table 4.

Comparative wear curves, as obtained directly from "Winducom-2006" software based data acquisition system, have been depicted in Fig. 2. It has been revealed that the wear data at the end of 900 s of sliding against the roller is minimum in quenched sample (26.1 micron) followed by normalized sample (71.8 micron). Original sample ends up with a final wear of 105.7 micron which is less than the wear value of annealed sample (120.7 micron). However, this does not mean the overall wear of original sample is less than that of its annealed counterpart.
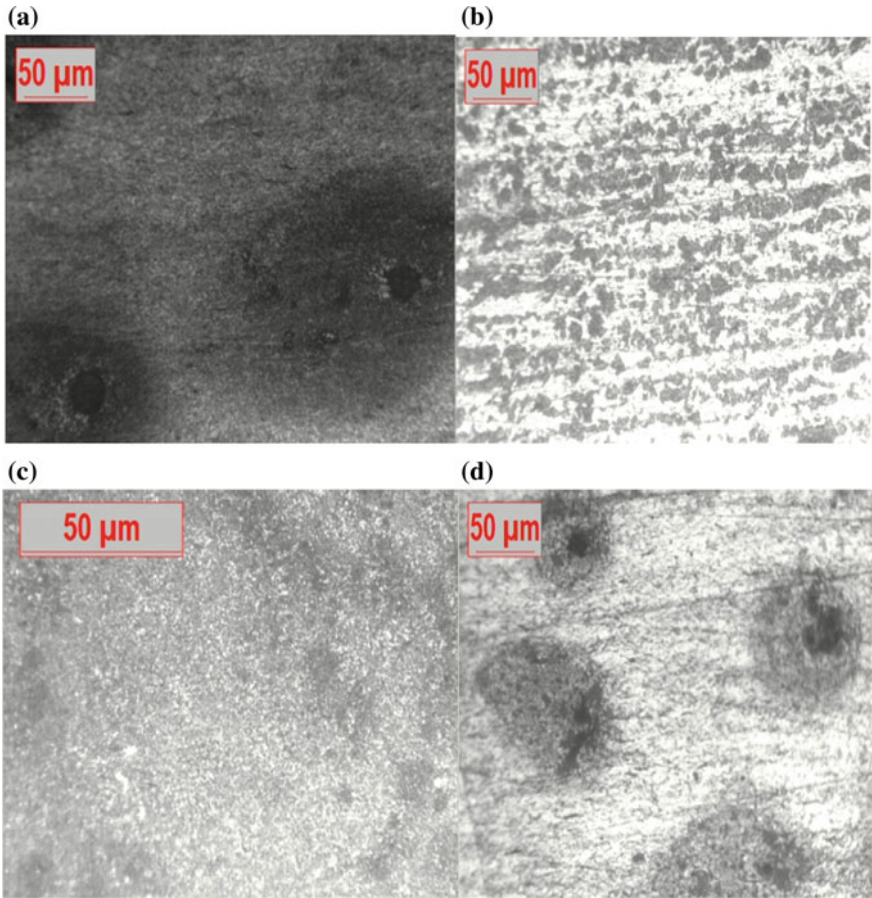
Fig. 1 Microstructures of **a** original **b** annealed **c** normalized and **d** oil quenched samples of medium carbon alloy steel

Table 4 Wear (micron) of different heat treated samples in regular time intervals

Heat treatment type	Wear (micron) in different times (s)								
	100	200	300	400	500	600	700	800	900
Annealed	61.5	69.8	75.9	83.5	84.9	95.2	103.0	118.6	120.7
Normalized	50.5	53.9	55.2	77.6	76.5	77.7	75.6	71.6	71.8
Quenched	11.9	16.7	19.7	22.2	23.7	23.8	23.7	23.5	26.1
Original	93.7	96.9	97.7	97.8	99.5	100.3	98.4	103.1	105.7
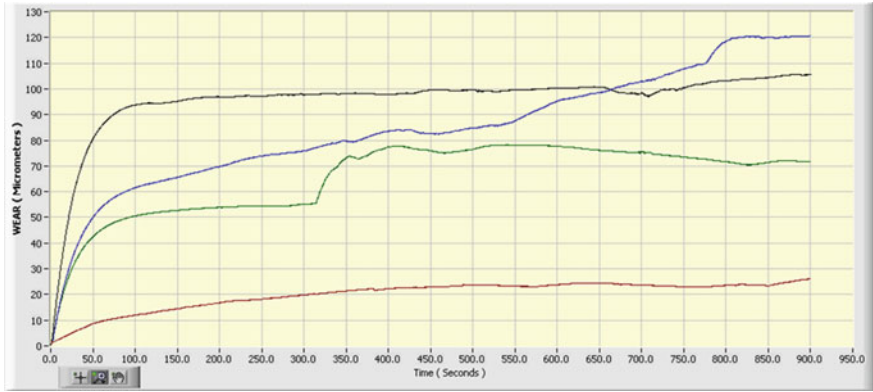
Fig. 2 Figure indicating comparative wear of different samples [maroon: quenched sample, green: normalized sample, blue: annealed sample, black: sample without heat treatment]
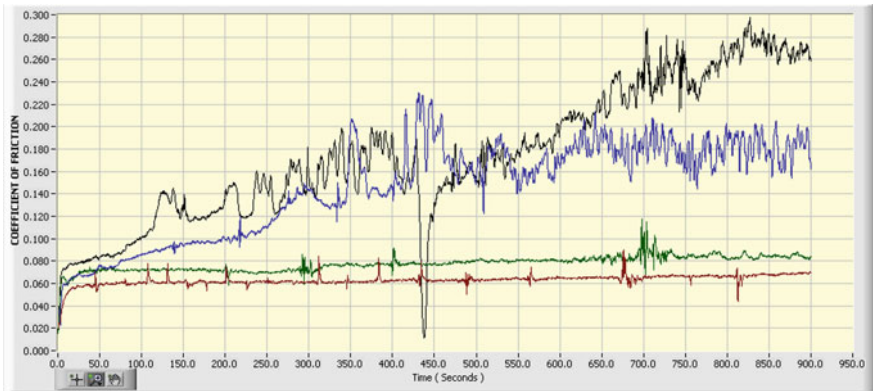
Fig. 3 COF curves [maroon: quenched, green: normalized, blue: annealed, black: original]

The comparative curves in Fig. 2 reveals very high initial wear of original sample and after 150 s of operation the stable trend in high wear is maintained. On the contrary, the wear of the annealed samples gradually increases from the very beginning and ends up with a maximum value, may be due to some local layer detachment from its surface or other reason. The weight loss data, as furnished in Table 3, are in good agreement with the wear data.

Comparative coefficient of friction (COF) curves have also been depicted in Fig. 3. These curves have also been generated directly from "Winducom-2006" software.

Coefficient of friction of oil quenched samples are minimum having an average value of 0.06 and the curve is stable all along. Normalized samples have a higher

COF than quenched counterparts with an average value of about 0.08 and the curve is almost stable. Other two samples show higher COF values with gradually increasing trend.

4 Conclusion

Some important heat treatments of medium carbon alloy steel have been accomplished in the present experimental study utilizing the available in-house facilities. This is a great value addition in the conceptual learning process.

Heat treatment of medium carbon alloy steel results in varied microstructures and hardness which govern the mechanical characteristics of the concerned steel. The particular type of heat treatment process should be selected according to the area and severity of the application.

Tribological characterization is the study of friction, wear and lubrication, if any, is considered as one of the important mechanical characterization processes and it has been discussed in the present experimental work. However, the friction and wear parameters have been calculated under dry sliding condition. Under the present operating conditions, annealed samples show maximum wear of 120.7 micron after 900 s of operation followed by original and normalized samples having wear of 105.7 and 71.8 micron respectively. Quenched samples have a minimum wear of 26.1 micron. Quenched samples also reveal all along low wear starting from its inception and maintain almost straight line trend (e.g., the graph as generated directly from Winducom-2006, Fig. 2). In other cases, the initial wears are very high up to 100 s of operation and then follow some stable pattern. The wear of annealed sample is increasing gradually up to 660 s. However, the wear is less than the other two samples. But after 660 s the wear has been increased and finally reaches to maximum. The study gives an average idea about friction and wear characteristics of medium carbon alloy steel after different heat treatment processes.

Future scope of work: More experiments under different parametric combinations of tribology test are to be carried out before coming to a concluding remark. Application of lubricants is another area of research in this regard. It is also planned to conduct tribological studies of the same material after austempering and martempering heat treatments.

References

1. Kumar S, Mukhopadhyay A (2016) Effect of microstructure on the wear behavior of heat treated SS-304 stainless steel. J Tribol Ind 38(4):445–453
2. Ludema KC (1996) Friction, wear, lubrication: a textbook in tribology. CRC Press, USA
3. Fontalvo GA, Mitterer C (2010) Comparison of the tribological properties of different cold work steels at temperatures up to 250 °C. In: 6th International Proceedings of Tooling Conference. Austria, pp 223–236

4. Leroux P (2010) Stainless steel analysis using tribology and 3D metrology. NANOVEA, pp 1–9. http://www.nanovea.com
5. Niazi N, Nisar S, Shah A (2014) Austempering heat treatment of AISI 4340 steel and comparative analysis of various physical properties at different parameters. IJMSE**5** 10:6–11
6. Muddamsetty PLV, Radhika N (2016) Effect of heat treatment on the wear behavior of functionally graded LM13/B$_4$C composite. J Tribol Ind 38(1):108–114
7. Lindberg RA (1974) Processes and materials of manufacture. Prentice-Hall, New Delhi
8. Jaypuria SK (2009) Heat treatment of low carbon steel. In: B.E (Mechanical) project report. NIT Rourkela, pp 1–39
9. Naylor DJ, Cook WT (1992) Heat treated engineering steels. J Mat Sci Tech 7:405–538
10. Krauss G (1990) Steels: heat treatment and processing principles. ASM International Materials Park, OH
11. Tanwer AK (2014) Effect of various heat treatment processes on mechanical properties of mild steel and stainless steel. AIJRSTEM 8(1):57–68
12. Tukur SA, Dambatta MS, Ahmed A, Mu'az NM (2014) Effect of heat treatment temperature on mechanical properties of the AISI 304 stainless steel. IJIRSET 3(2):9516–9520
13. DUCOM (2006) User manual for safety, installation, operation and maintenance. WO No. 305, DUCOM, India
14. Parthasarathi NL, Borah U, Albert K (2013) Correlation between coefficient of friction and surface roughness in dry sliding wear of AISI 316L (N) stainless steel at elevated temperatures. J Comput Model New Technol 17(1):51–63
15. Chowdhury MA, Nuruzzaman DM, Roy BK, Islam A, Hossain Z, Hasan R (2013) Experimental investigation of friction coefficient and wear rate of stainless steel 202 sliding against smooth and rough stainless steel 304 counter-faces. J Frict Wear Res 1(3):34–41
16. Mukhopadhyay A, Mondal P, Saha R, Dutta S (2014) Optimization of process parameters during dry sliding wear of different weld zones of AISI-304 SS in a block-on-roller tribotester. In: Proceedings of National Conference IFMMT. Manipal University, Jaipur, India, pp 1–12 (2014)
17. Kumar S, Mukhopadhyay A (2016) Study of dry sliding tribo-characteristics of heat treated SS-304 stainless steel against En-8 stainless steel using a multi tribo tester. In: Proceedings of 2nd International Conference ICRIET-16. MAIT, Baddi, India, pp 258–262
18. Mukhopadhyay A (2016) SEM study of worn surface morphology of an indigenous 'EPDM' rubber. J Polym Test 52:167–173
19. Mukhopadhyay A (2014) Some tribological characterization of EPDM rubber. J Tribol Ind 36 (2):109–116
20. Mukhopadhyay A (2011) Effect of some lubricants on the flow characteristics of 'EPDM' rubber under compressive load. In: 6th International Proceedings on Conference on Tribology 'BALTRIB2011'. Kaunas University, Lithuania, pp 229–234

A Comprehensive Review of Materials Used for 4D Printing

Ajay Sharma and Ajay K. S. Singholi

Abstract Rapidly 4D printing has made tremendous growth in diverse fields such as healthcare, aerospace, manufacturing industry, and advanced manufacturing systems. This technology is found to have a greater potential while considering the daily applications and the economy. Besides this 4D printing allows the conversion of a 3D printed structure to perform some interaction mechanisms by changing the functions based on the response time to parameters such as temperature, pressure, water, and light and so on. Also 4D printing is function of time, printer independent targets shape and functionality. Therefore, this paper conducted an exhaustive review of the recent researches in materials and designs leading to its use in a 4D printing process. This review also incorporates a detailed survey of smart material and multi-materials used to change the function and shape of those materials after printing. An attempt has been made in this paper to cover a more conclusive review in deciding the best appropriate material that may well be utilized in 4D printing process.

Keywords 4D printing · SMP · Smart materials · Smart design · PZT

1 Introduction

Rapid printing technology has excelled the traditional approach of 3D printing and continuously working on its advanced stage (4D printing) by adding fourth dimension of time. The revolutionary changes were brought by 3D printing technology in the field of manufacturing.

There is continuous focus on substantial progresses in 3D printing technology have been made relating to materials, printers and processes. Countries adapted

A. Sharma (✉)
USICT, Guru Gobind Singh Indraprastha University, New Delhi, India
e-mail: ajayrcert21@gmail.com

A. K. S. Singholi
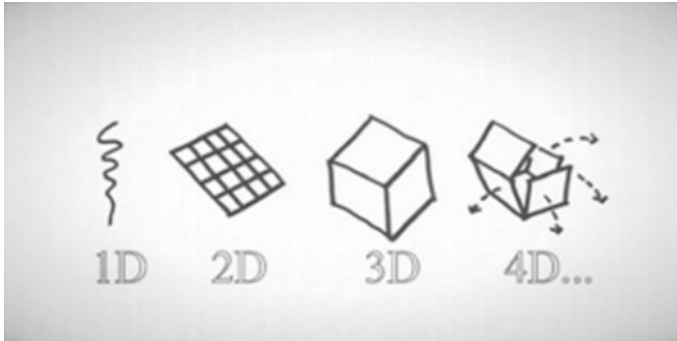GB Pant Engineering College, New Delhi, India

Fig. 1 A simple illustration of the concept of 4D printing [23]

additive manufacturing processes have declared 3D printing method as an innovative manufacturing method [1]. Applications of 3D printing have been applied in many fields like biomedical science, construction, space science, automobile, and automated factories, etc. [2]. 3D model is designed using the computer aided design, Solid Works, or different types of modeling software. As the 3D printing technology grown rapidly and occupied the place of traditional approach (static parts that show now change after printing), the emerging new dynamic approach is called as 4D printing technology. This term was first familiarized by Skylar Tibbits in TED conference (2013). This approach is similar as 3D printing except it embraces the fourth dimension of time besides 3D coordinates after printing [3]. As 4D printing illustration is defined in Fig. 1.

The more comprehensive definition of 4D is a predefined continuous changing of the 3D printed structure regarding shape, functionality, and property. 4D printed parts having dynamics in shapes, properties, and functionality [4, 5] on exposure of stimuli. The capacity of 4 D printing process is mainly dependent on the smart materials in the three-dimensional space. There are two stable states in a 4D printed object, and the object can shift from one state to another under the exposure of stimuli [6]. 4D printing differs from 3D printing only on the two points that is Smart material and smart design. So, smart materials for 4D printing should be fully programmed for predefined possible changes in the printed part. The main characteristic of the 4D printing method is smart material which is flexible to make changes in the final printed part in response to the stimuli exposure. The 4D printed structure is created by the combination of different materials in the proper distribution into one printed structure [7]. Stimulus is required to trigger the alterations of shape or property of a 4D printed structure. The stimuli which are generally used in 4D printing thus include water, heat, and light [4]. The stimulus responsive material is one of the most critical components of 4D printing. They are of many categories. The desired shape of a 4D printed structure is not accomplished by simply exposing the smart materials to stimuli [8]. To make 4D structures with combination of design with the smart materials, the new printers must be used with some modifications.

The recent progresses have encashed the smart materials for 3D printed parts with functional behavior or 4D printing. The recently developed materials in 4D printing uses the property of water absorption to create 4D printed structure [3]. The materials that respond to temperature for example shape memory polymers and alloys (i.e., SMPs and SMAs) are established 4D materials due to their capabilities of expansion and contraction. Photo (or light) responsive materials are finding place as 4D printing materials as 3D printed structure shows change in color after exposure of light. The photo (or light) responsive materials are finding their spaces in stickers, shopping bags, aerospace structure, photo-voltaic, and biomedical devices, etc. Bio materials are main category of smart materials in 4D printing. 4D printing is showing tits usefulness in various healthcare applications ranging from nano-particle design to tissue engineering to manufacturing of human scale biomaterials [1, 3, 9]. The important consideration of smart design in 4D printed objects is clear in the creation of self-assembling origami, where a thin flat sheet naturally folds into a complicated 3D component on the induction of stimuli [4].

Overcoming the concern of low value of mechanical strength & durability of printed active composite will widen the scope of 4D printing into making of artificial muscles that subjected to extreme stress of range of 40–80 MPa [10]. The overall survey on the types of materials of the 4D printing is explained in the following section.

2 Materials in 4D Printing

In additive manufacturing for the construction of a part or object, materials for example plastics, ceramics, and metals are commonly practiced as 3D printing materials. Though, all materials are not applicable to 4D printing as they do not respond when exposed to stimuli. Moreover this also can be explained that a final structure made by 3D printing method doesn't show any change over a period of time when any stimuli is introduced. So, selection of a proper material is important for creating a 4D printed part. The materials structures in 4D printing are classified as based on smart materials and those are based on design are conventional materials. Regarding additive manufacturing, materials structures can be further classified as single material and multi-material structures. Further multi-material structures classified into discrete and composite and porous materials [11]. Tibbit in his research applied rigid plastic and active expandable polymer materials in the experiments [12]. 4D printing materials must be having properties of low glass transition temperature and for proper distribution must be of suitable viscosity [2]. Besides SMPs, wood, fibers and botanical cellulose, with smart behavior are good candidate materials for 4D printing as all shows behavior when exposed to heat, light or water.

2.1 Shape Memory Alloys

Shape memory alloys are the developing smart materials which have dual shape changing capacity. Shape memory materials are stimulus responsive materials. These alloys when exposed to the proper stimulus they transform with predefined shape from one to another. The concept has been extended to direct thermal actuation or indirect actuation. The applications are found in many areas of everyday life. Medical parts, self-deployable parts in spacecraft are the areas used. Shape memory polymer requires the combination of polymer and then it is programmed. The structure of the polymer is deformed and is put into irregular shape. The polymer gains its final form whenever external energy is applied. The activating agent is heat [13, 14]. Figure 2 shows the time series of shape memory tube.

The material used in cell is polymethacrylyate polymer (Dileep. 2017). Shape memory alloys do have some limitations such as low modulus, low strength and low operating temperature.

Ge et al. [15] proposed method of 4D printing which creates high-resolution multi-material 4D printing using highly tailorable SMPs on a projection micro stereolithography. By optimizing the constituents and their percentage, the flexibility of the methacrylate based copolymer networks enabled highly tailorable SMP thermomechanical properties including elastic modulus (~ 100 MPa), glass transition temperature(T_g), and the failure strain (up to 300%).

Zarek and team designed a shape memory 4D airway stent in the temporary state. These alloys are used in biomedical applications. The shape memory recovery is triggered, and then the stent recovers its original shape matching the target anatomy. Thus, personalized 4D medical devices can be fabricated with any geometry in medical applications [16].

2.2 Piezoelectric Materials

Piezoelectric materials are also finding great interest of researchers due to their property of transforming mechanical energy to electric energy or vice versa. Chen and his team in study demonstrated that piezoelectric composite slurry with nanoparticles of $BaTiO_3$ can be used in 3D printing using mask image projection based stereolithography technology to make a 4D part [17].

Further piezoelectric ink made of Pb (Zr 0.53 Ti 0.47) O3 (PZT) particles with a normal size of 170 nm and settled with polyacrylic acid built by Kuscer et al. [18]. This ink was streamed onto a platinized alumina substrate and very much dispersed in a blend of water and glycerol 155, then utilized for the manufacture of thick films (up to 6 m) by piezoelectric inkjet printing. The printing system was effectively performed at room temperature with 21 µm nozzle, a 20 µm drop dispersing and jetting amplitude of 15 V at 2 Hz of greatest working frequency.
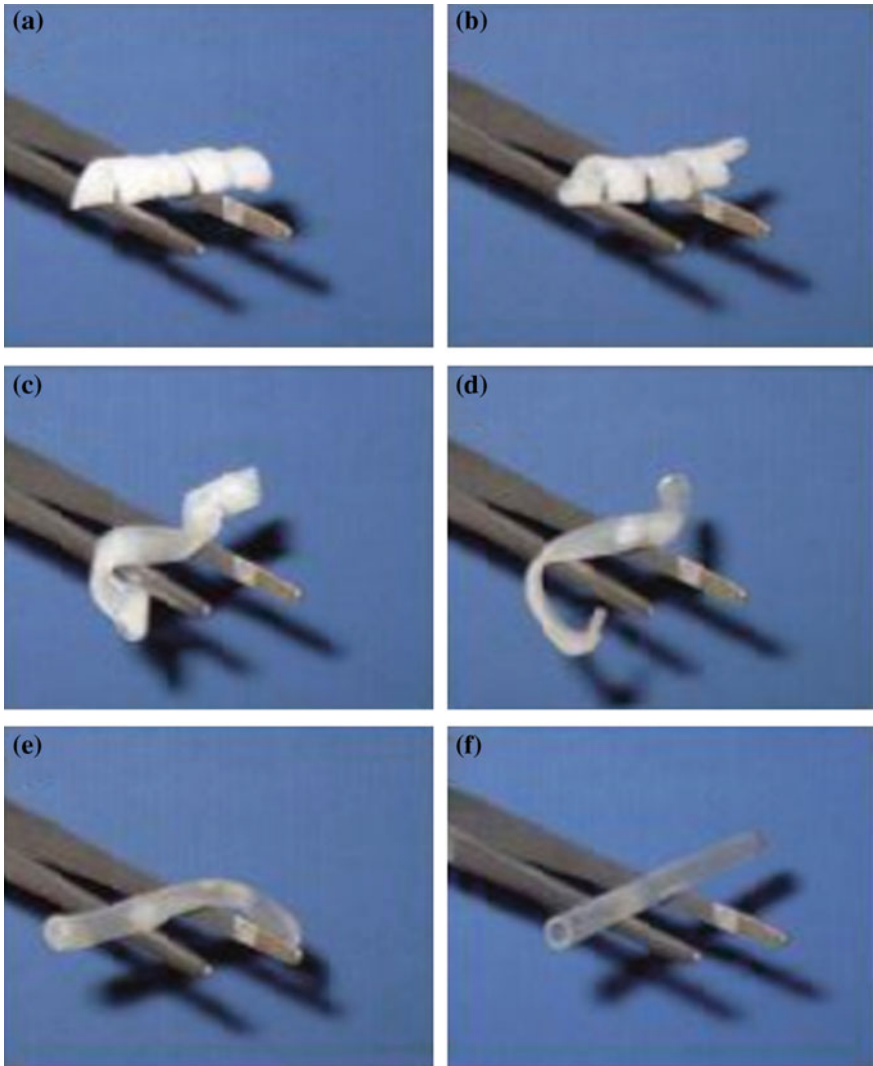
Fig. 2 Timeline of shape memory tube [13]

A low temperature piezoelectric (PZT) with 0–3 availability composite creation and utilized screen printed process and adaptable materials by Almusallam [19]. The optimized composition had proportion weightage as 12/1 (PZT/polymer), showing a relative dielectric of 146 (at 1 kHz) and a greatest d33 of 70 pC N-1 to alumina substrate.

Thus, the piezoelectric materials are used further for 4D printing as its most commonly used in 3D printing.

2.3 Magnetostrictive Materials

Like piezoelectric material, a magnetostrictive material uses a magnetic energy and converts this energy into mechanical energy and vice versa. Terbium, Iron, dysprosium (D), etc. are most common magnetostrictive materials. These materials can be utilized as transducers and actuators where magnetic energy is utilized to cause shape change. The application incorporates telephone receivers, oscillators, sonar scanning, and hearing aid, damping systems, and positioning equipment. The advance researches of magnetostrictive material alloys with compatible properties will help the 4D printing method [12]. These find applications in Stimuli responding material in structures, sensing, and actuation and so on. Magnetostrictive films are in use as micro-pumps since the inception of Micro Electro Mechanical Systems (MEMS) [20, 21]. 4D Printing technologies presents a solution of comparatively low cost and robust tool for production of magnetostrictive sensors and actuators.

Fig. 3 4D printing responsive to thermal behavior [2]

Light sensitive self-changing materials

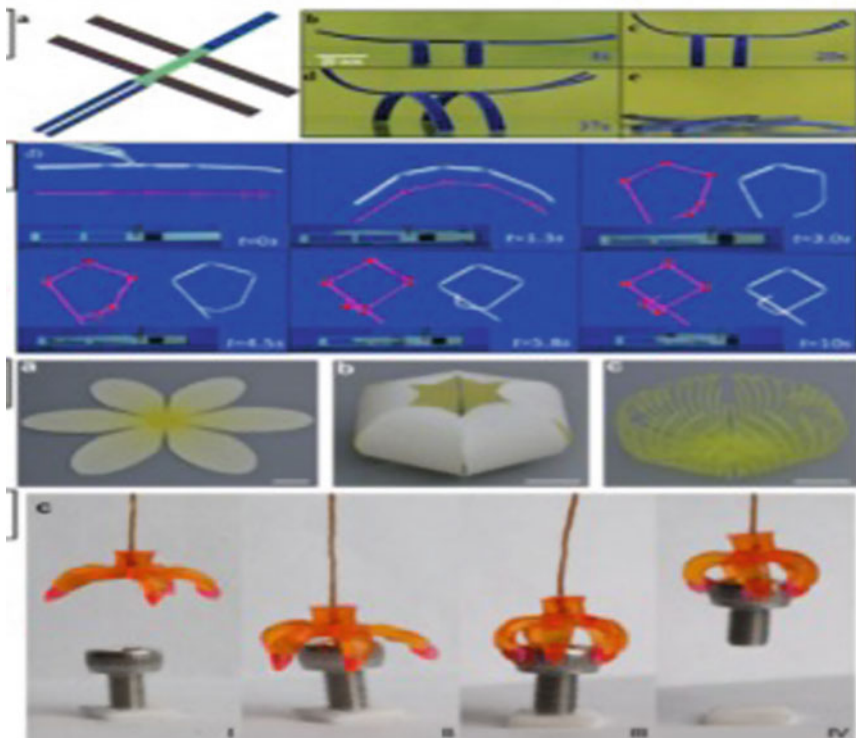Liu et al. [22] proposed the method for smart polymers activated by light by making hinges of the pre stressed polystyrene sheets, printed with black color ink. The techniques use infrared light to raise the temperature of the material beyond its glass transition temperature (T_g). The temperature of the black ink areas rises quickly and also bend quickly compare to the remaining material. The ink printed on the top of the sheets turns towards the light direction and ink printed on the bottom side of a transparent layer bends away from the light direction. By adjusting the geometry of ink, ink width, and number of printed lines produces distinctive turning points, twisting angle, and light power necessities (Fig. 3).

3   Conclusion

4D printing has the capabilities to enhance the functions of a product made through 3D printing technology. The feature of 4D printing is concerned with developing a product through smart material, smart design, exposure to stimuli and mathematical modeling. The process of 4D printing enables innovative and useful applications which are difficult to achieve through conventional rapid prototyping techniques. As 4D printing is obtaining popularity because of its functionality concerning time, smart materials, new designs for the printing process, it has enormous of applications from daily lives to the global manufacturing applications. This process helps in reduction of the manufacturing time and the human effort and labor required assembling the machine. The smart materials emerged in 4D printing technology is discussed and is reviewed. Thus, the comprehensive review of all smart materials and multi-materials used for the 4D printing technology is made in this research and found that smart materials are best and efficient in 4D printing and further research is conducted to improve and maximize the potential applications of the 4D printing process.

References

1. Gao W, Zhang Y, Ramanujan D, Ramani K, Chen Y, Williams CB, Wang CCL, Shin YC, Zhang S, Zavattieri PD (2015) The status, challenges, and future of additive manufacturing in engineering. CAD Comput Aided Des 69:65–89
2. Shin DG, Kim TH, Kim DE (2017) Review of 4D printing materials and their properties. Int J Precis Eng Manuf Green Technol 4:349–357
3. Choi J, Kwon O-C, Jo W, Lee HJ, Moon M-W (2015) 4D printing technology: a review. 3D Print Addit Manuf 2:159–167
4. Ge Q, Dunn CK, Qi HJ, Dunn ML (2014) Active origami by 4D printing. Smart Mater Struct 23(9):094007
5. Campbell TA, Tibbits S, Garrett B (2014) The next wave : 4D printing programming the material world. Atlantic Council

6. Leist SK, Zhou J (2016) Current status of 4D printing technology and the potential of light-reactive smart materials as 4D printable materials. Virtual Phys Prototyp 11:249–262
7. Raviv D, Zhao W, McKnelly C, Papadopoulou A, Kadambi A, Shi B, Hirsch S, Dikovsky D, Zyracki M, Olguin C, Raskar R, Tibbits S (2014) Active printed materials for complex self-evolving deformations. Sci Rep 4:1–8
8. Roy D, Cambre JN, Sumerlin BS (2010) Future perspectives and recent advances in stimuli-responsive materials. Prog Polym Sci 35:278–301
9. Pati F, Jang J, Ha DH, Won Kim S, Rhie JW, Shim JH, Kim DH, Cho DW (2014) Printing three-dimensional tissue analogues with decellularized extracellular matrix bioink. Nat Commun 5:1–11
10. Ramakrishna S, Mayer J, Wintermantel E, Leong KW (2001) Biomedical applications of polymer-composite materials: a review. Compos Sci Technol 61:1189–1224
11. Vaezi M, Chianrabutra S, Mellor B, Yang S (2013) Multiple material additive manufacturing-Part 1: a review: this review paper covers a decade of research on multiple material additive manufacturing technologies which can produce complex geometry parts with different materials. Virtual Phys Prototyp 8:19–50
12. Tibbits S (2014) 4D printing: multi-material shape change. Archit Des 84:116–121
13. Langer R, Tirrell DA (2004) Designing materials for biology and medicine. Nature 428: 487–491
14. Behl M, Lendlein A (2007) Shape-memory polymers are an emerging class of active polymers that. Mater Today 10:20–28
15. Ge Q, Sakhaei AH, Lee H, Dunn CK, Fang NX, Dunn ML (2016) Multimaterial 4D printing with tailorable shape memory polymers. Sci Rep 6:1–11
16. Zarek M, Mansour N, Shapira S, Cohn D (2017) 4D Printing of Shape Memory-Based Personalized Endoluminal Medical Devices. Macromol Rapid Commun 38:1–6
17. Chen Z, Song X, Lei L, Chen X, Fei C, Chiu CT, Qian X, Ma T, Yang Y, Shung K, Chen Y, Zhou Q (2016) 3D printing of piezoelectric element for energy focusing and ultrasonic sensing. Nano Energy 27:78–86
18. Kuscer D, Noshchenko O, Uršič H, Malič B (2013) Piezoelectric properties of ink-jet-printed lead zirconate titanate thick films confirmed by piezoresponse force microscopy. J Am Ceram Soc 96:2714–2717
19. Almusallam A, Yang K, Cao Z, Zhu D, Tudor J, Beeby SP (2014) Improving the dielectric and piezoelectric properties of screen-printed Low temperature PZT/polymer composite using cold isostatic pressing. J Phys Conf Ser 557
20. Linear S, Crosslinked S, Thermoplastic S, Shape-memory LSES, Industrial A, Smps P (2018) Shape-memory polymer, pp 1–10
21. Grabham NJ, White NM, Beeby SP (2000) Thick-film magnetostrictive material for MEMS. Electron Lett 36:332–334
22. Liu Y, Boyles JK, Genzer J, Dickey MD (2012) Self-folding of polymer sheets using local light absorption. Soft Matter 8:1764–1769
23. Young, M (2016) ALL3DP.com

Integrated Topsis-Moora Model for Prioritization of New Bike Selection

Sumit Chawla, Saurabh Agrawal and Ranganath M. Singari

Abstract Nowadays purchasing two wheeler especially bike in this fluctuating market is backbreaker task for the customers due to lots of complex specifications like mileage, style, life span, cost and suspension, etc. To tame this problem, we have many techniques available with us like multi-criteria decision-making (MCDM), fuzzy logic, etc. We have used MOORA (Multi-Objective Optimization on the basis of Ratio Analysis) and TOPSIS (Technique for Order Preference by Similarity to Ideal Solution and these methods are one of the best techniques among MCDM because it gives best results and it is used by most of the researcher. Using this technique, we find out the best optimal bike from the customer point of view based on their requirements. First time MOORA and TOPSIS methods are used together to solve this type of problem. Main ten attributes were identified through literature review, and discussion with the experts from the Indian automobile industry. Integrated TOPSIS-MOORA approach is proposed for prioritizing alternatives based on four selected attributes. Perusal of literature indicates that these methods have not been applied earlier for selection of new bikes in Indian automobile industry. Six Indian automobile companies were selected for evaluation of this methodology. Results indicate that best optimal bike based on customer requirements. Fuel economy, style, cylinder capacity and cost are top four prioritized factor taken in this study. The findings will be useful for every new customer and all automobile industry.

Keywords CDM · TOPSIS · MOORA · Bike selection · Relative closeness · Positive and negative ideal solutions · Priority · Normalized decision matrix

S. Chawla (✉)
Bharati Vidyapeeth's College of Engineering, New Delhi, Delhi, India
e-mail: chawlasumit4@gmail.com

S. Agrawal · R. M. Singari
Delhi Technological University (Formerly DCE), Delhi, India

1   Introduction

Buying a bike is an arduous task for customers. Customer wants to spend their money in good products which fulfills their needs. Normal middle class man wants to buy a bike which is economical to their budget. Even in the budget range of customers, many options are available which make customer decision for bike selection more challenging. The last decade has seen remarkable growth in the automobile industry because automobiles become the daily routine need for everyone. Due to the presence of global automobile companies and tremendous expansion of automation, Indian markets are filled with vast varieties of automobile.

Fourteen bike alternatives are determined based on best bikes of 2017. Six alternatives among them are used in this study Necessary data like specification parameters are taken from www.bikedekho.com/best-bikes. Table 1 shows the specification parameter of bikes.

2   Literature Review

With the help of decision-making process, we can select the ideal alternatives in line with the requirements of the customer. MCDM gives best solution in this type of case [7]. Rathi et al. [14] express a best way for identification of critical factors

Table 1 Specification parameter of bikes

Best Bikes in India 2017	On road price (Delhi) (approx.) (Rs)	Mileage (kmpl)	Cylinder capacity
Honda navi	43,000	60	109
Royal Enfield Himalayan	1,82,000	33.5	411
Honda shine	61,500	65	124.7
Bajaj V	63,000	57	125
Royal Enfield classic 350	1,53,000	37	346
KTM duke 200	1,57,000	35	199.5
Bajaj Pulsar 150	85,000	65	149
Yamaha YZF R15	1,30,000	40	149
Hero Splender Ismart	58,000	92	97.2
Suzuki Hayabusa	15,22,000	17	1340
Royal Enfield Bullet	1,28,000	40	346
Harley Davidson	5,47,000	17.4	749
TVS Apache	1,05,000	35	197.7
TVS Sport	42,800	95	99.7

responsible for machine failure in center less grinding machine. Srikrishna et al. [15] proposed a new procedure for four wheeler selection in line with the best alternative using TOPSIS model. Nima Zoraghi et al. [12] presents a fuzzy MCDM model for ranking the service quality in hotels.

Rajnish Kumar et al. [13] finds the best material for engineering design, based on criteria weights are calculated and alternatives are ranked using TOPSIS method.

Moreover, studies on automobile choice have mostly focused on developed country consumers with very little focus on automobile brand choice in developing countries especially in sub-Saharan Africa and India, etc. [5, 6, 9, 18].

MCDM is a very popular approach that in complicated materials selection problem more than one MCDM methods to be applied for the best decision [17]. TOPSIS and MOORA are selected for this problem because they are very efficient MCDM methods for solving real life problems like general bike selection problem due to its outstanding features and rational correlation with the previous studies. Many MCDM techniques like AHP, ANP, SAW, TOPSIS, MOORA, ELECTRE, VIKOR, COPRAS, PROMETHEE, DEMATEL, SMART, PSI, WPM, EVAMIX and GTMA, etc., have been applied to solve MCDM problems over last many years.

3 Methodology

In this study, TOPSIS model is developed for bike selection using seven-step unique approaches and to identify the best alternative for customers. The type of best alternative depends on customer. For some customers, economy is main criteria and for some customers, style and pick up of bike are main criteria. Based on weights of criteria results will vary.

3.1 Selection Criteria

For proper selection of bike according to customer point of view, we have to compare performance parameters of these bikes. The performance parameters taken for this study are Cost, Mileage (Fuel economy), cylinder capacity (CC), and style. Although thousands of bikes are present in market and it is very difficult to compare the performance parameter of all of them. So for our study, we have taken six bikes which are Hero Splender Ismart, Honda Navi, Bajaj pulsar 150, Royal Enfield bullet, TVS Sport and Honda Shine (Fig. 1).
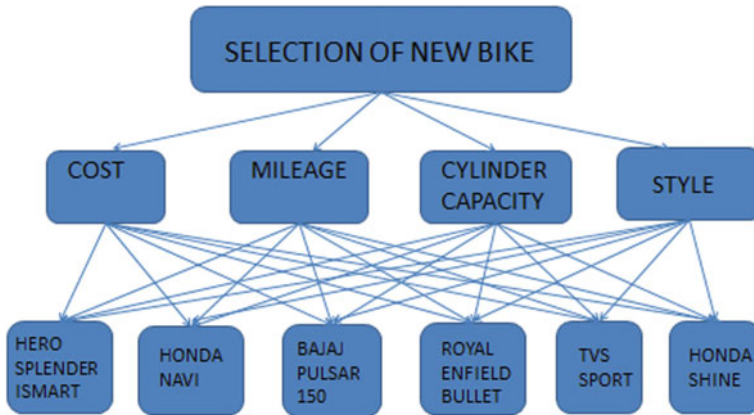
Fig. 1 Selection criteria of TOPSIS

3.2 TOPSIS Method

It is one of the best methods among all MCDM techniques for selecting the best alternatives in real-life problems [8].

Step 1: The first stage of this method is to construct **Decision Matrix (DM)**. (**Typed all equations again**)

$$DM = [x_{ij}]_{m \times n} \tag{1}$$

where i (i = 1….. m) and j (j = 1…. n) are the criterion index and alternative index respectively; m is the number of potential sites.
Step 2: Calculate a normalized decision matrix (NDM)

$$NDM = R_{ij} = \frac{x_{ij}}{\sqrt{\sum_{i=1}^{m} x_{ij}^2}} \tag{2}$$

Step 3: Determine the weighted decision matrix

$$V = v_{ij} = w_j \times R_{ij} \tag{3}$$

Step 4: Identify the Positive and Negative Ideal Solution

$$PIS = A^+ = \{v_1^+, v_2^+ \dots, v_n^+\}, \, where : v_j^+$$
$$= \{(\max i \,(v_{ij}) \, if \, j \in J); \, (\min i \,(v_{ij}) \, if \, j \in J')\} \tag{4}$$

$$PIS = A^- = \{v_1^-, v_2^- \ldots, v_n^-\}, \ where : v_j^-$$
$$= \{(\min i \ (v_{ij}) \ if \ j \in J); \ (\max i \ (v_{ij}) \ if \ j \in J')\} \tag{5}$$

where, J is related with the beneficial attributes and J' is related with the non-beneficial attributes [19].

Step 5: **Find the separation distance** of each alternative from ideal and non-ideal solution.

$$S^+ = \sqrt{\sum_{j=1}^{n} (v_j^+ - v_{ij})^2} \qquad i = 1\ldots\ldots m \tag{6}$$

$$S^- = \sqrt{\sum_{j=1}^{n} (v_j^- - v_{ij})^2} \qquad i = 1\ldots\ldots m \tag{7}$$

where, i = criterion index, j = alternative index.

Step 6: **Measure the relative closeness** of each location to the ideal solution.

$$C_i = \frac{s_i^-}{s_i^+ + s_i^-} \ , \ 0 \leq C_i \leq 1 \tag{8}$$

Step 7: **Rank the preference order** from higher relative closeness values to lower relative closeness values.

3.3   The MOORA Method

First two steps are almost similar to TOPSIS method. The MOORA methodology is shown below[1]

Step 1: The first step of MOORA method is to find decision matrix X in which x_{ij} represents performance index of ith alternative w.r.t jth attribute, i = 1, 2, …, m and j = 1, 2, …, n:

$$X = [x_{ij}]_{m \times n} \tag{9}$$

Step 2: Find normalized decision matrix (NDM).

$$NDM = x_{ij}^* = \frac{x_{ij}}{\sqrt{\sum_{i=1}^{m} x_{ij}^2}} \tag{10}$$

Step 3: The overall performance score of each alternative y_i^* in Eq. (11).

$$y_i^* = \sum_{j=1}^{k} x_{ij}^* - \sum_{j=k+1}^{n} x_{ij}^* \tag{11}$$

Here, k and (n–k) are the number of criteria to be maximized and minimized, respectively. If we want to give importance order to the criteria, then we can use the weightages also in the formula as seen Eq. (12) [4, 11].

$$y_i^* = \sum_{j=1}^{k} w_j x_{ij}^* - \sum_{j=k+1}^{n} w_j x_{ij}^* \tag{12}$$

AHP method is simple to use, we used this method for obtaining weights in our study.

Step 4: Finally, values of y_i^* obtained from step 3 are arranged in descending order in order to get ranking of alternatives. Higher values of y_i^* gives higher rank of alternative.

The ration system part of MOORA method is shown in first four steps. Remaining steps show reference point part.

Step 5: Tchebycheff Min–Max metric is given in Eq. (13) [1–3].

$$\min_i \{ \max_j \left| s_j - x_{ij}^* \right| \} \tag{13}$$

s_j is the jth coordinate of the reference point which shows those alternatives having most desirable performances with respect to j_{th} criterion. For determining s_j, Eq. (14) may be used [16].

$$s_j \{ _{\min_i x_{ij}^*,}^{\max_i x_{ij}^*} \tag{14}$$

$\max x_{ij}^*$ for criteria to be maximized & $\min x_{ij}^*$ for criteria to be minimized.

If we want to give importance order to the criteria, then we can use the weightages also in the formula (13) and it can be reformulated as seen Eq. (15).

$$\min_i \{ \max_j \left| w_j s_j - w_j x_{ij}^* \right| \} \tag{15}$$

Step 6: At last best alternative is selected based on minimum deviation value from reference point [10].

3.4 Application of TOPSIS Technique

This case study is associated with the automobile showroom which is the part of automobile industry. The Showroom management wants to sell the bikes to the customers. The R & D department is responsible for pinpoint the alternatives and choose the best bikes for the customers. We did this study for the showroom as well as for R & D department and determined the criteria according to the needs of the customer.

This entire numerical and linguistic variable used in Table 2 is converted to approx. score out of 10 as shown in Table 3.

4 Result and Discussion

The positive ideal (A^+) and the negative ideal (A^-) solutions are

$$A^+ = \{0.1912, 0.0486, 0.101 \text{ and } 0.0975\}$$

$$A^- = \{0.1116, 0.0358, 0.0702 \text{ and } 0.1512\}$$

Table 2 Criterion parametric values

Criteria's	Alternatives					
	Hero Splender Ismart	Honda Navi	Bajaj Pulsar 150	Royal Enfield Bullet	TVS Sport	Honda Shine
Mileage (kmpl)	92	60	65	40	95	65
Style	Good	Better	Good	Extreme	Good	Better
Cylinder Capacity (CC)	97.2	109.19	149	346	99.7	124.7
Cost (Rs) (approx.)	58,000	43,000	85,000	1,28,000	42,800	61,500

Table 3 Elements of decision matrix

Alternatives	Criteria's			
	Mileage (kmpl)	Style	Cylinder capacity (CC)	Cost (Rs) (approx.)
Hero Splender Ismart	9.2	7	6.8	7
Honda Navi	7.2	8.2	7.3	6
Bajaj Pulsar150	8.1	7.3	8.3	8
Royal Enfield Bullet	5.5	9.5	9.8	9
TVS Sport	9.4	7.3	7.1	5.8
Honda Shine	8.1	8.3	7.8	7.4
Weights	0.4	0.1	0.2	0.3

The separation distance is calculated using Eq. (7).

$$S^+ = \{0.03914, 0.0522, 0.04922, 0.0960, 0.030 \text{ and } 0.0433\}$$

$$S^- = \{0.0827, 0.0617, 0.0578, 0.0333, 0.0961 \text{ and } 0.061\}$$

The relative closeness values are calculated using Eq. (8).

$$C_i = \{0.3212, 0.4582, 0.4595, 0.7424, 0.238 \text{ and } 0.4151\}$$

So, relative closeness values show the best optimal bike according to customer requirements is Royal Enfield Bullet and 2nd best choice is Bajaj pulsar 150 (Figs. 2 and 3).

4.1 Results (Using MOORA Method)

Using steps 1 and 2, we will get same values of decision matrix and normalized values of decision matrix table as given in Table 3 and 4 respectively. $\sum_{j=1}^{k} x_{ij}^*$, this value is calculated by adding weighted normalized values of three beneficial criteria

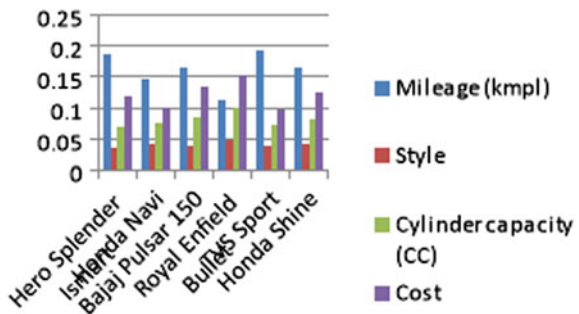
Fig. 2 Weighted values of decision matrix

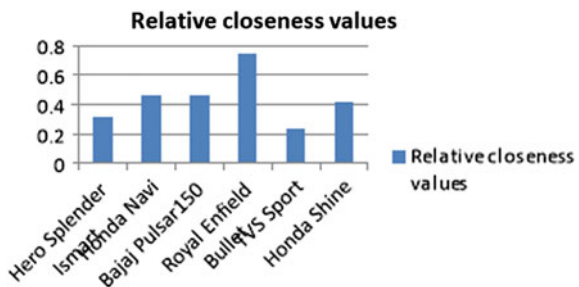Fig. 3 Relative closeness values of different bikes

Table 4 Normalized values of decision matrix

Alternatives	Criteria's			
	Mileage (kmpl)	Style	Cylinder capacity (CC)	Cost (Rs) (approx.)
Hero Splender Ismart	0.468	0.358	0.351	0.392
Honda Navi	0.366	0.419	0.376	0.336
Bajaj Pulsar150	0.412	0.373	0.428	0.448
Royal Enfield Bullet	0.279	0.486	0.505	0.504
TVS Sport	0.478	0.373	0.366	0.325
Honda Shine	0.412	0.424	0.402	0.414

Table 5 Weighted values of decision matrix

Alternatives	Criteria's			
	Mileage (kmpl)	Style	Cylinder capacity (CC)	Cost (Rs) (approx.)
Hero Splender Ismart	0.1872	0.0358	0.0702	0.1176
Honda Navi	0.1464	0.0419	0.0752	0.1008
Bajaj Pulsar150	0.1648	0.0373	0.0856	0.1344
Royal Enfield Bullet	0.1116	0.0486	0.1010	0.1512
TVS Sport	0.1912	0.0373	0.0732	0.0975
Honda Shine	0.1648	0.0424	0.0804	0.1242

which are mileage, style and cylinder capacity. Similarly, $\sum_{j=k+1}^{n} x_{ij}^*$ is taken directly from single non-beneficial criterion which is cost. y_i^* shows overall performance score of each alternative. Based on their performance score values ranking is decided (Tables 5, 6 and Fig. 4).

Table 7 shows the descending order of deviations from the reference point.

Table 6 Overall performances of the alternatives

Alternatives	$\sum_{j=1}^{k} x_{ij}^*$	$\sum_{j=k+1}^{n} x_{ij}^*$	y_i^*	Ranking
Hero Splender Ismart	0.2932	0.1176	0.1756	2
Honda Navi	0.2635	0.1008	0.1627	4
Bajaj Pulsar150	0.2877	0.1344	0.1533	5
Royal Enfield Bullet	0.2612	0.1512	0.11	6
TVS Sport	0.3017	0.0975	0.2042	1
Honda Shine	0.2876	0.1242	0.1634	3

Fig. 4 Overall performance
score using MOORA method
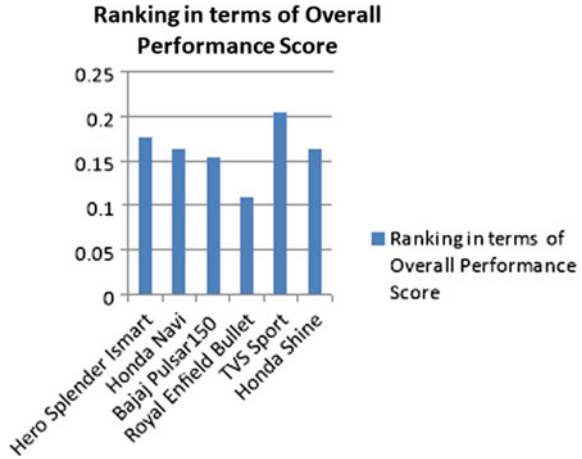
Table 7 Deviation from the reference point

Alternatives			Criteria's			
	Mileage (kmpl)	Style	Cylinder capacity (CC)	Cost (Rs) (approx.)	Maximum values	Ranking
Hero Splend. Ismart	0.004	0.0128	0.0308	0.0201	0.0308	4
Honda Navi	0.0448	0.0067	0.0258	0.0033	0.0448	2
Bajaj Pulsar	0.0264	0.0113	0.0154	0.0369	0.0369	3
Royal Enfield Bullet	0.0796	0	0	0.0537	0.0796	1
TVS Sport	0	0.0113	0.0278	0	0.0278	6
Honda Shine	0.0264	0.0062	0.0206	0.0267	0.0267	5

5   Conclusions

Using TOPSIS method of multi-criteria decision-making (MCDM), we find a seven
step procedure to select the best new bike among the given alternatives in the
market. By applying this method on various process parameters, technical speci-
fications, under different cases, it is concluded that proposed model is simple in use
and is able to find final ranking preferences in descending order in terms of relative
closeness values w.r.t. ideal solution. This proposed model also helps in comparing
the relative performances of different bikes. From both methods TOPSIS and
MOORA, we get best bike alternative for the customer is Royal Enfield Bullet.
These results can be varying based on the weightages and customer interest.

The MOORA method gives the overall performance of alternatives w.r.t various
criteria. This method is easy to apply, flexible and represents subjective part of
selection process [7].

References

1. Brauers WKM Zavadskas EK (2006) The MOORA method and its application to privatization in a transition economy. Control Cybern 35(2):445–469
2. Brauers WKM, Zavadskas EK (2009) Multi objective optimization with discrete alternatives on the basis of ratio analysis. Intellect Econ 2(6):30–41
3. Brauers WKM, Zavadskas EK, Turskis Z, Vilutiene T (2008) Multiobjective contractor's ranking by applying the MOORA method. J Bus Econ Manag 9(4):245–255
4. Chakraborty S (2011) Application of the MOORA method for decision making in manufacturing environment. Int J Adv Manuf Tech 54(9–12):1155–1166
5. De Haan P, Mueller MG, Peters A (2006) Does the hybrid Toyota Prius lead to rebound effects? Analysis of size and number of cars previously owned by Swiss Prius buyers. Elsevier Ecol Econ 58:592–605
6. Diamantopoulos A, Schlegelmilch B, Palihawadana D (2011) The relationship-between-country of origin-image and brand -image as drivers of purchase-intentions: a test of alternative perspectives. Int Mark Rev 28(5):508–524
7. Esra et al (2017) The multi-objective decision making methods based on MULTIMOORA and MOOSRA for the laptop selection problem. J Ind Eng Int 13:229–237
8. Hwang CL, Yoon K (1981) Multiple attribute decision making: methods and applications. Springer, New York
9. Lieven, T., Mu hlmeier, S., Henkel, S. and Waller, J.F. (2011) Who will buy electric cars? An empirical study in Germany. Transportation Research Part D (16):236–243
10. Karande P, Chakraborty S (2012) Application-of-multi-objective-optimization-on-the-basis-of-ratio-analysis (MOORA) method for materials selection. Mater Des 37:317–324
11. Madic M et al (2015) Non-conventional machining processes selection using multi-objective optimization on the basis of ratio analysis method. J Engg Sci Tech 10(11):1441–1452
12. Nima Zoraghi et al. (2013) A fuzzy-MCDM-model-with-objective and subjective-weights for evaluating service-quality in hotel-industries. J Ind Eng Int. https://doi.org/10.1186/2251-712x-9-38
13. Kumar R et al (2013) Selection of material for optimal design using multi-criteria decision making. Procedia Mater Sci 6:590–596
14. Rathi Rajeev, Khanduja Dinesh, Sharma SK (2016) Efficacy of fuzzy MADM approach in Six Sigma analysis phase in automotive sector. J Ind Eng Int 12:377–387
15. Srikrishna S et al (2014) A new car selection in the market using TOPSIS technique. IJERGS 2:177–181
16. Stanujkic D et al (2012) An objective multi-criteria approach to optimization using MOORA method and interval grey numbers Technol Econ. Dev Econ 18(2):331–363
17. Hadi Seyed et al (2017) A comprehensive MCDM-based approach using TOPSIS, COPRAS and DEA as an auxiliary tool for material selection problems. Materials 121:237–253
18. Tang Z, Lou J, Xiao J (2011) Antecedents of intention to purchase mass customized products. J Prod Brand Manag 20(4):316–326
19. Wang L et al (2007) Selection of optimum maintenance strategies based on a fuzzy analytical hierarchy process. Int J Prod Econ 107(1):151–163

Numerical Simulations of Bore-Finishing Tool Lubrication System to Achieve Minimum Quantity Lubrication Using the Discretized Phase Model

Rohan V. Sawant and Chandrakant R. Sonawane

Abstract Cooling as well as lubrication is essential for almost all types of metal cutting/machining processes. Nowadays, the Minimum Quantity Lubrication (MQL) technique has been found very popular and is been used widely during metal cutting/machining over the flood lubrication. In contrast to flood lubrication, minimum quantity lubrication uses only a few drops of lubrication (5–50 ml/h) in machining. Hence, the reduction in the quantity of lubricant compared to the circulated quantities of conventional metal-working fluid systems is the key feature of MQL. However, the supply of the adequate quantity lubrication as well as homogenous (air–oil) mixture is essential to avoid dry-out conditions at machine tool. In this paper, the numerical simulation of the lubrication system used for the bore finishing machine line is presented. The lubrication system uses the minimum quantity lubrication controlled by a distributor system having a common pipe carrying lubricant. This pipe has multiple outlets (13 outlets) supplying the lubricant at the respective 13 boring tool machines. The Discretized Phase Model is used to simulate the continuous medium (air) interacted with injection (oil) particles. Various flow rates, as well as supply (distributor) pressures, are simulated in order to obtain the homogenous distribution of lubricating oil. From the simulation results, it is seen inlet distributor pressure of 6 bar, inlet velocity of 39 m/s and with an oil injection rate of 50 ml/h are optimum, as well as homogenous air–oil distribution at all 13 lubricant outlets.

Keywords Minimum quantity lubrication · MQL · Water/oil droplets · Discretized phase model · Simulation

R. V. Sawant · C. R. Sonawane (✉)
Symbiosis Institute of Technology, Symbiosis International (Deemed University), Pune, Maharashtra, India
e-mail: chandrakant.sonawane@sitpune.edu.in

1 Introduction

In today's manufacturing era, it is expected that the cutting fluid not only performs a tool cooling requirements but also most of the other functions such as lubrication, removing metal particles and protecting workpiece and the tool from corrosion. However, conventional cutting fluids systems have few disadvantages like their high cost, environmental impact as well as it adversely affects the health of workers. Hence, concepts like dry machining, minimum quantity lubrication, solid lubrication, cryogenic cooling, gaseous cooling, sustainable cutting fluids, and nano fluids are in development as well as in utilization. Among this, Minimum Quantity Lubrication (MQL) is developed tremendously in the cooling fluid as the best alternative.

In the MQL process, a minute (minimum) amount of lubricant is directly applied to the cutting tool–workpiece interface. In contrast to flood lubrication, the minimum quantity of lubrication uses only a few drops of lubrication (approx. 5–50 ml/h) in machining. This supplied amount is sufficient to provide effective lubrication, hence avoiding the wastage or excess supply. MQL is found to be very effective in a wide variety of metal cutting processes, including sawing, turning, milling, drilling, etc. There are two basic types of MQL delivery systems: external feed system and internal feed system. Figure 1 shows the general classification of devices types for MQL. Figure 2 shows the type of lubrication feed.

A number of researchers had worked on the various aspects of MQL used for various machining processes. Kuzu et al. [1] conducted the thermal modeling of the deep-hole drilling process under MQL conditions. They investigated the temperature distribution of a compacted graphite iron (CGI) workpiece in minimum quantity lubrication (MQL) deep-hole drilling. Guo et al. [2] performed grinding on nickel-based alloy for the evolution of the lubrication performance of mixtures of castor oil with other lubricants in MQL. Zhang et al. [3] focused on the tool life and
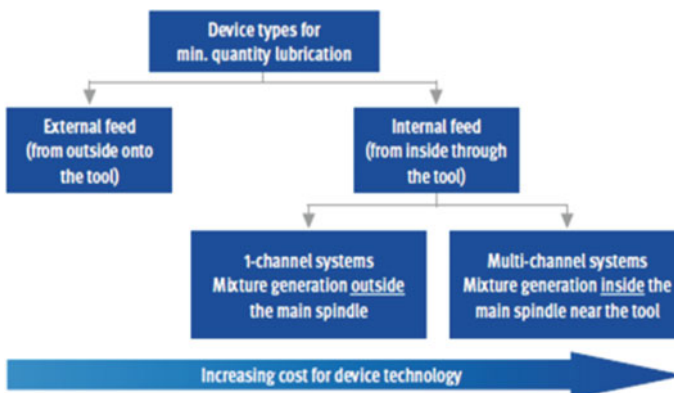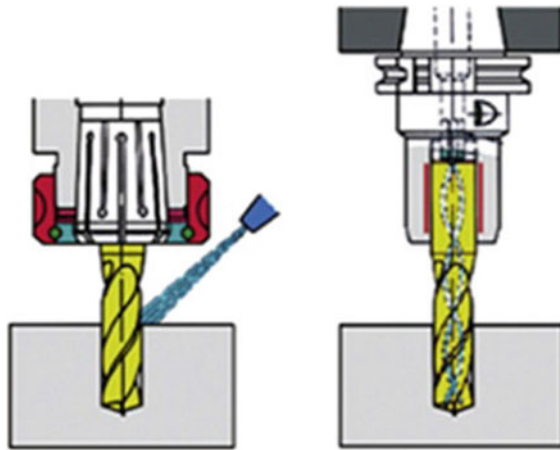

Fig. 1 Device types for MQL

cutting forces in end milling Inconel 718 under minimum quantity cooling lubrication with vegetable oil. They had found that MQCL cutting with biodegradable vegetable oil effectively improves the machinability and helps in the extension of tool life and reducing cutting forces.

Breitenbach et al. [4] focused on the study of a single drop impact onto a heated wall and his study is motivated by a wide range of industrial applications such as spray cooling fuel injection and atomization, or particle formation and encapsulation in a fluidized bed. Obikawa et al. [5] studied on the minimum quantity lubrication (MQL) to analyze the machining with the different lubrications other than flood coolant. MQL is to be used with < 1 ml/h, which is 10–100 times smaller compared with conventional consumed oil in the industry. They designed nozzles for MQL turning of Inconel 718 and their performances were investigated based on tool life and surface finish. They also controlled oil mist flow and the distance from the nozzle to the tooltip for enhancing the cutting performance of MQL machining, especially in the micro-liters lubrication range.

Park et al. [6] conducted an experiment to study the droplet size, the droplet size distribution, and the wetting angle. They utilized the Confocal Laser Scanning Microscopy (CSLM), wavelet filtering, and image processing algorithms for capturing droplet geometry and distribution for commercially available MQL oils. The wetting angles of the oils were measured by depositing oil droplets onto TiSiN and TiAlN-coated inserts. They studied particle distribution in the range of 10–100 µm. From the literature survey, it has been found that numerical analysis is being used by a number of researchers for finding the outcome of different machining operations like mass flow rate and particles distribution.

In this paper, numerical simulation of the lubrication system used for bore-finishing machine line is presented. The Discretized Phase Model is used to simulate the continuous medium (air) interacted with injection (oil) particles. The results are discussed for various flow rates, as well as supply (distributor) pressures in order to obtain the homogenous distribution of lubricating oil.

2   Modeling: Problem Under Consideration

Figure 3 shows the typical 1-channel and 2-channel systems. These systems eliminate investment into the sump, recyclers containers pump, and filtration devices. There is no cost for cleaning and drying the chips before their disposal or cleaning of the workpiece before the next process.

Figure 4 shows the geometry of the CAM bore-finishing tool; usually used for finishing operations for CAM bore. The lubrication system uses the minimum quantity lubrication controlled by a distributor system having a common pipe
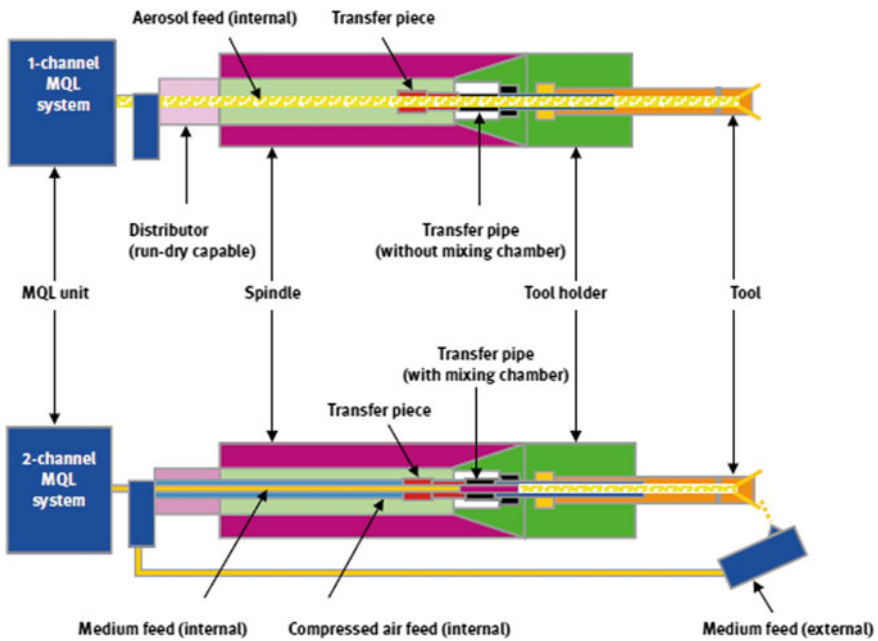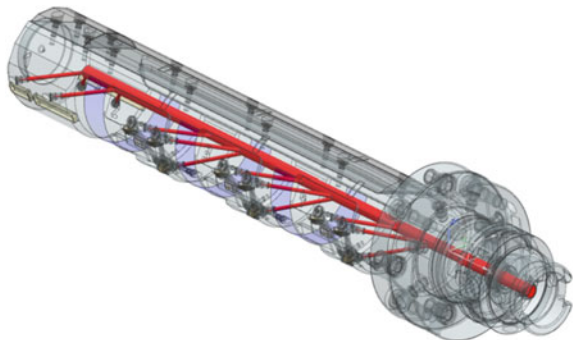

Fig. 3   Typical 1-channel and 2-channel systems
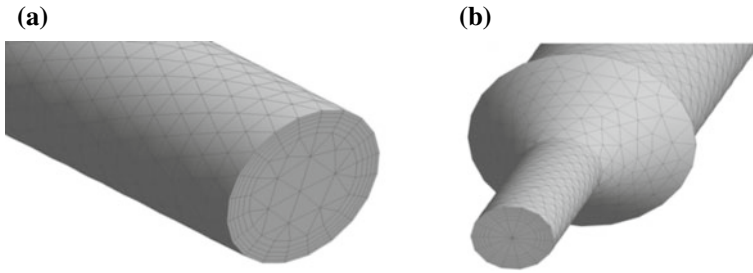
Fig. 4   CAM bore-finishing tool

Fig. 5 Details of a mesh generated for CAM bore finishing tool. **a** mesh at the coolant inlet, **b** mesh at the coolant outlet
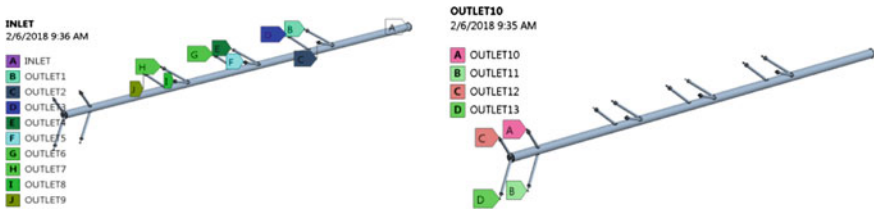

Fig. 6 Boundary conditions used during CFD simulations

carrying lubricant. The red zone shows the numerical domain of the MQL lubrication system under consideration. This pipe has multiple outlets (13 outlets) supplying the lubricant at respective 13 boring tool machine. It comprises of pressurized air and water/oil lubricant. It helps in reducing the heat generated in tool and flown down the chips with lubricant.

Figure 5a and b show the mesh view of coolant inlet and outlet, respectively. A hybrid mesh (combination of hexahedral and tetrahedron) with 777520 mesh elements and 308537 number of nodes. The hexahedral mesh is created near the pipe wall, which takes care of the proper boundary condition implementation.

Figure 6 shows the various boundary conditions used during the CFD simulation.

3 Numerical Method

The commercial code FLUENT 16.1 was used for current numerical analysis. The incompressible flow through the lubrication system is solved using SIMPLE [7] numerical scheme. The lubricant injected is tracked and solved using the Discrete Phase Model (DPM). The DPM is a multiphase model in which the dispersed phase is tracked in a Lagrangian reference frame, whereas a continuous phase is modeled

Fig. 7 Discrete phase model
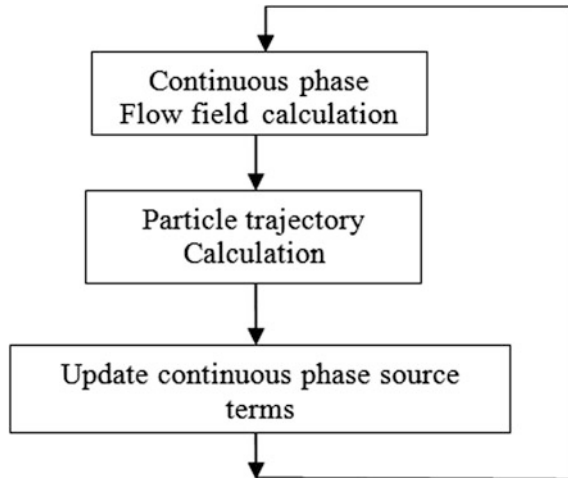
by a Eulerian method. Hence, DPM process is considered as a Eulerian–Lagrangian approach.

Figure 7 shows the typical flow of solution followed during current numerical computations. The dispersed phase is solved by tracking a large number of particles (bubbles, or droplets) through the calculated flow field. The trajectory of the injected lubricant is calculated by integrating the particle force balance equation as

$$\frac{du_i^p}{dt} = F_d(u_i - u_i^p) + \frac{g_i(\rho_p - \rho)}{\rho_p} + \frac{F_i}{\rho_p}$$

where

$F_d(u_i - u_i^p)$ = drag force, which is a function of relative velocity between the injected particles phase and continues phase.

$\frac{g_i(\rho_p - \rho)}{\rho_p}$ = gravity force, which is negligible in the current computations due to horizontal layout of the lubrication system as well as the density difference is also a negligible one. And

$\frac{F_i}{\rho_p}$ = additional force, if present. No additional forces acting hence taken as zero.

The two phases, i.e., compressed air and injected (dispersed) oil here are considered having a one-way coupling, i.e., particle motion gets affected by the continuous phase, but continuous phase is not affected by particle flow.

The particle–wall interactions are also considered and two types of interaction boundary conditions, i.e., (i) Trap: The particles are collected on the wall boundary condition and (ii) Reflect: The Particle bounces off the wall and user-prescribed coefficient of restitution are applied. Also, to the particle which leaves the flow
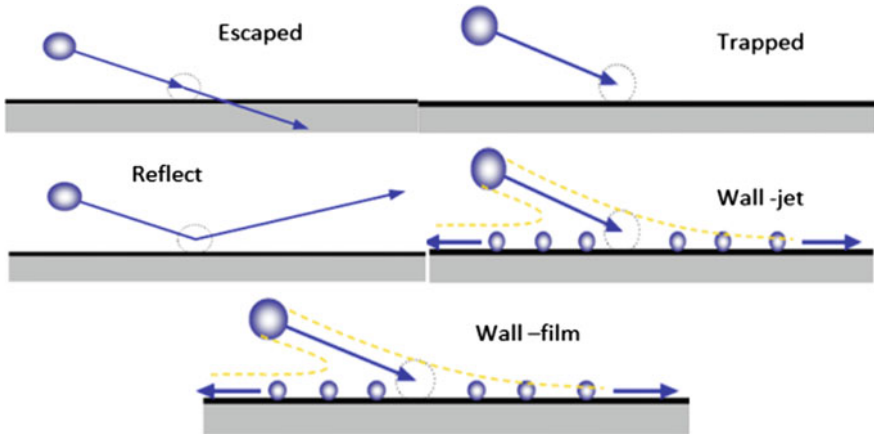
Fig. 8 Summary of the various wall–interactions conditions

domain, usually the escape condition is applied to inlet and outlets. Figure 8 shows the summary of various interaction boundary conditions applied at the wall.

The oil injected is defined as a surface injection where particle streams are injected from a surface (from inlet). The particle diameter is distributed in the range of 5–10 µm. Rosin-Rammler expression is used for oil particle (liquid sprays) representation of the droplet distribution. Here, the complete range of sizes is divided into an adequate number of discrete intervals; each represented by a mean diameter for which trajectory calculations are performed. For the Rosin-Rammler type, the mass fraction of droplets of diameter greater than d is given by

$$Y_d = e^{-\left(\frac{d}{\underline{d}}\right)^n}$$

where $\underline{d}$ is the size constant and n is the size distribution parameter. The Rosin-Rammler distribution also used to determine the distribution of mass flow among particle sizes.

4 Results and Discussion

The main objective is to find the flow distribution of the injected lubricant from the coolant domain. For this, the simulation domain is rotated at 1000 rpm. Also, the total domain is divided into 4 zones, where Zone 1, 2, and 3 contains 3 outlets, whereas, Zone 4 contains 4 outlets. Figure 9 shows the typical zone distribution adapted for the current simulation.
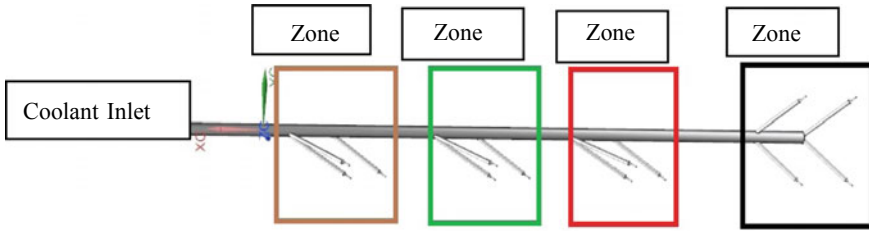
Fig. 9 Extracted coolant domain zone distribution

Table 1 Summary of inlet flow conditions for MQL lubrication system

Sr. No.	Mass flow rate of the dispersed phase (oil) used (ml/h)	Mass flow rate of the dispersed phase (oil) used (kg/s)	Percentage of the dispersed phase (oil) used (%)	Diameter of the dispersed phase (oil) used (μm)
1	15	0.35e-05	10	5–10
2	30	0.7 e-05	10	5–10
3	50	1.16667e-05	10	5–10
4	60	1.4 e-05	10	5–10

The Discretized Phase Model is now solved to simulate the continuous medium (air) interacted with injection (oil) particles. Various flow rates, as well as supply (distributor) pressures, are simulated in order to obtain the homogenous distribution of lubricating oil. Table 1 shows a summary of various mass flow rate and pressure inlet conditions used.

After running the simulation, particles summary is obtained where escaped particles, trapped particles, and incomplete particles are represented. Particles distribution along with start time and end time is given. Table 2 shows the mass flow rate distribution of particle with respect to various outlets as well as the area-weighted velocity magnitude attended during MQL flow.

During simulation, the total number of oil particles tracked are 1480, out of which 1045 particles escaped through various outlets. It is also observed that the total number of particles aborted are zero, the total number of particles trapped at various locations are 433, the total number of particles evaporated are zero, also the total number of particles incomplete are 2. Table 3 shows a summary of oil particle distribution through various outlets. Hence, it can be seen that 28% oil particles escaped from Zone 1, 15% from Zone 2, 16.7% from Zone 3 and 40.3% from Zone 4.

Total escaped particles = 1045
Zone 1: 114 + 94 + 85 = 293 percentage zone 1: 28%
Zone 2: 32 + 79 + 46 = 157 percentage zone 2: 15%
Zone 3:55 + 53 + 66 = 174 percentage zone 3: 16.7%
Zone 4:107 + 98 + 109 + 107 = 421 percentage zone 4: 40.3%

Table 2 Distribution of oil particle through various outlet

Boundary conditions	Mass flow rate(kg/s)	Velocity magnitude (m/s)	Boundary conditions	Mass flow rate (kg/s)	Velocity magnitude (m/s)
Inlet	0.0159275	39.91	Outlet 7	−0.00122	361.43
Outlet 1	−0.001231	364.62	Outlet 8	−0.001221	360.76
Outlet 2	−0.001229	361.07	Outlet 9	−0.001223	362.86
Outlet 3	−0.001233	361.75	Outlet 10	−0.001221	364.62
Outlet 4	−0.001226	360.61	Outlet 11	−0.001229	364.99
Outlet 5	−0.001224	363.27	Outlet 12	−0.001218	364.05
Outlet 6	−0.001229	362.64	Outlet 13	−0.001218	365.60
			Net	5.546e-06	364.98

Table 3 Summary of oil particle distribution through various outlets

DPM condition	Boundary condition	Number of particles	DPM condition	Boundary condition	Number of particles
Incomplete	–	2	Escaped	Outlet 7	55
Trapped	Wall	433	Escaped	Outlet 8	53
Escaped	Outlet 1	114	Escaped	Outlet 9	66
Escaped	Outlet 2	94	Escaped	Outlet 10	107
Escaped	Outlet 3	85	Escaped	Outlet 11	98
Escaped	Outlet 4	32	Escaped	Outlet 12	109
Escaped	Outlet 5	79	Escaped	Outlet 13	107
Escaped	Outlet 6	46			

Diameter Distribution plot: The particles size with injection input vary from 5 µm to 10 µm. Heavy particles that are escaped are very less in number compared with lighter particles. The heavy particles move toward the wall due to centrifugal force. A particle with different diameters is shown in Fig. 10.

Particle velocity plot: As the particles are moving along with the continuous flow of pressurized air, particles allow extra flow from the continuous flow. In the main pipe, particles move at very slow speed; when it moves into the 13 different branches it starts moving at a faster rate. At the outlets, due to the nozzle, sudden velocity rise takes place in each particle. The average velocity of the particle is 341 m/s. Figure 11 shows the contour plots for velocity magnitude.

Table 4 shows a summary of the percentage of the dispersed phase (oil) through various zones for various mass flow rate conditions. It can be seen that the mass flow rate of 50 ml/h produces the optimum particle distribution. It is seen that Rosin-Rammler distribution actually distributes the particles with different diameters and according to the mass flow rate. It has been also seen that the mass flow rate is higher at the mean diameter, whereas it goes on decreasing toward both sides. Figure 12 shows the histogram representing variation in particle diameters with an
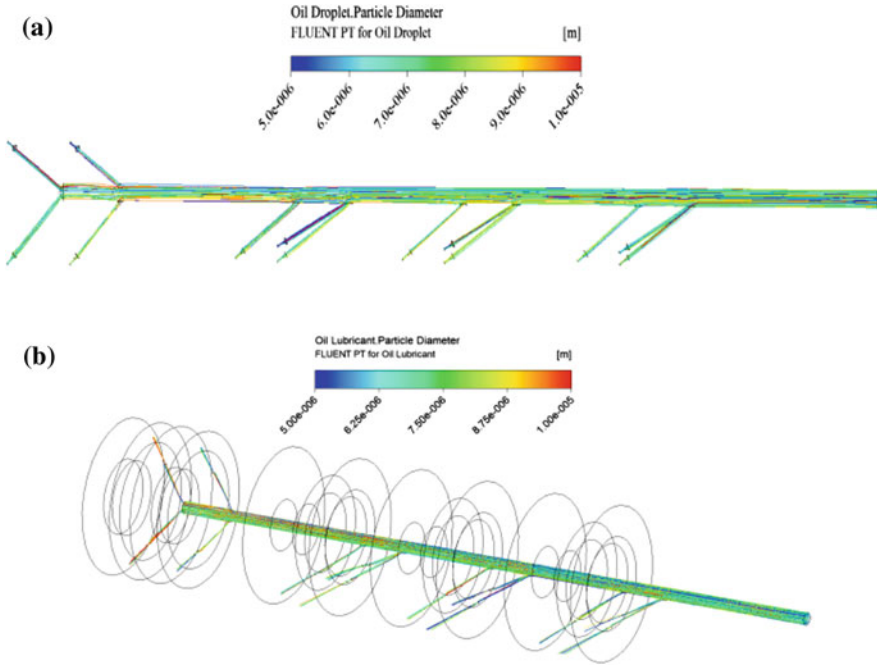
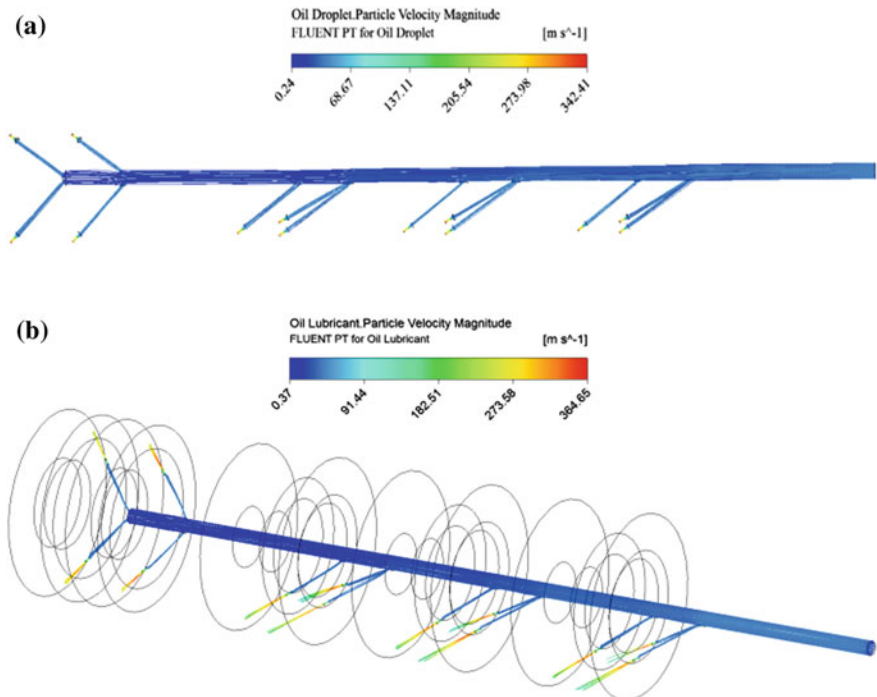**Fig. 10** Oil droplet particle diameter **a** for mass flow rate 15 ml/h **b** 50 ml/h

Fig. 11 Oil droplet particle velocity magnitude **a** for mass flow rate 15 ml/h **b** 50 ml/h

Table 4 Percentage of the dispersed phase (oil) through various zones for various mass flow rate conditions

Sr. No.	Mass flow rate of the DPM (oil) (ml/hr)	Percentage of the dispersed phase (oil) (%)			
		Zone-1	Zone-2	Zone-3	Zone-4
1	15	26	19	19	35
2	30	26	19	19	35
3	50	27	19	20	35
4	60	27	19	19	34
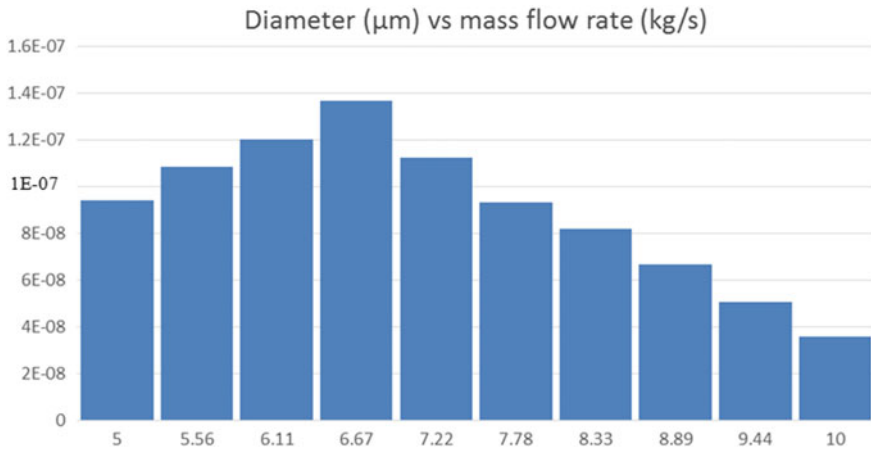
Fig. 12 Histogram representing variation in particle diameters with escaped mass flow rate (kg/s) from Outlet 2

escaped mass flow rate (kg/s) from Outlet 2. It gives a clear idea that 6.67 µm diameter has a high mass flow rate. A similar histogram was studied at all outlets and similar results are observed. Hence, it is concluded that 10 µm diameter carries a less mass flow rate compared with others.

5 Conclusion

In this paper, DPM analysis is successfully applied to simulate minimum quantity lubrication conditions used for CAM bore finishing tool. The oil is injected at various mass flow rates ranging from 15 to 60 ml/hr. In all simulations, it has been observed that the percentage of particles escaping are more for Zone 1 and Zone 4 as compared with Zone 2 and Zone 3. It is also concluded that oil mass flow rate of 50 ml/hr distributes the particle in even manner. The particle distribution model used, i.e., Rosin-Rammler distribution helps in distributing the mass with all

particles with a different diameter, hence mass distribution varies for each outlet. It has been also observed that particle velocity increases suddenly after escaping from coolant domain to the air domain. This mainly happens due to the change in pressure and density of operating continuous medium. It is been noted that a particle with a higher diameter has less mass flow rate when it compared with other particles diameters.

References

1. Kuzu AT, Berenjib KR, Ekim BC, Bakkala M (2017) The thermal modeling of deep-hole drilling process under MQL condition. J Manuf Process 29:194–203 (2017). https://doi.org/10.1016/j.jmapro.2017.07.020
2. Guo S, Li C, Zhang Y, Wang Y, Li B, Yang M, Zhang X, Liu G (2016) Experimental evaluation of the lubrication performance of mixtures of castor oil with other vegetable oils in MQL grinding of nickel-based alloy. J Clean Prod xxx:1–17 (2016). https://doi.org/10.1016/j.jclepro.2016.10.073
3. Zhang S, Li JF, Wang YW (2012) Tool life and cutting forces in end milling Inconel 718 under dry and minimum quantity cooling lubrication cutting conditions. J Clean Prod 32:81–87. https://doi.org/10.1016/j.jclepro.2012.03.014
4. Breitenbach Jan, Roisman Ilia V, Tropea Cameron (2017) Heat transfer in the film boiling regime: Single drop impact and spray cooling. Int J Heat Mass Transf 110:34–42. https://doi.org/10.1016/j.ijheatmasstransfer.2017.03.004
5. Obikawa T, Kamata Y, Asano Y, Nakayama K, Otieno AW (2008) Micro-liter lubrication machining of Inconel 718. Int J Mach Tools Manuf 48:1605–1612 (2008). https://doi.org/10.1016/j.ijmachtools.2008.07.011
6. Park K-H, Olortegui-Yumel JA, Joshil S, Kwonl P, Yoon M-C, Lee G-B, Park S-B (2008) Measurement of droplet size and distribution for Minimum Quantity Lubrication (MQL). In: International conference on smart manufacturing application 9–11 Apr 2008
7. Patankar SV (1980) Numerical heat transfer and fluid flow. Taylor & Francis. ISBN 978-0-89116-522-4

Development of Collision Avoidance System Using Fuzzy Logic

Ujjwal Deep Agarwal, Shishir Sinha, Rajeev Srivastava, Saurav Pathak and Shiv Raushan

Abstract The collision avoidance system is the present state-of-the-art hardware/ software integration for preventing an impending collision. The developed algorithm functions in two stages. It first warns the driver and if the driver fails to respond in time, it applies the brakes automatically to avoid the collision or reduce its severity. This paper deals with the development of a suitable mathematical model for Collision Avoidance System. Analysis and Simulation of the mathematical model has been done in MATLAB®. Simulation studies with On–Off and Fuzzy Logic Controller are compared and usefulness of Fuzzy Inference System (FIS) has been established. With two fuzzy inputs namely (slip ratio and rate of change of slip ratio) and one output (fraction of Brake Pressure required), optimum braking force is achieved. An iterative method is used to optimize the FIS controller. A new definition of critical distance has also been developed for optimization of the assessment of critical distance.

Keywords Fuzzy inference system (FIS) · Slip ratio · Critical distance

1 Introduction

According to the National Crime Records Bureau, Ministry of Home Affairs, GOI [1], more than 5,00,000 accidents occur in India every year. Data also illustrate that more than 70% of accidents happen due to the negligence of the driver. In the wake of increasing number of accidents and the fatalities caused due to them, most of the automobile manufacturers all over the world are trying to develop Driverless vehicles have achieved varying degrees of success. However, in a developing country like India, having narrow roads and less regard for traffic rules, concept of driverless cars is not quite feasible to be introduced in one go, but it could be done in number of stages first by introducing Collision Avoidance System, followed by

U. D. Agarwal (✉) · S. Sinha · R. Srivastava · S. Pathak · S. Raushan
MNNIT Allahabad, Allahabad 211004, UP, India
e-mail: udagarwal111@gmail.com

Throttle Control thus achieving full Longitudinal Control System and then integrating Steering Control to achieve fully autonomous vehicle system. This paper is concerned with the development of collision avoidance system.

The usefulness of collision avoidance system in preventing accidents or reducing their severity has already been established [2]. It has been estimated that of the total fatalities caused due to accidents, 12% are due to loss of control and systems like collision avoidance system can prevent up to 70% of these accidents. Collision of cars is divided into mainly four types—1. Head-on Collision 2. Rear-end collision 3. Side collision 4. Pedestrian Collision. This paper focuses on rear-end collision and pedestrian collision to develop an integrated Collision Warning and Mitigation system for vehicles in Indian Conditions.

Another important component that has to be factored in while designing the control system, is its ability to decide if the situation is critical or not and act accordingly. A safety spacing policy [3] based control methodology is applied, which relies on the ability of sensors to detect the relative velocity of the target vehicle with respect to the host vehicle and relative distance between the vehicles to assess if the situation is critical. The decision is made on the basis of deceleration required and whether it lies or not in the comfort braking zone of 0.3–0.7 g.

The braking process of any vehicle has a very high nonlinear character and also the process characteristics change with the road surface contact conditions. One of the biggest problems faced while designing a controller for the Collision Avoidance System is to factor in this nonlinear behavior and varying road surface contact conditions, into the control system. The different tyres have different characteristics, but the situations while braking can be easily approximated by using appropriate "Tyre Model". Though many tyre models are available such as Pacejka Magic Formula Model, Road-Tyre Friction Model, Dugoff's Tyre Model [4, 5], etc. In this paper, Road-Tyre Friction Model is used to establish the balance between true road-tyre friction behavior and computation time required by the processor. In practical implementation of this method, parameters of this model can be tuned to imitate actual road-tyre condition while maintaining sufficient accuracy.

For the parameters used in the Road-Tyre Friction Model in this paper, a slip ratio value of 0.2 generates the most efficient braking performance [5]. But while braking, slip ratio variation is highly nonlinear and does not have a predefined mathematical model to describe its behavior. But this absence of mathematical model is negated by using fuzzy logic in the controller and training the controller in order to achieve optimum slip ratio value. This way our model can closely follows the actual Anti-Lock Braking System (ABS) being used in vehicles.

In this paper, the methodology to develop the control system is described step by step from the vehicle dynamics calculation to vehicle accident risk assessment along with optimization of the slip ratio with FIS training. The developed control system is then simulated for various practical situations on Simulink and then on the basis of the results and graph obtained, inference is drawn and the results are validated with other research papers.

2 Methodology

2.1 Vehicle Dynamics

Due to complexities involved in full vehicle model in brake force analysis and the control system design, Quarter Car model, which is generally used for analysis of ABS systems, it is used to appropriately approximate the results. Two governing equations are formed by balancing the force in the longitudinal direction and balancing the torque about the wheel center (Fig. 1).

$$m\frac{dv_x}{dt} = -\mu F_N \tag{1}$$

Balancing torque at the wheel center

$$J_e \alpha_e = \mu R F_N - T_b \tag{2}$$

Slip ratio [4] is defined as follows:

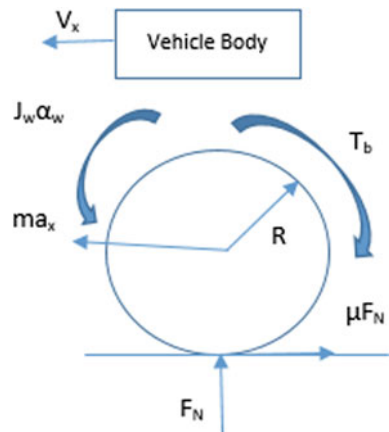$$\lambda = \frac{v_x - \omega R}{v_x} \tag{3}$$

By applying the control system on the above equations, we can control the variation of the slip ratio and thus can optimize the braking force.

2.2 Tyre Model

Road-Tyre Friction model.
Road Tyre friction model [5] gives the value of coefficient of friction as a function of linear velocity (V_x) and slip ratio (λ).

Fig. 1 Quarter car model

$$\mu(\lambda, V_X = \left[C_1\left(1 - e^{-c_2\lambda}\right) - C_3\lambda\right]e^{c_4 v_x} \tag{4}$$

$$F_x = \mu F_N \tag{5}$$

Here C1, C2, C3, and C4 are constants.

2.3 Critical Distance Calculation

Calculation of critical distance between the vehicles at which the controller will take over the braking action is very important for the development of control algorithm. Critical Distance is the threshold separation between the host vehicle and the target vehicle after which the system will autonomously apply brakes to avoid collision. In the developed definition, the system calculates the real-time braking distance of the vehicle taking into consideration the cases when the leading/target vehicle is decelerating with 'lvd' m/s^2. Two velocity ranges have been considered in which two different methods of the critical distance calculation are incorporated. These ranges are as follows (Fig. 2):

$$(a)\ (V_h - V_1) \le 1.12\ \text{m/s} \tag{6}$$

$$(b)\ (V_h - V_1) \succ 1.12\ \text{m/s} \tag{7}$$

The following two cases are analyzed by the controller:
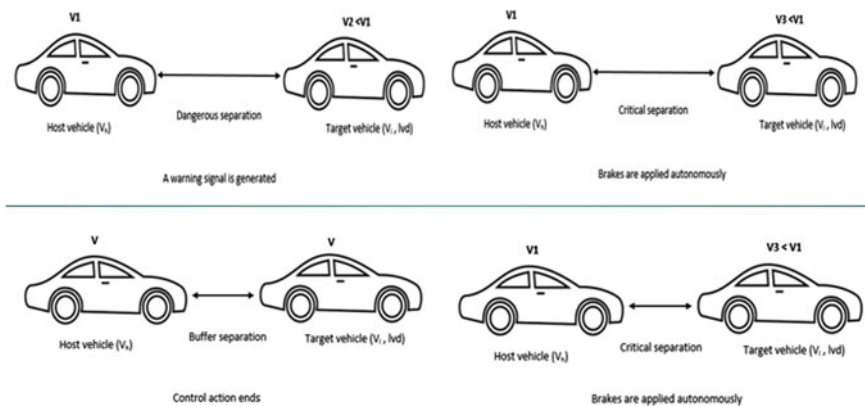
$$(V_h - V_1) \le 1.12\ \text{m/s}$$

Fig. 2 Different critical situations for application of brakes

$$dis_{cr} = ((V_h - V_1) \times (rth + rts)) + \frac{lvd \times (rts + rth)^2}{2} \qquad (8)$$

1. $$(V_h - V_l) > 1.12 \, \text{m/s}$$

$$dis_{cr} = (\max(discc_c) - \max(v\_diss1)) + (V_h - V_1) \times rts + \frac{lvd \times rts^2}{2} \qquad (9)$$

Following equations show the relationship between various distances:

1. $d_{dis} = (V_h - V_l) * 6 + \frac{lvd*6^2}{2}$
2. d_min is considered to be equal to 1 m
3. $criticl_{dis} = dis_{cr} + d\_min$
4. $d\_cri = d_{dis} + criticl_{dis}$

Where,

d_{dis}: dangerous separation distance during which driver will be warned continuously

dis: separation between host and leading vehicle

dis_{cr}: distance required by the controller to just prevent the collision when it takes autonomous braking action

d_min: minimum safe separation between the vehicles

d_cri: separation at which warning signal goes to the driver

$criticl_{dis}$: separation at which controller kicks in and takes autonomous braking action

V_h: host vehicle velocity

V_l: leading vehicle velocity

$diss_c$: displacement of leading vehicle during autonomous braking action

v_diss1: displacement of host vehicle during autonomous braking action

rts: reaction time of system

rth: reaction time of human driver

lvd: leading vehicle deceleration

Control action of the controller is as follows:

- If $dis > d\_cri$: Condition is Normal
- If $criticl_{dis} < dis$ and $dis < d\_cri$: Condition is Dangerous. Controller will give warning to the driver
- If $dis < critcl_{dis}$: Condition is critical. Braking action of the controller will start to act.

3 Controller Design

Fuzzy Logic is applied to design the control system. The controller decides when to warn the driver or apply the brakes automatically with the help of Fuzzy predictor based on the distance analysis. The fuzzy logic system consists of three parts: fuzzifier, inference engine, and defuzzifier [6, 7]. In the fuzzy control, first the fuzzifier takes two inputs, namely, 'Slip ratio' and 'rate of change of slip ratio', the inference engine figures out the fuzzy output based on safety assurance created by tuning as shown in Table 1, finally, the defuzzifier calculates the emergency braking system control signals using the centroid method (Figs. 3, 4, 5, 6 and Table 1).
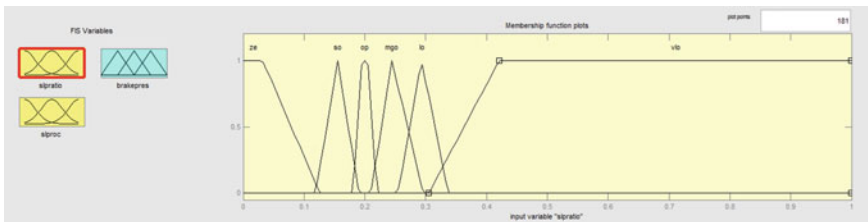
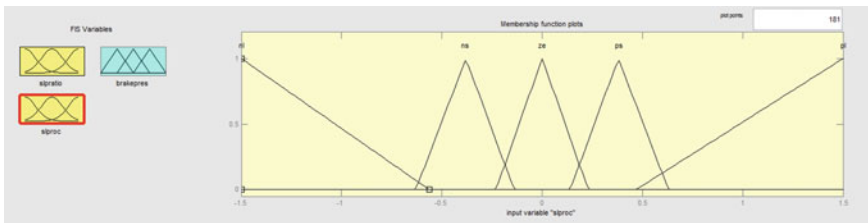

Fig. 3 Membership function plot for input 1—slip ratio

Fig. 4 Membership function plot for input 2—rate of change of slip ratio
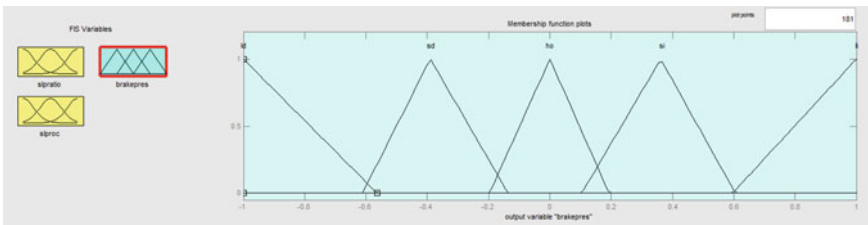
Fig. 5 Membership function plot for output variable—brake pressure
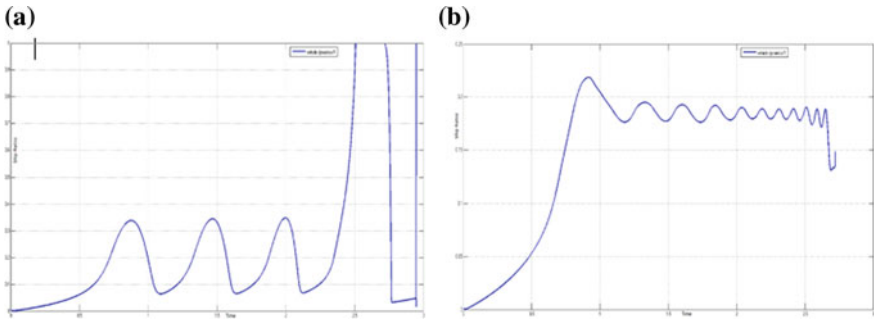
Fig. 6 **a** and **b** Left to right: Variation of slip ratio with time in FLC with 3-input membership functions, Variation of slip ratio with time in FLC with 5-input membership functions

Table 1 Values of membership functions of output variable (brake pressure) of fuzzy logic controller based on membership functions of input variables (slip ratio and rate of change of slip ratio)

slproc slpratio	Nl	Ns	Ze	Ps	Pl
Ze	N/A	N/A	Li	Li	Si
So	Li	Li	Si	Si	Ho
Op	Li	Si	Ho	Sd	Id
Lgo	Ho	Sd	Sd	Sd	Id
Lo	Ld	Sd	Ld	Ld	Id
Vlo	Ld	Ld	Ld	Ld	Id

Slpratio—Slip ratio
slproc—Slip ratio rate of change
Nl—negative large
Ns—negative small
Ze—zero
Ps—positive small
Pl—positive large
So—smaller than optimum
Op—optimum
Lgo—little greater than optimum
Lo—larger than optimum
Li—large increment
Vlo—very large than optimum
Si—small increment
Ho—hold
Sd—slight decrement
Ld—large decrement

Fig. 7 **a** and **b** Left to right: Variation of jerk with time in case of ON/OFF controller, Variation of jerk with time in case of fuzzy logic controller

4   Results and Discussion

A detailed analysis of the results obtained from the simulation of autonomous braking system using various controllers has made it clear that Fuzzy controller produces quite desirable results with minimum deviation. Th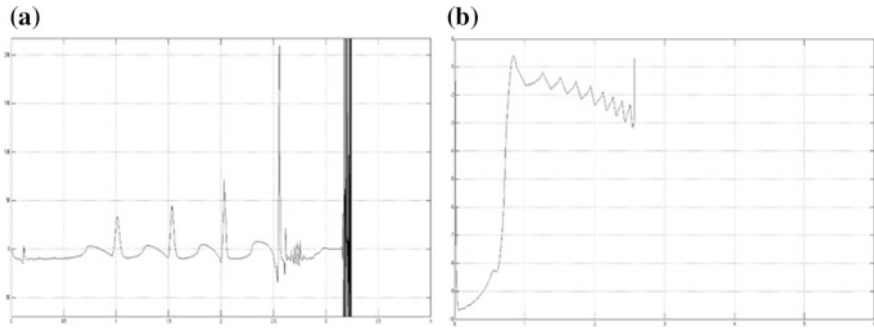e desired value is achieved earlier in case of ON/OFF controller than as compared to Fuzzy Logic controller. The braking force produced by Fuzzy controller is stable throughout in contrast to that produced by ON/OFF controller.

It can be observed from Fig. 7a that at regular interval, high values (50–200 m/s^3) of jerk is observed which is quite uncomfortable in case of on–off controller. It is clear that ride is quite uncomfortable during braking action. Additionally, it may cause excessive wear and tear of tires. In case of fuzzy logic controller, relatively lower (1–10 m/s^3) values of jerk (Fig. 7b) are there which are more comfortable than ON/OFF controller. Fuzzy controller adequately represents actual ABS. Thus, this model can be used to predict the criticality of the situation (Table 2).

Table 2 Table depicting stopping time and slip ratio variation of different tyre models and controller combinations

System	Stopping time	Slip ratio variation
Road tyre friction model	3.3 s	Steep variation
Without controller	3.8 s	Steep variation
Road tyre friction model with on–off controller	3.3 s	Smooth variation initially but high-frequency fluctuation in the end
Road tyre friction model with fuzzy logic controller (3 MFs)	3 s	Smooth variation but with high deviation from mean value of 0.2
Road tyre friction model with fuzzy logic controller (5 MFs)	2.7 s	Smooth variation with low standard deviation around 0.2

5 Conclusion

In this paper, an attempt is made to analyze the effect of controller on the slip ratio variation while braking along with considering the effect on the stopping time and stopping distance. The system is modelled with a quarter car vehicle dynamics and differential equation of motion is formulated. The slip ratio and rate of change of slip ratio are taken as control parameters as they efficiently represent the stability and steerability of the vehicle while braking. Various controllers are studied and their effects are observed by simulating the situation in MATLAB Simulink environment. The time history of the wheel, stopping distance of the vehicle, and slip ratio variation are obtained for benchmarking from problems available in the literature. The collision avoidance system has been designed to prevent collision or at least mitigate the effect of collision by either warning the driver or taking autonomous actions when driver fails to judge the criticality of the situation. The state of situation is judged by comparing the current parameters with critical parameters. The road tyre friction model has been used to formulate the mathematical model for slip ratio variation and optimum braking force generation. Two separate controllers, on–off controller and fuzzy logic controller, have been designed. A comparison between results obtained from both the controller shows that fuzzy logic controller reduces the stopping time and thus stopping distance to a larger extent as compared to on/off controller. In addition to that fuzzy controller provides smooth and continuous decrease in velocity as compared to that of on/off controller. The brake force obtained is also more consistent with much lesser fluctuation over on/off controller. Hence, the Fuzzy logic controller allows for optimum brake force generation and reduces the jerk involved by providing smooth variation in braking force. Thus, Fuzzy logic controller adequately represents actual ABS in modern vehicles and can be used to predict critical distances with sufficient accuracy in real time. Statistical method of control is used while developing the control action of the fuzzy logic controller.

References

1. http://ncrb.gov.in/StatPublications/ADSI/ADSI2015/chapter-2%20suicides-v1.pdf
2. Bosch report on study on effect of electronic stability programme in Indian specific conditions
3. Zhao MO, EL Kamel A (2009) A safety spacing policy and its impact on highway traffic flow. In: IEEE transaction on intelligent vehicle symposium Xi'an, China, June 2009, pp 960–965
4. Rajmani (2006) Vehicle dynamics and control. Springer, New York
5. Sharkawy AB (2010) Genetic fuzzy self-tuning PID controllers for antilock braking systems. Eng Appl Artif Intell 23:1041–1052
6. Balcones D, Llorca DF, Sotelo MA, Gavil´an M, Alvarez S, Parra I, Oca˜na M Real-time vision-based vehicle detection for rear-end collision mitigation systems. Department of Electronics, University of Alcal´a, Alcal´a de Henares, Madrid, Spain
7. Dhivya P, Murugesan A (2015) Intelligent car braking system with collision avoidance and ABS. Int J Comput Appl (0975–8887). In: National conference on information and communication technologies (NCICT 2015)

Flexural Properties of Silver Date Palm Leaf Reinforced Polyester Composites

B. P. Sharma, R. Gangawani, S. Akhtar, G. S. Rao and Umesh Kumar Vates

Abstract An attempt has been made to fabricate a new composite material by incorporating silver date palm fiber as reinforcement in the polyester resin. The composites have been fabricated up to a maximum volume fraction of fiber about 0.467. The flexural behavior of fabricated composites was investigated as a function of fiber content. It has been observed that the flexural strength of the composite material increases with an increase in fiber content up to 0.26 volume fraction and starts decreasing with an increase in volume fraction of the fiber. It is found that the maximum flexural strength of the composite is 377.69 MPa for the volume fraction 0.26 which is about 1.25 times greater than that of plain polyester resin. These results show that there could exist a solid bond between the fiber and resin at a volume fraction of 0.26. It has been concluded that using silver date palm fiber as reinforcement in plain polyester resin plays a major role in terms of high flexural strength of a new fabricated composite material.

1 Introduction

The natural fibers extracted from plants such as vakka, sisal, banana, and bamboo have many attractive benefits over synthetic fibers. These fibers are cheaper, easily available, low density, and they are also recyclable and eco-friendly. Therefore, the natural fiber reinforced composites are emerging as realistic alternatives to replace the synthetic fiber reinforced composites in many applications. These composites exhibit high tensile, flexural strength, and resistance to fracture when the suitable coupling agents are used for making the bond between the hydrophilic natural fibers and hydrophobic matrix.

B. P. Sharma (✉) · R. Gangawani · S. Akhtar · G. S. Rao · U. K. Vates
Department of Mechanical Engineering, Amity University Noida, Noida, Uttar Pradesh, India
e-mail: bpsharma15482@gmail.com

The mechanical behavior of sisal, hemp, and banana fiber reinforced composites using novolac resin, with and without maleic anhydride treatment was investigated [1]. It has been observed that the maleic anhydride treatment when applied on the fibers increases mechanical properties like the modulus of elasticity, flexural modulus, and impact strength. The tensile behavior of elephant grass fiber reinforced composites fabricated from retting, chemical extraction, and treated by $KMnO_4$ was reported [2]. It is found that the fibers treated by $KMnO_4$ have shown significant improvement in tensile strength and modulus compared to that of the fibers extracted by retting and manual process. The fabrication and testing of thermoplastics and thermosetting composites reinforced with commonly used natural fibers like coir, banana, hemp, and sisal with or without chemical treatment by different methods were studied by many researchers [3–7]. The effect of moisture content on mechanical properties of natural fibers such as jute, coir, sisal, flax, kenaf, and abaca was investigated by Symington et al. [8]. It has been observed that the jute fiber showed superior mechanical properties than other fibers. An attempt was made by Ratna Prasad et al. [9] to study mechanical properties of sisal, bamboo, and jowar fiber reinforced composites. It has been observed that the tensile modulus of jowar fiber reinforced composite is better than sisal and bamboo fiber reinforced composites. The tensile properties of different natural fiber reinforced composites made from jute, kenaf, hemp, coir, and sisal ware reported by Wambua paul et al. [10] and found that hemp fiber reinforced composite exhibited highest tensile strength values whereas coir showed the lowest. The tensile strength and impact behavior of rice straw polyester composites have been investigated by Ratna Prasad et al. [11]. It has been found that the rice straw fiber reinforced composites exhibited higher tensile and impact strength compared to that of pure polyester resin.

Though a huge amount of research work has been reported on various natural fibers and its composites, no work has been reported on flexural behavior of a silver date palm leaf fiber reinforced polyester composites. Thus, the aim of this work is to introduce a newly identified natural fiber, i.e., silver date palm leaf as reinforcement in the development of new composite materials for lightweight vehicle applications and to investigate the flexural properties of a silver date palm leaf fiber reinforced polyester composites.

2   Experimental Procedure

2.1   Materials

The source of this fiber is leaves of silver date palm tree, which grows in all parts of India, as shown in Fig. 1. Unsaturated polyester resin, methyl ethyl ketone peroxide (catalyst), and cobalt naphthenate (accelerator) were procured from ICA (Pvt) Ltd.

Fig. 1 Silver date palm tree

(Delhi, India). Rubber molds are prepared according to ASTM standards (100 mm*25 mm*3 mm). Thin transparent plastic sheets are used to cover the molds from one side for arresting the air. Five sets of bend specimens of each volume fraction (0.2, 0.26, 0.33, 0.4, and 0.46) have been fabricated as per ASTM D 790 M.

2.2 Preparation of Fiber

Initially, leaves were separated from the stems of the silver date palm tree and kept in water for about 2 to 3 h and followed by washing with normal water, so as to clean dust that might have presented on the leaves owing to their exposure to the environment. The wet fibers were dried under the sun for a few hours and subsequently dried in the furnace at 70 °C for 1 h. After that the fibers have been cut to the required length.

2.3 Composite Preparation

In the current research work, the composites have been prepared using hand layup method. For 100 ml of the polyester resin, 1.5% of catalyst and accelerator were added. The composites were fabricated, gradually by filling the mixture of resin into the mold and unidirectional fibers, starting and ending with alternative layers of resin. Subsequently, a thin transparent plastic sheet has been placed on the mold

from one side to arrest the air by pressing the sheet gently with the steel rule and instantly followed by applying a compressive pressure of 0.05 MPa on the mold. Then the specimens were allowed to cure for one day. Nevertheless, the movement of the fiber in the mold should be minimized for yielding sound quality fiber reinforced composites. Then the specimens were also post-cured at 70 °C for 1 h after being removed from the mold.

2.4 Flexural Testing of Composites

The dimensions of the flexural test specimens are 100 mm in length, 25 mm width, and 3 mm thick. Three-point bend tests were conducted on five identical specimens of each volume fraction as per ASTM D 790 M for measuring flexural properties. All the specimens were tested at a crosshead speed of 0.5 mm/min, using an electronic tensile testing machine at ITS Engineering College, Greater Noida Uttar Pradesh.

3 Results and Discussions

3.1 Flexural Properties of Silver Date Palm Fiber Reinforced Composites

The fabricated bend specimens for various volume fractions (0.2, 0.26, 0.33, 0.4, and 0.46) are shown in Fig. 2. It is evident from the figure that all specimens were made with care and free from porosity. The fractured bend specimens have been also presented in Fig. 3 for reference. The flexural properties of silver date palm leaf fiber reinforced composites along with those of some important existed natural fibers were presented in Table 1 [12]. It was clear from the values that silver date palm fiber reinforced composite exhibited highest flexural strength than that of the established fibers and the plain polyester resin as shown in the table.

The variation in flexural properties of silver date palm leaf fiber with increasing volume fraction was presented in Table 2. It can be seen from the results that the flexural strength increases with an increase in volume fraction of the fiber and the maximum flexural strength of the composite are found to be 377.69 MPa for the volume fraction 0.26 which is about 1.254 times greater than that of a plain polyester resin. It has also been observed that the flexural strength of silver date palm fiber reinforced composite increases up to a volume fraction 0.26, and starts
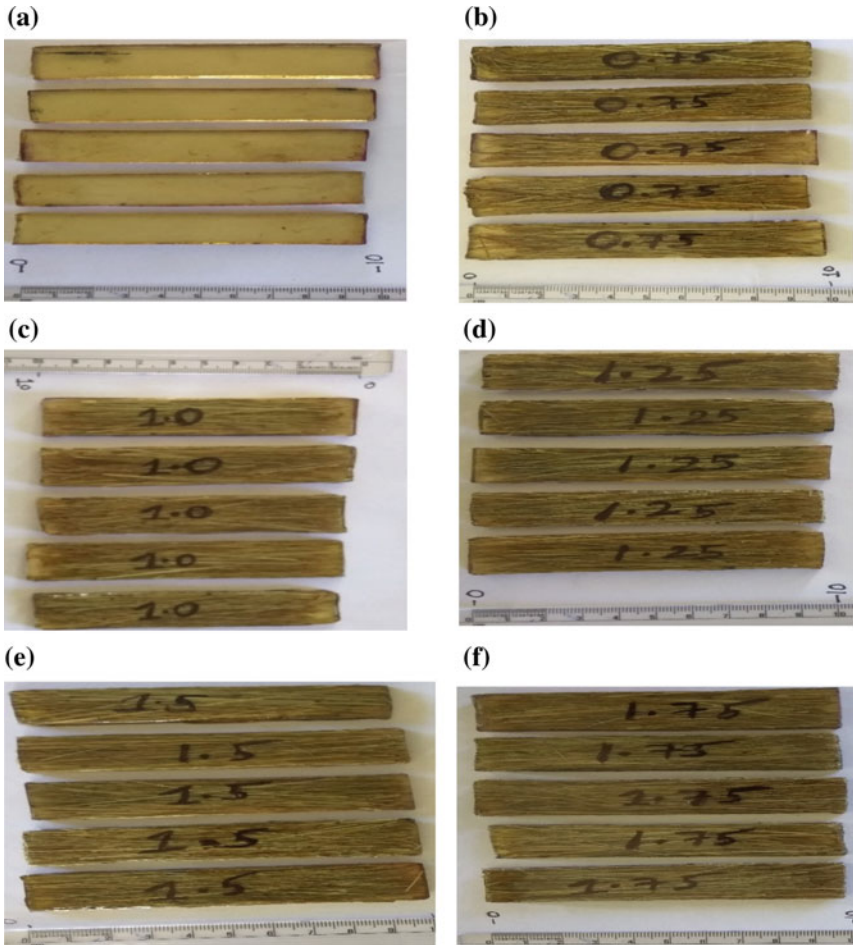
Fig. 2 Fabricated bend test specimens of various volume fractions **a** 0 **b** 0.20 **c** 0.26 **d** 0.33 **e** 0.40 and **f** 0.46

decreasing with the increase in volume fraction of the fiber in the composite material. It clearly indicates that reinforcing small amount of the fiber in resin improves significant flexural strength of the composite up to the volume fraction 0.26. This is mainly due to solid bonding of silver date palm fiber with resin.
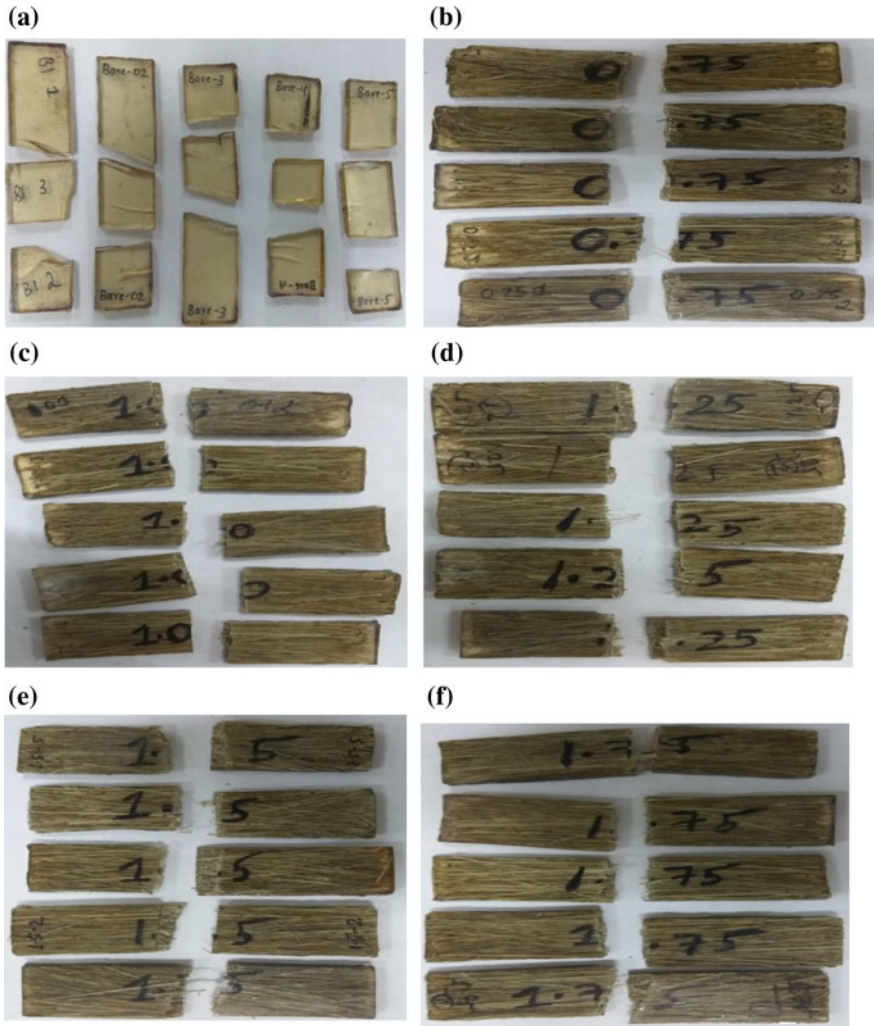
Fig. 3 Bend test specimens after failure for various volume fractions **a** 0 **b** 0.20 **c** 0.26 **d** 0.33 **e** 0.40 and **f** 0.46

Name of the composite	Ultimate flexural strength (MPa)
Plain polyester resin	66.0
Vakka	93.79
Sisal	98.1
Banana	91.40
Bamboo	127.1
Silver date palm tree fiber	377.69

Table 1 Flexural properties of silver date palm leaf fiber along with other natural fiber reinforced composites

Table 2 Flexural properties of silver date palm leaf fiber with various volume fractions

S. no	Volume fraction	Ultimate tensile strength (MPa)
1.	0	301.01
2.	0.20	313.23
3.	0.26	377.69
4.	0.33	326.99
5.	0.40	311.83
6.	0.46	311.83

4 Conclusions

- A lightweight composite material has been fabricated using silver date palm tree leaf fiber as reinforcement in polyester resin matrix.
- The density of the fiber is found to be 500 kg/m^3.
- It has been observed that the flexural strength of the composite increases with an increase in fiber content up to 0.26 volume fraction and further decreased with increasing volume fraction of fiber.
- It is found that the maximum flexural strength of the composite is 377.69 MPa for the volume fraction 0.26 which is about 1.25 times greater than that of plain polyester resin.
- It has been concluded that using silver date palm fiber as reinforcement in plain polyester resin plays a major role in terms of high flexural strength of a new fabricated composite material.

References

1. Mishra S, Naik JB, Patil YP (2000) Com Sci Tech 60:1729
2. Rao KMM, Prasad AR, Babu MR, Rao KM, Gupta AVSSKS (2007) The tensile behavior of elephant grass fiber reinforced composites fabricated from retting, chemical extraction and treated by KMnO$_4$. J Mater Sci 42:3266–3272. https://doi.org/10.1007/s10853-006-0657-8
3. Li Y, Mai YW, Lin Y (2000) Sisal fibre and its composites: a review of recent developments. Compos Sci Tech 60:2037–2055
4. Singh B, Gupta M, Verma A (1996) Influence of fiber surface treatment on the properties of sisal–polyester composites. Polym Compos 17:910–918
5. Manikandan Nair KC, Diwan SM, Thomas S (1996) Tensile properties of short sisal fiber reinforced polystyrene composites. J Appl Polym Sci 60:1483–1497
6. Geethamma VG, Joseph R, Thomas S (1995) Short coir fibre-reinforced natural rubber composites: effects of fibre length, orientation and alkali treatment. J Appl Polym Sci 55:583–594
7. Mishra S, Naik JB, Patel YP (2000) The compatibilising effect of maleic anhydride on swelling and mechanical properties of plant-fibre-reinforced novolac composites. Compos Sci Tech 60:1729–1735

8. Symington MC, Banks WM, West OD, Pethrick RA (2009) Tensile testing of cellulose based natural fibers for structural composite applications. J Compos Mater 43:1083–1086
9. Prasad AR, Rao KM (2011) Mechanical properties of natural fiber reinforced polyester composites: jowar, sisal, and bamboo. Mater Des 32(8–9):508–513
10. Wambua P, Ivens J, Verpoest I (2003) Natural fibers: can they replace glass in fibre reinforced plastics? Compos Sci Technol 63:1259–1264
11. Prasad AV, Rao K, Gupta AVSSKS (2007) Tensile and impact behavior of rice straw-polyester composites. Indian J Fiber Text Res 32:399–403
12. Rao KM, Rao KM, Prasad AR (2010) Fabrication and testing of natural fiber reinforced composites: vakka, sisal, bamboo, banana. Mater Des 31:508–513

Tensile Behavior of Silver Date Palm Leaf Reinforced Polyester Composites

B. P. Sharma, R. Pugalia, Ashish, G. S. Rao and Umesh Kumar Vates

Abstract In the current study, a lightweight composite material has been fabricated using silver date palm tree leaf fiber as reinforcement in polyester resin matrix. The fibers are extracted using retting and manual process. The density of the fiber is found to be 500 kg/m^3. The composites have been fabricated up to a maximum volume fraction of about 0.58. The tensile properties of the composites were investigated as a function of fiber content. It has been observed that the tensile strength of the composite increases with an increase in fiber content up to 0.41 volume fraction and decreases with an increase in volume fraction of the fiber. It is found that the maximum tensile strength of the composite is 200.5 MPa for the volume fraction 0.41 which is about 1.67 times greater than that of plain polyester resin. These results show that there could exist a solid goring bond between the fiber and resin at a volume fraction of 0.41. It has been concluded that using silver date palm fiber as reinforcement in plain polyester resin plays a major role in terms of high tensile strength of a new fabricated composite material.

1 Introduction

The natural fibers extracted from plants such as vakka, sisal, banana, and bamboo have many attractive benefits over synthetic fibers. These fibers are cheaper, easily available, low density, and they are also recyclable and eco-friendly. Therefore, the natural fiber reinforced composites are emerging as realistic alternatives to replace the synthetic fiber reinforced composites in many applications. These composites exhibit high tensile strength and resistance to fracture when the suitable coupling agents are used for making the bond between the hydrophilic natural fibers and hydrophobic matrix.

B. P. Sharma (✉) · R. Pugalia · Ashish · G. S. Rao · U. K. Vates
Department of Mechanical Engineering, Amity University Noida, Noida, Uttar Pradesh, India
e-mail: bpsharma15482@gmail.com

The mechanical behavior of sisal, hemp, and banana fiber reinforced composites using novolac resin, with and without maleic anhydride treatment was investigated [1]. It has been observed that the maleic anhydride treatment when applied on the fibers increases mechanical properties like the modulus of elasticity, flexural modulus, and impact strength. The tensile behavior of elephant grass fiber reinforced composites fabricated from retting, chemical extraction, and treated by $KMnO_4$ was reported [2]. It is found that the fibers treated by $KMnO_4$ have shown significant improvement in tensile strength and modulus compared to that of the fibers extracted by retting and manual process. The fabrication and testing of thermoplastics and thermosetting composites reinforced with commonly used natural fibers like coir, banana, hemp, and sisal with or without chemical treatment by different methods were studied by many researchers [3–7]. The effect of moisture content on mechanical properties of natural fibers such as jute, coir, sisal, flax, kenaf, and abaca was investigated by Symington et al. [8]. It has been observed that the jute fiber showed superior mechanical properties than other fibers. An attempt was made by Ratna Prasad et al. [9] to study mechanical properties of sisal, bamboo, and jowar fiber reinforced composites. It has been observed that the tensile modulus of jowar fiber reinforced composite is better than sisal and bamboo fiber reinforced composites. The tensile properties of different natural fiber reinforced composites made from jute, kenaf, hemp, coir, and sisal ware reported by Paul et al. [10] and found that hemp fiber reinforced composite exhibited highest tensile strength values whereas coir showed the lowest. The tensile strength and impact behavior of rice straw polyester composites have been investigated by Ratna Prasad et al. [11]. It has been found that the rice straw fiber reinforced composites exhibited higher tensile and impact strength compared to that of pure polyester resin.

Though a huge amount of research work has been reported on various natural fibers and its composites, no work has been reported on tensile properties of a silver date palm leaf fiber reinforced polyester composites. Thus, the aim of this work is to introduce a newly identified natural fiber, i.e., silver date palm leaf as reinforcement in the development of new composite materials for lightweight vehicle applications and to investigate the tensile properties of a silver date palm leaf fiber reinforced polyester composites.

2 Experimental Procedure

2.1 Materials

The source of this fiber is leaves of silver date palm tree, which grows in all parts of India is shown in Fig. 1. Unsaturated polyester resin, methyl ethyl ketone peroxide (catalyst), and cobalt naphthenate (accelerator) were procured from ICA (Pvt) Ltd. (Delhi, India). Rubber molds are prepared according to ASTM standards

Fig. 1 Silver date palm tree

(160 mm*12.5 mm*3 mm). Thin transparent plastic sheets are used to cover the molds from one side for arresting the air. Five sets of tensile specimens of each volume fraction (0.25, 0.33, 0.41, 0.5, and 0.58) have been fabricated as per ASTM D638-89.

2.2 Preparation of Fiber

Initially, leaves were separated from the stems of the silver date palm tree and kept in water for about 2–3 h and followed by washing with normal water, so as to clean dust that might have presented on the leaves owing to their exposure to the environment. The wet fibers were dried under the sun for few hours and subsequently dried in the furnace at 70° C for 1 h. After that, the fibers have been cut to the required length.

2.3 Composite Preparation

In the current research work, the composites have been prepared using hand lay-up method. For 100 ml of the polyester resin, 1.5% of catalyst and accelerator were added. The composites were fabricated, gradually by filling the mixture of resin into the mold and unidirectional fibers, starting and ending with alternative layers of resin. Subsequently, a thin transparent plastic sheet has been placed on the mold from one side to arrest the air by pressing the sheet gently with the steel rule and instantly followed by applying a compressive pressure of 0.05 MPa on the mold. Then the specimens were allowed to cure for one day. Nevertheless, the movement

of the fiber in the mold should be minimized for yielding sound quality fiber reinforced composites. Then the specimens were also post-cured at 700 C for 1 h after being removed from the mold.

2.4 Tensile Testing of Composites

The dimensions of the tensile test specimens are 160 mm in length, 12.5 mm width, and 3 mm thick. The tensile tests were conducted on five identical specimens of each volume fraction as per ASTM D638-89. All the specimens were tested at a crosshead speed of 1 mm/min, using an electronic tensile testing machine at ITS Engineering College, Greater Noida, Uttar Pradesh.

3 Results and Discussions

3.1 Tensile Properties of Silver Date Palm Fiber Reinforced Composites

The fabricated tensile specimens for various volume fractions (0.25, 0.33, 0.41, 0.5, and 0.58) are shown in Fig. 2. It is evident from the figure that all specimens were made with care and free from porosity. The fractured tensile specimens of the same have been presented in Fig. 3. The tensile testing results of silver date palm tree leaf fiber reinforced composites along with those of some important existed natural fibers were presented in Table 1 [12]. It was clear from the values that the tensile strength of silver date palm fiber reinforced composite is better than those of all the available fibers and the plain polyester resin as shown in the table. It was found that the density of silver date palm tree fiber was much lower than that of the established fibers like sisal, banana, and bamboo which was an attractive parameter in designing lightweight materials.

The variation in tensile properties of silver date palm leaf fiber with increasing volume fraction was presented in Table 2. It can be seen from the results that the tensile strength increases with an increase in volume fraction of the fiber and the maximum tensile strength of the composite are found to be 200.5 MPa for the volume fraction 0.41 which is about 1.67 times greater than that of a plain polyester resin. It has been also observed that the tensile strength of silver date palm fiber reinforced composite increases up to a volume fraction 0.41, and starts decreasing with the increase in volume fraction of the fiber in the composite material. It clearly indicates that reinforcing small amount of the fiber in resin improves significant tensile strength of the composite up to the volume fraction 0.41. This is mainly due to the increased area of bonding in the interfacial region between the matrix and the fibers.
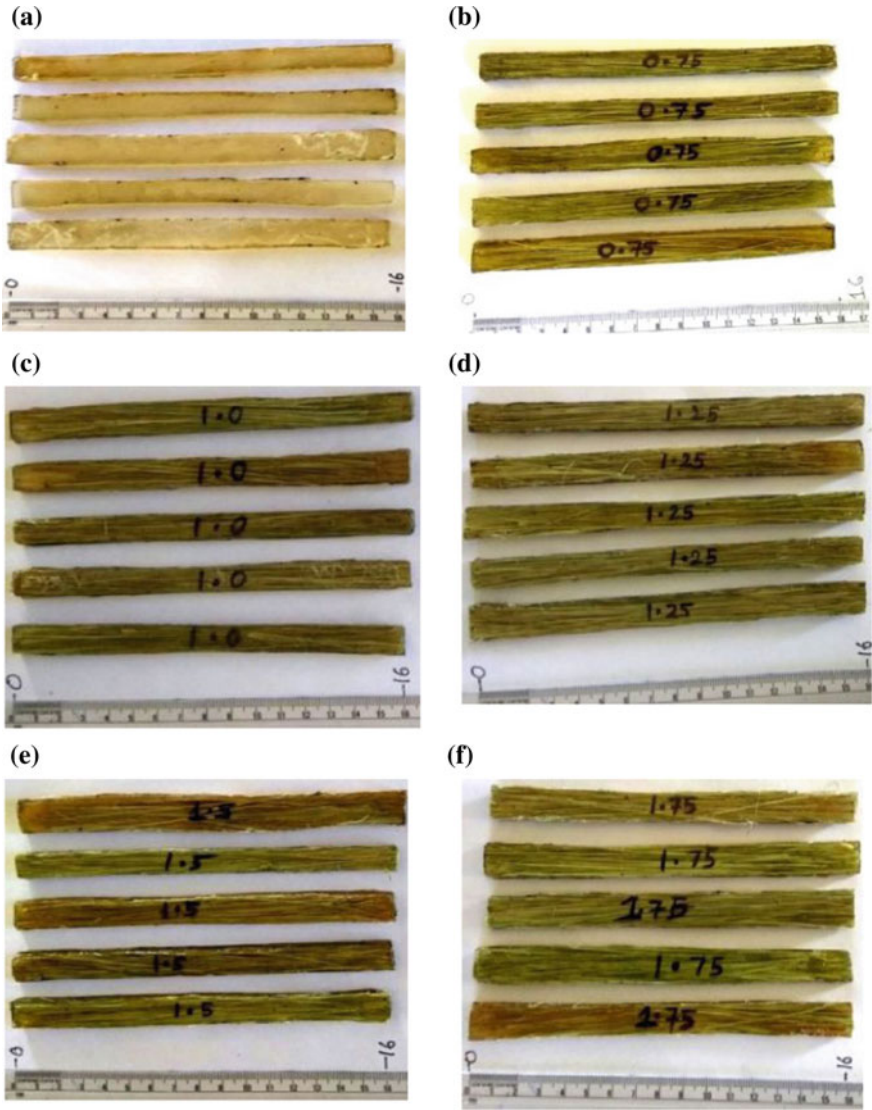
Fig. 2 Fabricated tensile test specimens of various volume fractions **a** 0 **b** 0.25 **c** 0.33 **d** 0.41 **e** 0.5 and **f** 0.58
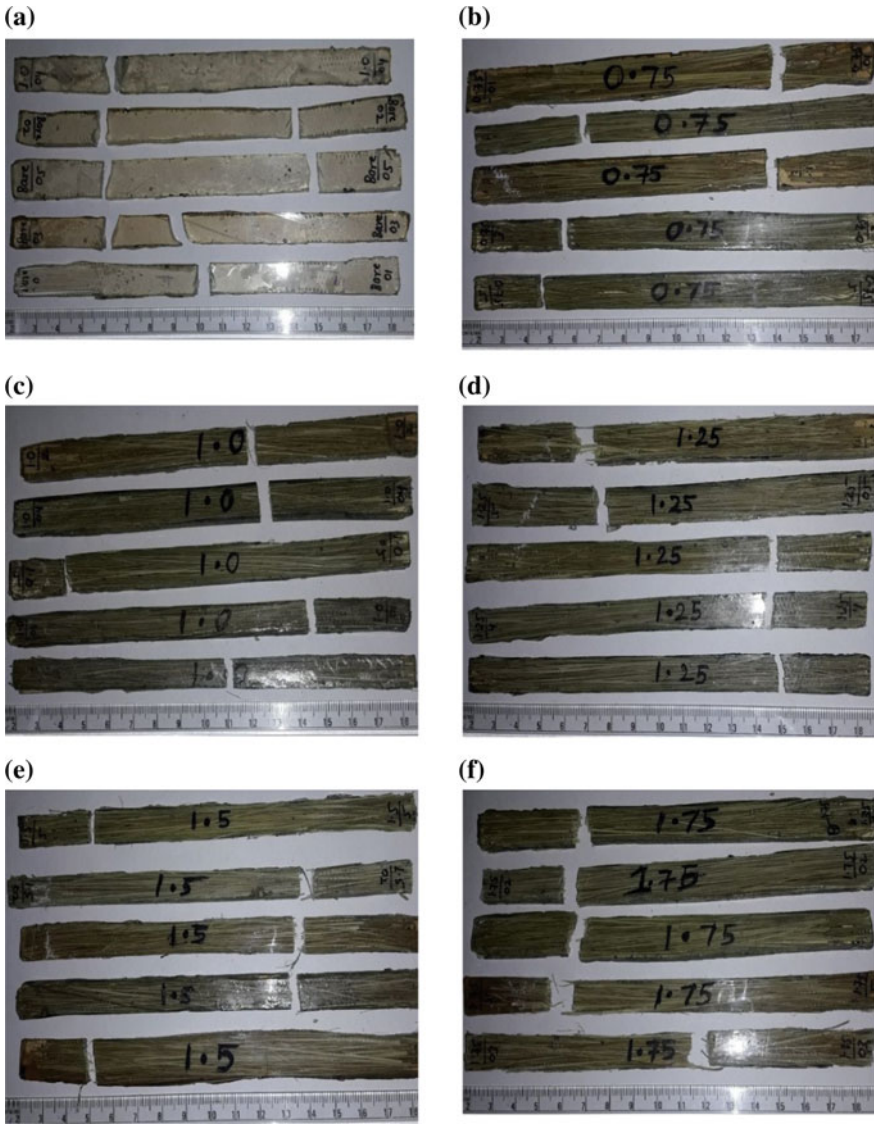
Fig. 3 Tensile test specimens after failure for various volume fractions **a** 0 **b** 0.25 **c** 0.33 **d** 0.41 **e** 0.5 **f** 0.58

Table 1 Tensile properties of silver date palm leaf fiber along with other natural fiber reinforced composites

Density (Kg/m^3)	Name of the fiber	Ultimate tensile strength (MPa)
1074	Plain Polyester	15.7
500	Silver date palm tree leaf	200.5
1450	Sisal	50.0
1350	Banana	60.9
910	Bamboo	121.5

Table 2 Tensile properties of silver date palm leaf fiber with various volume fractions

S. no	Volume fraction	Ultimate tensile strength (MPa)
1.	0	119.7
2.	0.25	154.7
3.	0.33	156.8
4.	0.41	200.5
5.	0.50	192.5
6.	0.58	135.1

4   Conclusions

- A lightweight composite material has been fabricated using silver date palm tree leaf fiber as reinforcement in polyester resin matrix.
- The density of the fiber is found to be 500 kg/m^3.
- It has been observed that the tensile strength of the composite increases with an increase in fiber content up to 0.41 volume fraction and later decreased.
- It is found that the maximum tensile strength of the composite is 200.5 MPa for the volume fraction 0.41 which is about 1.67 times greater than that of plain polyester resin.
- These results show that there could exist a solid goring bond between the fiber and resin at a volume fraction of 0.41. It has been concluded that using silver date palm fiber as reinforcement in plain polyester resin plays a major role in terms of high tensile strength of a new fabricated composite material.

References

1. Mishra S, Naik JB, Patil YP (2000) Com Sci Tech 60:1729
2. Murali Mohan Rao K., Ratna Prasad AV, Ranga Babu MNV, Mohan Rao K, Gupta AVSSKS (2007) The tensile behavior of elephant grass fiber reinforced composites fabricated from retting, chemical extraction and treated by KMnO$_4$ J Mater Sci (2007) 42:3266–3272 https://doi.org/10.1007/s10853-006-0657-8

3. Li Y, Mai YW, Lin Y (2000) Sisal fibre and its composites: a review of recent developments. Compos Sci Tech 60:2037–2055
4. Singh B, Gupta M, Verma A (1996) Influence of fiber surface treatment on the properties of sisal–polyester composites. Polym Compos 17:910–918
5. Manikandan Nair KC, Diwan SM, Thomas S (1996) Tensile properties of short sisal fiber reinforced polystyrene composites. J Appl Polym Sci 60:1483–1497
6. Geethamma VG, Joseph R, Thomas S (1995) Short coir fibre-reinforced natural rubber composites: effects of fibre length, orientation and alkali treatment. J Appl Polym Sci 55:583–594
7. Mishra S, Naik JB, Patel YP (2000) The compatibilising effect of maleic anhydride on swelling and mechanical properties of plant-fibre-reinforced novolac composites. Compos Sci Tech 60:1729–1735
8. Symington MC, Banks WM, West Opukuro D, Pethrick RA (2009) Tensile testing of cellulose based natural fibers for structural composite applications. J Compos Mater 43:1083–6
9. Ratna Prasad AV, Mohan RK (2011) Mechanical properties of natural fiber reinforced polyester composites: jowar, sisal, and bamboo. Mater Des 32(8–9):508–513
10. Paul W, Jan I, Ignaas V (2003) Natural fibers: can they replace glass in fibre reinforced plastics? Compos Sci Technol 63:1259–1264
11. Ratna Prasad AV, Mohan Rao K, Gupta AVSSKS (2007) Tensile and impact behavior of rice straw-polyester composites. Indian J Fiber Text Res 32:399–403
12. Murali Mohan Rao K, Mohan Rao K, Ratna Prasad AV (2010) Fabrication and testing of natural fiber reinforced composites: vakka, sisal, bamboo, banana. Mater Design 31:508–513

Shape Optimization of the Flywheel Using the Cubic B Spline Curve

Prem Singh and Himanshu Chaudhary

Abstract This paper presents the shape optimization of the flywheel using the uniform cubic B-spline curve. The performance of the flywheel can be evaluated by its energy storing capacity defined as kinetic energy per unit mass. The kinetic energy per unit mass depends on the geometry of flywheel. Therefore, a profile of flywheel is modeled using a uniform cubic B-spline parametric modeling method. Then shape optimization model is formulated with the objective of maximizing the kinetic energy per unit mass of the flywheel under the design constraints of the mass of the flywheel and the maximum value of total stress. The y coordinates of control points are taken as design variables which distribute along the radial direction. Then the formulated problem is solved by using Jaya algorithm. The proposed approach is applied to the flywheel of the agricultural thresher machine. It is found that the optimized shape of flywheel stores the more energy to the existing shape of the flywheel of the thresher machine.

Keywords Flywheel · Kinetic energy · Jaya algorithm · Cubic B-spline · Thresher machine

1 Introduction

The primary objective of the flywheel is stored the kinetic energy under the given mass as much as possible. The mass of flywheel is constrained due to the availability of space and cost. The kinematic energy can be enhanced by the optimum shape of the flywheel. So, there are most efforts made by the researcher on shape optimization of flywheel such as the shape of flywheel has been optimized using

P. Singh (✉) · H. Chaudhary
Mechanical Engineering Department, Malaviya National Institute of Technology Jaipur, Jaipur, Rajasthan, India
e-mail: premsingh001@gmail.com

H. Chaudhary
e-mail: hchaudhary.mech@mnit.ac.in

conventional optimization technique [1]. In some other works, coefficients of Fourier series and Fourier sine series are used as design variables to maximize the ratio of inertia to volume and kinetic energy with the maximum stress, maximum thickness, and maximum mass as constraints for optimal shape of the flywheel. These series represent the thickness as a function of the radius. The radial and tangential stresses of the flywheel are computed using a two-point boundary value differential equation to find out the maximum stress [2, 3]. The exact optimal shape is determined under the constraints of the geometry, which is derived from arbitrary design parameters using discrete optimization [4]. Injection island genetic algorithm is proposed to optimize the shape of flywheel under the kinetic energy as an objective function [5]. The shape of the flywheel is optimized for different kind of heterogeneous materials using conventional optimization techniques [6]. A nonlinear optimization problem is formulated with the objective to maximize the energy density (stored energy per unit mass) using the parametric geometry modeling method. Then, this problem is solved using the downhill simplex method [7]. However, polynomial expansion, Fourier series, and Fourier sine series are used for finding flywheel shapes. But these methods are limited by the number of coefficients and do not describe the degree of curve. Most researchers have been focused on conventional optimization techniques. These techniques are comparatively less efficient and, also increase the computational cost.

In this paper, the shape optimization model is formulated using the Cubic B-spline curve. B-Spline curves have the following advantages over the other curves as these curves have local control and are not limited by control points. Then, the optimization problem is solved by advanced optimization techniques as Jaya algorithm. The results of the optimized shape of the flywheel are compared with the existing flywheel shape of the thresher machine that shows the energy storage capacity is better compared to the existing flywheel of the thresher machine.

The paper is organized in the following sequence: Sect. 2 describes the parametric optimization model of the flywheel. The optimization problem formulation is presented in Sect. 3. The optimization algorithm based on Jaya is presented in Sect. 4. A numerical example based on the flywheel design of thresher machine is shown in Sect. 5. Finally, conclusions are given in Sect. 6.

2   The Optimization Model of Flywheel Based on B-Spline Curve

In this section, the thickness distribution of flywheel along the radial direction is represented by the cubic B-spline curve as shown in Fig. 1. R_i and R_o are the inner and outer radius of flywheel, respectively. The flywheel is symmetric in X and Y directions. The curve interpolates or approximates a set of control points as $p_1, p_2, \ldots, p_n$ and defined in Eq. (1) [8, 9]. X and Y coordinates of control points are taken as radius and the thicknesses of flywheel, respectively.

Fig. 1 The symmetric profile of flywheel
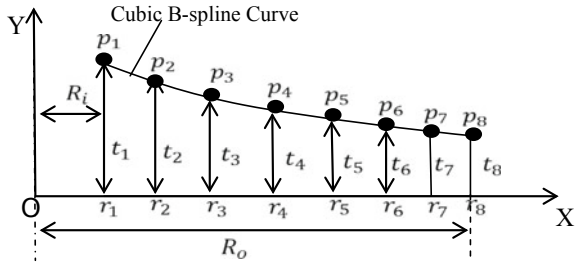
$$p(u) = \sum_{i=1}^{n} N_{i,k}(u)p_i, \quad 0 \leq u \leq S \tag{1}$$

where parameter k controls the degree of curve and in case of a cubic B-spline curve, the value of k is 4. $N_{i,k}(u)'s$ are B-spline blending functions, which are defined by the following expression;

$$N_{i,k} = (u - u_i)\frac{N_{i,k-1}(u)}{u_{i+k-1} - u_i} + (u_{i+k} - u)\frac{N_{i+1,k-1}(u)}{u_{i+k} - u_{i+1}} \tag{2}$$

Where

$$N_{i,1} = \begin{cases} 1, & u_i \leq u \leq u_{i+1} \\ 0, & elsewhere \end{cases} \tag{3}$$

where $N_{i,1}$ is a unit step function and u_i are called the parametric knots.

The coordinates of any point on the ith segment of the curve for periodic B-spline curves are given as

$$r^i(u) = \frac{a_1 r_i + a_2 r_{i+1} + a_3 r_{i+2} + a_4 r_{i+3}}{6} \tag{4}$$

$$t^i(u) = \frac{a_1 t_i + a_2 t_{i+1} + a_3 t_{i+2} + a_4 t_{i+3}}{6} \tag{5}$$

where

$$\left.\begin{aligned}
a_1 &= -u^3 + 3u^2 i - 3ui^2 + u^3 \\
a_2 &= 3u^3 + u^2(3 - 9i) + u(9i^2 - 6i - 3) - 3i^3 + 3i^2 + 3i + 1 \\
a_3 &= -3u^3 + u^2(9i - 6) + u(-9i^2 + 12i) + 3i^3 - 6i^2 + 4 \\
a_4 &= u^3 + u^2(-3i + 3) + u(3i^2 - 6i + 3) - i^3 + 3i^2 - 3i + 4
\end{aligned}\right\} i - 1 \leq u \leq i \tag{6}$$

2.1 The Design Parameters of Flywheel

The mass and kinetic energy are the parameters of the flywheel which describe the performance of the flywheel. These parameters for each segment is calculated using the expression for $r^i(u)$ and $t^i(u)$ given in Eqs. (4) and (5), respectively, as

$$mass = 2\pi\rho \sum_{i=1}^{n-k+1} \int_{u_{i-1}}^{u_i} t^i(u)r^i(u)\frac{dr^i(u)}{du}du \qquad (7)$$

$$I = 2\pi\rho \sum_{i=1}^{n-k+1} \int_{u_{i-1}}^{u_i} t^i(u)\big(r^i(u)\big)^3\frac{dr^i(u)}{du}du \qquad (8)$$

where ρ is the density of the material of flywheel.

2.2 Stresses Analysis of Flywheel

The tangential and radial stresses occur due to centrifugal forces during the operation of the flywheel. The following relationship between tangential and radial stresses for each segment has been obtained based on the force balance on a small element of flywheel [10].

$$\frac{d}{dr^i(u)}\big(t^i(u)r^i(u)\sigma_r^i\big) - t^i(u)\sigma_\theta^i + \rho\big(r^i(u)\big)^2 t^i(u)\omega^2 = 0 \qquad (9)$$

$$\big(\sigma_\theta^i - \sigma_r^i\big)(1+\upsilon) + r\frac{d\sigma_\theta^i}{dr^i(u)} - r^i(u)\upsilon\frac{d\sigma_r^i}{dr^i(u)} = 0 \qquad (10)$$

where σ_r^i and σ_θ^i are tangential and radial stresses for each segment, respectively. Let us define a stress function F^i for each segment as

$$F^i = t^i(u)r^i(u)\sigma_r^i; \sigma_r^i = \frac{F^i}{t^i(u)r^i(u)};$$

Solving for σ_θ as

$$\sigma_\theta^i = \frac{1}{t^i(u)}\left(\frac{dF^i}{dr^i(u)} + \rho\big(r^i(u)\big)^2\omega^2 t^i(u)\right) \qquad (11)$$

A second ordinary differential equation is obtained as

$$r^2 \frac{d^2F}{dr^2} + r \frac{dF}{dr} - F + (3+v)\rho r^3 \omega^2 t - \frac{r}{t} \frac{dt}{dr} \left(r \frac{dF}{dr} - vF \right) = 0 \qquad (12)$$

Equations (11) and (12) are written in parametric form for each segment by converting the independent variable r into u by using chain rule of differentiation as

$$\sigma_\theta^i = \frac{1}{t^i(u)} \left(\frac{\frac{dF^i}{du}}{\frac{dr^i(u)}{du}} + \rho \left(r^i(u) \right)^2 \omega^2 t^i(u) \right) \qquad (13)$$

$$
\left(r^i(u) \right)^2 \frac{dr^i(u)}{du} \frac{d^2F^i}{du^2}
$$
$$
+ \left\{ r^i(u) \left(\frac{dr^i(u)}{du} \right)^2 - \left(r^i(u) \right)^2 \frac{d^2r^i(u)}{du^2} - \frac{\left(r^i(u) \right)^2}{t^i(u)} \frac{dr^i(u)}{du} \frac{dt^i(u)}{du} \right\} \frac{dF^i}{du}
$$
$$
+ \left\{ v \frac{r^i(u)}{t^i(u)} \frac{dt^i(u)}{du} \left(\frac{dr^i(u)}{du} \right)^2 - \left(\frac{dr^i(u)}{du} \right)^3 \right\} F^i
$$
$$
+ (3+v)\rho \omega^2 t^i(u) \left(r^i(u) \right)^3 \left(\frac{dr^i(u)}{du} \right)^3 = 0 \qquad (14)
$$

The Eq. (14) is the second order differential equation with the independent variable "u" and dependent variable "F". In case of flywheel design, two boundary conditions are usually known, such as radial stresses are zero at the inner and outer radius. Then, the Eq. (14) represents a two-point boundary value problem with a second order differential equation. Then the equation is solved by Runge Kutta method using B Spline property.

Once radial and tangential stresses are known at each point of each segment, total stresses at each point are calculated using the application of distortion energy theory as

$$\sigma_t = \left(\sigma_r^2 + \sigma_\theta^2 - \sigma_r \sigma_\theta \right)^{1/2} \qquad (15)$$

3   Formulation of the Optimization Problem

The radius of the flywheel between R_i to R_o is equally divided. Hence, the X coordinates of control points are fixed and given as $r_i = r_1 + \frac{(r_2 - r_1)(i-1)}{n-1}$. Furthermore, the Y coordinates as thicknesses are taken as the design variables and are expressed in the vector form as $\mathbf{x} = [t_1 t_2 t_3 \ldots \ldots \ldots t_n]^T$ Where n represents the control points or design variables between R_i to R_o. The optimization problem is posed as

$$minimize f(x) = -\left(\frac{I\omega^2}{2 \times mass}\right)$$

$$Subjected\ to \quad g_1(x) = mass - max(mass) \leq 0 \qquad (16)$$

$$g_2(x) = \max(\sigma_t) - \sigma_a \leq 0$$

$$LB_i \leq x_i \leq UB_i \qquad i = 1, \ldots \ldots, n$$

The negative sign in the expression of the objective function implies that the function is being maximized. LB_i and UB_i are the lower and upper bounds on the ith design variable, n represents the number of design variables.

4 Optimization Algorithm

After formulating the optimization problem, it can be solved either by classical methods or nature–inspired based optimization algorithms. The gradient-based conventional algorithms use the gradient information of the objective function concerning the design variables. These methods converge on the optimum solution near to the starting point and thus produce a local optimum solution [11].

Nature inspired based optimization algorithms such as GA, PSO, and Ant colony optimization algorithm require their algorithm-specific control parameters. However, teaching-earning-based optimization algorithm does not need any algorithm-specific control parameters. It uses two phases (teacher phase and the learner phase) for its working [12]. Further, Jaya algorithm is nature inspired based optimization algorithms. It has only one phase, and it is comparatively simple and easier to understand [13]. A flowchart of Jaya algorithm is shown in Fig. 2.

5 Numerical Examples: The Flywheel of Thresher Machine

The proposed method is applied to the flywheel of agricultural thresher machine. Thresher machine is the most basic post-harvested machine. A thresher machine detaches the grains from harvested crops by a combination of impact and rubbing action with minimum effort and time. However, the flywheel is an import element of thresher machine. The function of the flywheel in the thresher machine is to minimize the variations in the speed of PTO shaft due to torque fluctuations of the threshing drum. The material properties and design parameters of flywheels are given in Table 1 and 2, respectively [14]. The upper and lower limits of design variables are taken as $0.010 \leq x_i \leq 0.060\ where\ i = 1, 2, ., ., ., ., .8$

The optimization problem as explained, in Eq. (16) is solved using Jaya algorithm. These algorithms are coded in MATLAB. These algorithms are run for 150
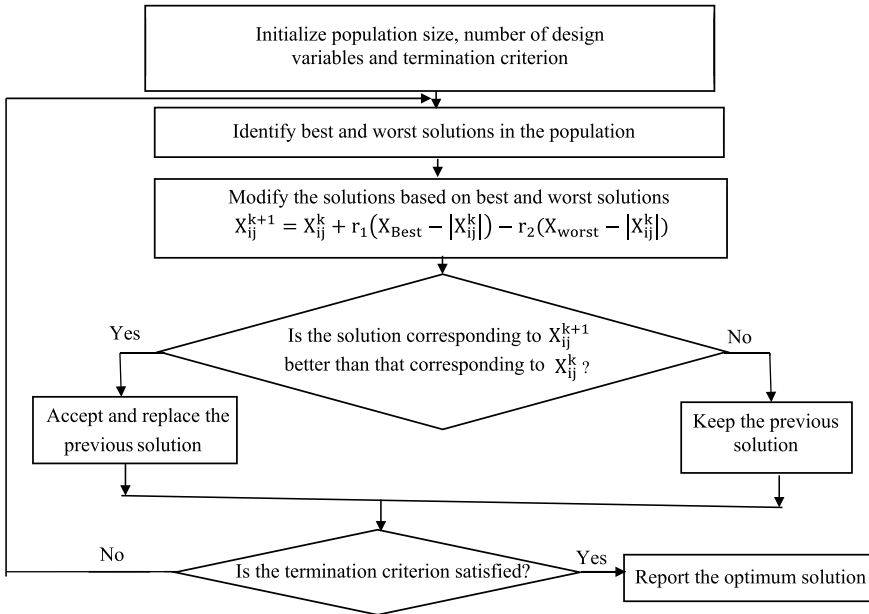
Fig. 2 Flowchart of Jaya algorithm

Table 1 Material properties of the flywheel

Material	Density (kg/m^3)	Elastic modulus (Gpa)	Poisson's ratio
Cast Iron	7200	210	0.3

Table 2 Design parameters of the flywheel

Control points (n)	Inner radius R_i (m)	Outer radius R_o (m)	Angular velocity ω (rad/sec)	Max. mass (kg)	σ_a (N/mm^2)
8	0.060	0.500	65.45	115	150

iterations to obtain the best objective function value and corresponding design variables. The convergence chart of the best objective function values is shown in Fig. 3. The comparison of optimum results obtained from Jaya algorithm with the design data of existing constant thickness flywheel of thresher machine [14] is given in Table 3, and the best value of the objective function is shown in bold.

The optimized shape of flywheel corresponding to the Jaya algorithm with the original shape of thresher machine flywheel is compared in Fig. 4. The profile of optimized flywheel is divided into three sections as thin at the middle section, thicker at the inner, and outer section while the original flywheel has a constant

Fig. 3 The convergence of
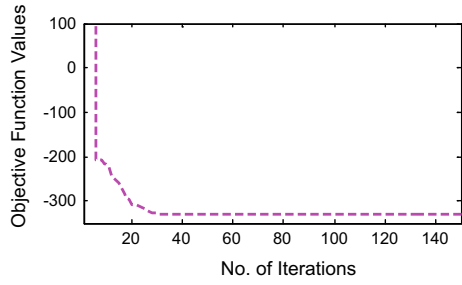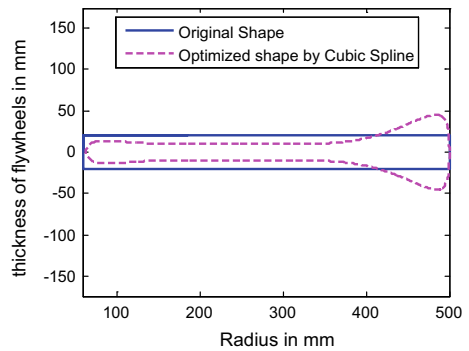the best objective function
values

Table 3 Optimum values for the geometry of flywheel

Optimum values	Design data of existing flywheel [14]	Jaya algorithm
$t_1(m)$	0.020	**0.0187**
$t_2(m)$	0.020	**0.01**
$t_3(m)$	0.020	**0.01**
$t_4(m)$	0.020	**0.01**
$t_5(m)$	0.020	**0.01**
$t_6(m)$	0.020	**0.01**
$t_7(m)$	0.020	**0.06**
$t_8(m)$	0.020	**0.01**
M (kg)	115	**115**
$f(\mathbf{x})$	−271.585	**−331.179(21.94%)**

Fig. 4 Comparison of the
shape of the flywheel

thickness profile over the entire section. Moreover, the optimized shape of flywheel obtained from Jaya algorithm stores 21.94% more energy compared to the existing flywheel of the thresher machine.

6 Conclusion

In this paper, the shape optimization model of the flywheel using uniform cubic B-spline curve is formulated by considering kinetic energy per unit mass as an objective function with some design constraints. This formulated problem is solved to find the optimum thickness distribution using Jaya algorithm. The proposed methodology is applied to the flywheel of agricultural thresher machine. It is seen that the optimized shape of flywheel stores 21.94% more energy compared to the actual shape of the flywheel of thresher machine.

References

1. Sandgren E, Ragsdell KM (1983) Optimal flywheel design with a general thickness form representation. J Mech Trans Autom Design 105:425–433
2. Ebrahimi ND (1988) Optimum design of flywheels. Comput Struct 29(4):681–686
3. Ghotbi Ehsan, Dhingra Anoop K (2012) A bi-level game theoretic approach to optimum design of flywheels. Eng Optim 44(11):1337–1350
4. Berger M, Porat I (1988) Optimal design of a rotating disk for kinetic energy storage. Trans ASME 55:164–170
5. Eby DJ, Averill RC, Goodman E, Punch W (1999) Optimal design of flywheels using an injection island genetic algorithm. Artif Intell Eng Design Anal Manuf 13:389–402
6. Huang J, Fadel GM (2000) Heterogeneous flywheel modeling and optimization. Mater Des 21 (2):111–125
7. Jiang L, Zhang W, Ma GJ, Wu CW (2017) Shape optimization of energy storage flywheel rotor. Struct Multidisc Optim 55(2):739–750
8. Zeid R (2009) Sivasubramanian, CAD/CAM – theory and practice. Tata McGraw-Hill, New Delhi, India
9. Mortenson ME (2006) Geometric modeling. McGraw Hill Education (India) Private Limited, New Delhi, India
10. Timoshenko SP, Goodier JN (1970) Theory of elasticity, 3rd edn. McGraw-Hill, New York
11. Arora JS (2012) Introduction to optimum design, 3rd edn. Reed Elsevier India Private Limited, India
12. Rao RV (2015) Teaching learning based optimization algorithm: and its engineering applications. Springer
13. Rao RV (2016) Jaya: a simple and new optimization algorithm for solving constrained and unconstrained optimization problems. Int J Ind Eng Comput 7(1):19–34
14. Varshney AC (2004) Data book for agricultural machinery design. Central Institute of Agricultural Engineering, Bhopal, India

Nonlinear Dynamic Response Analysis of Cylindrical Roller Bearings Due to Unbalance

Patra Pravajyoti, Saran V. Huzur and Suraj Prakash Harsha

Abstract The paper contains a detailed analysis of dynamic behavior of cylindrical roller bearings for unbalanced rotor conditions due to speed variations and internal clearances. The system behaves nonlinearly due to various reasons such as stiffness and damping at the contact points (due to Hertzian contact force between rollers and races), radial internal clearance, and speed associated with unbalanced rotor force. Presently, the differential equations that show the dynamics of the cylindrical roller bearings have been obtained using Lagrange's equation and solved numerically using modified Newmark-beta method. The tools like orbit plots, phase portraits, Poincaré maps, and FFT plots are helpful for analyzing various motion behavior. The obtained response showed the sensitive behavior of the system from periodic to quasiperiodic and chaotic with speed and clearance variations for unbalanced rotor conditions. The analysis is an attempt to show an interaction between existing frequencies due to change in speed and clearance variations, which will be helpful for analyzing the current condition of a healthy cylindrical roller bearing.

Keywords Cylindrical roller bearings · Speed · Radial internal clearance · Modified Newmark-beta method

P. Pravajyoti (✉) · S. V. Huzur · S. P. Harsha
Department of Mechanical and Industrial Engineering, Indian Institute of Technology Roorkee, Roorkee 247667, Uttarakhand, India
e-mail: pravajyoti@gmail.com

S. V. Huzur
e-mail: vhsaran@gmail.com

S. P. Harsha
e-mail: spharsha@gmail.com

1   Introduction

Dynamic study of the roller bearings requires understanding the physics behind the nonlinear contacts and sources of vibration which are important to monitor the present health condition. In the present world, roller bearings are used in highly sophisticated and high-speed machinery where the unwanted vibration in the radial direction caused a severe effect on the performance of the roller bearings. The reasons behind vibration occurred even in a healthy bearing are first, the eccentricity present in the bearing axis and the rotor axis and second, variable compliance effect of the bearings because of the cage rotation. An NU-205 radially supported roller bearings is taken into account to study the nonlinear behavior due to unbalance caused by radial internal clearance and speed variation. The main purpose of radial internal clearance is to compensate for thermal expansion, but it also adds the nonlinearity to the rotor bearing system [1]. Rotating machinery without unbalancing is almost unimaginable. The unbalance effect adds the rotating frequency (X) effect on the variable compliance effect (VC), which makes the system behavior more unpredictable even for healthy bearings. Variable compliance vibration, which is the change of dynamic stiffness of the bearing as the rolling element complement undergoes its orbital motion. So, it is also speed-dependent as a function of cage speed (relative to a stationary outer race) multiplied by the number of rolling elements.

Previously, many researchers had formulated the mathematical model for different types of bearings. Gupta [2, 3] considered the roller-cage dynamics while allowing the skewing motion for both cylindrical and tapered roller bearings. Tiwari and Gupta [4] and Tiwari et al. [5] analyzed the dynamic behavior of a balanced and unbalanced ball bearing system by changing both the clearance and hysteresis damping. Harsha [6] studied the dynamical behavior of the balanced roller bearing system considering the effect of geometrical defectiveness like radial internal clearance and waviness with speed variations. Ghafari [7, 8] investigated the effect of radial internal clearance and localized defect under balanced rotor condition. Mohammadpour et al. [9] considered the effect of preloading and interference fitting on the dynamics of roller bearings. Cui et al. [10] took a 4-DOF roller bearing system considering both speed and radial clearance.

A number of attempts had been made in past using various motion analyzer tools and phenomenon to monitor the actual health condition and to represent in a more convenient way to understand the dynamic behavior of the roller bearings. Kappaganthu and Nataraj [11] studied the roller dynamics by using the fft and Lyapunov exponents. The system nonlinearity which produces phenomenon like bifurcation and routes to chaos have been well explained by Mevel [12]. Patra et al. [13] tried to give a pattern to find a relation between speed and unbalanced cylindrical roller bearings. A comparison between experimental and simulated data of vibration induced in a coupled disk/rotor system, with clearance effect is performed by Flowers and Fangsheng [14]. Lynagh et al. [15] developed an experimental setup to study the vibration spectra of a high-speed spindle for an angular

contact ball bearing. Life of a bearing can also be customized by the radial clearances. Oswald et al. [16] gave a relation for the life expectancy of both roller and ball bearings for a wide range of radial clearances.

Hence, a period doubling and intermittency clearly indicates the routes to chaos and makes the response more unpredictable for a change in radial internal clearance or speed of rotation.

2 Problem Formulations

A multi-body dynamic model of a cylindrical roller bearing is considered in Fig. 1. The outer race is kept constant and the contacts between rollers and races are considered to be Hertzian contacts.

From Fig. 1, the elastic deformation between rollers and both the raceways can be calculated geometrically as

$$
\begin{aligned}
\delta_{ir} &= (r + \rho_R + cl) - \chi_j \\
\delta_{or} &= R - (\rho_j + \rho_R + cl)
\end{aligned}
\tag{1}
$$

For the elastic deformation to be considered, both δ_{ir} and δ_{or} are need to be positive, i.e., when both deformations are in compression in nature.

Fig. 1 Mass spring model of the cylindrical roller bearing
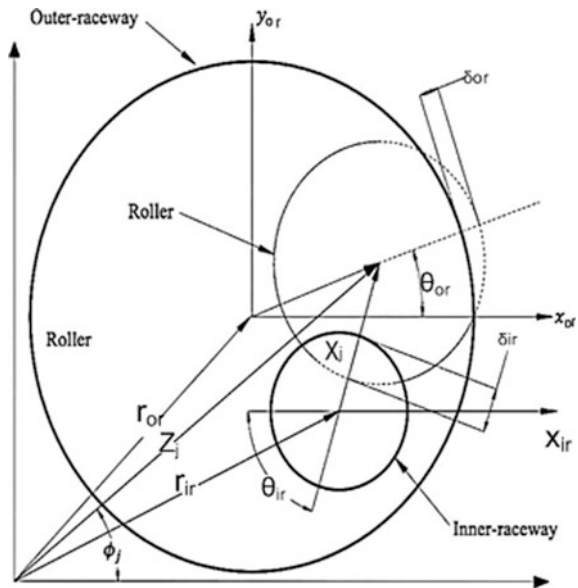
3 Contact Stiffness

Harris [1] gave the relation for Hertzian elastic deformation taking place between rollers and raceways. The contact is considered as a nonlinear spring-mass system and the stiffness and deformation relation is given as

$$\delta = \frac{4.05}{10^5} \frac{Q^{0.925}}{l_{eff}^{0.85}} \, (mm) \tag{2}$$

$$K = 56065.703 \, l_{eff}^{0.92} \left(\frac{N}{mm^{1.08}} \right) \tag{3}$$

4 Dissipative Force for Roller Bearings

A material or hysteretic damping is considered in the model at the contact zone of the rollers and raceways. Hunt and Crossley [17] gave a relation to the loss of damping energy at the contacts as

$$\begin{aligned}
E_d &= \int \left(C_{ir} K_{eq} \, (\dot{\delta}_{ir})_+^q + C_{or} K_{eq} \, (\dot{\delta}_{or})_+^q \right) \partial \dot{\delta} \\
&= \frac{10}{9(q+1)} \sum_{j=1}^{N_R} C_{ir} K_{ir} \delta_{ir_+}^{10/9} \, \dot{\delta}_{ir_+}^{q+1} + C_{or} K_{or} \delta_{or_+}^{10/9} \, \dot{\delta}_{or_+}^{q+1}
\end{aligned} \tag{4}$$

where C_{ir} and C_{or} are the damping factors between the inner race and outer race with roller.

A mathematical model derived by using Lagrange's Equation, for cylindrical roller bearings have been developed. The kinetic energy and potential energy contributed by the inner race, outer race, rollers are formulated and to obtain the equations of motion, these are differentiated with respect to the generalized coordinates ρ_j, x_{ir} and y_{ir}.

For the generalized coordinates ρ_j equation of motion is

$$\begin{aligned}
&m_j \ddot{\rho}_j + m_j \rho_j \dot{\theta}_j^2 + m_j g \, \sin \theta_j + \frac{1}{2} \frac{\partial \left[K_{ir} \left[\delta_{ir}^{10/9-1} \right]_+ \right]}{\partial \rho_j} [\delta_{ir}]_+^2 - \left[K_{ir} \left[\delta_{ir}^{10/9} \right]_+ \right] \frac{\partial \chi_j}{\partial \rho_j} + \frac{1}{2} \frac{\partial \left[K_{or} \left[\delta_{or}^{10/9-1} \right]_+ \right]}{\partial \rho_j} [\delta_{or}]_+^2 \\
&+ \left[K_{or} \left[\delta_{or}^{10/9} \right]_+ \right] + \frac{10}{9} \sum_{j=1}^{N_R} \left\{ C_{ir} (K_{ir}) \, \delta_{ir_+}^{10/9} (-\chi_j)^q \frac{\partial \dot{\chi}_j}{\partial \dot{\rho}_j} \right\} + \frac{10}{9} \sum_{j=1}^{N_R} C_{or} (K_{or}) \delta_{or_+}^{10/9} (-\dot{\rho}_j)^q = 0
\end{aligned} \tag{5}$$

For the generalized coordinates x_{ir} equation of motion is

$$m_{ir}\ddot{x}_{ir} - \sum_{j=1}^{N_R} \left[K_{ir} \left[\delta_{ir}^{10/9} \right]_+ \right] \frac{\partial \chi_j}{\partial x_{ir}} + \frac{10}{9} \sum_{j=1}^{N_R} \left[C_{ir} K_{ir} \left[\delta_{ir}^{10/9} \right]_+ (-\dot{\chi}_j)^q \frac{\partial \dot{\chi}_j}{\partial x_{ir}} \right]$$
$$= F_u \sin \omega t \tag{6}$$

For the generalized coordinates y_{ir} equation of motion is

$$m_{ir}\ddot{y}_{ir} + m_{ir}g - \sum_{j=1}^{N_R} \left[K_{or} \left[\delta_{or}^{10/9} \right]_+ \right] \frac{\partial \chi_j}{\partial y_{ir}} + \frac{10}{9} \sum_{j=1}^{N_R} \left[C_{ir} K_{ir} \left[\delta_{ir}^{10/9} \right]_+ (-\dot{\chi}_j)^q \frac{\partial \dot{\chi}_j}{\partial y_{ir}} \right]$$
$$= W + F_u \cos \omega t$$
$$\tag{7}$$

Above set of equations are nonlinear $(N_R + 2)$ order differential equations. Rotor mass and unbalanced effect due to that has been added and no other external load interacts with the system. The "+" sign in the subscript indicates that the deformation associated with compression is only allowed.

From Fig. 1 expression for "χ_j" can be obtained as

$$x_{ir} + \chi_j \cos \theta_x = x_{or} + \rho_j \cos \theta_j,$$
$$y_{ir} + \chi_j \sin \theta_x = y_{or} + \rho_j \sin \theta_j$$
$$\chi_j = \left[(x_{or} - x_{ir})^2 + \rho_j^2 + 2\rho_j(x_{or} - x_{ir}) \cos \theta_j + 2\rho_j(y_{or} - y_{ir})\sin \theta_j + (y_{or} - y_{ir})^2 \right]$$
$$\tag{8}$$

Nonlinear systems are very sensitive to the initial conditions. Due to shaft weight, an initial displacement and velocity are considered at the inner race, i.e., $x_{ir} = y_{ir} = 10^{-6}m$ and $\dot{x}_{ir} = \dot{y}_{ir} = 0$.

5 Results and Discussions

A numerical study has been done to predict the behavior of the cylindrical roller bearings due to speed and radial internal clearance. An unbalance force 15% of radial load is considered for NU-205 cylindrical roller Bearings. Motion analyzer like Orbit plot, Poincare Plot, and FFT are studied to analyze the dynamic behavior. Unbalance effect combined with speed and radial clearance makes the system behavior more unpredictable. This paper is an attempt to show the combined effect of all three parameters. First, a radial internal clearance of 30 microns is considered with speed variation of 3000 rpm, 5000 rpm, and 8000 rpm, then keeping the speed fixed to 8000 rpm, clearance is changed to 45 and 60 microns. Due to unbalance there is a clear interaction between rotation frequency (X) and variable compliance frequency (VC), which indicates the bi-periodic nature of the system.

Figure 2 shows the motion characteristics of an unbalanced cylindrical roller bearing for 3000 rpm and 30 microns radial clearance. A chaotic nature is observed from the horizontal and vertical Poincare maps (Fig. 2b, c). From the frequency response plot (Fig. 2d) X and VC are present at 50 Hz and 249 Hz. Other peaks are also observed at the interactions of VC and X. Figures 3d and 4d are the response plots for 5000 rpm and 8000 rpm with 30microns clearance, where "Xs" and "VCs" are at 83 Hz, 415 Hz, and 133 Hz, 664 Hz, respectively. As we increase the speed density of the region covered by the phase space and orbit space is also getting denser. It shows the chaotic nature involved in the system. The amplitudes of the vertical displacement are also increased with increase in speed. From the frequency response plots, we can observe a clear interaction between rotational frequencies and compliance frequencies. A particular pattern can be drawn from the above interaction, i.e., $m(VC \pm X)/N$, where N is a factor (N = 1/1000) considered the rotational speed of the shaft and m is constant.

As we further increase the radial clearances to 45 and 60 microns, it can be observed that in the frequency response plot the position of the major peaks is at the same place but the amplitude of vibration changes. It shows the effect of the design parameters like radial internal clearance on system dynamics. The system behaves aperiodic in nature and from the Poincaré plot it is clear that a fine layer structure of strange attractor is created in the phase space. So, the system response is highly nonlinear in nature (Figs. 5 and 6).
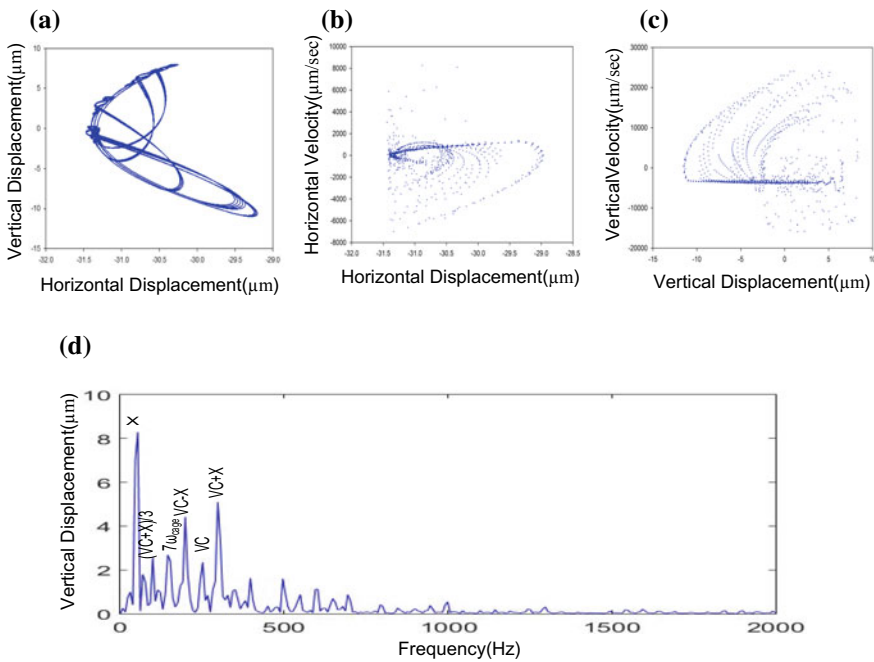

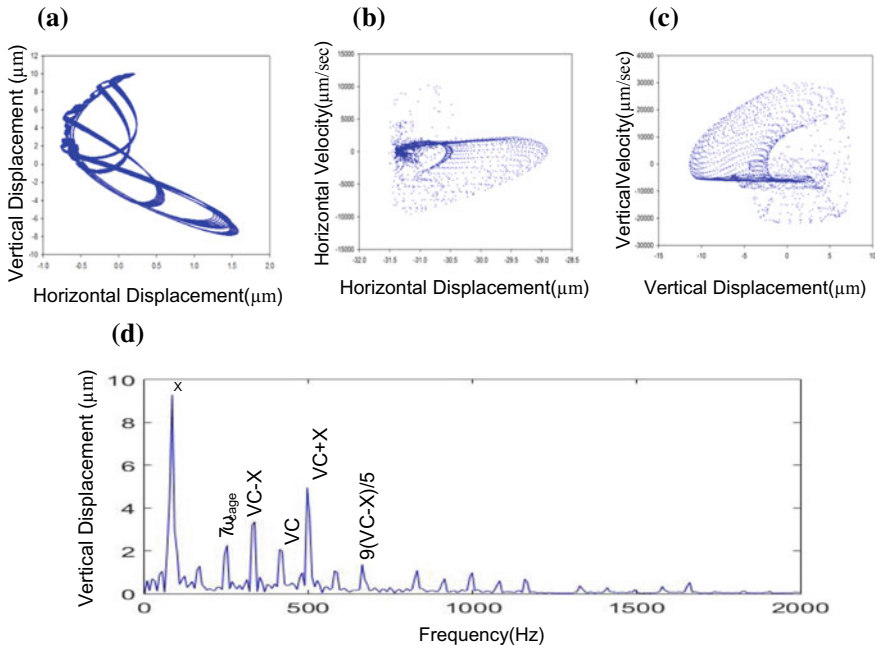**Fig. 2** **a** Orbit plot, **b** Horizontal Poincare plot, **c** Vertical Poincare plot, **d** FFT for 3000 rpm and 30 microns

(a)

(b)

(c)

(d)

Fig. 3 **a** Orbit plot, **b** Horizontal Poincare plot, **c** Vertical Poincare plot, **d** FFT for 5000 rpm and 30 microns

(a)

(b)

(c)

(d)
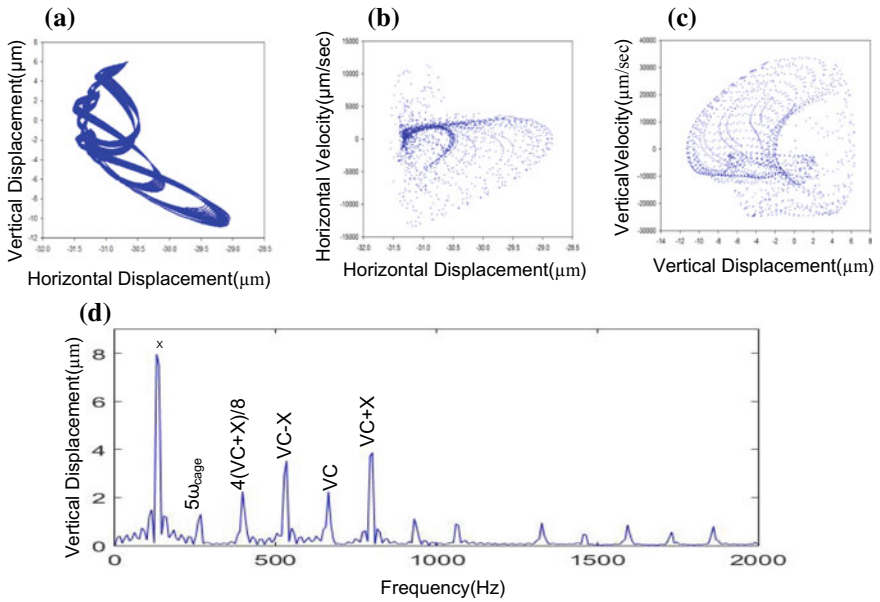
Fig. 4 **a** Orbit plot, **b** Horizontal Poincare plot, **c** Vertical Poincare plot, **d** FFT for 8000 rpm and 30 microns
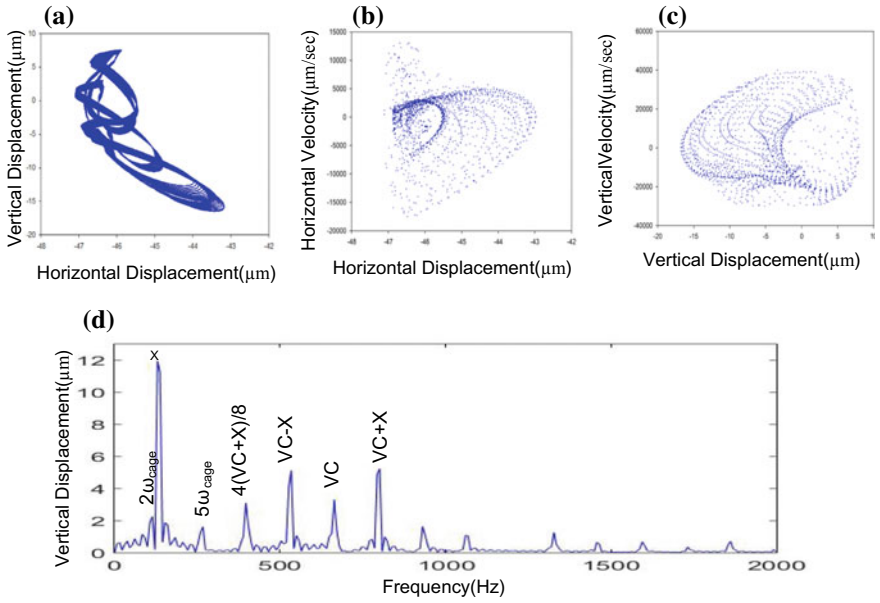
Fig. 5 **a** Orbit plot, **b** Horizontal Poincare plot, **c** Vertical Poincare plot, **d** FFT for 8000 rpm and 45 microns
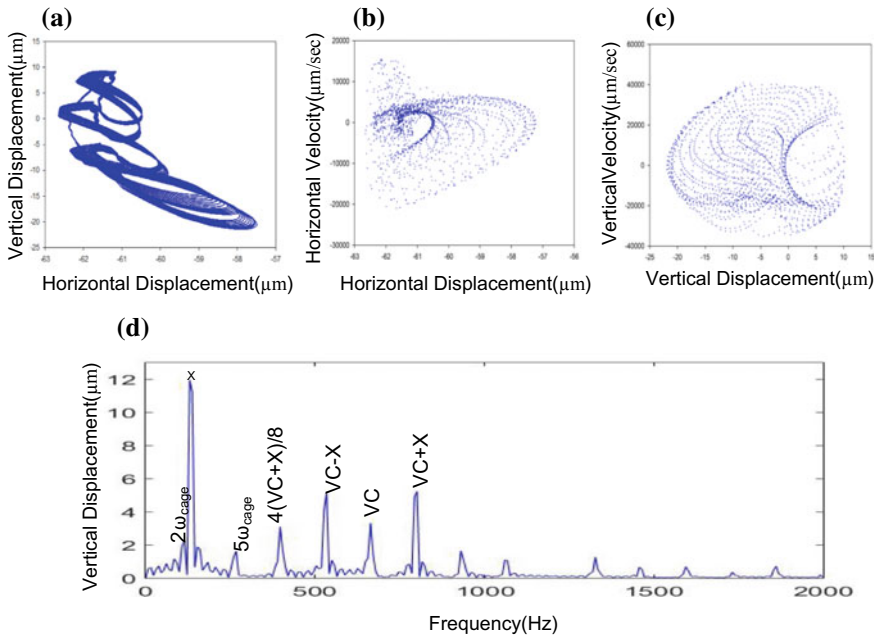

Fig. 6 **a** Orbit plot, **b** Horizontal Poincare plot, **c** Vertical Poincare plot, **d** FFT for 8000 rpm and 60 microns

6 Conclusion

Parameters like speed and radial clearance are completely controllable as per our need, but still, the responses that we get are completely nonlinear in nature and highly sensitive. So, an attempt is made to study the dynamic behavior of cylindrical roller bearings for a change in speed and/or radial internal clearance.

(a) For an increase in speed, the system behaves completely nonlinear in nature and a dense part of the strange attractor is formed at the innermost layer of the Poincare plot which indicates the chaotic nature of the system.
(b) With the increase in speed, the density of the phase space is even denser.
(c) A pattern can be observed due to the interaction between the rotational frequency and varying compliance frequency in the frequency response plots by changing the speed, i.e., $m(VC \pm X)/N$.
(d) With the increase in radial clearance, the amplitude of the vibration is also higher.

References

1. Harris T, Mindel M (1973) Rolling element bearing dynamics. Wear 23:311–337
2. Gupta PK (1979) Dynamics of rolling-element bearings Part I: cylindrical roller bearing analysis. J Lubr Technol 101:293–302
3. Gupta PK (1989) On the dynamics of a tapered roller bearing. J Tribol 111(2):278–287
4. Tiwari M, Gupta K (2000) Effect of radial internal clearance of a ball bearing on the dynamics of a balanced. J Sound Vib 238(5):723–756
5. Tiwari M, Gupta AK, Prakash O (2000) Dynamic response of an unbalanced rotor supported on ball bearings. J Sound Vib 238(5):757–779
6. Harsha SP (2006) Nonlinear dynamic analysis of a high-speed rotor supported by rolling element bearings. J Sound Vib 2006(a):290(1–2): 65–100
7. Ghafari SH, Abdel-Rehman EM, Golnaraghi F (2010) Vibrations of balanced fault-free ball bearings. J Sound Vib 329(9):1332–1347
8. Ghafari SH, Abdel-Rahman EM, Golnaraghi F, Ismail F (2007) Chaos in healthy ball bearings. In: ASME international mechanical engineering congress and exposition, proceedings (IMECE), vol. 9, pp 369–376
9. Mohammadpour M, Johns-Rahnejat PM, Rahnejat H (2015) Roller bearing dynamics under transient thermal-mixed non-Newtonian elastohydrodynamic regime of lubrication. Proc Inst Mech Eng Part K J Multi-body Dyn 229(4):407–423
10. Cui L, Liu C, Zheng J (2009) Study on nonlinear vibration and dynamic characteristics of rigid. Eng Conf Detc 2009-86161, (86):1–7
11. Kappaganthu K, Nataraj C (2011) Nonlinear modeling and analysis of a rolling element bearing with a clearance. Commun Nonlinear Sci Numerical Simul 16(10):4134–4145
12. Mevel B, Guyader JL (2008) Experiments on routes to chaos in ball bearings. J Sound Vib 318(3):549–564
13. Patra P, Saran VH, Harsha SP (2018) Nonlinear dynamic response analysis of cylindrical roller bearings due to rotational speed. Proc Inst Mech Eng Part K J Multi-body Dyn, 1–12

14. Flowers G, Fangsheng W (1996) Disk/shaft vibration induced by bearing clearance effects: analysis and experiment. J Vib Acoust 118(2):204–208
15. Lynagh N, Rahnejat H, Ebrahimi M, Aini R (2000) Bearing induced vibration in precision high speed routing spindles. Int J Mach Tools Manuf 40(4):561–577
16. Oswald FB, Zaretsky EV, Poplawski JV (2012) Effect of internal clearance on load distribution and life of radially loaded ball and roller bearings. Tribol Trans
17. Hunt KH, Crossley FR (1975) Coefficient of restitution interpreted as damping in vibro impact. J Appl Mech 42(2):440–445